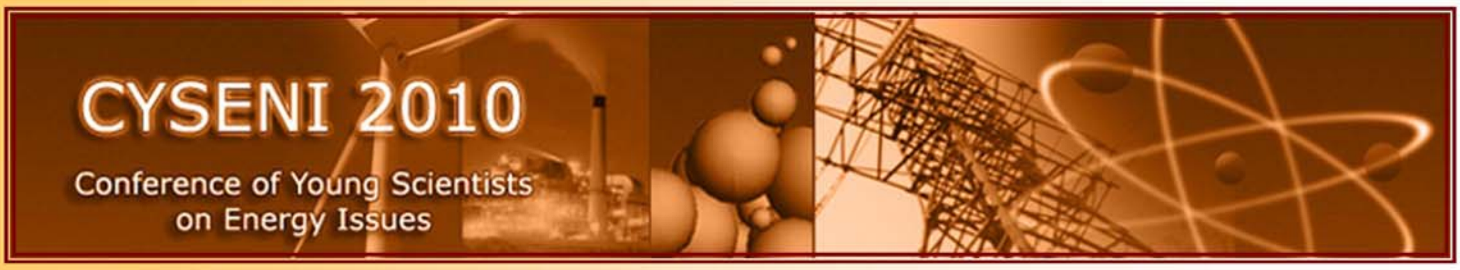

Conference of Young Scientists on Energy Issues

ISSN 1822-7554

Conference proceedings
www.cyseni.com
27—28 May, 2010

Dear Reader of the Proceedings,

Conference of ***Young Scientists on Energy Issues 2010*** is already a seventh conference.

Initiative came from young, enthusiastic researchers who realised that around ourselves we do have young, smart and science-oriented young people in the energy field, who need an event to come together and share their views, ideas, and success and disappointment stories. The very beginning was year 2004, when young researchers with the supervision of experienced scientists from only Lithuanian Energy Institute organised a conference. In 2005 it became a national conference with participants from Kaunas University of Technology, Vilnius Gediminas Technical University, Vilnius University, Vytautas Magnus University – in fact from all science and education institutions of Lithuania involved in energy-related topics. Year 2006 was devoted to strengthen status of the conference among young researchers and their experienced supervisors and bring the message that only joint efforts in a small country we can reach our targets. In 2007 organising committee decided to put emphasis on regional and international dimension. In the conference we had papers from neighbouring countries – Belarus and Poland. We realised that facing challenges in energy research we have to bring together as many young researchers as possible to create a critical mass to be competent and competitive for the future research. Thus, conference is not only increasing the competence with involvement of best experienced scientists as peer reviewers, involving the review process participants of the conference as educational exercise, but also expanding geographically. In 2008 we already had papers and participants from Belarus, Estonia, Latvia, Lithuania, Russia, and India. In 2009 we had papers from Belarus, Estonia, Italy, Latvia, Lithuania, Nigeria, and Ukraine. Young scientists in the conference of Young Scientists on Energy Issues 2009 have an auditorium to share their views and findings of the research, a possibility to evaluate achievements and hear critical comments for the improvements. In 2010 we had 76 young scientists' papers from various Lithuanian science and research institutions and that foreign institutions Latvia, Estonia, Belarus, Ukraine, Italy, Germany, Norway, Nigeria.

We will keep this momentum in the future ***Young Scientists on Energy Issues*** conferences as well. Thus, we already now invite you to conference of ***Young Scientists on Energy Issues 2011***, which will be held in 26–27 May, 2011 in Kaunas, Lithuania.

Organisers

CONTENT

I. HYDROGEN AND FUEL CELLS (5)

II. RENEWABLE ENERGY SOURCES AND THEIR USE (8)

III. SMART ENERGY NETWORKS (2)

IV. ENERGY EFFICIENCY AND SAVINGS (7)

V. KNOWLEDGES FOR ENERGY POLICY MAKING (6)

VI. INVESTIGATIONS IN THE FIELDS OF THERMAL PHYSICS, FLUID MECHANICS AND METROLOGY (6)

VII. NANOSCIENCES AND NANOTECHNOLOGIES, INVESTIGATIONS ON MULTIFUNCTION MATERIALS (16)

VIII. INVESTIGATIONS OF COMBUSTION AND PLASMA PROCESSES (7)

IX. GLOBAL CHANGE AND ECOSYSTEMS (7)

X. FUSION ENERGY (2)

XI. NUCLEAR FISSION AND RADIATION PROTECTION (8)

CYSENI 2010, May 27–28, Kaunas, Lithuania
ISSN 1822-7554, www.cyseni.com

CARBON DISTRIBUTION IN Mg FILMS IRRADIATED BY PLASMA IN C_2H_2 GASE

A. Bačianskas
Vytautas Magnus University
Vileikos 8 str., LT-44404, Kaunas – Lithuania
Phone: 868434213
Email: Aliusb@draugas.lt

L.L. Pranevičius
Lithuanian Energy Institute,
Vytautas Magnus University
Breslaujos 3 str., LT-44403 Kaunas – Lithuania
Vileikos 8 str., LT-44404, Kaunas – Lithuania
Phone: 868744187
Email: L.Pranevicius@gmf.vdu.lt

D.Milčius
Lithuanian Energy Institute,
Vytautas Magnus University
Breslaujos 3 str., LT-44403 Kaunas –Lithuania
Vileikos 8 str., LT-44404, Kaunas – Lithuania
Phone: 8-37-401909
Email: Milcius@mail.lei.lt

ABSTRACT

2 µm thick Mg films were magnetron sputter deposited on stainless steel (AISI 316L) substrates and hydrogenated in low pressure plasmas using C_2H_2 and Ar gas mixtures at 2-10 Pa pressure. The separation of hydrogen from hydrocarbon compounds and storage in Mg films have been performed by molecular ion implantation of CH_x^+ ions so avoiding hydrogen gas purification process. The depth profiles of H and C atoms in hydrogenated Mg films have been analyzed by Nuclear Reaction Analysis (NRA) and secondary ion mass spectrometry (SIMS), respectively, techniques. It is shown that carbon atoms accommodate in the 30 nm thick surface layer while H atoms are homogeneously distributed across the entire Mg film thickness after 0.5 h of plasma treatment under 1 kV bias voltage at 10 Pa working gas pressure. Results are explained considering transport kinetics of C and H atoms along grain boundaries of nanocrystalline Mg film.

Keywords: Magnesium films, Molecular implantation, Hydrogen separation

1. INTRODUCTION

Mg-based materials have attracted extensive attention for application in the hydrogen storage technology due to the high storage capacity of the hydride phase, nearly 7.6 wt.% of hydrogen iclude with Mg to form MgH_2. Unfortunately, the hydride phase of Mg-based materials is very stable and shows poor hydrogen absorption and desorption kinetics even in the range of temperature 300–350 ^{0}C. In the past few years, substantial improvement in the hydrogen absorption and desorption kinetics have been achieved by several different methods [1] . The most effective methods realized so far are based on structural refinements of the material and the addition of proper catalysts. Nanocrystalline and amorphous magnesium-based alloys demonstrate the promising performance as hydrogen storage materials. Nanoscale particles are advantageous over bulk materials as they have a larger solid/gas interface area and shorter hydrogen diffusion paths, yielding potentially faster kinetics for gas absorption and desorption. The strong tendency of surfaces for oxidation modifies the hydrogen absorption and desorption. Small impurity levels of oxygen and water can result in the formation of surface oxides. For example, the nanocrystalline Mg and MgH_2 samples handled under controlled inert gas atmospheres at room temperature are covered by 3–4 nm thick oxide barrier layer [2]. The presence of a dense native oxide layer serves as a barrier for hydrogen diffusion from the surface into the bulk, and from the bulk to the surface. So the study of the reactivity to oxygen and air and the passivation of Mg based materials is a major area of interest in this field, both from a practical and fundamental point of view. The accommodation efficiency of equilibrium molecular hydrogen in metals and alloys is extremely low in comparison with that of the non-equilibrium hydrogen [3]. In the present work, the plasma technologies are used to produce hydrides avoiding surface barriers hindering hydrogen transport from the surface into the bulk.

2. EXPERIMENTAL

2.1. Mg film deposition and characterization.

The film deposition rate was determined from the slope of the sample weight change obtained using a microbalance with a weight uncertainty of 2 μg. Before each experiment, the chamber was pumped to the background pressure of $2 \cdot 10^{-5}$ Pa. With a shutter placed between the target and the substrate with high purity (99,99) Mg, the chamber was filled with argon to the working pressure of 5.10^{-1} Pa. The distance between the target and substrate was fixed at 130 mm. The microstructure of the films was analyzed in air by X-ray diffraction (XRD (D8 discovery)) with the 2Θ angle diffractometer in the range of 20-70° using CuKα radiation in steps of 0.05°. Peak position and full-width of peak at half minimum intensity were obtained by fitting the measured peaks with two Gaussian curves in order to find the true peak position and width corresponding to monochromatic Kα1 radiation. The average crystallite dimension of the films, D, was calculated using the formula

$$D = 0.9\lambda/(\beta \cos\Theta), \qquad (1)$$

neglecting the micro strain, where λ is the X-ray wavelength, Θ is the Bragg diffraction angle and β is the full-width of the peak after correction for the instrument is broadening.

2.2. Film plasma irradiation

For studies of H separation in Mg films by molecular ion implantation, the Mg-coated samples were moved into a vacuum chamber and attached to the water cooled sample holder made of graphite (99.9% purity) disc 6 mm-thick and 75 mm in diameter. Experiment scheme is shown in Fig. 1.

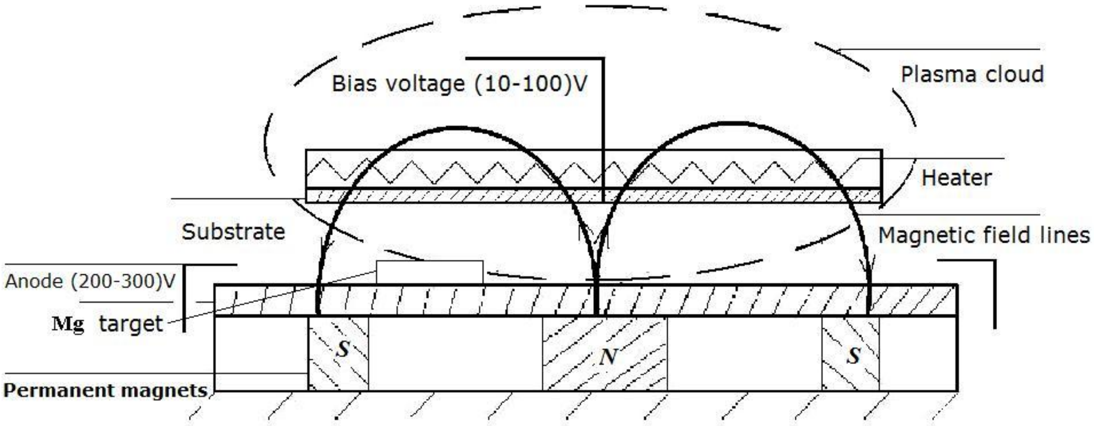

Fig. 1. Scheme of experiment. Plasma in crossed electric and magnetic fields is highly ionized and unhomogeneous

The chamber was evacuated to approximately 10^{-5} Pa pressure by a cryogenic pump. C_2H_2 and argon gases were introduced into the vacuum chamber via a mass flow controller. A DC power supply was used to produce plasma that was source of ions for irradiation of Mg film. Plasma was used as source for ion irradiation by $CHx+$ ions and its parameters such as ion flux and electron density were also measured using a Longmuir probe at 20 mm above the Mg sample located at the center of the ground electrode. The plasma measured parameters were the following: electron concentration – $8 \times \cdot 10^{10}$ cm^{-3}, electron temperature – 3.1 eV, sheath bias – 11 V and ion flux – $5.5 \times \cdot 10^{15}$ $cm^{-2} \cdot s^{-1}$ for fixed experimental conditions such plasma source power – 83 W, Ar gas pressure – 0.4 Pa, Ar gas flow rate – 0.85 $cm^3 \cdot min^{-1}$, C_2H_2 gas flow rate – 0.15 $cm^3 \cdot min^{-1}$ substrate temperature – 470 K.

The substrate temperature was measured during irradiation by a thermocouple which was attached to the stainless steel substrate. Under the previous conditions, a steady state temperature of 470±10 K was reached after five minutes of irradiation.

The intensity of ion irradiation is highly unhomogeneous for used magnetron plasma. This effect is known and described in [4]. The irradiation experiments were done at two working gas pressures: (i) at 0.4 Pa ($\lambda = 3 \times 10^{-2}$ m), (ii) and at 3.6 Pa ($\lambda = 3.3 \times 10^{-3}$ m). After plasma treatment of Mg coating, three characteristic regions on the Mg coating surface were distinguished: (i) the central region, where C adsorption rate exceeded plasma substrate erosion rate and continuous C film was grown, (ii) the region of intensive plasma irradiation, where plasma substrate erosion rate exceeded C deposition rate, and (iii) transfer region, where plasma erosion rate was about equal to C deposition rate (0.15 $cm^3 \cdot min^{-1}$).

Table 1. The parameters of magnetron used for plasma generation in Ar and C_2H_2 gas mixture

Sample	Gas Ratio $cm^3 \cdot min^{-1}$	Pressure, Pa	Current, mA	Voltage, V	Time, min
1	Ar/C_2H_2 0.85/0.15	0.5	250	500	6
2	Ar/C_2H_2 0.85/0.15	0.8	250	500	6
3	Ar/C_2H_2 0.85/0.15	0.5	100	500	30
4	Ar/C_2H_2 0.85/0.15	1.2	250	560	6

After plasma treatment, analysis of C distribution in Mg film was performed. The depth profiles of C were measured by secondary ion mass spectrometry (SIMS(kore technology)) profiling using 1.5 keV Ar^+ with a current of about 70 nA and a spot diameter around 2 µm. The ion beam was scanned over a 150x150 μm^2 area. The sputtering yield of Mg was 1.6 while that of C was about 0.9, as estimated using the transport of ions in matter (TRIM) Monte Carlo code [5]. These conditions gave sputter rate of about 2 $nm \cdot s^{-1}$. The effect of preferential sputtering on the surface erosion rate was neglected.

The Nuclear Reaction Analysis (NRA) with $^{15}N^{2+}$ ions for H distribution profiles was performed on the films at the Dresden-Rossendorf Tandem accelerator. The NRA measurements using the very sharp resonance in the reaction cross-section of ^{15}N on H at 6.385 MeV have been used to obtain high resolution hydrogen depth profiles. The resulting depth profiles yield dependences of concentration versus depth in at/cm². The elemental loss has been investigated for the elastic recoil detection analysis(ERDA) measurements by saving the spectra at 10 regular intervals during the measurement. The analyzed area is about 2x1 mm² for ERDA and 1x1 mm² for NRA. Different areas have been used for the ERDA and NRA measurements.

3. RESULTS

Fig. 2 a and b include SIMS distribution profiles of C in Mg film after irradiation with C_2H_2 plasma during 0.5 h under 0.5 kV bias voltage for two different areas (sample 3): (i) C sputtering rate prevails C deposition rate , and (ii) C deposition rate prevails C sputtering rate. It is seen that in the case, when C film growth during deposition is eliminated by sputtering (Fig. 2a) , the penetration depth of C atoms is about 30 nm, i.e. slightly higher than the C penetration depth into Mg after plasma ion implantation calculated by stopping and range of ions in matter (SRIM) program. In the case when C deposition prevails sputtering (Fig. 2b), Mg film after hydrocarbon plasma irradiation is covered by 280 nm thick C film. The penetration depth of C into Mg film is equal to about 50 nm.

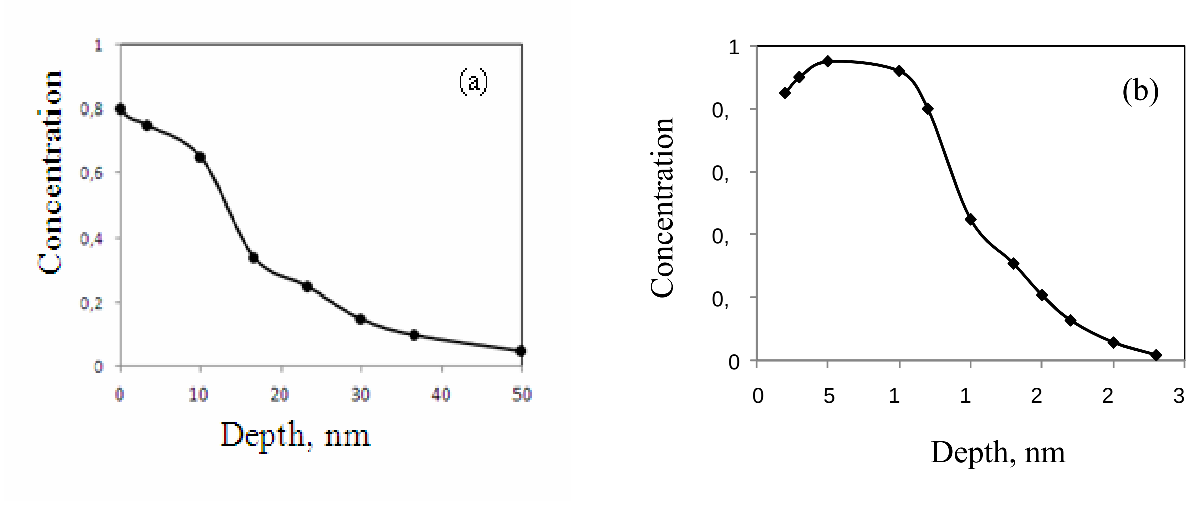

Fig. 2. Distribution of C in Mg film plasma: a – C sputtering rate prevails C deposition rate, and b – C deposition rate prevails C sputtering rate (sample 3)

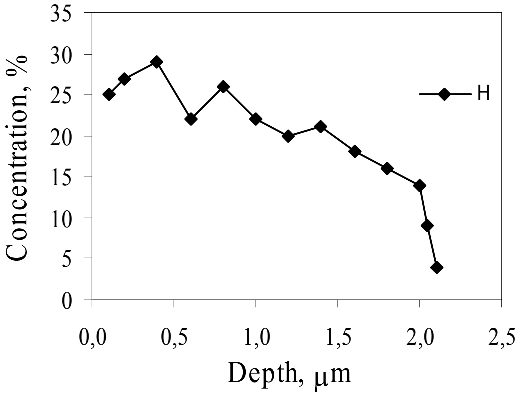

Fig. 3. Distribution of hydrogen in plasma hydrogenated Mg film

Fig. 3 includes NRA distribution profiles of H across the thickness of Mg film after 0.5 h of hydrogenation and 1 kV bias voltage (sample 3). Hydrogen is distributed in the bulk across the entire film thickness with a maximum concentration of about 30 at.% in the near-surface region.

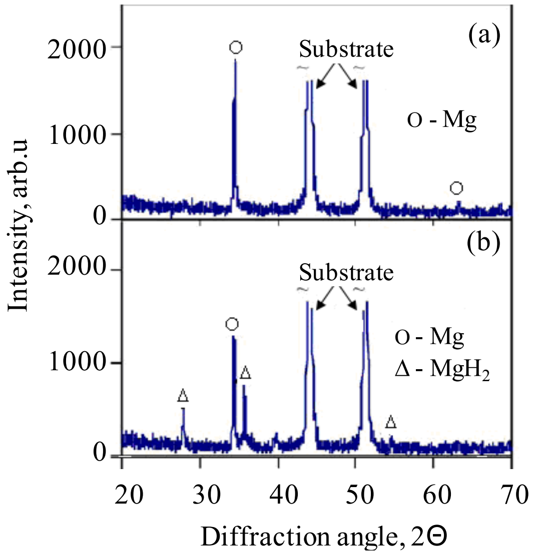

Fig.4. XRD patterns of Mg films: a – as-deposited, and b – after plasma treatment (sample 3)

XRD patterns of Mg films before and after hydrogenation (Fig. 4a)includes a single characteristic peak for h-Mg (002) at 34.5° with a width corresponding to a mean crystallite size about 95 nm. After 30 min of hydrogenation(Fig. 4b), the intensity of the h-Mg (002) peak decreases with a width that corresponds to a mean crystallite size of about 65 nm.

4. DISCUSSIONS

The distribution profiles of C in Mg film (Fig. 2) are in agreement with predictions which follow from theory of simultaneous ion deposition and implantation [5]. The questions remains how to explain anomalous deep penetration depth of hydrogen. There have been different attempts how to explain deep hydrogen penetration. In studies [1, 2], it is suggested that the excess of chemical potential on the surface relative to grain boundaries for nanocrystalline materials produces a net flow of adsorbates into the grain boundaries generating high compressive stress. Under plasma irradiation, the surface is both chemically and physically distinct from the bulk. Differences in chemical potentials between energetically activated surface, bulk and grain boundaries have been established. The transport of C and H atoms from the surface layer into the bulk depends on the difference of chemical potentials of surface and grain boundaries and on kinetic properties of C and H atoms moving along the interface of grain boundaries. Below 450 K, the C transport along grain boundaries is limited by slow kinetics of C atoms at the interface and C atoms accumulate in the near surface region. Meanwhile, the H atoms diffuse through grain boundaries and are distributed across the entire film thickness. In this way, separation of C and H atoms is realized in the bulk of Mg film. Further investigations to find depencev of C and H distribution profils on time and incident in energy are needed.

5. CONCLUSIONS

It is shown that at temperature 470 K the kinetics of C atoms along grain boundaries of nanocrystalline Mg film is slow, while the H atoms are transported deeply into the bulk. After plasma implantation, C atoms are located in the near surface region within about 30 nm and hydrogen atoms are distributed along the entire thickness of Mg film with a concentration of ~30 at. % in the near-surface region and ~15 at. % at the interface with the substrate. Further investigations are needed for deeper understanding of C and H atoms transport mechanism in nanocrystalline materials under plasma treatment.

REFERENCES

1. *Surfau and Coating Technology.* L. Pranevicius, E. Wirth, D. Milcius, L.L. Pranevicius and A. Kanapickas, 203 (2009), 998 p.
2. *Applied Surfau Science.* P. Fielitz, G. Borchardt, M. Schmucker, H. Schneider and P. Willich, 203–204 (2003), 639 p.
3. *Journal of Applied Physic.* A.I. Livshits, F. Sube, M. Soloviev, M. Notkin and M. Bacal, 84 (1998), 2558 p.
4. *B.Bobrovaitė, Study of carbon impurity in tungsten, daktaro disertacija*. Kaunas, VDU. 2008.
5. *The Stopping and Range of Ions in Solids.* J.F. Ziegler, J.P. Biersack and U. Littmark, , Pergamon Press, New York, (1985).

CYSENI 2010, May 27–28, Kaunas, Lithuania
ISSN 1822-7554, www.cyseni.com

ELECTRON AND PROTON CONDUCTIVE POLYMER MEMBRANES FOR FUEL CELLS

J. Hodakovska, G. Chikvaidze, J. Kleperis
Institute of Solid State Physics, University of Latvia
Kengaraga 8, LV-1063, Riga – Latvia
Phone: +371 67262145
Email: julia_h_lv@yahoo.co.uk

ABSTRACT

Global environmental concerns have ignited research to develop energy generation technologies which leave minimal ecological damage concerns of global climate change. These are driving nations all around the world to develop electric power generation technologies and transportation technologies which reduce carbon dioxide emissions. Renewable sources are one of the most discussed topics in this area of research, but the other problem is also to store energy in environmental-friendly way. Hydrogen is considered the fuel of choice for both the electric power and transportation industries. Nowadays between most expensive materials to be used in hydrogen technologies are membranes and membrane – electrode assemblies. In our work an idea is to develop the multilayered electron/proton conducting membrane using available polymers. Material for possible fuel cell applications is made from electron and proton conductive compounds: 2 different polymers (sulfonated poly (ether-ether-ketone) (SPEEK) and polyaniline (PANI)) are used for this purpose. The membranes were characterized by Fourier Transform Infrared (FTIR) and Raman spectra. Thermogravimetric analysis (TGA) and conductivity measurements of simple SPEEK and complex membranes SPEEK/PANI are performed to assess their suitability in fuel cell applications and thermal stability. The proton and electron conductivities of such multilayered membranes were found from impedance measurements and preliminary data were reported.

Keywords: polymer membrane, fuel cells, proton conductivity, electron conductivity

1. INTRODUCTION

Energy related topics are one of the most actual not only for scientists, but also for all humankind. Without this valuable resource we would not be able not only to develop our knowledge or improve our life, but even more – we would loose nearly all, what is associated with word “comfort”. Understanding of such a danger and the fact, that now humankind is highly dependant on non-renewable energy sources, has put any topic, related with possible problem solution, in focus of vast number both specialists and interested.

For quite a long time fuel cells were one of the technologies, which would allow humankind to avoid pollution due to fact, that resulting product of reaction is either enviromental friendly (e.g. water) or is produced in much more smaller amount (e.g. CO_2). For this reason alkaline fuel cells were chosen for space missions, where danger of bad air could turn into mission fail. Applications on Earth are also paid a lot of attention, since pollution is becoming significant problem, both due to life quality and climate changes [1, 2]. As a most easy way out of energy deficit, the renewable sources are named, but this type of sources is extremely dependant on availability (e.g. day time for Sun, un-classified time periods for Wind, Water in rivers only in spring etc.), so the question of energy storage in this case is raised. As one of the possible environment-friendly ways would be using hydrogen, because of it’s small weight, large combustion energy and availability in different compounds [3]. Then polymer electrolyte fuel cells could be a way to regain energy from hydrogen with only water as end-product, thus having no dangerous pollution at all.

Fuel cell working principles are known, but still there are possible a lot of improvements, making this topic full of challenges [4]. Some of the best-known topics are catalyst development and search for polymer, which would have good proton conductivity at optimal temprature for specified usage. Another problem is good contact between all component parts: membrane, electrodes and field flow plates, current collectors. Now to create membrane-electrode assembly, the polymer membrane and carbon cloth coated with catalyst are used. Due to different structures it is difficult to have good contact between conterminous parts.

In our work we are exploring the possibility to create the new material for electrode on base of membrane material (sulfonated poly(ether-ether-ketone) (SPEEK) in our case) by adding electron conductive material (polyaniline (PANI)).

2. EXPERIMENTAL

2.1. Samples

For experiments two polymers were used: SPEEK as a proton conductive compound and polyaniline as a possbile electron conductive part. Poly(ether-ether-ketone) (PEEK) was one of the first of the 'new generation' of engineering thermoplastics introduced and was developed by ICI in 1977 and first marketed in 1978. The material is one of the polyaryletherketone family – a group of partially crystalline polymers that are suitable for use at high temperatures. The polyether ether ketones have repeating monomers of two ether and ketone groups and PEEK is one of the highest rated thermoplastic materials in terms of heat resistance. The useful properties of the material are retained at temperatures as high as 315°C. The materials have excellent chemical resistance, high strength and good resistance to burning but equally the high cost of these materials makes applications limited to those where the properties are very necessary. The SPEEK is one of the possible Nafion`s replacement in polymer membrane fuel cells . It's conductivity is based on SO_3H groups and absorbed water. First factor is named "sulfonation degree" (SD); commonly SD is 100% in case all repeatable units have 1 group (n=1, m=0). PANI is one of the common polymers used as electron conductor and exists in 3 forms, only one of them (y=50%) is conductive (Fig. 1). H. Gharibi *et al.* [5] report that PANI is reducing necessary platinum ammount, which could have good influence on pricing.

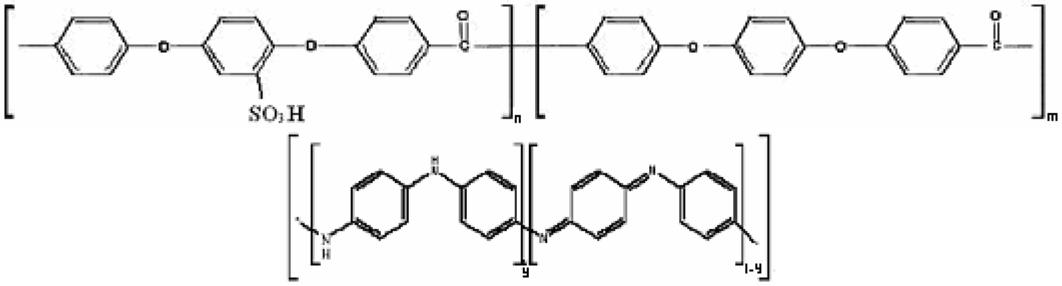

Fig. 1. Molecular structures of SPEEK and PANI

SPEEK was prepared from poly(ether-ether-ketone) (PEEK) supplied by Aldrich and according to procedure described elsewhere [6]. We used PANI in non-conductive form (emeraldine base) with molecular weight of 60000 g mol^{-1}, supplied by Aldrich. To evaluate an effect on conductivity of SPEEK, no additional dopand was used and PANI was only in non-conductive form.

In this work the samples of two types are reported only: 100 wt% SPEEK and with 10 wt% of PANI.

2.2. Methodology

2.2.1.FTIR

To determine the sulfonation degree of polymer, the Furje transform Infrared (FTIR) spectroscopy was used. Infrared spektra were recorded using Bruker Equinox 55 FTIR spektrometer. Spectra were recorded in interval from 500 cm^{-1} to 1700 cm^{-1} with resolution of 0.5 cm^{-1}. For raw PEEK material due to it's bad solubility, the diffused reflection method was used and measured data were mathematically treated to receive absorbance. For new synthesized SPEEK membranes, the light transmition spectrum was measured directly.

2.2.2.Water uptake

To determine the water uptake of membrans, a simple method was used. Small sample (with area around 1 cm^2) was cut out from membrane, weighted and then left in deionized water for 24 hours. Then samples were taken out from water and weight gain was determined using following equation:

$$WaterAbsorbtion = \frac{M_{membrane+water} - M_{membrane}}{M_{membrane}}$$

2.2.3.Conductivity

Membrane samples were placed in water for 24 hours before conductivity measurements. The relative humidity in conductivity cell was kept constant 100% during all measurements.

Proton conductivity was measured with Becktech conductivity cell [7]. Four electrode scheme was used (Fig. 2) to determine in-plane conductivity of membrane. During conductivity measurements at different temperatures, the saturated water vapours were provided to cell with self-made special experimental setup. The constant current from DC power source (potentiostat VoltaLab PGZ301) is applied to electrodes 1 and 2; generated voltage is measured between electrodes 3 and 4 with Welleman DVM850BL multimeter.

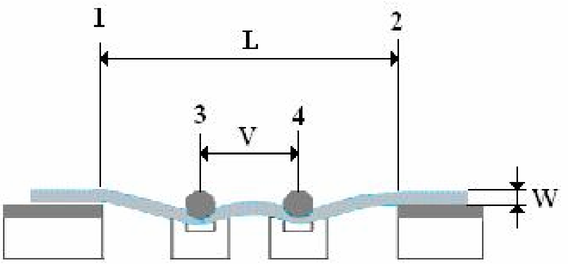

Fig. 2. Proton conductivity measurement scheme. Distances L and V are fixed; the thickness of membrane (W) is dependant from the sample

3. RESULTS AND DISCUSSION

To determine the presence of sulfonated sites in synthesized membranes, the FTIR spectra of PEEK and SPEEK samples were compared (Fig. 3). Due to different measurement methods (diffuse reflectance and direct transmission) and absorbtion values, both spectra were normalized for better understanding. Some changes between spectra were observed. The peak at around 1500 cm^{-1}, which corresponds to C-C bond, splits into two in SPEEK sample due to hydrogen replacement with SO_3H group. Also for SPEEK sample the new peaks appear, which indicate sulfur and oxygen bound and it's stretching vibrations. Since sulfur appears only after sulfonation, all the mentioned lines clearly indicate the positive results of sulfonation process.

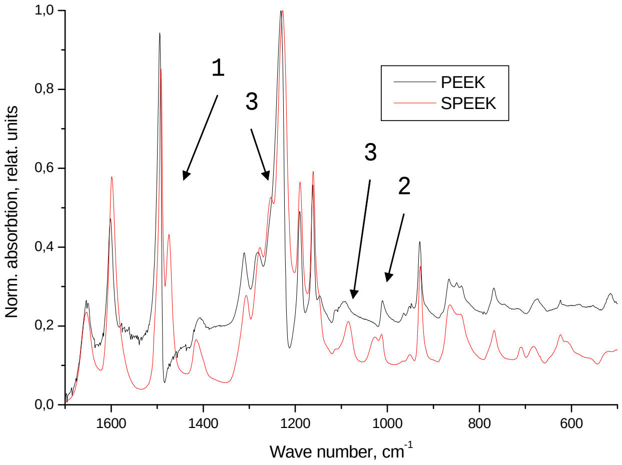

Fig. 3. PEEK and SPEEK normalized absorbtion spectrum. Numbers are showing following peaks: 1 – C-C bond at 1470 cm^{-1} and 1493 cm^{-1}; 2 – S=O bond at 1022 cm^{-1}; 3 – O=S=O simetrical and assimetrical stretching vibrations at 1080 cm^{-1} and 1250 cm^{-1}accordingly

Water absorbtion degree in membrane is important parameter due to next contardictory facts: SPEEK proton conductivity is dependant from water, absorbed by membrane, and water absorbtion makes membrane to swell, deforming it. This two effects make water absorbtion capacity both positive and negative gactor, and balance is needed. Since PANI polymer absorbs nearly no water (below 1 wt%), an overall water absorbtion of 2 – component composite membrane is decreased, comparing to SPEEK membrane. At the same time the water uptake in our composite membrane is not close to zero, indicating possibility to have also comparably good proton conductivity.

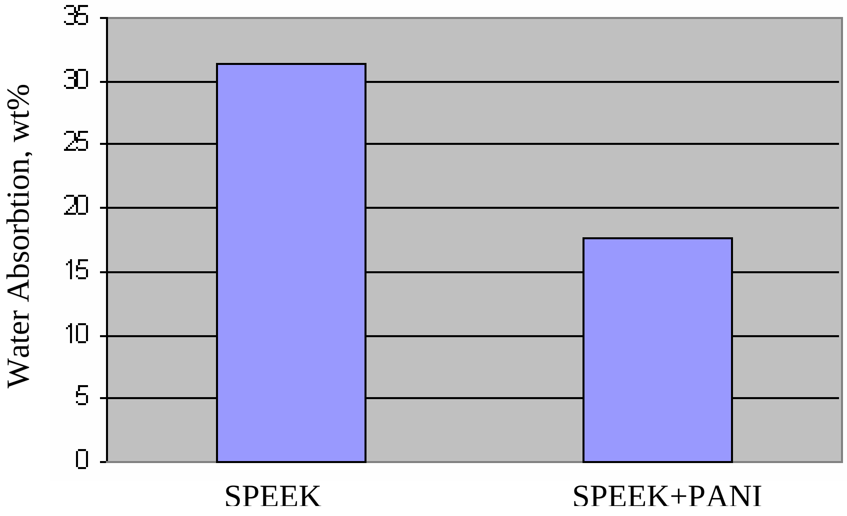

Fig. 4. Water absorbtion of SPEEK membrane and composite SPEEK/PANI membrane

The most important parameter for our membrane is proton conductivity, and measured values showed (Fig. 5), that for composite membrane the conductivity decreased significantly (3–4 times depending from temperature region).

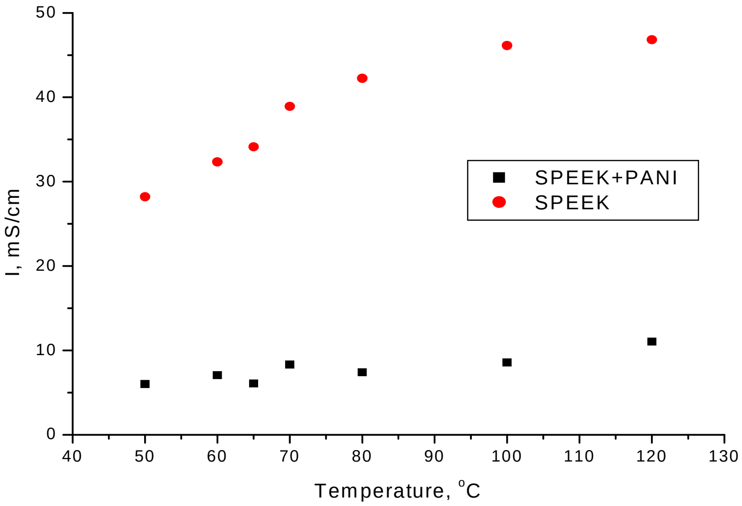

Fig. 5. Proton conductivity for SPEEK membrane and composite SPEEK/PANI membrane

One of the possible reason for signifficant conductivity decrease could be the possibility of SPEEK polymer to play the dopant role and PANI changes in direction of increasing “y” value (Fig. 1.). This process decreases the number of SO_3H groups, which are responsible for proton conductivity in membrane. To increase the proton conductivity, another dopant polymer could be used, e.g. some acid. As it was seen from preliminary impedance spectra of composite SPEEK/PANI membrane, an electronic conductivity is found to be insignifficant. It would be suggested that PANI transformation to electron conductive form also woould increase the conductivity of composite membrane. Further research is needed to improve proposed composite membranes in this area.

4. CONCLUSIONS

Experimental results show, that adding polymer PANI to polymer SPEEK decreases proton conductivity of composite membrane. Electronic conductivity without dopand is too small to use membrane also as electron conductor. Improvement of membrane material is planed to create appropriate composite membrane with both types of conductivity by adding dopant.

5. ACKNOWLEDGMENT

We would like to thank ESF (European Social Fund), National State Program in Energetic and University of Latvia for financial support in researches.

REFERENCES

1. Hoogers G. edition *Fuel Cell Technology Handbook*, CRC Press LLC, 2003, ISBN 0-8493-0877-1.
2. Barbir. F. *PEM Fuel Cells. Theory and Practice*, Elsevier Academic Press, 2005.
3. Lanz A., Heffel J., Messer C. Hydrogen Fuel Cell Engines and Related Technologies December 2001 College of the Desert, Palm Desert, CA, USA.
4. Norby T. Solid-state protonic conductors: principles, properties, progress and Prospects, Solid State Ionics 125, 1999, p. 1–11.
5. Gharibi H., Zhiani M., Mirzaie R.A., Kheirmand M., Entezami A.A., Kakaei K., Javaheri M. Investigation of polyaniline impregnation on the performance of gas diffusion electrode (GDE) in PEMFC using binary of Nafion and polyaniline nanofibers, Journal of Power Sources 157, 2006, p. 703–708.
6. Nunes S.P., Ruffmann B., Rikowski E., Vetter S., Richau K. Inorganic modification of proton conductive polymer membranes for direct methanol fuel cells, Journal of Membrane Science 203, 2002, p. 215–225
7. BekkTech`s procedures for performing in-plane membrane conductivity testing. Report on US DOE Contract # DE-FC36-06GO16028 (2008), 18 p.

CYSENI 2010, May 27–28, Kaunas, Lithuania
ISSN 1822-7554, www.cyseni.com

THE HYDROGEN PERMEATION RATE THROUGH THE METAL MEMBRANE AT MEMBRANE SEPARATION OF HYDROGEN FROM SYNTHESIS-GAS

N.V. Kolyago
The A.V. Lukov Institute of Heat and Mass Transfer NAS Belarus
Belarus, 220072, Minsk, P.Brovka str., 15
Phone: +375(017) 284 12 42
Email: kolyago@hmti.ac.by

ABSTRACT

The present work reports the results of investigation of hydrogen separation from synthesis-gas. A mathematical model that describes the process of hydrogen separation from synthesis-gas in tubular and plane-frame elements on the basis of metal membrane has been developed. The effects of the convectional external diffusional and intramembrane resistances on the mass transfer in a gas-separating element, degree of hydrogen dissociation at adsorption on the surface of metal membrane are taken into account. The integro-differential equation is obtained which makes it possible to calculate the most important characteristics of the membrane separation, that is, the rate of hydrogen mass transfer through the metal membrane taking into account external diffusion convective and intramembrane diffusion resistances, degree of hydrogen dissociation, the physical properties of synthesis-gas, the physiochemical properties of membrane, the technological parameters of the process and the geometry and dimensions of the membrane element. The procedure of calculation of the hydrogen permeation rate has been proposed on the basis of received solution. The advantage of this procedure is that the integro-differential equation of the hydrogen permeation rate can be converted to the ordinary nonlinear differential equation of first order in separable variables. It is solved by the Runge–Kutta method of fourth order. In present work the influence of temperature on the processes of mass transfer in membrane metal gas-separating elements are analyzed.

Keywords: hydrogen, gas separation, metal membrane, hydrogen permeation rate

1. INTRODUCTION

Since hydrogen has a number of advantages over other energy resources, in the last years there have been strong developments in technology for hydrogen separation from hydrogen-containing mixtures. The separation technology used in H_2 production depends on the application, the desired H_2 purity and the downstream impact of CO or N_2. Synthesis-gas is a mixture of hydrogen and carbon monoxide predomination. Today it is one of the most widespread fuels and may be source of hydrogen-containing products. CO:H_2 ratio depends on method of synthesis-gas production and it is varying from 1:1 to 1:3 [1]. Four different H_2 purification technologies are widely practiced in industry; these include: 1) absorption, both chemical and physical, 2) adsorption, 3) membranes and 4) cryogenic processes [2].

In the last decade of the previous century and at the beginning of the new one, there has been a considerable upswing of interest in devices that separate gas mixtures of various compositions on the basis of membranes [3, 4]. This is ascribed to the fact that the traditionally used technologies have reached their limit from the viewpoint of their further optimization and adaptation to the increased requirements of industry. The use of membrane facilities allows to intensify the process of gas separation considerably. Among the advantages of the membrane method are the ecological purity, reliable operating, compactness, explosion – and fire-safety, flexible characteristics of separation and their smooth regulation, the mobility of the process [5].

Over 700 patents have been issued since 2000 for hydrogen selective membranes. Hydrogen selective membranes such as metal ones have been evaluated for commercial hydrogen separation. Because hydrogen in membrane is transported in dissociated form, metal membranes can be almost 100% selective towards hydrogen (ultra pure hydrogen is containing little (< 1 ppm) or no carbon oxides). Among hydrogen metal membranes, Pd – based membranes remain the most promising [2].

However, not only must one solve a number of technological problems for membrane processes of gas separation to be commercialized, but one must also create calculation methods for these processes. The underlying principles of mechanisms of separation of gas mixtures in membranes is at the study stage. This is attributable to a multitude of factors that influence the process: a wide range of gas mixtures varying in their physical properties; diverse implementation of membrane separation (shape of the channel, excess pressure, initial concentration, etc.); membranes varying in the material and, as a consequence, in their physiochemical properties exerting their influence on permeability and selectivity. To do this, it is necessary to know the main mechanisms of convective hydrogen separation.

To calculate modules incorporating membranes one has to solve a conjugate problem of convective mass transfer in the head channel and of mass transfer through the membrane. In this case, the external diffusion resistance in the head and drainage channels is usually ignored and the gas composition is assumed to be equal everywhere over their cross sections because of the high diffusivity of gases at comparatively low pressures and the low penetrability and selectivity of the membrane [5, 6]. However, the development of high-selectivity metal and polymeric membranes, which can be used at high pressures in the head channel, has changed the situation. In apparatus with such membranes the external diffusion resistance is comparable with the resistance to the internal mass transfer in the membrane. Such a problem for a polymeric membrane has been posed for the first time and solved in [7, 8], but hydrogen dissociation on metal membrane is left out of account. Therefore, it makes sense to calculate the operation of apparatus in the presence of external and intramembrane diffusion resistances, hydrogen dissociation on metal membrane.

In [3, 4] consideration is given to some laws that govern mass transfer in membrane elements on the assumption that injection of a gas mixture does not change the properties of the main flow, whereas the gas dynamics of the flow is independent of the separation process on a membrane and is determined by the relations that follow from Berman’s solutions [9]. In [5, 10], the laws governing mass transfer in the head channel of the membrane element are considered on the basis of the analogy with the heat-transfer problem. The disadvantage of these works is that in the case of the membrane element of gas-separating module it is necessary to solve a more complex problem of conjugate mass transfer in the head channel and membrane, when the magnitude of the rate of gas penetration is the unknown quantity and cannot be assigned a priori as a boundary condition.

The aim of the present investigation is to determine the most important characteristic of the membrane separation of synthesis-gas – the rate of hydrogen mass transfer through the metal membrane taking into account external diffusion convective and intramembrane diffusion resistances, hydrogen dissociation on metal membrane.

2. MATHEMATICAL MODEL

2.1. Formulation complex problem of conjugate mass transfer in membrane unit

For the analysis of the gas separation and prediction of hydrogen permeation rate it is necessary to create mathematical models providing the description of the main processes that influence on the transfer substances.

The main processes determining the gas separation include [11]: convective mass transfer in the head channel, mass transfer through the membrane, convective mass transfer in the drainage channel. Hydrogen transport through the membrane can best be described by the solution/diffusion mechanism: hydrogen is adsorbed on one side of the membrane, splits into two atoms, diffuses through the metal matrix, and recombines and desorbs at the permeate side (Fig. 1). The level of influence of processes can be differ from various physiochemical properties of a membrane, technological parameters of the process.

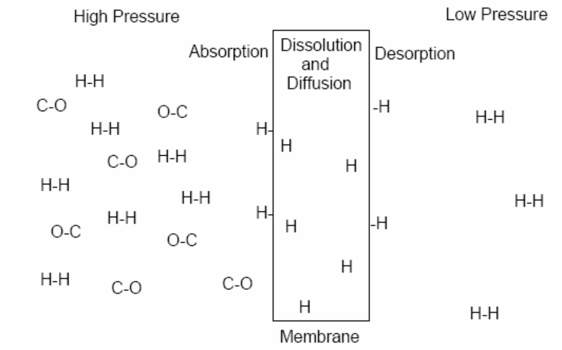

Fig. 1. Basic processes determining the hydrogen separation

Apparatus with tubular and plane-frame elements are used for hydrogen separation. A synthethisis-gas with a hydrogen concentration c_0 enters into the head channel of the membrane element (Fig. 2).

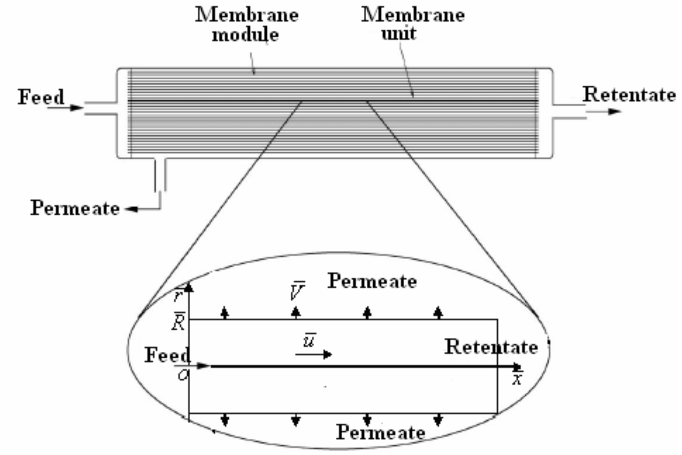

Fig. 2. Diagram of membrane separation of synthesis-gas mixture: membrane unit – cell containing a drainage and head channels, a membrane to separate the streams of feed, permeate, and retentate; membrane module – manifold assembly containing membrane unit; permeate – stream containing penetrants that leaves a membrane module; retentate – stream that has been depleted of penetrants that leaves the membrane modules without passing through the membrane to the downstream; $\overline{r}$ is the radial coordinate, m; R is the radius (halfwidth) of the channel, m; $\overline{u}$ is the longitudinal projection of the velocity, m/sec; $\overline{V}$ is the rate of penetration of hydrogen through the membrane, m/sec; $\overline{x}$ is the longitudinal coordinate, m

As a result of the different penetration rates of hydrogen and carbon monoxide during flow through the membrane, the composition of the mixture undergoes a change. In the head channel the fraction of the hydrogen is decreased as a result of passage through membrane and the concentration of the carbon monoxide is increased. The gas mixtures from the head and drainage channels are delivered from the membrane element. The resistance of the drainage channel is not taken into account in this work.

When gas separation is implemented in practice, gas separation circuits are used, including hollow-fiber and flat-frame units based on the membranes with different separation characterictics (Fig. 3). Since carbon monoxide penetrability coefficient tent to zero, the metal membrane is regarded as semipermeable membrane (only hydrogen passes through the membrane).

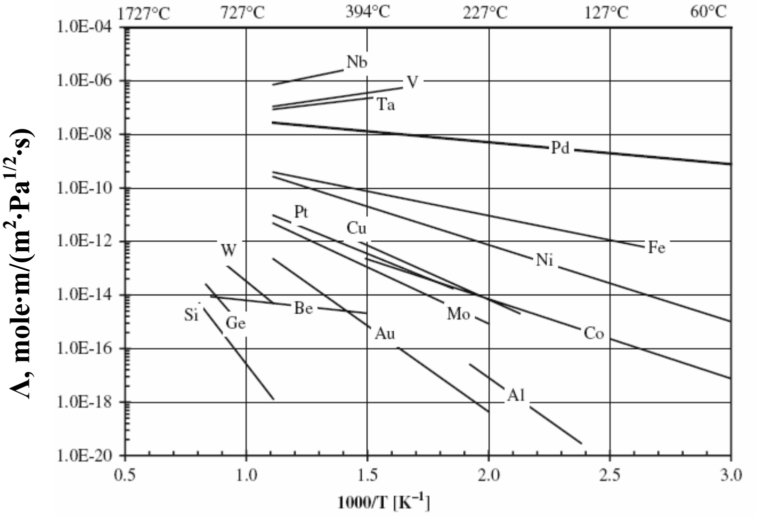

Fig. 3. Temperature dependence of hydrogen penetrability coefficient through metals [11]

The flow in the head channel is two-dimensional and symmetrical relative to the channel axis, laminar, steady, and fully developed at the entrance to the channel. The synthesis-gas is incompressible, the process is isothermal, the coefficients of viscosity and diffusion are constant. The bulk viscosity and barodiffusion are neglected. The coefficients of viscosity are described by a viscosity equation of Wilke for gas mixtures [12]. The coefficients of diffusion are described by a Chepmen-Enskii method [12]. The hydrogen penetrability coefficient Λ is usually independent of gas concentration in the membrane and is described by Arrhenius theory [13].

The continuity equation, the equation of motion (in projections), and the equation of convective diffusion can be written in dimensionless form as

$$\frac{\partial u}{\partial x}+r^{-\alpha}\frac{\partial\left(r^{\alpha}\upsilon\right)}{\partial r}=0, \tag{1}$$

$$\frac{\partial p}{\partial x}=\frac{1}{\mathrm{Re}\,\varepsilon}\left[r^{-\alpha}\frac{\partial}{\partial r}\left(r^{\alpha}\frac{\partial u}{\partial r}\right)\right], \qquad \frac{\partial p}{\partial r}=0, \tag{2}$$

$$u\frac{\partial c}{\partial x}+\upsilon\frac{\partial c}{\partial r}=\frac{1}{\mathrm{Pe}_D\varepsilon}r^{-\alpha}\frac{\partial}{\partial r}\left(r^{\alpha}\frac{\partial c}{\partial r}\right), \tag{3}$$

where $u=\bar{u}/u_0$ is the dimensionless longitudinal projection of the velocity; u_0 is the mean flow rate at the input of the channel, m/sec; $x=\bar{x}/L$ is the dimensionless longitudinal coordinate; $L=1$ m is the caliber of length of the channel, m; $r=\bar{r}/R$ is the dimensionless radial coordinate; $\alpha=0$ corresponds to a plane-frame unit and $\alpha=1$ corresponds to a tubular unit; $\upsilon=\bar{\upsilon}L/(u_0R)$ is the dimensionless radial projection of the velocity; $\bar{\upsilon}$ is the radial projection of the velocity, m/sec; $p=\bar{p}/(\rho u_0^2)$ is the dimensionless pressure; $\bar{p}$ is the pressure, Pa; ρ is the density, kg/m^3; $\mathrm{Re}=u_0R/\nu$ – Reynolds number; ν is the kinematic viscosity, m^2/sec; $\varepsilon=R/L$ is the ratio between two characteristic sizes of the channel; c is the concentration of the hydrogen; $\mathrm{Pe}_D=u_0R/D$ is the diffusional Peclet number; D is the diffusion coefficient, m^2/sec.

The boundary conditions can be written as
at the input to the channel (at $x=0$):

$$c=c_0,\ p=p_0,\ u=\frac{\alpha+3}{2}\left(1-r^2\right), \tag{4}$$

at the axis (plane) of symmetry (at $r=0$):

$$\frac{\partial u}{\partial r}=0,\ \upsilon=0,\ \frac{\partial c}{\partial r}=0, \tag{5}$$

on the membrane (at $r=1$)

$$u=0,\ \left.\left[\left(1-c(x,r)\right)\upsilon(x,r)+\frac{1}{\mathrm{Pe}_D\varepsilon}\frac{\partial c(x,r)}{\partial r}\right]\right|_{r=1}=0, \tag{6}$$

$$\upsilon(x,1)=V(x)=\frac{\Lambda M}{\delta_{\mathrm{m}}\varepsilon}\left(\frac{p(x)c_{\mathrm{w}}(x)}{\rho}\right)^{\frac{1}{2}}, \tag{7}$$

where substript 0 is the value at the input of the channel; $V=\bar{V}L/(u_0R)$ is the dimensionless rate of penetration of hydrogen through the membrane; Λ is the penetrability coefficient, mole·m/(m^2·Pa$^{1/2}$·sec); M is the molar mass of the hydrogen, kg/mole; substript w is the value at the wall of the channel; δ_{m} – effective thickness of the membrane, m; exponent 1/2 is degree of hydrogen dissociation at adsorption on the surface of metal membrane.

Hydrogen transport through Pd-based membranes is commonly described by Sieverts' law which results from the coupling of two main processes: adsorption of molecular hydrogen and its dissociation into atoms, at the upstream membrane surface ($H_2 \rightarrow 2H$) and vice versa at the downstream surface of the metal membrane and the atomic hydrogen diffusion in the metallic lattice.

As follows from the formulation of the problem, the continuity equation, the equation of motion, and the equation of convective diffusion are interconnected since the unknown rate of mass transfer through the membrane $V(x)$ depends on the concentration and pressure of the gas at the wall. The problem will be solved on the assumption that $V(x)$ is known. In this case, the equation of motion and the equation of convective diffusion can be solved independently.

In solving the equations of continuity and motion (1), (2), subject to boundary conditions (4)–(6), we find the distributions of the rates and pressure in the membrane channel:

$$u(x,r)=\frac{\alpha+3}{2}\left(1-(\alpha+1)\int_0^x V(x)dx\right)\left(1-r^2\right), \tag{9}$$

$$\upsilon(x,r)=\frac{(\alpha+1)(\alpha+3)}{2}V(x)\left(\frac{r}{\alpha+1}-\frac{r^3}{\alpha+3}\right), \tag{10}$$

$$p(x)=p_0-\frac{(\alpha+1)(\alpha+3)}{\mathrm{Re}\,\varepsilon}\int_0^x\left(1-(\alpha+1)\int_0^x V(x)dx\right)dx\,. \tag{11}$$

2.2. Analytical semi-integral method

To analyze the equation of convective diffusion (3) a semi-integral method is proposed. The essence of the method is that the distribution of concentration in the diffusion layer is determined directly from the equation of convective diffusion in the region adjacent to the membrane. Using the continuity equation (1), the equation of convective diffusion can be written in a conservative form:

$$\frac{\partial\left(r^\alpha u(1-c)\right)}{\partial x}+\frac{\partial\left(r^\alpha \upsilon(1-c)\right)}{\partial r}=-\frac{1}{\mathrm{Pe}_D\varepsilon}\frac{\partial}{\partial r}\left(r^\alpha\frac{\partial c}{\partial r}\right). \tag{12}$$

Since the diffusion Prandtl number is small (0.7–1) for gas mixtures, the diffusion boundary-layer zone occupies a small part of the membrane channel in a laminar regime and so can be ignored.

We propose to solve the equation of convective diffusion (12) at the boundary conditions (5), (6) by a semiintegral method. The essence of this method is as follows. We write Eq. (12) in the form

$$\frac{\partial\left(r^\alpha u(1-c)\right)}{\partial x}+\frac{\partial}{\partial r}\left[\frac{1}{\mathrm{Pe}_\mathrm{D}\varepsilon}r^\alpha\frac{\partial c}{\partial r}+r^\alpha\upsilon(1-c)\right]=0. \tag{12}$$

Let us drop the first term of the equation and integrate the remainder with respect to *r* at the boundary conditions (5), (6). As a result, we obtain

$$c(x,r)=1-\left(1-c_\mathrm{w}(x)\right)\exp\left(-\mathrm{Pe}_D\varepsilon V(x)\left(\frac{\alpha+5}{8}-\frac{\alpha+3}{4}r^2+\frac{\alpha+1}{8}r^4\right)\right). \tag{13}$$

The concentration distribution (13) is true for the region near the membrane. To determine such a distribution everywhere over the cross section of the membrane channel, we will derive an integral equation of mass balance. For this purpose, let us integrate Eq. (13) with respect to *r* from 0 to 1 at the boundary conditions (5) and (6):

$$\frac{\partial}{\partial x}\int_0^1 r^\alpha u(1-c)dr=0. \tag{14}$$

The condition (14) means that the mass balance for carbon monoxide is carried out. This expression can be written, in view of (4), as

$$\int_0^1 r^\alpha u(1-c)dr=\frac{1-c_0}{\alpha+1} \tag{15}$$

To determine the dependence $c_{\mathrm{w}}(x)$, we substitute relation (13) into formula (15) and, using expression (9), obtain

$$\int_0^1 r^{\alpha}\left(1-r^2\right)\exp\left(-\mathrm{Pe}_D\varepsilon V(x)\left(\frac{\alpha+5}{8}-\frac{\alpha+3}{4}r^2+\frac{\alpha+1}{8}r^4\right)\right)dr = \\ =\frac{2\left(1-c_0\right)}{(\alpha+1)(\alpha+3)\left(1-(\alpha+1)\int\limits_0^x V(x)\,dx\right)\left(1-c_{\mathrm{w}}(x)\right)}. \tag{16}$$

For membrane separation of gases small values of $\mathrm{Pe}_D\varepsilon V(x)$ are typical, hence the exponent can be expanded into a Taylor's series, and we can restrict ourselves to the first two terms of expansion, neglecting terms of the order $\left(\mathrm{Pe}_D\varepsilon V(x)\right)^2$:

$$\exp\left(-\mathrm{Pe}_D\,\varepsilon V(x)\left(\frac{\alpha+5}{8}-\frac{\alpha+3}{4}r^2+\frac{\alpha+1}{8}r^4\right)\right)= \\ =1-\mathrm{Pe}_D\,\varepsilon V(x)\left(\frac{\alpha+5}{8}-\frac{\alpha+3}{4}r^2+\frac{\alpha+1}{8}r^4\right)+O\left(\left(\mathrm{Pe}_D\,\varepsilon V(x)\right)^2\right). \tag{17}$$

As a result, we find

$$c_{\mathrm{w}}(x)=1-\frac{1-c_0}{\left(1-(\alpha+1)\int\limits_0^x V(x)\,dx\right)\left(1-\frac{5\alpha+17}{(\alpha+5)(\alpha+7)}\mathrm{Pe}_{\mathrm{D}}\varepsilon V(x)\right)}. \tag{18}$$

Substituting (11) and (18) into (7), we obtain an equation for hydrogen permeation rate *V*(*x*):

$$V(x)=\frac{\Lambda M}{\varepsilon\delta_{\mathrm{m}}\sqrt{\rho}}\sqrt{p_0-\frac{(\alpha+1)(\alpha+3)}{\mathrm{Re}\,\varepsilon}\int\limits_0^x\left(1-(\alpha+1)\int\limits_0^x V(x)dx\right)dx}\,\times \\ \times\sqrt{1-\frac{1-c_0}{\left(1-(\alpha+1)\int\limits_0^x V(x)\,dx\right)\left(1-\frac{5\alpha+17}{(\alpha+5)(\alpha+7)}\mathrm{Pe}_{\mathrm{D}}\varepsilon V(x)\right)}}\,. \tag{19}$$

The integral equation obtained allows one to calculate the most important characteristic of the membrane separation of synthesis-gas – the rate of hydrogen mass transfer through the metal membrane taking into account external diffusion convective and intramembrane diffusion resistances, the physical properties of synthesis-gas, the physiochemical properties of membrane, the technological parameters of the process and the geometry and dimensions of the membrane element.

3. DETERMINATION OF THE HYDROGEN PERMEATION RATE

3.1. The procedure of calculation of the hydrogen permeation rate

The procedure of calculation of the hydrogen permeation rate has been proposed on the basis of received solution (19) that will enable us to analyze the process of separation of the mixture in the gas-separating unit with metal membranes and to evaluate the prospects for searching metal alloy suitable for manufacture of membrane unit to isolate hydrogen from synthesis gas.

Let us transform the equation (19) to a differential one. To find the dependence of the hydrogen penetration rate on the longitudinal coordinate *x*, we use simplifying assumption. Using the expression for the dependence of pressure on the longitudinal coordinate *x* (11) at the characteristic values of the membrane separation of synthesis-gas, we estimate from above the pressure in unit, having assumed that $V(x) = V$:

$$p(x) = p_0 - \frac{(\alpha+1)(\alpha+3)}{\mathrm{Re}\,\varepsilon}x + \frac{(\alpha+1)^2(\alpha+3)}{\mathrm{Re}\,\varepsilon}\frac{x^2}{2}V. \qquad (20)$$

Since the second and third terms are small in comparison with the remaining terms, it can be neglected within one unit. In this case, Eq. (19) takes the form

$$V(x) = \frac{\Lambda M}{\varepsilon\delta_{\mathrm{m}}}\sqrt{\frac{p_0}{\rho}\left(1 - \frac{1-c_0}{\left(1-(\alpha+1)\int\limits_0^x V(x)\,dx\right)\left(1-\frac{5\alpha+17}{(\alpha+5)(\alpha+7)}\mathrm{Pe_D}\varepsilon V(x)\right)}\right)}. \qquad (21)$$

For this purpose we introduce the notation $\int\limits_0^x V(x)\,dx = \varphi(x)$, $V(x) = \varphi'(x)$ and pass from the variable $V(x)$ to a new variable $\varphi(x)$:

$$\varphi'(x) = \frac{\Lambda M}{\varepsilon\delta_{\mathrm{m}}}\sqrt{\frac{p_0}{\rho}\left(1 - \frac{1-c_0}{\left(1-(\alpha+1)\varphi(x)\right)\left(1-\frac{5\alpha+17}{(\alpha+5)(\alpha+7)}\mathrm{Pe_D}\varepsilon\varphi'(x)\right)}\right)}. \qquad (22)$$

There are three techniques to solve Eq. (22): 1) reduction of Eq. (22) to cubic equation for the hydrogen penetration rate and analytic solution found by the Cardano method; 2) reduction of Eq. (22) to quadratic equation and analytic solution for the hydrogen penetration rate; 3) reduction of Eq. (22) to linear equation and analytic solution for the hydrogen penetration rate. These solutions hold equally at membrane hydrogen separation. Now these solutions may be any conceivable solution of Eq. (22). For mathematical simplicity, reduction of Eq. (22) to linear equation is used.

For membrane gas separation the square root of Eq. (22) can be expanded into a Taylor's series. In this case, Eq. (22) takes the form

$$\varphi'(x) = \frac{2\left(1-\frac{1-c_0}{1-(\alpha+1)\varphi(x)}\right)}{2\left(1-\frac{1-c_0}{1-(\alpha+1)\varphi(x)}\right)^{\frac{1}{2}}\left(\frac{\Lambda_1 M_1}{\varepsilon\delta_{\mathrm{m}}}\sqrt{\frac{p_0}{\rho}}\right)^{-1} + \frac{1-c_0}{1-(\alpha+1)\varphi(x)}\frac{5\alpha+17}{2(\alpha+5)(\alpha+7)}\mathrm{Pe_D}\varepsilon}. \qquad (23)$$

The integral equation of the hydrogen permeation rate (21) can be converted to the ordinary nonlinear differential equation of first order in separable variables (23). It is solved by the Runge–Kutta method of fourth order.

To check the developed method of calculation of the gas separation numerical and experimental data is compared. The experiments on separation of hydrogen from synthesis-gas are produced by Laboratory of Membrane Mass Transfer of the A.V. Luikov Heat and Mass Transfer Institute of the National Academy of Sciences of Belarus using the experimental testing membrane type set with the replaceable working elements that are tubular palladium-nickel membranes. A satisfactory agreement of the calculation results and experimental data is observed. It makes the model more adequate to the processes taken place in the practice. The model can be used for gas separation process modeling in metal semipermeable membrane elements under the conditions that degree of gas dissociation at adsorption on the surface of metal membrane is 1/2.

3.2. The influence of temperature on process of hydrogen separation from synthesis-gas

In present work the influence of temperature on prosess of hydrogen separation from synthesis-gas (hydrogen ranges 0.25 mass fraction, carbon monoxide ranges 0.75 mass fraction) is investigated . Temperature is the most important factor that determines the viscosity of gas, diffusion, hydrogen penetrability coefficient, and as a result, the hydrogen penetration rate through metal membrane. It has been estimated that hydrogen penetrability coefficient is described by Arrhenius theory. The theoretical researches are carried out for $Pd_{3.18}/Ni_{96.82}$ membrane. The inconsistency of the temperature effect is observed (Fig. 4). It has been established that the temperature rise increases convective external diffusion resistance. This is one of the reasons why degree cleanliness of retentate decreases and retentate requires afterpurification. Alternatively, the inverse effect is observed. Since the hydrogen penetrability coefficient dependences on temperature, the output of hydrogen increases.

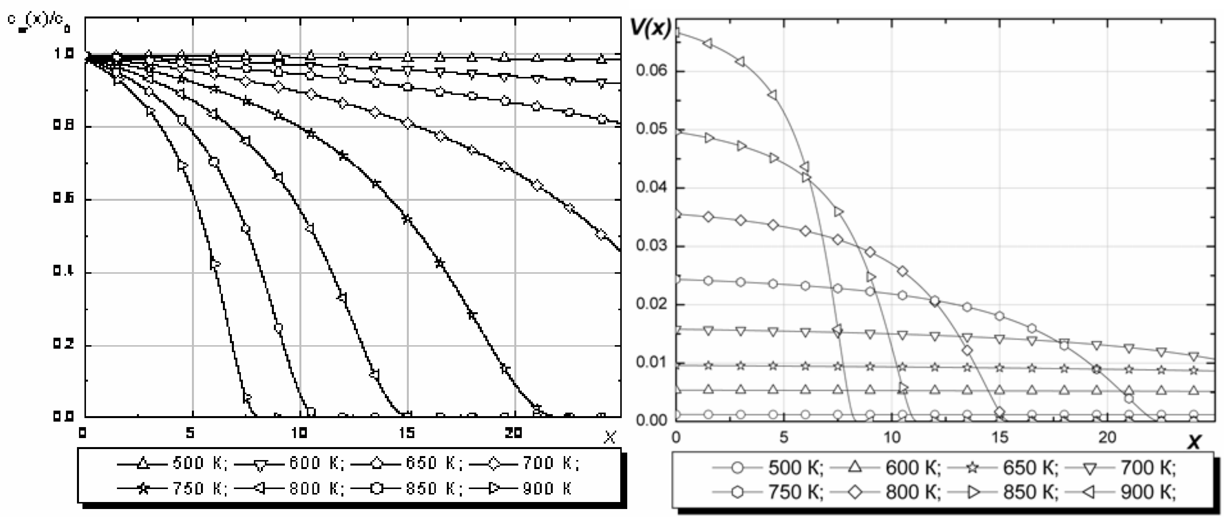

a b

Fig. 4. Concentration of hydrogen on the Pd-Ni membrane surface (a) and hydrogen permeation rate (b) vs. longitudinal coordinate for different temperature (c_0=0.25 mass fric., $\overline{p}$=1.5 MPa, u_0=0.05 m/s)

It should be kept in mind in research that the state of Pd-based membrane depends strongly on its mechanical, chemical, and thermal properties. Research has shown that membrane can be deformed by heat load case of a long time operating.

4. CONCLUSIONS

1. A mathematical model that describes the process of hydrogen separation from synthesis-gas in a unit on the basis of metal membrane with account for convective external and intramembrane diffusion resistances, degree of hydrogen dissociation at adsorption on the surface of metal membrane has been developed.
2. A semi-integral method for investigating the conjugate problem of hydrogen mass transfer through metal membrane and mass exchange in head channel is suggested.
3. The procedure of calculation of the hydrogen permeation rate has been proposed taking into account external diffusion convective and intramembrane diffusion resistances, degree of hydrogen dissociation, the physical properties of synthesis-gas, the physiochemical properties of membrane, the technological parameters of the process and the geometry and dimensions of the membrane unit.
4. The inconsistency of the temperature effect is observed. Such approach ultimately will make it possible to develop a highly efficient membrane apparatus.

5. ACKNOWLEDGEMENT

This work was carried out with support by the National Academy of Sciences of Belarus through the project “Hydrogen-08”. The author is grateful to Prof. V.I. Baikov for useful discussions of results.

REFERENCES

1. AMOSOVA, O.L., MALYKH, O.V., TEPLJAKOV, V.V. Integrated membrane/PSA method for hydrogen recovery from multicomponents gas mixture of biotechnology and petrochemistry. *Membranes*, 2008, Vol. 38, No 2, p. 26–39.
2. *Separation Technology R&D Needs for Hydrogen Production in the Chemical and Petrochemical Industries* // A Chemical industry Vision 2020 Initiative to help identity future R&D needs – Link to the internet <http://www.chemicalvision2020.org/pdfs/h2_report.pdf, 2005>.
3. BAZILE, A., GALLUCHCHI, F., YULLIANELLI, A. Researches of Institute membrane technologies (National centre of science of Italy ITM-CNR) on reception of hydrogen in membrane plants. *Membranes*, 2007, Vol. 34, No 2, p. 3–22.
4. MULDER, M. *Basic principles of membrane technology*. Kluwer Academic Publishers, 1996.
5. DYTNERSKII, YU.I., BRYKOV, V.P., KAGRAMANOV, G.G. *Membrane Separation of Gases*. Moskow: Khimiya, 1991.
6. CARAVELLA, A., BARBIERI, G., DRIOLI, E. Concentration polarization analysis in self-supported Pd-based membranes. *Separation and purification technology*, 2009, Vol. 66, p. 613–624.
7. BAIKOV, V.I., KOSTAREVA, I.YU., PRIMAK, N.V. Theory of membrane separation of binary gas mixtures. *Journal of Engineering Physics and Thermophysics*, 2004, Vol. 77, No 5, p. 999–1004.
8. BAIKOV, V.I., PRIMAK, N.V. Membrane selective separation of binary gas mixtures. *Journal of Engineering Physics and Thermophysics*, 2007, Vol. 80, No 2, p. 382–387.
9. BERMAN, A.S. Laminar flow in channels with porous walls. *J. Appl. Phys.*, 1953, Vol. 24, No 9, p. 1232–1235.
10. EROSHENKO V.M., ZAICHIK, L.I. *Hydrodynamics and Heat- and Mass Transfer on Permeable Surfaces* . Moscow: Nauka, 1984.
11. BOSE, A.C. [et al.] *Inorganic Membranes for Energy and Environmental Applications*. DOI 10.1007/978-0-387-34526-0 10, Springer Science + Business Media, LLC 2009.
12. REID, R.C., PRAUSNITS, J., SHERWOOD, T.K. *The properties of gases and liquids.* Leningrad: Khimiya, 1971.

INVESTIGATION OF Mg-Ti THIN FILMS HYDRIDING KINETICS

S. Tuckute, M. Lelis
Faculty of Nature Sciences, Vytautas Magnus University
Vileikos str. 8, Kaunas, LT-44404 – Lithuania
Phone: +370 37 327 910
Email: s.tuckute@gmail.com

D. Milcius, M. Lelis, R. Motiejuniene
Centre for Hydrogen Energy Technologies, Lithuanian Energy Institute
Breslaujos str. 3, Kaunas, LT-44403 – Lithuania
Phone: +370 37 401909
Email: milcius@mail.lei.lt

ABSTRACT

Magnesium hydride is a promising material for hydrogen storage but the slow hydriding and dehydriding kinetics limit its practical application. Identification of effective catalyst is a subject of great interest in developing MgH_2 system as a potential hydrogen storage medium. A thin layer of Ti acts as a catalyst. The main emphasis of this study was to investigate Mg–Ti–H system hydrogenation properties. For this purpose nanocrystalline Mg-Ti films were deposited onto quartz substrates using magnetron co-sputtering technique and hydrogenated at 10 bar H_2 pressure in the temperature range from 200 up to 300 °C during 6 h. The synthesised samples were characterized by X-ray diffraction, and surface morphology were observed by means of scanning electron microscopy (SEM).The experimental results show that the growth of the initial hydride layer may be blocked by the surface oxide barrier layer formed during hydrogenation. The growing hydride phase in the bulk generates stresses that induce cracks and holes in the oxide barrier formed during the initial stages of hydrogenation, and hydrogen release.

Keywords: Mg-based hydride, Coupling, Thin films, Hydrogen storage

1. INTRODUCTION

Hydrogen is considered to be one of the most attractive clean energy sources of the future energy and transport system. In this context the hydrogen storage is one of the key challenges in developing hydrogen economy. The common storage methods such as high-pressure gas or liquid hydrogen storage cannot fulfil future storage goals. On the other hand chemical or physically combined storage of hydrogen in other materials has potential advantages over traditional storage methods [1]. Many metals and metal alloys can safely store hydrogen, but in most cases hydrogen storage capacities are considerably low (<3 wt.%). Among them magnesium is one of the most attractive and promising material for hydrogen storage applications because it has high hydrogen capacity (~7.6 wt% by weight, and 150 kg H_2 m^{-3} by volume), it also benefits of being light weight, low cost, innoxiuos and rich in natural resources. In general, the magnesium hydride, MgH_2, is synthesised by a chemical reaction of Mg with hydrogen under 573–673 K and 10–400 bar [2]. So in practice this way to produce MgH_2 is not effective, because the enthalpy of MgH_2 formation is very high (−76 kJ/mol H_2), furthermore, it requires temperatures in excess of 573 K (high reaction temperature) to decompose it into H_2 and bulk Mg [3] and slow hydriding–dehydriding kinetics limit its applications and hence seriously hinder its development. Activation barrier for the H_2 desorption is considerably high (0.38 eV) due to the ionic-like character of the Mg–H bonding [4]. The results indicate that this Mg–H interaction is related to the thermodynamic stability of MgH_2. To solve these problems, it has been reported that doping Mg with a transition metal can weaken the Mg–H bond and reduce the stability of the hydride, thus promoting the hydrogenation/dehydrogenation performance of Mg [3]. In order to investigate the kinetics of magnesium hydride in this work it was decided to use magnetron sputtering technology and to deposit Mg-Ti thin films.

The Mg-Ti system was chosen for two reasons. Firstly, we expected that adding of titanium catalyst will help to improve the hydrogenation kinetics. Secondly, it is expected that titanium should work as destabilising agent for magnesium hydride, therefore, dehydrogenation should take step at lower temperature.

The others authors studies reported promising results, such as improved kinetics, however, the state-of-the-art materials are still far from meeting the aimed target for their transport applications. Therefore, further research work is needed to achieve the goal by improving development on hydrogenation, thermal and cyclic behaviour of metal hydrides [1].

It was expected by this study to show that using complex Mg and Ti alloys can improve hydrogen kinetics for more economical applications.

2. EXPERIMENTAL METHODOLOGY

The 1.2 μm thick Mg-Ti films were deposited on quartz substrates using a physical vapour deposition system equipped with two independent DC magnetron sputtering sources. The purity of Ti and Mg targets was 99.95% and each target disk was of 100 mm in diameter. Magnetrons were placed at a distance of 6 cm (Mg) and 12 cm (Ti) in front of the sample holder which was biased by negative voltage of -100 V. The bias voltage was used to extract positive Ar^+ ions from surrounding plasma and to initiate additional bombardment of sample which improves relaxation of the growing film (better crystallinity and lower micro strains). Before each experiment vacuum system equipped with mechanical and diffusion pumps enabled to reach a base pressure of $2x10^{-3}$ Pa. Afterwards, Ar (99.999%) gas was injected to the vacuum chamber and its flow rate was controlled to keep a constant pressure of 0.3 Pa. Then prior to the thin film deposition process, sputtering targets were pre-cleaned for 5 minutes with keeping shutter closed. Finally, the co-deposition of Mg and Ti was performed for 3 min.

Further details about the deposition parameters can be found in Table 1.

Table 1. Parameters for the deposition of Mg-Ti coatings by reactive dc magnetron sputtering

Cathode	Mg	Ti
Substrate	quartz	
Distance between the target and substrate, cm	6	12
Magnetron voltage, V	400	365–370
Magnetron current, A	1.4	0.8
Gas	Ar	
Working pressure, Pa	0.3	
Deposition time, s	180	

Subsequently the samples were exposed in air and moved into a stainless steel chamber for hydrogenation. The set-up was cleaned with a flow of high purity (99.999%) hydrogen before loading. The series of samples deposited at the same conditions were hydrogenated at 8 bar hydrogen pressure for 6 hours at different temperatures of 200 °C, 220 °C, 240 °C, 260 °C, 280 °C and 300 °C. The sample temperature was measured and adjusted by using a chromel-alumel thermocouple attached to the outside wall of the hydrogenation cell. The heating rate was around 5 degrees per minute, hydrogenation time – 6 hours, cooling down was a passive process and took around 3-4 hours.

Structural and microstructural analysis of the magnesium–titanium samples before and after the hydrogenation was performed by X-ray diffraction (XRD) and scanning electron microscopy (SEM). The XRD experiments were carried with the 2Θ angle diffractometer (Bruker D8 Discover) in the range of 20–70° using CuKα radiation in steps of 0.02°. After the XRD structural analysis was done the microstructural and morphological investigations were performed in JEOL JSM5600 scanning electron microscope.

3. RESULTS AND DISCUSSIONS

3.1. XRD analysis

Fig. 1. shows a representative XRD pattern of the synthesised Mg-Ti sample and data base references for pure elemental ingredients (pure Mg and pure Ti). The single observed diffraction peak with intermediate peak position (between Mg and Ti) before hydrogenation (Fig. 1) confirms that the starting material embodies single crystalographic phase of Mg with Ti atoms dissolved in its matrix.

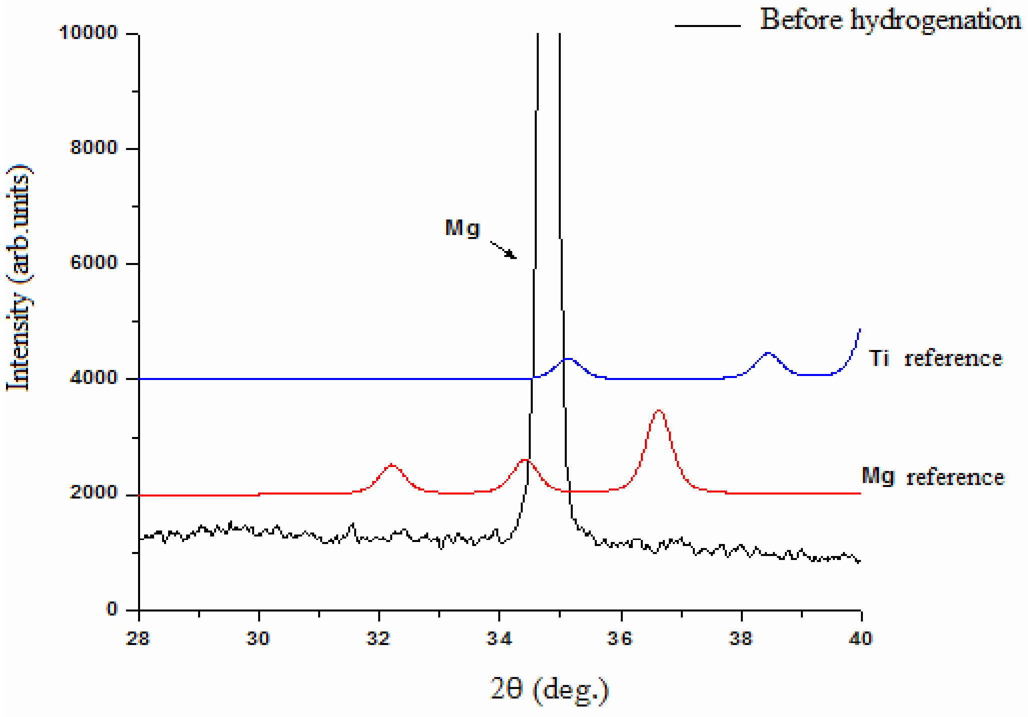

Fig. 1. X-ray diffraction patterns of Mg-Ti films before hydrogenation

Representative interval of X-ray diffractograms of sputter deposited Mg-Ti films hydrogenated at different temperatures are shown in Fig. 2. The general trend shows that the intensity of the MgH_2 (110) peaks grows with the increase of temperature of the hydrogenation, whereas intensity of initial Mg peak is decreasing. However, there are several points to be stressed. First of all, we can see that at the lowest hydrogenation temperature (200 ^{0}C) no hydride phase formation is observed, thus evidently hydrogen did not pass the activation energy barrier for one or several reaction steps consisting of surface penetration, bulk diffusion, nucleation and agglomeration. As one would expect the increase in hydrogenation temperature should allow overcoming potential barriers. Indeed, when sample is hydrogenated at 220 ^{0}C a new peak corresponding to t-MgH_2 (1 1 0) appears. The intensity of later peak is even increased for the next temperature level (sample hydride at 240 ^{0}C) and the increase of peak intensity is natural and reasonably expected as higher temperature results in better chances for hydrogen to overcome activation energy barriers. But this prediction is already broken for sample hydrogenation at 260 ^{0}C as intensity of t-MgH_2 (1 1 0) peak is decreased. Furthermore, we can see that for this temperature another crystallographic orientation (1 0 1) is much more favourable. Surprisingly, additional increase of the hydrogenation temperature up to 280 ^{0}C makes (1 1 0) more favourable again. Moreover, we observe very steep increase peak intensity. The XRD profile of sample hydrogenated at T = 300 ^{0}C shows MgH_2 (1 1 0), MgO (2 0 0), MgH_2 (2 2 0) and MgO (2 2 0) peaks from the hydride Mg-Ti film and no traces of Mg. Therefore, after the hydrogenation process at 300 ^{0}C temperature, thin film is completely hydrogenated. At this hydrogenation temperature the energy of arriving hydrogen is enough to effectively overcome activation energy barrier effects in Mg-Ti-based films. We also observe that MgO oxides formation begins at about 300 ^{0}C. This could be explained that at highest investigated temperature, oxygen is released from the walls of hydrogenation chamber. On the other hand minor amounts of oxygen may come from the film interaction with the quartz substrate, giving it reacted with Mg forming MgO.

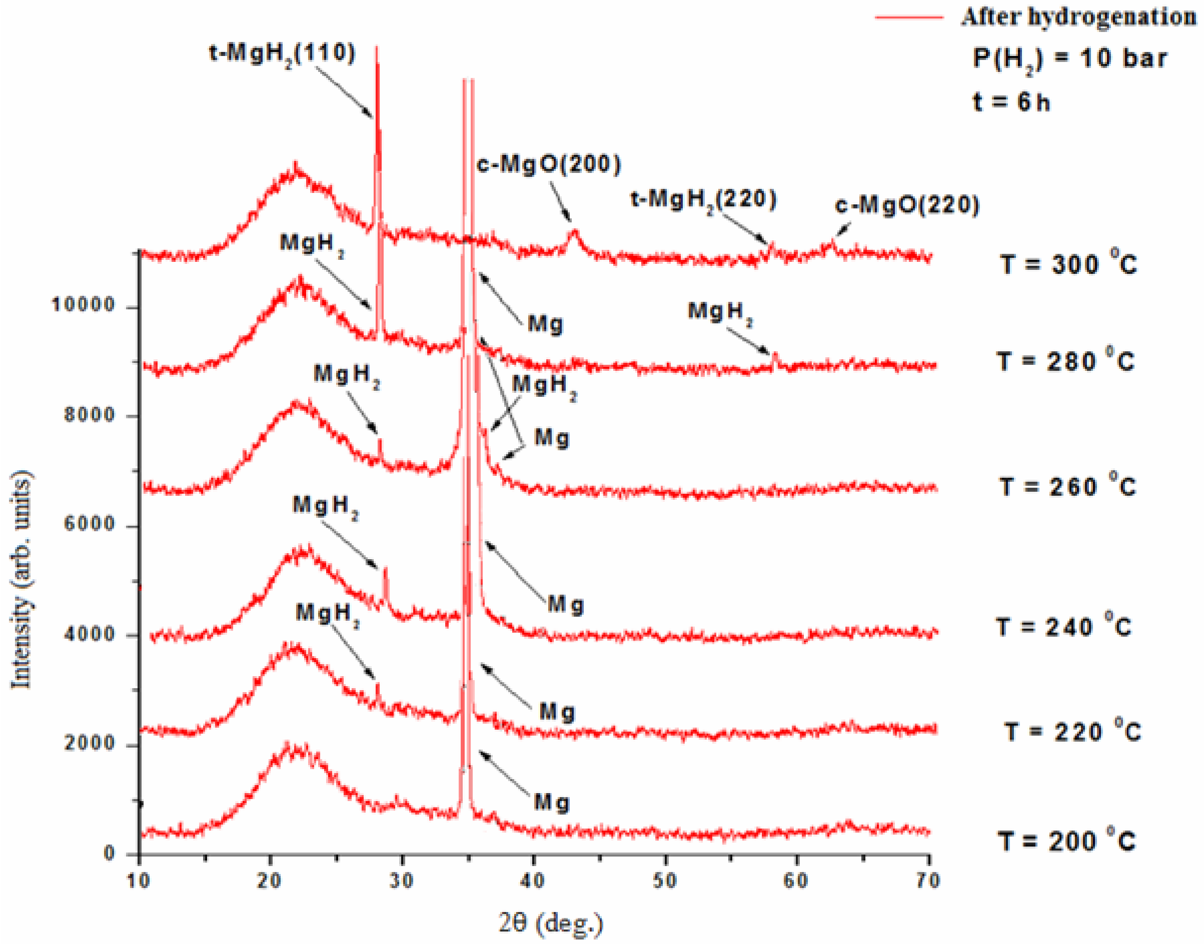

Fig. 2. The representative interval of XRD diffractograms of Mg-Ti films after hydriding at different temperatures: 200 °C, 220 °C, 240 °C, 260 °C, 280 °C and 300 °C for 6h

3.2. SEM analysis

The surface morphology was investigated by SEM in the as-deposited state and after different temperatures of hydrogenation. Fig. 3a - f and Fig. 4a – f shows SEM micrographs of magnesium (with titanium impurities) hydride before and after hydrogenation at different temperatures, respectively. As it is stated bellow the changes of surface topography provides us with complementary information about the phenomena observed in X-ray diffractograms.

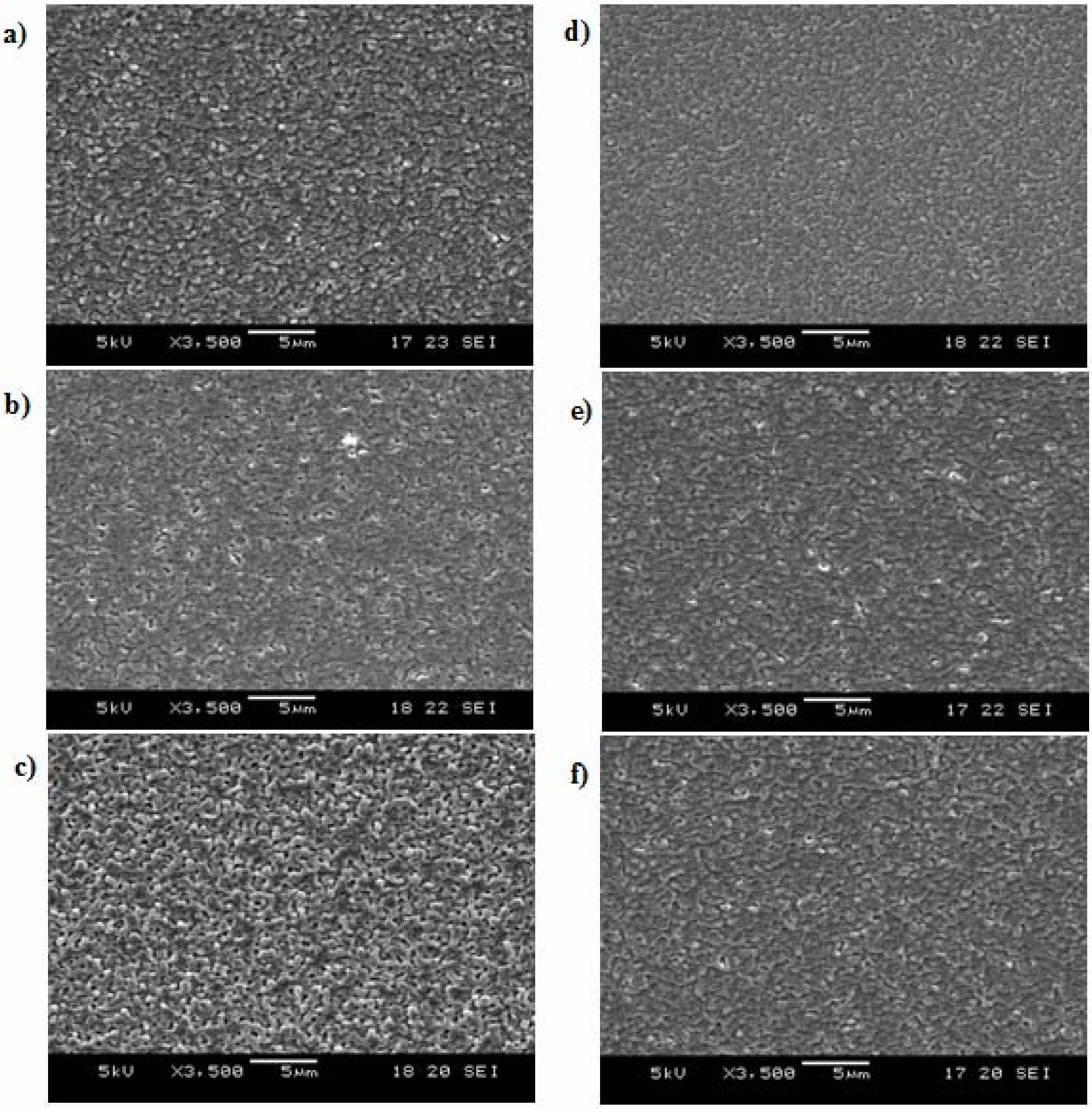

Fig. 3. SEM surface views of as deposited Mg–Ti films (deposition conditions kept constant)

As shown in Fig. 3. a-f, the as-deposited Mg-Ti films are not homogenously dense and consists of great number of micropores ranging up to 100 nm in diameters. The micropores form a sponge type structure which provides affective channels for hydrogen transport from film surface to the bulk. No major difference between individual sample surface morphology was observed.

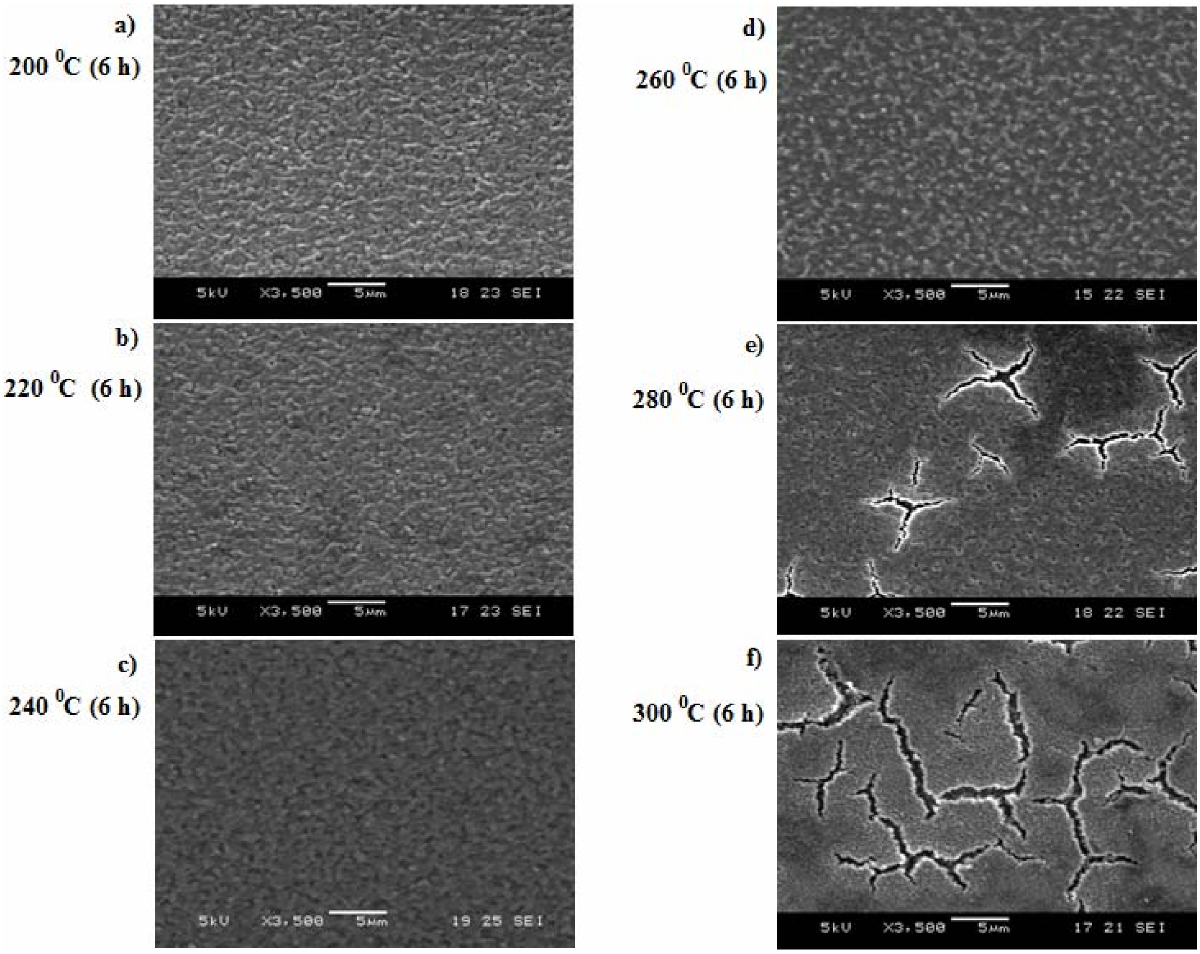

Fig. 4. SEM surface views of Mg–Ti films after different temperatures of hydrogenation: a) 200 ^{0}C, b) 220 ^{0}C, c) 240 ^{0}C, d) 260 ^{0}C, e) 280 ^{0}C and f) 300 ^{0}C for 6 h.

The SEM images after hydrogenation are shown in Fig. 4. a-f. After hydrogenation at 200 ^{0}C temperature Mg-Ti film demonstrates surface which is comparable to the images from as-deposited films. For the hydrogenation temperatures of 220–260 ^{0}C the SEM images shows a slow transition from initial microporous towards dense surface structure. Meanwhile, for the higher temperatures (280-300 ^{0}C) we observe formation of cracks. The amount and size of cracks is higher at 300 ^{0}C. It is well known that Mg tends to disintegrate due to volume expansion upon hydrogenation. In the case of Mg thin films; this phenomenon is accompanied by the formation of cracks of the layers because of the build up of compressive stresses during the hydrogenation process [5]. These SEM observations can be explained by following model:

i) initial Mg-Ti films consists of great amount of micro cracks, which provide very efficient channels for hydrogen transport, however, at lowest investigated temperature the energy of arriving hydrogen is too low to overcome the surface barrier and almost no hydride formation is observed;

ii) increase of the hydrogenation temperature up to 220-240 ^{0}C provides enough energy for hydrogen to overcome surface barrier, therefore it penetrates several atomic surface layers and nucleation of MgH_2 starts, however, the hydrogenation is not fast as hydrogen diffusion through MgH_2 is limited by even higher activation energy then throughout pure Mg;

iii) apart from the mentioned effects, increase of the temperature induce mass transport effects in the film which finally results in final “closing” of the micropores at hydrogenation at 260 ^{0}C (indications are already visible at 220-240 ^{0}C;

iv) at 280–300 ^{0}C temperature the hydrogen energy is enough to effectively diffuse through MgH_2 phase and hydride of the film proceeds much faster. At this point hydrogenation works as reaction self-catalyst because transition from metal to hydride phase also introduce huge stresses and produce cracks which helps hydrogen to diffuse into the bulk. Surface deformations and lattice stresses are well known to accelerate the H diffusion process [6]. It also enhances fracturing and particles size reduction, resulting in an increase of the specific surface for hydrogen adsorption.

Another confirmation for the proposed model can be found in SEM cross-section images. As shown in Fig. 5, the cross-sectional SEM reveals a typical columnar structure of Mg-Ti film after hydrogenation with a mean height h ≈ 1.2 µm. For 200 ^{0}C and 280 ^{0}C temperatures columnar structure includes many well defined boundaries which are open and may serve as channels for the transportation of hydrogen from the surface into the bulk, whereas, for 240 ^{0}C the structure is denser.

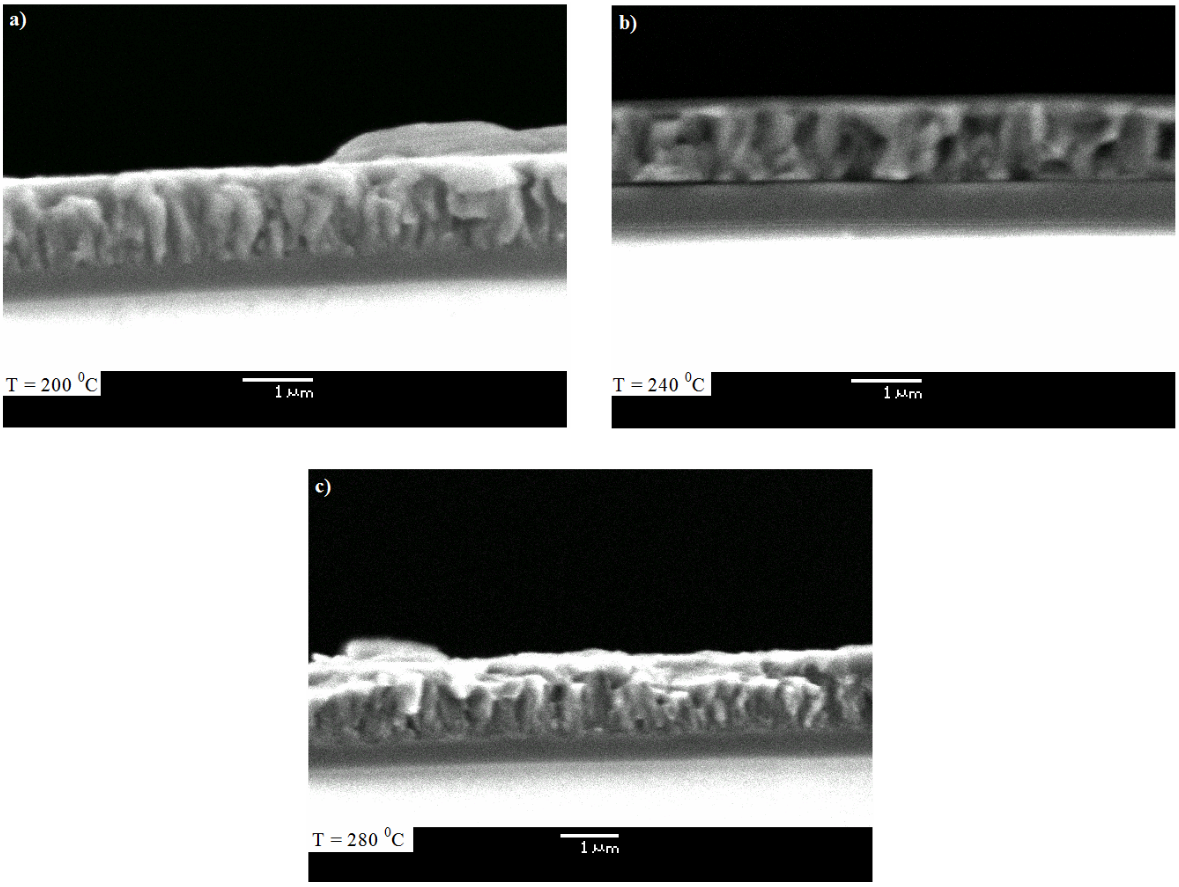

Fig. 5. Typical cross-sectional view SEM images of Mg-Ti films on quartz substrates after hydrogenation at different temperatures: a) 200 ^{0}C, b) 240 ^{0}C and c) 280 ^{0}C

4. CONCLUSIONS

In the present work we successfully synthesised Mg-Ti thin film samples with single crystallographic phase. Investigation of these samples hydrogenated at various temperatures has showed dissimilar behaviour at different temperatures. We were able to identify three temperature zones T < 240 ^{0}C, T ~ 260 ± 20 ^{0}C and T > 280 ^{0}C which activates different hydrogenation affects. The exact mechanisms of such different behaviour is not clear, however, received results allowed to propose a hydrogenation model based on different routes for hydrogen transport from surface to the bulk. Differences of the discussed activation energies lead to the non-linear changes in hydrogenation kinetics during temperature increase.

5. ACKNOWLEDGEMENT

This work was supported by Nordic Energy Research under Contract 06-Hydr-C15-Nordic Center of Excellence on Hydrogen Storage Materials.

REFERENCES

1. SAKINTUNA, B.; LAMARI-DARKRIM, F.; HIRSCHER, M. Metal hydride materials for solid hydrogen storage: A review. *International journal of hydrogen energy*, 2007, Vol. 32, No 9, p. 1121–1140.
2. STAMPTER, J.F.; HOLLY. C.E.; SHUTTLE, J.F. Alloying effects of transition metals on chemical bonding in magnesium hydride MgH2. *Acta Materialia* 2004, Vol. 52, No 2, p. 521–528.
3. POZZO, M.; ALFÈ, D. Hydrogen Dissociation and Diffusion on Transition Metal(=Ti,Zr,V,Fe,Ru,Co,Rh,Ni,Pd,Cu,Ag)-doped Mg(0001) Surfaces. *International Journal of Hydrogen Energy*, 2009, Vol. 34, No 4, p. 1922–1930.
4. ZEPPELIN, Von F.; REULE, H.; HIRSCHER, M. Hydrogen desorption kinetics of nanostructured MgH_2 composite materials. *Journal of Alloys and Compounds*, 2002. Vol. 330-332, p. 723–726.
5. FERRERI, R.D.; SRIDHARAN, M.G.; GARCIA, G.; PI,F. and VIEJO, J.R. Hydrogenation properties of pure magnesium and magnesium–aluminium thin films. *Journal of Power Sources*, 2007, Vol. 169, No 1, p. 117–122.
6. BOBET, J.-L.; EVEN, C.; NAKAMURA, Y.; AKIBA, E.; DARRIET, B. Synthesis of magnesium and titanium hydride via reactive mechanical alloying Influence of 3d-metal addition on MgH2 synthesize. *Journal of Alloys and Compounds*, 2000, Vol. 298, No 1–2, p. 279–284.

CYSENI 2010, May 27–28, Kaunas, Lithuania
ISSN 1822-7554, www.cyseni.com

WATER ELECTROLYSES POWERED WITH INDUCTIVE SPIKES

M. Vanags, J. Kleperis, G. Bajars
Institute of Solid State Physics of University of Latvia
Kengaraga 8, LV-1006 - Latvia
Phone: +371-67262145
Email: sf11053@gmail.com

ABSTRACT

Special power supply based on inductive spikes (kick-back voltage impulses) is made for water electrolysis cell. Different electrodes and electrolyte solutions were tested. The voltage and current characteristics are measured as oscillogramms, from which the double layer charge time is calculated and efficiency of electrolysis estimated. Separate current and voltage pulses on oscillogramms were integrated to calculate power in one pulse and to estimate efficiency. It is determinate, that charging time of double layer between electrode and electrolyte solution isn't dependent from an area and material of the electrode. Nevertheless, using direct, not kick-back voltage pulses, the dependence from an area and material of the electrode is clearly observed. This mean that the length of kick-back voltage pulses is so small (microsecond) that no additional double layer is formed between electrode and solution. It is proved that efficiency of electrolysis is higher for kick-back voltage powered cell, as for traditional DC electrolysis. Efficiency isn't dependent from supplied power when electrolysis is made with kick-back voltage pulses, because DC constituent is quit small, and is independent from material of the electrode.

Keywords: hydrogen evolution reaction, kickback voltage, pulse electrolyses

1. INTRODUCTION

Hydrogen is considered to be best energy carrier in future [1]. Hydrogen is main constituent in Universe, but available only in compounds on the Earth. Nevertheless hydrogen could be produced, stored and consumed in several ways, including direct burning. But the most efficient is hydrogen chemical burning in fuel cell due high theoretical efficiency, reaching 83% for hydrogen's higher heating value and 94.5% for lower heating value [1]. The European Commission has established a Hydrogen and Fuel Cell Technology Platform to facilitate and accelerate the development and deployment of cost competitive world class European Hydrogen and Fuel based energy systems and component technologies for application in transport, stationary and portable power [2].

One of the main problems to be solved is the high cost of hydrogen [1]. Water electrolysis is known more than 130 years already, and different technologies are developed giving power consumption around 3.6 kWh/m^3 (high temperature electrolysis) and 4.1 kWh/m^3 (room temperature alkaline electrolysers and proton exchange membrane electrolysis) [3]. Lower hydrogen production costs is for technologies using closed thermo-chemical cycles, but only in places where huge amount of waste heat is available (for example, nuclear power stations [3]).

Nevertheless what will be the hydrogen price today, in future only hydrogen obtained from renewable resources using electricity from renewable energy sources will save the World, – as it was stated in 2nd World's Hydrogen Congress in Turkey (see for example [4]). For Latvia the hydrogen obtained in electrolysis using electricity from renewables (wind, Sun, water) also would be the best solution to move to Hydrogen Economics [5]. That is because all renewables (wind, Sun, water in rivers) in Latvia's geographical situation are giving non-stable and interrupt power, for which the storage solutions are necessary. Usage of hydrogen as energy carrier to be produced from electricity generated by renewables, stored and after used in fuel cell stack to generate electricity is the best solution. Efficient and stable electrolysers are required for such purposes. Smaller electrolysis units are necessary also for technical solutions were hydrogen is produced and used directly on demand, for example, hydrogen welding devices [6], hydrogen powered internal combustion cars [7].

Direct current (DC) power typically is used for electrolysis, nevertheless pulse powering also is proposed [8]. Using a mechanically interrupted DC power supply, [9, 10] Bockris et all noticed next interesting phenomena: immediately upon application of voltage to an electrochemical system, a high but short – lived current spike was observed. When the applied voltage was disconnect, significant current continues to flow for a short time. In 1985, Ghoroghchian and Bockris [11] designed a homo-polar generator to drive an electrolyser on pulsed DC voltage. They concluded that the rate of hydrogen production would be nearly twice as much as the rate for DC. Our previous researches [5, 12] also has shown that the application of short and high voltage pulses yields the highest possible electrolyses current and even reach step charging effect [12]. The dynamics of current and voltage, when inductive kickback voltage (IKV) pulses are used to power electrolysis cell with steel electrodes and KOH solution, we described previously [5, 12].

In this work the response of electrochemical cell to IKV pulses is investigated. Special cell was constructed to allow the change of distance between electrodes.

2. EXPERIMENTAL SETUP

Self-made electrolysis cell was used in experiments (Fig. 1). It is made from polyacetal corp with two stainless steel SUS316L electrodes. One electrode is fixed but second is moving and connected to micro-screw. Special sealing holes are made to avoid micro-screw holder material to contact electrolyte. Before experiments sealing holes are filled with isolating mastic. Electrochemical cell is in a form of hollow with diameter 40 mm, but steel electrodes are squares with area 2 cm^2. Before experiments electrodes were mechanically polished and washed with acetone and deionised water. As electrolyte the KOH solution with concentrations 0.1–0.5 M are used. During experiments the distance between electrodes was varied from 1 to 5 mm.

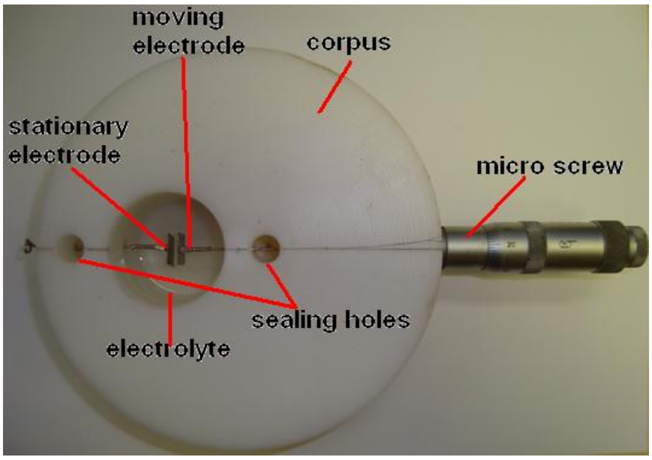

Fig. 1. Experimental cell design

IKV pulses were generated with an electric circuit (Fig. 2) consisting from pulse generator, DC power source, field transistor BUZ350 and blocking diode. Special transformer is wound as bifilar from two wires twisted together. Square pulses from generator are used to conduct field transistor, connected in series with DC power source. Obtained voltage pulses powers the primary winding in bifilar transformer. After each square pulse in this broad band bifilar transformer very sharp and high kick back pulse with opposite polarity is induced in secondary winding of transformer due to the collapse of magnetic field induced in the coil. Pulses of induced kickback voltage are directed through blocking diode and resulting high voltage pulses with width around 1 μs are used to power electrolysis cell. Two beam oscilloscope GWinstek GDS-2204 is used to register voltage and current (voltage drop on an etalon resistance) in circuit powering electrolysis cell.

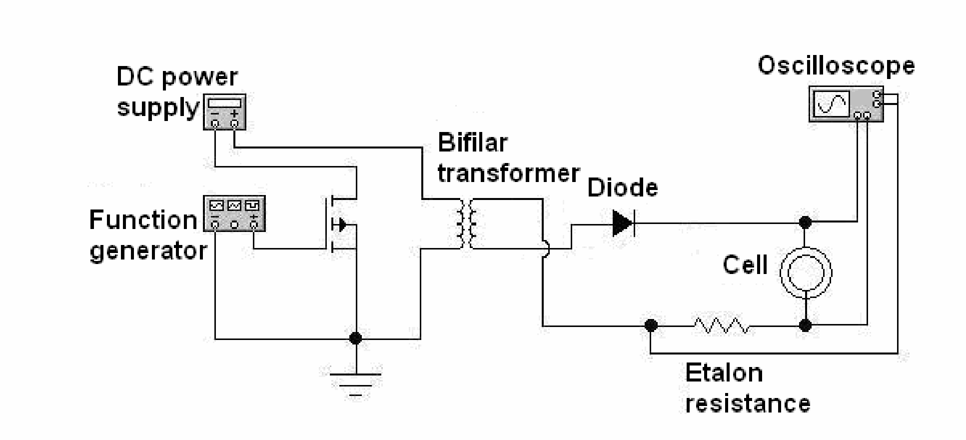

Fig. 2. Experimental circuit for generation of inductive kickback voltage pulses IKV

3. RESULTS AND DISCUSSION

Next regularity is seen in oscillograms of voltage pulses for steel electrodes at variable distances in deionised water (Fig. 3) – as larger the distance between electrodes, as higher amplitude of pulse.

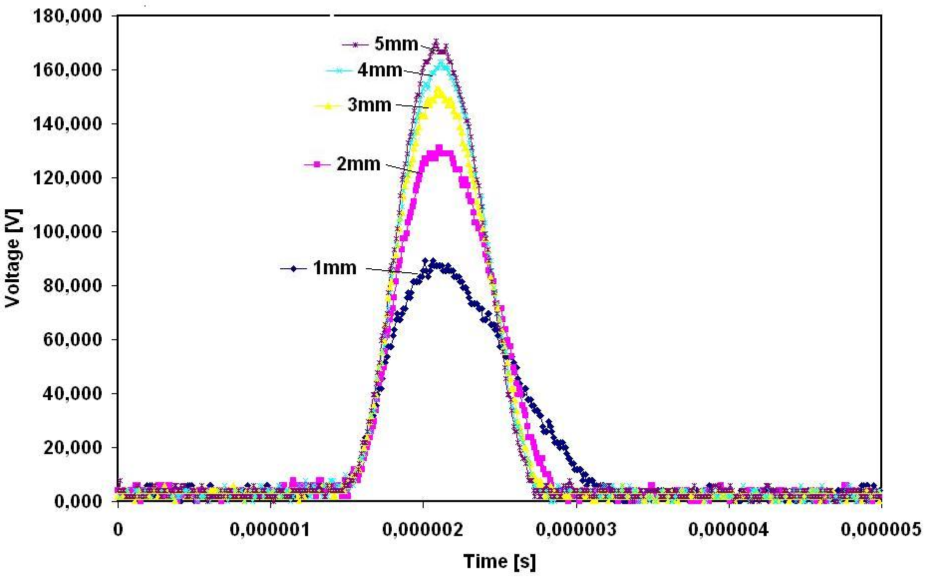

Fig. 3. Voltage pulses on steel electrodes in deionised water

For one distance between electrodes the pulses of current and voltage (Fig. 4) does not match in time – the current is ahead the voltage as it is on capacitive element.

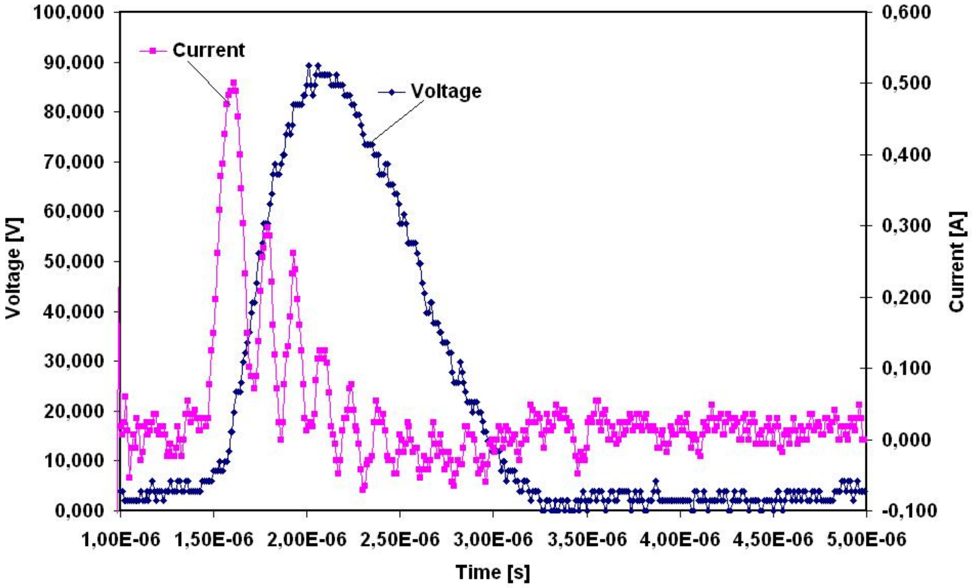

Fig. 4. Voltage and current pulses on steel electrodes (distance 1 mm) in deionised water

Voltage oscillograms of steel electrodes in KOH solution differs very much from oscillograms in deionised water (Figure 5). Pronounced first charging pulse is observed with next long discharge tail. From the distance between electrodes only amplitude of registered voltage pulse changes, the forms are equal. Also the change of electrolyte concentration does not influence the form of pulse, only amplitude decreases with increasing concentration.

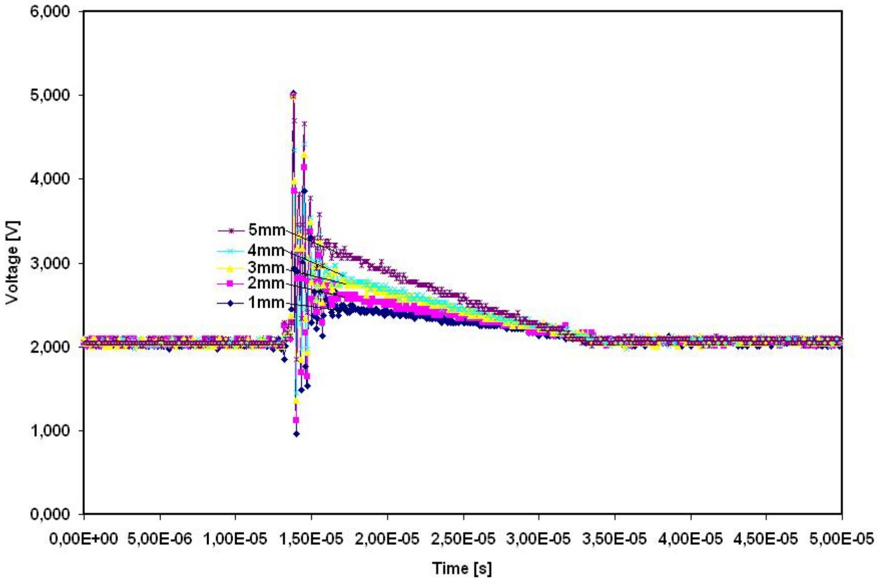

Fig. 5. Voltage pulses on steel electrodes in 0.3 M KOH solution

For one distance between electrodes in 0.3 M KOH electrolyte the pulses of current and voltage (Fig. 6) match in time and are with similar behaviour – sharp charging peak followed with long discharge tails. Only in deionized water there are no tails as for voltage as well as for current pulse.

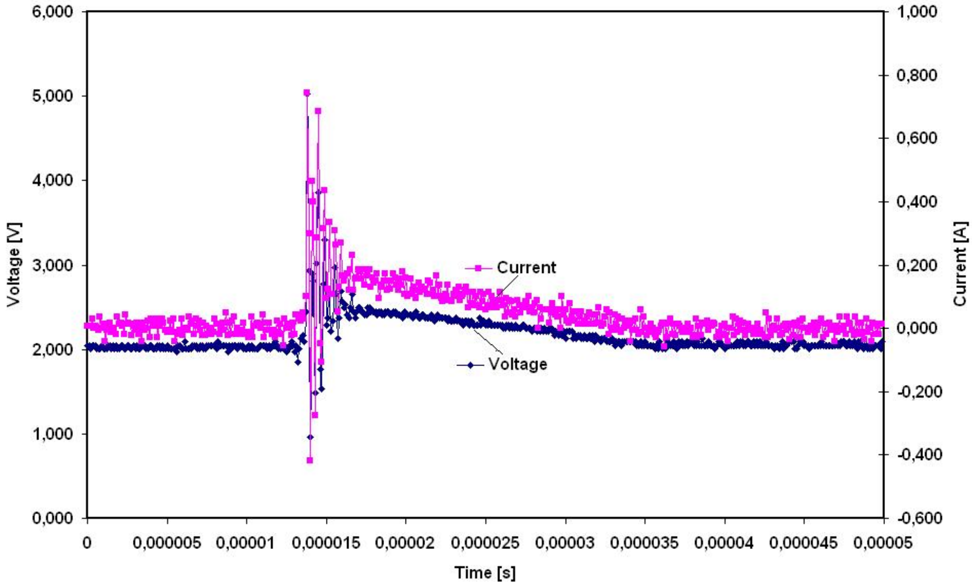

Fig. 6. Voltage and current pulses on steel electrodes (distance 0.1 mm) in 0.3 M KOH solution

The concentrations of H_3O^+ and OH^- ions in deionized water are quit small. The amplitude of voltage increases when the distance between electrodes increases. As it can be noticed from Fig. 3, the falling front of voltage pulse is extended only when the distance between electrodes is 1 mm. In such small distance also small concentrations of H_3O^+ and OH^- ions can influence the voltage pulse. But in KOH solutions when concentrations of K^+, H_3O^+ and OH^- ions are high, the pulse tails are very long. This encourages an idea that at higher concentrations of ions in electrolyte, the hydrogen evolution reaction on steel electrode occurs. The tail of voltage and current pulse characterize the intensity of hydrogen evolution process but first sharp peaks could be connected with charging of double layer. The chain of events in an electrolysis process could be next: immediately with applying pulse the double layer charging starts, and after about 1.5 μs the voltage drop begin. Nevertheless blocking diode in power circuit (Fig. 2) prevents the voltage drop. Only way to decrease the voltage is through hydrogen evolution reaction. This reaction must be very effective because the double layer charging occurred when current and voltage were displaced in phase, what later transformed to hydrogen discharge reaction.

Comparing calculated values of energy and charge in separate pulses (Table 1) it can be seen that pulse energy is approximately equal for all concentrations of KOH solutions – about 6 μJ. Pulse charge for KOH solutions also is constant – about 2 μC, while differs very much from value for deionized water.

The energy used in power circuit during one pulse is compared with energy generated by IKV on an electrolysis cell (Table 2). As it is seen, the power generated by IKV pulse is higher as energy used in power circuit.

Table 1. Calculated values of energy and charge in pulses at all measured situations

Solution concentration	Space between electrodes [mm]	Pulse energy [μJ]	Pulse charge [μC]
Dejonised water	1	4.82	0.153
	2	3.47	0.124
	3	3.68	0.109
	4	3.94	0.104
	5	4.26	0.115
0.1 M KOH	1	5.69	1.96
	2	6.17	1.96
	3	6.57	1.98
	4	6.86	1.79
	5	6.82	1.71
0.2M KOH	1	5.88	2.24
	2	5.85	2.05
	3	6.18	2.00
	4	6.28	1.96
	5	6.23	1.88
0.3M KOH	1	5.49	2.09
	2	5.72	2.10
	3	6.00	2.15
	4	5.43	1.99
	5	5.88	1.89
0.4M KOH	1	5.95	2.29
	2	5.58	2.16
	3	5.98	2.09
	4	5.78	2.02
	5	6.00	2.10
0.5M KOH	1	6.01	2.47
	2	5.96	2.31
	3	5.81	2.22
	4	5.67	2.06
	5	5.41	2.16

Table 2. Comparison of energies used to power circuit and generated by IKV

Solution concentration	Power supply DC current [mA]	Power supply DC voltage [V]	Power supply DC power [W]	Direct pulse energy in period [μJ]
Deionized water	17	1	0.002	1
0.1M KOH	32	1	0.015	2.1
0.2M KOH	35	1	0.017	2.4
0.3M KOH	35	1	0.017	2.4
0.4M KOH	35	1	0.017	2.4
0.5M KOH	35	1	0.017	2.4

So that in energy balance equation the chemical energy transformed to hydrogen mass during electrolysis process is important, it is necessary to measure evaluated hydrogen during pulse electrolysis. In our previous research [11] the current efficiency value 50% was determined. The charge which will transform to hydrogen is equal to 1 μC (Table 1) and it includes about 10^{13} electrons or $0.5*10^{13}$ hydrogen molecules. The mass of $0.5*10^{13}$ hydrogen molecules is about 1.6*10^{-14} kg, and to burn this amount at higher heating value (140MJ /kg) the energy during one pulse – 2.3 μJ can be obtained. This energy is very close to the value used in power circuit (Table 2), what is giving the 100% outcome for electrolysis.

Question is opened about the nature of law responsible for the coefficient of current in electrolysis with IKV pulse – while the increase on 50% can't be observed? It should be very fundamental law, defining energy conservation law, likely as displacement current in Maxwell's equation No 3.

4. CONCLUSIONS

Electrolysis with inductive kickback voltage pulses in the cell with stainless steel SUS 316L electrodes and water - KOH solution electrolyte proves:

1. Amplitudes of voltage pulses increases with increasing the distance between electrodes;
2. Energy of pulses in electrolysis cell is constant for any distance between electrodes when KOH solution electrolyte is used in any concentration;
3. The charge of pulses also is constant for any distance between electrodes and any concentration of solution;
4. Electrolysis efficiency in the cell with inductive kickback voltage feeding reaches 100%.

5. ACNOWLEGMENTS

Authors acknowledge the ESF (European Social Fund), National State Program in Energetic and University of Latvia for financial support in researches.

REFERENCES

1. S.A. Sherif, F. Barbir, T.N. Veziroglu, M. 2006. Forecasts, scenarios, visions, backcasts and roadmaps to the hydrogen economy: A review of the hydrogen futures literature. Solar Energy, vol. 78, 2005, p. 647–660
2. R. Council Regulation (2008), No 521/2008, Setting up the Fuel Cells and Hydrogen Joint Undertaking. Official Journal of the European Union, L 153/1, 20 p.
3. Schultz, K.R., Brown, L.C., Besenbruch, Hamilton, G.E., 2003. Large – scale production of hydrogen by nuclear energy for the hydrogen economy, Proceedings of of National Hydrogen Association Annual Conference, April 6-9, 2003, Washington, DC, USA, general Atomics Report GA-A24265, 16 p.
4. Spazzafumo, G., 2007. An alternative to the long-term roadmaps: a pathmap just for today. Proceedings International Hydrogen Energy Congress and Exhibition IHEC 2007, Istanbul, Turkey, 13–15 July 2007, 5 p.
5. Vanags, M., Shipkovs, P., Kleperis, J., Bajars, G., Lusis, A., 2007. Water Electrolyses – Unconventional Aspects. in: T.N. Veziroglu, M.O. Alniak, S. Yalcin (Eds.), Selected Articles on Hydrogen Phenomena "As the Memory of IHEC 2007 on the Occassion of UHK 2009", Umuttepe Kitabevi, Kocaeli Universitesi (2009), 39–45.
6. Finc, R., 2005. Performance Welding Handbook. Published by Motorbooks International, St. Paul, Mn (USA), 160 p.
7. Halter, F., Foucher, F., Moreau, B., Mounaïm-Rousselle, C., 2007. Combined effects of hydrogen addition and dilution in a spark-ignition engine. Proceedings International Hydrogen Energy Congress and Exhibition IHEC 2007, Istanbul, Turkey, 13–15 July 2007, 6 p.

8. Gutmann., F., and Murphy, O.J., 1983. The electrochemical splitting of water. In Book: Modern Aspects Of Electrochemistry, Ed. by R.E. White, J.O'M. Bockris, B.E. Conway, Plenum Press, NewYork, Vol. 15, Chap. 1, p. 1, 1983.
9. Bockris, J.O'M., Potter, E.C., 1952. J.O'M. The mechanism of cathodic hydrogen evolution reaction. J. Electrochem. Soc., Vol. 99, p. 169–176.
10. Bockris, J.O`M., Ammar, I.A., Huq, A.K.S., 1957. The mechanism of the hydrogen evolution reaction on platinum, silver and tungsten surfaces in acid solutions. J. Chem. Phys, Vol. 61, p. 879–886.
11. J. Ghoroghchian, J.O'M. Bockris, Hydrogen Energy, Vol. 10 (1985), p. 101–112.
12. M. Vanags, J. Kleperis, G. Bajars, G. Vaivars. Water electrolysis – traditional and uncommon aspects. Conference of Young Scientists on Energy, Kaunas, Lietuva, 28. – 29. maijs, 2009.g.
13. Meyer, S.A., 1986. Electric pulse generator. US Patent 4613779.

CYSENI 2010, May 27–28, Kaunas, Lithuania
ISSN 1822-7554, www.cyseni.com

EFFECT OF AMBIENT TEMPERATURE ON COMERCIAL PHOTOVOLTAIC SOLAR CELLS

J. Blums, M. Vanags, J. Kleperis
Institute of Solid State Physics of University of Latvia
Kengaraga str. 8, LV-1063 Riga – Latvia
Phone: +371 26013926
Email: jb05008@lu.lv

ABSTRACT

0.6 kW solar panels were installed at our institute in the beginning of 2009, and collected data showed that harvested power is dependant not only on Sun irradiation, but also on the temperature of panels. In summer at sunny days the collected power was higher, when wind exceeds 2m/s. Power dependence of commercial photovoltaic silicon panel on temperature was tested. We found linear power dependence in temperature interval 33-162 ^{o}C accordingly to data of producer and theoretical predictions. Also the decrease of the output power measured experimentally (-0.55 %/°C at 33 °C) exceeded the values reported in technical instruction for crystalline silicon solar cells (KS-180). Obtained results are discussed and possible explanations given. New constructions and materials are discussed to improve the efficiency of solar panels.

Keywords: Solar cells, temperature dependence, efficiency coefficient

1. INTRODUCTION

Human in his everyday life recognises that energy is necessary to make any job. Nowadays humans are developing different technologies which are coming more powerful and consume more energy. Nowadays fossil energy resources are consumed more and more, and forecasts predict limited amounts on Earth, to be exhaust in next 30–50 years. What can be done to get additional energy? There are three solutions:

1) to develop and use energy saving technologies;
2) to find new energy sources and resources;
3) to develop the existing technologies.

Regarding energy harvesting from Sun, there are two most popular processes – solar batteries and solar collectors. Solar batteries transform Sun radiation to electricity and solar collectors – to heat. An actual question for both systems is efficiency – how to increase it? Solar energy is becoming popular in Baltic States nowadays, not only with thermal collectors to heat up water, but also with photovoltaic solar panels. The licenses with guarantied electricity purchase (4 times exceeding defined rates for electricity produced by largest power generating stations of J/S Company Latvenergo) for 2 MW solar power installations are sold in Latvia in the end of last year already. Therefore interest in available photovoltaic modules and their technical characteristics is growing in Latvia.

For solar batteries efficiency is dependent also on temperature, and the higher the temperature, the lower efficiency [1, 2]. In my work the reasons for lower efficiency of solar battery at higher temperatures are analysed and some experiments to explain it performed.

2. THEORETICAL EXPLANATION OF TEMPERATURE DEPENDANCE

Basic theoretical aspects of solar battery shortly are discussed below. Efficiency coefficient of solar battery depends on many aspects, and for better understanding the temperature dependence on next parameters will be analyzed: J_{SC} – closed circuit current density, V_{OC} – open circuit voltage, *ff* – filling factor of volt-amperic characteristic [1-3].

2.1. Temperature dependence on closed circuit current density J_{SC}

J_{SC} dependence on temperature can be described mostly with the diffusion length of the minor part of all charge carriers:

$$L = \left(\frac{\mu * k * T * \tau}{q} \right)^{\frac{1}{2}}, \tag{1}$$

were μ – mobility of charge carriers, k – Bolcman constant ($1.38 \cdot 10^{-23}$ J/K = $8.64*10^{-5}$ eV/K), T – temperature, τ – life time of minority charge carriers, q – charge of electron ($|q|=1.6*10^{-19}$ C).

Experimentally it is shown that life time of electrons τ_n increases constantly with temperature T increase (approximately proportional to $T^{1.5}$, when $T \approx 300$ K at low injection level). The temperature dependence on mobility of charge carriers μ is defined by basic scattering mechanism of them. For silicon crystal with low level of introduced impurities the mobility of charge carriers can be expressed with $\mu \sim T^{-2}$, therefore diffusion length L practically isn't a temperature function.

The temperature change is inducing the displacement of the edge of optical absorption spectra, which is the reason for the changes in J_{SC}. This change is relatively small – for silicon crystal $(\Delta J_{SC}/J_{SC})/\Delta T \approx 0.03\%/°C$.

From experiments it is known that J_{SC} is almost constant with temperature increase for the most of qualitative solar batteries.

2.2. V_{OC} and *ff* dependence on temperature

The decrease of V_{OC} and *ff* with temperature increase is determined from changes in concentration of self-substance charge carries n_i. Saturation current density J_0 with temperature increase grows exponentially, what cause almost linear decrease of V_{OC}:

$$V_{OC} = \left(\frac{k * T}{q} \right) * \ln \left(\frac{J_{SC}}{J_0} \right) \tag{2}$$

$$ff = \frac{P_m}{V_{OC} * I_{SC}}, \tag{3}$$

where P_m – maximal power corresponding to optimal load in volt-amperic characteristic, I_{SC} – short-circuit current. Usually *ff* decreases quickly with temperature increase.

The efficiency coefficient of solar energy transformation for solar battery made from silicon crystal with homogenic interface transition is expressed by:

$$\eta_S = \frac{V_{OC} * J_{SC} * ff}{P_S}, \tag{4}$$

where P_S – energy of Sun radiation falling to Solar battery. It is known that efficiency coefficient is maximal in temperature region from -150 to -100°C [1], but around +25°C, the η_S is changing by speed $\Delta\eta_S/\Delta T \approx -0.05\%/°C$.

2.3. Temperature dependence of I_{SC}, V_{OC}, *ff* and η_S all together

Above discussed parameters (I_{SC}, V_{OC}, *ff* un η_S) can be measured experimentally and their temperature dependences are shown in Fig. 1 [1].

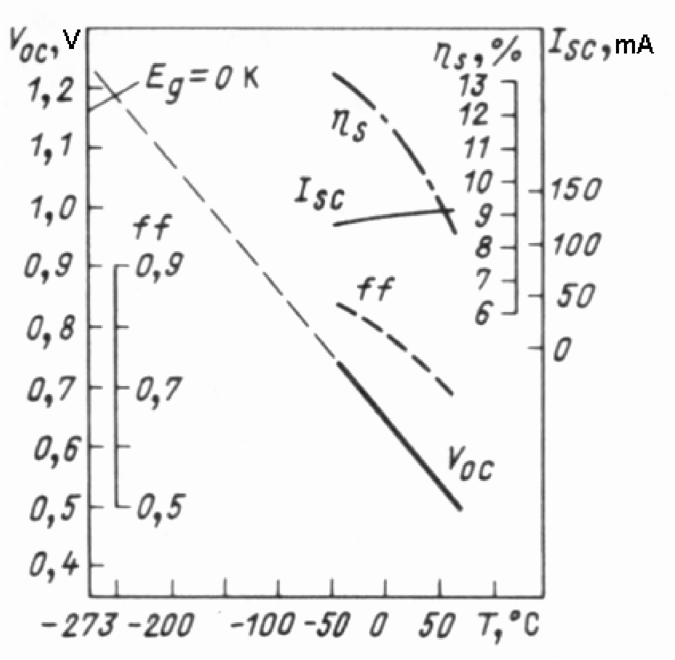

Fig. 1. I_{SC}, V_{OC}, *ff* and η_S dependence on temperature for solar battery with active area 4 cm^2 at light radiation 140 mW/cm^2. Curve $V_{OC}(T)$ is extrapolated to T=0 K

2.4. What is going on at low temperatures?

At low temperatures there are specific problems at operation of solar batteries. If the mobility of charge carriers is described with scattering on impurities, then remarkable decrease of L and hence with the decrease of J_{SC} is also possible. Also contact problems would arise at low temperatures, losing their electronic conductor nature, therefore filling factor can be reduced drastically. Nevertheless for solar batteries based on silicon crystals this problem is solved with making p$^+$ layer and related interface.

3. METHODOLOGY

3.1. Experimental setup

Experiments were performed using the following setup (Figs. 2 and 3). Fig. 2 shows the whole experimental setup and Fig. 3 specifies the sample inside the heater camera.

Solar battery is heated with special heater, and halogen lamp is used as light source. Microcontroller is used to read temperatures T_1 and T_2 from thermocouples. Volt–amperic characteristics are measured using special electronic circuit connected to computer. At different temperatures the volt–amperic characteristics are measured and collected in computer. Power, filling factor and other parameters are calculated at every temperature.

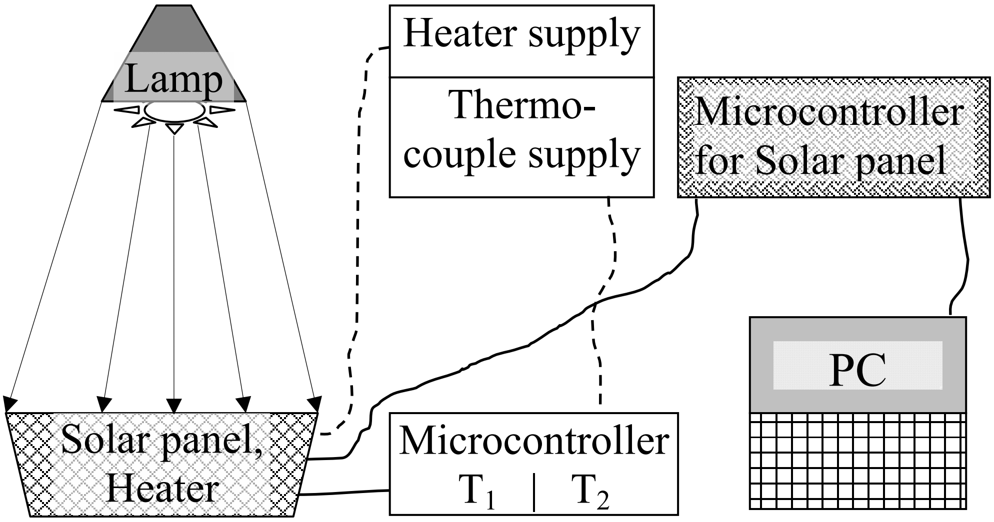

Fig. 2. Equipment overview for experiments made in our work

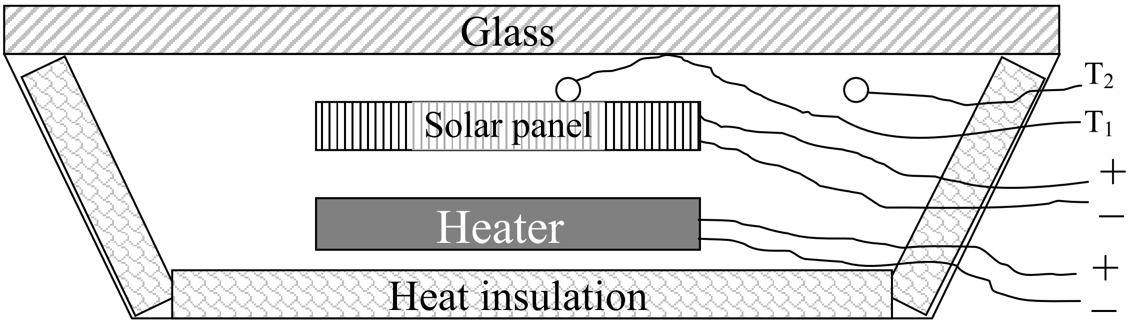

Fig. 3. Solar panel and construction of heater camera

4. RESULTS AND DISCUSSION

We made three different experiments to measure temperature effect on efficiency of solar batteries. One experiment was made with large commercial silicon solar panel (1.281 m^2). Measurements were arranged in special hot room equipped with two light sources (halogen lamps). Separate measurement circuit made from old resistivity magazine, ampere meter and voltmeter were used to register volt-amperic curves, because this solar panel has large power exceeding the limits of electronic circuit used in next measurements. Smaller solar battery (43.12 cm^2) was used for second and third experiments. Special equipment was made (Figures 2 and 3) using electric heater (second experiment) and thermo-battery (third experiment) to cover temperature region from room temperature till +162 ^oC.

In our work the results of the second experiment are described. The following problems were indicated in our experiments: uniform lighting is difficult to arrange for large solar battery in hot room, halogen lamp must be used for short time periods because of quick heating and affecting the temperature of solar battery.

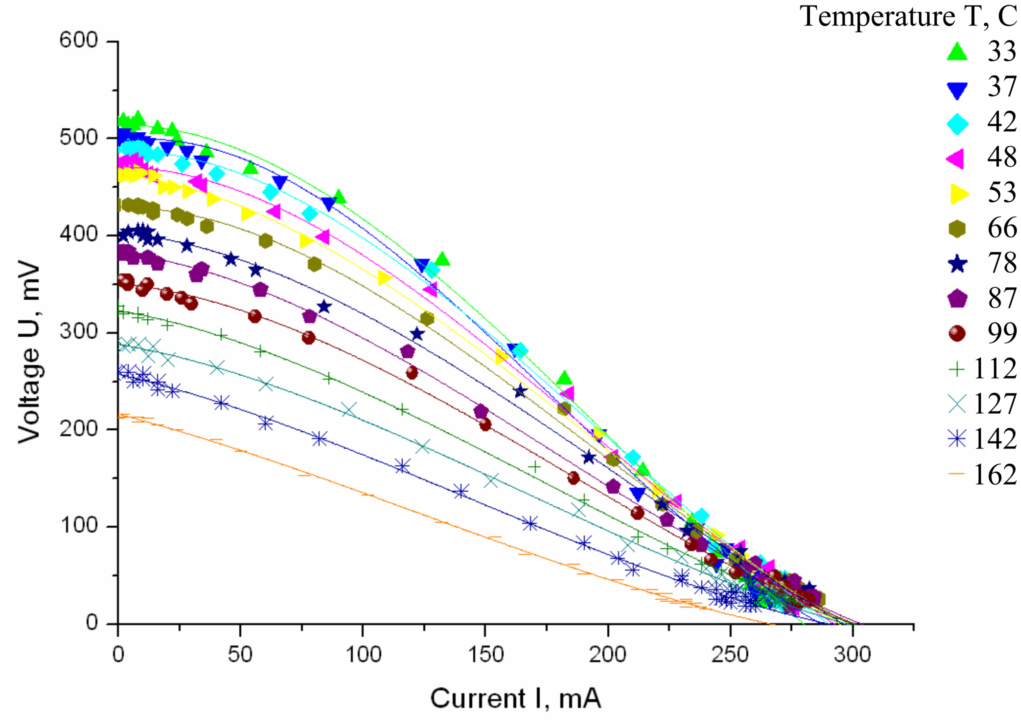

Fig. 4. Volt-amperic characteristics of silicon solar battery at different temperatures

As it is seen from Fig. 4, the produced voltage U of a solar cell decreases with temperature T at open circuit and also under the load.

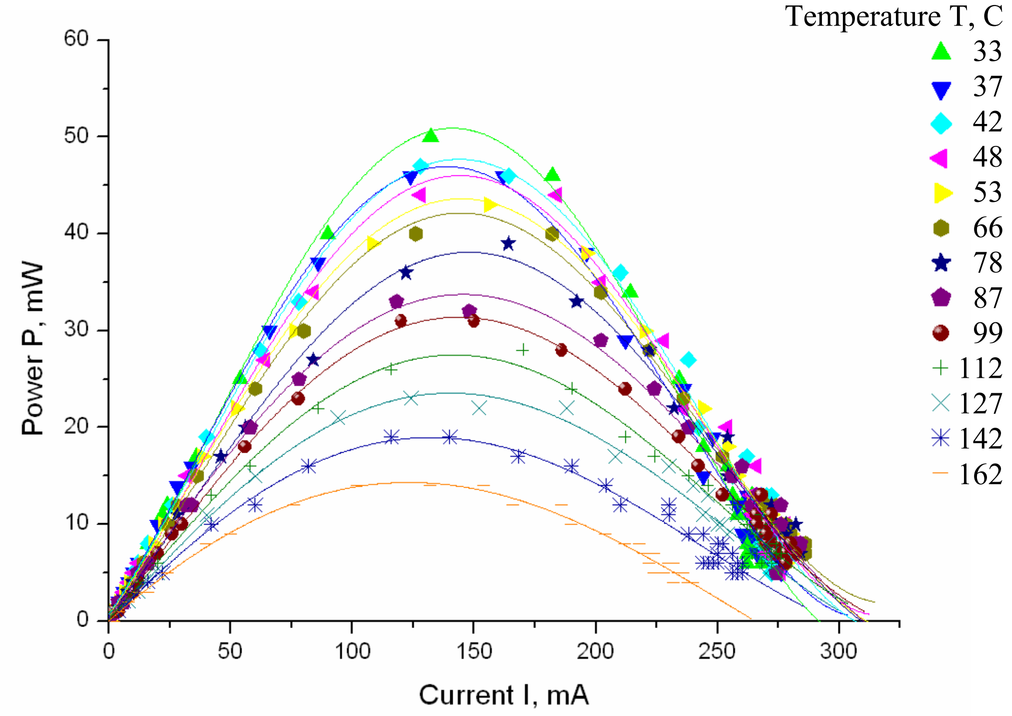

Fig. 5. Solar cell output power P dependence on current I at different temperatures

As it is seen from Fig. 5, the produced power P of a solar cell decreases with temperature T.

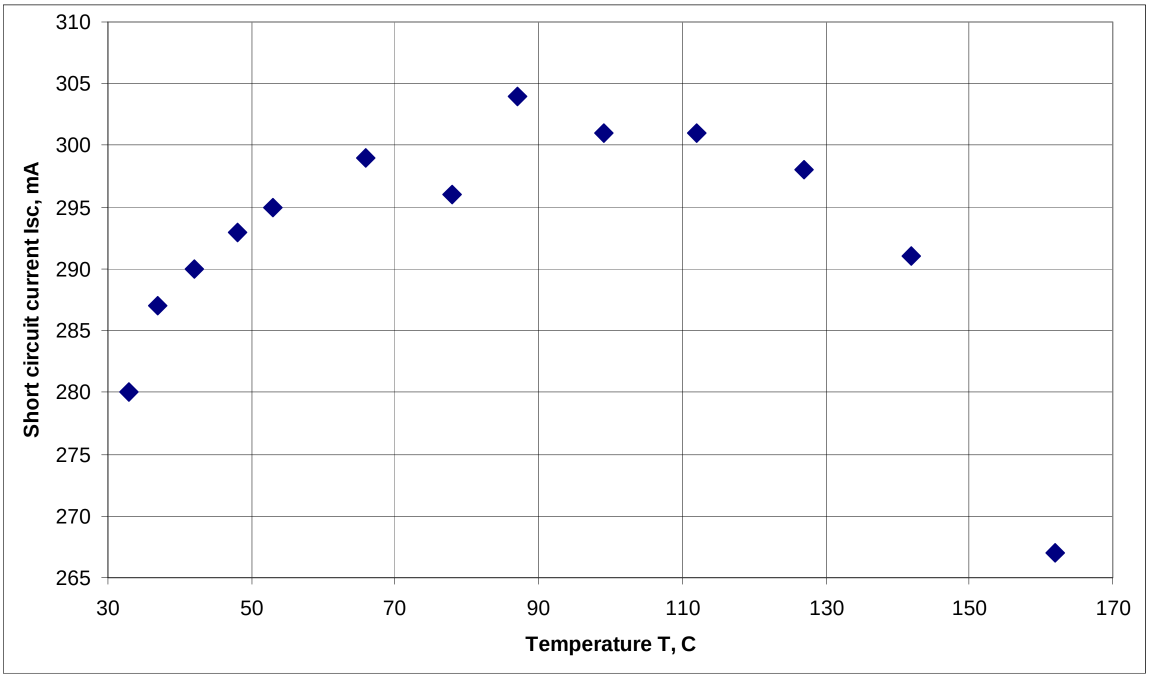

Fig. 6. Solar cell short circuit current I_{SC} dependence on temperature T

As it is seen from Fig. 6, the increase of I_{SC} is observed till temperature ≈ 90°C and beyond this temperature the short circuit current of battery decreases. The character of temperature dependence of short circuit current is rarely analyzed in literature at such high temperatures. More results are necessary to explain measured results.

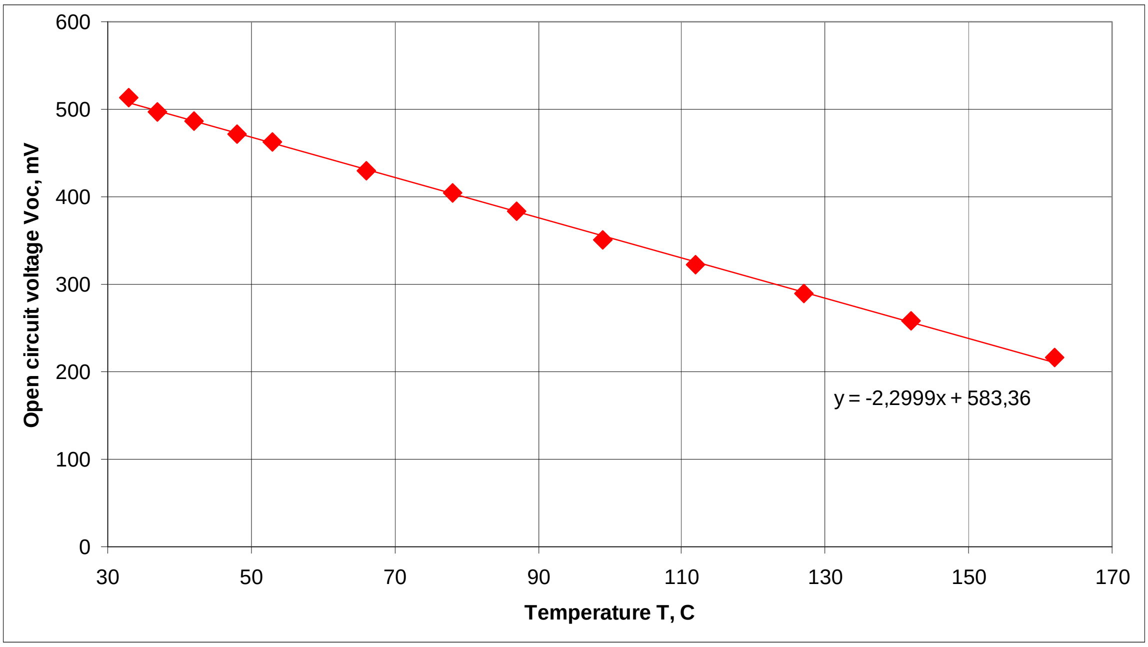

Fig. 7. Solar cell open circuit voltage V_{OC} dependence on temperature T

Open circuit potential V_{OC} linearly decreases with the rate of 2.3 mV/°C, which corresponds to scientific literature [1].

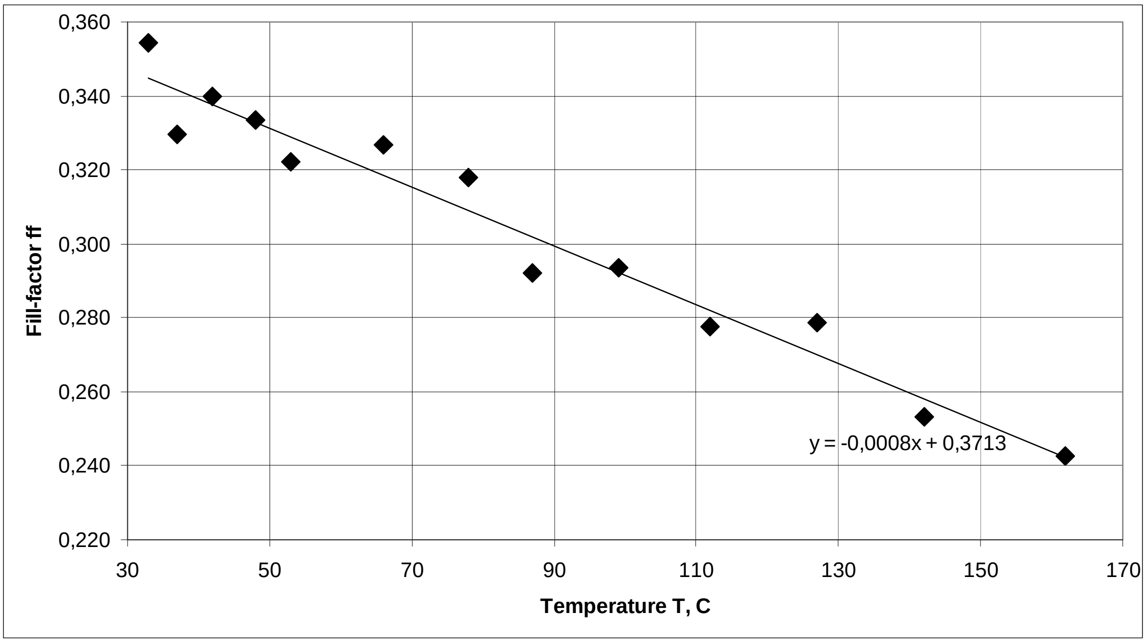

Fig. 8. Solar cell fill-factor ff dependence on temperature T

In our experiments we found that ff decreases linearly with rate of approximately 0.0008/°C, and in absolute values from ≈0.350 at 30 °C till ≈0.240 at 160 ^{o}C.

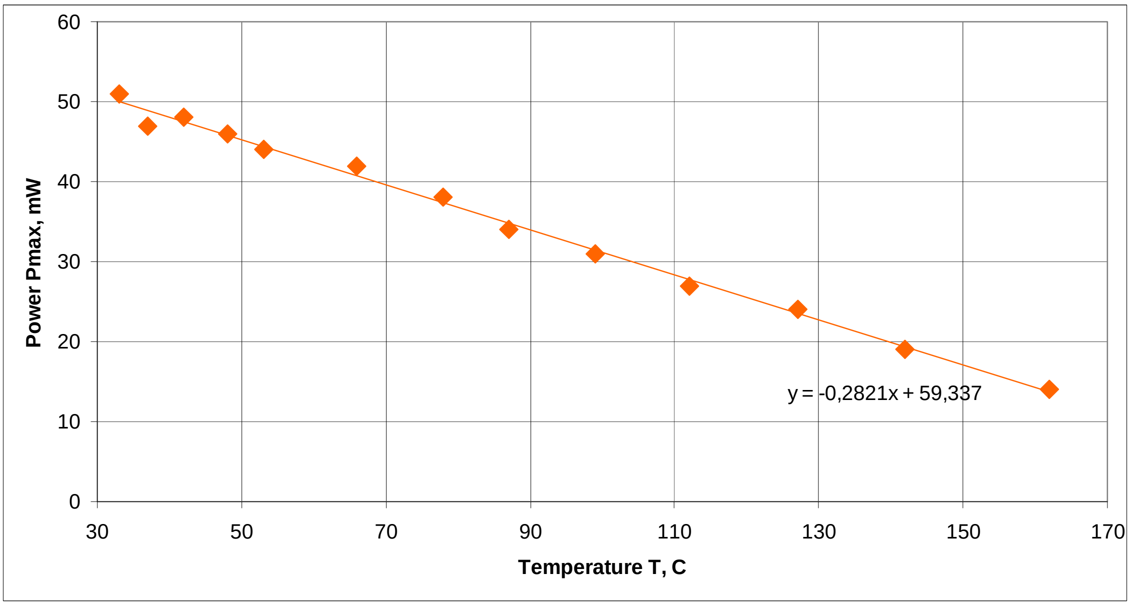

Fig. 9. Solar cell maximum output power P_{max} dependence on temperature T

Our results show that total power of solar battery P_{max} decreases linearly with rate of 0.28 mW/°C in temperature region from 33 till 162 ^{o}C. The efficiency coefficient η_S will be determined when light intensity P_S used in experiments will be determined (in process). Nevertheless we can conclude that also efficiency of solar panel will decrease linearly with increasing the temperature. This is concluded from formula (4). In this formula energy of Sun radiation falling to Solar battery P_S only changes the tilt of the maximal power P_m curve.

The problem of temperature dependence of efficiency for solar cells can be solved in two different means. The first one is to develop Solar cell materials and construction itself. The second is connected with heat removal from the Solar cell, for example, using refrigerant solution like in Solar heat collector. Ideal solution is "two in one" – combining the Solar cell with the Solar collector. In such a way the Solar cell will be cooled and produced electric power increased simultaneously with additional heat collected in the form of hot water.

5. CONCLUSIONS

The investigation of the dependence of solar battery parameters related with the efficiency on different temperatures is made. Next results are obtained:

a) short circuit current of solar battery increases till ≈ 90°C and decreases with further temperature increase;
b) open circuit potential V_{OC} linearly decreases with the rate of 2.3 mV/°C;
c) filling factor ff decreases linearly with rate approximately 0.0008/°C, and in absolute values from ≈0.350 at 30 °C till ≈0.240 at 160 °C;
d) the total power of solar battery P_{max} decreases linearly with rate of 0.28 mW/°C in temperature region from 33 till 162 °C.

6. ACKNOWLEDGMENT

JB thanks to ESF (European Social Fund) for financial support in study and researches.

REFERENCES

1. Фаренбрух А., Бьюб Р. *Солнечные элементы: Теория и эксперимент*/ Пер. с англ. под ред. М.М. Колтуна. – М.: Энергоатомиздат, 1987. – 280 с.: ил.
2. Radziemska E. The effect of temperature on the power drop in crystalline silicon solar cells. *Renewable Energy*, Vol. 28, 2003, p. 1–12
3. Russian Wikipedia http://ru.wikipedia.org Search words "Солнечная батарея"and "Фотоэлемент"

CYSENI 2010, May 27–28, Kaunas, Lithuania
ISSN 1822-7554, www.cyseni.com

DIFFICULTIES, BARRIERS AND POSSIBILITIES TO DEFINE THE DEMAND AND POTENTIAL RESOURCES OF WOOD BIOMASS FUEL ON REGIONAL LEVEL

E.F. Dzenajavičienė, S. Masaitis
Lithuanian Energy Institute
Laboratory of Regional Energy Development
Breslaujos str. 3, LT-44403 Kaunas – Lithuania
Phone: +370-37-401935
Email: farida@mail.lei.lt

ABSTRACT

While working with regional energy development projects or trying to assess regional potential of wood fuel for energy generation, it appeared that there is lack of statistical data or any justified professional assessments. The data on actual use of such fuel is available from the data of district heating sector only, however, origin of the fuel is not known: is it produced locally in the region or imported from other regions, or even from abroad. National statistics provides data on producers and users of fuels starting from certain size of the company only. Forestry and wood processing industry branch data bases are not full and usually do not provide information, which is considered as confidential. The forestry sector data which is the main provider of such fuel gives more or less precise statistics on state owned forests only. At the mean time, private forests in average make more than 30% of the all forests area in the country. Wood fuel consumption in individual residential sector and industry appear to provide very uncertain information. This led to the need of specific statistical data and requires some necessary corrections to currently available statistics.

The paper makes attempts to define the main difficulties and barriers as well as explore existing possibilities to refine current regional use and potential for wood fuel in Lithuania which is actual issue for regional energy planning.

Keywords: regional development, forestry resources, wood fuel

1. INTRODUCTION

Increased interest in wider use of available local renewable energy sources is related to the new energy policy targets drawn in EU and national energy strategies. The targets can be reached by sustainable energy planning at regional level. Such planning is foreseen in draft Renewable energy law introduced to Parliament.

The lack of exact data on available resources and actual demand is the main obstacle in regional planning of mastering renewable energy sources and particularly wood fuel in Lithuania. Data here means regional statistics, national justified and professional data, data of certain economic sectors like household, energy sector, industry, etc. In this paper we'll try to overview available data on potential resources and consumption of forestry biomass, problems and difficulties, which occur while regional planning and will suggest some ideas for staticts improvement for regional planning needs.

2. DEMAND – SUPPLY ANALYSIS ON REGIONAL LEVEL IN LITHUANIA

Sustainable energy planning on regional level is extremely complicated task for Lithuania. The main difficulty is that all energy sector (except heating) was always highly centralised and energy companies, e.g. electricity, gas, fuel supply, do not provide relevant data for demand-supply analysis on regional/municipal level. This is evidently reflected in national statistics, which different from other sectors of economy do not provide any energy statistics on regional level.

Since the main area of interest of our research is wood biomass fuel, which is the main indigenous renewable energy source, here we restrict ourselves with mainly heating and partly electricity sectors on demand side and forestry and wood industry sectors on supply side for wider overview.

One of the most modern and currently applied method for regional development assessment is Life Cycle Analysis (LCA) [1]. This approach evaluates not just operation of any object but also energy costs and pollution from establishment to suspending. Such life-cycle approach is highly important in defining sustainability of bioenergy sector, as the main aim of regional sustainable energy development planning is sustainable energy generation, supply and consumption on regional level. Challenges of climate change, energy provision security and the need to make energy available for all consumers clearly shows that economic prosperity of the regions, social justice and the quality of environment depend on sustainable development of regional energy sector.

In case of wood fuel life cycle analysis should include the whole chain, starting with biomass production – transportation – conversion – transmission – efficient consumption and environmental issues (Fig. 1):

Fig. 1. Life Cycle approach for biomass energy

An increased production and use of biomass reduces consumption of finite resources such as oil, natural gas and coal. Thereby environmental benefits are provided and the increased use of bioenergy also contributes to the mitigation of climate change. The reduction of oil, coal and natural gas demand goes step by step through development of local renewable energy systems. Locally the energy supply is secured, community resilience improved and jobs created.

The Directive on the promotion of the use of energy from renewable sources sets national overall targets for the share of energy from renewable sources in gross final energy consumption which is 23% for Lithuania in 2020 [2]. Biomass is the main renewable energy source globally, in European countries and in Lithuania. It was expected that annual wood fuel production in year 2008 should be nearly 9000 GWh [3].

Approximately 59% of this fuel is consumed in individual houses, and approximately 23.6% in district heating sector. The rest amount is consumed by industry [4].

3. AVAILABLE STATISTICS ON WOOD RESOURCES

Based on above mentioned study [4] the following wood fuel resources at national level are available for energy production during years 2010–2025 (Table 1).

Table 1. Projections of wood fuel resources, thousand m^3 [4]

Wood fuel resources	***2010***	***2025***
Firewood	2664	3218
Residues from wood industry	1578	1627
Cutting residues	882	1085
Total:	***5124***	***5930***

Above figures are based on forest inventory and planned cuttings of mature stand. However, these figures do not represent regional data, which is required for the needs of regional planning at municipal level and here we'll present regional data, available in current statistics.

3.1. National Forestry statistics data

The total forestland area as of January 1, 2009 was 2,150,300 ha, covering 32.9% of the country's territory. The total growing stock was 426.9 million m^3. The area of mature stands in III-IV forest groups (which is the main source of forest production activities) has expanded to 358,000 ha, and mature growing stock has increased to 94.6 million m^3. The average forest area per capita increased to 0.64 ha, and growing stock volume – to 127 m^3. The average age of stands remained at 53 years. The gross annual increment increased to 13.8 million m^3 corresponding to 6.8 m^3/ha. The Lithuanian forests map is provided in Fig. 2. [5]

Moving from above general information we should go down to regional level and discuss regional data, which is available in national statistics. As we can see from the map, forests in Lithuania are distributed unevenly. Forestlands in different municipalities occupies from 10 to 84 % of total area.

Fig. 2. Lithuanian forest map. State Forest Survey service [5]

Department of Statistics under the Government of Lithuanian Republic provides very few regional data on forests, actually these are only 3 figures for each municipality or county: wood resources in 100 thousand m^3, forests area coverage in % and forest productivity in m^3/ha [6]. Unfortunately, these figures are not helpful in defining resources, available for energy purposes, which are significantly lower than forest productivity or total resources. Presence of protected areas, economic reasons reduce the volume of available resources significantly.

3.2. Forestry enterprises statistics

More comprehensive data is available as Forestry statistics, provided annually by State Forest Survey service [5]. Here you can find regional data, which shows annual resources and fellings by tree species, felling, haulage and transportation volumes, as well as wood sales, such as logs, pulpwood, fibrewood and fuel wood. All above mentioned data is provided by forestries. Information could be very helpful in defining annual resources, as felling volumes were rather constant during several recent years and well define tendencies in state forests, as well as in some cases private forests. Fuel wood figures could be used for assessment of resources, however here we meet with difficulties, related to administrational distribution of resources.

There are 60 municipalities in Lithuania and only 42 forestries. We can make an assumption, that 9 town municipalities (Vilnius, Kaunas, Klaipėda, Šiauliai, Panevėžys, Alytus, Palanga, Birštonas, and Visaginas) are not supposed to be involved in forests activities. Another thing is that there are 3 forestries, which are named after locations in already existing municipalities with forestries – Dubravos (Kaunas regional municipality), Nemenčinės (Vilnius regional municipality) and Valkininkų (Varėna regional municipality), which provides additional potential for mentioned municipalities, however reduces total number of forestries to 39, bearing in mind that we still have 51 regional municipalities. The reason is that the boundaries of forestries are not the same as those of municipalities. Some forestries are located in the area of several municipalities, in other cases several forests form the area of single municipality, however there is no information on which share of forestry area is in specific municipality. For this reason, the assessment of municipal forest wood potential, based on actual fuelwood fellings is not accurate.

Another difficulty is defining the use of forestry cutting residues available for fuel.

We can state with certainty, that only Logs are to be used as industrial wood and would never be used for energy purposes (though there are cases of such wood chipping into wood fuel in Lithuania). From the attitude of sustainable forest management, only forest management residues and auxiliary products can be used for energy production, however, it may be feasible to use Pulpwood and Fiberwood for fuel in case there is no direct demand for these products.

Other rather complicated item is the amount of Cutting residues. According to some generalised data [8–12] nearly 30% of total wood volume can be considered as wood cutting residues. Such volumes are rather high in Lithuania in case we evaluate total annual forest volume growth. However, cutting residues are very closely linked to cutting volumes, which were rather constant between 5.5 and 6.5 mill. m^3 during recent ten years [5]. There are several studies, which evaluate the volumes of forest cutting residues [12, 13], however, only one study [13] evaluates environmental aspects, soil, water quality, which provides sustainable approach in biofuel production. The regional results of this assessment are shown in Fig. 3 and Table 2.

And the final remark concerns forests ownership issues. The share of state forests and the share of private ones and assigned to restitution forests are nearly the same. However, the problem is that economic activity (cuttings, thinnings, cleanings, sales, etc.) statistics is presented for state forests only. The only available data on regional level for private forests is trees constitution, area, trees volume, etc. Scare general data gives only approximate estimate of economic activity in private forests, which needed introduction of "common sense" criterion for wood volumes assessment, as private forests appeared to be of lower quality. This criterion is appr. 0.78 and is introduced in assessment of firewood volumes.

4. WOOD ENERGY CONSUMPTION DATA

As it was mentioned before, the main users of wood fuel in Lithuania are district heating sector, individual houses and industry. In year 2008 nearly 18% of fuel in district heating sector was from renewable energy sources, mainly wood fuel. Renewable energy sources used for heat production were: wood – 144186 toe, straw and biogas – 2098 toe and geothermal – 900 toe. For combined heat and power generation (CHP) 21165 toe of solid biofuel and 259 toe of biogas were used. [14]. The use of RES (mainly wood fuel) in individual houses was approximately 401 ktoe of total 766 ktoe, in 2007 which makes about 53% in final consumption. The rest of wood fuel is consumed mainly wood processing industry, which uses own technological residues in their own boiler-houses and drying chambers (appr. 85.3 ktoe) [4].

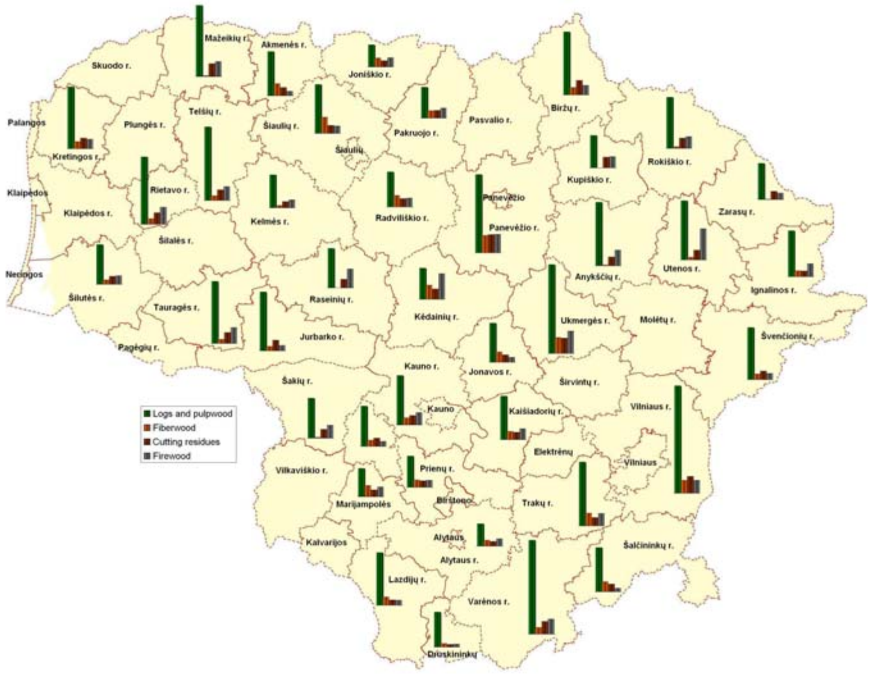

Fig. 3. Logs and Pulpwood, Fiberwood, Fuelwood and Forest cutting residues potential in Lithuanian Municipalities, thous. m^3 [5, 7]

Table 2. Forest wood potential by Forestries, thous. m^3 [5, 7]

Forestry	***Logs and pulpwood***	***Fiberwood***	***Cutting residues***	***Firewood***
Alytaus		12.4	10.4	15.9
Anykščių	136.4	1.6	19.2	33.4
Biržų	135.2	16.0	30.8	20.2
Druskininkų	75.4	7.3	5.8	6.5
Dubravos	52.9	5.7	9.0	7.1
Ignalinos	98.8	12.4	12.0	28.0
Jonavos	84.0	22.0	15.9	10.9
Joniškio	47.3	19.2	13.2	19.6
Jurbarko	126.7	9.5	22.5	11.5
Kaišiadorių	93.8	17.8	15.7	23.3
Kauno	53.5	9.5	11.2	19.4
Kazlų Rūdos	86.7	13.0	17.9	10.5
Kėdainių	66.9	30.4	22.3	54.8
Kretingos	133.0	15.2	23.0	20.4
Kupiškio	69.4	0.0	23.0	24.0
Kuršėnų	94.7	25.8	18.0	9.3
Marijampolės	60.6	24.3	14.8	20.9
Mažeikių	153.3	1.6	27.8	32.3
Nemenčinės	101.7	6.0	18.5	8.8
Pakruojo	66.3	16.0	16.3	21.4
Panevėžio	168.1	37.6	39.0	39.8
Prienų	67.4	16.1	13.7	15.4
Radviliškio	75.2	24.6	18.0	18.8
Raseinių	84.7	0.0	18.6	40.3
Rietavo	144.7	12.2	24.9	36.6
Rokiškio	109.9	3.8	22.1	25.3
Šakių	85.9	2.0	19.0	28.1
Šalčininkų	94.7	21.3	16.5	7.8
Šiaulių	105.1	34.7	17.4	15.8
Šilutės	85.6	9.8	17.3	18.3
Švenčionėlių	111.8	12.0	18.3	13.2
Tauragės	133.8	8.7	23.6	34.5
Telšių	158.3	10.0	22.7	29.6
Tytuvėnų	70.9	4.9	13.3	17.2
Trakų	137.5	27.0	18.0	26.5
Ukmergės	191.0	34.0	33.1	48.3
Utenos	127.4	5.6	20.6	67.4
Valkininkų	104.0	9.1	13.4	16.8
Varėnos	98.0	5.0	14.1	15.4
Veisiejų	113.4	18.0	11.1	10.7
Vilniaus	129.5	21.8	17.6	18.8
Zarasų	77.6	0.9	18.0	14.0
TOTAL	***4210.9***	***584.6***	***777.6***	***956.7***

4.1. District heating sector

District heating sector provides the best available data on wood fuel consumption for regional development planning purposes. Strong Lithuanian District heating Association, which unites most heat and electricity producers collect comprehensive data basis on the activity of district heating sector as well as wood fuel production via collaboration with Lithuanian Biomass Energy Association.

Fig. 4 shows distribution of installed heat production capacities using biomass fuel. The data provides figures for district heating sector and some biggest and available industrial installations.

The total number of approximately 360 biofuel boilers are installed with total capacity of 610 MW. 380 MW are installed in DH sector and about 202 MW in industry. Among them 45–50 boilers with total capacity of 9 MW are straw fired boilers [15]. Biggest installations are in Vilnius City, Klaipėda City, Kupiškis, Rokiškis, Ignalina, Mažeikiai and other municipalities. However, municipalities with biggest forest resources in the south of Lithuania (Fig. 2), still have rather high potential for such installations.

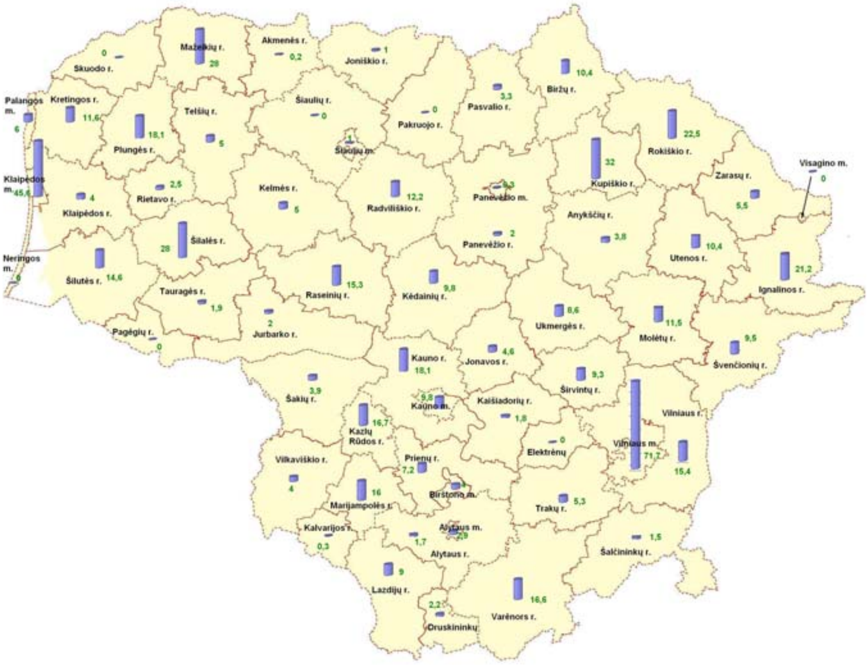

Fig. 4. Wood fuel using heat production capacities in Lithuanian municipalities, MW [15]

4.2. Individual sector, industry

As it was mentioned above, the largest amount of wood fuel is consumed by individual housing sector, most of which use firewood (appr. 2 mill. m^3), according to wood fuel amounts sold by State forestry companies [5] and private forest owners. Total number of forest owners is 232318, average private forest area 3.34 ha, the largest forest plot 1631.87 ha [16]. Unfortunately, there is no available data on cuttings in private forests. The Association of the Lithuanian producers and traders of wood products state, that households used about 2046 thousand m^3 of wood fuel in 2007 [17], however, this figure includes individual users and those connected to DH.

Besides, housing sector is not included into regular statistics. This sector is reflected via irregular questionnaires on household income and expenses, which are expressed in monetary units only and not provided on regional basis.

Concerning wood industry, there are two types of wood energy consumption:

1) Wood processing companies produce certain volume of wood residues, which is mainly used in the same companies as fuel for boiler-houses and wood drying chambers. This amount of wood fuel is not reflected in any statistics.

2) Wood fuel (firewood, wood waste, pellets and briquettes) industrial producers. Most of their production is exported (80% of briquettes and 95% of pellets [4], besides growing export of firewood) and not consumed in local market because of too high prices of such fuel. This aggregated statistics could be available in regional statistics since most companies must provide Fuel-energy balance sheet for the Department of Statistics. Availability of individual data is restricted as confidential. General data is presented in Table 3.

Table 3. Data on biofuel production in industry

Energy and fuel type	**Measure units**	**Produced**	**No of producers**	**Consumed**	**Import**	**Export**
Firewood and wood residues available for fuel	Thos. m^3	3885.6	N/A	2664.7	149.6	271.2
Sawdust briquettes	Thos. t	39.5	44	7.2	0.3	9.8
Wood pellets	Thos. t	87.6	8	0.2	-	94.9

5. DISCUSSIONS

This paper does not provide any scientific research but rather overview of national statistical data system, expert assessments, etc., which are required for the planning needs of wood energy sector on municipal level. The largest problem here is that energy sector was always considered as national, not regional issue. However, currently very urgent topics, such as use of RES, sustainability issues in biofuel and bioenergy production raise need for regional or in Lithuania's case municipal attitude towards energy sector planning and development.

Here the involvement of national Statistics Department could be highly valuable. Conversion of forestry area based forests statistics as well as regional statistics of energy demands is the urgent need, bearing in mind that all companies of more significant size provide fuel-energy balance sheets in their monthly and annual statistical reports.

Another topic is that biomass sustainability issues were never identified for energy sector of Lithuania yet. Greenhouse gases emissions are represented on national level only. We should start following good practice examples, which are numerous from more developed countries and which show, that high national goals are to be reached applying bottom-up rather than top-down planning and development method. Local inputs form "big" national output and not vice versa.

6. CONCLUSIONS

Overview of current situation in defining the demand and potential resources of wood biomass fuel on regional level disclosed:

- Department of Statistics under the Government of Lithuanian Republic provides very few regional data on forests, which is not sufficient in defining wood resources, available for energy purposes at municipal level.

- More comprehensive statistics could be available for fuel needs, however, here we meet with difficulties, related to administrational distribution and ownership of forest areas.
- Another difficulty is defining the use of forestry cutting residues available for fuel. From the attitude of sustainable forest management, only forest management residues and auxiliary products can be used for energy production, however, it may be feasible to use Pulpwood and Fiberwood for fuel in case there is no direct demand.
- Economic activity (cuttings, thinnings, cleanings, sales, etc.) statistics is presented for state owned forests only.
- District heating sector provides the best available data on wood fuel consumption for regional development purposes.
- Residential sector is not included into regular statistics. This sector is reflected via irregular questionnaires on household income and expenses, which are expressed in monetary units only and not provided on regional basis.
- Amount of wood fuel from wood processing companies, which is mainly used in the same companies as fuel for boiler-houses and wood drying chambers, is not reflected in any statistics.

REFERENCES

1. GUINĚE, J. ed. Handbook on Life Cycle Assessment: Operational Guide to the ISO Standards. Kluwer Academic Publishers, 2002.
2. DIRECTIVE OF THE EUROPEAN PARLIAMENT AND OF THE COUNCIL on the promotion of the use of energy from renewable sources amending and subsequently repealing Directives 2001/77/EC and 2003/30/EC.
3. Study on the energy production potential from renewable energy sources during 2008–2025. LEI Final report of applied - research study. Kaunas, December, 2007.
4. Action plan for promotion of the use of renewable energy sources during 2010–2020 in Lithuania. Lithuanian Biomass Energy Association LITBIOMA. Vilnius, 2008.
5. Lithuanian statistical yearbook of forestry 2009 / State Forest Survey service [referred on the 27th of January in 2010 y.] Link to the internet <http://www.lvmi.lt/vmt/leidiniai.php?form_currentid=470>
6. Forests resources in counties and municipalities 2006-2008/ Department of Statistics at Lithuanian Government [referred on the 27th of January in 2010 y.] Link to the internet <http://www.stat.gov.lt/lt/pages/view/?id=2503>
7. TEBĖRA, A. Wood resources, which could be used for fuel and it‘s accounting. Presentation data for BBN Project under INTERREG IIIB Programme. Kaunas College of Forests and Environment Engineering, 2005.
8. Analysis of perspectives for bioenergy development and measures for ensuring co-ordination between the investigations and technological development. Report of the research study. Lithuanian University of Agriculture. Akademija, 2007.
9. TEBĖRA, A., VAIČIUKYNAS, G. Branch volume measurements in stacks. Kaunas College of Forests and Environment Engineering, 2008.
10. TEBĖRA, A., VAIČIUKYNAS, G., ALĖKSĖJŪNAITĖ, A. Norms of tree branches volumes. Kaunas College of Forests and Environment Engineering, 2008.

11. ALĖKSĖJŪNAITĖ, A., TEBĖRA, A., VAIČIUKYNAS, G. Modelling and accounting of trees branches available for fuel. Kaunas College of Forests and Environment Engineering, 2007.
12. Assessment of forests cutting residues and ecologic risks from haulage activitues and elaborating recommendations. Report. Lithuanian Association of Independent Wood Surveyors. Akademija, 2008.
13. Model for assessment of wood cutting residues. Report of research study. Kaunas College of Forests and Environment Engineering, Girionys, 2007.
14. Overview of economic activity of district heating companies in 2008. Lithuanian District Heating Association. Vilnius, 2009.
15. STASIŪNAS, V. Lithuanian heat sector – current situation and barriers for development. Presentation at the conference “The most expensive heating season. Reasons and solutions”. October 22, 2008. Vilnius.
16. Realty register, data of 07/01/2008.
17. Lithuanian Forest Cluster. Association „Lietuvos mediena“. 2009.

WIND MEASUREMENTS IN ESTONIA

Indrek Pertmann
Tallinn University of Technology
Department of Thermal Engineering
Kopli 116, 11712 Tallinn – Estonia
Phone: +372 620 3915
Email: pertmann@sti.ttu.ee

ABSTRACT

Wind measurements are very important phase before setting up a single wind turbine or a wind farm. Without correct preliminary wind measurements in planned wind farm site, there can be over- or underestimation of wind conditions. If the wind farm project should be covered by loan, wind measurements are also preconditions for getting loan from the bank. Not any kind of wind data is sufficient to make accurate wind farm calculations. It is always cheaper to make correct and accurate wind measurements than to choose a wrong site or wind turbine type for the wind farm project. It is not reasonable to economize wind measurement costs. Economizing wind measurement costs, accuracy of measurement data will suffer and it will lead to sensor failures during measurement period. To make accurate wind turbine energy production prognoses, wind data from the height of future wind turbine is needed. Length of the measurement period must be at least one year.

Keywords – wind measurements, wind speed, wind direction, measurement mast, measurement sensors.

1. INTRODUCTION

Wind measurements are not only very important but in some cases also ineluctable. Accurate wind speed and direction data are important to determinate the best sites for wind turbine. Previous wind measurements are also needed, if the wind project owner needs a loan to finance a single wind turbine or wind farm.

Wind measurements can be made very simply and with low costs or even weather station wind data can be used, but in the wind industry it is not an option. Although correct and in-depth wind measurements are rather high-priced, it is cheaper to make accurate measurements than over – or underestimate wind speeds and make wrong wind farm energy production prognoses.

Accurate wind measurements assume many different stages. To investigate the wind resources within a given land area, the main three stages are:

- preliminary area identification;
- area wind resource evaluation;
- micrositing [1].

Initial site choosing can be made according to Estonian Wind Atlas [2] or weather station wind data, where are given average wind speeds 10 meters above the ground level, but for final conclusions and wind turbine production prognosis, additional more accurate wind measurements are needed.

The main focus of this study is to find out all the problems and hindrances that may occur during wind measurement period. Second task is to analyze requirements to the wind data needed for wind turbine production prognoses.

2. METHODOLOGY

Many different wind measurements were carried out in Estonia in order to investigate the importance of accurate wind measurements and problems, which may occur during measurement period. Wind measurements were made on different measurement mast types (tubular steel, lattice, tilt-up, telescope, fixed) and in different locations. To investigate the relevance of new measurement sensors some measurements were made with new sensors and others with already used sensors.

Elaborated wind measurements were carried out in the northern and eastern coast, where wind conditions are rather good. Nine investigated measurement points were Prangli, Türisalu, Virtsu, Uulu, Paldiski, Võiküla, Tamba, Roomassaare and Mäliküla. Exact locations are shown in Fig. 1 [3]:

Fig. 1. Wind measurement points in Estonia

Mast types and measurement heights of the nine measurement points were:

- Prangli measurement mast co-ordinates were E 25^{o}00´22.8´´ and N 59^{o}38´16.3´´;
- Sensors were mounted to 50-m GSM antenna mast, secured by guy-wires and sensor heights were- upper anemometer 44.5 m, lower anemometer 26.5 m and wind vane 26.5 m;
- Türisalu measurement mast co-ordinates were E 24^{o}20´06.6´´ and N 59^{o}24´47.9´´.
- Sensors were mounted to standard 40-m meteorological tubular mast and sensor heights were- upper anemometer 40.5 m, lower anemometer 20.5 m and wind vane 40.5 m;
- Pakri measurement mast co-ordinates were E 24^{o}02´51´´ and N 59^{o}22´46´´.
- Sensors were mounted to 80-m tubular telescope mast and sensor heights were- upper anemometer 75.2 m, middle anemometer 51.6 m, lower anemometer 33.7 m and wind vane 72.7 m;
- Virtsu measurement mast co-ordinates were E 23^{o}31´00´´ and N 58^{o}37´59´´.
- Sensors were mounted to 52-m GSM mast and sensor heights were- upper anemometer 52.3 m, lower anemometer 31.3 m and wind vane 52.3 m;
- Võiküla measurement mast co-ordinates were E 23^{o}23´27´´ and N 58^{o}33´13´´.
- Sensors were mounted to 46-m Võiküla substation lattice mast and sensor heights were- upper anemometer 46.5 m, lower anemometer 29.5 m and wind vane 46.5 m;
- Roomassaare measurement mast co-ordinates were E 22^{o}29´49´´ and N 58^{o}13´09´´. Sensors were mounted to standard 30.5-m tubular mast and sensor heights were- upper anemometer 30.5 m, lower anemometer 15.5 m and wind vane 30.5 m;

- Tamba measurement mast co-ordinates were E 23°41´12´´ and N 58°29´55´´;
- Sensors were mounted to 40.5-m tubular mast, secured by guy-wires and sensor heights were- upper anemometer 40.5 m, lower anemometer 20.5 m and wind vane 40.5 m;
- Mäliküla measurement mast co-ordinates were E 23°43´14´´ and N 58°26´36´´;
- Sensors were mounted to 70-m GSM mast and sensor heights were – upper anemometer 60 m, lower anemometer 31.8 m and wind vane 60 m;
- Uulu measurement mast co-ordinates were E 24°35´14.4´´ and N 58°17´34.2´´.
- Sensors were mounted to 50-m GSM mast and sensor heights were- upper anemometer 44.5 m, lower anemometer 26.5 m and wind vane 44.5 m.

In Prangli, Türisalu, Virtsu and Uulu wind measurements were made according to UNDP measurement program and are also basis to Baltic Wind Atlas [4].

All wind measurements lasted for at least one year in order to cover all twelve month wind speed and direction data. Wind speed measurements were made with one or two wind speed sensors (anemometers). In this research two types of cup anemometers were used – Thies Classic and Vector A100L2. If the future turbine mast is 80 meters high, then the wind speed measurements must be carried out in same height or calculated to that height. For calculating wind speeds to another height, wind data must come from at least two different heights to know the wind profile in this area.

All obstacles around the measurement masts were described by their characteristics (distance from mast, length, width, height and porosity). All obstacles around the mast are taken into account in order to clean wind data from effects of obstacles to wind flow, because they generate turbulence and therefore recorded wind speed data are influenced. For wind resource estimation WAsP or WindPRO programs must be used – those are two common used programs for wind climate analyses and wind farm planning. In this study WAsP 9 program was used. To calculate measurement area wind climate, map with contour- and roughness lines were created with WAsP map editor program. Map must cover at least 10-20 km area around the future wind turbine area.

After many different wind measurements the main problems that occurred during the measurement period were investigated. The best measurement mast and sensor types were determined on the basis of wind speed data accuracy and minimal disturbance.

3. RESULTS AND DISCUSSION

3.1. Measurement mast

There are different types of masts that can be used. There are two basic tower types - tubular steel and lattice. Both towers could be tilt-up, telescope or fixed. Towers may be either guyed or self-supporting. Two basic tower types are shown in Fig. 2:

It is important to place the measurement mast as far away as possible from the local obstacles like houses and trees. Selected location should also represent the majority of the site. In order to get accurate wind speed data, measurement mast should be exactly as high as the future wind turbine. In lower wind measurement mast two or three anemometers should be used.


a b

Fig. 2. Wind measurement mast types: a – lattice mast, b – tubular steel mast

At present most of the Estonian wind measurement masts are about 40 meters high. There are three basic options in use:

- measurement sensors are installed on the mobile mast;
- measurement sensors are installed on the substation mast;
- measurement sensors are installed on the independent wind measurement mast.

Basic measurement heights are 40 and 20 meters above the ground level, using two anemometers. Biggest measurement mast, used in our research, was 80 meters high and had three Vector A100L2 anemometers on three different heights.

3.2. Basic wind measurement sensors and correct installation

Two basic sensors to measure wind speed and direction respectively are anemometer and wind vane. In order to make more exact measurements, air temperature, air pressure and precipitation sensors are used.

There are many different types of anemometers: cup anemometers, windmill anemometers, hot-wire anemometers, sonic anemometers etc. Cup anemometers are preferred and mostly used. In order to make accurate energy prognoses anemometers, separately calibrated in the wind tunnel must be used. All anemometer calibrations are generally made in DEWI (Deutches Windenergie Institute).

There are certain rules for sensor mounting. Sensors must be mounted away from the mast because of the turbulence and shading caused by the measurement mast. Sensors are mounted on the booms; their location is shown in Fig. 3 [5].

Mostly two anemometers are mounted on the measurement mast. One anemometer should be placed centrally on the top of the mast. Only lightning protection can be placed next to the anemometer. The lower anemometer should be fitted approximately 20 meters lower than the upper anemometer and on a boom with length of at least 7 times the mast diameter. Anemometer should be staying 30–50 cm over the boom. The wind vane will also be placed on a boom but at least 1.5 meters below the upper anemometer [5]. Other components like logger shelter box and solar panel for power supply should be fitted as high as possible but within the reach of maintenance (generally 10 meters above the ground level).

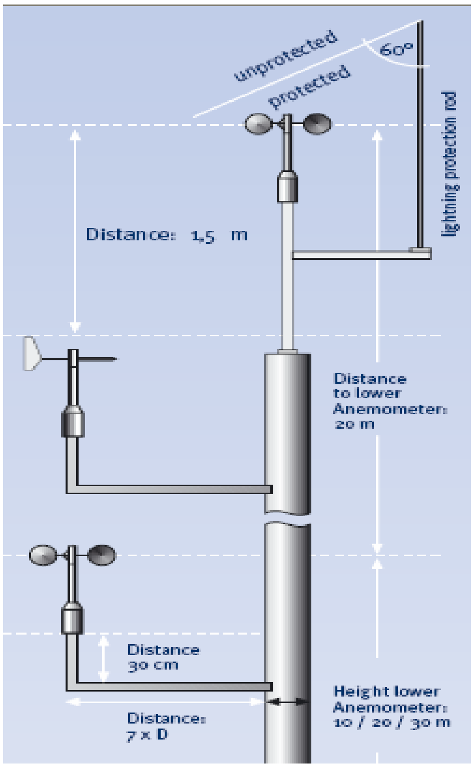

Fig. 3. Wind measurement mast sensor locations

3.3. Problems during wind measurement period

Main problems during wind measurement period are sensor faults, lightning, freezing in coastal areas, oxidation, also logger and sensors power supply.

Data loggers and sensors need power supply that can either be external power or solar power (solar panel). In remote areas the only option is to use an autonomous power supply system with solar panel. With both power supply systems there can be problems. External power supply is more reliable because power system problems are quite rare and they do not last very long. Solar power systems are more problematic in Estonian climate. There have been cases when there is not enough power to read the data because the sky was cloudy for a few weeks.

Winter temperatures are often below freezing point and sensor freezing is quite actual problem in Estonia. There have been several cases when sensors without heating were frozen and that lead to incorrect wind data or even several month gaps in data. In order to prevent freezing problems, sensors with heating must be used.

The best wind conditions in Estonia are in coastal areas and on islands. Air is salty and air humidity is high in costal areas, these conditions usually lead to oxidation of the measurement equipment.

The data logger on one coastal measurement mast was completely oxidized after three years of usage. Sensor cable oxidation cases have also appeared. Logger shelter box should be completely hermetic in order to prevent oxidation problems.

Vandalism is also one problem that should be to taken into account. To protect lower measurement equipment like logger shelter box, it is usually mounted approximately 10 meters above the ground level. Even when all the equipment is mounted high enough there can be some vandalism cases. For example somebody shot the solar panel on one of the measurements masts. To prevent vandalism problems measurement masts should be equipped with protective fence [6].

It is very important to supply the measurement mast with lightning protection. When measurement equipment is installed to the substation mast it is very important to use proper lightning protection. Substation mast ground wire is not enough because sensors can get direct lightning strikes.

3.4. Wind measurement data

In order to save money smaller wind energy developers and project managers want to use weather station wind data or used equipment for wind measurements and energy prognoses.

In Estonia weather station wind data is mostly measured at the height of 10 meters above the ground level. This measurement point is too low to make wind climate calculations and wind turbine production prognoses. Some weather stations are located very close to highways. It means that wind data is under the influence of cars, especially trucks. Other problems when using weather station data are forest and other local obstacles. With years the trees grow higher and it influences the wind data. In this case wind data shows that wind speed decreases year by year. In reality it is influence of higher forest or new obstacles.

Another problem with accurate wind data is used sensors. Generally wind sensors, which are used for a year or two, are not used in another measurement. If old anemometers and wind vane are used, they must be calibrated again before new measurement. It ensures the accuracy, but not other sensor faults. One problem with used anemometers is bound up with bearings. Bearings that have been used for many years could jam during the measurements. That will cause approximately two month gap to the measurement data.

This anemometer bearing broke up during the second measurement period. The separator broke up, balls stuck together and anemometer rotor jammed.

Oxidation is another problem with used components and that could also lead to data loss during the measurement period. One factor that could also have influence is sensor cable condition. Concatenated cables are always a weak point. They can break lose or air humidity could go into cables. Too long cables can influence the sensor signals and thereby also gathered wind data.

On the basis of gathered 12 month wind speed and direction data Weibull distribution with Weibull parameters and wind rose is usually calculated. It shows wind climate and prevalent wind directions in that area. 12 month wind data must be used for full representation of wind variations through the different seasons and therefore for more exact wind resource estimation. In Fig. 4 Pakri peninsula wind speed Weibull distribution, wind rose and wind profile are shown.

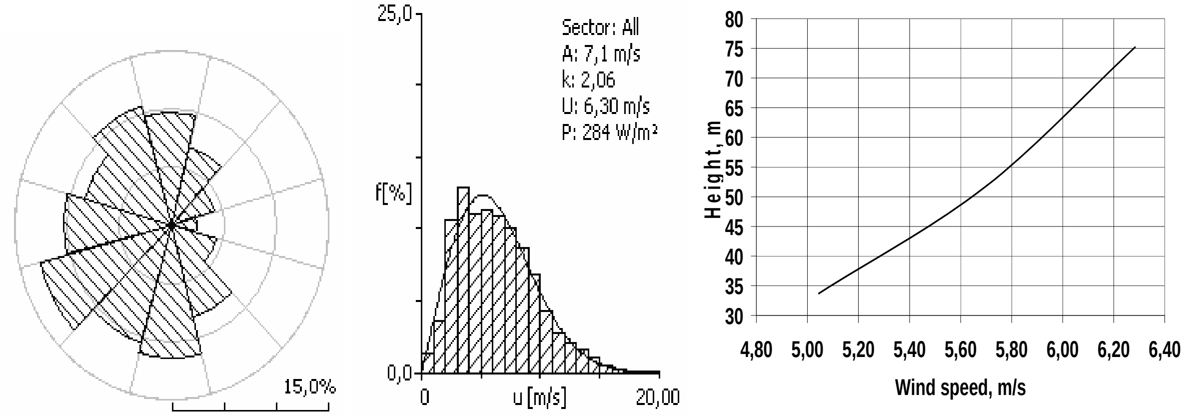

Fig. 4. Pakri wind measurements: wind rose, Weibull distribution and wind profile

A is Weibull parameter *A* (m/s), *k* is Weibull parameter *k* (Weibull distribution shape factor), *U* is average wind speed (m/s) and *P* is energy density (W/m^2). Figure shows that Pakri peninsula is a good place for wind turbines (average wind speed 6.30 m/s) and the prevalent wind direction is south-west [7]. Wind rose and Weibull distribution were calculated 75.2 m above the ground level. Measurement period was 12 month.

In Fig. 5 Muhu Island (Võiküla) wind speed Weibull distribution, wind rose and wind profile are shown.

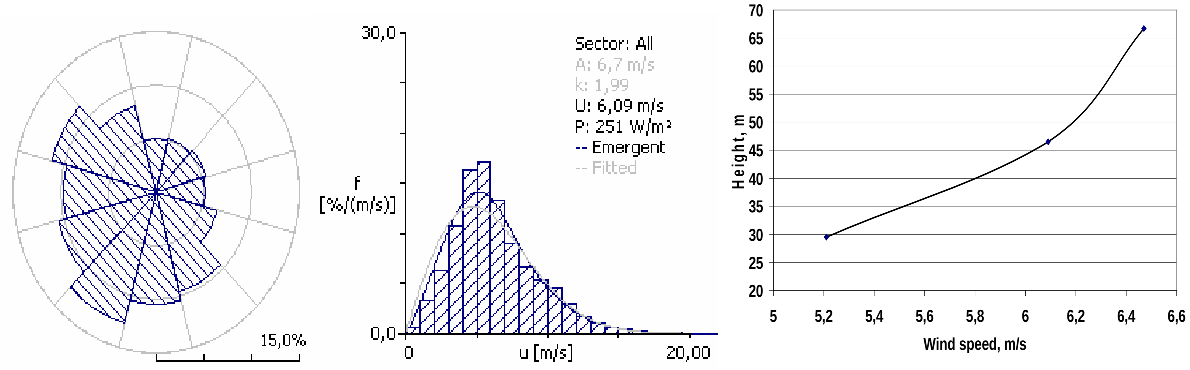

Fig. 5. Võiküla wind measurements: wind rose, Weibull distribution and wind profile

Võiküla wind rose and Weibull distribution were calculated 46.5 m above the ground level. Measurement period was 12 month.

In both measurements wind speed was measured with Vector A100L2 cup anemometers and wind direction with potentiometer wind vane W200P. All anemometers were calibrated in DEWI.

In Pakri prevalent wind direction is sector 9 (240^o) and in Võiküla sector 8 (210^o). Wind profiles in both measurement points show that to choose bigger mast for wind turbines means considerable growth in wind speeds.

In Fig. 6 Võiküla and Nasva average monthly wind speeds are shown.

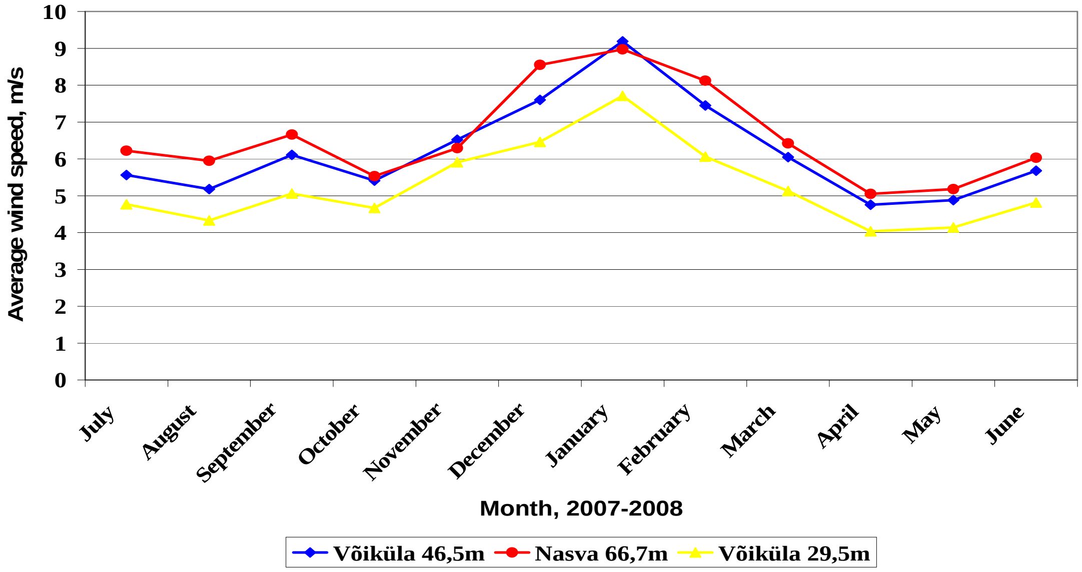

Fig. 6. Average wind speeds in Võiküla and Nasva

Võiküla wind measurements were affected by lightning strike and last 3 month measurement data was calculated by comparing it with Nasva wind turbine anemometer wind data. Nasva wind speed data correlates considerable good with Võiküla wind measurement data. When the wind speeds are bigger, anemometer at the top of wind turbine is more affected by turbine rotor (in January real wind speeds were bigger than registered with Nasva wind turbine anemometer).

All nine measurement point wind data had smaller or bigger periods of missing data. Data gaps were caused by long-standing power loss, GSM connection problems (to read out data), sensor faults etc. If there are GSM connection problems, which will last several weeks, logger memory gets full and that cause’s valuable data loss.

In Fig. 7 all 9 measurement points 12 month average wind speeds are shown.

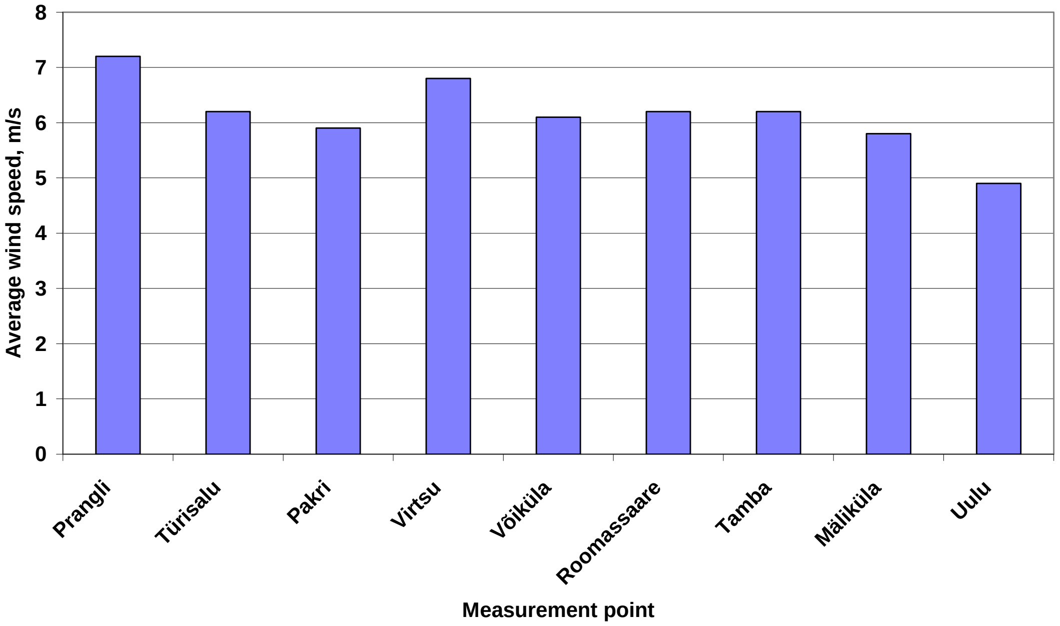

Fig. 7. Measurement points 12 month average wind speeds

All 9 measurement points 12 month average wind speeds are calculated 50 meters above the ground level with roughness class 2 (farm land with scattered houses and some higher vegetation). In Estonian coastal areas average wind speeds 50 meter above the ground level are mostly 6 m/s and in some places even higher. Those are reasonably good conditions for single wind turbines and wind farms.

For single wind turbine or wind farm production prognoses one year wind measurement data must be correlated with weather station long-term wind data. 20 year long-term weather station wind speed data is used, because wind turbine life expectancy is usually 20 years. In Fig. 8 three different weather stations 20 year long-term wind data are shown.

Virtsu and Jõhvi measurement masts are in coastal area, Tiirikoja in inland, near Lake Peipsi. 20 year average wind speed in Virtsu is 4.5 m/s, in Jõhvi 4.4 m/s and in Tiirikoja 3.1 m/s. Weather station wind data are registered 10 meters above the ground level. 20 year annual average wind speeds in Jõhvi were changing from 3.8 m/s to 4.7 m/s and to make detailed calculations with only one year wind speeds without long-term calculation could cause very big production prognosis under- or over estimation.

Measured 12 month wind data, correlated with nearest weather station 20 year long-term data, is basis to wind turbine production prognoses.

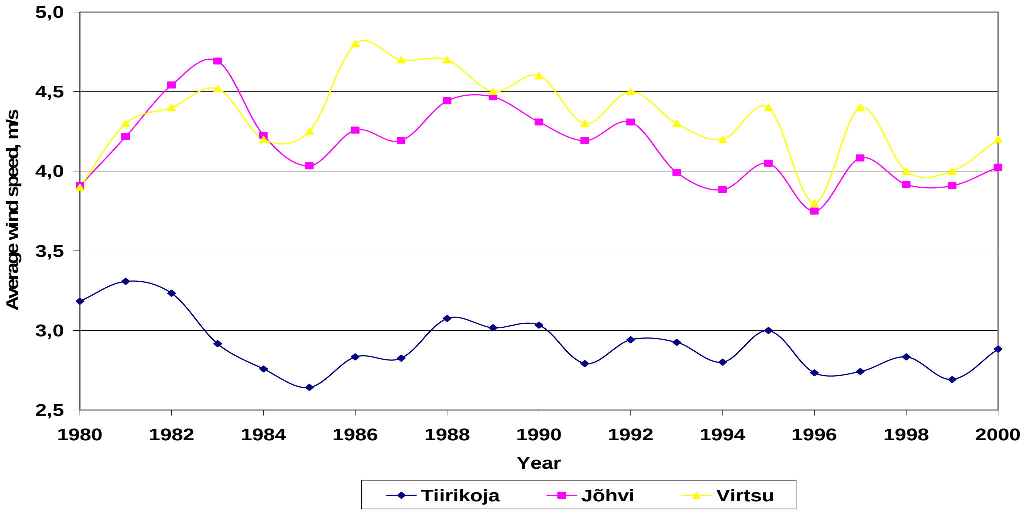

Fig. 8 Weather station long-term wind data

4. CONCLUSIONS

Wind measurements are very important and mostly even ineluctable phase before setting up the single wind turbine or a wind farm. Weather station wind data and low cost wind measurement data is not sufficient to make accurate wind climate analysis and wind turbine production prognoses.

In order to get correct wind measurements and accurate wind data following facts must be taken into account:

- new, accurate, calibrated and correctly installed sensors must be used (every measurement made with used equipment consisted bigger data gaps due to sensor or logger faults);
- measurement period must be at least 12 month, to cover all wind variations through different season;
- all lightning, freezing, oxidation and vandalism protection measures must be taken (several measurements, where one of those measures were not take into account, suffered data loss);
- for data analyses and production prognoses proper software (WAsP – Wind Atlas Analysis and Application Program, WindPRO) must be used;
- all obstacles around the wind measurement mast must be taken into account;
- all the roughness and contour lines about 10–20 km around the future wind farm area must be taken into account (allows to calculate wind conditions for every single wind turbine in their exact location);
- correlations with weather station long-term wind data must be made (calculations based on only one year wind measurements without long-term correlations would lead to under- or over estimation of average wind turbine production prognoses).

Wind measurements are rather expensive, but under- or overestimation of the area’s wind conditions and selection of wrong place or wrong turbines for the wind farm will cost much more than accurate wind measurements.

In Estonian coastal areas wind speed 50 meters above the ground level is approximately 6 m/s and it grows considerably comparing with higher measurement points.

REFERENCES

1. BAILEY, B.H.; MCDONALD, S.L. Wind resource assessment handbook. New York: AWS Scientific, 1997. 79 p.
2. Kull, A. Estonian Wind Atlas. Tartu: University of Tartu. 1996. 20 p.
3. http://www.hot.ee/martlei/Eesti%20Kaart.gif
4. Rathmann, O. The UNDP/GEF Baltic Wind Atlas. Roskilde: Riso National Laboratory, 2003. 36 p.
5. Messtechnik für Klimaforschung und Windenergieprognose. Berlin: Ammonit Gesellschaft für Messtechnik GmbH, 2000. 37 p.
6. PERTMANN, I. How to carry out correct wind measurements and what kind of problems may occur during the measurement period. Kuressaare: Tallinn University of Technology. 2006. 3 p.
7. PAIST, A., PARVE, T., KASK, Ü., NUUTRE, M., LOOSAAR, J., VESKI, A., PERTMANN, I. Biokütuste ja tuuleenergia alastest uuringutest Tallinna Tehnikaülikoolis. Tallinn: Estonia Academy of Sciences. 2007. 8 p.

CYSENI 2010, May 27–28, Kaunas, Lithuania
ISSN 1822-7554, www.cyseni.com

COMPARISION OF SOLAR COLLECTORS OPERATION METHODS

P. Shipkovs, A. Snegirjovs, M. Vanags, K. Lebedeva, J. Shipkovs
Institute of Physical Energetics
Aizkraukles 21, Riga, LV-1006 – Latvia
Phone: +371 67553537
Email: shipkovs@edi.lv

L. Vasilevska, M. Pankars
Riga Technical University
Azenes 16/20, Riga, LV-1048 – Latvia
Phone: +371 67615191
Email: lana.vasilevska@rtu.lv

ABSTRACT

Solar collector's operation methods investigated on the Institute of Physical Energetics (IPE) solar energy polygon according different parameters. The most common types of solar collector's operation were investigated and compared: by the time, by the heat carrier temperature differences of input and output, by the solar radiation intensity and operation control methods in various combinations.

Theoretical and practical advantages and disadvantages of using each control methods were analyzed.

Currently, companies that offer solar collectors, offer solar collectors complete set with all necessary equipments for the solar collector connection for hot water supply system, or for home heating operation system by the temperature difference of input and output. And no one of them does not offer solar collectors operation systems by the various parameters.

Except the manual operation system the worst solar collector's operation system is the operation system by time. Usually equipments of the operation system are primitive and those could not used for individual program for each day, so one program is used for all days of the solar collector's operation time. Thereby the fact that the weekly average value of solar radiation is changes, and changes the sun sunshine hours, then it is not possible fully use the obtaining solar energy in sunny days and fully use the solar collectors operation time of spring and autumn periods, in this time the heat storage tank will be more cooled than heated.

The solar collector operation system by the flow and return temperature is one type of solar collectors for operational system. Through this system can provide instantaneous accession and if it is necessary can regulate solar collector operation system; by this operation the system can get instantaneous maximum efficiency. It is necessary to find the optimal speed of heat carrier flows speed.

Solar collector's operation system could be regulated in accordance with the solar radiation intensity, by the boiler lower temperatures and by the outdoor air temperature to determine precisely the solar collector efficiency of the parameter changes. This may help to avoid the previous operation systems testing regime deficiencies.

The precision of solar collectors operation depends on the type of operation systems: heat losses and the collector efficiency calculation accuracy, the sensor is accuracy, the time between the regulation regimes, and the range of heat carrier pumps action operation sensors.

Keywords: solar energy, solar collectors, operation methods

1. INTRODUCTION

On the IPE solar energy polygon investigated solar collectors control methods according different parameters. Were investigated and compared the most common types of solar collector's types. There were analyzed theoretical and practical advantages and disadvantages of using each control methods.

Currently, a large number of companies that offer solar collectors, one-third of them offer solar collector complete set with all necessary equipments to the solar collector connection for hot water supply systems, or home heating. Only a few of them offered two or three solar collector operating control modes, where many differences are in the heat carrier pumps action operating range. And not one of them nor offers solar collectors control systems by the various parameters.

2. METHODS AND RESULTS

2.1. The operation methods of solar collectors

The solar collector control systems are designed for solar collector circulation pump control according changing weather conditions.

2.2. Operation by time

Apart from the manual operation system the weakest solar collector's operation system is the operation system by time. Usually equipment of the operation systems are primitive and those could not be used for individual program for each day, therefore one program is used for all days of the solar collector's operation time.

Thereby the fact that the weekly average value of solar radiation varies, and changes the sun sunshine hours, then it is not possible fully use the obtaining solar energy in sunny days and fully use the solar collectors operation time of spring and autumn periods, in this time the heat storage tank will be more cooled than heated.

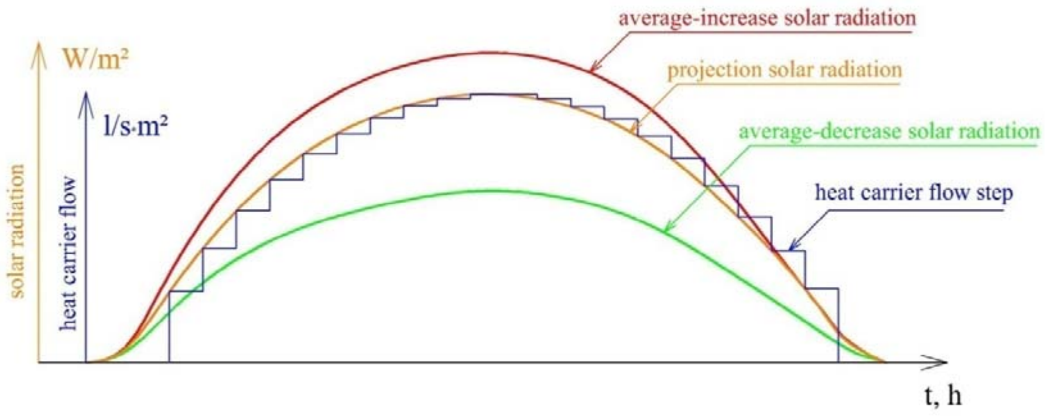

Fig. 1. Heating schedule that shows how the heat depends on the activity of all daily average solar radiation value, and potential of solar radiation deviation

Consequently these solar collector operation type is not widely used anymore.

If only there had been possible to determine operation programm for each day there bigest disadvantage would be connected with systems disability to appoint weather conditions and amount of energy from collector workplace and respectively to adapt for it. Therefore in claudy and rainy days the action of solar colletctors would cool aclumulation tunk.

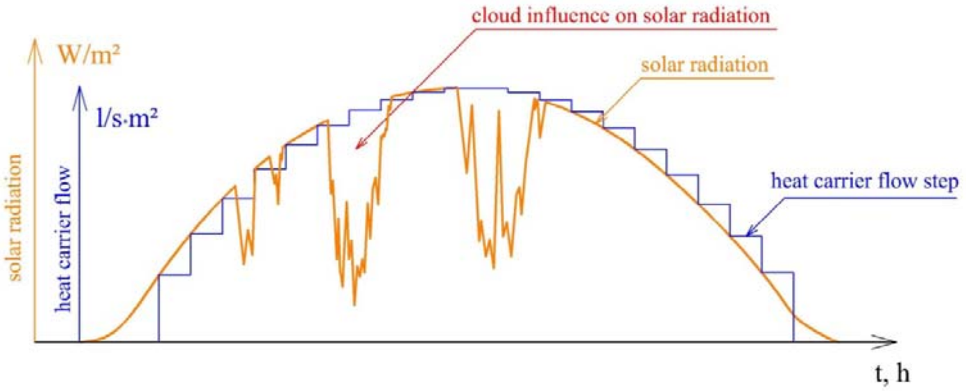

Fig. 2. Heating schedule that shows how the heat depends on the activity of each day average solar radiation value, and potential of solar radiation deviation of cloud activities

2.3. The operation of solar collector according to input and output temperature or output and input temperature of accumulation tank

The operation of solar collector according to temperature difference is needed two sensor of temperature. One is for input temperature measuring, but another for output. If the temperature sources store near solar collector the difference of temperature will be gotten. And if we know heatcarrier flow we will determine the energy which was produced by solar collector. But if temperature source will store very close to heat-exchanging apparatus will be gotten the energy which was produced by solar collector also included energy produced by solar collector pipes heat losses between heat-exchanging apparatus and solar collector. This technique is suitable for continuous heatcarrier flow.

To operate the systems at a temperature difference of one temperature source is positioned in the solar collector warmer point. If there is no such place the temperature source is stored at the gate of solar collector. This technique helps to determine the temperature of heatcarrier in solar collector even in stationary phase. The second temperature recourse is necessary to place in water accumulation tank – output pipe of heatcarrier. The pump is activated through a relay, which provided necessary temperature difference. Unfortunately, (in this way) by the operation of solar collectors we won’t count the heat loss flow conduits between the accumulating tank and solar collectors. Only the minimum temperature differences between the adopted dependence of pipeline length, usually it is from 1 to 8 K.

Turn on according to condition:

$$(T2 - T1) + a \text{ [K]}, \tag{1}$$

a – coefficient of temperature differences, which depends on the pipe lengths (3÷8), K.

Knockout temperature:

$$(T2 - T1) + b \text{ [K]}, \tag{2}$$

b – coefficient of temperature differences, which depends on the pipe lengths (1÷6), K.

After switching the temperature must be above the exit temperature of not less than one degree:

$$a > b \tag{3}$$

and

$$a - b \geq 1 \text{ [K]}. \tag{4}$$

Otherwise the low temperature changing the heat pumps are often turning on and off. This facility will promote accelerated aging and measuring inaccuracies due to thermal inertia.

Third temperature sensor may be placed in the water heat accumulated tank top point, which will signal about accumulation tank overheating. In the event of overheating is necessary to eliminate solar collector circulation pump operation, which will stop temperature increases in accumulation tank.

But the temperature of the solar collectors will rise sharply. IPE studies shows that, in the Latvian region in stationary phase the temperature in some solar collectors in the sunniest days can climb to 180 ºC. Solar collectors can withstand at the maximum temperature, solar collector can withstand from 300 ºC to 600 ºC, depending on the collector type and brand. Consequently solar collectors in the Baltic Sea region are not at risk of overheating.

Even in our climate may be a transient temperature rise above 160 ºC more profitable to use the temperature sensor with high thermal resistance. For example, the PT100 or PT1000 platinum temperature sensors, working from -200 ºC to 850 ºC range.

Management determines the temperature difference between the instantaneous system performance benefits and the opportunity to adjust the solar collector operation; the system allows getting the instantaneous maximum efficiency.

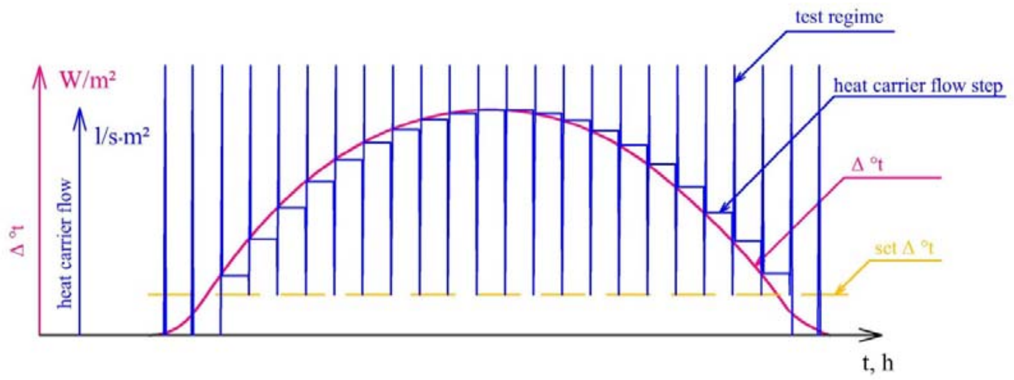

Fig. 3. Heat schedule that shows flow varies depends on temperature difference, including test regimes

The main energy loss will be in all test period (beginning at each step), the productivity will be tested at different flow rates.

2.4. The heat flow rate

To obtain maximum effectiveness it is necessary to provide the optimum heat flow rate. The speed decrease of heat flow increase heat losses in pipes, especially between the solar collector and the accumulating tank. But with increasing flow rate, decreases efficiency of heat exchanger and coolant flow will go with high temperatures which will promote increased energy loss.

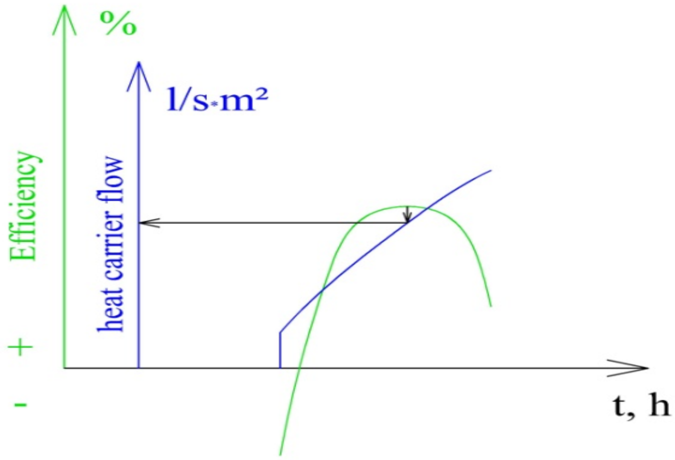

Fig. 4. Heating schedule shows the principle of automation control, depending on the heating temperature difference

At too small or too large flow rates of heat loss may even be greater than the absorbed solar energy collector amount. Particularly large losses, in the testing regime, will be near insufficient weather parameters of productivity, when all flow rates for heat productivity will be negative.

At that time the energy will be spent from the accumulation tank to the testing regime. But, while too little testing arrangements may be insufficiently precise look after weather changes and work with the lowest productivity, not as capable. Therefore, the testing regime and associated with a number of heat loss, as well as deviations from the operating system requires the operating mode is the main weaknesses of theses operation type.

2.5. Operation by solar radiation intensity

Very rarely, only on special order, the solar collectors are guided by the heat source – solar radiation intensity and acumulation tank button temperature.

You can adjust the management of the solar collector solar radiation intensity, the lower boiler temperatures and outdoor air temperature, if determine precisely the solar collector efficiency depends of the parameter changes. To calculate the size required for the flow to increase accuracy and increase reliability estimates would be useful to supplement the system with the flow and return temperature sensors.

If the heat capacity of the substance in the formula:

$$q = c * m * \Delta t, \tag{5}$$

where q – amount of energy, c - heat capacity of the substance, m - the mass, Δt - the temperature difference.

Distributed to the two parts of the formula over time:

$$\frac{q}{T} = \frac{c * m * \Delta t}{T} \tag{6}$$

from there, the energy divided by time is power:

$$\frac{q}{T} = P \tag{7}$$

and quantity of the substance divided by the time is flow:

$$\frac{m}{T} = Q, \tag{8}$$

flow rate depends on:

$$Q = \frac{P}{c * \Delta t}, \tag{9}$$

either:

$$Q = \frac{P_s * \eta_c - P_{c.h-l} - P_{p.h-l}}{c * \Delta t}. \tag{10}$$

P_s – solar radiation intensity, η_c – solar collector absorption efficiency, $P_{c.hl}$ – solar collector heat loss, $P_{p.hl}$ – piping heat losses;

whence:

$$P_{c.h-l} = (t_c - t_a) * K_c, \tag{11}$$

K_c – solar collector heat loss coefficient, t_c – temperature in the solar collector, t_a – ambient temperature,

and

$$P_{p.h-l} = \sum_{i=1}^{n} P_{p.h-l.\,n} = \sum_{i=1}^{n} (t_n - t_a) K_{p.\,n}. \tag{12}$$

t_n – given pipeline stage temperature (may be conditional or reversing flow temperature), $K_{P\,n}$ – given pipeline stage heat loss coefficient.

In the end are get heat loss coefficient of single stage:

$$K_p = \frac{l}{\sum R} = l/(\frac{1}{\pi * d_1 * \alpha_1} + \sum_{i=1}^{k} \frac{1}{2 * \pi * \lambda_k} * ln\frac{d_{k+1}}{d_k} + \frac{1}{\pi * d_2 * \alpha_2}) \tag{13}$$

l – pipe length, ΣR – isolated pipeline full thermal resistance, d_1 – inner diameter, α_1 – inner surface of the thermal conductivity coefficient, λ_k – given pipe layer heat conductivity coefficient, d_k – given the internal diameter of the pipe layer, d_{k+1} – given the pipeline layer of outer diameter, d_2 – insulation design surface diameter, α – thermal insulation design surface conductivity.

It can be avoided by pre-testing management systems deficiencies and the overall productivity of sunny days during the increase of approximately 9%.

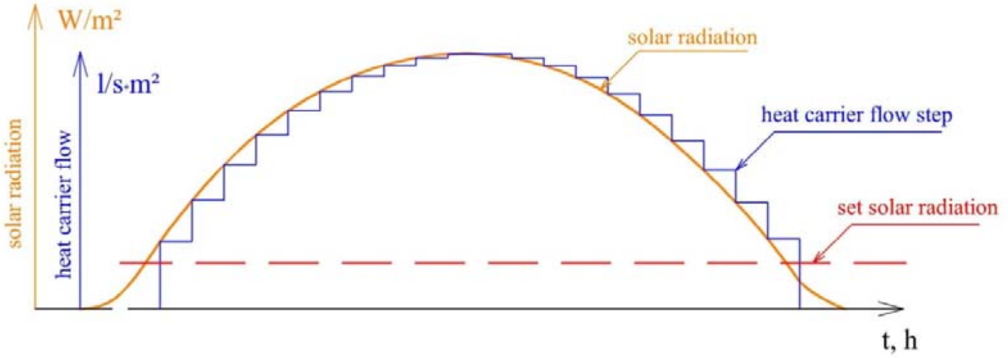

Fig. 5. Heat schedule that shows flow varies depends on solar radiation

Solar collectors work accureancy will depend on: (not including heat loss and the collector yield calculation accuracy) of solar radiation meter accuracy, the time between the adjustment times, and like all previous forms of management, the productivity of the heat pump range.

Weaknesses: no data on the solar collector output for different values of the intensity of solar radiation and solar collector heat loss, heat loss calculation must be precise; solar radiation measuring instruments are expensive, fast erosium process, neccesity of calibration every few years.

To get a solar collector yield at different values of the intensity of solar radiation and heat losses of solar collector needed to conduct the experiment. On the investigated IPE solar energy polygon are also subjected a series of experiments, the solar collector output for different values of the intensity of solar radiation and solar collector heat loss values.

2.5.1 Photo Voltaics like a solar radiation meter

Solar radiation meter accuracy should be similar to the heat pump operation control options. In less able to regulate the heat pump operation, the less can choose the intensity of solar radiation accuracy. Ex.: If solar collector systems are installed in the private home of one - two families, the solar collector operation can be controlled by a small solar panels productivity. But anyway it will be necessary to follow the solar techicque condition and every five years spanned the solar system productivity. Therefore, during the time period of solar battery activity there will be the productivity decrease (an average one per cent per annum).

3. CONCLUSIONS

To get most effectively function of solar collector systems, it is certainly necessary for automation, which regulates a capacity according to various parameters. Automation accuracy depends on the complexity of the system. Than more efficient is the system itself, than more automation response to small environmental changes. By contrast, system complexity makes the system less protected from damages and increased it costs. If are used latest automated technology it is possible to get accurately determined the solar collector system activation time and the required capacity without energy usage for the testing regimes. This is very important for regions with low solar radiation potential.

REFERENCES

1. *Planning and Installing Solar Thermal Systems*, United Kingdom: James & James, 2005. 300 p.
2. *Planning and Installing Photovoltaic Systems,* United Kingdom: James & James, 2008. 388 p.

CYSENI 2010, May 27–28, Kaunas, Lithuania
ISSN 1822-7554, www.cyseni.com

BIOMASS OF GRASSES AND PASTURES FOR UNUSUAL USE - BIOGAS PRODUCTION

V. Tilvikienė, Ž. Kadžiulienė, L. Šarūnaitė
Institute of Agriculture
Lithuanian Research Centre for Agriculture and Forestry
Instituto ave. 1 LT-58344 Akademija, Kėdainiai distr. – Lithuania
Phone: +370 347 37057
Email: vita@lzi.lt

ABSTRACT

Lithuania has aimed ensure that the share of renewable energy sources in final energy consumption in 2020 is not less than 23%. To achieve this goal all renewable energy sources as well as biomass from agriculture should be involved. On the other hand, the changing traditions of farming and the decrease in the number of livestock farms have prompt the search for alternative applications of grassland, one of which could be biogas production. The output and quality of biogas are directly dependent on biomass yield and chemical composition of plants. The potential of using perennial grasses for anaerobic digestion and one of the factors which influences the stability and productivity of biogas production, carbon to nitrogen ratio were analyzed. Pure swards of cocksfoot (*Dactylis glomerata* L), tall fescue (*Festuca arundinacea* Schreb.) reed canary grass (*Phalaris arundinacea* L.) and long term pastures consisting of white clover (*Trifolium repens* L.), lucerne (*Medicago sativa* L.), perennial ryegrass (Lolium perenne L.), and meadow grass (*Poa pratensis* L.) were used for the research. Grasses were grown in the soil characterized as loam *Endocalcari - Endohypogleyic Cambisol* in the centre of Lithuania (55˚ 24‘N). Annual dry matter yield of swards depended on the different swards and fertilization rates. Pure grasses produced from 9.0 up to13.7 t ha^{-1} dry matter in the first year of use. The yield of unfertilised pasture swards was more than 8.0 t ha^{-1} during the 10 years of sward use. The results showed that carbon to nitrogen ratio did not exceed the rates recommended for biogas production, but in pastures it did not reach the minimum values. Perennial grasses can be used for biogas production only after selecting the appropriate species or mixtures.

Keywords: perennial grasses, pastures, biomass yield, carbon to nitrogen ratio, biogas

1. INTRODUCTION

Increasing demand for energy, rising price of fossil raw materials and intensifying environmental pollution prompts to search for alternative energy sources. One of such sources is biomass, which is characterized by effective solar energy storage and wide possibilities of versatile conversion of biomass into biogas. For the formation of energy biomass of different grass species and varieties it is very important to identify such agro technical practices as optimal fertilization, cutting time and frequency. Optimal cutting time determines good plant digestibility and does not exert any negative effect on the yield [1, 2]

Biogas production can make use of most organic material in the absence of oxygen to produce methane for heat generation, electricity and also vehicle fuels. The ability to digest most of organic materials makes this process promising in achieving multiple environmental benefits while using renewable sources for bioenergy. Numerous crops could be available for anaerobic digestion [3, 4, 5, 6]. Biogas production of energy crops is of growing importance. Specific cultivation and harvesting technologies as well as specific genotypes are required when crops are used as renewable energy sources [7, 8, 9, 10].

Anaerobic digestion is a biotechnological process. The maintenance of optimum microbiological activity in the digester is crucial to gas generation and consequently is related to nutrient availability [3, 7]. Two of the most important macronutrients are carbon and nitrogen and a critical factor for raw material choice is the overall carbon to nitrogen ratio. Often the C/N ratio is used as an index of the suitability of organic material for methane rich biogas production but there is no agreement in the literature on the 'ideal' carbon to nitrogen ratio. A low carbon to nitrogen ratio, or too much nitrogen, can cause ammonia to accumulate which would lead to pH values above 8.5 which is toxic to methanogenic bacteria. When the C/N ratio is too wide, carbon cannot optimally be converted to CH_4 and the CH_4 production potential is not fully used.

A 10:1 carbon to nitrogen ratio is the optimal for sequencing batch reactor treatment of shrimp aquaculture wastewater [11]. On the other hand, many researches suggest that anaerobic digestion of manure, energy crops and many other sources of biomass requires a carbon to nitrogen ratio of between 20/1-30/1[8, 12, 13]. Biogas potential of different grasses varies from 400 l $kg^{-1}{}_{ODM}$ to 900 l $kg^{-1}{}_{ODM}$ depending of grass species and biomass quality [6]. The main focus of the underlying study was the difference of grass species and pastures and the influence of harvest time and nitrogen fertilization on dry matter yield and carbon to nitrogen ratio formation in biomass.

2. METHODOLOGY

Because of expected high biomass yield and optimal biomass quality for biogas production pure swards of cocksfoot (*Dactylis glomerata* L), tall fescue (*Festuca arundinacea* Schreb.) reed canary grass (*Phalaris arundinacea* L.) and long term pastures consisting of white clover (*Trifolium repens* L.), lucerne (*Medicago sativa* L.), perennial ryegrass (Lolium perenne L.), and meadow grass (*Poa pratensis* L.) were chosen for the research. Swards were cultivated in central Lithuania (55˚ 24'N).

Cocksfoot, tall fescue and reed canary grass were sown in 2008. The results from the firs year of use are analyzed. Pure swards were fertilized with mineral nitrogen fertilizers. The application rate of nitrogen was 90 kg ha^{-1} and 180 kg ha^{-1} per year. Fertilization of cocksfoot, tall fescue and reed canary grass was combined with harvesting. When the first cut was made at heading stage 1/3 of mineral nitrogen fertilizers were applied in early spring in the beginning of vegetation, second fertilization was made after first cut ant the third fertilization after the second cut. When the first cut was made at flowering stage ½ of mineral nitrogen fertilizers was applied in the beginning of vegetation and the other half after the first cut. Pastures were not fertilized.

During 1998–2006 a randomized block design field trial was carried out. The results for this study were taken from the year 2005–2006. The treatment involved four different swards consisting of: 1. white clover 40% + perennial ryegrass 60%; 2. white clover 40% + perennial ryegrass 30% + meadow grass 30%; 3. lucerne 60% + meadow grass 20% + perennial ryegrass 20%; 4. lucerne 30% + white clover 30% + perennial ryegrass 40%.

In the year 2009, pure grass swards were harvested three and four times per season, depending on the vegetation stage during the first cut. Pastures consisting of different swards were cut three times per season in 2005 and four times per season in 2006 because of the different weather conditions.

The grasses were cut using a mowing machine. The biomass yield of the grasses was determined by taking 4 samples from an area of 15 m^2 and weighing them. After that, harvested grass material samples of about 0.5 kg were taken to the laboratory and chopped to a ca. 1 cm partical size then weighted and dried in the oven in 105 ^{o}C temperature until constant weight. Dry matter yield was measured.

The total nitrogen and organic carbon were determined using the Dumas method (DIN/ ISO 13878).

3. RESULTS AND DISCUSSION

One of the main factors in selecting energy crops for biogas production is achieving large quantities of biomass feedstock [3; 14]. Dry matter yield of fodder grass swards can reach 6–13 t ha-1 in leys and 6–7 t ha^{-1} DM in pastures depending on management [15, 16, 17]. In our research, annual dry matter content of plant species of pure swards investigated varied from 8.3 to 13.8 t ha^{-1} (Fig. 1). In Lithuania, the biomass yield of the first cut of most perennial grasses can account for from 47% to 65% of the annual biomass yield when cut at the heading stage and about 6-10% more when cut at the flowering stage [18]. In the first year of our research the situation in cocksfoot sward was different. In the first cut at heading stage dry matter yield reached 3.0 t ha-1 and it was lower compared to the second cut when the dry matter yield was approximately 4 t ha-1. Cocksfoot harvested for the first time at flowering stage averaged 4.6 to 4.8 t ha^{-1} of dry matter when the sward was fertilized with both levels of mineral nitrogen. Dry matter yield of the second cut was 2.8 t ha^{-1} (fertilized with N_{90}) and 4.2 t ha^{-1} (fertilized with N_{180}). This shows that nitrogen fertilization had a great effect on biomass yield of the second cut. The dry matter yield of the third cut of cocksfoot as well as of tall fescue and reed canary grass was the lowest.

The dry matter content varied extremely between grass species. In the year 2009, tall fescue swards produced higher biomass yield compared to cocksfoot and reed canary grass. Till the flowering stage tall fescue accumulated around 5 t ha^{-1} of dry matter, in the second cut dry matter yield was 4 t ha^{-1}. Dry matter yield of the first cut made at flowering stage was 8 t ha^{-1}, of the second cut about 5 t ha^{-1}. The lowest values were obtained for reed canary grass biomass.

The biomass yield showed a clear dependence on nitrogen fertilization level within each grass species.

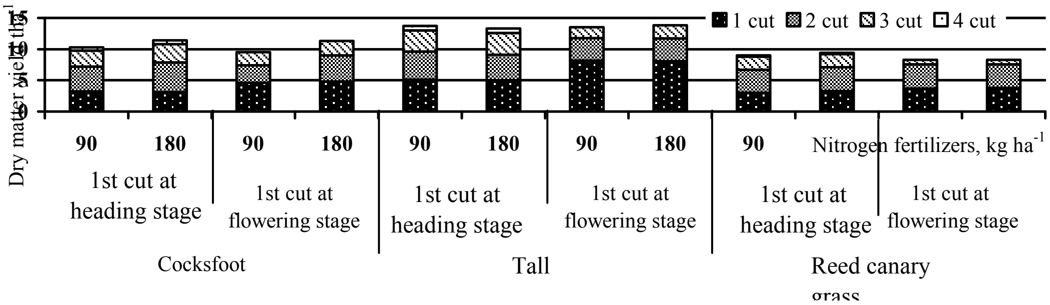

Fig. 1. The variation of annual biomass yield of cocksfoot, tall fescue and reed canary grass

The quantity of dry matter per unit area of production, determines the potential energy production capacity. The total annual dry matter yield of long term pastures consisting of white clover, lucerne, perennial ryegrass and meadow grass was primarily affected by the climatic conditions and less by sward composition (Fig. 2). The weather conditions in 2005 were conductive to the growth of sward, since warm and wet weather prevailed. In the first half of sward growing season all pastures produced the highest and almost similar dry matter yield. The yield of 3rd and 4th cuts of pastures with white clover was significantly lowest compared with that of pastures consisting of lucerne. The pasture with one type of legume (lucerne) grew intensively and produced 1.00 t ha^{-1} higher yield than the pasture consisting of lucerne and clover swards. In 2006, the summer period was dry and growing conditions were contrary to the previous year for perennial sward growth. The annual biomass yield of all pastures was in 2006 two times lower than in 2005. The yield was significantly higher or trend of increasing was obtained for lucerne/white clover/perennial ryegrass pasture compared with the yield of other pastures. Generally, pastures consisting of lucerne sward were more productive compared to white clover and grass pastures.

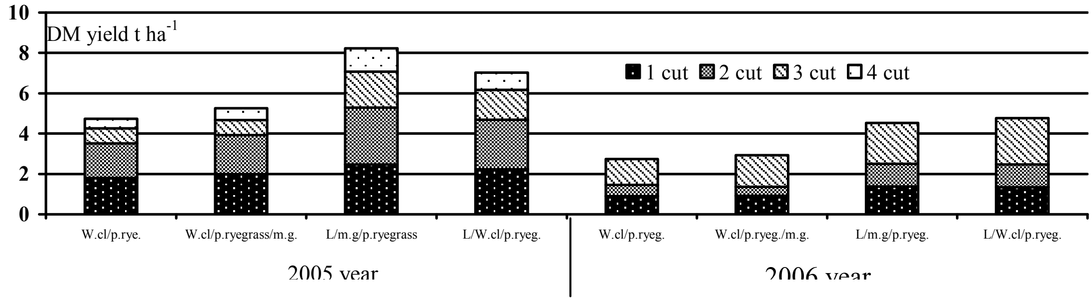

W.cl/p.rye – white clover/perennial ryegrass; W.cl/p.rye/m.g – white clover/perennial ryegrass/meadow grass; L/m.g/p.rye – lucerne/meadow grass/perennial ryegrass; L/W.cl/p.rye. – lucerne/white clover/perennial ryegrass.

Fig. 2. The variation of annual biomass yield of pastures

The stability of anaerobic digestion is influenced by many parameters one of which is carbon to nitrogen ratio which changed significant during plant growth [3; 19; 20]. In our research, in all treatments the carbon to nitrogen ratio was higher in the biomass harvested at flowering stage compared to the biomass harvested at heading stage.

As anaerobic bacteria consume carbon roughly 20–30 times faster than nitrogen, the carbon and nitrogen ratio in the biomass for anaerobic digestion is optimum 20–30 [21]. In the present study the most suitable C/N ratio was in the cocksfoot and tall fescue biomass during the first, second and third cuts when swards had been fertilized with 90 kg ha^{-1} nitrogen rate (Fig. 3).

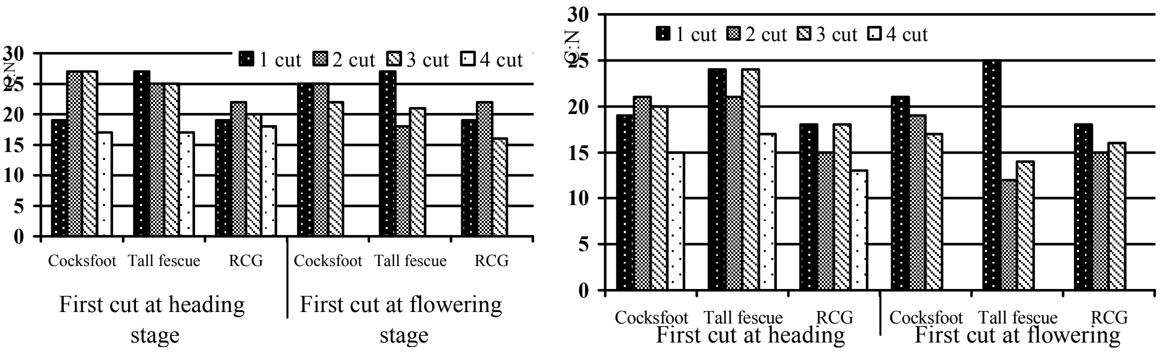

Pure swards, nitrogen fertilization rate 90 kg ha^{-1} Pure swards, nitrogen fertilization rate 180 kg ha^{-1}

Fig. 3. The variation of the ratio of carbon to nitrogen in the biomass of cocksfoot, tall fescue and reed canary grass

The C:N ratio of reed canary grass (all cuts) ranged within 16–22, it was the lowest value of all grasses. The higher level of nitrogen fertilization resulted in significant reduction of carbon to nitrogen ratio for most of the grasses grown in pure swards.

The results of our study indicated that the quality of digestible material as well as the carbon to nitrogen ratio depended on the cultivation and mostly on the climate. The pastures, presented in this paper produced lower carbon to nitrogen ratio in the year 2005 when the weather was warm and wet compared to the results of the year 2006 (Fig. 4). The highest carbon to nitrogen ratio was in the biomass during the second cut. The variation of the results of C/N ratio of pastures was 10.3–17.8. Even the highest values of C/N in biomass of different pastures did not reach the minimum ratio for biogas production.

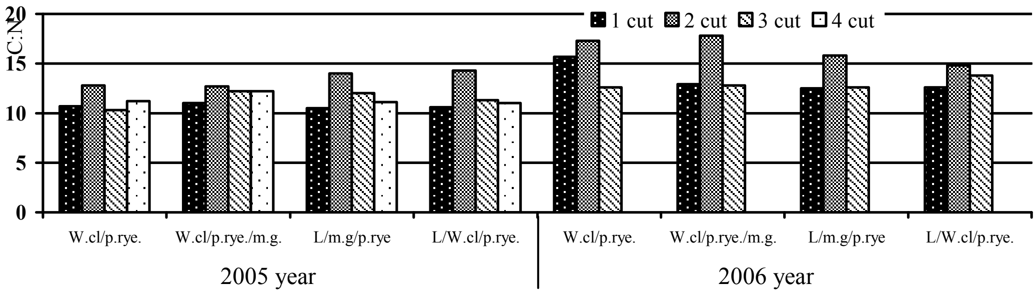

W.cl/p.rye – white clover/perennial ryegrass; W.cl/p.rye/m.g – white clover/perennial ryegrass/meadow grass; L/m.g/p.rye – lucerne/meadow grass/perennial ryegrass; L/W.cl/p.rye. – lucerne/white clover/perennial ryegrass.

Fig. 4**.** The variation of the ratio of carbon to nitrogen in the biomass of pure swards and mixtures

As it was mentioned before, the main task when selecting crops for anaerobic digestion is to achieve the highest biomass yield of the best quality. The results suggest that the carbon to nitrogen ratio of pure swards was higher in the biomass of more productive plants (Fig. 5).

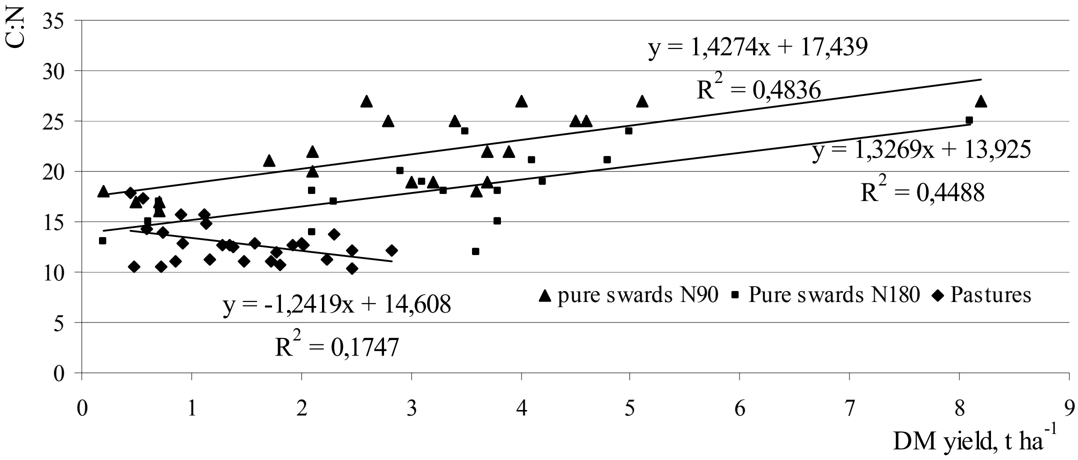

Fig. 5. The variation of carbon to nitrogen ratio in the biomass of pure swards and pastures

The highest values of C/N ratio did not exceed the ‘ideal’ ratio for biogas production. Different situation was measured in the biomass of pastures.

Most grassland currently is used for feeding domestic herbivores and it is argued that bioenergy production from grassland would displace part of the forages from their traditional role of feeding animals. As well as for fodder environmental impacts of grassland based biogas production depend on management intensity to a large extent and also on species, varieties and mixtures of grasses. The results of our research suggest that pure swards grown on arable land are more productive and have optimal carbon to nitrogen ratio for methane rich biogas production.

4. CONCLUSIONS

The results from the first experimental year suggest that cocksfoot and tall fescue are better than reed canary grass and pastures for biogas production in boreal conditions because they offer higher specific dry matter yields per hectare and have better carbon to nitrogen ratio for anaerobic digestion. More research is needed to prove that the selection of grasses for bioenergy is necessary to achieve the highest efficacy of biogas production.

REFERENCES

1. SEPPÄLÄ M., PAAVOLA T., LEHTOMÄKI A., RINTALA J. Biogas production from boreal herbaceous grasses – Specific methane yield and methane yield per hectare. Bioresource Technology, 2009, Vol. 100, p. 2952–2958.
2. MONTI A, BEZZI G, PRITONI G, VENTURI G. long-term productivity of lowland and upland switchgrass cytotypes as affected by cutting frequency. bioresource technol. 2008, 99:7425–7432.
3. AMON T., AMON B., KRYVORUCHKO V., MACHMULLER A., HOPFNER-SIXT K., BODIROZA V., HRBEK R., FRIEDEL J., POUTSCH E., WAGENTRISTL H., SCHREINER M., ZOLLITSCH W. Methane production through anaerobic digestion of various energy crops grown in sustainable crop rotations. Bioresource Technology, 2007, Vol. 98, p. 3204–3212.
4. BAUER, A. Potential of biogas production in sustainable biorefinery concepts. Proceedings of the 15th European Biomass Conference and Exhibition, Berlin, 2007 May 7–11.
5. MCKENDRY P. Energy production from biomass (Part 1): overview of biomass. Bioresource Technology 2002, Vol. 83, p. 37–46.
6. PROCHNOW A., HEIERMANN M., PLOCHL M., LINKE B., IDLER C., AMON T., HOBBS P.J. Bioenergy from permanent grassland – A review: 1. Biogas. Bioresource Technology, 2009, Vol. 100, p. 4931–4944.
7. AMON T., KRYVORUCHKO V., AMON B. Methane production from maize, grassland and animal manures through anaerobic digestion. Organic Waste Treatments: Safety Implications, 2004, p. 175–178.
8. BORJESSON P. Environmental efects of energy crop cultivation in Sweden: Identification and quantification. Biomass and Bioenergy, 1999, Vol. 16, p. 137–154.
9. LEHTOMÄKI, A., VIINIKAINEN, T.A. & RINTALA, J.A. Screening boreal energy crops and crop residues for methane biofuel production. Biomass and Bioenergy, 2008, Vol. 32, p. 541–550.
10. LEMEZIENE N., KANAPECKAS J., BUTKUTE B. Biodujų gamybai tinkamos paprastosios šunažolės (*Dactylis glomerata* L) veislės, selekcinės linijos ir ekotipai. Zemdirbyste – Agriculture, 2009, Vol. 96 (3), p. 36–46.
11. FONTENOT Q., BONVILLAIN C., KILGEN M, BOOPATHY R. Effects of temperature, salinity, and carbon: nitrogen ratio on sequencing batch reactor treating shrimp aquaculture wastewater. Bioresource Technology, 2007, Vol. 98, p. 1700–1703.
12. ARIFIANTARI P., HANDAJANI M., SEMBIRING T. ratio c/n effect to the degradation of organic material in traditional market waste (biowaste) by anaerobic process. Faculty of Civil and Environmental Engineering Institute Technology of Bandung [refered on the 20 of January in 2010] Link to the internet <http://kuliah.ftsl.itb.ac.id/wp-content/uploads/2009/04/re-15304024-sw-1-pratiwi-nur-a.pdf>
13. SINGHAL, V., RAI, J.P.N. Biogas production from water hyacinth and channel grass used for phytoremediation of industrial effluents. Bioresource Technology, 2003, Vol. 86, p. 221–225.
14. HEIERMANN M., PLÖCHL M., LINKE B., SCHELLE H., HERRMANN C. Biogas Crops – Part I: Specifications and Suitability of Field Crops for Anaerobic Digestion. Agricultural Engineering International: the CIGR Ejournal. Manuscript 1087, 2009, Vol. 11.

15. BRENCIENĖ V. Varpinių žolių palyginimas Vakarų Lietuvos velėniniame jauriniame ir velėniniame jauriniame glėjiškame dirvožemyje. Žemdirbystė: LŽI mokslo darbai, 1995, t. 46, p. 16–22.
16. DAUGĖLIENĖ, N. Žolininkystė rūgščiuose dirvožemiuose. Lietuvos žemdirbystės institutas. Arx_Baltica, Kaunas, 2002, 261 p.
17. KADZIULINE Z., KADZIULIS L. Botanical composition and stability of yield in legume/grass swards over eight years under grazing. Grassland Science in Europe, 2007, Vol. 12, p. 47–50.
18. KANAPECKAS J., LEMEŽIENĖ N., TARAKANOVAS P., NEKROŠAS S., AND PAPLAUSKIENĖ V. Plaukėjimo fazėje pjautų daugiamečių varpinių žolių derliaus ir jo vertės palyginimas. Žemės ūkio mokslai, 1999, Vol. 1, p. 10–16.
19. RACLAVSKÁ H., JUCHELKOVÁ D., ROUBÍČEK V. Utilisation of biomass and mixtures for the gas production // International conference on engineering education. – Coimbra, Portugal, 2007.
20. BUTKUTĖ B., PAPLAUSKIENĖ V. Daugiamečių varpinių žolių pašarinės vertės potencialas. Žemdirbystė-Agriculture, 2006, t. 93, Nr. 3, p. 172–187
21. DENNIS A., BURKE P.E. Dairy Waste Anaerobic Digestion Handbook, 2001, 57 p.

CYSENI 2010, May 27–28, Kaunas, Lithuania
ISSN 1822-7554, www.cyseni.com

SIMULATION OF A VERTICAL U-TYPE HEAT EXCHANGER FOR GEOTHERMAL SYSTEMS

M. Valantinavičius, V. Girdauskas
Department of Physics, Vytautas Magnus University
Vileikos str. 8, LT-44404, Kaunas – Lithuania
Phone: +37037327922
Email: mantas.valantinavicius@live.vdu.lt

ABSTRACT

Geothermal heating systems are becoming increasingly popular for public and individual buildings. But they have some disadvantages, most notable of which is that such systems require major investments into geological research and installation of heat exchanger. One of the most important components in this type of systems is a heat exchanger, supplying geothermal heat to heat pump. Selecting the proper parameters of a heat exchanger is critical for overall efficiency and installation costs of a geothermal heating system. Simulations of engineering parameters of heat exchangers are based on quite approximate methods. In this work, we carried out a Finite Element Method computer simulation of a vertical U-type heat exchanger using the COMSOL Multiphysics software package. We solved a 3D heat conduction problem, allowing more accurate assessment of vertical U-type heat exchanger parameters, such as the thermal resistance and heat flux, depending on geometry of the wells, grout and soil parameters.

Keywords: Geothermal heating systems; U-type heat exchanger; Heat transfer; 3D numerical borehole model

1. INTRODUCTION

Geothermal heating systems are becoming ever more popular because of increasing heating costs. For example, in Sweden there are more than 360000 geothermal heating systems installed.

Geothermal heating systems for buildings are relatively simple: liquid heat carrier circulates in a closed loop – underground heat exchanger, and the heat extracted from the soil is transferred to the heat pump that supplies heat to the building. A typical collector of a geothermal heating system is a vertical borehole with the depths of several tens of meters, and the diameter from 10 to 15 centimetres. In the borehole, two vertical pipes are installed, connected at the bottom of the borehole, through which the heat carrying liquid circulates. The borehole is filled with a grout enhancing the heat exchange between the liquid circulating in the pipes and the surrounding soil. Since the configuration of the collector pipes through which the liquid circulates in the borehole is similar to letter “U”, this type of vertical heat exchangers is referred to as U-type heat exchangers.

Since installation of a vertical U-type heat exchanger is rather expensive, estimation of thermal parameters of the heat exchanger with preferably highest accuracy is an important task. For example, increase in temperature of the heat carrying liquid of one degree Celsius at the exit from the heat exchanger increases efficiency of the geothermal heating system by 2 to 3 percent.

For calculation of the U-type heat exchanger parameters, approximate analytical methods are widely used: the linear source model [1], the cylindrical source model [2, 3] and various modifications [4] of these. The numerical solution methods for heat transfer and fluid flow equations are becoming ever more popular: finite differences, finite volumes and finite elements [5, 6].

Advantages of numerical methods, compared to analytical ones, include the possibility to simulate larger variety of heat exchanger and soil configurations with greater accuracy, unlimited by approximations characteristic of analytical methods. Application of specialized software for heat transfer simulations extended considerably the capabilities to use numerical methods for simulations of thermal properties of the heat exchangers.

In this contribution, we present the method for simulation of U-type thermal heat exchanger by means of the COMSOL MULTPHYSICS software package and discuss the results. We obtained the longitudinal and transversal temperature profiles of the heat exchanger and the borehole, examined the dependence of convective heat flow on velocity of the heat carrying liquid, and determined the dependence of the heat obtained on the soil thermal characteristics.

2. 3D BOREHOLE NUMERICAL MODEL

The scheme of the simulated U-type heat exchanger is presented in Fig. 1. It shows the vertical cross-section of the heat exchanger. The geometrical parameters used for simulation are presented in Table 1. The parameters of the heat carrying liquid (mixture of 40% of ethylene glycol and water), the borehole grout and various soils are presented in Table 2. The temperature of the liquid at the heat exchanger entrance is T_{in}, and at the exit - T_{out}. It is assumed that the fluid flow is laminar and its velocity profile is constant throughout the entire heat exchanger length:

$$v(r) = v_{\max}(1 - \frac{r^2}{R_0^2}) \tag{1}$$

Here, v_{max} is the flow velocity along the heat exchanger pipe axis; R_0 is the pipe inner radius. The assumption of laminar flow is correct for velocities $\bar{v} = 0.5 v_{\max} \le 0.26 m/s$, because $\mathrm{Re} = \rho \bar{v}(2R_0)/\mu \le 2300$ (the temperature of 40% water based ethylene glycol is $10\,^{\circ}C$ and $\mu = 4.1 \cdot 10^{-3} Pa \cdot s$). The cylindrical domain for solution of heat exchange problem between the heat exchanger and the soil is shown in Fig. 2. Its height is equal to the heat exchanger length excluding the bent section that connects the pipes at the bottom. The connecting section was simulated in such a manner that at the bottom cross section of the ascending pipe, the transverse profile of velocity and temperatuzre was the same as that at the bottom section of the descending pipe. It is assumed that the heat transfer through the top and bottom planes of the domain can be neglected due to small longitudinal temperature gradient in the heat exchanger. Since the plane containing the borehole and pipe axes is the collector symmetry plane, the heat transfer problem was solved for only half the cylindrical domain. Having performed the test calculations, the diameter of the cylindrical domain was selected in such a way that the temperature at its side surface can be considered equal to the unperturbed soil temperature T_{∞}. It is assumed that the unperturbed soil temperature is $10\,^{\circ}C$ and it is equal at all depths, because approximately from 13 meters depth soil temperature is constant [8].

Table 1. Geometrical characteristics of 3D model [7]

Geometric parameter	Value
Borehole depth	80 m
Borehole diameter	0.15 m
Internal pipe diameter	0.0274 m
External pipe diameter	0.0335 m
Pipe center to center distance	0.11 m

We use 3D finite element numerical model for solving the heat transfer problem, which is constructed using Comsol Multiphysics, general heat transfer module, software package.

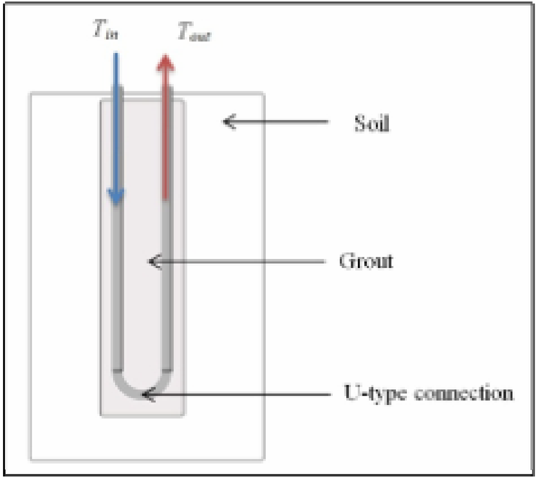

Fig. 1. Schematic diagram of U-type heat exchanger

The geometry was divided to triangular and quad shape grid, Fig. 2a, b. Predefine mesh size of the grout and fluid zone was generated by using extremely fine mesh Fig. 2b, the ground zone mesh was generated by using normal quad predefined mesh size. In order to get maximum mesh quality in fluid zone at the pipe wall, quad shaped mesh was used Fig. 2b. Vertically geometry is divided in a 240 equal layers in order to obtain appropriate quality of mesh geometry Fig. 2c.

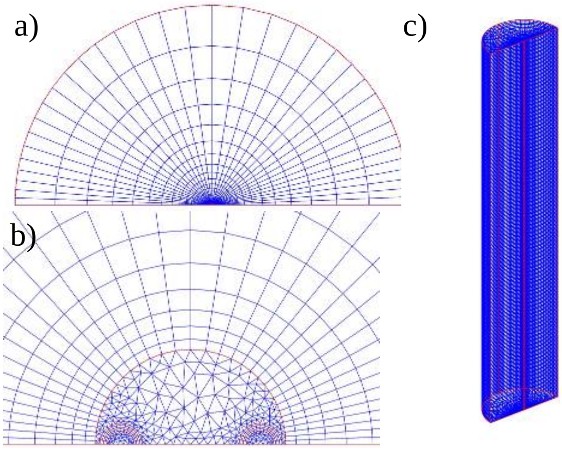

Fig. 2. 3D numerical model geometry

At the top of descending pipe, boundary condition was used as a constant temperature. At the bottom of the descending pipe the boundary condition is as a convective flux, and the same transversal temperature distribution is given to ascending pipe bottom using identity boundary pairs. Convective flux boundary condition is given at the top of ascending pipe. The continuity condition is used for the borehole and pipe wall. The top and the bottom of ground and grout boundary conditions are used as insulation.

Table 2. Materials properties [5]

Material	Density kg/m^3	Heat capacity J/(kg*K)	Thermal conductivity W/(m*K)
Pipe (polyethylene pipe)	950	2000	0.56
Ethylene glycol 40% by volume (water based)	1070	3537	1.445
Grout	1320	641.03	1.08
G1 Heavy clay (15% water)	1952	1408	1.65
G4 Heavy clay (5% water)	1952	983	1.2
G5 Light clay (water content 15%)	1285	1121	0.85
G6 Light clay (water content 5%)	1285	838	0.7
G2 Dense sand (water content 15%)	1925	1530	3.3
G3 Dense sand (water content 5%)	1925	840	2.2
G7 Light sand (water content 15%)	1285	1489	1.55

3. DISCUSSION OF THE RESULTS OF MODELING

We started by analyzing the influence of the fluid flow velocity in the heat exchanger on the outflowing liquid average temperature at the exit cross section $<T_{out}>$ and the convective heat flux

$$Q = Q_{in} - Q_{out}, \tag{2}$$

where Q_{in} is the inflow rate and Q_{out} is the outflow rate.

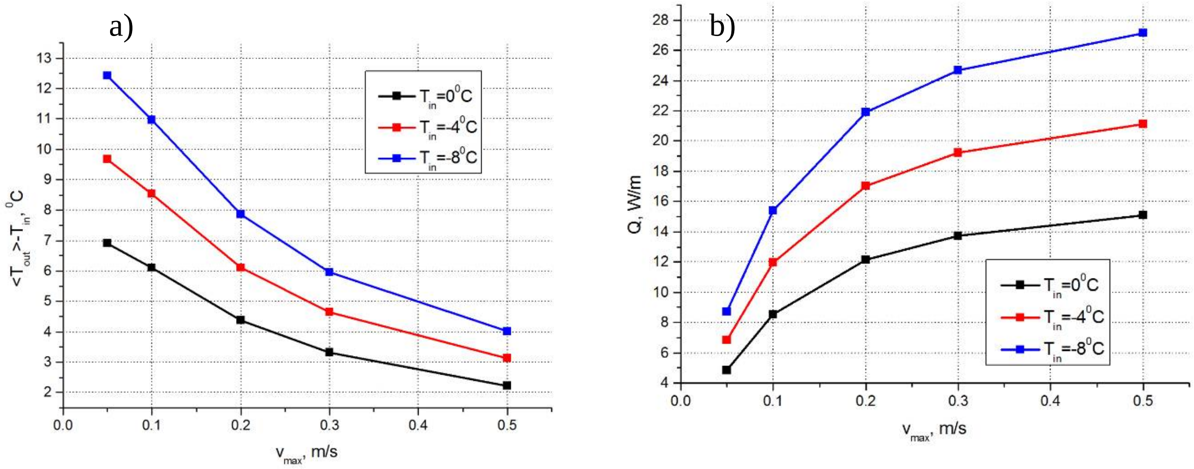

Fig. 3. Temperature difference of inflowing and outflowing fluid (a) and heat flux (b) dependences on the velocity of fluid

The change in temperature difference $<T_{out}>-T_{in}$, when T_{in} are different for different liquid temperatures at the inflow and the flow velocity v_{max} changes from 0.05 *m/s* to 0.5 *m/s*, is shown in Fig. 3a. It is seen that the difference between the inflowing and outflowing temperatures decreases as the flow velocity increases. The temperature difference is largest for the lowest temperature of the inflowing liquid. The transverse temperature profile at the collector exit in Fig. 4a shows that at higher flow velocities the liquid temperature raises noticeably in the boundary layer, and the temperature near the pipe axis remains lower than that of the walls of the pipe. Only when the flow velocity is 0.2 *m/s*, the liquid temperature is almost homogeneous throughout the entire outflow cross section. For even lower flow velocity, the liquid temperature at the outflow is higher near the pipe axis than at the wall.

Difference between the temperatures at the boundary layer and at the pipe axis is evident also in the longitudinal temperature profiles, Fig. 5a, the longitudinal temperature profile in Fig. 5a show that the temperature grows almost linearly at the boundary and at the axis in the largest part of the heat exchanger, except for the entrance and the exit. At the entrance, rapid rise of the temperature is noticeable at the boundary. Only after the rapid rise levels off and transforms into the linear growth at the boundary, the temperature begins to rise also at the pipe axis. The temperature growth rate declines near the exit, because of intense influence of heat transfer between the cold liquid at the heat exchanger entrance and the warm liquid at the heat exchanger exit. Interaction between the cold and warm pipe of the heat exchanger is more intense for lower liquid flow velocity is shown in Fig. 5b. Heat exchange can be so intense, that the temperature of outflowing fluid starts to drop.

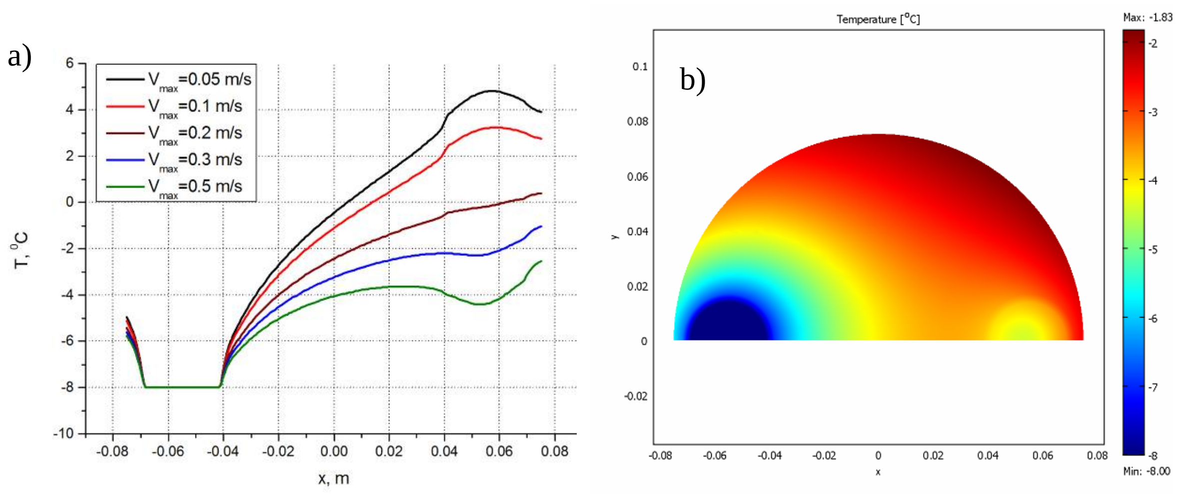

Fig. 4. Temperatures along the axis of symmetry of upper slice of borehole at different velocities of fluid (a) and at the entire upper slice of borehole, when the velocity of fluid is 0.3 *m/s* and T_{in}=-8 ^{o}C (b)

Dependence of heat flux per unit heat exchanger length on the liquid flow velocity and the temperature at the entrance are shown in Fig. 3b. It is seen that the laminar flow velocity ensuring the optimum heat exchanger performance is approximately 0.3 *m/s*. As the flow velocity further increases, the heat flux increases relatively insignificantly, and the temperature difference $<T_{out}>-T_{in}$ decreases. In the examined temperature range T_{in}, the optimum velocity does not depend on the liquid temperature at the entrance. As the incoming liquid temperature decreases, the heat flux received by the heat exchanger increases, because the temperature gradient between the heat exchanger and the soil increases. For the simulated 80 *m* long heat exchanger, decrease of T_{in} by four degrees led to increase of the heat flux by more than a factor of 1.3.

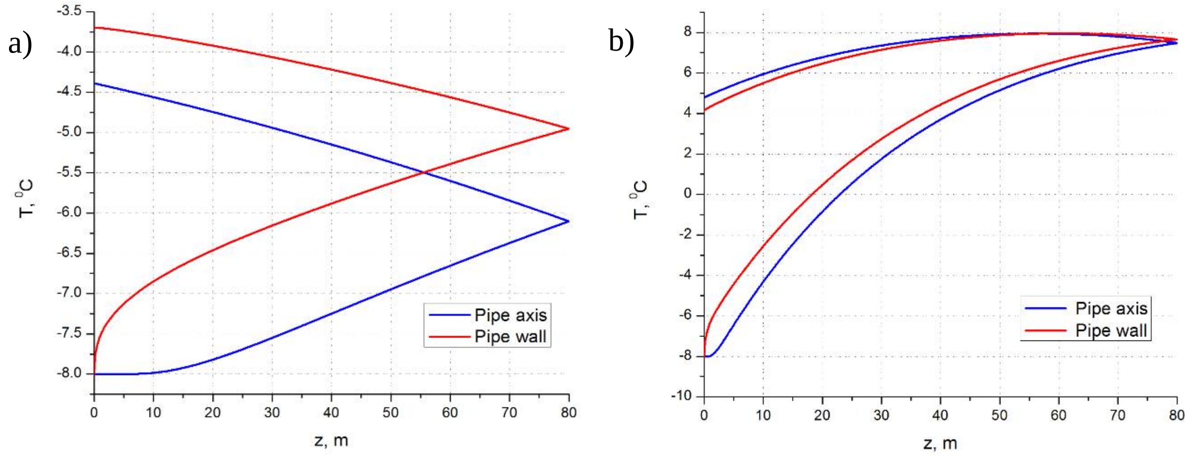

Fig. 5. Temperature of a fluid along the axis of pipe and the pipe wall, when fluid velocity is 0.5 *m/s* (a) and 0.05 *m/s* (b)

Since the thermal properties of different soils differ noticeably Table 2, calculations of the heat flux received by the heat exchanger and the temperature difference of the inflow and outflow liquids were performed for different soil types. It has been determined that for different types of soil, the heat exchanger heat flux can differ by more than 2.5 times (from 13.4 *W/m* to 35.9 *W/m*) Fig. 6a, and the temperature difference – by almost three times, Fig. 6b, for the same heat exchanger geometry and the grout, and for the same soil temperature far away from the heat exchanger. The highest heat flux and the temperature difference are obtained for the soil G2 (Dense sand (water content 15%)), and the lowest heat flux and the temperature difference is obtained for the soil G6 (Light clay (water content 5%)).

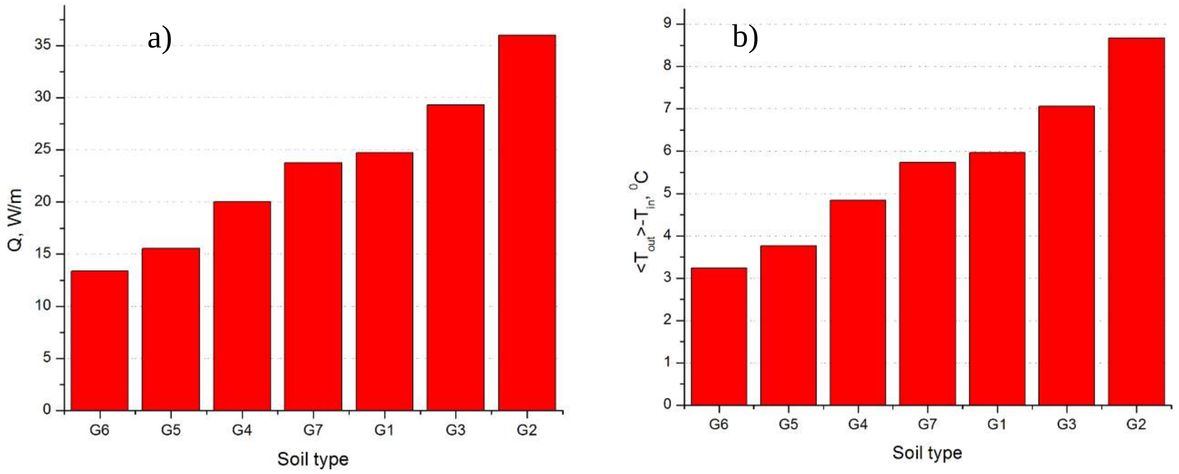

Fig. 6. The heat flux for the length of unit of geothermal heat exchanger (a) and temperatures differences of inflowing and outflowing fluid (b) for the different types of soil, when fluid velocity is 0.3 *m/s* and T_{in}=-8°C

4. CONCLUSIONS

In this work, we carried out a Finite Element Method computer simulation of a vertical U-type heat exchanger using the COMSOL Multiphysics software package. Heat exchange model was used taking into account different heat conduction values of soil, grout, collector pipe walls and liquid. For simulation of convective heat transfer, the model of laminar fluid flow was applied with parabolic velocity profile and identity pairs boundary conditions for the U-type junction at the collector bottom. Dependences of thermal parameters of the collector on the liquid flow velocity and its temperature at the inflow, as well as the thermal properties of the surrounding soil, were examined. It has been shown that the collector heat flux rises and the difference of the inflow and outflow liquid temperatures decreases with the increasing liquid flow velocity in the collector. Increase of the heat flux slows down when the flow velocity exceeds 0.3 m/s. It was shown that at low flow velocities, intense heat transfer takes place at the upper part of the collector between the descending and ascending collector pipes, therefore, the thermal efficiency of the collector is noticeably lower than that in case when the liquid flow velocity is higher than 0.3 m/s.

REFERENCES

1. INGERSOLL, L.R.; PASS H.J. *Theory of Ground Pipe Heat Source for the Heat Pump: Heating,* (1948) *Piping & Air Conditioning.* July: 119–122.
2. HELLSTROM, G., *Ground Heat Storage. Thermal Analysis of Duct Storage Systems I: Theory.* (1991) University of Lund, Department of Mathematical Physics. Lund, Sweden.
3. KAVANAUGH, S. *A Design Method for Commercial Ground-coupled Heat pumps.* (1995) ASHRAE Transactions. 101(2): 1088–1094.
4. SUTTON, M.G., COUVILLION R.J., NUTTER D.W., DAVIS R.K. *An Algorithm for Approximating the Performance of Vertical Bore Heat Exchangers Installed in a Stratified Geological Ragime.* (2002) ASHRAE Transactions. 108(2): 177–184.
5. ROTTMAYAR, S.P., BECKMAN, A., MICHELL, J. W. *Simulation of a single vertical U-tube ground heat exchanger in an infinite medium.* (1997) ASHRAE Transitions. 103(2): 651-659
6. ZENG, H., DIAO N., FANG Z. Heat transfer Analysis of boreholes in vertical heat ground heat exchangers*. (2003) International Journal of Heat and Mass transfer.* 46(23): 4467–4481
7. LIU JUN, ZHANG XU, GAO JUN, YANG JIE. *Evaluation of heat exchange rate of GHE in geothermal heat pump systems.* (2009) Renewable Energy 34 2898–2904.
8. SANNER, B., MANDS, E., SAUER, M., GURDMAN, E. *Technology, development, and routine application of Thermal Response Test.* Proceedings European Geothermal Congress. Germany, Unterhaching, 2007 May 30 – June 1.

CYSENI 2010, May 27–28, Kaunas, Lithuania
ISSN 1822-7554, www.cyseni.com

INVESTIGATION OF THE PERFORMANCE OF LOW CAPACITY BOILERS (UP TO 300 KW) FIRED WITH BIOFUEL

T. Vonžodas, A. Grigula
Lithuanian Energy Institute
Laboratory of Heat-Equipment Research and Testing
Breslaujos str. 3, LT-44403, Kaunas – Lithuania
Phone: +370-37-401864
Email: vonzodast@mail.lei.lt, grigula@mail.lei.lt

ABSTRACT

The growing public concern about environmental pollution and the strict requirements of the new EU normativedocuments for the sources of pollution encourage searching for the effective tools to reduce pollution by improving the construction of the equipment fired with various types of fuel, including wood fuel. The main part of wood fuel about 60% is consumed in the households, and only about 17-20% - in central heating boilerin in Lithuania. Therefore, it is very important that the small and middle size boilers fired with wood fuel would operate effectively and emit low amount of pollutants. The investigation and tests with different types of boilers are performed in order to achieve these goals. Various modifications of boilers fired by wood and wood pellets in order to evaluate their efficiency and pollution while they are operating at nominal and minimal output rated capacity were investigated. Considerable attention was dedicated to the possibility to reduce the concentration of unburned hydrocarbons CxHy, carbon monoxide CO and dust, as well as to foreseen specific improvements of the design. It was revealed that it is possible to reduce significantly emission levels: CxHy and CO concentrations of up to 80% and dust content – 50%, by improving combustion chamber of the boiler and air supply systems.

Keywords: Grate boiler, combustion

1. INTRODUCTION

The growing public concern about environmental pollution and the strict requirements of the new EU normative documents for the sources of pollution encourage searching for the effective tools to reduce pollution by improving the construction of the equipment fired with various types of fuel, including wood fuel.

1.1. The consumption of biofuel in Lithuania

In the last twenty years the use of biofuel has been increasing in Lithuania. But the growth has been declining because the consumption of biofuel jumped by 73% from 1992 till 1996 and only 24% from 1996 till 2000. Even lesser increase of the consumption of biofuel was from 2000 till 2004. The increase was only 12% in that year. The consumption of biofuel increased only by 5.8% from 2004 till 2008. This kind of increase of the consumption of biofuel can be simply explained. The resources of biofuel were consumed very poorly till 1992, therefore it was started to consume that unused fuel from 1992. [1, 2] Gradually it began to use it more and more. There are still much resources of biofuel in Lithuania. These resources can be enlarged by planting quick rotation plants into unused area of soil. In Fig. 1 the diagram shows the dynamics of the consumption of solid fuel in Lithuania.

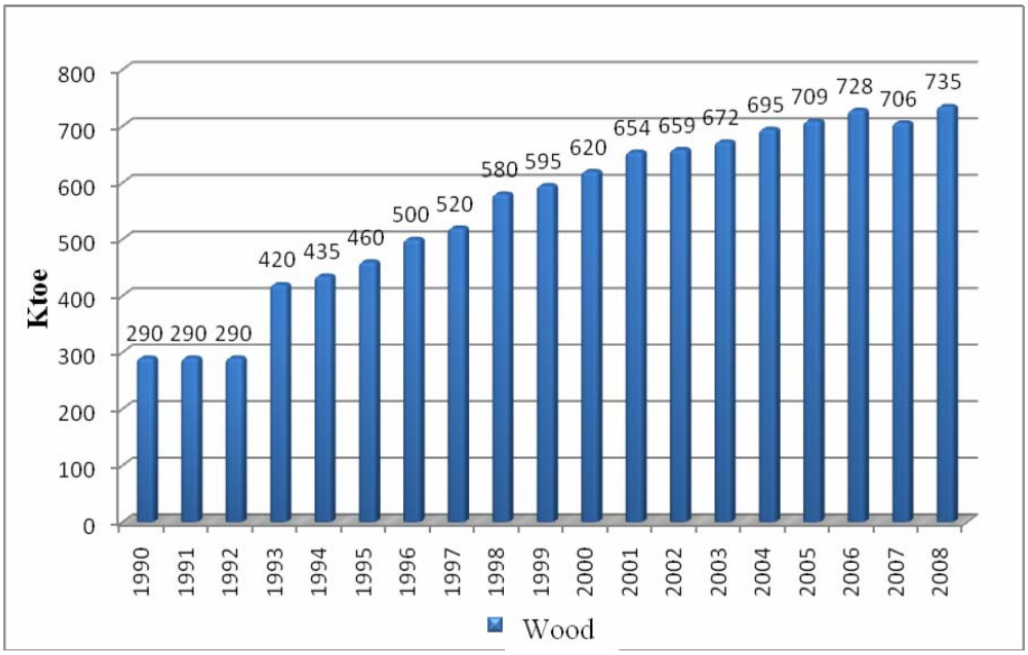

Fig. 1.Comsumption of solid biofuel in Lithuanian [1, 2]

The consumption of wood fuel should change after the directive of renewable energy resources is implemented. This directive declares that the consumption of biofuel should create 23% of final balance of energy till 2020. This should stimulate the increase of the consumption of wood fuel.

In Lithuania the main part of wood fuel (wood, pellets, briquettes of wood waste) is consumed in the households (about 60%), and only about 17–20% – in central heating boilerins for making thermal energy. Fig. 2 and Fig. 3 show that the consumption of wood fuel is quite constant in Lithuania.

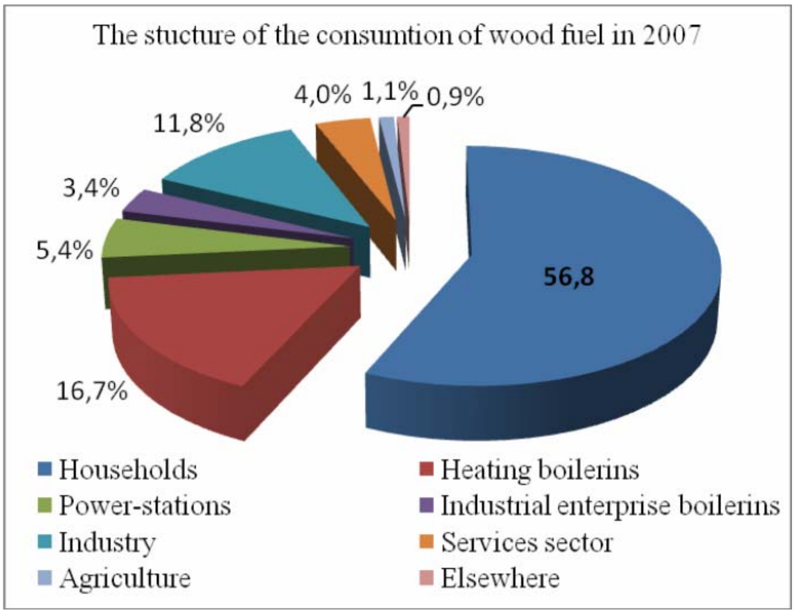

Fig. 2. Wood fuel consumption structure during 2007 [2]

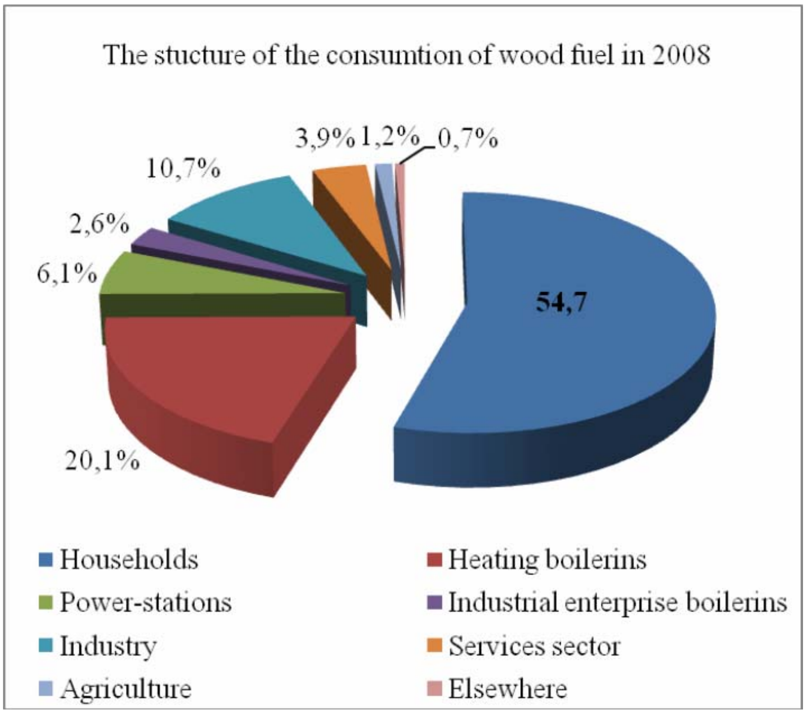

Fig. 3. Wood fuel consumption structure during 2008 [1]

Therefore, it is very important that the small and middle size boilers fired with wood fuel would operate effectively and emit low amount of pollutants. The investigation and tests with different types of boilers are performed in Lithuanian Energy Institute in order to achieve these goals.

2. RESEARCH METHODS

Tests of boilers fired by solid fuel were executed in the Thermal equipment testing and experimenting laboratory in Lithuanian Energy Institute. It was done by using the test bench that fulfills the requirements of standard “LST EN 303-5:2000” [3]. This appliance is used to test boilers and other similar equipments fired by solid, liquid and gas fuel (central heating boilers, momentary and volume water heaters, air heaters, stoves, etc.).

Nominal heat rating of these equipments should be less than 300 kW, water temperature in working conditions should be not higher than 95 °C, working pressure in the water system should be not higher than 6 bar. The equipments can be with atmospheric or compulsory air distention burners and air distention fans. Combution products that are ejected by these equipments can be condensed or not.

By using test bench it can be determined:

- thermal parameters: consumption of fuel, thermal power, thermal effectivenes, thermal loss;
- pollutants’ level: O_2/CO_2, CO, NO_x, C_xH_y, SO_2;
- hydraulic parameters: tightness and hardness of water system;
- hermetics of Gaseous system and hermetics of combustion’s products exclusion system;
- temperature of equipment’s surface, electrical and safety parameters.

While making boilers‘ test according to standard “LST EN 303-5:2000” [3] boilers fired by solid fuel are divided into three classes by the limits of pollutants‘ emission, feeding of fuel, origin of fuel and nominal heat output (Table 1). Permissible limits of emission are different in all classes. The first class is the worst and the third one is the best.

Table 1. Permissible limits of emission of boilers fired by solid fuel [3]

Stoking	Fuel	Nominal heat output kW	Emission limits								
			CO			H_xC_y			Dust		
			mg/m^{3}at 10 % O_2 *								
			class 1	class 2	class 3	class 1	class 2	class 3	class 1	class 2	class 3
Manual	Biogenic	≤50	25000	8000	5000	2000	300	150	200	180	150
		>50 to 150	12500	5000	2500	1500	200	100	200	180	150
		>150 to 300	12500	2000	1200	1500	200	100	200	180	150
	Fossil	≤50	25000	8000	5000	2000	300	150	180	150	125
		>50 to 150	12500	5000	2500	1500	200	100	180	150	125
		>150 iki 300	12500	2000	1200	1500	200	100	180	150	125
Auto-matic	Biogenic	≤50	15000	5000	3000	1750	200	100	200	180	150
		>50 to 150	12500	4500	2500	1250	150	80	200	180	150
		>150 to 300	12500	2000	1200	1250	150	80	200	180	150
	Fossil	≤50	15000	5000	3000	1750	200	100	180	150	125
		>50to 150	12500	4500	2500	1250	150	80	180	150	125
		>150 to 300	12500	2000	1200	1250	150	80	180	150	125

* referred to dry exit flue gas, 0^0 C, 1013 mbar

Boilers with the same capacity were chosen for this investigation. They were compared by concenctration of carbon dioxide (CO_2), carbon monoxide (CO), hydrocarbons (C_xH_y), dust and also by effectiveness.

Types of tested boilers:

- pellet boiler;
- grate boiler with forced draught;
- gas generative boiler.

Pellet boiler is fully automated. It is operated with programmable controller which controls the process of combustion by regulating the feeding of fuel and primary and secondary air. The feeding of primary and secondary air is regulated by the amount of oxygen in a chimney. This allows to combust the fuel effectively and to minimize pollution. This type of boilers also requires little care.

Grate boiler with forced draught is a boiler which burns the fuel on the grate. This type of construction is spread most widely. In this type of boilers the primary air is regulated by the thermo-regulator and the secondary air is regulated manually by combining and optimizing the mode of combustion.

Gas generative boiler burns fuel in two stages. In the first chamber the fuel burns with the deficit of air. In this case combustible gas is generated. This gas combust finally in the second chamber by feeding the secondary air. The primary and secondary air are fed by air ventilator which is operated with programmable controller according to the temperature of output water and the speed of temperature‘s change.

Wood pellets of net calorific value 18.317 MJ/kg, water moisture – 7–9% and wood of net calorific value 15.901 MJ/kg, water moisture – 13–17% were used for tests.

3. RESULTS

The concentrations of carbon dioxide (CO_2) are shown in the Fig. 4. As it can be seen from this figure, the combustion of pellet boiler is stable. In this case the exhaustion of carbon dioxide varies in narrow limits during the entire test. The combustion is not stable in other types of boilers. Therefore the concentration of CO_2 varies in wide limits during all the combustion time.

Carbon can react with oxygen in two ways during the combustion process:

When the oxygen is enough and the complete combustion is in process:

$C + O_2 = CO_2 + 33.6 \cdot 10^3$ kJ/kgC.

When the oxygen is not enough the carbon combusts not completely:

$2C + O_2 = 2CO + 9.9 \cdot 10^3$ kJ/kgC.

CO compound is combustible and reacts with oxygen:

$2CO + O_2 = 2CO_2 + 10.15 \cdot 10^3$ kJ/kgCO. [5]

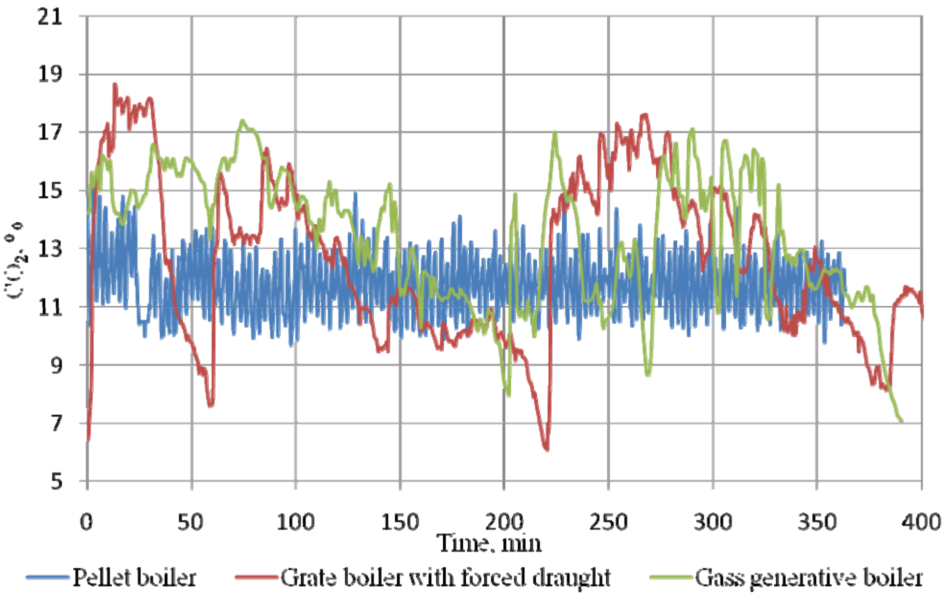

Fig. 4. Carbon dioxide concentration of boilersat nominal heating rate

A different view can be seen in a Figure 5 that shows the concentrations of carbon monoxide. The concentrations of carbon monoxide differ in all types of boilers. Gas generative boiler has the highest rate of carbon monoxide exhaustion. Carbon monoxide can appear in the smoke for a few reasons:

- the imperfections of the construction of the primary and secondary air feeding canals and low productivity of ventilator;
- the imperfect operating of programmable controller which calls the pulsations of the air flow made by ventilator and uneven combustion;
- the primary air, that gets into combustion chamber, is heated not enough.

These reasons could contribute to getting gas generative boiler into the worst first class by standard LST EN 303-5:2002.

The exhaustion of carbon monoxide (CO) in grate boiler depends on regulating the feeding of primary and secondary air properly. The smoke-consumer which is installed in the chimney helps to ensure the constant draught and more stable combustion. Because of the quite perfect construction of this boiler the acieved results allowed let to put this boiler to the best class.

It should be mentioned, that the jumps of carbon monoxide concentration depend on the time and type of the fuel's combustion on the grate. The fallen fuel without the gaps of air combusts with the deficit of air. Therefore the concentration of carbon monoxide (CO) becomes higher [4].

Pellet boiler reaches the best results because it has constant and good combustion, qualitative fuel and good control. The pulsation (the jumps) can be seen in the diagram of carbon monoxide (CO) concentration of the pellet boiler. These jump appears because of the fuel's feeding into the combustion chamber. The fuel is fed by the specified doses. When a new dose of the fuel is fed the concentration of the carbon monoxide jumps up. It comes back when the combustion becomes constant.

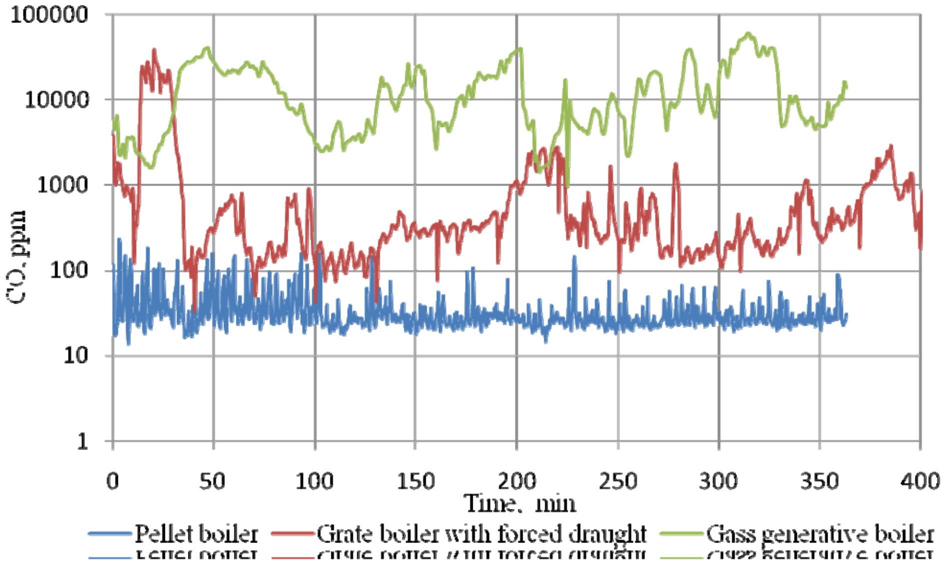

Fig. 5. Carbon monoxide concentration of the boilers at nominal heating rate

The concentration of hydrocarbons (C_xH_y) can be seen in the diagram below (Fig. 6). As it can be seen the same tendency remains for the hydrocarbons (C_xH_y) as for the carbon monoxide (CO). The difference of the concentrations is for the same reasons as it was mentioned before. The gas generative boiler distinguishes from others extremely. The hydrocarbons' exhaustions of the pellet boiler are constant during all the test.

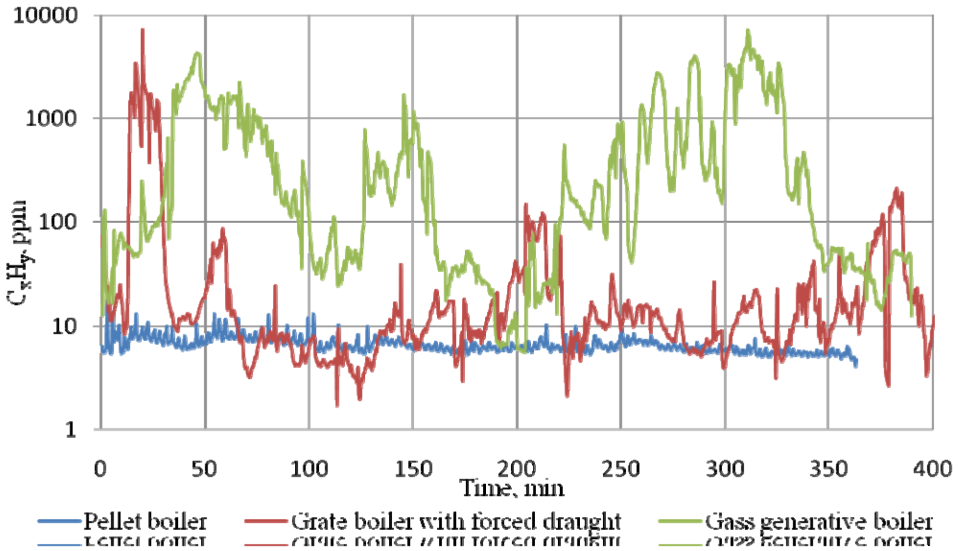

Fig. 6. C_xH_y concentration of the boilers at nominal heating rate

As it can be seen from the diagram of the dust concentration (Fig. 7), the pellet boiler exhausts about four times smaller concentration of the dust. This difference appears because the pellet fuel has better properties and the pellet boiler combusts this fuel effectively. Gas generative boiler exhausts smaller concentrations of dust as compared with grate boiler. It is because the gas generative boiler has two stages of combustion.

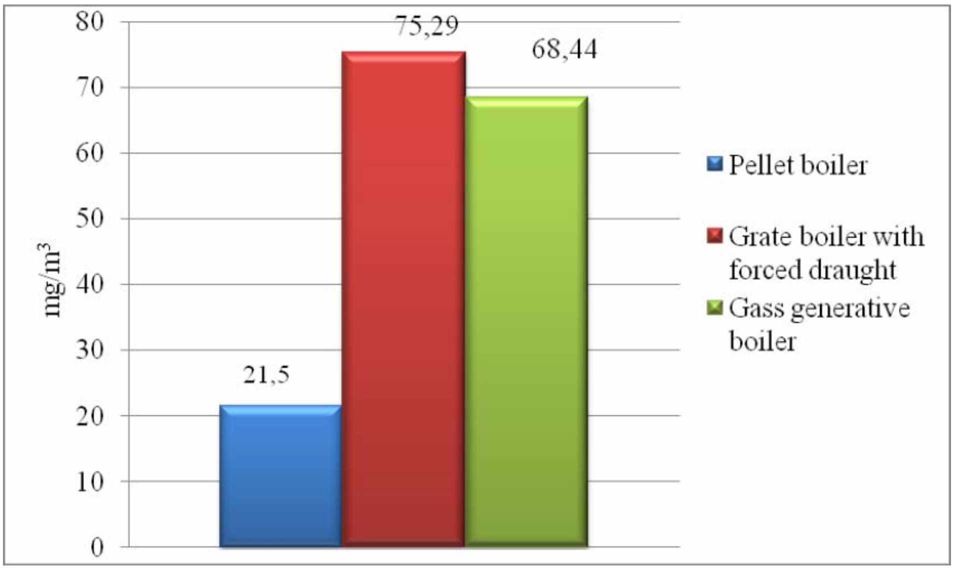

Fig. 7. The dust concentration of the boilers at 10% O_2

All the discussed results are shown in the diagram of efficiency below (Fig. 8). It can be seen that the pellet boiler has the greatest coefficient of efficiency as compared with other boilers. This coefficient can be greater than 90%. This is because the pellet boiler has a better fuel quality and this fuel can be combusted more effectively. Gas generative boiler is in the worst first class but it lags from the grate boiler not so much. Therefore it can be considered that the gas generative boiler could compete with the grate boiler after improving the gas generative boiler‘s construction.

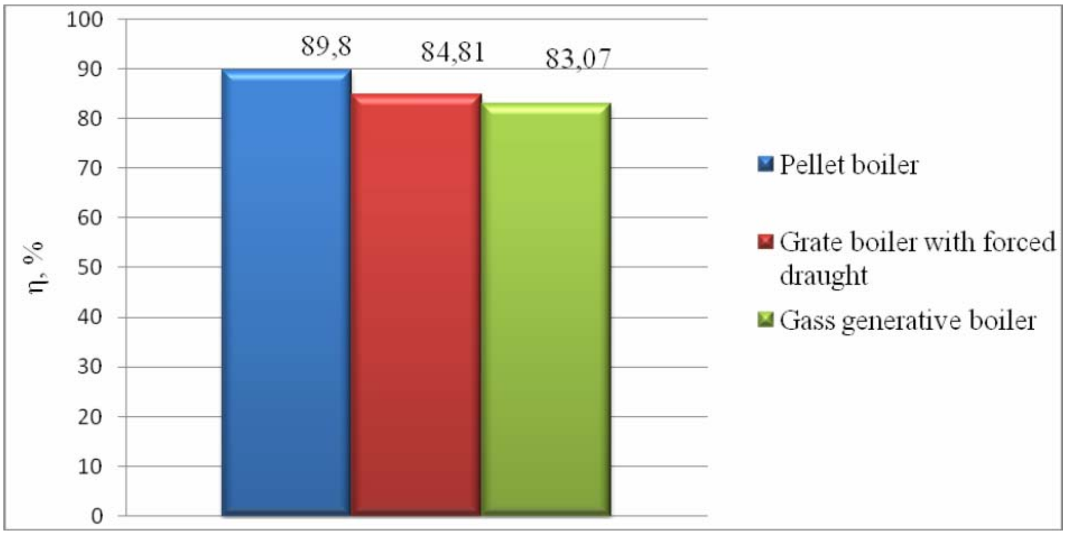

Fig.8. The boiler efficiency coefficient

4. CONCLUSIONS

1. The greater attention should be paid to increasing the efficiency of boilers fired by wood fuel and to minimize their emission of pollutants. For example, the process of combustion can be mechanized and automated by using bonded wood fuel.
2. Despite of the boiler type, better parameters of the combustion process can be achieved by improving the construction of the boiler‘s furnace and the construction of the air feeding canals.
3. It could be said that the manufacturers in Lithuania should guarantee that their products fulfill the requirements of the second or third class of boilers by standard LST EN 303-5:2000 in order to remain competitive in the market of boilers.

REFERENCES

1. Kuro ir energetikos balansas 2008.- Statistikos departamentas. Vilnius, 2009.
2. Kuro ir energetikos balansas 2007.- Statistikos departamentas. Vilnius, 2008.
3. LST EN 303-5:2000 heating boilers – part 5: heating boilers for solid fuels, hand and automatically stocked, nominal heat output of up to 300 kW – terminology, general requirements, testing and marking // European standard.
4. R. Bauer, M. Golles, T. Brunner, N. Dourdoumas, I. Obernberger. *Modelling of grate combustion in a medium scale biomass furnace for control purposes* // Biomass and bioenergy, Vol. 30, 2010, p. 1–11.
5. J. Tissari, J. Lyyraanen, K. Hytoonen. *Fine particle and gaseous emissions from normal and smouldering wood combustion in a conventional masonry heater* // Atmospheric Environment, Vol. 42, 2008, p. 7862–7873.

CYSENI 2010, May 27–28, Kaunas, Lithuania
ISSN 1822-7554, www.cyseni.com

TECHNOLOGICAL PECULIARITIES OF STRAW CONVERSION TO ENERGY

L. Zidonis, S. Sinkunas, E. Puida
Kaunas University of Technology
Department of Thermal and Nuclear Energy
K. Donelaicio 20, LT-44239 Kaunas – Lithuania
Phone: +370 687 27658
Email: Lukas.Zidonis@gmail.com

ABSTRACT

The world-wide efforts to reduce the carbon dioxide emissions by replacing fossil fuels with renewable energy sources determine the interest of utilizing the large amounts of agricultural waste (primarily straw) for energy generation purposes. Utilization of straw for energy generation entails some specific technological aspects that should be addressed before the straw fired plants are competitive to traditional plants fired with fossil fuels. The aim of the article is to present these technological aspects and provide the basis for further straw fuel processing and combustion investigations.

The article reveals the main physical characteristics of straw and their impact on the combustion behavior. Since the consistence of straw fuel is import for combustion processes, the issues of straw logistics, pretreatment and densification are approached. The peculiarities and main technologies of straw combustion are described. The reasons of straw ash formation, slagging and fouling and the impact of these processes on burning appliances are picked up. The characteristics of chimney emissions are revealed.

Keywords: densification, slagging, fouling, initial smoldering, early flaming, late flaming, afterflame smoldering, glowing

1. INTRODUCTION

Agricultural residues emerge as a waste from agricultural activities. The straw is the main agricultural residue emerging from grain breeding processes in Lithuania. There are other types of agricultural residues, for example coffee or rice husks, sugarcane stems, etc. in other countries.

The references provide different numbers about the yield of straw in Lithuania and fluctuate every year. The straw yield depends on the area and vegetative features of seeded crops, the crop fertility and farming practice used. While exact yield is not specified, it is in the range of 3.5–4.0 Mt/year.

The share of straw that could be utilized as a fuel is another uncertain value which as the rule of thumb is taken 15–20% of the total amount. The rest is ploughed back into the soil, burnt on the field or used as bedding for animals.

Straw available for utilization could provide the energy potential of about 3 200 GWh per year (about 12% of annual gross energy consumption in Lithuania). To make a comparison, in Denmark, there were 2.6 megatons of total 6.5 megatons straw yield utilized for energy generation, what constituted about 40% [1].

The current utilization level of straw as a fuel is low despite the quite large generation quantities. Straw is produced in rural regions and since it has low density, high transportation costs emerge; it is often uneconomical to use it as the main fuel in large power stations.

Another reason is the lack of sufficient information and availability of the necessary technology concerning straw combustion.

2. PHYSICAL CHARACTERISTICS AND THEIR IMPACT ON COMBUSTION PROCESS

Unlike the conventional fuels, some physical and chemical properties of straw fuel complicate their processing and combustion. The main physical characteristics of straw are presented in Table 1 [2]:

Table 1. Straw physical characteristics.

No	Physical characteristic	Quantity
1	Moisture content, %	10-20
2	Volatile mater, %	>70
3	Ash content, %	3-4
4	Ash melting temperature, °C	800-1100
5	Calorific value wt, MJ/kg	14.4–15.0
6	Calorific value mf, MJ/kg	18.2–18.7

The higher moisture content – the poorer ignition, reduced the combustion temperature, which in turn hinders the combustion of the reaction products and consequently affects the quality of combustion. A larger quantity of flue gas is also formed during the combustion of high moisture content fuels. This leads to large dimensions of the flue gas treatment equipments.

Higher contents of volatile matter indicate that the fuels are easier to ignite and to burn, although the combustion is expected to be rapid and difficult to control. The high volatile matter contents affect the overall combustion process – care must be taken to achieve complete combustion of the volatiles to ensure higher combustion efficiency and low emissions of CO, hydrocarbons and aromatic hydrocarbon.

A peculiar ash problem, which is normally experienced during the combustion of straw, is the low melting temperature of the ash. This is due to the presence of specific chemical elements in the fuel. The problems attributed to low melting temperatures of the ashes from straw are bed agglomeration in fluidized bed as well as fouling, scaling and corrosion of the heat transfer surfaces. This issue will be revealed in details in chapter 5.

3. LOGISTICS, PRETREATMENT AND DENSIFICATION

The loose straw has very low density to compare it to coal or even wood. For transportation, storage, feeding into furnaces and combustion of straw, it may be necessary to upgrade the raw biomass by increasing its bulk density. This is achieved by densification.

Densification is one of the residues handling processes which includes collection, storage and transportation and can also involve treating, grinding and drying. The advantages of densified biomass are:

- the more uniform combustion can be achieved;
- the possibility of unexpected combustion in storage is reduced;
- the transportation, storage and feeding is made more efficient.

The factors which determine the densification process are moisture content, particle size, form, fibrous and non-fibrous nature as well as lignin contents.

Straw, has structural tubes of highly crystalline cellulose, protected by a waxy outer surface, and can be effectively densified only after destroying the structure through chopping or milling [3]. Where possible, an addition of materials containing some natural binders such as sawdust, bark, corn stalk can lead to the production of higher quality briquettes and pellets. However, the basic problem often encountered in the use of densified straw is the cost of densification. The main densification techniques normally used are baling, briquetting and pelleting.

3.1. Baling

Generally the roll and cubic forms of straw bales (Fig. 1) are produced after the yield is reaped.

Fig. 1. The roll and cubic forms of straw bails

Common straw bale dimensions and weight are presented in Table 2. The bulk density is 70–150 kg/m^3, the heating values: 260–360 kWh/m^3.

Table 2. Ordinary bale dimensions and weight

No.	Bale type	Dimensions, m	Weight, kg
1	Roll bales	Diameter: 1,2 – 1,8; Length: 1,2 – 1,5;	200-340
2	Large cubic bales	1,2 x (0,7–0,9) x (2,35-3)	180-350
3	Small cubic bales	0,5 x 0,4 x (0,8–1,2)	up to 20

The straw is collected and densified by automotive or pulled equipments (Fig. 2) [4].

Fig. 2. The automotive pulled densifying equipments

The straw can be chopped at the same time they are collected, but it is economically justified only if the transportation distance to storage place is rather short.

3.2. Briquetting and pelleting

Briquetting and pelleting (Fig. 3) technologies are more advanced, requiring more expensive equipment and energy and therefore raise the costs of the straw fuel. The application of these techniques must be economically feasable.

Fig. 3. The straw briquettes and pellets

The purpose of briquetting and pelleting is to increase the bulk density required especially if transport and storage are the major concerns. For example, the bulk densities of straw briquettes and pellets are around 450–650 kg/m^3 which are 5–10 times higher than baled straw and the energy content increases from 260–360 to 1800–2800 kWh/m^3 [5].

Compared to briquetting, pelletization has several advantages (Table 3), including higher press output and acceptance of materials with wider range of moisture contents [5].

Table 3. Comparison of straw pelletization and briquetting methods.

No	Factor	Pelletization	Briqueting
1	Moisture content, %	10–20	10–15
2	Maximum output of press, t	4–6	1–1.5
3	Energy consumption (chopping and pressing), kWh/t	80–90	40–50
4	Straw preparation	must be finely chopped	need not be finely chopped
5	Combustion systems used	automatized systems can be used	the same combustion systems as for peat and wood can be used

However, the raw materials for pelletization must be chopped and milled whereas for briquetting, chopping of straw may be sufficient. The design of briquetting machinery is also simpler. Fig. 4 presents a schematic layout of a briquetting press unit [6].

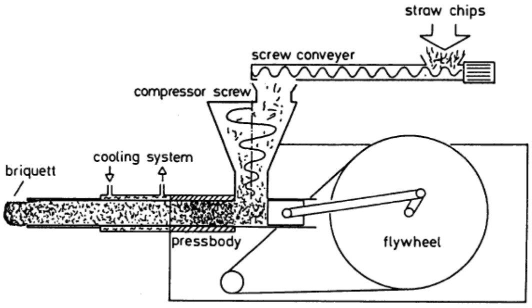

Fig. 4. Schematic layout of a briquetting press unit

Besides the need of using densification technologies for straw fuel handling purposes there is demand for transportation vehicles and store premises. These items are not further revealed in this paper since their impact on straw fuel combustion processes is insignificant.

4. COMBUSTION PROCESS

Whatever form of straw is used for burning - unprocessed, baled, briquettes or pelleted – understanding of the combustion process is required in order to achieve higher efficiency and to effectively design and operate the combustion systems. The inter-related events through which solid fuel undergoes during combustion are drying, pyrolisis, gasification and final combustion. Combustion process for a small biomass particle is presented in Fig. 5 [7].

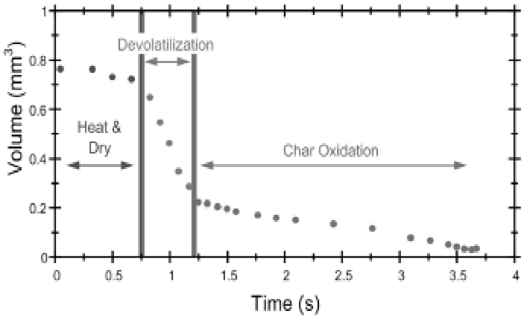

Fig. 5. Combustion process for a small biomass particle

Drying and pyrolysis/gasification will always be the first steps in straw combustion process. The relative importance of these steps will vary, depending on the combustion technology implemented, the fuels properties and the combustion process conditions. A separation of drying/pyrolisis/gasification/gas and char combustion, as in staged-air combustion, may be utilized.

4.1. Drying

Moisture evaporates at low temperatures (< 100°C). Since vaporization uses energy released from the combustion process, it lowers the temperature in the combustion chamber, which slows down the combustion process.

4.2. Pyrolysis (devolatilization)

Pyrolysis can be defined as thermal degradation (devolatilization) in the absence of an externally supplied oxidizing agent. The pyrolysis products are mainly tar and carbonaceous charcoal, and low molecular weight gases. In addition, CO and CO_2 can be formed in considerable quantities. Temperature, pressure, heating rate and reaction time are all variables that affect the amounts and properties of the products formed.

4.3. Gasification (devolatilization)

Gasification can be defined as thermal degradation (devolatilization) in the presence of an externally supplied oxidizing agent. However, the term gasification is also used for char oxidation reactions with, for example. CO, or H_2O. While pyrolysis is usually optimized with respect to a maximum char or tar yield, gasification is optimized with respect to a gas yield. Temperatures of 800–1100°C are used. The gas contains mainly CO, H_2O, H_2, CH_4 and other hydrocarbons. Gasification can be carried out with air, oxygen, steam or CO_2, as oxidizing agents.

4.4. Final combustion (oxidation)

Combustion can ideally be defined as a complete oxidation of the fuel. The hot gases from the combustion may be used for direct heating purposes in small combustion units, for water heating in small district heating boilers, to heat water in a boiler for electricity generation in larger units, as a source of process heat, or for water heating in larger district heating systems. Drying and pyrolysis/gasification will always be the first steps in a solid-fuel combustion process.

5. ASH FORMATION, SLAGGING AND FOULING

Straw have high contents of chemical elements that determine the low melting point which may lead to various problems during combustion. The chemical composition of straw is presented in Table 4 [2].

Table 4. The chemical composition of straw (%).

No.	Straw type	C	H	O	N	S
1	Wheat	48,53	5,3	39,08	0,28	0,05
2	Barley	45,67	6,5	38,26	0,43	0,11
3	Rape	35,93	4,6	38,48	0,57	0,34
4	Maize	47,09	5,4	39,79	0,81	0,12

Deposit formation can be classified as either slagging or fouling [8]:

- slagging refers to the deposits in a molten or highly viscous state, found in the flame section of the furnace and therefore subjected to radiant heat;
- fouling refers to deposits built up largely by species that have vaporized and then condensed, and it occurs in the cooler furnace region where the heat exchanger equipment is located (Fig. 6).

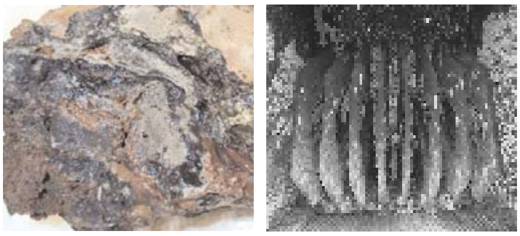

Fig. 6. Slagging and fouling deposits formed during straw combustion

The undesirable effects of deposits formation are [9]:

- retardation of heat transfer and the decrease of the capacity and efficiency of the boiler;
- restriction of flow through the boiler and cause of mechanical damage;
- accumulation of deposits in hoppers and on grates in forms that are unmanageable by the de-ashing facility, leading to shutdown;
- those deposits are associated with corrosion.

Straw contain Si and K as their principal ash-forming constituents; in addition they also have higher Cl content relative to other biomass fuels. These properties generally lead to severe ash deposition and problems at high or moderate combustion temperatures. The primary sources of these problems are:

- reaction of alkali with silica to form alkali silicates that melt or soften at low temperatures (usually > 700ºC);
- reaction of alkali with S to form alkali sulphates on combustor heat transfer surfaces;

K is the dominant source of alkali in most biomass fuels and it has a central role in both processes. An increasing K concentration in straw tends to accompany increasing ash content, thus indicating an inherent source of K. In addition, many of the agricultural byproducts contain high K concentrations - up to 0.021%, depending on nutrition used [7]).

6. COMBUSTION TECHNOLOGIES

The purpose of the combustion system is to supply fuel and combustion air such as to facilitate the distribution and mixing of the fuel with air, to initiate ignition and maintain combustion, to dry and volatilize the fuel, to position the flames in areas where heat release is needed and to reach a high burn-out at low pollutant emission. The design of the appropriate equipment depends on the type, the amount and the characteristics of the fuel and the desired energy form (heat, steam, electric power). Further design aspects concern the relationship of the residue combustion system to other systems in the same plant (i.e. independent or integrated operation), the disposal methods needed for the residues and environmental factors.

For the design of efficient large-scale straw combustion systems a lot of parameters have to be taken into account. These parameters are the mean value and the variability of moisture, the volatile matter content, ash content, ash composition, agglomeration characteristics and the energy content of the fuel. Further, the furnace design will depend on the emission limits that have to be kept.

There are two main categories of straw combustion burners, according the fuel supply manner – the periodic fuel supply burners and continual fuel supply burners.

6.1. Periodic fuel supply burners (PFSB)

PFSB usually burn baled straw. The air for combustion is supplied by natural draught or by fan. The example of such kind of furnace is presented at Fig. 7 [10].

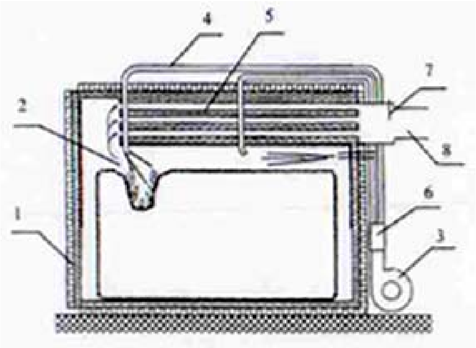

Fig. 7. Furnace with PFSB. 1 – door; 2 – combustion chamber; 3 – fan; 4 – air supply duct; 5 – heat exchanger; 6 – valve; 7 – sensors; 8 - chimney nipple

The advantage of PFSB is quite simple construction, low investments, the possibility to burn solid bales. The major disadvantages however are quite significant – the fuel load burns out quite fast, the combustion process is uneven, the burners are heavily automated, the efficiency is lower than of continual fuel supply burners. These disadvantages determine that PFSB burners are used for residential heating purposes only.

6.2. Continual fuel supply burners (CFSB)

These types of burners usually are designed to combust chopped or densified straw. Pellet-fired burners usually consist of the following components [11].

- fuel supply system with auger;
- storage hopper;
- electric supply air fan;
- combustion chamber with burner;
- ash collecting and removal system;

- control, measurement and safety elements.

The combustion is organized in combustion chamber where the fan blows pressurized air and pushes the fume to the upper chamber zone. The combustion process is intensive and concentrated in a small burning volume Fig. 8.

Fig. 8. Pellet burner

Combustion of chopped straw as a single fuel is not widely practiced, but co firing it with other fuels such as wood or coal is quite common. The range of combustion technologies is presented in Fig. 9 [7].

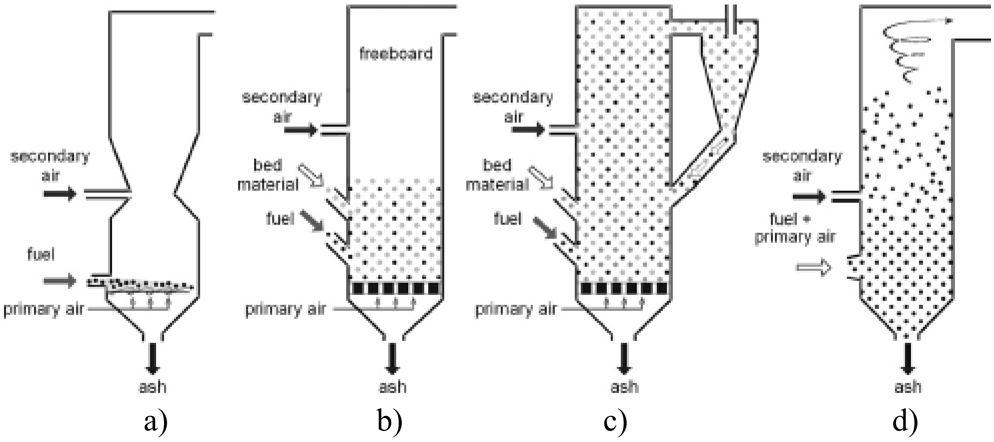

a) b) c) d)

Fig. 9. Combustion technologies: a) fixed bed; b) bubbling fluidized bed; c) circulating fluidized bed; d) pulverized fuel

Fixed bed combustion systems include grate furnaces and underfeed stokers. Primary air passes through a fixed bed, in which drying, gasification and charcoal combustion take place. The combustible gases produced are burned after secondary air addition has taken place usually in a combustion zone separated from the fuel bed.

Within a fluidized bed furnace, biomass fuel is burned in a self-mixing suspension of gas and solid-bed material into which combustion air enters from below. Bubbling fluidized bed (BFB) and circulating fluidized bed (CFB) combustion can be distinguished depending on the fluidization velocity.

Pulverized fuel (PF) combustion is suitable for fuels available as small particles (average diameter smaller than 2mm). A mixture of fuel and primary combustion air is injected into the combustion chamber. Combustion takes place while the fuel is in suspension and gas burnout is achieved after secondary air addition.

7. CHIMNEY EMISSIONS

It is of great importance to study the emissions of specific organic compounds to air during combustion before straw can be widely used as residential or industrial fuel. The smoke contains many different compounds which can affect health and the environment.

Emissions from incomplete combustion reflect the chemical composition of the fuel and indicate the compounds that can be emitted during, e.g., start-ups and temporary disturbances.

Chimney emissions depend on chemical composition, moisture content of straw and the combustion process. Table 5 presents the highest level of straw combustion pollutants observed [12].

Table 5. Straw combustion pollutants.

No.	**Pollutant**	**Automatic load boilers with continual combustion**		**Recurring load boilers**
		mg/m^3	kg/MWh	mg/m^3
1	Carbon dioxide CO_2	517939	1357	517939
2	Carbon monoxide CO	500–2000	5,240	1000–4000
3	Sulphur dioxide SO_2	170	0,445	170
4	Nitrogen oxides NO_x	400	1,048	400
5	Airborne particulates (dust)	150	0,393	200

Organic compounds in the emissions from incomplete combustion of straw were determined in M. Olson (2006) laboratory study [13]. M. Olson stated that the straw pellet combustion can be divided into five sequential stages. The pictures of these stages are presented in Fig. 10.

Fig. 10. Straw pellet combustion stages

Characterizing features and chimney emissions during combustion stages are described below:

1. Moisture evaporated and volatile compounds were released during the first stage, *initial smoldering*. The total concentrations of organic compounds were high in comparison with the subsequent stages. The highest concentrations of furan and furan-related compounds such as 2.5 – dimethylfuran, 2 – furaldehyde and 5 – hydroxymethyl-2-furaldehyde were found during this stage. Furan-related compounds are decomposition products of the polysaccharides of the fuels (mainly cellulose, hemicelluloses and starch). Furan and benzofuran are possibly carcinogenic to humans. The concentrations of furans decreased with more efficient combustion.
2. Considerable amount of the virgin fuel was still visible during *early flaming*. The highest combustion efficiencies were measured, calculated as $(CO_2)/(CO_2+CO)$. The highest concentrations of carbon dioxide were found during early flaming.
3. There was no virgin fuel left, only charred surfaces in the *late flaming* stage. The early and late flaming stages both lasted for 1–2 min. During the early and late flaming stages, the concentration of oxygen in the smoke was 16–17%. The concentrations of organic compounds were generally very low during the late flaming phase, although somewhat higher for peat/wood pellets. Major compounds emitted were methane, phenol and vanillin (GuCHO). Generally, the emissions from early and late flaming were low.

4. When flaming ceased, the short *afterflame smoldering* stage was entered. The concentrations were higher for after-flame smoldering than for initial smoldering. Predominant organic compounds emitted were methane, ethane, ethene, propene, benzene, methylbenzene, naphthalene and phenol. Of the compounds studied, some have serious effects on health and the environment. When considering these factors, after-flame smoldering gave rise to the highest concentrations of hazardous compounds. However, these compounds are only formed during a short time period, which results in low total emissions.
5. Following the after-flame smoldering stage, the final *glowing* stage began. This continued for up to 20 min. Concentrations of organic compounds during the final glowing stage of straw and softwood pellets were very low, with methane, ethyne, benzene and vanillin (GuCHO) as the only prominent compounds. The carbon monoxide concentrations of all pellets were high during this stage, although this was not indicative of high concentrations of other compounds.

The results of this study indicated that straw is a fuel with relatively low deleterious emissions almost as low as the concentrations found in smoke from softwood pellets.

One possible way to decrease the total emissions from combustion is to keep combustion at the flaming combustion stages (2 & 3), with high efficiency and low emissions, as much as possible and to avoid unnecessary after-flame smoldering (4).

8. CONCLUSIONS

The issues concerning the utilization of straw for energy generation purposes have been presented in this paper. The article revealed the available energetical potential of straw in Lithuania, main straw physical characteristics and their impact on combustion, the process and forms of densification of straw, combustion process, the problems related to low melting temperatures of the ash of straw such as slagging and fouling, straw combustion technologies and emission characteristics. The following conclusions can be drawn:

1. The energetical potential of straw is about 3 200 GWh per year (about 12% of annual gross energy consumption) in Lithuania. This amount, if utilized, is very significant for Lithuanian energy sector.
2. The higher moisture content, higher contents of volatile matter and low ash melting temperatures are characteristics that must be considered when designing straw combustion appliances.
3. The bulk density of straw is low. Therefore densification may be required for effective transportation, storage and firing. Three forms of densification can be used – baling, briquetting and pelleting.
4. Combustion process consists of drying, pyrolisis, gasification and final combustion stages. These stages must be taken to account when designing combustion heat utilization systems.
5. A major difficulty that affects the burning of straw is the low melting point characteristic of ash. This property poses serious design and operation problems.
6. The way to decrease the total emissions from straw combustion is to keep it at the early and late combustion stages as much as possible and to avoid unnecessary after-flame smouldering.

REFERENCES

1. Židonis L., Šinkūnas S., Puida E. Utilization of solid biomass for energy generation in Lithuania. CYSENI 2009. Proceedings of annual conference of young scientists on energy issues. [CD]. Kaunas: Lithuanian Energy Institute. 2009 May 28–29.
2. Genutis A. Šiaudų kuro vartojimas Lietuvoje. Kaunas: Institute of Agriculture Engineering of Lithuanian University of Agriculture. 2006 10 06, p. 7.
3. Miles T, Miles J. Densification systems for agricultural residues. Washington DC: American Santosrican Chemical Society. 1980, p. 179–93.
4. Biekša D., Janulis M., Plankis V., Jaraminienė E. Šiaudų kuro naudojimo technologijų įvertinimas ir rekomendacijų tolimesniam jų naudojimui bei biokuro briketų iš smulkių šiaudų ir žolinių augalų paruošimo technologijos parengimas. Ataskaita. UAB Cowi. 2007.
5. Wilen C., Stahlberg P., Sipila K., Ahokas J. Pelletization and combustion of straw. Energy from biomass and wastes. London: Elsevier Applied Science. 1987, p. 469–83.
6. Brendo M. Joint enterprise and utilization of a briquetting plant for straw. Energy from biomass, 3rd E.C. Conference, London: Elsevier Applied Science. 1985, p. 773–7.
7. Van Loo S., Koppejan J. The Handbook of Biomass Combustion & Co-firing. Earthscan. 2008, p. 8–11.
8. Hamilton K. Feasibility Study: Grain-dust Burner. MSc Energy Systems and the Environment Thesis. 2005/2006.
9. Baxter L., Miles T., Miles J., Jenkins B., Milne T., Dayton D., Bryers R., Oden L. Behaviour of inorganic material in biomass-fired power boilers: Field and laboratory experiences. Fuel Processing Technology. 1998, V 54, N 1–3.
10. Žaltauskas A. Šiaudų panaudojimas kurui Lietuvoje. VĮ “Energetikos agentūra”, 2002.
11. Židonis L., Šinkūnas S., Puida E. Pelleted biomass fuel combustion technological peculiarities. Proceedings of annual conference of Šilumos energetija ir technologijos 2010. Kaunas: Technologija. 2010.
12. Grzybek A., Grandziuk P., Kowalczyk K. Sloma energetyczne paliwo. Warszawa. 2001, p. 72.
13. Olsson M. Wheat straw and peat for fuel pellets - organic compounds from combustion. Biomass & Bioenergy, No 30. 2006.

CYSENI 2010, May 27–28, Kaunas, Lithuania
ISSN 1822-7554, www.cyseni.com

MODERN PERFORMANCE MEASUREMENT SYSTEMS: THEORETICAL OPPORTUNITY OF APPLICATION IN THE ELECTRICITY SECTOR COMPANIES

L. Jasiukevičius
The Kaunas University of Technology
K. Donelaicio str. 20, LT-44239 Kaunas – Lithuania
Phone: +370 602 40884
Email: linas.jasiukevicius@gmail.com

N. Radziukynienė
Lithuanian Energy Institute
Laboratory of Systems Control and Automation
Breslaujos str. 3, LT-44403 Kaunas – Lithuania
Phone: +370 (37) 401944
Email: rutkauskaite@mail.lei.lt

ABSTRACT

This paper analyzes the theoretical possibilities of performance measurement systems' application in the electricity sector. The main goal of this analysis is to review the most popular modern performance measurement systems and evaluate their potential application in the electricity manufacturing companies. In order to achieve this goal, the disadvantages of traditional performance measurement systems as well as features and design's requirements of modern performance measurement systems are discussed in the article. Especially paper focuses on four the most widely spread systems in the world such as balanced scorecard, performance pyramid, performance prism and European foundation for quality management excellence model. In order to get deeper understanding about potential application of these performance measurement systems in the electricity sector companies, the specification of those companies' performance are discussed too. Finally, taking into account the features of these companies' performance, advantages and disadvantages of potential application of described systems in the electricity sector companies were analyzed.

Keywords: electricity sector companies, performance, performance measurement systems, application

1. INTRODUCTION

Strategic management in a constantly changing competitive environment has an important role in management of organization. In order to gain an advantage and new opportunities, organizations must be accept changes in their environment and respond to them more quickly than competitors. Therefore, the organizations must constantly monitor and analyze their performance and evaluate the results of the strategic goals' implementation. According to Rantanen *et al.*, [1], strategic goals‘ evaluation has become a widespread strategic management tool, and the demand to assess the results of company‘s strategy implementation is still growing. However, often the question arises what strategy is the most rational and suitable for organization and how reliably evaluate its implementation at any time and in any company‘s operational level [1], [2], [3].

According to Slatkevičienė and Vanagas P. [6], the company‘s performance measurement is inseparable from the management function. The performance measurement systems was started to develop as a tool for strategic management regulating two decades ago [3], [4]. It was understood that the traditional indicators of measurement mainly based on financial analysis were insufficient to assess all value creating factors in fast changing environment [4], [5], [6]. Considering the disadvantages of 'classical' systems, it was created much more advanced systems including wide spectrum of financial and nonfinancial, internal and external indicators. Each of these indicators has its own advantages and disadvantages. Therefore, one of the main challenges is to choose a set of indicators that would clearly reflect organization's performance and effectiveness of its implementation [3], [7], [8].

Recently, Lithuania is undergoing profound changes (electricity sector restructurization) in the sector of electricity. Implementation of European Union legislation's requirements is causing new performance conditions for this sector‘s companies [19]. The almost finished gradual process of liberalization of electricity generation, transmission and supply and the energy strategy's goals to connect electricity networks of Lithuania to Scandinavian countries and Poland not later than the end of 2016 allows presuming of increasing competition. Therefore, because of started market liberalization, the development and implementation of individual strategy of electricity companies will achieve a much greater role. However, such changes of performance conditions for the companies' which operated in regulated electricity sector for a long time can be a considerable challenge to increase their efficiency of performance through the strategic positioning. Because of activity‘s conditions changes, it is very important to find new means, which would be strategy effectively.

In the scientific literature it can be found a lot of articles analyzing various problems of performance measurement systems. However, the possibilities of performance measurement systems' application in the electricity sector were less analyzed. Haapasalo H., *et all.,* [2] analyzed the use of Balanced Scorecard in the Finnish energy sector. Bromley M. *et all.,* [21] described the successful example of implementation of an in-house version of the balanced scorecard in one of the UK's largest electricity companies 'EDF Energy'. Therefore, the evaluation of performance measurement systems' appropriateness in electricity sector remains the actual problem in Lithuania.

The goal of the paper – to review the most popular modern performance measurement systems, to evaluate and assess their opportunities of application in the electricity sector.

Tasks – to discuss the features of modern performance assessment system, to discuss the electricity sector companies operating features; to analyze the performance measurement systems for the electricity sector companies, to find their advantages and disadvantages.

Methods – analysis and synthesis of scientific publications.

2. THE EVALUATION AND REQUIREMENTS FOR MODERN PERFORMANCE MEASUREMENT SYSTEMS

The problem how to assess company‘s performance was one of the biggest challenges for many years. For a long time it was believed that financial indicators are the only one reliable information source describing the company. And a performance measurement was mainly understood as effectiveness and efficiency assessment process [8]. Modern performance measurement systems were widely developed since 1990. They supported strategic management functions. It was understood that only financial indicators of technological environment cannot assess the implementation of strategy [9], [10], [11]. Automation and computerization of managed processes have reduced a large part of operating costs (from 50 percents to less than 10). Therefore, the traditional accounting systems, proposing only financial rates, was no longer sufficient to evaluate company‘s performance, provide information and to make rational management decisions. Many authors acknowledge that despite the fact that financial indicators are defined, accurate and comparable, they have a lot of disadvantages [9], [11], [12], [13]:

- lacking strategic focus;

- encouraging local optimism and not being externally focussed;
- they tend to be insular or inward-looking;
- they fail to include the less tangible factors such as service quality, customer satisfaction, employee morale and so on;
- they are lagging indicators (they show what has happened in the past, and are poor predictors of tomorrow's performance);
- they provide not enough information on how to achieve company's operating goals or how to improve them.

Taking into account disadvantages of traditional indicators it was created modern performance measurement systems which were orientated to the strategic goals in fast – changing competitive environment [11]. One of the most important modern performance measurement systems‘ features are that all indicators are closely related to the companies' values and strategic goals in all levels of the implementation. These indicators include the main factors of company's performance assessment [2]. The results of performance show how successfully the company implements its strategic goals. Evaluation report takes a variety of different indicators. Some of them, such as financial analysis indicators, are the same for all organizations in order to compare the achievements of business opportunities. The other parts of indicators are unique, which depend on the goals of the organization and its environment, e.g. indicators covering internal business processes, customer relationships, employee training, development, company growth and etc., evaluation [4], [7]. Indicators integrated to the general performance system enables to get all necessary information for management decisions. All of this suggests that critical indicators of performance assessment have the main task to transform performance measurement system into the effective means of implementation of strategic goals.

However, it does not mean that in order to obtain clear picture about company's performance it is necessary to involve all performance indicators, which company is able to assess [8], [12]. Performance assessment would become inefficient, consuming a lot of time, because of searching and analyzing all of the results. It would be very difficult to control all the parameters. In order to get more efficient system it is necessary to have a indicators s simple as possible which can focus only on a real impact of company‘s management [6], [14]. Such as assessment of system optimization must guarantee operational feedback to company‘s leaders and employees.

Modern performance measurement system must be dynamic in time and the environment [5]. The indicators should be regularly reviewed and modified if necessary, in order to achieve that performance measurement system will always provide realistic data on the company‘s performance. This improvement of assessment system is one of the most important features of modern company‘s. According to Vanagas P. and Slatkevičienė G. [6] it is important to identify and stimulate company‘s development, to assess and improve achievements.

Slatkevičienė G. and Vanagas P. [6], analyzing performance measurement systems, highlight that performance assessment systems must be closely related to quality achievement. According to them, the business processes of continuous improvement, needs business process monitoring and assessment of the results. Therefore, according to these authors, modern performance measurement system must integrate the quality evaluation of organization's performance.

In conclusion, it can be stated that the measurement system and its requirements were changing together with technological and competitive environment. Technological progress and growing intangible capital‘s deposit to value – added process, has highlighted the importance of nonfinancial indicators and has set new requirements for performance measurement system. All of this has formed one of the most important company‘s strategic goals.

3. THE SPECIFICS OF COMPANIES IN ELECTRICITY SECTOR

In order to find the most suitable performance measurement systems for the companies operating in the electricity sector, it is very important to analyze their common features of performance. Considering the characteristics of this sector performance, it will be able to identify the most influenced factors for the companies' performance and based on them to determine the main indicators of companies' performance. It will allow to choose performance measurement system which would be closely linked to company‘s performance and it‘s goals [15].

All main operating characteristics of electricity companies are closely linked with each other. Electricity system consists of electricity generation, transmission, distribution and consumption companies. They operate in the same technical environment. This is due to the fact that electricity generation and consumption operate at the same time. Because it is not possible to store large amounts of electricity, it is very important to forecast it‘s demand. Electricity system must work reliably and safely, ensuring adequate power quality. Although the power system is not very flexible, especially in case of producers, it must ensure costumers' demand effectively.

The operation of electricity companies is regulated under strict rules, legislation, European Union (EU) directives, regulating different types of activity: trade, generation, import, reliability of electricity supply, electricity supply interruption, environmental and other conditions. Implemented EU directive on the electricity market liberalization has changed operation conditions in general [16], [18]. Therefore, power companies inevitable need to adapt to the competitive conditions of liberazed electricity sector. Also all costumers have opportunity freely to choose electricity suppliers since 2007. Competition between electricity companies is increasing, creating preconditions for declining electricity prices [17]. Customers can not select transmission and distribution networks, because of a natural monopoly. Lithuanian electricity connection to Scandinavian and Polish electricity networks will give opportunity for electricity producers to trade electricity not even in the Baltic region, but also throughout the EU market. This will provide more opportunities and increase competition. Lithuanian producers will have to compete with foreign producers [2]. Therefore, it is important to assess their possibilities and to choose a competitive performance strategy.

In Lithuania the main electricity producers are - Lithuanian power plant, Vilnius CHP, Kaunas CHP, Klaipėda CHP and Mažeikiai CHP. They generate the biggest part of electricity in Lithuanian. Essentially, it can be stated that in the Lithuanian electricity market dominate large power plants. In the future it could appear new “players” in the electricity market - new nuclear power plant, wind farms, new CHPs. Competition between market “players” will be sufficiently large. Lithuanian electricity producers will have strongly to compete with each other on both – internal and external markets. The generating companies should prepare to work under the new circumstances [19].

For successful electricity companies' work it is necessary to provide the funds needed to maintain, renew and expand infrastructure (electrical equipment maintenance and repairing, new elements of system installing).

No less important for energy companies is to have highly qualified staff who can constantly reach better results and to impose funding for personal training (to have an effective system for the promotion and successful work). Highly qualified personnel, rational management of all organizational levels let to attain its targeted goals [19].

Considering constantly changing electricity market situation, it is very important for companies to forecast their future factors (electricity demand, generating power, primary energy prices). Increased forecast accuracy factors can reduce costs.

The successful or not successful performance of electricity sector companies may be defined by the company‘s performance indicators and highlighting the following key indicators:

- income;
- profit/losses;
- constant and variable costs;
- commitments (debts, taken/given credits);
- investments;
- statistics of emergencies and breakdowns;
- amount of produced electricity;
- staff alteration;
- wages – fund.

4. MAIN PERFORMANCE MEASUREMENT SYSTEMS

In order to assess advantages, disadvantages and alternatives of company‘s performance the most common and modern performance systems are analyzed.

4.1. Balanced scorecard (BSC)

Balanced scorecard is one of the most popular performance measurement systems in the world developed by R. Kaplan and D. Norton [7]. This is a strategic planning and management system that is used extensively in business and industry, government and non-profit organizations worldwide to align business activities to the vision and strategy of the organization, improve internal and external communications, and monitor organization performance against strategic goals [7]. According to Anderson K. and McAdam R. [12], BSC’s strength lies in the way it integrates different classes of organizational performance – financial and non-financial, internal and external. Sližytė A. [20] states that it is the first organization’s performance measurement system, which in addition to the financial indicators that reflect past results’ evaluation includes the evaluation of non-financial indicators determining the future performance of the organization. This system aims to provide managers and supervisors by more “balanced” view on their activities and concentrate on critical areas of the organization’s activities [20].

The balanced scorecard enables organizations to translate a company's vision and strategy into implementation, working from 4 perspectives [7]:

Financial perspective. Kaplan and Norton do not disregard the traditional need for financial data. Timely and accurate funding data will always be a priority, and managers will do whatever necessary to provide it.

Customer perspective. Recent management philosophy has shown an increasing realization of the importance of customer focus and customer satisfaction in any business. In developing metrics for satisfaction, customers should be analyzed in terms of kinds of customers and the kinds of processes for which company is providing a product or service to those customer groups.

Internal business process. This perspective refers to internal business processes. Metrics based on this perspective allow the managers to know how well their business is running, and whether its products and services conform to customer requirements. The indicators used to measure this perspective measures achievement in the key processes that have the greatest impact on customers' satisfaction and the organization's financial goals. The examples of internal business processes' perspective can be the achievement of quality, costs, time and specified external requirements and other indicators level.

Learning and growth perspective. This perspective includes employee training and corporate cultural attitudes related to both individual and corporate self-improvement. In a knowledge-worker organization, people - the only repository of knowledge – are the main resource in the modern competitive environment. In this perspective metrics can be put into place to guide managers in focusing training funds where they can help the most.

Hence, balanced scorecard seeks that short-term financial goals would not become the indicators of company's performance. In this case, the financial measurement is only on of the perspectives. According to Kaplan S. and Norton P. [7], the balanced scorecard allows avoiding the gap between strategic goals and daily performance of organization, to evaluate and respond to stakeholders' needs and expectation, to evaluate strategy and to make necessary adjustments and optimize all internal process.

The failures of balanced scorecard are considered the lack of strategy for integration with everyday operations, the disregard of evaluation of workers and suppliers (as the stakeholders of organization) and the lack of methodology of perspectives' measurability [14].

4.2. Performance prism (PP)

Performance prism is a measurement system indicating the main factors of the organization effecting performance to be included in the performance measurement [20]. According to Anderson K. and McAdam R. [12], this system is very flexible and can be focused on both the narrow and general organization's performance aspects. Performance prism consists of five interrelated perspectives: stakeholder satisfaction, strategies, processes, capabilities and stakeholder contribution [12], [20]. Each of these perspectives has its own components, e.g. the strategy can be analyzed on the level of corporation, business unit, brand or service level, or even operational level. Together, these five perspectives provide a comprehensive and indeed an integrated framework for thinking about organizational performance.

According to Sližytė A. [20], under the performance prism the most important object of evaluation is stakeholder's satisfaction, i.e. the first it is necessarily to find out what is the stakeholders of organization and their requirements. As stated by Anderson K. and McAdam R. [12], nowadays the competitive success depends on management taking an inclusive approach on meeting the needs indeed, requirements of all stakeholders. Only the creation of value for stakeholders is a way to implement the strategy, to determine its processes of implementation and identify capacity of organization. Therefore, the main focus should be given on the satisfaction of stakeholders rather than the achievements of strategy evaluation. According to Sližytė A. [20], it cannot start from the implementation of strategy yet and therefore, that strategy is not a goal of organization, it is just a mean for achievement of the goals determining of how organization should perform that it would satisfy the requirements of stakeholders. This performance prism's feature is a contrary to the most other performance measurement frameworks' attitude that the strategy is the primary factor determining the measurement indicators At the same time this is performance prism's oneness.

Performance prism point of view, the strategy must be adapted to the organization's processes. Therefore, it has to be assessed capacity of the organization (personnel, experience, available technology, infrastructure and *et al.*) necessary for these processes perform and to create value for stakeholders [20].

The lack of performance prism is that it provides little information on how to identify appropriate indicators and how to use them that they would provide the most benefit.

4.3. Performance pyramid system (PPS)

Performance pyramid system (or *Strategic Measurement Analysis and Reporting Technique - SMART*) is a performance measurement framework that distinctly ties together the hierarchical view of business performance measurement with the business process view [11]. According to this framework, the hierarchical level of each unit has goals that are focused on the implementation of strategy and the increase of organisation's external and internal usefulness.

Performance pyramid prism consists of five levels: in the highest level there are strategy and vision of organisation. Organization determines the role of every single business unit and allocates resources. In the second level it is determined financial and competitive goals for every business unit. In the third level goals are tied in with customer satisfaction and measurement of flexibility or productivity. In the forth level that is design to measure units of organization, satisfaction of consumers, flexibility and productivity are expressed in quality, delivery, cycle time and lost assessment criterions. Last level presents the evaluation of day-to-day operations. According to performance pyramid system's model, the lowest level criterions are the main elements that determine the implementation of strategy. Therefore, in order to implement the strategy management efforts during evaluation must be direct from bottom up [19].

According to Anderson K. and McAdam R. [12] and Sližytė A. [20], the main advantage of the performance pyramid system is ability to describe how objectives are communicated down to the troop and how measures can be rolled up at various level in the organization. Every unit has its own goals and knows its responsibility. Lower hierarchical lever units' performance must satisfy the goals of higher level units. Also very important peculiarity of this framework that it makes explicit the difference between measures that are of interest to external parties; customer satisfaction, quality and delivery, and measures that are primarily of interest within the business's products, cycle time and waste. According to mentioned authors, the main problem with performance pyramid system is that it fails to specify, in any detail, either the form of the measures or the process for developing them, with no apparent scope for lead measures of performance.

4.4. European Foundation for Quality Management (EFQM) Excellence Model

The EFQM Excellence Model is a framework for organisational management system promoted by the European Foundation for Quality Management in 1992 and designed for helping organisations in their drive towards being more competitive. It is a practical tool to evaluate organisations' performance, identify areas for improvement and then stimulate for solutions [20]. It is enough flexible and can be used in various types of organisations large and small, in the public as well as the private sectors. This model can be used in four ways:

1. to help organizations develop their vision and goals for the future in a tangible, measurable way;
2. to help organizations identify and understand the systemic nature of their business, the key linkages and cause and effect relationships;
3. as a process which allows organizations to recognize its most successful customer experience (internal and external) and promote them to achieve the organizational target guided by their mission statements;
4. as self-assessment.

The EFQM Excellence Model is a non-prescriptive framework based on nine criterions that are divided into the "enablers" and "results". The "enabler" criterions such leadership, people, policy / strategy, partnership / resources and processes cover what an organization does. The 'results" criterions such as people results, customer results, society results and key performance results cover what an organization achieves. Innovation and learning is a continuous criterion throughout the model, arising from performance "results" and feedback acting "enablers" criterion. In EFQM Excellence Model importance of criterions is assessed by percentage (the greater importance, the greater impact on operational efficiency).

According to Sližytė A. [19], EFQM Excellence Model is more appropriate as diagnostic evaluation mean the operational rather than strategic level. However, even at the operational level EFQM Excellence Model measures the organization as a whole by focusing on a systematic approach to performance measurement, performance criterions are identified by the causal relations.

Slatkevičienė G. and Vanagas P. [6] identify such shortcomings of EFQM Excellence Model:

- it can measure performance of organization only episodically, the intervals between measurements are quite long. While organization implementing the principle of persistent improvement, it is important to continuously measure its results of performance;
- there is no methodology for how to consistently measure by the individual criteria blocks and hierarchical levels of organization.

5. COMPARISON OF PERFORMANCE MEASUREMENT SYSTEMS

In order to ascertain potential opportunities of applications of modern performance measurement system for the electricity sector companies comparative analysis of earlier discussed performance measurement systems was done. Performance measurement systems were analyzed in two steps:

- Performance measurement systems compared by criterions of evaluation;
- Performance measurement systems compared by performance specification of electricity sector companies.

The first section of performance measurement system comparison is the comparison by their criterions. In order to do analysis it is distinguished elements so called objects of organization's performance measurement that were described in the overview of systems (chapter 4). According to Sližytė A. [20], there is no unanimous opinion which objects of organization's performance measurement have to be included in the framework of organization's performance measurement.

As we can see in the Table 1, financial rates, implementation of strategy, satisfaction of consumers and internal processes of organization were the most frequently involved objects in the systems. Although financial rates are evaluated controversially, financial assessment is very important in all systems. According to Sližytė A. [20], financial rates reflect results of performance and have to be used by formulating goals of organization. However, they cannot be used as the main and the only one object of performance measurement of organization. Although PMP system is more orientated to measurement of stakeholders' satisfaction, the measurement of strategy implementation is one of fundamental objects of performance measurement of organization in all four performance measurement framework. The consumers are one of the most important stakeholders of organizations; their satisfaction is one of the success factors of organization. Internal processes of organization are particularly important, because successful development of organization is possible if they are concerted.

The object of workers' evaluation was identified in 3 of 4 systems (PMP, SMART, EFQM).

Stakeholder cooperation, capabilities of organization and resources, other stakeholder satisfaction, and innovations were identified in 2 of 4 systems. According to Sližytė A. [19], it is necessary to consider these measurement objects' influence and position in the performance measurement of organization then creating performance measurement system. According to the mentioned author, satisfaction of stakeholder is related to the participants' satisfaction of chain value influencing the productivity of chain value by investors' satisfaction that is determined by general result of organization's performance and so on.

Other objects such as quality, perfection, flexibility, external organization's process, learning, leadership, general results, social results, productivity, cycle of adaptation and the loss are identified in only 1 of 4 frameworks. Therefore they are not analyzed separately.

To safeguard electricity companies' functioning, it would be necessary to mention the main policies:

- in electricity market it is important to find consumers, to trade large amounts of electricity (if possible – in higher prices);
- finding of new fuel suppliers and ability to buy at lower prices and forecast trends in these markets;
- organizing the optimal performance of company allows to minimize operating costs, insures it‘s successful work.

Table 1. Objects of performance measurement systems

Objects of organization's performance measurement	**Performance measurement systems**			
	BSC	**PMP**	**SMART**	**EFQM**
Financial rates	*	*	*	*
Strategy implementation	*	*	*	*
Stakeholder satisfaction	*	*	*	*
Internal business process	*	*	*	*
Workers	-	*	*	*
Competition and goals	-	-	*	-
Capacity of organization, recourses	-	*	-	*
Other stakeholder satisfaction	-	*	-	*
Quality	-	-	*	-
Innovation	*	-	-	*
Perfection	*	-	-	-
Flexibility	-	-	*	-
External business processes	-	*	-	-
Learning	*	-	-	-
Stakeholder contribution	-	*	-	*
Leadership	-	-	-	*
General results	-	-	-	*
Social results	-	-	-	*
Productivity	-	-	*	-
Delivery time	-	-	*	-
Cycle time	-	-	*	-
Loss	-	-	*	-

Depending on the analysis of scientific literature became evident that the evaluation of performance measurement systems in electricity sector has varied continually with the companies technological and competitive environment. After analysis, often used in modern approach, performance measurement systems, (the second thing which) became evident that there is no single comprehensive performance measurement system. While each of them has its own advantages and disadvantages, modern approach, performance measurement systems, depending on the needs of the company, are considered as a tool for strategic goals' implementation. After inspected operating characteristics and conditions of electricity sector companies, it was made a conclusion that modern approach, performance measurement systems covers for the most part of measurement elements. It is also made the assumption that the gradual implementation of free Lithuanian electricity market, gain an important role of the individual strategy in electricity sector companies. This suggests that all analyzed modern performance measurement systems for electricity companies can be used as a tool of the strategy's implementation. This also encourages to analyze performance measurement systems of electricity companies more detail.

To complete the review of performance measurement systems as the tool of strategy's implementation in Lithuanian electricity generation, transmission and distribution companies, important:

- to clarify the implementation of a free electricity market impact of Lithuanian electricity generation, transmission and distribution companies, their strategy formulation and implementation;
- to analyze the peculiarity of performance measurement systems in electricity companies;
- to define the operational elements, indicators and strategic goals which have influence for the electricity companies;

In order to clarify these things it should be done the empirical researchs.

6. CONCLUSIONS

1. The understanding about performance measurement systems and its requirements has changed throughout time with changing technological and competitive business environment. According to the modern approach, performance measurement systems are considered as a tool for strategic goals' implementation of the company. Therefore, it must be flexible to the strategic changes and precisely reflect all organization's internal and external business process including both financial and non-financial also qualitative and quantitative criterions in order to get comprehensive view of organization's performance and implementation of strategic goals. Moreover, it has to be related to the evaluation of performance's quality, integrated through all levels of organization and to encourage its permanent perfection in order to ensure the effectiveness of organization's performance and strategy's implementation.
2. It was analyzed four of the most popular modern performance measurement systems in the paper in order to present their specifications. Balance Scorecard particularly focuses on implementation of strategy. It helps vision and strategy transform to organization's goals and criterions. According to Performance prism, the most important object of measurement is the satisfaction of all stakeholder therefore it is very important to find out their requirements. Performance Pyramid allows tying together distinctly the hierarchical view of business performance measurement with the business process view. Finally, EFQM Excellence Model seeks to evaluate organisations' performance, identify areas for improvement and then stimulate for solutions.

3. The analysis of performance measurement systems showed that all of them include the measurement of financial rates, implementation of strategy, satisfaction of stakeholder and internal business processes. However, other objects of organization's performance measurement differ in all systems. Therefore, it is possible to state that there is no performance measurement system that would include all objects of organization's performance.
4. There is no single comprehensive performance measurement system. All these systems have their advantages and disadvantages.
5. All analyzed modern approach, performance measurement systems for electricity companies, can be used as an implement of the strategy realization.
6. In exceptional cases, if there is a need to use more evaluation systems it is necessary to know what additional indicators must be evaluated and what disadvantages of the system are used.

REFERENCES

1. RANTANEN, H., KULMALA, HARRI I., LONNQVIST, A., KUJANSIVU, P. Performance measurement systems in the Finnish public sector. *International Journal of Public Sector Management*, 2007, Vol. 20, No. 5, p. 415–433.
2. HAAPASALO, H.; INGALSUO, K.; LENKKERI, T. A survey of BSC implementation in Finnish energy sector. *Benchmarking: an International Journal,* 2006, Vol. 13, No 6. p. 701–717.
3. WOUTERS, M., SPORTEL M. The role of existing measures in developing and implementing performance systems. *International Journal of Operation & Production Management,* 2005, Vol. 25, No 11, p. 1062–1082.
4. CHRISTAUSKAS, Č., KAZLAUSKIENĖ V. Modernių veiklos vertinimo sistemų įtaka įmonės valdymui globalizacijos laikotarpiu. *Ekonomika ir vadyba,* 2009, Nr. 14. ISSN 1822-6515.
5. UNAHABHOKHA, C., PLATTS, K, TAN, KIM H. Predictive performance measurement system. A fuzzy expert system approach. *Benchmarking: an International Journal.* 2007, Vol. 14, No 1, p. 77–91.
6. SLATKEVIČIENĖ, G., VANAGAS, P. *Veiklos kompleksinio vertinimo sistema: sudarymo teorija ir metodai. Monografija*. Kaunas: Technologija, 2001. 187 p. ISBN 9955-09-087-1.
7. KAPLAN, ROBERT S., NORTON, DAVID P. The Balanced Scorecard – Measures that Drive Performance. *Harvard Business Review.* 1992, January-February.
8. NEELY, A. The evolution of performance measurement research. *International Journal of Operation & Production Management.* 2005, Vol. 25, No 12, p. 1264–1277.
9. McADAM, R.; BAILIE, B. Business performance measures and alignment impact on strategy. *International Journal of Operation & Production Management.* 2002, Vol. 22, No 9, p. 972–996.
10. KENNERLEY, M., NEELY, A. A framework of the factors affecting the evolution of performance measurement systems. *International Journal of Operation & Production Management.* 2002, Vol. 22, No 11, p. 1222–1245.
11. KENNERLEY, M., NEELY, A. Measuring performance in a changing business environment. *International Journal of Operation & Production Management.* 2003, Vol. 23, No 2. p. 213–329.
12. ANDERSON, K., MCADAM R, A critique of benchmarking and performance measurement. Lead *Benchmarking: an International Journal*, 2004, Vol. 11, No 5, p. 464–483.

13. BOURNE, M.; MILLS. J., WILCOX, M.; NEELY, A., PLATTS, K. Designing, implementing and updating performance measurement systems. *International Journal of Operations & Production Management.* 2000, Vol. 20, No. 7, p. 754–771.
14. TONI, De A., TONCHIA S. Performance measurement systems. Models, characteristics and measures. *International Journal of Operation & Production Management,* 2001, Vol. 21, No 1/2, p. 46–70.
15. TAPINOS, E., DYSON, R. G., MEADOWS M. The impact of performance measurement in strategic planning. *International Journal of Productivity and Performance Management.* 2005, Vol. 54, No 5/6, p. 370–384.
16. LRS Nutarimas. Dėl nacionalinės energetikos strategijos patvirtinimo, 2007, sausio 18 d, Nr. X-1046, Žin. 2007, Nr. 11-430.
17. MULLER, R.; STEINERT, M.; TEUFEL, S. Successful diversification strategies of electricity companies: an explorative empirical study on the success of different diversification strategies of German electricity companies in the wake of the European market liberalization. *Energy policy*, 2008, No 36, p. 398–412.
18. WALSH, PHILIP R., SANDERSON, STUART M. Hybrid strategic thinking in deregulated retail energy markets. *International Journal of Energy Sector Management,* 2008, Vol. 2, No. 2, p. 218–230.
19. Lietuvos energija. Elektros rinka Lietuvoje, atmintinė. [Referred on the 3th of March in 2009 .]. Link to the internet <www.le.lt>
20. SLIŽYTĖ, A. Daktaro desertacija. Kompleksinio organizacijos veiklos vertinimo sistemos formavimas. 2009, Vytauto Didžiojo universitetas. Kaunas. p. 222. ISBN 978-9955-12-473-3.
21. RANTANEN, H., KULMALA, HARRI I., LONNQVIST, A., KUJANSIVU, P. Performance measurement systems in the Finnish public sector. *International Journal of Public Sector Management*, 2007, Vol. 20, No 5, p. 415–433.
22. BROMLEY, M., CUTHBERTSON, R., MARTINEZ, V., KENNERLEY, M. Insights from the Balanced Scorecard. Performance management at EDF Energy: ambition into action. *Measuring Business Excellence,* 2006, Vol. 10, No 3, p. 23–30.

CYSENI 2010, May 27–28, Kaunas, Lithuania
ISSN 1822-7554, www.cyseni.com

ESTIMATION OF OUTAGE PROBABILITY OF SCHEMES OF SWITCHGEARS FOR 110KV SUBSTATIONS

A. Lvovs, A. Mutule
Riga Technical University
Faculty of Power and Electrical Engineering
Kronvalda blvd. 1, LV-1070 – Latvia
Phone: (+371) 25970020, (+371) 67558616
E-mail: aleksandrs.lvovs@inbox.lv, amutule@edi.lv

ABSTRACT

The paper gives overview of methodology for calculations of reliability and outage probability of switchgears. The parameters of reliability for some types of 110kV substations` switchgears are calculated at the work. There are also compared switchgear schemes with different types of isolation – Air Insulated Switchgears (called AIS) and Gas Insulated Switchgears (called GIS). The calculations approved that two-busbar switchgear has higher reliability comparing to other schemes of switchgears. Calculations performed in the paper can help in making decision about usage of particular switchgear for each specific substation.

Keywords: outage probability, power supply, reliability, dependability, air insulated switchgear, gas insulated switchgear

1. INTRODUCTION

110kV substations are big power supply centres of cities and substations switchgears` reliability affects power supply reliability of large consumers' amount. Because of the fact, it is necessary to have information about switchgears` reliability. Consumers experience reliability of power supply, but for power supplying company more common term, related to reliability, should be used. The term, that can be used for power supply companies, is – dependability. That is so because dependability is characterised by such parameters: reliability performance, maintainability performance and maintenance support performance, and if reliability and maintainability performance depends on equipment, maintenance support performance depends on company's possibilities to ensure maintenance. Taking into account that possibilities of companies differ, in the work only reliability of switchgears is examined.

If the load of new or renovated substation and the parameters of dependability, including reliability and costs of equipment, it's maintainability performance and company's opportunities to ensure maintenance, for particular switchgears are known, it is possible to choose the best switchgear type for substation from technical and economical point of view. Sometimes technically more advanced switchgear has practically no advance in reliability comparing with not so advanced switchgears, e.g. switchgear with two busbars (4 lines) and switchgear with one busbar (two sections and 4 lines). However, difference in costs of such schemes can be considerable because of difference in number of elements (e.g. circuit-breakers) and in amount of maintenance works. Therefore, capital investments and dependability depend on each other and calculations of reliability should be performed.

In this article we will analyze reliability of some types of 110kV switchgears – Air Insulated Switchgears (further in text called – AIS) and Gas Insulated Switchgears (further in text called – AIS), in order to bring out the optimal type of switchgear for substations. As soon as maintenance staff and repair crews in Latvia, which realize maintenance of 110kV substations, are not permanently located at substations, and there are no persons on duty at substations, importance of reliability of 110kV substations increase.

As motive to carry out the analysis of reliability of switchgears was the fact that Distribution System Operator (DSO) of Latvia – JSC "Augstsprieguma tīkls" did not have any calculations as ones mentioned in the paper and no one could precisely (quantitatively) evaluate outage probability of 110 kV switchgears.

At the beginning of the paper there are given some facts about power supply networks of different European cities and exploitation of elements of the network. Some terminology is given too. Then methodology of calculations of reliability (this term has number of description 191-12-01 in [2] and is located in section 191–12 – Reliability performance measures), is given. After the methodology there are placed formulas for calculation of outage probability of the most popular 110 kV switchgears used in Latvia. At the end of the paragraph results of the calculations are demonstrated. Discussion of results and conclusions follow the results.

2. REVIEW OF POWER SUPPLY NETWORKS AND RELIABILITY AFFECTING FACTORS

Reviewing power supply schemes of Stockholm, Berlin, Moscow, Vilnius, Tallinn and Riga, we found some similarities, for example, high voltage transmission lines round the cities have a ring structure. There are diagonal interconnections between substations in the cities and radial lines from ring to the centre of city too. In Vilnius and Tallinn power supply network is created using two-chain power transmission lines. Such a structure of scheme is created to ensure high level of reliability of power supply because there is only one nominal voltage high voltage ring around the city. All other cities have more than one (usually two) high voltage "ring" and these "rings" have different nominal voltages. Overhead lines as well as cable lines are used in the cities, but in the future it is planned to create network using cables only. Usually two power transformers are installed at substations in those cities.

Efficiency (quality) of power network is determinated by group of properties that cause the ability of the system to perform needed functions. Usually such properties of power system are: reliability, economy, safety (security) and sometimes vitality of the system [1].

Requested reliability level for power network element is designed by engineers, realised in life by manufacturers and is maintained during exploitation. Element of power supply network is any part of the network that is used to produce, transform, transmit, distribute and to transform it to another kind of energy. Such elements are: generators, power transformers, autotransformers, reactors, current and voltage transformers, overhead and cable lines, distribution elements, transformer substations etc.

All elements mentioned above usually are brought under impact of different factors, which could be divided into four groups: mistakes in design and mounting, some factors of exploitation, environment factors and some other probabilistic factors like flashover to transport (cars, trains etc.), break of overhead line's pillar because of road accident, etc.

According to [2] there are such explanations of the terms:

- Dependability (191-02-03) – The collective term used to describe the availability performance and its influencing factors: reliability performance, maintainability performance and maintenance support performance. NOTE: dependability is used only for general descriptions in non-quantitative terms.
- Availability (performance) (191-02-05) – The ability of an item to be in a state to perform required function under given conditions at a given instant of time or over a given time interval, assuming that the required external resources are provided. NOTES: 1 – This ability depends on the combined aspects of reliability

performance, the maintainability performance and the maintenance support performance. 2 – Required external resources, other than maintenance resources do not affect the availability performance of the item. 3 – In French the term “disponibilite” is also used in the sense of “instantaneous availability” (see 191-11-01 in [2]).

- Reliability (performance) (191-02-06) – The ability of an item to perform a required function under given conditions for a given time interval. NOTES: 1 – It is generally assumed that the item is in a state to perform this required function at the beginning of the time interval. 2 – The term “reliability” is also used as a measure of reliability performance (see 191-12-01).
- Maintainability (performance) (191-02-07) – The ability of an item under given conditions of use, to be retained in, or restored to, a state in which it can perform a required function, when maintenance is performed under given conditions and using stated procedures and resources. NOTE: The term “maintainability” is also used as a measure of maintainability performance (see 191-13-01 in [2]).
- Maintenance support performance (191-02-08) – The ability of a maintenance organisation, under given conditions, to provide upon demand, the resources required to maintain an item, under a given maintenance policy. NOTE: The given conditions are related to the item itself and to the conditions under which the item is used and maintained.
- Reliability (symb. $R(t_1, t_2)$) (191-12-01) – The probability that an item can perform a required function under given conditions for a given time interval (t_1, t_2). NOTES: 1 – It is generally assumed that the item is in a state to perform this required function at the beginning of the time interval. 2 – The term “reliability” is also used to denote the reliability performance quantified by this probability (see 191-02-06).

3. METHODOLOGY OF CALCULATIONS OF RELIABILITY

Reliability of power supply for customers depends on power system element’s reliability and on structure of power network. It means that having the same customers and the same amount of generated power, power supply reliability can be different, e.g. for network formed by cable lines with a lot of interconnections and for network formed by overhead radial lines without interconnections. Duration and number of power supply interruptions also depends on equipment maintenance works. Reliability of element is determinated by quantity of failures of element during some period of time (e.g. one year) and fault repair time – T_{repair}. Usually term “failure rate” is used to quantify number failures of some type of elements during some period of time. Symbol used for Failure rate is λ. For cable or overhead lines λ is determinated by quantity of failures at 100 km of line. λ for an element and line can be calculated by using equations (1) and (2) respectively [3]:

$$\lambda = \frac{m}{n \cdot t}, \tag{1}$$

$$\lambda = \frac{m}{l \cdot t}, \tag{2}$$

where λ – failure rate;

m – number of failures of n elements per t years (typically per 1 year) (for elements) or number of failures of line per t years (typically per 1 year) and per l km (for lines);

n – number of monitored elements;

l – length of monitored line(-s), km (for calculations usually use l=100 km);
t – time of monitoring, year.

Usually λ value is bigger at the beginning and at the end of exploitation of an element. At the beginning of exploitation failures usually are caused by mounting mistakes or defect of any element. In case if equipment have been produced for long period of time and if mounting personnel has big experience of mounting works the first phase of exploitation could have the same λ value as the second phase. At the end of exploitation period failures appear because of wear of equipment. The diagram of failure rate λ dependence on time is shown at Fig. 1.

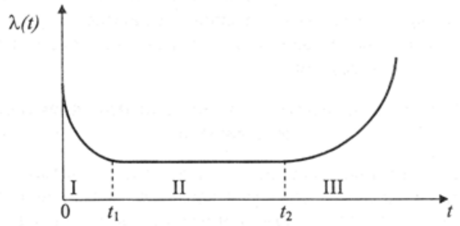

Fig. 1. Failure rate λ dependence on time

Calculations of outage probability will be performed using data from the second phase of exploitation.

In case if λ and T_{repair} values are known it is possible to calculate time of down-state T_{dn} and outage probability χ (see equations (3) and (4)). For Eqs. (3) and (4) T_{repair} is expressed in hours and it is assumed that failure rate λ is calculated for time period of 1 year, i.e. 8760 hours.

$$T_{dn} = \lambda \cdot T_{repair} \tag{3}$$

$$\chi = \frac{T_{repair} \cdot \lambda}{8760} \tag{4}$$

Usually electrical equipment and network consists of many elements. Because of that network usually is shown as diagram or structural scheme to show how elements interact and what will happen if one or more elements are damaged and have failure.

In case if some elements are connected in series, as shown at Fig. 2, failure rate of such chain can be calculated using Eq. (5). Outage state probability for connection shown at figure 2 can be calculated using Eq. (6).

$$\lambda_{series} = \lambda_1 + \lambda_2, \tag{5}$$

where λ_1 – failure rate for the first element;
λ_2 – failure rate for the second element.

$$\chi_{series} = \chi_1 + \chi_2, \tag{6}$$

where χ_1 – outage probability for the first element;
χ_2 – outage probability for the second element.

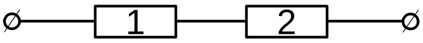

Fig. 2. Series connection of elements

In case if some elements are connected in parallel, as shown at Fig. 3, failure rate of such chain can be calculated using Eq. (7). Outage state probability for connection shown at figure 3 can be calculated using Eq. (8).

$$\lambda_{parallel} = \lambda_1 \cdot \chi_2 + \lambda_2 \cdot \chi_1, \tag{7}$$

where $\lambda_1 \cdot \chi_2$ – failure rate for the first element;

$\lambda_2 \cdot \chi_1$ – failure rate for the second element.

$$\chi_{parallel} = \chi_1 \cdot \chi_2 \tag{8}$$

where χ_1 – outage probability for the first element;
χ_2 – outage probability for the second element.

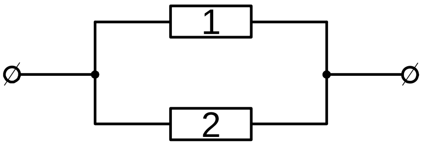

Fig. 3. Parallel connection of elements

Sometimes elements are physically connected in parallel, but at diagram they should be connected in series like it is shown at Fig. 2. Such situation can be for two generators working in parallel. Together they can provide as much power as we need, but if one of them fails, the second will be overloaded and should be disconnected too.

More complicated situation for calculations of outage probability and reliability is for schemes with bypass as shown at Fig. 4. Structure of such type of schemes determinates using mathematical logic (De Morgan's laws). Evaluation of reliability of such scheme is realized using theory of probability [4]. As logical link between elements during calculations is used sign of conjunction $\wedge$ (also known as: logical multiplication or AND operation) or sign of disjunction $\vee$ (also known as: disjunction operation or OR operation). Calculating reliability for schemes with bypass usually make some variants with the shortest ways of transmitting energy. For making the shortest ways for energy transmitting some different hypotheses (called "incompatible hypotheses") are used. For one hypothesis one element is expected to be absolute reliable, but for another hypothesis the same element is expected to be with failure.

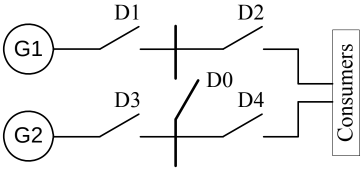

Fig. 4. Power supply scheme: G1 and G2 – generators, D1, D2, D3, D4 – circuit breakers, D0 – switched busbar circuit-breaker

Using scheme shown at Fig. 4 we can see, that consumer can get power from any of two generators and by any feeder. So in this case there are only the following ways:

- generator G1, circuit-breakers D1 and D2;
- generator G2, circuit-breakers D3 and D4;
- generator G1, circuit-breakers D1, D0 and D4;
- generator G2, circuit-breakers D3, D0 and D2.

Using method of incompatible hypotheses, reliability (probability of proper work without failures) of an object can be determinated using equation (9).

$$P(t) = \sum_i P(H_i) \cdot P(Y_i), \tag{9}$$

where $P(H_i)$ – probability of implementation of hypothesis i;

$P(Y_i)$ – probability of all elements` working state for hypothesis i.

Some elements before and after busbars and switched busbar circuit-breaker could be joined as series connected elements as explained above. At Fig. 5 there is shown scheme with joined generators and circuit-breakers. It also could be called functional scheme of scheme showed at Fig. 4.

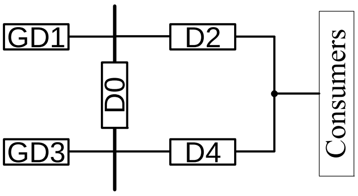

Fig. 5. Functional scheme of power supply scheme

From Fig. 5 we can see that scheme is not series connected, nor parallel connected. Let us make two incompatible hypotheses for element D0:

- H_1 – D0 is absolutely reliable;
- H_2 – D0 has failure.

Structural scheme for calculations for hypothesis H_1 is shown at Fig. 6. Working state requirements for this situation are given by Eq. (10).

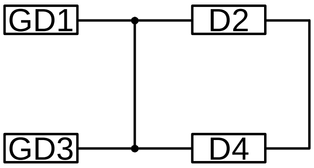

Fig. 6. Structural scheme for calculations for hypothesis H_1

$$Y_1 = (GD1 \vee GD3) \wedge (D2 \vee D4)\,. \tag{10}$$

Structural scheme for calculations for hypothesis H_2 is shown at Fig. 7. Working state requirements for this situation are given by Eq. (11).

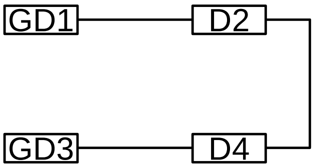

Fig. 7. Structural scheme for calculations for hypothesis H_2

$$Y_2 = (GD1 \wedge D2) \vee (GD3 \wedge D4)\,. \tag{11}$$

Reliability of the object can be determinated by Eq. (12) according to Eq. (9).

$$P(t) = P(H_1)\cdot P(Y_1) + P(H_2)\cdot P(Y_2)\,. \tag{12}$$

For example described above:

- probability of implementation of hypothesis H_1: $P(H_1)=P(D_0)$ – probability of D0 perform a required function;
- probability of implementation of hypothesis H_2: $P(H_2)=Q(D_0)=1-P(D_0)$ – outage probability of D0;
- probability of working state of scheme in case of hypothesis H_1:

$$P(Y_1) = [1-(1-P_{GD1})\cdot(1-P_{GD3})]\cdot[1-(1-P_{D2})\cdot(1-P_{D4})], \qquad (13)$$

where P_{GD1}, P_{GD3}, P_{D2}, P_{D4} – probability of elements GD1, GD3, D2, D4 to perform a required function;

- probability of working state of scheme in case of hypothesis H_2:

$$P(Y_2) = [1-(1-P_{GD1}\cdot P_{D2})\cdot(1-P_{GD3}\cdot P_{D4})]. \qquad (14)$$

Eqs. (13) and (14) can be explained using De Morgan's laws. For Eq. (13) "not (P or Q) = (not P) and (not Q)" law is used for expressions in parenthesis, because scheme for hypothesis H_1 will not work only in case if both GD1 and GD3 or D2 and D4 will not work. For equation (14) "not (P and Q) = (not P) or (not Q)" law is used for expressions in parenthesis, because scheme for hypothesis H_2 will not work in case if at least one element in each chain (chain GD1 and D2 and chain GD2 and D4) will not work.

The final Equation for calculations of reliability of discussed object can be written using equation (12):

$$P(t) = P(D0)\cdot[1-(1-P_{GD1})\cdot(1-P_{GD3})]\cdot[1-(1-P_{D2})\cdot(1-P_{D4})]+$$
$$+(1-P(D0))\cdot[1-(1-P_{GD1}\cdot P_{D2})\cdot(1-P_{GD3}\cdot P_{D4})] \qquad (15)$$

4. CALCULATION OF OUTAGE PROBABILITY OF SCHEMES OF 110KV SWITCHGEARS

To calculate the possibility of a full loss of power supply for 110kV substation (because of damage of 110kV switchgear), some assumptions are used:

1) Switchings are made in one hour $\chi = \frac{1*\sum\lambda}{8760}$;

2) One defect (fault) can be eliminated in 12 hours $\chi = \frac{12*\sum\lambda}{8760}$;

3) Once a year 110kV transformer has maintenance for 8 hours;

4) Once in 25 years 110kV transformer has overhaul, that lasts for two weeks;

5) Once in 4 years for 16 hours 110kV line or 110kV line's connection has maintenance. This time is used only for overhead lines. The same time in needed to repair busbar;

6) All 110kV lines are cable or overhead lines. All lines have equal length (for cable and overhead lines length is different);

7) All substations are equipped with identical equipment;

8) All outgoing lines are connected to power supply centres.

The aim of using different colours for different parts of Eq. (16) is to tell what kind of activity is done after each type of failure. Depending on equation's part colour, such activities should be performed: green – switchings should be performed, red – defect (fault) should be eliminated, blue – repair works for busbar or maintenance works for line or line's connection should be performed, pink – transformer repair or maintenance works should be performed.

Calculations are performed for outage probability χ, because it is easier to make such calculations (in this case subtraction is not needed, e.g. $(1-P_{D0}) = \chi_{D0}$).

At Fig. 8 and 9 there are given 4 types of schemes of switchgears usually used in Latvia for 110kV substations.

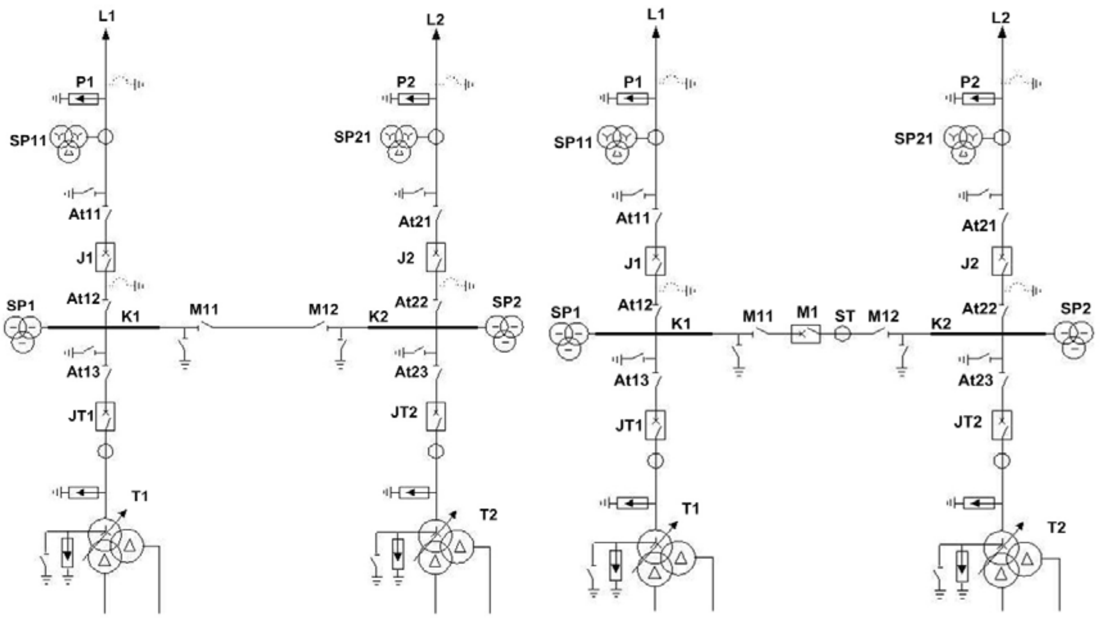

a) b)

Fig. 8. Schemes of 110kV switchgears: a) Substation with one busbar (two sections) without switched busbar circuit-breaker (two 110kV lines); b) Substation with one busbar (two sections) with switched busbar circuit-breaker (two 110kV lines)

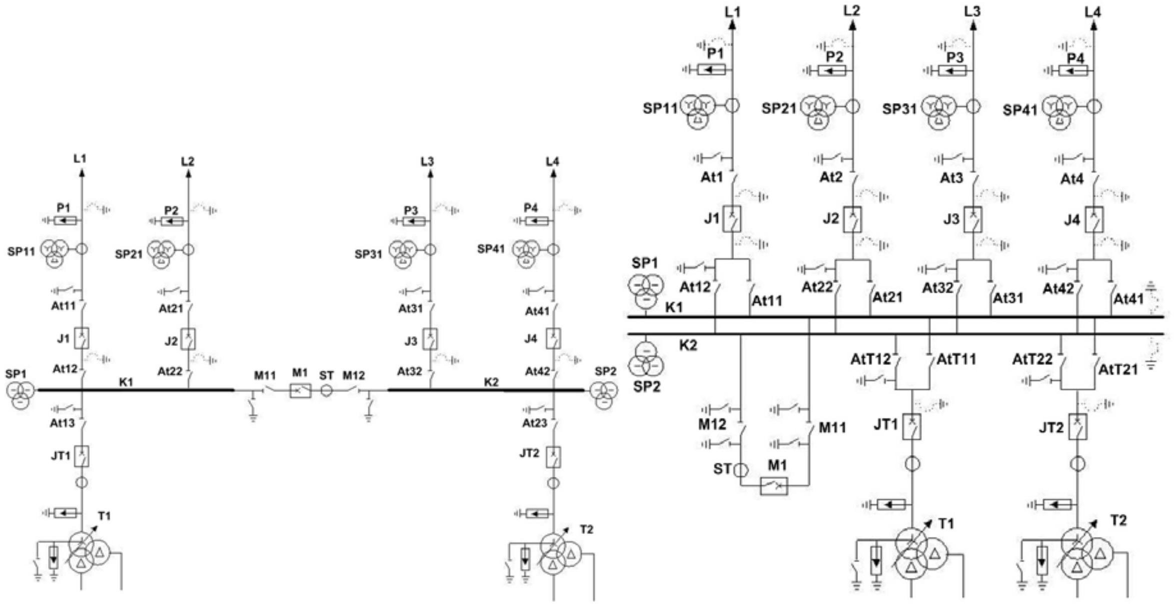

Fig. 9. Schemes of 110 kV switchgears: a) Substation with one busbar (two sections) with switched busbar circuit-breaker (four 110 kV lines); b) Substation with two busbars and bus coupler circuit-breaker (four 110 kV lines)

Table 1 illustrates failure rate's λ values for different elements of 110 kV switchgears. Different failure rate's λ values for some elements (e.g., spark gap, voltage/current transformer, etc.) depending on type of switchgear (AIS or GIS) are explicable by better environmental conditions for elements used with GIS. Using GIS, all elements, including voltage/current transformers, disconnectors etc., are located in metal enclosure filled by SF_6, so, air humidity, icing and other weather occurrences almost do not affect these elements. Data in software's LDM-AD`04 database are based on statistics of exploitation of high voltage equipment of substations in Latvia. As there are only few (not more than 15) GIS substations is Latvia and time period of exploitation of such substations is insignificant, λ values for GIS elements are based on information provided by manufacturers (presentation of GIS equipment of SIEMENS company in Institute of Physical Energetics).

Table 1. Failure rate's λ values for switchgear equipment from software's LDM-AD`04 database [5]

Element	Description (AIS / GIS)	λ	
		Air Insulated Switchgears	Gas Insulated Switchgears
Line	Overhead line (cable line), for length – 100 km	8.6 (0.86)	
Spark gap	PBC-110 / PEXLIM R,Q,P,E	0.01	0.0036
Voltage/current transformer	EJOF-123 / CPA/CPB	0.001	0.0007
Disconnector	PLHD-2-110/2000 / HAC-EV	0.08	0.0026
Circuit-breaker	BBY-110/40-2000 / LT3AP1 (Siemens)	0.07	0
Busbar	-	0.01	0.01
Transformer	Sum of transformer`s, spark-gap`s and multi-purpose transformer parameters	0.024	0.024

Calculations for scheme shown at Fig. 8 a):

$$
\begin{aligned}
\chi_1 = {} & \frac{12*12}{8760*8760} *[(\lambda_{L1}+\lambda_{P1}+\lambda_{SP11}+\lambda_{At11}+\lambda_{J1}+\lambda_{At12}+\lambda_{SP1}+\lambda_{K1}+\lambda_{At13}+\lambda_{M11}+\lambda_{JT1}+\lambda_{T1}) * \\
& * (\lambda_{L2}+\lambda_{P2}+\lambda_{SP21}+\lambda_{At21}+\lambda_{J2}+\lambda_{At22}+\lambda_{SP2}+\lambda_{K2}+\lambda_{At23}+\lambda_{M12}+\lambda_{JT2}+\lambda_{T2})] + \mathbf{\{1\}} \\
& + \frac{1}{8760} *[(\lambda_{J1}+\lambda_{At12}+\lambda_{SP1}+\lambda_{K1}+\lambda_{At13}+\lambda_{JT1}+\lambda_{M11}+\lambda_{M12}+\lambda_{J2}+\lambda_{At22}+\lambda_{SP2}+\lambda_{K2}+\lambda_{At23}+\lambda_{JT2}) + \\
& + (\frac{12*12}{8760*8760} *(\lambda_{T1}*\lambda_{JT1\ non.op.}))+ (\frac{12*12}{8760*8760} *(\lambda_{T2}*\lambda_{JT2\ non.op.})) + (\frac{12*12}{8760*8760} * \\
& * (\lambda_{L1}+\lambda_{P1}+\lambda_{SP11}+\lambda_{At11}) *\lambda_{J1\ non.op.}) +(\frac{12*12}{8760*8760} * (\lambda_{L2}+\lambda_{P2}+\lambda_{SP21}+\lambda_{At21}) *\lambda_{J2\ non.op.})] + \mathbf{\{2\}} \\
& + (\chi_{L1maint..} + \chi_{L1conn.maint.})* \frac{12}{8760} *(\lambda_{L2}+\lambda_{P2}+\lambda_{SP21}+\lambda_{At21}+\lambda_{J2}+\lambda_{At22}+\lambda_{SP2}+\lambda_{K2}+\lambda_{At23}+\lambda_{M12}) + \mathbf{\{3\}} \\
& + \chi_{K1maint.} * \frac{12}{8760} *(\lambda_{L2}+\lambda_{P2}+\lambda_{SP21}+\lambda_{At21}+\lambda_{J2}+\lambda_{At22}+\lambda_{SP2}+\lambda_{K2}+\lambda_{At23}+\lambda_{M12}+\lambda_{JT2}+\lambda_{T2}) + \mathbf{\{4\}} \\
& + \chi_{T1maint.} * \frac{12}{8760} *(\lambda_{At22}+\lambda_{SP2}+\lambda_{K2}+\lambda_{At23}+\lambda_{M12}+\lambda_{JT2}+\lambda_{T2}) + \mathbf{\{5\}} \\
& + (\chi_{L2maint.} + \chi_{L2\ conn.maint.}) * \frac{12}{8760} *(\lambda_{L1}+\lambda_{P1}+\lambda_{SP11}+\lambda_{At11}+\lambda_{J1}+\lambda_{At12}+\lambda_{SP1}+\lambda_{K1}+\lambda_{At13}+\lambda_{M11}) + \mathbf{\{6\}} \\
& + \chi_{K2maint.} * \frac{12}{8760} *(\lambda_{L1}+\lambda_{P1}+\lambda_{SP11}+\lambda_{At11}+\lambda_{J1}+\lambda_{At12}+\lambda_{SP1}+\lambda_{K1}+\lambda_{At13}+\lambda_{M11}+\lambda_{JT1}+\lambda_{T1}) + \mathbf{\{7\}} \\
& + \chi_{T2maint.} * \frac{12}{8760} *(\lambda_{At12}+\lambda_{SP1}+\lambda_{K1}+\lambda_{At13}+\lambda_{M11}+\lambda_{JT1}+\lambda_{T1})\ \mathbf{\{8\}},
\end{aligned}
\tag{16}
$$

where {1….8} describes outage probability of switchgear shown on Fig. 8.

{1} – describes outage probability that is caused by fault of one element clashing with another element's fault. At least one element should restore it's capability;

{2} – describes outage probability that is caused by fault of one element or fault of one element clashing with another element's fault. Switchings should be made.

{3} – describes outage probability that is caused by fault of one element clashing with line's L1 or it's connection maintenance;

{4} – describes outage probability that is caused by fault of one element clashing with busbar section's K1 maintenance;

{5} – describes outage probability that is caused by fault of one element clashing with transformer's T1 maintenance;

{6} – describes outage probability that is caused by fault of one element clashing with line's L2 or it's connection maintenance;

{7} – describes outage probability that is caused by fault of one element clashing with busbar section's K2 maintenance;

{8} – describes outage probability that is caused by fault of one element clashing with transformer's T2 maintenance.

Calculations for other schemes have been performed using the same principles in Microsoft Office Excel software. Table 2 gives us results of calculations.

Table 2. Full-load loss probability and time of outage state for various switchgear schemes for air insulated and gas insulated cases

Switchgear (according to figure)	**Cable lines (length – 5 km)**		**Overhead lines (length – 50 km)**	
	χ	**Time of outage state, min/year**	χ	**Time of outage state, min/year**
1 busbar, no circuit breaker, 2 lines	$9.7926*10^{-5}$ $(4.81147*10^{-6})$	51.4 (2.5)	$1.57*10^{-4}$ $(5.6270*10^{-5})$	82.5 (29.6)
1 busbar, 1 circuit breaker, 2 lines	$1.29032*10^{-5}$ $(5.87724*10^{-7})$	6.8 (0.389)	$7.19253*10^{-5}$ $(5.20464*10^{-5})$	37.8 (27.4)
1 busbar, 1 circuit breaker, 4 lines	$1.16407*10^{-5}$ $(3.56668*10^{-7})$	6.1 (0.187)	$1.16747*10^{-5}$ $(3.88451*10^{-7})$	6.1 (0.204)
2 busbars, 1 circuit breaker, 4 lines	$1.1222*10^{-5}$ $(2.3454*10^{-7})$	5.9 (0.123)	$1.1222*10^{-5}$ $(2.3454*10^{-7})$	5.9 (0.123)

5. DISCUSSION OF RESULTS

From the results we can see, that, as it was expected, the most reliable switchgear is switchgear with two busbars and bus coupler circuit-breaker between busbars, but the worse switchgear, from reliability point of view, is one busbar switchgear with two sections without switched busbar circuit-breaker between sections.

In case of network formed by cable lines number of connected lines, if it is more than two lines, do not affect reliability level a lot. Another situation is with overhead lines, where number of connected lines affects result a lot.

Comparing outage probabilities for switchgear with two busbars and bus coupler circuit-breaker and four 110 kV lines with switchgear with one busbar (two sections) with switched busbar circuit-breaker and four 110kV lines in spite of network structure – cable or overhead lines, it is clear that such scheme doesn't give us much better outage probability value. Therefore, it would be useful to use such switchgear scheme only for 110 kV distribution points and for 330/110 kV substations. Such scheme can be used for substations where three transformers are installed.

According to the results usage of GIS instead of AIS helps to improve reliability level a lot in cities and countryside. Usage of GIS in city substation improves reliability level dramatically. For rural substations, where network is formed mainly with overhead lines, reliability level increases, but, unfortunately, reliability level doesn't increase so fast as in cities, because of big role of reliability of overhead lines on power supply interruptions. Taking into account rising land prices, shortage of land and high power loads, usage of GIS in cities is necessary and reasonable. If power transit through substation is needed, scheme shown at figure 8 b) should be used and in case of GIS, high voltage network practically does not affect power supply reliability. For rural substations, it could be better to install just circuit-breaker between sections to improve reliability level, because price of GIS is approximately twice higher than for AIS and GIS becomes economically inefficient. In this case economical calculations should be performed. Sometimes it is economically better not to improve reliability of power supply, but just pay penalty for energy not supplied.

6. CONCLUSIONS

The aim of calculations presented in the paper is to quantify outage probability of 110 kV switchgears. Results showed that:

1. Usage of circuit breaker between sections and GIS instead of AIS increases reliability dramatically for substations located in rural and countryside territories;
2. Number of lines connected to substations, affect reliability of power supply a lot only in case of overhead lines and if number of connected lines is under 4;
3. Switchgear with two busbars and bus coupler circuit-breaker practically doesn`t have advantage in reliability of power supply.

The research is very useful for transission network planning, becase results of calculations can be used to compare suitability of different types of switchgears for particular substation, taking into account objective judgement about reliability of the scheme of switchgear and it`s type (AIS or GIS). Results of calculations will be used further to assess reliability of power supply of cunsumers located in middle and low voltage network and to analyze impact of different types of reliability improvement enterprises to power supply reliability. All the results will be used in doctoral dissetration development.

This work has been supported by the European Social Fund within the project „Support for the implementation of doctoral studies at Riga Technical University”.

EIROPAS SOCIĀLAIS FONDS

EIROPAS SAVIENĪBA

REFERENCES

1. СКОПИНЦЕВ, В.А., ЧЕМОДАНОВ, В.И., ЧИЧИНСКИЙ, М.И. Оценка надёжности работы электрической сети. *Трактат* НМЦ НЭС, Москва, 2004, 37 p.
2. LVS IEC 50-191:1990, Starptautiskā elektrotehnikas vārdnīca, 191. nodaļa: Drošums un pakalpojumu kvalitāte (IEC 50-191:1990, *International Electrotechnical Vocabulary, Chapter 191: Dependability and quality of service)*. Rīga: Latvijas Nacionālais standartizācijas un metroloģijas centrs, 1998, 63 p.
3. KRIŠĀNS, Z.; OĻEINIKOVA, I. *Elektroenerģētisko uzņēmumu vadības pamati.* Rīga: Rīgas tehniskā universitāte, 2007, 158 p. ISBN 978-9984-32-985-7.
4. КАЛЯВИН, В.П.; РЫБАКОВ, Л.М. *Надёжность и диагностика элементов электроустановок.* Санкт-Петербург: Элмор, 2009. 331 p. ISBN 5-7399-0150-2.
5. KRIŠĀNS, Z., OĻEINIKOVA, I., MUTULE, A., KUTJUNS, A. LDM-AD'04 versija2, Apraksts instrukcija (instruction for computer software LDM-AD`04). Latvian Academy of Sciences, Institute of Physical Energetics, Power system mathematical modelling laboratory, 2004., 82 p.

CYSENI 2010, May 27–28, Kaunas, Lithuania
ISSN 1822-7554, www.cyseni.com

FINAL ENERGY CONSUMPTION IN LITHUANIA FROM THE HOUSEHOLD SECTOR PERSPECTIVE

Renata Dagiliūtė, Genovaitė Liobikienė
Department of Environmental Sciences of Vytautas Magnus University
Vileikos str. 8, Kaunas LT-44404, Lithuania
Phone: (8 37) 327 904
Email: r.dagiliute@gmf.vdu.lt
g.liobikiene@gmf.vdu.lt

ABSTRACT

The household sector plays a major role in final energy use. Declining household size, increasing overall number of households, growing number of appliances means that household energy will continue to grow in Lithuania. Since 2000 electricity consumption has been increasing by 5% annually and during the period from 2000 to 2007 electricity consumption has risen by 40%, heating energy by 2% in Lithuanian household sector. It is estimated that electricity consumption in Lithuanian household sector will tend to grow. However, government policies aimed at reducing energy use have focused on technical elements rather than changes in behaviour. Informed how to save the energy and to use it efficiently energy consumers could help to reduce energy consumption.

Therefore this study aims to analyze the Lithuanian energy consumption and energy saving behaviour in household sector. The research is based on quota sample survey and is backed up with some relevant studies.

The results of survey show that 68% of respondents declared that in the last five years their electricity consumption increased, following the most significant increase in number of home appliances (81.4%). Despite rapid energy consumption growth, 60% of respondents in general claimed to be saving energy, 51.3% claimed to be saving the thermal energy for heating. However energy saving was determined by energy prices, incomes, but not by ecological awareness. Only 8.7% of respondents save energy concerning environment pollution, 16 % of respondents save concerning less use of resources. On the purpose to increase energy efficiency in household sector lifestyle changes, environmental education and promotion of energy efficient goods and services is necessary.

Keywords: energy consumption, household sector, attitudes and behaviour

1. INTRODUCTION

Sustainable development has gained an international attentions in the lasts decades, aiming to decouple environmental impacts from economy growth [1, 2]. Increasing eco-efficiency both: production and consumption is accepted to be appropriate, thought not sufficient strategy for sustainability goals. Very often eco-efficiency gains are offset by increasing consumption [3].

Acknowledged values, cultural, social and psychological factors determine final decisions for purchasing and consuming [4]. Very often consumption is related not only to fulfillment of basic needs, but creates social meanings and becomes symbols of social values [5]. Unsustainable consumption patterns are especially characteristic to industrialized, developed countries. It is estimated that household consumption will double until 2030 in European Union (hereinafter – EU) [6]. About 70% of all environmental impact directly (using water and energy) and indirectly (using goods and services) is caused by households in EU [7, 8]. In EU, as well as in Lithuania, one third of all final energy used within economy is consumed in households, contributing to climate change, air pollution and related problems, as energy consumption issues are multidimensional. Questions of energy efficiency, energy supply dependency, and energy price and fuel poverty are often discussed and are linked to political, social and environmental aspects [9].

As it was already mentioned, households consume one third of overall final energy and final energy demand is constantly increasing in household sector [10]. The main drive is considered to be increasing incomes. As some studies reveal, increase by 1% in incomes leads to 0.1–0.4% increase in final energy consumption [11]. Increase in final energy consumption is also driven by shrinking household size and growing number of home appliances (TV, DVD, computers and etc.). Usually at the same time the living space per person is increasing leading to the increase of thermal energy for heating and electricity consumption, too [2]. It is estimated, that one person consumes nearly twice more energy in a single person household than a person in three person household [12]. Increasing age of populations also is one of the drivers for energy consumption. Older persons spend more time at home and therefore use relatively more energy [13]. H.C. Moll and K.J. Noorman and others (2005) estimated that due to this reasons older people more intensively use gas and electricity to compare to younger persons.

As mentioned, technological gains in eco-efficiency alone are not enough as they are often offset by increased overall consumption. Here, very important role is played by personal values and attitudes. Therefore the social factors are becoming of importance and the need to reshape lifestyles and attitudes as well as behaviour in daily lives is needed [6, 14, 15].

Therefore, this paper aims to analyze the main changes in household final energy consumption, to discuss main drivers as well as attitudes and behaviour of consumers regarding energy saving and energy efficiency in Lithuanian households. The paper is organized as follows. Firsts, some methodological issues are presented, and then, some insights about changes in final energy consumption in household sector of Lithuania are given. Some attitudes and behaviour regarding energy efficiency of the consumers are presented in the third section, and, finally, conclusions are drawn.

2. DATA AND METHODOLOGICAL ISSUES

Paper is based on the data from Statistical Office of Lithuania and quota sample survey. Analysis of the energy consumption trends covers 1990–2007 year period. To reveal on going changes year 1990 is treated as a base year.

To reveal the main trends in consumers’ attitudes and behaviour towards environment a consumer survey was conducted. As the results of quota sample survey often follow the results of representative surveys, the quota sample survey was conducted in 2006 (May-August). 343 respondents (52.6% female and 47.4% male) filled in the questionnaire prepared by the authors. The sex structure and the age structure (with some deviations) of the respondents correspond to that of Lithuania. Though results of the survey do not represent the whole population of Lithuania, some conclusions on prevailing trends of consumers’ attitudes and behaviour could be done. The number of respondents is sufficient to secure significance of the results nearly by 95%. It should have been mentioned that energy issues constituted only one part of the questions in conducted survey.

Analysis is mainly based on descriptive statistics. The analysis of possible drivers is based on the interrelation analysis (Kendall’s τ-b correlation coefficients). Correlations were considered to be statistically significant at $p < 0.05$. SPSS 12.0 for Windows and Microsoft Excel software was used for data analysis and presentation.

3. HOUSEHOLD ENERGY CONSUMPTION IN LITHUANIA 1990–2007

After the collapse of former Soviet Union, changes in political, economical and social life highly influenced the consumption patterns of households in Lithuania. When looking to the final energy consumption in household sector (Fig. 1) in overall terms decreasing trends are observed. During the analyzed period overall final energy consumption decreased by 27%. The main drivers for these positive changes were introduction of appropriate metering measures, increased control and fast growing prices especially for the district heating (the biggest share of energy consumed in households is for heating purposes (70%), about 14% is consumed for hot water preparation, and 12% for lighting and electronic devices at home [6]). Only since 1995 the price for the district heating for final household consumers increased about 4 times, natural gas – more than 2 times and consumption of thermal energy for heating in household sector decreased nearly twofold (43%).

Then analyzing separately thermal energy for heating and electricity consumption, quite different trends are observed during economy growth period especially from 2000. After continuously decrease during 1990–2000, consumption of thermal energy for heating (not adjusted to the outdoor temperature) showed some stabilization and minor fluctuations from 2000. In addition to that, it should be mentioned that, energy consumption intensity in household sector is still very high. It is estimated that renovation of multi-blockhouses could reduce relative consumption of thermal energy for heating per square meter by 30% [16].

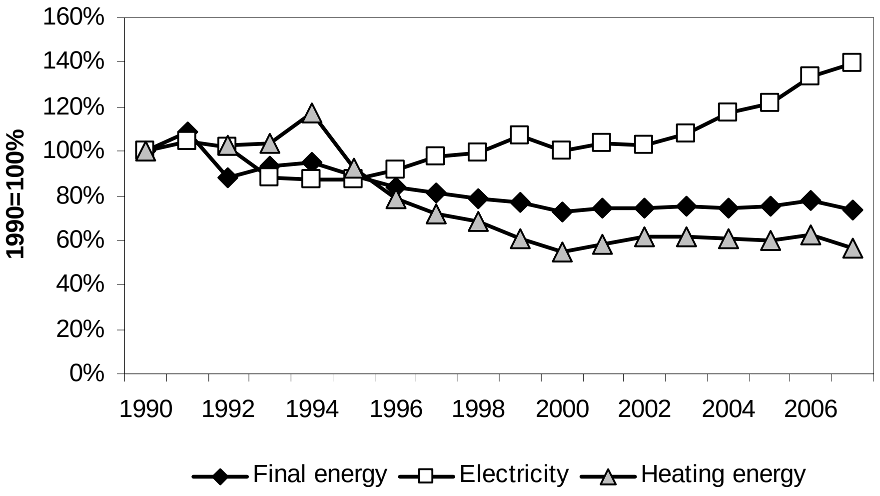

Fig. 1. Overall final energy, electricity and thermal energy for heating consumption trends in Lithuanian household sector 1990–2007 (based on: Statistical Office of Lithuania)

Some opposite trends are seen when electricity consumption is analyzed. After slight decrease during transitional decline, electricity consumption in Lithuanian household sector was on continuous increase. And recent growth of this indicator by 40% from 2000 is challengeable from the point of sustainability. This tendency was driven by decreasing size of household. From 1995 household size in Lithuania decreased by 15% from 2.76 to 2.39 persons per household while per capita living area increased by 21%. Also households became more luxurious with more home appliances (increased by 83%), more electronic and communication tools (increased nearly twofold) that require more and more recourses of electricity to fulfill daily needs. Despite the fact that the eco-efficiency of these appliances is constantly increasing and their exploitation requires less energy, the number of durable goods is increasing and electricity consumption is growing in Lithuanian household sector [17]. Still as compared to EU-15 there are less home appliances per 100 households in Lithuania.

Having in mind discussed drivers, it is estimated that electricity consumption in Lithuanian household sector will tend to grow by 4.1–5% per year depending on economy growth rates [18].

4. ATTITUDES TOWARDS ENERGY ISSUES AND BEHAVIOUR OF HOUSEHOLD CONSUMERS

As it was already discussed, technological efficiency gains are often offset by increased consumption. Therefore trying to increase energy efficiency not only production phase, but consumption phase should be addressed, too. Consumers' lifestyle, attitudes, individual perceptions and behaviour play very important role in achieving sustainability.

The results of our survey highly correspond with the consumption trends discussed in the previous section then we indicated relatively fast growth of electricity consumption and number of home appliances. More than a half of respondents declared that in the last five years their consumption increased and the most significant was increase in number of household appliances (81.4%), followed by 67.1% increase in electricity consumption (Fig. 2). The relationship analysis showed than significantly faster number of household appliances grew in households with higher incomes ($\tau_b = -0.153$, $p < 0.05$) and in households of younger respondents ($\tau_b = -0.202$, $p < 0.05$).

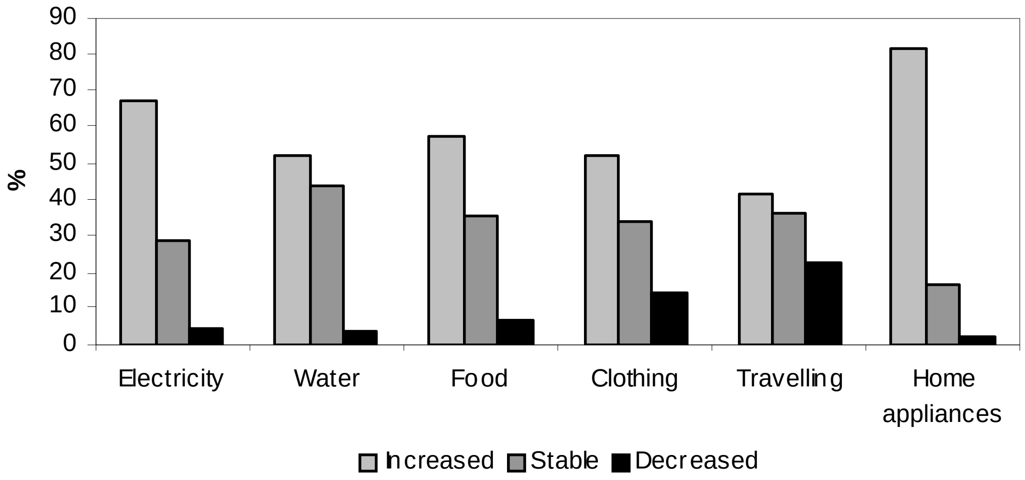

Fig. 2. Changes in consumption during last five years in respondents' households in % of all households under analysis (based on survey results)

Nevetheless, increase in incomes would lead to the further consumption increase not only for cultural and social needs of respondents, but will determine further growth of household appliances in 30% of households of the respondents as our results reveal (Fig. 3). In the separate question whether respondents are planning to buy some new household durable goods, 36.2% of the respondents confirmed these intensions, some of them, 14.7% were not sure about this. However, these tendencies let us make some assumptions that electricity consumption is going to grow further, as it was also indicated by V. Miskinis (2004) and other authors [18].

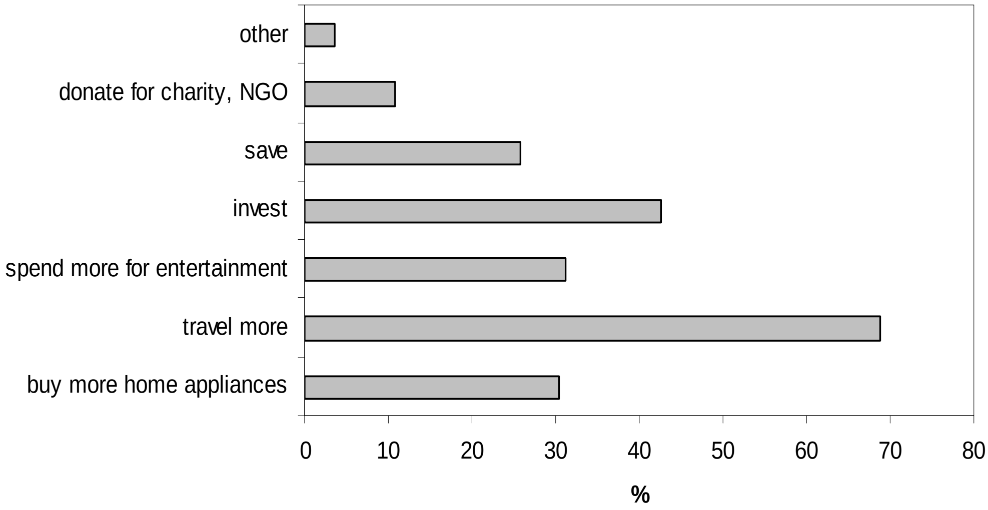

Fig. 3. Consumption activities induced by higher income (based on survey results)

Despite rapid electricity consumption growth, general energy saving activities declared by the respondents should be evaluated positively from the point of sustainable consumption. 60% of respondents in general claimed to be saving energy, 51.3% claimed to be saving the thermal energy for heating, 50% – gas (Fig. 4). This could be induced by relatively high heating prices, as 70% of all energy consumed goes for the heating in the household sector and proportionally heating bills are much higher. On the other hand, thermal energy for heating and gas had the largest share on the respondents only seldom or never performing saving activities. Though high heating prices is one of the drivers for saving thermal energy, deeper analysis revealed that respondents who were not likely to save heating energy lived in blockhouses and were provided by district heating. The attitudes and behaviour of these respondents to some extend could be determined by the fact, that usually, individual saving activities are very limited in the flats of blockhouses. To addition to that, there is no individual metering system applied in such old-fashion blockhouses. This situation to some extend creates no incentives for saving thermal energy for heating and limits the willingness to save. Therefore, not only technological issues, but information (in this case on building renovation, modernization of thermal energy distribution units and on other possibilities) is very important as Dagiliute *et al*. (2009) state [19].

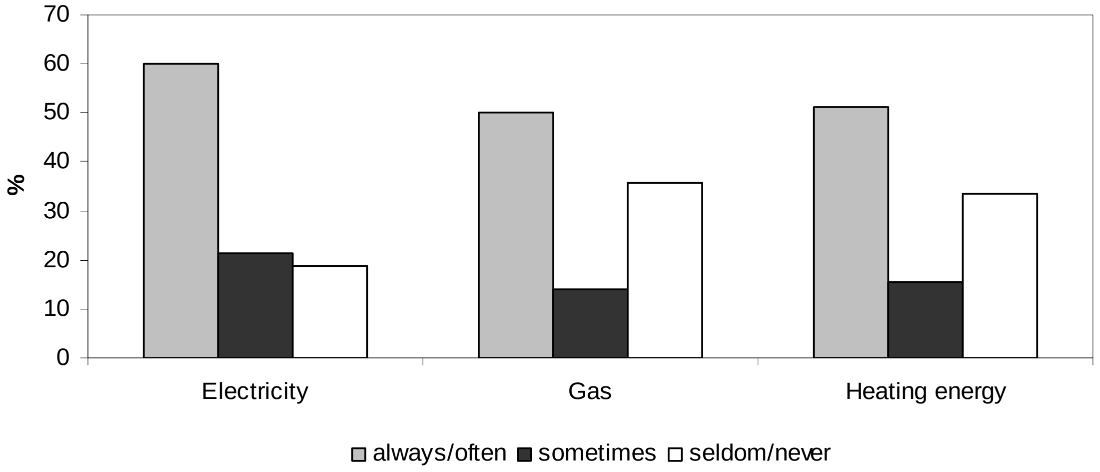

Fig. 4. Frequency of saving activities in respondents' households (based on survey results)

On the other hand, those who claimed to save energy were driven mostly by economical reasons. As results show, energy saving was determined by energy prices, incomes, but not by ecological awareness (Fig. 5). Only 8.7% of respondents save energy concerning environmental pollution, 16% of respondents save concerning less use of resources. Those respondents were living in private houses, using gas or firewood for the heating. Therefore this is also mostly driven by economic motives, than really environmental perceptions.

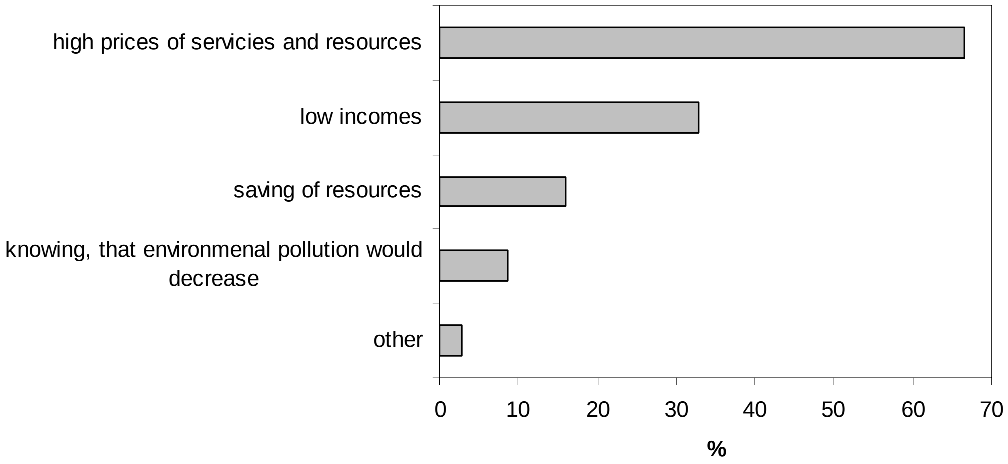

Fig. 5. Incentives for final energy saving in respondents' households (based on survey results)

On the purpose to increase energy efficiency in household sector lifestyle changes, environmental education and promotion of energy efficiency goods and services is necessary. As results show, consumers often lack information on environment and energy efficiency related issues (eco products and etc.). Together with these measures some technological solutions and adequate supporting measures should be applied, enable consumers to express their environmental and saving perceptions. This complex approach is needed if significant improvements in energy and especially electricity consumption are to be achieved.

5. CONCLUSIONS

1. In Lithuanian households consumption of thermal energy for heating during economy growth period was stabile and minor fluctuated, however, electricity consumption was continuously increasing during the period under analysis.
2. The results of the survey correspond to the electricity consumption trends in Lithuanian households. 68% of respondents declared that in the last five years their electricity consumption increased, following the most significant increase in number of home appliances (81.4%). Striving for life styles and life quality of the West might lead to the further increase in electricity consumption in Lithuanian households, driven by growing number in home appliances, even having in mind improvements in their energy efficiency and price growth for electricity.
3. Thought technological, technical and economical instruments are of importance for energy efficiency increase; final household consumers play a major role when making saving and purchasing decisions. As study reveals more than half of Lithuanian consumers declare to be saving energy and this is mostly driven by economic factors (prices for energy, incomes).
4. Existing infrastructural, technical and legislative conditions, as well as the lack of information very often limits consumer possibilities to save final energy, especially in multi-blockhouses. Information, education and promotion of energy efficient goods and services could be the major factors for increasing energy efficiency. Clearly and timely

provided information on possible options and their effectiveness could induce consumer's energy saving activities (via behaviour, via chosen technological solutions, products and services), that could lead to increased energy efficiency and mitigation of energy related social, economic and environmental problems.

6. ACKNOWLEDGEMENTS

Authors would like to thank an anonymous and two official reviewers whose comments and suggestions have helped to improve the manuscript.

REFERENCES

1. SUN, J. W. Dematerialization and Sustainable development. *Sustainable Development*, 2000, Vol. 8, p. 142–145.
2. EUROPEAN COMMUNITIES. Energy, Transport and Environment Indicators, Luxemburg: Office for Official Publications of the European Communities. 2005, p. 183.
3. BINSWANGER, M. Technological progress and sustainable development: what about rebound effect? *Ecological economics*, 2001, Vol. 36, p. 119–132.
4. SPANGENBERG, J.H., LOREK, S. Environmentally sustainable household consumption: fro aggregate environmental pressures to priority fields of action. *Ecological Economics*, 2002, Vol. 43, p. 127–140.
5. MONT, O., PLEPYS, A. Sustainable consumption progress: should we be proud or alarmed? *Journal of Cleaner production*, 2008, Vol. 16, p. 531–537
6. EEA. Household consumption and the environment. EEA Report, 2005, No 11/2005, Copenhagen, p. 68
7. TUKKER, A, JANSEN, B. Environmental impacts of products. A detailed review of Studies. *Journal of Industrial Ecology*, 2006, Vol. 10, No 3, p. 159-182
8. TUKKER, A., COHEN, M.J., DE ZOYSA, U., HERTWICH, E., HOFSTETTER, P. INABA, A., LOREK, S., STO, E. The Oslo Declaration on Sustainable Consumption. *Journal of Industrial Ecology*, 2006, Vol. 10, No. 1-2, p. 9–14.
9. DAGILIŪTĖ, R., MŽAVANADZĖ, N. Sustainability Innovations as the Way Out of the Current Economy Crisis. Proceedings of an International Conference on Interdisciplinary Research Crisis: Catalyst for Creativity and Innovation. Klaipėda: LCC International University. 2009 March 27–28, (accepted in LCC Liberal Arts Studies).
10. MIGUEZ, J.L., PORTEIRO, J., LOPEZ-GONZALEZ L.M., VICUNA J. E., MURILLO S., MORAN J.C., GRANADA E. Review of the energy rating of dwellings in the European Union as a mechanism for sustainable energy. *Renewable & Sustainable Energy reviews*, 2006, Vol. 10, p. 24−45.
11. FUCHS, D. A, LOREK, S. An Inquiry the Impact of Globalization on the Potential for "Sustainable Consumption" in Households. Report No 2/01. Program for Research and Documentation for a Sustainable Society, Oslo, 2001, p. 80.
12. MOLL, H.C., NOORMAN, K.J., KOK, R., ENGSTROM, R., THRONE-HOLST, H., CLARK, Ch. Pursuing More Sustainable Consumption by Analyzing Household Metabolism in European Countries and Cities. *Journal of Industrial Ecology*, 2005, Vol. 9, No 1–2, p. 259–275.
13. HAAS R., SCHIPPER L. Residential energy demand in OECD-countries and the role of irreversible efficiency improvements. *Energy Economics,* 1998, 20, p. 421–442.
14. COGOY, M. The consumer as a social and environmental actor. *Ecological Economics*, 1999, Vol. 28, p. 385–398.

15. HALME, M., JASCH, C., SCHARP, M. Sustainable home services? Toward household services that enhance ecological, social and economic sustainability. *Ecological Economics*, 2004, Vol. 51, p. 125–128.
16. LITHUANIAN HOUSING STRATEGY. The Government of the Republic of Lithuania, January 21, 2004, decision No 60, p. 20
17. DAGILIŪTĖ, R. JUKNYS, R. Sustainability of Household Consumption in Lithuania. *Aplinkos tyrimai inžinerija ir vadyba*, 2009, Nr. 1 (47), p. 63–68.
18. MIŠKINIS, V., KONSTANTINAVIČIŪTĖ, I., NORVAIŠA, E., DEKSNYS, R. Energijos poreikių namų ūkio sektoriuje prognozės. *Energetika*, 2004, Vol. 1, p. 17–24.
19. DAGILŪTĖ, R., VENSLOVIENĖ, J., LIOBIKIENĖ, G. The need and the importance of environmental information for sustainable development. Proceedings of International conference Human and Nature Safety. Kaunas: LZUU. 2009 May 13-14 ISSN 1822-1823, p. 113–116.

CYSENI 2010, May 27–28, Kaunas, Lithuania
ISSN 1822-7554, www.cyseni.com

HEAT-INSULATING PAINT EFFICIENCY ESTIMATION

S.M. Danilova-Tretiak, V.L. Dragun, V.G. Leschenko
A. V. Luikov Heat&Mass Transfer Institute of NAS of Belarus
Brovki 15, Minsk 220072 – Belarus
Phone: (+375)172841250
Email: dts@hmti.ac.by

ABSTRACT

Heat losses reduction through building walls is an actual question. It allows improving energy effectiveness of buildings structures. In this paper the results of heat-insulating paint efficiency estimation are presented. The estimation is performed on the basis of distance thermophysical diagnostics which is complex investigation of the object thermal state by infrared thermography and analysis of thermophysical properties of wall components including the paint itself. The problem is solved at different ambient conditions. Heat flux was accepted as the criterion of heat-insulating material applicability. The material is admitted as improper if calculated value of heat flux exceeds standardized one. Comparative analysis is carried out for three different structures really applied in building construction. The cases when paint was coated on plaster with underlaid heat-insulating material (two sorts of paint are considered) and directly on concrete panel are regarded. The optimal values of thermal conductivity are denoted for heat-insulating material and paint. The paint layer thickness is also determined. The results are important for achievement and improvement of required thermal parameters of buildings structures.

Keywords: heat loss, heat-insulating material, heat-insulating paint, thermal conductivity

1. INTRODUCTION

Improvement of building structures energy efficiency is important problem and many scientists and engineers try to solve it by different ways. But the aim is the same - heat losses reduction through buildings walls. As for heat losses they could be reduced due to good thermal insulation. There are no materials which can turn back heat flux fully but there are ones which can restrict it more or less effectively.

A lot of heat-insulating materials are proposed on building materials market. Most unordinary of them is heat-insulating paint. It is a compound of special binding polymeric material on water basis and hollow evacuated glass-ceramic balls 10–100 μm in diameter. Paint layer dries to strength dense water-proof membrane. Peculiarities of the membrane give energy-saving properties to the paint coat. Glass microspheres serve as a filter for heat flux in infrared spectrum reflecting and scattering a part of heat.

In the paper presented we consider heat-insulating paint as addition or even alternative to other traditional heat-insulating materials. We have determined geometrical and thermophysical parameters of different materials which will provide building walls heat-saving enhancement.

2. METHODOLOGY

We suggest the distance thermophysical diagnostics as the method of building materials and structures efficiency analysis. This diagnostics is complex investigation of the object thermal state by infrared thermography and its mathematical modeling under different conditions. In some cases thermal control might be active that is to say additional temperature gradient is created between inner and outer walls of structure [1]. Thermophysical properties of multilayer structure components could be determined by solving of inverse problem of thermal conductivity under condition that the object temperature is known from thermographic data. The results of thermographic inspection imply that:

1) one-dimensional steady-state heat transfer is realized inside of the wall at the moment of inspection;
2) internal (external) air temperature is constant along inner (outer) surface of the wall;
3) surface temperature is uniform that is defectless wall is regarded;
4) convective heat transfer coefficient is uniform on external surface of the wall.

To describe the object thermal state mathematically the thermal conductivity equation is used. In the case of multilayer object the equation is assigned to each layer characterized by its own parameters. Temperatures and heat fluxes are assumed to be equal on the boundaries of layers.

Standardized temperature inside building (domestic one) is equal to 18 ^{o}C. Thermal state of building walls is estimated at different thermal properties of insulation, ambient temperatures and wall-air convection conditions. Heat flux is accepted as the criterion of heat-insulating material applicability [2]. The material is admitted as improper if calculated value of heat flux exceeds standardized one. Heat flux through the unit of area allowing for surface-air heat transfer and one across the whole width of the wall can be calculated according the equation:

$$q = \frac{t_i - t_e}{R}, \tag{1}$$

where t_i – internal air temperature, t_e – external air temperature, R – heat transfer resistance. Standardized values (in Belarus) of heat transfer resistance at different ambient temperatures are presented in Table 1.

Table 1. Heat transfer resistance for domestic building's wall at different ambient temperatures

t_e, ^{o}C	-25	-15	-10	-5
R, $m^2 \cdot {}^{o}C/W$	3.12	2.56	1.75	1.75

Boundary conditions for the problem under solving allow for radiative and convective heat transfer between outer wall surface and air. Emissivity ε of outer wall surface determines radiative heat transfer. It can be valued from special tables or from Table 2 for materials regarded in the problem under solving. Heat transfer across the whole width of the wall is determined by thermal conductivity λ of used materials. The values are presented in Table 2.

Table 2. Physical properties of building materials

Material	Concrete panel	Plaster
ε	0.92	0.92
λ, W/m·^{o}C	1.75	0.80

The program Elcut® 5.1 Professional Edition [3] is used for modeling of two-dimensional fields by the method of finite elements. Among modeled fields are temperature, its gradient, heat flux and heat losses.

Only blind walls are considered in modeling. It is assumed that the wall consists of several layers made to be a tight. Due to this fact we can give condition of temperature contingency on layers boundaries. It causes some degree of approximation in calculations because real surfaces are rough so close-contact is almost impossible and there is air space between layers. Air space reduces equivalent thermal conductivity of multilayer wall because of low air thermal conductivity. The lower thermal conductivity is the lower heat losses through the wall are. So we neglect air space existence.

The building wall considered here consists of (Fig. 1): 1 – concrete panel, wall thickness is 0.30 m; 2 – heat-insulating material, wall thickness is 0.12 m; 3 – plaster, thickness is 0.004 m; 4 – heat-insulating paint, thickness is 0.001 m. Heat-insulating paint of two sorts was examined in the paper.

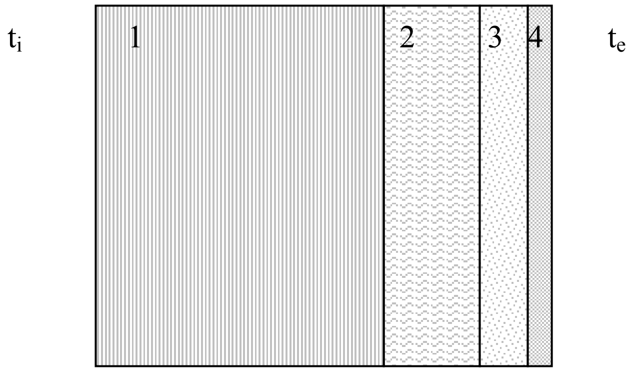

Fig. 1. Building wall under consideration

Thermal conductivity of heat-insulating material is varied to determine more optimal value and ones of 0.050; 0.045; 0.040 W/m·°C are considered. The values correspond to materials proposed on Belorussian market. Plaster and paint (of sort 1) thermal conductivities equal 0.8 W/m·°C and 0.15 W/m·°C correspondingly.

3. RESULTS AND DISCUSSION

Values of maximal heat flux q through the unit of domestic building wall surface area at different ambient temperatures (peculiar to Belarus) are presented in Table 3.

Table 3. Maximal heat flux through building wall at different ambient temperatures

t_e, °C	10	0	-10	-15
q, W/m^2	4.57	10.29	16.00	12.89

Then we determine heat flux through the wall at different convection conditions. Heat flux is calculated for each convective heat transfer coefficient at different ambient temperatures. In Fig. 2 graphs of heat flux against ambient temperature are presented for heat-insulating materials of different thermal conductivities. Convective heat transfer coefficient α are assumed to be equal a) 5 W/m^2·°C, b) 23 W/m^2·°C, c) 45 W/m^2·°C. Both in Fig. 2 and on following figures the values of maximal heat flux through building wall at corresponding ambient temperatures are denoted as color points (in the legend it can be seen as "normal").

It can be seen that values of heat flux don't exceed standardized ones at all ambient conditions considered here. But if we take heat-insulating material with thermal conductivity of 0.050 W/m·°C then calculated heat flux is 98% of standardized value at ambient temperature 15 °C and wind velocity 10 m/s. So, if ambient conditions would be more rigorous the structure regarded wouldn't enough energy-effective. So, heat-insulating material with thermal conductivity of 0.045 W/m·°C or less should be chosen. Decrease of thermal conductivity from 0.050 to 0.045 W/m·°C leads to heat flux through the wall fall by 10%.

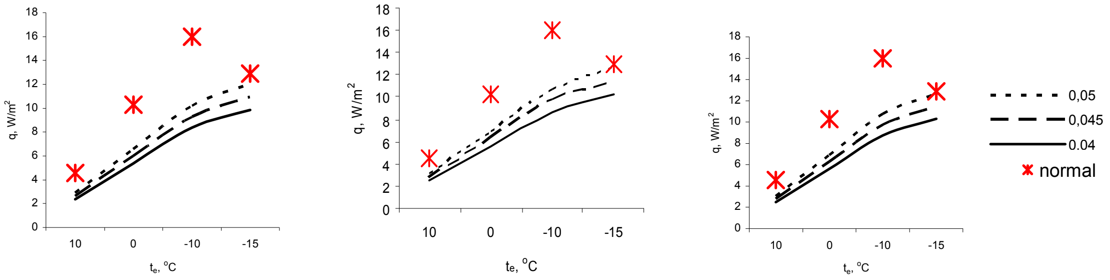

a) b) c)

Fig. 2. Heat flux versus ambient temperature

More modern sorts of heat-insulating paints have less value of thermal conductivity – 0.001 W/m·°C [4–6]. It should be noted that it is not natural thermal conductivity. Heat-insulating paint gives quasi-vacuum layer of insulation which almost blocks heat flux. It is due to rarefied air in microspheres. Radiative part of heat losses is reduced significantly due to high reflection. The paint surface emits three times as less as brick or concrete. To take into account both of heat transfer mechanisms so called "effective thermal conductivity" was introduced. It is calculated value.

In Fig. 3 the results of heat flux calculation are presented for structure from Fig. 1 with paint coat of sort 2 (with low thermal conductivity). The results correspond to wind velocity of 10 m/s. Wind velocity variation doesn't cause heat flux calculated value excess over the standardized one more than 70%.

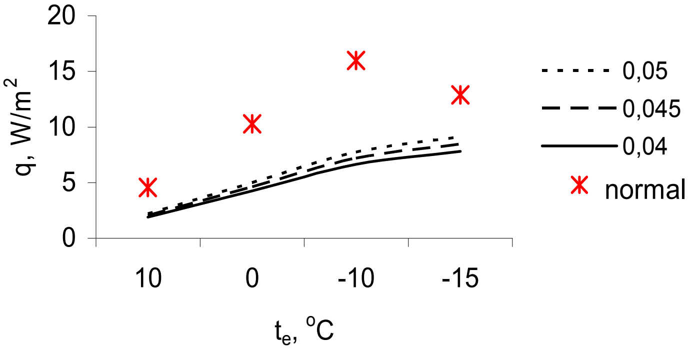

Fig. 3. Heat flux versus ambient temperature at different values of thermal conductivities of heat-insulating material

Thermal field (by Elcut®) inside of building wall is shown in Fig. 4 (thermal conductivity of heat-insulating material equals 0.045 W/m^2·°C). Ambient temperature is -15 °C, wind velocity is 10 m/s. Temperature gradient in the layer 1 (inner concrete wall from the side of living space) is no more than 2 °C. That is to say the heat-saving effect of this structure is acceptable.

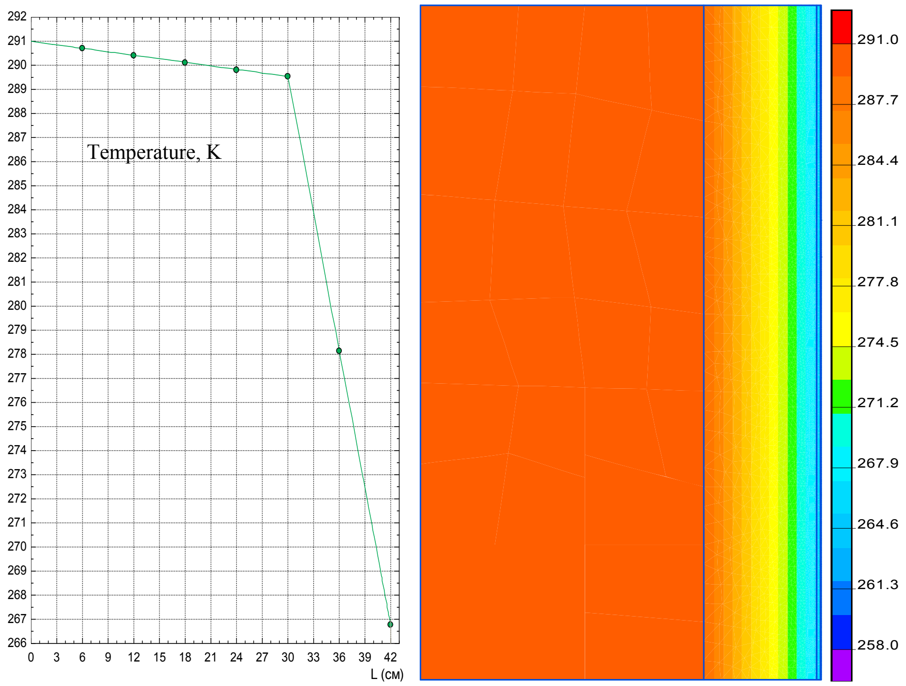

Fig. 4. Thermal field inside of structure «concrete panel – heat-insulating material – plaster – heat-insulating paint of sort 2

The comparative analysis of three walls heat-saving effect was carried out (Table 4): 1 – concrete panel – heat-insulating material – plaster; 2 – concrete panel - heat-insulating material – plaster – heat-insulating paint of sort 1; 3 – concrete panel - heat-insulating material – plaster – heat-insulating paint of sort 2. Heat-insulating material thickness is 12 cm, its thermal conductivity is 0.045 W/m·°C.

Table 4. Heat flux through the wall at different convection conditions (for ambient temperature of -15 °C).

α, W/m²·°C	**q, W/m²**		
	building wall		
	1	2	3
5	11.15	10.94	8.23
23	11.46	11.41	8.49
45	11.52	11.49	8.54

We can see that using of heat-insulating paint of sort 1 leads to negligible reduction of heat losses (within 2%) through the wall. While other paint (sort 2) exhibits better heat-saving – heat losses are 25% reduced. The maximal calculated heat flux doesn't exceed 70% of standardized one.

Low thermal conductivity of paint sort 2 determines its appropriate heat-saving effect. So it's an actual task to simplify the wall structure considered here. Such paints can be coated directly on concrete panel. Paint thermal conductivity is assumed to be equal 0.001 W/m·°C. The paint layer thickness which is necessary for appropriate heat saving is determined. We can see from Fig. 5 that paint sort 2 with layer thickness of 3 mm provides heat flux values through unit of the wall area within the mark.

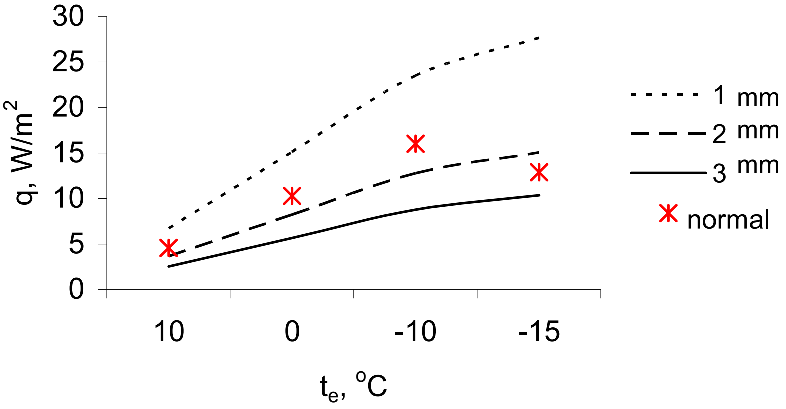

Fig. 5. Heat flux versus heat-insulating paint thickness

4. CONCLUSIONS

So the distance thermophysical diagnostics as complex investigation of the object thermal state by infrared thermography and its mathematical modeling under different conditions allows estimating of structural integrity and efficiency of structure at the moment and foreseeing of its thermal state changes at different conditions and properties of components.

Heat-insulating paint coating with thickness of 3 mm leads to reduction of heat flux through building wall. If paint thermal conductivity is $\lambda = 0.001$ W/m·°C the value of heat flux doesn't exceed the 70% of standardized one.

Coating the paint directly on concrete panel simplifies structure of the wall. The layer with thickness of 3 mm provides heat flux values through unit of the wall area within the mark.

REFERENCES

1. The method of non-destructive control of heat-saving properties of building wall. Patent BY 12812 C1, 2010.
2. MALYAVINA E.G. *Building heat losses*. Moscow: Avok-press, 2007. 144 p. (rus).
3. Elcut® 5.1. Modeling of two-dimensional fields by finite elements method. User manual. St-Petersburg, 2003.
4. Heat-insulating compound ThermalTech. TC BY 400084698.171-2005.
5. Anticorrosive and heat-insulating material on the basis of hollow microspheres. Patent RF №2251563, 2005.
6. Heat insulating liquid-ceramic material. Patent RF №2342415, 2008.

CYSENI 2010, May 27–28, Kaunas, Lithuania
ISSN 1822-7554, www.cyseni.com

CASE STUDY OF LOW ENERGY BUILDING IN LITHUANIA

R. Džiugaitė
Vilnius Gediminas Technical University,
Department of Buildings Energetics
11 Sauletekio str., LT-10223, Vilnius – Lithuania
Phone: +370 655 35 450
Email: rasa.dziugaite@vgtu.lt

ABSTRACT

Nowadays buildings consume more energy than any other sector of the European economy. It is recognized that they account for around 40% of energy consumption. The building sector offers the largest potential for energy savings, which can reduce the negative impact on the environment. Therefore, building designers have to focus on the energy performance of their building designs. This means that they have to consider new buildings constructions, improve energy efficiency of buildings and energy systems, develop low energy (sustainable, passive) building concepts and promote renewable energy sources.

The design of the low energy building requires parametric studies via simulation tools in order to optimize the design of the building envelope, heating, ventilation and air conditioning systems. Therefore, the article's subject is the tools, which are used for computing the energy performance of the buildings and finding out the optimal solutions to select the best system configuration and energy sources mix. Also, this article shows an example of low energy building project in Lithuania that minimizes the use of energy for heating in cold period and promotes the multi-energy systems, which integrate renewable energy sources.

Keywords: low energy buildings, multi-energy systems, optimization, energy performance, simulation

1. INTRODUCTION

As buildings account for 40% of total energy consumption in the EU, reduction of energy consumption and the use of energy from renewable energy sources in the buildings sector constitute important measures needed to reduce the EU's energy dependency and greenhouse gas emissions [1]. The EU addressed the problem by introducing Energy Performance of Buildings Directive (EPBD), which was updated on 29th of January in 2010. The new definition for „nearly zero energy building" has been presented and it means a building with a very high energy performance and a significant share of energy supply from renewable energy sources. One of the targets is that all new buildings in EU should be "nearly zero energy building" by the end of 2020 [2]. However, it means that the design of a low energy building requires a common calculation methodology of the energy performance of building; also Member States of EU shall to set the minimum requirements for energy performance of building at a national level and building elements. Furthermore, the design of a low energy building should comply with the environmental impact, indoor thermal comfort and internal quality, investment cost, etc [3]. Equally, the parametric studies via simulation tools have to be performed in order to optimize the design of the low energy building envelope and HVAC systems considering the local climatic conditions of the concrete case study.

Therefore, this paper aims to set up a research that shows a variety of simulation tools which can help the designers to choose the optimal solution regarding building thermal insulation, building orientation, glassed surface area, windows type, envelope air-tightness, building thermal inertia, efficiency of equipments and HVAC systems, renewable energy sources, etc. Also, this article shows a case study of low energy building in Lithuania that promotes the multi-energy systems, which integrate renewable energy sources, in order to cover the thermal loads of a building. This case study shows several examples of multi-energy source building systems, which combine thermal solar energy, heat pumps, ventilation unit with heat recovery.

2. OVERVIEW OF BUILDING ENERGY PERFORMANCE SIMULATION PROGRAMS

The most appropriate calculation and simulation tools of low energy buildings and passive houses, which are available today, are described in Table 1.

Table 1. Features and capabilities of building energy performance simulation programs

Program	Data requirements	Capabilities, simulation features	Calculation scope	Validation
Energy Plus	Weather data (climate data of Kaunas is available), detailed building input data	Simulation manager, heat and mass balance simulation module and building systems simulation module [4]	Simulation of building energy performance and designing of energy efficient systems	IEA SHC Task 12, IEA SHC Task 22
TRNSYS	Weather data (climate data of Kaunas is available), building input data, definition of the energy systems	Detailed multi-zone building model, including solar thermal and photovoltaic systems, low energy buildings, HVAC systems, renewable energy systems, cogeneration, fuel cells [5]	Designing of energy efficient systems	IEA SHC Task 12, IEA SHC Task 22
SIMIEN (Norwegian-developed)	Climate data (only for 30 different locations in Norway [7]), building input data	Dynamic simulation and calculation of heat and cooling effects, power demand, heat balance, energy supply for months or whole year, energy savings, energy costs [7]	Simulation of indoor climate and energy use in buildings	NS 3031
Passive House Planning Package (German-developed)	Surface areas of envelope, thermal characteristics of materials, thermal bridges, ventilation system, efficiency of heat recovery, location of building	Energy calculations, design of ventilation system, sizing of the heating and cooling loads, the heating and DHW systems, calculations of auxiliary electricity, primary energy requirements [7]	Planning and verifying the passive houses	LST EN ISO 13790: 2008 *(original EN 832:1998)*

Table 1. Features and capabilities of building energy performance simulation programs

Program	Data requirements	Capabilities, simulation features	Calculation scope	Validation
BSim (Danish-developed)	Weather data (no climate data for locations of Lithuania is available), building input data, equipments and energy systems	Simulation and calculation of thermal indoor climate, energy consumption, daylight conditions, moisture and energy transport in constructions and spaces, electrical yield from building integrated photovoltaic systems [5]	Energy design of buildings and moisture analysis	IEA SHC Task 12
IDA ICE (Swedish-developed)	Weather data, building input data, internal loads and schedules, equipments and energy systems	Dynamic multi-zone simulation of the building, its systems, and controllers [6]	Modelling thermal indoor climate and the energy consumption of the building	IEA SHC Task 12, IEA SHC Task 22
DEROB-LTH (Swedish-developed)	Weather data, building input data, internal loads and schedules, equipments and energy systems	Calculations of peak loads, energy demand, temperatures, thermal comfort for a building, the influence of solar isolation and shading devices on the energy balance in the building [8]	Modelling thermal indoor climate and the energy consumption of the building	*(is not explored)*
PolySun (Swiss – developed)	Weather data, geographic location, energy load profile, hydraulic scheme, costs, horizon characteristics	Calculation of the efficiency of the single components of solar or photovoltaic systems, selection of the most appropriate components [7]	Simulation of thermal solar collectors, photovoltaic systems, heat pumps	LST EN 12975-2:2006
Heat 2, Heat 3	Using the generated inputs	Modelling heat transfer, transient simulations, automatic calculation of the linear thermal transmittance [7]	Modelling thermal bridges, U-values for building construction parts, surface temperatures, heat losses to the ground from a house	LST EN ISO 10211: 2008, LST EN ISO 10077-2: 2006

Considering the availability of the weather data for the certain location, the capabilities of the tool and the ability to explore the software as a primer user at the beginning of modelling, Energy Plus has been chosen to perform the energy performance simulation for the presented case study. EnergyPlus software and weather data for Kaunas have been downloaded at no cost from the EnergyPlus web site.

3. CASE STUDY

In this case a created model of a single family house is presented as low energy building. It has been assumed, that this building is located in Kaunas. The plan of the house is shown in Figure 1. The total living area is 140 m^2, the hight of the rooms is 3.0 m.

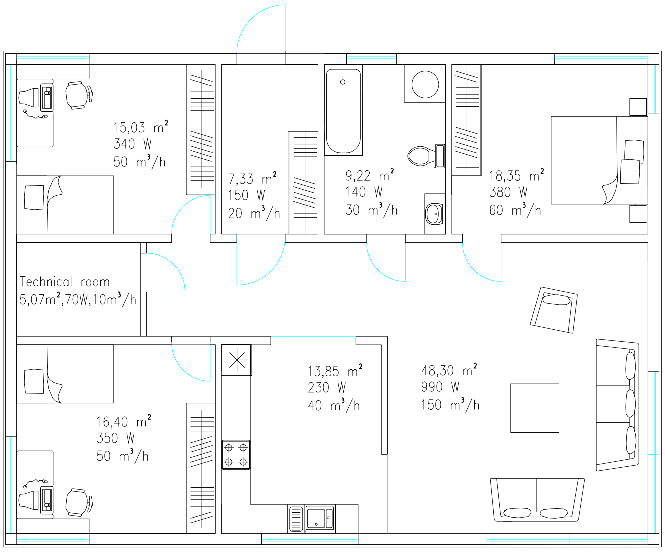

Fig. 1. Case study – low energy building

3.1. Climate data

Kaunas, located at latitude N 54° 52', has an average yearly temperature of 6.3ºC [9]. The heating degree days for Kaunas are 3789, representing the cold climate region. In this cold climate, meeting the energy targets set for the high-performance buildings requires that the building envelope, including the windows, has to have a very low U-value, a very little infiltration, so good air quality has to be ensured using mechanical ventilation with heat recovery.

The cold climate creates special limitations on supplying energy from solar gains. KAUNAS – LTU IWEC Data has been used to simulate monthly average temperatures and solar radiation with EnergyPlus software [16]. Calculated monthly average temperatures and solar radiation are shown in Fig. 2.

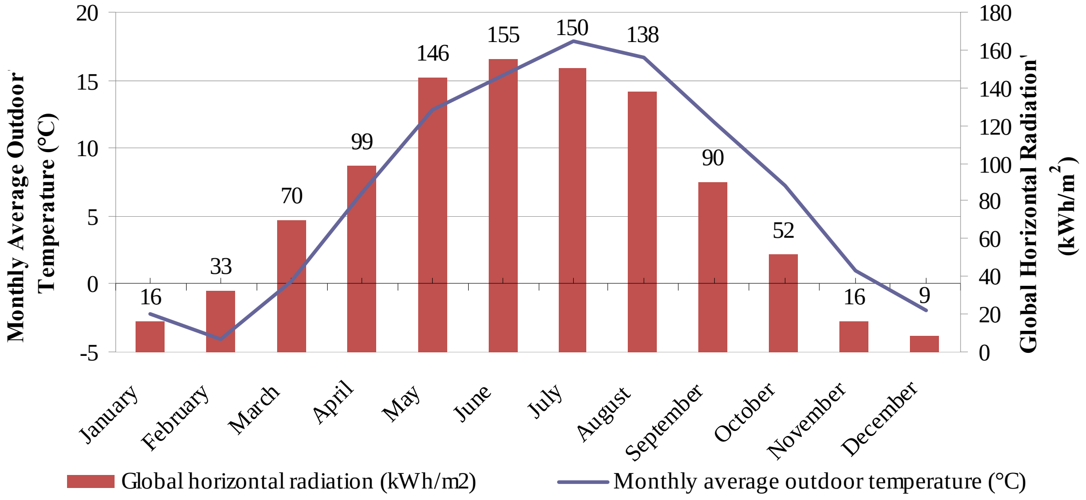

Fig. 2. Monthly average outdoor temperature and global horizontal solar radiation in Kaunas

As can be seen from Fig. 2, most of the solar radiation occurs in summer. The annual amount of sunshine hours is 1751 [10]. Total annual solar energy (direct and diffuse) amount fallen on the horizontal surface in Kaunas is 976 kWh/ m^2.

3.2. Building description

Low-energy house has been chosen for this case study. This building fulfills the following requirements [11]:

- an annual heat demand for heating is 47 kWh/m² per year. Cooling of this building is not considered in this case;
- total primary energy consumption for heating, hot water and electricity is 101 kWh/m² per year. Household electricity is not included as a part of the energy targets;
- an air tightness of building construction is 0.6 h^{-1} at 50 Pa, resulting in approximately 0,05 h^{-1} infiltration rate under normal conditions;
- a heat recovery ventilation system, with a heat recovery rate of over 80% and high-efficiency electronically commutated motors (ECM), is used to maintain air quality;
- specific fan power efficiency rating (SFP) is 1.5 kW/(m^3/s);
- since the building is essentially airtight, the rate of air change is 1.0 h^{-1}. All ventilation ducts are insulated and sealed against leakage;
- average internal gains, caused by lighting, electrical equipments and people, is 4 W/m^2;
- the internal temperature is 21°C, in order to maintain thermal comfort in the rooms. For studies of energy demand and peak load, the maximum allowed internal temperature is 25°C. Above this temperature, the occupants are assumed to reduce the air temperature by using shading devices.

The exterior walls and roof of the building are in wooden lightweight frame construction with mineral wool as insulating material. Superinsulation is used to significantly reduce the heat transfer through the walls, roof and floor compared to conventional residential buildings. The windows are chosen with exceptionally low U values, triple-pane insulated glazing (with a good solar heat-gain coefficient, low-emissivity coatings, krypton gas fill, and 'warm edge' insulating glass spacers) with air-seals and specially developed thermally-broken window frames. The U values of the building components are shown in Table 2.

Table 2. The U-values of the low energy building components

Building component	**U value (W/m^2K)**
External walls	0.078
Roof	0.068
Floor	0.132
Windows	0.746
External door	0.80

All these requirements for low energy residential buildings have been implemented and used for the energy performance simulations in EnergyPlus.

3.3. Energy performance of the building

3.3.1. Space heating demand

The monthly space heating demands of the building, calculated according to [12], are shown in Fig. 3.

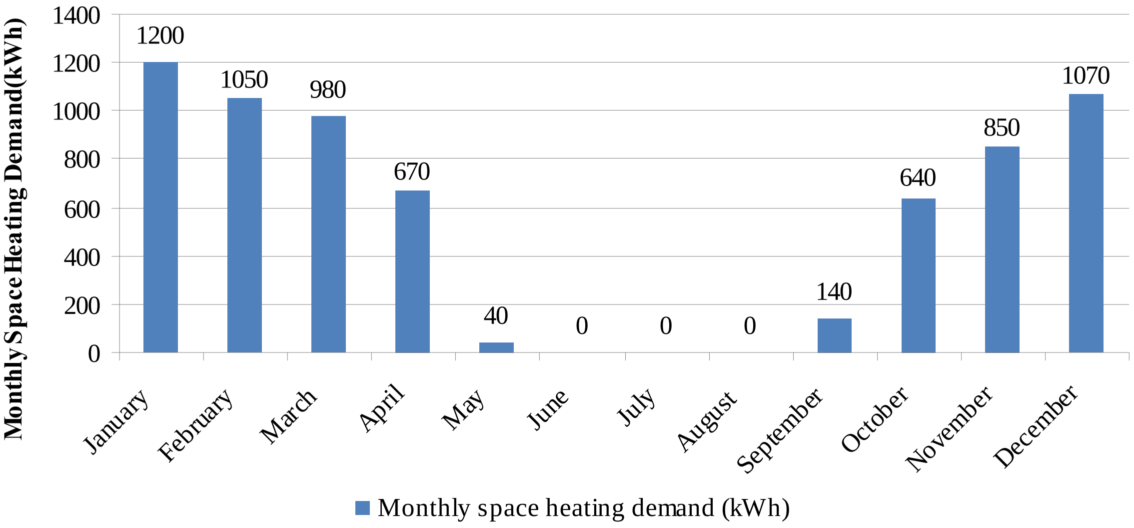

Fig. 3. Monthly space heating demand

As can be seen from Fig. 3, for the heating season from September to May, the annual space heating demand is 6640 kWh, or approximately 47 kWh/m^{2}a, when the design internal temperature is 21°C. Useful solar gains and internal gains in the low energy building shoul be calculated by a verified calculation method, accordingly they are not taken into consideration during the calculation of annual space heating demand.

3.3.2. Peak load for space heating

Total building heat loss is 2650 W, when external temperature is -22°C in Kaunas and maintained internal temperature of the rooms is 21°C. Transmission heat loss and ventilation heat loss were evaluated, when total building heat loss were calculated, according to the requirements of [12].

The balance point temperature is used in order to indicate the energy performance of a building. The balance point temperature is the outdoor temperature at which a comfortable indoor temperature can be kept without running the heating system [13]. The simulation of the internal temperatures of the building has been performed using EnergyPlus (see Fig. 4), when the heating system is not working. The simulation is performed without direct solar radiation.

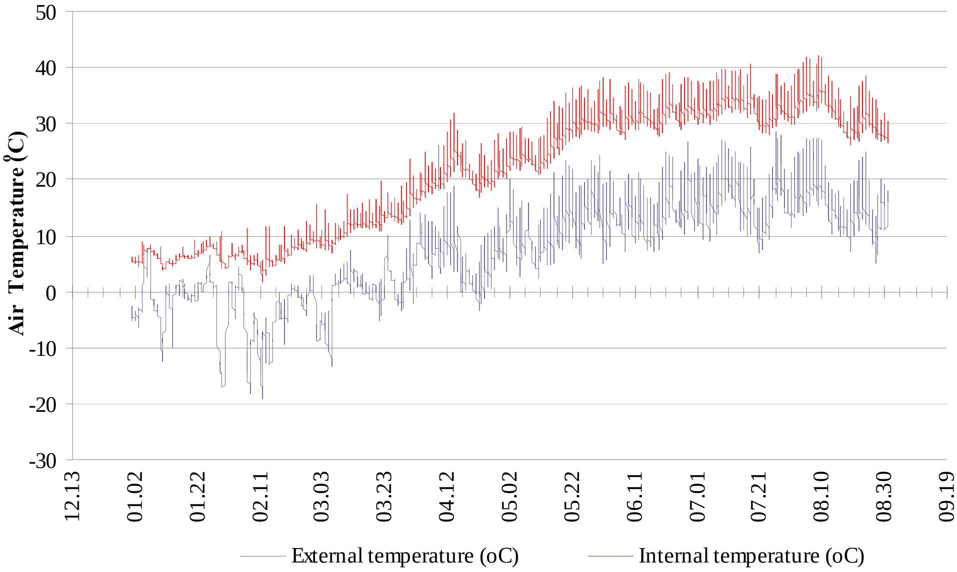

Fig. 4. The simulation of the internal temperatures of the building

According to the results of the simulations, the balance point temperature is approximately 8°C at which internal temperature of the rooms will be 20°C. As can be seen from Fig. 4, the peak loads occur in January and February, when the heat load for heating is 2650 W. Also near peak loads occur some hours in March, likely in December. From the middle of May shading devices and mechanical ventilation have to be used, in order to reduce excess temperatures.

3.3.3. Domestic hot water (DHW) demand

The net DHW heat demand is approximately 21 kWh/(m^2 a) or 2940 kWh/a for two adults and two children, who are living in a single family house [13]. The DHW temperature is set to 55ºC and the average DHW consumption per person is 40 litres per person per day. Consequently, the model single family house consumes 160 litres of domestic hot water per day [13].

3.3.4. The solutions of multi-energy systems

The required heat load for the heating of the low energy building is very low, so the particular energy source has to be selected, although renewable energy sources have to be used, when there are such low loads. Therefore, the possibility to integrate the thermal solar energy system is shown in this case study.

In order to assure the required air quality, a balanced mechanical ventilation system with heat recovery is chosen in the both introduced solutions (see Fig. 5).

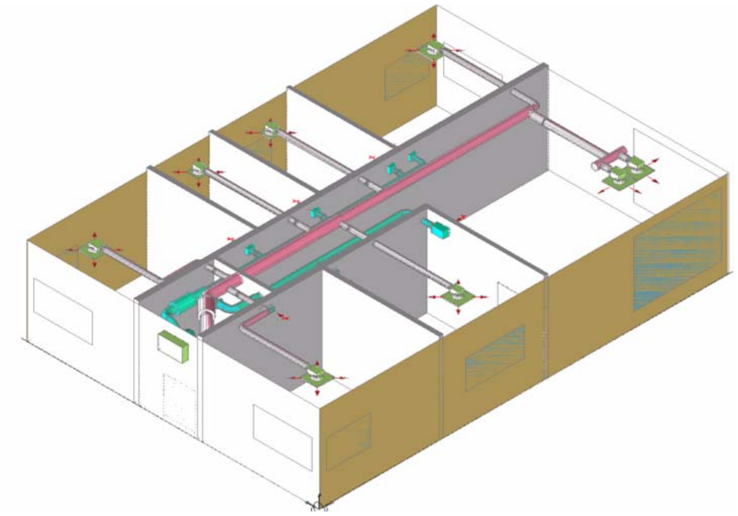

Fig. 5. Designed mechanical ventilation system of the low energy building

The multi-energy systems are foreseen in the low energy building, in order to maintain heating, ventilation and preparation of domestic hot water.

3.3.4.1. *Compact ventilation and heating device with integrated exhaust air heat pump (CVHD) and thermal solar system*

One of the solutions of the multi-energy systems can be a compact ventilation and heating device with integrated exhaust air heat pump (CVHD) and thermal solar system, shown in Fig. 6.

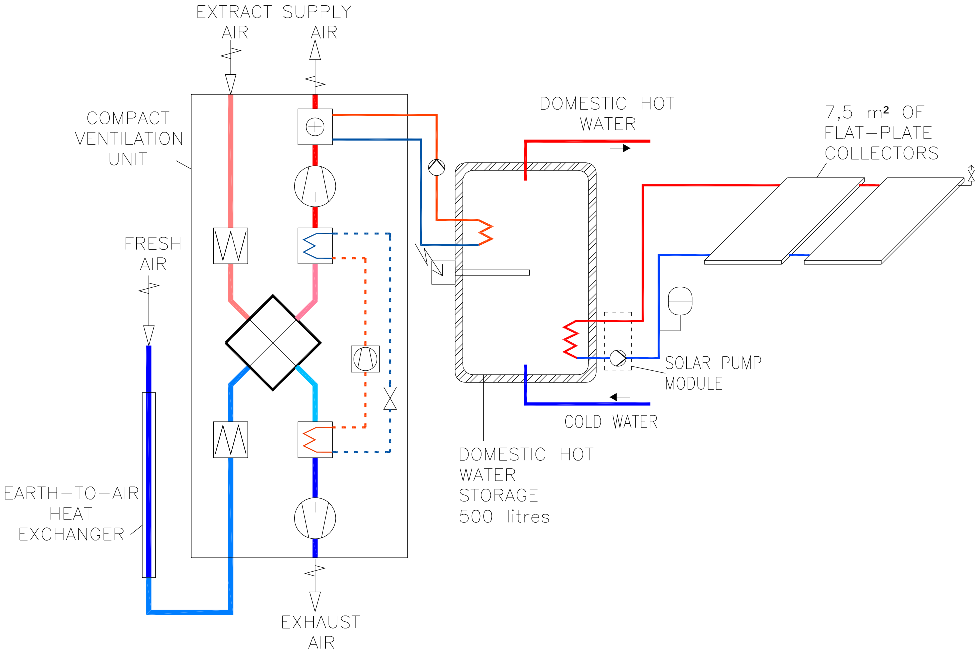

Fig. 6. Compact ventilation and heating device with integrated exhaust air heat pump (CVHD) and thermal solar system

The air is supplied with an air-to-air heat exchanger, which has a heat recovery efficiency of 85%, according to the pruducer. The ventilation rate is 0.5 h^{-1} or the amount of supplied and exhaust air is 410 m^3/h. Additional heat for supply air is distributed by a waterborne heating battery with a capacity of 3.55 kW (25 W/m^2). The maximum supply air temperature is 41°C, when the design external temperature is -22°C. The remnant heat in the exhaust air after the air-to-air heat exchanger does not yield very much heat. However, when there are no peak loads, the heat demand is very low, that it can be realised almost completely by the remnant exhaust air enthalpy. This discovery was published in 1995 by Wolfgang Feist [14]. Also, earth warming tubes (200 mm diameter, 40 m long at a depth of 1.5 m) is buried in the soil to act as earth-to-air heat exchanger and pre-heat the fresh air for the ventilation system. Compact ventilation and heating device with integrated exhaust air heat pump has the posibility to connect thermal solar system. Therefore, 7,5 m^2 of flat-plate solar collectors are foreseen at an angle of 30° and a storage tank of 500 l is assumed according to the results of sensivity analysis to key solar active parameters, performed by [13]. The electric heating element is integrated in the storage tank, when peak loads occur. The solar collector area is assumed for achieving 100% coverage of the heat demand during summer.

3.3.4.2. Outdoor air - water heat pump with thermal solar system

The second solution of the multi-energy systems can be an outdoor air - water heat pump with thermal solar system, shown in Fig. 7.

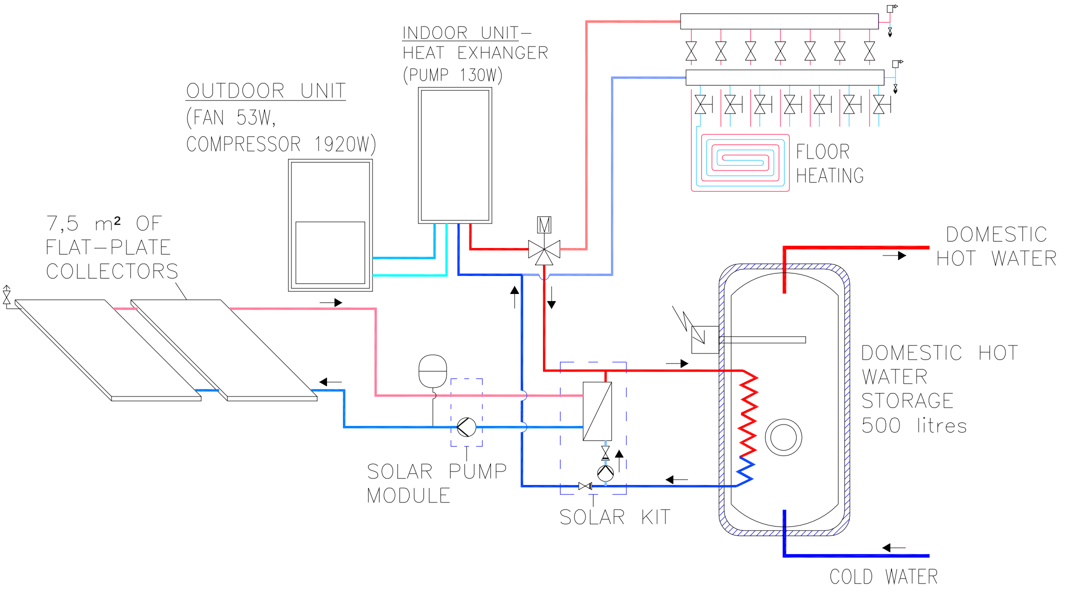

Fig. 7. Outdoor air - water heat pump with thermal solar system

In this case, the outdoor air-water based combi plant supplies heat to domestic hot water preparation and space heating. The heat is distributed in the building by a low temperature heat distribution system (underfloor heating). The heat pump heats the water from 45°C to 85°C according to producer. As heating demand in the low energy building is low, the heat pump achieves high coefficient of performance (COP) and also covers a maximum share of hot water needs, when the outdoor temperature is higher than -10°C according to the technical data of producer. The heat pump has the posibility to connect thermal solar system. Therefore, 7.5 m^2 of flat-plate solar collector are foreseen at an angle of 30° and a storage tank of 500 l is assumed. The electric heating element is integrated in the storage tank, when peak loads occur. The solar collector area is assumed for achieving 100% coverage of the heat demand during summer. In order to ensure indoor air quality, mechanical ventilation system with heat recovery (85%) and electrical heating battery (880 W) are foreseen.

3.3.5. Energy demand

These two alternatives described above can be compared according to the energy consumption. The required energy demand includes space heating, domestic hot water demand and electricity for mechanical systems (fans, pumps, compressors). Household electricity is excluded. The energy consumption results are shown in Fig. 8.

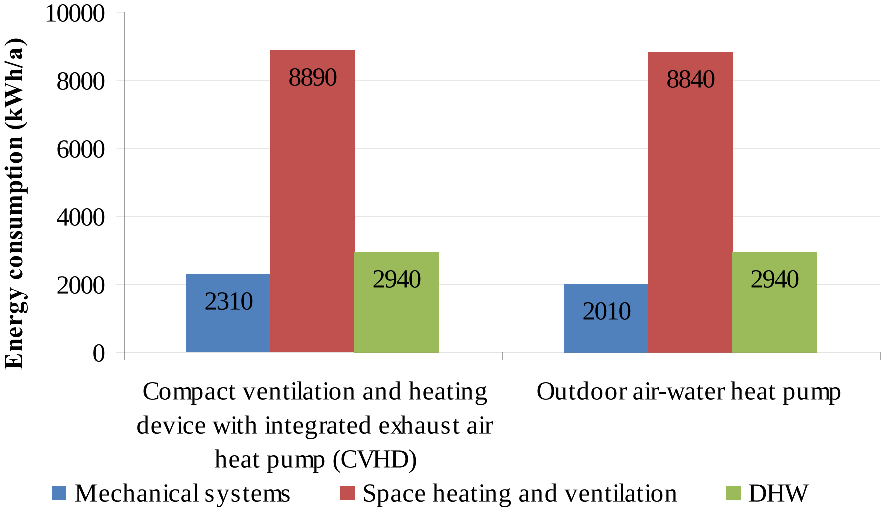

Fig. 8. Total energy consumption of two proposed solutions

As can be seen from Fig. 8, the energy consumption of these two multi-energy systems is similar. However, the useful collector output and the remaining auxiliary demand, needed to cover the DHW and space heating demands, have to be evaluated. More comprehensive studies have to be performed during the evaluation of the total energy use of the multi-energy systems [15].

4. CONCLUSIONS

1. The case study of the low energy building has shown that well-insulated and air-tight construction of the building envelope are the crucial factors for achieving low energy demands, i. e. the peak load for space heating is only 2650 W.
2. Air-tight construction of the low energy building requires to keep a good air quality in the rooms, therefore the balanced ventilation system with heat recovery is esential in both proposed solutions of multi-energy systems.
3. The introduced solutions of multi-energy systems can be implemented only in the low energy buildings, which have low energy demands. Otherwise, these systems will be insufficient and do not maintain the required thermal comfort in the rooms. Therefore, better insulated buildings have to be designed than that required according to current building standards, in order to implement Renewable Energy Strategy.
4. The annual space and domestic water heating demand is low (11830 kWh/a for solution with CVHD and 11780 kWh/a for solution with outdoor air – water heat pump), the capital investment in the heating system has to be kept small. Therefore, the solution with CVHD is more favourable, because the initial investments for installation of the current system will be lower.

5. ABBREVIATIONS

HVAC – Heating, Ventilation and Air Conditioning

LTU IWEC – International Weather of Lithuania for Energy Calculations
DHW – Domestic Hot Water
CVHD – Compact ventilation and heating device with integrated exhaust air heat pump

REFERENCES

1. *Intelligent Energy Project report.* The beauty of efficiency: European Commission, 2008. Link to the internet <http://ec.europa.eu/energy/intelligent/library/doc/ka_reports/buildings08_en.pdf>.
2. *Energy Performance of Buildings Directive.* European Commission, 2010. Link to the internet <http://www.euractiv.com/en/energy-efficiency/energy-performance-buildings-directive/article-187130>.
3. CHLELA, F., HUSAUNNDEE, A., INARD, C., RIEDERER, P. A new methodology for the design of low energy buildings. *Energy and Buildings*, 2009, Vol. 41, p. 982–990.
4. CRAWLEY, D. EnergyPlus: creating a new-generation building energy simulation program. *Energy and Buildings*, 2001, Vol. 33, p. 319–331.
5. CRAWLEY, D., HAND, J., KUMMERT, M., GRIFFITH, B. Contrasting the capabilities of building performance simulation programs. NINTH INTERNATIONAL IBPSA CONFERENCE. Montréal, Canada. 2005 August 15–18.
6. *IDA Indoor Climate and Energy software home page.* Link to the internet <http://www.equa.se/eng.ice.html>.
7. *A handbook for planning of passive and low energy buildings.* Energy effective housing for the future: Sintef Energiforskning AS, 2006. Link to the internet <http://www.lavenergiboliger.no/hb/lavenergi.nsf/frmwebPublikasjoner?ReadForm>.
8. *DEROB-LTH software home page*. Link to the internet <http://www.ebd.lth.se/english/software/derob-lth/>.
9. RSN 156-94 Building Climatology.
10. *Data of Lithuanian Science and Studies Foundation program.* Solar and other renewable energy sources for agriculture. Link to the internet <http://msi.lms.lt/publish/straipsn/pop_saule1.html>.
11. prNS 3700:2009 Criteria for low energy and passive houses – Residential buildings.
12. STR 2.09.04:2008 Capacity of building heating system. Heat demand for space heating.
13. HASTINGS, S. Robert; WALL, Maria. *Sustainable Solar Housing. Volume 1 – Strategies and Solutions.* London: Earthscan, 2007. 292 p. ISBN-13: 978-1-84407-325-2.
14. Passive House Institute home page. Link to the internet <http://www.passivhaustagung.de/Passive_House_E/compact_system_passive_house.htm>.
15. FABRIZIO, E., CORRADO, V., FILIPPI, M. A model to design and optimize multi-energy systems in buildings at the design concept stage. *Renewable Energy*, 2010, Vol. 35, p. 644–655.
16. *Weather Data Sources*. International Weather for Energy Calculations (IWEC). Link to the internet <http://apps1.eere.energy.gov/buildings/energyplus/weatherdata_sources.cfm#IWEC>.

ENERGY EFFICIENT BUILDING MANAGEMENT SYSTEM DEVELOPMENT FOR HEATING, VENTILATION AND AIR CONDITIONING EQUIPMENT IN BUILDING

Andris Krūmiņš*, E. Dzelzītis, R. Belinskis, M. Baduns, N. Bogdanovs
Riga Technical University, Latvia
Institute of Heat, Gas and Water technology,
Riga Technical University
Āzenes 16-20, LV 1010, Rīga – Latvia
Phone: +371 29178589
Email: andrisk@lafivents.lv

ABSTRACT

This paper describes energy efficient building management system development for heating, ventilation and air conditioning equipment in buildings. Building management system has survived three development stages: a) decrease of necessary labour amount; b) decrease of necessary time for fault diagnostics and maintenance; c) energy efficiency. A lot of objects in Latvia are built with building management system (BMS), but just few of them correspond to all requirements. Very important is BMS user interface for effective control of units, which includes control parameters (on/off, time schedules, setpoints), regulation parameters (PID regulators coefficients, min / max values), trendlogs and event messages.

We have done research in three objects in Latvia, two of them are trading centres (located in Riga and Madona); one object is office building (located in Riga).

Our experience in office building in Riga showed, that corresponding usage of BMS functions (time schedules, energy management) is very important for building owner. From year 2007–2008 BMS was used to achieve very good comfort in premises without caring about energy consumption and unit working hours. After economical crises in Latvia (middle of 2008), office-building owner invite us to help limit energy consumption, but still required good comfort conditions in office building during of working hours. We made corrections to time schedules, heating and cooling systems control algorithms (BMS is done with Alerton controllers). Energy consumption analyse (2007–2009) showed, that energy consumption after all improvements in BMS can be decreased by 20%.

Results of our investigations are definition of all necessary BMS functions and unit control algorithms. Paper results can be used for installation of new BMS in office and trading centre buildings. According to our investigation results, we made appropriate BMS for Madona trading centre.

Keywords: building management system, energy efficiency, control algorithms

1. CONTROL SYSTEM ANALYSE OF SHOPPING CENTRE IN RIGA

Our experience in Shopping centre in Riga showed, that BMS work efficiency depends not only from controllers producer (Trend control systems), but from installation company and programmers work quality. We were invited to analyse reasons of high temperature in premises during a winter (more than 23 degrees Celsius) and high-energy consumption (more than in another similar shops). Our investigation showed, that BMS did not corresponds to any above mentioned requirement of good control systems.

Our investigation showed, that existing BMS has several serious problems:

- inadequate ventilation equipment adjustment (not correct time schedules, no supply air volume regulation);
- an incorrect algorithm for calculating supply air temperature;
- insufficient air-handling equipment control parameters from BMS visualisation software;
- not correct heating centre regulation according to outside air temperature;
- mistakes in indoor and outdoor lighting control. Lighting control was turned to "HAND" regime and was controled from security.

Due to Trend dealer inability to fix all mistakes, we made replacement of existing control system to DEOS controllers and software.

These systems where connected to DEOS control system:

a) two air handling units (AHU1 and AHU2);
b) heating centre with four heating circuits (for radiators, air curtains, ventilation and hot water);
c) lighting control (3 groups of indoor premises lighting, 9 groups of outdoor lighting).

Table 1. The main parameters of air handling units

Description	**AHU I**	**AHU II**
Electrical power of supply / exhaust fans, kW	4/2.2	15/11
Total pressure supply / exhaust fans, Pa	784/646	1005/588
Air flow of supply / exhaust fans, m^3/h	6360/4560	25500/23000
Temperature efficiency of heat exchanger	61.1%	42.7%
Nominal heating power of water heating coil, kW	41.4	53.4

We used energy efficient and tested algorithms for control of air handling units, heating centre and lighting [2], [3], [5]. The main goals for savings was:

a) CO_2 detector installation in air handling units exhaust air ducts. Air volume of air handling units was calculated according to CO_2 level un premises. Setpoint of CO_2 was 650 ppm. Minimal speed of supply and exhaust fans was determined as 30 Hz;
b) cascade temperature regulation of air handling units. Air handling units supply air temperature was calculated according to room temperature. Minimum supply air temperature was determined as 15^oC;
c) air handling units work according to time schedules, synchronized with shop working time;
d) finding of correct heating curves for each heating circuit with temperature decrease during a night;
e) indoor lighting control according to time schedule, synchronized with shop working time. Time of BMS is synchronized with internet time;
f) outdoor lighting control according to outside light detector measurements. Each group is turned on by individual setpoint of light level. Each group has time schedule, which gives opportunity to turn on light just in shopp working time or during a night.

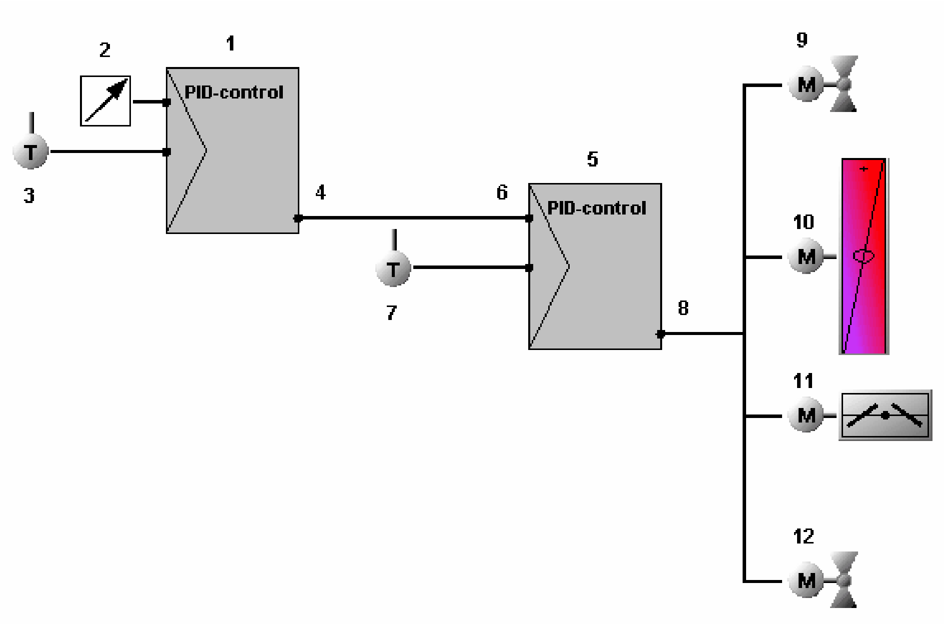

Fig. 1. Cascade regulation of air handling unit

Used abbreviations in Fig. 1. 1 – exhaust air temperature controller; 2 – exhaust air temperature setpoint device; 3 – exhaust air temperature sensor; 4 – controller output signal; 5 – supply air temperature control; 6 – supply air temperature setpoint; 7 – supply air temperature sensor; 8 – controller output signal; 9 – heating valve; 10 – heat recovery; 11 – mixed air dumper; 12 – cooling valve.

BMS visualisation software gives all information about air handling unit sections and operation data.

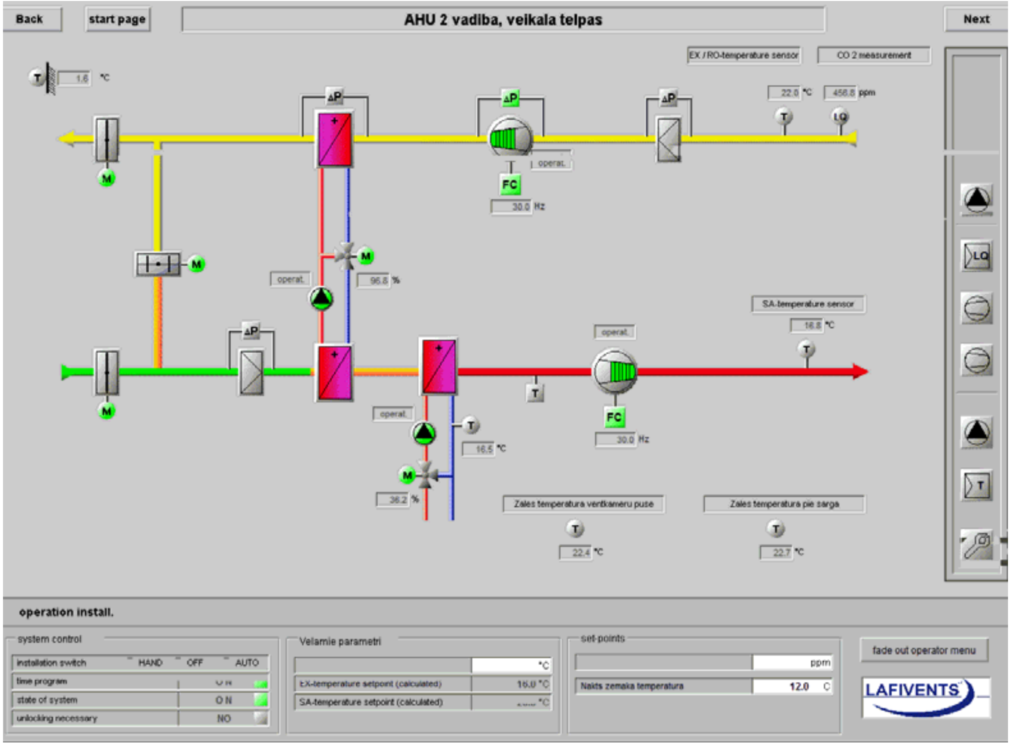

operation install.

system control

installation switch HAND OFF AUTO
time program ON
state of system ON
unlocking necessary NO

Velamie parametri

°C
EX-temperature setpoint (calculated) 16.0 °C
SA-temperature setpoint (calculated) [illegible] °C

set-points

ppm
Nakts zemaka temperatura 12.0 C

Fig. 2. Air handling unit control from BMS software

1.1. Energy consumption analyse

Replacement of existing control system to DEOS controllers with energy efficient algorithms was connected with our confidence about energy savings potential. Possible energy savings were calculated with Matlab and Simulink software [4], with A. Krumins developed simulation software, described in [1]. Before control system replacement we got data of consumed electrical and gas energy for each month. Our aim was to reduce energy consumption by 20%.

Control system was replaced in August 2009.

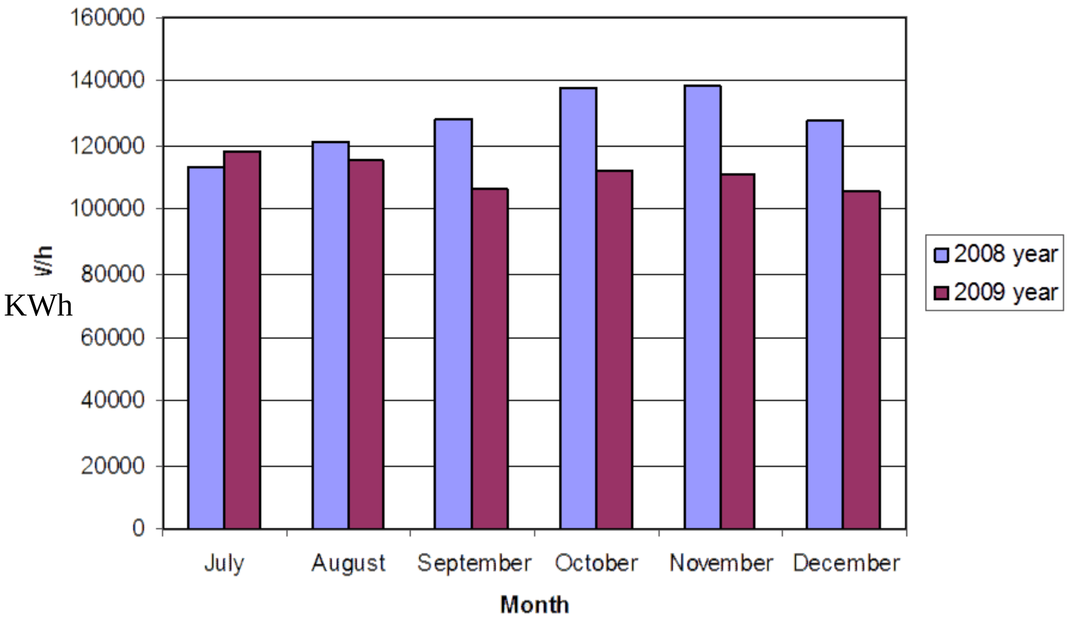

Fig. 3. Electrical energy consumption comparing in years 2008–2009

Fig. 3 shows that, the new control system allows to reduce electrical energy consumption by 16%. The main energy saving is achieved with decrease of air volume exchange in shops and correct lighting control.

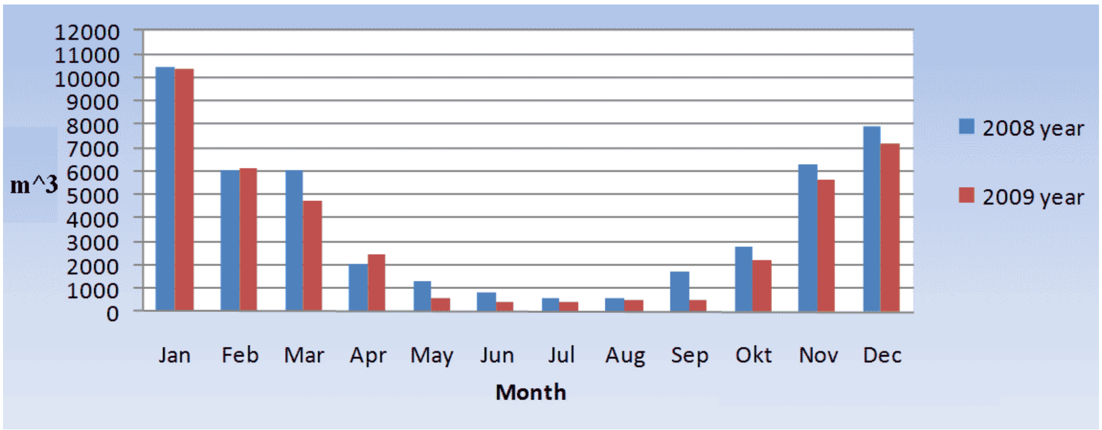

Fig. 4. Gas consumption comparing in years 2008–2009

Fig, 4 shows that, the new control system allows to reduce gas consumption by 17%. The main energy saving is achieved with decrease of air volume exchange in shops, cascade temperature control (during a day shop is heated by lights, which allows to decrease supply air temperature) and correct heating curves for heating centre.

Table 2. Energy consumption from August till end of December in years 2008–2009

Energy consumption	2008	2009
Electrical energy consumption, kWh	653793	550104
Gas consumption, m^3	19271	16008

Electrical energy price per kWh in 2009 is 0.071 Ls/kWh, price for gas is 0.25 Ls/ m^3. Total saving at the end of 2009 was about 8000 Ls. Installation cost of DEOS control system was 8325 Ls with VAT. We can see that payback time was 5 months.

2. CONTROL SYSTEM ANALYSE OF OFFICE BUILDING IN RIGA

Building management system controls and supervises:

- 5 air handling units;
- three chillers;
- heating centre;
- 2 gas boilers ;
- climate control of 61 rooms (control of room temperature);
- control of lighting.

Building management system was started in 2007. Building management system had correct control algorithms for climate control and HVAC units control. BMS installator company instructed about all possibilities of algorithms to building owner service department. Unfortunately service department was more concerned about stable climate in premises rather than energy economy. Such functions as time schedules, temperature decrease during a night, where not used. At the end of 2008 there were a change of home owner and we were invited to help new home owner to run building more efficiency.

Investigation of current setpoints, unit working hours and temperatures of premises during a night and day was done by trendlogs.

Trendlogs were used to find out possibility to decrease temperature during a night in premises. It was neccessary to find out room climate preperation time, because we had to save energy without influence on comfort.

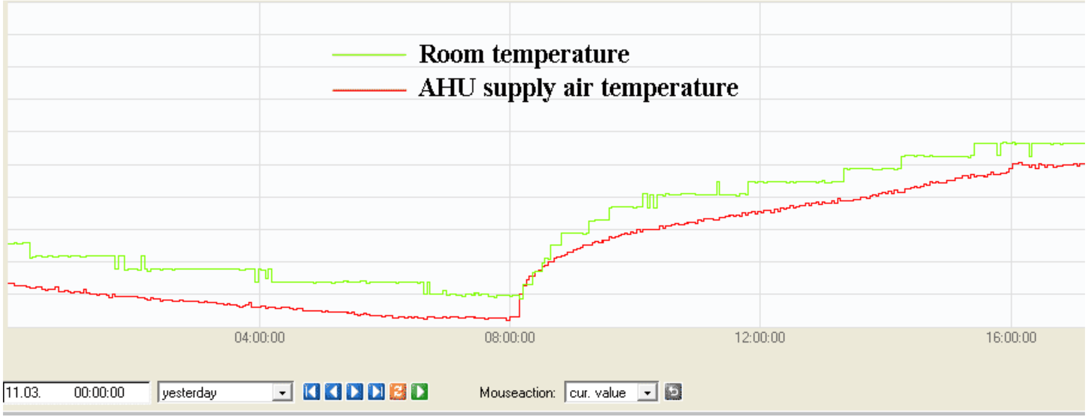

Fig. 5. Trendlogs

2.1. Energy consumption analyse

After analyse of trendlogs, several energy efficient steps were done:

1) time schedules corrections for air handling unit operation;
2) temperature decrease of rooms during a night;
3) cooling system deactivation during a night;
4) optimal startup of room climate systems (radiators, fancoils);
5) correction of lighting control time schedules and light level setpoints.

Energy savings was achieved starting from year 2009.

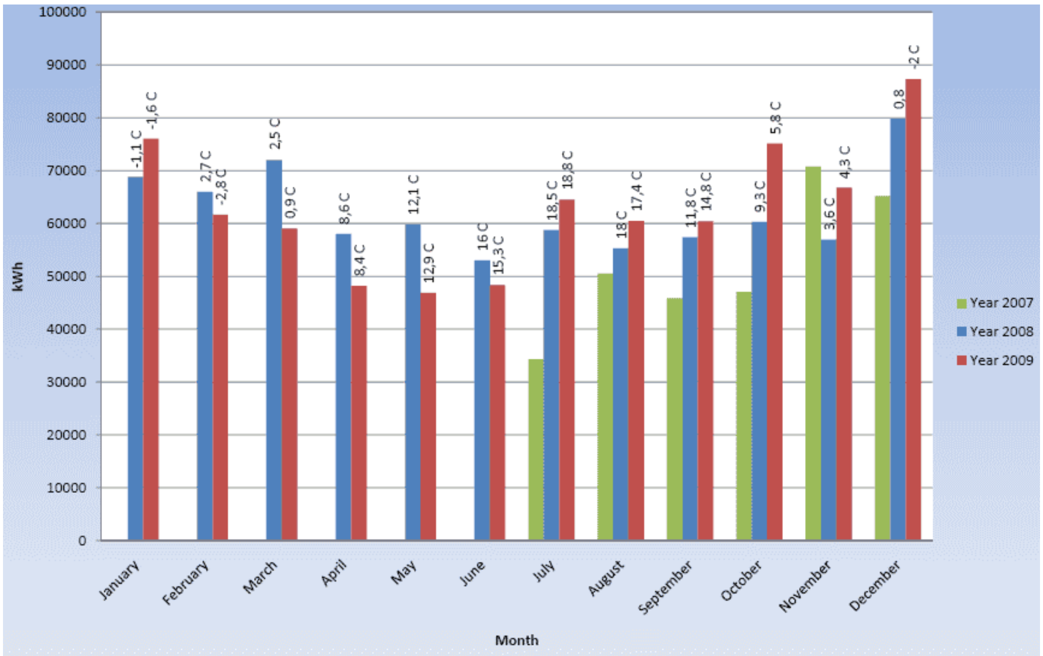

Fig. 6. Consumption of electrical energy

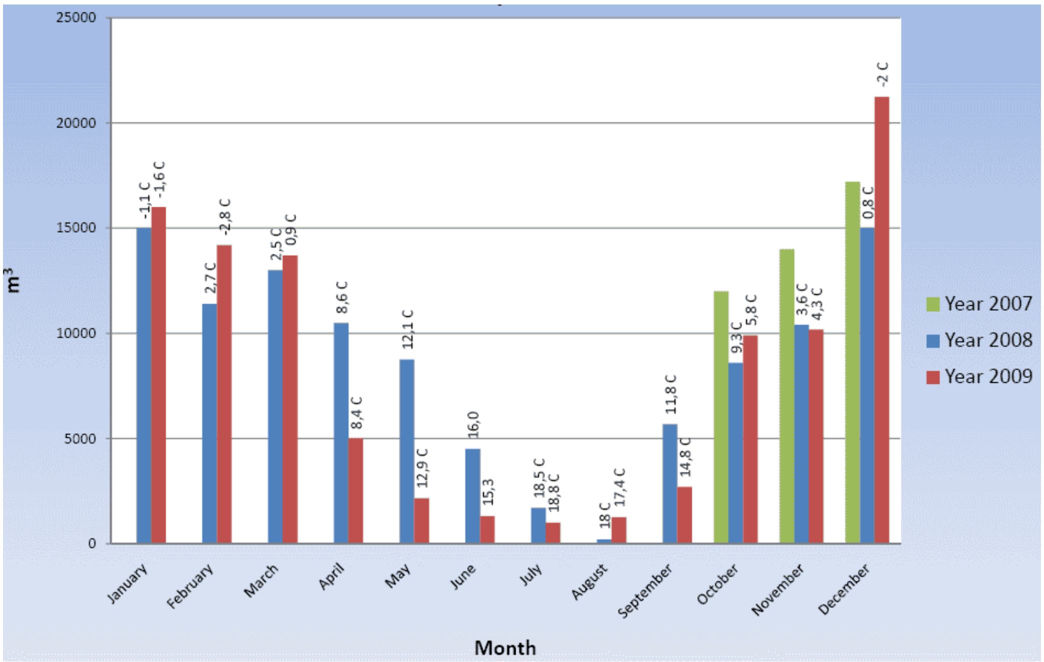

Fig. 7. Consumption of gas

Fig. 6 and Fig. 7 show electrial energy and gas consumption in years 2007–2009. Building was fully occupied at the end of 2007. In July of 2009 additional building was completed and that we can see also in energy consumption figures.

It is possible just to compare energy consumption in period from February till end of June in years 2008–2009.

Table 3. Energy consumption from February till end of June in years 2008–2009

Energy consumption	2008	2009
Electrical energy consumption, kWh	308838	264097
Gas consumption, m^3	41150	36377

Results shows, that BMS can be used as energy saving tool. Electrical energy consumption is decreased by 14%, gas consumption is decreased by 12%. Total saving at the end of 2009 was about 4300 Ls.

3. DEVELOPMENT OF APPROPRIATE BUILDING MANAGEMENT SYSTEM

Our investigation shows, that results of Building management system working efficiency depends from installator proffessional working skills, used control algorithms for HVAC systems, and friendly user interface. Usually local personal is responsible for energy savings, and they shall understand all functions of BMS.

This main idea was implemented in development of BMS for Madona trading centre.

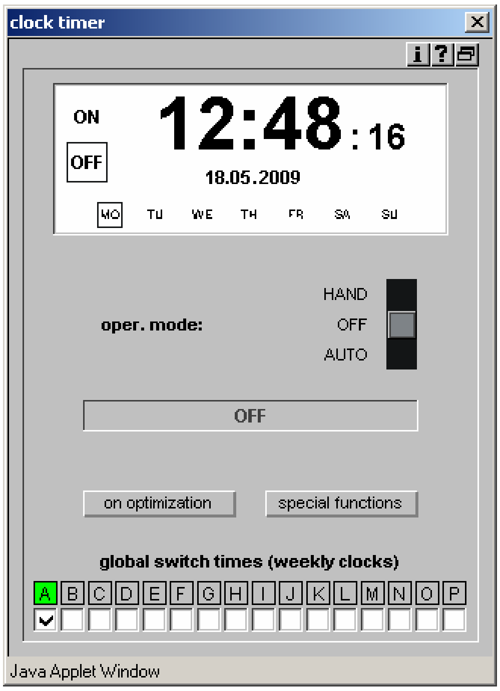

Fig. 8. Time Schedule

Each BMS function has help button "?". For example, pressing this button for time schedule function, user can get all necessary information about all regimes, for example, what means "Hand", "Off", "Auto". We made very high attention to used algorithms and their possibilites to save energy consumption without changes in comfort. We worked together with local personal and tried to explain all functions and possibilities of BMS.

BMS supervision software has additional functions as "Event server". In case of alarm, inadequates temperatures or other parameters, alarm message is transferred to mobile phones as SMS and e-mails. This function allows to decrease problem solving time and also saves energy.

4. DISCUSSION

Installation, programming and maintenance of BMS are complex job. Usually in Latvia a lot of local companies are using different BMS controllers and software. It means that after BMS installation home user can ask for service just from this company. If home user wants to ask help from other companies, then mainly it is not possible, because other companies are not familiar with existing BMS and functions.

5. CONCLUSIONS

Necessary BMS functions, control algorithms, communication protocols shall be described in one common regulation. In Latvia there is no such norm, and that is in favour of BMS Installation Company, not homeowner. We think, that next job is to make regulation for all necessary BMS functions, control algorithms, visualisation software capabilities, and energy saving functions. Our experience show, that BMS can save up to 17% of consumed energy without changes in mechanical system.

REFERENCES

1. A. Krumins, Optimization of the control of ventilation systems, doctoral thesis, Riga, 2008. – 113 p.
2. R. Carlson, Understanding Building Automation Systems: Direct Digital Control, Energy Management, Life Safety, Security Access Control, Lighting, Building Management Programs, Kingston MA: R.S. Means Co., 1991.
3. J. Levenhagen, HVAC Controls and Systems, New York: McGraw-Hill, 1993.
4. MATLAB, SIMULINK, The MathWorks, Inc., 2007.
5. Recknagel E. Taschenbuch für heizung und klimatechnik einschliesslich warmwasser – und kältetechnik. – München: Oldenbourg, 2004. – 2036 p.

BUILDING ENERGY CONSUMPTION FOLLOWING ENERGY CERTIFICATE *VIS A VIS* OF REAL ENERGY CONSUMPTION DATA

R. Mikučionienė, V. Martinaitis
Vilnius Gediminas technical university
Saulėtekio av. 11, LT-10223 Vilnius – Lithuania
Phone: (+370 5) 2744718
Email: ruta.kausylaite@vgtu.lt

ABSTRACT

The purpose of the Energy Performance of Buildings directive implementation in EU was to reduce the energy consumption in building sector and make it more efficient. The calculated energy consumption was chosen as an indicator of energy performance certification for implementation of the Energy Performance of Buildings directive in Lithuania. The calculated energy consumption and real energy consumption of few buildings was compared. The calculated energy consumption was evaluated by the Lithuanian norm STR 2.01.09:2005 „Building Energy performance. Certificate of energy performance“. The real energy consumption was recalculated to normal year. The average of two years of the real energy consumption was taken into account for comparison. Old administrative and residential buildings were analyzed. All objects were partially renovated. The difference of results and the reasons for it are presented in the article. The building energy consumption following energy certificate is only theoretical value, which depends on building envelope, but not on engineering systems. The main reasons of different results are: insufficient evaluation of engineering systems and ineffective building energy management systems.

Keywords: energy certification, energy rating, building, energy consumption

1. INTRODUCTION

Energy consumption in buildings was one of the concerns in Europe 20 years ago, and still the energy performance in the building sector is a sore point today. The Energy Performance of Buildings directive 2002/91/EC (Directive) [1] was implemented to reduce energy consumption and to increase efficiency of energy usage in the building sector. One of the Directives objectives was the building energy performance certificate (building certificate).

Lithuania started the life as an independent country 20 years ago. All regulations and norms were yet to be created. Started from scratch, the regulations were new and innovative. The regulations of district heating stated, that heat meters should be installed in every segment of the heat supply chain [2]. Since district heating supplies heat for 63% of the buildings in the cities of Lithuania, today there are heat meters in most of the buildings across the country, and it is possible to evaluate real heat consumption in each building.

It is noted in the Directive, that certificate should be calculated according to the technique based on “the amount of energy actually consumed or estimated to meet the different needs associated with a standardized use of the building, which may include, *inter alia*, heating, hot water heating, cooling, ventilation and lighting.” [1]. Therefore, each country can choose to evaluate actual or estimated energy consumption. In the European standard EN 15217:2005 “Energy performance of buildings – Methods for expressing energy performance and for energy certification of buildings” [3] these methods are described as operational rating (OR) (rating based on energy use) and asset rating (AR) (rating based on calculations of the energy used). The terms operational rating and asset rating are used, as it is described in [3].

In this paper the methods of energy certification for buildings are analysed, and results of energy performance certificates of few administrative and residential buildings in Lithuania are presented. The calculated energy consumption and real energy consumption of these buildings were compared.

2. ENERGY RATINGS

In 2005 European countries chose the rating methods for certification in order to implement the Directive. Some countries chose the asset rating (AR) (Lithuania was among them) some chose the operational rating (OR). The certificate can be based on either the operational or the asset rating. Both methods have their advantages and disadvantages.

An asset rating highlights the intrinsic potential of the building while a measured rating makes it possible to take into account the impact of building management:

- For new buildings OR is not available, so AR based on design data is the only way to rate. The same problem is for certification of the project (not build yet), so the AR should be used;
- OR certificate will no longer be valid after a change of building occupant or a change of the style of building management, but the AR does not include these indicators at all;
- AR does not depend on actual weather and indoor conditions [4], [5].

Countries which had older energy efficiency policy history chose the operational rating (OR) as the main rating and AR for new buildings only. Among these are Belgium, Germany, France, Ireland, Sweden, United Kingdom [6]. In those countries, where both ratings (AR and OR) are available or required, the energy certificate should have two columns [3]. In accordance with recommendations [3], building energy certification scheme for existing buildings should be implemented by the use of operational rating (OR).

3. CERTIFICATION RESULTS VIS A VIS OF REAL ENERGY CONSUMPTION IN LITHUANIA

Lithuania has chosen the asset rating, and the Lithuanian norm STR 2.01.09:2005 „Building Energy performance. Certificate of energy performance“[7] was created accordingly. Four buildings with different purpose were chosen for the calculation: two administrative and two residential buildings. The calculated energy consumption or AR was evaluated by the Lithuanian norm for certification STR 2.01.09:2005 [7], using the software for certification “NRG-sert”. According to this norm, the delivered energy for heating, preparation of domestic hot water and electricity was taken into account. The parameters used for asset rating and described in [7] are:

- indoor temperature for all types of the buildings analyzed in the paper is 20°C;
- mean outdoor temperature of the heating season is 0,6°C;
- duration of heating season – 220 days.

The real heat consumption, alias OR, was recalculated to normal year [8] using the method of degree-days. The OR was evaluated by metered real consumption of 2 years. The period of meters was 1 month. The consumption of heat for hot water preparation was evaluated by the consumption of hot water in cubic meters and multiplied by norm 0.051 MWh for 1 m^3 hot water preparation [9]. The recalculation to normal year was done using normal and real indoor temperature equal 18°C.

By evaluating the real consumption, the delivered energy for heating, preparation of domestic hot water and electricity was summed in order to compare it with the AR. The average of two years of real energy consumption was taken into account.

All objects were built before 1992 and at the time of evaluation, had been partially renovated. The characteristics of buildings are below:

- automatic regulation, dependent on outdoor temperature had been installed in all substations for heat preparation of buildings;
- new tight windows (Heat transfer coefficient U=1.7 W/m^{2}K) and doors had been installed;
- all other part of the envelope had typical heat transfer coefficients for buildings built before 1992;
- ventilation system was natural only;
- heating system was without regulation.

This section represents the results of both OR and AR calculations for administrative and residential buildings.

3.1. Results of administrative building

Two administrative buildings where analyzed, and results of OR and AR calculations are presented in Fig. 1.

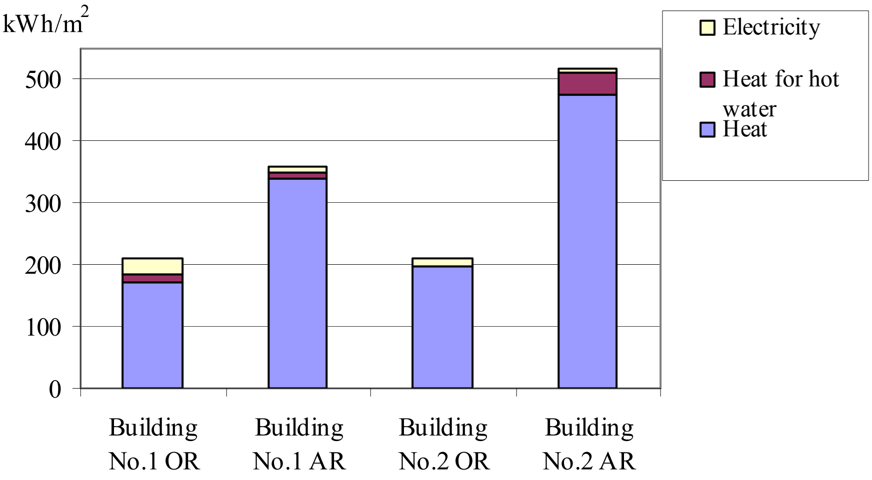

Fig. 1. Comparison of OR (operational rating) and AR (asset rating) of administrative buildings

In administrative building No 1, the sum of delivered energy for AR is approximately 40% higher than the sum for OR. The amounts of heat between the AR and OR differ twice. The value of heat for hot water has the smallest effect for the difference, and the actual electricity consumption is 3 times higher than that, evaluated for AR.

Analyzing the results of the building No 2, the sum of delivered energy for AR is 250% higher than the sum for OR. The main reason of the difference is the difference between amounts of heat, same as for the building No 1. Hot water in this (No 2) building is prepared using electricity and in the OR is evaluated together with the amount of electricity. That is the reason why the value of the real electricity consumption is higher then in AR.

3.2. Results of residential building

Two residential buildings where analyzed, and results of OR and AR calculations are presented in Fig. 2.

Both residential buildings are dormitories, where habitants are students, and the bills for tenancy do not depend on consumed energy. The calculations where done by using the software “NRG-sert”. The type of the building was chosen “other residential buildings”. The same calculation where done assuming that type of the building is “hotels”. The estimated energy rate for both types of buildings was the same, so the dormitories where attributed to other residential buildings, because it is more logical.

In residential building No 3, the sum of delivered energy for AR is approximately 33% lower than that of OR. However, the evaluated amount of heat in the AR is higher by 70% than the real consumption. The values of heat used for preparation of hot water and electricity have unusual differences – the measured consumption of heat for preparation of hot water is almost 6 times higher than the evaluated, and electricity consumption is 4 times higher than the evaluated by AR. The aforementioned differences can be caused by ineffective use of hot water and electricity.

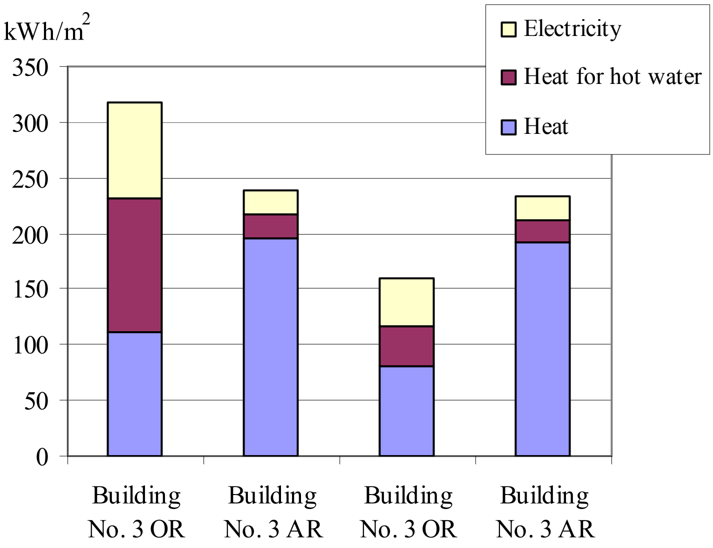

Fig. 2. Comparison of OR (operational rating) and AR (asset rating) of residential buildings

Analyzing results of building No 4, the sum of the delivered energy for AR is 30% higher than the sum for OR. The evaluated amount (AR) of heat is twice as high as the real consumption (OR), and the real consumption of heat for preparation of hot water and the consumption of electricity is twice as high than that of AR. Such difference is caused by ineffective use of hot water and electricity, as in the Building No 3.

Columns of both buildings in total look different, but tendency is the same: the real consumption of heat in both buildings (columns OR) is less than is AR columns, and electricity and heat for hot water consumptions are high than in AR columns.

3.3. Conclusions of the results

Concluding the results presented in sections 3.1 and 3.2 it is seen, that the real consumption of heat for preparation of hot water and electricity depends mostly on behavior of the inhabitants and the building management system. It is not enough to evaluate the purpose of the building, because the habitants of different buildings with the same purpose can have different awareness and knowledge about energy efficiency.

The results show, that the evaluated amount of heat following energy certificate is only theoretical value, which depends on building envelope, while the influence of engineering systems is undervalued. The simplified charts of heat balance for AR and OR are presented in Fig. 3.

It is seen that the calculated heat balance consist of heat losses through the envelope, heat losses caused by infiltration, heat gains and energy used in ventilation system. It is difficult to make the same balance for actual heat consumption, because the meter is in the heat substation only, and exact evaluation of each part of the heat balance is impossible, however, assumptions can be made, and evaluated according the reading of a meter.

In the beginning of this section it was stated, that all analyzed buildings have only natural ventilation. Therefore, the amount of heat lost through ventilation and infiltration should actually be lower, than evaluated by [7]. Another factor can be low infiltration in the building. All analyzed buildings had new tight windows, and sufficient infiltration for natural ventilation can be achieved only by opening windows (factor of inhabitant's behavior) [10]. And if windows are tightly closed all the time, the value of heat losses through the infiltration will be lower.

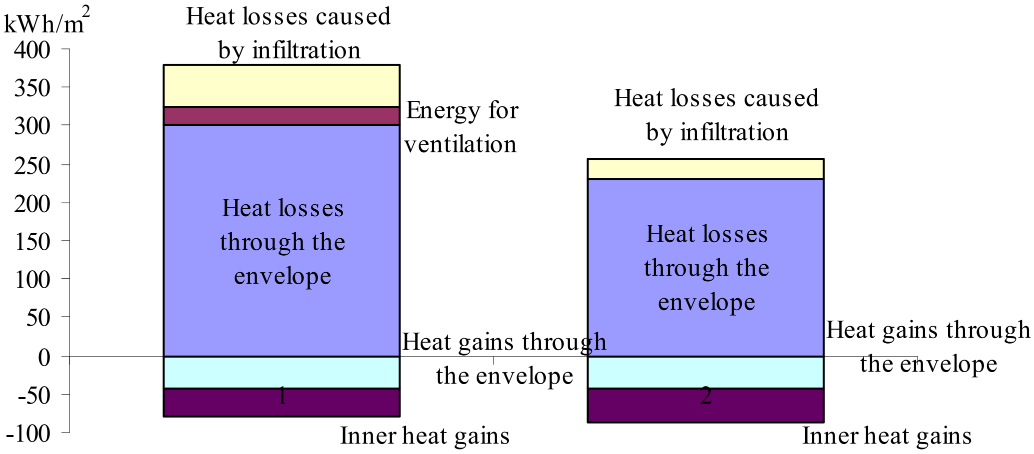

Fig. 3. Calculated (1st column) and recalculated actual (2nd column) heat balance

In case of administrative buildings, it is complicated to evaluate actual heat gains, since during office hours inner heat gains can possibly be higher.

The main difference is in heat losses through the envelope. When type of constructions is known in old buildings, it is not difficult to evaluate heat transfer coefficients with sufficient accuracy. The difference can be less than 10%. The one of the factors for difference in heat losses should be the actual indoor and outdoor temperatures. The actual heat consumption is recalculated to normal year using mean indoor temperature (18°C in this case) during heating season and monthly mean outdoor temperatures. So the actual number of degree days is not accurate. It is exceptionally complicated to evaluate mean indoor temperature in administrative buildings, where people are present for at most 60 hours per week. In case heating season lasts 200 days, disparity of 2 °C in temperatures difference will cause more than 10% disparity in the amount of degree days.

Therefore assumptions and adjustments, used for real consumption heat balance, are:

- insufficient air infiltration – heat losses caused by infiltration are twice as lower;
- inner heat gains are 20 % higher than those calculated theoretically;
- heat losses through the envelope were adjusted in order to get the heat balance. Adjustment was made with the assumptions, that actual mean indoor temperature is lower than the evaluated in degree days (difference in 13%) and the values of heat transfer coefficients of the envelope are smaller by approximately 10%.

Considering energy, the energy balance should be followed all the time, despite the procedure or technique accomplished. Assumptions and thermal rates should be adjusted to the real energy consumption of few years, in order to get the energy balance. Otherwise the calculations will not indicate the real status, and should not be trusted.

The main factors of difference in results OR vis a vis AR are: behavior of inhabitants, energy management and actual indoor and outdoor temperatures. The behavior of inhabitants and intelligent building management can effect energy consumption, because such factor as number of people and activity, regulation possibilities (thermostats), equipment usage, natural ventilation, hot water demand and etc. are strongly dependent on the occupants or manager of the building and can result energy use in large variations, even for the same climate and building type [4], [10]. It is complicated to evaluate the aforementioned factors using AR, but more precise evaluation of engineering systems and their types of regulation can make these differences smaller.

4. CONCLUSIONS

Countries which had older energy efficiency policy history had chosen the operational rating (OR) as the main rating and AR is used for new buildings only.

In Lithuania the ssset rating (AR) is used to evaluate energy performance of building. The delivered energy is evaluated and the sum of energy for heating, preparation of domestic hot water and electricity is taken into account. Such way of calculation can make evaluation of CO_2 complicated, because different kinds of energy are summed without recalculation to primary energy source.

The difference of results in comparison of AR and OR in Lithuania on the average is about 40%. The reason of this difference is that evaluation of AR does not take into account human behavior and energy management, and other thermal rates of the building are evaluated insufficiently.

Indoor and outdoor temperatures have big influence for actual energy consumption. Especially the variation of indoor temperatures can show how intelligent is the building management and regulation of energy systems. These parameters should be evaluated to certificate of the building, because it shows the quality of building in context of energy use. Thereby, looking back in recommendations [3] the operational rating should be used for energy performance of existing buildings.

REFERENCES

1. Directive 2002/91/EC of the European parliament and the Council of 16 December 2002 on the energy performance of buildings. Official Journal of the European Communities. 2003. 4.1.2003, p. 65–71.
2. Lietuvos centralizuoto šilumos tiekimo apžvalga 1990–2007. Lietuvos šilumos tiekėjų asociacija, 2007.
3. EN 15217:2005 “Energy performance of buildings – Methods for expressing energy performance and for energy certification of buildings”. European committee for standardization. 2007, p. 25.
4. PEREZ-LOMBARD, L., ORTIZ, J., GONZALEZ, R., MAESTRE, I.R. A review of benchmarking, rating and labelling concepts within the framework of building energy certification schemes. *Energy and Buildings,* 2009, No 41, p. 272–278.
5. P155 Energy performance certificates EN 15217 "Energy performance of buildings – Methods for expressing energy performance and for the energy certification of buildings". CENSE. 2009, p. 6.

6. Towards an Energy Efficient European Building Stock. An RICS Status Report on the Implementation of Directive 2002/91 on the Energy Performance of Buildings (EPBD) in the EU Member States. 2009, p. 65.
7. STR 2.01.09:2005 „Building Energy performance. Certificate of energy performance“. Vilnius: Ministry of environment of the republic of Lithuania, 2005.
8. RSN 159-94 “Building climatogoly”. Vilnius: Ministry of environment of the republic of Lithuania, 1995, p. 120.
9. Atskirų energijos ir kuro rūšių sąnaudų normatyvų būstui šildyti ir karštam vandeniui ruošti nustatymo bei taikymo metodika. Vilnius: Valstybinė kainų ir energetikos kontrolės komisija. 2007, p. 6.
10. MALIAVINA, E. G. The air exchange calculation of natural ventilation in multi-storeyed dwellings. *Energy for buildings*. Proceedings of the sixth International Conference. Vilnius: Technika, 2004, p. 464–470.

CYSENI 2010, May 27–28, Kaunas, Lithuania
ISSN 1822-7554, www.cyseni.com

OPTIMAL RENOVATION PERIODICITY OF THE SCHOOL BUILDINGS IN TERMS OF THEIR LIFE CYCLE ENERGY CONSUMPTION AND GREENHOUSE GAS EMISSIONS. CASE STUDY

L. Užšilaitytė
Vilnius Gediminas Technical University
Department of Building Energetics
Saulėtekio al. 11, LT-10223, Vilnius-40 – Lithuania
Phone: +370 674 46 983
Email: Lina.Uzsilaityte@ap.vgtu.lt

ABSTRACT

There is no strict regulation how often buildings should be renovated. Today we face situation when depreciated buildings are not renovated due to the lack of financial resources and thus keeping these buildings in a state not complying with 6 essential requirements for buildings. Decisions to renovate buildings usually are based on economical evaluations, not taking into account energy and environmental benefits of the renovation. However such approach is not sufficient from the point of view of sustainable buildings maintenance. Economical evaluations are important while choosing different alternatives of the building renovation. However estimation how often and to what extent building should be renovated based only on economical evaluations is not sufficient. Energy and environmental components become relevant to be included into these evaluations. Goal of this study is to estimate optimal renovation periodicity of the two school buildings in terms of their life cycle energy consumption and greenhouse gas emissions. Results of the study showed that the most reasonable renovation periodicity of the buildings under consideration is 12–24 years depending on the initial energy performance of the building.

Keywords: energy efficiency, building renovation, life cycle analysis, greenhouse gas emissions

1. INTRODUCTION

Inefficient use of energy is a topical issue which is encountered all over the world. Need to reduce energy consumption is induced by number of reasons. Scarce energy resources and increased energy dependency forces to look for the alternative energy sources and limit energy consumption. European Union is dependent on external energy suppliers [1]. In Lithuania this problem is even more relevant as approximately 90 % of primary energy is imported and almost all this energy is imported from one country. Stabilisation of climate change is very limited without stabilising energy consumption. Actions in energy efficiency field solve not just climate change problems, but also help to ensure security of supply and decrease energy dependency [1].

While seeking to increase energy efficiency, European Union set a goal to save 20 % of energy and reduce greenhouse gas emissions by 20 % by 2020 [2]. The last challenge of the European Union is to start building nearly zero energy buildings since 2020.

In Lithuania as well as in the whole world 40 % of final energy is consumed in buildings [3, 4]. In European Union buildings contribute 36 % of greenhouse gas emissions [5]. The growth rate of new buildings added to the housing stock is currently estimated at around 1–1.5%, the number of buildings removed from the stock is about 0.2–0.5 %, and the number of refurbishments accounts roughly 2% of the housing stock a year [5]. In Lithuania statistics of construction of new buildings is similar; however increase of energy consumption is higher than increase of the new building area [4]. These numbers show that it is important to pay more attention to the increase of energy efficiency in exiting buildings.

Renovation is a phase of a building life cycle when energy performance of the building characteristics can be substantially increased. There is no strict regulation how often buildings should be renovated. Today we face situation when depreciated buildings are not renovated due to the lack of financial resources and thus keeping these buildings in a state not complying with 6 essential requirements for buildings set by the Directive 89/106/EEC [6]. Decisions to renovate buildings usually are based on economical evaluations. However such approach is not sufficient from the point of view of sustainable buildings maintenance. Benefits of the renovation are not limited just to the decrease of energy expenses and increase of building value. Renovation allows solving global problems such as energy dependency and negative impact on environment of the energy sector.

Goal of this study is to estimate optimal renovation periodicity of the two school buildings in terms of their life cycle energy consumption and greenhouse gas emissions.

2. METHODOLOGY

Energy is used in all phases of the building life cycle – building construction, operation, maintenance, demolition. Therefore seeking for a comprehensive analysis it is relevant to analyse building using life cycle analysis.

Life cycle analysis is widely used in design of industrial products [7]. It is also applied for buildings: to compare different construction materials [8, 9, 10]; to analyse different energy systems [11, 12, 13]; to analyse the whole building [14, 15]. However renovation separately usually is not analysed.

In this study life cycle analysis is used for evaluation of the impact of the building renovation periodicity on its life cycle energy consumption and greenhouse gas emissions.

Evaluation starts from analysis of the building structure and estimation of the possible building renovation frequency. This analysis is followed by energy and pollution calculations.

In this study building construction, operation and renovation phases are considered. Building maintenance phase is not considered because of negligible its effect in comparison to the construction, operation and renovation. Building demolition phase is not considered as it is assumed that building lifetime can be extended beyond its standard lifetime.

2.1. Analysis of the building structure

Building life cycle evaluation starts with the analysis of the building structure. Before formation of the building life cycle building lifetime has to be estimated. Building is constructed of parts (passive and active technical systems) and elements (e. g. heating system is composed of piping, insulation, valves etc.). Every building part and element has its own lifetime [16, 17]. In order to keep building complying with 6 essential requirements for buildings, when the lifetime of the part or element of the building ends it has to be replaced or renovated. Lifetimes of structural parts and elements of the building forms maximal intervals between building major renovations (simultaneous replacement or improvement of the building passive and active technical systems with a view of major improvement of the whole building physical and energy performance).

2.2. Building life cycle energy consumption

Total energy consumption during building lifetime (TE, MWh) includes primary energy consumed for installation and renovation of the active and passive building technical systems (embodied energy, EE, MWh) and operational energy (OE, MWh) used in active technical systems of the building:

$$TE_n = \sum_{i=1}^{n} EE_i + \sum_{i=1}^{n} OE_i \,, \tag{1}$$

where: n – age of the building, years; i – year under consideration.

Embodied energy consumption includes primary energy used for construction (EE_0^c, MWh) and renovation (EE_i^{ren}, MWh) of the building:

$$EE_i = EE_0^c + EE_i^{ren} \,. \tag{2}$$

Embodied energy is calculated as sum of the primary energy used for production of the building elements and materials and primary energy used for transportation of the building elements and materials to the building site:

$$EE = \sum_{j=1}^{m} M_j \cdot \kappa_j^{e,pr} + \sum_{j=1}^{m} M_j \cdot l_j \cdot \kappa_j^{e,tr} \,, \tag{3}$$

where: m – number of elements or materials; j – element or material; M – amount of element or material, t, kg, m^3, units; $\kappa^{e,pr}$ – energy indicator of the production of the element or material (kWh/kg, kWh/m^3, kWh/unit); l – length of transportation of the element or material, km; $\kappa^{e,tr}$ – energy indicator of the transportation of the element or material, kWh/(t·km).

Operational energy includes energy value of the fuel used for production of heat and electricity delivered to the building:

$$OE_i = OE_i^e / (\eta_i^{ep} \cdot \eta_i^{et}) + OE_i^h / (\eta_i^{hp} \cdot \eta_i^{ht}) \,, \tag{4}$$

where: OE_i^e – annual consumption of electricity used for lighting, in equipment and technological processes, MWh; η_i^{ep} – annual electricity production efficiency; η_i^{et} – annual electricity transportation efficiency; OE_i^h – annual consumption of heat used for heating, ventilation and hot water preparation, MWh; η_i^{hp} – annual heat production efficiency; η_i^{ht} – annual heat supply efficiency.

The most acceptable alternative is the one which total energy consumption is the lowest.

Total energy consumption depends on the variation of characteristics of building energy performance and energy supply systems (efficiency of heat and electricity generation and transportation). Factors determining building energy consumption are divided into internal and external.

Internal factors are characteristics of the building constructional parts and engineering systems and their elements. External factors are characteristics of the energy supply systems. These characteristics change due to technological progress, change of the regulations and consumers behaviour and their demands.

2.3. Building life cycle pollution

Analogically as total energy consumption the total pollution (greenhouse gas emissions) of the building lifetime is calculated. Greenhouse gas emissions are expressed in equivalent of amount of carbon dioxide. Total pollution (TP) includes operational greenhouse gas emissions (OP) and embodied greenhouse gas emissions (EP):

$$TP_n = \sum_{i=1}^{n} EP_i + \sum_{i=1}^{n} OP_i \tag{5}$$

Embodied emissions include emissions which occur during construction (EP_0^c, tCO_{2eq}) and renovation (EP_i^{ren}, tCO_{2eq}) of the building:

$$EP_i = EP_0^c + EP_i^{ren}. \tag{6}$$

Embodied emissions due to production and transportation of the elements and materials are calculated:

$$EP = \sum_{j=1}^{m} M_j \cdot \kappa_j^{p,pr} + \sum_{j=1}^{m} M_j \cdot l_j \cdot \kappa_j^{p,tr}, \tag{7}$$

where: $\kappa^{p,pr}$ – pollution indicator of the production of the element or material $kgCO_{2eq}/kg$, $kgCO_{2eq}/m^3$, $kgCO_{2eq}$/unit; $\kappa^{p,tr}$ – pollution indicator of the transportation of the element or material, $kgCO_{2eq}/tkm$.

Operational emissions include emissions due to heat and electricity production:

$$OP_i = OE_i^e / (\eta_i^{ep} \cdot \eta_i^{et}) \cdot \tau_i^e + OE_i^h / (\eta_i^{hp} \cdot \eta_i^{ht}) \cdot \tau_i^h, \tag{8}$$

where: τ_i^e – pollution indicator of the electricity production, tCO_{2eq}/MWh; τ_i^h – pollution indicator of the heat production, tCO_{2eq}/MWh.

The most acceptable alternative is the one which total lifetime pollution is the lowest.

2.4. Decision making

In this study optimal building renovation periodicity is determined according to two criteria – total energy consumption and total pollution. In order to have one criteria for decision making, 3E (energy, economy and ecology) method [18] was used transforming it into 2E (energy and ecology) method. 2E criterion is calculated:

$$2E = e_n \cdot s_e + p_n \cdot s_p, \tag{9}$$

where: e_n – non-dimensional value of the total energy consumption (non-dimensional value express the same results of the variants under consideration but in percents, e. g. zero value is set to the minimal result, one – to the maximum, other values are between zero and one); p_n – non-dimensional value of the total emissions; s_e, s_p – weight coefficients. Decision-maker assesses the weight coefficients of each criterion under consideration.

Non-dimensional values are calculated:

$$e_n = 1 - \frac{TE_{\max} - TE_n}{TE_{\max} - TE_{\min}}, \tag{10}$$

$$p_n = 1 - \frac{TP_{\max} - TP_n}{TP_{\max} - TP_{\min}}. \tag{11}$$

In this study it is assumed that both energy and pollution criteria are equally important and each of their weight is equal 0.5.

3. RESULTS AND DISCUSSIONS

3.1. Buildings characteristics and assumptions

In this study two school buildings are analysed. Those buildings are different in date of design; size and construction (see Table 1).

Table 1. Buildings characteristics

	1st building	**2nd building**
Location	Vilnius	Vilnius
Year of design	1974	1986
Number of pupils	1284	216
Useful area, m^2	6228	2306
m^2/pupil	5	11
Work shifts	2	1
Walls construction	Concrete panels	Clay bricks, mineral wool
Heating system	Water, radiators	Water, radiators
Ventilation of classrooms	Natural	Mechanical

The analysed building lifetime is 100 years [19]. According to the construction of the building the maximal time until its renovation is 30 years. Calculations are made for the alternatives when renovation is performed every 10–30 years. When time intervals between renovations are 10 years, building is renovated 9 times during the considered lifetime. When time intervals between renovations are 24–30 years, building is renovated 3 times.

Assumptions on external factors:

1. Initial heat generator efficiency of the 1st building – 80 %, 2nd building – 84 %, after renovation – 94 %.
2. Initial electricity production and transportation efficiency is 30 %. Electricity production efficiency increase by 0.3 %, o transportation – 0.1 % per year.
3. Energy consumption and emissions of the materials and elements production and transportation are constant. Data for embodied energy and emissions calculations are taken from SimaPro data bases [20].
4. Heat production emissions 0.299 tCO_{2ekv} / MWh, assuming that heat is produced in the boiler using natural gas. Electricity generation emissions 0.315 tCO_{2ekv} / MWh.

Assumptions on internal factors:

1. Requirements on building thermal characteristics changes every 10 years. Calculations are made for three scenarios of the requirements of thermal characteristics tightening: values of the heat transmission coefficients decrease by 10 %, 30 % and 50 % every 10 year (minimal heat transmission coefficients of opaque envelopes is 0.08 W/m^2K, windows – 0.70 W/m^2K). Heat transmission coefficients of the buildings under consideration are presented in Table 2 and Table 3.
2. Electricity consumption during buildings lifetime is constant. It is assumed that energy efficiency increase is compensated by new equipment installed in the building (pumps, fans, computers, air conditioners etc.).
3. After the renovation heating systems are installed with thermostats, balancing valves and possibility to decrease internal temperature during non-working hours.
4. After the renovation ventilation systems with heat recovery is installed in buildings.
5. When heat gains exceed heat demand of the building, air heating system is installed and radiator system is left as a duty heating system.

6. During building renovation phase only those building parts and elements are taken into account which have big share in total material balance: heat insulation production, roof and walls facing materials production, windows production, heating pipes and devices materials production, ventilation ducts materials production, air-handling units production, water supply and sewerage pipes materials production, electricity pipes and cables materials production.

Table 2. Heat transmission coefficients of the 1st building

Envelope	**Heat transmissions coefficient, U (W/m^2K)**									
	Construc-tion	**Decades**								
		I	**II**	**III**	**IV**	**V**	**VI**	**VII**	**VIII**	**IX**
	Values of the coefficients decrease by 10 %									
Wall	0.75	0.69	0.62	0.56	0.51	0.45	0.41	0.37	0.32	0.30
Roof	0.77	0.69	0.62	0.56	0.51	0.45	0.41	0.37	0.33	0.30
Floor	0.35	0.28	0.25	0.23	0.20	0.18	0.16	0.15	0.13	0.12
Window	2.5	1.71	1.71	1.71	1.69	1.21	1.21	1.21	0.95	0.95
	Values of the coefficients decrease by 30 %									
Wall	0.75	0.54	0.38	0.26	0.18	0.13	0.09	0.08	0.08	0.08
Roof	0.77	0.54	0.38	0.26	0.18	0.13	0.09	0.08	0.08	0.08
Floor	0.35	0.22	0.15	0.11	0.08	0.08	0.08	0.08	0.08	0.08
Window	2.5	1.71	1.21	0.95	0.70	0.70	0.70	0.70	0.70	0.70
	Values of the coefficients decrease by 50 %									
Wall	0.75	0.39	0.19	0.10	0.08	0.08	0.08	0.08	0.08	0.08
Roof	0.77	0.39	0.19	0.10	0.08	0.08	0.08	0.08	0.08	0.08
Floor	0.35	0.16	0.08	0.08	0.08	0.08	0.08	0.08	0.08	0.08
Window	2.5	1.21	0.70	0.70	0.70	0.70	0.70	0.70	0.70	0.70

Table 3. Heat transmission coefficients of the 2nd building

Envelopes	**Heat transmissions coefficient, U (W/m^2K)**									
	Construc-tion	**Decades**								
		I	**II**	**III**	**IV**	**V**	**VI**	**VII**	**VIII**	**IX**
	Values of the coefficients decrease by 10 %									
Wall	0.46	0.40	0.38	0.33	0.30	0.27	0.24	0.22	0.20	0.18
Roof	0.40	0.37	0.32	0.29	0.26	0.24	0.21	0.19	0.17	0.15
Floor	0.35	0.31	0.28	0.25	0.23	0.20	0.18	0.17	0.15	0.13
Window	2.50	1.23	1.23	1.23	1.23	1.23	1.23	1.21	0.73	0.73
	Values of the coefficients decrease by 30 %									
Wall	0.46	0.32	0.22	0.16	0.11	0.08	0.08	0.08	0.08	0.08
Roof	0.40	0.28	0.20	0.14	0.10	0.08	0.08	0.08	0.08	0.08
Floor	0.35	0.24	0.17	0.12	0.08	0.08	0.08	0.08	0.08	0.08
Window	2.50	1.23	1.23	0.73	0.70	0.70	0.70	0.70	0.70	0.70
	Values of the coefficients decrease by 50 %									
Wall	0.46	0.23	0.11	0.08	0.08	0.08	0.08	0.08	0.08	0.08
Roof	0.40	0.20	0.10	0.08	0.08	0.08	0.08	0.08	0.08	0.08
Floor	0.35	0.17	0.09	0.08	0.08	0.08	0.08	0.08	0.08	0.08
Window	2.50	1.21	0.70	0.70	0.70	0.70	0.70	0.70	0.70	0.70

3.2. Results

3.2.1. 1st building

The lowest total energy consumption (28 161 kWh/m^2) of the 1st building is counted when building renovation frequency is 12 years and standard heat transmission coefficients become lower by 50 % every 10 years. The highest total energy consumption (32 107 kWh/m^2 – 14 % higher) is counted when building renovation frequency is 30 years and standard heat transmission coefficients become lower by 10 % every 10 years.

The lowest total pollution (7 152 kg CO_{2eq}/m^2) is counted when building renovation frequency is 16 years and standard heat transmission coefficients become lower by 50 % every 10 years. The highest total pollution (7 721 kg CO_{2e}/m^2 – 8 % higher) is counted when building renovation frequency is 30 years and standard heat transmission coefficients become lower by 10 % every 10 years.

Results of 2E criteria are presented in Fig. 1. The lowest 2E is when building renovation frequency is 12 years and standard heat transmission coefficients become lower by 50 % every 10 years.

When standard heat transmission coefficients become lower by 30 % every 10 years, the lowest 2E criteria is counted when building renovation frequency is 12 years too. When standard heat transmission coefficients become lower by 10 % every 10 years, the lowest 2E criterion is counted when building renovation frequency is 10 years.

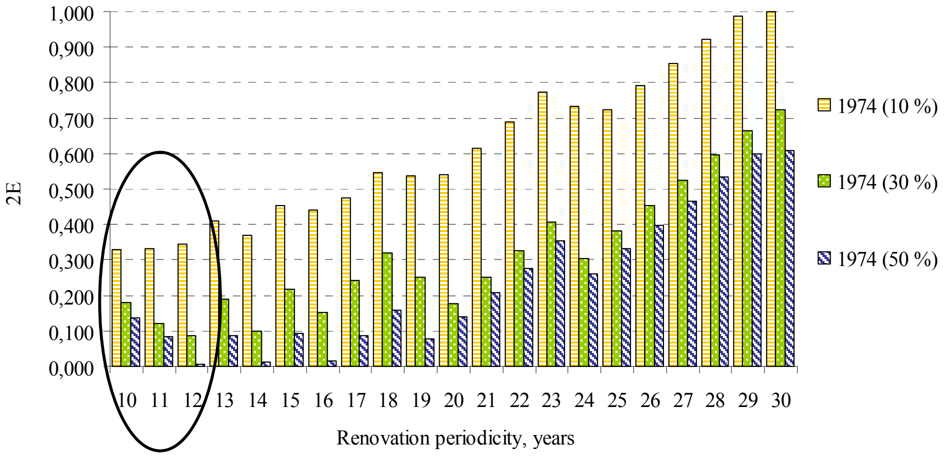

Fig. 1. 2E values of the 1st building

In order to check how initial building energy performance influences the results, calculations are made for scenarios when initial building energy performance corresponds to the requirements of the regulations of the years 1999 [21] and 2005 [22]. Results are presented in Fig. 2 and Fig. 3.

When initial building energy performance corresponds to the requirements of the regulation of the year 1999, the lowest 2E is counted when building renovation frequency is 24 years.

When initial building energy performance corresponds to the requirements of the regulation of the year 2005, the lowest 2E is counted when building renovation frequency is 24 years and standard heat transmission coefficients become lower by 50 % every 10 years.

When standard heat transmission coefficients become lower by 30 % every 10 years, the lowest 2E criteria is counted when building renovation frequency is 24 years too. When standard heat transmission coefficients become lower by 10 % every 10 years, the lowest 2E criteria is counted when building renovation frequency is 25 years.

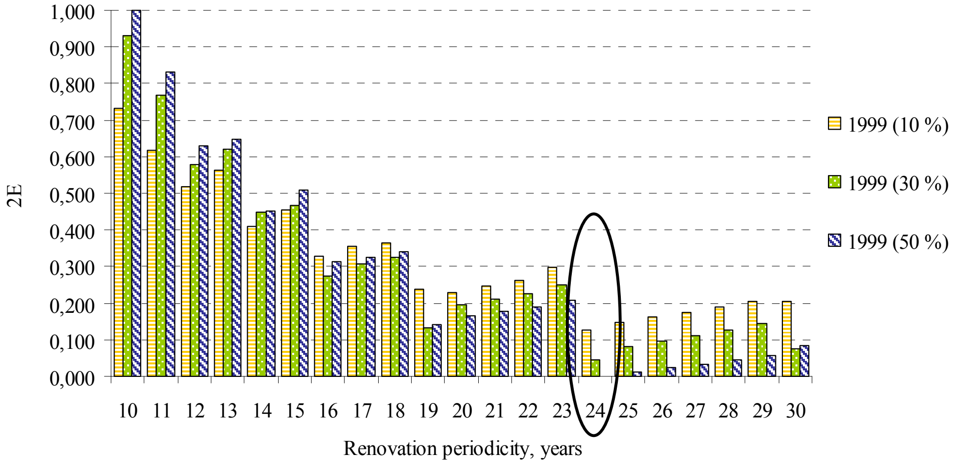

Fig. 2. 2E values, when initial energy performance of the 1st building corresponds to the requirements of the regulation of the year 1999

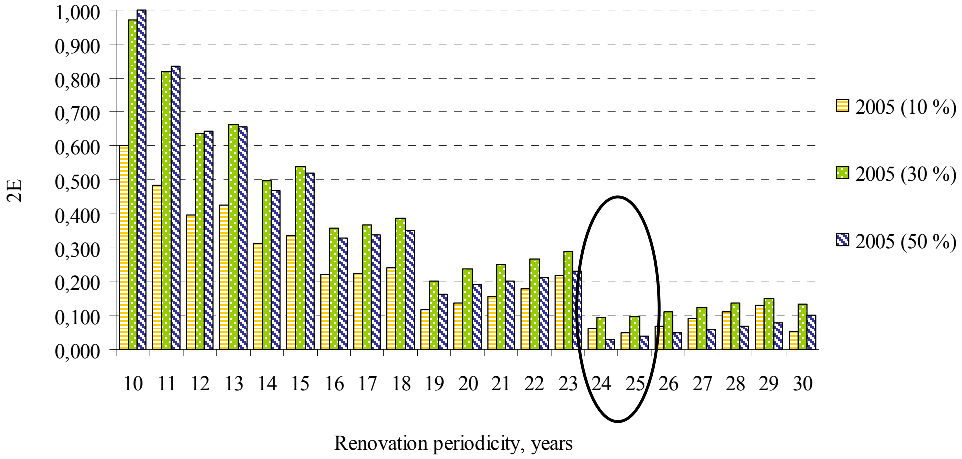

Fig. 3. 2E values, when initial energy performance of the 1st building corresponds to the requirements of the regulation of the year 2005

3.2.2. 2nd building

The lowest total energy consumption (18 147 kWh/m^2) of the 2nd building is counted when building renovation frequency is 20 years and standard heat transmission coefficients become lower by 50 % every 10 years. The highest total energy consumption (21 533 kWh/m^2 – 19 % higher) is counted when building renovation frequency is 30 years and standard heat transmission coefficients become lower by 10 % every 10 years.

The lowest total pollution (5 081 kg CO_{2eq}/m^2) is counted when building renovation frequency is 20 years and standard heat transmission coefficients become lower by 50 % every 10 years. The highest total pollution (5 663 kg CO_{2e}/m^2 – 11 % higher) is counted when building renovation frequency is 30 years and standard heat transmission coefficients become lower by 10 % every 10 years.

Results of 2E criteria are presented in Fig. 4. The lowest 2E is counted when building renovation frequency is 20 years and standard heat transmission coefficients become lower by 50 % every 10 years.

When standard heat transmission coefficients become lower by 30 % every 10 years, the lowest 2E criteria is counted when building renovation frequency is 15 years. When standard heat transmission coefficients become lower by 10 % every 10 years, the lowest 2E criteria is counted when building renovation frequency is 16 years.

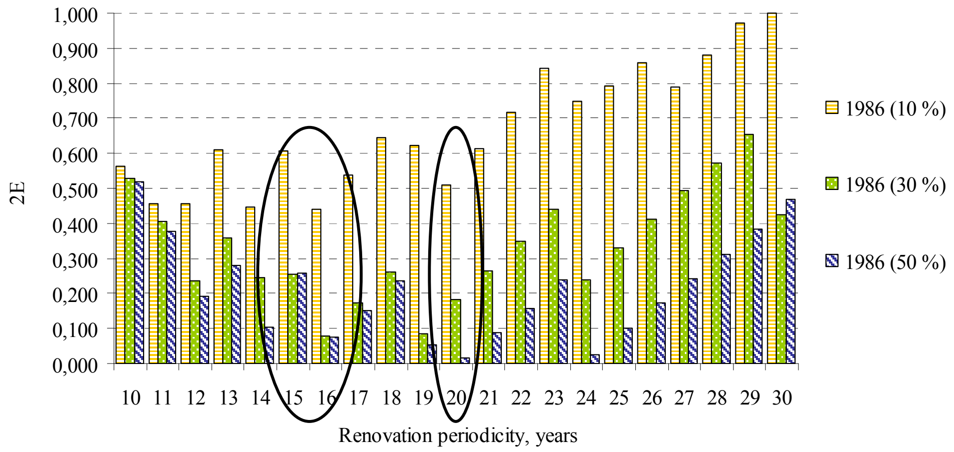

Fig. 4. 2E values of the 2^{nd} building

In order to check how initial building energy performance influences the results, calculations are made for scenarios when initial building energy performance corresponds to the requirements of the regulation of the year 2005. Results are presented in Fig. 5.

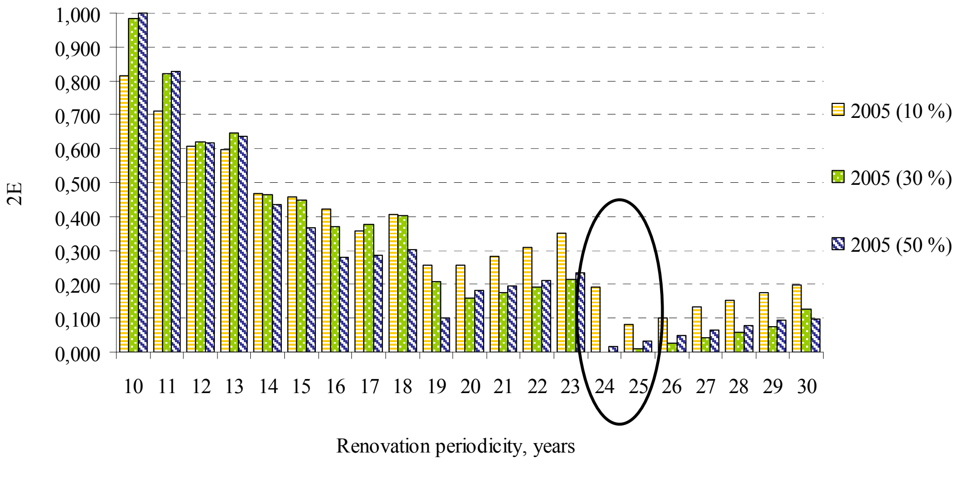

Fig. 5. 2E values, when initial energy performance of the 2^{nd} building corresponds to requirements of the regulation of the year 2005

When initial building energy performance corresponds to the requirements of the regulations of the year 2005, the lowest 2E is counted when building renovation frequency is 24 years and standard heat transmission coefficients become lower by 30 % every 10 years.

When standard heat transmission coefficients become lower by 50 % every 10 years, the lowest 2E criteria is counted when building renovation frequency is 24 years too. When standard heat transmission coefficients become lower by 10 % every 10 years, the lowest 2E criteria is counted when building renovation frequency is 25 years.

4. CONCLUSIONS

1. It is relevant to evaluate building renovation periodicity according to the renovation frequency impact on its lifetime energy consumption and impact on environment.
2. Taking into account tendency that requirements for buildings thermal characteristics tend to become more stringent, it is reasonable to renovate buildings while increasing their energy efficiency earlier then they totally depreciate.
3. The lower initial building energy performance and scope of the renovation (in terms of energy efficiency increase) is the more frequent renovation is reasonable. The higher initial building energy performance and scope of the renovation is the more frequent building renovation becomes less reasonable.
4. In case of the 1st building:
   - the lowest 2E value is counted when building is renovated every 12 years and standard heat transmission coefficients becomes lower by 50 % every 10 years;
   - when initial building energy performance corresponds to the requirements of the regulations of the years 1999 and 2005, the lowest 2E value is counted when building is renovated every 24 years and standard heat transmission coefficients become lower by 50 % every 10 years.
5. In case of the 2nd building:
   - the lowest 2E value is counted when building is renovated every 20 years and standard heat transmission coefficients become lower by 50 % every 10 years;
   - when initial building energy performance corresponds to the requirements of regulation of the year 2005, the lowest 2E is accounted when building is renovated every 24 years and standard heat transmission coefficients become lower by 30 % every 10 years.
6. While analysing building renovation and seeking to evaluate real energy and pollution reduction effect, it is reasonable to pay attention to the embodied energy consumption. Taking into account only operational energy consumption and emissions, frequent renovation is reasonable if it increases energy efficiency. Whereas embodied energy and emissions, which are the higher the more frequent is renovation, determines less frequent renovation expediency.

REFERENCES

1. Commission of the European Communities. Green Paper – A European Strategy for Sustainable, Competitive and Secure Energy, 2006. [referred on the 15th of February in 2010 y.]. Link to the internet < ec.europa.eu>
2. Council of the European Union. Brussels European Council 8/9 March 2007, Presidency Conclusions, 2007. [referred on the 3rd of January in 2009 y]. Link to the internet <register.consilium.europa.eu>
3. International Energy Agency. Energy efficiency requirements in building codes, energy efficiency policies for new buildings. France: International Energy Agency, 2008. [referred on the 15th of february in 2010 y.]. Link to the internet <www.iea.org>
4. Department of Statistics under the Government of the Republic of Lithuania [referred on the 15th of February in 2010 y.]. Link to the internet <www.stat.gov.lt>
5. Energy Efficient Buildings European Initiative. Research priorities for the definition of a multi-annual roadmap and longer term strategy. Energy Efficient Buildings European Initiative, 28 December 2009. [referred on the 15th of February in 2010 y.]. Link to the internet <www.e2b-ei.eu>

6. Council Directive 89/106/EEC of 21 December 1988 on the approximation of laws, regulations and administrative provisions of the Member States relating to construction products. *Official Journal*, 1989, L 40, p. 12–26.
7. Directive 2005/32/EC of the European Parliament and of the Council of 6 July 2005 establishing a framework for the setting of eco-design requirements for energy-using products and amending Council Directive 92/42/EEC and Directives 96/57/EC and 2000/55/EC of the European Parliament and of the Council. *Official Journal*, 2005, L 191, p. 29–58.
8. ABEYSUNADRA, Y.U.G., BABEL, S., GHEEWALA, SH. A matrix in life cycle perspective for selecting sustainable materials for buildings in Sri Lanka. *Building and Environment*, 2009, Vol. 44, p. 997–1004.
9. GERILLA, G. P., TEKNOMO, K., HOKAO, K. An environmental assessment of wood and steel reinforced concrete housing construction. *Building and Environment*, 2007, Vol. 42, p. 2778–2784.
10. XING, S., XU, ZH., JUN, G. Inventory analysis of LCA on steel- and concrete-construction office buildings. *Energy and Buildings*, 2008, Vol. 40, p. 1188–1193.
11. NYMAN, M., SIMONSON, C. J. Life cycle assessment of residential ventilation units in a cold climate. *Building and Environment*, 2005, Vol. 40, p. 15–27.
12. SHAH, V.P., DEBELLA, D.C., RIES, R.J. Life cycle assessment of residential heating and cooling systems on four regions in the United States. *Energy and Buildings*, 2008, Vol. 40, p. 503–513.
13. YANG, L., ZMEUREANU, R., RIVARD, H. Comparison of environmental impacts of two residential heating systems. *Building and Environment*, 2008, Vol. 43, p. 1072–1081.
14. SCHEUER, CH., KEOLEIAN, G.A., REPPE, P. Life cycle energy and environmental performance of a new university building: modelling challenges and design implications. *Energy and Buildings*, 2003, Vol. 35, p. 1047–1064.
15. VERBEECK, G., HENS, H. Life cycle inventory of buildings: A calculation method. *Building and Environment,* 2010, Vol. 45, p. 1037–1041.
16. Aplinkos ministerija, VšĮ Būsto ir urbanistikos plėtros fondas. *Rekomendacijos R 27-01. Statinių ir jų dalių gyvavimo skaičiuojamosios trukmės įvertinimas*. Vilnius: Rekona, 2002. 35 p.
17. Lietuvos standartas LST EN 15459:2008 Energetinės pastatų charakteristikos. Pastatų energetinių sistemų ekonominio įvertinimo procedūra. Lietuvos standartizacijos departamentas, 2008, p. 50.
18. ROGOŽA, A., ČIUPRINSKAS, K., ŠIUPŠINSKAS, G. The optimisation of energy systems by using 3E factor: the case studies. *Journal of Civil Engineering and Management*, 2006, Vol. XII, No 1, p. 63–68.
19. Statybos techninis reglamentas STR 1.12.06:2002 Statinio naudojimo paskirtis ir gyvavimo trukmė. *Valstybės žinios*, 2002, Nr. 109, p. 4837.
20. Pre Consultants bv, SimaPro 7 Software, Data Base.
21. Statybos techninis reglamentas STR 2.05.01:1999 Pastatų atitvarų šiluminė technika. *Valstybės žinios*, 1999, Nr. 41, p. 1297.
22. Statybos techninis reglamentas STR 2.05.01:2005 Pastatų atitvarų šiluminė technika. *Valstybės žinios*, 2005, Nr. 100, p. 3733.

CYSENI 2010, May 27–28, Kaunas, Lithuania
ISSN 1822-7554, www.cyseni.com

SUSTAINABILITY OF BIODIESEL MARKET – A SYSTEMS CASE STUDY OF PROBLEM IN GERMANY

H. Ardawatia
System Dynamics Group, Department of Geography
University of Bergen
Fosswinckels Gt. 6, Bergen 5020, Norway
Email: ardhimanshu@gmail.com

ABSTRACT

Due to environmental and energy security reasons, an increasing need is being felt around the world to find carbon neutral, efficient, cost-effective and sustainable energy solutions. This is also true for liquid fuel for transport purpose as the liquid fossil fuel resources are depleting fast with demand increasing day by day. Biodiesel is one such alternative to fossil fuels for transportation purposes and it is being promoted by different governments through different policies. However, in spite of different policies implemented at large organizational and governmental levels, biodiesel market has not been able to reach a point where it can survive without support from governments in terms of tax rebates, subsidies etc. Further, sustainability of biodiesel has still got question marks.

Germany has promoted biodiesel market by introducing tax rebates and subsidies and for some years such policies led to a steep growth in biodiesel production capacity and production in German industry. However, such growth remained short-lived and within a decade the market switched from almost exponential growth to a steady decline. In this study, German biodiesel market behavior has been analyzed by investigating the feedback dynamics in this sector in context of different policies, thereby throwing light on the sustainability issues and possibilities of the biodiesel sector.

Keywords: Biodiesel, Fossil fuel, carbon neutral, Feedback Dynamics, Policies, Sustainability

1. INTRODUCTION

Need to explore and use alternative and renewable sources of energy is becoming critical as the world population and thus demand increases and fossil fuels get depleted. This holds true for all energy requirements – cooking, electricity, industry, transport fuel and heating. On top of that, growing concerns about global warming (which, in part, has been attributed to green-house gas (GHG) emissions from use of conventional fossil fuels) has led to increased concerns over habitable ecosystem conditions on earth. Further, even renewable energy may not necessarily be carbon-neutral. Thus, interest has been increasing towards finding alternative sources of energy which are renewable and ever more carbon-neutral than existing energy sources (including renewable and fossil fuels). Currently, for transport needs, only electricity and liquid bio-fuels (e.g., biodiesel) seem feasible. Electric or hybrid vehicles are still found to, indirectly, emit GHGs because the electricity used in their batteries is primarily generated from GHG emitting fossil fuels. Further, vehicles need to have completely new engines or modified engines to be able to use electricity. Electricity is also consumed in many other areas of need and, therefore, large amounts of electricity needs to be generated (cheaper sources of which still are the ones which emit green house gases). On the other hand, biodiesel, which is a methyl ester of natural fatty acids produced via transesterification of fats and vegetable oils and is renewable, can be used directly in diesel engines. For Germany it is particularly a practical option as a number of vehicles in the country already use diesel engines.

This case study is about German Biodiesel sector due to the fact that Germany has been the market leader in biodiesel all these years. German biodiesel sector developed at steady pace since 1990 as the national and European biofuel policies took shape but it showed some signs of decline in the last 2-3 years (details later in the article). It is difficult to say whether this downturn is just normal as part of a larger cycle of industry development or whether it is an indication of a larger issue of the future. Several reports (mainly news reports and organizational report releases) have pinpointed on some reasons (e.g., the green fuel tax policy, the splash-and-dash tax loophole in USA etc.) for the recent issues in the German biodiesel market. However, such report about these trends can be, several times, biased towards certain categories of stakeholders and regions or political contexts and therefore an objective view with a scientific basis (natural, social, political) is needed. Further, although, it is possible to consider different parts of the whole issue seperately but it is hard to get a coherent understanding of the whole problem using that approach. Therefore, a systems understanding of the whole problem could be more effective as first step in identifying interlinked parameters and their dynamics. Therefore, this review article aims to analyze the German biodiesel market scenarios using systems approach. This is done by investigating the dynamics and interplay of reinforcing and counteracting feedback loops and delays in the German biodiesel market and supply chain system and suggesting possible hypotheses in context of different policies.

1.1. German Biodiesel Market

German biodiesel sector started to pick up as the national biofuel policy started to take effect to jumpstart the biodiesel market development around 1990. It started to show sharper growth from 1999-2001 period onwards as comprehensive European biofuel policy started to take shape (European Biodiesel board, 2009, [1]). Over the years, the German government has showed political will to support biofuel programs by introducing and continuing various policies including tax rebates and subsidies. Germany followed a fiscal policy of giving full tax exemption for unlimited volumes of biofuels to create a favourable and stable market condition for biodiesel (Thuji, van E., et al, 2006, [2]). The agricultural sector in Germany also firmly lobbied for the introduction of biofuels. In all, political commitement, active market actors, financial benefits (e.g., tax reduction) and growth of end-user market led to a booming biodiesel sector in Germany. These efforts steadily culminated in Germany becoming world's largest producer and consumer of biodiesel. Several big and small companies increasingly invested towards increasing production capacity and production as consumption and sales forecast looked good. Production capacity, production and consumption grew steadily until 2005. However, it showed decline in production from 2007 onwards one critical reason being increase of biodiesel tax by government to 9 Euro cents per litre with regulation to increase it step-wise to 45 Euro cents per litre by 2012 (Hogan, M., 2007, [12]). This was followed by somewhat slower decline in Production capacity (Fig. 1).

Although it is a bit early to say what kind of trend will follow in the coming years but it is certainly a concern for biodiesel related industries and organization. It is natural to worry about this trend because if the trend continues, it might culminate in monetary and job losses and possible company closures. Some companies have already started decreasing production but the production capacity has been taking time to level off due to the steps taken earlier by the companies in terms of investment in infrastructure and capital. Sustainability of German biodiesel market is a question mark in the light of current policies which the government changes and modifies from time to time. Such complex issues are rarely single-faceted but are multi-faceted. Sustainability of a sector depends on optimal policies which are developed after considering all possible parameters and their dynamics in the system.

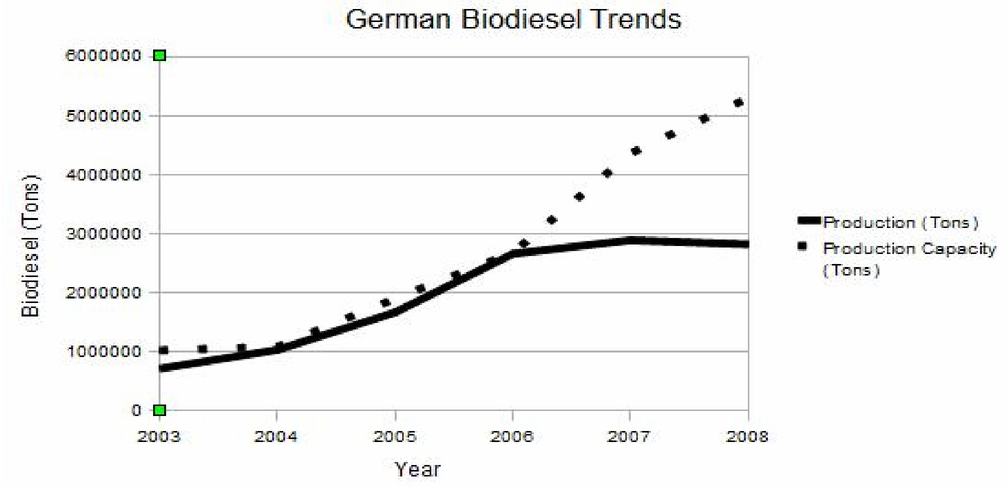

Fig. 1. Biodiesel Production capacity and production trends in Germany (Production data for 2009 is unavailable while production capacity was logged upto 5200000 tons which is a decrease from 2008 data. Concrete data unavailable before 2003.) (Source: European Biodiesel Board, 2009, [1])

Therefore, a system level analysis is done to identify key parameters and feedback loops in the system, dynamics of which could be an important endogenous factor for the current situation, apart from the exogenous factors.

2. METHODOLOGY

To have a holistic and integrated understanding of the whole situation, causal loop diagrams from the system dynamics methods have been used to reflect on the current situation. Causal Loop Diagrams (CLD) are an important tool for representing the feedback structure and capturing hypotheses about the causes of dynamics in systems (Sterman, J., 2000, [3]). CLD consists of variables (parameters) connected (with positive or negative denotion) signifying the causal influences among them. A positive (+) link signifies increase of effect with increase of cause (and decrease of effect with decrease of cause) while a negative (-) link signifies the opposite (effect decreases if cause increases and effect increases if cause decreases). Thus, with several variables linked causally in the system, important feedback loops (reinforcing and counteracting) can be identified. Different sectors were first formulated separately into causal loops diagrams which were then integrated into a large causal loop system. This helped understand the various sectors and parameters in context of the whole system and vice versa. Some parameters have been aggregated into single parameters for the sake of simplicity. If a simulation model were to be built further, such aggregated parameters would be dis-aggregated into other parameters as per the needs, accuracy and boundary conditions of the model.

3. RESULTS & DISCUSSION

Upon decomposition of the system, different sectors and feedback loops were revealed. As is usual with different markets, a supply-demand sector always exists. In the case of Biodiesel also, "supply-demand" sector exist but it is not one supply and demand sector but three. These supply-demand sectors have altogether three reinforcing (positive) feedback loops. Another sector which we can call the "development sector" here has four balancing (counteracting / negative) feedback loops. The two sectors are inter-related and the feedback loops interact endogenously and result in dynamics of the system. The sectors and feedback loops are discussed below:

3.1. Supply-Demand Sector

The supply-demand sector in this case has three sub – supply-demand sectors. In the biodiesel supply chain, the biodiesel supply-demand, the by-product supply-demand and the cost sub-sectors are the three main sub-sectors. These three sub-sectors are also part of three counteracting feedback loops (denoted by B5, B6, B7 in the following text) in this case. These loops are counteracting loops because effect of any parameter, if traced all through the loop, has a counteracting or balancing or negative effect on the growth of that parameter itself.

3.1.1. *Biodiesel supply-demand sub-sector*

The supply chain of biodiesel starts with fuel crop cultivation (mostly rapeseed in case of Germany). Initially, the increase in fuel crop (rapeseed in case of Germany) cultivation leads to more production of vegetable oil which further leads to higher production of biodiesel. More biodiesel in the market leads to higher supplies and thus decrease in biodiesel price. Price is further decreased due to government support in the form of tax rebate and subsidies. A higher biodiesel price can decrease the attractiveness of biodiesel for customers (and vice versa) and if the mineral oil price is low, the attractiveness decreases further. The more the attractiveness, the higher the consumption and thus higher the biodiesel demand. Higher biodiesel demand leads to higher vegetable oil demand putting increasing pressure on fuel crop cultivation resources and thus increasing the cultivation cost. This higher cultivation cost can decrease the rapeseed cultivation. Fig. 2 shows the Biodiesel supply-demand sub-sector and also counteracting feedback loop (B1) in this sector. Attractiveness of Biodiesel for Customers can be given by a simple equation (Equation 1)

Attractiveness of Biodiesel for Customers = Mineral Diesel Price / Biodiesel Price (1)

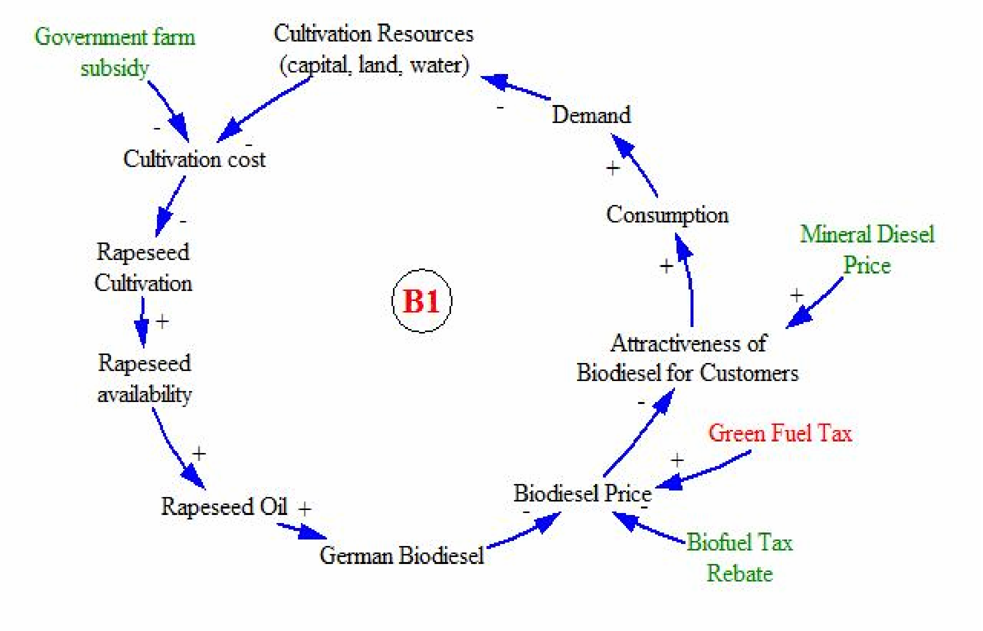

Fig. 2. Counteracting feedback loop B1 in the Biodiesel supply-demand sub-sector

3.1.2. *By-product supply-demand sub-sector*

Similar to the biodiesel supply-demand sub-sector, another counteracting loop (B2) exists in the by-product supply-demand sub-sector (Fig. 3). This sub-sector emphasizes the importance of by-products in the overall biodiesel sector and how revenues from by-products can influence the biodiesel price. The loop polarity in this case is also reinforcing because of the same reasons as explained above.

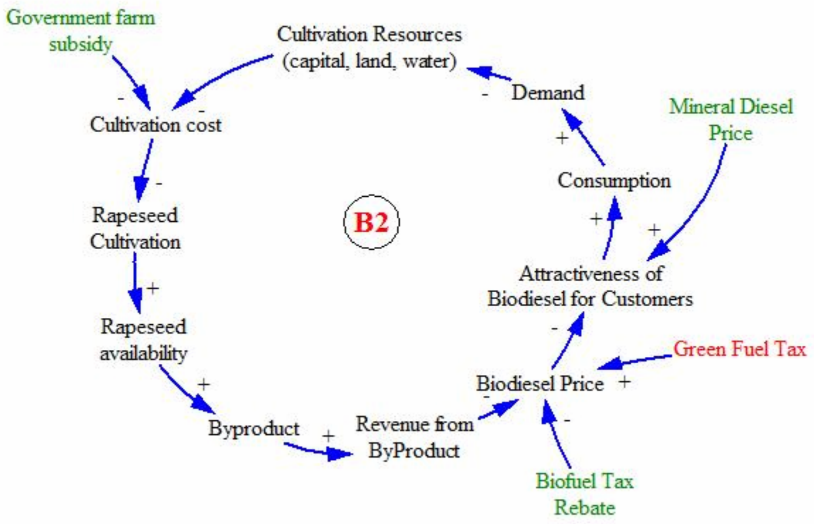

Fig. 3. Counteracting feedback loop B2 in the By-product supply-demand sub-sector

3.1.3. *Cost sub-sector*

This sector (Fig. 4) signifies how high demand can put pressure on resources thus increasing their cost. The higher the resource cost, the higher the cultivation cost and the higher the cultivation cost, the higher the rapeseed cost and further German biodiesel cost which further leads to increase of the overall biodiesel price (affected by other exogenous factors which are discussed later). It is assumed, for simplicity sake, that German biodiesel production cost directly translates to German biodiesel price (which is further adjusted based on foreign biodiesel price, taxes etc). This also constitutes another counteracting loop (B3).

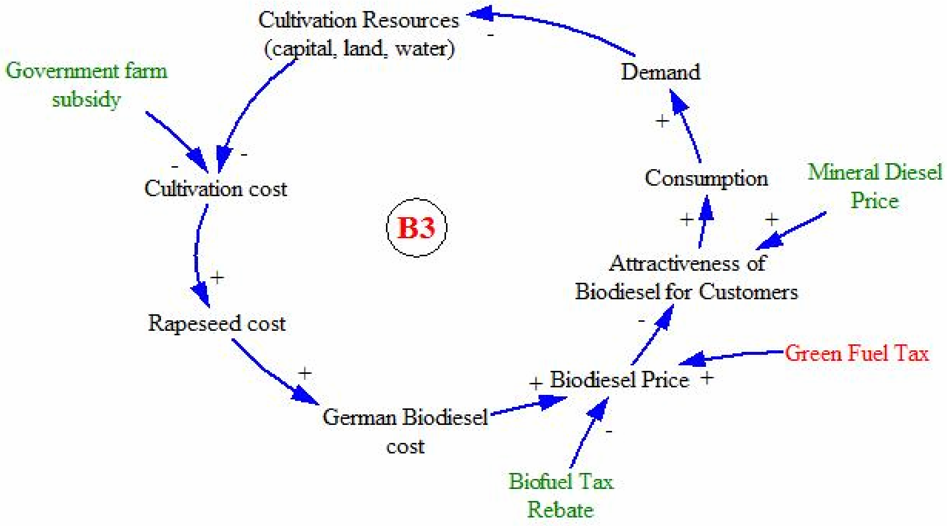

Fig. 4. Counteracting feedback loop B3 in the Cost sub-sector

3.2. Development Sector

Development sector is composed of one more balancing (counteracting) loop (denoted by B4) and three reinforcing feedback loops (denoted by R1, R2, R3). These loops are reinforcing because effect of any parameter, if traced all through the loop, eventually reinforces the growth of the said parameter. The sub-sectors in the development sector are production-attractiveness sub-sector, biodiesel production capacity sub-sector, rapeseed cultivation capacity sub-sector and by-product development sub-sector.

3.2.1. Production-attractiveness sub-sector

The balancing loop B4 plays the major role in this sub-sector (Fig. 5). This sub-sector signifies the role of higher prices in increasing the attractiveness for the industry to build more production capacity. Such higher production capacity further increases German biodiesel volumes thus increasing the supply. Higher biodiesel volumes in market can lead to lower prices which can further lower the attractiveness for producing biodiesel.

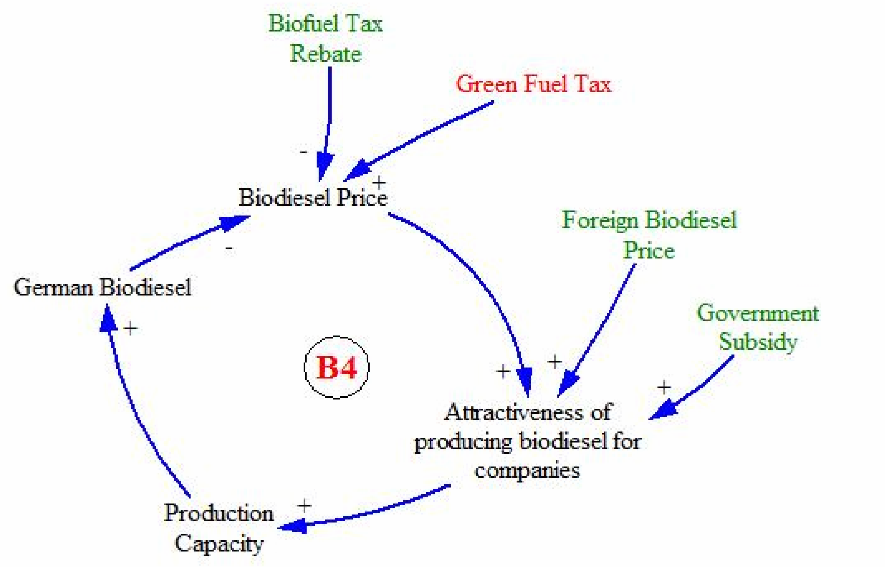

Fig. 5. Counteracting feedback loop B4 in Production-attractiveness sub-sector

3.2.2. Biodiesel Production capacity sub-sector

This sub-sector (with reinforcing loop R1) brings the customer perspective in the picture. The lower biodiesel prices can increase its attractiveness for customers thus further increasing consumption (in this case, it is assumed that price attractiveness (as compared to mineral diesel oil) is directly translated to product (biodiesel) attractiveness). Higher consumption leads to higher revenues which lead to higher investments in upstream processes like towards increasing biodiesel production capacity which increases biodiesel volumes in the market thus decreasing price. Fig. 6 shows this sub-sector and the reinforcing loop R1.

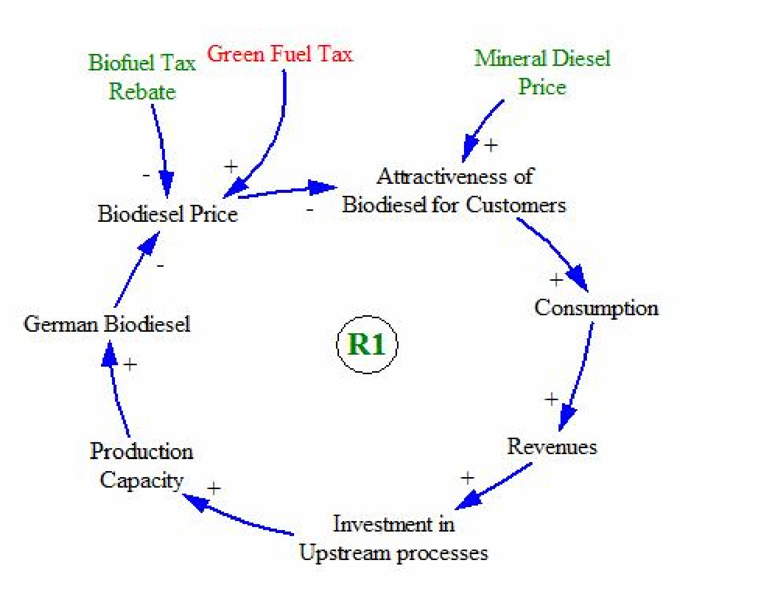

Fig. 6. Reinforcing Loop R1 in Biodiesel Production capacity sub-sector

3.2.3. *Rapeseed Cultivation capacity sub-sector*

This sub-sector is similar to the biodiesel production sub-sector except that the higher revenues generated from higher consumption lead to higher investment in building higher rapeseed cultivation capacity which affects parameters further in the loop causing the overall loop polarity to be reinforcing (positive) This loop is R2 and the sub-sector is shown in Fig. 7.

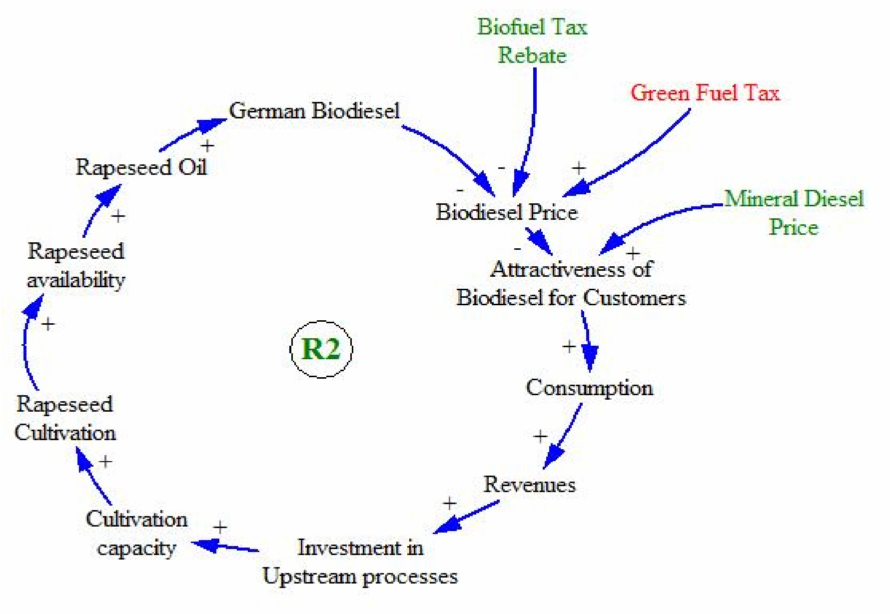

Fig. 7. Reinforcing feedback loop R2 in Rapeseed Cultivation capacity sub-sector

3.2.4. *By-product development sub-sector*

This sub-sector is similar to the previous sector, except that by-products are involved in this sub-sector. Inclusion of by-products in the industry can help offset costs through the revenue generated through sale of by-products. The higher the revenue from by-products, the lower the biodiesel price. This culminates into the reinforcing loop R3 (Fig. 8).

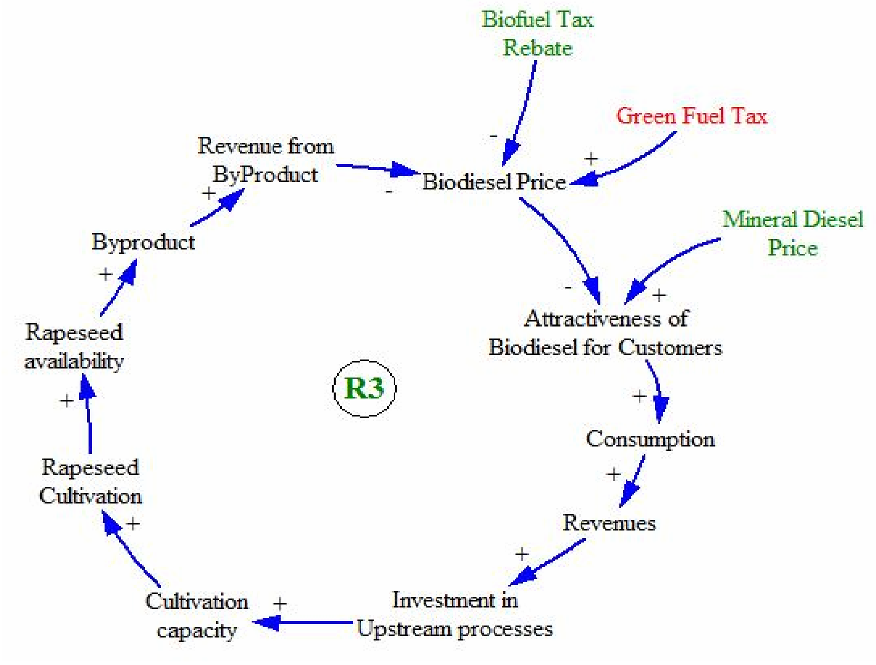

Fig. 8. Reinforcing feedback loop R3 in By-product development sub-sector

It is worthwhile noting that several exogenous factors play a role in these sub-sectors and feedback loops by controlling different parameters. In this case, these exogenous factors are identified to be Foreign biodiesel price, Biofuel tax rebate, Green fuel tax, Mineral oil price, Government farm subsidy and Government subsidy. The government support is considered exogenous here because it is not affected endogenously by any of the parameters in biodiesel sector but by political will and environmental concerns and possibly by the mineral oil sector's dynamics. The mineral oil price is considered exogenous here because in context of the current biodiesel sector status it is largely independent (at least at this time point) and depends mostly on its own supply and demand. Similarly, the Foreign biodiesel price is considered exogenous because it is influenced by the foreign countries' biofuel policies in terms of incentives and taxes which fuel growth or decline in those countries.

These parameters are exogenous and as is evident they can have strengthening or weaking effects on different loops. For example, Biofuel tax rebate negatively influences the biodiesel price while Green fuel tax positively influences the Biodiesel price. Increase in mineral oil price increases the attractiveness of biodiesel for customers. Increase in Government subsidy increases attractiveness of producing biodiesel for companies. Similarly, Foreign biodiesel price positively influences the attractiveness of producing biodiesel for companies in the sense that it increases the chances of growth of indigenous industry due to price difference. Last but not the least, Government farm subsidy negatively influences the cultivation cost. Therefore, these are the first choice for governments as policy parameters for the puspose of affecting the behaviour of the whole system. An integrated causal loop diagram of the German biodiesel sector is shown in Fig. 9. It shows how the above described feedback loops interact with each other and how each of their dynamics could affect the other loops.

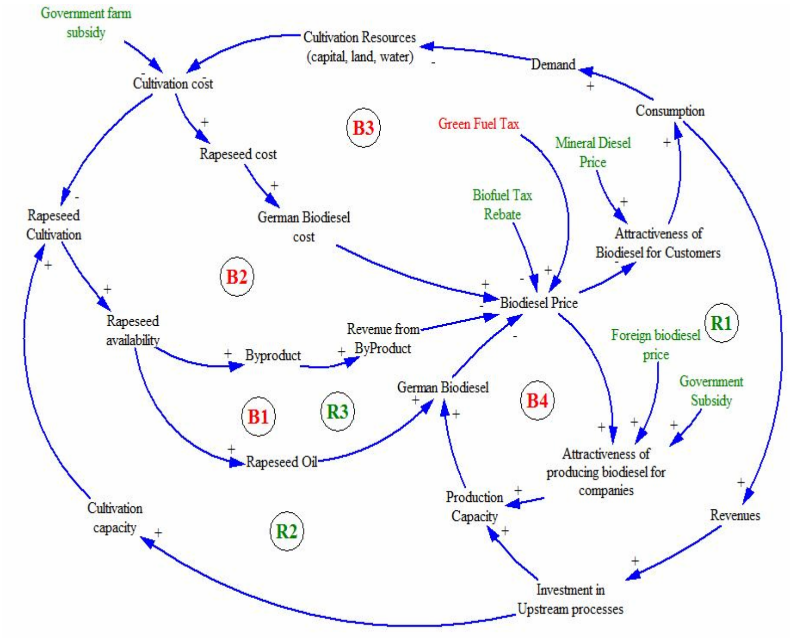

Fig. 9. Integrated Causal Loop Diagram of German Biodiesel sector (Loop names B1, B2, B3 and B4 are counteracting loops. Loop names R1, R2, R3 are reinforcing loops. R1, R2, R3, B4 are in the Development Sector. B1, B2, B3 constitute the supply-demand sector)

According to systems theory (Sterman 2000, [3]), reinforcing feedback loops are responsible for exponential growth behaviour while counteracting loops are responsible for goal-seeking behaviour. More than one balancing loop with "delays" in the process can lead to oscillatory behaviour. There are certainly several "delays" or "time-lags" in the biodiesel sector. These include both material delays and information delays. For example, it takes time to cultivate rapeseed and produce biomass (material delay) and it takes time to "perceive" demand and take action to fulfill that demand (information delay). There are several such delays in this system. From the graph in Fig. 1, it seems likely that initially the reinforcing loops were strong thus leading to almost exponential growth while in the last 2–3 years the balancing loops gained more strength (which is reflected in the goal-seeking behaviour of the production and production-capacity curves). The production-capacity curve does not show such fast goal-seeking behaviour as the production curve. This could be because of the fact that the capital and infrastructural investments are made in advance for production capacity based on market speculations (which until 2–3 years ago looked good). This dynamics correlates with the market and policy developments in the German biodiesel sector in the last 10 years (approximately). Initially, the reinforcing loops were strong and became stronger because of tax rebates and farm subsidies because the Government (German and EU) had ambitious biodiesel targets. Several companies jumped in and the sector grew almost exponentially. However, over the last 3–4 years, the rapeseed prices increased manifold thus increasing the production cost for rapeseed oil and subsequently biodiesel. This was compounded by the new German biofuel tax (Evans, J., 2008, [4]) which decreased the price competetiveness of the biodiesel produced indigenously. It did not end there – several US companies started taking advantage of the loophole in the 2004 US energy legislation according to which the biodiesel companies in the US would get tax credit for biodiesel that is blended with petroleum diesel (1 cent per percent of biodiesel). With this, the US companies imported cheaper biodiesel from other countries, blended 1% petroleum diesel in that biodiesel (making it B99) and exporting it to Germany (popularly known as splash and dash). These companies thus got 99 cents in tax credits per litre of biodiesel which helped their biodiesel to be sold much cheaper in Germany than the indigenous German biodiesel (Lancellotti, A, 2009, [5]). This further strengthened the balancing loops.

In general, rising fuel crop prices (due to demand and competetion with food crops (Sandvik S., 2008, [6]; Elmendorf D.W. et. al., 2009, [7])), decreasing mineral oil prices, government biodiesel tax and other factors described above have been attributed for higher price of biodiesel (Krawczyk, T., 1996, [8]) and has led to decreasing consumption and production trends. This has led Germany to recently announce that biodiesel blends would be limited by mandate to 5.25% of total diesel sales instead of 6.25% announced in the past as a 2009 target (Lane, J., 2008, [9]). Thus, continous changes of energy policy at short intervals is also assumed to be responsible for the uncertainty in the system and further leading to uncerainty in sustained and growth oriented investments in the biodiesel sector in Germany and overall sustainability of the biodiesel sector.

From the above discussion, we can see that apart from exogenous factors, sustainable development and growth possibility could also arise when we consider some endogenous factors. For example, feedstocks (here rapeseed) could be substituted or diversified with some other biodiesel source and it could bring feedstock security in supply part of the market system. Similarly, it could be worth while considering the by-product supply chain for finding lucrative leverage in the whole system. Change of feedstock to non-food sources such as algae could be worth observing. Algae is already being experimented with in different organizations for the purpose of harnessing biodiesel from different strains of algae (Chisti, Y., 2007, [10]) (Algae has seperated resource needs as compared to rapeseed). Further, by simulations with proper bondary condition, it could be estimated as to “how much” tweaking with such parameters would yield “how much” change in behaviour of the overall system and whether there could be any “side-effects”. The likelihood of devising optimal policies could well increase based on such efforts.

4. CONCLUSIONS

The German biodiesel market scenarios were analysed by understanding the interplay and dynamics of feedback loops in the system. This review article analysed the German biodiesel situation from a systems perspective which had been lacking in most studies yet. The gap between different studies and analyses has been bridged by taking the systems approach. Some parameters were treated as exogenous to keep the focus on the particular issue of German Biodiesel market. It is not very difficult to see the role of such exogenous parameters and events and how these can be used for policy leverage. However, the systems view and understanding of dynamics of feedback loops and delays in this system also throws light at some endogenous parameters (e.g., feedstock source and diversity, by-products) which can be tackled for finding leverage in the system.

This review study has resulted in a hypothesis about dynamics of feedback loops in the German biodiesel market system. Although basic behaviour can be predicted in this way to some extent, it is difficult to predict the future behaviour without system dynamics model simulation. This lays the foundation for future studies where in this hypothesis can be put into a system dynamics model (Sterman, J., 2000, [3]) which can be simulated to replicate the historic behaviour (to emphasize the accuracy of how the model captures the overall situation) (Forrester, J.W., 1969, [11]) and to predict future behaviour of key parameters in different scenarios (for example, changing of certain parameters to weaken or strengthen certain loops in realistic conditions). Simulation could help determine whether there will be cycles in the future or growth or further decline. The parameters which have been considered exogenous in this review article can be tested for their effects on the overall behaviour and checked whether there can be any endogenous causes of these and other parameters. Further, it can also be checked whether endogenizing them makes much difference in how accurately the model captures the situation. New feedback loops might also emerge as the system is dis-aggregated further for modeling purpose. Such studies is being pursued currently by the author.

In the end, I would like to emphasize that it is likely that due to high political and societal stakes and general commitment to reduce emission of GHGs, biodiesel sector won't be allowed to vanish in Germany by responsible actors. However, in general, severe fluctuations in such sectors can have severe side-effects and therefore, optimal systems based policy need to be in place for sustainable development and growth of the biodiesel sector. Further, if some energy souce better than biodiesel (in terms of efficiency, feasibility, cost competetiveness, carbon neutrality and sustainability) is developed for transportation needs, such system models could be helpful in understanding and managing those sectors too and policies based on such models could be helpful in catalysing sustainable development of those sectors.

REFERENCES

1. European Biodiesel Board Database, 2009 (http://www.ebb-eu.org/stats.php#)
2. THUJI, van E., DEURWAARDER, E.P. *European Biofuel Policies in Retrospect.* Report from Energy Recearch Center of Netherlands, 2006, Project Number 7.7706.
3. STERMAN, J. *Business Dynamics: Systems Thinking and Modeling for a Complex World*. Boston: McGraw-Hill, 2000. 982 p. ISBN 0-07-231135-5.
4. EVANS, J. *Taxing time for Eurpean Biodiesel.* Biodiesel Magazine, 2008 (http://www.biodieselmagazine.com/article.jsp?article_id=2386)
5. LANCELLOTTI, A. *The Splash and Dash is over: How can the Brazilian Biodiesel be Competitive.* Frost & Sullivan Consulting, 2009 (http://www.frost.com/prod/servlet/market-insight-top.pag?Src=RSS&docid=156819622)
6. SANDVIK, S. *Impacts of peak oil and food based biofuel production on long-term food security- A dynamic policy model.* Master Thesis (2008), System Dynamics Group, University of Bergen , Norway.
7. ELMENDORF, D.W. *The impact of ethanol use on food prices and Greenhouse-gas emissions.* Congressional Budget Office Paper 2009, (Congress of the United States).
8. KRAWCZYK T. *Biodiesel-alternative fuel makes inroads but hurdles remain.* INFORM 7, 1996, p. 801–829.
9. LANE, J. *German Biodiesel taxes to rise 40 percent in January: Producers cry extinction.* Biofuel Digest, 2008 (http://www.biofuelsdigest.com/blog2/2008/07/31/german-biodiesel-taxes-to-rise-40-percent-in-january-producers-cry-extinction/).
10. CHISTI, Y. Biodiesel from Algae. *Biotechnology Advances*, 2007, Vol. 25, p. 294–306.
11. FORRESTER, J.W. *Urban Dynamics,* Waltham: Productivity Press, 1969, 285 p. ISBN-10-0262060264.
12. HOGAN, M. *Analysis-German tax hits Europe's biggest biodiesel market,* 2007 (http://uk.reuters.com/article/idUKL0231973020070202)

CYSENI 2010, May 27–28, Kaunas, Lithuania
ISSN 1822-7554, www.cyseni.com

STRATEGIC SELF MANAGEMENT: COMPARISON OF ENERGY ACCOUNTING METHODS FOR ENERGY PRICE EVALUATION OF THE LITHUANIAN ENERGY SECTOR

K. Biekša, A. Klevienė
Lithuanian Energy Institute
Laboratory of Regional Energy Development
Breslaujos str. 3, LT-44403 Kaunas - Lithuania
Phone: +370 680 16985, +370 37 401982
Email: bieksa@mail.lei.lt, audrone@mail.lei.lt

ABSTRACT

A concept of sustainability became a core element of our modern-day life. Nevertheless our lifestyle is not nearly enough sustainable up to this day. Even our intellectual wealth is far away from the origin of everlasting approach. We all were witnesses last year when a crisis has reminded that we live in fragile world where not only the environment and ecosystems are vulnerable, but where nowadays economic growth and social activities are in the certain limits. National development strategy, the persistent structure of energy management institutions and the finance accounting system gives a priority to the economic growth and the management of the economy, while the environment protection and the sustainable development tasks are left aside as needful, but not of a primary importance. While economic activities show recovery signs the energy prices in Lithuania are dramatically increasing. Politicians and economists emphasize the closure of Ignalina nuclear power plant and dissolution of Leo LT partnership as the main factors of changes of energy prices. Nonetheless the main factors of energy sector growth ignore the environmental costs of economic activities. “Environmental accounting”, “green accounting”, “ecological footprint” methods provide basis to include such accountings into all kind of energy costs. Sustainable development paradigm extends accounting elements from pure economical to environmental and nature’s sources. It’s become true to evaluate and account all possible sources and cost, which are necessary for actual energy sector and will be necessary for future generations. Using concepts, ideas and indicators of sustainable development the comparison of energy accounting methods, their variations, possibilities, limitations, indicators and actuality of implementation will be examined. The most attentions of the article will be focused on identification of methodological problems of energy accounting economy in Lithuania and investigation of possibilities to use green accounting methods of sustainable development of energy sector.

Keywords: sustainable development, accounting models, green accounting, environmental accounting, ecological footprint, renewable recourses, RES (renewable energy resources)

1. INRODUCTION

Nowadays became obvious, that human knowledge about nature, society and economy development and their interactions is not sufficient for safe use them in practice. Natural resources eventually became the domain of economics, where the economy is an open system within the ecosphere, importing useful resources from the natural world and exporting wastes (pollution) back to the environment. The environment provides services that we must have and cannot supply. All economic activity is thus enabled by the natural environment and all economic production is actually consumption of natural resources. The economic growth suggests that the scarcest factor now is natural capital or natural resources, which with human economic activity continue to draw down. Our priority number one is to stop further depletion of natural resources as soon as possible. However essentially is easier to prepare asset accounts first, using approaches of *weak* and *strong* sustainability.

Weak sustainability requires that the combined *value* of all assets remains constant and where it is possible to substitute one form of capital by another, so natural capital can be depleted or the environment degraded as long as there are compensating investments in other types of capital.

Strong sustainability is based on the concept that natural capital is a complement to manufactured capital, rather than a substitute. Renewable resources can be exploited only at the natural rate of net growth. The use of non-renewable resources should be minimized and used only at the rate for which renewable substitutes are available. Emissions of wastes should not exceed the assimilative capacity of the environment. The indicator of sustainability requires that all natural capital is measured in physical units.

In the last 50 years Gross Domestic Product (GDP) was considered not simply as tool for economic management but also as indicators of economic performance and economic wellbeing, and of a country's "income". GDP measures economic activity in terms of the amount of final demand satisfied by economic output, however, activity has many negative external effects. These can often be described as environmental externalities: pollution of air, water and soil caused by production. Some of the damage caused by this pollution is reflected in the national accounts, since output figures are lower than they would otherwise have been. Environmental damage directly affects human welfare and this loss is not reflected in the national accounts. Examples of this loss of welfare are the discomfort of breathing polluted air. This defensive expenditure does not contribute to welfare, but because it is final expenditure, it is counted as part of GDP.

2. ECONOMIC GROWTH AND ENERGY INTESNITY LEVEL

The most rapid growth in the Lithuanian economy during the period from 2000 to 2008 was observed in 2003 (10.2%), after the recovery from the Russian crisis (in 1999, GDP went down by 1.1%). Later the GDP growth rate in Lithuania was among the most rapidly growing in the EU-27 countries (annual growth rate around 7%). However, the global financial crisis, which had started at the end of the summer of 2008, and the consequent economic difficulties made a major impact on the Lithuanian economy. In 2008, the GDP growth rate significantly slowed down and stood at 2.8%. In 2008, provisional GDP at current prices amounted to LTL 111.2 billion. GDP per capita in purchasing power standards amounted to 33111, i.e. 61% of the EU-27 average [1].

Indicators of the Lithuanian GDP (using Purchasing Power Parities) and final electricity consumption per capita are between the lowest in the EU countries. Final energy consumption during the last five years period has increased by 19.3%. Due to the closure of Unit 1 at Ignalina NPP total primary energy has decreased by 6% in 2005 and net electricity export decreased by 59%. However the level of energy intensity in Lithuanian economy is 432.5 and it is one of the highest in EU countries, compare average level of 169.3 in EU countries, or with lowest 103,1 in Ireland [1].

3. LITHUANIAN ELECTRICTY SECTOR

There are three main activities of the Lithuanian electricity market – power generation, electricity transmission and supply (distribution). The principle of electricity market is that the electricity transmission and supply companies are having monopoly rights. AB "Lietuvos energija" is an owner of transmission network (110-330kV) and is an energy market operator. There are three public suppliers of electricity through a distribution network: two companies (AB RST and AB VST, where after 2010 July 1st are planning to establish one distribution company) own the distribution networks and one state enterprise "Visaginas energija" has rights to distribute electricity in Visaginas town. There are several minor companies which operatetheir own distribution networks directly connected to the transmission network. A share of networks in electricity market and the amount of purchasing electricity are shown in a table below.

Table 1. The amount of electricity supplied to electricity market in 2008

Suppliers	**Amount of electricity, MWh**	**Market share, %**
Independent suppliers	1312	13
AB “RST”	4598	44
AB “VST”	4351	42
Public supplier “Visagino energija”	66	1
TOTAL	10327	100

Source: Energy market regulation // Report. National control commission for price and energy regulation, Vilnius, 2008.

The total installed capacity of power generators in Lithuania was around 5000 MW, and total gross production around 13900 MWh in year 2008. The final consumption of electricity in all economic sectors was around 9040 MWh. The Ignalina Nuclear Power Plant (NPP) was the dominant producer of electricity in the Lithuanian energy sector, as it produced about 71% of all electricity produced nationally. The electricity produced at Ignalina NPP was used not only for domestic purposes, but is exported as well. Following the Accession Agreement to the EU, Lithuania closed the first reactor on 31st December 2004 and the second reactor closed at the end of 2009. The share of electricity produced in Ignalina NPP will be taken over mainly by the Lithuanian Power Plant and the largest combined heat and power plants at Vilnius and Kaunas [4].

The total amount of electricity produced at Ignalina NPP was 9893.7 GWh in year 2008. About 5688 GWh were sold in contractual prices and 1344 GWh were sold additionally in auctions, an about 2127 GWh were exported [3].

The energy production capacity will exceed the energy consumption demand in the period of 2009–2011. However deficits of maximum available power are planned from 2010. To cover this deficit Lithuania is planning to buy the lack of power from the neighboring energy systems. Also the share of renewable energy source is planned to increase, for example capacity of installed wind generators is planned to increase up to 200 MW. According EU directive 2009/28/EB on the promotion of the use of energy from renewable sources use of renewable energy resources (RES) the national overall target for the share of energy from renewable sources in gross final consumption of energy in 2020 is 23%, or 10% from the total electricity consumption by year 2025. However according EU directive 2001/77/EC the amount of energy produced at RES compare to total energy production should achieve 12%, or production of electricity at RES should achieve 7% by year 2010. The total installed RES power capacity is about 115 MW by year 2008 (see table no.2 below) and the energy production in RES was about 595 GWh in year 2008, where a major part of electricity or 400 GWh were produced in hydropower plants, wind energy sector produced 131 GWh and biomass sector – 65 GWh [3].

Table 2. Electricity generation capacity in Lithuania, 2008

Power sources	**Install power, MW**	**Available power, MW**	**Energy supply in GWh**
Ignalina AE	**1300**	**1183**	**9140**
Lithuanian power plant	1800	1732	779.7
Mažeikių power plant	160	148	125.7
Vilniaus power plant	372	355	535.8
Kauno power plant	170	161	616.8
Kauno energy	8	7	-
Klaipėda energy	11	9	14.2
Panevėžio power plant	35	33	164.4
Industrial power plants	98	96	129.2
Total in CHP	**2654**	**2541**	**2365.8**
Kaunas HE	101	51	325.7
Kruonio HA	900	760	586.4
Small hidro power plants	26	26	74.4
Total in hidro power plants	**1027**	**837**	**986.5**
Biomass power plants	21	21	64.8
Wind generators	68	68	130.9
Total biomass/wind	**89**	**89**	**195.7**
Other power plants	**-**	**-**	**97.9**
TOTAL	***5070***	***4650***	***12785.9***
Longterm reserve needed		**1300**	
Power balance (overproduction)		**1300**	
Total final powr/consumption		**2050**	**8398**
Industry			2055
Households			2794
Agriculture			226
Other			3323

Source: Security of supply in the Lithuania electricity energy market // Monitoring report. Ministry of Energy. 2009.

4. REGULATION OF ELECTRICTY PRICES

Looking back to a time than a major part of electricity were produced at Ignalina NPP the average price for electricity production in domestic market was approved to 7.03 cents/kWh in 2009. However the National commission of energy price regulation and control decided that after the examining the calculations of production costs some of production costs can be reduced and it confirmed the 6.11 cents/kWh for the average price in the domestic market. Commission confirmed additional amount of 27.9 mill. Lt [3] as necessary expenditure and it was included in the public service obligations (PSO).

Production prices (electricity and reserve power) and the independent supply electricity prices are non-regulated, unless the independent electricity suppliers take up more than 25% of electricity sales market in Lithuania. The prices for electricity transmission, distribution and public supply are regulated by setting the upper price limits. Adjustable public tariff include all social categories of users - the population, small, medium and large business.

The upper limits of public tariff rate are fixed for each public suppliers individually every year. The public tariff of electricity consists of the generation, transmission services, distribution services in the medium and low voltage networks and the service of electricity supply. Public tariff rate depends on the production price volatility.

The volume of produced electricity at AB “Lithuanian power plant” has increased from 600 MWh in year 2008 to 800 MWh in year 2009 [16]. Electricity generation is necessary to maintain the existing equipment readiness. Therefore unstable work schedule of power generators are significantly increasing fuel costs. After assessment of influence of gas price and its transportation costs, the accumulated stocks of fuel and availability to use renewable source for electricity production, the price of public service obligation for energy production in AB “Lithuanian power plant” was set to 37.35 cents/kWh, where about 94% of the energy production price goes for fuel costs.

In Figures below you can see approximate evaluation of electricity price components, which makes final tariff for regulated market in 2009 and prognosis for 2010. A price of electricity production is calculating using formula: Final tariff – (VAT + transmission + distribution + PSO) = electric power price [7].
Regulated energy price components are presented in picture below.

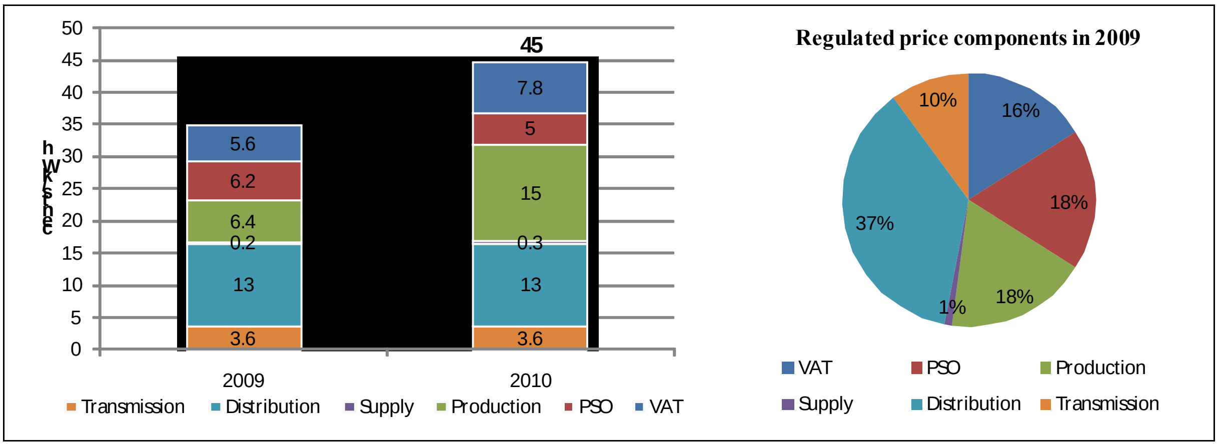

Fig. 1. Regulated electric power price components
Source: www.enefit.lt Enefit Co. the Lithuanian subsidiary of Eesti Energia AS Co

National control commission for prices and energy has provided the following calculation of average price of production of electricity. Electricity provided from producers or independent suppliers additional [2].

Table 3. The energy price for public use in year 2008 in cents/kWh

Components of electric price	Price cents/kWh
Additional price/ Actions	9.13
Energy transmission service price (330-110kV electric grids)	3.59
Energy distribution (35-6kV electric grids) RST/VST	6.75/7.45
Energy distribution (0,4kV electric grids) RST/VST	7.15/7.59
Energy price of public supplier RST/VST	0.21/0.20

Source: Energy market regulation // Report. National control commission for prices and energy, Vilnius, 2008.

The price for distribution of electric power consists of the following price components: price of transmission of electric energy through high/low voltage grids, additional price/action price and price of public service obligations (PSO). Additional price is the supply of reserve power to keep electric grid stable and reliable.

The public service obligations (PSO) consist of financial support allocated to producers of renewable energy, electricity produced in cogeneration plants, supply security and maintenance of nuclear wastes and their storage. The PSO tariff has increased about 24%

from 2003. The average PSO tariff was 3.72 cents/kWh in 2008. Cost of production of electric power at CHPP has increased by 88% consequently PSO tariff has increased by 70% (6.2 cents/kWh) in 2009. To keep continues reserve of power balance includes additional costs, which are about 57% from all electricity production costs. The energy production at RES has increased as well. Consequently it had an impact for PSO tariff. The components of PSO tariff are shown in picture below.

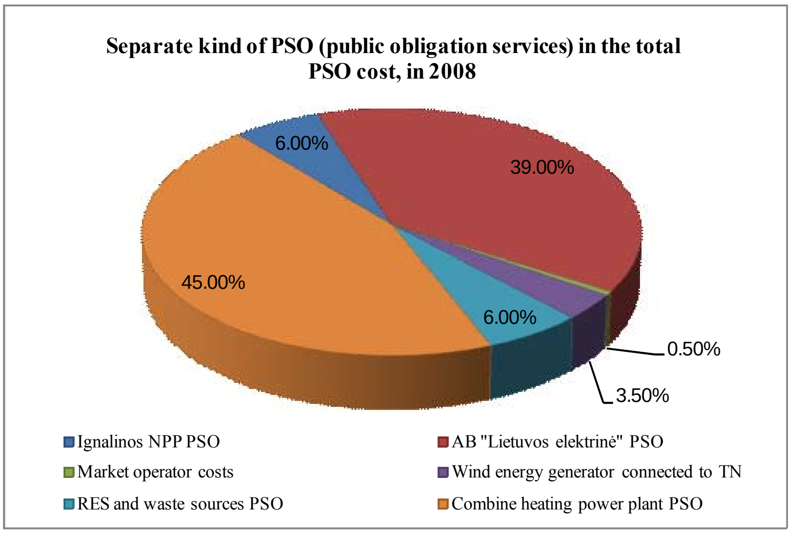

Fig. 5. The price of public service obligation (PSO)
Source: Security of supply in the Lithuanian electricity market //
Monitoring report. Ministry of Energy. 2009

5. DEVELOPMENT OF ELECTRICTY MARKET

On December 28, 2009 the National Control Commission for Prices and Energy regulation granted Baltpool Company a license to pursue the activity of electricity market operator in the Republic of Lithuania from January 1, 2010. Baltpool Co. is the electricity market operator of Lithuania. Baltpool Company was established by Litgrid company which is a daughter company of Lietuvos Energija AB. The main function of the Baltpool company is to organize electricity trade. Administered by Baltpool Co. the wholesale electricity trade in Lithuania is carried out in two ways: the trade at Lithuanian power exchange and bilateral trade between electricity generators and suppliers. Baltpool organizes wholesale electricity trade at the Lithuanian power exchange in cooperation with Nord Pool Spot – the power exchange operating in the Nordic countries. The participants of the Lithuanian power exchange are generators and suppliers from Lithuania and neighboring power systems. Electricity generated in Lithuania or imported from abroad is purchased for consumption in Lithuania and for export to neighboring energy systems. The trade is carried out on a day-ahead basis: all electricity delivery agreements are arranged day-ahead for each hour of the following day.

Electricity market regulator Baltpool company announced the data from electricty trade market for year 2010. Average purchasing price for electricity in an energy stock market was 13.9 cents/kWh in January. The amount of electricity sold in January was 536 GWh and a turnover was around 74.474 mill Litas. The situation in February was as following: Average purchasing price for electricity in an energy stock market was 15.3 cents/kWh in February. The amount of energy sold in February was 490 GWh and a turnover was around 75.104 mill. Litas.

Table 3. Participants of the electricity energy market

Licensed activities	Number of licenses	Number of active participants in the market
Transmission of electricity	1	1
Distribution of electricity	3	3
Supply of electricity	26	11
Public supply	6	3
Independent electricity supply	20	8

Source: Security of supply in the Lithuania electricity energy market // Monitoring report. Ministry of Energy. 2009.

6. CALCULATIONS OF EXTERNAL COSTS FOR ELECTRICITY

The accounting principles used in the energy sector of Lithuania are based mainly on the economic growth indicators, while the environment protection and the sustainable development tasks are left aside. The green accounting system includes environmental services, environmental damages, defensive expenditures and resource depletion factors. The direct contribution of *environmental services* to human welfare is not reflected in produced output. Two broad methods have been used to value degradation: *cost-based methods* and *damage-based methods*. *Cost-based methods* – how much would it cost to avoid the energy generation of residuals by changing production and consumption patterns. *Damage-based method is an* evaluation the damage caused by the current level of residual energy generation.

In 1991, the European Commission together with the US Department of Energy launched a joint research project ExternE to assess the environmental externalities of energy use. The label "ExternE" became a recognized "brand", the scientific quality of the work was well accepted on the international level, national and international organizations got used to referring to the ExternE numbers as a standard source for external cost data. Seven major types of damages have been assessed within the ExternE methodology. The main categories are human health (fatal and non-fatal effects), effects on crops and materials [10].

After the closure of the Ignalina NPP, thermal power plants using imported fossil fuel and releasing great amounts of various contaminants (sulphur, nitrogen, carbon oxides, solid particles and others) will become the main electricity producers. Significant increase of pollutants emitted into the atmosphere will have a great negative effect on both natural environment and people's health. The result of chemical pollution impact – acidification by sulphur and nitrogen oxides and gases causing greenhouse effect, i. e. temperature rise – at the same time negatively influences all the ecosystems. Therefore, it is very important to introduce effective measures for the reduction of regional and global pollution [9].

Lithuania signed the United Nations Convention on Climate Change (UNFCCC) as an Annex I Party in 1992 and ratified it in 1995. The Kyoto Protocol was signed in 1998 and ratified in 2002. Lithuania undertook an obligation to reduce its greenhouse gas emissions by 8% below 1990 levels during the first commitment period 2008–2012 [4].

Renewable sources are favorable for the reduction of environmental pollution. The RES plants working without greenhouse gas and other pollutant emissions can reduce negative influence on the ecosystems, can maintain the environment ecologically less polluted and can make the implementation of the international protocols easier. Conventions and directives would also provide the possibility to join trade in CO_2 emissions, thus, improving the economic and ecological situation of the country. This energy development trend is motivated by rapidly changing global climate (global warming). Emission factor for electricity production (EF_{LE}) at Lithuanian PP was estimated ex-ante, based on production of electricity and heat. The emission factor calculated based on fuel consumption from 2002 to 2005 is considered conservative, as Lithuania PP has been preparing to use higher share of orimulsion and decrease the share of natural gas, in an attempt to reduce dependence on single supplier of gas, Russia. External cost of electricity generation in Lithuania is calculated based on the emission into atmosphere of classical pollutants from the main electricity generation sources provided in table 4 below. The main electricity generation sources were Ignalina NPP, Vilnius CHP, Lithuanian PP, Kaunas CHP, Kaunas HPP, Kruonis HPP. Lithuanian external costs from electricity generation are presented in table 5 below.

Table 4. Emission of pollutants from electricity generation sources in 2005 (thous.t)

Power plants	**SO_2**	**Nox**	**NH_3**	**NMVOC**	**PPM_{25}**	**PPM_{coars}**
Lithuania PP	3.26	0.96	0	0.00002	0.00008	0.002
Vilnius CHP	0.15	0.63	0	0.01	0.003	0.00006
Mažeikiai CHP	3.67	0.23	0.000001	0.02	0.09	0.01
Kaunas CHP	0.0002	0.02	0	0	0.003	0
Ignalina NPP	0	0.01	0	0.004	0.005	0.00001
Total emissions in electricity generation, thou.t	8.9	3.6	0.0001	0.08	0.28	0.02

Source: D.Štreimikienė, R.Pušinaitė. External cost of electricity generation in Lithuania

Table 5. External cost of electricity generation in Lithuania in 2005, thous. Eur

	Lithuania PP	Vilnius CHP	Mažeikiai CHP	Kaunas CHP	Ignalina NPP	Total external cost in electricity sector
Human health						
NH_3	0.00	0.00	0.01	0.00	0.00	0.40
NMVOC	0.00	0.00	0.00	0.00	0.00	26.10
Nox	3795.50	2494.60	920.10	1.60	47.60	14392.60
PPM_{25}	0.00	1.20	34.00	1.30	1.90	0.00
PPM_{coars}	16.50	0.70	156.90	0.00	0.20	252.30
SO_2	14400.80	639.70	16192.00	1.80	0.00	39416.80
Biodiversity losses						
NH_3	0.00	0.00	0.00	0.00	0.00	0.20
NMVOC	0.00	0.00	0.00	0.00	0.00	0.00
Nox	564.60	371.10	136.90	8.90	7.10	2141.10
SO_2	453.70	20.20	510.10	0.20	0.00	1241.80
Impact on crops						
NH_3	0.00	0.00	0.00	0.00	0.00	0.00
NMVOC	0.00	0.00	0.00	0.00	0.00	2.80
Nox	123.50	81.10	29.90	1.90	1.50	468.10
SO_2	-45.70	-2.00	-51.40	0.00	0.00	-125.10
Impact on materials						
Nox	70.80	46.50	17.20	1.10	0.90	268.50
SO_2	610.40	27.10	686.30	0.10	0.00	1670.70
Total external costs in electricity sector, thous.Eur	19990.00	3680.70	18632.60	16.80	59.30	59756.50
Electricity production GWh	1073.00	1164.00	160.00	695.00	10338.00	14784.00
External cost EUR/kWh	0.02	0.003	0.12	0.00002	0.00001	0.004
External cost Cents LTL/kWh	6.45	1.04	40.44	0.01	0.00	1.40

Source: D.Štreimikienė, R.Pušinaitė. External cost of electricity generation in Lithuania

External costs in Lithuania are not fully integrated though Lithuanian power plants pay pollution taxes for atmospheric emissions; however these taxes are very low comparing with the external cost per ton of pollutants emitted into the atmosphere. The comparison of pollution taxes and external costs is presented in Table 6 [10].

Table 6. Comparison of external cost and pollution taxes in Lithuania, in Lt/t

	Damage cost	Tariffs, 2004-2009
SO_2	16300	311
No_x	16400	587
V_2O_5	38000	11485
Particulates	1345.5	184

Source: D.Štreimikienė, R.Pušinaitė. External cost of electricity generation in Lithuania

The pollution taxes are very low in Lithuania comparing with the external costs of pollution, however an increase in pollution taxes needs to be implemented through the ecological tax reform, then an increase in pollution taxes should be compensated by reduction in other taxes (profit, income, VAT) maintaining the budget revenues constant and not shifting tax burden on economy. Under the Kyoto Protocol Lithuania is committed to reduce its greenhouse gas emissions by 8% to 46.854 Mt CO_2e in the period of 2008–2012. About 74% of GHG emissions are from energy sector: extraction, transportation, storage, distribution, reuse, burning or production. The major part of GHG are emission of CO_2 – 70%, about 16% – methane, about 10% – NO_x. Total annual emission of CO_2 in Lithuania in year 2000 were 16,1 Mt (or 4.8 t/capita).

Implementing Joint Implementation projects in Lithuania, where the result is the reduction in the power use or power generation which would indirectly reduce the amount of generated power in the installations of the allowance trading scheme, it is offered to use the pollution factor equal to 0.629 t CO_2/MWh of the electricity generated. In the period of 2005–2007 average annual number of allocated allowances for installations listed in the NAP was 11.47 million. It corresponds to the average pollution of Lithuanian condensing power plant for one MWh of the generated electricity in 2002–2005. Another 1.36 million of allowances (that is 0.27 million per year) will be sold in the auctions. It is estimated, that because of closure of Ignalina NPP and increased production of power by industrial and energy sector's thermal power plants, will additionally emit 23.57 Mt of CO_2 during 2008–2012. After deduction of 2% allowances for the auctioning and deduction of 4.04 Mt which goes to the reserve for the new entrants for promotion of efficient cogeneration, 19.14 million allowances are put into reserve related to closure of Ignalina NPP. The allowances from this amount will be allocated for the existing power plants which according to their agreement with Ministry of Economy of Lithuania intend considerably increase the power production compensating for the influence of the closure of Ignalina NPP.

The external costs used to calculate this indicator are based upon the sum of three components: climate change damage costs associated with emissions of CO2; damage costs (such as impacts on health, crops etc) associated with other air pollutants (NOx, SO_2, NMVOCs, PM10, NH3), and other non-environmental social costs for non-fossil electricity-generating technologies [13]. Based on the methodology used the external costs of electricity production have fallen considerably between 1990 and 2004 in almost all Member States. However, the average external costs still represented between 1.8–6.0 Eurocent/kWh in the EU in 2004 [13]. These costs are very significant and reflect the dominance of fossil fuels in the generation mix.

Traditional fossil systems (coal, oil and to a lesser extent natural gas) exhibit the highest external costs for electricity generating technologies, in the range of 1.1 Eurocents/kWh (for advanced gas technologies) to 24.1 Eurocents/kWh (for traditional coal plants using the higher bound estimate of damage costs) [13]. These fuels accounted for about 54% of all electricity production in 2004. Renewable energy shows the lowest damages per unit of electricity.

7. CONCLUSIONS

- Energy is a substantial factor influencing the future development of our society. Strongly increased demand, volatile prices with a tendency to rise over the next year, severe impacts on the environment, energy security is energy issues which are high on the political agenda. Energy consumption is closely linked to individual behavior, development and dissemination of new technologies requires the acceptance of the public. Thus it is essential to understand people's knowledge, attitudes and perceptions of energy matters in general and of energy technologies in particular.
- The total installed capacity of power generators in Lithuania was around 5000 MW, and total gross production around 13900 MWh in year 2008.
- Looking back to a time when a major part of electricity was produced at Ignalina NPP the average price for electricity production in domestic market was approved to 6.11 cents/kWh in 2009. The new energy market regulator Baltpool company announced the average purchasing price for electricity 13.8 cents/kWh in January and 15.3 cents/kWh in February.
- Average price for electricty in 2009 transmission is 3.6 cents/kWh (10%), for distribution – 13 cents/kWh (37%), for supply – 0.2 cents/kWh (1%), production 6.4 cents/kWh (18%), PSO – 6,2 cents/kWh (18%), VAT tax – 5.6 cents/kWh (16%).
- Average price for electricity in 2010 transmission is 3.6 cents/kWh (8%), for distribution – 13 cents/kWh (29%), for supply – 0.3 cents/kWh (1%), production – 15 cents/kWh (34%), PSO – 5 cents/kWh (11%), VAT tax – 7.8 cents/kWh (17%).
- According EU directive 2009/28/EB on the promotion of the use of energy from renewable sources use of renewable energy resources (RES) the national overall target for the share of energy from renewable sources in gross final consumption of energy in 2020 is 23%, or 10% from total electricity consumption by year 2025.
- The principal targets of EU directives – GHG emissions should not exceed Kyoto target (8% reduced GHG emission level in 1990); CO_2 emissions should decline by 32% from 2004 level in 2010; SO_2 emissions should decline by 3% from 2004 level in 2010; NO_x emissions should decline by 21% from 2004 level in 2010.
- After the closure of the Ignalina PP, thermal power plants using imported fossil fuel and releasing great amounts of various contaminants (sulphur, nitrogen, carbon oxides, solid particles and others) will become the main electricity producers. Significant increase of pollutants emitted to the atmosphere will have a great negative effect on both natural environment and people's health.
- Based on the ExternE methodology used for evaluation of external costs of electricity production the costs have fallen considerably between 1990 and 2004 in almost all EU Member States. However, the average external costs still represented between 1.8–6.0 Eurocent/kWh in the EU in 2004 [13]. However in Lithuania this would increase the average electricity price by about 1.4 Lt cent/kWh in Lithuania [13].

REFERENCES

1. Statistical yearbook of Lithuania 2009 // Statistic Lithuania, Vilnius, 2009, ISSN 2029-3631, p.704. http://www.stat.gov.lt
2. Energy market regulation. Report // National control commission for price and energy regulation, Vilnius, 2008, p. 24.

3. Security of supply in the Lithuania electricity energy market // Monitoring report. Ministry of Energy. 2009, p. 41.
4. National greenhouse gas emission inventory report 2008 of the Republic of Lithuania. Annual report under the UN Framework convention on climate change // Ministry of Environment, Vilnius, December 2008.
5. Electricity market operator "Baltpool". http://www.baltpool.lt
6. R.Fernandez. External cost of electricity production // European environment agency. 2006, p. 35.
7. Enefit company, the Lithuanian subsidiary of Eesti Energia AS Co., http://www.enefit.lt
8. About energy prices in 2007 year // Presentation of National Control Commission for Prices and Energy regulation, 2007, http://www.regula.lt, p. 17.
9. Bronius Jaskelevičius. Kyoto Protocol requirement and wind energy evolution in Lithuania // Ekologija. 2007. Vol.53. No.3.P.1-8
10. Extern E: Externalites of energy // European Comission, Directorate General XII, Science Research and Development, Luxembourg, 1995, p. 266–366.
11. Policies & Measures and Projections of Greenhouse Gas Emissions in Lithuania. Report // Ministry of Environment of the Republic of Lithuania, Vilnius, 2009.
12. Benaiciai wind power project 2nd monitoring report // Environmental investment group, 2009 septemeber 23, ver 2.1, p. 9. JI project design documents www.unfccc.com
13. D.Štreimikienė, R.Pušinaitė. External cost of electricity generation in Lithuania // Environmental research, engineering and management, 2008, No 2(44), p.33–40.
14. Dalia Štreimikienė, Inga Konstantinavičienė. JT Bendrosios klimato kaitos konvencijos įsipareigojimų įgyvendinimo galimybės atsižvelgiant į šiltnamio dujų emisijų Lietuvoje mažinimo priemones // Energetika, ISSN 0235-7208. 2003. Nr. 1, p. 28–37.
15. Inga Konstantinavičienė, Vaclovas Miškinis. Atmosferos taršos energetikos sektoriuje imitacinis modeliavimas // Energetika, ISSN 0235-7208 . 2002. Nr. 2, p. 23–28.
16. Information database on JI projects: Climate change, Joint implementation // Information about JI projects, www.laaif.lt

CYSENI 2010, May 27–28, Kaunas, Lithuania
ISSN 1822-7554, www.cyseni.com

SPREAD OF ENERGY SUPPLY DISTURBANCES IN THE NETWORK SYSTEMS

L. Martišauskas, J. Augutis
Lithuanian Energy Institute
Laboratory of Nuclear Installation Safety
Breslaujos str. 3, LT-44403, Kaunas – Lithuania
Phone: +370 37 401938, +370 37 401973
Email: linasm@mail.lei.lt , juozas@mail.lei.lt

J. Augutis
Vytautas Magnus University
K. Donelaičio str. 58, LT-44248, Kaunas – Lithuania
Phone: +370 37 203775
Email: j.augutis@adm.vdu.lt

ABSTRACT

Energy supply disturbances play a considerable role in security of energy supply. Level of energy security varies regarding occurrence of energy supply disturbances. Thus, it is very important to analyse energy disturbances: affect to energy systems (disturbance distribution in the network systems), how systems cope with the disturbance, probability of occurrence and consequences of energy disturbance.

Spreading of energy supply disturbance in the network systems is analysed in the paper. Mathematical model of the potential energy disturbances spread in the network systems is developed and presented. Energy supply disturbances are characterized in parameters of disturbance duration, price and supply deviations of basic supply scenario, fuel type etc. Disturbances occur with different severity level and cause consequences of various severities according to the parameters of energy supply disturbances. Theory of Markov chains is used, distributions of different energy disturbances in the network systems are analysed as well as issues of their stability. Theoretical results are illustrated by simulation of some potential energy disturbances. Probability of disturbance occurrence is calculated, distribution of disturbance hazard in the network system is evaluated and stability conditions are defined.

Keywords: security of energy supply, energy supply disturbances, network systems, mathematical simulation

1. INTRODUCTION

Priorities of every country's energy security is ensuring reliable energy supply and functionality of energy infrastructure, diversification of energy supply sources, reduction of dependence on energy resource import (by reducing energy intensity and switching to alternative or renewable energy resources).

Threats to energy security include the political instability of several energy producing and supply countries, the manipulation of energy supplies, the competition over energy sources, attacks on supply infrastructure, as well as accidents and natural disasters [1].

The International Energy Agency (IEA) [2] "energy security" describes as "the uninterrupted physical availability at a price which is affordable, while respecting environment concerns". The need to increase "energy security" was the main objective underpinning the establishment of the IEA. According to IAE, energy security has many aspects: long-term energy security is mainly linked to timely investments to supply energy in line with economic developments and environmental needs. On the other hand, short-term energy security is the ability of the energy system to react promptly to sudden changes in supply and demand. Another way to look at energy security is to study the different energy sources (coal, oil, gas, nuclear, renewables), intermediate means (electricity, refineries) and transportation modes (grids, pipelines, ports, ships). All of these have risks of supply interruptions or failures, challenging the security of undisturbed energy supply [2].

High focus of this article is an analysis of energy supply disturbances and their impact or effect to energy system.

2. ENERGY SYSTEM

The total energy system, from generation and supply to demand undergoes continuous change. Supply options (renewables, intermittent sources, clean fossil options with CO_2 removal and storage) emerge and are developed at the cost of other options. Energy use is growing (especially electricity and transport fuels) and is influenced by growth and decline of various economic sectors. The energy infrastructure (merging electricity, heat, gas, fuels supply and demand, including storage) is an essential element of the total energy system. The energy infrastructure is typically a “slow and inert” component of the energy system. Modifications require considerable investments and once choices are made, energy infrastructure is in place for decades, possibly resulting in lock-in situations for the longer term. Preferences may therefore emerge to make use of the existing infrastructure as far as possible to avoid expensive changes. On the other hand, existing energy infrastructure is sometimes a key barrier for introducing new supply or energy efficiency measures [3].

Energy system is a complex system. It consists of energy supply network as a complex systems with interdependencies. The energy system is composed of primary energy sources (nuclear, fossil, renewable etc.), energy generators from fuel (energy source) and energy supply networks (electricity, gas, oil, heat etc.). Each of energy supply network is another system with many links of transmission and distribution networks. The main purpose of every energy supply network is to provide energy to the consumer. The main objective of the consumer is to get energy at an affordable price and in reliable way.

Three stages of each energy generator in its life cycle can be drawn: 1) research, testing and prototype, 2) operation and maintenance, 3) waste management and decommissioning.

Let’s mark energy sources as $E_1, E_2, \ldots, E_N$; transmission networks as $T_1, T_2, \ldots, T_N$; distribution networks as $D_1, D_2, \ldots, D_N$ and consumers or end-users as $C_1, C_2, \ldots, C_N$. All these components compose energy network system. In a simple way it can be drawn as shown in the scheme:

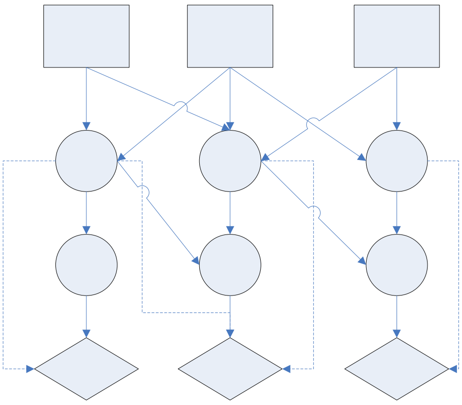

Fig. 1. Simple scheme of energy system

Energy system can be affected by some hazards or disturbances. These disturbances come in three types: technical, economical and socio-political. Every energy system must have ability to cope with energy supply disturbances. More about energy supply disturbances and how well the energy supply network reacts to disturbances it is facing is described in more detail further.

2.1. Energy supply disturbances

The importance of energy supply and energy supply disturbances and concepts of them is determined in the previous papers (Augutis et al. [4, 5]).

Disturbances of energy system are external natural events or external events related to the human being activity, which may disturb energy system or some elements of the system work. Three types of energy disturbances – technical, economical and socio-political – are considered in this methodology.

2.1.1. Parameters of energy supply disturbance

Each of energy supply disturbance is characterized in parameters. All values of energy supply disturbance parameters can be ranked in points due to its severity. The concept of basic scenario is needed to describe disturbance parameters. The basic scenario shows a current situation of energy sector when primary energy supply disturbances do not exist till 2025, fuel and primary energy sources are supplied as it was predicted by demand for electric energy and heat production; also prices of primary energy sources or fuel change by average high forecasts.

Parameters of energy supply disturbance:

1) Fuel type or primary energy source of restricted supply – φ_i. For instance, oil products (fuel oil), gas, nuclear fuel, fossil, renewable etc.
2) Part of energy supply deviation of basic supply scenario – δ_i.
   It is primary energy supply amount reduction in percent of basic supply scenario. Each type of primary energy supply reduction is from 0% to 100% for basic scenario supply amounts in appropriate period.
3) Duration of primary energy sources or fuel supply interruption – t_i, $0 < t < \infty$. This parameter shows duration of energy supply interruption.
4) Price deviation of fuel or primary energy sources from predicted price projected in basic scenario – σ_i. There is committed a period of predictable price increase. The maximum price deviation must be chosen.

A set of various energy supply disturbances is obtained from different values of disturbance parameters. To evaluate probability of disturbance occurrence, probabilities of parameters values occurrence is needed. These probabilities should be assessed by experts and/or obtained from statistical data. The probability matrix of disturbance parameters values is obtained (Table 1).

Table 1. Values and probabilities of energy disturbance parameters

	Value	**Probability**
Fuel type or primary energy source	Oil	$P(\varphi_1)$
	Gas	$P(\varphi_2)$
	Nuclear	$P(\varphi_3)$
	Renewable	$P(\varphi_4)$
	Coal	$P(\varphi_5)$
	…	…
Part of energy supply deviation of basic supply scenario	0 %	$P(\delta_1)$
	20 %	$P(\delta_2)$
	40 %	$P(\delta_3)$
	…	…
Duration of primary energy resources or fuel supply interruption	1 month	$P(t_1)$
	3 months	$P(t_2)$
	6 months	$P(t_3)$
	…	…
Price deviation of fuel or primary energy resources from predicted price projected in basic scenario	10 %	$P(\sigma_1)$
	20 %	$P(\sigma_2)$
	30 %	$P(\sigma_3)$
	…	…

where $\sum_{i=1}^{N} P(\varphi_i)=1$, $\sum_{i=1}^{N} P(\delta_i)=1$, $\sum_{i=1}^{N} P(t_i)=1$, $\sum_{i=1}^{N} P(\sigma_i)=1$.

Evaluation of country‘s general functioning of energy system should use this matrix, where probabilities of this matrix should be obtained from evaluation of experts and/or statistical data.

Energy supply disturbance is a function of parameters: $D(\varphi,\delta,t,\sigma)$. Since all disturbance parameters are independent, probability of disturbance occurrence is obtained from multiplication of appropriate probabilities of disturbance parameters:

$$P(D)=P(\varphi_i)\cdot P(\delta_i)\cdot P(t_i)\cdot P(\sigma_i),\ i=1,2,\ldots,N. \tag{1}$$

2.2. Barriers of energy system

It is very important to know how well the energy supply network reacts to disturbances it is facing. Each of the energy systems itself is a system of barriers to these disturbances. The energy system is expected to activate various barriers to cope with the potential energy supply disturbances. Some energy systems have safety systems as a barrier, e. g., power system barriers: switchers, control systems, dispatcher etc.

3. METHODOLOGY OF THE SPREAD OF ENERGY SUPPLY DISTURBANCES IN THE NETWORK SYSTEMS

Let’s suppose that energy system has N components. These components are network nodes. Existing relations between components can be depicted with an oriented graph with network nodes. In this way we have network with nodes and transitions from one node to another. Energy system all the time can be affected by some disturbances. Energy supply disturbances spread in the network system from one component to another and, thus, disturbance reaches all the network nodes after a certain number of steps, which are called cycles in this methodology. Disturbance is transferred from one node to another in one cycle. In this case, the cycle can be described as a period of time. Disturbance after a certain number of cycles would stabilize in the network system, i.e. disturbance converges to the steady state System components may have barriers, a response to energy disturbance. Barrier mitigates disturbance or even destroys it, therefore barriers in the energy system may be some safety systems. If the network nodes have barriers, energy supply disturbance after a certain number of cycles should be destroyed or at least be mitigated. Methodology of the spread of such disturbances in the network systems is proposed further. Methodology is developed according to methodology described in Augutis and Uspuras monograph (section 2) [6] with some changes and applications to energy sector.

3.1. Sources of energy supply disturbances

As it was already mentioned in this paper, disturbance comes in three types: technical, economical and socio-political. Energy supply disturbance will be noted as *H*. Source of disturbance is one of the network nodes in which disturbance can arise or occur. Energy supply disturbance can access neibhouring nodes and spread further to other nodes in the next step. Let's begin with investigating a case, in which one network node is a point source with disturbance level $H_1(0)=H$. Dependencies between network components or network flow matrix will be marked as follows: $Q=\left[q_{ij}\right]$, where $i,j=1,2,\ldots,N$.

3.2. Energy supply disturbance distribution in Markov chains

Let's suppose that we have a network with *N* nodes. Disturbance from the node *i* can be transferred only to one node *j*, which is selected according to transition probability P_{ij}. Thus, during each cycle, disturbance can occur in only one network node. An assumption is made that transition probabilities have Markov [8] feature. If the disturbance that exists in node *i* after *n* cycles will be marked as $X(n)$, thus

$$P_{ij}=P\big(X(n)=j\big|X(n-1)=i\big)=P\big(X(n)=j\big|X(1)=i_1,X(2)=i_2,\ldots,X(n-1)=i_{n-1}\big). \quad (2)$$

This way the process $X(n)$ will be Markov chain with finite set of the states $\{1,2,\ldots,N\}$. The homogeneous Markov chain should also be discussed since P_{ij} is not dependent on *n*. Let's mark disturbance occurrence probability in the *i* node after *n* cycles $\pi_i(n)$. It is clear that $\sum_{i=1}^{N}\pi_i(n)=1$.

Now it can be returned to the disturbance level calculation in each node after *n* cycles. Naturally, it is possible to determine only average disturbance level $\bar{H}_i(n)$ in each node since disturbance after *n* steps is a random value. If we would also make an assumption that all the network line flows are equal to 1, the following would be obtained:

$$\bar{H}_i(n)=\frac{1}{n}\sum_{k=1}^{n}H\cdot\pi_i(k)=\frac{H}{n}\sum_{k=1}^{n}\pi_i(k), \quad (3)$$

here H – the disturbance level that has occurred in one of the network nodes during zero cycle, i.e. we hold that this node is a point source of the disturbance.

From the theory of the Markov chains is known that state probabilities after *n* cycles are described using recursive formulas:

$$\left[\pi_1(1),\pi_2(1),\ldots,\pi_N(1)\right]=\left[\pi_1(0),\pi_2(0),\ldots,\pi_N(0)\right]\cdot\left[P_{ij}\right], \tag{4}$$

or in matrix form:
$\vec{\pi}(1)=\vec{\pi}(0)P$, here $P=\left[P_{ij}\right]$ - transition probability matrix and $\vec{\pi}(0)=[1,0,\ldots,0]$, if we make an assumption that the point source of the disturbance is located in the first node.
Then it follows:

$$\vec{\pi}(2)=\vec{\pi}(1)P=\left(\vec{\pi}(0)P\right)P=\vec{\pi}(0)P^2,\ i,j=1,2,\ldots,N. \tag{5}$$

Given that $\vec{\pi}(0)=[1,0,\ldots,0]$, we receive:

$$\vec{\pi}(n)=\vec{\pi}(n-1)P=\vec{\pi}(0)P^{n-1}=\left[P_{11}^{(n-1)},P_{12}^{(n-1)},\ldots,P_{1N}^{(n-1)}\right]. \tag{6}$$

Thus, we can calculate the average disturbance level in the node *i* after *n* cycles $\bar{H}_i(n)$ recursively, using the following formula:

$$\bar{H}_i(n)=\frac{H}{n}\sum_{k=1}^{n}P_{1i}^{(k-1)}, \tag{7}$$

here $P_{1i}^{(k-1)}$ is the *i* element of the first line of matrix P^{k-1}.

3.3. Marginal distribution of the energy supply disturbance in the network system with barriers

In the majority of energy network systems disturbance in its whole or in part is eliminated during certain time of a number of cycles. Of course, if the source of the disturbance in such systems was a point source (single), the disturbance would be entirely destroyed or minimized to the secure level by the system during certain period of time or after a certain number of cycles. In the energy systems, however, sources of disturbances may be inexhaustible, i.e. infinitive and, at the beginning of every cycle, the disturbance can renew.
In this subsection we will analyse the marginal energy supply disturbances in energy network systems with the infinitive disturbance sources and node barriers.

The barrier of the network node *i* is considered as the value of the number B_i ($0\le B_i\le 1$), by which the disturbance level *H* that occurs in this node is multiplied. Thus, when $B_i=1$, disturbance is fully transmitted, and when $B_i=0$, all of the disturbance, that makes way to the node *i* to be destroyed.

Let's assume that the first node of the network is the infinitive source of disturbance that increases disturbance level by the value *H* during each new cycle. Firstly, we shall make an assumption that a marginal disturbance distribution exists under such conditions, i.e.

$$\lim_{n\to\infty}H_i(n)=H_i,\ \text{where}\ i=1,2,\ldots,N. \tag{8}$$

Then, if at the end of each cycle the disturbance level that is located in the node is multiplied by the value of barrier $0\le B_i\le 1$, and the node in which the source of disturbance is located, does not have barrier (let's say it is the first one), in this case disturbance level in the first node will not change, if it is reduced by the value H after each cycle, i.e.

$$H_2q_{21}+H_3q_{31}+\ldots+H_Nq_{N1}=H_1\left(q_{12}+q_{13}+\ldots+q_{1N}\right)-H\,. \tag{9}$$

In the second node, the incoming disturbance level multiplied by the barrier value B_2 has to be equal to the outgoing disturbance level:

$$B_2\left(H_1q_{12}+H_3q_{32}+\ldots+H_Nq_{N2}\right)=H_2\left(q_{21}+q_{23}+\ldots+q_{2N}\right).$$

The case is analogous with the other nodes:

$$B_j\left(H_1q_{1j}+H_2q_{2j}+\ldots+H_{i-1}q_{i-1j}+H_{i+1}q_{i+1j}+\ldots+H_Nq_{Nj}\right)=H_i\left(q_{i1}+q_{i2}+\ldots+q_{iN}\right),$$
$$j=2,3,\ldots,N\,.$$

Joining those equations we get a system of linear equations:

$$\begin{cases}H_2q_{21}+H_3q_{31}+\ldots+H_Nq_{N1}-H_1\widehat{q}_1=-H;\\ H_1q_{12}+\ldots+H_Nq_{N2}-H_2\widehat{q}_2/B_2=0;\\ \ldots\\ H_1q_{1N}+\ldots+H_{N-1}q_{N-1N}-H_N\widehat{q}_N/B_N=0.\end{cases} \tag{10}$$

This system can be written in the form of matrix

$$\tilde{Q}\overline{H}=\overline{C}\,. \tag{11}$$

The main matrix of this system is:

$$\tilde{Q}=\begin{bmatrix}-\widehat{q}_1 & q_{21} & q_{31} & \cdots & q_{N1}\\ q_{12} & -\widehat{q}_2/B_2 & q_{32} & \cdots & q_{N2}\\ \cdots & \cdots & \cdots & \cdots & \cdots\\ q_{1N} & q_{2N} & q_{3N} & \cdots & -\widehat{q}_N/B_N\end{bmatrix},$$

constants vector $\overline{C}=\left[H,0,\ldots,0\right]^T$, and unknown vector $\overline{H}=\left[H_1,H_2,\ldots,H_N\right]^T$.

To investigate the existence of the marginal distribution, disturbance distribution $\vec{H}(n)$ will be expressed as iterative equation. As there is the barrier, we shall introduce a diagonal matrix

$$B=\begin{bmatrix}B_1 & 0 & 0 & 0\\ 0 & B_2 & 0 & 0\\ \cdots & \cdots & \cdots & \cdots\\ 0 & 0 & 0 & B_N\end{bmatrix}.$$

Now we can express the system of equations this way:

$$\left[H_1(n+1),H_2(n+1),\ldots,H_N(n+1)\right]=\left[H_1(n),H_2(n),\ldots,H_N(n)\right]\times B\times Q+\left[H,0,\ldots,0\right], \tag{12}$$

here $Q=\begin{bmatrix} q_{11} & q_{12} & \cdots & q_{1N} \\ q_{21} & q_{22} & \cdots & q_{2N} \\ \cdots & \cdots & \cdots & \cdots \\ q_{N1} & q_{N2} & \cdots & q_{NN} \end{bmatrix}$.

We mark $\vec{H}(n)=\left[H_1(n),H_2(n),\ldots,H_N(n)\right]$, $\vec{H}(0)=\left[H,0,\ldots,0\right]$ and obtain that

$$\vec{H}(n+1)=\vec{H}(n)\cdot B\cdot Q+\vec{H}(0). \qquad (13)$$

In the case of point source (single) of disturbance distribution we obtain that

$$\vec{H}(n+1)=\vec{H}(n)\cdot B\cdot Q. \qquad (14)$$

4. NUMERICAL SIMULATION AND RESULTS

Numerical simulation is based on European power system. The European AC (alternating current) transnational transmission network has been modelled with an equivalent representation (Fig. 2.) where each country (or aggregate of countries, such as Balkans) is presented by a node, interconnected with the neighbouring countries via equivalent lines. For the analysis, an oriented graph with 20 nodes and 37 links was chosen. In this case, European UCTE (Union for the Coordination of Transmission of Electricity) countries constituted a set of nodes and the network of transmission lines – a set of links.

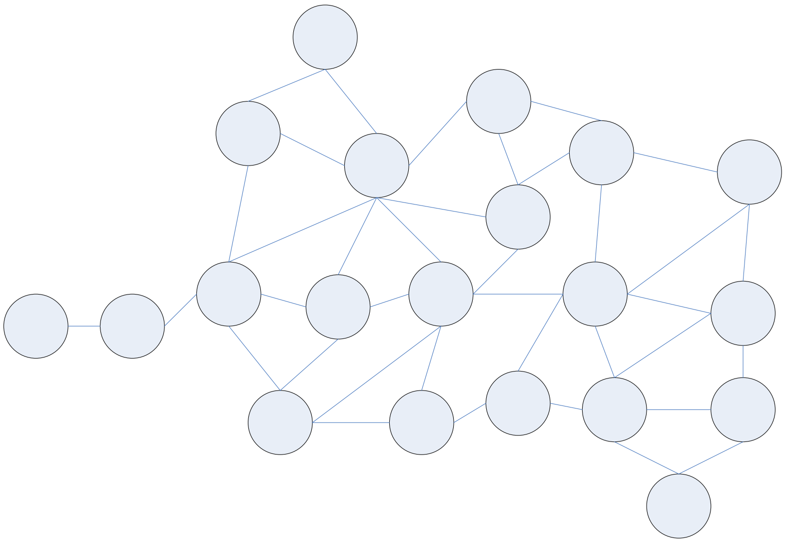

Fig. 2. Equivalent representation of the European AC transmission network

Abbreviations used in the Fig. 2.: PT – Portugal, ES – Spain, FR – France, IT – Italy, BL – Belgium and Luxembourg, CH – Switzerland, DE – Germany and Denmark West, NL – The Netherlands, SI – Slovenia, AT – Austria, CZ – Czech Republic, PL – Poland, HR – Croatia, HU – Hungary, SK – Slovak Republic, BX – Balkan countries (Albania, Bosnia and Herzegovina, Kosovo, Montenegro, Republic of Macedonia, Serbia), GR – Greece, BG – Bulgaria, RO – Romania, UA_W – Ukraine West.

Flow matrix is calculated according to transmission capacity between neighbouring countries. Statistical data used are transmission capacity equal to the corresponding cross-border Net Transfer Capacity (NTC). NTC values have been provided by ENTSO-E (European Network of Transmission System Operators for Electricity) [7]. As far as the NTC values (for both flow directions) are concerned, the latest ENTSO-E available data (Summer 2009: see [7]) have been used.

The main purpose of the numerical simulation, using developed methodology, is to determine how occurred energy supply disturbance effects power system, which countries it has reached the fastest and where is the highest disturbance level and how it is distributed across European countries.

The case of system with barriers was analyzed, when the disturbance source is one country, then disturbance occurs and causes a certain level of damage and we are interested in how disturbance spreads to other countries. Yet it is assumed that the power system has barriers to protect against disturbance or to reduce the level of it. Since the issue is power system, the barriers could be various safety systems and controllers. Another assumption is made that the disturbance is not a point source, but it is an inexhaustible, i.e. infinitive and, at the beginning of every cycle, the disturbance can renew. Expected results are disturbance distribution in the network nodes, how many number of cycles (time) are needed to stabilization and where is the highest disturbance level. Values of network barriers are calculated according to how many links country have with other countries. The country has more interconnections, the value of barrier is lower, i.e. the major level of disturbance is destroyed, because it has more possibilities of electricity supply.

The source of disturbance was selected 7th node Germany and Denmark West. During each cycle it is supplemented with a relative disturbance unit, which is equal to 1 ($H = 1$). Physical meaning of such disturbance is a hazard to the country not to be supplied with electricity from neibhouring countries. For example, if in the country (source of disturbance) due to some reasons is a shortage of electric power, thus it needs to import power from neibhouring countries. In that case disturbance level shows a hazard not to get power due to some other disturbances (not only technical). Since the disturbance level is generated during each cycle, in some nodes total disturbance level (after some number of cycles) can exceed 1. The disturbance level was estimated using equation (13). Modelling results are given in Table 2 and Fig. 3.

Table 2. Disturbance distribution in the European AC transmission network

No.	**Country**	**Disturbance level**	**No.**	**Country**	**Disturbance level**
1.	Portugal	0.0174	11.	Czech Republic	0.3008
2.	Spain	0.0703	12.	Poland	0.3326
3.	France	0.3642	13.	Croatia	0.0129
4.	Italy	0.1058	14.	Hungary	0.0600
5.	Belgium and Luxembourg	0.3333	15.	Slovak Republic	0.1878
6.	Switzerland	0.1668	16.	Balkan countries	0.0099
7.	Germany and Denmark West	1.1816	17.	Greece	0.0027
8.	The Netherlands	0.1751	18.	Bulgaria	0.0069
9.	Slovenia	0.0696	19.	Romania	0.0192
10.	Austria	0.2872	20.	Ukraine West	0.0483

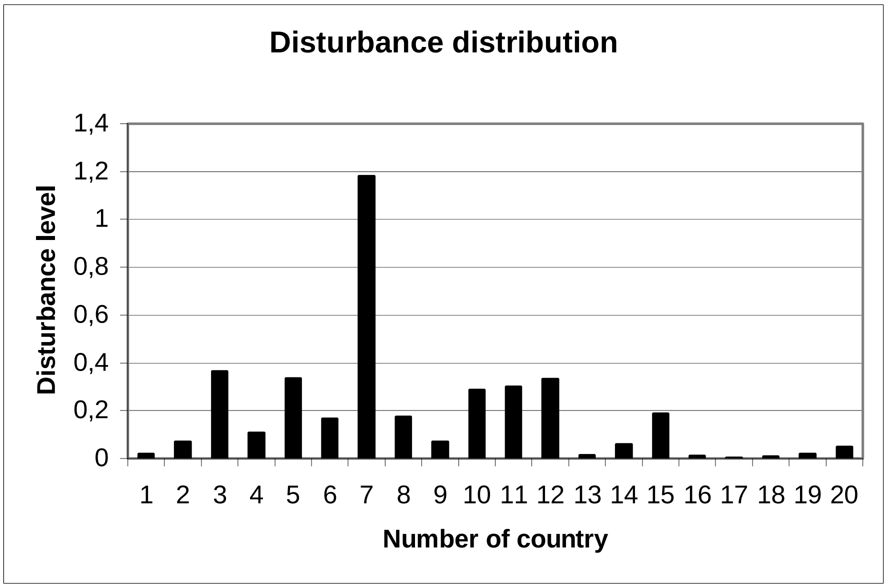

Fig. 3. Disturbance level in the European AC transmission network countries

The presented results are settled after 200 iterations, but their stabilized even after 50 cycles. As we see from the table and figure, the highest disturbance level is in the source of disturbance (Germany and Denmark West). Since this node has many interconnections with other countries, the neighbouring countries are affected by the disturbance as well, but its level is lower several times. If the countries are far from sources of disturbance, the level of disturbance is becoming lower and lower, in some of them even close to zero.

Calculations were made with other countries also taking them as sources of disturbance, but the results and conclusions were very similar: if a disturbance occurs, it mostly affects only the country where it occurs and even some neighbouring countries with which it has interconnections. However, disturbance level in other countries are several times lower.

5. SUMMARY AND CONCLUSIONS

The main aim of the paper is to present the developed energy supply disturbance distribution mathematical model and its analysis. The cases of disturbance spread in Markov chains and network systems were analyzed, where nodes have barriers or resistance to the disturbance characteristics. Theoretical results were illustrated by numerical simulation of European AC transnational transsmission network.

From the obtained results such conclusions could be drawn:

- In the case of infinitive source of disturbance, the highest disturbance level after certain number of cycles is in the source of disturbance.
- Other nodes are affected, but disturbance level is several times lower.

REFERENCES

1. WESLEY, M., Power plays: Energy and Australia’s security. Australian strategic policy institute, Australia, 2007. 66 p. ISBN 9781921302169.
2. *International Energy Agency (IAE)*. [referred on the 18th of February 2010]. Link to the internet <http://www.iea.org/subjectqueries/keyresult.asp?KEYWORD_ID=4103>
3. SIMS, R.E.H., SCHOCK, R.N., ADEGBULULGBE, A., FENHANN, J., KONSTANTINAVICIUTE, I., MOOMAW, W., NIMIR, H.B., SCHLAMADINGER,

B., TORRES-MARTKNEZ, J., TURNER, C., UCHIYAMA, Y., VUORI, S.J.V., WAMUKONYA, N., ZHANG, X. Energy supply. In Climate Change 2007: Mitigation. Contribution of Working Group III to the Fourth Assessment Report of the Intergovernmental panel on Climate Change [B. Metz, O.R. Davidson, P.R. Bosch, R. Dave, L.A. Meyer (eds)], Cambridge University Press, Cambridge, United Kingdom and New York, NY, USA.

4. AUGUTIS, A., KRIKŠTOLAITIS, R., ŠIDLAUSKAS, K., MARTIŠAUSKAS, L., MATUZIENĖ, V. Modelling of energy supply disturbances in network systems // Reliability, risk and safety: theory and applications. London: Taylor & Francis Group, 2010. Vol. 3. ISBN 978-0-415-55509-8, p. 1035–1041.
5. MARTIŠAUSKAS, L., AUGUTIS, J. Mathematical modelling of security of energy supply disturbance scenarios // 6th annual conference of young scientists on energy issues CYSENI 2009, Kaunas, Lithuania, 28–29 May, 2009. Kaunas: LEI, 2009. ISSN 1822-7554, p. 212–222.
6. AUGUTIS, J., UŠPURAS, E. Risk of technologies: monograph // Kaunas: Lithuanian Energy Institute, Vytautas Magnus University, 2006. 248 p. ISBN 9986-492-89-0.
7. *European Network of Transmission System Operators for Electricity (ENTSO-E)*. [referred on the 18th of February 2010]. Link to the internet <http://www.entsoe.eu/>
8. RABINER, L., JUANG, B. An introduction to hidden Markov models. IEEE ASSP Magazine, p. 4–16, 1986.

CYSENI 2010, May 27–28, Kaunas, Lithuania
ISSN 1822-7554, www.cyseni.com

TOWARDS A SUSTAINABLE ENERGY TRANSITION? RENEWABLE ENERGY DEVELOPMENT IN HUNGARY

M. Prantner
Wuppertal Institute for Climate, Environment and Energy
42103 Wuppertal Döppersberg 19 - Germany
Phone: +49 - 202-2492-193
Email: magdolna.prantner@wupperinst.org

ABSTRACT

With the EU Eastern enlargement process the new member states had to undergo a complete political and economic transformation from centrally planned to market economies and a substantial re-orientation of the economic ties from the former Eastern Bloc to the EU. However, the EU enlargement signalizes the culminating event, the transformation process has not finished yet. The energy sector reflects this development process; its transition started in the middle of the 1990s. Various radical processes took place and the EU directives have largely been implemented, such as the improvement of the renewable energy production and consumption. Nevertheless, the energy sector still faces serious challenges in order to reach a more sustainable society.

All the same, the current research activities in the energy sector tend to ignore the special conditions of political and economic transition in Central and Eastern Europe as well as the implications of membership in the European Union.

The purpose of the paper is to analyse this transition process of the energy and renewable energy sector in Hungary as one of the new EU member states. The aim is to highlight the institutional, social and political factors – besides the technical and economic ones that presently receive most attention – in the dynamics of the Hungarian renewable energy policy. What are the driving forces and what are the barriers for deployment of the renewable energy production technologies in Hungary? What can other transition countries learn from the Hungarian development? The research will not only identify the specific characteristics of the Hungarian transformation process, but the conclusions will also draw a more differentiated picture of the more sustainable energy market development in other transition countries.

Keywords: Hungary, renewable energy policy, renewable energy market

1. INTRODUCTION

In line with the overall strategy of sustainable development the EU decided to support, encourage and promote energy production from renewable sources. Other main advantages of using renewable energy sources are the favourable impacts on the overall competitiveness of European industry, and the positive effects on regional development and employment. Therefore, the new European directive on the promotion of the use of energy from renewable sources (2009/28/EC) aims at covering 20% of the overall energy needs from renewable energy sources by 2020.

Although, different renewable energy policies exist in the EU for decades, the 2020 – targets challenge every member states: in order to reach the targets, it is necessary to draft appropriate renewable energy development strategies in every member state.

Until now relatively little attention has been paid to renewable energy and energy policy development in the new member states. The research debate either seeks to find the „best incentives” on promotion of renewable energy sources scrutinising the situation in the forerunner countries or analyse the implications of renewable energy use in developing countries, while the proper research on transition countries is almost totally missing [1].

The energy sector in the new member states is more vulnerable because of its heritage from the centrally planned era (e.g. import dependency, lower reliability, high energy intensity, environmental problems). The extended use of domestic renewable energy sources can be seen as a possible alternative to develop sustainable energy use. But existing barriers pose a challenge for the future. These characteristics show inherent differences in the energy sectors of the old and new member states.

The future analyses should put more emphasis on institutional and social dimensions of energy policy besides the technical and economic aspects. Although policy incentives are important, other actors are involved in the renewable energy market (e.g. firms, utilities, special interest groups, consumers), whose interests might be different in the new EU member states. Presently, market conditions and public awareness in the old EU member states are more mature than that of the new EU member states. The lack of policy consensus and coherent long-term strategies in the Central and Eastern European countries presumably results from several factors [2], including conflicting interests of energy suppliers and users, and lack of knowledge about the dynamics of energy systems. A comprehensive analysis is needed to understand the transition of energy systems in the new member states and the differences between the old and new member states, in order to create optimal incentives for renewable energy utilisation in Central and Eastern European countries. A proper analysis should also include perceptions, strategies and actions of stakeholder groups and attach greater importance to their socio-economic situation.

The aim of the research is to increase the understanding of the dynamics of the energy systems and to gain insight into the possibilities and limitations of renewable energy policies in Central and Eastern Europe. However, the analysis of the renewable energy development in the whole region goes beyond the limits of the paper, therefore this study focuses on the development of the most considerable renewable energy sectors in Hungary from the early 1990 until recently. The paper concentrates on the wind and biomass sector, because these technologies made the most significant progress during the analysed time period (see Fig. 4.). The paper describes the development and deployment of these renewable energy technologies in Hungary with focus on the specific driving forces and lagging factors taking into account the various actors on the energy market.

2. USED METHODOLOGY

Ohlhorst [3] Schenk et al [4] and Verbong and Geels [5] put forward a new kind of policy analysis using a socio-technical and multi-level theory on transitions. This approach allowed them to distinguish between different actors' characteristics in the electricity sector. Therefore it enables a better understanding of motivation, behaviour and outcomes. It offers valuable indications on how to set up more efficiently an effective support policy in relation to the target groups and taking into account their specific needs [6, 7, 4].

The existing written literature about the Hungarian renewable energy development does not ensure the equal treatment of the different stakeholders and their relations from all aggregation level. Therefore it was necessary to collect information from all kind of stakeholders of the Hungarian renewable energy market. In order to collect proper information from all aggregation levels, the research included detailed field analysis, too. The interviews of various stakeholders can verify the classification of different development phases, and the interview's results may change them. The empirical analysis is based on data collection using structured questionnaires and interviews with experts and different stakeholders. During 2009, 45 interviews were accomplished covering all significant stakeholder groups of the Hungarian renewable energy sector. The process of these in-depth interviews followed the main existing literature on expert interviews and qualitative content analysis, like Lamnek [8] and Gläser and Laudel [9]. The aim of the interviews was to receive information, facts and background knowledge from political, industrial, societal and academic stakeholders. The interviewees identified the specific driving forces and barriers of the country and the renewable energy sector.

Based on these desk and field analyses the research work is to formulate an extended analysis including the special aims and behaviour of the different actors in Hungary. This contains both the institutional dynamics of innovation processes and the relationships between all relevant actors.

3. HUNGARIAN RENEWABLE ENERGY MARKET DEVELOPMENT

3.1 Market transformation process: establishment of essential preconditions

The journey from the centrally planned economy to market economy has taken Hungary, like the other formerly socialist countries of Central and Eastern Europe (CEE) and the Soviet Union, through a painful restructuring process. At the same time the transformation process was essential to establish the institutional preconditions for alternative energy production – like setting up the market based rules and regulations, foundation of necessary regulatory institutions, unbundling the energy production chain.

The Hungarian energy industry was a vertically integrated, state owned monopoly until 1990. During the centrally planned era there was no separate elaborated national energy policy. In the early 1990s, after the switch-over to market economy, the break-up of the former international barter trade as well as the adoption of the market conditions required the establishment of a national energy policy based on widespread social and political consensus [10]. The first Hungarian energy policy concept was approved by the Hungarian Parliament in 1993. In 1994 the Gas Act founded the Hungarian Energy Office (HEO), the energy regulatory institution in Hungary.

The privatisation of the Hungarian energy sector started in 1995. The Hungarian government sold the electricity companies to European strategic investors within nine months. The remained unsold production, transmission and generation plants belonged to the still state owned MVM Rt. (Hungarian Power Companies Ltd.) [2].

The privatisation and the regulatory changes increased the efficiency, the renewal and updating of the Hungarian energy sector. The majority of the power plants, the gas and electricity supplying companies went to foreign ownership. However, the privatisation did not help to reduce the country's import dependence, which is still above the EU-27 average [Eurostat database].

The Act CX of 2001 started the liberalisation process of the electricity sector in Hungary. The act ensured the most important and progressive preconditions for competition. It initiated a step-by-step liberalisation process, that started in 2003 allowing consumers with a consumption over 6,5 GWh/year to change supplier. After 2004 all non-household costumers were allowed to step to the free market. Since 2008 the electricity market is open for all end users. Some elements of market regulation are very well developed such as the electricity network regulation. On the other hand, other elements, such as the creation of fully functioning wholesale markets, are lagging behind. The government has adopted all relevant EU market incentives, but the power of incumbents remained. In 2005, the government's decision to integrate the transmission system operator (MAVIR) into the MVM Rt. reduced the independence of MAVIR, and threatens the development of the liberalisation process [11].

Further consequences of the transition process were the swift away from coal towards other, less polluting fuels, associated with less energy intensive technologies, which followed by rapid structural change. The more flexible private sector responded sooner to the market price signs [12].

Nevertheless, detrimental carbon lock-in effects have been smitten the Hungarian energy sector as well. Large monolithic energy system abated technological lock-in to centralised energy structures and conventional fuels. The carbon lock-in [13] raises through the conservation of fossil fuel based infrastructures in spite of their known environmental externalities and the apparent existence of cost-neutral or even cost-effective alternative solutions. Rational action in face of climate change would internalise environmental externalities arising from fossil fuel use and remove fossil fuel use supporting subsidies. Nevertheless, instead of systematically correcting market and policy failures, the government expanded fossil fuel subsidy and institutional policy.

The Hungarian energy system seems to be locked into fossil fuel based technological systems. During the 90's the natural gas grid was extended with huge state financial support. In 1980 only 25% of the residential sector was connected to the natural gas grid. In 1990 the share of connected homes achieved 40%, and the share jumped to around 80% lately [14]. The residential prices of electricity and gas remained controlled until recently [15]. Between 2003 and 2006 the Hungarian government spent around 330 Mrd HUF[1] on residential gas price subsidies [16]. Therefore the majority of the Hungarian population switched from traditional fuel wood or coal to natural gas firing. As a result, in 2005 the natural gas demand of the population amounted to 4.8 billion m^3 [10].

The drivers behind the enormous energy and gas subsidies were dual. On the one hand the gas sector had a good organised lobby power, which helped to keep governmental subsidised gas prices for consumers [17; 18]. On the other hand, the governmental policy aimed to keep energy prices low for certain categories of residential consumers. From that subsidies benefited a large number of the potential voter groups, which made residential energy prices a political question.

As a consequence, the immense growth of natural gas consumes increased gas imports from Russia [Eurostat data]. Energy intensity remain high as compared to those in the old EU members. The structural changes, although having positive impact in most of the countries in transition, have not contributed in a significant way to the reduction of energy intensity [12].

3.2 Influence of EU accession process

As a consequence of the EU accession procedure the EU directives stimulated new energy policy standards on the governmental level:

- establishment of an efficient national energy market opening as part of the single European energy market, increase the competitiveness of the economy and serve the interest of the energy consumers;
- maintaining and increasing the stability of energy supply;
- environmental requirements, like the stringent emission standards, the renewable energy directive, introduction of CO_2 emission trading;
- increase publicity and public information.

From the renewable energy market development point of view, three EU directives have differentiated importance for Hungary, especially the directive 2001/77/EC on the promotion of electricity produced from renewable energy sources (RES) and the directive 2003/87/EC to establish a scheme for greenhouse gas emission allowance trading.

The EU RES-directive stipulated Hungary 3.6% national indicative target for the contribution of renewables to total electricity consumption by 2010 from the base year 1999 value of 0.7%.

---

[1] 1.26 Mrd EUR

The target has been reached and exceeded in 2005 (see

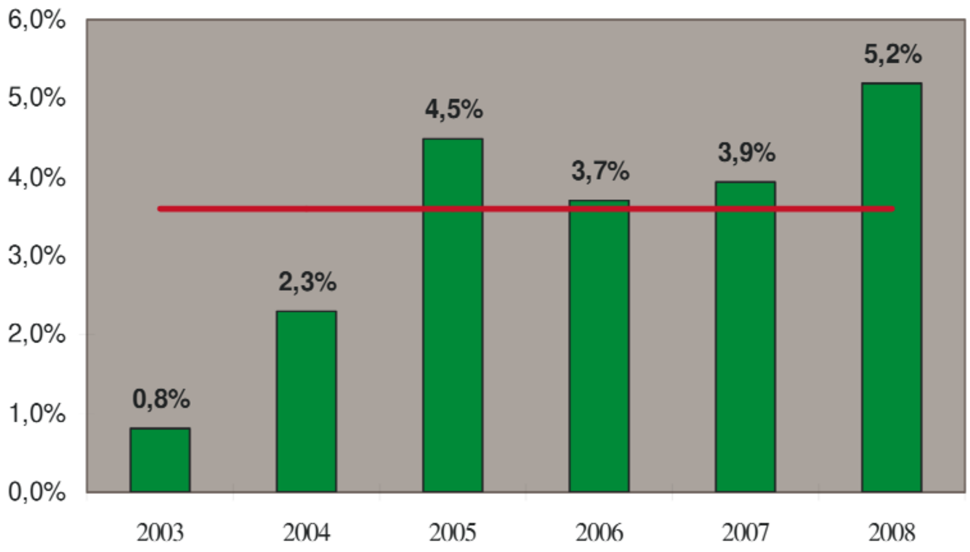

Fig. 1.)

Hungary ratified the Kyoto Protocol in 2002 and introduced the EU Emission Trading System (EU-ETS) in compliance with the Community directions on the 1st of January 2005. The country is obliged to reduce greenhouse gas emissions within its territory by 6% compared to the average levels of 1985 – 87 during the period of 2008 – 2012. Due to the restructuring of the economy forced by the political change in 1989/90 and subsequent decline in production, considerable reduction in greenhouse gas (GHG) emissions was experienced. These low levels, despite increasing production and gross domestic product (GDP) were maintained to these days. In fact, in 2004 the national emissions were 31% below base year levels, and there is no further national reduction target beyond the Kyoto commitment. From the government's point of view Hungarian climate policy is not necessary because the Kyoto targets can be reached easily and without any restrictions.

This means, that there was no more pressure from international environmental regulations since 2005, neither the climate convention nor the EU-directive 2001/77/EC can be regarded as a further direct driving force for renewable energy development in Hungary (only indirectly through the flexible mechanisms of the Kyoto protocol).

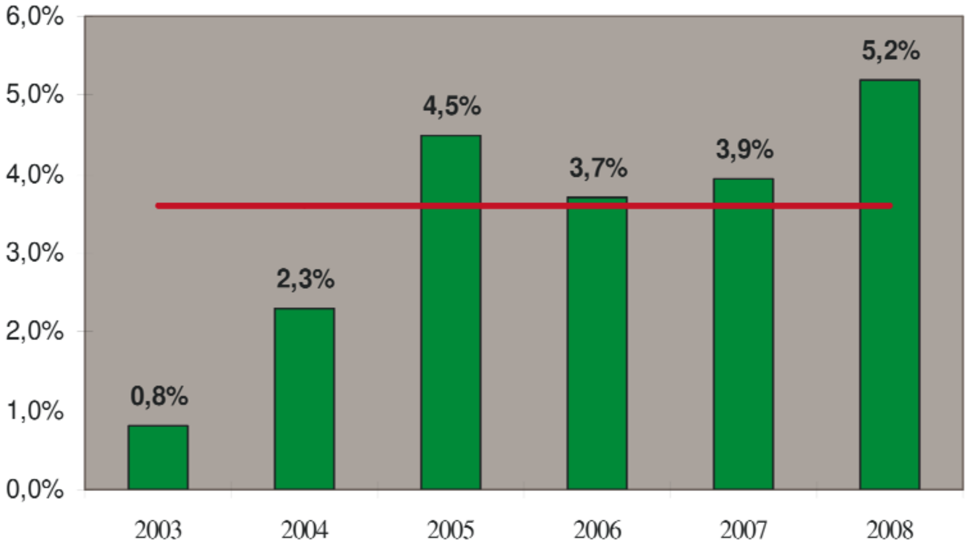

Fig. 1. Development of generation of RES-electricity and the EU 2010-target [19]

4. DEVELOPMENT OF THE RES ELECTRICITY SECTOR

4.1 Introduction of the feed-in tariff system in Hungary

The preparation of the renewable energy support scheme was one of the tasks of the Hungarian Energy Office (HEO). The economists of the office decided on a one-price feed-in support scheme, because, according to the former president of the office [11], this solution provided the best investment security. Furthermore, the HEO sought a solution, that has a smallest affects on the national budget [11].

The Electricity Act Nr. CX of 2001 introduced the feed-in obligation and fix feed-in tariff for renewable electricity over the capacity threshold of 0.1 MW. The HEO conducted a survey on external costs of conventional energy generation. Partly based on this study, the HEO set up fixed purchase price at HUF 23 (€ cent 8.23) per kWh subject to yearly indexation by official consumer price index [11; 20].

Subsequent modifications of the Ministerial Decree 56/2002 first set up two distinguished periods with different feed-in tariffs: peak and off-peak. Later, off-peak was split into two sub-categories, allowing for the discrimination of the plummeting “pit” period of the very early hours, and a broader period in the week-end nights. The decree distinguished furthermore between weather dependent (wind and solar) and weather independent (hydro power, biomass, biogas and geothermal) RES. While the same level of remuneration was paid from weather dependent electricity sources, three different tariff levels are applied for other technologies, depending on the time the electricity was produced. All weather independent renewable plant is encouraged by the tariffs to schedule their production according to the grid load profile. Peak tariffs are almost 14% higher than off-peak tariffs, and pit tariffs are almost 60% lower than off-peak tariffs. In 2005 the Electricity Act raised the feed-in tariffs in a sustainable manner [20]. The definition of peak, off-peak and pit periods are set administratively in a ministerial decree.

The feed-in tariffs were valid until 2010 according to the Energy Act of 2001, however, these were extended until 2015 by the amendment of the Electricity Act in 2009.

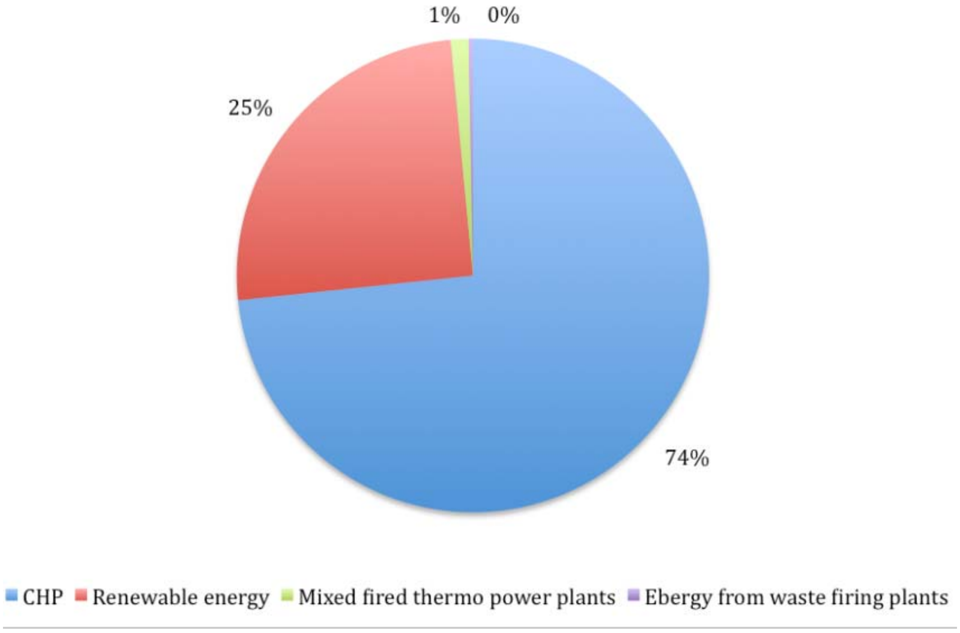

Fig. 2. Amount of subsidy for categories in 2008 (in %) [19, 21]

The new energy decree of 2001 involved the cogeneration as well, and extended the compulsory purchase of electricity cogenerated with district heating (CHP) up to 20 MW. The Minister of Economy was responsible to determine the compulsory purchase and the order of subsidies of cogenerated energy and for electricity from renewable energy sources. The feed-in prices were favourable and guaranteed until 2011. In 2002 a new decree raised the upper limit of the compulsory purchase category up to 50 MW. As a consequence, even big CHP plants received generous feed-in tariffs, which were partly even more attractive than for renewable energy sources. Both the renewable and CHP technology received its subsidies from the same “green” fund, which caused frictions between the different technologies. *Fig. 2* shows, that 74% of the feed-in tariffs was paid to CHP plants, while only 25% went to renewable energy sources in 2008.

4.2 Development of electricity production from wind power

According to the IEA study of 1995 [22], the wind power potential of Hungary was regarded as rather low. The wind resources were considered as limited by the geographical position of the country and the rather flat topography. The IEA stated in 1995, that the wind power equipment is unlikely to find a commercial market. The first wind power plants were established in Hungary as pilot projects in the early 2000's before the feed-in tariff regulation.

The new Hungarian Electricity Act of 2001 changed the investment inclination gradually, and created favourable investment climate [23]. The ordinance about the feed-in tariff was effective in 2003, and offered generous feed-in tariffs for wind energy investments. *Fig. 3* shows the development of installed wind energy capacity and electricity production from wind resources.

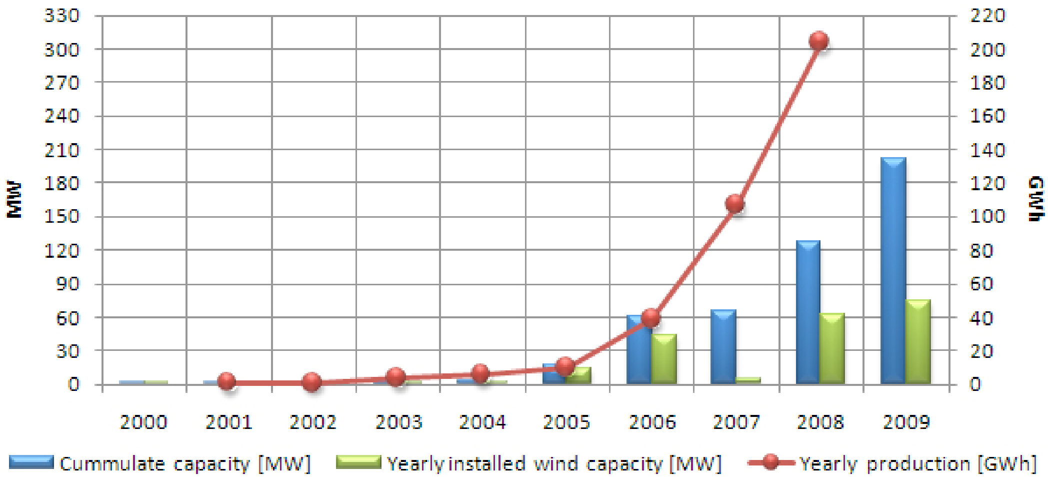

Fig. 3. Development of installed wind energy capacity and electricity production from wind resources 2000–2009 [26]

The wind power investments became "popular", until the end of 2005 around 3000 MW wind park stood in different development stages [24]. After the measurement of local wind resources, the project developers received their permits during a tree-step licensing process: environmental permit, building permit, and grid connection permit.

The ordinance 246/2005 restricted the regulating environment and prescribed a fourth step to obtain a small power plant licence from the Energy office as well [24]. Furthermore, due to balancing reasons the grid operator (MAVIR) advised restrictions in wind power plant licensing. The transmission system operator was concerning about the secure operation of the grid due to increasing amount of flexible power plants, which led to limitation of grid access for new wind energy installations. The Hungarian Energy Office introduced a 330 MW upper barrier for wind generation capacity until 2010. However, on the tender received 1138 MW wind generation applications. Only 51% of the proposed projects were successful obtaining a permit [17].

The permit laid down, how much electricity could the wind power plant produce under the feed-in system every year. The energy office determined the period of the feed-in tariff system individually according to the payback period of the wind power investment (10–15 years) [17].

The 389/2007 governmental decree was introduced in a very short time, within the end of December 2007, and took into effect in 1. January 2008 [23; 24]. It set new rules: the wind power plants were required to give production schedule a day ahead. If the difference from the real production exceeded +/- 30%, the wind power plant had to pay surcharge.

The Hungarian Meteorological Service was, however, not prepared to offer detailed wind data, which would be indispensable for proper electricity production prognoses. The surcharge for several wind project entrepreneur was equivalent to a 10 – 20% decrease of the feed-in tariffs [24].

The aim of the Energy Office that wind energy investors will invest into the wind predictions of the meteorological service was not fulfilled. On the other hand, the Energy Office did not spend the incomes from these surcharges to the development of the Hungarian wind prognosis either. [17] For want of better the Hungarian wind power plant operators used the services of European wind prognosis providers. After a year the Energy Office alleviated the strict rules of the production forecast: the tolerated difference between forecast and real production was extended to +/-50% [17].

In August 2009 the HEO organised a new tender for 410 MW additional wind energy capacities, which offers new prospects for Hungarian wind energy investors [25].

The Hungarian wind energy market development clearly shows, that the introduced feed-in tariff system made a favourable investment climate for market near renewable energy technologies, like the electricity production from wind resources. The electricity production from wind power with feed-in tariffs became nearly as competitive as the conventional sources. Nevertheless, the market development started rather unexpectedly. The introduced different administrative hurdles moderated the new wind capacity growth.

4.3 Development of electricity production from biomass resources

In 1989 fuel wood was estimated to contribute 0.32 MToe to the Hungarian total primary energy supply (TPES), mostly consumed by the residential heating sector. Further approximately 2.82 PJ was accounted for other biomass like forestry wastes, straw and other agricultural wastes [27].

However, during the 90's, the Hungarian residential heating sector changed radically. The natural gas grid was gradually expanded, and almost every settlement was connected to that. Between 1990 and 1997 the number of connected towns and villages more than quadrupled [28] and the number of connected households grow over 3.5 million in 2006 [15].

Therefore the majority of the Hungarian population switched from traditional fuel wood or coal to natural gas firing, which was generously supported by state subsidies. As a result the natural gas demand of the population increased constantly, while at the same time, the consumption of residential fuel wood decreased substantially [29; 30].

The development affected the fuel wood market: while the overall area of the Hungarian forestries grew continually, permanent oversupply evolved on the fuel wood market. The fuel wood prices remained constant during the latest 90's. The forestries started to lift up their exports. New export markets were opened up in Austria and in Italy. The production of new products started, such as charcoal. However, these efforts did not help on the substantial overproduction of fuel wood. The sale of fuel wood was possible only on discounted prices; therefore the exploitation was reduced as well. However, due to technological and environmental reasons, the decrease of exploitation could not be adapted to the decreased market demand of fuel wood [29]. The situation of the forestries was untenable: the selling price (3200 - 3300 HUF/m^3) of fuel wood was under the price costs (4500 HUF/m^3). In this situation the interests of the forestry met with the coal power plant sector.

The Hungarian conventional coal power plants had to undergo substantial changes during the 1990's. Coal mining was in favour during the communist regime. The coal sector received huge amount of cross subsidies. After the collapse of the communist system, the coal sector entered a major financial crisis. Since the political changes of 1990, coal's importance in the Hungarian energy mix has decreased. The majority of the Hungarian coalmines and power generation was economically not profitable. Therefore the government started to rationalise the coal industry and scheduled to close the most ineffective mines [28].

From 2000 the government decided to eliminate state operational subsidies. Coal power plants received no more state aid except to finance the remaining mine closures [15].

In line with the rationalisation process, the EU accession procedure required the introduction of several environmental measures, standards and directives, which affected the power production additionally. The transportation of the EU environmental acquis to the Hungarian legal order and the implementation of the major tasks was a part of the EU enlargement process. The Environmental chapter was opened in December 1999 and closed in December 2002. All candidate countries have requested transitional measures and technical adaptations. As a result of negotiation, clarification and substantial additional efforts by the candidate countries, several of these requests have been withdrawn. Finally, limited transitional periods have been granted to Hungary in relation to sulphur content of large combustion plants until 2004 [31].

The first large combustion plant directive (88/609/EEC) was adopted by the European Council on 24 November 1988, and then amended by Council directive 94/66/EEC in 1994. It was revised on 23 October 2001 (directive 2001/80/EC). The national environmental policies of the candidate countries have principally been initiated by the directives of 88/609/EEC and 94/66/EC. However, the most crucial influence was made by the Large Combustion Plant Directive (2001/80/EC).

The first directive set national emission ceilings for emissions of SO_2 (sulphur dioxide) and NO_x (nitrogen oxides) from existing LCPs, and absolute emission limit values for SO_2, NO_x and dust for individual new installations based on Best Available Technology (BAT). The amendment of 1994 established an emission limit value for SO_2 for those new plants burning solid fuels with a rated thermal input between 50 and 100 MW_{th}. The emission limit values for SO_2, NO_x and dust set by this directive 2001/80/EC are considerably stricter than the ones included in directive 88/609/EC. Notably the directive establishes new requirements for plants licensed before 1 July 1987. Directive 2001/80/EC encourages the combined generation of heat and power and sets specific emission limit values for the use of biomass as fuel.

The Hungarian power sector was mainly affected by the strict SO_2 emission limits. The Hungarian coal, which was mainly used in the power plants, had high sulphur content. Furthermore the outdated, simple pulverised coal combustion technology was not capable to keep sulphur within the combustion residues. The coal power plants had three options to choose:

- close down the power plant;
- introduce substantial environmental investments, such as filters, etc.;
- switch to another fuel technology [32; 33].

At the end of 2001, experts and interests of the coal power and the forestry sector met with each other. The partners recognised, that their interests overlap each other. It was followed by a rapid development: in December 2001 a disintegrator was already put into operation temporarily at one coal power plant site, the trial production period started in the following year. Since 2003 the forestry's supply fuel wood on regular basis [29].

The development was followed by other coal power plants in Hungary [32]: in the next years 1465 GW new electricity production capacity based on biomass were connected to the national grid.

As the consequence of the rapid fuel combustion change Hungary reached its RES 2010-target already in 2005. Fig. 4. shows the crucial role of solid biomass source in the development of installed renewable energy capacity. Furthermore the government was afraid of spending more money on green electricity production. Therefore since 2005 every RES power plant has a yearly upper generation limit prescribed by the Hungarian Energy Office.

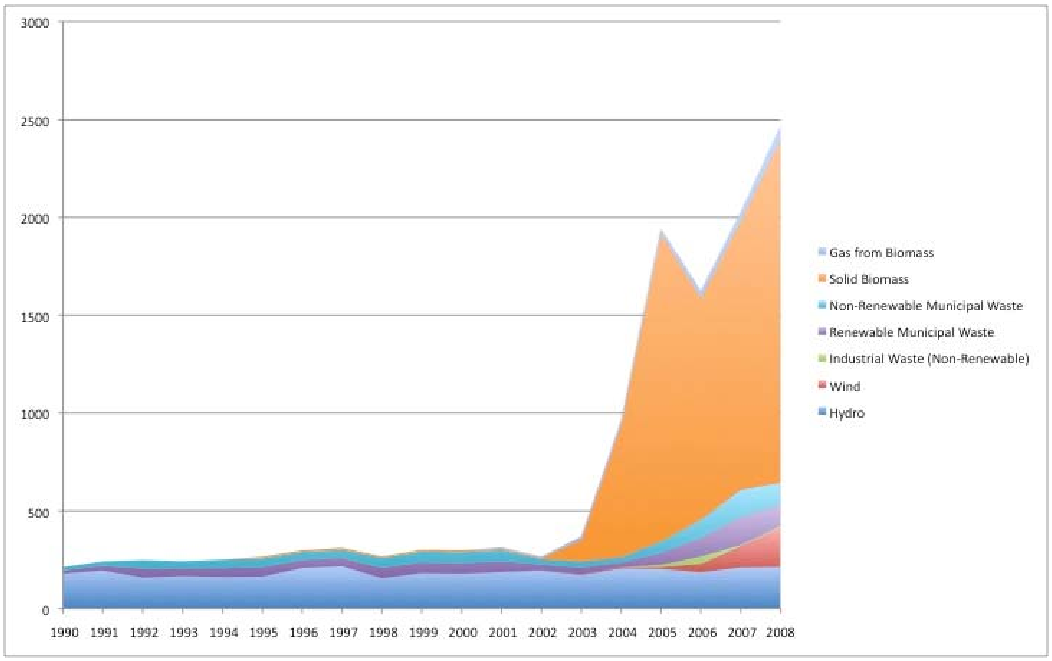

Fig. 4. Development of installed renewable energy capacity 1990 - 2008 (in MW) [Source: Eurostat]

Simultaneously, the Hungarian fuel wood market followed the development of the renewable electricity generation. The gross scale electricity generation from solid biomass abolished the fuel wood export. Furthermore, after 2004 fuel wood import turned up. Nowadays the share of fuel wood in the whole wood production accounts for around 50%, while its share is still increasing.

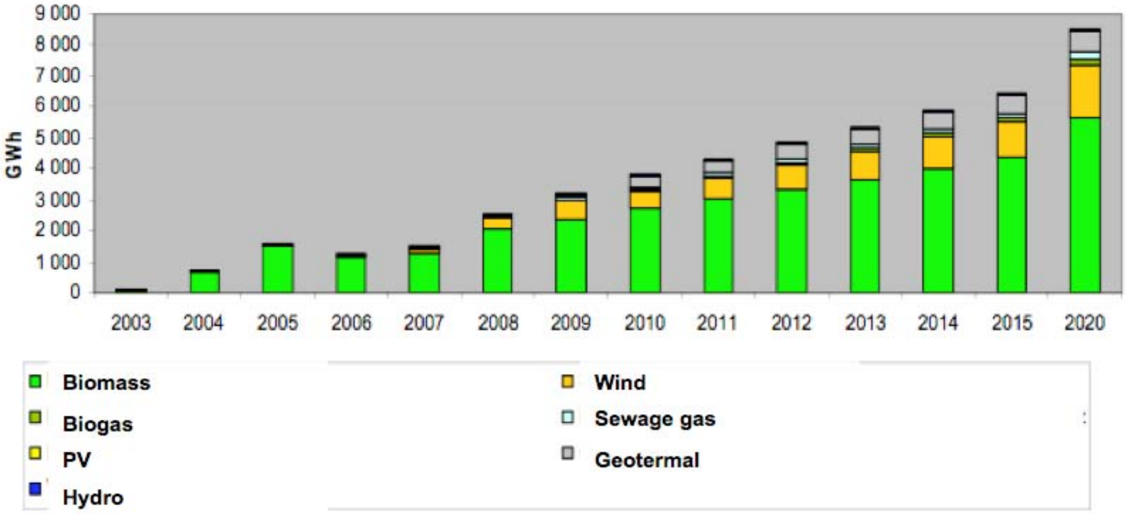

Fig. 5. Hungarian green energy strategy until 2020, (added electricity in GWh) [34]

However, recent studies [30] show, that there is no more available, sustainable produced fuel wood in the Hungarian resource market any more. Hungary cannot reach its 2020-target without any sectoral change.

The strategy (

Fig. 5) of the Hungarian government indicates, that Hungary wants to achieve its 2020-RES-targets to increase the biomass based electricity production. However, recent studies show, that under recent production circumstances there are no more biomass available for further growth in biomass based electricity production.

5. CONCLUSIONS

In the last 20 years Hungary followed the most convenient solution to reach the international agreed targets. Both the EU 2010-target on renewable electricity and the Kyoto commitment were no real driving factors, because the targets were “too easy to reach”. The government has adopted all relevant EU market incentives, but the sectoral changes have not started yet. The strong lobby power of the conventional energy sources and the disadvantageous effect of the carbon lock-in intensified the situation.

The energy system seems to be locked into fossil fuel based technological systems: the Hungarian governments subsidised heavily the conventional energy production, especially the residential gas use. As a positive consequence, the Hungarian energy use were swift away from coal towards other, less polluting fuels. On the other hand, the energy import dependency gradually increased as well.

The introduced feed-in tariff system stipulated mainly the market-near renewable energy technologies, like the electricity production from wind resources. However, the government introduced different administrative hurdles that caused a decline in the favourable investment climate. The main driver behind the enormous biomass electricity capacity development was not the EU RES-directive. The most crucial influences were made by the Large Combustion Plant Directive. After an extremely rapid development process, substantial amount of new electricity production capacity based on biomass were connected to the national grid. Therefore Hungary reached its 2010-RES target already in 2005.

On the same time the Hungarian governments were not willing to achieve any further target beyond the international agreements in order to reach a more sustainable energy system. The national strategy was to jump on the bandwagon in the very last minute and do not spend more effort than necessary. In fact, Hungary reached its renewable targets, but the countries performance is not a good practice for others.

One of the main advantages of using renewable energy sources are the favourable impacts on the overall industry and the positive effects on regional development and employment. However, these positive effects of increased renewable energy use did not have an impact on the country. The absence of long-term transparent renewable energy policy and the unclear governmental strategy did not provide enough investment capacity for the manufacturing sector. Nowadays, there is little current prospect of an industrial policy spin-off in Hungary both because of the nature of the recent policy and because of the "late mover disadvantage". The impact of the renewable energy sector development remained low on the Hungarian job market.

The recent policy system, the existing cross-subsidies in the energy sector and the inflexibility of the actual energy system do not stimulate efficient use of biomass energy sources. However, the future renewable energy policy of Hungary is based on additional use of domestic biomass resources. Although, under recent production circumstances, there is no more biomass available for further growth in biomass based electricity production. Hungary has to make significant efforts and gradual structural changes to reach its 2020-target.

REFERENCES

1. NILSSON L.J., PISAREK M., BURIAK J., et al. Energy policy and the role of bioenergy in Poland. *Energy Policy*. 2006; Vol. 34, No 15, p. 2263–2278.
2. dr. KADERJÁK P. Preconditions of Electricity Market Integration in Seven Central and Southern Eastern European Countries. In: Towards More Integration of Central and Eastern Energy Markets. Budapest, Hungary; 2006.
3. OHLHORST D. *Windenergie in Deutschland: Konstellationen, Dynamiken und Regulierungspotenziale im Innovationsprozess*. Wiesbaden: Vs Verlag; 2009. p. 257
4. SCHENK N.J., MOLL H.C., SCHOOT UITERKAMP A.J. Meso-level analysis, the missing link in energy strategies. *Energy Policy*. 2007, Vol. 35, No. 3, p. 1505–1516.
5. VERBONG G., GEELS F. The ongoing energy transition: Lessons from a socio-technical, multi-level analysis of the Dutch electricity system (1960–2004). *Energy Policy*. 2007 Vol. 35 No 2, p. 1025–1037.
6. SZARKA J. Wind power, policy learning and paradigm change. *Energy Policy*. 2006, Vol. 34, No 17, p. 3041–3048.
7. EGMOND C., JONKERS R., KOK G. One size fits all? Policy instruments should fit the segments of target groups. *Energy Policy*. 2006, Vol. 34, No 18, p. 3464–3474.
8. LAMNEK S. *Qualitative Sozialforschung*, 1-2 Bde. München, Weinheim: Psychologie Verlag Union.; 1995.
9. GLÄSER J., LAUDEL G. *Experteninterviews und qualitative Inhaltsanalyse: als Instrumente rekonstruierender Untersuchungen*. VS Verlag für Sozialwissenschaften, September 2006. p. 347
10. CSUTI J. General Review of the Energy Market of the Hungarian Republic. *EuroHeat&Power*. 2007, Vol. 4, No I/2007, p. 32–39.
11. Interview with Péter Kaderják, Director, REKK, (Former president of the Hungarian Energy Office) 17.03.2009.
12. ÜRGE-VORSATZ D., MILADINOVA G., PAIZS L. Energy in transition: From the iron curtain to the European Union. *Energy Policy*. 2006, Vol. 34, No 15, p. 2279–2297.
13. UNRUH G.C. Understanding carbon lock-in. *Energy Policy*. 2000 Vol. 28, No 12, p. 817–830.
14. DUDÁS G. Index - Gazdaság - Előbb-utóbb lesz gázáremelés. 2006. Available at: http://index.hu/gazdasag/magyar/gazar/ [Accessed March 14, 2010].
15. IEA. *Energy Policies of IEA Countries: Hungary 2006*.; 2007. Available at: http://www.oecdbookshop.org/oecd/display.asp?lang=en&sf1=DI&st1=5L9HZQF6457D [Accessed March 14, 2010].
16. FÜLÖP O. Ösztönzött pazarlás – Lakossági energiaárak állami támogatása 2003–2009. Budapest, Hungary: Energia Klub; 2009. Available at: http://www.energiaklub.hu/hu/tanulmanyok/?id=77 [Accessed October 12, 2009].
17. Interview with Csaba Kovács and Tamás Tóth, Head of Department and Economic analyst, Hungarian Energy Office, Department of Economic Research and Environmental Protection 23.03.2009
18. Interview with Ferenc Bohoczky and dr Tibor Laklia, Senior counsels of the Ministry of Transport, Telecommunication and Energy 31.08.2009.
19. MAGYAR ENERGIA HIVATAL. A kötelező átvétel keretében megvalósult villamosenergiaértékesítés 2008-ban. 2009. Available at: http://www.eh.gov.hu/gcpdocs/200907/microsoft_word__2008_evi_kat_ertekeles_veglegesdoc_20090721132837.pdf [Accessed March 14, 2010].
20. dr. PÁL G., PRANTNER M., MEZŐSI A. Renewable Electricity: ambrosia or delicatessen? A survey of electricity markets. In: Towards more integration of Central

and Eastern European Energy Markets; Book of the C3EM project of REKK.; 2006: p. 185–221.

21. CSÁKÁNY G. Utilisation of wind energy in Hungary in 2009. Available at: www.nrg-systems.hu/ewec_presentation.ppt [Accessed March 14, 2010].
22. IEA. *Energy Policies of Hungary - 1995 Review*.; 1995. Available at: http://iea.org/publications/free_new_Desc.asp?PUBS_ID=1224 [Accessed March 14, 2010].
23. Interview with Andrea Molnár, Secretary, Légáram Alapítvány / EMSZET Első Magyar Szélerőmű Kft 12.03.2009
24. Interview with Gábor Csákány, Managing director, NRG Systems Kft. 25.03.2009
25. Interview with Prof. Dr. Péter Tóth, Chairman of Wind Energy Associacion / Associate professour, Széchenyi István University, 25.08.2009
26. MAGYAR SZÉLENERGIA TÁRSASÁG: Statistics. 2009. Available at: http://www.mszet.hu/index.php?mid=53 [Accessed March 14, 2010].
27. IEA. *Energy Policies of Hungary - 1991* Review.; 1992. Available at: http://iea.org/publications/free_new_Desc.asp?PUBS_ID=1367 [Accessed March 14, 2010].
28. IEA. *Energy Policies of IEA Countries - Hungary - 1999* Review.; 1999. Available at: http://iea.org/publications/free_new_Desc.asp?PUBS_ID=1174 [Accessed March 14, 2010].
29. Interview with László Jung, Egererdő ZRt, CEO 26.08.2009
30. REGIONAL CENTER FOR ENERGY POLICY RESEARCH (REKK). Erdészeti és ültetvény eredetű fás szárú energetikai biomassza Magyarországon (Biomass energy potential of the Hungarian forestry and agricultural sector). Budapest, Hungary: REKK; 2009.
31. EUROPEAN COMMISSION - Enlargement: Negotiations of the chapter 22: Environment. Available at: http://ec.europa.eu/enlargement/archives/enlargement_process/future_prospects/negotiations/eu10_bulgaria_romania/chapters/chap_22_en.htm [Accessed March 14, 2010].
32. Interview with László Szegő, Vice president pf Pannon Holding ZRt. 16.03.2009
33. Interview with Frigyes Németh CEO, Bakony Power Plant ZRt. 30.04.2009.
34. HUNGARIAN MINISTRY OF ECONOMY AND TRANSPORT. Magyarország megújuló energiaforrás-felhasználás növelésének stratégiája 2007-2020.; 2007. Available at: http://www.khem.gov.hu/feladataink/energetika/strategia/energiapolitika/meguj.html [Accessed March 14, 2010].

Hungarian legal acts:

Hungarian energy policy concept from 1993
Gas Act from 1994
Electricity Act of 2001
Ministerial Decree 56/2002
Ministerial Decree 246/2005
New Electricity Act of 2007

EU directives:

The Large Combustion Plant Directive (88/609/EEC)
Commission Regulation No 94/66/EEC
Directive on the promotion of electricity produced from renewable energy sources in the internal electricity market (2001/77/EC)
Directive on the limitation of emissions of cer tain pollutants into the air from large combustion plants (2001/80/EC)

Directive establishing a scheme for greenhouse gas emission allowance trading within the Community (2003/87/EC)
Directive on the promotion of the use of energy from renewable sources (2009/28/EC)

Databases:

Eurostat
OECD
Hungarian Statistical Office (KSH)
HEO webpage: Webpage of the Hungarian Energy Office:
http://eh.gov.hu/home/html/index.asp?msid=1&sid=0&HKL=1&lng=2
MSZET, 2010: Statistical data of the Hungarian Wind Energy Associacion:
http://www.mszet.hu/index.php?mid=53

CYSENI 2010, May 27–28, Kaunas, Lithuania
ISSN 1822-7554, www.cyseni.com

DEVELOPMENT OF SUSTAINABLE ENERGY POLICY OF REGIONS

M. Stankevičius
Lithuanian Energy Institute
Breslaujos str. 3, LT-44403 Kaunas – Lithuania
Phone: +370 688 96835
E-mail: m.stankevicius@mail.lei.lt

ABSTRACT

World economic growth is to significant extent dependable on the sufficiency of the Fossil Fuel (FF) resources as well as on the sustainability of its supply. Extensive growth of the World population (from 2.6 billion in the 1950 m. till 6.8 billion in the 2009) further increases demand for FF which makes it a powerful weapon for FF monopolies seeking to have dominance in the selected regions. On the other hand increasing utilization of FF is one of the contributing factors impacting climate change. Despite of the factors listed above and increasing consensus that only the synergy of renewable energy resources, renaissance of the nuclear power, development of the science and technology innovation and dispersion of the "best practice" and "know-how" could ensure reliability of energy supply across the regions and social groups, some of the World countries develop their policy of energy development based only on a short-term analysis while using consumer orientated approach as a standard. In Lithuania, energy development is intensely regulated by the National Law instruments. Common practice for the local municipalities is to place major resources to achieve short term goals therefore it can be argued, that successful integration of "bottom up" approach would have a positive impact on their effectiveness. All these questions raise new challenges for the development of the theory of energy economics making it one of the most important factors providing the guidelines for the sustainable energy policy.

This paper provides review of energy development in Lithuania. Furthermore the paper provides introduction of energy economics theory to indicate methods for the formulation of regional sustainable energy policy.

Keywords: sustainable development, energy economics, energy policy, welfare.

1. INTRODUCTION

The energy use in Lithuania is considered as a basic driving force that impacts environment. It is a major contributor to environmental problems of global concern, such as climate change, acidification, and urban air pollution. Energy is crucial for economic and social development, quality of life and consumption level. According to sustainable development concept it is necessary to incorporate sustainable development goals into all sectoral policies [1]

Sustainable energy development is energy production and consumption with guaranty for long-term human and each country's development objectives in all social, economic and environmental aspects [2].

Analysis of current situation in energy sector could help to indicate the issues for sustainable energy policy development.

The review of existing situation probably indicates common situation in all countries where energy development is organized on the principle as "top down". Successful integration of the "bottom up" approach could have a positive impact on their effectiveness. Various questions raise new challenges for the development of the theory of energy economics making it one of the most important factors providing the guidelines for the sustainable energy policy, development and implementation of legislation.

2. THE GUIDELINES OF LITHUANIAN NATIONAL ENERGY STRATEGY

2.1. Electricity generation

Average annual instantaneous electricity power demand ranges from 1100 MW_e till 1500 MW_e. 160 companies have permissions for electricity production in Lithuania. The biggest producers are allocated as follows: Lithuanian Power Plant – 1800 MW_e, district heating central heating plant (thereinafter – CHP) (city of Vilnius, Kaunas, Panevezys, Klaipeda, Siauliai etc.) – about 670 MW_e, the wind turbines – about 70 MW_e, the Kaunas hydro power plant – 101 MW_e. Other about 290 MW_e (SC “Achema”, SC “Lifosa”, SC “Mazeikiu Nafta”). Lithuanian electricity market development plan (prepared by Ministry of Energy), approved by the Government of Lithuania in 2009 by resolution No 740 (Government news, 2009, no. 85-3603) provides the amount of supported electricity production in 2010 that reaches 4.5 TWh_e. After 26th November 2009, Minister of Energy signed the order, by which the supported electricity production divided as follows:

- 2.5 TWh_e – Lithuanian Power Plant;
- only 1.05 TWh_e for Lithuanian district heating CHP plants;
- other – Renewable energy sources.

The priority to generate cost valued 70% of supported electrical power is accrued to Lithuania power plant (power plant generate electricity within 30% of effectiveness), while the Lithuanian district heating power plants are able to achieve approx. 90% of effectiveness. The effectiveness of district heating power plants is higher than that of Lithuania power plant due to CHP plants turbine condensers cooled with return district heating water from the network, after – preheated district water is used to serve city heat demands for heating and hot water, while Lithuania power plant heats the “Elektrenai Lake”.

Annually Lithuanian electrical power demand is about 9 TWh_e. Other issue is that supported electricity cost (supported amount total 4.5 TWh_e) fall only on Lithuania residents, when all private companies buying electricity in trading market. In April of 2010 supported electricity for residents price was 9.6÷14.2 € cent per one kWh_e, when all private companies have possibilities to buy electricity in trade market price 5.2 € cent per one kWh_e.

2.2. Renewable energy sources, district heating, investments

European Parliament and Council Directive 2009/28/EB provide that each member state shall adopt a National renewable energy action plan [5]. It is hard to say if the quality and adopted schemes will prove to be good in Lithuania’s action plan because of the lack of knowledge, understanding of existing situation and political strength of purposes of the Government.

Resolution No 307 of Lithuanian Government, approved in 2004, limits expansion of biofuel-fired boilers. Resolution indicates that total installed capacities of biofuel-fired boilers in 2010 must not exceed 730 MW_{th}.

Follow information of the Lithuanian district heating association - investments into district heating CHP plants start to be not really attractive because of new rules and regulations for basic price conversion methodology. Basic price in the previous methodology was recalculated every four years; which ensures the return of investment.

Lithuanian government, confirmed “Order description for the electrical power generated by using renewable energy sources, production and purchase promotion” within resolution

No 1474 in year 2001. Order provides quotation for power generated by using renewable energy sources (thereinafter – RES) till year of 2009. Document indicates electricity purchasing and promotion schemes. This document contravenes with the goals indicated for Lithuania in Directive 2009/28/EB till the year of 2020. The new order, providing support and promotion for electricity produced from RES, is not prepared.

Europe will enter into force stringent environmental requirements for large combustion installations (thereinafter – LCI) from the year 2016. Currently, the EU Directive 2001/80/EC and future environmental requirements for solid particles, SO_2, NO_x, CO, for LCI can be implemented using best available technologies (hereinafter - BAT) [6]. If present situation in district heating and CHP plants will dominate in future, it is likely that the majority of district heating companies will not be able to invest the necessary capital. Taxes for pollution can be an unbearable burden for the district heating companies. In the future, the environmental tax burden could likely fall on the shoulders of taxpayers. It is necessary kick start of improvements in the investment environment as soon as possible so that district heating companies could start projects. The government could also consider changing existing conversion methodology for basic price. There is still need to decide on municipal waste for energy generation of landfill storage.

2.3. Implementation of national energy strategy

Lithuanian Government approved resolution No. 1442 (Implementation Plan for National Energy Strategy 2008-2012 (thereinafter – NESP)) in year 2007. Currently investments to energy projects in Lithuania and amounts of projects declared in NESP shows that only 30% of the investment projects are actually launched. Government declare (NESP) that purpose for Lithuania is to build new modern electricity generating equipment in accordance with BAT within total power of approximately 930 MW_e. New installations will meet not only BAT, but also all environmental demands for LCI. From 930 MW_e about 121 MW_e electricity could be generated using RES (biomass and biodegradable fraction of industrial and municipal waste). Preliminary calculations show that the new more efficient power plants could significantly improve the country's overall energy production efficiency. Investments in the energy sector could stimulate the economy, heat and electricity market could achieve higher competitiveness, new jobs places could be created. The new CHP plants could be contributing factor to reach 20 percent of efficiency till year of 2020.

2.4. Permits. Licenses. Entry restrictions

One of the perfect competition conditions is the fact that there is no market entry and exit barrier. Lithuania has a rich body of laws regulation for the electricity and heat producers and suppliers. Ministry of Energy, National Control Commission for Prices and Energy, National Energy Inspection issue permits, licenses, certificates, allowing the producers or (and) suppliers to produce, supply energy or (and) operate energy facilities.

Access to energy networks is regulated by Energy law, District Heating law, Electricity law and other legislation. Often, technical conditions for new producers (or suppliers) to connect power generation facilities to the grid are not well economically proportioned. It is hard for energy producers and suppliers to get the permits. The government could reduce bureaucracy if Order of permits for manufacturers and suppliers to generate and supply of energy would be canceled.

The clear and well known criteria for preparation of technical conditions to connect the energy networks could be prepared, now e.g. wind power plants together with hydropower station have poor possibilities to connect to the grid (wind power plants <200 MW_e). Wind parks generate supported electricity in non stable regime, the regulation and reservation cause big issues for National electricity grid operator (National enterprise). The problems could be solved if Kruonio Hydro accumulative power plant (owner – National electricity grid) (thereinafter- KHAPP) (owns >900 MW_e with the additional investments could go up to 1800 MEW_e) could reserve and regulate power for e.g. wind parks. The government could prepare roles and regulations for KHAPP to sell the regulation and reservation electricity as services for private wind power parks. The future wind power plants could have easy access to connect facilities to the electricity grid, because expansion of the electricity grid would be implemented through the capital from KHAPP.

3. THEORETICAL PROBLEMS OF SUSTAINABLE ENERGY DEVELOPMENT

The review of exiting situation above helps indicates energy issues. There is a similar energy sector issues in the most of countries where energy development organized on the principle as "top down". Successful integration of the "bottom up" approach would have a positive impact. Various questions raise new challenges for the development of the theory of energy economics making it one of the most important factors providing the guidelines for the sustainable energy policy.

3.1. The problem of creation conditions for perfect competition

Economic issues in economic theory are analyzed by using method of welfare analysis. Perfect competition economy is a decentralized pricing system, which has no external compulsion on what to produce and what to purchase, what to sell and so on. This is decided by individual users, business managers, and owners of resources. Perfect competition needs to operate a number of conditions:

a) there is a lot of sellers and buyers and each of them takes only small part of the market,
b) there is no entry and exit barriers,
c) one buyer or seller doesn't have power to impact price level, because they have no monopoly in the market,
d) product homogenity,
e) there are all of the sources of goods and services,
f) welfare for the individual and society are equal,
g) transaction costs equal zero,
h) a resource belongs to all users.

Implementation of the principles of perfect competition in energy sector could be the foundation to develop sustainable energy policy in regions. The classical approach to solving problems above presents applied welfare analysis. Efficient resource allocation occurs in the way energy is priced. At any time, the price of the energy resource should reflect its marginal social cost .This implies that any divergence between social and private cost arising as a consequence of the market failures (for example, public goods or externalities) should be corrected by internalizing such external costs. To assure the equivalence of price and marginal costs, a competitive market framework is required. Monopoly elements are to be eliminated if prices are not equal marginal costs. Applied welfare analysis allows to quantify the welfare loss associated with any given market failure. This enables policy makers to focus on the market distortions. But even though a policy change leads to an aggregate welfare gain, certain groups may suffer deleterious income distribution loss. Again this implies need to create welfare system to redress burdens imposed on the poor as a consequence of an efficiency generating policy change.

The main problem that according theoretical concept the market consists of economic agents operating under perfect competition conditions. All market based mechanisms provide for efficient resource allocation just under perfect competition which is not available in reality.

There are no accepted methodological approach allowing to evaluate efficiency of projects in terms of sustainability on the regional level. There are several methodological achievements in this field which can be used to solve the problem. The solution proposed in my article include the synthesis of rational methods used in practice but these methods are integrated by applying the new approach towards evaluation of sustainability on local level [3].

The concept of sustainable energy development can't be separated from the understanding of additional negative and positive social – economic effect of energy efficiency measures, energy savings, implementation of RES. For example, projects on energy efficiency improvements allow to save energy costs and have the multiple effects on new jobs creation, disperse across the community both socially and spatially, involving small and medium size enterprises. The indicators to be used describe the contribution of energy projects to a sustainable economic development, the medium- and long-term trends and the inter-relationship between them and the typical energy indicators (saved toe, improved energy efficiency, percentage of RES).

3.2. Local approach of sustainable energy development

It is widely accepted that integrated complex of environmental, social and economic policy is easier to implement in towns, regions, and state costs and financing from structural funds should, where possible, permit to achieve more than one goal of sustainable development policy. Organizing and implementing institutions, actors, support tools, order, etc., are needed for regional sustainable development. Municipalities may have significant role in promotion of sustainable development as local authorities have more functions in energy sector, and such opportunities should be used.

Just is case of huge demand progressive technologies may have economic background for successful development. The awareness of energy consumers usually contain just scraps and fragments in comparison to the full effective knowledge, which forms demand based on public benefit.

Demand of RES technologies is not adequately restricted by slow demand rates. The main problem is measuring of public interest. It is expressed through continuous supply of energy resources in future, solving of social problems in rural areas, environmental solutions and also inability of private sector to invest in current conditions.

From the attitude if the security of supply we can't consider the security of energy supply distractedly from consumers. Besides, security of energy supply is just the part of complicated phenomenon – energy safety, which includes national, technical and many other aspects. In one case, e.g. gas supply, consumers will be large aggregated ones – power energy system, in other cases, e.g. use of solar energy is still considered as expensive, exotic energy resource, and its use is limited. Still it is not private matter, as energy is vitally important economic sector. Tiring to escape from simplified, short-term, fragmented assessment and see energy sector as a whole with defined aspects in distant future, we must define common denominator for all energy aspects. Such attitude requires non-standard solutions.

Territorial aspect means implementation of management principle for assessment of energy resources sustainability aspects – defining of responsibilities.

Prospective organizational and financing form of technologies integration using Structural funds are towns and regional energy programs. However, integration of RES may be more successful after reliable methodological assessment of positive effect for solving social, economic, rural development problems in regional development context.

Comprehensive economic policy and it's most important legal – economic tools, applying of which would permit to correct market errors and disproportions. Here the main problem – inadequacy of social prices and actual prices. The background for RES promotions will be formulated on the basis of theoretical analysis. Scientific and practical problem will be solved while evaluating links between energy development and economic growth with providing possibilities to solve social and security problems.

Organizational mastering forms are extremely important for RES mastering, which is more accepted by foreign countries. These are various regional or municipal programs, which include RES projects to solve energy supply and environmental (biogas plants in stock-raising farms and municipal waste incineration plants) and social problems in rural areas as well as many other functions in the context of sustainable development. There are many examples of effective practices: they perform RES market establishment and awareness raising functions. These examples should be investigated, scientifically generalized and proposals prepared for applying in Lithuania's conditions.

4. FRAMEWORK FOR LOCAL SUSTAINABLE ENERGY PROGRAMMES

Methodological approach above is suitable for sustainability assessment using regional social-economic-environmental indicators, as increasing of security of energy supply, new jobs, new enterprises, additional economic product, greenhouse gas reduction. The methodology of integration of sustainable energy projects into local/regional development programs has been elaborated as a key to integrate sustainable energy projects into the regional deployment level [4].

To some extent the energy supply system is quite efficient, simply because it is optimized also from an economic point of view. This does not necessarily imply that it is optimized from the view of total cost, including the *external cost*, such as environmental cost. Even with those externalities included, however, optimizing the supply technologies constitutes a *sub-optimizing* only as compared to considering the whole energy chain.

Integrated Resource Planning, IRP, is a methodology which should avoid the sub-optimizing. The idea of IRP (or Least Cost Planning, which is a similar concept) is that we should not optimize the single links in the chain, but the chain as a whole. So far the IRP has been interpreted to include only the links up to the energy services. As an example, if it is less costly to save a kWh of electricity in the end-use than to produce a kWh, then the investments should be directed not to building new supply, but to save secondary energy and hence provide the energy services at the lowest cost. If this was taken seriously in Western Europe, for instance, there would hardly be a need for any new electricity supply system for a decade or two, since the investment in electricity savings would be more profitable, both from an economic and an environmental point of view. In most developing countries, an IRP would lead to a much lower need to invest in expensive supply systems.

It is important to recognize that you cannot optimize the energy chain as a whole by separately optimizing the single links. You cannot optimize and sub-optimize at the same time. Each time an investment is made in an electricity supply in order to optimize the supply, it is a sub-optimization, because it might have prevented the money to be invested in more efficient end-use technologies, even if that would be more cost-effective and hence optimal. In economic terms: a more optimal electricity system is one that gives the consumer the energy services at a lower bill (including environmental externalities). The kWh-price might very well be for instance 20% higher in a more optimal system if the electricity consumption is say 40% lower.

It must be taken into account that each country has its own problems, which are to be solved according to the situation in a particular country. Following the Netherlands' experience of climate policy management, an overall framework of the sustainable energy strategy could be presented as follows:

- Municipal Sustainable energy policy should be based on a covenant between government and local bodies.
- Local Sustainable energy plans are based on the national Sustainable energy strategy.

Implementation of National sustainable energy strategy should be supported by sharing the tasks on the increased share of renewables and energy efficiency improvements between regions and authorities. Moreover, the Structual fund (thereinafter – SF) programming period 2007–2013 is crucial for the implementation of sustainable energy into practice. It should be focused on the regional and local sustainable energy programmes as a whole (not only on vertical themes).

The fact that municipalities can link their climate policy to their own local themes, makes climate policy to be defined as vivid, specific and recognisable. This removes the risk of vagueness and the feeling that it has no relevance to local issues. Improved traffic situations, sustainable business parks, healthier houses and less pollution: these are the points that enter the picture thanks to climate policy. Municipal climate policy is then easy to sell and it continues to working because of its supporting base and image. From the organisational point of view, too, climate policy brings benefits for a municipality. Municipal climate policy works according to a model of policy options. This enables the municipality to give shape to sustainable, realistic aims within a clearly defined structure.

Establishing a regional market rather than local renewable energy market could help to ensure a market of a sufficient size and enhance the competition. In addition, a regional approach could be an important element in the Kyoto follow-up work.

In the Netherlands, wind energy parks and biomass power plants are often implemented on a regional scale. For individual municipalities, however, local opportunities also present themselves. The purchase of green power for their own buildings, constructing new buildings with an optimum sun-facing position, supporting the marketing of solar energy: all these things are within the reach of every municipality and contribute substantially to reducing CO_2 in built-up areas.

Municipalities occupy a key role when it comes to energy saving in existing housing. They are involved right from the beginning in renovation and restructuring plans and have a decisive contribution to make to energy saving and energy provision. They can make agreements with housing associations about the quality of energy in the rental sector. The municipality can also exert its influence on individual homeowners. For example, it can approach homeowners specifically to suggest that they have their energy consumption analysed. This will enable homeowners to make responsible choices from the available measures to both save energy and increase their own comfort.

However, there is a need to support this process, and the most feasible solution could be based on the local programming approach.

The main methodological problem is to integrate energey efficiency and RES projects into regional/local development procedures, so that energy elements may compile an integral uniformity in terms of regional / local goals. The most difficult problem is to have municipal officials that are willing and cooperative. A very important issue is to define a possible external positive effect of energy project in the framework of local/regional policy directions (financed by SF), and summarize these effects as a total input of energy projects' implementation.

An additional positive effect on energy saving, energy efficiency measures and RES most often compile with the local and regional development objectives:

- RES, being indigenous sources of energy improve the security of energy supply and diversity of the fuel mix.
- RES have advantages for regions, in which power and heat supply costs are considerably higher than average costs in the country. Thus the use of RES – electricity and heat in small isolated systems can also help to avoid or delay expensive extensions to the grid.
- Some RES are a labour intensive form of industry and create jobs especially at location sites in rural areas.

Method of evaluation of the above named advantages to be included into the evaluation process in feasibility studies is under elaboration.

5. CONCLUSIONS

1. The procedures for permits and licensing could be changed to improve the entrance and exit conditions for energy marked players.
2. Successful integration of “bottom up” method for sustainable energy development would have a positive impact on effectiveness if the authorities (municipalities, government) will be capable generate and implement ideas. It is necessary to organize training for municipal staff responsible for the energy sector. Municipal experts must be trained to collect the data and develop business plans for investment. It would be useful to obligate the local authorities to develop own energy development plans and coordinate them with responsible national institutions for policy implementation (e.g. Ministry of Energy) and EU directives.
3. The sustainable energy development in regions could be achieved more efficient if responsible institution for development of National energy strategy would be capable to take the Master role to organize competitions for municipal authorities for investment projects. Projects could be financed by environmental pollution taxes, excise duty for natural gas and so on.

REFERENCES

1. European Commission’s report. (2004). Link to the internet: http://europa.eu.int/eur-lex/pri/en/dpi/cnc/doc/2004/com2004_0029en02.doc
2. V. Klevas. D. Šreimikienė. The basics of Lithuanian energy economy. Monograph, 2006, No 1, p. 17–44.
3. V. Klevas., D. Streimikiene., A. Klevienė. Sustainability assessment of the energy implementation in regional scale // Renewable and Sustainable Energy Reviews, 2009 N 13, p. 155–166.
4. V.Klevas., M. Antinucci. Integration of national and regional energy development programs in Baltic States // Energy Policy. – 2004. – No 3, p. 345–355.
5. European Parliament and Council Directive 2009/28/EB. Link to the internet: http://eur-lex.europa.eu/LexUriServ/LexUriServ.do?uri=OJ:L:2009:140:0016:0062:EN:PDF
6. European Parliament and Council Directive 2001/80/EC. Link to the internet: http://eur-lex.europa.eu/LexUriServ/LexUriServ.do?uri=OJ:L:2001:309:0001:0001:EN:PDF

CYSENI 2010, May 27–28, Kaunas, Lithuania
ISSN 1822-7554, www.cyseni.com

AIR VELOCITY MEASUREMENTS USING ULTRASONIC ANEMOMETER: ERRORS AND DISCREPANCIES

A. Bertašienė
Lithuanian Energy Institute
Laboratory of Heat Equipment Research and Testing
Breslaujos str. 3, LT–44403 – Lithuania
Phone: +370 37 401865
Email: agne@mail.lei.lt

ABSTRACT

Ultrasonic anemometers are widely used in many applications in the field of outdoor measurements of the wind velocity vectors. Recently indoor air measurements are in rapid progress. Wide variety of new sonic instruments induces more detailed analysis of application possibilities and instruments characteristics. 1 D, 2D and even 3D ultrasonic anemometers are available for velocity, turbulence, and temperature studies.

Though sonic anemometers have been studied in field measurements for more than two decades new designs and new possibilities make research more complicated and are evoking larger complex of errors and deviations.

Several types of anemometers are described in the paper and observed errors as well as predicted ones are discussed. Comparison of velocity values are depicted using ultrasonic anemometer fitted under laboratory conditions, portable sonic and laser anemometers. For higher velocities static Pitot tube and convergent nozzle values are taken as reference ones. Different test facility conditions are under research to find installation effects. Fluid flow development in the channel and temperature impacts on response time or even velocity value is revealed.

The conclusion was made that different conditions of air velocity reproduction initiated high discrepancies of measured values. Probe orientation and transducer shadowing makes effects on true value transferred.

Keywords: air velocity, ultrasonic anemometer, measurement errors, installation effects

1. INTRODUCTION

Air/gas flow measurements are one of the most talking point studying modern industry issues. Air/gas flows use in various different kinds of industrial technological processes, heating/conditioning systems and controlling microclimate in living/working places urge the consumer to be involved into detailed research of microclimate behaviour in a certain medium with its leading factors. In scientific point of view air velocity distribution measurements are significant in a sense that they display mass and energy transfer consistent pattern.

Air flow measurement techniques are based on different principles and methods as well [1]. Taking into account aims and condition peculiarities measurement instruments are selected. The most essential for instrument selection is the cost issue as well as low velocity range measurement capabilities in practice.

The latter problem is evident when operating with widely usable mechanical instruments such as cup, vane anemometers [2] and conventional static Pitot tubes [3]. Thermal anemometry (TA) that is very sensitive for flow environmental conditions (temperature, humidity and contamination) has its own limitations based on velocity threshold around 10–15 cm/s [3–4]. Low velocity range for hot wire systems requires special and frequent recalibrations. Air flow meters having operating principles of wave methods are the most promising for nowadays but are of small cost effectiveness. Laser Doppler velocimetry (LDV or LDA) technique has the potential of being a valuable tool for fluid velocity measurements in wide range of velocities [5] and sampling frequencies providing valuable information regarding flow pattern and behaviour but the need for release of seed particles limits its applications as well as high cost of the systems. An alternative nonintrusive method that can be used for airflow pattern predictions is numerical simulation via computational fluid dynamics (CFD) computer models [6] that knowing geometry and boundary conditions teamwise with physical models of laden in the medium particle response to the predicted field gives a visual view of exploratory object. However employing CFD models in real experimental applications has serious limitations, and their validation comes into narrow nonconfident field with limited configuration.

As most of nowadays applications come into microscale fields regarding to low velocity values an experimental technique that may contribute to airflow studies and help validation of CFD models is direct measurements using sonic anemometry [7]. This technique provides highly accurate 1, 2 or 3 dimensional (1D, 2D, 3D) measurements of velocity vector components in the range of centimetres per second. Ultrasonic methods due to their simplicity, cheapness and prompt response to fluctuations are widely used in gas flow measurements. The applications cover the range from micrometeorology to optical propagation.

2. ULTRASONIC ANEMOMETER

2.1. Advantages and disadvantages of anemometer

Sonic (ultrasonic) anemometer (UA) avoid many problems associated with the traditional rotating anemometer and vane sets inertia of moving parts, bearing wear, contamination from dust and ice, frequent maintenance, having no starting threshold or special fluid preparation with particles. The accuracy of the sonic anemometer is inherently stable because its accuracy is determined primarily by the distance between the transducers. The small size and fixed orientation of the transducers allow them to be heated at minimum power expense to prevent icing.

Using acoustic measurement principle, the airflow velocity does not need to be converted into another value, as it is in thermoanemometry. Equipping the device with suitable metrological features (measurement range, sensitivity and accuracy) takes place on the construction level and does not require calibration in an aerodynamic tunnel. UA is characterized by a wide measurement range, ranging from hundredths of m/s to tens m/s. The precision of velocity and airflow direction measurements depends only on the precision of the transit time values t_1, t_2 and d (sound pulse path length) measurements. The devices response to airflow velocity and direction (eliminating of the transducers characterised by relatively high inertia) variation is very fast. The speed of reaction depends on the frequency of emitting the sound pulses. Practically speaking, the measurement can be taken as often as a few hundred times per second [7].

But anyway UA has its own disadvantages as well. Main disadvantages of sonic anemometers include:

- high complexity of electronic systems emitting and registering sound pulses and fragile sensors construction,
- division of vertical and horizontal measuring axes (occurring in some types of anemometers),
- spatial averaging of airflow velocity to the area where measuring paths are distributed (definite spatial resolution),

- occurring flow disturbances – "shadowing" – caused by the circumflow of air around cantilevers and sensors.

The fact that data collected by sonic anemometer is not continuous loses on significance in most cases when we know that probing can be done with very high frequency [7].

Main sources of errors during measurement by means of acoustic anemometers are:

- wrong spatial orientation of the anemometer,
- declination from vertical axis (it should not exceed 1°),
- incorrect setting of the device's azimuth,
- disturbances of flow caused by cantilevers and sensor heads.

In extreme cases the flow velocity may be underestimated by about 10%. Atmospheric deposits and raindrops sediment on sensors, intense precipitation or dust suspensoid – causing disturbances in flow of sound pulses between sensors; electronic disturbances, impacting the quality of reception of sound pulses – their influence is mineralised in the process of construction [7].

Anyone who has tested sonic sensors in a wind tunnel soon discovers the major drawback to sonic anemometry. The physical construction of the sensor provides obstacles to airflow that modify the sensed velocity within the sample volume. Designers of most 3-D research grade sonic anemometers using six transducers go to great length to minimize the cross section of the device to the dominant horizontal wind. Many of these anemometers have three transducers pointing upward and three companion transducers pointing downward. Thus, no path is directly in line with the direction of expected maximum wind speed, minimizing adverse effects of turbulence. When wind flows past the transducer, it must move around the unit's body. This creates local pressure gradients that may become turbulent. The pressure gradient can decrease the efficiency of transfer from electrical energy to sonic energy (and conversely, from sonic energy to electrical energy) in the transducers, decreasing the received signal strength. The pressure gradients also modify the sonic propagation, much like the bending of light at the boundary between two materials of different indices of refraction, adding to the decrease of received signal strength.

At the same time, the turbulence increases the acoustic noise. The drop in the S/N ratio prevents the anemometer from achieving top wind speed performance. Wind tunnel tests indicate that the effects of turbulence increase when the path between transducers is parallel to the wind. This is a problem for orthogonal geometry sonic anemometers because they have only two basis vectors and need both to determine the horizontal wind velocity. This is where the three-transducer geometry shines. Because the geometry provides one redundant basis direction, the parallel or near parallel basis can be discarded, and the sensor can still find a solution for wind velocity with the other two bases.

2.2. Operation principle

The method of acoustic measurement of airflow is based on the phenomenon of the impact of airflow velocity on the velocity of sound wave spread (Doppler effect). The sonic anemometers working principle is based on measuring time of sound pulses travel in opposite directions, in the same moment, along a known measurement path.

The measurement of single component of wind velocity vector is conducted by means of a set of two transducers, typically piezoelectric devices, placed concentrically against each other in a defined distance, emitting and registering sound pulses. Sonic anemometers are composed of two or three such sets (measuring axes), creating a frame of reference where specific components of wind velocity vector are measured (Fig. 1). In devices in which two axes are installed only horizontal components are measured, in devices equipped with three such axes, also the vertical component is registered [8].

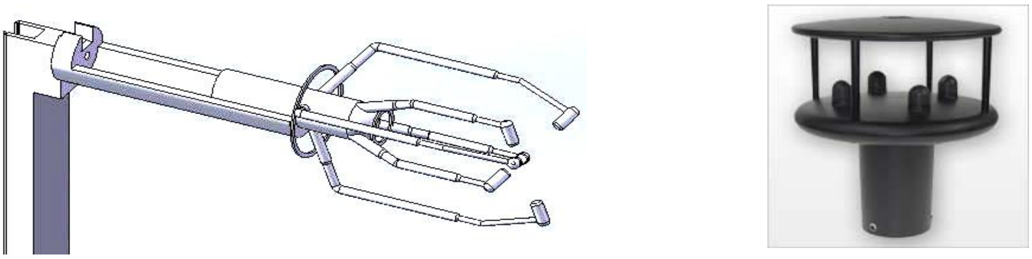

a) 3D Kaijo Sonic 600 DE [9] b) 2D Windsonic, GILL Instruments

Fig. 1. Different type of UA transducers' configuration

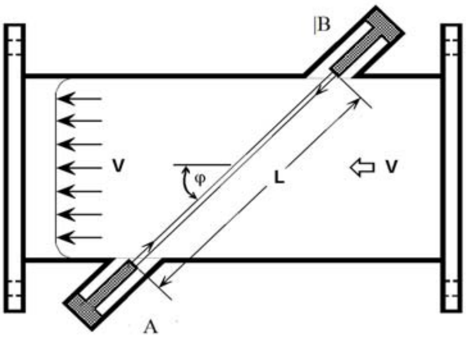

Fig. 2. Detailed scheme of UA installed in the channel: A, B – niches for transducers

As it was mentioned using UA time difference of ultrasound propagation downward and upward to air flow directions is defined. Air velocity using UA in Fig.2 is calculated via:

$$c = \frac{2L}{\left(t_1 + t_2 - 2t_{el}\right)}, \tag{1}$$

$$v = \frac{\left[(L - \Delta L)/2\cos\varphi\right]\left(t_2 - t_1\right)}{\left[\left(t_2 - \Delta L/c - t_{el2}\right)\left(t_1 - \Delta L/c - t_{el1}\right)\right]}, \tag{2}$$

here t_1, t_2 – signal propagation time between transducers down the flow (1) and upwards (2), c – sound velocity; $t_{el1,2}$ – signal delay in electric circuit down the flow (1) and upwards (2), $L = L_0 + \Delta L$ – distance between transducers, ΔL – measured distance elongation due to transducers installation into the niches made in pipe wall, L_0 – distance from pipe wall

Using the latter UA to reproduce air velocity value signal propagation times, length of signal path that intersects with air velocity propagation direction at an angle φ and sound velocity in a still medium should be measured. As air velocity distribution could be nonuniform in the cross-section of the pipe it should be know in advance before averaging velocity along sound ray path.

KAIJO UA enables to measure three dimensional (X(axial), Y, Z) velocity vector derived from the propagation time of the ultrasonic waves between each of three pair of transducers and signal processing unit provides a scalar value of the air velocity:

$$v = \sqrt{v_x^2 + v_y^2 + v_z^2}\ . \tag{3}$$

3. EXPERIMENTAL RESULTS AND DISCUSSION

All the experiments related to the topic are made in a test rig that is depicted in a Fig. 3. In previous publications [3, 5, 10] good correlation of UA values with the measured by LDA and calculated from convergent nozzle ones was shown. Resolution of laboratory UA is from

0.03–0.04 m/s giving stable values up to 10 m/s but used to measure mean velocity only. UA is arranged at the initial sector of the channel the influence of developing boundary layer is weak and values of UA could be treated as local velocity at the central core of the channel axis with high accuracy taking into account coefficient of proportionality. After detailed analysis it could be stated velocity uncertainty that shows very similar level to the LDA one. Contribution factors and total expanded uncertainty is given in a Table 1.

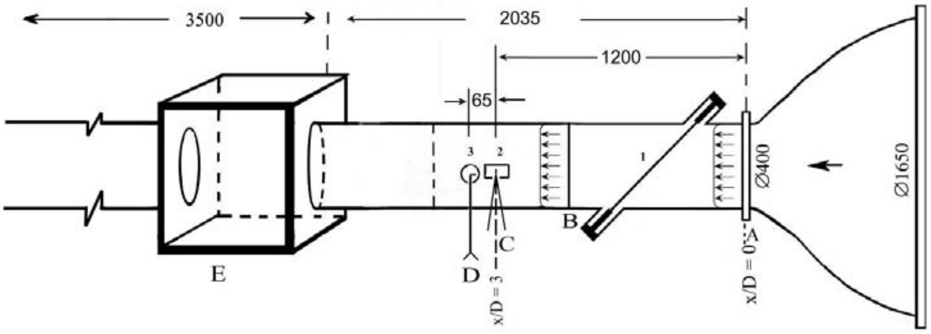

Fig. 3. Test facility: 1 – UA measurement plane, 2 – a window for LDA measurements (C plane) and 3 – a hole for instrument under calibration (D plane). A, B, E – measurement planes

Table 1. Total UA uncertainty and contribution components

Sources of uncertainty	**Estimate**	**Standard uncertainty**	**Distribu-tion**	**Sensiti-vity coeffi-cient**	**Contri-bution to the uncer-tainty, %**
Sound velocity uncertainty					
Distance between transducers, L	0.5922 m	± 0.021 mm	Rectangular	1	0.0014
Signal delay time,	$15.5 \cdot 10^{-6}$ s	± 0.02 μs	Rectangular	1	$3 \cdot 10^{-4}$
Signal propagation time measurement downstream, t_2	1700 μs	± 0.02 μs	Normal	1	0.00112
Signal propagation time measurement upstream, t_1	1774 μs	± 0.02 μs	Normal	1	0.00111
Temperature, T	20 ºC	0.07 ºC	Rectangular	0.5	0.0118
Humidity, φ	50 %	0.69 %	Triangular	1	0.002
Air molar mass, μ	28.9626 kg/kmol	0.001	Normal	-0.5	0.001
Gas constant R	8314.51 J/mol·K	0.00007	Normal	0.5	$2.43 \cdot 10^{-7}$
Adiabatic coefficient, κ (for air)	1.4001	0.0001	Normal	0.5	0.0021
Acceleration, g	9.8145 m/s^2	0.001	Normal	0.5	0.0029
Air velocity uncertainty					
Velocity of sound calculation, c	344.035 m/s	0.1186	Normal	1	0.0048
Repeatability	0.05 m/s 0.2 m/s 1.0 m/s 10.0 m/s	0.00196 m/s 0.00184 m/s 0.00148 m/s 0.00263 m/s	Normal	-	3.8854 0.9836 0.1477 0.0286

Reproducibility	0.05 m/s 0.2 m/s 1.0 m/s 10.0 m/s	0.00375 m/s 0.00359 m/s 0.00341 m/s 0.00320 m/s	Normal	-	7.504 1.795 0.341 0.032
Signal propagation time measurement downstream, t_2	1700 μs	± 0.02 μs	Normal	1	0.00116
Signal propagation time measurement upstream, t_1	1774 μs	± 0.02 μs	Normal	1	0.00115
Angle between transducers, α	45.65°	± 0.5 °	Rectangular	1	0.6324
Length of distance under flow $L_0=L-\Delta L$	0.5594 m	± 0.021 mm	Rectangular	1	0.00217
Air velocity in the channel, m/s					**0.05** **0.2** **1.0** **10.0**
Expanded uncertainty (k=2), %					17 4.3 1.5 1.3

The major factors contributing total air velocity uncertainty are angle between transducers determination and value repeatability and reproducibility coming up from velocity reproduction by the test rig. Sound velocity determination is very dependent on ambient conditions (T and φ) variation.

Trying to analyse peculiarities of flow development in the channel air velocity change in the centre (maximum velocity) has been shown by Fluent using laminar model. Fig. 4. shows maximum velocity growth in the channel, the initial inlet region from convergent nozzle with 1650/400 mm diameters is characterized by unsettled flow that needs at least 2–3D (D-diameter of the channel, 400 mm) to be set. At the distance x/D=3, the plane where LDA measurements basically are done (C plane, Fig. 3.), the flow reaches establishment phase and downwards the flow remains unchanged with slightly growing boundary layer.

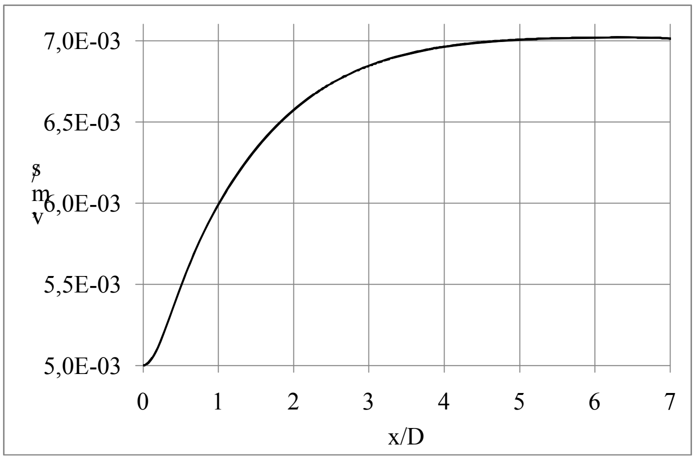

Fig. 4. Axial velocity development from the nozzle outlet modelled by FLUENT, $v = 0.005 m/s$

The flow establishment is confirmed by the experiment with 2D Windsonic portable UA made by GILL and depicted in Fig.1.b. The instrument was tackled on the peel and dragged along the channel from the nozzle outlet, initial region of the channel, near the wall. Despite this UA enables to measure two velocity vectors it shows flow angle (α, °) upcoming towards as well, revealing vorticity. From angle measurement results one could state that the flow has a uniform profile though for low velocities it was noticed that flow is vortical

(Fig. 5). This phenomenon could influence air velocity measurement accuracy and real velocity value overall. It happens due to the uneven flow transversely the perimeter of inlet channel. At the very beginning of the initial region in the channel air drag could develop along the axis and the intensity could alter in essence when lowering velocity.

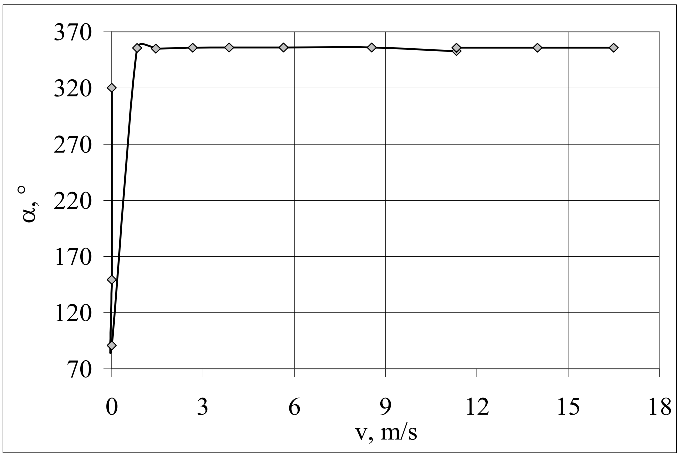

Fig. 5. Instantaneous axial velocity vector angle in dependence of axial velocity magnitude

When speaking about low velocities, low Reynolds (Re) region ($1.3 \cdot 10^3$–$5 \cdot 10^3$), transitional flow regime starts manifesting with its instabilities in a manner of Tollmien-Shlichting waves that basically exist at the boundary layer. When increasing velocity these waves transform into turbulent vortices in fully developed turbulent flow. Low turbulence degree in turbulent region, when decreasing velocity from $v = 0.15 m/s$, (Fig. 6) sharply increases when transitional flow region, $v = 0.05 \div 0.15 m/s$, is reached. And moreover turbulence intensity variation is uneven.

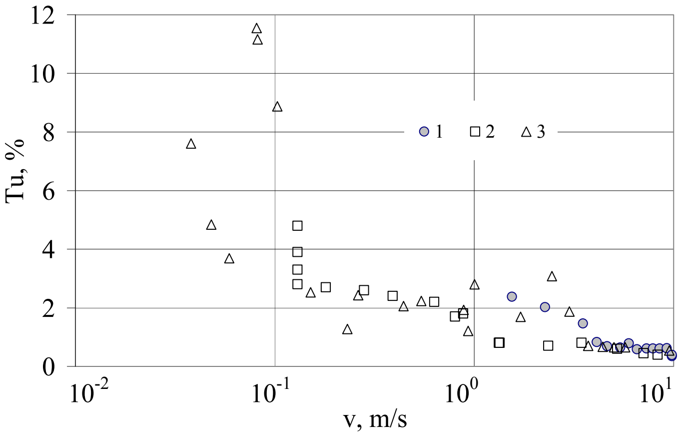

Fig. 6. Measurement of turbulence in the channel by: 1 – 1D UA, 2 – TA, 3 – LDA

The transitional region is very sensitive to various disturbances but suppressing them transitional region could be shifted towards higher Re range or reinforcing them could be shifted the region towards much lower Re values. Regrettably, this phenomenon is complicated and poorly explored. Turbulence intensity (Tu, %) evoked by various scale and high frequency vortices in turbulent flow does not make any sense to local velocity measurements but for low velocities involving transitional region it influences velocity measurements and could be a considerable contribution to result uncertainty especially for values of instruments sensitive to Tu variation. In Fig. 6 one can see a Tu degree measured by different instruments in different scale (LDA in 1.5 mm, TA in 30 mm and UA in 400 mm volume) but is of similar magnitude. Small scale Tu is cut off when measuring with UA and only large scale pulsations are averaged in 400 mm pipe.

Investigations of flow using 3D Kaijo Sonic UA confirm the propositions made in the paper. Three velocity components reveal flow pulsations in X (axial velocity direction), Y and Z directions and are depicted in Fig. 7 and 8. In Fig. 7 standard deviations in m/s of each velocity vector pulsation in dependence of axial velocity show that with velocity increase all components pulsations absolute values are of similar magnitude and increase non gradually especially at low velocities.

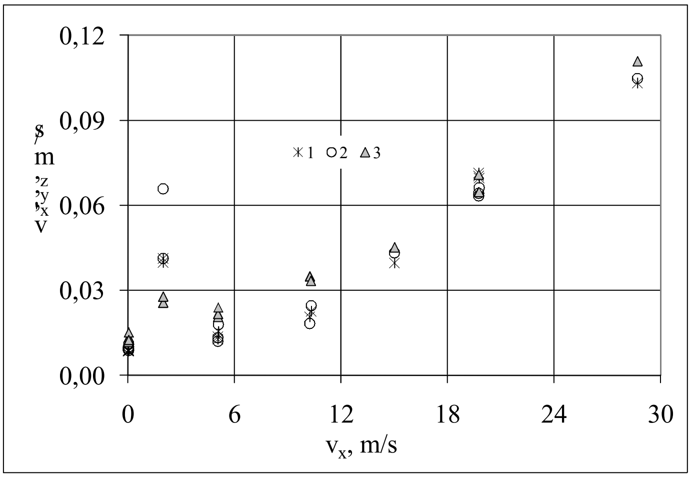

Fig. 7. Standard deviations of velocity component pulsation in dependence on axial velocity increase (velocity pulsations $v'_{x,y,z}$ in 1-2-3 respectively Y, Z and X directions, v_x – axial (longitudinal) velocity component)

At 2 m/s ($Re = 5.3 \cdot 10^4$) a sudden pulsation augmentation is observed, relative value of which increases greatly (Fig. 8). Further with axial velocity increase pulsations settle into the range of 0.4 % confirming sharp flow structure reformation in transitional regime and remaining stable later as turbulent flow starts to develop. In all measured velocity range transverse components are small showing longitudinal flow domination in the channel.

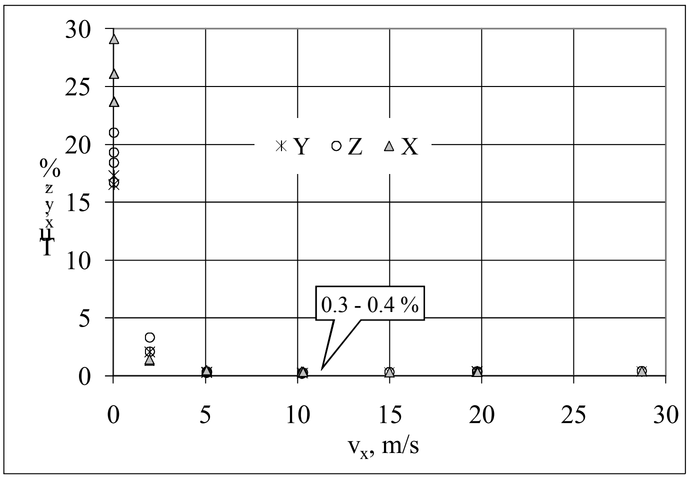

Fig. 8. Relative flow turbulence in X, Y and Z directions

So, transverse pulsations influence is weak except for low velocities it manifests (Fig. 9). For lower than 2 m/s the level of these pulsations increases up to 2.5% when for all the rest velocities is ~0.5%.

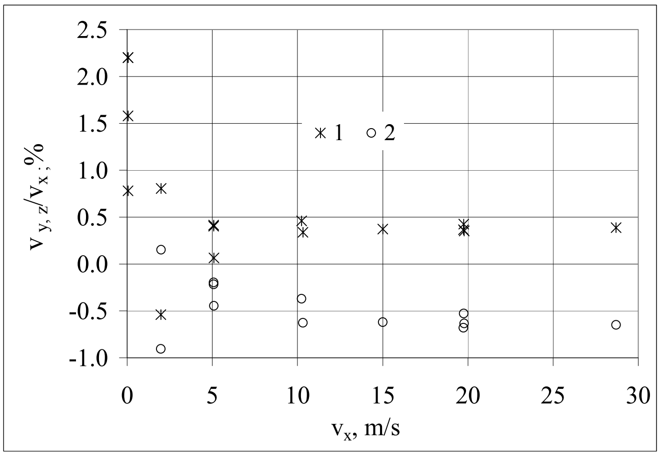

Fig. 9. Flow vorticity along the channel

Reformation of flow structure during transitional process makes a considerable impact to low velocity value reproduction that was evident in result scattering during EURAMET intercomparison participants [11] and uncertainty level increase due to velocity value reproducibility and repeatability depending not only on instrument resolution and accuracy.

Fig. 10. shows a very relative results of uncertainties of high accuracy instruments – LDA and ultrasonic ones – portable KAIJO and laboratory UA. Transitional flow regime is characterized by sharp increase of uncertainty up to 20%. For a wide range velocity measurement uncertainty does not exceed 0.7% with LDA, 2% with UA.

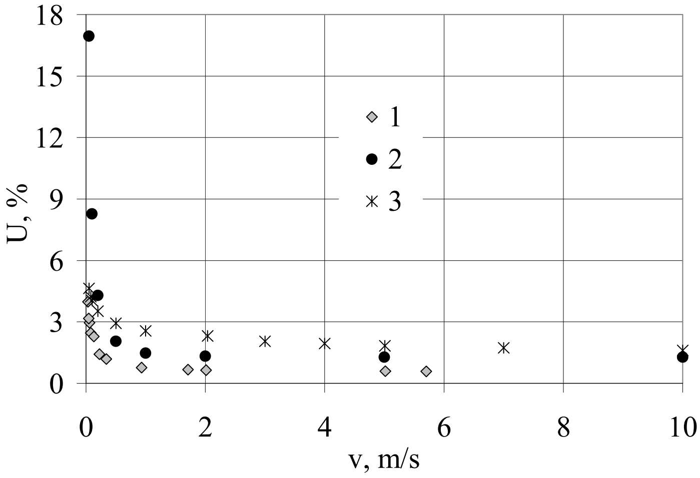

Fig. 10. Total uncertainty comparison of: 1 – LDA, 2 – UA 1D, 3 – 3D UA Kaijo SONIC

4. CONCLUSIONS

Transitional flow regime could be divided into two zones. First one, when $\mathrm{Re} = 10^3 - 5 \cdot 10^3$, longitudinal instabilities dominate in the flow structure and evoke high transverse velocity value components. It could be attributed as early initial stage of instabilities development and the question has no reply if flow suck phenomenon influences this zone and the range of it. In the second zone ($\mathrm{Re} = 5 \cdot 10^3 - 1(5) \cdot 10^4$) instabilities intensity is increasing up to vortices structure that is typical when developing of turbulent flow. The region displays pulsation increase. High flow sensitivity for low Re to various disturbances causes transitional flow regime zones displacements. Instruments accessing this region acts in different manner and measurements become complicated and with no repeatable consistent pattern.

REFERENCES

1. DAUGELĖ A., ILGARUBIS V., JANUŠAS V. National standard of air velocity. Methods of realization. *Measurements,* 2002, No 3 (23), p. 13–20. ISSN 1392–1223.
2. HUNTER R.S. Wind speed measurement and use of cup anemometers. 1999. [Referred on the 9th of February, 2010]. Link to the internet< http://www.ieawind.org/Task_11/RecommendedPract/11%20Anemometry_secondPrint.pdf >
3. PEDIŠIUS A., JANUŠAS V., BERTAŠIENĖ A.. Low air velocity measurement characteristics' variation due to flow regime. *Int. journal of mechanical, industrial and aerospace engineering.* 2009, Vol. 3, No 1, p. 25–29. ISSN 2073-056X.
4. BERTAŠIENĖ A.. Air conditions evaluation quality and accuracy in residential and working places using measuring thermal anemometers. *Science – Lithuanian future*. Building engineering systems. 2009, Vol. 1, No 1, p. 18– 1. ISSN 2029-2341.
5. BERTAŠIENĖ A., DAUGELĖ A., JANUŠAS V. Investigation of practical application of laser Doppler anemometer. *Measurements*. 2006, No 2 (38), p. 5–10. ISSN 1392-1223.
6. JANUŠAS V., ILGARUBIS V., DAUGELĖ A.. Research of air velocities reproduction. *Measurements*. 2004, No 2 (30), p. 11–14. ISSN 1392-1223.
7. PIASECKI J., SAWINSKI T.. Acoustic measurements of airflow in speleo-climatological studies. *Karst and Cryokarst, Studies of the Faculty of Earth Sciences University of Silesia.* 2007, No 45, p. 237–256. ISSN 1895-6777.
8. LOCKYER R. A sonic anemometer for general meteorology. 1996. Copyright by Helmers Publishing Inc. [Referred on the 5th of January, 2010]. Link to the internet < http://www.vaisala.com/files/A_Sonic_Anemometer_for_General_Meteorology.pdf>
9. TERAO Y., VAN DER BEEK M., YEH T.T., MULLER H. Final report on the CIPM air speed key comparison (CCM.FF-K3). 2007.
10. BERTAŠIENĖ A., JANUŠAS V.. Different flow regimes and test facility constructions impact on a stable low air velocity value reproduction. Proceedings of the 7th IASME/WSEAS Int. conference on FLUID MECHANICS and AERODYNAMICS. 2009, August 20–22, p. 163–169. ISSN: 1790-5095.
11. BERTAŠIENĖ A.. Research of medium conditions' and flow perturbations' influence on reproduced air velocity values. CYSENI 2009. 6th annual conference of young scientists on energy issues [CD]. Kaunas: LEI, 28–29 May, 2009, p. 253–263. ISSN 1822-7554.

MODELLING OF MIXED CONVECTION HEAT TRANSFER IN AN INCLINED FLAT CHANNEL USING TURBULENCE TRANSITION MODELS

G. Drumstas
Lithuanian Energy Institute
Laboratory of Nuclear Engineering
Breslaujos str. 3, LT44403 Kaunas – Lithuania
Phone: +37037401889
Email: d.giedrius@mail.lei.lt

ABSTRACT

In this paper we present the results on numerical investigation of the local opposing mixed convection heat transfer in the laminar-turbulent (transition) region in the inclined flat channel (inclination angle $\varphi = 60^{\circ}$ from horizontal position) using Ansys Fluent 12 code. Modelling was performed using *kkl-ω, SST and Reynolds Stress low-Re stress-ω* models. The data of modelling, using turbulence transition models, have been compared with experimental data and previous results of numerical modelling using *laminar* model. Numerical investigations have been performed for the same conditions as during the experiment with airflow pressure of 0.4 MPa and at the Reynolds numbers of $1.9 \cdot 10^3$, 2.4 10^3, $3.1 \cdot 10^3$, $4.7 \cdot 10^3$ and Grashof numbers $1.5 \cdot 10^9$, $1.7 \cdot 10^9$, $1.9 \cdot 10^9$, $2.4 \cdot 10^9$ respectively. There is some difference between the results generated using different turbulence transition models, but in all cases modelling results demonstrate that vortices exists near the upper and bottom heated walls.

Keywords: opposing mixed convection, inclined flat channel, transition region, numerical modelling

1. INTRODUCTION

For modern nuclear and thermal energy technologies, computer, chemistry and other technologies reliability requirements are very important. So, designers of such technologies must have the detailed information about the processes including thermal ones that very often define the reliability and operation lifetime of the equipment.

Heat and momentum transfer in single-phase flows in case of complex processes under effect of buoyancy, are still not investigated in details. Due to the importance of the problem for engineering applications a lot of researchers concentrated their attention to the turbulent mixed convection heat transfer investigations in vertical circular tubes. Wide investigations on this problem for turbulent flow in the vertical and horizontal channels were performed at the High Temperature Institute in Moscow [1], at the Manchester University [2, 3] and at the Lithuanian Energy Institute (LEI) [4–6]. At the LEI also investigations of the turbulent mixed convection in the inclined flat channels with one side heating (under effect of stable and unstable air density stratification) have been performed [7–9]. It was revealed that heat transfer is closely related to the channel inclination angle in case of the stable density stratification but heat transfer practically does not depend on the channel inclination angle in case of the unstable air density stratification.

Investigations of heat transfer in the laminar-turbulent transition region under the effect of buoyancy are rather limited. The flow character in pipes in a laminar-turbulent transition region was investigated in [1, 10–12]. In paper [13] the results on numerical investigation of the local opposing mixed convection heat transfer in a vertical flat channel with symmetrical heating for laminar and vortex airflow (at p = 0.1; 0.2 and 0.4 MPa and Re numbers from 1500 up to 4310, with Gr_q number variation from $1.65 \cdot 10^5$ to $3.1 \cdot 10^9$) were presented. The new correlations were suggested for determination of the non-dimensional distance at which the flow stability is lost in the flat channel with opposing flows. In another paper [14] the detailed results on experimental and numerical investigation of the local opposing mixed convection heat transfer in a vertical flat channel with symmetrical heating ($q_{w1} \approx q_{w2} \approx$ const) in the laminar-turbulent transition region were presented. It was shown that as the influence of the buoyancy becomes stronger the circulating flows appear along the channel. These flows cause asymmetry of velocity profiles and increase in heat transfer up to $Re \approx 8 \cdot 10^3$, when p = 0.4 MPa. The experiments were performed at airflow of different pressures (0.1, 0.2 and 0.4 MPa) in the range of Re from $2 \cdot 10^3$ to $5 \cdot 10^4$ and Gr_q up to $1.5 \cdot 10^{10}$. In the paper [15] the results on experimental investigations of the local opposing mixed convection heat transfer in the same vertical flat channel with symmetrical heating in the laminar-turbulent transition region at higher air pressures (0.7, 0.8 and 1.0 MPa) when buoyancy effect is prevailing in the range of Re from $2 \cdot 10^3$ to $4 \cdot 10^4$, and Gr_q up to $1.0 \cdot 10^{11}$ were presented. The experimental data show similar tendencies in the heat transfer at higher air pressures (0.7 –1.0 MPa) as it was revealed at smaller air pressures (0.2–0.4 MPa). But at higher air pressures the transition from the vortical flow regime to the turbulent one does not causes such drastic decrease in heat transfer as it was noticed at smaller air pressures (for p = 0.2 MPa at $Re \approx 4000$, for p = 0.4 MPa at $Re \approx 8000$). The recent review of the mixed convection in the channels including transition region was presented in [16]. Poskas et al. [17] presented the preliminary results on experimental investigations of the local opposing mixed convection heat transfer in the inclined flat channel (inclination angle $\varphi = 60^o$ from horizontal position) with symmetrical heating in the laminar-turbulent transition region at 0.4 MPa air pressures when buoyancy effect is prevailing in the range of $Re = 1.5 \cdot 10^3 – 5.3 \cdot 10^4$, and Gr_q up to $1.5 \cdot 10^{10}$. The experimental data show similar tendencies in the heat transfer as it was revealed in vertical channel. There are only minor differences in the local heat transfer for upper (stable density stratification) and bottom (unstable density stratification) walls.

In this paper the results on numerical investigations of the local opposing mixed convection heat transfer in the laminar-turbulent transition region in the same flat channel with inclination angle $\varphi = 60^o$ from horizontal position is presented. Numerical two-dimensional simulations were performed for the same channel and for the same conditions as in experiments using Fluent code. Simulations were performed at air pressure p = 0.4 MPa with symmetrical heating for the Reynolds numbers of $1.9 \cdot 10^3$, $2.4 \cdot 10^3$, $3.1 \cdot 10^3$, $4.7 \cdot 10^3$ and Grashof numbers $Gr_{qin} = 1.5 \cdot 10^9$, $1.7 \cdot 10^9$, $1.9 \cdot 10^9$, $2.4 \cdot 10^9$ respectively.

2. METHODOLOGY

In this paper results on two-dimensional numerical modelling of opposing mixed convection (upward oriented flow due to natural convection and downward oriented flow due to forced flow) in inclined flat channel (height – 0.0408 m, length – 6 m, hydrodynamic unheated length – 2.5 m, heated (calorimeter) length 3.5 m) with two sides symmetrical heating ($q_{w1} = q_{w2}$ = const) are presented for steady state flow conditions in airflow. The modelling was performed using turbulence transition models: *kkl-ω*, *SST*, and *Reynolds Stress low-Re stress-ω* model.

The *k-kl-ω* model is considered to be a three-equation eddy-viscosity type, which includes transport equations for turbulent kinetic energy k, laminar kinetic energy k_L, and the inverse turbulent time scale ω [18]. The transition SST model is based on the coupling of the *SST k-ω* transport equations with two other transport equations, one for the intermittency and one for the transition onset criteria, in terms of momentum-thickness Reynolds number [19]. The low-Re stress-omega model is a stress-transport model that is based on the omega-ω equations and LRR (Launder, Reece and Rodi) model [20].

The modelling has been carried out using Ansys FLUENT 12 code. It is a contemporary computational fluid dynamics code, which is used for modelling the fluid flow and heat transfer in complex two-dimensional or three-dimensional systems [21]. This code solves the main flow and energy equations. In this case a control volume based technique is used which is based on division of the domain into discrete control volumes using a computational grid (which at the same time describes channel geometry).

The steady state mean flow equations to be solved in the two dimensional problem are:

conservation of mass (continuity),

$$\frac{\partial(\rho u_x)}{\partial x}+\frac{\partial(\rho u_y)}{\partial y}=0 \tag{1}$$

conservation of the u_x and u_y momentum,

$$\rho u_x\frac{\partial u_x}{\partial x}+\rho u_y\frac{\partial u_x}{\partial y}=-\frac{\partial p}{\partial x}+2\frac{\partial}{\partial x}\left(\left(\mu+\mu_t\right)\frac{\partial u_x}{\partial x}\right)+\frac{\partial}{\partial y}\left(\left(\mu+\mu_t\right)\left(\frac{\partial u_x}{\partial y}+\frac{\partial u_y}{\partial x}\right)\right)\pm\rho g\sin\varphi\ , \tag{2}$$

$$\rho u_x\frac{\partial u_y}{\partial x}+\rho u_y\frac{\partial u_y}{\partial y}=-\frac{\partial p}{\partial y}+2\frac{\partial}{\partial y}\left(\left(\mu+\mu_t\right)\frac{\partial u_y}{\partial y}\right)+\frac{\partial}{\partial x}\left(\left(\mu+\mu_t\right)\left(\frac{\partial u_x}{\partial y}+\frac{\partial u_y}{\partial x}\right)\right)+\rho g\cos\varphi \tag*{3)}$$

and energy equation.

$$\rho u_x\frac{\partial i}{\partial x}+\rho u_y\frac{\partial i}{\partial y}=\frac{\partial}{\partial x}\left(\left(\frac{\mu}{\Pr}+\frac{\mu_t}{\Pr_t}\right)\frac{\partial i}{\partial x}\right)+\frac{\partial}{\partial y}\left(\left(\frac{\mu}{\Pr}+\frac{\mu_t}{\Pr_t}\right)\frac{\partial i}{\partial y}\right). \tag*{4)}$$

Boundary conditions are:

- At the inlet to the experimental setup longitudinal air velocity u_x is equal to inlet velocity u_{in}, transversal velocity $u_y = 0$. Air enthalpy i at the inlet to the calorimeter is equal to the inlet air enthalpy i_{in}.
- On the walls ($y = 0$ and $y = h$) longitudinal u_x and transversal u_y velocities are equal to 0. Heat flux on the calorimeter walls are $q_{w1} = q_{w2} =$ const.

In the course of modelling process, it is very important to create the proper grid, since in most cases it defines the accuracy of the modelling and the stability of the solution. The grids 30 x 2200, 50 x 6000 and 60 x 7500 were tested in [22] and finally the grid 60 x 7500 was selected, because the tests show good agreement of results for last two grids. In this paper else more higher grid 80 x 7500 was used (Fig. 1).

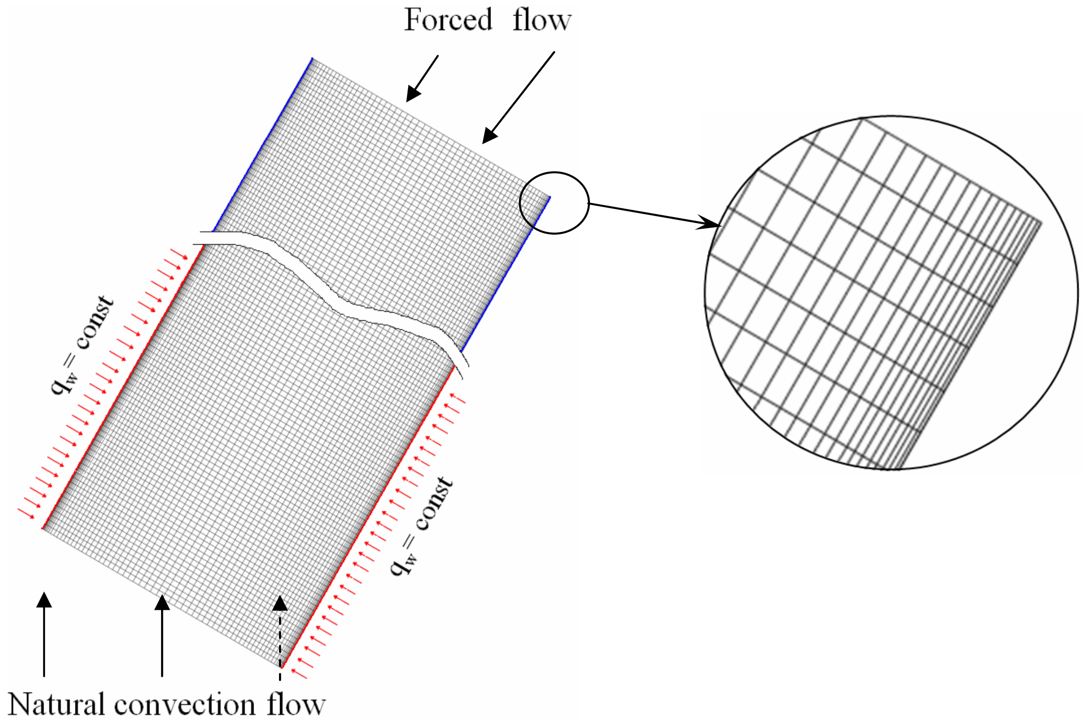

Fig. 1. Computational domain and partial view of the grid

3. RESULTS

The velocity profiles for various transitional models: *kkl-ω*, *SST*, *Reynolds Stress low-Re stress - ω* and *laminar*, for $Re_{in} = 3.1 \cdot 10^3$ are illustrated in Fig. 2.

We can see that using *kkl-ω* model (Fig. 2a) the flow in the central part of the channel is always downward oriented for all x/d_e (the direction of forced flow), but velocity profiles at some x/d_e are asymmetric. The flow structure shows backward flow near both walls (Fig. 3). At $x/d_e = 1.9$ (Fig. 2a, curve 1) the backward flow near the both channel walls occupies almost the same part of the cross-section, and the maximum velocity is at $y/h \approx 0.5$. At $x/d_e = 3.9$ (Fig. 2a, curve 2) the backward flow is asymmetric and near the bottom (right) wall occupies a larger part of the cross-section than that near the upper (left) one, and the maximum velocity is at y/h ≈ 0.5 also. At $x/d_e = 22.3$ (Fig. 2a, curve 3) the flow is almost symmetric as well and near the both channel walls is also oriented upwards, but in comparison with $x/d_e = 3.9$, the backward flow occupies smaller part of the cross-section near the both walls. It is seen that maximum velocity of the flow has moved a little bit to the central position $y/h \approx 0.5$. For other x/d_e ($x/d_e = 30.4$) (Fig. 2a, curve 4) the velocity profile is very similar to the previous one, but the backward flow near the both walls becomes weaker. Almost the same situation we observe at the largest x/d_e ($x/d_e = 42$) (Fig. 2a, curve 5), but here the backward flows near the both walls are the weakest ones. The maximum velocity of the downward flow is at $y/h \approx 0.5$ for both x/d_e ($x/d_e = 30.4$ and $x/d_e = 42$).

Using *SST* model (Fig. 2b) we observe very similar situation as it was with *kkl-ω* model that the flow in the central part of the channel is also always downward oriented for all x/d_e, and velocity profiles are asymmetric at some x/d_e as well. But in general it can be stated that velocity profiles are less fullfilled and gains more parabolic shape comparing with *kkl-ω* model case. Along the channel also backward flow exists at the walls.

The parabolic shape of velocity profiles are also visible in case of *Reynolds Stress low-Re stress - ω* model, but the distribution along the channel is more chaotic, because the model shows vortexes at the beginning of heated channel. The maximum velocity is moving in the region $y/h \approx 0.45–0.6$.

In case of *laminar* modeling (Fig. 2d) the vortexes exist near channel walls. The chequerwise circular flow takes place at the walls. As a result, the velocity profile becomes distorted and the flow in the center of the channel gains sinusoid character. The direction of flow in the central part of the channel is downward oriented for all x/d_e (the direction of forced flow), but the velocity profiles are always asymmetric, and in almost all cross-sections (except x/d_e = 22.3) near the upper (left) wall occupies much larger part of the cross-section than that near the bottom (right) one, and the maximum velocity is at $y/h \approx 0.4$.

Variation of heat transfer along the channel for different Re using different models is illustrated in Fig. 4. As it can be seen, the appearance of the circular flows near the walls (in case of *laminar* modelling (Fig. 4a and Fig. 4b)) at the very beginning of the channel greatly influences the heat transfer variation along the channel. Flow structure obtained from *laminar* modeling case shows that the highest vortexes are at the beginning of the heating section and the scale of vortexes is diminished along the channel [23]. Therefore at the beginning of the heating section heat transfer is more intensive.

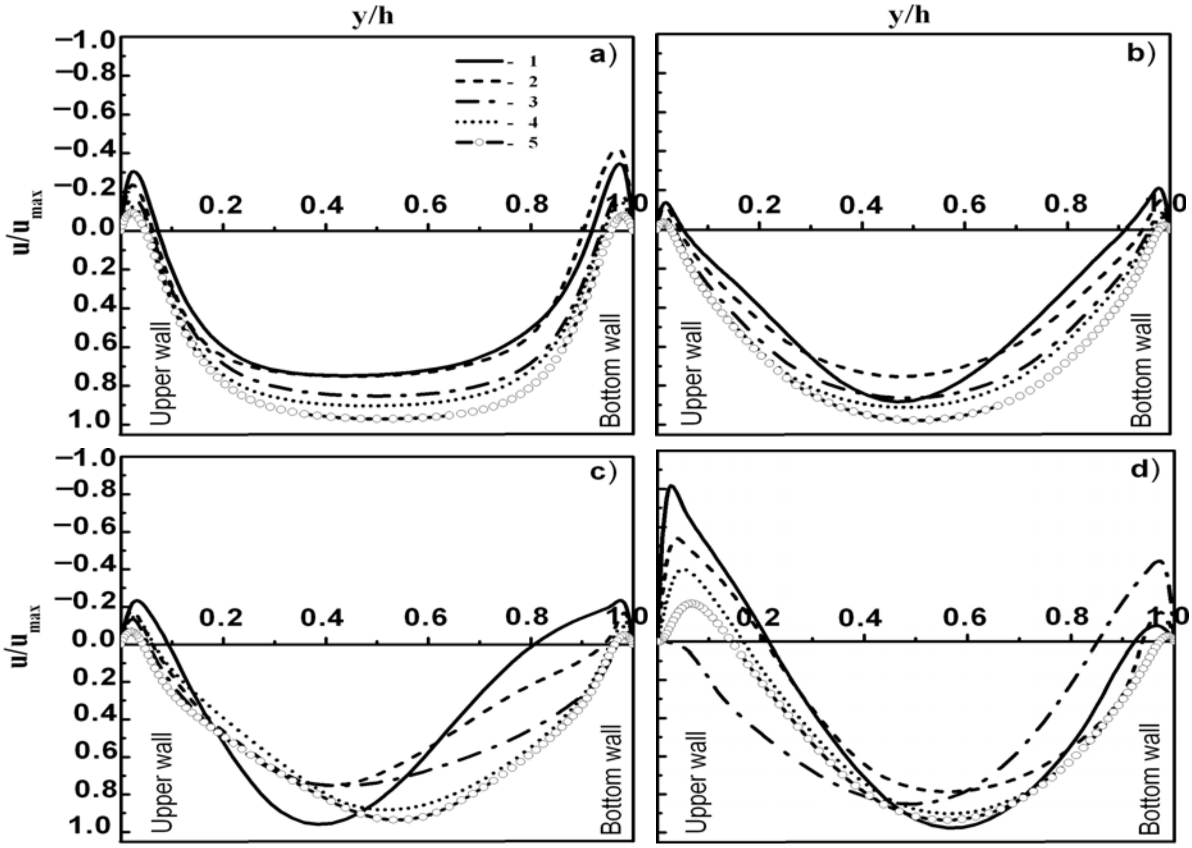

Fig. 2. The dynamics of velocity profiles for $Re_{in} = 3,1 \cdot 10^3$, $Gr_{qin} = 1.9 \cdot 10^9$ using: a) *kkl-ω*, b) *SST*, c) *Reynolds Stress low-Re stress-ω* and d) *laminar* [23] models. 1 curve – $x/d_e = 1.9$; 2 – 3.9; 3 – 22.3; 4 – 30.4; 5 – 42.

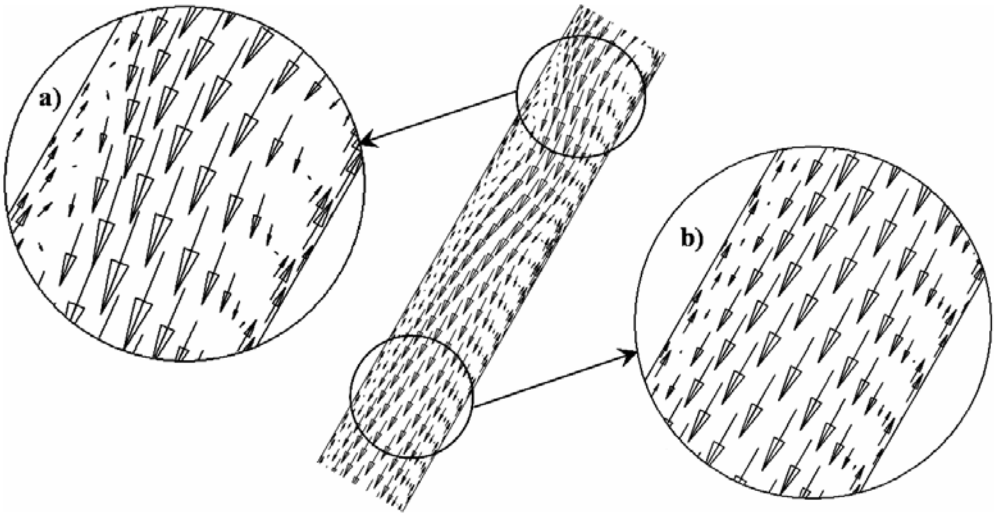

Fig. 3. Flow structure at the beginning (a) – $x/d_e \approx 0.3$ and b) $x/d_e \approx 1.9$) of heated channel using *kkl-ω* model for $Re_{in} = 3.1 \cdot 10^3$, $Gr_q = 1.9 \cdot 10^9$

Analyzing heat transfer variation from upper wall for lowest Re number ($Re_{in} = 1.9 \cdot 10^3$) it can be stated that *laminar* model gives higher results at the beginning of the heating section till $x/d_e \approx 5$ and lower results at the heat transfer stabilized region from $x/d_e \approx 22$ till 42 comparing with experimental data (Fig. 4a).

For higher Re numbers heat transfer variation character remains similar, but the regions where modeling results are higher or lower that experimental data are different i.e. for $Re_{in} = 2.4 \cdot 10^3$ *laminar* model gives higher results till $x/d_e \approx 7$ and lower results from $x/d_e \approx 22$ till 42 (Fig. 4c). For $Re_{in} = 3.1 \cdot 10^3$ *laminar* model gives higher results till $x/d_e \approx 15$ and lower results from $x/d_e \approx 30$ till 42 (Fig. 4e). For $Re_{in} = 4.7 \cdot 10^3$ *laminar* model gives higher results till $x/d_e \approx 25$ and lower results from $x/d_e \approx 35$ till 42 (Fig. 4g) comparing with experimental data.

Fig. 4 demonstrates clear difference between intensity of heat transfer from upper (stable air density stratification) and bottom (unstable air density stratification) walls. This difference is decreasing with increasing of x/d_e, but for all x/d_e heat transfer from bottom wall is higher than from upper one.

Analyzing heat transfer variation from bottom wall for lowest Re number ($Re_{in} = 1.9 \cdot 10^3$) we can observe that at the beginning of the heating section modeling results practically coincide with experimental data and from $x/d_e \approx 10$ till 42 are lower than experimental ones (Fig. 4b). In case of higher Re number ($Re_{in} = 2.4 \cdot 10^3$) *laminar* model gives a little bit higher results till $x/d_e \approx 10$ and lower results from $x/d_e \approx 18$ till 42 (Fig. 4d). For else more higher Re number ($Re_{in} = 3.1 \cdot 10^3$) modelling gives higher results till $x/d_e \approx 15$ and lower results from $x/d_e \approx 18$ till 42 (Fig. 4f) and for the highest Re number ($Re_{in} = 4.7 \cdot 10^3$) *laminar* model gives higher results till $x/d_e \approx 20$ and lower results from $x/d_e \approx 20$ till 42 (Fig. 4h) comparing with experimental data.

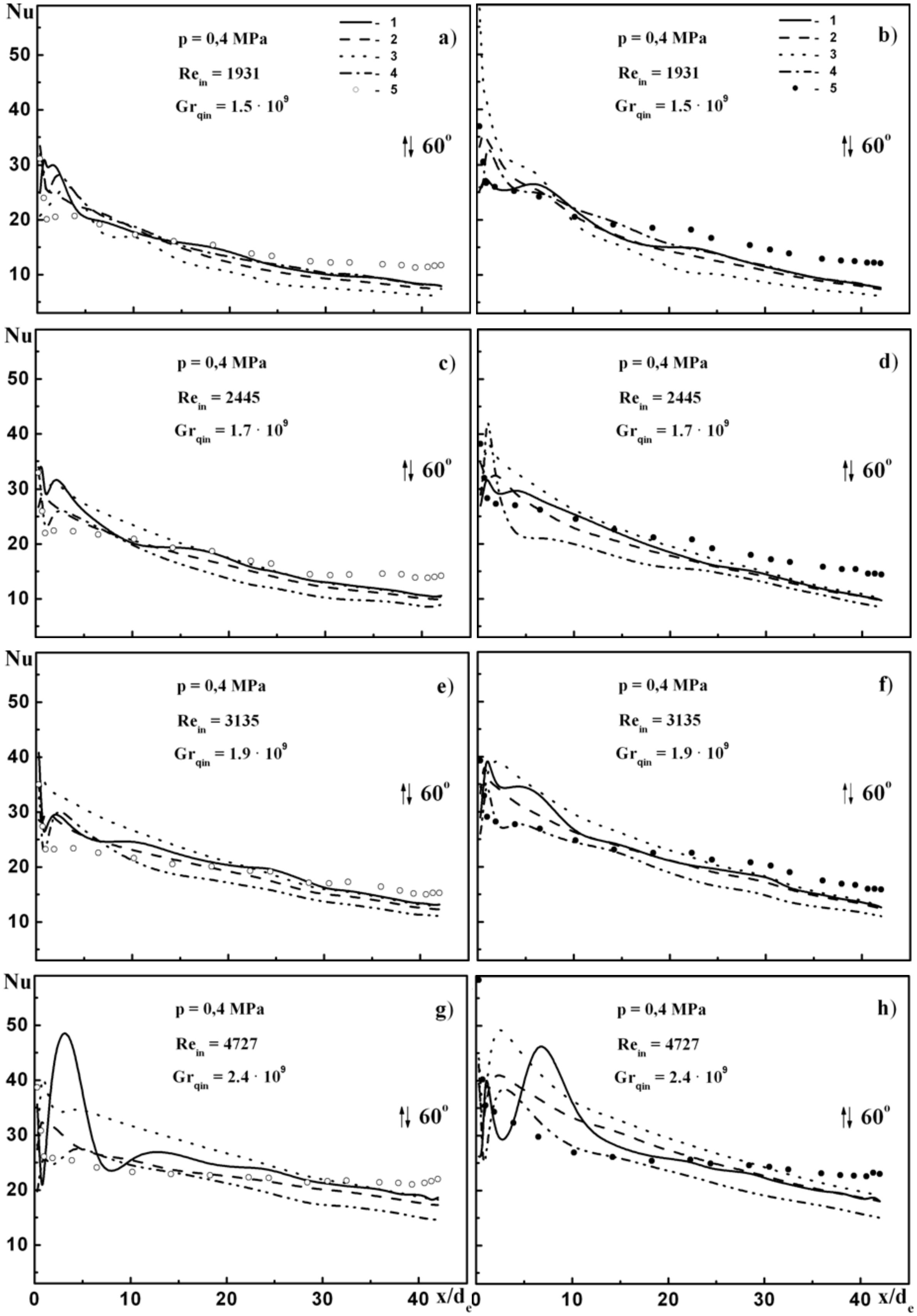

Fig. 4. Variation of heat transfer along the channel for different Re using different models: 1 – *laminar* model, 2 – *kkl-ω* model, 3 – *SST* model, 4 – *Reynolds Stress low-Re stress-ω* model; 5 – experiments. a, c, e, g – upper wall; b, d, f, h – bottom wall

The flow structure in case of transition models (*kkl-ω*, *SST* and *Reynolds Stress low-Re stress-ω*) also shows vortexes at the very beginning of the heating section, therefore heat transfer intensity is similar comparing with *laminar* modeling case. In the heat transfer stabilized region there are no vortexes observed in case of transition models, therefore heat transfer intensity practically in all analyzed cases are lower than in case of *laminar* modeling and the correlation with experimental data is worse.

Correlation between numerical modelling results and experimental data in the heat transfer stabilized region for $Re_{in} = 1.9 \cdot 10^3$ is better using *laminar* and *Reynolds Stress low-Re stress-ω* transition model where difference is about 32 % for upper wall and about 37% for bottom wall. For higher Re numbers ($Re_{in} = 2.4 \cdot 10^3 – 4.7 \cdot 10^3$) correlation between numerical modelling results and experimental data in the heat transfer stabilized region is better using *laminar* and *SST* transition model where difference varies from 14 – 27% for upper wall and from 19 – 33% for bottom wall.

Finally it can be stated that used turbulence transition models do not improve prediction of the mixed convection heat transfer in the transition region in comparison with *laminar* model.

4. CONCLUSIONS

Analysis of the numerical modelling data on opposing mixed convection in transition region in an inclined flat channel (inclination angle $\varphi = 60^o$ from horizontal position) with symmetrical heating leads to the following conclusions:

1. Modelling results demonstrate the vortex structure of the flow at the beginning of the channel and vortex flow (laminar model) or backward flow (transition models) at higher x/d_e.
2. Used turbulence transition models do not improve prediction of the mixed convection heat transfer in the transition region in comparison with *laminar* model.

REFERENCES

1. Petukhov B.S., Polyakov A.F. and Strigin B.K. Heat transfer investigations in tubes under viscous-gravitational flow, Energija, Moscow, Vol. 1, 1968.
2. Jackson J.D., Cotton M.A., and Axell B.P. Studies of mixed convection in vertical tubes. Review, International Journal of Heat Fluid Flow, Vol. 10, No 1, 1988, p. 2–15.
3. Jackson J.D., Influences of buoyancy on velocity, turbulence and heat transfer in ascending and descending flows in vertical passages, Proceedings of the 4th Baltic Heat Transfer Conference. Advances in Heat Transfer Engineering, Kaunas, Lithuania, August 2003, p. 57–78.
4. Vilemas J., Poskas P., and Kaupas V. Local heat transfer in a vertical gas-cooled tube with turbulent mixed convection and different heat fluxes, International Journal of Heat and Mass Transfer, Vol. 35, No 10, 1992, p. 2421–2428.
5. Vilemas J., and Poskas P. Effect of body forces on turbulent heat transfer in channels, LEI-Bigell House, Kaunas-New York, 1999.
6. Poskas P., and Poskas R. Turbulent opposing mixed convection heat transfer in a vertical flat channel with one side heating, International Journal of Heat Transfer Engineering, Vol. 25, No 2, 2004, p. 17–23.
7. Poskas P. and Poskas R. Local turbulent opposing mixed convection heat transfer in inclined flat channel for stably stratified airflow, International Journal of Heat and Mass Transfer, Vol. 46, No 21, 2003, p. 4023–4032.

8. Poskas P. Poskas R. and Sabanskis D. Local turbulent opposing mixed convection heat transfer in inclined flat channel for unstably stratified airflow, International Journal of Heat and Mass Transfer, Vol. 48, No 5, 2005, p. 956–964.
9. Poskas P., Poskas R. and Sabanskis D. Comparison of the turbulent opposing mixed convection heat transfer in inclined flat channel for stably and unstably stratified airflows, Proceedings of the 6th World Conference Experimental Heat Transfer, Fluid Mechanics, and Thermodynamics, Matsushima, Miyagi, Japan, April 2005 (Published on CD-ROM).
10. Scheele G.F., Rosen E.M. and Hanratty T.J. Effects of natural convection on transition to turbulence in vertical pipes, Canadian Journal of Chemical Engineering, Vol. 38, 1960, p. 67–73.
11. Scheele G.F., and Hanratty T.J. Effects of natural convection instabilities on rates of heat transfer at low Reynolds numbers, American Institute of Chemical Engineers Journal, Vol. 9, No 2, 1963, p. 183–185.
12. Petukhov B. S., Polyakov A. F., and Strigin B. K., Heat transfer investigations in tubes under viscous-gravitational flow, Energija, Moscow, Vol. 1, 1968.
13. Poskas P., Poskas R. and Sirvydas A. Modelling of the opposing mixed convection heat transfer in a vertical flat channel in the regions of a laminar and vortex flow, Proceedings of the 4th. International Conference on Heat Transfer, Fluid Mechanics and Thermodynamics, Cairo, Egypt, September 2005 (Published on CD-ROM).
14. Poskas P., Poskas R. and Sirvydas A. Opposing mixed convection heat transfer in the vertical flat channel in a laminar-turbulent transition region, Proceedings of the 13th. International Heat Transfer Conference, Sydney, Australia, August 2006 (Published on CD-ROM).
15. Poskas P., Poskas R. and Sirvydas A. Opposing mixed convection heat transfer in the vertical flat channel in a laminar-turbulent transition region under prevailing effect of buoyancy, Proceedings of the 5th European Thermal-Sciences Conference, Eindhoven, the Netherlands, May 2008 (Published on CD-ROM).
16. Poskas P. and Poskas R. Mixed convection in the channel flows, Heat Transfer Research, Vol. 40, No 1, 2009, p. 31–56.
17. Poskas R., Poskas P. and Drumstas G. Opposing mixed convection heat transfer in an inclined flat channel in a laminar-turbulent transition region, Proceedings of the 7th World Conference on Experimental Heat Transfer, Fluid Mechanics and Thermodynamics, Krakow, Poland, June 2009 (Published on CD-ROM).
18. D.K. Walters and D. Cokljat. A three-equation eddy-viscosity model for Reynolds-averaged Navier-Stokes simulations of transitional flows. Journal of Fluids Engineering, 130, December 2008.
19. F.R. Menter, R.B. Langtry, S.R. Likki, Y.B. Suzen, P.G. Huang and S. Volker. A Correlation Based Transition Model Using Local Variables Part 1 – Model Formulation. (ASME-GT2004-53452), 2004.
20. D.C. Wilcox. Turbulence Modelling for CFD. DCW Industries, Inc., La Canada, California, 1998.
21. Fluent, Inc., 2005. FLUENT User's Guide.
22. A. Sirvydas, R. Poskas. Numerical Investigations of Opposing Mixed Convection Heat Transfer in Vertical Flat Channel // 2. Vortex Flow in Case of Symmetrical Heating, Power Engineering, No 1, 2006, p. 9–15.
23. G. Drumstas. Modelling of mixed convection in an inclined flat channel // CYSENI-2009, LEI. 2009, Kaunas.

NOMENCLATURE

b	channel width (m)
c_p	specific heat (J/(kg K))
d_e	equivalent diameter of the channel [$d_e = 2hb/(h+b)$](m)
Gr_q	Grashof number defined by the heat flux specified on the surface [$Gr_q = g\cdot\beta\cdot d_e^4\cdot q_w/\nu^2\cdot\lambda$]
g	acceleration due to gravity (m/s^2)
h	channel height (m)
i	enthalpy (J/kg)
Nu	Nusselt number [$Nu = \alpha d_e/\lambda$]
Pr	Prandtl number [$Pr = \mu c_p/\lambda$]
p	pressure (Pa)
q	heat flux density (W/m^2)
Re	Reynolds number [$Re = ud_e/\nu$]
T	temperature (K)
u	local flow velocity (m/s)
x	axial coordinate measured from start of heating (m)
y	transverse coordinate

Special characters

α	heat transfer coefficient [$\alpha = q_w/(T_w - T_f)$] (W/(m^2 K))
β	volumetric expansion coefficient (1/K)
φ	inclination angle (degree)
λ	thermal conductivity (W/(m K))
ν	kinematics viscosity (m^2/s)
μ	dynamic viscosity (Pa s)
ρ	density (kg/m^3)

Subscripts

in	at the inlet
f	in the flow
w	at the wall
x	axial coordinate
y	transverse coordinate
1	first wall
2	second wall

CYSENI 2010, May 27–28, Kaunas, Lithuania
ISSN 1822-7554, www.cyseni.com

FLAT HEAT PIPES WITH SINTERED POROUS STRUCTURE FOR THERMAL MANAGEMENT SYSTEMS OF FUEL CELLS

O.S. Filatova
A.V. Luikov Heat and Mass Transfer Institute
of the National Academy of Sciences of Belarus
P. Brovki, 15, Minsk, 220071 – Belarus
Phone: +375 17 284 2138
Email: filatova@hmti.ac.by

ABSTRACT

Hydrogen is considered to be one of the most preferable alternatives to organic fuel for transport applications and power engineering overall. Hydrogen usage in energy production processes leads to great decrease of environment pollution. Fuel cells based on direct transformation of chemical energy of hydrogen and hydrogenous fuel into electric energy became a perfect solution for further development.

Fuel cells have been used widely in different application fields due to their high performance coefficient, high reliability and absence of harmful impact. However, a large amount of wasted heat requires an effective thermal management. Such system needs to remove heat fluxes during fuel cell operation as well as to provide uniform temperature distribution on the surface of electrodes. Heat pipes are particularly suited to these requirements owing to their efficiency and ability to transfer high heat fluxes.

Flat heat pipe with sintered capillary porous structure is presented as a base of fuel cell thermal management system. Heat flux densities over 100 W/cm^2 have been observed without any critical dry-out during experiments. Used samples had different porosity and grain diameter. Water was used as a working fluid and experiments were carried out at saturation temperatures 70, 80 and 90ºC. Application of flat heat pipes can be considered as a successful way to maintain necessary temperature regime and to increase total fuel cell performance.

Keywords: capillary porous structure, evaporation, heat pipe, thermal management, fuel cell

1. INTRODUCTION

Fuel cells (FC) known as electrochemical generators with high efficiency are considered as perspective energy sources. The main advantages are high performance coefficient and absence (or very low level in some cases) of harmful pollutions. Depending on construction, maximum performance of contemporary FC is about 40–60%. Owing to chemical reactions of hydrogen or hydrogenous compounds and oxygen electric energy is generated as well as heat dissipation occurs. The problem of heat dissipation is very important for sustainable functioning of FC. Membrane FCs have special requirements on temperature and humidity determined. Incoming reactant gases should have a certain temperature. Moreover, not only a temperature value of electrodes but also uniformity of temperature field makes a great influence on FC performance and reliability. Overheating and local dry-out of a membrane may cause FC failure. That is why FC stacks require an appropriate thermal regulation. Besides observance of these conditions such thermal management system is able to increase the whole FC system efficiency by using waste heat as secondary source of heat energy instead of removing of dissipated heat into atmosphere [1].

Among the main methods of thermal control of FC, natural and forced convection, liquid cooling, heat removing by thermal conductivity and heat transfer at phase changes have gained a widest distribution [2]. Heat pipes belong to the latest method that enables to remove high heat fluxes and can be easily fabricated at the same time.

Flat heat pipes are very efficient heat transfer devices. Phase change phenomena occurring inside allow them to transport heat fluxes of high level with small temperature gradients. Heat pipes are widely studied all over the world as a base of thermal regulation systems of electronic components (especially diodes, thyristors, PC chips). In recent years another interesting application of heat pipes has appeared. Due to great performance characteristics, heat pipes can be applied for thermal management systems of fuel cells. The concept of heat pipes application and using of heat pipe phenomenon in thermal regulation of fuel cells is described in [3]. Author of [4] has proposed a method of embedding a set of cylindrical miniature heat pipes inside bipolar plate of FC. Investigations of flat heat pipes with micro grooves are illuminated at [5]. Flat heat pipes can be easily mounted on heat dissipation source and do not need high technologies for holes drilling. An alternative design of carbon bipolar plate containing flat heat pipe is also mentioned in [2].

Nowadays evaporation heat transfer is one of the most promising technologies in electronics cooling and power engineering thermal management. Absence of moving parts makes cooling system more reliable and quiet. Intensification of heat transfer process by using of enhanced heat transfer surfaces leads to sufficient reduce of cooling system weight, size and energy consumption. Evaporation heat transfer can be strongly increased by covering the surface with a porous layer in good thermal contact with base [6]. Numerous investigations, e.g. [7], confirm enhancement of heat transfer coefficient in several (up to 10) times compared to the smooth surface.

Porous coatings should have advanced system of capillary channels, high effective thermal conductivity and enough mechanical strength, good mechanical contact with heat transfer surface (base, walls). In addition, porous structure should have long-termed resistance to erosion and vibration effects. Moreover, it should be producible and reasonably priced. Porous structure of sintered copper powder is a promising solution, meeting the above mentioned requirements [8]. Capillary-porous wick is responsible for heat transfer capability of heat pipe, therefore right choice of capillary structure is of a great importance. Since theoretical prediction of evaporation heat transfer in porous structures is rather complicated due to description of porous structure (especially taking into account a variety of its types and specificity), experimental study is essential in such investigations.

The main object of experimental investigation is to obtain a value of heat transfer coefficient of porous structures saturated with liquid. This allows to evaluate critical heat flux transferred by porous structure that makes possible to choose an appropriate structure for given conditions.

2. EXPERIMENTAL SETUP

Experimental samples of porous structure were produced by sintering of copper particles that form a structure of 2 mm thickness. This porous layer covers a thin copper plate of rectangular shape. Grain diameter is equal to 20 and 200 µm, porosities of the samples are 0.5 and 0.57. Given values of porosities were obtained by adjustment in conditions of sintering process. Copper plate with porous structures under investigation makes a base of flat heat pipe, which has a massive lateral walls (Fig. 1). Transparent lid of heat pipe made from pyrex glass allows visualization of phase change processes occurring inside the pipe during the tests (Fig. 2).

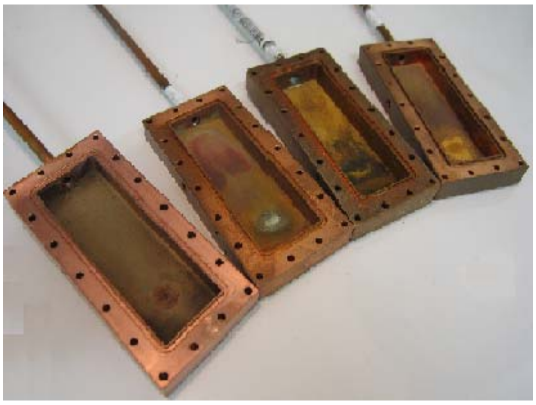

Fig. 1. Photograph of tested heat pipes with samples of porous structures

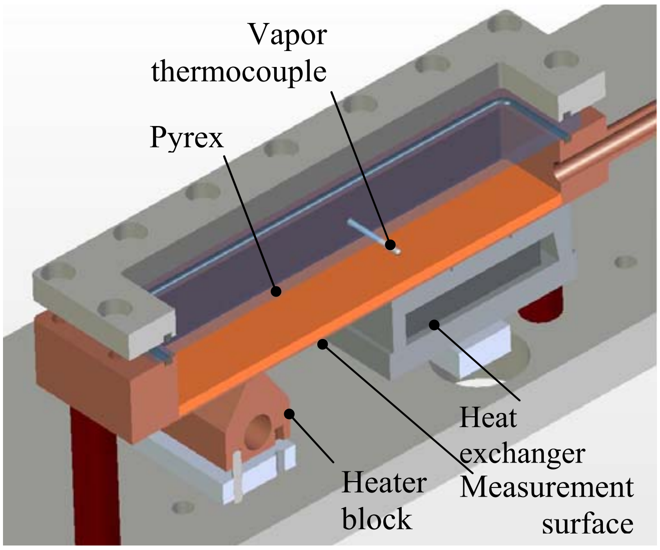

Fig. 2. Schematic diagram (cross-cut) of the heat pipe

Water was chosen as a working fluid in the experiments. During preparation process the porous structure of each sample was purified and oxidized in order to improve wetting characteristics.

An electric heater was attached to the copper base to ensure heat input. Heat removing from other end of the heat pipe is realized by heat sink with running fluid. To prevent heat losses insulation was made around this assembly.

During the experiment electric current was applied to the heater, which was placed to emulate the heat of a component to be cooled [9]. As a result a certain heat flux came to the copper base of heat pipe through the area of appr. 0.5 cm^2. The heat flux spreads through copper base to porous structure, causing heating and evaporation of working fluid. Generated vapor came to the space between porous structure and glass lid of heat pipe, and then condensed at the upper cooled part (evaporation zone was disposed below condensation one). The greater loaded heat flux, the lower temperature of a cooling fluid in the condenser. Constancy of vapor temperature was provided by thermostat temperature regulation. Condensed liquid phase returned to the evaporation zone through capillaries of porous structure. Liquid supply of porous structure in evaporation zone was mainly caused by capillary forces. Gravitational forces participate in liquid return to the evaporation zone in some extent as well. Thus liquid was returned to the heating zone and evaporated again.

The experiments were realized at saturation temperatures of 70, 80 and 90ºC and heat load from 0 to approximately 210 W (it depended on the tested sample). To control temperature seven thermocouples were fixed on the surface of copper base of heat pipe and one thermocouple was inserted into vapor space to measure saturation temperature. Schematic diagram of experimental setup is shown on Fig. 3. The tested heat pipe 1 was placed inside an insulation box 2, which was attached to a tilting mechanism 3. Electrical current for a heater was yielded by a power supply 4. Cooling fluid flowed through a heat sink and was thermally managed by the thermostat 5. A commutating device 6 for thermocouples was used to centralize data acquisitions. Experimental managing was realized using a program on personal computer 7. When a signal of certain heat load given to the electric heater and desirable vapor saturation temperature set, steady state was reached for investigated sample while heat removal intensity was fitting.

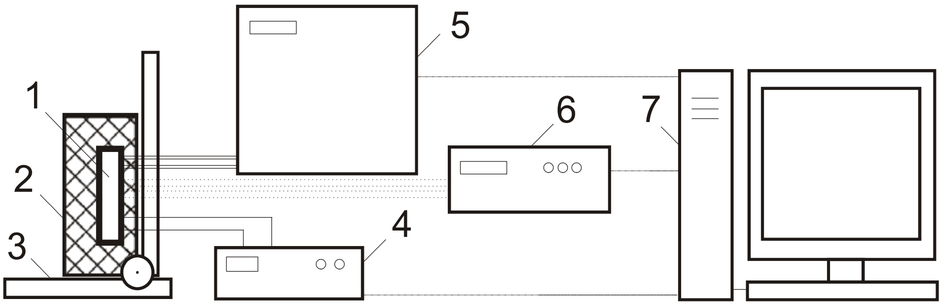

Fig. 3. Experimental setup: 1 – heat pipe (porous structure), 2 – insulation, 3 – tilting mechanism, 4 – power supply, 5 – thermostat, 6 – thermocouple commutator, 7 – data acquisition system (PC)

3. CALCULATIONS OF THE EFFECTIVE CONDUCTIVITY OF POROUS STRUCTURES AND EXPERIMENTAL RESULTS

The thickness of heat pipe base was only 0.5 mm and the area heat flux applied to was very small (about 0.5 cm^2). These circumstances admited to suppose that heat flux spreads mainly in direction from heater towards the porous structures. The aim was to determine coefficients of effective conductivity of porous structures saturated with liquid. For their evaluation a task of conductivity of multi-layer wall was considered on the base of experimental results. The data of thermocouples readings at low heat loads at initial stages of heating process were used. The coefficient of effective conductivity λ_{eff} of saturated porous structure was calculated by:

$$\lambda_{eff} = \frac{\delta}{\frac{t_1 - t_3}{q} - \frac{\delta_{Cu}}{\lambda_{Cu}}}, \qquad (1)$$

δ is the thickness of a porous structure, δ_{Cu} is the thickness of a copper base of the heat pipe, λ_{Cu} is the coefficient of thermal conductivity of copper, t_1 is temperature of a base, t_3 is adiabatic temperature, q is applied heat flux density.

On the other hand, thermal conductity of porous structure can be predicted theoretically. Faghri [10] described several calculations aiming to evaluation of effective conductivities of porous wicks. Maxwell expression (2) for conductivity of a heterogenous material of randomly dispersed, randomly sized spheres was chosen for the further analysis because of the better agreement with experimental results calculated by (1):

$$\lambda_{eff} = \lambda_s \left(\frac{2 + \lambda_l / \lambda_s - 2\varepsilon(1 - \lambda_l / \lambda_s)}{2 + \lambda_l / \lambda_s + \varepsilon(1 - \lambda_l / \lambda_s)} \right), \tag{2}$$

λ_l and λ_s are coefficients of thermal conductivity of liquid and solid copper particles respectively, ε is porosity of a porous structure. The values of the coefficients are given in Table 1.

Table 1. Characteristics of tested samples of porous structures

Sample	**Grain diameter, µm**	**Porosity**	**Eff. thermal conducty of saturated wick, W/m/K**	**Eff. thermal conductity of saturated wick and base, W/m/K**
S 1	20	0.57	129.3	181
S 2	200	0.5	154.5	200
S 3	20	0.5	154.5	200

Purification and oxidization of the samples has enriched wetting characteristics of the samples S1–S3. Wetting capabilty was inspected visually. Comprehensive tests showed enhancement of the conductivity *G* of the samples calculated as:

$$G = \frac{Q}{t_{ev} - t_{cond}}, \tag{3}$$

where Q is applied heat flux, t_{ev} is mean evaporator temperature, t_{cond} is condenser temperature. For example, for S1 conductivity has rised approximately from 1.4 to 4.7 W/K for heat load diapason of 50–100 W at 80 and 90 °C.

During the experimental investigations of the heat pipes high heat flux values have been observed without critical dry-out of the tested porous structures. Even in the case of local dry-out of the regions directly above the evaporator (at the place of maximum heat input), heat pipe remained functioning. Indeed, evaporation which occured on the border of the dry area was sufficient enough to transfer high heat flux densities [9]. Experimental curves illustrating dependencies of heat flux vs. overheating of porous structures are shown at Fig. 4. The order of data scattering did not allowed to make any important conclusions.

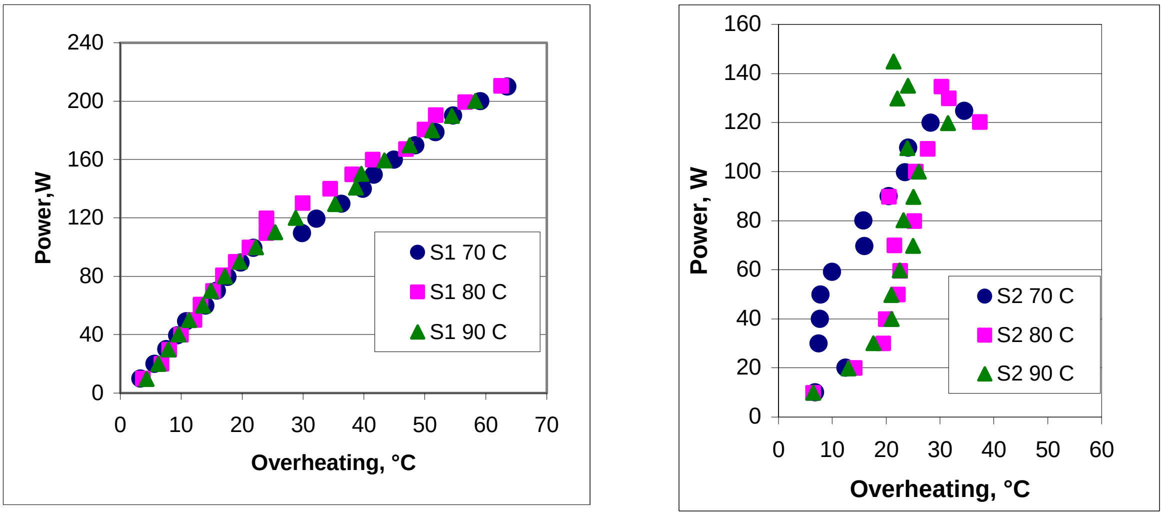

a) S1 b) S2

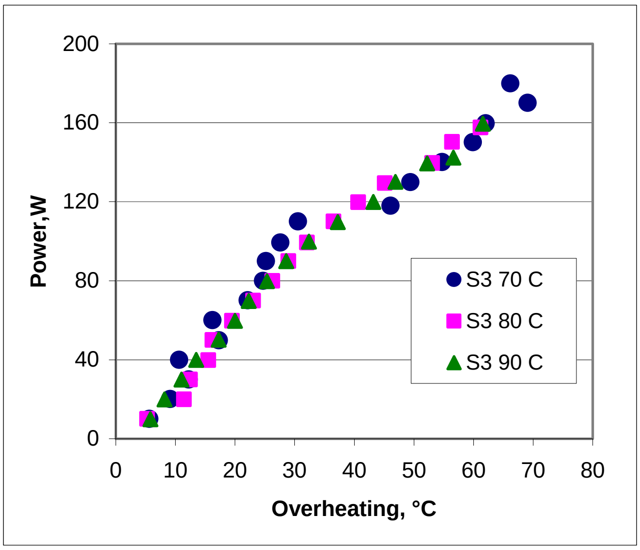

c) S3

Fig. 4. Heat flux vs. overheating of porous samples S1, S2, S3

The dependencies of heat flux vs. overheating of porous structures at different saturation temperatures are shown at Fig. 5. From the analysis of the diagrams it becomes evident that sample S1 shows best performance characteristics.

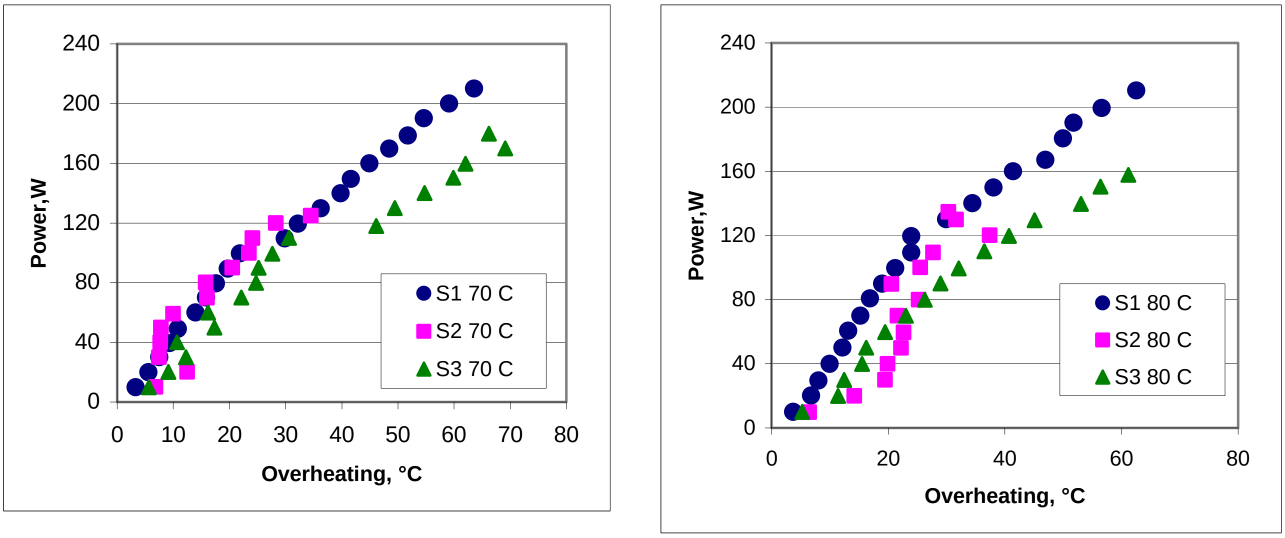

a) 70 ºC b) 80 ºC

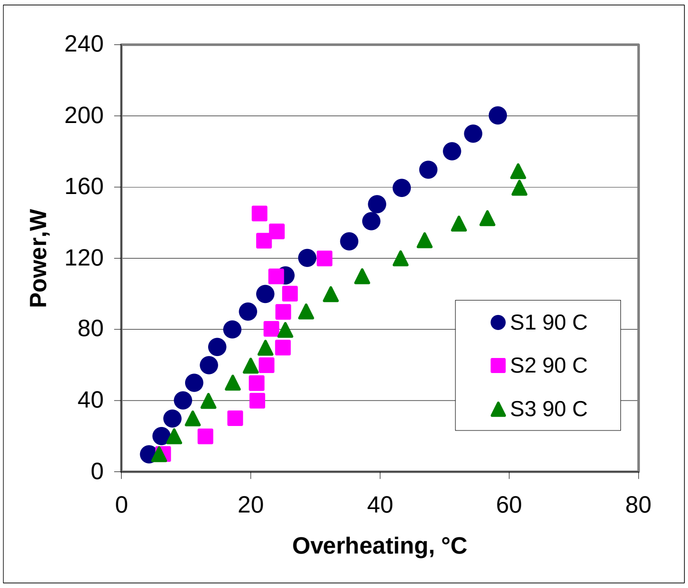

c) 90 ºC

Fig. 5. Heat flux for each sample as function of saturation temperature.

Deviation of the dependencies for the sample S2 might be caused by peculiarities of heater mounting during the experiments. Consequently additional correction of given data must be provided.

4. A METHOD OF DETERMINATION OF HEAT LOSES

Although the thermal loses during the set of experiment have been minimized due to the construction of the heat pipe and providing of insulation, their calculation was necessary for more accurate estimation of heat flux applied to porous structures and consequently for heat transfer coefficient value of the structures under investigations. In order to determine heat loses and actual applied heat flux, evaporation area was divided into two rectangular zones: directly above the evaporator and the surrounding area. The borders of the latter one were constrained by the thermocouples location on the base of the heat pipe (Fig. 6). In turn the surrounding area was divided into zones in four directions by the diagonals of the rectangle (Fig. 7).

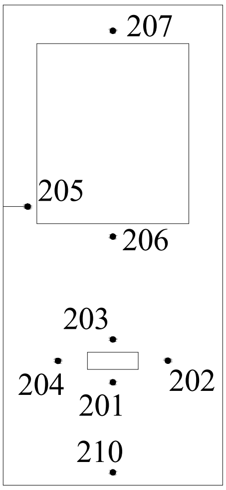

Fig. 6. Scheme of thermocouples location on the base of heat pipe

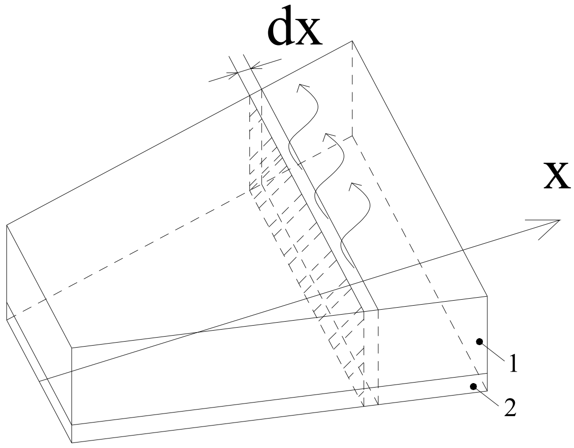

Fig. 7. An element for the heat flux calculations. 1 – porous layer, 2 – copper base

In this task it was necessary to calculate effective thermal conductivity λ_{eff}^* of the multi-layer trapezoid edge. Its thermal resistance was calculated by formula for parallel connection. The values determined by

$$\lambda_{eff}^* = \frac{\lambda_1\delta_1 + \lambda_2\delta_2}{\delta_1 + \delta_2}, \tag{4}$$

where δ_1 is copper base thickness with thermal conductivity $\lambda_1 = \lambda_{Cu}$, δ_2 is thickness of porous layer saturated with liquid with thermal conductivity $\lambda_2 = \lambda_{eff}$ (determined by Eq.(2)), are established at Table 1 (see above).

Due to differing coefficients of thermal conductivity it was assumed that heat transfer was performed in *x* direction only through the copper base with thickness δ_1 and evaporation was occurring from the surface of the saturated porous layer with thickness δ_2. But when considering thermal conductivity of the copper base it is possible to regard this base owning the total thickness of the whole edge, including copper base as well as porous stucture above. Because of the insulation there was no heat transfer on the lower base of heat pipe.

At first approximation heat transfer coefficient from surface of porous structure was evaluated as

$$\alpha = \frac{\lambda_{eff}}{\delta_2}, \tag{5}$$

where λ_{eff} is thermal conductivity of saturated porous layer.

Considering the temperature of the upper side of trapezoidal edge equal to vapor temperature $t_{vap} = const$, constant temperature of the edge at the cross-cut *t*, governing equation concerning excess temperature $\theta = t - t_{vap}$ according to Fourier and Newton-Richman laws was concluded as

$$\frac{d^2\theta}{dx^2} + \frac{1}{x}\frac{d\theta}{dx} - \frac{\alpha}{\lambda\delta}\theta = 0. \tag{6}$$

Boundary equations were next:

$$\theta\big|_{x=x_i} = \theta_i, \tag{7}$$

$$\left.\frac{d\theta}{dx}\right|_{x=z_j} = 0, \tag{8}$$

where $x_i, i=\overline{1,4}$ x_i, i=1..4 is distance in chosen direction to the thermocouple near the heater with reading θ_i, $z_j, j=\overline{1,4}$ z_j, j=1..4 is distance in the same direction to the isolated border. At calculation of distance in the direction of condenser zone, z is being distance to the available thermocouple. After the analysis of the experimental data it has been concluded that heat transfer on this border was absent.

The general solution of the Eqn. (6) with conditions (7–8) is a combination of Bessel's functions *J* and *Y*:

$$\theta = J\left[0, i\sqrt{\frac{\alpha}{\lambda\delta}}x\right]C_1 + Y\left[0, -i\sqrt{\frac{\alpha}{\lambda\delta}}x\right]C_2. \tag{9}$$

Comparing calculated temperature profiles with experimental ones a new approach of the heat transfer coefficient must be determined, allowing calculation the real value of supplied heat flux density, coming to the porous structure. Preliminary evaluation showed heat loses equal to approximately 30% of heat input.

5. CONCLUSIONS

Three samples of capillary porous structure of sintered copper powder were examined at saturation temperatures of 70, 80 and 90ºC and heat load from 0 to approximately 210 W (depending on the tested sample). During experimental investigations high values of coming heat flux were observed without critical overheating.

In spite of local dry-out of the regions directly above the heater place, heat pipes maintained stable functioning. The obtained results allowed to conclude that evaporation on the border of the dry area was sufficient enough to transfer high heat flux densities, and capillary structures were able to maintain necessary capillary head for liquid return.

Analysis of the experimental data showed the best performance characteristics for the sample S1 with grain diameter of 20 μm and porosity of 0.57. Flat heat pipes were shown to be capable to transfer heat flux densities over 100 W/cm^2 and to ensure thermal management of fuel cells.

A method of evaluation of thermal loses has been proposed.

REFERENCES

1. VASILIEV L.L., VASILIEV L.L., Jr. Heat pipes for fuel cells thermal control. 5th Heat Powered Cycles Conference, Berlin, Germany, September 7–9, 2009.
2. FILATOVA O.S. Heat pipes for fuel cells thermal management. CYSENI 2009. Proceedings of annual conference of young scientists on energy issues. [CD]. Kaunas: Lithuanian Energy Institute. 2009 May 28–29.
3. FAGHRI, A. GUO, Z. Integration of Heat Pipe into Fuel Cell Technology. *Heat Transfer Engineering*, 2008, Vol. 29, Number 3, p. 232–238.
4. FAGHRI A., Micro Heat Pipe Embedded Bipolar Plate for Fuel Cell Stacks, U.S. Patent Pub. No. 2005/0026015, 2005.

5. RULLIERE R., LEFEVRE F., LALLEMAND M. Prediction of the maximum heat transfer capability of two-phase heat spreaders – Experimental validation. *Int. Journal of Heat and Mass Transfer*, 2007, Vol. 50, p.1255–1262.
6. VASILIEV L.L., ZHURAVLYOV A.S. Heat transfer enhancement with propane boiling and evaporation on the porous coatings of tubes. Transport Processes and Interfacial Phenomena in Multiphase Systems, Summaries of Symposium, Madras, India, 2004, p. 10–11.
7. WANG J., CATTON I. Enhanced evaporation heat transfer in triangular grooves covered with a thin fine porous layer. *Applied Thermal Engineering*, 2001, Vol. 21, p. 1721–1737.
8. VASILIEV L.L., MAZIUK V.V., KULAKOV A.G., RABETSKY M.I., VUKOVIC M. Miniature heat-pipe thermal performance prediction tool – software development. *J. Applied Thermal Engineering*, 2001, Vol. 21, p. 559–571.
9. LOSSOUARN D., ROMESTANT C., BERTIN Y., FILATOVA O. Heat flux density characterization in heat pipes using capillary porous media. Preprints of 14th Int. Heat Pipe Conference, Florianopolis, Brazil, April 22–27, 2007.
10. FAGHRI A., *Heat pipe science and technology*, Taylor & Francis, USA, 1995, 874 p.

CYSENI 2010, May 27–28, Kaunas, Lithuania
ISSN 1822-7554, www.cyseni.com

MEASUREMENTS OF TURBULENT TRANSFER AND MIXING AVERAGED CHARACTERISTICS IN A TURBULENT JET FLOW USING A TALBOT INTERFEROMETER METHOD

I.N. Shatan
A.V. Luikov Heat and Mass Transfer Institute
of National Academy of Sciences of Belarus
15 P. Brouki Str., Minsk BY-220072 – Republic of Belarus
Phone: +375(17)2842246
Email: 2eshnik@gmail.com

ABSTRACT

The present study is concerned with applying of a Talbot effect-based technique for analyzing flows with random phase inhomogeneities. It is shown that this method is a powerful tool for diagnostics of turbulent gas flows. Some of the applied potentialities of the technique are shown by measurements of averaged values of admixture concentration in the two-dimensional turbulent helium jet issuing into air space. Averaged helium concentrations throughout the flow field are determined using local light refraction index measurements with a high spatial resolution from a long-exposed Talbot image of the jet.

Talbot effect, shear flow, turbulence

1. INTRODUCTION

Currently, optical diagnostic methods are widely used for experimental studies of gas-dynamic flows. Its using allow to achieve a qualitative visual image of the investigated processes, but also to measure quantitative characteristics of the flows with high accuracy and high resolution. Optical methods give the possibility to diagnose a wide range of physical phenomena occurring during mixing and transfer processes in turbulent flows, flow of gas through a nozzle, propagation of shock waves, chemical reactions, plasma beams collisions, and other ultrafast and high-temperature processes.

The self-imaging effect of intensity distributions of a coherent monochromatic radiation field with a periodically modulated front known as the Talbot effect [1] can be used for diagnostics of flows with phase inhomogeneities [2–12]. In particular, this principle forms the basis of the moiré technique, implying that a test object is placed between two light-illuminated gratings, and then a value and type of inhomogeneities are estimated from the distortion of the moiré picture [13, 14]. To enhance the potentiality of the moiré technique, a scheme called the Talbot interferometer is used. In this method a receiving grating is positioned in the self-imaging plane of the first grating, with the intent of upgrading the measurement range and sensitivity [15–17]. The application of optical methods based on the self-imaging effect for analyzing turbulent flows has a number of features that derive from the hydrodynamic nature of such flows, namely, from the existence of fluctuations in time and space. This is peculiar to the optical properties of a medium. In this case, an instantaneous value of a local refraction angle measured by a Talbot interferometer can be considered as a sum of time-averaged and rms fluctuation values. While averaging, the random displacement of unit light intensity maxima, or of Talbot image (talbotgram) elements from the middle position causes to blur them. So, the displacement of the center of a unit element is as a whole related to the mean local refraction angle, whereas the light intensity distribution within a unit element depends on the spectral density of angle fluctuations.

The efficiency of the method based on the Talbot effect to study objects with phase inhomogeneities can be significantly enhanced by digital technology [3]. The proposed method of digital Talbot-interferometry provides data on the parameters of turbulent flows by using computer processing of experimental results [11, 12, 19–22].

The purpose of this work was to measure the averaged characteristics of turbulent helium jet issuing into air space.

2. EXPERIMENTAL SETUP

The optical scheme of the setup for measuring the statistical characteristics of turbulent flows using Talbot interferometer is shown in Fig. 1. A collimator transforms the He-Ne laser radiation having passed through an aperture diaphragm and a neural filter into a wide-aperture light beam with an approximately plane wave front. A Talbot grating that represents a thin film with a system of equally spaced holes of orthogonal arrangement is tightly pressed between a pair of plane-parallel plates of high optical quality and is placed into the laser beam region just behind the collimator. A plane nozzle is placed at some distance from the grating (no more than at the distance z_1). Depending on a required sensitivity of the technique, an imaging screen is mounted in the self-imaging plane of the Talbot image at the distance z_N from the grating. The length z_N determines the position of self-imaging planes where the light intensity distribution repeats the one over the grating:

$$z_N = \frac{p^2 \cdot N}{2\lambda}. \tag{1}$$

In this equation p is a Talbot grating period, N is a number of the self-imaging plane and λ is a wavelength of the incident laser radiation. The screen image is recorded with a required space and time resolution using a CCD camera.

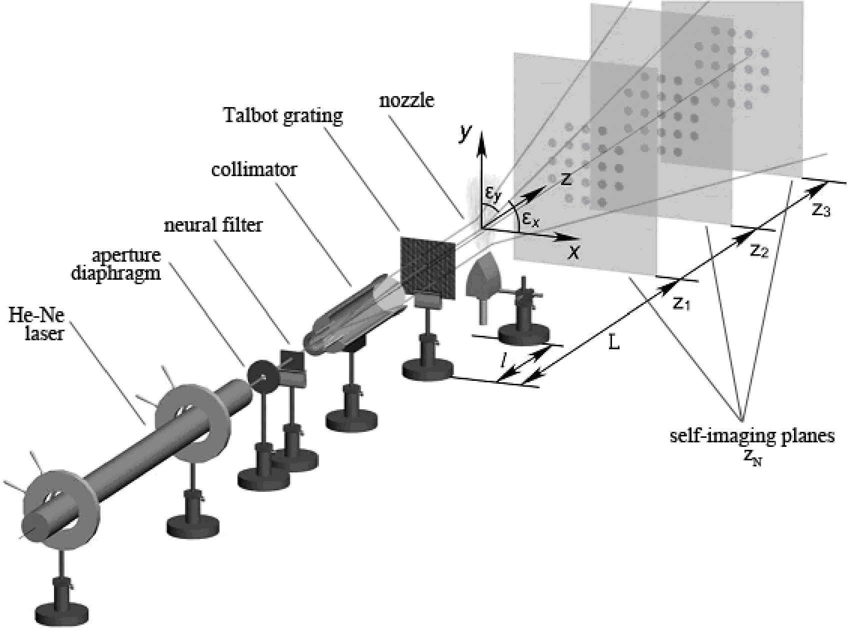

Fig. 1. Optical scheme of the setup based on the Talbot effect which is used for studying the statistical characteristics of turbulent flows

A two-dimensional helium jet was formed by a nozzle installed at the distance l just behind the Talbot grating (Fig. 1). An outlet nozzle cross section was 1.8×40 mm in size. For uniform flow distribution over the cross section of the jet, the nozzle throat was located at the bottom of the convergent part of a rectangular channel provided with a system of honeycombs. A gas was fed through a receiver with a constant pressure. A gas velocity at the nozzle throat was $u = 10$ m/s. The Reynolds number of the flow was $Re_l = 4.8\cdot10^3$.

The neutral density filter which has a constant attenuation across the wide range of wavelengths and the inlet aperture of a photo camera were chosen in a such way that an optimal amount of light could be obtained on a CCD-matrix with exposures sufficient for averaging of turbulent fluctuations.

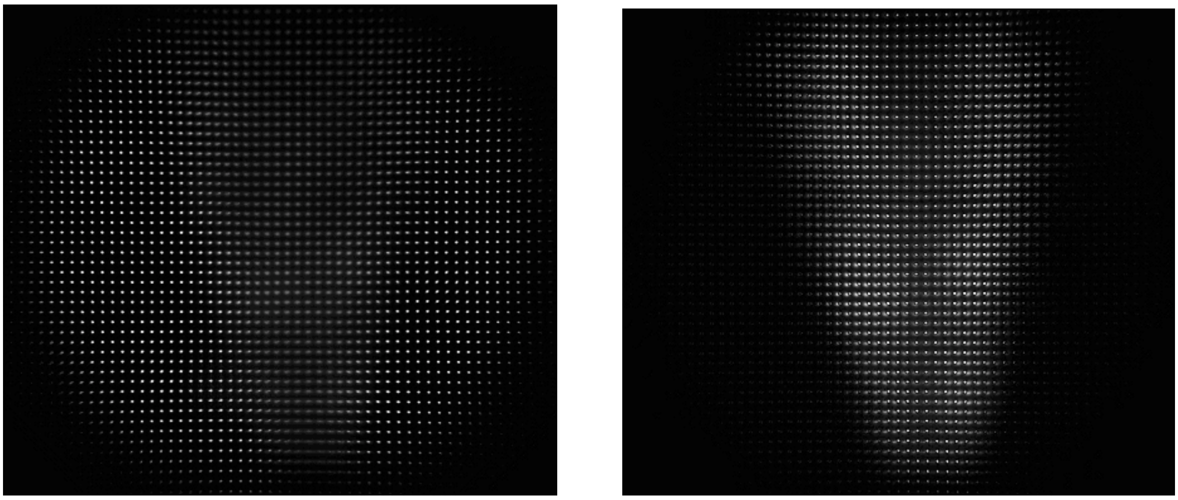
(a) (b)

Fig. 2. The talbot image of a helium jet (a) and a difference between this image and initial one (b)

The talbot image of a turbulent axisymmetric helium jet (Fig. 2, a) was recorded by diode target array of «Canon 300D» camera. The exposure of the image was sufficient for the averaging of refractive index turbulent fluctuations. Fig. 2, b showes the difference between helium jet talbotgram and initial unperturbed talbotgram. It is seen that the presence of a helium jet causes a shift of the perturbed isolated Talbot elements from their initial positions. Effect of turbulence leads to a change in the intensity distribution in perturbed single elements (i.e., bluring of spots) [20, 21].

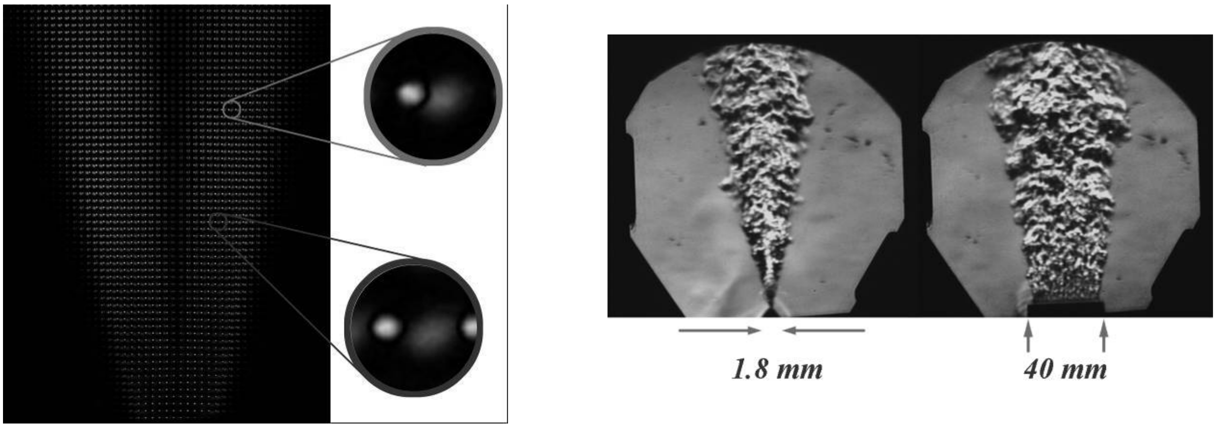

(a) (b)

Fig. 3. Light intensity distributions in the unit element of the Talbot image before and after light passing through the two-dimensional turbulent jet (a) and the schlieren photo of the jet (b)

The difference between intensity distributions in the self-imaging plane of the initial unperturbed pattern and pattern with helium jet also is shown in Fig. 3, a. Fig. 3, b demonstrates a schlieren photo of the jet. It is seen that along with the local displacement of unit intensity maxima throughout the flow field $\bar{\Delta}_i = (\Delta X_i, \Delta Y_i)$ caused by the averaged refraction angles, these maxima undergo significant blurring due to turbulent fluctuations. In addition, the fluctuations essentially transform the light intensity distribution in a unit element into approximately elliptical shape with different values of the ellipse major-to-minor half-axes ratio and the slope angle of these half-axes to the x-axis. It points to the fact that the field of turbulent fluctuations is inhomogeneous and non-isotropic.

3. CALCULATION OF AVERAGED HELIUM CONCENTRATION THROUGHOUT THE FLOW FIELD

For small refraction angles of a light beam in an optical inhomogeneous medium (e.g., light propagates in a turbulent gas flow), the Euler equations can be written in simplified form [18]

$$\tan(\varepsilon_x) \approx \int_{z_1}^{z_2} \frac{d\{\ln[n(x,y,z)]\}dz}{dx}; \quad \tan(\varepsilon_y) \approx \int_{z_1}^{z_2} \frac{d\{\ln[n(x,y,z)]\}dz}{dy}, \tag{2}$$

where $n(x,y,z)$ is a field of refrective index, ε_x and ε_y are projectionesof light deflection angel on *x* and *y* axis respectively. If a nozzle throat is positioned along the optical axis of a Talbot interferometer and a flow is directed vertically upwards (see Figure 1), then it can be approximately assumed that the functions $\frac{\partial n}{\partial x}$ and $\frac{\partial n}{\partial y}$ do not depend on the coordinate *z*. Then equations (2) assume the form

$$\varepsilon_x = \frac{1}{n}\frac{\partial n}{\partial x}\Delta z, \qquad \varepsilon_y = \frac{1}{n}\frac{\partial n}{\partial y}\Delta z, \tag{3}$$

where Δz is spatial length of the optical inhomogeneity. Fig. 4 plots the distributions of averaged deflection angles of a light beam in the jet cross section at the distance *y* = 30*D* from the nozzle throat. Here *D* = 1.8 mm is a transverse size of the nozzle.

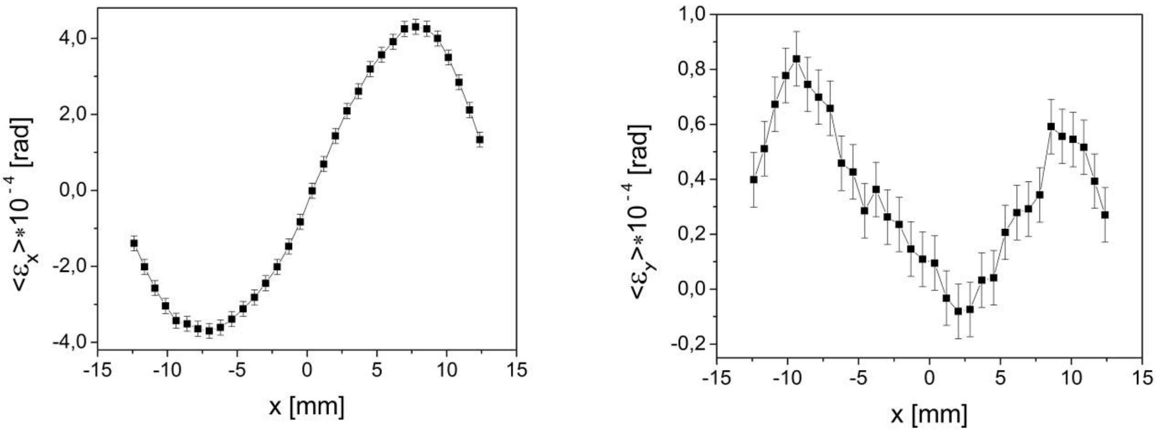

(a) (b)

Fig. 4. Distributions of averaged deflection angles of a light beam $\langle \varepsilon_x \rangle$ (a) and $\langle \varepsilon_y \rangle$ (b) in the jet cross section at *y* = 30*D*

Eq. (3) can be numerically integrated when a value of refractive index in an undisturbed medium is known. Absolute values of refractive index in a turbulent jet can be found by the formula

$$n(x,y) = n(x_0, y) + \int_{x_0}^{x} \frac{\partial n}{\partial x}(x,y)dx \,. \tag{4}$$

Taking into account that in processing an averaged Talbotgram we have to deal with a discrete set of data, relation (4) can be written in recurrence form

$$n(x_i) = n(x_0) + \sum_{k=1}^{i} \frac{n(x_k)\cdot \overline{\varepsilon_k}}{\Delta z}\cdot \Delta x_k \,. \tag{5}$$

Fig. 5, a plots the distribution of the averaged refractive index in the jet cross section calculated by formula (5) from the initial data in Fig. 4.

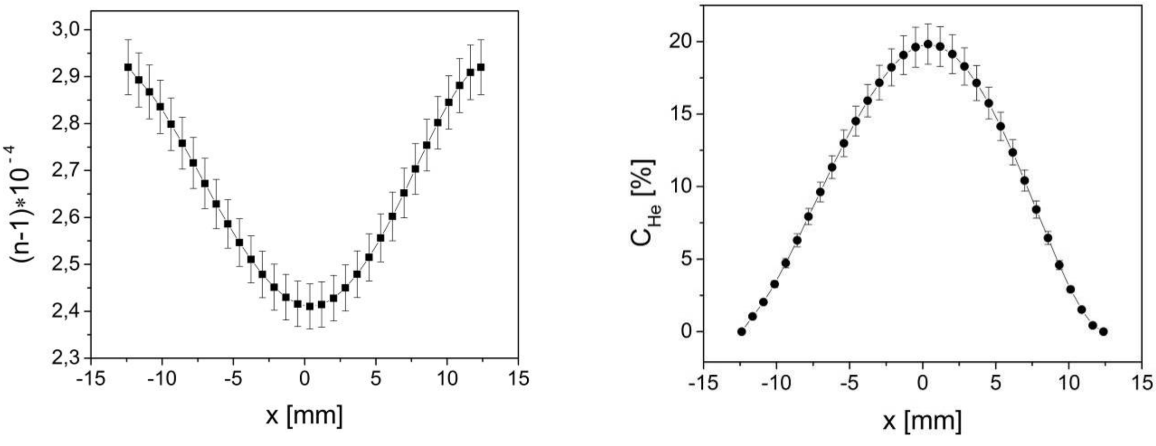

(a) (b)

Fig. 5. Distributions of averaged refractive index (a) and helium concentration (b) in the jet cross section at the distance $y = 30D$ from the nozzle throat

The obtained distribution of the medium refractive index can be used for calculating an averaged helium concentration throughout the flow field. Considering a helium-air mixture as binary and assuming that refractive index values for gas mixtures differ slightly from unity, we write the Lorenz-Lorentz formula [18] in the form of the following system of equations

$$\begin{gathered} \overline{n-1} = 2\pi\left(\overline{C_{He}}a_{He} + \overline{C_{air}}a_{air}\right) \\ \overline{C_{He}} + \overline{C_{air}} = \overline{C} \end{gathered} \,, \tag{6}$$

where $\overline{C_{He}}$ and $\overline{C_{air}}$ are the averaged concentrations of helium and air in the jet, while a_{He} and a_{air} are the polarizability of helium and air molecules, respectively. Fig. 5, b shows the calculation results on the averaged concentration of helium in the jet obtained by formulas (3), (5) and (6).

4. CONCLUSIONS

The applied potentialities of the technique based on Talbot effect are illustrated by the results of measurement of averaged values of a turbulent jet issuing into the drown air space.

The possibility of measuring the spatial distribution of averaged admixture concentration makes this method very promising in investigations of turbulent mixing.

Carried out investigations give reason to conclude that Talbot effect-based technique is a powerful tool for diagnostics of turbulent gas flows. The method is simple to implement, requires no additional optical elements and it is illustrative. Due to the small number of optical elements, it is little prone to external disturbances and can be used in industrial conditions.

REFERENCES

1. TALBOT F. Facts relating to optical science. IV. Philos. Mag., Vol. 9, p. 401–407, 1836.
2. SHAKHER C., NIRALA A. A review on refractive index and temperature profile measurements using laser-based interferometric techniques. Optics and Lasers in Engineering, Vol. 31, p. 455–491, 1999.
3. SHAKHER C., DANIEL A., NIRALA A. Temperature profile measurement of axysimmetric gaseous flames using speckle photography, speckle shearing interferometry, and Talbot interferometry. Opt. Eng., Vol. 33, p. 1983–1988, 1994.
4. SPAGNOLO G, AMBROSINI D, PAOLETTI D. Displacement measurement using the Talbot effect with a Ronchi grating. J. Opt. A: Pure Appl. Opt., Vol. 4, p. 376–380, 2002.
5. ANDREYEV A, GINZBURG V, RAMISHVILI N. The use of the Talbot effect in dynamic measurements of deformed liquid/gas interface surface shape. Opt. Communs., Vol. 73, No 6, p. 429–433, 1989.
6. QI-CAN Zhang, XIAN-YU Su. An optical measurement of vortex shape at a free surface. Optics and Laser Technology, Vol. 34, No 2, p. 107–113, 2002.
7. STRICKER J, ZAKHARIN B. 3-D turbulent density field diagnostics by tomographic moiré technique. Experiments in Fluids, Vol. 23, No 1, p. 76–85, 1997.
8. KORYAKOVSKY A, MARCHENKO V. Датчик волнового фронта на основе эффекта Тальбота. J. Tech. Phys, Vol. 51, No 7, p. 1432–1438, 1981.
9. VOINOV Yu, ZUEV G., KORYAKOVSKY A. О возможности исследования оптического качества газовых потоков методом тальбот-интерферометрии. Крат. сообщ. по физике ФИАН, № 1 (1984) p. 13–17.
10. BOREISHO A, KORYAKOVSKY A, MARCHENKO V. Исследования оптического качества газовых потоков, формируемых сопловыми блоками сотовой конструкции. J. Tech. Phys, Vol. 55, No 10, p. 1943–1949, 1985.
11. DOROSHKO M., PENYAZKOV O., RANKIN G., KHRAMTSOV P., SHIKH I. Talbot effect-based technique study of two-dimensional turbulent flow past a horizontal cylinder. Heat and Mass Transfer–2005, Minsk, pp. 210–214, 2005.
12. DOROSHKO M., PENYAZKOV O., RANKIN G, KHRAMTSOV P., SHIKH I. Talbot effect-based technique in measurements of an axis-symmetrical turbulent jet. JEPTER, No 5, 2006. Vol. 79, № 5. p. 94–99.
13. EBBENI J. Nouveaux aspects du phenomene de moiré. Nouv. Rev. Opt., Vol. 1, No 5, p. 333–342, 1970; Vol. 1, No 6, p. 353–358, 1970.
14. NAKANO Y., MURATA K. Measurements of phase objects using Talbot effect and moiré techniques. Appl. Opt., Vol. 23, No 14, p. 2296–2299, 1984.
15. LOHMANN A., SILVA D. An interferometer based on the Talbot effect. Opt. Communs., Vol. 2, No 9, p. 413–415, 1971.

16. LIM C., SRINIVASAN V. Talbot interferometer with computer generated gratings. Opt. Communs., Vol. 44, No 3, p. 219–222, 1983.
17. TAKEDA M., KOBAYASHI S. Lateral aberration measurements with a digital Talbot interferometer. Appl. Opt., Vol. 23, No 11, p. 1760–1764, 1984.
18. VASILIEV L. Schlieren Methods. Nauka Press, Moscow, 1968.
19. WAY J., LIBBY P. Hot wire probes for measuring velocity and concentration in helium-air mixtures. AIAA J., Vol. 8, p. 976–977, 1970.
20. DOROSHKO M.V., KHRAMTSOV P.P., PENYAZKOV O.G., SHIKH I.A. Measurements of admixture concentration fluctuations in a turbulent shear flow using an averaged Talbot image // Experiments in Fluids. 2008. Vol. 44, p. 461–468.
21. DOROSHKO M.V., KHRAMTSOV P.P., PENYAZKOV O.G., SHIKH I.A. Измерение пульсаций концентрации в сдвиговом турбулентном потоке методом осредненных тальбот-изображений // ИФЖ. 2008. Vol. 81, № 1, p. 49–54.
22. DOROSHKO M.V., KHRAMTSOV P.P., PENYAZKOV O.G., SHIKH I.A. Исследование статистических характеристик пульсаций плотности в пограничном слое за фронтом ударной волны // Тепло- и массоперенос–2007. Minsk, 2007. p. 213–219.

HEAT TRANSFER BETWEEN NON-STANDARD IN–LINE TUBE BUNDLE AND VERTICALLY UPWARD AQUEOUS FOAM FLOW

J. Gylys, T. Zdankus, M. Gylys, A. Ingilertas
Kaunas University of Technology
Energy Technology Institute
K. Donelaicio str. 20–212 LK, LT–44239 Kaunas, Lithuania
Phone: +370 37 300444
Email: jonas.gylys@ktu.lt

R. Jonynas
Kaunas University of Technology
Department of Thermal and Nuclear Energy
K. Donelaicio str. 20, LT–44239 Kaunas, Lithuania
Phone: +370 37 300445
Email: rolandas@afterma.lt

ABSTRACT

In this article the results of experimental investigation of heat transfer between non – standard inline tube bundle and vertically upward two – phase foam flow are presented. Compressor, foam generation accessory, experimental channel with integrated tube bundle, measurement devices and auxiliary installation were the main parts of experimental equipment. Statically stable aqueous foam was used as two – phase coolant in this investigation. Non–standard in–line tube bundle was constructed out of seven rows of tubes (diameter d = 0.02 m, amount of tubes in a row: 1st = 5, 2nd = 4, 3rd =4, 4th = 5, 5th = 4, 6th = 4, 7th = 5). The spaces between the centers of tubes in a row across the tube bundle was s_1 = 0.03 m and the distance between axis piloted out through tubes centers in horizontal rows was s_2 = 0.03 m. Tubes in a second row were moved into the right side considering the first row with a distance s_3 = 0.01 m. The third row tubes were moved with the same distance s_3 = 0.01 m to the right side regarding the second row tubes. Fourth row tubes were aligned horizontally the same way as the first. The fifth, sixth and seventh rows were stated complexly like a mirror–image of first three rows. Due to the complicated array of tubes in the bundle that was defined above was named “non-standard”. The experimental investigation results are as follows: the dependence of heat transfer intensity on flow velocity and volumetric void fraction of aqueous foam was determined. Influence of tube position of the bundle on heat transfer intensity was investigated either. Moreover, the experimental results were summarized by criterion equations.

Keywords: aqueous foam, two phase foam flow, heat transfer, non-standard in–line tube bundle

1. INTRODUCTION

The application of aqueous foam (two–phase system) as a coolant [1] has a number of advantages in comparison with single–phase coolants. For example, delivering the coolant to the place of heat exchange requires lower flow rates as well as lower energy consumption. Two–phase foam flow can obviously reduce material expenditures too. A totally new, modern and economic heat exchanger with simple and safe exploitation using two–phase foam flow in heat transfer could be created.

Aqueous foam flow has various peculiarities which always exist in heat transfer processes such as drainage of liquid from foam [2], diffusive transfer of gas between bubbles [3], division and collapse of foam bubbles [3, 4]. These phenomena are closely related with each other and make the application of heat transfer processes in the foam flow in analytical study extremely complicated. That is why experimental approach is selected as the most suitable for our previous and present investigation [1, 5, 6].

Typical heat exchangers usually consist of several vertical parts in which coolant changes its direction from vertical upward to vertical downward and vice versa [7, 8]. Tube bundles of different types and geometry [7, 8] may also be used in heat exchangers. Therefore we performed an investigation where the heat transfer between staggered [5] and in–line [6, 9] tube bundles and vertical upward and downward after turning foam flow were used.

The objectives of this investigation are to determine the optimal type (and geometry – in our previous and future works) of tube bundle which guarantees the heat transfer to two–phase aqueous foam flow at maximum level. The dependence of heat transfer intensity in the non–standard tube bundle on foam flow velocity and volumetric void fraction was determined and discussed in this work either.

2. EXPERIMENTAL SET-UP

The experimental equipment (Fig. 1) consisted of these following parts: vertical experimental channel with integrated non–standard in–line tube bundle, gas and liquid control valves, gas and liquid flow meters, liquid storage reservoir, liquid level control reservoir, compressor with receiver, electric current transformer and stabilizer. Cross section of the experimental channel had the dimensions of 0.14 x 0.14 m^2; its' height was 1.8 m. Walls of the channel were made from the transparent material so that the foam flow could be observed visually.

Statically stable foam – one type of aqueous foam – was used as a coolant for the experiments. Statically stable foam flow was generated from the water solution with detergents. The concentration of detergents was constant at 0.5% level in all the experiments. Solution (water-detergent) was supplied from the reservoir onto the special perforated plate. Foam flow was generated during gas and liquid contact. Foam flow parameters control was fulfilled using gas and liquid valves.

The perforated stainless steel plate with a thickness of 2 mm for foam generation was installed at the upside of the experimental channel; orifices were located in a staggered order with diameter equal to 1 mm and 5 mm spacing between the centers of the holes.

Non–standard in–line tube bundle (Fig. 2) was constructed out of seven rows of tubes (diameter d = 0.02 m, amount of tubes in a row: 1st = 5, 2nd = 4, 3rd =4, 4th = 5, 5th = 4, 6th = 4, 7th = 5). The spaces between the centers of tubes in a row across the tube bundle were s_1 = 0.03 m and the distance between axis piloted out through tubes centers in horizontal rows was s_2 = 0.03 m. Tubes in a second row were moved into the right side considering the first row with a distance s_3 = 0.01 m. The third row tubes were moved with the same distance s_3 = 0.01 m to the right side regarding the second row tubes. Fourth row tubes were aligned horizontally the same way as the first. The fifth, sixth and seventh rows were stated complexly like a mirror – image of the first three rows. Due to this kind of complicated array of tubes, the tube bundle was named "non-standard".

"Non-standard" tube bundle tubes at the different positions was labeled A1, B1 … G1, G3 (Fig. 2a). In-line tube bundle used for comparison of results presented in Figure 2b.

One tube – calorimeter was heated electrically. This tube was made of copper and had an external diameter of 0.02 m. The ends of the heated tube was sealed and insulated to prevent heat loss through them.

During the experiments calorimeter was placed instead of one of the bundle's tube. An electric current value of heated tube was measured by an ammeter, the voltage – by a voltmeter. Temperature of the calorimeter surface was measured by eight calibrated thermocouples: six of them were placed around the central part of the tube and two of them were placed in both sides of the tube with a distance of 50 mm from the central part. Temperature of the foam flow was measured by two calibrated thermocouples: one in front of the bundle and one behind it.

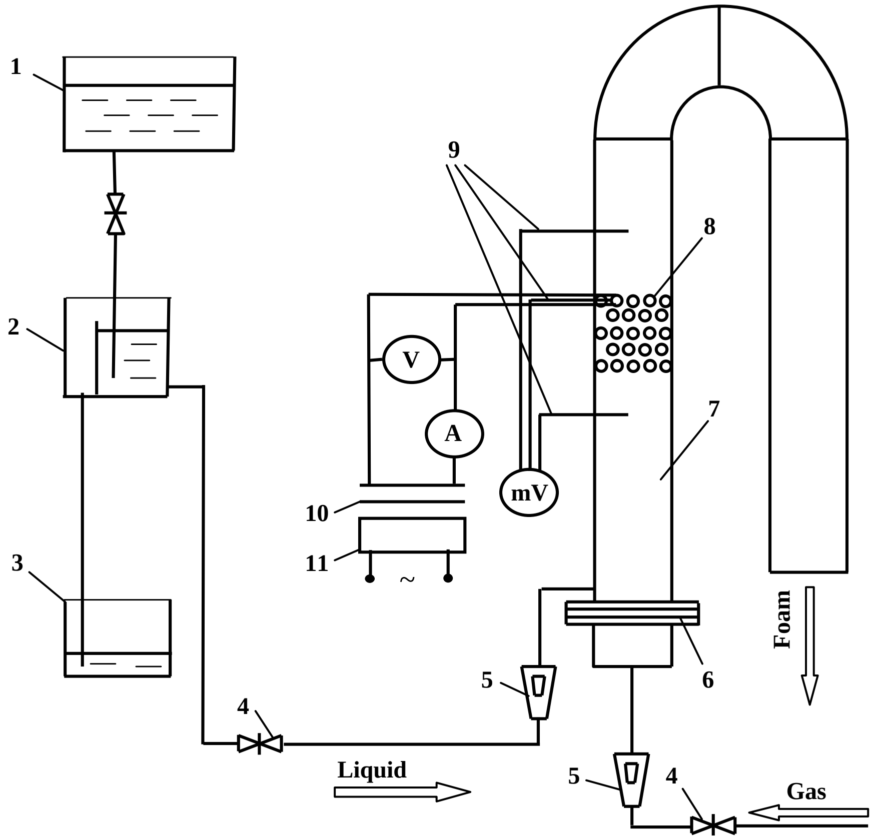

Fig. 1. Experimental set–up scheme: 1–liquid reservoir; 2–liquid level control reservoir; 3 – liquid receiver; 4 – gas and liquid control valves; 5 – flow meters; 6 – foam generation plate; 7 – experimental channel; 8 – tube bundle; 9 – thermocouples; 10 – transformer; 11–stabilizer

Measurement accuracies for flows, temperatures and heat fluxes were as follows: 1.5%, 0.15÷0.20% and 0.6÷6.0%.

During the experimental investigation the relationship between an average heat transfer coefficient h from one side and foam flow volumetric void fraction β and gas flow Reynolds number Re_g from the other side was obtained:

$$Nu_f = f(\beta, Re_g). \tag{1}$$

Nusselt number was computed by formula:

$$Nu_f = \frac{hd}{\lambda_f}. \tag{2}$$

Here λ_f is the thermal conductivity of the statically stable foam flow, W/(m·K), computed by the equation:

$$\lambda_f = \beta\lambda_g + (1-\beta)\lambda_l. \tag{3}$$

An average heat transfer coefficient was calculated as:

$$h = \frac{\overline{q_w}}{\Delta T}. \tag{4}$$

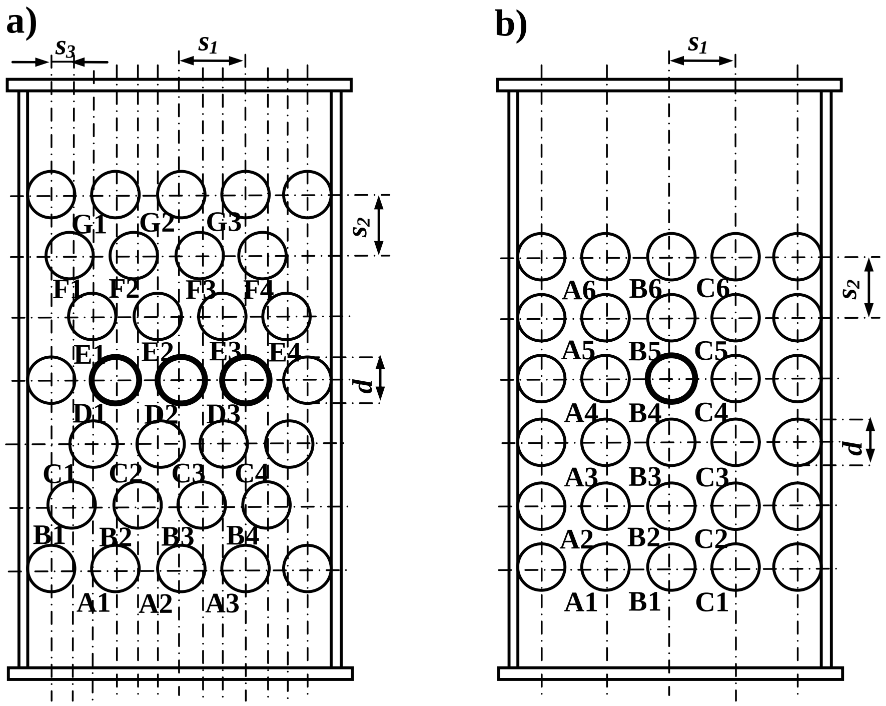

Fig. 2. Non–standard in–line (a) and in–line 1.5x1.5 (b) tube bundles in upward foam flow

Gas Reynolds number of foam flow was computed by formula:

$$Re_g = \frac{G_g d}{A \nu_g}. \tag{5}$$

Foam flow volumetric void fraction was expressed by the equation:

$$\beta = \frac{G_g}{G_g + G_l}. \tag{6}$$

Experiments we performed within limits of Reynolds number range for gas (Re_g): 190÷440 (laminar flow regime) and foam volumetric void fraction (β): 0.996÷0.998. Gas velocity for foam flow was changed from 0.14 to 0.32 m/s.

3. RESULTS

The heat transfer intensity of the tubes located at the different places across and along the non-standard in–line tube bundle to vertical upward foam flow was investigated experimentally. In the foam flow case heat transfer intensity of the different tubes is under the influence of distribution of local flow velocity and local foam void fraction across and along the channel. The third factor which influences the heat transfer intensity of tubes is the foam structure.

With increasing of foam flow gas Reynolds number Re_g within the limits 190÷440 (Fig. 3), heat transfer intensity (Nu_f) of the tube D1 from the fourth horizontal line of the bundle increases by 2.2 times (from Nu_f=375 to Nu_f=811) for foam volumetric void fraction β = 0.996, and by 2.2 times for β=0.997 (from Nu_f=324 to Nu_f=724), and by 2.1 times for β = 0.998 (from Nu_f = 262 to Nu_f = 551). The heat transfer intensity of the tube D1 is on average by 1.3 times higher to the wettest foam flow (β = 0.996) in comparison to the drier foam flow (β=0.997) and by 1.7 times higher in comparison to the driest foam flow (β = 0.998).

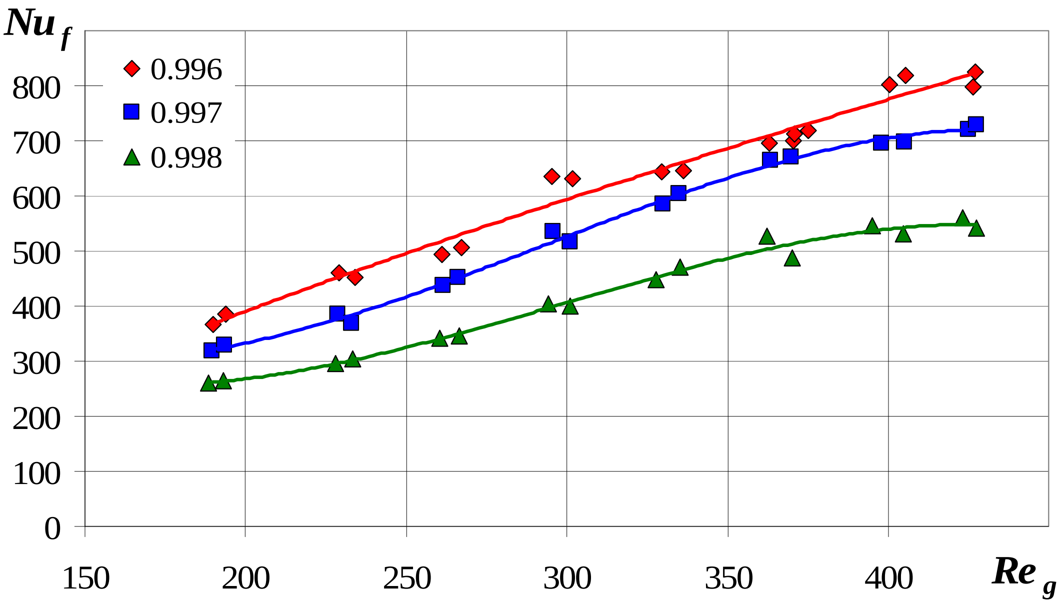

Fig. 3. Heat transfer intensity of the tube D1 from the fourth horizontal line of the tubes of the non–standard in–line bundle to upward foam flow; β=0.996, 0.997 and 0.998

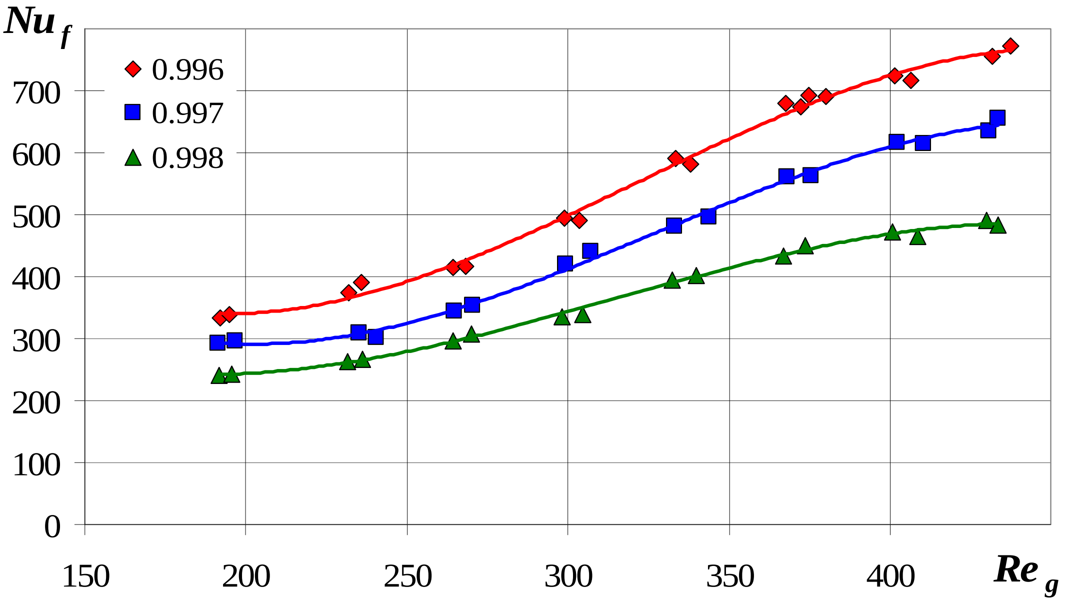

Fig. 4. Heat transfer intensity of the tube D2 from the fourth horizontal line of the tubes of the non–standard in–line bundle to upward foam flow; β=0.996, 0.997 and 0.998

Data of the heat transfer intensity of the tube D2 from the fourth horizontal line of the tubes of the non–standard in–line bundle to upward foam flow for Re_g=190÷440 and β=0.996, 0.997 and 0.998 is shown in Fig. 4. By increasing of Re_g from 190 to 440, heat transfer intensity (Nu_f) of the tube D2 to upward foam flow increases by 2.3 times (from Nu_f=335 to Nu_f=764) for wettest foam flow (β=0.996), and by 2.2 times for foam flow with β=0.997 (from Nu_f=295 to Nu_f=644), and twice for foam flow with β=0.998 (from Nu_f=241 to Nu_f=487). The heat transfer intensity of the tube D2 is on average by 1.4 times higher to the wettest foam flow (β=0.996) in comparison to the drier foam flow (β=0.997) and by 1.7 times higher in comparison to the driest foam flow (β=0.998).

The heat transfer intensity of the tube D3 to upward foam flow (Fig. 5) increases by 2.2 times (from Nu_f=359 to Nu_f=775) for foam flow with β=0.996, twice for β=0.997 (from Nu_f=308 to Nu_f=617), and by 1.8 times for β=0.998 (from Nu_f=260 to Nu_f=460) and for Re_g=190÷440. The heat transfer intensity of the tube D2 is on average by 1.4 times higher to the foam flow with β=0.996 in comparison to foam flow with β=0.997 and by 1.8 times higher in comparison to the foam flow with β=0.998.

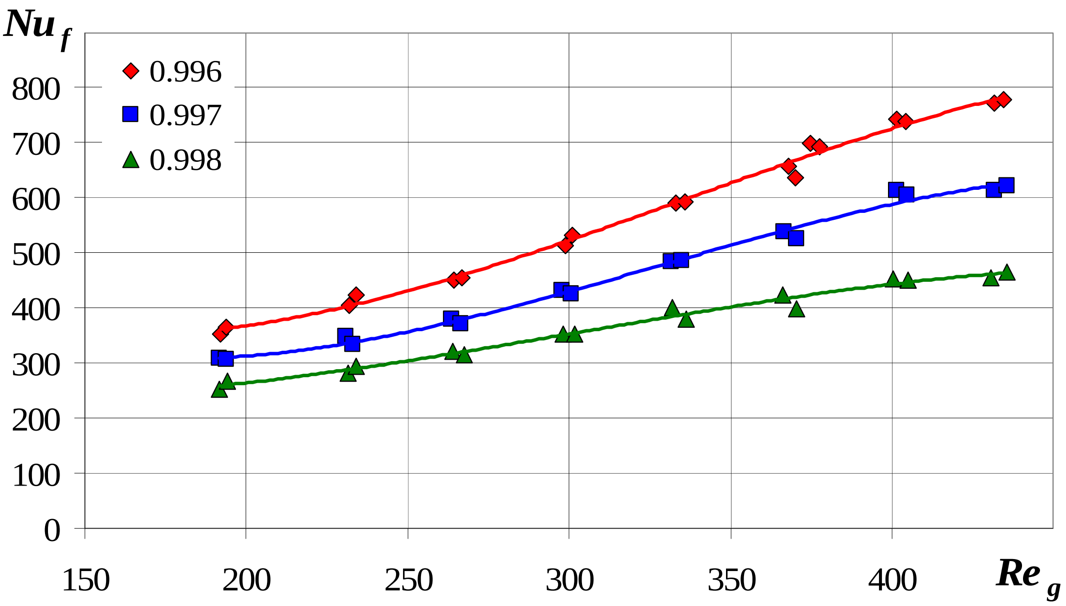

Fig. 5. Heat transfer intensity of the tube D3 from the fourth horizontal line of the tubes of the non–standard in–line bundle to upward foam flow; β = 0.996, 0.997 and 0.998

The heat transfer intensity of the tubes located in the different places in the fourth horizontal line of tubes of the non–standard in–line tube bundle is not the same. The heat transfer intensity of the tube D1 is highest, the heat transfer intensity of tube D3 is less than that of the tube D1 and heat transfer intensity of the tube D2 is less than that of the tubes D1 and D3. The values of heat transfer intensity of the tubes D2 and D3 are almost the same when the volumetric void fraction of the foam flow is equal to 0.997 and 0.998 for Re_g=190÷440. The heat transfer intensity of the tube D1 is on average by 8% higher than that of the tube D3 and by 11% higher than that of the tube D2 for β=0.996 and Re_g=190÷440. The heat transfer intensity of the tube D1 is on average by 18% higher than that of the tubes D3 and D2 for β=0.997 and by 14% higher than that of the tubes D3 and D2 for β=0.998 (Re_g=190÷440).

The tube D2 is located in the centre of the cross–section of the experimental channel and it's located in the centre of the fourth horizontal line of tubes of the non–standard in–line tube bundle. In our previous work the heat transfer process between tubes of the in–line tube bundle 1.5x1.5 (Fig. 2. – Tube B4 was located in the middle of the fourth horizontal line) and upward vertical foam flow was investigated [6, 9]. Comparison of heat transfer intensity of the tubes D2 (of the non–standard tube bundle) and B4 (of the in–line tube bundle 1.5x1.5) to the upward foam flow at the volumetric void fraction β=0.996, 0.997 and 0.998 is shown in Fig. 6. Heat transfer intensity of the tube D2 is higher than that of the tube B4 on average by 1.34 times for β=0.996, by 1.25 times – for β=0.997 and 0.998 (Re_g=190÷440). This phenomenon can be explained by more intensive turbulisation of foam flow in the case of the non–standard in–line tube bundle.

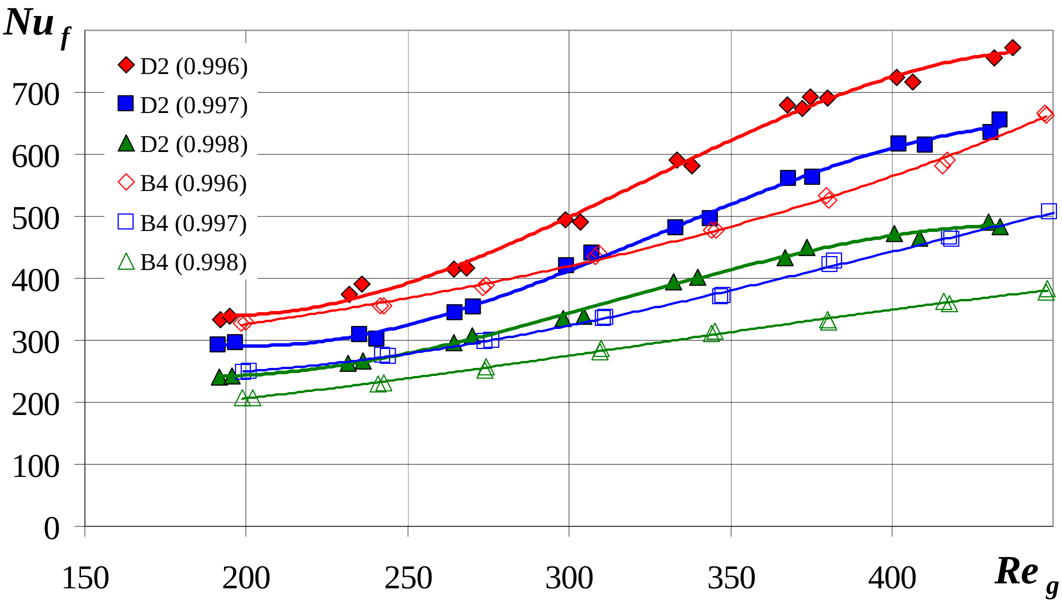

Fig. 6. Heat transfer intensity of the tubes D2 and B4 from the fourth horizontal tube lines of the non–standard and in–line bundles to upward foam flow; β=0.996, 0.997 and 0.998

Experimental results of investigation of heat transfer from the non–standard in–line tube bundle to upward foam flow were generalized by criterion equation (7) using dependence between Nusselt number Nu_f and gas Reynolds Re_g number. This dependence within the interval 190 < Re_g < 440 for the non–standard in–line tube bundle in upward foam flow with the volumetric void fraction β=0.996, 0.997, and 0.998 can be expressed as follows:

$$Nu_f = c\beta^n Re_g^m \tag{7}$$

For the tube D1 in the upward foam flow: c=0.75, n=–233, m=20.9(1.042–β).
For the tube D2 in the upward foam flow: c=2.34, n=275, m=82.4(1.010–β).
For the tube D3 in the upward foam flow: c=12.80, n=518, m=127.3(1.004–β).

4. CONCLUSIONS

The heat transfer process between tubes of the non–standard in–line tube bundle and upward statically stable foam flow was investigated experimentally. It was determined dependency of heat transfer intensity of the tubes bundle on foam flow velocity and volumetric void fraction of foam.

The three main parameters of foam flow influence on heat transfer intensity of different tubes of the bundles were as follows: changes of foam structure along the experimental channel, distribution of local flow velocity and distribution of local foam void fraction across and along the experimental channel.

The results showed that the heat transfer intensity of the middle tube (D2) from the fourth (further line of the bundle) horizontal tubes line was smaller than that of the side tubes (D1 and D3). The heat transfer of the side tubes (D1 and D3), which were located at the same distance from the centre of the channel, was found to be different. The heat transfer intensity of the tube D1 was determined to be higher than that of the tube D3.

The heat transfer intensity of the tubes from the fourth horizontal tubes' line in the non–standard in–line tube bundle is higher than that of the tubes in the in–line tube bundle 1.5x1.5.

The criterion Eq. (7) should be applied for calculating the heat transfer intensity of tubes from further lines of non–standard in–line tube bundle's to upward vertical statically stable foam flow.

NOMENCLATURE

A – cross section area of experimental channel, m^2; c, m, n – coefficients; d – outside diameter of tube, m; G – volumetric flow rate, m^3/s; h – average coefficient of heat transfer, W/(m^2·K); Nu – Nusselt number; q – heat flux density, W/m^2; Re – Reynolds number; $\overline{T}$ – average temperature, K; β – volumetric void fraction; λ – thermal conductivity, W/(m·K); ν – kinematic viscosity, m^2/s. Indexes: f –foam; g – gas; l – liquid; w – wall of heated tube.

REFERENCES

1. J. Gylys. Hydrodynamics and Heat Transfer Under the Cellular Foam Systems // Kaunas, Technologija, 1998, p. 50–314.
2. V. Nguyen, Anh, Liquid Drainage in Single Plateau Borders of Foam, Journal of Colloid and Interface Science, 249, 2002, p. 194–199.
3. V. Tichomirov. Foams. Theory and Practice of Foam Generation and Destruction // Moscow, Chimija, 1983, p. 11–106.
4. J.F. Sadoc, N. Rivier, Eds., Foams and Emulsions, NATO ASI Series, 1997.
5. J. Gylys, S. Sinkunas, T. Zdankus, Analysis of staggered tube bundle heat transfer to vertical foam flow, J. International Journal of Heat and Mass Transfer, 51(1–2), 2008, p. 253–262.
6. J. Gylys, T. Zdankus, S. Sinkunas, V. Giedraitis. Study of In–line Tube Bundle Cooling in Vertical Foam Flow, WSEAS Transactions on Heat and Mass Transfer, Iss. 6, Vol. 1, 2006, p. 632–637.
7. A. Zukauskas. Convectional Heat Transfer in Heat Exchangers // Moscow, Nauka, 1982, p. 245–268.
8. T. Kuppan. Heat Exchanger Design Handbook // New York: Marcel Dekker, 2000, p. 229–303.
9. J. Gylys, S. Sinkunas, T. Zdankus, Analysis of tube bundle heat transfer to vertical foam flow, J. Engenharia Termica, 4, 2005, p. 91–95.

CYSENI 2010, May 27–28, Kaunas, Lithuania
ISSN 1822-7554, www.cyseni.com

EVALUATION OF WATER VOLUME AND FLOW RATE MEASUREMENT CAPABILITIES BY REFERENCE FACILITY

Eugenijus Maslauskas
Lithuanian Energy Institute
Breslaujos str. 3, LT-44403 Kaunas
Phone: +370 37 401860
Email: maslauskas.e@mai.lei.lt

Andrius Bončkus
Lithuanian Energy Institute
Breslaujos str. 3, LT-44403 Kaunas
Phone: +370 37 401861
Email: andriusb@mail.lei.lt

ABSTRACT

Reference facility for reproduction of flowing water volume is constructed and operates now in Lithuanian Energy Institute. Measurement of water volume is realized by using gravimetric method. Usually, measurement accuracy is expressed by evaluation of measurement capability or, in other words, by expanded uncertainty of measurement result. Therefore always there exists task to reduce measurement uncertainty. So, in presented report not only investigation and improvement of separate component of facility but also the level of uncertainty reached are analyzed.

On the first stages, the uncertainty was evaluated by conventional statistical method. Using the information accumulated during the investigation of uncertainty sources, the mathematical model was comprised, the distribution laws for each input values were ascribed and standard uncertainty values were calculated.

Then sensitivity coefficients were calculated by differentiating the model's equations in respect of every input value, correlation coefficients were evaluated according to interdependence of input values and total standard uncertainty was finally found.

Considering probability distributions of input values, the probability distribution law of output value and coverage factor corresponding the to a coverage probability were chosen.

Naturally in such case, few problems dealing with determination of probability distribution of input values and its interdependence arise. It is also probable to evaluate erroneously the probability distribution of output value as well as nonlinearity of mathematical model.

To remove the problems mentioned above, Monte Carlo method was used for calculation of measurement uncertainties. This method is based on numerical simulation of experiment and processing the sequence of results received by statistical methods. This method enables to evaluate more precisely distribution law of output value and possible nonlinearity of mathematical model.

The use of both models enabled to qualify more exactly expanded uncertainty of water volume and flow rate measurement.

Keywords: flow, uncertainty, gravimetric method, Monte Carlo, test facility, statistical

1. INTRODUCTION

The Monte Carlo method has many advantages over statistical method in the estimation of expanded uncertainty: method is relatively simple to implement even in complicated measuring system with complicated mathematical model; there aren't subjective solution in estimation correlation coefficients of correlatives values; setting the distribution function of output size and the calculation of the expanded uncertainty. These advantages allow the

Monte Carlo method used to calculate not only the uncertainty of new measurement instrument, but also verify calculation estimated uncertainty with statistical method.

The measurement capability of test facility 3E was calculated using EA-4/02 method [1], but goal of this work is to verify these estimating, using Monte Carlo method.

2. TEST FACILITY

Scheme of flow meters calibration facility shown in Fig. 1. Functioning of this facility is based on the gravimetric method; it is recognized as the most accurate flow measurement method. Water is weighed in high-precision scales, and then converted into mass volume. Mass is corrected according to the buoyancy of which depends on the specific weather conditions. Density, required for calculating of volume in facility 3E, is calculated using the water density formula in release 1997 of IAPWS [2]. The data required for calculation of density, are taken from temperature and pressure transducers in the measurement section. Calculation buoyancy of water in weighing tank requires measured values of water temperature and environment conditions.

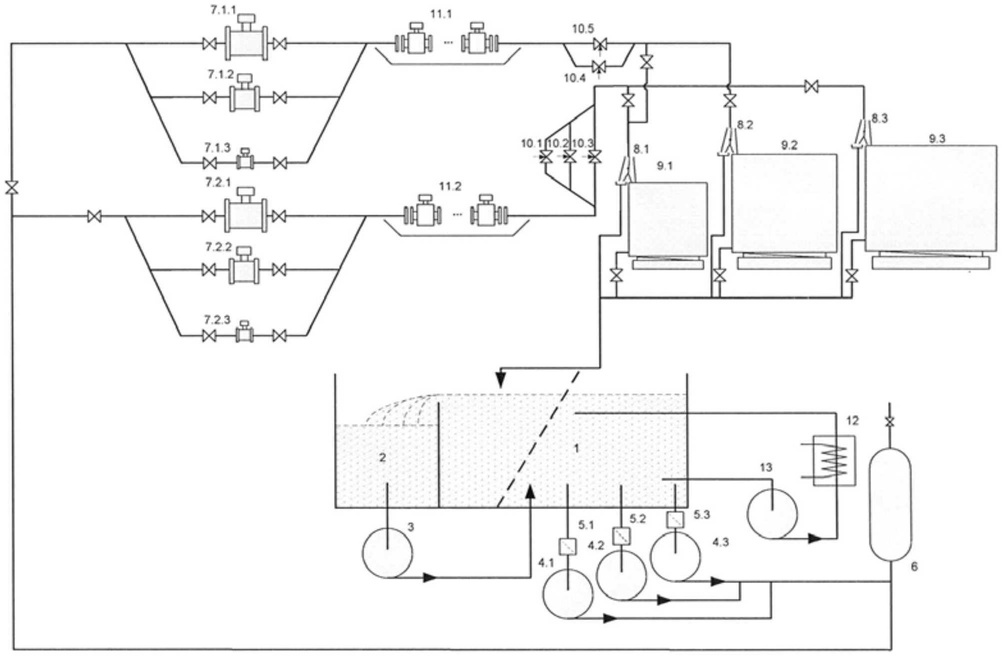

Fig. 1. Reference facility 3E

The facility consists of two parallel lines with flow-meters for measuring flow 7.2.1–7.2.3 in first and 7.1.1–7.1.3 in the second lines. The maximal flow rate of the first line is 100m^3/h. Here the water is weighed with 9.1 and 9.3 scales (up to 1400 kg). The maximum available flow rate in second line is 15m^3/h. Here the water is weighed with 9.1 and 9.2 scales (up to 500 kg). Three pumps 4.1, 4.2 and 4.3, are controlled by frequency converters to adjust the required flow. To ensure stable height of water column up to the pumps, the tank is divided into two sections. Water pump 3 keeps maximal level of water in the main section. The water excess is draining back. If it is necessary, the temperature is heightening in the reservoir using the heating element 12 with regulator. Pressure vessel 6 compensates flow and pressure pulsation. Valve system 10.1–10.5 and pumps control flow and pressure. Diverter 8.1–8.3 directs flow from the return line in to the weighting tank and back.

3. MONTE CARLO METHOD

Monte Carlo method is based on processing of the statistical results of the digital experiment. Beginning of operation sequence using Monte Carlo method is the same as beginning using statistical method for calculating uncertainty. Mathematical model is structured a more detailed of the device. Uncertainties and their distributions of all dimensions in the mathematical model are found. Later the mathematical experiment is executed. Number of iterations is picked, random values arrays of all incoming dimensions are generated according to theirs distributions. The output value is estimated for each realization. The output array is composed, mean and standard uncertainty are calculated. Coverage interval of output size is computed according coverage probability.

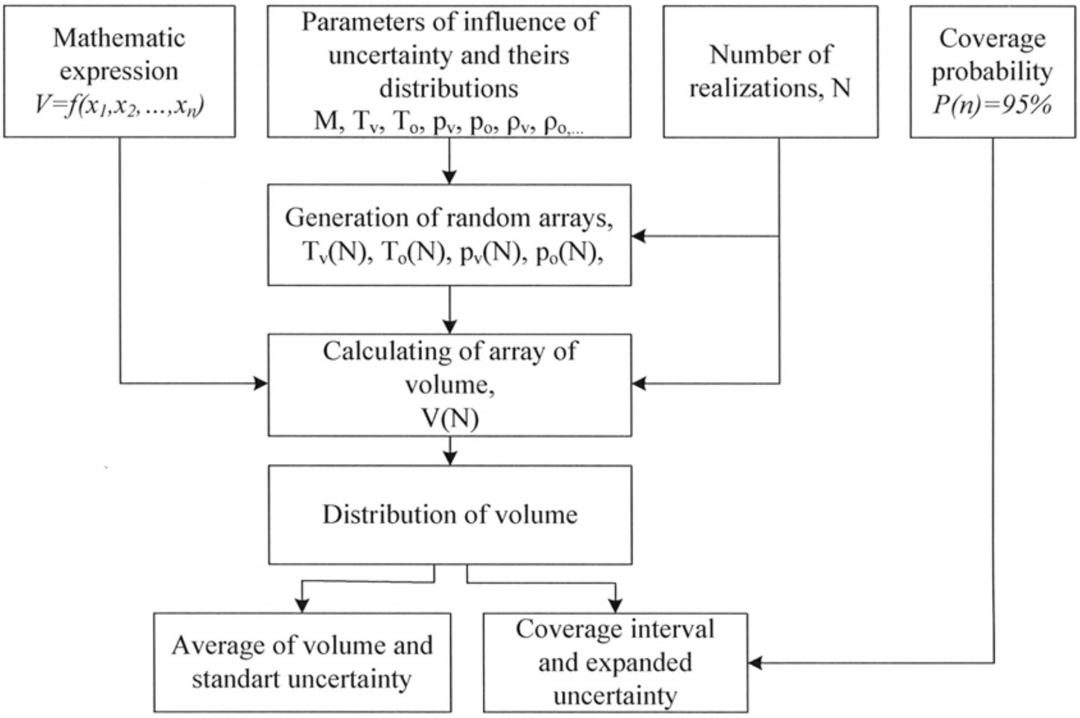

Fig. 2. Monte Carlo method

Monte Carlo method allows to objective evaluates the expanded uncertainty and the distribution of output dimension. Using of this method makes possible to do verification of the reliability of the statistical method using.

4. MATHEMATICAL MODEL

The volume of water measured on the calibration facility is calculated using the formula:

$$V_{et} = k\frac{m_{sv} + \Delta m}{\rho_{v1}} + \Delta V_{kr} + \Delta V_T + \Delta V_{Pl}, \tag{1}$$

where V_{et} – reference volume, k – coefficient of buoyancy, m_{sv} – scale reading, Δm – scale calibration correction, ρ_{v1} – water density in the measurement section, ΔV_{kr} – correction of volume caused by of uneven work of diverter, ΔV_T – correction of volume caused by evaporation, ΔV_{Pl} – correction of volume caused by temperature expansion of pipeline.

Since Archimedes power put up the water, so it is evaluated with coefficient of buoyancy:

$$k = \frac{1-\rho_o/\rho_s}{1-\rho_o/\rho_{v2}}, \tag{2}$$

where ρ_o – air density, ρ_{v2} – density of water in weighing tank, ρ_s – density of reference weight of calibration scales, ρ_s = 8000 kg/m^3.

Volume of pipe after flow meters and water volume in weighing tank is changed, because temperature of pipe shifts. Temperature expansion of pipes from start to end of measure is evaluated using the formula:

$$V_{pl} = V_i(1 + a_\alpha \Delta t), \tag{3}$$

where V_i – volume of pipes at measure start, a_α – temperature expansion coefficient of volume, Δt – temperature shift from start to end of measure.

Volume correction for water evaporation is calculated:

$$V_T = W\tau, \tag{4}$$

where W – speed of water loss, τ – time of measurement.

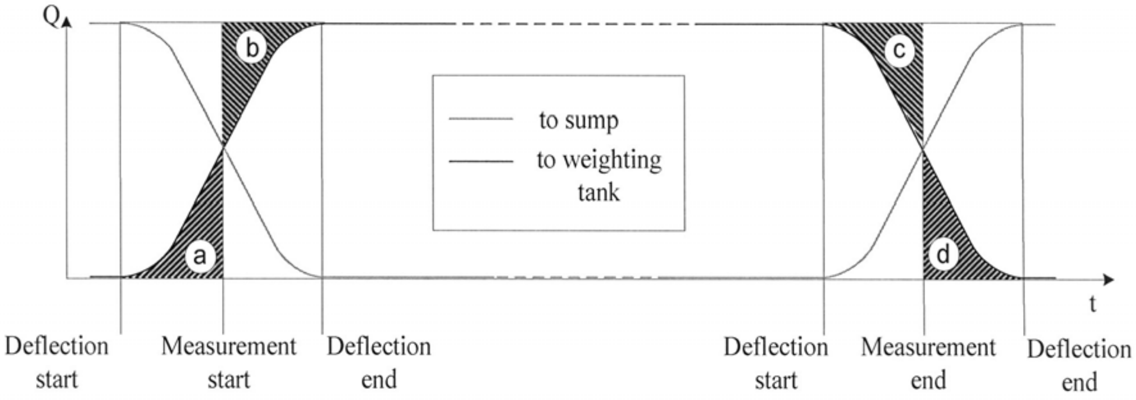

Fig. 3. Influence of diverter

Fig. 3 shows the diagram of diverter operation. Measure start is midpoint between region a and b, and end – between region c and d. Volume a and d get in weighing tank not during measure time. Volume b and c get to sump during measure time. If $V_a+V_d=V_b+V_c$, that uncertainty $V_{kr}=0$, and:

$$V_{kr}= (V_a+V_d)-(V_b+V_c). \tag{5}$$

All volumes depend on diverter operation time and flow instability.

Table 1 shows incoming parameters, their standard uncertainties and distributions, that influence on uncertainty of volume, when it is measured in both lines in maximum flow: I – 100 m^3/h and II - 15 m^3/h. Parameters were collected from the technical documentation of devices, calibration certificates and measurements, experiments, needed to identify obscure values such as the water evaporation, influence of diverter, capacity of pipeline after flow meters.

Table 1. Parameters affecting uncertainty of volume measurement.

Flow	**15**		**100**			m^3/h
Parameter	Value	St. uncertainty	Value	St. uncertainty	Distribution	Dimension
Weighing results	500	0.0058	1400	0.0058	Rectangular	kg
Correction of balance calibration	0	0.0030	0	0.0535	Normal	kg
Water temperature of working section	20	0.05	20	0.05	Normal	ºC
Water temperature change of working section	0	0.17	0	0.17	Rectangular	ºC
Water pressure of working section	200	0.5	200	0.5	Normal	kPa
Water pressure change of working section	0	1.73	0	1.73	Rectangular	kPa
Water density of working section	0.9983	0.00025	0.9983	0.00025	Normal	kg/dm^3
Air temperature	20	0.1	20	0.1	Normal	ºC
Air temperature change	0	1.15	0	1.15	Rectangular	ºC
Atmospheric pressure	101.325	1	101	1	Normal	kPa
Air humidity	45	1	45	1	Normal	%
Air density	0.00120	$1.8^{x}10^{-6}$	0.00120	$1.8^{x}10^{-6}$	Normal	kg/dm^3
Water temperature in weighing tank	20	0.05	20	0.05	Normal	ºC
Water temperature change in weighing tank	0	0.58	0	0.58	Rectangular	ºC
Water density in weighing tank	0.9982	0.00025	0.9982	0.00025	Normal	kg/dm^3
Diverter influence	0	0.069	0	0.44446	Normal	dm^3
Water evaporation	0	0.020	0	0.066	Normal	dm^3
Temperature expansion of tube	0	0.0004	0	0.0031	Normal	dm^3

5. COMPUTATIONS RESULTS

The uncertainty was calculated with Monte Carlo method using MATLAB software. The number of iterations was selected N = 10^6, according to the OIML G 1 – 101:2008 [3]. It was calculated for the first and second lines for maximal flows. Input values were presented in table 1. The mathematical model was used of the formula (1). Coverage probability was chosen P = 0.95. Standard uncertainty calculated according to:

$$u(x_i) = \sqrt{\frac{1}{n(n-1)}\sum_{k=1}^{n}(x_{i,k} - \overline{x_i})^2}\ , \tag{6}$$

The output array elements were distributed in equal intervals by size and calculated frequencies to trace the distribution law. The volume array elements were sorted by size, to find the expanded uncertainty. $M = N(1-P)$ mostly remote elements to the higher and lower direction from the average were rejected. If distribution law is symmetrical, the average of remaining maximal and minimal values will be expanded uncertainty:

$$u_e(x_i) = \pm \frac{V_{\max 0,95} - V_{\min 0,95}}{2}. \tag{7}$$

If distribution law is not symmetrical:

$$\begin{cases} u_e(x_i)_+ = V_{\max 0,95} - V_{mean} \\ u_e(x_i)_- = V_{\min 0,95} - V_{mean} \end{cases}. \tag{8}$$

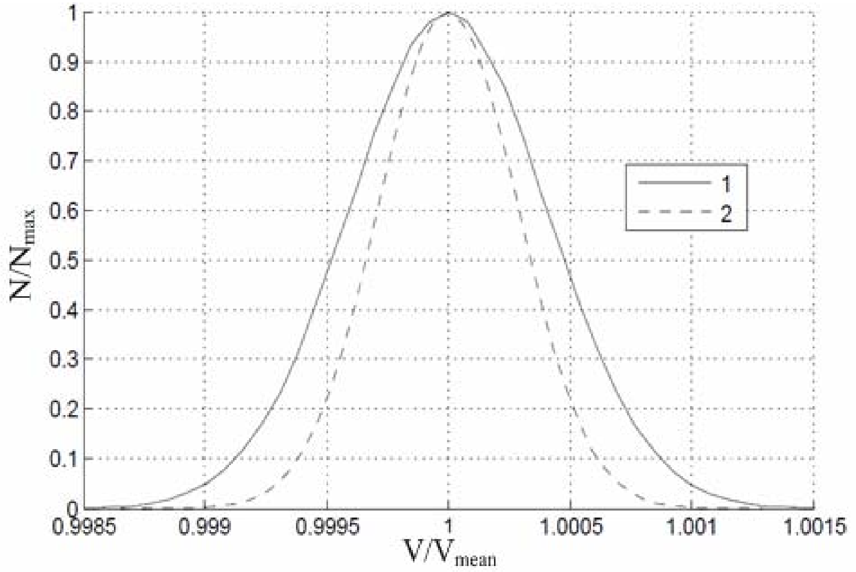

Fig. 4. The distribution law of volume, where 1 – first line, 2 – second line

As shown in Fig. 4, the uncertainty of first line on the maximum flow is greater than that of the second lines (more wide distribution). This is caused by diverter operating time and greater value of diverter timing error of first line (weight and overall dimensions of diverters of the first line is major than that of the second line). The maximum measured volume increases in 3 times, but flow – in 7 times and the measuring time at the maximum flow, is only t = 50.4 s. These reasons (diverter timing error increases and the measurement time decreases) determine the increase diverter uncertainty component. So, near the density uncertainty, which has normal distribution, close-sized diverter uncertainty with normal distribution emerges.

Table 2. Results of calculating with Monte Carlo and statistical method

Parameter	First line		Second line	
	Monte Carlo method	(EA-4/02) method	Monte Carlo method	(EA-4/02) method
Volume, l	501.381	501.381	1403.867	1403.867
Standard uncertainty, l	0.144	0.146	0.570	0.575
Expanded uncertainty, l	0.281	0.292	1.119	1.151
Expanded uncertainty, %	0.056	0.058	0.080	0.082

We can see from the Table 2, that obtained results are very similar, estimated by both the Monte Carlo method and the statistical method. Obtained volumes in the first and second lines are the same in both methods. In our case expanded uncertainty, calculated with Monte Carlo method, is obtained slightly smaller than calculated with statistical method.

6. CONCLUSIONS

Measurement capability of flow test facility 3E was estimated using Monte Carlo method by the maximum at flow rate in the first ($Q = 100m^3/h$) and in the second line ($Q = 15m^3/h$).

It was compared the results estimated using EA-4/02 and Monte Carlo methods.

Distribution law was obtained normal, as it was estimated with EA-4/02 method.

The standard and expanded uncertainties estimated using Monte Carlo method were closed to the values obtained using EA-4/02 method.

REFERENCES

1. EA-4/02 . Expression of the Uncertainty of Measurement in Calibration. 1999.
2. The International Association for the Properties of Water and Steam. Release on the IAPWS Industrial Formulation 1997 for the Thermodynamic Properties of Water and Steam. 1997.
3. OIML G 1 – 101:2008. Evaluation of measurement data -Supplement 1 to the "Guide to the expression of uncertainty in measurement" - Propagation of distributions using a Monte Carlo method.
4. ISO/IEC Guide 98-3/Suppl.1:2008. Propagation of distributions using a Monte Carlo method.
5. PAPADOPOULOS, C.E.; YEUNG, H. Uncertainty estimation and Monte Carlo simulation method. Flow Measurement and Instrumentation. 2001, No 12, p. 291–298.

CYSENI 2010, May 27–28, Kaunas, Lithuania
ISSN 1822-7554, www.cyseni.com

IMPACTS OF DIFFERENT SOLVENTS AND SUBSTRATES ON PROPERTIES OF ZINC OXIDE NANOROD LAYERS PREPARED BY CHEMICAL SPRAY PYROLYSIS

K. Annert, M. Vent, T. Dedova, E. Kärber, I. Oja Acik,
O. Volobujeva, A. Mere, M. Krunks
Department of Materials Science
Tallinn University of Technology
Ehitajate tee 5, 19086 Tallinn – Estonia
Phone: +3726203369
Email: katre88@hotmail.com

V. Mikli
Centre for Materials Research
Tallinn University of Technology
Ehitajate tee 5, 19086 Tallinn – Estonia
Phone: +3726203150
Email: miku@staff.ttu.ee

ABSTRACT

Highly structured ZnO layers comprising hexagonal nanorods were prepared by spray pyrolysis deposition from zinc chloride aqueous and alcoholic solutions with pH=2 and 5. Bare glass, differently processed ITO covered, and SnO_2 covered glass were used as substrates. The nanorod layers were deposited at tin bath temperatures of 480°C and 550°C. The effect of the substrate on nanorods growth was achieved by depositing onto different substrates and changing the structure of the ITO covered glass by treating it chemically. Morphology of the nanorods and their distribution on the substrate was examined with the help of surface and cross-sectional views of Scanning Electron Microscopy (SEM). The deposition on treated substrates resulted in more uniform structures compared to non-treated ones. Nanorods deposited from aqueous solution were thicker and longer than nanorods deposited from alcoholic solutions. Deposition of solutions with pH=2 supports formation of layers with separately standing rods. Photoluminescence (PL) and X-ray Diffraction (XRD) results suggest that ZnO nanorods prepared by spray pyrolysis are of high optical and crystalline quality. Additionally, according to PL studies, intense UV-emission is characteristic of ZnO independent of growth temperature, the concentration of oxygen vacancy related defects is lower in ZnO nanorods deposited at 550°C.

Keywords: Zinc oxide; Nanorods; Chemical spray pyrolysis; Surface morphology; Photoluminescence

1. INTRODUCTION

Zinc oxide nanostructured layers comprising nanorods are very attractive for various applications such as new generation solar cells with different sensitizers [1–4], high efficient gas sensors [5], ultraviolet detectors [6], etc.

Well-aligned single-crystalline ZnO nanorod arrays have been prepared by vapour-liquid-solid (VLS) [7], chemical vapour deposition (CVD) [8] and metal organic CVD (MOCVD) [9] techniques. Wet-chemical methods such as growth in the solution [1, 2, 10] or electrochemical deposition [3] have been mainly used to produce ZnO nanorod layers for photovoltaic applications. However, one of the drawbacks of the solution growth methods is the relatively long processing time.

Chemical spray pyrolysis has the advantage over the other methods being a less time and expenses consumable, catalyst and template free method to prepare ZnO nanostructures. Development of ZnO nanorods by spray technique is controlled by the growth temperature, precursor concentration in spray solution, type of solvent and surface morphology of the substrate [11–14]. Recently, we reported extremely thin absorber solar cells with conversion efficiency of 4% could be prepared on spray deposited ZnO nanorods using thin spray pyrolysis deposited $CuInS_2$ absorber layer [15].

The aim of the research is to characterize the impact of different substrates and solvents on the properties of chemical spray pyrolysis deposited ZnO nanorods. This paper is based on our previous results [11, 12, 16, 17].

2. METHODOLOGY

ZnO nanorods were deposited by spray pyrolysis method using an aqueous or ethanol containing aqueous solution of zinc chloride ($ZnCl_2$, Aldrich, purity 98%). The concentration of $ZnCl_2$ in spray solution was 0.1 mol/l. Acidity of spray solution was held around pH=5 or pH=2. Solution pH of 2 was adjusted by addition of HCl. The precursor solution was pulverized with the help of compressed air onto bare glass, indium tin oxide (ITO), and SnO_2 covered glass substrates placed on a soldered tin bath. Two types of ITO covered glass (A and B) with similar thickness of about 1 mm have been used. Type A: ITO (further named as ITO-A) with rough surface and non-uniform grain size (thickness of 150 nm, medium grain size ca. 100 nm). Type B: (further named as ITO-B) ITO with rough surface and non-uniform grain size (thickness of 150 nm, medium grain size ca. 40 nm). Both types of substrates (originally non-treated) were additionally chemically treated which resulted in smoother surface. The deposition temperature (T_s, temperature at substrate surface) was 550 ^oC in case of aqueous solution and 480 ^oC in case of alcohol containing solution with accuracy of ± 5 °C using an electronic temperature controller. The solution volume was 50 ml and the flow rate and carrier gas flow rate were maintained between 2.2 and 2.4 ml/min and 8 l/min, respectively.

The surface morphology and cross-sectional images of the layers were examined by high-resolution scanning electron microscopy (SEM) on a Leo Supra 35 or Zeiss EVO-MA15. The optical properties were investigated by photoluminescence (PL) measurements at room temperature (300 K) using a He–Cd laser (325 nm) as an excitation source. X-ray diffraction (XRD) patterns were recorded by a Bruker AXS D5005 diffractometer using the Cu-Kα radiation (λ=0.1542 nm).

3. RESULTS AND DISCUSSION

3.1 Deposition of ZnO nanorods by spray on different substrates

In order to study the effect of substrate morphology on the ZnO nanorods formation and development we examined the nanorods growth on different substrates.

Fig. 1 (a–f) presents SEM micrographs of the ZnO nanorod structures formed on different substrates such as glass, ITO with various surface structures and SnO_2. For a comparison, the surface morphology of the bare substrates is depicted in insets of Fig. 1 (b–e).

ZnO nanorods grown on glass substrate are presented in Fig. 1a. As it can be seen on SEM micrograph, large well-shaped hexagonal prisms with diameter of 300-400 nm and length of 2 µm (cross-sectional image not presented) are formed [11, 16]. It was also found that both, the increase of the substrate temperature and precursor concentration, resulted in increased dimensions of the rods [11, 12].

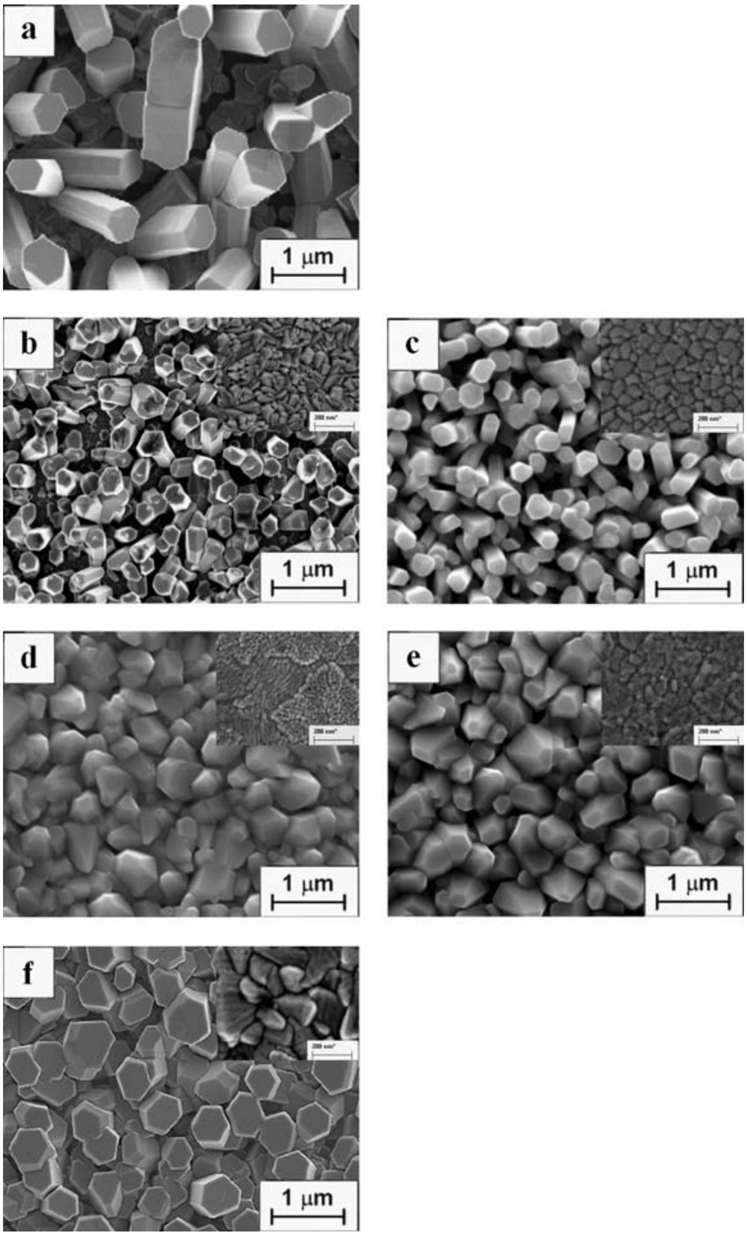

Fig. 1. SEM micrographs of bare substrates (insets) and ZnO layers deposited from the $ZnCl_2$ aqueous solution at T_s=550°C onto a) glass, b) non-treated ITO-A, c) chemically treated ITO-A, d) non-treated ITO-B, e) chemically treated ITO-B, f) non-treated SnO_2

According to the SEM surface views (Fig. 1b, c), a structured film consisting of hexagonally shaped crystals was formed in case of ITO-A. Though, ZnO nanorods grown onto non-treated substrate (Fig. 1b) appear to be in different shape and length. However, using chemically treated ITO-A as a substrate (Fig. 1c) resulted in more uniform ZnO crystals with diameter of 200 nm and length of 800 nm (cross-sectional image can be seen on Fig. 2a).

Deposition on non-treated ITO-B (Fig. 1d) resulted in asymmetric ZnO structures with various shapes and sizes. Deposition on chemically treated ITO-B (Fig. 1e) led to the formation of ZnO with more defined hexagonally shaped pyramidal-like forms in different sizes with average diameter of 400 nm on ITO surface and average length of 600 nm (cross-sectional image not presented).

As it can be detected from SEM micrographs, ZnO hexagonal crystals grown on SnO_2 covered glass (Fig. 1f) are relatively fat and short with diameter about 700 nm and length 250 nm (cross-sectional image not presented), thus, well-shaped nanorods have not been developed [16].

The results obtained indicate that the development of nanorods strongly depends on the substrate microstructure. Generally, it is known that the most successful approach to grow well aligned nanorods is the use of a seed layer for site-selective nucleation [18, 19]. In our experiment, the density of nuclei was definitely higher in case of smaller-grained ITO (ITO-B) and SnO_2 covered glass, and thus the number of crystals formed in the early stage of growth can also be high. Obviously, the coalescence of adjacent crystals occurs during the growth, resulting in the layer composed of fat crystals [12, 16]. It was also discovered that using chemically treated ITO substrates can result in more uniform ZnO nanorod structures [12]. Consequently, in order to grow well-shaped ZnO nanorods by spray pyrolysis method chemically treated larger-grained ITO (in this case, for example ITO-A) or a seed layer should be used as a substrate.

3.2 Effect of solution pH on the development of ZnO rods

In order to study the effect of the solution pH on the formation of ZnO nanorods we deposited series of samples at the spray solution pH of 2 or 5 onto treated ITO-A substrate. Fig. 2 depicts the SEM micrographs of the ZnO nanorods sprayed from aqueous solutions with pH=2 (Fig. 2a) and pH=5 (Fig. 2b) onto treated ITO-A. SEM micrographs (Fig. 2a, b) indicate the formation of well-shaped hexagonal nanorods, irrespective of the spray solution pH. ZnO nanorods deposited from spray solution with pH=2 (Fig. 2a) were uniform in both, size and distribution, with diameter of about 200 nm and length of about 800 nm. Using spray solution with pH=5 (Fig. 2b) resulted in rods that were slightly thinner and more densely located but not as uniform as rods that were deposited from solution with pH=2.

In order to compare the density of ZnO crystals which were formed by spraying the solution with pH= 2 and 5 onto the treated ITO-A the image analysis of SEM microphotos were carried out by the Media Cybernethics Image-Pro 3 system. According to the analysis, the spraying solution with pH=5 (Fig. 2b) resulted in ZnO layer with density of crystals (mean diameter of ZnO crystals ~200 nm, length ~800 nm) as high as 212 per analyzed area of 24μm^2 (~9x10^{6}mm^{-2}). Deposition of the solution with pH=2 resulted in ZnO layer showing larger deviation in diameter of crystals (Fig. 2a). According to the image analysis of SEM microphotos in Fig. 2a, the number of crystals was lower – 166 per the area analyzed (~7x10^{6}mm^{-2}) [17].

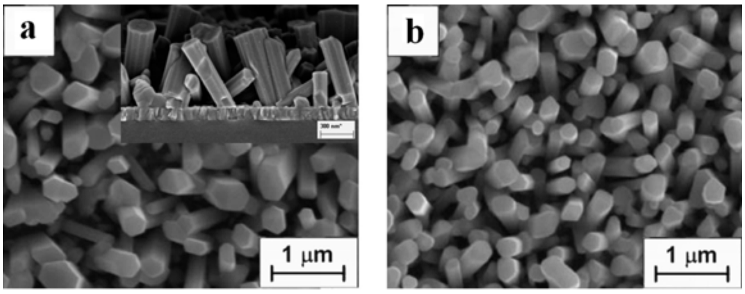

Fig. 2. SEM micrographs and cross-section (inset) of ZnO layers deposited from the $ZnCl_2$ aqueous solution with a) pH=2 and b) pH=5 onto treated ITO-A. T_s=550°C

Nevertheless not directly proved, the changes in the layer morphology depending on the solution pH refer to the possibility that partial dissolution of initially formed seed crystals occurs in the nucleation stage due to spray of an acidic solution. As a result, the number of growing crystals is reduced and their further coalescence can also be avoided. It is not excluded as well that solution pH has effect via controlling the hydrolysis of $ZnCl_2$ precursor in spray solution. The use of acidic solutions offers an alternative way besides thiocarbamide containing solutions [13] for obtaining separately standing ZnO nanorod layers on ITO electrode by spray pyrolysis method [17].

3.3 Effect of organic solvent on the development of ZnO rods

Another approach is to add alcohol into the spray solutions as it is well-known that alcoholic solvents have low surface tension and viscosity, which facilitates the formation of small spray droplets [20]. For example, most of ZnO thin films have been deposited by spray of alcoholic solutions [21]. In order to study the effect of organic solvent on the ZnO nanorods formation we sprayed alcohol containing solution onto the treated ITO-A substrate. Additionally the effect of the alcoholic solution pH on the formation of ZnO nanorods was examined by depositing series of samples at the spray solution pH of 2 or 5.

Fig. 3 depicts the SEM micrographs of the ZnO nanorods sprayed from alcoholic solutions with pH=2 (Fig. 3a) and pH=5 (Fig. 3b) and aqueous solution with pH=2 (Fig. 3c) onto treated ITO-A.

Deposition of alcohol containing spray solution with pH=2 (Fig. 3a) led to well-shaped hexagonal nanorods with a length of ca. 300 nm and average diameter of about 70 nm, but also small (diameter of 50 nm) and fat (diameter of 200 nm) crystals were formed. Nanorods deposited from alcohol containing spray solution with pH=5 (Fig. 3b) were more uniformly located ZnO crystals with diameter of about 70-80 nm, length of about 400 nm and density of coverage of about 40 rods/μm^2 [16]. For a comparison, the spray of aqueous solution with pH=2 (Fig. 3c) led to the growth of significantly thicker (diameter of about 200 nm) and longer (length of about 800 nm) ZnO nanorods compared to those obtained by spraying alcohol containing solutions.

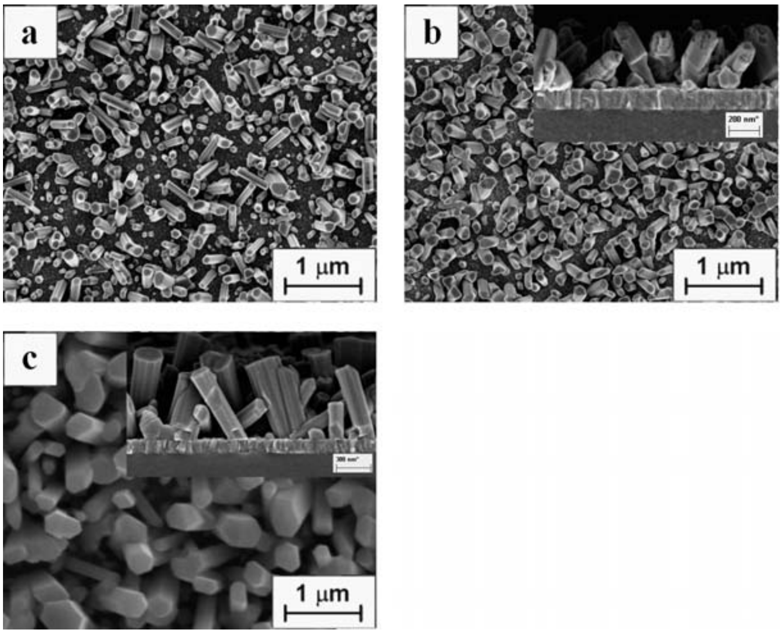

Fig. 3. SEM micrographs and cross-section (inset) of ZnO layers deposited from the $ZnCl_2$ alcoholic solution with pH=2 (a) and pH= 5 (b) at T_s=480°C and aqueous solution with pH=2 (c) at T_s=550°C onto treated ITO-A

Our results show that the use of alcoholic solutions instead of aqueous ones allows to obtain nanorods which are sparsely located and significantly thinner. Another remarkable advantage of using of alcoholic solutions is the possibility to reduce the deposition temperature [16].

3.4 Electrical and optical properties of ZnO nanorods

3.4.1 XRD study

XRD measurements were performed to study nanorods composition and their orientation.

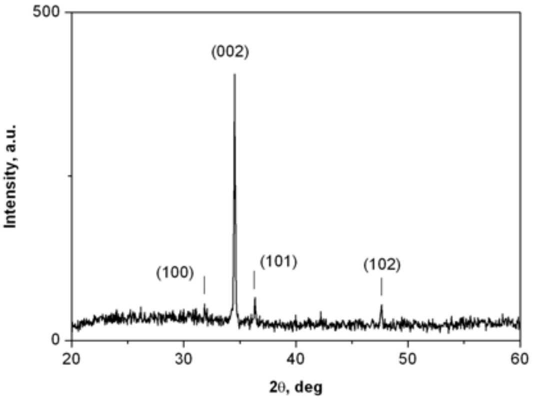

Fig. 4. XRD patterns of ZnO layers deposited from the $ZnCl_2$ aqueous solution onto glass substrate. T_s=550°C [11]

The X-ray diffractogram of the structured layer deposited at 550 °C onto glass substrate is presented in Fig. 4. The strong (002) reflection and weak reflections of the (101) and (102) planes of the ZnO wurtzite form (PDF 36-1451) can be detected in the diffractogram. The ratio of the intensities of (002) and (101) reflections (I002/I101) between 5.5 and 8.6 is characteristic of the samples consisting of well-shaped hexagonal columns. For a powder sample, the I_{002}/I_{101} is 0.44. Thus, according to XRD, ZnO crystals are c-axis-oriented [11].

3.4.2 Photoluminescence study (PL)

PL studies were performed to evaluate and compare the optical properties of ZnO nanorods deposited from aqueous (Ts=550 °C) and alcohol (Ts=480 °) containing solution.

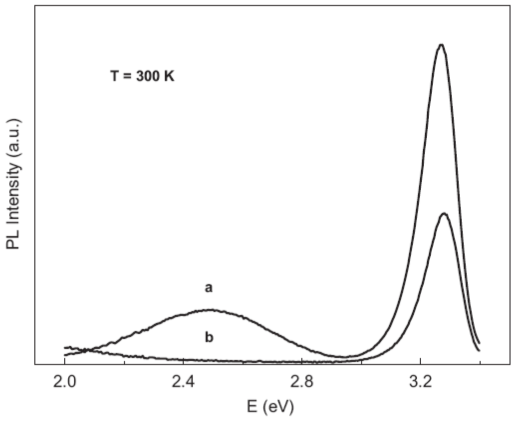

Fig. 5. Photoluminescence spectra of ZnO nanorod layers deposited from: a) alcoholic (T_s=480 °C) and b) aqueous (T_s=550 °C) solutions.
Spectra are recorded at room temperature [17]

The room-temperature PL spectrum of ZnO nanorod layer deposited from alcohol containing solution at 480 °C (Fig. 5a) shows a broad emission band centered around 2.5 eV in the visible spectral region and an intense UV-emission band centered around 3.27 eV. The green PL emission band is not present in the spectrum of the sample prepared from aqueous solution at 550 °C (Fig. 5b). Instead, a rise of the PL signal in the low-energy range of the spectrum is observed. It is generally accepted that UV-emission band is mainly due to the recombination of bound excitons in ZnO. The green PL emission band is assigned to the oxygen vacancies in ZnO, this luminescence being due to the recombination of photogenerated hole with singly ionized oxygen vacancies [22]. While the green emission band is being observed in oxygen deficient samples, the orange PL emission is seen in oxygen rich samples [23]. Correlation between the green and orange PL emission intensity and free-carrier density has been established—the green PL emission decreases and the orange PL emission increases while increasing the annealing temperature in oxidative conditions [22]. Thus, it can be concluded that the concentration of oxygen vacancies related defects is lower in the material deposited at higher temperature being also expressed in lower density of carriers [17].

4. CONCLUSIONS

ZnO nanorods could be grown on glass, indium tin oxide, and SnO_2 covered glass substrates by chemical spray pyrolysis using zinc chloride aqueous and alcoholic solutions. The formation of nanorods strongly depends on the underlayer microstructure. To avoid coalescence of growing crystals the density of nuclei should be carefully controlled.

According to SEM study, spray pyrolysis deposition of acidic zinc chloride solutions (pH=2) instead of those with pH=5 offers a new approach to grow ZnO nanorod layer with separately standing crystals on ITO substrate where, ordinarily, coalescence of growing crystals occurs easily. As a result, the density of ZnO crystals on the substrate is decreased, however, their size distribution is broadened.

According to PL studies, the concentration of oxygen vacancy related defects is lower in ZnO nanorods deposited at 550 °C compared to those deposited at 480 °C. Intensive UV-emission prevails in PL spectra independent of the growth temperature or solution pH and refers that spray deposited ZnO has relatively high crystal quality.

ACKNOWLEDGEMENTS

Financial support by the Estonian Ministry of education and Research (Target Financing Project SF0140092s08), Estonian Science Foundation (Grants ETF6954, ETF8509) is gratefully acknowledged.

REFERENCES

1. BAXTER, J.B., AYDIL, E.S. Dye-sensitized solar cells based on semiconductor morphologies with ZnO nanowires. *Solar Energy Materials and Solar Cells*, 2006, Vol. 90, No 5, p. 607–622.
2. GREENE, L.E., LAW, M., YUHAS, B.D., YANG, P.D. ZnO−TiO_2 Core−Shell Nanorod/ P3HT Solar Cells. *The Journal of Physical Chemistry C*, 2007, Vol. 111, No 50, p. 18451–18456.
3. Tena-Zaera, R., Ryan, M.A., Katty, A., Hodes, G., Bastide, S., Lévy-Clément, C. fabrication and characterization of zno nanowires/cdse/cuscn eta-solar cell. *comptes rendus chimie*, 2006, Vol. 9, No 5–6, p. 717–729.

4. KRUNKS, M., KATERSKI, A., DEDOVA, T., OJA ACIK, I., MERE, A. Nanostructured solar cell based on spray pyrolysis deposited ZnO nanorod array. *Solar Energy Materials and Solar Cells*, 2008, Vol. 92, No 9, p. 1016–1019.
5. YANG, Z., LI, L.-M., WAN, Q., LIU, Q.-H., WANG, T.-H. High-performance ethanol sensing based on an aligned assembly of ZnO nanorods. *Sensors and Actuators B: Chemical*, 2008, Vol. 135, No 1, p. 57–60.
6. LUPAN, O., CHOW, L., CHAI, G., CHERNYAK, L., LOPATIUK-TIRPAK, O., HEINRICH, H. Focused-ion-beam fabrication of ZnO nanorod-based UV photodetector using the in-situ lift-out technique. *Physica Status Solidi (A)*, 2008, Vol. 205, No 11, p. 2673–2678.
7. HUANG, M.H., MAO, S., FEICK, H., YAN, H., WU, Y., KIND, H., WEBER, E., RUSSO, R., YANG, P. Room-Temperature Ultraviolet Nanowire Nanolasers. *Science*, 2001, Vol. 292, No 5523, p. 1897–1899.
8. YI, G.-C., WANG, C., PARK, W.I. ZnO nanorods: synthesis, characterization and applications. *Semiconductor Science and Technology*, 2005, Vol. 20, No 4, p. 22–34.
9. PARK, J.Y., JUNG, I.O., MOON, J.H., LEE, B.-T., KIM, S.S. Temperature induced shape change of highly aligned ZnO nanocolumns. *Journal of Crystal Growth*, 2005, Vol. 282, No 3–4, p. 353–358.
10. KIEVEN, D., DITTRICH, T., BELAIDI, A., TORNOW, J., SCHWARZBURG, K., ALLSOP N., LUX-STEINER, M. Effect of internal surface area on the performance of ZnO/In_2S_3/CuSCN solar cells with extremely thin absorber. *Applied Physics Letters*, 2008, Vol. 92, No. 15, p.153107 1-3.
11. KRUNKS, M., DEDOVA, T., OJA ACIK, I. Spray pyrolysis deposition of zinc oxide nanostructured layers. *Thin Solid Films*, 2006, Vol. 515, p. 1157–1160.
12. DEDOVA, T., KRUNKS, M., GROSSBERG, M., VOLOBUJEVA, O., OJA ACIK, I. A novel deposition method to grow ZnO nanorods: Spray pyrolysis. *Superlattices and Microstructures*, 2007, Vol. 42, p. 444–450.
13. DEDOVA, T., VOLOBUJEVA, O., KLAUSON, J., MERE, A., KRUNKS, M. ZnO nanorods via spray deposition of solutions containing zinc chloride and thiocarbamide. *Nanoscale Research Letters, Nanoexpress*, 2007, Vol. 2, p. 391–396.
14. ALVER, U., KILINÇ, T., BACAKSIZ E., NEZIR, S. Temperature dependence of ZnO rods produced by ultrasonic spray pyrolysis method. *Materials Chemistry and Physics*, 2007, Vol. 106, No 2–3, p. 227–230.
15. KRUNKS, M., KÄRBER, E., KATERSKI, A., OTTO, K., OJA ACIK, I., DEDOVA, T., MERE, A. Extremely thin absorber layer solar cells on Zinc Oxide nanorods by chemical spray. *Solar Energy Materials and Solar Cells*, 2010, accepted, doi: http://dx.doi.org/10.1016/j.solmat. 2010.02.036
16. DEDOVA, T., KRUNKS, M., MERE, A., KLAUSON, J., VOLOBUJEVA, O. Preparation of shape and size-controlled zinc oxide nanostructures by chemical spray pyrolysis technique. Materials Research Society Symposium Proceedings 957: Warrendale, PA. 2007, p. 0957–K10-26.
17. KRUNKS, M., DEDOVA, T., KÄRBER, E., MIKLI, V., OJA ACIK, I., GROSSBERG, M., MERE, A. Growth and electrical properties of ZnO nanorod arrays prepared by chemical spray pyrolysis. PHYSICA B. Proceedings of the Third South African Conference on Photonic Materials. South Africa: Mabula Game Lodge. 2009 March 23–27.
18. SHI, Y., YANG, Z., CAO, H., LIU, Z. Controlled *c*-oriented ZnO nanorod arrays and *m*-plane ZnO thin film growth on Si substrate by a hydrothermal method. *Journal of Crystal Growth*, 2010, Vol. 312, No 4, p. 568–572.

19. FUGE, G.M., HOLMES, T.M.S., ASHFOLD, M.N.R. Ultrathin aligned ZnO nanorod arrays grown by a novel diffusive pulsed laser deposition method. *Chemical Physics Letters*, 2009, Vol. 479, No 1–3, p. 125–127.
20. PATIL, P.S. Versatility of chemical spray pyrolysis technique. *Materials Chemistry and Physics*, 1999, Vol. 59, No 3, p. 185–198.
21. KRUNKS, M., MELLIKOV, E. Zinc oxide thin films by the spray pyrolysis method. *Thin Solid Films*, 1995, Vol. 270, No. 1–2, p. 33–36.
22. VANHEUSDEN, K., WARREN, W.L., SEAGER, C.H., TALLANT, D.R., VOIGT, J.A., GNADE, B.E. Mechanisms behind green photoluminescence in ZnO phosphor powders. *Journal of Applied Physics*, 1996, Vol. 79, No 10, p. 7983–7990.
23. STUDENIKIN, S.A., GOLEGO, N., COCIVERA, M. Density of band-gap traps in polycrystalline films from photoconductivity transients using an improved Laplace transform method. *Journal of Applied Physics*, 1998, Vol. 84, No 9, p. 5001–5004.

CYSENI 2010, May 27–28, Kaunas, Lithuania
ISSN 1822-7554, www.cyseni.com

PREPARATION AND CHARACTERIZATION OF $Li_{1.4}Ti_{1.9}P_3O_{12}$ SUBSTITUTED BY NB SOLID STATE ELECTROLYTE CERAMICS

V. Venckutė, J. Banytė
Vilnius University
Faculty of physics
Saulėtekio al. 9/3, LT-10222 *Vilnius – Lithuania*
Phone: 852366064
Email: vilma.venckute@ff.stud.vu.lt

ABSTRACT

In the present work we report the technological conditions for the solid phase reaction synthesis of $Li_{1.4}Ti_{1.9}P_3O_{12}$ substituted by $Nb_{0.1}$ powder, sintering of the ceramics, the results of the investigations of X-ray diffraction (XRD) from the powder, X-ray photoelectron spectroscopy (XPS) and electrical properties of the ceramics in the frequency range from 10Hz to 3GHz in the temperature range from 300K to 600K. The results of the X-ray diffraction patterns study shown that $Li_{1.4}Ti_{1.9}P_3O_{12}$ compound substituted by Nb belongs to hexagonal symmetry (space group $R\overline{3}c$) with six formula units in the lattice. The results of the investigations of Ti2p, P2p, Nb3d, O1s and Li1s core level XPS shown that substitution of $Li_{1.4}Ti_{1.9}P_3O_{12}$ compound by $Nb_{0.1}$ influence the values of binding and splitting energies of Ti2p, P2p, Nb3d spin-orbit doublets. It is discussed about peculiarities of the Li ions transport of the investigated ceramics.

Keywords: ceramics, synthesis, sintering, NASICON, XRD, XPS, electrical conductivity

1. INTRODUCTION

The development of fast lithium conductors is important for applications in high-energy Li-ion batteries [1, 2] and electrochemical sensors [3]. It is known that $LiTi_2P_3O_{12}$ compound with the NASICON-type structure is a pure ionic conductor [4,5]. It has been used as a host compound for substituting Ti^{4+} ion by different three valence ions and a series of new Li-ion conductors have been found [4, 5]. The system $Li_{1+x}M_xTi_{2-x}(PO_4)_3$ (where M = Al, Sc, Y, Fe, Cr) seems to be the most suitable for Li^+ ionic transport in the framework [4, 6]. Conductivity increases rapidly then Ti^{4+} is partially substituted by $M^{III} + Li^+$ ions in the above mentioned system [4] or P^{+5} substituted by Si^{+4} [7]. High ionic conductivity of above mentioned solid electrolyte compounds with NASICON - type structure stimulate further investigation and make the materials promising for applications in the functional elements of solid state ionics. In the present work we report the technological conditions for the synthesis of $Li_{1+4x}Ti_{2-x}Nb_yP_{3-y}O_{12}$ (where x = 0.1; y = 0, 0.1) powder, sintering of the ceramics, the results of the investigations of X-ray diffraction (XRD) from the powder, X-ray photoelectron spectroscopy (XPS) and electrical properties of the ceramics in the frequency range from 10 to $3\cdot10^9$ Hz in the temperature range from 300 to 600 K.

2. EXPERIMENTAL

Conventional solid state reaction method was employed to prepare $Li_{1.4}Ti_{1.9}P_3O_{12}$ compound. Required amounts of chemicals Li_2CO_3 (purity 99.999 %), TiO_2 and $NH_4H_2PO_4$ (extra pure) were heated at temperature $T = 723$ K for 20 h. After heating the mixture was placed in ethyl alcohol and milled in a planetary mill for 12 h. The obtained powder was heated at temperature 973 K for 8 h, at 1173 K for 3h and at 1273 K for 2.5h. After each heating the mixture was placed in ethyl alcohol and milled in a planetary mill. Finally, the mixture was dried at $T = 393$ K temperature for 24 h. The procedure was repeated three times. The powders of $Li_{1.4}Ti_{1.9}Nb_{0.1}P_{2.9}O_{12}$ compound have been synthesized by a solid state reaction method too. Li_2CO_3 , TiO_2, $NH_4H_2PO_4$ and Nb_2O_5 (extra pure) were used. The stoichiometric mixture was heated at temperature 723 K for 20 h. After heating the mixture was placed in ethyl alcohol and milled in a planetary mill for 24 h. The obtained powder was heated at temperature 1073 K for 3 h, at 1173 K and 1373 K for 3h and at 1473 K for 2 h. After each heating the mixture was placed in ethyl alcohol and milled in a planetary mill. Then mixture was dried at $T = 393$ K temperature for 24 h.

The structure parameters were obtained using Brucker D8 Advance equipment at room temperature from the X-ray powder diffraction patterns in the region $2\Theta = 6$–80 degree, step 0.02 degree, time per step 1–8 sec., $CuK_{\alpha1}$ radiation (40 kV, 40 mA). The lattice parameters were deduced by fitting the XRD patterns with software TOPAS.

The ceramic samples were used for XPS and impedance measurements. The powder was uniaxially cold pressed at 300 MPa. The $Li_{1.4}Ti_{1.9}P_3O_{12}$ and $Li_{1.4}Ti_{1.9}Nb_{0.1}P_{2.9}O_{12}$ ceramics were sintered in air for 1h at temperatures 1343 K and 1473 K respectively. Chemical bonding states of the constituent elements of the surfaces of ceramics were examined by X-ray photoelectron spectroscopy. XPS were recorded by LAS-3000 (ISA-Riber) surface analysis equipment. The instrument was equipped with double-pass cylindrical mirror analyzer MAC2. The XPS spectra were obtained by using Mg Kα ($h\nu = 1253.6$ eV) radiation at an average of 10 scans with step size of 0.05 eV. Before the measurement the samples were kept in a preparation chamber (residual pressure $1.6\cdot10^{-6}$ Pa) of the experimental setup for one day. The residual pressure in the analyzer chamber was $1.3\cdot10^{-8}$ Pa. In order to extract the core-level shifts and relative intensities of these components, a curve-fitting procedure was utilized. The fitting of the core-level data was performed using a nonlinear fitting procedure (software XPSPEAK 41).

Platinum electrodes were prepared on sintered cylindrical samples by conductive Pt paste (GVENT Electronic Materials LTD) fired at 1073 K. For the measurements of electrical impedance in the frequency range (10-$2\cdot10^6$) Hz vector voltmeter-amperemeter method was used. The network with the sample was affected by the narrow spectra radio pulse. Voltage and current of this network were measured by two channel computer oscilloscope TiePie Handyscope HS3. For alternating current measuring the special current – voltage converter, allowing accurate vector current converting, was used. The accurate complex impedance ($\tilde{Z} = Z' - iZ''$) of the sample was computed by computer from the time functions of signals, measured by both scope channels. The measurements in the frequency range ($3\cdot10^5$-$3\cdot10^9$) Hz were performed by Agilent Network Analyzer E5062A connected to coaxial line, the part of inner conductor of which was replaced by the sample. The impedance of the sample was calculated from transmission and reflection parameters of such network. The temperature measurements of the ceramics in the low and high frequency ranges were performed in the range 300–600 K by Digital Thermometer TMD90A. The temperature was controlled by a computer connected to DC power supply Mastech HY 30005.

3. RESULTS AND DISCUSSION

The results of XRD data analysis shown that investigated compounds belong to hexagonal symmetry (space group $R\bar{3}c$), but in both compounds some peaks realted to $LiTiPO_5$ exist (Fig. 1). The lattice parameters, unit cell volume (V), density ($d_{\text{X-ray}}$) and formula units in the lattice (Z) of the investigated compounds are presented in Table 1. It was used geometrical and mass measurements of the ceramics for the investigation of relative density. The relative density of the ceramics was found to be 94 % of the theoretical density.

Table 1. Summary of X-ray diffraction results for $Li_{1.4}Ti_{1.9}P_3O_{12}$ and $Li_{1.4}Ti_{1.9}Nb_{0.1}P_{2.9}O_{12}$ compounds at room temperature

Compound	***a*** **(Å)**	***c*** **(Å)**	***V*** **(Å^3)**	$d_{X\text{-ray}}$ **(g·cm^{-3})**	***Z***
$Li_{1.4}Ti_{1.9}P_3O_{12}$	8.5137(2)	20.8587(5)	1309.36	2.93	6
$Li_{1.4}Ti_{1.9}Nb_{0.1}P_{2.9}O_{12}$	8.5267(23)	20.8608(53)	1313.49	2.97	6

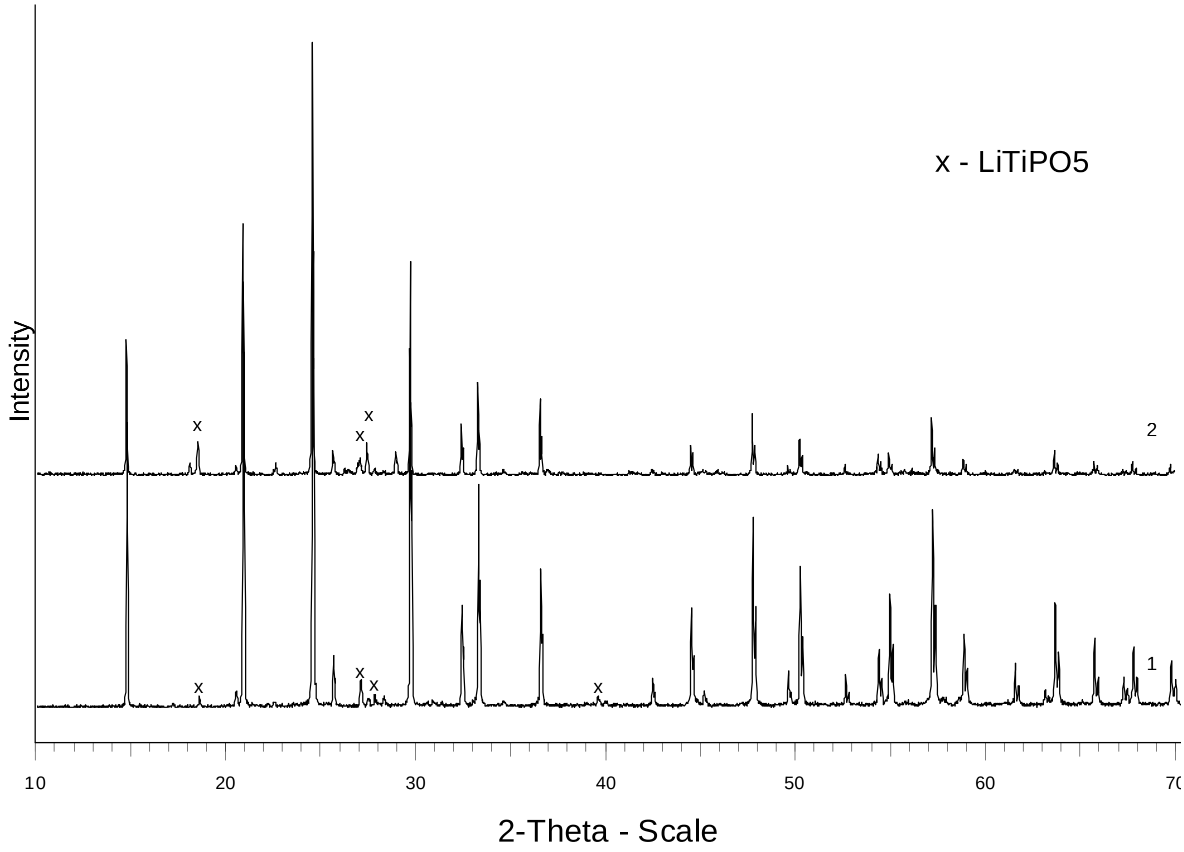

Fig. 1. The powder XRD patterns of $Li_{1.4}Ti_{1.9}P_3O_{12}$ (1) and $Li_{1.4}Ti_{1.9}Nb_{0.1}P_{2.9}O_{12}$ (2) compounds

XPS spectra of surface of $Li_{1.4}Ti_{1.9}P_3O_{12}$ and $Li_{1.4}Ti_{1.9}Nb_{0.1}P_{2.9}O_{12}$ ceramics are shown in Fig. 2 a–e. To exclude any effects on the values of binding energies due to charging of the sample during the XPS analysis, all data were corrected by a linear shift such that the peak maximum of the C 1s binding energy of adventitious carbon corresponded to 284.6 eV. Ti 2p, P 2p, Nb 3d, O 1s, and Li 1s core level XPS spectra were fitted.

Ti 2p spectrum is shown in Fig. 2 a. The spectrum shows spin-orbit doublet of Ti $2p_{3/2}$ and Ti $2p_{1/2}$ as in [8]. The spin-orbit doublets assembled two low and high binding energy peaks. The lower energy peaks of Ti $2p_{3/2}$ spectra are in the range from 458.5 eV to 459.1 eV. The higher binding energy peaks of $Ti2p_{1/2}$ spectra are in range from 459.7 eV to 460.1 eV. The splitting energies between $2p_{3/2}$ and $2p_{1/2}$ for both compounds is 5.8 eV. The authors [8] reported that binding energy splitting between $2p_{3/2}$ and $2p_{1/2}$ in $LiM_{0.05}Mn_{1.95}O_4$ (M=Ni, Fe and Ti) solid electrolytes is 5.4 eV. Ti 2p spectrum has been deconvoluted into two spin-orbit doublets. The $2p_{3/2}$ peaks at lower binding energy are associated with a lower oxidation state (Ti^{3+}). The peaks at higher $2p_{3/2}$ binding energy are associated with the Ti^{4+} state [9]. The ratio of Ti^{+4} and Ti^{+3} was determined by fitting and estimating the area of each doublet and it corresponds to different amounts of Ti^{4+} and Ti^{3+} states. The different amount of Ti^{+4} and Ti^{+3} was found in Li conducted solid electrolytes such as $LiM_{0.05}Mn_{1.95}O_4$ (M=Ni, Fe and Ti) [8] or Li_2O–Al_2O_3–(TiO_2 or GeO_2)–P_2O_5 glass–ceramics [9]. The results of XRD investigation showed that in the synthesized compounds some lines related to $LiTiPO_5$ exist as a mixture. The values of the binding and splitting energies and amounts of Ti^{4+} and Ti^{3+} states in atomic % are presented in Table 2.

The deconvolution of the P 2p XPS spectra of $Li_{1.4}Ti_{1.9}P_3O_{12}$ and $Li_{1.4}Ti_{1.9}Nb_{0.1}P_{2.9}O_{12}$ ceramics into two peaks is shown in Fig. 2 b. The deconvolution of the P2p core level XPS spectra can be associated with different amounts of P^{5+} and P^{3+} states in the investigated ceramics. The P^{5+} and P^{3+} states in the ceramics can be assigned to group PO_4^{3-} and group PO_3^{-} respectively (Table 2).

Fig. 2 c shows the fitting pattern of O 1s XPS spectra of $Li_{1.4}Ti_{1.9}P_3O_{12}$ and $Li_{1.4}Ti_{1.9}Nb_{0.1}P_{2.9}O_{12}$ ceramic surfaces. It can be seen that the O 1s core level XPS spectra has been deconvoluted into four peaks. The O 1s some peaks are attributed to the lattice oxygen at the normal sites of the NASICON structure and other O 1s are assigned to the chemisorbed oxygen in the forms O^{2-}, O_2^{-}, and in hydroxyl environment (O_H) as in $La_{0.6}Sr_{0.4}Co_{1-y}Fe_xO_3$ ceramics [10].

Table 2. The amounts of elements with different binding energies and energy splitting of the spin-orbit doublets of $Li_{1.4}Ti_{1.9}P_3O_{12}$ and $Li_{1.4}Ti_{1.9}Nb_{0.1}P_{2..9}O_{12}$

	Binding energy, eV	**Splitting energy, eV**	**Amount, at. %**
$Li_{1.4}Ti_{1.9}P_3O_{12}$			
O 1s	529.8		34.3
	530.8		29.7
	531.9		21.7
	532.9		14.3
P 2p	132.2	0.95	72.1
	133.9	0.95	27.9
Ti3p	458.5	5.8	67.2
	459.7	5.8	32.8
Li 1s	54.4		61.7
	55.4		38.3
$Li_{1.4}Ti_{1.9}Nb_{0.1}P_{2.9}O_{12}$			
O 1s	529.9		7.2
	530.9		50.9
	532.0		32.7
	533.0		9.2
P 2p	132.8	1.0	50.4
	133.6	1.0	49.6
Li 1s	55.4		100.0
Nb 3d	207.2	2.8	69.9
	208.1	2.8	30.1
Ti 2p	458.8	5.8	49.9
	459.9	5.8	50.1

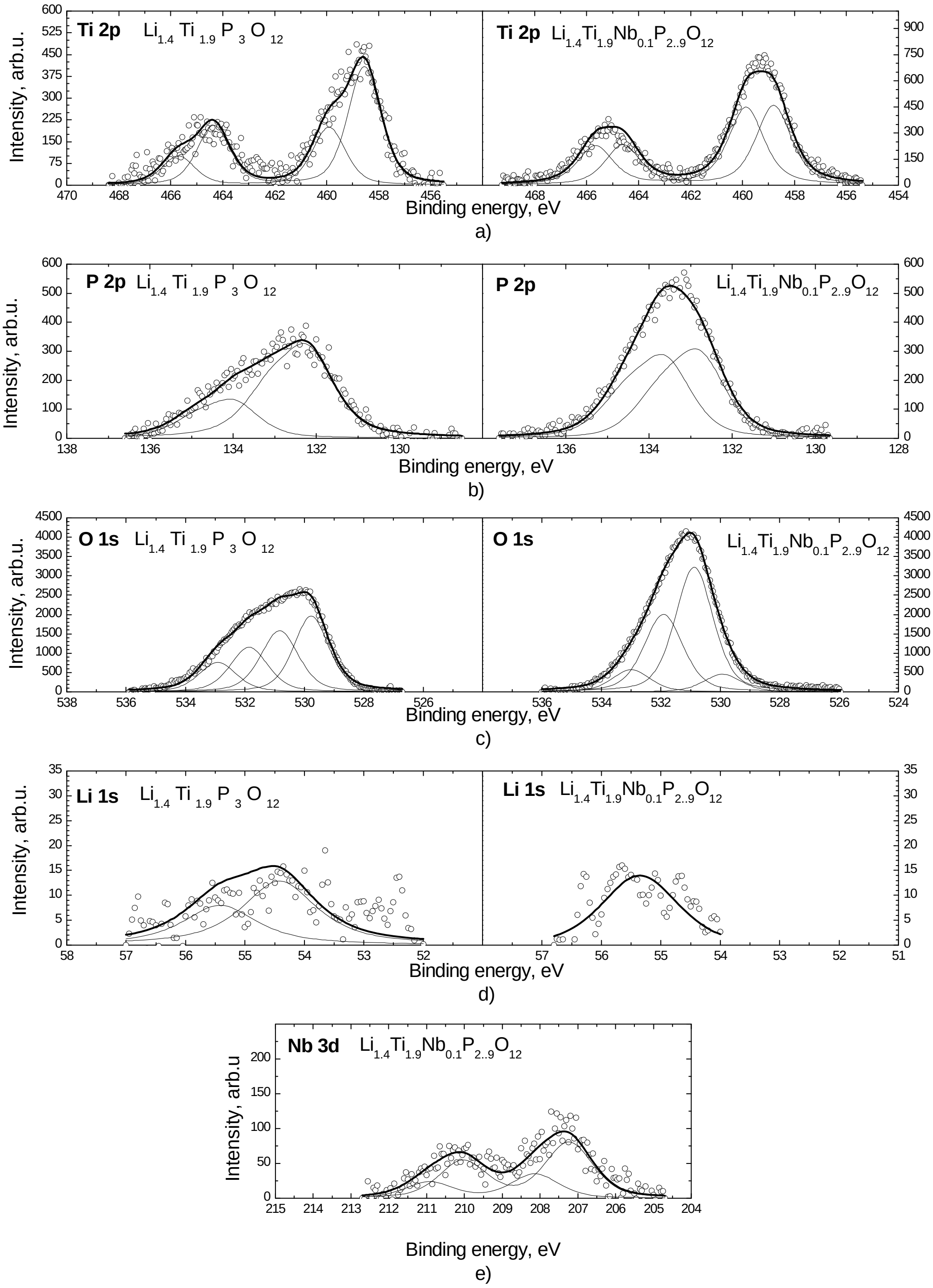

Fig. 2. Ti 2p (a), P 2p (b), O 1s (c), Li 1s (s) , and Nb 3d (e) core level XPS spectra

Li 1s core level XPS spectra of the investigated ceramics are shown in Fig. 2 d. Li 1s signal is of very low intensity and the fitting of the patterns is very complicated. Li 1s core level XPS spectra of $Li_{1.4}Ti_{1.9}P_3O_{12}$ has been deconvoluted into two peaks. One peak is at lower binding energy (54.4 eV), other peak is at higher binding energy (55.4 eV). In the ceramics with y= 0.1 exist only one peak at 54.5 eV (Table 2). It is reported that the Li 1s core level XPS peak is at binding energy around 55.8 eV [11]. For the $Li_{0.8}CoO_4$ composition single Li 1s peak has been observed at 55.4 eV but for Li rich compositions such as $LiCoO_4$

and $Li_{1.2}CoO_4$ an intense peak is at 55.4 eV, a shoulder peak around 55.05 eV has also been observed [12]. The authors concluded that Li ions occupy two different positions. The results of the NMR study of $LiTi_{2-x}Zr_x(PO_4)_3$ composition have shown that Li ions occupies two different positions in the lattice, too [13].

Fig. 2 e shows Nb 3d spectra of investigated ceramics. The spectrum shows spin-orbit doublet of Nb $3d_{5/2}$ and Nb $3d_{3/2}$ as in $LiNbO_3$ [14] or potassium lithium niobate [15] crystals. The deconvolution of the Nb 3d core level XPS can be associated with different amounts of Nb^{5+} and Nb^{4+} [14] or lower Nb^{3+} valence states in the investigated ceramics.

The presence of a mixed valence states of atoms plays a large role in controlling the structure and electronic states in oxygen deficient ceramics [17]. Elemental composition of $Li_{1.4}Ti_{1.9}P_3O_{12}$ and $Li_{1.4}Ti_{1.9}Nb_{0.1}P_{2.9}O_{12}$ ceramic surfaces have been estimated from XPS spectra and is shown in Table 3.

Table 3. Elemental composition of $Li_{1.4}Ti_{1.9}P_3O_{12}$ and $Li_{1.4}Ti_{1.9}Nb_{0.1}P_{2.9}O_{12}$ ceramic surfaces

Composition	**Elements, at. %**				
	Ti	P	O	Li	Nb
$Li_{1.4}Ti_{1.9}P_3O_{12}$	5.9	16.8	65.4	11.9	
$Li_{0.9}Ti_{2.2}Nb_{0.1}P_3O_{11}$	12.9	17.3	63.7	5.3	0.9

The two relaxation dispersions have been found in complex conductivity and impedance spectra of the studied ceramics. The one in the high frequency region was attributed to Li^+ ion relaxation in the bulk and the intermediate frequency range dispersion was caused by ion blocking effect at grain boundaries of the ceramics. Frequency dependences of the real part of complex conductivity of $Li_{1.4}Ti_{1.9}P_3O_{12}$ and $Li_{1.4}Ti_{1.9}Nb_{0.1}P_{2.9}O_{12}$ ceramics measured at temperature T = 530 K are shown in Fig. 3. The dispersion regions shift to higher frequencies while temperature is increased. Bulk (σ_b) and total (σ_{tot}) conductivities were derived from impedance complex plain $Z''(Z')$ and conductivity complex plain $\sigma''(\sigma')$ plots. The characteristic $Z''(Z')$ and $\sigma''(\sigma')$ plots of $Li_{1.4}Ti_{1.9}P_3O_{12}$ and $Li_{1.4}Ti_{1.9}Nb_{0.1}P_{2.9}O_{12}$ ceramics at temperature T = 530 K can be seen in Fig. 4 and Fig. 5, respectively. Temperature dependences of σ_b and σ_{tot} are shown in Fig. 6 and Fig. 7, respectively. σ_b and σ_{tot} of investigated ceramics change according to Arrhenius law in the studied temperature range. The date of the measurements of σ_b and σ_{tot}, their activation energies (ΔE_b) and (ΔE_{tot}) are summarized in Table 4. The results of the investigation have shown that insertion of Nb in to the $Li_{1.4}Ti_{1.9}P_3O_{12}$ system leads the decrease of total and bulk conductivities and increase their activation energies. The temperature dependences of real part of dielectric permittivity (ε') and tangent losses ($\tan\delta$) were carried out at frequency of 1 GHz and are presented in Fig. 8 and Fig. 9, respectively. The increase of the values of ε' with temperature of the investigated compounds can be caused by contribution of the migration polarization of lithium ions, vibration of lattice and electronic polarization. The increase of $\tan\delta$ with temperature is related to the contribution of conductivity in the investigated temperature region.

Table 4. σ_b, σ_t and their activation energies of $Li_{1.4}Ti_{1.9}P_3O_{12}$ and $Li_{1.4}Ti_{1.9}Nb_{0.1}P_{2.9}O_{12}$ ceramics at 530 K

Compound	**σ_b, S·m^{-1}**	**ΔE_b, eV**	**σ_t, S·m^{-1}**	**ΔE_t, eV**
$Li_{1.4}Ti_{1.9}P_3O_{12}$	2.07	0.18	0.244	0.29
$Li_{1.4}Ti_{1.9}Nb_{0.1}P_{2.9}O_{12}$	0.22	0.38	0.022	0.44

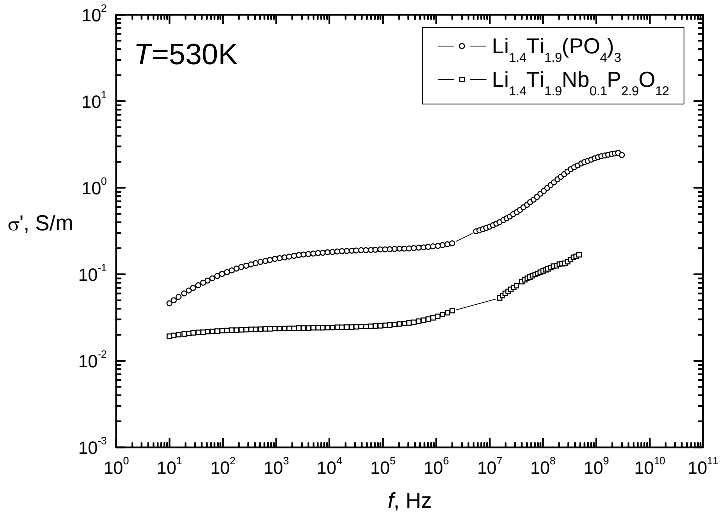

Fig. 3. Frequency dependences of the real part of conductivity of $Li_{1.4}Ti_{1.9}P_3O_{12}$ and $Li_{1.4}Ti_{1.9}Nb_{0.1}P_{2.9}O_{12}$ ceramics

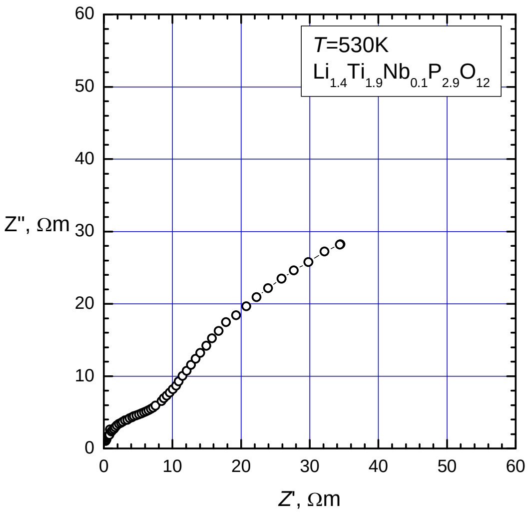

Fig. 4. Characteristic impedance complex plain plot of $Li_{1.4}Ti_{1.9}Nb_{0.1}P_{2.9}O_{12}$ ceramics

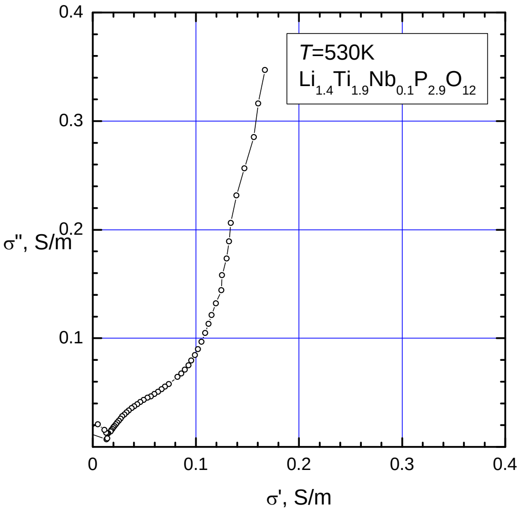

Fig. 5. Characteristic conductivity complex plain plot of $Li_{1.4}Ti_{1.9}Nb_{0.1}P_{2.9}O_{12}$ ceramics

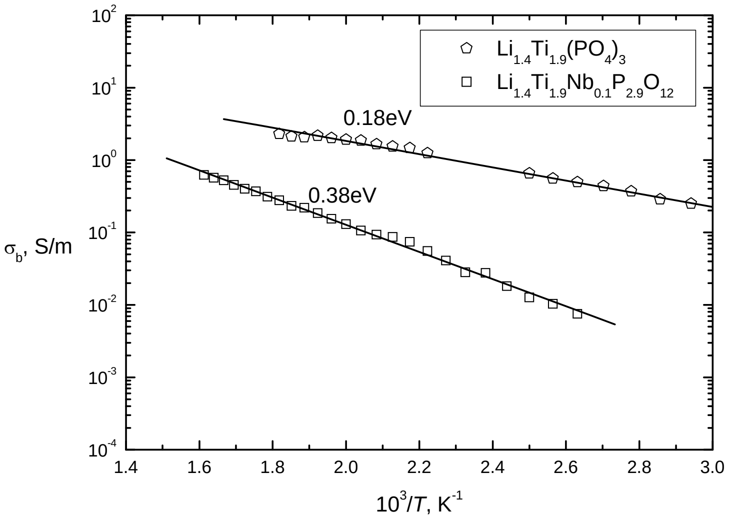

Fig. 6. Temperature dependences of bulk conductivities of $Li_{1.4}Ti_{1.9}P_3O_{12}$ and $Li_{1.4}Ti_{1.9}Nb_{0.1}P_{2.9}O_{12}$ ceramics

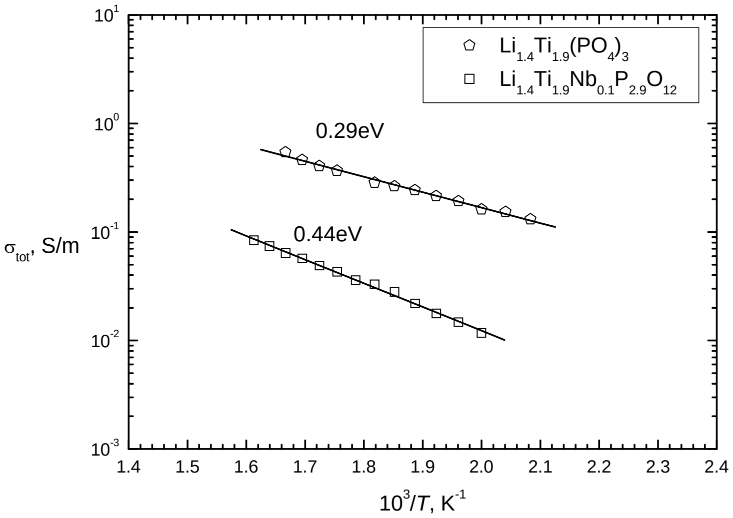

Fig. 7. Temperature dependences of total conductivities of $Li_{1.4}Ti_{1.9}P_3O_{12}$ and $Li_{1.4}Ti_{1.9}Nb_{0.1}P_{2.9}O_{12}$ ceramics

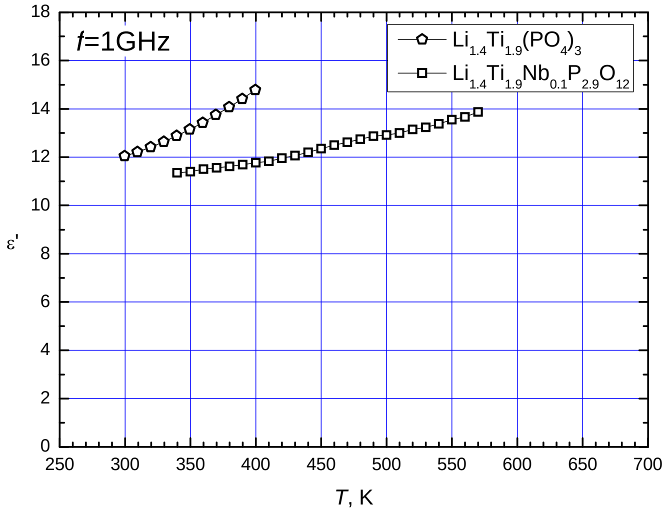

Fig. 8. Temperature dependences of dielectric permittivity of $Li_{1.4}Ti_{1.9}P_3O_{12}$ and $Li_{1.4}Ti_{1.9}Nb_{0.1}P_{2.9}O_{12}$ ceramics

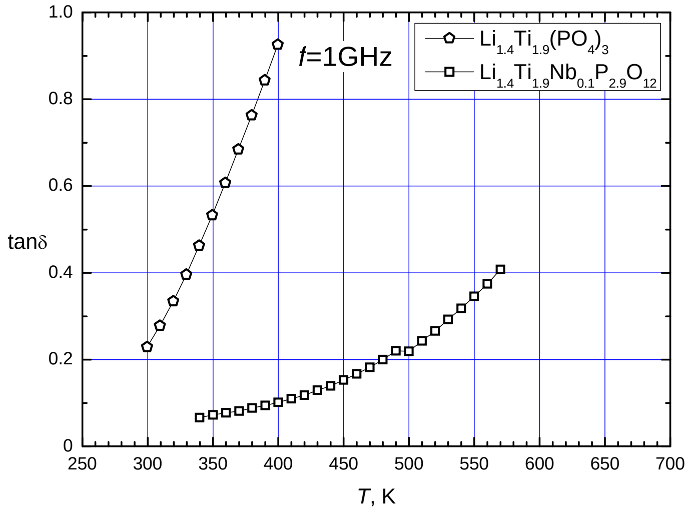

Fig. 9. Temperature dependences of tanδ of $Li_{1.4}Ti_{1.9}P_3O_{12}$ and $Li_{1.4}Ti_{1.9}Nb_{0.1}P_{2.9}O_{12}$ ceramics

4. CONCLUSIONS

The powder of $Li_{1.4}Ti_{1.9}P_3O_{12}$ and $Li_{1.4}Ti_{1.9}Nb_{0.1}P_{2.9}O_{12}$ has been prepared by solid state reaction and corresponding ceramics have been sintered. The results of XRD has shown that investigated compounds belong to hexagonal symmetry (space group $R\bar{3}c$). Ti 2p, P 2p, Nb 3d, O 1s and Li 1s core level XPS spectra were fitted. The results of the investigation of XPS suggested that Ti ions are at Ti^{3+} and Ti^{4+} oxidation states. It was ascertained that there are four different kinds of oxygen on the ceramic surface, including lattice oxygen, chemisorbed oxygen in the forms O^{2-}, O_2^{-}, and oxygen in hydroxyl environment (O_H). The deconvolution of the P2p core level XPS can be associated with different amounts of P^{5+} and P^{3+} states in the investigated ceramics. The P^{5+} and P^{3+} states in the ceramics can be assigned with group PO_4^{3-} and group PO_3^{-} respectively. The deconvolution of the Nb 3d core level XPS can be associated with different amounts of Nb^{5+} and Nb^{4+} or lower Nb^{3+} valence states in the investigated ceramics.

Impedance spectroscopy study of the ceramics in the frequency range 10 - 10^9 Hz in the temperature range from 300 to 600 K revealed that insertion of Nb in to the $Li_{1+4x}Ti_{2-x}P_3O_{12}$ (where x = 0.1) ceramics leads to the decrease of total and bulk conductivities and increase their activation energies. Also insertion of the Nb in to the system leads to the lowering of the value of ε'.

ACKNOWLEDGEMENTS

A.F.Orliukas is acknowledged for discuss.

A. Dindune, J. Ronis, Z. Kanepe are acknowledged for XRD investigation and synthesis of the powders.

Vilma Venckutė aknowledges Student Research Fellowship Award from Lithuanian Science Council for support.

REFERENCES

1. V. Thangadurai, J. Schwenzel, and W. Weppner *Ionics* 11, 11 (2005).
2. M. Broussely, J.P. Planchot, G. Rigobert, D. Vireu, and G. Sarre, J. Power Sources 68, 8 (1997).
3. F. Salam, P. Birke, and W. Weppner, Electrochem. Solid-State Lett. 2, 201 (1999).
4. H. Aono, E. Sugimoto, Y. Sadaoka, N. Imanoka, and G. Adachi, J. Electrochem. Soc. 137, 1023 (1990).
5. M.A. Subramanian, R. Subramanian, and A. Clearfield, Solid State Ionics, 18/19, 562 (1986).
6. H. Aono, E. Sugimoto , Y. Sadaoka , N. Imanaka , G-y. Adachi, Solid State Ionics. 40/41, 38 (1990).
7. A.Dindune, A.Kežionis, Z.Kanepe, E. Kazakevičius, R.Sobiestianskas, A.Orliukas, J.Inorg. Phosphor. Chemistry, 10, 387 (1999).
8. Qi-Hui Wu, Jin-Mei Xu, Quan-Chao Zhuang, Shi-Gang Sun , Solid State Ionics. 177, 1483 (2006).
9. B.V.R. Chowdari, G.V. Subba Rao, G.Y.H.Lee, Solid State Ionics. 136–137, 1067 (2000).
10. Qing Xu, Duan-ping Huang, Wen Chen, Hao Wang, Bi-tao Wang, Run-zhang Yuan , Applied Surface Science, 228, 110 (2004).
11. J. Swiatowska-Mrowiecka , Soline de Diesbach, V. Maurice, S. Zanna, L. Klein, E. Briand, I. Vickridge, P. Marcus, J. Phys. Chem. C 112,11050 (2008).
12. M.S. Bhuvaneswari, S. Selvasekarapandian, Shinobu Fujihara, Shinnosuke Koji, Solid State Ionics, 177, 121 (2006).
13. K. Arbi, J.M. Rojo, J. Sanz, J. Europ. Ceram. Soc., 27, 4215 (2007).
14. R.J. Iwanowski, M. Heinonen, I. Pracka, J. Raczynska, K. Fronc, J.W. Sobczak, J.Alloys and Compounds, 286, 162 (1999).
15. Byeong-Eog Jun, Chung-Sik Kim, Hyung-Kook Kim, Jung-Nam Kim, Yoon-Hwae Hwang, J. Korean Phys. Soc., 46, 100 (2005).
16. Jia-Yan Luo, Li-Juan Chen, Yu-Jun Zhao, Ping He, Yong-Yao Xia, Journal of Power Sources, 194, 1075(2009).

CYSENI 2010, May 27–28, Kaunas, Lithuania
ISSN 1822-7554, www.cyseni.com

SOOT PARTICLES CHARACTERIZATIONS AT PYROLYSIS OF ETHYLENE IN SHOCK TUBE

Y.A. Baranyshyn, O.G. Penyazkov
A.V.Luikov Heat and Mass Transfer Institute
15, P. Brovka str., 220072 – Belarus
Phone: 375 17 284 23 87
Email: baranishin-83@mail.ru

K.N. Kasparov, L.I. Belaziorava
B. I. Stepanov Institute of Physics,
68, Independence av., 220072 – Belarus
Phone: 375 17 284 17 55

ABSTRACT

Soot is formed in most power installations, besides, black carbon is a widely used industrial product. That is why the soot formation has attracted the attention of scientists for many years. The research technique development allows extending the understanding of this process. Nowadays the experimental investigation of the behaviour of soot particle temperature during their formation and growth is of interest for scientists. The experimental results on carbon nanoparticles produced at pyrolysis of the ethylene – argon mixture (5% C_2H_4 – 95% Ar) at temperatures 2000–3400 K behind the reflected shock wave in a shock tube are presented in the present report. The photoemission method with 1 μs time resolution was used to register the particles temperature and further formed soot was analysed with bitmapped electron microscope. It is found that in the soot formation process at the beginning of registration the temperature of particles was higher by about 550–900 K than the gas temperature, but it decreased fast and became lower by about 400–650 K than the last one. The temperature rate change was about 10^6 K/s. The mean diameter of the initial carbon nanoparticles decreased from 55 to 27 nm with temperature growth from 2000 to 2800 K.

Keywords: soot temperature measurement, pyrolysis, shock tube.

1. INTRODUCTION

Soot formation is a complicated process that has attracted scientists' attention for many years. Today there are a lot of experimental and theoretical materials on this theme [1–3], but researches in this field are still actual [4, 5]. It can be explained by some reasons. At first, soot (black carbon) is an industrial product and it is necessary to know optimal production conditions [1, 6]. Secondly, soot nano- and submicron particles are formed in engines and industrial power installations cause negative consequences in their operation. This problem has to be analysed and solved. Thirdly, small soot particles are one of the main pollutants that influence heat and mass transfer in atmosphere and mankind's health [7]. Fourthly, research technique development allows getting a deeper insight into the understanding of this complicated process.

Usually optical in-situ methods are used to research carbon particles parameters during soot formation and growth in gas. The main methods are represented by modulated absorption/emission (MAE) pyrometry [8], laser extinction and laser-induced incandescence (LII) [9, 10]. The first of them enables determining soot particles temperature by measuring both laser radiation absorption (at one or two wavelengths) in the volume with soot and the intensity of radiation emitted from this volume (at the same wavelengths). The second allows determining a particles diameter during soot formation by laser radiation absorption registering at certain wavelength. LII is used to research the behaviour of particles temperature and size due to particles pulse laser heating and a further analysis of radiation intensity at some wavelength. But it is necessary to know optical properties of soot substance and emissivity of carbon particles in order to use these methods. A priori, such data for all experimental conditions are unknown; besides, the emissivity of carbon particles depends on their temperature and size, so it can change during the research process.

In this paper we present the results on soot formation at the ethylene–argon mixture pyrolysis behind the reflected shock wave in the shock tube. The photoemissive method is adopted for measurements of particles temperature [11, 12]. It is based on registering soot particles radiation and analysing the photoelectron energy distribution, possesses high time resolution (1 μs), allows detecting fast temperature changes (10^8 K/s). The emissivity of carbon particles in this case doesn't affect significantly the result. The size of initial carbon particles has been determined by bitmapped electron microscope.

2. METHODOLOGY

The studies of soot particles formation and growth were carried out in the stainless steel shock tube 7.1 m long and 50 mm in diameter. The reflected wall of the tube was flat. The ethylene – argon mixture (5% C_2H_4 – 95% Ar) was used as a working gas. In our study the pyrolysis temperature was 2000–3400 K. The pressure of the gas behind the reflected shock wave was 7.0–11.5 atm and the density was 1.61–1.63 kg/m^3. In all our experiments pyrolysis took place behind the reflected shock wave.

The shock tube test section is presented in Fig. 1. High-frequency pressure sensors were situated in the wall of the tube test section and in the reflected wall. These enabled us to register the shock wave motion and pressure variations inside the tube. These data were then used to calculate the shock wave velocity and, according to the 1-D shock relations and the assumption of vibrational equilibrium and frozen chemistry [13, 14], to determine gas parameters (temperature, pressure, density) behind the incident and reflected shock waves.

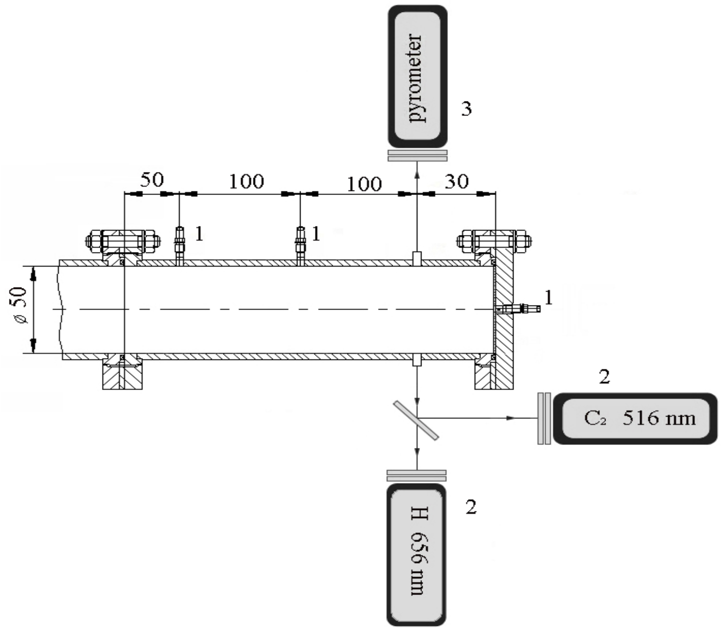

Fig. 1. Scheme of the shock tube test section: 1 – high-frequency pressure sensors, 2 – photomultipliers with colour filters, 3 – pulse photoemissive pyrometer

Two quartz rods with a diameter of 8 mm were mounted into the side of the wall of shock tube opposite to each other. Through the one rod we detected the soot radiation using a home-made pulse photoemissive pyrometer for the next temperature calculation. In some experiments remissive neutral colour filters with the transmitting efficiency 3–70% were placed in front of the pulse photoemissive pyrometer to detect carbon particle radiation without signal pining. The accelerating voltage of the pulse photoemission pyrometer was 1100 V and the retarding voltage realizing the separation of photoelectrons was –0.6 V. Through the second rod the luminosity of C_2 radicals (transitions $A^3\Pi - X^3\Pi$) at the wavelength of λ = 516.5 nm and hydrogen atoms (transitions H_α) at the wavelength of λ = 656.3 nm was detected. For this purposes we used 2 photomultipliers with colour filters λ_{max} = 516.2 nm ($\Delta\lambda_{0.5}$ = 4.6 nm) and λ_{max} = 656.2 nm ($\Delta\lambda_{0.5}$ = 2.6 nm) respectively. The data obtained make it possible to find a mixture induction time for C_2 and H.

Soot produced at pyrolysis was analysed under a bitmapped electron microscope Carl Zeiss Supra 55. For soot collection the stainless steel plates fixed at the reflected wall of the shock tube were employed.

3. RESULTS

In the first experiments of soot particles formation it was found that the soot temperature deceased from the near gas temperature to the steady value (Fig. 2). The rate of temperature change was about 10^6 K/s. The identical temperature behaviour of particles was obtained for all gas temperatures behind the reflected shock wave in the range 2000–3400 K. A gas and steady soot temperature difference for different pyrolysis temperatures is presented in Fig. 3. One can see that the particles temperature became lower by 400–650 K than the gas one. Such fast temperature decreasing of particles to the steady value can be attributed to radiative cooling to the temperature, at which radiative cooling is compensated by gas heating.

In the above experiments we used the remissive neutral colour filters in front of the pulse photoemissive pyrometer with objectives to increase the measurement time range and to detect carbon particles radiation without signal pining. Then we carried out series of experiments for the same initial conditions (the similar post shock conditions) without using the remissive neutral colour filters in front of the pyrometer or using filters with a higher transmitting efficiency (Fig 4). This was made for careful measurement of soot temperature at the initial stage when there appears particles radiation.

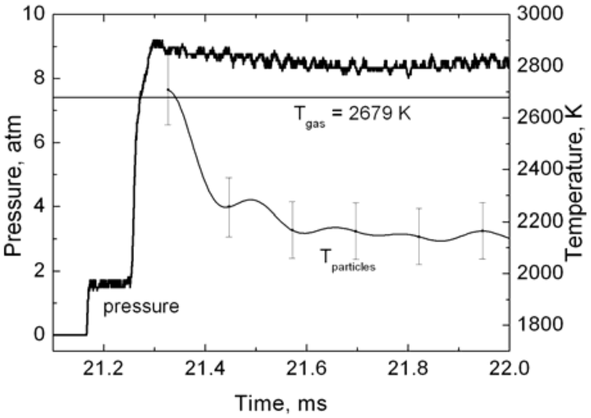

Fig. 2. Pressure and the soot particles temperature at the pyrolysis temperature of 2679 K

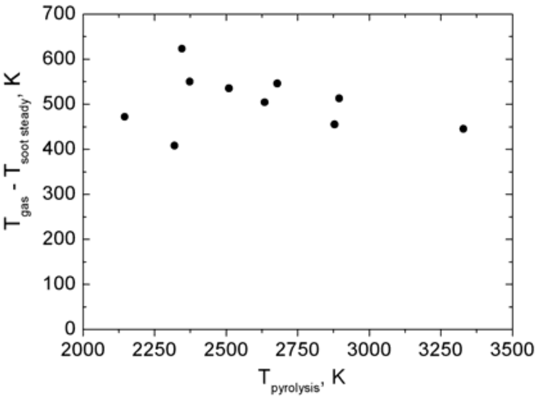

Fig. 3. Difference between gas and steady soot temperatures at different pyrolysis temperatures

In this case, the particles temperature in different experiments was higher than the gas one by 550–900 K (Fig. 5), but also decreased fast to the value lower than the gas temperature. It is difficult to find a correct dependence between particles overheating and pyrolysis temperature from Fig. 5 because of the use of the remissive neutral color filters in some experiments. But it is clear that due to latent heat release during soot particles formation the soot temperature can exceed significantly the gas one.

For low pyrolysis temperatures (< 2400 K) the temperature of black carbon particles did not exceed significantly the gas temperature. The reason for this is the low intensity of particles radiation at these temperatures.

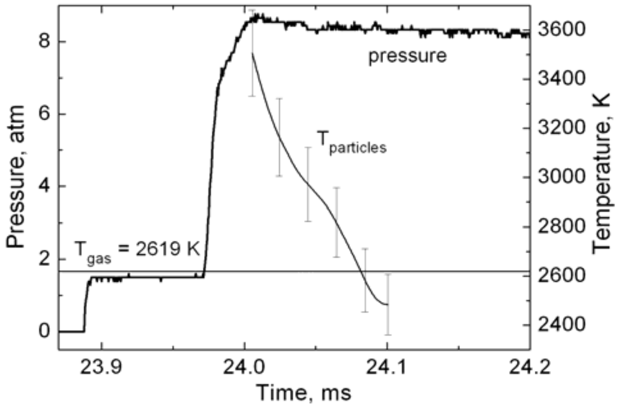

Fig. 4. Pressure and the soot particles temperature at the pyrolysis temperature of 2619 K

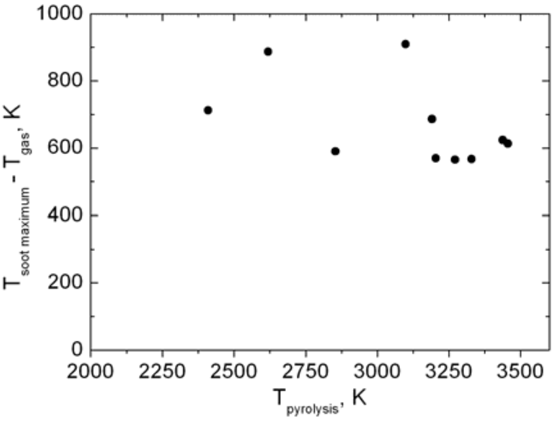

Fig. 5. Difference between maximum soot and gas temperatures at different pyrolysis temperatures

As mentioned above, in our experiments we registered the luminosity of C_2 radicals and hydrogen atoms. Its typical behaviour is seen in Fig. 6. Registering the luminosity allowed determining a mixture induction time (Fig. 7). It was found that with temperature growth in the range 2000 – 3400 K the induction time decreased from 1.50 to 0.03 ms and from 1.70 to 0.25 ms for C_2 and H respectively, and the temperature of particles became steady long before the end of the pyrolysis process.

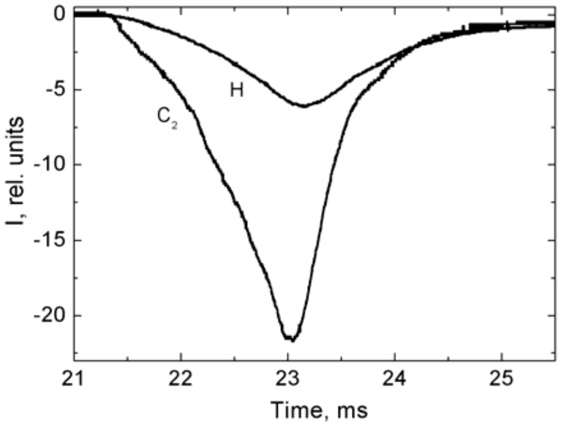

Fig. 6. Luminosity of C_2 radicals and hydrogen atoms at the pyrolysis temperature of 2679 K

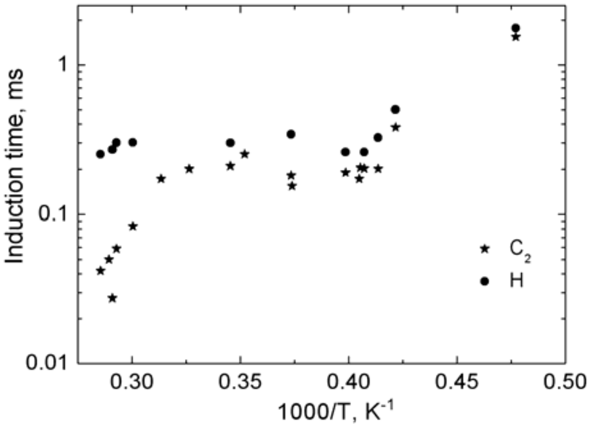

Fig. 7. Induction time

The analysis of soot under the bitmapped electron microscope (Fig. 8) showed that the mean diameter of primary carbon particles decreased from 55 to 28 nm with pyrolysis temperature growth from 2100 to 2800 K. Such a decrease of the particles diameter can be explained by more intense evaporation of carbon atoms from soot particles.

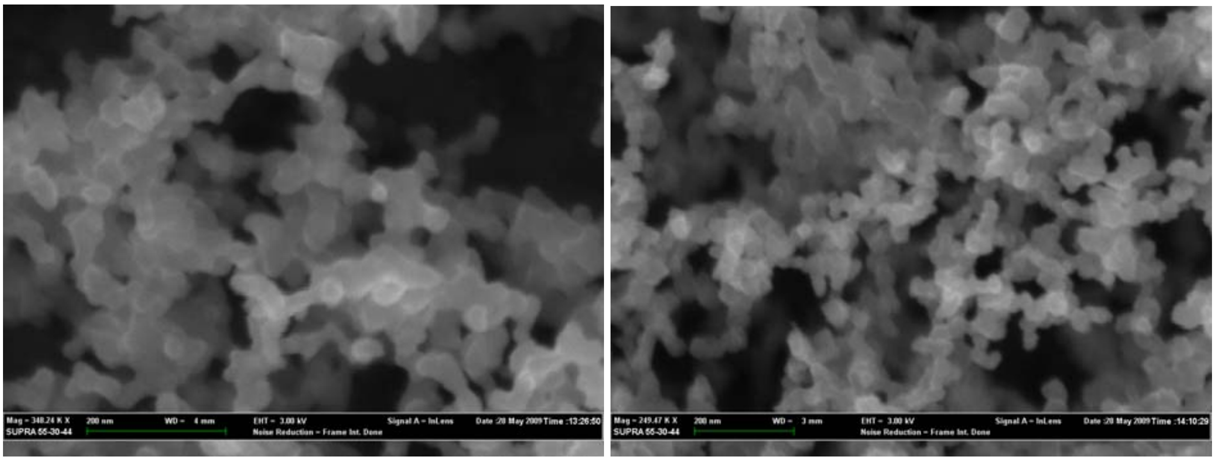

a) *b)*

Fig. 8. Electron picture of soot at the pyrolysis temperatures of 2146 K (*a*) and 2679 K (*b*)

4. CONCLUSIONS

The study of soot formation in the ethylene – argon mixture in the shock tube was carried out. Photoemissive temperature measurements showed that at first the soot temperature was higher than the gas one (550–900 K), but decreased fast (~ 10^6 K/s) and reached its steady value lower by 400–650 K than the gas temperature. It contradicts the idea of the isothermal soot formation, but agrees with the predictions and experimental results of some authors [15, 16].

The soot analysis showed that the mean diameter of primary carbon particles decreases in the range of 55–28 nm when the pyrolysis temperature is increased from 2100 to 2800 K. It can be due to intense evaporation of carbon atoms from the initial soot particles during their formation and growth in the ethylene pyrolysis process.

This project was sponsored by State Research Programs “Hydrogen” and “Nanotechnologies and Nanomaterials”.

REFERENCES

1. TESNER, Pavel A. *Formation of Carbon from the Gas-phase Hydrocarbons.* Moscow: Khimiya 1972. 136 p.
1. WAGNER, H. Soot formation in combustion. 17th international symposium on combustion. Pittsburgh: the Combustion Institute. 1979, p. 3–19.
2. KENNEDY, I. Models of soot formation and oxidation. Progress in energy and combustion science, 1997, Vol. 23, p. 95–132.
3. Soot formation in combustion: round table discussion. Ed. H. BOCKHORN. Heidelberg: Springer Verlag, 1991.
4. Combustion generated fine carbonaceous particles. Proceedings of international workshop ed. H. BOCKHORN [et al.]. Anacapri. 2007, 651 p.

5. BAKIROV, F.G.; ZAKHAROV, V.M.; POLESHCHUK, I.Z.; SHAIKHUTDINOV, Z.G. *Formation and Burning of Soot during the Combustion of Hydrocarbon Fuels*. Moscow: Mashinostroenie, 1989, 128 p.
6. GOLDBERG, Edward D. *Black Carbon in the Environment: Properties and Distribution.* New York: John Wiley and Sons, 1985, 216 p.
7. JENKINS, T., HANSON, R. Soot pyrometry using modulated absorption/emission. Combustion and flame. 2001, Vol. 126, No 3, p. 1669–1679.
8. BHASKARAN, K., ROTH, P. The Shock tube as wave reactor for kinetic studies and material systems. Progress in energy and combustion science, 2002, Vol. 28, p. 151–192.
9. MELTON, L. Soot diagnostics based on laser heating. Applied Optics, 1984, Vol. 23, p. 2201–2208.
10. KASPAROV, K. Heated body temperature measurement by spectrometry of photoelectrons. Measurement science and technology, 1998, Vol. 9, p. 1388.
11. KASPAROV, K.N. A photoemission method of temperature measurement. Two methods of a procedural error determining. Measurement technique, 2004, Vol. 8, p. 62.
12. SOLOUKHIN, REM I. *Shock Waves and Detonations in Gases*. Moscow: Fizmatgiz, 1963. 175 p.
13. GAYDON, A.G.; HURLE, I.R. *The Shock Tube in High-temperature Chemical Physics.* New York: Reinhold Publishing Corporation, 1963. 427 p.
14. ZHIL’TSOVA, I., ZASLONKO, I., KARASEVICH, Yu., WAGNER H. Nonisothermal effects in the process of soot formation in ethylene pyrolysis behind shock waves. Kinetics and catalysis, 2000, Vol. 41, No 1, p. 87–101.
15. ISHII, K., OHASHI, N., TERAJI, A., KUBO, M. Soot formation in hydrocarbon pyrolysis behind reflected shock waves. 22nd international colloquium on the dynamics of explosions and reactive systems. [CD]. Minsk. 2009 July 27–31.

CYSENI 2010, May 27–28, Kaunas, Lithuania
ISSN 1822-7554, www.cyseni.com

HETEROGENEOUS DROPLETS GROWTH IN A DIFFUSION CHAMBER

A.A. Brin, S.P. Fisenko
A.V. Luikov Heat and Mass Transfer Institute
15, P. Brovki Str., 220072, Minsk, Belarus
Phone: +375 17 2842222
Email: brin@hmti.ac.by

ABSTRACT

For the description of growth of heterogeneous droplets, containing the nanoparticle inside, in a laminar flow diffusion chamber a new mathematical model is proposed. The mathematical model is comprised by three equations: the first one is for the description of the gas-vapor mixture temperature (energy balance), the second equation is for the vapour density (mass balance), and the third one is for heterogeneous droplet growth. This model takes into account the vapor depletion due to the condensation on nanoparticles. For small initial concentrations of nanoparticles the wall temperature affects on the final heterogeneous droplet radius. The increase of the initial number density of nanoparticles leads to the smaller droplets sizes for all wall temperatures considered.

Keywords: condensation, heterogeneous droplets, diffusion chamber

1. INTRODUCTION

An efficient method for the registration of nanoparticles is detecting of heterogeneous droplets, which are formed by means of the supersaturated vapor condensation on nanoparticles. The sketch of a laminar flow diffusion chamber with a porous hot wall is shown in Fig. 1.

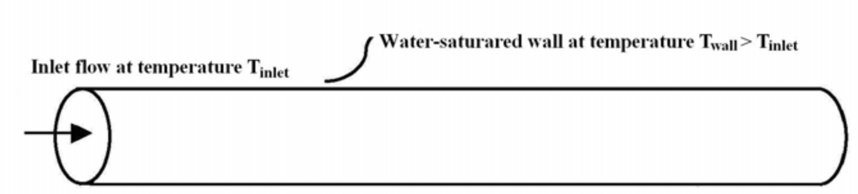

Fig. 1. Diffusion chamber with a water saturated porous wall

The operation principle of this chamber is as follows. The cold gas flow with nanoparticles enters the cylindrical chamber with the wall temperature T_{wall} and the saturated water vapor mixes with the gas flow. Vapor diffusion and heat conduction occur simultaneously in the radial direction. Hot water is evaporated into a cold gas flow and, thereby, a supersaturated gas-vapor mixture is formed.

In this work the condensation of water vapor on a dense cloud of nanoparticles moving in non-uniform fields of temperature and vapor supersaturation is simulated. For the simulation the new mathematical model is used, which was discussed in [1–3]. Previous numerical results were obtained for small values of the initial number densities of nanoparticles at the chamber inlet. The main attention in this paper is given to the growth of heterogeneous droplets for large values of the initial number density of nanoparticles. In this case the heat and mass transfer in a laminar flow diffusion chamber is influenced by the droplet growth.

2. MATHEMATICAL MODEL

In the laminar flow diffusion chamber the profile of a gaseous mixture velocity $u(r)$ has the parabolic character:

$$u(r) = 2u_0\left[1-\left(r / R\right)^2\right]. \tag{1}$$

Our mathematical model is comprised by three equations: the first one is for the description of the gas-vapor mixture temperature (energy balance), the second equation is for the vapour density (mass balance), and the third one is for heterogeneous droplet growth. The first equation is:

$$u(r,z)\frac{\partial T(r,z)}{\partial z} = \frac{1}{\rho_m c_m}\cdot\left[\frac{1}{r}\frac{\partial}{\partial r}\left(\lambda_m(T(r,z))r\frac{\partial T}{\partial r}\right)\right] + I_t\left[n(r,z)-n_s(T(r,z))\right], \tag{2}$$

where $I_t\left[n(r,z)-n_s(T(r,z))\right]$ is the heat source relevant to the release of the latent heat of the phase transition during vapor condensation on heterogeneous droplets.

The second equation is for the mass balance with a sink for vapor depletion:

$$u(r,z)\frac{\partial n(r,z)}{\partial z} = \frac{1}{r}\frac{\partial}{\partial r}\left(D(T(r,z))r\frac{\partial n}{\partial r}\right) + I_n(r,z)\left[n(r,z)-n_s(T(r,z))\right], \tag{3}$$

where the term $I_n(r,z)\left[n(r,z)-n_s(T(r,z))\right]$ describes a reduction in the vapor density resulting from its condensation on the droplets.

It can be shown that the contribution of the thermodiffusion is quite small for a laminar flow diffusion chamber; therefore, this effect is ignored in Eqs. (2) and (3).

The growth of a heterogeneous droplet, containing the nanoparticle inside, is described by the following equation:

$$\frac{\partial R_d(r,z)}{\partial z} = L(R_d(r,z))\frac{n(r,z)-n_s(T(r,z))}{u(r,z)}, \tag{4}$$

where $L(R_d)$ describes the isothermal mass transfer for droplets. This function depends on the Knudsen number $Kn = \lambda_d/R_d$ and can be written as following:

$$L(R_d) = \frac{Dm}{\rho_l R_d}\left(\frac{1}{1+(D/R_d)\sqrt{2\pi m/kT}}\right). \tag{5}$$

It exactly describes the droplet growth in the free-molecular regime and the continuous regime, respectively. In the calculations the water vapor diffusion coefficient D is assumed to be a function of temperature and concentration.

There is an important parameter, so called the Kelvin radius R_K:

$$R_K = \frac{2\sigma v}{kT\ln(S)}. \tag{6}$$

If the initial radiuses of nanoparticles are greater than the R_K, then a fast growth of droplets in the free-molecular regime takes place. As shown below the final radiuses of heterogeneous droplets do not depend on the initial ones.

3. NUMERICAL RESULTS

Some results of the numerical simulation are presented in Figs. 2-5. The curves are plotted as follows: 1 is for r/R = 0.1; 2 is for r/R = 0.6; 3 is for r/R = 0.9. We use the following initial parameters: chamber radius R = 0.005 m, mixture velocity u_0 ~ 0.15 m/s, inlet gas flow temperature T_{inlet} = 288 K, chamber wall temperature T_{wall} = 310 K, number density $N_d = 10^7$ nanoparticles/m^3. Also, we assume that all nanoparticle radiuses are larger than the Kelvin radius. For three radial positions the mixture temperature profiles are shown in Fig. 2.

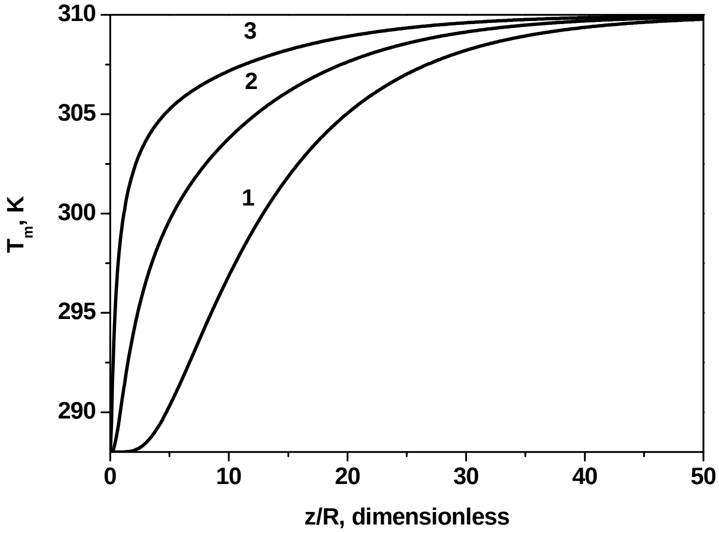

Fig. 2. Temperature profiles along the chamber axis

Characteristic length l_t of the temperature change, according to [4], is

$$l_t = 1.6 u_0 R^2 \rho_m c_m / \lambda_m b^2 , \quad (7)$$

where b is the smallest positive root of the equation $J_0(b) = 0$; J_0 is the Bessel function of the zeroth order. It is seen from Fig. 2 that the mixture temperature adjusts to the wall temperature at an axial position of approximately 40 R; l_t is about 13 R. According to the Eq. (7), the larger the mixture velocity the larger this distance. As the Lewis number is about one, the characteristic length l_v for the change of the vapour density is about l_t.

The local saturation $S(r,z)$ is defined by the following expression:

$$S(r,z) = n(r,z) / n_s(T(r,z)) . \quad (8)$$

Thus, for the calculation of the saturation we need to know the water vapour density $n(r,z)$. Saturation profiles of water vapour are shown in Fig. 3. The maximum saturation S is near the hot porous wall. For given conditions the maximum supersaturation of water vapour is about 1.45.

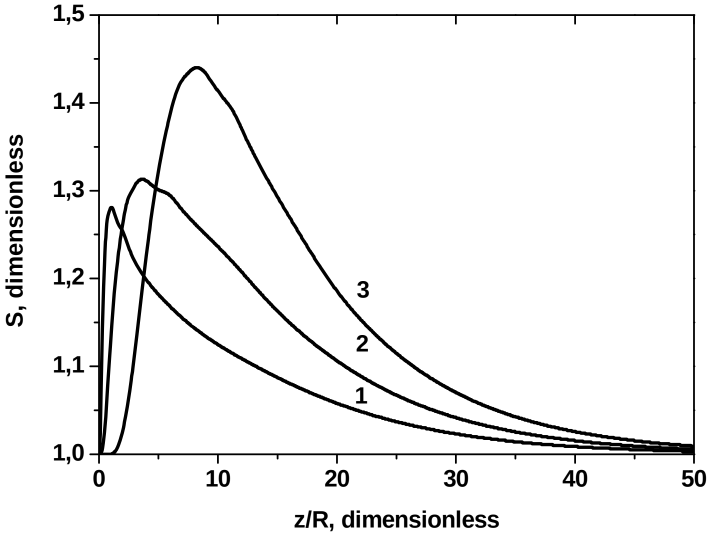

Fig. 3. Saturation profiles of mixture along the chamber axis

The growth of heterogeneous droplets versus the distance is shown in Fig. 4. Note that for all these conditions, the droplets grow to optically detectable sizes. A weak dependence of the final droplet radius on its radial position is observed. We see that the fastest growth of heterogeneous droplets take place below a distance of 15 *R*.

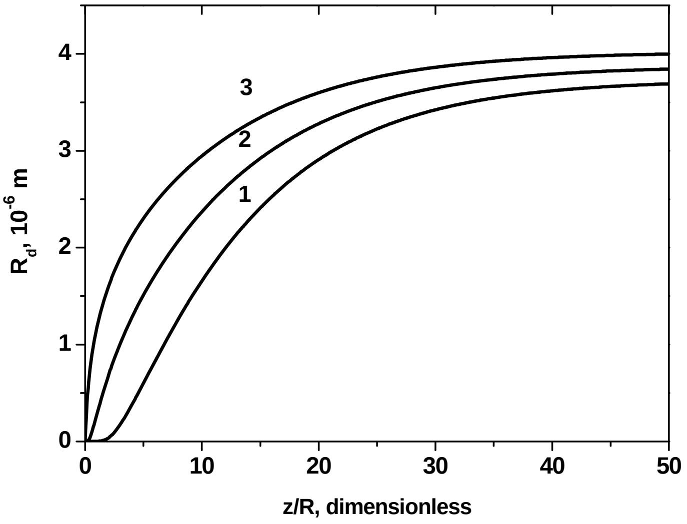

Fig. 4. Growth of heterogeneous droplets along the chamber axis

The wall temperature T_{wall} is one of the governing parameters of the chamber performance. For three initial number densities of nanoparticles (“a” is for $N_d = 10^7$ nanoparticles/m^3; “b” is for $N_d = 10^9$; “c” is for $N_d = 10^{10}$) the final radiuses of heterogeneous droplets versus T_{wall} are shown in Fig. 5. The calculations are made for the fixed length of the chamber of 0.1 m. For small initial concentrations of nanoparticles the wall temperature affects on the final heterogeneous droplet radius. The increase of the initial number density of nanoparticles leads to the smaller droplets sizes for all wall temperatures considered. The physical reasons of this effect are the vapor depletion and the fast increasing of temperature of the gas-vapor mixture.

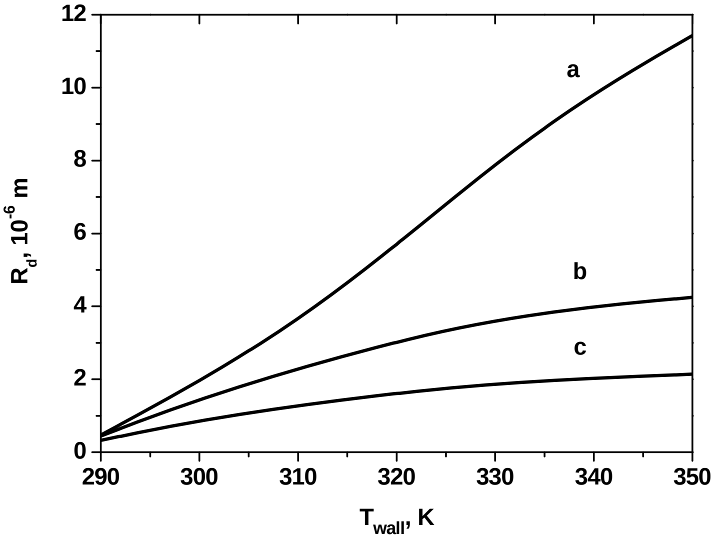

Fig. 5. Final droplet radius versus wall temperature

Thus, using the water vapour as a condensing substance, the laminar flow diffusion chamber can be applied for the effective registration of nanoparticles if $N_d < 10^{11}$ nanoparticles/m^3. Additionally, the water covering reduces the Brownian diffusion of nanoparticles, which is important for safety problems of nanotechnology.

4. CONCLUSIONS

For the description of growth of heterogeneous droplets, containing the nanoparticle inside, in a laminar flow diffusion chamber a new mathematical model is proposed.

It was shown that the wall temperature affects on the final heterogeneous droplet radius for small initial concentrations of nanoparticles. Increasing of the initial number density of nanoparticles leads to the smaller droplets sizes for all wall temperatures considered.

REFERENCES

1. BRIN, Anton A. Vapor condensation on carbon nanoparticles in a laminar flow diffusion chamber. *Proc. NAS of Belarus. Series of Phys.Tech. Sci.*, 2005, Vol. 5, p. 14–16.
2. BRIN, Anton A.; FISENKO, Sergey P. Heterogeneous condensation of a steam on nanoparticles in a laminar flow diffusion chamber. *J. Eng. Phys. Thermophys.*, 2006, Vol. 79, p. 212–216.
3. BRIN, Anton A.; FISENKO, Sergey P. Growth and motion of heterogeneous water droplets in laminar flow diffusion chambers. *Colloid Journal*, 2007, Vol. 69, No 6, p. 679–684.
4. BRIN, Anton A.; FISENKO, Sergey P. Heat and mass transfer and condensation interference in a laminar flow diffusion chamber. *Intern. J. Heat Mass Transfer*, 2006, Vol. 49, No 5/6, p. 1004–1014.

CYSENI 2010, May 27–28, Kaunas, Lithuania
ISSN 1822-7554, www.cyseni.com

SIMULATION OF TEMPERATURE DISTRIBUTION IN THIN ACTIVE LASER MEDIUM DISK

M. Gabalis, V. Girdauskas
Department of Physics
Vytautas Magnus University
Vileikos str. 8, LT-44404 Kaunas – Lithuania
Email: Martynas.Gabalis@fc.vdu.lt

ABSTRACT

In design of high average power lasers one common problem is the heat generated in the active laser medium. Heating of active medium causes undesirable changes in the parameters. Temperature gradient causes thermal stresses, which may lead to damaging of the active medium upon exceeding the threshold values. These problems can be solved by a thin disk active medium geometry: one side of the thin disk is in contact with cooler. Such composition leads to more efficient heat transfer due to the large surface area of cooler. This work discusses the problem of the heat transfer in a thin disk Nd:YAG disk medium, starting with formulation of the problem and concluding with numerical solutions: the maximum temperature of the thin disk, the cross sectional area temperature distribution dependence on thickness of the disk, absorption coefficient, incident angle and focusing of the pump beam. It will be shown that maximum temperature is attained on the surface of the disk and that focusing of pump beam results a lower increase of temperature.

Keywords: solid state laser, temperature distribution, thin disk laser

1. INTRODUCTION

Thin disk laser is a special kind of solid state laser, which was introduced in 1990s. The main difference from conventional rod lasers is the geometry of the active laser medium – the laser crystal is a thin disk. The heat generated is extracted dominantly through one end face (Fig. 1).

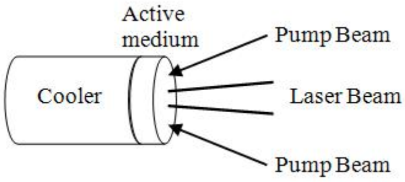

Fig. 1. Schematic view of thin laser disk geometry

In design of such solid state lasers, one must solve a problem of controlling the phenomenon that occurs as a result of heat generated in active medium disk [1]. This phenomena consist of thermal stresses, pump beam distortion and depolarization. Heating causes undesirable changes in active medium parameters: reduction of thermal conductivity, rise of both thermal expansion coefficient and temperature coefficient of refractive index. Temperature gradient causes thermal stresses, which can even destroy active medium.

Heat generation in active laser medium is related to quantum defect – pump photon energy is higher than that of photon of output radiation. The difference between those energies stays in active laser medium in form of heat. This is why one demands to use medium that is characterized by low quantum defect [2].

Temperature itself and its gradient in active laser medium can be reduced by a thin disk active medium geometry. Its main advantage is large cooling area and small temperature gradient along the axis perpendicular to the laser beam axis [3].

Analytical solution to heat transfer problem for thin disk is known only for simple situation: when pump beam incident perpendicularly to the top of active laser medium and beam's width in active medium stays constant [4]. However, when pump beam incident at some angle and/or is focused, the usual way to solve problem is to use numerical methods.

This work discusses numerical simulation of the temperature distribution in Nd:YAG active medium disk and results gained. Calculations were performed with respect to the different incident pump beam geometries, different values of active laser medium disk thickness and absorption coefficients. Also the effect of thermal conductivity dependence on temperature is discussed.

2. PROBLEM FORMULATION

The geometry of the heat transfer problem is shown in Fig. 1. Active laser medium disc is placed on a copper disc. The diameter of copper disk is twice as big as of active medium disk. The bottom of copper disk is cooled with water. Other faces of the disks are in contact with surrounding medium – air. Incident pump beam strikes top of the active medium at a certain angle (solid line) or perpendicularly (dashed line). Because of the different refractive index of active medium with regard to air, the beam which incidents at some angle, changes its direction inside the medium (angle θ differs from γ). The coordinates axes used in calculation are also shown in Fig. 2, except for y coordinate – which is perpendicular to xz plane. For radial coordinates z direction is left the same and radial coordinate r is pointing towards the side of the disks with r = 0 at the center.

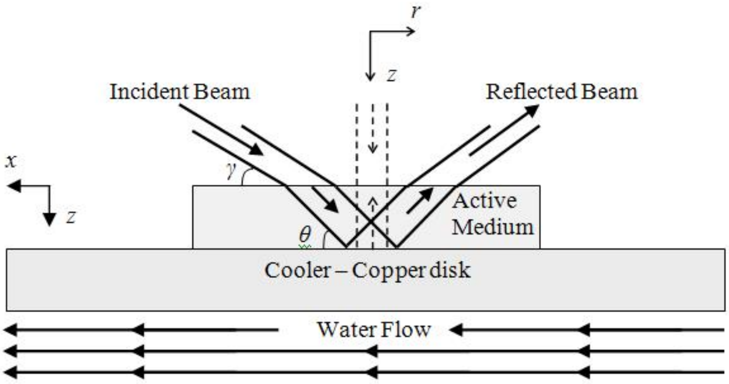

Fig. 2. The geometry of heat transfer problem

Temperature distribution problem for the geometry shown in Fig. 2 was solved with several assumptions made. Between both disks there is perfect thermal contact – heat flux is continuous, the bottom of the copper disk is set to be at constant temperature that is equal to the temperature of water. All other faces are set in heat isolating state, which is a good approximation, because of small heat transfer coefficient between both mediums (YAG and cooper) and air. Also light reflection at the top of active medium is neglected, while at the bottom light is fully reflected.

Fig. 2 shows pump beam with a constant width, but the case with focused beam will be discussed as well. All together, temperature distribution was calculated for four situations. First – angle θ is 90° (Fig. 2: dashed line), second – $\theta = 45°$ (Fig. 2: solid line). For those both cases pump beam width is set to be a constant. Third – $\theta = 45°$ and pump beam is focused in such a way, that its waist is at the bottom of active medium disk, and fourth – $\theta = 45°$, pump beam is focused as in previous case and thermal conductivity dependence on temperature is taken into account.

Temperature distribution calculation was based on the 3D steady state heat conduction differential equation:

$$\nabla\left(k(T)\nabla T(x,y,z)\right)+Q(x,y,z)=0, \tag{1}$$

where symbol ∇ denotes del operator, $k(T)$ is temperature dependent thermal conductivity of active medium, and $Q(x,y,z)$ – heat source. However, this equation can be simplified if we assume that thermal conductivity is constant (which is good approximation for small temperature interval). In this case Eq. (1) becomes:

$$\nabla^2 T(x,y,z)+\frac{Q(x,y,z)}{k}=0. \tag{2}$$

For the perpendicular incident beam we can go even further and simplify Eq. (2) to 2D radial differential equation:

$$\frac{1}{r}\frac{\partial}{\partial r}\left(r\frac{\partial T(r,z)}{\partial r}\right)+\frac{\partial^2 T(r,z)}{\partial r^2}+\frac{Q(r,z)}{k}=0 \tag{3}$$

r is radial coordinate. Boundary conditions used in Eqs. (1), (2) and (3) are:

$$\left.\frac{\partial T}{\partial n}\right|_{\Gamma_o}=0, \tag{4}$$

$$\left.T\right|_{\Gamma_f}=T_0, \tag{5}$$

$$k\left.\frac{\partial T}{\partial n}\right|_{\Gamma_A}=k_A\left.\frac{\partial T}{\partial n}\right|_{\Gamma_A}, \tag{6}$$

where Γ_0 are boundaries in contact with air, Γ_f – boundary in contact with water and Γ_A – boundary between active medium and copper disk. T_0 express temperature of the water, which is constant, k – thermal conductivity of active medium and k_A – thermal conductivity of copper. Eq. (3) requires an extra boundary condition:

$$\left.\frac{\partial T}{\partial r}\right|_{r=0}=0, \tag{7}$$

which express the symmetry of temperature distribution with respect to z axis. The only heat source in Eqs. (1), (2) and (3) will be non-radiate transitions inside the part of active medium in which pump beam absorption occurs. If we assume that absorption is independent of medium temperature and neglect diffraction of the pump beam inside the active medium, then heat source is linearly proportional to the pump beam intensity (whose profile has a Hyper-Gaussian shape) and for perpendicular beam can be expressed as:

$$Q(x,y,z)=\alpha\eta\frac{P}{\pi w_0^2}e^{-\alpha z}e^{-\left(\frac{x^2+y^2}{w_0^2}\right)^p}, \tag{8}$$

where α is active medium absorption coefficient, η – power transfer efficiency (part of the absorbed pump power that generates heat), P – pump beam power, w_0 – pump beam width and p – order of Hyper-Gaussian profile. However, for the problem in this paper, heat source must consist of two terms – one for incident pump beam and other for reflected (Fig. 2). In 2D radial problem modification of Eq. (8) is taken:

$$Q(r,z)=\alpha\eta\frac{P}{\pi w_0^2}e^{-\left(\frac{r^2}{w_0^2}\right)^p}\left(e^{-\alpha z}+e^{-\alpha(2L-z)}\right), \tag{9}$$

where the first term in the sum corresponds to heat source of incident beam, the second – of reflected. For 3D problem, when pump beam incident at some angle, transformation of coordinates were used. Pump beam axis is turned around y coordinate and beam itself is shifted along coordinate x, so that y coordinate is unchanged. With this modification made, heat source is expressed in Eq. (10):

$$Q(x,y,z)=\alpha\eta\frac{P}{\pi w_0^2}\left(e^{-\alpha z_I}e^{-\left(\frac{x_I^2+y^2}{w_0^2}\right)^p}+e^{-\alpha z_R}e^{-\left(\frac{x_R^2+y^2}{w_0^2}\right)^p}e^{-\alpha\frac{L}{\cos\theta}}\right), \tag{10}$$

where L is the thickness of active medium disk and terms z_I, x_I are the transformed coordinates for incident beam, and z_R, x_R – for reflected beam:

$$x_I=(x-L\tan\theta)\cos\theta+z\sin\theta, \tag{11}$$

$$z_I=\frac{z}{\cos\theta}, \tag{12}$$

$$x_R=(x+L\tan\theta)\cos\theta-z\sin\theta, \tag{13}$$

$$z_R=\frac{L-z}{\cos\theta}. \tag{14}$$

For focused pump beam term w_0 in Eq. (10) is replaced by expression (11):

$$w(z)=w_0\sqrt{1+\left(M^2\frac{\lambda(z-z_0)}{\pi w_0^2}\right)^2} \tag{15}$$

relating beam width with the coordinate z. M^2 is beam quality parameter and λ – beam wavelength. Eqs. (1), (2) and (3) were solved numerically by finite elements method with “Comsol Multiphysics” software. Numerical values of parameters in equations above, which were used in calculations are given in Table 1:

Table 1. Parameters used in calculation

Parameter	**Numerical value**
w_0	0.2 [mm]
P	40 [W]
p	20
D	12 [mm]
d	24 [mm]
η	0.3
k	12 [W/(mK)]
k_A	400 [W/(mK)]
T	20 °C

where *D* is diameter of active medium disk and *d* – of copper disk.

3. RESULTS AND DISCUSSIONS

3.1. Perpendicular incident pump beam

For perpendicular incident beam equation (3) was solved. Calculations were made for different active medium disk thicknesses and absorption coefficients. Values of the active medium disk thicknesses were taken in range from 0.5 mm to 1.5 mm with increasing step of 0.25 mm. Calculated temperature distribution in both active medium and copper disk, with $\alpha = 6$ cm^{-1} and $L = 1.5$ mm, is shown in Fig. 3.

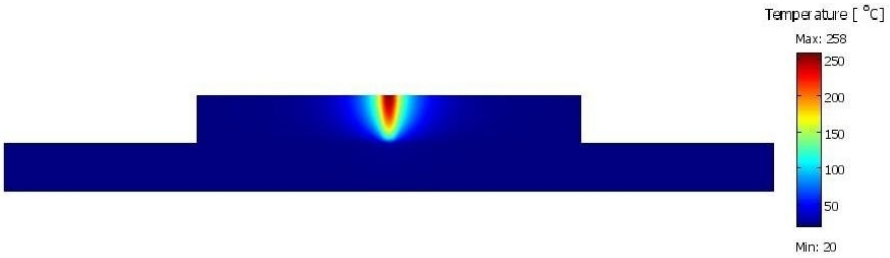

Fig. 3. Temperature distribution in both disks in plane (*zr*)

Temperature at the center on the top of the coopers disk is about 26 °C and at the whole bottom (the side that is in contact with water) is equal to 20 °C. While this difference may be considered small, temperature difference between top and bottom in active medium disk is much bigger and reach value of about 232 °C. For larger values of active medium disk thickness maximum temperature grows (Fig. 4(b)), and temperature along radial coordinate spreads outside more (Fig. 4(a)). This is a result which could be expected because of larger region inside active medium disk where pump beam absorption occurs – that is more heat is generated in active medium disk.

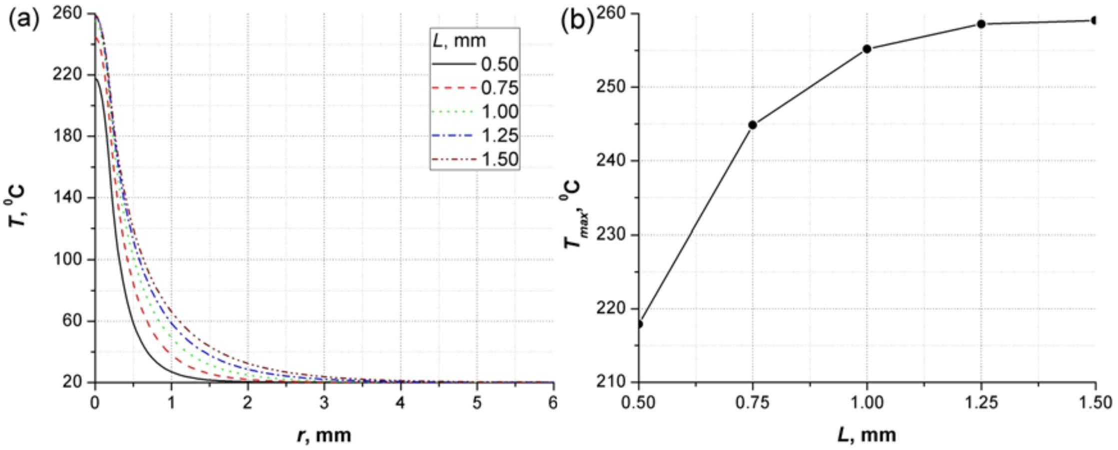

Fig. 4. (a) Temperature distribution along radial coordinate and (b) maximum temperature for different thickness *L*. Absorption coefficient $\alpha = 6$ cm^{-1}

For bigger values of absorption coefficient maximum temperature and temperature along both coordinates *z* and *r* also increase (Fig. 5). Maximum temperatures in active medium disk differ from one in copper disk quite much (Fig. 5(a)). Maximum temperature in copper disk for absorption coefficient values from region 4÷9 cm^{-1} differs from 26 °C only for about 4%. For some approximation it is possible to neglect existence of copper disk and perform temperature distribution calculations only in active medium disk with assumption that its bottom has constant temperature. This approximation was used to get results discussed in the following part of this paper.

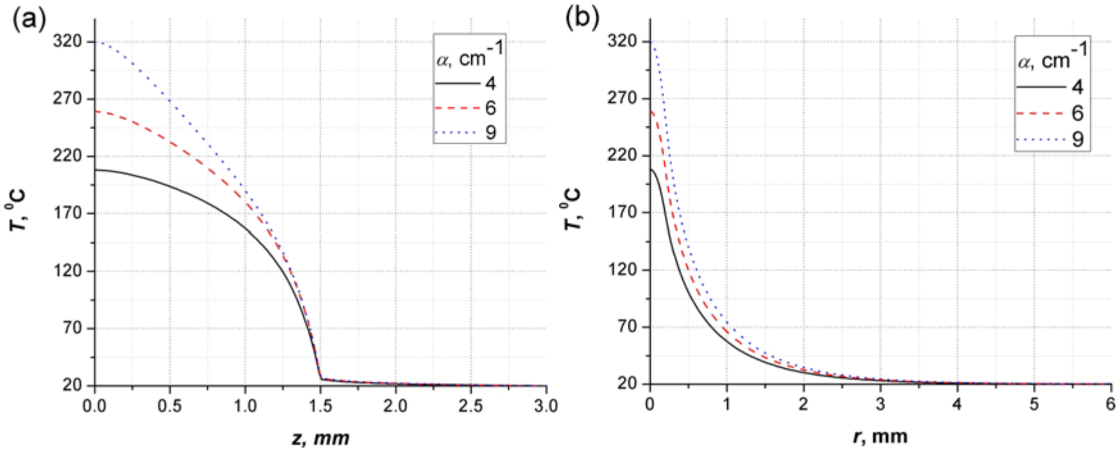

Fig. 5. Temperature distribution: (a) along coordinate *z* (interval from 1.5 mm to 3 mm belongs to copper), (b) along radial coordinate *r*. Active medium disk thickness L = 1.5 mm

3.2. At 45^0 angle incident pump beam

For oblique incident pump beam Eq. (2) with heat source given by equation (10) is solved. As mentioned above, copper disk was neglected and temperature at the bottom of the active medium disk was set to be equal to 20 °C – a situation which could reflect a very thin copper disk. Angle θ was set to be equal to 45°, thickness of active medium disk L = 1.5 mm, absorption coefficient α = 6 cm^{-1} and pump beam width w_0 = 0.2 mm. Heat source in active medium disk replicates geometry of pump beam (Fig. 6). Local maximums of heat source are located at the top of active medium disk, where pump beam incidents, and at the bottom, where heat sources from incident and reflected beams compose.

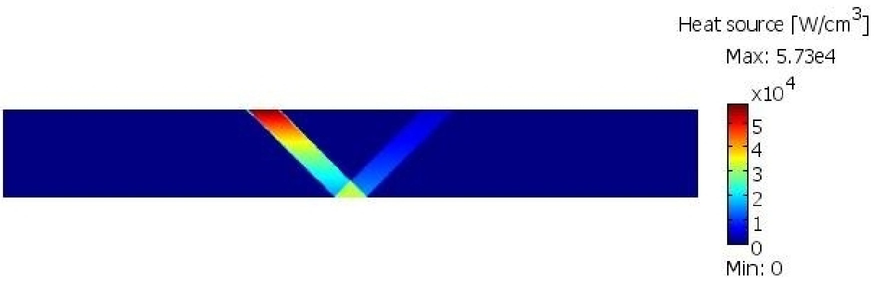

Fig. 6. Heat source in the plane (*x,y=0,z*) of active laser medium disk

Maximum temperature in active medium disk is 233 °C (Fig. 7). Although its value is less than the one in perpendicular incident pump beam case (Fig. 2), power dissipated here is larger (10.8 W vs. 9.8 W of the total 40 W pump beam power). Lower maximal temperature mainly is caused by the fact that incident and reflected pump beams compose in smaller region, and partly because of larger heat source volume inside medium, what results wider temperature spread (Fig. 7 vs. Fig. 2).

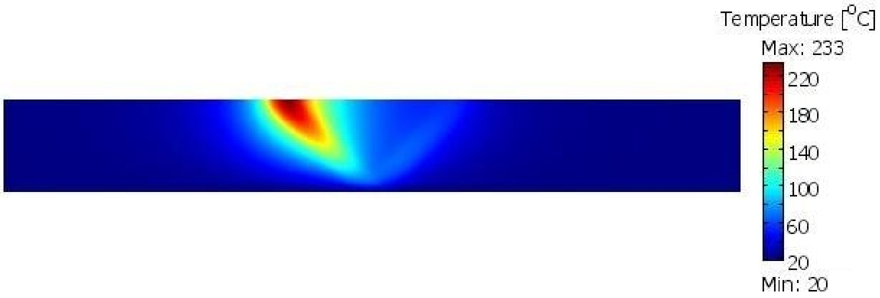

Fig. 7. Temperature distribution in the plane (*x,y=0,z*) of active laser medium disk

On the top of the active medium disk there are two temperature peaks (Fig. 8 (b)). For smaller values of absorption coefficients second peak (corresponding to reflected beam) becomes bigger, while the first one – smaller.

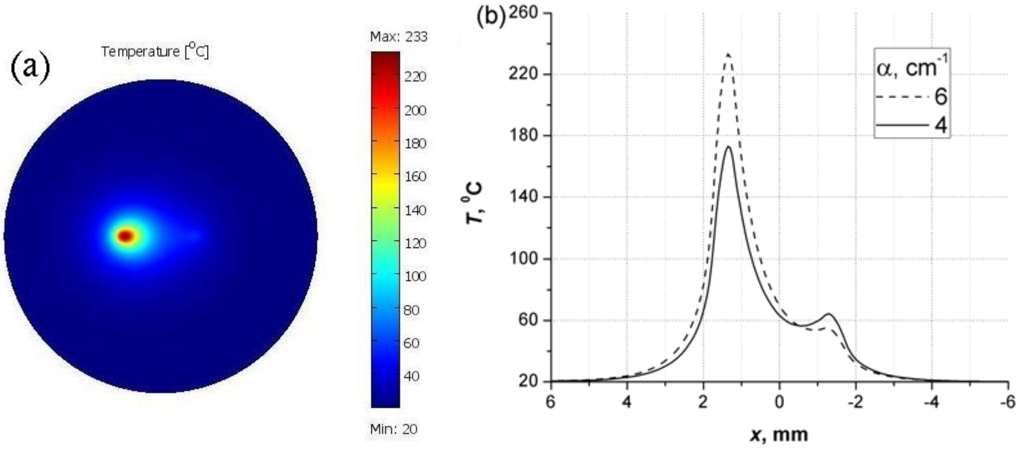

Fig. 8. Temperature distribution: (a) on the top of the disk and (b) along coordinate *x*

3.3. Focused pump beam

Focused pump beam changes its width along the way through active medium disk, heat source also replicates this geometry (Fig. 9). In this case maximum heat source is generated at the bottom of the disk, that is where pump beam waist, equal to w_0 = 0.2 mm, was set. Pump beam was focused in such a way, that its width at the waist is 0.2 mm and at 50 mm distance from waist – 5 mm (parameter M^2 in equation (15) equal to 78). Other parameters were the same as those in previous discussion.

Fig. 9. Heat source in the plane (*x,y=0,z*) of active laser medium disk

Temperature distribution compared to the one of unfocused beam (Fig. 7) does not differ much (Fig. 10). But maximum temperature is notably less – about 149 °C (233 °C for unfocused pump beam) – result partly influenced by the fact, that only 7.6 W of the total 40 W pump power becomes heat in active medium. Other reason for this is that maximum heat source is at the bottom of the disk – at the boundary where largest heat sink is produced.

To get the same power dissipation as in the case for constant width pump beam (10.8 W) 56 W pump beam can be used. Maximum temperature then is 204 °C – still smaller. Conclusion from this result could be this – in order to get lower values for maximal temperature one should keep in mind use of focused pump beam.

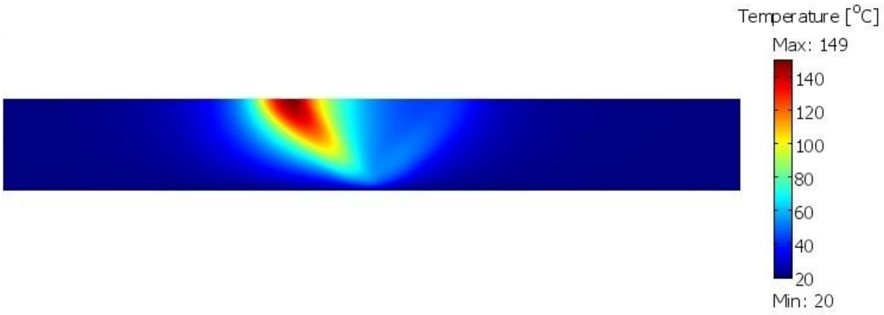

Fig. 10. Temperature distribution in the plane (*x,y=0,z*) of active laser medium disk

3.4. Influence of temperature dependent thermal conductivity

Temperature distribution calculation based on solving equation (1) used empirical expression (16) [5] for thermal conductivity:

$$k(T) = (7.28 - 7.3c)\left(\frac{204}{T - 96}\right), \tag{16}$$

where c is the doping concentration, which value in calculations were set to zero. This was done in order to see the temperature distribution of Nd:YAG crystal itself. Use of temperature dependent thermal conductivity gives raise to maximum temperature (Fig. 11). Fig. 11 (b) summarizes results with all pump beam geometries discussed. Perpendicular pump beam gives largest maximum temperature and focused – lowest. Affect of temperature dependent thermal conductivity is quite large (Fig. 11(b)) – maximum temperature raise about two times.

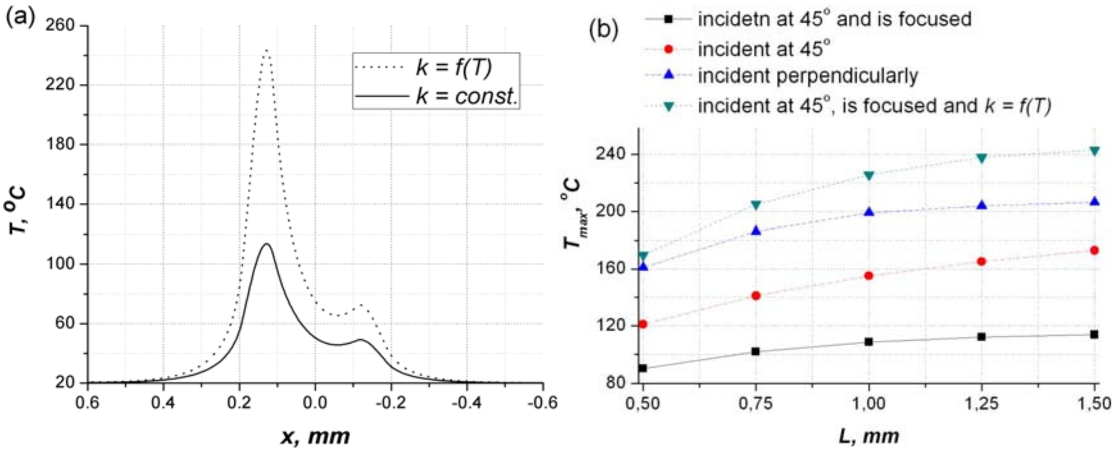

Fig. 11. (a) Temperature at the top of active medium disk along coordinate x, thickness of the disk L = 1.5 mm, pump beam is focused, α = 4 cm^{-1}. (b) Maximum temperature dependent on thickness of the disk for different incident beam geometries, α = 4 cm^{-1}

4. CONCLUSIONS

This work presents the results of temperature distribution calculations in a thin active laser medium disk using finite elements method. Calculations were performed for different geometries of incident pump beam, different values of the disks thickness and absorption coefficient. Also, temperature dependent thermal conductivity was discussed. It was shown that larger values of absorption coefficient and disk thickness result maximum temperature raise. Increasing disk thickness from 0.5 mm to 1.5 mm increase maximum temperature about 20%. Temperature peak was located at the top of the disk. Maximum temperature with the same pump power absorbed is gained with perpendicular incident pump beam, while minimum - with focused pump beam. This difference is about 30%. Temperature dependent thermal conductivity gives significant increase in maximum temperature – about two times.

Results discussed in this article will be used for calculating laser beam aberration and thermal lens effect in thin disk active laser medium.

ACKNOWLEDGEMENTS

This work was supported by the Lithuanian State Science and Studies Foundation under project No B-41/2009.

REFERENCES

1. KEMP A.J., VALENTINE G.J., BURNS D. Progress towards high-power, high-brightness neodymium-based thin-disk lasers. *Progress in Quantum Electronics*, 2004, Vol. 28, p. 305–344.
2. CHÉNAIS S., DRUON F., FORGET S., BALEMBOIS F., GEORGES P. On thermal effects in solid state lasers: the case of ytterbium-doped materials. *Progress in Quantum Electronics*, 2006, Vol. 30, p. 89–153.
3. GIESEN A., SPEISER L., PETERS R., KRÄNKEL C., PETERMAN K. Thin-disk laser come of age. *Photonics Spectra*, 2007, Vol. 41, p. 52–58.
4. KOECHNER W. *Solid-State Laser Engineering*. Springer-Verlag Berlin Heidelberg New York, 2008. ISBN-10: 1-4419-2117-6.
5. NAJAFI M., SEPEHR A., H. GOLPAYGANI A.; SABBAGHZADEH J. Simulation of thin disk laser pumping process for temperature dependent Yb:YAG property. *Optics Communications*, 2006, Vol. 282, p. 4103–4108.

CYSENI 2010, May 27–28, Kaunas, Lithuania
ISSN 1822-7554, www.cyseni.com

DETERMINATION OF CHARGE CARRIER DENSITY IN ZINC OXIDE NANORODS PREPARED BY CHEMICAL SPRAY PYROLYSIS

E. Kärber, T. Dedova, I. Oja Acik, M. Krunks, A. Mere
Department of Materials Science, Tallinn University of Technology
Ehitajate tee 5, 19086 Tallinn – Estonia
Phone: +3726203369
Email: erki.krbr@gmail.com

V. Mikli
Centre for Materials Research, Tallinn University of Technology
Ehitajate tee 5, 19086 Tallinn - Estonia

ABSTRACT

The electrical properties of nanostuctured, undoped n-type ZnO layers (ZnO_{NR}), comprising hexagonal nanorods, were studied. The aim was the determination of charge carrier density in ZnO_{NR}. The C-V characteristics of ZnO_{NR}/Hg Schottky barrier contact were obtained in order to determine the active area of the contact via a newly proposed model for the capacitance of the ZnO_{NR}/Hg Schottky barrier; Mott-Schottky plot of the C-V characteristics was applied in order to determine the carrier density. Carrier densities in the order of 10^{14} to 10^{16} cm^{-3} were determined, dependent on the growth temperature of the ZnO_{NR}. Higher densities were acquired in case of lower deposition temperatures. The origin of the carriers is related to the intrinsic defects of ZnO_{NR}. Higher growth temperature is likely to reduce the concentration of the oxygen vacancies as electron donors. Annealing or doping of the ZnO_{NR} is needed in case higher carrier densities are required.

Keywords: ZnO, Nanostructures, Electronic properties, Hg probe

1. INTRODUCTION

ZnO layers of hexagonal nanorods (ZnO_{NR}), prepared by chemical spray pyrolysis [1], were studied. Optical transparency and light scattering ability due to high internal surface area makes ZnO_{NR} suitable for solar cell window layer application [2]. However, the aim of this work was the determination of the charge carrier density (from here on: carrier density) in the n-type ZnO_{NR} layers, indicating high resistivity according to preliminary measurements.

The determination of electrical parameters in lateral direction, regarding the substrate, is not available due to discontinuous cross section of the nanostructured layer. However, the main difficulty in case of electrical characterization perpendicular to the substrate is the determination of the electrically active interface area (from here on: active area) of the ZnO_{NR} and contact material.

Different methods for the determination of electrical properties of ZnO single nanorods have been applied, yet requiring considerable time and effort. The conductors used to contact ZnO_{NR} are: Pt-covered cantilever of atomic force microscope (AFM) forming a Schottky contact on an individual ZnO nanorod grown on a conductive substrate (ITO) [3], AFM cantilever on a ZnO_{NR}/Au Schottky diode array grown on conductive ZnO layer [4]; Ni/Au conductors in order to manufacture ohmic contacts to single ZnO nanowire FET (Field Emission Transistor) [5]; ohmic Ti/Au conductors defined by electron beam lithography (EBL) on a ZnO nanorod separated from the substrate [6]; Ag conductors forming rectifying Schottky nanocontacts on a separated ZnO nanorod [7].

The characterization of bulk ZnO_{NR} layers has been done by means of a counter electrode (ITO), pressed on the ZnO_{NR} layer grown on ITO [8]; impedance spectroscopy (IS) of n-ZnO_{NR}/liquid junction [9]; investigations of n-Si/n-ZnO and p-Si/n-ZnO heterojunction [10]. However, the studies of previous references are limited to current-voltage (I-V) characteristics, with an exception of the electrochemical characterization by IS [9] suitable for the determination of carrier density. In addition, carrier density has been evaluated from the field-effect based transport measurements as-well [5], based on the I-V characteristics.

In this paper, a method for the evaluation of the active area of bulk n-ZnO_{NR} and Hg Schottky contact, is discussed. The active area and the carrier density are determined from capacitance vs bias voltage (C-V) measurements of the Schottky barrier. The advantage of this method is the determination of the active area by concurring identical electrical measurements to determine the carrier density, as opposed to visual evaluation by scanning electron microscope (SEM) images, yielding an exact area of the working contact, i.e. the effective area.

2. EXPERIMENTAL

The ZnO_{NR} layers were prepared on glass/ITO substrate by chemical spray pyrolysis (CSP) deposition of zinc chloride solutions at substrate temperatures 480 °C and 550 °C.

The electrical characterization of ZnO nanocrystals was carried out using mercury (Hg) probe to form the ZnO_{NR}/Hg Schottky barrier. The mercury drop with an area of ca 7 mm^2 was applied onto ZnO_{NR} to form a rectifying contact, confirmed by diode-like I-V characteristics recorded by four-point probe method on Autolab PGSTAT-30 potentiostat. Due to the high surface tension of Hg, short circuiting was avoided with ITO which served as the second, negative electrode. In addition, it was assumed that the contact forms only with the top of the ZnO nanorods.

C-V measurements of the ZnO_{NR}/Hg Schottky barrier were recorded at 10kHz, 20 mV AC on the same apparatus. The active area of the contact and the carrier density of the ZnO_{NR} was obtained from $1/C^2$–V plot, according to the Mott-Schottky model [11]. The series resistance of the ZnO_{NR} was evaluated from linear part of the I–V characteristics of the forward biased ZnO_{NR}/Hg barrier, while having subtracted the series resistance of the substrate.

3. RESULTS

3.1. Determination of the active ZnO_{NR}/Hg contact area

In order to exlude the air volume of the ZnO_{NR} layer, that is, to evaluate the active area only, a model is proposed for the capacitance of ZnO_{NR}/Hg Schottky barrier (Fig. 1).

The total capacitance C_0 of the ZnO_{NR} layer between ITO and Hg drop, can be expressed as:

$$C_0 = C_1 + C_2 \tag{1}$$

Here, C_1 is the capacitance caused by the active area of ZnO_{NR}/Hg contact, acting as a Schottky barrier capacitor and C_2 is due to the air gap, partially filled with ZnO nanorods which do not take part of the Schottky barrier capacitance. Thus, C_2 is considered as an air gap with relative permittivity $\varepsilon \approx 1$.

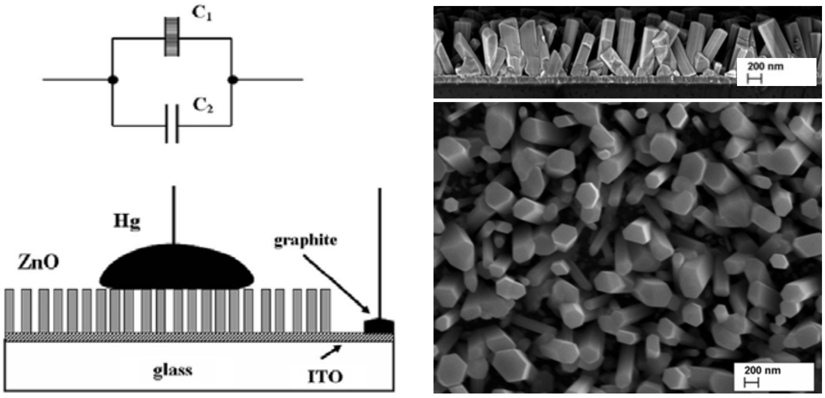

Fig. 1. Left: Sketch of the ZnO_{NR}/Hg contact and the model of capacitance. Right: SEM images of ZnO_{NR} array, deposited at 550 °C. The length of the particular nanorods is ca 800 nm, and length to width ratio is ca 3

In case a full depletion of the ZnO_{NR} is achieved via applied bias voltage, then, according to the model of parallel plate capacitor and the considerations in previous section, equation (1) can be represented as

$$C_0 = \frac{\varepsilon_0 \cdot \varepsilon_1 \cdot A_1}{L} + \frac{\varepsilon_0 \cdot (A - A_1)}{L} \tag{2}$$

Here, A is the area of the Hg drop, ε_1 is the relative permittivity of ZnO (ε_1=8.5), ε_0 is the electric constant ($8.85\cdot10^{12}$ F/m) and L is the thickness of the ZnO_{NR} layer, determined from SEM cross-sectional image (Fig. 1). While A corresponds to apparent contact area of the mercury drop, the active area A_1 of ZnO_{NR}/Hg contact is derived from equation (2):

$$A_1 = \frac{C_0 \cdot L - \varepsilon_0 \cdot A}{\varepsilon_0 (\varepsilon_1 - 1)} \tag{3}$$

In order to calculate A_1, the total capacitance C_0 is obtained from $1/C^2$ = *const*, at the reverse bias region of $1/C^2$–V plot (Fig. 2).

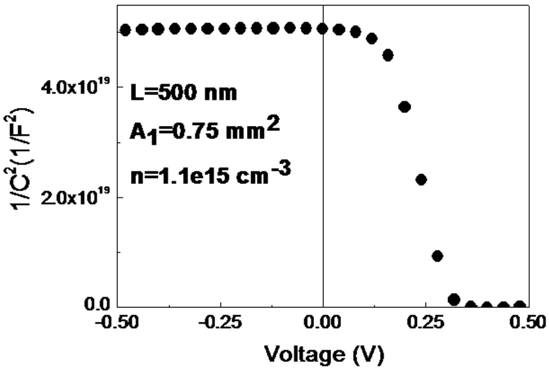

Fig. 2 Mott-Schottky plot of the ZnO_{NR}/Hg barrier

The presence of the horizontal part of the $1/C^2$–V plot is assigned to the fulfillment of the requirement of the full depletion of the ZnO_{NR}. In case this requirement is not fulfilled, the model is inapplicable and active area must be evaluated by other means, e.g. from SEM image.

Thus, the active ZnO_{NR}/Hg area is estimated from the $1/C^2$–V plot of the ZnO_{NR}/Hg Schottky barrier, according to equation (3), assuming the full depletion of the ZnO_{NR}. This step is needed for the determination of the carrier density of the ZnO_{NR} layer.

3.2. Determination of carrier density in ZnO_{NR}

Carrier density *n* of the ZnO_{NR} is determined from the negative slope of $1/C^2$–V plot (Fig. 2), according to the Mott-Schottky formula:

$$n = \frac{2}{q\varepsilon_0\varepsilon_1 A_1^{\;2}} \frac{dV}{d\left(\frac{1}{C^2}\right)}, \tag{4}$$

where q is the elementary positive charge ($1.60 \cdot 10^{-19}$ C). The active area A_1 of the ZnO_{NR}/Hg contact is evaluated as presented in paragraph 3.1.

4. DISCUSSION

Relatively low n-type carrier densities 10^{14} to 10^{16} cm^{-3} were determined in ZnO_{NR}, dependent on the growth temperature of the ZnO_{NR}. Higher carrier densities were acquired in case of lower deposition temperature of 480°C and lower carrier densities were obtained in case of higher deposition temperature of 550 °C

As ZnO_{NR} were undoped, the origin of the carriers is intrinsic. Thereof interstitial zinc (Zn_i) and oxygen-vacancies (V_O) as electron donors is the cause of n-type conduction in ZnO_{NR}. The contribution of V_O is known to be dominant in the sense of n-type conductivity, while n-type defects are dominant as a whole, making the achievement of p-type ZnO_{NR} difficult [12].

Regarding our study, the higher growth temperature was likely to reduce the concentration of the oxygen vacancies as electron donors due to thermodynamically more favorable conditions for the crystal formation. In order to increase the carrier density in ZnO_{NR}, the concentration of oxygen vacancies needs to be increased by annealing in vacuum or zinc rich atmosphere [11]. Another option is the addition of suitable group III elements (Al, Ga, In) as n-type dopants, of which Ga is structurally most suitable due to similar covalent bond length of Ga–O and Zn–O [13]. The production of p-type ZnO has been done by N–In co-doping [14].

As an extension of the discussed method for the evaluation of the carrier density, it allows an estimation of the substrate coverage via the A_1/A ratio.

5. CONCLUSIONS

Carrier density in ZnO_{NR} was determined via a proposed model for the determination of the electrically active interface area of ZnO_{NR}/Hg Schottky contact. Carrier densities in the order of 10^{14} to 10^{16} cm^{-3} were determined in ZnO_{NR}, deposited at 550 °C and 480 °C, respectively. The origin of carriers in ZnO_{NR} is related to intrinsic defects, most likely oxygen vacancies. The lower depositing temperature and annealing or doping is needed in case higher carrier densities are required.

6. ACKNOWLEDGEMENT

Financial support by Estonian Ministry of Education and Research (SF0140092s08) and Estonian Science Foundation (ETF6954) is acknowledged.

REFERENCES

1. KRUNKS, M.; DEDOVA, T.; OJA ACIK, I. *Thin Solid Films*, 2006, Vol. 515, Issue 3, p. 1157–1160.
2. KRUNKS, M.; KATERSKI, A.; DEDOVA, T.; OJA ACIK, I.; MERE, A. *Solar Energy Materials & Solar Cells*, 2008, Vol. 92, Issue 9, p. 1016– 1019.
3. NAJAK, J.; KASUJA, J.; WATANABE, A.; NOZAKI, S. *Journal of Physics: Condensed Matter*, 2008, Vol. 20, No 195222.
4. PARK I, W.; YI, G-C.; KIM, J.W.; PARK, S.M. *Applied Physics*, 2003, Vol. 82, No 24.
5. PARK Young, J.; OH, H.; KIMB, J-J.; KIMA Sub, S. *Journal of Crystal Growth*, 2006, Vol. 287, p. 145–148.
6. ZHOU, H.; FALLERT, J.; SARTOR, J.; DIETZ J.B. R.; KLINGSHIRN, C.; KALT, H.; WEISSENBERGER, D.; GERTHSEN, D.; ZENG, H.; CAI, W. *Journal of Applied Physics Letters*, 2008, Vol. 92, No 132112.
7. ZHANG, N.; YU, K.; LI, L.; ZHU, Z. *Applied Surface Science*, 2008, Vol. 254, p. 5736–5740.
8. KIM, Y.; SHANG, H.; CAO, G. *Journal of Sol-Gel Science and Technology*, 2006, Vol. 38, No 1, p. 79–84.
9. MORA-SERO, I.; FABREGAT-SANTIAGO, F.; DENIER, B.; BISQUERT, J.; TENA-ZAERA, R.; ELIAS, J.; LÉVY-CLÉMENT, C. *Applied Physics Letters*, 2006, Vol. 89, No 203117.
10. SUN, M.; ZHANG, Q.-F.; WU, J.-L. *Journal of Physics D: Applied Physics*, 2007, Vol. 40, p. 3798–3802.
11. TUNG T., R. *Materials Science and Engineering: R: Reports*, 2001, Vol. 35, Issues 1–3, Chapter 5.3.1.
12. SUN, F.; SHAN, C.X.; WANGA, S.P.; LI, B.H.; ZHANG, J.Y.; ZHANG, Z.Z.; ZHAO, D.X.; YAO, B.; SHEN, D.Z.; FAN, X.W. *Applied Surface Science*, 2010, Article in Press (On the origin of intrinsic donors in ZnO, DOI: 10.1016/j.apsusc.2009.12.040).
13. XU, C.; KIM, M.; CHUN, J.; KIM, D. *Applied Physics Letters*, 2005, Vol. 86, No 133107.
14. SUN, H.; ZHANG, Q.; ZHANG, J.; DENG, T.; WU, J. *Applied Physics B*, 2008, Vol. 90, p. 543–546.

CYSENI 2010, May 27–28, Kaunas, Lithuania
ISSN 1822-7554, www.cyseni.com

CZTS ($Cu_2ZnSnSe_4$) CRYSTAL GROWTH FOR USE IN MONOGRAIN MEMBRANE SOLAR CELLS

I. Klavina, J. Raudoja, M. Altosaar, E. Mellikov, D. Meissner
Institute of Materials Science, Tallinn University of Technology,
Ehitajate tee 5, 19086 Tallinn, Estonia
Phone: +3726203362
Email: ingaklav@inbox.lv

T. Kaljuvee
Laboratory of Inorganic Materials, Tallinn University of Technology,
Ehitajate tee 5, 19086 Tallinn, Estonia
Phone: +3726203362
Email: tiidu@staff.ttu.ee

ABSTRACT

In order to save the world's climate a continuous growth of Photovoltaic (PV) by at least about 20% per year will be needed during the coming decades leading to installation of several ten TW_p in 2050. However, both current thin film materials, i.e. CdTe and CI(G)S contain resource limited elements (Te and In) which do not allow for such an extensive use. The only currently available very promising new material is CZTS, as yet investigated only in few research laboratories. Powder crystals with a diameter of about 50 μm have proven already to yield solar efficiencies of more than 10 % yielding cell efficiencies of more than 6 %. By varying the composition of the melt-grown $Cu_2ZnSn(S_xSe_{1-x})_4$ materials, especially the sulphur to selenium ratio, the band-gap as determined from quantum efficiency spectra of photo current generation can be shifted between below 1.0 to above 1.7 eV, i.e. across the complete range of band-gaps able to generate the highest possible solar energy conversion efficiencies of single band-gap as well as of tandem solar cells. A production process is currently developed for the first complete roll-to-roll production of flexible solar modules. The present study deals with possible chemical reactions between the binary precursor compounds CuSe, SnSe, ZnSe in molten CdI_2 as flux material in vacuum ampoules. The aim is to find suitable preparation conditions for the synthesis of $Cu_2ZnSnSe_4$. Differential thermal analysis (DTA) was used for the determination of thermal effects and their enthalpies. Phase compositions in mixtures of binary precursors and CdI_2 were determined by X-ray diffraction (XRD) Energy-dispersive X-ray spectroscopy (EDX) and Raman spectroscopy. Closed quartz vacuum ampoules were used for heating/cooling processes of mixtures and empty ampoule as reference. The chemical route of formation of $Cu_2ZnSnSe_4$ starting from binary chalcogenides is discussed.

Keywords: $Cu_2ZnSnSe_4$, solution growth, XRD, EDX, Raman and DTA

1. INTRODUCTION

Solar cells converting absorbed solar light into electrical energy by the photovoltaic effect are a promising alternative to the use of non-renewable and polluting fossil fuels in the today's world situation of growing energy needs and increasing environmental concern. Research and development in new, exotic and simple materials and devices, and innovative, but simple manufacturing processes need to be pursued in a focused manner.

Conventionally, photovoltaic materials are inorganic semiconductors, which form suitable junctions with materials of the other type of conductivity and exhibit a PV effect when exposed to light, but only a few of them are commercially interesting. A solar cell absorber should be a direct band gap semiconductor material with a band gap of 1–1.5 eV with a high optical absorption (>10^4 cm^{-1}), high quantum efficiency of excited carriers, long diffusion length, low recombination velocity, and should be able to form a good electronic junction [1]. For example, alloys and compounds of I–III–VI ternaries (on the base of $CuInSe_2$) and related quaternaries like $Cu_2ZnSnSe_4$ where relatively high cost. In is changed by Zn and Sn, can form a host of suitable photovoltaic materials [2]. However, it must be emphasized that with increasing number of components, the phase diagrams of these materials are quite complicated [3] and due to this it is difficult to produce homogeneous single phase absorber materials. As a rule, monograin growth in different molten fluxes results in homogeneous material [4]. The isothermal heating of precursor materials in the presence of liquid phase of a suitable solvent material (flux) leads to the formation of semiconductor materials with single-crystalline grain structure and narrow-disperse granularity, so called monograin powders. In our previous reports [5, 6] we showed, that monograin powders of $Cu_2ZnSnSe_4$ and also $Cu_2Zn_{1-x}Cd_xSn(Se_{1-y}S_y)_4$ solid solutions with tailored chemical composition could be prepared by isothermal recrystallization of initial binary compounds in molten KI. $Cu_2ZnSnSe_4$ powder crystals grown in molten KI had tetragonal shape with rounded grain edges. By XRD analysis the powders had stannite structure (space group $I\overline{4}2m$) [5]. Potassium iodide has high melting temperature (686 ^oC) and due to this rather high contamination of synthesized absorber material with potassium and iodine is predicted. Solvent materials with lower melting temperatures are therefore preferred. In the present paper the formation of $Cu_2ZnSnSe_4$ from binary CuSe, ZnSe and SnSe in molten CdI_2 (melting temperature 390 ^oC) is studied and the chemical interactions between initial binary compounds with CdI_2 are investigated using SEM, EDX, DTA and Raman spectroscopy.

2. METHODOLOGY

For determination of temperatures of phase changes and interactions between initial binaries and flux material differential thermal analysis (DTA) was used. Following samples were studied: CdI_2+CuSe, CdI_2+ZnSe, CdI_2+SnSe, CdI_2, CdI_2+CuSe+ZnSe+SnSe, CdI_2+CuSe+SnSe. The total mass of mixtures was kept constant – 0.25 g. The mass ratios of binary compounds and CdI_2 were equal to 1:1. Compounds were mixed by grinding in a mortar and sealed into degassed quartz ampoules. As the reference the empty degassed and sealed quartz ampoule was used. Heating rate 5 ^oC/min was applied during two heating runs from room temperature to 800 ^oC and cooling down to 300 ^oC.

The samples for Raman and XRD measurements were prepared as follows: 1 g mixtures of CuSe + ZnSe + SnSe in relations of Cu-deficient composition of $Cu_2ZnSnSe_4$ with Cu/Zn+Sn=1.85 and CdI_2 were annealed in degassed quartz ampoules at temperatures: 370 ^oC, 400 ^oC, 590 ^oC, 740 ^oC for 1h. The ampoules were quenched in water. The used temperatures were a little bit higher than those for the detected peaks in DTA curves. The ampoules were opened and the powder was studied by Raman, EDX, XRD and SEM. For more deep investigation of interactions between ZnSe and molten CdI_2 a single crystalline sample of ZnSe was heated in CdI_2 at 740 ^oC for 1 week. After opening this ampoule CdI_2 was removed by washing with DI water. Room temperature Raman spectra were recorded by using a Horiba`s LabRam HR high resolution spectrometer equipped with a multichannel CCD detection system in backscattering configuration. In micro-Raman measurements, the incident laser light with a wavelength of 532 nm can be focused on the sample within a spot of 1 µm in diameter. Samples were studied by using Zeiss Ultra 55 SEM. Composition was determined by EDX method using a Röntec EDX X-flash 3001 detector and the Thermo Noran Maxray ER Parallel Beam Spectrometer. For XRD Rigaku PDXL Ultima IV apparatus with D/teX Ultra line detector was used. For DTA – Lab sys SETERAM was used.

Results of DTA were compared with phase diagrams of systems Cu-Se (Fig. 1), Zn-Se, Sn-Se available from literature [7].

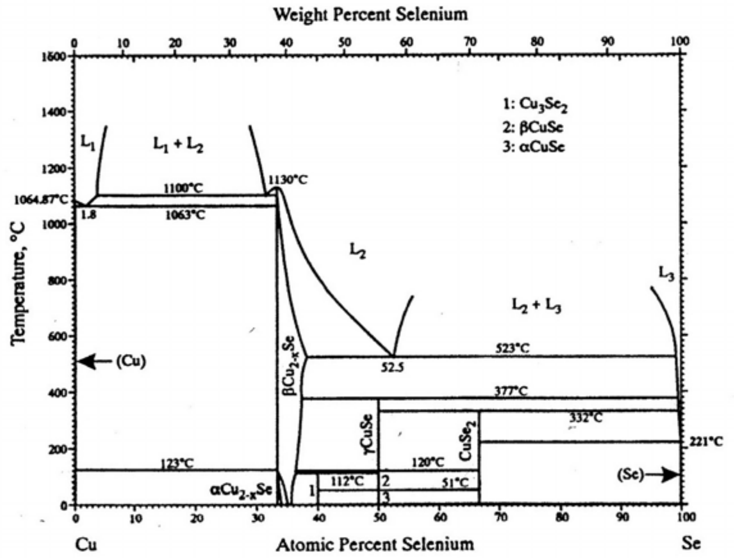

Fig. 1. Phase diagram of system Cu-Se [7]

3. RESULTS AND DISCUSSIONS

3.1. Differential thermal analysis (DTA)

3.1.1. Quasi-binary systems

Comparison of DTA curves presented in Fig. 2 with corresponding phase diagrams of semiconductor compounds gave the next findings: DTA peaks can be attributed to phase changes for the mixture of CuSe + CdI_2 (Fig. 2a) as follows – at 51 °C α-CuSe transforms to β-CuSe, which transforms to γ-CuSe at 119 °C the endothermic peak at 217 °C, near the melting point of Se, indicates that used CuSe contains an undetermined amount of elemental Se. The endothermic peaks at 304 and 354 °C can not be assigned to phase changes of CuSe. The next endothermic peak in vicinity of 368 °C could be attributed to the melting process of CuSe+CdI_2 mixture. After this peak an exothermic peak follows at 385 °C that probably is connected with dissolution of CuSe in molten CdI_2. The undissolved β-$Cu_{2-x}Se$ melts at 636 °C [5].

In the other binary systems there were found no other peaks than an endothermic peak followed by an exothermic peak in the vicinity of CdI_2 melting point. DTA curve of the mixture CdI_2 + ZnSe shows an endothermic peak at 381 °C followed by an exothermic peak at 388 °C (Fig. 2b) and DTA curve of the mixture SnSe + CdI_2 shows an endothermic peak at 359 °C and an exothermic peak at 384 °C (Fig. 2c). The common feature for all the investigated quasi-binary systems is that after endothermic peak attributable to melting process an exothermic peak occurs.

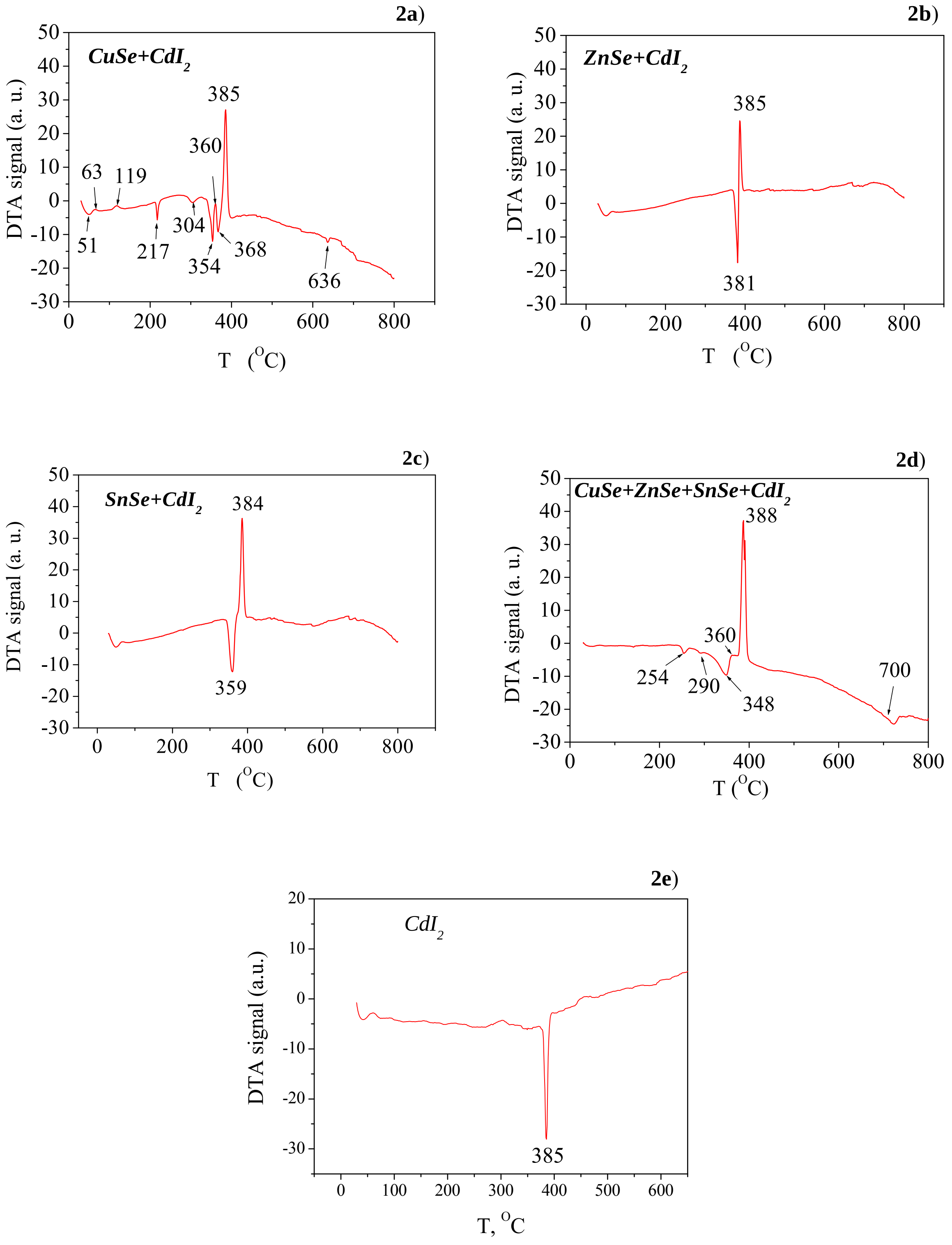

Fig. 2. DTA heating curves of quasi-binary systems (2a, 2b, 2c), the sample of the mixture for quaternary CZTSe synthesis (2d) and also CdI_2 (2e)

3.1.2. $CuSe+ZnSe+SnSe+CdI_2$

From the first DTA heating curve presented in Fig. 2d it is seen that there are more pronounced endothermic peaks at 254, 290 and a wide peak at 348 °C followed by an exothermal peak at 388 °C. The endothermic peak near 700 °C can be attributed to the melting of ternary compound Cu_2SnSe_3 (685–697 °C) determined by Dudchak et.al. [6]. In the cooling curve of the studied system there was only one endothermic peak in the vicinity of melting point of the mixture at 366 °C that can be attributed to the solidification process of the molten phase.

3.2. Raman analysis

In the Table 1 the experimental results of Raman spectroscopy for the mixture of $CuSe+ZnSe+SnSe+CdI_2$ heated at several temperatures for 1 hour are presented. Raman spectroscopy data reveal that the formation of CZTSe is detectable already at 370 °C, lower than melting temperature of pure solvent CdI_2 but higher than melting temperature of the mixture of precursors. The CZTSe Raman peak at 171 cm^{-1} in spectrum of the sample heated at 370 °C is shifted to 174 cm^{-1} for samples annealed at higher temperatures. This shift is typical for CZTSe materials where Zn is partly substituted with Cd. It is common for all used heating temperatures that some part of SnSe and $SnSe_2$ is remained as non-reacted, even at 740°C. No CZTSe Raman peaks were found in un-crushed sample heated at 740 °C. It means that the surface of formed CZTSe grains is completely covered by SnSe-$SnSe_2$. In all samples there is also determined the presence of solid solution $Zn_xCd_{1-x}Se$.

Table 1. Data of Raman analysis for the mixture of $CuSe+ZnSe+SnSe+CdI_2$ heated at several temperatures for 1 hour

Annealing temperature °C	**Raman peaks, cm^{-1}**	**Component**	**Reference**
370	240-242	ZnSe-CdSe	Experiments and [10]
	109–111, 143–147	SnSe	[8]
	171, 194	CZTSe	[6]
400	238–242, 476–477	ZnSe-CdSe	Experiments and [10]
	109–111, 143–147	SnSe	[8]
	194, 383	CZTSe	[6]
590	240-242	ZnSe-CdSe	Experiments and [10]
	109–111, 143–147	SnSe	[8]
	194	CZTSe	[6]
740	94–98	ZnSe-CdSe	Experiments and [10]
	109–111, 143–147, 187–188	SnSe, $SnSe_2$	[8, 9]

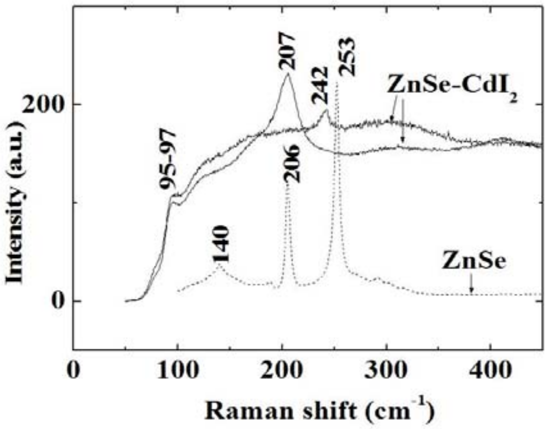

Fig. 3. The Raman spectrum of the sample ZnSe-CdI$_2$ heated at 740 °C for 1 week. Dashed line is Raman spectrum of a single crystalline ZnSe sample

Raman spectra of the mixture of ZnSe-CdI$_2$ heated at 740 °C for 1 week (see Fig. 3) showed peaks at 95–97 cm^{-1} region, at 206-207 and at 242 cm^{-1}. For comparison, a Raman spectrum of a single-crystalline ZnSe sample is given. It is seen that the peak at 253 cm^{-1} in Raman spectrum of single-crystalline ZnSe is shifted to 242 cm^{-1} in Raman spectra of ZnSe samples heated in CdI$_2$. The shift of the peak position is the conformation to the formation of solid solution of ZnSe-CdSe. (Raman peak of pure CdSe is at 209 cm^{-1} as measured separately and not shown in Fig. 3).

3.3. SEM, EDX and XRD analyses

3.3.1 *ZnSe-CdI$_2$*

In Fig. 4 SEM photos from different places of the sample of single crystalline ZnSe heated in CdI$_2$ are presented. Fig. 4a gives information about 2 different areas of the sample – black and orange. External surface is not homogeneous, the colour contrasts from black to red and even orange. From EDX analyses (see Table 2) the black area (see Fig. 4b) surrounding the orange part consists of Cd, Se and I. By XRD CdSe crystalline phase is determined for this black part. The orange part consists mainly of Cd, Zn and Se and $Cd_3Zn_7Se_{10}$ crystalline phase is determined by XRD. The most probable is that after the formation of molten phase the chemical change reaction (1) occurs in the molten phase followed by the formation of solid solution $Zn_xCd_{1-x}Se$ through the reaction (2). The possible reactions could be written as following:

$$ZnSe + CdI_2 \rightarrow CdSe + ZnI_2 \qquad (1)$$

$$x\, ZnSe + 1-x\, CdSe \rightarrow Zn_xCd_{1-x}Se \qquad (2)$$

The occurrence of iodine in the black parts can be attributed to CdI$_2$ enclosed between solid crystals of $Zn_xCd_{1-x}Se$ due to the fast crystallisation of them during the quenching process. Fast crystallization can be also derived from the formation of leaf- (Fig. 4c) and flower-like (Fig. 4d) shape of crystals.

Table 2. EDX analyses data for the sample ZnSe-CdI_2 (heated at 740 °C for 1 week)

Place of EDX analysis	Colour	Concentration , mole %			
		Zn	Se	Cd	I
Fig. 4a	Orange	31.2	48.9	17.5	0
Fig. 4a	Black	0	29.7	51.4	18.9
Fig. 4b	Black	10.7	42.9	39.3	7.0
Fig. 4c	Black “leaves”	3.9	38.9	43.8	13.4
Fig. 4d	Black “flower”	3.7	30.0	40.4	25.8

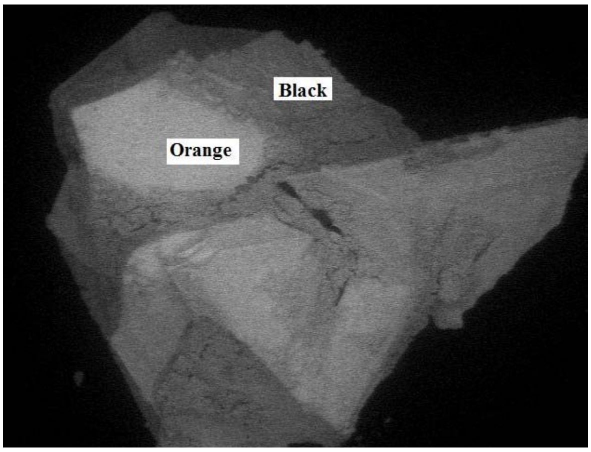

Fig. 4a

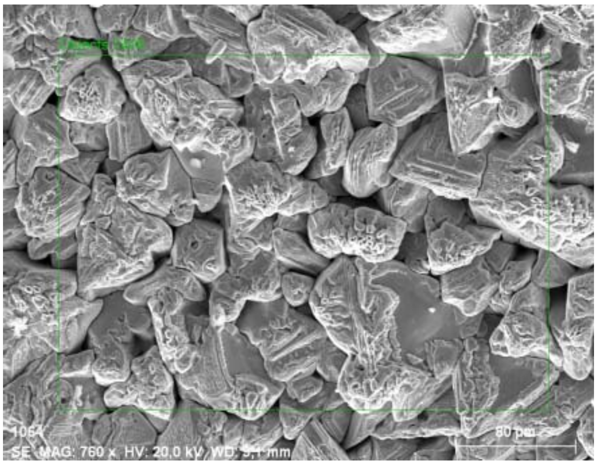

Fig. 4b

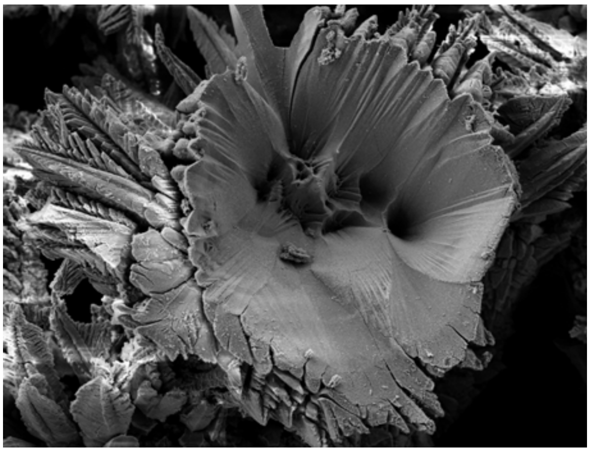

Fig. 4c

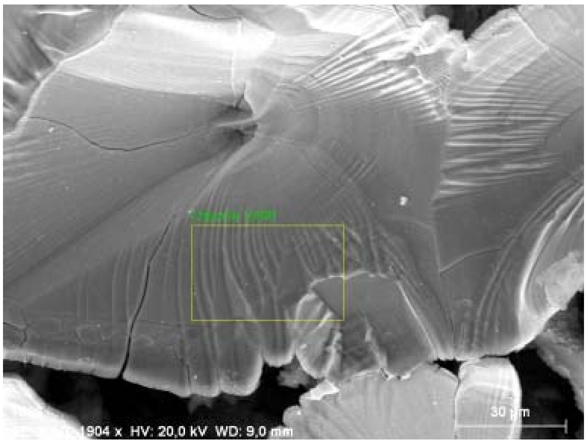

Fig. 4d

Fig. 4. SEM photos from different places of the ZnSe-CdI_2 sample
(heated at 740 °C for 1 week)

3.3.2 *CuSe-CdI_2*

By XRD the sample CuSe-CdI_2 heated at 400 °C contained CdSe, $Cu_{1.75}Se$, Cu_3Se_2 and elemental selenium. By this finding the DTA exothermic peaks in the vicinity of CdI_2 melting temperature could belong to the exchange reactions of copper selenides with CdI_2. It is one more evidence for the statement that formed liquid phase is the main mediator for diffusion and chemical interactions.

3.3.3 *CuSe+ZnSe+SnSe+CdI$_2$*

XRD analyses show that the formation of CZTSe in CdI$_2$ involves several steps. In samples heated at 370 °C $Cu_2CdSnSe_4$, $SnSe_2$ and ZnSe were found. At 400 °C $Cu_{1.8}Se$, Cu_2SnSe_3 and SnSe prevailed. At 590 °C $Cd_{0.22}Zn_{0.78}Se$, CuI and $Cu_2ZnSnSe_4$ existed. At 740 °C beside $Cu_2ZnSnSe_4$ also CuSe and Cu_4Se_3 were detected. By EDX analysis the crystals of CZTSe grown in CdI_2 contain about 3 mole % of Cd. On the basis of the results of Raman and XRD measurements it can be derived that Se, released due to the phase change of CuSe to $Cu_{1.8}Se$, can combine with SnSe resulting in $SnSe_2$ that dissolves in molten CdI_2 and deposits on the surface of formed particles of $Cu_2(Zn_xCd_{1-x})SnSe_4$ during the quenching process.

It is one more evidence for the statement that formed liquid phase is the main mediator for diffusion and chemical interactions.

4. CONCLUSIONS

Comparison of DTA curves revealed that the common features for all the investigated quasi-binary systems – precursor binary compound mixed with CdI_2 – are that melting of mixtures started at lower temperatures than melting of pure CdI_2 and that after endothermic peak attributed to the melting process an exothermic peak occurred. By SEM, DTA, EDX and Raman spectroscopy data it can be concluded that all chemical interactions were induced by formation of liquid phase both in separate quasi-binary systems of precursor compound-CdI_2 and in the mixture for quaternary CZTSe synthesis. In the case of ZnSe-CdI_2 chemical exchange reaction occurred and as a result CdSe and ZnI_2 was formed. Similar reactions were found for CuSe-CdI_2. Raman analysis gave the data, that the formed surface of CZTSe crystals was covered by SnSe-$SnSe_2$. In all samples there was also determined the presence of solid solution $Zn_xCd_{1-x}Se$ and conformed the formation of pentanary $Cu_2(Zn_xCd_{1-x})SnSe_4$. The formation of multiphase products makes the useage of CdI_2 as a solvent for synthesis of single phase monograin powders of CZTSe complicated.

5. ACKNOWLEDGEMENTS

This work was supported by the Estonian Ministry of Education and Research by Contract No. SF0140099s08. Dr. O. Volobujeva is gratefully acknowledged for SEM and EDX spectroscopy and Dr. A. Mere for XRD measurements.

REFERENCES

1. CHOPRA, K. L., PAULSON, P. D., DUTTA, V. Thin-Film Solar Cells: An Overview. PROGRESS IN PHOTOVOLTAICS: RESEARCH AND APPLICATIONS Prog. Photovolt: Res. Appl. 2004; 12:69–92 (DOI: 10.1002/pip.541).
2. RAULOT, J.M. DOMAIN, C., GUILLEMOLES, J.F. Ab initio investigation of potential indium and gallium free chalcopyrite compounds for photovoltaic application. *Journal of Physics and Chemistry of Solids*, 2005, Vol., p. 2019–2023.
3. MATSUSHITA, H., MAEDA, T., KATSUI, A., TAKIZAWA, T. Thermal analysis and synthesis from the melts of Cu-based quaternary compounds Cu–III–IV–VI$_4$ and Cu$_2$–II–IV–VI$_4$ (II=Zn,Cd; III=Ga,In; IV=Ge,Sn; VI=Se). *J. Cryst. Growth*, 2000, Vol. 208, p. 416.
4. MELLIKOV, E., HIIE, J. ALTOSAAR, M. Powder materials and technologies for solar cells. *Int. J. Materials and Product Technology*, 2007, Vol. 28, No 3-4, p. 291–311.
5. ALTOSAAR, M., RAUDOJA, J., TIMMO, K., DANILSON, M., GROSSBERG, M.,

KRUSTOK, J., VAREMA, T., MELLIKOV, E. $Cu_2ZnSnSe_4$ Monograin Powders for Solar Cell Application Proceedings of the 2006 IEEE WCPEC-4, Hawaii, 2006 May 7–12.

6. ALTOSAAR, M., RAUDOJA, J., TIMMO, K., DANILSON, M., GROSSBERG, M., KRUSTOK, J., MELLIKOV, E. $Cu_2Zn_{1-x}Cd_xSn(Se_{1-y}S_y)_4$ solid solutions as absorber materials for solar cells. *Phys. stat. Sol.*, 2008, Vol. (a) 205, No. 1, p. 167–170.
7. CHAKRABATI, D. J.; LAUGHLIN, D. E.: *Bull. Alloy Phase Diagrams 2* 1981. 305 p.
8. SMITH, A. J., MEEK, P. E., LIANG, W. Y. Raman scattering studies of SnS_2 and $SnSe_2$. *J. Phys. C: Solid State Phys.*, 1977, Vol. 10, p. 1321.
9. BOSCHER, N. D., CARMALT, J. C., PALGRAVE, R. G., PARKIN, I. P., Atmospheric pressure chemical vapour deposition of SnSe and $SnSe_2$ thin films on glass. *Thin Solid Films*, 2008, Vol. 516, p. 4750–4757.
10. KONTOS, A. G., RAPTIS, Y. S., STRABURG, M., POHL, U. W., BIMBERG, D., Raman study of nitrogen-doped ZnSSe/GaAs epilayers. *Thin Solid Films*, 2003, Vol. 428, p. 185.

CYSENI 2010, May 27–28, Kaunas, Lithuania
ISSN 1822-7554, www.cyseni.com

FABRICATION OF THREE-DIMENSIONAL NANOSTRUCTURES BY LASER POLYMERIZATION TECHNIQUE

M. Malinauskas, A. Žukauskas, G. Bičkauskaitė, M. Rutkauskas, K. Belazaras, H. Gilbergs, P. Danilevičius, V. Purlys, D. Paipulas, T. Gertus, R. Gadonas and A. Piskarskas
Laser Nanophotonics Group
Department of Quantum Electronics
Physics Faculty, Vilnius University, Sauletekio ave. 9, bld. III
LT-10222 Vilnius – Lithuania,
Tel.: +37060002843
Email: mangirdas.malinauskas@ff.vu.lt

D. Baltriukienė, V. Bukelskienė
Institute of Biochemistry
Vivarium, Mokslininkų 12, LT-08662 Vilnius – Lithuania

A. Gaidukevičiūtė
Foundation for Research and Technology Hellas (FORTH)
Division Institute of Electronic Structure and Laser (IESL)
P.O. Box 527, Heraklion, Crete 711 10, Greece

ABSTRACT

Laser Multi-Photon Polymerization (LMPP) is a direct writing technique offering three-dimensional (3D) nanostructuring of photopolymers. In this report, we present LMPP principles, our constructed versatile fabrication system and an overview of recent advances. Based on non-linear light-matter interaction, tightly focused intense laser beam can initiate photochemical modification which is tightly localized in space within femtoliter volume. There is no restriction in the sample translation trajectory, thus point-by-point photomodification can be induced with no geometrical restrains. As the sample is scanned according to Computer Aided Design (CAD) model, the trace of the focused beam materializes the object. After exposure, the sample is immersed into an organic solvent in order to remove the unmodified material, thus results in free standing 3D structure on a substrate. The LMPP fabrication system employs 75 fs pulse duration laser light of 515 nm central wavelength. Large working field (100 mm x 100 mm x 50 mm in X, Y and Z directions) linear-motor stages are used for the precise sample positioning with up to 10 nm resolution. The fabricated functional microstructures are: microlenses, photonic crystals, phase and fluorescent gratings, artificial scaffolds for cell growth, cantilevers and tubules. Conventional optical and fluorescence, scanning electron and atomic force microscopes are used to characterize the fabricated microstructures. Biological experiments proved the structured materials to be biocompatible framework for tissue forming cells and, therefore, to be used as scaffolds for artificial tissues and applied for regenerative medicine. The microstructures show perfect quality and can be fabricated with high repeatability as well as be integrated into more complex Micro-Opto-Electro-Mechanical (MOEM) or Lab-On-Chip (LOC) devices. Variety of photosensitive materials can be used for this type of manufacturing, among them are: epoxies (SU-8), acrylates (AKRE), hybrid organic-inorganic (ORMOCERs and ORMOSILs) and biodegradable (PEG-DA) materials. In brief, high throughput, possibility to use various photosensitive materials combined with flexibility and easy scaling makes LMPP a versatile 3D nanostructuring technique for diverse applications in microoptics, photonics, biomedicine, micromechanics and microfluidics.

Keywords: femtosecond laser, nonlinear absorption, photopolymerization, nanolithography, three-dimensional microstructures, photonics, microoptics, micromechanics, artificial scaffolds, stem cells growth, regenerative medicine

1. INTRODUCTION TO MICRO/NANOSTRUCTURING

Interest in down-scaled functional micro/nano devices is growing steadily as low-cost and high-efficiency devices are being applied wider in everyday life. During last decades, efforts in improving the fabrication methods of such components have advanced dramatically. UV lithography [1], electron beam writing [2], X-ray lithography [3] and nanoimprint [4] are widely used for nanostructuring, however, these methods are not flexible, cost efficient and limited for 3D formation. Recently, development of less expensive technical routes for industrial applications has emerged. It is represented by ink jet and 3D printing [5, 6], dip coating [7] and selective laser sintering [8] techniques. However, these methods are lacking fabrication resolution and are limited to usable materials. During last decade a non-linear lithography technique employing ultrafast laser has emerged as Laser Multi-Photon Polymerization (LMPP) [9]. Illustrations showing method's feasibility and flexibility for production of 3D microstructures are shown in Fig. 1. Direct 3D writing in photopolymers enables rapid, flexible and cost efficient fabrication of microstructures required in fields of photonics [10–12], microoptics [13, 14], microfluidics [15, 16], biomedical components [17,18] and tissue engineering [19,20]. Compared to its anterior alternative, UV micro-stereolithography [21, 22], it offers higher spatial resolution and easier fabrication of true 3D structures [23, 24]. Novel hybrid materials are expected to ensure higher structuring resolution and control optimized mechanical, optical and electrical or even magnetic properties [25, 26]. Possibility to selectively metalize these nanostructures provides opportunity to make it applicable in plasmonics or metamaterials production [27–30]. Using LMPP technique, near 100 nm spatial structuring resolution was demonstrated [31–33] (prototype systems are already commercially available [34–37]), but the structures were not much bigger than several tens or hundreds of micrometers. It complicates the nano-featured microstructures practical applications or even characterization of their properties. This implies that demand of 3D micro/nanostructures over a large area is still high [38–40]. For example, larger photonic crystals or microlens arrays can increase their applicability; artificial scaffolds have to be big enough for the biologist or surgeon for comfortable handling.

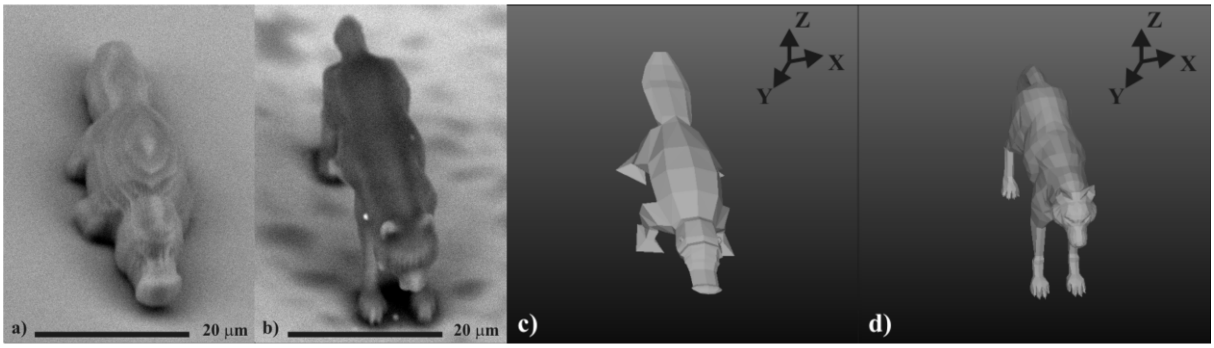

Fig. 1. Scanning electron microscopy images of micro-animals fabricated via LMPP technique: micro-platypus and micro-wolf out of SZ2080 and AKRE37 materials, a) and b), respectively. c) and d) depicts STL models of the produced micro-objects

Summing up, the field of direct writing based on LMPP technique has advanced to a level of practical applications. However, several issues are still to be solved, among them – efficient micro/nanostructuring of larger areas and on various transparent as well as opaque substrates. In this paper, we present constructed LMPP system, designed for rapid fabrication over a large area for applications in photonics, microoptics, micromechanics and microfluidics, especially focusing on production of artificial polymer scaffolds for tissue engineering [41–43].

2. LASER MULTIPHOTON NANOPOLYMERIZATION TECHNIQUE

2.1. Principles of non-linear laser writing in polymers

LMPP is a direct writing technique based on point-by-point photomodification of photosensitive material. A tightly focused laser beam induces non-linear light-matter interactions, which quasi-instantly triggers radical polymerization chain-reactions which convert monomers to polymer. Due to multi-photon absorption, laser light is absorbed only in the vicinity of the focus and absorption is negligible in the outer region of the focus. This enables energy to be introduced in an ultra-localized volume (*voxel*), deep in the droplet of the pre-polymer, transparent to VIS or NIR light. In this manner, the translated focal spot leaves a photomodified trace inside the bulk, so that it becomes insoluble in organic solvents. After immersing the sample in the developer bath the unexposed part of the material is washed out revealing the 3D model as a materialized structure. Fabrication steps are shown in Fig. 2.

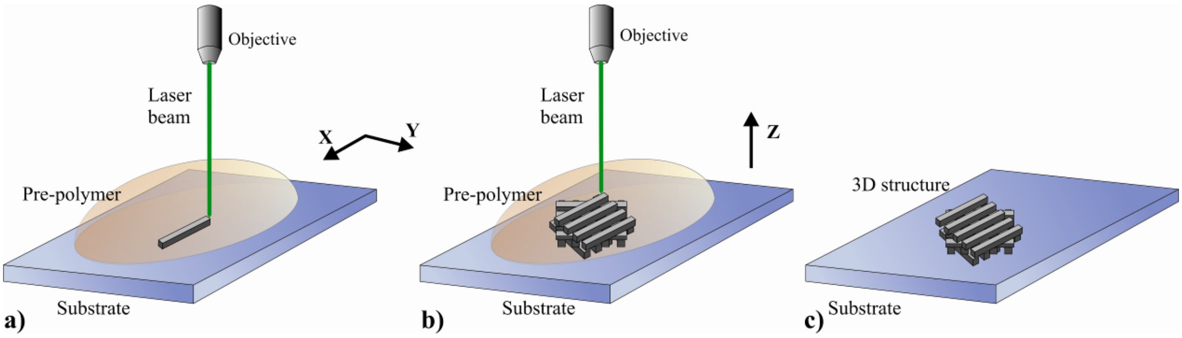

Fig. 2. The LMPP fabrication process: a) femtosecond beam is tightly focused into a droplet of photopolymer and point-by-point solidifies it from the liquid (or gel) state; b) layer-by-layer 3D computer model is materialized; c) after development the unexposed part of the pre-polymer material is removed and 3D structure is revealed

The size of the generated voxels depends on the laser power and exposure time. Their diameter (*d*) and length (*l*) dimensions can be estimated theoretically [14]:

$$d = \frac{\lambda}{NA}\sqrt{\ln\frac{I^2 t\beta\tau v}{I_{th}}}; \qquad (1)$$

$$l = \frac{2z_R}{n}\sqrt{\exp\left(\frac{1}{2}\left(\frac{dNA}{\lambda}\right)^2\right)-1}; \qquad (2)$$

here λ, NA, I, t, τ, v, I_{th}, z_R, n is laser radiation wavelength, numerical aperture, intensity in the vicinity of the focus, exposure time, pulse duration, repetition rate, polymerization threshold intensity, Rayleigh range and refractive index, respectively. β is experimentally obtained constant. Actual value of β depends on various photoinitiator properties, such as two-photon absorption cross-section, quantum yield of absorbed photo-energy conversion to chemical energy (generation of radicals) and concentration of the photoinitiator itself. As shown in Eq. (1) and (2), the dimensions of the voxels can be minimized by optimizing the irradiation dose. Despite achievable sub-100 nm spatial resolution [44, 45] for some application demands, it is more important to have highly reproducible structuring resolution. Moreover, ultra-fine featured structures are extremely sensitive to chemical treatment which complicates microstructure extraction from the solvent [46–48]. Experimentally obtained structuring resolutions in the used materials are provided in the Results section.

2.2. Femtosecond laser three-dimensional nanopolymerization setup

The goal of our experiments was to construct an LMPP system and test it for 3D micro/nanostructuring of photopolymers over a large area. A schematic illustration of the fabrication system is shown in Fig. 3. An Yb:KGW femtosecond laser oscillator (*Pharos, Light Conversion. Co. Ltd.*) was used as an irradiation source. The laser parameters were: 75 fs pulse duration, 200 kW peak power, 1030 nm and 515 nm (second harmonic) central wavelengths, 80 MHz repetition rate. The expanded femtosecond laser beam was guided through the objective, where it was focused into the volume of the photopolymer. The sample was mounted on XYZ wide range positioning stages. The positioning system "*AltSCA-2*" consisted of combined linear motor driven stages [49] (*Aerotech, Inc.*): for XY translation - *ALS130-100* and for Z translation - *ALS130-50*. These stages ensured an overall travelling range of 100 mm into X and Y directions and 50 mm in Z direction and supported a scanning speed of up to 300 mm/s.

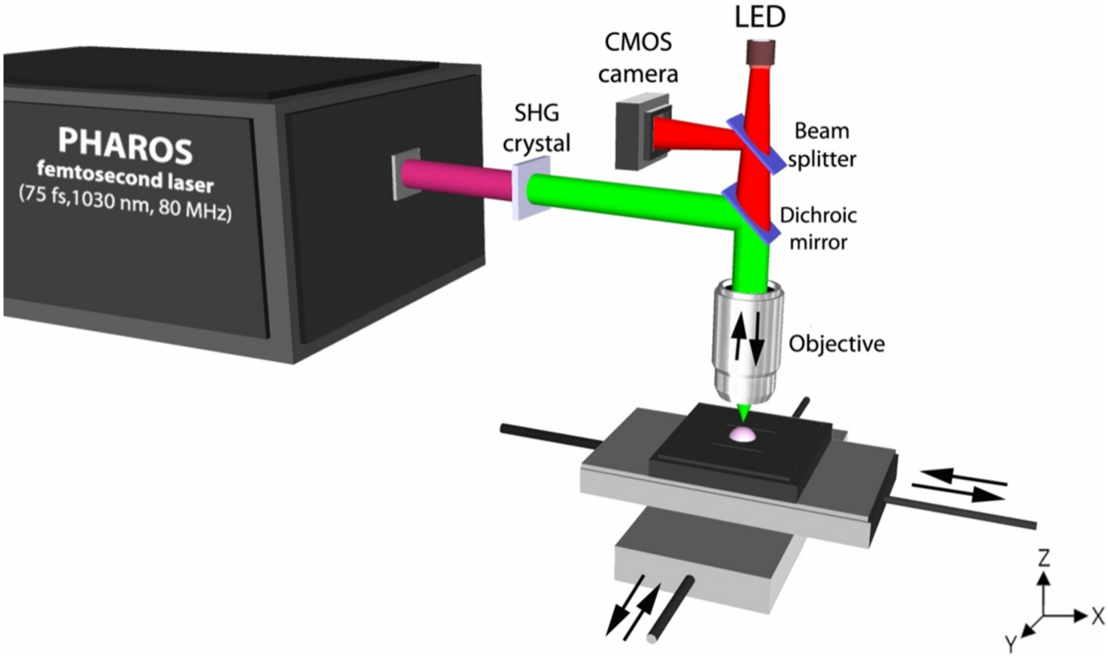

Fig. 3. The LMPP fabrication setup: a femtosecond laser beam is frequency doubled using a non-linear KTP crystal and tightly focused via microscope objective to the pre-polymer droplet spread on the substrate. For fabrication monitoring in real time the LED illumination is guided through the same objective and reflected from the sample to a CMOS camera

Upon irradiation, the pre-polymer underwent a transition from liquid to solid (or from gel to solid) which resulted in a change of the refractive index. This can be used for real time monitoring of the manufacturing process through wide field transmission microscopy. A microscope was built by assembling its main components: an LED source of red light, a CMOS (*mvBlueFOX-M102G, Matrix Vision GmbH*) camera, and a video screen. The ability to image photostructuring process, while performing LMPP, is an important feature for a successful fabrication. It is of utmost importance for the microstructures to be properly anchored to the substrate, so that they could survive the washing step of the unsolidified resin. Control of all equipment was automated via custom made computer software *"3D-Poli"* specially designed for LMPP applications. By moving the sample three-dimensionally, the laser focus position inside the photopolymer changed, thus enabling the writing of complex

3D structures. Structures could be imported from Computer Aided Design (CAD) files or programmed directly. Since it is a serial direct writing approach, it can be time consuming to process huge volumes using highest resolution. In order to increase manufacturing throughput we were able to scale up and speed up the fabrication by changing the laser beam focusing objectives in the range from 100x NA = 1.4 to 8x NA = 0.2, sacrificing resolution (from below 200 nm to up to 20 µm [41]) for manufacturing speed.

Rapid and flexible production is an important factor for the technology to be widely applied. Fabrication duration (*t*) of specific 3D structure can be estimated by Eq. 3:

$$t = \frac{xyzF}{Rv}. \tag{3}$$

Here *x, y* and *z* are the dimensions of the structure*, F* - filling factor, *R* - resolution and *v* is sample scanning speed. It is obvious that increase of the structure size affects the fabrication time dramatically, though appropriately chosen *R* and *F* can reduce it, while scanning speed *v* is a user set parameter and is limited only by the sample positioning stages. For example, it takes 60 h to fabricate a 3D woodpile structure having dimensions of 5 x 5 x 0.02 mm^3 at 1000 µm/s sample scanning speed. In comparison, only 1 h is needed to produce a 2D grid having lateral dimensions of 10 x 10 x 0.05 mm^3 at scanning speed 500 µm/s. Though the fill factors (*F*) (corresponding to total processed volume) of both structures were comparable, the structuring resolution (*R*) was different: 500 nm and 20 µm. Another example could be fabrication of woodpile structure with lateral and axial period of 8 µm and 2 µm, having an overall structure size of 800 x 800 x 40 µm^3 and roughly 0.5 filling ratio. If the sample is translated at 1000 µm/s speed it would take just 25 min to manufacture it using NA = 0.25 objective. In comparison to 7 h, needed for fabrication of identical structure using NA = 1.25 objective.

However, if huge volumes are needed to be polymerized, and high feature resolution is required, a sophisticated strategy to overcome this drawback of time consuming fabrication can be recurred. For example, if a cantilever with a sharp tip is needed, the huge volume cantilever can be fabricated using low NA objective and then, the sharp tip can be fabricated with high NA objective. This combination enables fabrication of relatively large (mm in overall scale) volumetric structures with submicrometer feature resolution.

3. PHOTOSENSITIVE POLYMER MATERIALS

We have used four different negative photoresins in our experiments. Organic-inorganic hybrids SZ2080 (FORTH) [26, 50] and Ormocore b59 (Micro Resist Technology GmbH) [12, 19], acrylate based AKRE19 [24, 39] and biodegradable PEG-DA-258 (PolyEthylenGlycol Di-Acrylate of M.w. = 258, Sigma-Aldrich GmbH) [42, 51]. The pre-polymers were photosensitized by adding 1 wt.% of thioxanthen-9-one or 2-benzyl-2-dimethylamino-1-(4-morpholinophenyl)-butanone-1 photoinitiators (Sigma-Aldrich GmbH). Ormocore b59 was used as received. To increase the functionality of the materials, they can be chemically bonded or doped with inorganic or organic ingredients upon demand [26, 52]. Chemical formulas and developers for the used materials are listed in Table 1. Samples for the fabrication were prepared by drop-casting or spin-coating the pre-polymer on a substrate (cover glass, metal plate or plastic pad). Scanning Electron Microscopy (SEM) was applied to investigate the microstructured scaffolds.

Table 1. Photosensitive pre-polymer materials

Material	**Chemical formula**	**Developer**
SZ2080	$C_4H_{12}SiZrO_2$	methyl isobutyl ketone:isopropanol (1:1)
Ormocore b59	$C_4H_{12}Si_2O_2$	methyl isobutyl ketone:isopropanol (1:1)
AKRE	$C_{18}H_{21}N_3O_9$	ethyl alcohol
PEG-DA-258	$C_8H_{10}O_4$	water

4. RESULTS

4.1. Fabricated three-dimensional microstructures

The possibility to flexibly change the CAD model enables easy modification of the 3D structures' architecture (see Fig. 4). In this way not only overall size, but porosity and fill factor can be controlled precisely. This important feature corresponds to the structures' interaction with light at nano-scale (when feature resolution $R \sim \lambda$) and biocompatibility at micro-scale (when feature resolution is in the range of 10-100 µm). Both of these factors influence the stiffness (flexibility) of the whole structure at macro-scale. The maximal obtained structuring resolution in the used materials is given in Table 2. As it is seen, the aspect ratio of the voxels' dimensions (l/d) varies depending on the chosen material. AKRE19 shrinks, yet ensures highest structuring resolution, SZ2080 shrinks negligibly, thus provides quality structuring, and PEG-DA-258 shrinks the most, resulting to almost symmetrical voxels. As discussed earlier, using the LMPP approach it is straightforward to increase fabrication throughput, sacrificing spatial resolution, by adjusting introduced laser power or focusing optics, if needed [41].

Table 2. Experimentally obtained structuring lateral (d) and longitudinal (l) resolutions in used materials, with writing parameters: pulse energy $E_p = 0.125$ nJ (corresponding to $I = 0.5$ TW/cm^2 intensities when focused with NA = 1.4 microscope objective) and $v = 100$ µm/s sample translation speed

Material	***d*, nm**	***l*, nm**
AKRE19	180	550
SZ2080	220	670
PEG-DA-258	1070	1110

Three-dimensional microstructures, which could be applied as components in micromechanics and microfluidics, were successfully fabricated and shown in Fig. 5. It demonstrates feasibility to produce elements without any geometrical restrains and being intertwined which each other as well as having a hollow inside. Fabricated woodpile photonic crystal and artificial scaffold template (of 10 x 10 mm^2 area) over the large area is shown in Fig. 6. Diffraction pattern from collimated 405 nm light incident to photonic crystal (area – 5 x 5 mm^2, 40 layers) made out of SZ2080 material on the cover glass substrate is seen on the screen (Fig. 6. a)). In Fig. 6. b), a 2.5D grating having 100 µm lateral period and 10 x 10 mm^2 overall size produced on stainless steel surface is shown. Similar structures were tested for the rabbit myogenic stem cell proliferation and results are depicted in Fig. 7. As seen from the pictures, cell growth is widespread and comparable in both scaffold templates manufactured out of Ormocore b59 [17–19] material, well known for biomedical applications, and novel SZ2080 material. This shows a potential to use it for further cell growth and tissue engineering experiments. SZ2080 being designed expressly for LMPP micro/nanostructuring [26, 58] offers much more quality fabrication possibilities.

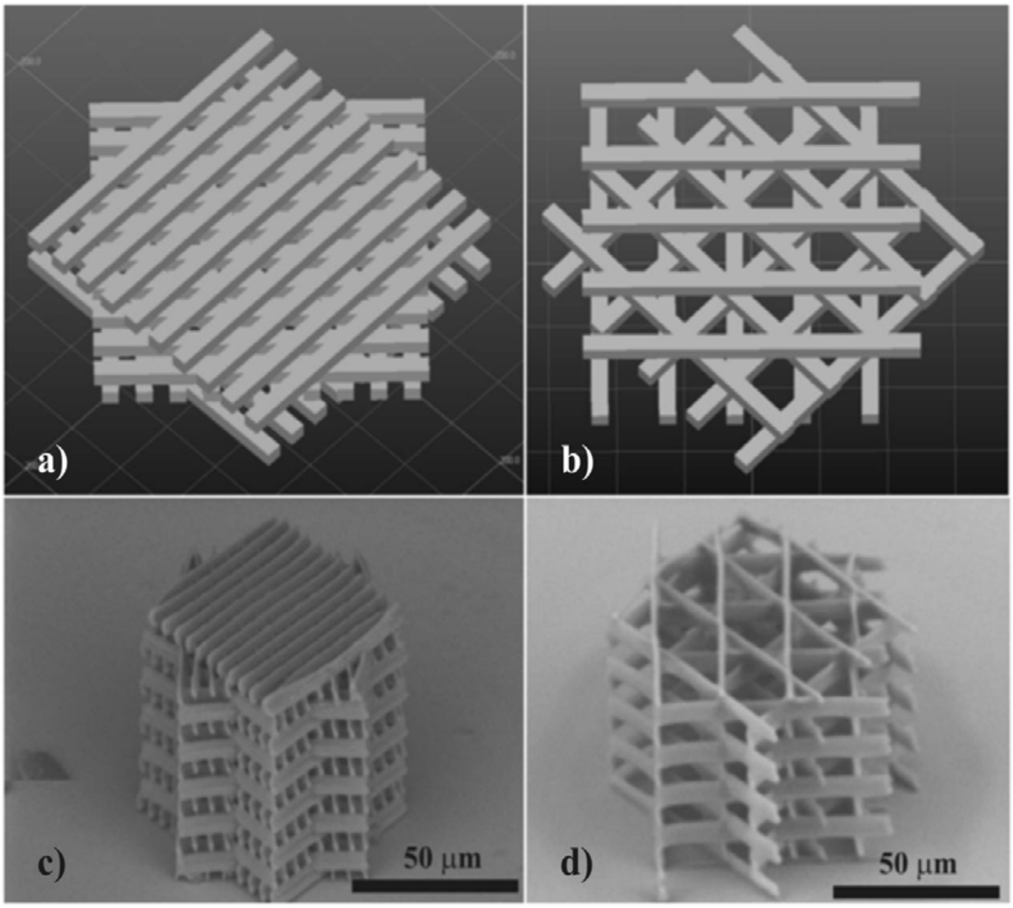

Fig. 4. CAD models (a) and (b), and LMPP fabricated 3D rotating woodpile scaffolds out of SZ2080 material (c) and d)). The structures are of the same size and geometry but having different periodicities, left and right, respectively

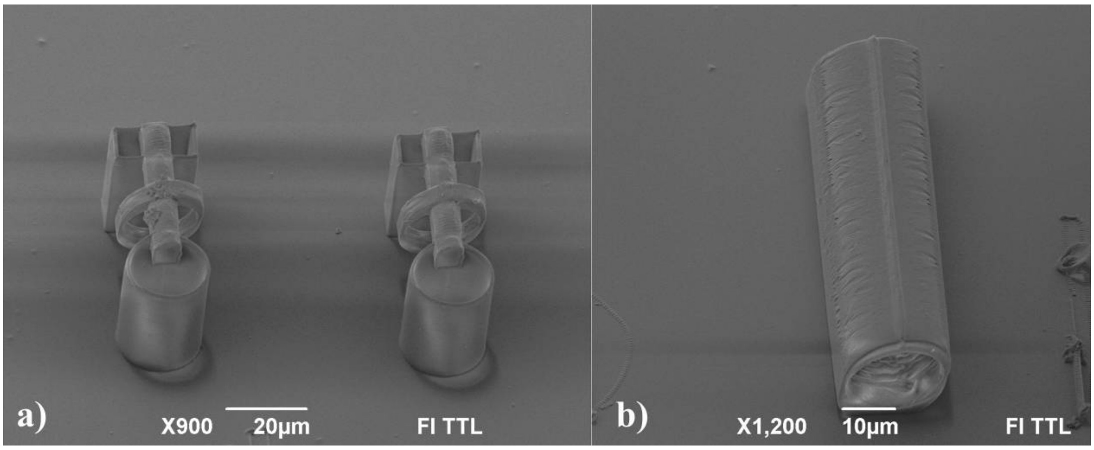

Fig. 5. Components out of SZ2080 for micromechanics and microfluidics: a) a free movable micro-ring on a micro-rod based on rectangular and circular hollow wells, b) micro-tubule having diameter of 20 µm

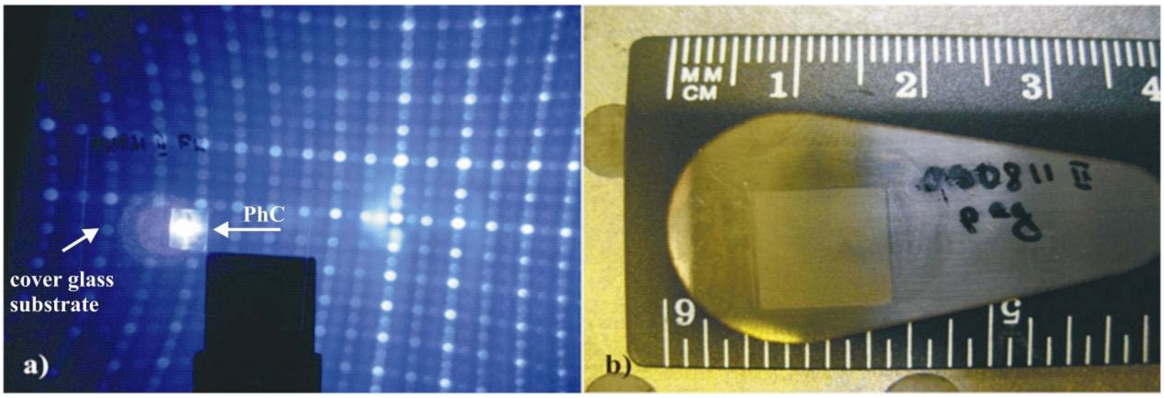

Fig. 6. a) Diffraction pattern of 405 nm light propagating through 5 x 5 x 0.02 mm^3 photonic crystal out of SZ2080, with 2 µm lateral and 0.5 µm longitudinal periods. b) 10 x 10 mm^2 2.5D grating scaffold out of PEG-DA-258 having 100 µm period on stainless steel substrate

4.2. The material and structure biocompatibility tests

The biocompatibility of microstructures as scaffolds for tissue engineering was assessed according to adult stem cell expansion on them. The scaffold provides housing for the cells, therefore, it must ensure a friendly environment in which cell proliferation, differentiation and migration can occur. However, fabrication of artificial tissue is followed by two different kind of mechanism by which the cells interact with the surface. The first of them is cell adhesion to polymeric scaffold and the second is relationship with other cells. Both they determine quality of the artificial tissue.

In our experiments, rabbit muscle-derived adult stem cells were used for cell-based biocompatibility testing of fabricated microstructures. Myogenic stem cells were isolated from skeletal muscle tissue and grown in Iscove’s modified Dulbecco minimum essential medium (Sigma) supplemented with 10% foetal calf serum (Sigma) in multiple polystyrene tissue culture plates (Orange). We have studied the possibility to expand cell growth on the tested scaffolds in two steps. The first portion was stained with vital dye PKH26 (red fluorescent cell membrane label), the second cell part was stained with vital dye PKH67 (green fluorescent cell membrane label). The second portion of the cells was introduced after 72 h after the first seeding. The scaffolds with the cells were examined after 168 h cultivation. The cells on Ormocore b59 as well as on SZ2080 scaffolds seemed to be alive. Both colours of the cells were registered and are shown in Fig. 7. Two colours imagery of the artificial tissue present fully-fledged relations between scaffold-cell as well as cell-cell.

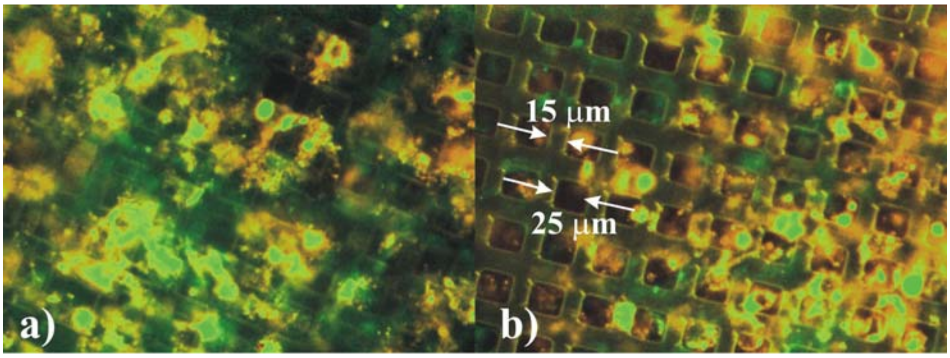

Fig. 7. Optical microscopy images of adult rabbit myogenic stem cells expanded on LMPP microstructured scaffolds out of a) Ormocore b59 and b) SZ2080 materials, respectively. Line thickness and height is 15 μm and pore size is 25 x 25 μm^2. The first layer consists of red cells, and the second layer is of green cells, age of culture is 168 hours. No significant cell growth differences using different materials were found

5. CONCLUSIONS

Direct structuring by LMPP enables rapid and flexible production of 3D micro/nanostructures. We have presented a constructed system based on femtosecond VIS light combined with precise high speed linear motion translation stages designed for fabrication over the large areas. Our fully automated LMPP setup is user friendly for modeling and managing production of 3D structures as well as for easy change of geometrical parameters, if needed. Samples of up to several cm in overall size can be successfully processed by nanometer or micrometer resolution. Point-by-point serial writing is relatively slow in manufacturing structures of huge volume, but change of focusing optics can dramatically increase fabrication throughput while keeping ultra-fine features. Another advantage of the LMPP method is the diversity of usable photopolymers. Materials having good optical, mechanical, chemical characteristics or biocompatibility (biodegradability) can be freely chosen depending on final application. In this paper, we have demonstrated rapid fabrication of 3D microstructured polymers over a large area on glass, plastic and metal substrates. It can be used for further investigations in photonics, microoptics, micromechanics, microfluidics and cell proliferation. Results of stem cell expansion show a potentiality for this technique to be used in tissue engineering experiments in the near future.

6. ACKNOWLEDGEMENTS

This work was supported by the Lithuanian State Science and Studies Foundation Grants B09/08 (Laser Micro-Processing with High Repetition Femtosecond Pulses) and B-07041 (Development of the models to regenerate heart structures employing stem and specialized cells also biological tissues) as well as The research leading to these results has received funding from the EC's Seventh Framework Programme (LASERLAB-EUROPE, grant agreement No 228334, OPTOBIO). The authors would like to thank the Erasmus internship program for H. Gilbergs' internship grant. We gratefully acknowledge M. Farsari (Institute of Electronic Structure and Laser, Foundation for Research and Technology Hellas, Heraklion, Crete, Greece, bmm@iesl.forth.gr) for providing zirconium containing sol-gel hybrid photosensitive material SZ2080. Lastly, authors are grateful to dr. A. Ovsianikov (Nanotechnology Department, Laser Zentrum Hannover, Hanover, Germany) and A. Gaidukevičiūtė (Institute of Electronic Structure and Laser, Foundation for Research and

Technology Hellas, Heraklion, Crete, Greece) for fruitful discussions regarding LMPP fabrication.

REFERENCES

1. P.P. Naulleau, C.N. Anderson, J. Chiu, P. Denham, S. George, K.A. Goldberg, M. Goldstein, B. Hoef, R. Hudyma, G. Jones, C. Koh, B. La Fontaine, A. Ma, W. Montgomery, D. Niakoula, J. Park, T. Wallow and S. Wurm. 22-nm Half-pitch extreme ultraviolet node development at the SEMATECH Berkeley microfield exposure tool // Microelectron. Eng. 86(4-6), 2009, p.448–455.
2. G. R. Sunne. Electron Beam Lithography for Nanofabrication // PhD thesis, University of Barcelona, Barcelona, 2008, p. 17–21.
3. E. Di Fabrizio, R. Fillipo, S. Cabrini, R. Kumar, F. Perennes, M. Altissimo, L. Businaro, D. Cojac, L. Vaccari, M. Prasciolu and P. Candeloro. X-ray lithography for micro- and nano-fabrication at ELETTRA for interdisciplinary applications // J. Phys.: Condens. Matter 16(33), 2004, p. 3517-3535.
4. H. Schift. Nanoimprint lithography: An old story in modern times? A review // J. Vac. Sci. Technol. B 26(2), p. 458–480, Mar/Apr (2008).
5. M. Walther, A. Ortner, H. Meier, U. Löffelmann, P. J. Smith and J. G. Korvink. // Terahertz metamaterials fabricated by inkjet printing”, Appl. Phys. Lett. 95(25), 251107, 2009.
6. T. Boland, X. Tao, B.J. Damon, B. Manley, P. Kesari, S. Jalota and S. Bhaduri. Drop-on-demand printing of cells and materials for designer tissue constructs // Mat. Sci. Eng. C 27(3), p. 2007, p. 372–376.
7. H. Benkreira and M. I. Khan. Air entrainment in dip coating under reduced air pressures // Chem. Eng. Sci. 63(2), 2008, p. 448–459.
8. K.H. Tan, C.K. Chua, K.F. Leong, C.M. Cheah, P. Cheang. M.S. Abu Bakar and S. W. Cha. Scaffold development using selective laser sintering of polyetheretherketone-hydroxyapatite biocomposite blends // Biomaterials 24(18), 2003, p. 3115–3123.
9. S. Maruo, O. Nakamura and S. Kawata. Three-dimensional microfabrication with two-photon-absorbed photopolymerization // Opt. Lett. 22, 1997, p. 132–134.
10. V. Mizeikis, K. K. Seet, S. Juodkazis and H. Misawa. Three-dimensional woodpile photonic crystal templates for the infrared spectral range // Opt. Lett. 29, 2004, p.2061–2063.
11. M. Deubel, G. von Freymann, M. Wegener, S. Pereira, K. Busch and C. M. Soukoulis. Direct laser writing of three-dimensional photonic-crystal templates for telecommunications // Nat. Mater. 3(7), 2004, p. 444-447.
12. J. Serbin, A. Ovsianikov and B. Chichkov. Fabrication of woodpile structures by two-photon polymerization and investigation of their optical properties // Opt. Express 12, 5221-5228 (2004).
13. R. Guo, S. Xiao, X. Zhai, J. Li, A. Xia and W. Huang. Micro lens fabrication by means of femtosecond two photon photopolymerization // Opt. Express 14, 810-816 (2006).
14. M. Malinauskas, H. Gilbergs, A. Žukauskas, V. Purlys, D. Paipulas and R. Gadonas. A femtosecond laser-induced two-photon photopolymerization technique for structuring microlenses // J. Opt. 12(3), 2010, 035204.
15. S. Maruo, A. Takaura and Y. Saito. Optically driven micropump with a twin spiral microrotor // Opt. Express 17, 2009, 18525-18532.

16. D. Wu, Q. D. Chen, L. G. Niu, J. N. Wang, J. Wang, R. Wang, H. Xia and H. B. Sun. Femtosecond laser rapid prototyping of nanoshells and suspending components towards microfluidic devices // Lab. Chip. 9(16), 2009, 2391–2394.
17. R. J. Narayan, C. Jin, A. Doraiswamy, I. N. Mihailescu, M. Jelinek, A. Ovsianikov, B. N. Chichkov and D. B. Chrisey. Laser processing of advanced bioceramics // Adv. Eng. Mater. 7(12), 2005, 1083–1098.
18. A. Ovsianikov, B. Chichkov, O. Adunka, H. Pillsbury, A. Doraiswamy and R. J. Narayan. Rapid prototyping of ossicular replacement prostheses // Appl. Surf. Sci. 253(15), 2007, 6603-6607.
19. A. Ovsianikov, S. Schlie, A. Ngezahayo, A. Haverich and B. N. Chichkov. Two-photon polymerization technique for microfabrication of CAD-designed 3D scaffolds from commercially available photosensitive materials // J. Tissue. Eng. Regen. Med. 1, 2007, p. 443–449.
20. F. Claeyssens, E. A. Hasan, A. Gaidukevičiūtė, D. S. Achilleos, A. Ranella, C. Reinhardt, A. Ovsianikov, X. Shizhou, C. Fotakis, M. Vamvakaki, B. N. Chichkov and M. Farsari. Three-Dimensional Biodegradable Structures Fabricated by Two-Photon Polymerization // Langmuir 25(5), 2009, p. 3219-3223.
21. Y. M. Ha, J. W. Choi, S. H. Lee. Mass production of 3-D microstructures using projection Microstereolithography // J. Mec. Sci. and Technol. 22(3), 2008, 5154-521.
22. I. B. Park, Y. M. Ha and S. H. Lee. Cross-section segmentation for improving the shape accuracy of microstructure array in projection Microstereolithography // Int. J. Adv. Manuf. Technol. 46, 151–161(2010).
23. D. Y. Yang, S. H. Park, T. W. Lim, H. J. Kong, S. W. Yi. Yang, H. K. and Lee, K. S., “Ultraprecise microreproduction of a three-dimensional artistic sculpture by multipath scanning method in two-photon photopolymerization // Appl. Phys. Lett. 90(1), 013113 (2007).
24. M. Malinauskas, H. Gilbergs, V. Purlys, A. Žukauskas, M. Rutkauskas and R. Gadonas. Femtosecond laser-induced two-photon photopolymerization for structuring of micro-optical and photonic devices // Proc. SPIE 7366, 736622 (2009).
25. K. E. Gonsalves, L. Merhari, H. Wu and Y. Hu. Organic-Inorganic Nanocomposites: Unique Resists for Nanolithography // Adv. Mater. 13(10), 703–714, (2001).
26. I. Sakellari, A. Gaidukevičiūtė, A. Giakoumaki, D. Gray, C. Fotakis, M. Vamvakaki, M. Farsari, C.Reinhardt, A.Ovsianikov, B. N. Chichkov. Direct laser writing of photonic nanostructures // Proc. SPIE 7392, 73920Y (2009).
27. T. Tanaka, A. Ishikawa and S. Kawata. Two-photon-induced reduction of metal ions for fabricating three-dimensional electrically conductive metallic microstructure // Appl. Phys. Lett. 88(8), 081107 (2006).
28. V. Mizeikis, S. Juodkazis, R. Tarozaitė, J. Juodkazytė, K. Juodkazis and H. Misawa. Fabrication and properties of metalo-dielectric photonic crystal structures for infrared spectral region // Opt. Express 15, 8454-8464 (2007).
29. M. S. Rill, C. Plet, M. Thiel, I. Staude, G. von Freymann, S. Linden and M. Wegener. Photonic metamaterials by direct laser writing and silver chemical vapour deposition // Nat. Mater. 7, 543 - 546 (2008).
30. L. Vurth, P. Baldeck, O. Stephan and G. Vitrant. Two-photon induced fabrication of gold microstructures in polystyrene sulfonate thin films using a ruthenium(II) dye as photoinitiator // Appl. Phys. Lett. 92(17), 171103 (2008).
31. S. H. Park, T. W. Lim, D. Y. Yang, R. H. Kim and K. S. Lee. Improvement of Spatial Resolution in Nano-Stereolithography Using Radical Quencher // Macromol. Res. 14(5), 559–564 (2006).

32. W. Haske, V.W. Chen, J.M. Hales, W. Dong, S. Barlow, S.R. Marder and J.W. Perry. 65 nm feature sizes using visible wavelength 3-D multiphoton lithography // Opt. Express 15(6), 3426–3436 (2007).
33. X. -Z. Dong, Z. S. Zhao and X. M. Duan. Improving spatial resolution and reducing aspect ratio in multiphoton polymerization nanofabrication // Appl. Phys. Lett. 92(9), 091113 (2008).
34. http://www.nanoscribe.de/
35. http://www.lzh.de/sites/default/files/brochures/machinesfor2and3dmicroandnanotechnology.pdf
36. http://www.newport.com/file_store/Optics_and_Mechanics/AppsNote37.pdf
37. http://www.teemphotonics.com/products/microfab.html
38. S. Passinger, A. Ovsianikov, R. Kiyan, C. Reinhardt, A. Ostendorf and B. N. Chichkov. Two-Photon Polymerization for industrial applications // Proc. of LPM2007-the 8th International Symposium on Laser Precision Microfabrication, (2007).
39. M. Malinauskas, V. Purlys, M. Rutkauskas and R. Gadonas. Two-photon polymerization for fabrication of three-dimensional micro- and nanostructures over a large area // Proc. SPIE 7204, 72040C (2009).
40. J. Stampfl, R. Inführ, K. Stadlmann, N. Pucher, V. Schmidt and R. Liska. Materials for the fabrication of optical waveguides with two photon photopolymerization // Proc. of the Fifth International WLT-Conference on Lasers in Manufacturing, Munich, (2009).
41. M. Malinauskas, V. Purlys, M. Rutkauskas, A. Gaidukevičiūtė and R. Gadonas. Femtosecond Visible Light Induced Two-Photon Photopolymerization for 3D Micro/Nanostructuring in Photoresists and Photopolymers // Lithuanian J. Phys., to be printed (2010).
42. M. Malinauskas, P. Danilevičius, D. Baltriukienė, M. Rutkauskas, A. Žukauskas, Ž. Kairytė, G. Bičkauskaitė, V. Purlys, D. Paipulas, V. Bukelskienė and R. Gadonas. 3D artificial polymeric scaffolds for stem cell growth fabricated by femtosecond laser // Proc. of Northern Optics 2009 conference to be printed in special issue Lithuanian J. Phys., (2010).
43. M. Malinauskas, V. Purlys, A. Žukauskas, M. Rutkauskas, P. Danilevičius, D. Paipulas, G. Bičkauskaitė, L. Bukelskis, D. Baltriukienė, R. Širmenis, A. Gaidukevičiūtė, V. Bukelskienė, R. Gadonas, V. Sirvydis and A. Piskarskas. Large Scale Laser Two-Photon Polymerization Structuring for Fabrication of Artificial Polymeric Scaffolds for Regenerative Medicine // Proc. of ICO-Photonics: Emerging Trends & Novel Materials in Photonics 2009, to be printed (2010).
44. K. Takada, H. B. Sun and S. Kawata. The study on spatial resolution in two-photon induced polymerization // Proc. SPIE 6110, 61100A (2006).
45. Y. Li, H. Cui, F. Qi, H. Yang and Q. Gong. Uniform suspended nanorods fabricated by bidirectional scanning via two-photon photopolymerization // Nanotechnology 19, 375304 (2008).
46. S. H. Park, K. H. Kim, T. W. Lim, D. Y. Yang and K. S. Lee. Investigation of three-dimensional pattern collapse owing to surface tension using an imperfection finite element model // Microelectron. Eng. 85(2), 432 - 439 (2008).
47. Q. Sun, S. Juodkazis, N. Murazawa, V. Mizeikis and H. Misawa. Freestanding and movable photonic microstructures fabricated by photopolymerization with femtosecond laser pulses // J. Micromech. Microeng. 20, 035004 (2010).
48. M. Malinauskas, G. Bičkauskaitė, M. Rutkauskas, D. Paipulas, V. Purlys and R. Gadonas. Self-Polymerization of Nano-Fibers and Nano-Membranes Induced by Two-Photon Absorption // Proc. of Northern Optics 2009 conference to be printed in special issue Lithuanian J. Phys., (2010).

49. http://www.altechna.com/
50. A. Ovsianikov, J. Viertl, B. Chichkov, M. Oubaha, B. MacCraith, I. Sakellari, A. Giakoumaki, D. Gray, M. Vamvakaki, M. Farsari and C. Fotakis. Ultra-Low Shrinkage Hybrid Photosensitive Material for Two-Photon Polymerization Microfabrication // ACS Nano 2(11), 2257–2262 (2008).
51. A. Ovsianikov, B. N. Chichkov, M. Malinauskas, S. Schlie, A. Ngezahayo, S. Gittard, R. Narayan. Two-photon polymerization of poly(ethylene glycol) materials for biomedical applications // (submited).
52. A. Žukauskas, M. Malinauskas, L. Kontenis, V. Purlys, D. Paipulas, M. Vengris and R. Gadonas. Organic Dyes Doped Microstructures for Optically Active Functional Devices Fabricated via Two-Photon Polymerization Technique // Proc. of Northern Optics 2009 conference to be printed in special issue Lithuanian J. Phys., (2010).

CYSENI 2010, May 27–28, Kaunas, Lithuania
ISSN 1822-7554, www.cyseni.com

NONLINEAR HIGH-DOSE, LOW-ENERGY ION IMPLANTATION MODEL

D. Maželis
Vytautas Magnus University
K. Donelaicio str. 58, LT-44248, Kaunas – Lithuania
Phone: +370 672 23944
Email: darius.mazelis@fc.vdu.lt

ABSTRACT

The paper presents the study of ion high dose implantation effects on the distribution of implanted ions and atoms of solid. The study is based on the analysis of rate equations describing simultaneous action of different processes, such as ion implantation, preferential ion sputtering, adsorption, cascade mixing and thermal diffusion. Emphasis is made on the studies of distribution profiles of implanted species. The existing models are based on assumptions about continuity of solid and fulfilment of normalization condition. They do not consider the facts that composition of solid changes during ion implantation and implanted atoms initiate growth of implanted layer. It is shown that these assumptions can be source of inaccuracies in calculations of profiles of implanted atoms.

A new alternative model is proposed. Kinetic equations for ion implantation and relaxation processes are modified. Changes of composition of material during the implantation and process of the target growth due to accommodation of implanted species are taken into account. Obtained calculation results are compared to the existing models.

Keywords: Ion implantation, nonlinear model, distribution profiles

1. INTRODUCTION

The understanding of processes on the surface of solids is necessary condition for an interpretation of various surface properties. With the help of ion beams the surface properties can be controllable handled. From one side, ion beams can be used as a tool to get fundamental understanding about the surface structure and composition, from the other side, as an instrument to change surface properties for different applications. The answer to the question, how do the properties of solid after high-flux, low-energy ion irradiation at elevated temperature change approaching the surface from the bulk is still the object of intensive discussions.

During ion beam interaction with solids, surface properties of material change as result of various ion beam initiated processes, such as ion implantation, preferential ion sputtering, adsorption, cascade mixing and thermal diffusion [1]. Each of these processes are well investigated, there are many models describing these processes separately. For example SRIM program [2] is widely used that can calculate behavior of different energy ions implanted into different materials. But this program cannot simulate several interaction processes acting simultaneously and to obtain distribution profiles of implanted species across modified surface layer after ion irradiation. The aim of this work is to develop a common model of ion beam interaction with solids. Ion implantation model described in this paper includes some new elements regarding modeling of relaxation processes after insertion of implanted atoms in the solid and may be adapted to the general model described in detail in [1, 3].

2. BASIC OF ION IMPLANTATION

Ion implantation is a materials engineering process by which energetic ions can be implanted into another solid, thereby changing the physical properties of the solid [4]. It is thermodynamically non equilibrium process. The energy of the ions, as well as the ion species and the composition of the target determine the depth of penetration of the ions in the solid. A monoenergetic ion beam will generally have a broad depth distribution. The mean penetration depth is called project range R_p. The mean range can vary from a few nanometers to a micrometer. The number of incident ions to the surface of solid is called fluence, F, while dose, D, is equal to the number of ions which cross the surface of the solid [1]. In this paper we will assume that F=D, because only ions implanted into the bulk are considered in this work. Moving in solid ions lose their energy by collisions with the target atoms and energy losses resulting in constant ion stopping as a result of interaction with target electrons and nucleus. For large ion energies, electronic stopping is dominant. With the decrease of incident ion energy, the nuclear energy losses become prevailing. Penetration length of ion in material can be found in the assessment of its energy losses:

$$R(E)=\int_0^E \frac{dE}{N(S_n(E)+S_e(E))}\,, \tag{1}$$

where N – concentration of material atoms, $S_n(E)$ – cross section of nuclear stopping, $S_e(E)$ – cross section of electronic stopping. But the length of penetration trajectory is not equal to the mean implantation range, because after collision with atom of solid, ion may be recoiled in all directions. Therefore, distribution of implanted atoms has a statistical nature. In the simplest case the profile of the implanted atoms in the solid can be presented as a Gaussian distribution [3]. In this work, the distribution profile of implanted ions was obtained by the computer program SRIM2010 [2].

3. MODELS

3.1 Main assumptions of the existing ion implantation model

Existing model of ion implantation is widely used for many practical applications. All equations and parameters of the model are comprehensively presented in literature [1, 3]. There are considered the applications of the model for simulation of experimental results of ion implantation and other implantation induced processes in the studies of interaction of first wall materials of thermonuclear reactor with plasma and formation of metal hydrides [5, 6].

Concentration of implanted species changes due to ion implantation as

$$\left(\frac{dc_i^{(K)}}{dt}\right)_{IMP.} = w_i^{(K)}\cdot i_i\,, \tag{2}$$

where $w_i^{(K)}$ – the frequency probability of implantation of i type ion into the K-th monolayer of target, i_i – the flux of incident i type ions expressed in relative units.

Ion implantation process increases relative concentration of implanted component in target. It means that condition of normalization for relative concentrations

$$\sum_i c_i = 1 \tag{3}$$

is not held. That’s why process of relaxation has to be introduced. A part of implanted i atoms from K-th monolayer is moved into K+1 monolayer:

$$\Delta c_i^{(K)} = c'^{(K)}_i \cdot \left(1 - \frac{1}{\sum_i c'^{(K)}_i} \right), \tag{4}$$

where $c'^{(K)}_i$ is concentration obtained by equation (2). The final concentration of i atoms in the K-th monolayer after implantation and relaxation processes is

$$c_i^{(K)} = c_{i_{notnorm}}^{(K)} - \Delta c_i^{(K)}, \tag{5}$$

where $\Delta c_i^{(K)}$ is total amount of surplus i type atoms in the K-th monolayer, expressed in the following way

$$\Delta c_i^{(K)} = c_{i_{notnorm}}^{(K)} \left(1 - \frac{1}{\sum_i c_{i_{notnorm}}^{(K)}} \right). \tag{6}$$

In this equation, $c_{i_{notnorm}}^{(K)}$ is equal to concentration, obtained not only due to implantation, but also due to relaxation from K-1 monolayer:

$$c_{i_{notnorm}}^{(K)} = c'^{(K)}_i + \Delta c_i^{(K-1)}. \tag{7}$$

3.2 Nonlinear ion implantation model

The penetration range of implanted atoms depends on the composition of solid. For targets of different elemental composition, the energy losses of ions and theirs penetration range varies. In the model, the distribution of implanted atom ion is defined by implantation frequency probability $w_i^{(K)}$ for different target monolayers K. The i atom concentration in the K-th monolayer changes due to ion implantation calculated by equations presented above can give significant inaccuracies in determination of penetration depth for the case of high-dose ion implantation when the target composition changes during the process, but implantation probability $w_i^{(K)}$ stays unchanged.

Implantation probability of carbon ion into K-th monolayer as a function of magnesium monolayer number was calculated by the stopping and range of ions in material software package SRIM2010. Obtained results presented in Fig. 1 (curve 1). After intensive irradiation by carbon ions target near surface layer may be saturated by carbon atoms. Implantation probability profile of carbon ions in carbon material calculated by SRIM2010 is also shown in Fig. 1 (curve 2).

As it is shown in the Fig. 1, the mean carbon ion implantation range in magnesium is approximately 18 monolayers, while in isotropic carbon, almost two times smaller, about 10 monolayers.

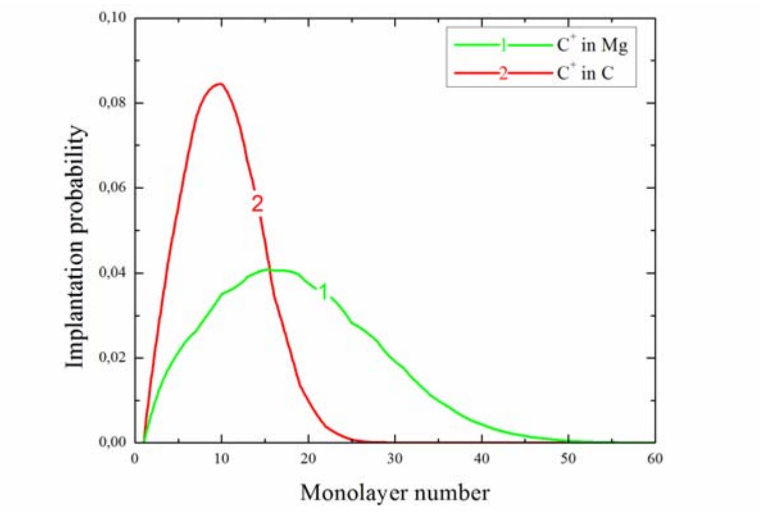

Fig. 1. Distribution profiles of carbon ions in magnesium (curve 1) and isotropic carbon (curve 2) targets, as a function of target monolayer number. Energy of carbon ions – 1.0 keV

In the modified model, it is considered that the target composition changes due to ion implantation and it may be expressed as:

$$\left(\frac{dc_i^{(K)}}{dt}\right)_{IMPL.} = i_i \sum_j \left(w_{ij}^{(K)} \frac{\sum\limits_K c_j^{(K)}}{K} \right), \tag{8}$$

where i_i is flux of i type ions, $w_{ij}^{(K)}$ – implantation probability of i ions into the K-th monolayer of target, when target is composed of j atoms.

The process of relaxation described in existing models transfers part of target atoms into deeper monolayers. In this way the growth of target due to ion implantation is neglected. In the modified model, the part of target atoms from K-th monolayer is transferred into K-1 monolayer:

$$\left(\frac{dc_i^{(K-1)}}{dt}\right)_{REL.} = c_i^{(K)} \left(1 - \frac{1}{\sum\limits_i c_i^{(K)}} \right). \tag{9}$$

Normalization, that makes the sum of concentrations of all components in one monolayer equal to 1, gives

$$\left(\frac{dc_i^{(K)}}{dt}\right)_{NORM.} = c_i^{(K)} \left(\frac{1}{\sum\limits_i c_i^{(K)}} \right). \tag{10}$$

When the part of target atoms driven by the relaxation process arrives into the first monolayer, they start to form a new monolayer on the top introducing some atoms into it from the bulk. Some atoms part of the first monolayer become atoms of the second monolayer. It does not change composition of the first monolayer, but the other monolayers, starting from the second, must be recalculated by equation

$$\left(\frac{dc_i^{(K)}}{dt}\right)_{\text{MONOL.RECAL.}} = \left(c_i^{(K-1)} - c_i^{(K)}\right)\left(\sum_i \left(c_i^{(1)}\right) - 1\right), \tag{11}$$

where $c_i^{(1)}$ is not normalized concentration of i atoms of the first monolayer.

4. COMPARISON OF THE MODELS AND DISCUSSION

The computation program was built on the basis of ideas disclosed above. FORTRAN90 was used as programming language. Classical fourth-order Runge-Kutta method was used for numerical solution of models equations.

Probability distribution profiles in dependence on the monolayer depth number for carbon ions implanted in magnesium and carbon calculated by SRIM2010 are shown in the Fig. 1. Flux of carbon ions was assumed equal to 0.1 per one surface atom per second. No other simultaneously acting processes were simulated for the simplicity of obtained results interpretation.

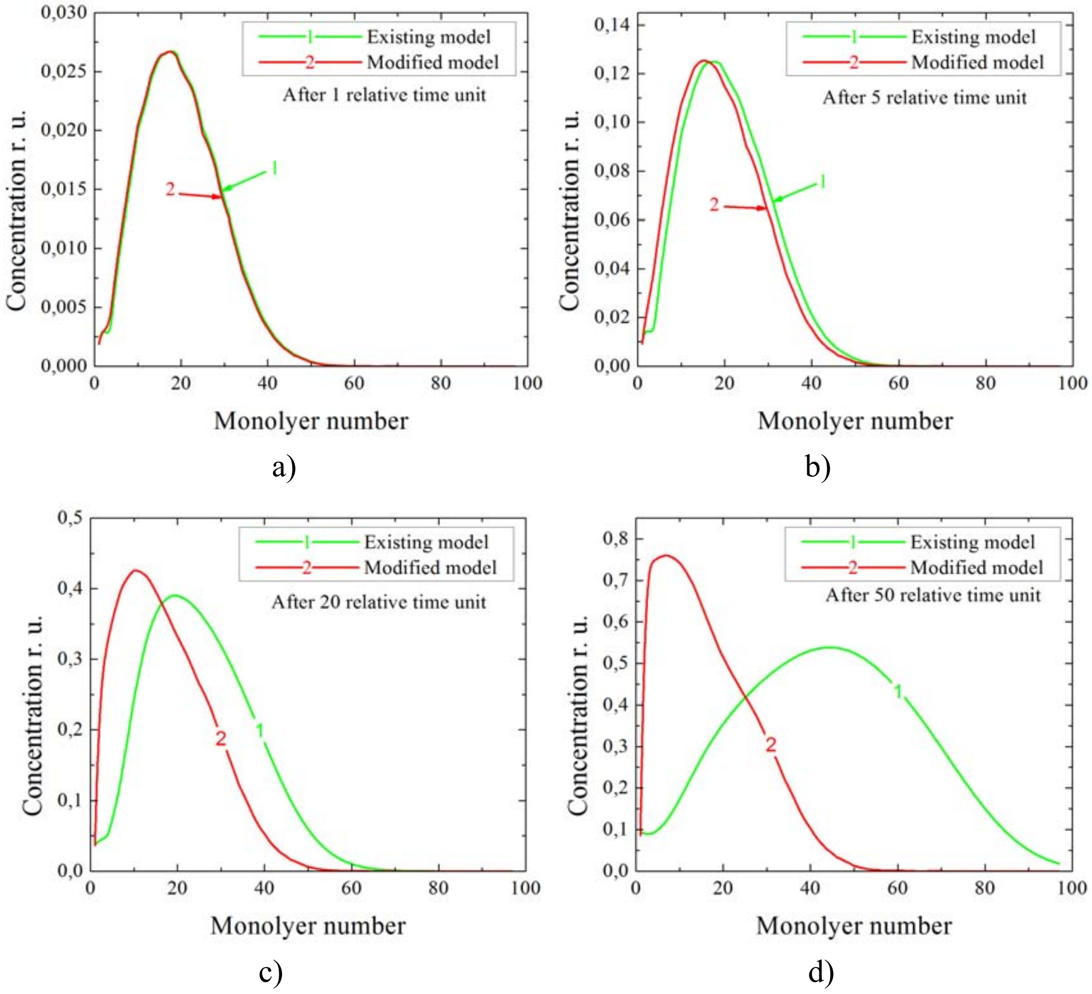

a) b)

c) d)

Fig. 2. Comparison of calculated distribution profiles for different irradiation fluences. Concentration profile obtained according model [1] (curve 1) and modified model (curve 2)

It is easy to see in the Fig. 1, differences between the profiles obtained by different models depend on the dose of implanted atoms. After t=1 (Fig. 2a) when implantation dose is small, there are no noticeable differences between the considered models. Composition of a target is almost unaffected by implanted atoms. Therefore, it can be assumed that a profile of implantation probability is constant during all process. We can see that the mechanism of relaxation does not give an impact in the range of low doses.

After t=20 (Fig. 2c) concentration of implanted atoms becomes large enough and we see differences between results obtained by different models. The concentration peak of implanted atoms obtained by model [1] is much deeper than a concentration peak calculated by modified model. In a case of t=50 (Fig. 3) the depth of concentration profile obtained by existing model is about two times deeper than used calculated profile of implantation probability. Any other except relaxation transport mechanism of implanted atoms was not simulated.

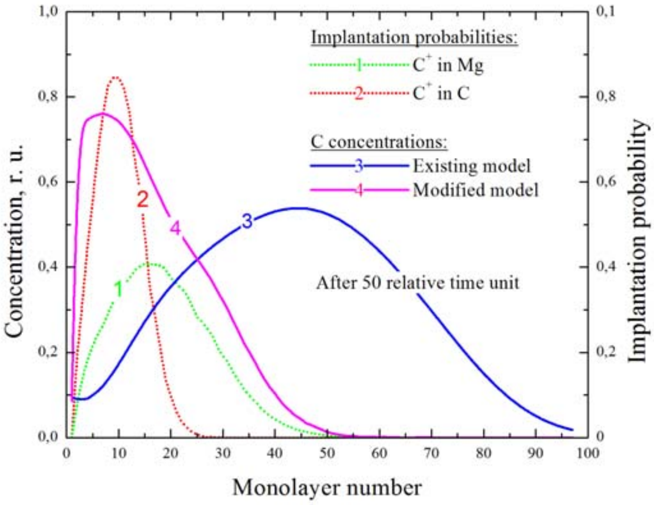

Fig. 3. Comparison of implantation probability profiles of carbon ions into magnesium and carbon (curves 1 and 2, respectively) and calculated distribution profiles of existing and modified models (curves 3 and 4, respectively)

Differences between the distribution profiles of implanted species obtained by existing and modified models can be explained by the differences of implantation probability for different materials. In the existing model implantation probability profile stays constant during all process. In the modified model this profile depends on the composition of target.

In conclusion, new approach for relaxation process in implanted solids is considered. In the case of high fluences and low ion energies, when concentration of implanted atoms is comparable with concentration of matrix atoms, it is suggested to keep continuity of the solid performing relaxation by pushing atoms to the surface rather than into the bulk.

ACKNOWLEDGEMENTS

Author would like to express sincere thank to prof. L. Pranevičius for his support and help to understand subject and prepare this work. Paper author also grateful to PhD M. Povilaitis for his help create program code for models comparison.

REFERENCES

1. PRANEVIČIUS, L. *Coating technology: ion beam deposition.* Warwick, Rhode Island: Satas & Associates, 1993. 451 p. ISBN 0-9637993-0-4.
2. *SRIM - The Stopping and Range of Ions in Matter.* Link to the internet <http://www.srim.org/>
3. GALDIKAS, A., PRANEVIČIUS, L. *Ion beam surface processing: Composition and morphology.* Kaunas: Technologija, 1998. 158 p. ISBN 9986-13-653-9.

4. MILČIUS D., TEMPLIER C., RIVIER J.-P., PRANEVIČIUS L.L., PRANEVIČIUS L. High-flux, low-energy implantation effects on the composition of the altered layer. *Surface and Coatings Technology,* 2002, Vol. 156, p. 214–218.
5. PRANEVIČIUS, L. *New materials for hydrogen storage.* Kaunas: Lithuanian Energy Institute, 2005. 185 p. ISBN 9986-492-86-6.
6. POVILAITIS, M. Simulation of plasma interaction with the first wall of thermonuclear reactor. CYSENI 2008. Proceedings of annual conference of young scientists on energy issues. [CD]. Kaunas: Lithuanian Energy Institute. 2008 May 28–29.

CYSENI 2010, May 27–28, Kaunas, Lithuania
ISSN 1822-7554, www.cyseni.com

IN– AND ACROSS–PLANE CONDUCTIVITY MEASUREMENTS ON YSZ THIN FILMS

E. Navickas[1,2], M. Gerstl[1], J. Fleig[1]
[1] *Institute of Chemical Technologies and Analytics*
Vienna University of Technology
Getreidemarkt 9-164/EC, 1060 Vienna – Austria
[2] *Institute of Materials Science*
Kaunas University of Technology,
Savanoriu 271, 50131 Kaunas – Lithuania
Phone: +370 656 22196
Email: edvinas.navickas@stud.ktu.lt

ABSTRACT

The conductivity of yttria stabilized zirconia (YSZ) bulk materials is well investigated and understood, while the results for the thin film case are contradictory with values varying from one publication to another. The conductivity of thin YSZ films can be measured perpendicular and lateral to the thin film plane. Both types of measurements are important, because they reveal any potential anisotropy of the conductivity due to the microstructural effects of the thin film. In this contribution the in-and across-plane conductivity was measured with impedance spectroscopy by applying a special geometry of micropatterned electrodes. For the in-plane measurements YSZ coatings were synthesized onto sapphire wafers with insulating behavior to both electronic and ionic currents. For the across-plane measurements YSZ thin films were synthesized onto silicon wafers, which have a low electronic resistance. For both measurements thin films of YSZ with thicknesses ranging from 60 nm to 200 nm, were synthesized by pulsed laser deposition (PLD). In- and across–plane conductivity values are discussed in comparison to measurements on a YSZ single crystal.

Keywords: YSZ thin films, ionic conductivity, microelectrodes, conductivity anisotropy, pulsed laser deposition

1. INTRODUCTION

Ceramic ion conducting materials play an important role in fuel cells, batteries, and sensors. Yttrium stabilized zirconium (YSZ) is one of the most important ionic conductors, and used as electrolyte in solid oxide fuel cells (SOFC) due to its ionic conductivity and thermal stability. Bulk properties of YSZ are widely investigated and understood, while results obtained on thin films are still contradictory. The activation energies of the ionic conductivity in thin films vary from one paper to another. A higher conductivity in thin films is discussed in terms of the increased role of interfaces. In some studies it was shown that when decreasing the film thickness the conductivity increases [1, 2]. However, other studies reported that the ionic conductivity is independent of the films thickness [3]. In some publications it was emphasized that due to interfacial effects the conductivity increases for very thin films [1, 2], while in others an effect of the interface was not observed [3]. Most of these studies dealt with the in-plane conductivity and there are much less studies considering the across-plane conductivity in films of nanometer thickness. Most of the studies which investigated the across-plane conductivity used films with a thickness in the micrometer range [4, 5]. Further in- and across-plane conductivity studies could help to evaluate the conductivity anisotropy of YSZ films which, among others may come from the effect of different numbers of grain boudaries and the effect of the interface.

YSZ thin films can be synthesized by various methods, such as chemical vapour deposition [7, 9] ultrasonic spraying [8], electron beam evaporation [10] etc. A very convenient method for thin film deposition in the nanometer range is pulsed laser deposition [11]. In this work thin films of YSZ were prepared by pulsed laser deposition. To investigate the role of the microstructure on the conductivity, thin films were synthesized onto two different substrates. For perpendicular (across-plane) measurements thin films were synthesized onto silicon substrates which have a higher conductivity than YSZ. For the in-plane measurements, YSZ films were deposited onto highly resistive sapphire substrates. The conductivity anisotropy was detemined from the in- and across-plane conductivity measurements by impedance spectroscopy.

2. EXPERIMENTAL

YSZ thin films were prepared by pulsed laser deposition (PLD) onto silicon (100) and sapphire (0001) substrates. For the ablation an eximer KrF laser (248 nm) was used with a beam spot size of 2 cm^2. The repetition rate was 5 Hz, the fluence of the beam was 2 J/cm^2. The laser beam entered the chamber at an angle of 45^0 and hit the rotating YSZ target. The distance between the target and the substrate was 6.3 cm, the oxygen pressure during the deposition 0.4 mbar. The substrates were preheated during the deposition. Heater set temperature during the deposition was 800 ^{o}C. The substrate temperature during the deposition process was also measured with an IR pyrometer. A sketch of the PLD system is shown in Fig. 1. The deposition rate was 1 nm/min. YSZ targets were synthesized by unaxial pressing of 8% Y_2O_3 doped ZrO_2 powder (Tosoh, Japan). Pressed pellets were annealed at 1200 ^{o}C for 10 hours. After annealing the pellets were polished. The thickness of the layers on the silicon wafers was determined by ellipsometry and from scanning electron microscope (SEM) cross section photos.

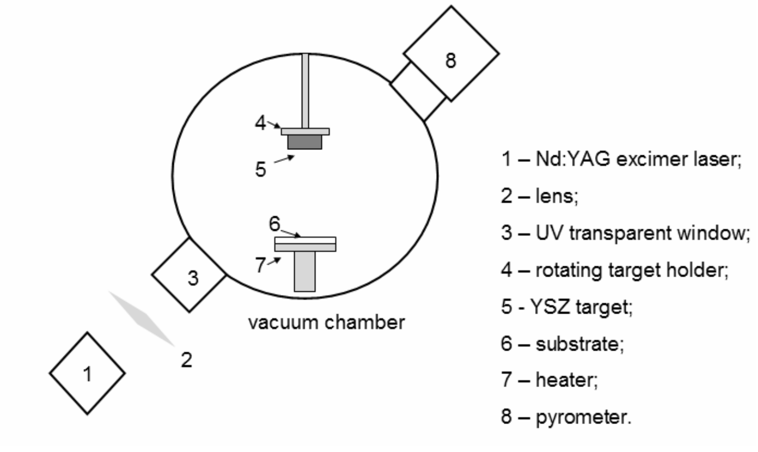

Fig. 1. Pulsed laser deposition system

The phase composition of the synthesized layers was determined by X- ray diffraction method. X-ray diffraction measurements were done with Philips X'Pert (Cu anode, $\lambda = 1.54$ Å) diffractometer. The crystallite size was estimated by using an atomic force microscope (AFM) VEECO nanoscope 5. Electrical properties of the synthesized samples were measured by impedance spectroscopy (Novocontrol Alpha) in a frequency range from 1 Hz to 1 MHz. The measurements were done in the temperature range from 100 ^{o}C to 450 ^{o}C. Fitting of the impedance spectrum was accomplished with the ZView software. To avoid a possible short-circuit through pinholes in the YSZ film circular microelectrodes with different diameters (100, 50 and 40 μm) were used for the perpendicular conductivity measurements. The bottom of the substrate was covered with silver paste. This measurement geometry is shown in Fig. 6a. For the in-plane conductivity measurements two stripe electrodes on top of the YSZ layer were used as shown in Fig. 3a. In both cases micropatterned electrodes were prepared by UV lithography from gold films deposited by magnetron sputtering.

3. RESULTS

3.1. In-Plane Measurements

For the in-plane measurements YSZ thin films on a saphhire substrate were used. XRD measurements are shown in Fig. 2a and demonstrate that YSZ layers exhibiting the cubic phase were sucessfully synthesized. For comparison the XRD pattern of the pure sapphire substrate is also shown in Fig. 2a. The YSZ thin film thickness was estimated from the known deposition rate (200 nm). For the crystallite size evaluation AFM measuremens of the surface morphology were used. YSZ thin films grow with a columnar structure and from the AFM measuments we can see (Fig. 2 b) that the mean crystallite size is approximately 30 nm. Electrical characterization of the samples was done in the AC mode with a microcontact electrode measurement stage. One semicircle was found in impedance spectra (Fig. 3b), and the corresponding resistance includes contributions from both grain and grain boudaries resistances. Separation of the grain and grain boundary conductivity with such a geometry is not possible due to the high stray capacitance of the substrate. Measurements of the impedance were done in the temperature range from 100 ^{0}C up to 550 ^{0}C. The impedance spectrum was fitted with one parallel RQ element, where Q is a constant phase element and R is a resistance. The conductivity of the layer was calculated from the equation $\sigma = L/(R*k*d)$, where L is the distance between the gold electrodes, R = resistance, k = the length of the electrodes, and d = thin film thickness. The calculated conductivities are plotted in the Arrhenius diagram in Fig. 8a.

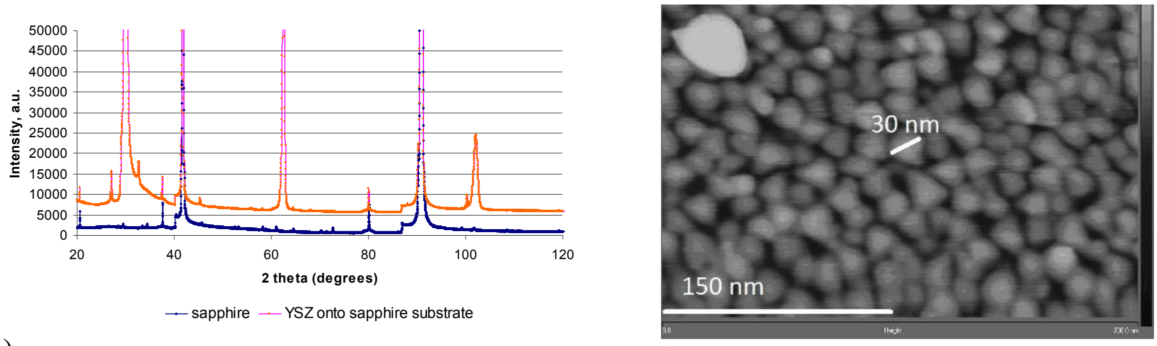

a)

b)

Fig. 2. a) XRD of a YSZ thin film on a substrate and of the pure substrate; b) AFM surface measurements of the YSZ film

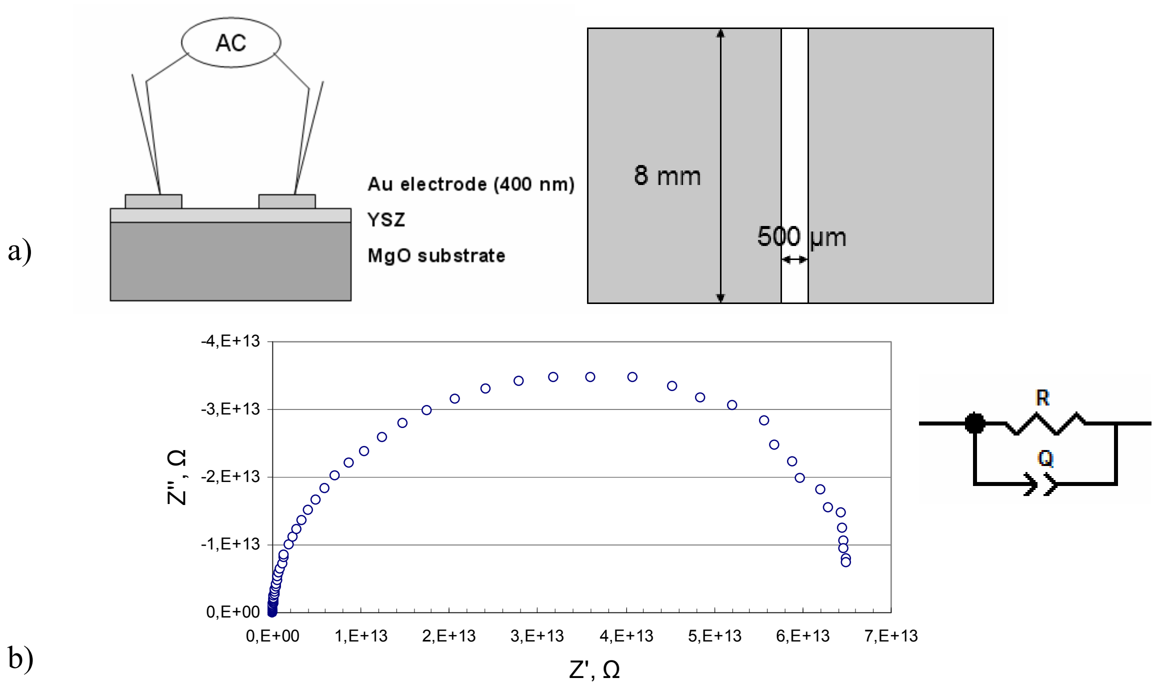

Fig. 3. a) Sketch of the measurement geometry of the in-plane measurements;
b) Impedance spectra of an in-plane measurement at 300 °C

3.2. Across-Plane Measurements

The measurement geometry for the across-plane conductivity measurement is demonstrated in Fig. 6a. For such experiments YSZ layers on silicon wafers are used. During the pulsed laser deposition in oxygen environment it is not possible to avoid oxidation of the silicon wafer, moreover the native silica layer was not removed before the deposition. Hence, an insultating layer exists between YSZ and Si. YSZ films with different ablation times were synthesized to investigate possible conductivity correlations with the film thickness. The thickness of the samples was determined by ellipsometer measurements. To avoid possible errors and uncertainties thickness measurements were performed four times on each sample. It was taken into account that the silicon refractive index is 1.5 and that of YSZ is 2.1. The thicknesses of the YSZ films determined by ellipsometry measurements were 30, 60 and 100 nm. Their structure was again analyzed by XRD and the diffractograms are shown in Fig. 5a.

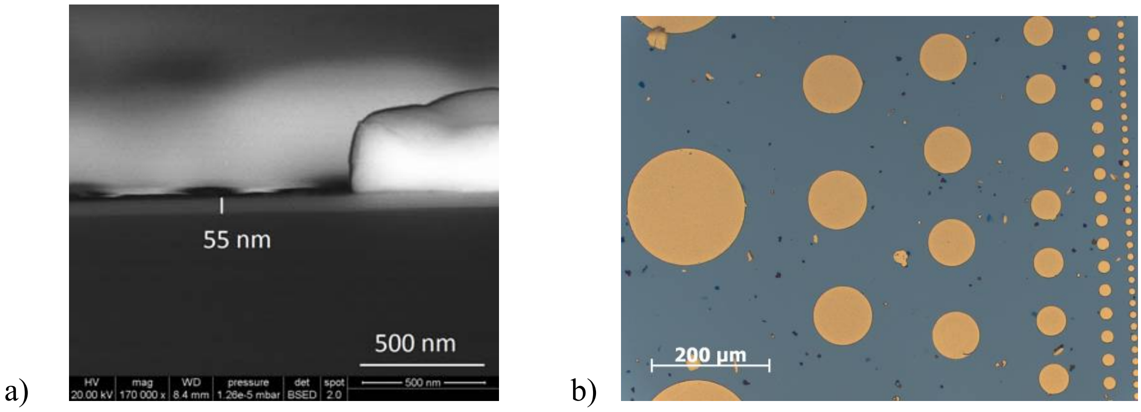

Fig. 4. a) Cross section image of a gold electrode/YSZ thin film/Silicon measured in the SEM back scattering mode; b) micropatterned gold electrodes

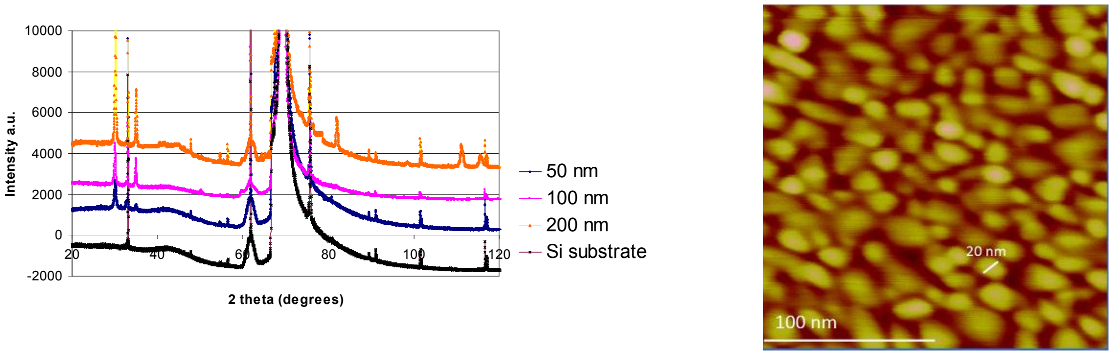

a) b)

Fig. 5. a) XRD patterns of synthesized YSZ thin films onto silicon wafers; b) AFM surface measurements of the film

It can be concluded that a cubic YSZ phase was successfully synthesized onto the silicon wafer. AFM measurements were done to evaluate the crystallite size of the film. Measurements are represented in Fig 5 b and show that the mean width of the columns is 20 nm. To minimize the shortcircuit possibility micropatterned electrodes were used in such across-plane measurements. The corresponding gold electrodes on the YSZ layer are shown in Fig. 4b. Different radius of the circular electrodes were investigated for a better separation of YSZ and Si conductivities.

The impedance measurements were conducted in a frequency range from 1 Hz to 1 MHz. The temperature of the heating table was changed from 100 ^{0}C to 450 ^{0}C. A tungsten needle was attached to the circular gold electrodes, while another one was used to contact the silver counter electrode on the bottom of the sample.

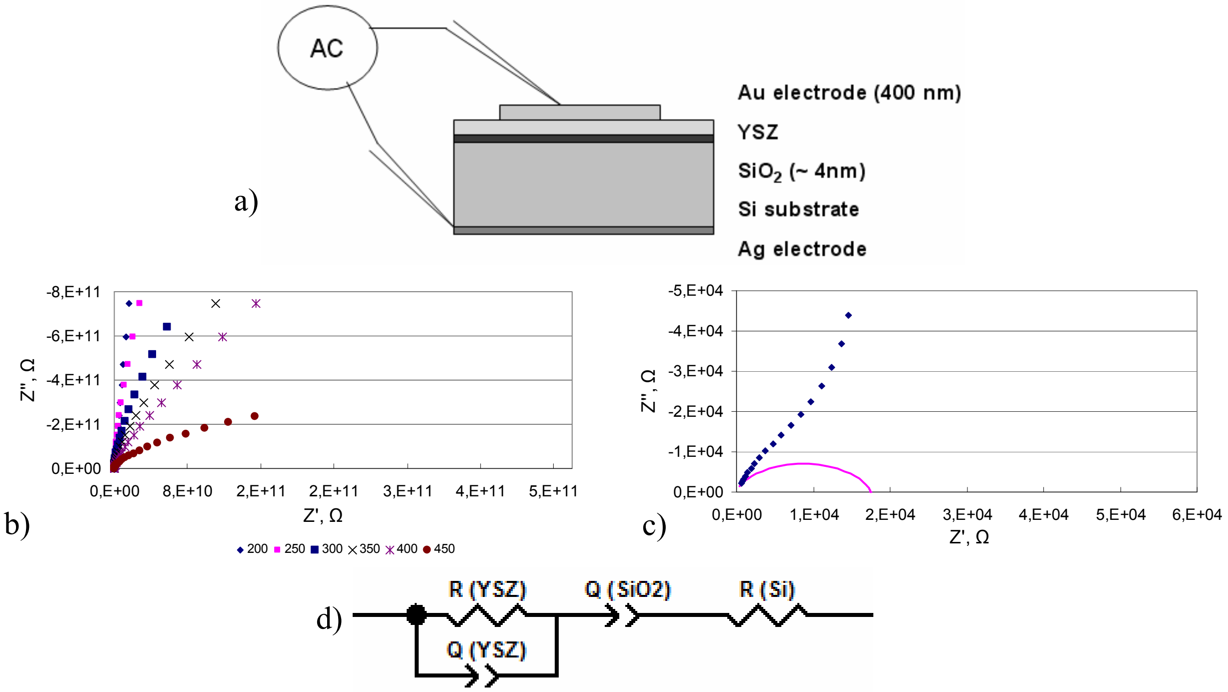

a) b) c) d)

Fig. 6. a) Across-plane measurement sketch of the structure Au/YSZ/SiO2/Si/Ag; b) Across-plane impedance spectra measured for different temperatures (200 ^{0}C – 450 ^{0}C); c) High frequency part of an across-plane impedance spectrum; d) Equivalent circuit for the across-plane measurement

The impedance spectrum shows a strong effect due to a blocking capacitance, which reflects the silica layer (Fig 6 b). In the high frequency range, however, (from 1 MHz to 50 kHz (depending on temperature) a part of a semicircle appears (Fig 6 c), which is the result of ion conduction across the the YSZ film. The impedance spectrum was fitted with a RQ element, which corresponds to the YSZ film, serially connected to the blocking capacitance of silica. The conductivity of silicon, which changes with temperature, was also taken into account by a resistor. (Fig 6d). Across-plane measurements were done for different film thicknesses and different diameters of the circular electrodes. The conductivity of the layer was calculated as $\sigma = d/(\pi * r^2 * R)$, where d is the thickness of the YSZ thin film, r = radius of the circular microelectrode, R = measured resistance. Calculated conductivities correlate with those of YSZ single crystals, independent of the YSZ film thickness (Fig. 9). The blocking capacitance of the silica was constant over time and did not vary with temperature, but changed with the radius of the electrode.

3.3. Across-Plane Impedance Simulation

Additional impedance simulations were done with the equivalent circuit shown in Fig. 6d using the ZView software. The simulation results show how the separability of YSZ and silica becomes worse with increasing silica layer thickness. By changing the silica layer thickness the silica capacitance is modified. It is seen in Fig. 7b that for an additional silica layer of 79 nm thickness, there is hardly any possibility to separate the two phases in order to see an effect of YSZ, i.e. to perform successful perpendicular measurements.

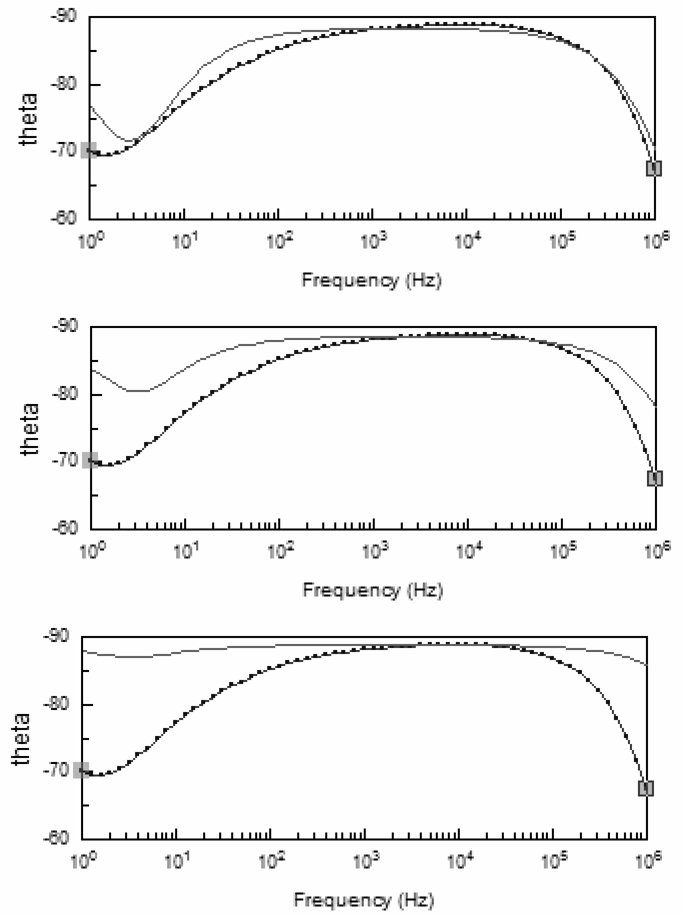

a) C=123 pF,
D = 4 nm

b) C= 50 pF,
D = 16 nm

c) C = 10 pF,
D = 79 nm

Fig. 7. Simulated (solid line) Bode plots with different thickness of silica layer and measured Bode plot (solid line with dots) with the native silica layer

3.4. Anisotropy Evaluation from in- and Across-Plane Conductivities

For comparison impedance measurements were performed on single crystals of YSZ covered by platinum electrodes. The conductivity of the YSZ single crystal, the perpendicular YSZ film and the lateral YSZ film measurements are shown in an Arrhenius plot in Fig. 8. Activation energies of the conductivity were calculated according to Eq. (1).

$$\sigma = A\exp\left(-\frac{E}{kT}\right) \tag{1}$$

where σ is the conductivity, A = pre-exponential factor, E = activation energy, k and T – Boltzmann constant and temperature, respectively.

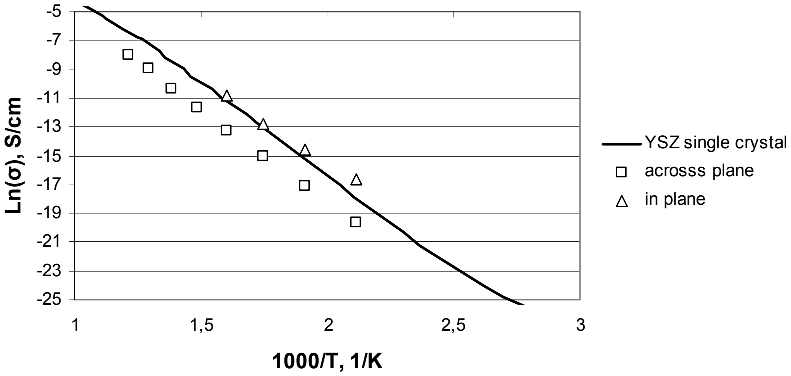

Fig. 8. Arrhenius plots of different YSZ films and a YSZ single crystal

The across-plane conductivity is much higher than the in-plane conductivity. This could be due to the different number of grain boudaries to pass. Different activation energies might be caused by an effect of the substrate. Arrhenius plots of across plane measurements of YSZ thin films with different thicknesses are shown in Fig. 9. The activation energies of the across-plane conductivities do not depend on thickness and the conductivity values are the same, except for the measurements at low temperatures which might be due to additional conduction paths protons.

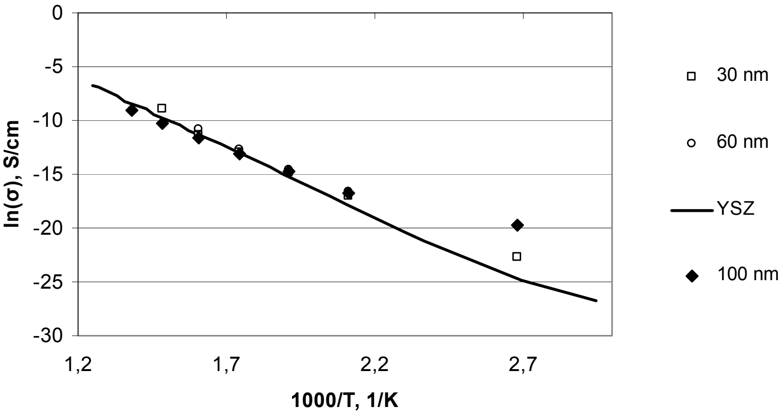

Fig. 9. Arrhenius plots of across-plane measurements with different film thicknesses

4. CONCLUSIONS

YSZ thin films with cubic phase were successfully synthesized onto sapphire and silicon substrates. The study showed that across-plane measurements are possible despite a native silica layer. The native silica layer may even be useful to avoid shortcircuits by cracks or holes in YSZ thin films which easily appear in films in the nanometer range. Simulations of impedance spectra showed that across-plane measurements would not be possible with thicker silica layers. Comparison of in- and across-plane conductivities shows, that the in-plane conductivity is lower than that of across-plane measurements. The activation energies of the conductivities may differ due to the effect of the substrate (mismatch of lattice parameters). To better understand the anisotropy of the conductivity the thin films case, studies of in- and across-plane conductivities on the same substrate are needed.

REFERENCES

1. KOSACKI, I., ROULEAU, C., BECHER, M. P., BENTLEY, J., LOWNDES, D.H. Nanoscale effect on the ionic conductivity in highly textured YSZ thin films, *Solid State Ionics,* 2005, Vol. 176, p. 1319–1326.
2. KOSACKI, I., ROULEAU, C.M., BECHER, M., P. BENTLEY, J., LOWNDES, D.H., Surface/interface – Related Conductivity in Nanometer Thick YSZ Films, *Electrochemical and solid state letters*, 2004, Vol. 12, p. 459–461.
3. GUO, X., VASCO, E., MI, S., SZOT, K., WACHMAN, E., WASER, R. Ionic conduction in zirconia films of nanometer thicness, *Acta materiala,* 2005, Vol. 53, p. 5161–5166.
4. KWON, H.O., CHOI, G.M. Electrical conductivity of thick film YSZ, *Solid State Ionics,* 2006, Vol. 177, p. 3057–3062
5. JOO, J.H., CHOI, G.M. Electrical conductivity of YSZ film grown by pulsed laser deposition, *Solid State Ionics,* 2006, Vol. 177, p. 1053–1057.
6. HARTMANOVA, M., GMUCOVA, K., JERGEL, M., THURZO, I., KUNDRACIK, F., BRUNEL, M. Characterization of ceria/yttria stabilized zirconia grown on silicon substrate, *Thin Solid Films,* 1999, Vol. 345, p. 330–337.
7. WANG, H.B., XIA, C.R., MENG, G.Y., PENG, D.K. Deposition and characterization of YSZ thin films by aerosol assited CVD, *Materials Letters*, 2000, Vol. 44, p. 23–28.
8. GARCIA – SANCHEZ, M.F., PENA, J., ORTIZ, A., SANTANA, G., FANDINO, J., BIZARRO, M., CRUZ – GANDARRILA, F., ALONSO, J.C. Nanostructured thin films for solid oxide fuel cells deposited by ultrasonic spray pyrolysis, *Solid state Ionics,* 2008, Vol. 179, p. 243–249.
9. CHUN, S.Y., MIZUTANI, N. The transport mechanism of YSZ thin films prepared by MOCVD, *Applied surface science*, 2001, Vol. 171, p. 82–88.
10. LAUKAITIS, G., DUDONIS, J., ORLIUKAS, A. F., MILČIUS, D. Properties of YSZ thin films deposited by e-beam technique, *Solid State Ionics*, 2008, Vol. 179, p. 182–187.
11. INFORTUNA, A., HARVEY, A.S., GAUCKLER, L.J. Microstructures of CGO and YSZ Thin Films by pulsed laser deposition, *Adv. Funct. Mater.*, 2008, Vol. 18, p. 127–135.

CYSENI 2010, May 27–28, Kaunas, Lithuania
ISSN 1822-7554, www.cyseni.com

STRUCTURAL AND ELECTRIC PROPERTIES OF NANOSTRUCTURED SPINEL FERRITES OBTAINED BY AUTO-COMBUSTION METHOD

A. Shutka, G. Mezinskis, A. Pludons, S. Lagzdina
Institute of Silicate Materials
Azenes 14/24, LV-1048 – Latvia
Phone: +371 67089141
Email: gundarsm@ktf.rtu.lv

ABSTRACT

The $NiFe_2O_4$, $ZnFe_2O_4$ and $CoFe_2O_4$ ferrites were prepared by auto-combustion method. Method involves the preparation of aqueous solution containing corresponding metal nitrates and organic compound - citric acid. Metal nitrates acting as oxidants were also used as cation sources, whereas an organic compound was employed as fuel. In the next step dried gel from achieved solution were obtained which was directly transformed into nanosized oxide mixture after temperature initiated oxidation-reduction reaction. Finally obtained oxide mixtures were anealed at 800 ^{o}C. The morphology of combustion reaction products were investigated by scanning electron microscopy (SEM). The structural evolution of spinel ferrites and its crystallite sizes at different process stages are investigated by X-Ray diffraction and Fourier transform infrared techniques (FT-IR). The X-ray diffraction patterns after anealing confirm the single-phase spinel structure for the synthesized ferrites. The average crystallite sizes for different compounds were found to be ranging from 33 to 40 nm. The FT-IR measurements show two fundamental absorption bands which are assigned to the vibration of octahedral and tetrahedral complexes characteristic to the structure of spinel. Powder surface area was measured using the multi point Brunauer-Emmet-Teller method (BET). BET results shows, that after anealing sub-micrometer sized primary particles have been agglomered into larger secondary particles. Atomic force microscopy (AFM) was used to study particle dimensions. AFM images reveal particles in the nanosize range (10-70 nm). Room temperature electrical resistivity measurements of the spinel ferrites were measured by conventional two probe method.

Keywords: Nanoparticles, combustion reaction, ferrite, athom force microscopy, electric properties

1. INTRODUCTION

Spinel ferrite nanoparticles are attractive materials for modern industries such as electrical engineering, electronics and information. The ferrites made from nanoparticles are intensively studied due to their unusual electric and magnetic properties. The properties of nanosized particles are in general attributed to the small size, large surface to volume ratio and structural characteristics. As a result nanoparticles could launch comparatively different properties from those of materials prepared by the use of particles with sizes over hundred nanometers [1].

It is well known that the spinel ferrite structure with molecular formula $MeFe_2O_4$ can be described as a cubic close packed arrangement of oxygen atoms, which contains two cation sites for metal cation occupancy. There are 8 A-sites where metal cations are coordinated tetrahedrally and 16 B-sites, which posses octahedral coordination. When sublattice A contains Me^{2+} ions, and sublattice B contains Fe^{3+} ions, the ferrite has a normal spinel structure. If the A-sites are completely occupied by Fe^{3+} ions and B-sites are randomly taken up with Me^{2+} and Fe^{3+}, the structure is attributed as an inverse spinel [2].

Bulk zinc ferrite has a long been known as an antiferomagnetic material and it poses a normal spinel structure where the A site contains all the Zn^{2+} ions. The $NiFe_2O_4$ is a ferromagnetic material in which structure nickel ion due to its superior radius (0.74 Å) [3], in comparison with Fe^{3+} radius (0,67 Å) [1], tends to occupy B sublattice states by making an inverse spinel structure [4]. Recent investigations have suggested that the cation distribution in nanosized $ZnFe_2O_4$ and $NiFe_2O_4$ is partly inverted which means, that both sites contain a fraction of the Me^{2+} and Fe^{3+} cations [5, 6]. The $CoFe_2O_4$ usually forms an inverse spinel structure and independently from preparation technique, as well as particle size it has a high magnetic anisatropy and saturation magnetization [7].

These structural modifications of nanosized ferrite materials increases its potential technological applications, which means that effective, relatively easily method with low energy consumption is significant. Method of ferrite powder preparation strongly affects not only the size of powders but also characteristic properties, thus the aim of present report is to characterize structure and some properties of various spinel ferrites obtained by sol-gel auto-combustion method.

2. METHODOLOGY

In order to obtain zinc, nickel and cobalt ferrites, corresponding metal nitrates as iron nitrate ($Fe(NO_3)_3 \cdot 9H_2O$) and nickel nitrate ($Ni(NO_3)_2 \cdot 6H_2O$) or zinc nitrate ($Zn(NO_3)_2 \cdot 6H_2O$) or cobalt nitrate ($Co(NO_3)_2 \cdot 6H_2O$) were weighted accurately according to the required molar proportion and dissolved in distilled water. Then 1 mole citric acid monohydrate ($C_6H_8O_7 \cdot H_2O$) was added to nitrate solution. To reach pH value to about 7 of prepared solution, ammonia water (NH_4OH) was used. During the last step highly viscous gel was formed after intensive stirring and evaporation at 100°C temperature. The resulting gel was heated up to 250 °C to initiate combustion, and as a result the as-burnt product powder mixture of different oxide compounds was obtained. Finally, attained oxide mixture for 1h was annealed at 800 °C temperature by using heating rate 15 °C/min.

X-ray diffraction patterns of the combustion reaction and annealed powders were recorded for 2θ from 5° to 60° at scan rate of 2° min^{-1} using X-ray diffractometer Rigaku Ultima+ with $Cu_{K\alpha}$ radiation (λ=1.5418 Å).

The IR absorption spectra of calcinated powders were recorded in the wave number range of 4000–400 cm^{-1}, by using Shimadzu Prestige-21 spectrometer. Sample preparation for FTIR measurements included mixing ferrite powder with potassium bromide (KBr) powder.

Morphology of auto-combustion reaction products was characterized by using scanning electron microscopy Hitachi TM 1000. The particle dimensions of annealed ferrites were collected with Digital Instruments CP-II scanning probe microscope, Veeco Instruments Inc. by using non-contact mode. The particle sizes were determined from AFM topographical analysis data taking into account at least 100 particle measurements. Samples for AFM analysis were prepared by dispersing ferrite particles in heptane with subsequent ultrasound treatment to destroy particle aglomerates. The drop of suspension onto mica sheet was analyzed after drying.

The specific surface area was determined by the physical adsorption of N_2 performing the multi-point BET calculation method using a Surface Area and Pore Size Analyser NOVA 1200e.

DC resistivity measurements were performed by the convenctional two probe method with tera-ohmmeter E6-13A. The samples for resistivity measurements were used in the form of circular pellets with the thickness of 1mm and 10 mm in diameter, which were pressed from auto-combustion reaction products at the pressure of 20 MPa using 5 wt % propanol-2 as a binder. Pelets were heated with heating rate of 15 °C/min, and sintered at 1100 °C for 2 hours. The samples were overlayed on either side with high purity conductive silver paint to ensure good electric contacts.

3. RESULTS AND DISCUSSIONS

3.1. Phase analysis of products

The X-ray diffraction patterns of as-burnt and annealed $ZnFe_2O_4$, $NiFe_2O_4$ and $CoFe_2O_4$ samples are presented in Fig. 1, Fig. 2 and Fig. 3, respectively.

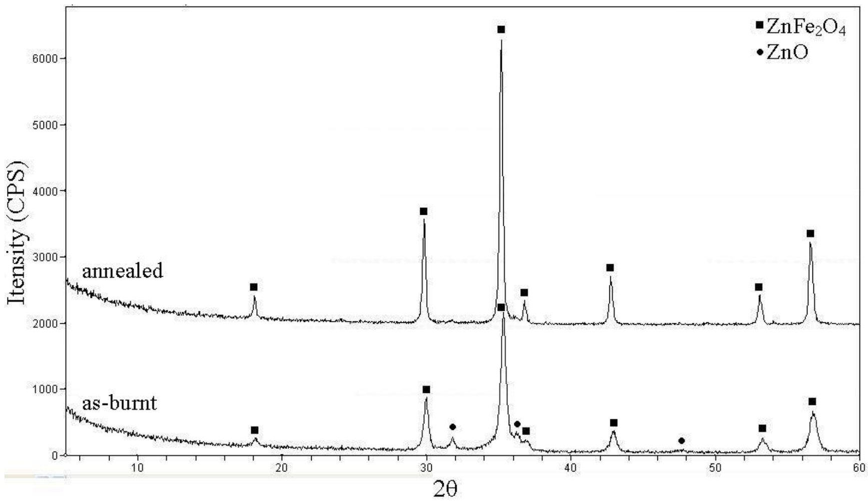

Fig. 1. XRD pattern of as-burnt and annealed $ZnFe_2O_4$

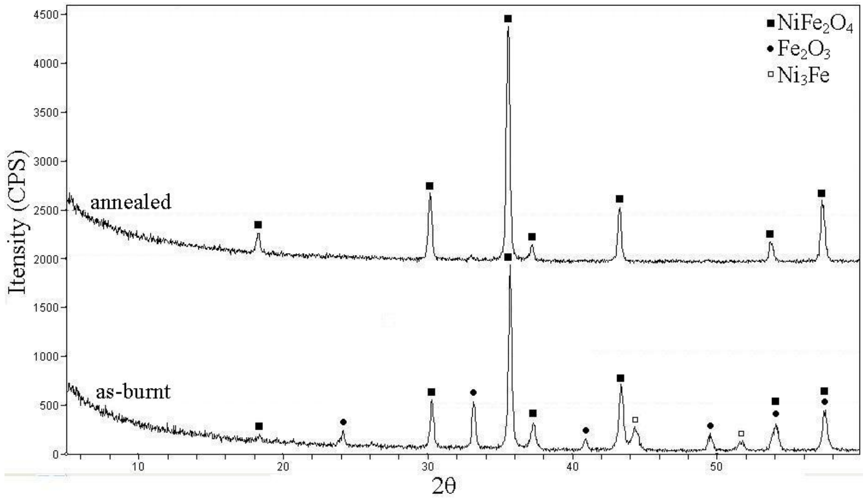

Fig. 2. XRD pattern of as-burnt and annealed $NiFe_2O_4$

The XRD patterns of as burnt products besides cubic spinel structure indicates presence of other minor phases caused by impurities. When annealing in 800 ºC temperature is carried out, the product seemed to contain single-phase $ZnFe_2O_4$, $NiFe_2O_4$ and $CoFe_2O_4$ ferrites because only characteristic peaks of spinel structure are observed ensuring phase purity. The crystallite size (Table 1) determined from the most intense diffraction peaks (311) for the different prepared ferrite compounds, applying Debye-Scherrer equation show that the crystallite size in all cases is at nanometer dimensions and increases with taking annealing at 800 ºC. The lattice parameter ‘a’ of the as-burnt and annealed ferrites was determined by using the formula [9]:

$$a = \frac{\lambda}{2}\frac{\left(h^2 + k^2 + l^2\right)^{1/2}}{\sin\theta} \tag{1}$$

where λ is the wavelength of Cu*K*α, (hkl) are the Miller indices, and θ is the diffraction angle of corresponding (hkl) plane. Parameter ‘a’ for all compositions were calculated from the (220) plane due to its occupied by both A and B sublattice ions [10]. As we can see in Table 1, the lattice parameter in all cases increases by taking ferrite treatment at elevated temperature, that suggests the formation of a compositionally stoichiometric ferrite compound [9]. Generally observed ‘a’ values for annealed ferrite compounds is in good agreement with other authors obtained results for nanosized ferrites [11, 12].

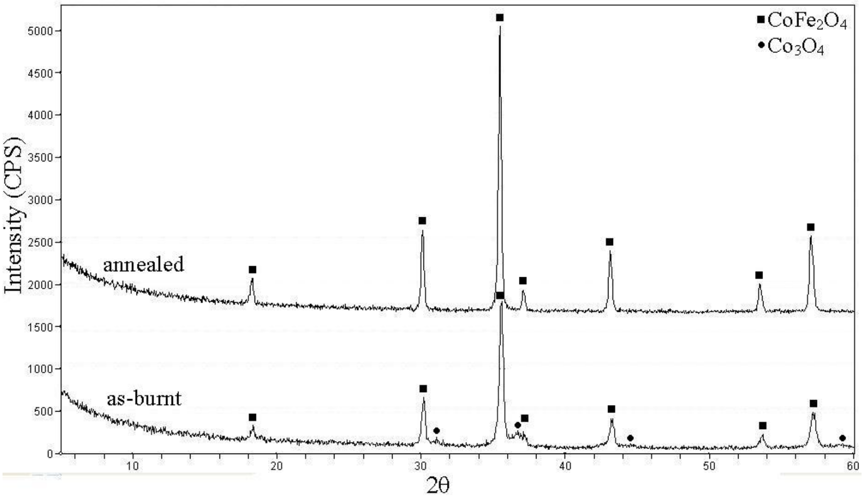

Fig. 3. XRD pattern of as-burnt and annealed $CoFe_2O_4$

3.2. Infrared analysis

From rsults presented at Fig. 4 we can observe typical spinel ferrite absorption bands, which is attributed as metal oxygen vibrations. The first one, V_1, is mostly notice in the range between 600–540 cm^{-1} [13], corresponds to intrinsic streching vibrations at tetrahedral site and second one, V_2, is observed in the diapason 450–385 cm^{-1}, corresponds to octahedral-metal streching [11]. Thease absorption bands are highly sensitive to changes in interaction between oxgen and cations, as well as particle dimensions for nanomaterials [13].

In our study V_1 bands (Table 1) in all cases are higher for annealed samples, what can be explained with stoichiometric compound formation, as well as Fe^{3+} ion replacement with bigger Zn^{2+}, Ni^{2+} or Co^{2+} ion.

Table 1. Various properties of ferrite powders synthesized by sol-gel auto-combustion method

Ferrite	**a, Å**	**D, nm**	**V_1, cm^{-1}**	**V_2, cm^{-1}**	**Specific surface area m^2/g**	**ρ, Ω·cm**
as-burnt $ZnFe_2O_4$	8.4191	20.0	547.8	409	36.4	-
annealed $ZnFe_2O_4$	8.4618	34.7	549.5	412.5	8.0	$5.8 \cdot 10^5$
as-burnt $NiFe_2O_4$	8.3416	28.2	578.7	-	36.4	-
annealed $NiFe_2O_4$	8.3744	33.1	584.4	-	5.2	$9.24 \cdot 10^5$
as-burnt $CoFe_2O_4$	8.3648	24.0	578.0	-	32.6	-
annealed $CoFe_2O_4$	8.3865	34.9	586.0	-	25.4	$4.78 \cdot 10^6$

For $NiFe_2O_4$ and $CoFe_2O_4$ ferrites we could not observe an accurate value of V_2 vibrations due to spectra was recorded in range of 4000–400 cm^{-1} but octahedral state vibrations for thease samples are located below 400 cm^{-1}.

Generally all spectra indicate broad bands around 3450 cm^{-1}, 1600 cm^{-1} and 950 cm^{-1} showing evidence for O↔H streching vibrations. The vibration band located at 2337 cm^{-1} belongs to KBr.

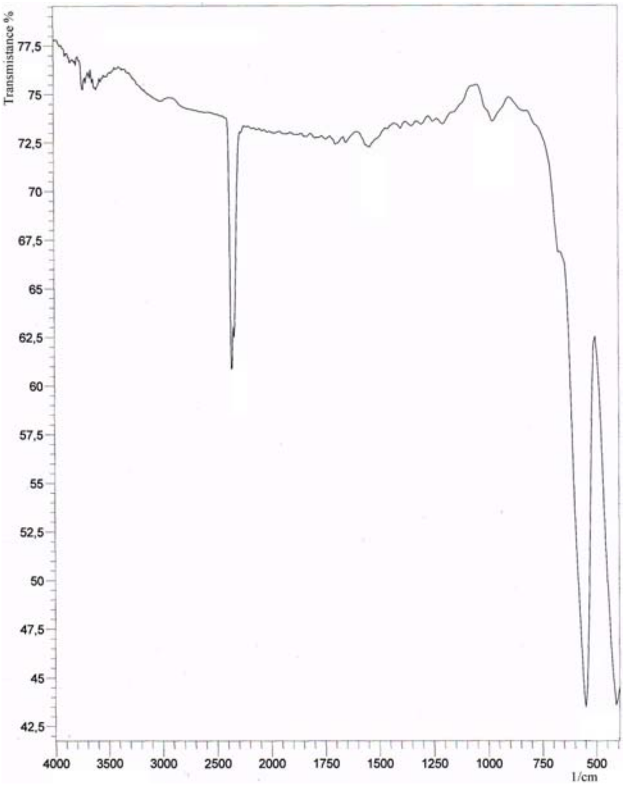

Fig. 4. IR spectrum of spinel $ZnFe_2O_4$ ferrite

3.3. Powder characterization

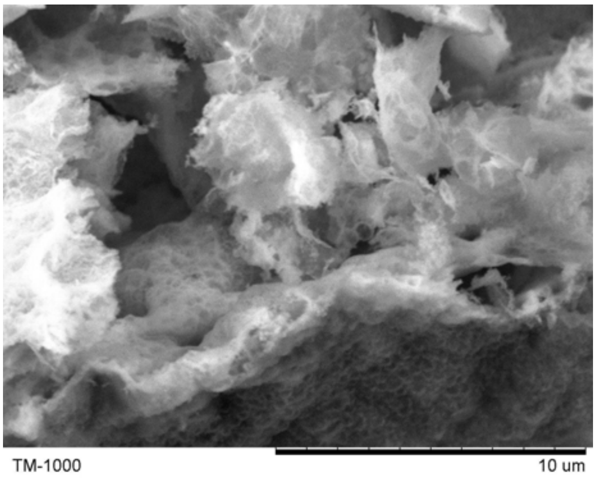

Fig. 5. SEM microphotography of the $CoFe_2O_4$ as-burnt powder

It is to be noted, that in auto-combustion reaction forms highly porous and fluffy products. From gained image (Fig. 5) we can see sub-micrometer sized primary particles which are agglomerated into larger secondary particles. In the same time from obtained photograph is hard to evaluate shape and size of individual particles.

Non-contact AFM topographical images and topographical analysis of $ZnFe_2O_4$, $NiFe_2O_4$ and $CoFe_2O_4$ are shown in Fig. 6, Fig. 7 and Fig. 8, respectively. As we can observe from topographical analysis, ferrite powders consists of individual particles and superior sized clusters (Fig. 6-3, Fig. 7-1, Fig. 8-2), which presumably consists of smaller individual particles as like as it was concluded in the work of Dias et al. [14].

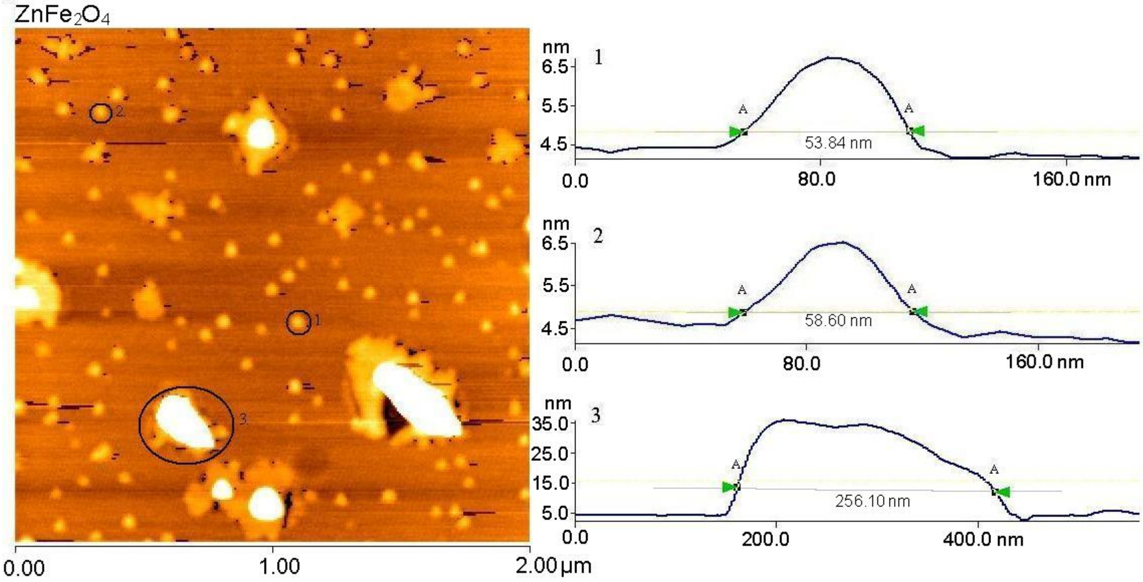

Fig. 6. AFM topographical image and topographical analysis of $ZnFe_2O_4$

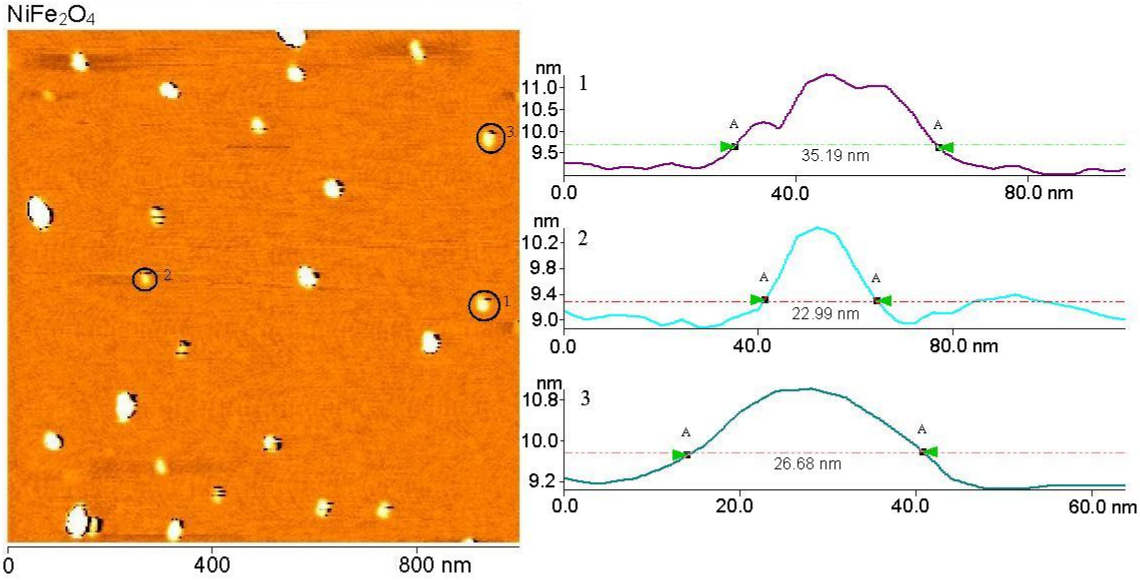

Fig. 7. AFM topographical image and topographical analysis of $NiFe_2O_4$

Measured particle sizes for $ZnFe_2O_4$ were 25-70 nm, $NiFe_2O_4$ 10-45 nm and for $CoFe_2O_4$ 10-40 nm. In the case of $ZnFe_2O_4$ there are bigger particles and clusters. Zinc ferrite superior average particles and clusters sizes, can be explained that by the Zn^{2+} ion presence at spinel structure tends to increase a combustion reaction temperature resulting with intensification of individual particle growth [15], as well as due to liquid phase presence of zinc at sintering process, attributed to its low melting point (470 ^{o}C), which draws the particles together because capillary forces takes place [16].

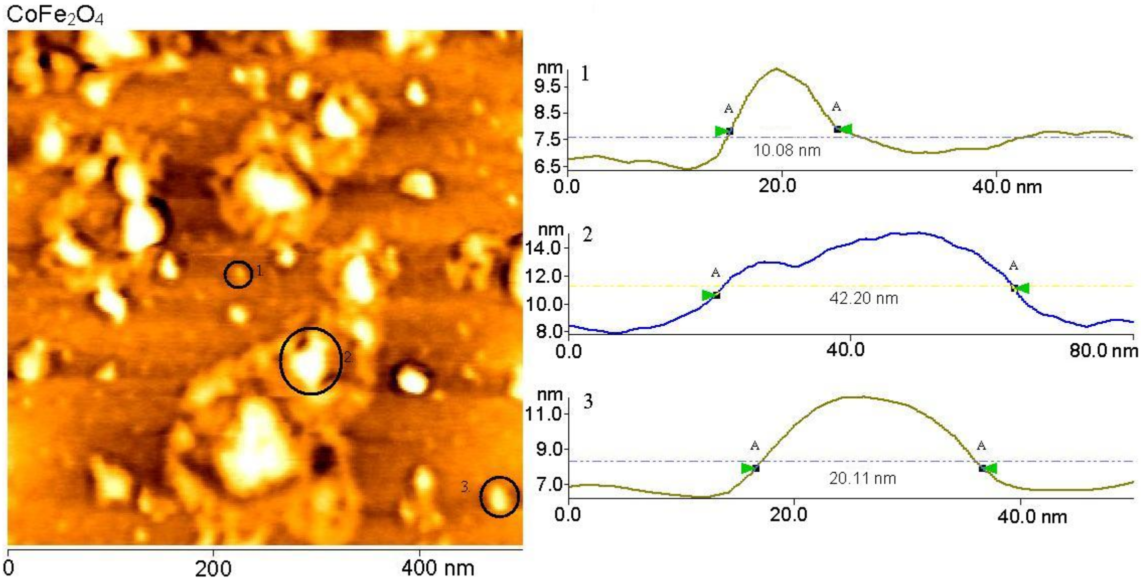

Fig. 8. AFM topographical image and topographical analysis of $CoFe_2O_4$

Measured specific surface areas of the samples are presented in Table 1. From the specific surface area values of as-burnt powders we can conclude that auto combustion reaction products have a mesoporous character. In result of heating at 800 ºC for 1 hour, products showed a clear decrease of the surface areas, from what we can conclude that sub-micrometer sized primary particles have been agglomerated into larger secondary particles.

3.4. DC resistivity

Measured electrical resistivity values are shown in Fig. 9 and Table 1. The comparetively high resistivity values is due to spinel ferrites belongs to the group so-called hopping semiconductors. The basic conduction mechanism for spinel ferrites at room temperature is attributed to hopping of electrons between one cation to another [17] and not due to thermal creation of charge carriers.

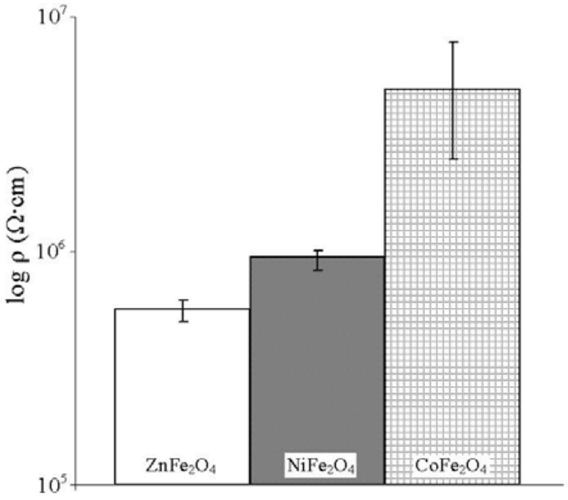

Fig. 9. Electrical resistivity of ferrites

The electron hopping at room temperature is also observed only in equal sublattice sites, because the distance between the metal cations at B sublattice are smaller than the distance between A and B site adherent cations. Therefore the electron hopping between A and B sites compared with B and B sites under normal conditions has a very small probability [18].

Observed electrical propertes could also be attributed to small grain sizes which results with larger number of insulating grain boundaries which act as barriers to the flow of electrons [19]. Generally observed results are in good agreement with other authors obtained experimental results [20, 21].

4. CONCLUSIONS

A convenient combustion synthesis has been developed and can be used to synthesize ultrafine and highly crystalline spinel ferrites with high purity.

The FT-IR studies and lattice parameter changes shows that by taking annealing at 800ºC temperature, compositionaly stoichiometric ferrite compounds are formed.

The topographical images obtained from AFM indicates that ferrite powders consist of nanometer-sized individual particles, as well as particle clusters.

Measured DC resistivity values were comparatively high corresponding to the nature of spinel ferrite materials.

ACKNOWLEDGMENTS

Scientific investigations and results which are presented in this work were financed by the European Social Fund.

REFERENCES

1. GUL, I.H., AHMED, W., MAQSOOD, A. Electrical and magnetic characterization of nanocrystalline Ni-Zn ferrite synthesis by co-precipitation route. *Journal of Magnetism and Magnetic Materials,* 2008, Vol. 320, p. 270–275.
2. DALIYA, S.M., RUEY-SHIN, J. An overview of the structure and magnetism of spinel ferrite nanoparticles and their synthesis in microemulsions. *Chemical Engineering Journal,* 2007, Vol. 129, p. 51–65.
3. EL-SAYED, A.M. Influence of zinc content on some properties of Ni-Zn ferrites. *Ceramics International,* 2002, Vol. 28, p. 363–367.
4. PAIVA, J.A.C., GRACA, M.P.F., MACEDO, M.A., VALENTE, M.A. Spectroscopy studies of NiFe2O4 nanosized powders obtained using coconut water. *Journal of Alloys and Compounds,* 2009, Vol. 485, p. 637–641.
5. WANG, Z., SCHIFERL, D., ZHAO, Y., O’NEILL, C. High pressure Raman spectroscopy of spinel-type ferrite $ZnFe_2O_4$. *Journal of Physics and Chemistry of solids,* 2003, Vol. 64, p. 2517–2523.
6. CHINNASAMY, C.N., NARAYANASAMY, A., PONPANDIAN, N., JOSEYPHUS, J.R, JEYADEVAN, B., TOHJI, K., CHATTOPADHYAY, K. Grain size effect on the Neel temperature and magnetic properties of nanocrystalline $NiFe_2O_4$ spinel. *Journal of Magnetism and Magnetic Materials,* 2002, Vol. 238, p. 281–287.
7. CHINNASAMT, C.N., SENOUE, M., JEYADEVAN, B., PERALES-PEREZ, O., SHINODA, K., TOHJI, K. Synthesis of size-controlled cobalt ferrite particles with high coercivity and squareness ratio. *Journal of Colloid and Interface Science,* 2003, Vol. 263, p. 80–83.
8. COSTA, A.C., TORTELLA, E., MORELLI, M.R., KAUFMAN, M., KIMINAMI, R.H. Effect of heating conditions during combustion synthesis on the characteristics of $Ni_{0,5}Zn_{0,5}Fe_2O_4$ nanopowders. *Journal of Materials Science,* 2002, Vol. 37, p. 3569–3572.

9. HWANG, C.C., TSAI, J.S., HUANG, T.H., PENG, C.H., CHEN, S.Y. Combustion synthesis of Ni-Zn ferrite powder-influence of oxygen balance. *Journal of Solid state Chemistry,* 2005, Vol. 170, p. 382–389.
10. HE, X., SONG, G., ZHU, J. Non-stoichiometric NiZn ferrite by sol-gel processing. *Materials Letters,* 2005, Vol. 59, p. 1941–1944.
11. MOUALLEM-BAHOUT, M., BERTRAND, S., PENA, O. Synthesis and characterization of Zn1-xNixFe2O4 spinels prepared by a citrate precursor. *Journal of Solid State Chemistry,* 2005, Vol. 178, p. 1080–1086.
12. SILEO, E.E., RODENAS, L.G., PAIVA-SANTOS, C.O., STEPHENS, P.W., MORANDO, P.J., BLESA, M.A. Correlation of reactivity with structural factors in a series of Fe(II) substituted cobalt ferrites. *Journal of Solid State Chemistry,* 2006, Vol. 179, p. 2237–2244.
13. MARYKUTTY, T., GEORGE, K.C. Infrared and magnetic study of nanophase zinc ferrite. *Indian Journal of Pure & Applied physics,* 2009, p. 81–86.
14. DIAS, A., BUONO, V., VILELA, J., ANDRADE, M., LIMA, T. Particle size and morphology of hydrothermally processed MnZn ferrites observed by atomic force microscopy. *Journal of Materials Science,* 1997, Vol. 32, p. 4715–4718.
15. COSTA, A., SILVA, J., CORNEJO, D., MORELLI, M. Magnetic and structural properties of $NiFe_2O_4$ ferrite nanopowder doped with Zn^{2+}. *Journal of Magnetism and Magnetic Materials,* 2008, Vol. 320, e370-e372.
16. AJMAL, M., MAQSOOD, A. AC conductivity, density related and magnetic properties of $Ni_{1-x}Zn_xFe_2O_4$ ferrites with the variation of zinc concentration. *Materials Letters,* 2008, Vol. 62, p. 2077–2080.
17. MANGALARAJA, R., MANOHAR, A., GNANAM, F. Direct current resistivity studies of $Ni_{1-x}Zn_xFe_2O_4$ prepared through flash combustion and citrate gel decomposition techniques. *Materials Letters,* 2003, Vol. 57, p. 2662–2665.
18. GUL, I.H., MAQSOOD, A. Structural, magnetic and electrical properties of cobalt ferrites prepared by the sol-gel route. *Journal of Alloys and Compounds,* 2008, Vol. 465, p. 227–231.
19. RAO, B.P., RAO, K.H. Effect of sintering conditions on resistivity and dielectric properties of Ni-Zn ferrites. *Journal of Material Science,* 1997, Vol. 32, 6049-6054.
20. BAYOUMI, W. Structural and electrical properties of zinc-substituted cobalt ferrite. *Journal of Material Science,* 2007, Vol. 42, p. 8254–8261.
21. EL-SAYED, A.M. Electrical conductivity of nickel-zinc and Cr substituted nickel-zinc ferrites. *Materials Chemistry and Physics,* 2003, Vol. 82, p. 583–587.

CYSENI 2010, May 27–28, Kaunas, Lithuania
ISSN 1822-7554, www.cyseni.com

OBTAINING OF CARBON NANOMATERIALS IN A FLUIDIZED BED

S.V. Vasilevich, A.M. Sidorovich, E.K. Buchilko
A. V. Luikov Heat and Mass Transfer Institute
National Academy of Sciences of Belarus
15 P. Brovka St., Minsk, 220072, Belarus
Phone: +375 17 2841089
Email: svasilevich@yandex.ru

ABSTRACT

The possibility of obtaining carbon nanomaterials from such local recoverable materials as plant biomass and waste polymers has been proven. The two-phase technique of obtaining carbon nanomaterials from gaseous products of pyrolysis of a vegetative biomass and waste polymers in a fluidized bed has been suggested and the installation has been described. The suggested two-phase technique has been tested experimentally. It is shown by the experiments that carbon nanotubes obtained by the two-stage technique of synthesis of carbon nanomaterials from plant biomass are of much higher quality compared to those obtained by single-stage pyrolytic synthesis. There is every reason to believe that it would also improve the quality of carbon nanomaterials obtained from polymers.

Keywords: nanomaterials, Carbon nanotubes, Fluidized bed, Biomass

1. INTRODUCTION

Thanks to their unique properties, carbon nanomaterials (CNMs) – nanotubes (CNTs) and nanofibers (CNFs) became a perspective material for many industries. However, a high cost of production and a limited quantity of a synthesized material (10–100 g/hour) restrict their use in the industrial market. Existing technologies use graphite, carbon monoxide or hydrocarbons as a raw material for construction a carbon "skeleton" of CNTs. In some methods, thermolysis of hydrocarbons or materials containing carbon that uses metal catalytic centres is applied. In any case, these methods require extreme operating conditions, which, along with expensive raw materials, defines a high cost of a product and restricts the range of application of nanomaterials.

Recently, new methods directed to large-scale production of CNTs have appeared which open a possibility of their wide practical application in various areas. An analysis of different variants of hardware design of such processes allows one to distinguish, among the most perspective ones, a technology with a fluidized bed (FB) reactor where fine-grained particles of catalyst are fluidized by a carbonaceous gas [1–4]. The known advantages of a fluidized bed - isothermicity and high efficiency of a reactor attained at the expense of a substantial increase of the catalyst surface , allow one to obtain a uniform product and to automate the process. Besides, fluidized bed reactors can be used for organization of a continuous process. Simultaneously, there appeared the information on the possibility of using wastes of plastic as a potential source of carbonaceous raw materials for obtaining CNMs. Their application allows simultaneous solution of two problems: to reduce a cost of raw materials and to solve a problem of waste utilization [5].

The present work is aimed at investigation of the possibility of obtaining multiwalled carbon nanotubes (MWCNTs) by thermochemical conversion of polymer plastic in a fluidized bed of an inert material (sand) that is fluidized by nitrogen.

2. THE EXPERIMENTAL SETUP

The studies were carried out on the experimental setup that makes it possible to obtain CNMs in a fluidized bed not only from carbonaceous gases, but also from vegetative biomass. The schematic of the experimental setup is show in Fig. 1.

The basic units of setup are reactor 1 for synthesis of carbon nanotubes which is connected by a gas supply system 2 with a gasification reactor 3 .

The first stage (gasification) reactor 3 with an inner diameter of 55 mm is made of heat-resistant steel. The reactor height over a gas-distributing grating 4 is 0.5 m. The gas-distributing grating consists of a 1.5-cm-thick layer of chamotte crumbs confined between double layers of a heat-resistant grid with a mesh of 0.5 mm.

A fluidized bed of inert material particles (quartz sand) 6 is formed on the gas-distributing grating 4 of the gasification reactor. Nitrogen entering from the gas supply system 2 is used for fluidization of the bed of the inert disperse material 6.

The (CNMs synthesis) reactor 1 with an inner diameter of 50 mm and a height of 1 m is made of heat-resistant steel (Fig. 1) and is installed above the first stage (gasification) reactor downstream the course of gases. A possibility of reactor off-line operation with the use of ready gas-reagent (acetylene, ethylene, propylene) is provided.

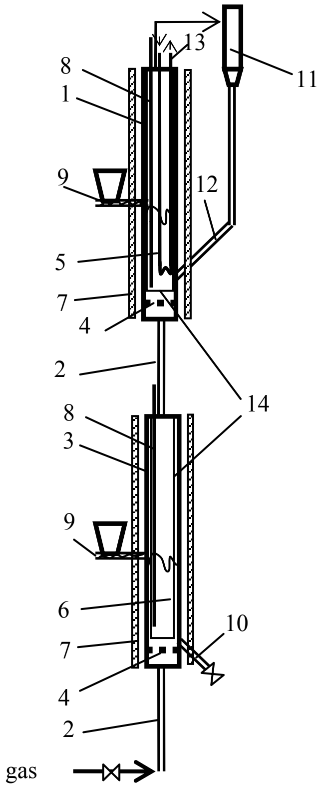

Fig. 1. The schematic of the experimental setup for obtaining CNTs from carbonaceous gases and biomass in FB: 1) reactor of CNTs synthesis; 2)system of gas supply; 3) reactor of biomass gasification; 4) gas distributor; 5, 6) fluidized bed; 7) electric heater; 8) thermocouple; 9) biomass feeder; 10) drainage of FB material; 11) cyclone-separator; 12) material recirculation line; 13) nickel plate; 14) quartz insert

The fluidized bed of the catalysts 5 represented by sawdust impregnated by ferric nitrate lies on the gas-distributing grating 4 of reactor 1. The carbonaceous gas formed in reactor 3 is used for fluidization of bed 5. The reactors 1 and 3 are equipped with external electric heaters

7 with the help of which the bed temperature can be increased to 800°C. The temperature is measured by the chromel-coppel thermocouples 8. The reactors are also equipped with screw feeders 9 for supply of wood raw materials. Reactor 1 is fed with the catalyst and reactor 3 with raw materials for obtaining a carbonaceous gas. The reactor is supplied by a cyclone separator 11, which serves for additional trapping of nanotubes, and also by a vertical nickel plate 13 where carbon nanotubes settle. Reactor walls are insulated from the catalyst contained in the bed by a quartz insert 14 to prevent sedimentation of nanotubes on the reactor walls. In the lower part of a reactor 3 a device to drain the inert disperse material 10 on termination of the experiment is installed.

2.1. Experimental Technique

The fluidized bed temperature in the reactors of both stages was maintained the same and equal to 650°C. In the first-stage reactor the bed material was sand with an average particle size of 0.26 mm, the fluidizing gas was nitrogen with the volumetric flow rate 0.3 nl/s. Sawdust with a humidity of 8%, or polyethylene (PE) waste, which were supplied to the reactor 3, served as a raw material for obtaining the carbonaceous gas. In the second-stage reactor the rate of gas filtration was somewhat higher because of release of volatiles in their pyrolysis.

The sawdust impregnated by ferric nitrate was used as the catalyst for CNTs synthesis. The sawdust forms a bed 5 in the CNTs synthesis reactor 1. The samples of the product were taken from the surface of the nickel plate placed in reactor 1 and from the cyclone-separator 11, installed behind the second-stage reactor.

A typical procedure of the experiment was as follows.

First, reactors 1 and 8 were brought to the operating mode. When the temperature in a fluidized bed 6 reached 550 °C and that in bed 5 reached 650°C air supply to reactor 8 was stopped and switched to nitrogen supply. The raw materials for gasification (sawdust or polyethylene granules) were fed by screw feeder 9 to reactor 3 where gasification with obtaining of carbonaceous gas took place. Simultaneously, disperse catalyst was supplied to reactor 1 by feeder 9. The carbonaceous gas obtained as a result of gasification of wood raw materials entered reactor 1. Synthesis of carbon nanotubes in reactor 1 is carried out in a fluidized bed 5 on the disperse catalyst in the form of the sawdust impregnated by ferric nitrate, which is fluidized by accending flow of the gas-reagent, being a gasification product. As the process of synthesis goes on the agglomerates of carbon nanotubes accumulate in reactor 1 of the synthesis of carbon nanotubes on the catalyst and a nickel plate 13. Particles of the catalyst with settled on them nanotubes that were carried away from reactor 1, got to cyclone-separator 11 where nanotubes settled, and catalyst particles were returned to reactor 1 through the system of recirculation 12.

After each experiment the fluidized bed reactor was cooled by a free air stream, and the flue ducts behind the reactor downstream the course of gases were demounted. The internal surfaces of the walls of the reactor and flue ducts were cleaned. During the experiments the deposits on the vertical nickel plate or the stainless steel grid, fixed in the freeboard region of the reactor were gathered and analyzed. The deposits and samples of the bed material were analyzed by a scanning electron microscope *Supra 55 Carl Zeiss* and spectral microanalyzer *INCA 350*.

3. RESULTS AND DISCUSSION

3.1. Use of Wood as a Raw Material for Gasification

Typical results of the experiments using the sawdust as a raw material for obtaining the carbonaceous gas are presented in Figs 2–4.

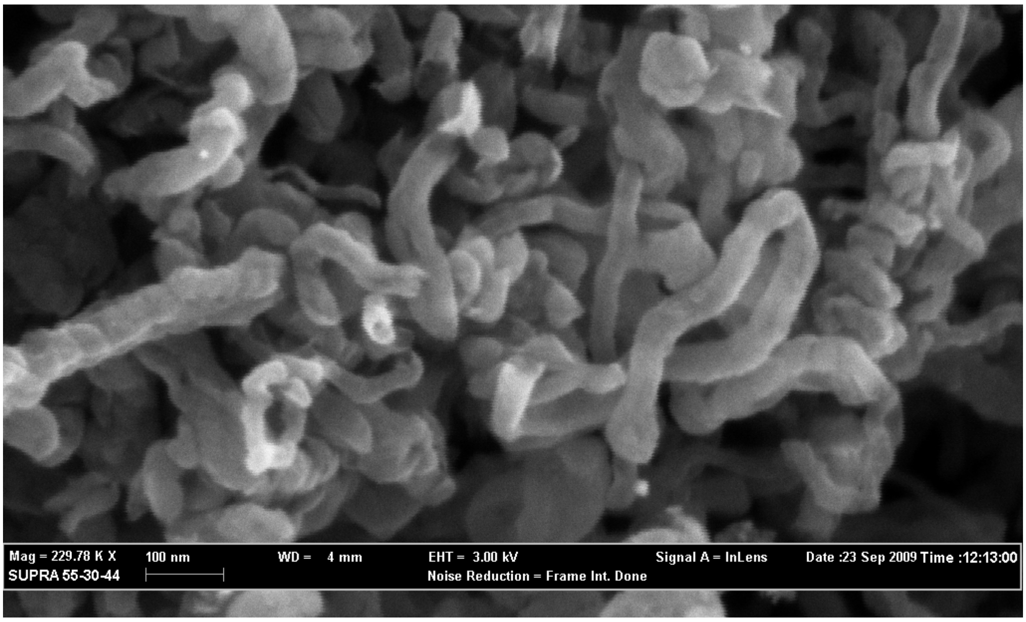

Fig. 2. Carbon nanotubes synthesized from the products of pyrolysis of wood biomass on a surface of the nickel plate (scale: 100 nm)

Deposits on the surface of the nickel plate (Fig. 2) consist of a continuous "carpet" of interweaved CNTs with a diameter D = 30÷50 nm and a length L >> D (the authentic estimation of the length of tubes is complicated in connection with their interweaving). There occurdouble tubes braid in original "plaits" with an outer diameter 75÷100 nm.

The spectral composition of crude CNTs is C – 97.23 at.%, O – 2.77 at.% which indicates an insignificant amount of moisture in the studied samples.

Fig. 3 shows a microphoto of solid material particles trapped in the cyclone-separator behind the second-stage reactor after calcination in a muffle furnace at a temperature of 300°C for 8 hours. The particle surface is covered by a "carpet" from CNTs synthesized from the products of wood biomass pyrolysis.

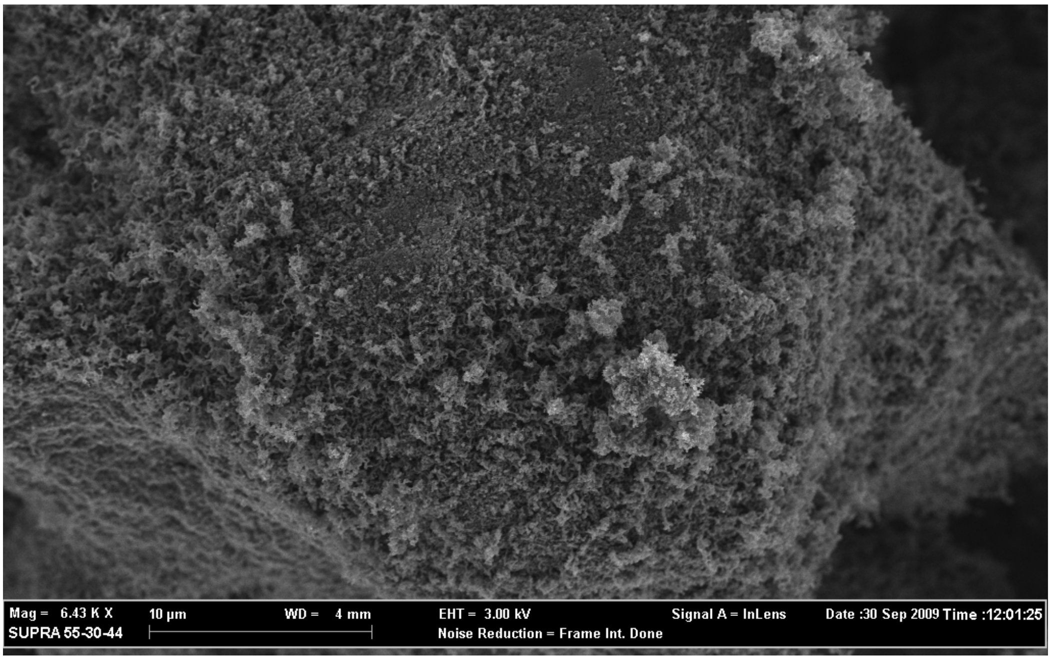

Fig. 3. The sample of particles from the cyclone-separator, with CNTs deposits synthesized from the products of pyrolysis of wood biomass (scale: 10 μm)

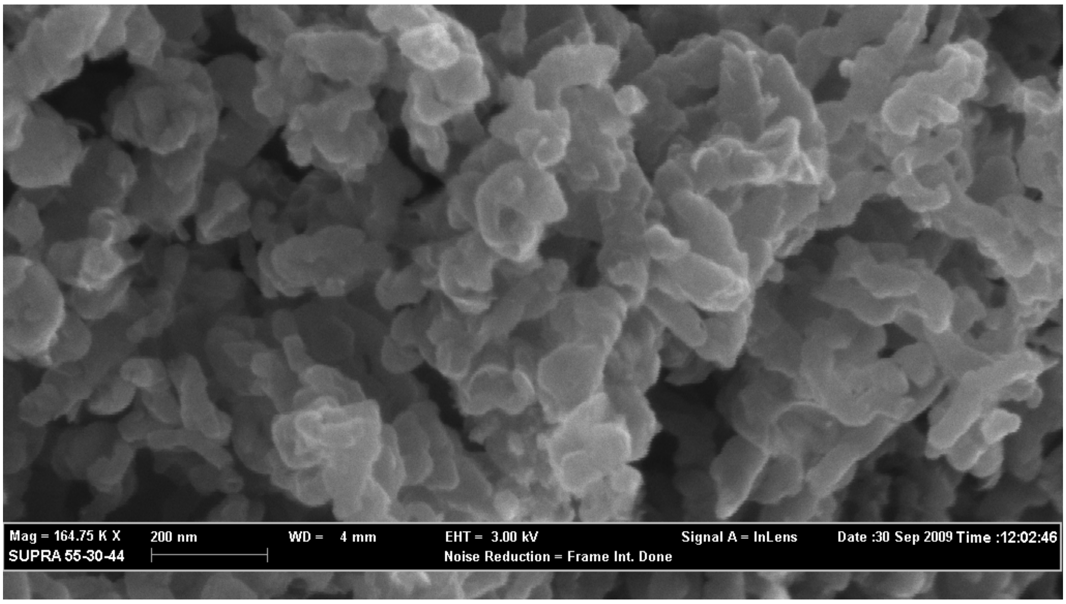

Fig. 4. Carbon nanoparticles synthesized from the products of pyrolysis of wood biomass on a surface of quartz particles from the cyclone-separator (scale: 200 nm).

The large-scale samples of the corresponding CNTs are presented in Fig. 4. A diameter of tubes is close to D ≈ 50 nm, the length is much larger than a diameter that is clearly seen in the figure although quantitative estimates of their length are difficult because of the crookeedness and interweaving of tubes.

The spectral composition of annealed CNTs is C – 97.03 at.%, O – 2.61 at.%, and Ni – 0.36 at.%. A small impurity of oxygen most likely is connected to the content of moisture in the investigated sample, and nickel traces point to the role of nickel atoms as a catalyst in the synthesis process and a "basis" for CNTs "growing" on a nickel substrate. As a tube breaks off from the substrate, atoms of Ni possiblly remain in its basis.

3.2. Use of Polyethylene as Raw Material for Gasification

Figs. 5–7 present the results of investigation of CNTs synthesis from products of pyrolysis of high-pressure PE waste. An average weight of a particle is equal to 0.15 g. The total time of the experiment is about 5 hours. An average flow rate of raw materials is 36 g/h, the used weight of raw materials is 180, the fluidized bed temperature is 650°C.

Fig. 5 shows the general view nanostructural deposits on a surface of a bed material particle (quartz sand) sticking to a nickel plate at a height h = 0.2 m over the upper boundary of FB. In the figure one can see many nanotubes (fibers) with a diameter D ≈ 30÷70 nm a length of which is difficult to be estimated because of crookedness. It is possible to discriminate the braids twisted in dense spirals from two and more CNTs with a diameter to 200 nm.

The spectral composition of nanostructures shown in Figure 5 includes C – 97.34 at.%, O – 2.16 at.%, Ni – 0.5 at.%. The content of nickel indicates that its atoms can serve as the basis for CNTs being formed.

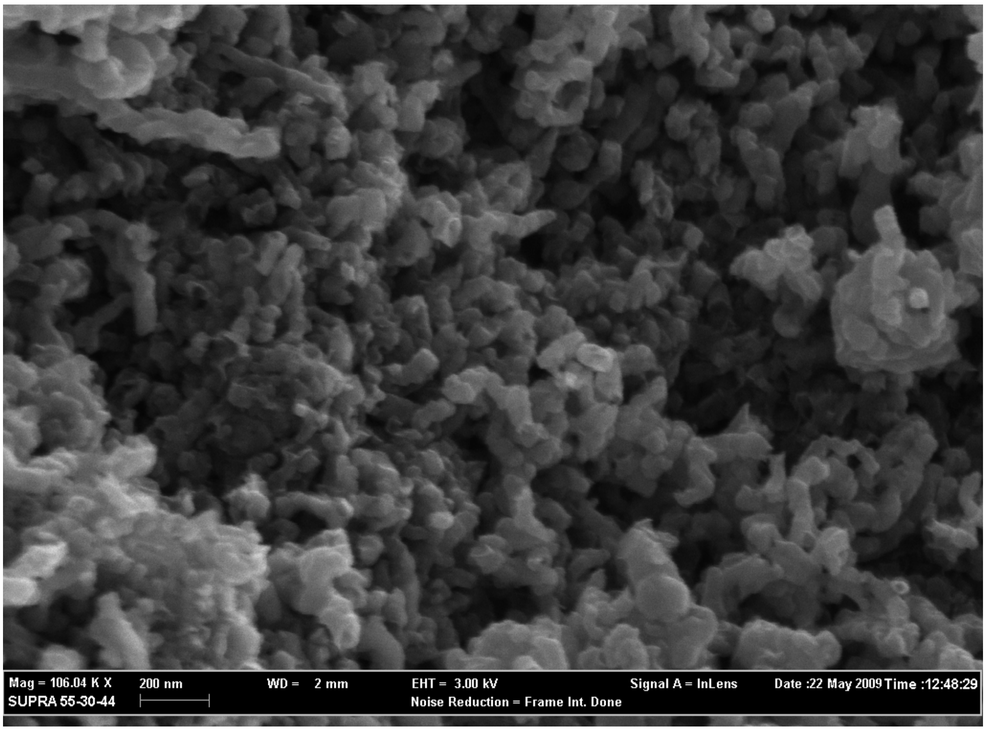

Fig. 5. The microphotos of nanostructural deposits obtained as a result of pyrolysis of PE waste, on a surface of particles carried away from a bed (altitude over a bed h = 0.2 m; scale: 200 nm)

In Fig. 6, a crude sample of the material collected in the cyclone-separator behind a reactor is shown. As follows from figure, the particles in the cyclone-separator become covered by a thick layer of gums that condense here despite the presence of external thermal insulation.

Spectral measurement of the content of crude samples from the cyclone-separator (C – 24.72 at.%, O – 49.8 at.%, Si – 24.47 at.%, Al – 1.0 at.%) indicate a great amount of impurity in the samples of the carried away bed material (sand) that mainly consists of silicon dioxide and aluminosilicate impurities.

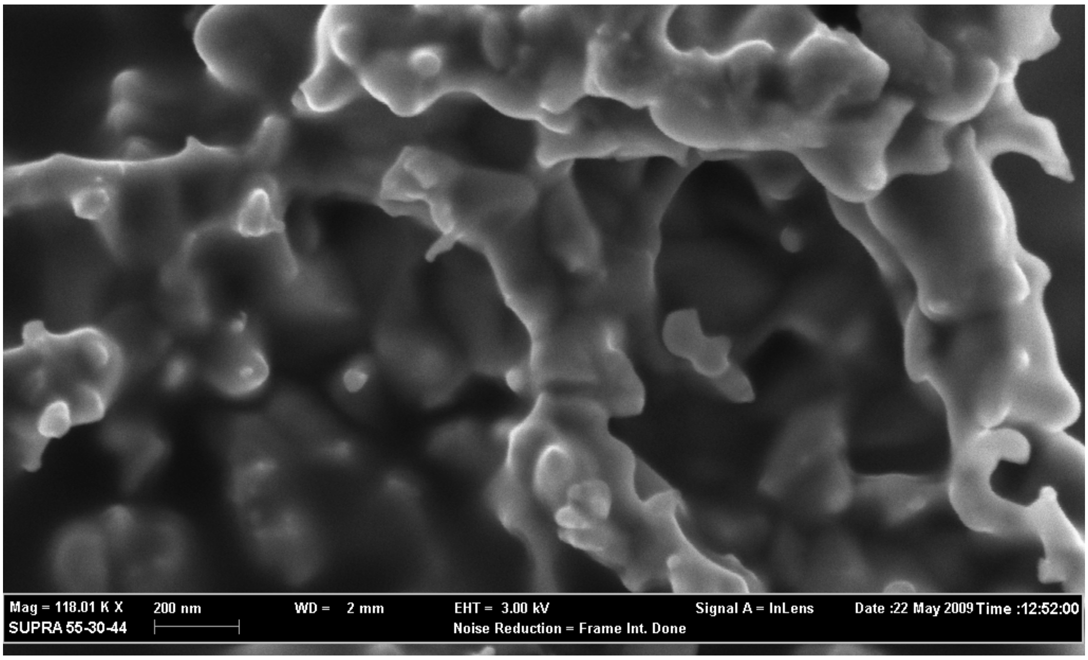

Fig. 6. The microphotos of the sample of material from the cyclone-separator taken in synthesis of CNTs from the products of PE pyrolysis (scale: 200 nm)

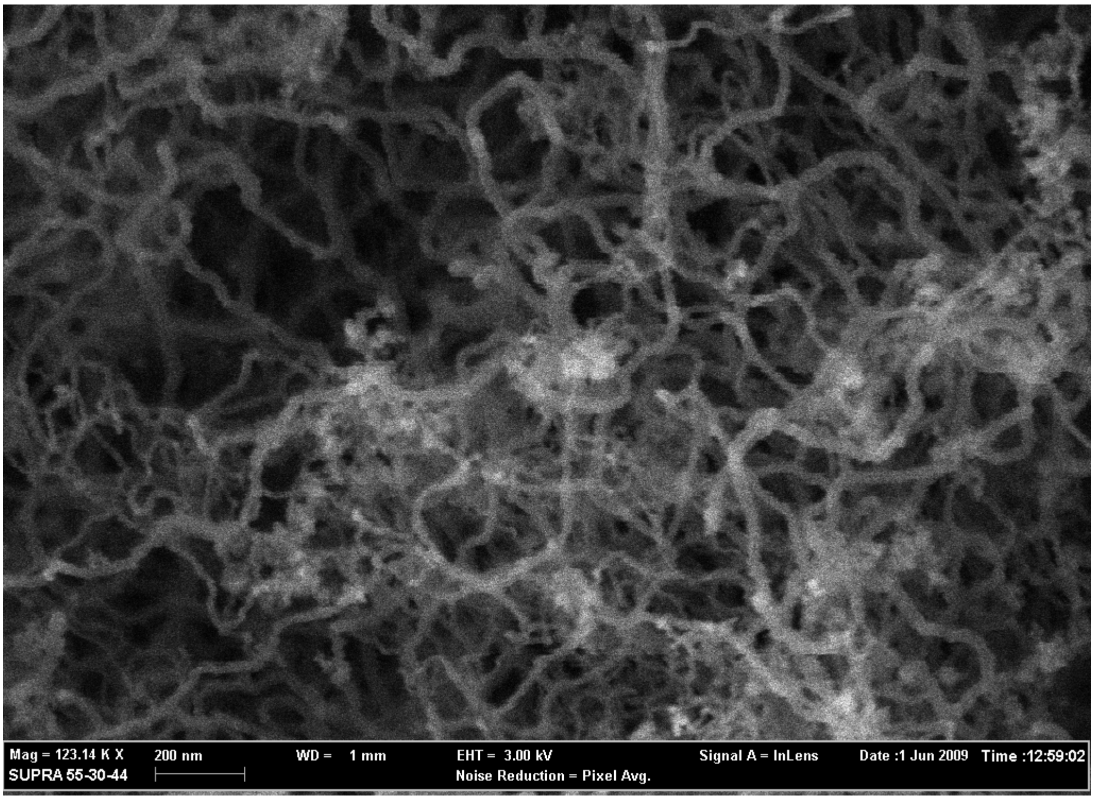

Fig. 7. The microphotos homogeneous carbon nanotubes, gained from the products of pyrolysis of PE waste (scale: 200 nm)

On annealing the samples taken from the cyclone-separator in the muffle furnace at a temperature of 300°C for 15 hours, the following spectral composition of them was obtained: C – 98.41 at.%, Fe – 1.59 at.%. Apparently, sand impurities have been taken away from the samples by melted gums. The annealed CNTs samples synthesized from the products of pyrolysis of PE wastes in the fluidized bed are shown in Fig. 7.

In Fig. 7, a strongly magnified massif of homogeneous nanotubes is shown. The given CNTs samples possess the best morphological properties from all previous data: diameter D = 15÷40 nm, length of visible horizontal projections not less than 1000 nm, and a maximum ratio L/D = 250÷700.

4. CONCLUSIONS

A possibility of obtaining carbon nanomaterials by pyrolysis of biomass and polymer materials in a fluidized bed of an inert material is confirmed experimentally. There are all bases to assume that this will allow one to raise the quality of CNTs obtained from biomass and polymers. We have submitted the application for a patent for the given way of obtaining CNTs. The patent pending No. a20091704 as of 01.12.2009.

REFERENCES

1. LUO G., LI Z., WEI F. et al. Physica B, 2002. V. 323, p. 314.
2. WANG Y., WEI F., LUO G. Physica B, 2002. V. 323, p. 327.
3. LI Z., LUO G., WEI F., WANG Y. CHINESE J. Proc. Eng., 2002. V. 2, p. 224.
4. WANG Y., WEI F., LUO G. et al. Chem. Phys. Lett., 2002. V. 364. No 5–6, p. 568.
5. MASTELLONE M.L. Thermal treatments of plastic wastes by means of fluidized bed reactors // Doctor of Engineering Thesis. Dept. Chemical Engineering, University "Federico II" of Naples. 2000.

CYSENI 2010, May 27–28, Kaunas, Lithuania
ISSN 1822-7554, www.cyseni.com

ZNO THIN FILMS AS TRANSPARENT CONDUCTIVE OXIDES BY CHEMICAL SPRAY PYROLYSIS

M. Vent, K. Annert, E. Kärber, M. Krunks
Tallinn University of Technology, Department of Materials Science
Ehitajate tee 5, 19086-Estonia
Phone: +372 620 3369
Email: vendike@gmail.com

ABSTRACT

ZnO is an abundant and low cost material and its electrical conductivity can be varied in wide range by doping with suitable elements. ZnO thin films are extensively used as window layers in solar cells, for example in amorphous silicon solar cells and thin film solar cells based on chalcopyrite absorbers. ZnO is one potential candidate to substitute indium tin oxide (ITO; In_2O_3:Sn) and fluorine doped tin oxide (FTO; SnO_2:F) as transparent and conductive electrode for various applications if prepared electrically highly conductive. In present study ZnO thin films were prepared by low cost chemical spray pyrolysis method on glass substrates from solutions of $Zn(CH_3COO)_2{\cdot}2H_2O$ in a mixture of de-ionized water and isopropyl alcohol. Doping material $InCl_3$ was added into the spray solution to obtain conductive films. The films were grown at substrate temperatures between 350°C and 550°C in air. The structural, optical, morphological and electrical properties of ZnO thin films were studied. These properties depend on the deposition temperature, concentration of the doping material in solution and solution spraying rate. According to XRD, undoped ZnO films are highly c-axis orientated, ZnO:In films show preferential (101) orientation. ZnO:In films have smooth surface and show optical transmittance of 80-85% in visible spectral region. Electrical resistivity as low as $4{\cdot}10^{-3}$ Ωcm was obtained in the films deposited from solutions with $[In^{3+}]/[Zn^{2+}]$=2-4 at.% at tin bath temperatures close to 450°C using spray rate of 3-4 ml/min.

Keywords: Zinc oxide; Spray pyrolysis; Thin films; Indium

1. INTRODUCTION

Zinc oxide (ZnO) is a widely used semiconductor material for many different applications such as gas sensors, ultrasonic oscillators and transducers, reflecting coatings and transparent and conductive layers in photovoltaic devices [1–3]. Its direct optical band gap (3.3 eV) is wide enough to transmit most of the useful solar radiation in $CuInSe_2$ based solar cells [2, 4]. Furthermore, ZnO is a good candidate to substitute indium tin oxide (ITO; In_2O_3:Sn) and fluorine doped tin oxide (FTO; SnO_2:F) as transparent and conductive electrode for various applications if prepared electrically highly conductive [2]. In present work ZnO thin films are prepared by chemical spray pyrolysis which is found to be cheap and simple method to produce large area thin films [1–2, 4].

It has been found in earlier studies that parameters such as zinc source, the concentration of zinc in spray solutions, growth temperature, doping material and doping concentration have strong effects on optical transmittance, structural and electrical properties of sprayed ZnO thin films [1–2, 4]. The aim of this study is to give an overview of the previous worldwide studies and our recent results on formation of uniform, optically transparent and electrically conductive ZnO thin films by chemical spray pyrolysis. We studied the effect of indium concentration in spray solution, growth temperature and spraying rate to the structure, optical transmittance and electrical resistivity of the films.

2. METHODOLOGY

Zinc oxide thin films were prepared by spraying of zinc acetate ($Zn(CH_3COO)_2\cdot2H_2O$, Merck, 99.5%) in a mixture of deionized water and isopropyl alcohol (2:3 by volume) onto heated glass substrate (25mm x 25mm x 1mm). The glass substrates were placed on a soldered tin bath. Compressed air was used as carrier gas. The concentration of $Zn(CH_3COO)_2\cdot2H_2O$ at spray solution was fixed to 0.2 mol/l for every series. A few millilitres of acetic acid was added to the solution to avoid precipitation of zinc hydroxide. Indium(III)chloride ($InCl_3$) prepared from indium (extra pure) and hydrochloric acid was used as doping agent added to the spray solution. Indium to zinc concentration (in future as [In]) was varied from 0 up to 5 at. %. The tin bath temperature (T_{Sn}) varied from 350°C up to 550°C. The growth temperature of thin films is approximately about 100°C lower that tin bath temperature.

X-ray diffraction (XRD) patterns of sprayed thin films were recorded using a Rigaku Ultima IV diffractometer with monochromatic Cu K_α radiation. The optical transmittance spectra were recorded in the wavelength range of 200-2000nm on a Jasco V-670 UV-VIS-NIR spectrophotometer. The surface morphology of the films was examined by scanning electron microscopy (Zeiss HR FESEM Ultra 55). Electrical resistivity of the thin films was measured by Van der Pauw's method.

3. RESULTS AND DISCUSSIONS

3.1. Summary of previous worldwide studies on deposition of transparent and conductive ZnO thin films by chemical spray pyrolysis

Different spraying systems, set-ups and spray modes have been used by many research groups to deposit ZnO thin films. The zinc source, doping material and solvent are also different, not to mention precursor solution concentration, doping material level and growth temperature. A summary of main film deposition parameters and properties of the films obtained is presented in Table 1.

Table 1. Summary of literature survey on deposition doped ZnO thin films by spray pyrolysis. CSP – Pneumatic chemical spray pyrolysis; USP – Ultrasonic spray pyrolysis; T_{sub} – substrate temperature (°C); T – optical transmittance in visible region (%); XRD – preferred crystallite orientation; ρ – resistivity (Ωcm)

Film deposition parameters						**Film properties**			
Spray mode	**Zinc source**	**Zinc conc.**	**Dopant source**	**Dopant conc.**	**T_{sub}, °C**	**T, %**	**XRD**	**ρ, Ωcm**	**Ref.**
CSP	$Zn(C_2H_3O_2)_2$	0.7M	$H_3\mathbf{B}O_3$	1 at.%	450	>90	(002)	$2.5\cdot10^{-3}$	[5]
CSP	$Zn(C_2H_3O_2)_2$	0.2M	$\mathbf{Al}C_{15}H_{21}O_6$	3 at.%	475	>85	(002)	$4.3\cdot10^{-3}$	[6]
CSP	$Zn(C_2H_3O_2)_2$	0.1M	$\mathbf{Al}\ (NO_3)_3$	0.15 at.%	450	>90	(101)	-	[7]
CSP	$Zn(C_2H_3O_2)_2$	0.2M	$\mathbf{Ga}C_{15}H_{21}O_6$	2 at.%	425	>80	(002)	$7.4\cdot10^{-3}$	[8]
CSP	$Zn(C_2H_3O_2)_2$	0.1M	$\mathbf{Ga}Cl_3$	5 at.%	350	>85	(002)	$1.5\cdot10^{-3}$	[9]
CSP	$Zn(C_2H_3O_2)_2$	0.2M	$\mathbf{In}Cl_3$	1 at.%	350	-	(002)	$10\cdot10^{-3}$	[2]
USP	$Zn(C_2H_3O_2)_2$	0.2M	$\mathbf{In}(C_2H_3O_2)_3$	3 at.%	370	>80	(101)	$2.9\cdot10^{-3}$	[10]
CSP	$ZnC_{10}H_{14}O_4$	0.5M	$\mathbf{In}Cl_3$	3 at.%	475	>80	(101)	$3.0\cdot10^{-3}$	[11]
USP	$Zn(C_2H_3O_2)_2$	0.2M	$\mathbf{In}(C_2H_3O_2)_3$	3 at.%	370	83	-	$3.0\cdot10^{-3}$	[12]
CSP	$ZnC_{10}H_{14}O_4$	0.2M	$\mathbf{In}(NO_3)_3$	2.5 at.%	475	>85	(101)	$3.0\cdot10^{-3}$	[13]
CSP	$ZnC_{10}H_{14}O_4$	0.5M	$\mathbf{In}(C_2H_3O_2)_3\cdot H_2O$	3 at.%	475	77	(101)	$2.1\cdot10^{-3}$	[14]
CSP	$Zn(C_2H_3O_2)_2$	0.1M	$\mathbf{In}(NO_3)_3$	3 at.%	450	>85	(101) (002)	$4.0\cdot10^{-3}$	[15]

According to literature review two main zinc sources such as zinc acetate and zinc acetylacetonate and four main doping elements such as boron, aluminium, gallium and indium were used to obtain conductive ZnO films. Zinc concentration varies from 0.1M up to 0.7M and the most useful dopant concentrations altered from 0.15 at.% to 3 at.%. Doping of the films was attained by adding salt of the dopant element into the spray solution. All thin films presented in Table 1 are more than 80% optically transparent in visible spectral region and their resistivity varies from $1.5\cdot10^{-3}$ Ωcm to $10\cdot10^{-3}$ Ωcm. It is noticeable that indium compounds ($InCl_3$, $In(NO_3)_3$, etc.) are the most widely used dopant sources although there is no matter what kind of In compound to use for doping with indium [14]. Indium doped ZnO films show preferred orientation along (101) plane, however doping with gallium and boron do not cause changes in the crystallites preferred orientation compared to undoped ZnO films with c-axis orientated crystallites [5, 8–14]. Electrically conductive films were prepared at substrate temperatures from 350°C up to 475°C. Usually the home-made set-up is used and therefore every group has to find parameters which will work on their spraying system to prepare optically transparent and electrically conductive ZnO thin films.

3.2. Our results

Studies on preparation of doped and undoped ZnO thin films by chemical spray pyrolysis were initiated at Tallinn University of Technology (TUT) in 1995 [1]. It was found that increasing substrate temperature increases optical transmittance of undoped and indium-doped (up to 1 at.%) films [1]. The dopant concentration has also effect on optical transmittance [4]. It has been shown that for the use of dopant in amount of 1 at% or less in spray solution the preferred orientation is (002), otherwise it is (101) [2, 4].

Recently, the studies for deposition of zinc oxide thin films at TUT were reactivated due to need to develop transparent conductive ZnO window layers for solar cells [16].

3.2.1. The effect of indium concentration in spray solution on properties of ZnO thin films

$InCl_3$ was used as indium source and the atomic percentage of indium in spray solution was varied from 0 at.% to 5 at.%, other deposition parameters such as zinc concentration, tin bath temperature and spraying rate were kept constant. The X-ray diffraction patterns of ZnO and ZnO:In thin films grown at T_{Sn}=450°C are shown in Fig. 1. All peaks in XRD spectra belong to ZnO (JSCP file No.: 00-036-1451) and therefore no other compounds are in the films. Undoped ZnO thin film shows very strong (002) peak, thus the film is c-axis oriented (see Fig. 1). Doping with indium decreases the intensity of the (002) peak and increases relative intensity of (100), (101), (102) and (110) peaks. At dopant concentration of 3 at.% in spray solution the (101) peak is the most intense. The result obtained is in accordance with earlier studies [2, 4, 10] and shows that crystallites in the film are grown (101) plane parallel to the substrate.

It was found that ZnO thin films were milky and foggy while indium doped ZnO thin films (ZnO:In) were clear and transparent. Optical transmittance spectra for ZnO and ZnO:In indicate that the interference maxima of ZnO thin film are not as strongly formed as they are for ZnO:In thin films (see Fig. 2). Similar tendency is characteristic of the films deposited at T_{Sn}=550°C. The optical transmittance of ZnO:In is higher than 80% in visible region of the spectrum. The difference in optical transmittance between undoped and doped films is caused by their different surface morphology. SEM pictures were done to study thin film surface (see Fig. 3).

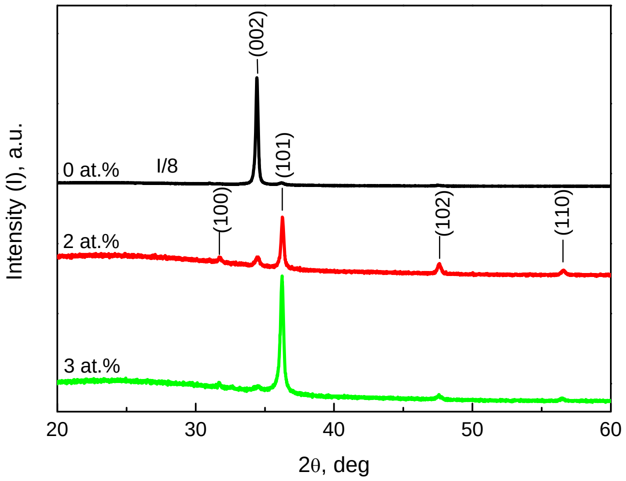

Fig. 1. XRD patterns of sprayed undoped ZnO and indium doped ZnO thin films (In concentration in solution 2 at.% and 3 at.%) deposited at T_{Sn}=450°C with similar spraying rate of ca. 3 ml/min.

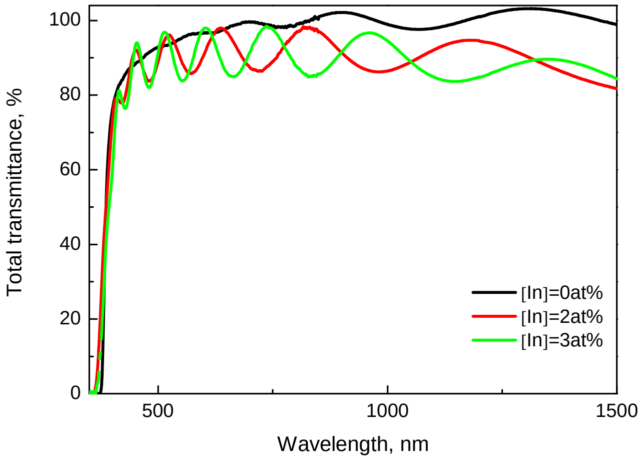

Fig. 2. Total transmittance spectra of sprayed ZnO and ZnO:In thin films deposited at T_{Sn}=450°C with similar spraying rate of ca. 3 ml/min.

a) b)

Fig. 3. SEM pictures of sprayed ZnO thin films. a) undoped ZnO thin film; b) ZnO:In thin film ([In]=3 at.%). Films were deposited at T_{Sn}=450°C

Undoped ZnO thin films surface is not uniform and the crystallites on the ZnO thin film surface resemble needles and roses-like crystals as shown in our recent study [17]. According to SEM, ZnO:In thin film (Fig. 3b) is composed of tetragonal grains and is more homogeneous.

The effect of indium concentration in spray solution on electrical resistivity of ZnO:In thin films deposited at tin bath temperatures of 350°C, 450°C and 550°C is shown in Table 2.

Table 2. Electrical resistivity (in Ωcm) of ZnO thin films depend on the indium concentration in spray solution. The films were deposited at tin bath temperatures of 350°C, 450°C and 550°C using solution spraying rate 2.6–3.0 ml/min.

	Indium concentration in spray solution			
T_{Sn}, °C	**1 at.%**	**2 at.%**	**3 at.%**	**4 at.%**
350	0.25	0.15	0.028	0.049
450	0.085	0.0044	0.0054	0.0049
550	0.069	0.014	0.014	0.012

Increase in In concentration in spray solution has effect on electrical resistivity of ZnO deposited at 350°C, 450°C or 550°C. Independent of the growth temperature, the [In] = 1 at.% was not sufficient to reduce electrical resistivity of ZnO. Doping effect becomes clearly visible starting from 2 at.% using deposition temperature of 450°C. Undoped ZnO film has high resistivity ($\rho = 50$ Ωcm). Addition of indium in amount of 1 at.% into the spray solution results in resistivity of 0.085 Ωcm. ZnO films with the lowest resistivity of 0.004–0.005 Ωcm were achieved when deposited at T_{Sn}=450°C with 2–4 at.% of In in spray solution. Effect of indium concentration is also observed in the films deposited at 550°C, where the lowest resistivity ($\rho = 0.01$ Ωcm) for this deposition temperature was obtained with [In]=2–4 at.% in spray solution.

3.2.2. The effect of growth temperature on properties of indium doped ZnO thin films

To study the effect of the growth temperature on properties of ZnO:In thin films, the In concentration in spray solution was selected to be 3 at.% and films were deposited at 400°C, 450°C, 500°C and 550°C. The X-ray diffraction profiles of ZnO:In thin films deposited at different temperatures with 3 at.% in starting solution are presented in Fig. 4. According to XRD, there are minor changes with the deposition temperature in the interval 400–500°C. ZnO: In films show preferential growth along (101) plane, increase in deposition temperature weakens the intensities of the (102) and (103) planes.

The UV-VIS transmittance spectra of ZnO: In thin films deposited at different temperatures showed (not presented) that all films were more than 80% transparent in visible spectral region. Hence, the optical transparency of ZnO:In thin films deposited at different temperatures is similar.

The resistivity of ZnO: In films (3 at.% of In in solution) decreases from 0.28 Ωcm to 0.004 Ωcm when deposition temperature increases from 350°C to 450°C (see Fig. 5). Further increase in deposition temperature leads to an increase in resistivity and the film deposited at 550°C shows resistivity in the order of 0.01 Ωcm. According to the electrical resistivity measurements T_{Sn}=350°C is not sufficient to deposit electrically conductive ZnO:In thin films. Deposition temperatures above 500°C are also not recommended as electrical resistivity of the films is up to three times higher than in the films deposited at 450°C.

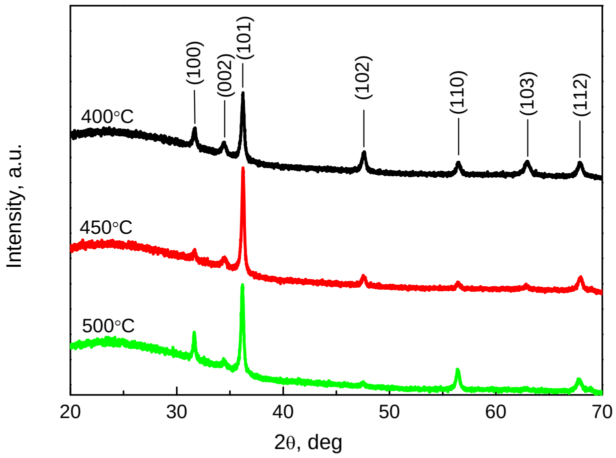

Fig. 4. XRD patters of sprayed ZnO:In films deposited at different temperatures with similar spraying rate of ca. 3 ml/min and constant indium concentration in spray solution (3 at.%)

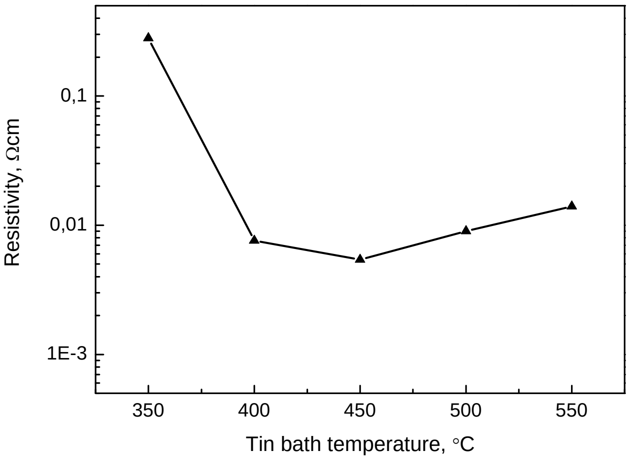

Fig. 5. Effect of deposition temperature on electrical resistivity of ZnO:In films. Indium concentration in spray solution is 3 at.%, spray rate ca. 3 ml/min.

3.2.3. *The effect of spraying rate on properties of indium doped ZnO thin films*

To study the effect of spraying rate on properties of ZnO:In, the films were prepared at T_{Sn} = 400, 450 and 550°C with indium concentration of 3 at.%, spray rate was varied from 1.8 to 4.2 ml/min. The X-ray diffraction patterns of ZnO:In thin films deposited at 450°C using three different spray rates are presented in Fig. 6. With an increase in spraying rate the intensity of the (102) peak is increasing and of the (110) is decreasing. Thus, the spray rate has only some effect on orientation of the crystallites in the film deposited at 450°C with different spray rate.

The optical transmittance spectra of ZnO:In thin films sprayed with different spraying rate showed (not presented) that the optical transparency of all the films deposited at 450°C was more than 80%.

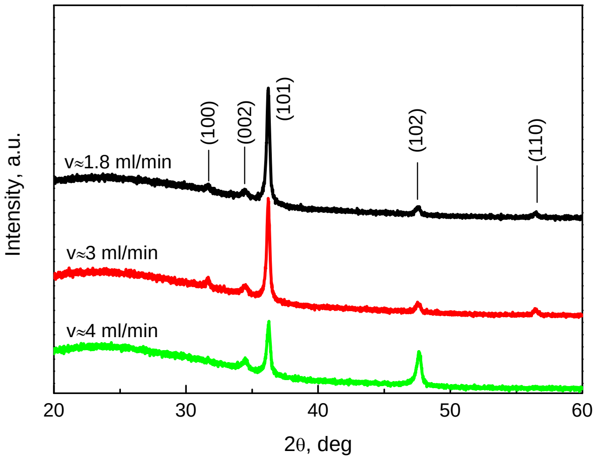

Fig. 6. XRD patterns of sprayed ZnO:In thin films deposited at T_{Sn}=450°C with different spraying rates with constant indium concentration in spray solution (3 at.%)

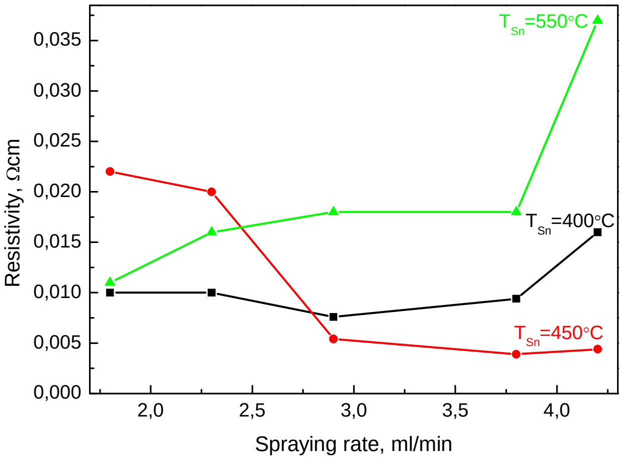

Fig. 7. The effect of spraying rate to electrical resistivity of ZnO:In thin films deposited at different temperatures with 3 at.% of indium in spray solution.

Fig. 7 presents the electrical resistivity of ZnO films prepared at different temperatures depend on the solution spray rate. It can be seen that resistivity of the films obtained with the spray rate of ca. 1.8 ml/min is 0.01–0.02 Ωcm depend on the deposition temperature. For the films deposited at 400°C and 450°C the resistivity values of 0.008 and 0.005 Ωcm, respectively were obtained with the deposition rate close to 3 ml/min. Relatively conductive films with resistivity of 0.004 Ωcm could be obtained at 450°C also with higher spray rates (ca 3.8 ml/min). At the same time spray rates higher than 3 ml/min at 400°C were found to increase ZnO film resistivity. Thus, the solution spray rate is an important parameter controlling the film electrical properties. This observation is in accordance with the earlier results when ZnO films were prepared by pulsed spray with mean spray rate of 0.7 ml/min at 450°C [18]. Electrical resistivity of ZnO: In films prepared by pulsed spray mode was as high as 30–40 Ωcm [18]. ZnO: In films deposited at T_{Sn} = 550°C show electrical resistivity higher than 0.01 Ωcm and using spray rate above 4.0 ml/min causes significant increase in the film resistivity.

4. CONCLUSIONS

A summary of published studies on preparation of electrically conductive and optically transparent ZnO films by chemical spray pyrolysis method was presented. In experimental part of the current work undoped and indium doped zinc oxide thin films were prepared by chemical spray pyrolysis method using pneumatic continuous spray mode and deposition temperatures in the range of 350°C-550°C. According to XRD, undoped ZnO films are highly c-axis orientated. Doping with indium from $InCl_3$ affects the crystallites orientation in the film. Using In concentracion higher than 1 at.% in the solution the crystallites are grown (001) plane parallel to the substrate. ZnO:In films have smooth surface and show optical transmittance of 80–85% in visible region of the spectrum. It has been shown that low spray rates (< 2 ml/min) and growth temperatures above 500°C result in electrical resistivities above 0.01 Ωcm. ZnO films with electrical resistivity of 0.004 Ωcm, which is close to the best values reported in literature, can be deposited by spray of zinc acetate solutions with In concentration of 2–4 at.% in the spray solution using tin bath temperatures close to 450°C and solution spray rate of 3.0–4.0 ml/min.

5. ACKNOWLEDGEMENT

Dr. A. Mere is gratefully acknowledged for his help with X-ray diffraction measurements and Dr. O. Volobujeva is acknowledged for SEM studies.

6. REFERENCES

1. KRUNKS, M., MELLIKOV, E., BIJAKINA, O., VAREMA, T., MEISSNER, D. Formation and properties of chemically sprayed ZnO films. *Proceedings of the SPIE*, 1997, Vol. 2968, p. 129–134.
2. KRUNKS, M., MELLIKOV, E. Zinc oxide thin films by the spray pyrolysis method. *Thin Solid Films*, 1995, Vol. 270, p. 33–36.
3. JAGADISH, C.; PEARTON, S.J. *Zinc Oxide Bulk, Thin Films and Nanostructures.* Oxford: Elsevier, 2006. 589 p. ISBN-13: 978-0-08-044722-3.
4. KRUNKS, M., BIJAKINA, O., MIKLI, V., VAREMA, T., MELLIKOV, E. Zinc oxide thin films by spray pyrolysis method. *Physica Scripta*, 1999, Vol. T79, p. 209–212.
5. PAWAR, B.N., JADKAR, S.R., TAKWALE, M.G. Deposition and characterization of transparent and conductive sprayed ZnO:B thin films. *Journal Of Physics and Chemistry of Solids*, 2005, Vol. xx, p. 1–4.
6. GÓMEZ-POZOS, H., MALDONADO, A., DE LA LUZ OLVERA, M. Effect of the [Al]/[Zn] ration in the startin solution and doposition temperature on the physical properties of sprayes ZnO:Al thin films. *Materials Letters*, 2007, Vol. 61, p. 1460–1464.
7. KAID, M.A., ASHOUR, A. Preparation of ZnO-doped Al films by spray pyrolysis technique. *Applied Surface Science*, 2006, Vol. 256, p. 3029–3033.
8. GÓMEZ, H., DE LA LUZ OLVERA, M. Ga-doped ZnO thin films: Effect of deposition temperature, dopant concentration, and vacuum-thermal treatment on the electrical, optical, structural and morphological properties. *Materials Science and Engineering B*, 2006, Vol. 134, p. 20–26.
9. RAMAKRISHNA REDDY, K.T., GOPALASWAMY, H., REDDY, P.J., MILES, R.W. Effect of gallium incorporation on the physical properties of ZnO films grown by spray pyrolysis. *Journal of Crystal Growth*, 2000, Vol. 210, p. 516–520.

10. WIENKE, J., BOOIJ, A.S. ZnO:In deposition by spray pyrolysis – Influence of the growth conditions on the electrical and optical properties. *Thin Solid Films*, 2008, Vol. 516, p. 4508–4512.
11. LUCIO-LÓPEZ, M.A., LUNA-ARIAS, M.A., MALDONADO, A., DE LA LUZ OLVERA, M., ACOSTA, D.R. Preparation of conducting and transparent indium-doped ZnO thin films by chemical spray. *Solar Energy Materials & Solar Cells*, 2006, Vol. 90, p. 733–741.
12. WIENKE, J., VAN DER ZANDER, B., TIJSSEN, M., ZEMAN, M. Performance of spray-deposited ZnO:In layers as front electrodes in thin-film silicon solar cells. *Solar Energy Materials & Solar Cells*, 2008, Vol. T92, p. 884–890.
13. MALDONADO, A., DE LA LUZ OLVERA, M., TIRADO GUERRA, S., ASOMOZA, R. Indium-doped zinc oxide thin films deposited by chemical spray starting from zinc acetylacetonate: effect of the alcohol and substrate temperatures. *Solar Energy Materials & Solar Cell*, 2004, Vol. 82, p. 75–84.
14. LUCIO-LÓPEZ, M.A., MALDONADO, A., CASTANEDO-PÉREZ, R., TORRES-DELGADO, G., DE LA LUZ OLVERA, M. Thickness dependence of ZnO:In thin films doped with different indium compounds and deposited by chemical spray. *Solar Energy Materials & Solar Cells*, 2006, Vol. 90, p. 2362–2376.
15. CASTAÑEDA, L., GARCIA-VALENZUELA, A., ZIRONI, E.P., CAÑETAS-ORTEGA, J., TERRONES, M., MALDONADO, A. Formation of indium-doped zinc oxide thin films using chemical spray techniques: The importance of acetic acid content in the aerosol solution and the substrate temperature for enhancing electrical transport. *Thin Solid Films*, 2006, Vol. 503, p. 212–218.
16. KRUNKS, M., KATERSKI, A., DEDOVA, T., OJA ACIK, I., MERE, A. Nanostructured solar cell based on spray pyrolysis deposited ZnO nanorod array. *Solar Energy Materials and Solar Cells*, 2008, Vol. 92, p. 1016–1019.
17. DEDOVA, T., KLAUSON, J., BADRE, C., PAUPORTE, TH., NISUMAA, R., MERE, A., VOLOBUJEVA, O., KRUNKS, M. Chemical spray deposition of zinc oxide nanostructured layers from zinc acetate solutions. *Physica Status Solidi*, 2008, Vol. 205, p. 2355–2359.
18. KLAUSON, J. ZnO õhukesed kiled pideva ja pulseeriva pihustamise meetodil. – Master's thesis, Tallinn, 2007.

THE ELECTRICAL PERCOLATION SHIFT IN POLYISOPRENE – NANOSTRUCTURED CARBON COMPOSITE

J. Zavickis, A. Linarts, M. Knite
Riga Technical University
Institute of Technical Physics
Azenes str. 14-322, LV-1007 – Latvia
Phone: +371 29794188
Email: juriszavickis@inbox.lv

ABSTRACT

Previous research approved polyisoprene – nanostructured carbon composite (PNCC) as a prospective material for use as a piezoresistive pressure sensing material in finger pressure range. The major advantage of this material would be hyperelastic flexibility compared with conventional ceramic piezoelectric pressure sensing elements as well outstanding sensitivity for small (<1 Bar) pressures. The PNCC is made when highly structured particles of good conductor (Printex XE2 carbon black) and necessary curing ingredients are dispersed into elastomer matrix (Thick Pale Creppe natural polyisoprene) and vulcanized afterwards. There electrical percolation of PNCC greatly depends on mixing method used. In our work we try to use ultrasound as an alternative way to disperse filler. The roll mixed, mechanically mixed in solution and ultrasound mixed in solution PNCC samples were made. The critical concentrations of electrical percolation were determined and critical indexes were calculated for all types of PNCCs using linear trendlines on log-log plots. The piezoresistive behavior of PNCCs was evaluated and compared.

Keywords: polyisoprene, carbon, nanostructured, composite, piezoresistive

1. INTRODUCTION

1.1. Prime novelty statement

Increasing demand of compressive and strain sensors requires a new materials to be designed for particular application. Usually the pressure and strain sensors are rigid structures, connected with difficulties to integrate them into structure being monitored. Attempts were made to design a flexible pressure and strain sensor made of filled polymer or elastomer. Recent research approved PNCC to be a prospective material for current needs. At certain concentrations of conductive filler these composites shows remarkable reversible tensoresistive and piezoresistive effect [1]. In this work we present an attempt to use PNCC as a perspective material for flexible pressure sensor elaboration. We have estimated the electrical percolation threshold shift for various piezoresistive composites, depending on filler dispersing technique used. We believe that our research will lead to a new kind of functional sensor composite material, which could be used for intelligent sensing in robotics and other smart structures.

1.2 The concept

The conductive polymer-composites for stress and/or strain sensing can be obtained when electrically conducting particles (carbon black, graphite powder, carbon fibers, particle of metals) are implanted into an insulating polymer matrix [2–6]. A continuous insulator-conductor transition is observed in two-component systems at gradual increase of the number of randomly dispersed conductor particles in an insulator matrix. Most often such transitions, called percolation transitions, are described by the model of statistical percolation [7-8]. The volume concentration of conductor particles V_C at which the transition proceeds is called the percolation threshold or critical point [8].

In the vicinity of percolation threshold, the specific electrical conductivity of the composite σ changes as

$$\sigma \sim \left|V - V_c\right|^t, \; if\; V > V_c, \tag{1}$$

where t is the non-universal critical index [8]. According to concept of piezoresistivity, in the sharpest region of the percolation threshold the composite should be the most sensitive to external mechanical action (the region of interest shown in Fig. 1) as well the percolation threshold is expected to shift to lower concentration region, if more effective filler dispersing method is used [1, 9].

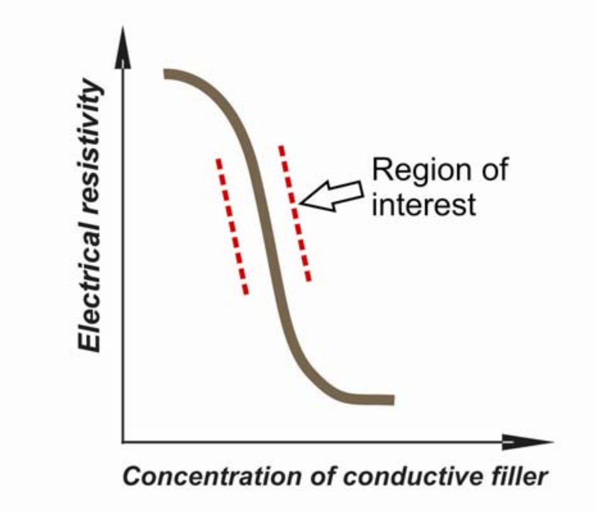

Fig. 1. The schematic illustration of the percolation threshold for carbon filled conductive composites

This means - to gain more piezoresistive sensitivity, the sharpest possible percolation threshold should be acquired with lowest possible fraction of conductive filler, although resulting in more economically effective use of filler.

2. METHODOLOGY

2.1. Making the samples

The polyisoprene – nanostructured carbon composite raw rubber is made from Thick Pale Creppe polyisoprene natural rubber, necessary curing ingredients and high structure carbon black (HSCB). Commercially available Degussa Printex Xe2 HSCB (average particle diameter of 30 nm, DBP absorption value 380 ml/100 g and specific surface area of 950 m^2/g) was used as desired electroconductive filler. The concentration of conductive filler was expressed as “parts per hundred rubber”, adopted from rubber chemistry, later mentioned as p.h.r. in text and figures, which means mass parts of filler per 100 mass parts of natural polyisoprene.

Three types of PNCC raw rubbers were fabricated using different methods for dispersing the conductive filler.

1) Roll mixed PNCC was obtained directly mixing all curing ingredients and HSCB into polyisoprene on cold rolls (Fig. 2.).

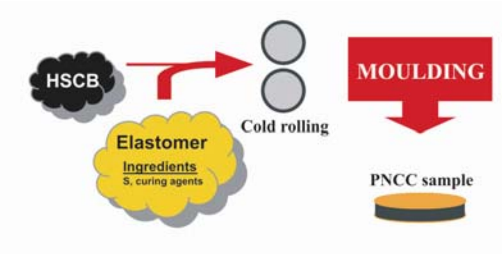

Fig. 2. The making schematics of roll mixed PNCC sample

2) Chloroform solution mechanically mixed (further in text - mechanically mixed) PNCC were made by first mixing curing ingredients (except HSCB) into polyisoprene matrix using cold rolls. Obtained raw rubber was dissolved into chloroform and necessary amount of HSCB was added. Then solution was homogenized by high speed mechanical mixing with small glass beads for 30 minutes. Afterwards the solution was poured into glass plate for chloroform to evaporate and films were obtained. Acquired films were then homogenized using cold rolls with the possible smallest aperture (Fig.3.).

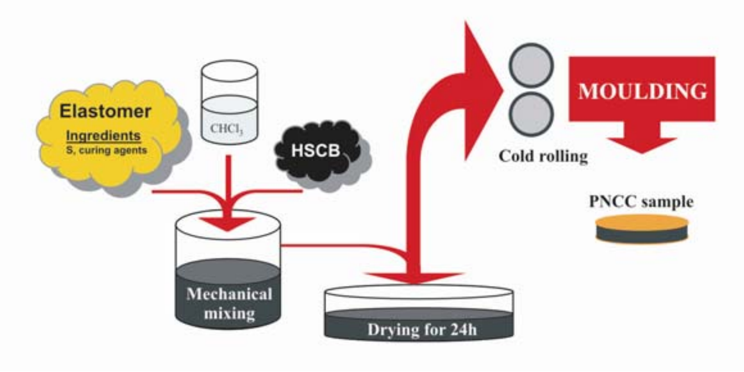

Fig. 3. The making schematics of mechanically mixed PNCC sample

3) Chloroform suspension ultrasound mixed (further in text - US mixed) PNCC were made by first mixing curing ingredients (except HSCB) into polyisoprene matrix using cold rolls. The HSCB was dispersed separately into chloroform using Hielscher UP200S ultrasound homogenizator for 5 minutes. Specific power was 1 W/ml. Afterwards the filler dispersion in chloroform was added to raw rubber/chloroform mixture and stirred in room temperature for 24 h. Then solution was poured into glass plate for chloroform to evaporate and PNCC films were obtained. Acquired films were then homogenized using cold rolls with smallest possible aperture (Fig. 4.).

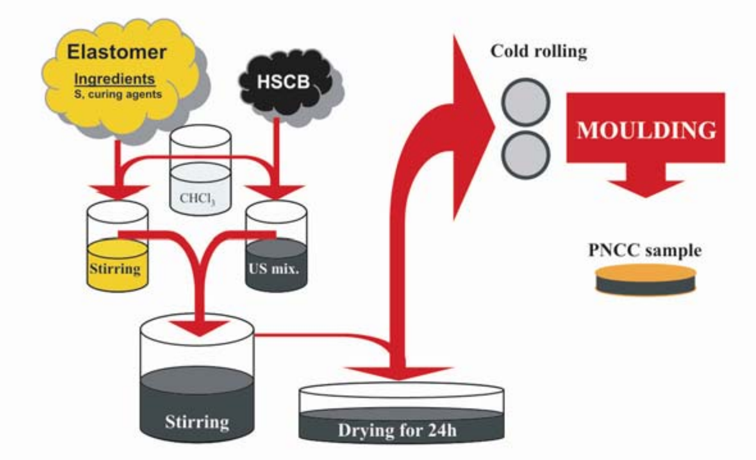

Fig. 4. The making schematics of US mixed PNCC sample

Flat shaped samples in average thickness of 1mm were made by curing raw rubbers in hot stainless steel mould using Rondol™ thermostated press at 150 ºC for 15 to 20 minutes. The sandpaper polished brass foil mould inserts were used to acquire good electrical connection for measurements.

The samples were shelf aged in room temperature for at least 24 h after processing before any electrical measurements were made.

2.2. Instruments and measurements

Before vulcanization the raw rubber compositions was tested on Monsanto rheometer for optimal curing time.

The initial electrical resistivity of the samples was measured using Agilent A34970A digital multimeter/multiplexer and Keithley Model 6487 Picoammeter/Voltage source. The mechano-electrical testing was done using Zwick/Roell Z2.5 universal material testing machine, coupled and synchronized with Agilent A34970A digital multimeter/multiplexer. The samples of lower regions of percolation thresholds were not measured for piezoresisitivity, because the upper resistivity range of the dynamic measuring equipment was limited to 10^8 Ω. The evaluation of the results and trend line fitting was done using Origin8 data analysis and graphing software.

3. RESULTS AND DISCUSSION

First of all initial electrical resistivity of all samples was measured. The percolation transitions obtained from these measurements are displayed in Fig. 5.

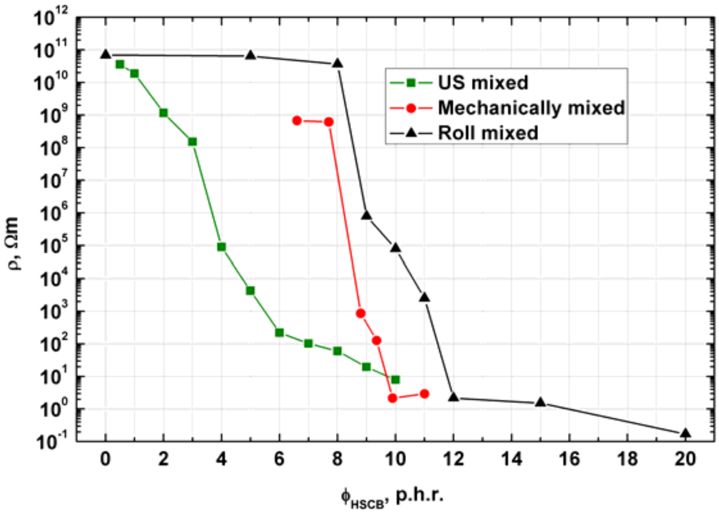

Fig. 5. The specific electrical resistivity as a function of filler fraction for differently prepared PNCCs

As it can be seen, the percolation transition for roll mixed and mechanically mixed PNCC is much steeper than for US mixed PNCC, so theoretically, the better piezoresistive action can be expected. To ease up further investigation, at this point the specific electrical resistivity was converted into specific electrical conductivity. The experimental data were carefully fitted by statistical percolation theory predicted dependence of conductivity on filler concentration (so called "scaling law")

$$\sigma = \sigma_0 (\Phi - \Phi_C)^t . \tag{2}$$

The critical concentrations (Φ_c) corresponding to the percolation threshold were found out for all types of PNCCs (Fig. 6.).

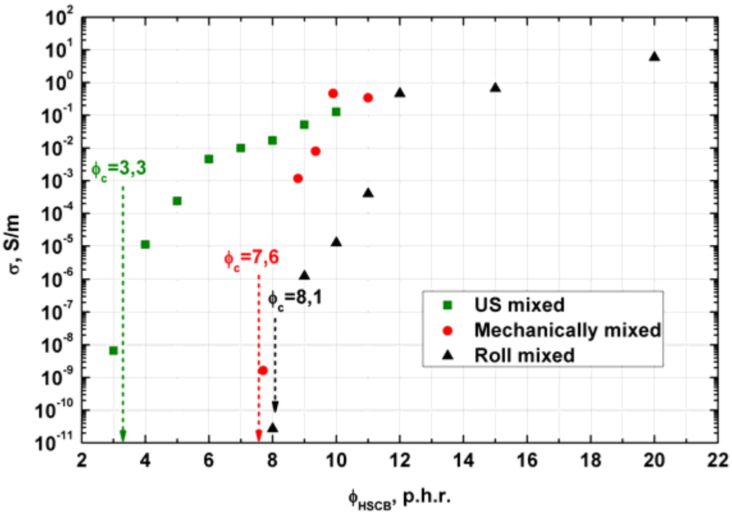

Fig. 6. The specific electrical conductivity as a function of filler fraction for differently prepared PNCCs and their critical concentrations Φ

To properly do this, experimental results was plotted $\log\sigma$ versus $\log(\Phi-\Phi_c)$ (Fig .7) by incrementally varying of Φ_c until the best linear fit was obtained [10].

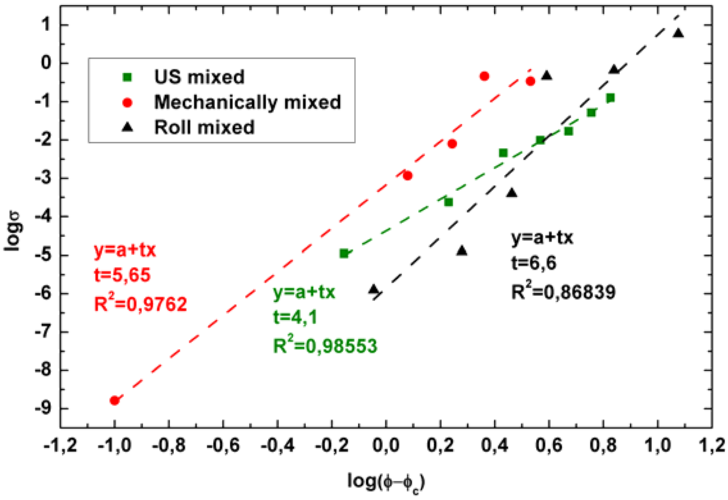

Fig. 7. The linear fitting of conductive part of the logσ versus $\log(\Phi-\Phi_c)$ plot for differently prepared PNCCs.

As it is seen in Fig. 5. and Fig. 6. the mechanical mixing with glass beads in chloroform solution doesn't add much effect on lowering the percolation threshold. In the same time, the chloroform suspension sonicated PNCC provides as much as 2.5 times lower percolation threshold. According to Kilbride et al. [10], the slope of the linear fit trend line of $\log\sigma$ versus $\log(\Phi-\Phi_c)$ plot (see Fig.7) corresponds to the critical index *t*. According to Yakubowicz et al. [11] *t* can be interpreted as average number of simultaneous contacts each conductive particle forms with its neighboring ones. In other words, the critical index describes the complexity of the direct conductive grid, formed by HSCB particles. And as a fact - the larger the *t*, the more sharper the percolation transition appears. Accordingly to this assumption the comparison of critical indexes in Fig. 7 has good correlation with the sharpness of percolation transitions obtained in Fig. 5. This means, that sonication reduces the complicity of HSCB structure, possibly resulting from more uniform distribution of sizes of HSCB aggregates. At the same time, the better distribution of smaller particles should lead to major increase of the role of tunneling currents. According to Bauhofer [12] the intensity of tunneling currents between closely distributed but non-touching conductive particles can be expressed by dependence

$$\ln \sigma_{DC} \propto \Phi^{-\frac{1}{3}}. \tag{3}$$

When plotting the conductive part of percolation threshold as logσ versus $\Phi^{-1/3}$, the coefficient of determination R^2 of its linear fit is proportional to the contribution of tunneling currents mechanism to conductivity (Fig. 8).

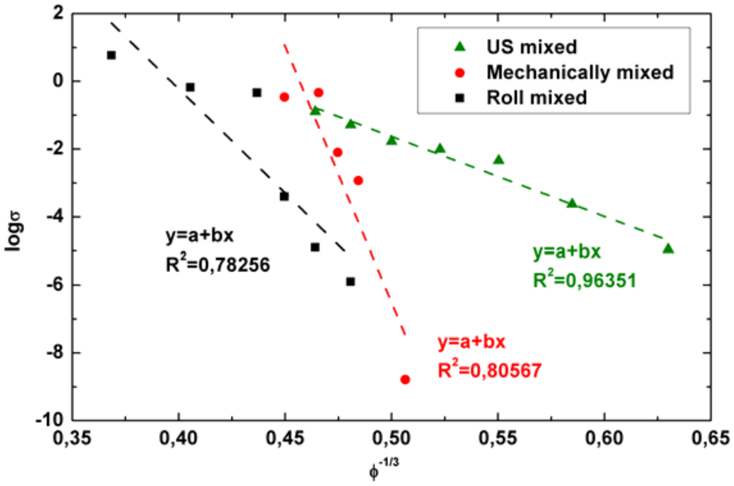

Fig. 8. The linear fit of the logσ versus $\Phi^{-1/3}$ plot for differently prepared PNCCs

The piezoresistive properties (ΔR/R₀, %) under applied external one-dimensional pressure P up to 1 Bar were determined for roll and US mixed PNCC samples (Fig. 9 and 10). Unfortunately, we were unable to perform these measurements on mechanically mixed PNCC, due to proper sample shape unavailability.

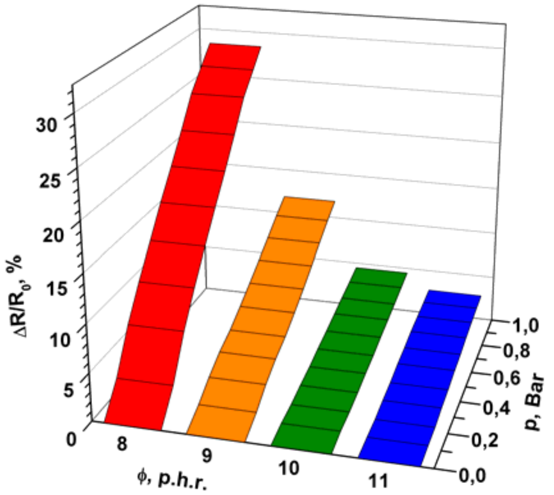

Fig. 9. The piezoresistive behavior of roll mixed PNCCs

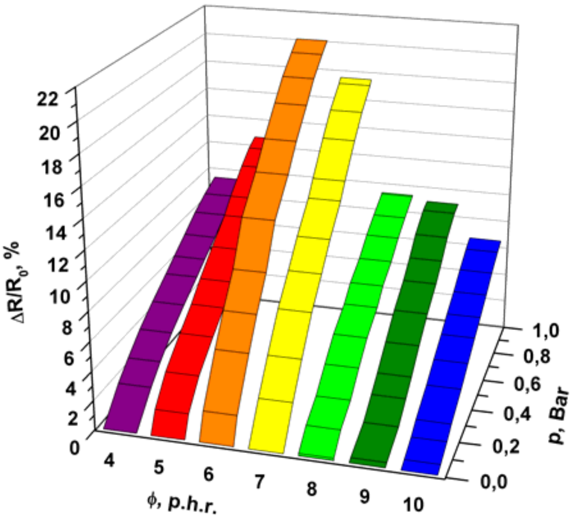

Fig. 10. The piezoresistive behavior of US mixed PNCCs

The measurements of piezoresistive behavior prove that roll mixed PNCCs exhibit large dependence of piezoresistivity on HSCB concentration. The maximal piezoresistivity for mechanically mixed PNCC is found in the lower concentration end of percolation transition (8 p.h.r. on black curve in Fig. 5.). At the same time, the maximal piezoresistivity for US mixed PNCC if found in upper concentration region of percolation transition (6 p.h.r. on red curve in Fig. 5).

This phenomenon can be explained as follows: It is believed, that during mechanical deformation, the inter-particle slippage occurs due to excessive share forces and conductive channels are partly destroyed, resulting in positive piezoresistivity. The conducting channels in roll mixed PNCC are mainly formed by larger HSCB agglomerates. For this reason better piezoresistivity is observed at lower concentrations of percolation transition, where shunting is limited due to small filler concentration. At higher filler concentrations the shunting of conductive channels comes into play reducing the overall piezoresistivity. On contrary the conducting channels in US mixed PNCC consist of well distributed smaller HSCB primary particles, which exhibit better mobility when compared to aggregates, thus more complete conductive grid breakdown is achieved even at larger fractions of filler.

4. CONCLUSIONS

The character of percolation for PNCC is clearly dependant on the mixing method used to disperse HSCB. The US mixed PNCC provided up to 2.5 times lower percolation threshold, in the same time reducing the overall sharpness of percolation transition. The correlation was found between the critical index of percolation, the sharpness of percolation transition and the maximum piezoresisitivity of PNCC. The use of ultrasound for dispersing HSCB in suspension instead of direct roll or mechanical mixing in solution reduces the structure of conductive filler, evidenced by increasing relevance of tunneling currents and noticeably shifting the percolation threshold to lower concentration region. The change of electrical resistivity for roll mixed PNCC can reach up to 30% under applied external one-dimensional pressure of 1 Bar. The maximal piezoresistivity also shifts from lower concentration end of percolation transition for roll mixed PNCC up to higher concentration end of percolation transition for US mixed PNCC. The most believable cause of this is the increased mobility of smaller and better distributed HSCB particles.

5. ACKNOWLEDGEMENTS

The research was supported by the Council of Science of Latvia and by Latvian National Research Program in Materials Science.

This work has been supported by the European Social Fund within the project „Support for the implementation of doctoral studies at Riga Technical University”.

REFERENCES

1. KNITE, M., TETERIS, V., POLYAKOV, B., ERTS, D. Electric and elastic properties of conductive polymeric nanocomposites on macro- and nanoscales. *Material science and engineering: C*, 2002, Vol. 19, No 2, p. 15–19.
2. ANELI, J., N., ZAIKOV, G., E., KHANANASHVILI, I., M. Effects of mechanical deformations on the structurization and electric conductivity of electric conducting polymer composites. *Journal of applied polymer science*, 1999, No 74, p. 601–621.
3. ZHANG, X., W., PAN, Y., ZHENG, Q., YI, X., S. Time dependence of piezoresistance for conductor-filled polymer composites. *Journal of polymer science part B: polymer physics*, 2000, Vol. 38, p. 2739–2749.
4. DAS, N., C., CHAKI, T., K., KHASTGIR, D. Effect of axial stretching on electrical resistivity of short carbon fibre and carbon black filled conductive rubber composite. *Polymer international*, 2002, Vol. 51, p. 156-163.
5. WU, T., M., CHENG, J., C. Morphology and electric properties of carbon black-filled poly(e-caprolactone)/poly(vinyl butyral) nanocomposites. *Journal of applied polymer science*, 2003, Vol. 88, p. 1022–1031.
6. WU, T., M., YAN, M.,C., CHENG, J., C. Thermoelectric properties and morphology of carbon black-filled poly(e-caprolactone)/poly(vinyl butyral)/clay nanocomposites. *Polymer*, 2003, Vol. 44, No 8, p. 2553–2562.
7. STAUFER, D.; AHARONY A., *Introduction in to percolation theory*. Washington DC: Taylor & Francis, 1992. 198 p.
8. BALBERG, I. A comprehensive picture of the electrical phenomena in carbon black–polymer composites. *Carbon*, 2002, Vol. 40, p. 139–143.
9. KNITE, M., TETERIS, V., KIPLOKA, A., KAUPUZS, J, Polyisoprene-carbon black nanocomposites as tensile strain and pressure sensor materials. *Sensors and actuators, A: Physical*, 2004, Vol. 110, No. 1–3, p. 142–149.
10. KILBRIDE, B., E., COLEMAN, J., N., FRAYSSE, .J, FOURNET, P., CADEK, M., DRUDY, A. Experimental observation of scaling laws for alternating current and direct current conductivity in polymer-carbon nanotube composite thin films. *Journal of applied physics*, 2002, Vol. 92, No 7, p. 4024–4030.
11. JACUBOWICZ, J., NARKIS, M. Dielectric behavior of carbon black filled polymer composites. *Polymer engineering and science*, 1986, Vol. 26, No 22, p. 1568–1573.
12. BAUHOFER, W., KOVACS, Z. A review and analysis of electrical percolation in carbon nanotube polymer composites. *Computer science and technology*, 2009, Vol. 69, No 10, p. 1486–1498.

FORMATION OF $Cu_2ZnSnSe_4$ THIN FILMS ABSORBERS FOR SOLAR CELLS

R. Zhang[1], J. Iliyna[1] , L. Kaupmees[1], T. Raadik[1] , J. Raudoja[1], M. Altosaar[1], O. Volobujeva[1], E. Mellikov[1], T. Varema[1], H. Dikov[2], M. Ganchev[1]

1- Materials Science Institute
Tallinn University of Technology, Ehitajate tee 5,
19086 – Tallinn, Estonia
Phone: +3726203374
Email: rz.renzhang@gmail.com

2- Central Laboratory Solar Energy&New Energy Sources
Bulgarian Academy of Sciences,
1786 Sofia, 78 Tzarigradsko shaussee blvd, Bulgaria

ABSTRACT

To understand codeposition of all components of $Cu_2ZnSnSe_4$ (Cu_2ZnSnS_4) electrochemical behaviour of pyrophosphate formulations was investigated. A preliminary analysis using cyclic voltammetry performed for each individual component showed that proposed ligand ($P_2O_7^{4-}$) is suitable for one step codeposition of elements. Presence of the metalloids either Se or S ions (SeO_3^{2-} or SO_3^{2-}) causes an obvious depolarization in depositing of the metal constituents and of the chalcogens itself. This phenomenon indicates that there is a potential interval for induced codeposition in the system Cu-Zn-Sn-Se-S. At higher catodhic potentials where components are deposited in limiting diffusion currents almost stoihiometric Cu_2ZnSnS_4 was deposited.

During the electrodeposition of alloy Cu-Sn layers to avoid oxidation Sn^{2+} ions on the counter electrode the bath volume was separated as anode and cathode part by an ion selective membrane.

The electrodeposited in Potentiostatic conditions thin stacked layers were selenized in an isothermal quartz tubular reactor. Ratio of metal components in selenized films was adjusted through appropriate choice of composition and thickness of the constituent layers. The influence of annealing conditions on crystalline structure, phase composition, surface morphology and photoluminescence of obtained $Cu_2ZnSnSe_4$ thin films is discussed and peculiarities of formation $Cu_2ZnSnSe_4$ thin films determined.

1. INTRODUCTION

Future development of thin film photovoltaics depends on deployment of low cost and easy up scalable deposition methods for abundant and non-toxic compounds [1]. Ternary chalcopyrites $CuInS_2$ (CIS) and $Cu(In,Ga)Se_2$ were promise solution but increasing price of rare metals In and Ga changed unfavorably the cost-efficiency ratio. Replacement of III group metals with cheap and widespread Zinc and Tin serve another opportunity for diversification and industrialization of compound thin film photovoltaics [2]. $Cu_2ZnSnSe_4$ (CZTSe) is a structure analog of CIS where III group (Indium or Gallium) atoms are exchanged with Zinc and Tin. CZTSe is a perspective material with direct band gap near 1.44 eV close to the optimum for the solar irradiation spectra and high absorption coefficient ranging 10^4 cm^{-1} [3].

There are numerous investigations on the sulphur compound Cu_2ZnSnS_4, exploring either atom beam sputtering [4] and thermal evaporations [5] and electron beam evaporated precursors processed in H_2S atmosphere [6]. Later were developed electrodeposition routes [7, 8] for formation of substrate metallic precursors subjected subsequently on sulfurization.

Abou-Ras et al. [7] exploited a particularly elaborated electrolyte for formation of metallic alloy Cu-Zn-Sn precursor layers [9] for building of solar cells.

On the aspect of the selenium compound are developed CZTSe thin layer absorbers by pulsed laser ablation [10], one step RF magnetron sputtering [11] or with sequential selenization [12] as well as synthesis from melts [13]. The recent developed low sulphur containing thin film $Cu_2ZnSn(S,Se)_4$ solar cell has given Voc = 516 mV, Jsc = 28.6 mA/cm^2 and FF 65 % with overall World record efficiency 9.66% [14].

This work presents results of investigations on formation of $Cu_2ZnSnSe_4$ absorber layers by sequential electrodeposition of alloy Cu-Zn and Cu-Sn stacked precursors followed by reactive annealing in atmosphere of selenium vapors.

2. EXPERIMENTAL DETAILS

Electrodeposition of precursor layers was performed on potentiostatic condition with Wenking Bank PGstat 3440 in three-electrode configuration at room temperature (20°C). Reference was a saturated silver chloride electrode (Ag/AgCl: 3M KCl) and counter electrode was platinum gauze with much higher active surface than cathode. The working electrodes were molybdenum covered (near 1 μm thick) soda-lime glass substrates sized approximately 1 x 2.5 cm^2 or molybdenum foils by the same dimensions. Solutions for deposition Cu-Zn and Cu-Sn layers contained 0.6M potassium pyrophosphate and salts of Cu^{2+}, Zn^{2+} and Sn^{2+} following formulations in [15]. Due to oxidizing ability of Sn^{2+} on anode or by the oxygen from air the electrolytic cell for deposition of bronze layers was divided and anode compartment was isolated trough an ion (Na^+) selective membrane. Anolyte was 0.2M Na_2CO_3 and to keep constant cation equilibrium concentrations for membrane the catolyte contained 0.2M $Na_4P_2O_7$ and 0.4M $K_4P_2O_7$ as well as 0.1M Hydroquinone playing role as antioxidant.

Substrate layers Cu-Zn/Cu-Sn were selenized at isothermal conditions in evacuated 5 cm long quartz ampoules at 530°C – 560°C during 15 minutes at 1.5 m long thermal tubular reactor. In order to simulate fast thermal annealing samples with ampoules were situated in preliminary preheated quartz holder pipe – ticker 2 mm, longer 60 cm and with inner diameter 2.5 cm. After that the pipe with ampoule inside was comparatively slowly moved out for cooling down to near 50°C until another 20 minutes. Estimated annealing temperature profile is shown schematically on Fig. 1. Annealing experiments as reactive selenization for 1 hour at 560°C were performed for preliminary preheated in vacuum 150 Torr during 1 hour at 400°C metal alloy sub layers.

Scanning electron microscopy investigations and EDX composition measurements were performed on Hitachi TT1000 unit supplied with X-ray source and detector equipment with accelerating voltage 15.0 kV and acquisition time 90 sec. High resolution micrograms and fine impurities composition measurements were done on Zeiss ULTRA 55 at accelerating voltage 1.74 kV. The room temperature (RT) micro – Raman spectra were recorded by Horiba LabRam 800 high-resolution spectrometer equipped with a multichannel detection system on backscattering configuration. Spectrometer operates by Green 532 nm wavelength laser focused within a 1 μm spot diameter providing the incident light with spectral resolution 0.5cm^{-1}.

X – ray diffraction analysis (XRD) were performed on Rigaku Ultima IV with Cu – Kα radiation (λ=1.5418Å) and 4 kV accelerating voltage The diffracted beam was scanned in steps by 0.01° for 2 sec in angular range from 10 to 80 degrees in 2Θ. A comparison with JCDPS file cards [16] was made to assign the observed peaks. Phases manifested at least with three reflexes are taken into considerations. Optical investigations for determining the type and width of the band gap were carried out on UV-VIS-NIR spectrophotometer JASCO V-670 in the range 200 to 2500 nm.

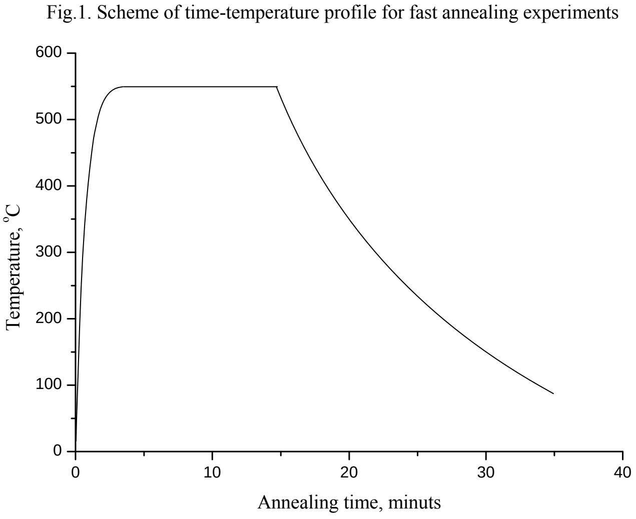
Fig.1. Scheme of time-temperature profile for fast annealing experiments

Fig. 1. Thermal profile for selenization of thin alloy Brass – Bronze layers

3. RESULTS AND DISCUSSION

The electrochemical behavior of the elements was elaborated by potentio-dynamic investigations on Glassy Carbon Electrode (GCE) and by Classical Differential Polarography on Dropping Mercury Electrode (DME). All potentials here are set versus Saturated Ag/AgCl Reference Electrode if is not mentioned other and data are presented in Tabl. 1.

Table 1.1 Differential Polarography and Dynamic Voltammetry data for aqueous solution of Cu^{2+}, Zn^{2+},Sn^{2+}, $S_2O_3^{2-}$ and SeO_3^{2-} in 0.6M $K_4P_2O_7$

Cation	PickPot/$_{\mathrm{lMDE/polgr}}$	vsAg/AgCl	PickPot$_{\mathrm{DinVA/GCE}}$	vsAg/AgCl
Cu2+	E_p'		E_p'	-538mV
	E_p''	-1318mV	E_p''	-850mV
Sn2+	E_p'	-963mV	E_p'	
	E_p''	-1260mV	E_p''	-1230mV
Zn2+	E_p'	na	E_p'	-1650mV
	E_p''		E_p''	
$S_2O_3^{2-}$	E_p'	+48mV	E_p'	
	E_p''	-250mV	E_p''	-1050mV
SeO_3^{2-}	E_p'	-926mV		
	E_p''	-982mV		
	E_p'''	-1744mV		

Surprisingly tin appears at more positive potentials than copper in MDE. Tin reduces on two waves – at – 963 mV and at – 1260 mV. The first can be ascribed on step reduction of Sn^{4+} to Sn^{2+} or adsorption phenomena. Last is for full reduction of tin and was confirmed by dynamic curve also with individual response at –1230 mV

Copper appears at –1318 mV. One can expect appearance of copper reduction wave before reduction wave for Tin. But if are taken into consideration the activity of ligand ions

($P_2O_7^{4+}$) which fix Cu^{2+} much more stronger than Sn^{2+} the picture seems quite reasonable. Dynamic voltammetry presents two waves: first at –538 mV is attributable of the Redox couple Cu^{+}/Cu^{2+} and second – for reduction of Cu^{2+} to elemental Cu^{0}.

Unfortunately, it was not possible to registrate reduction of Zn^{2+} ions to elemental Zn on DME. As it is well known the deposition potential for Zn^{2+} to Zn is quite negative and the reaction is accompanied usually with intensive Hydrogen evolution. In the same condition Dynamic voltammetry has shown a wave with peak at –1650mV.

The as presented investigations are base for development of complex electrolyte for as depositing of multi component alloy and compound material layers.

Tabl. 2. Thin compound layer compositions, deposited at –1500 mV from respective electrolyte compositions – El-15, El-16 and El-17(see Fig. 2)

-1.5V (vs.Ag/AgCl)	a.%Cu	a.% Zn	a.% Sn	a.% S
El 15	21.99	18.65	5.09	54.25
El 16	19.87	11.75	13.22	55.14
	20.66	13.74	11.55	54.04
El 17	18.08	10.06	14.81	57.03

In co-deposition of metals with Tiosulphate have been obtained layers with different sulphur concentration achieving almost near stoichiometric composition (See Tabl. 2.).

Selenium appeared in co-deposits near and below -1.3 V (vs. Ag/AgCl) but on higher cathodic potentials miss probably due to formation of H_2Se. At near -1.5V(vs. Ag/AgCl) from electrolyte with appropriate metals ion (Cu^{2+}, Sn^{2+} and Zn^{2+}) ratio in 0.6M $K_4P_2O_7$ (El 16) were deposited metal alloy Cu-Zn-Sn layers close behind to stoichiometric composition for formation of $Cu_2ZnSnSe_4$ after selenization (Fig. 3).

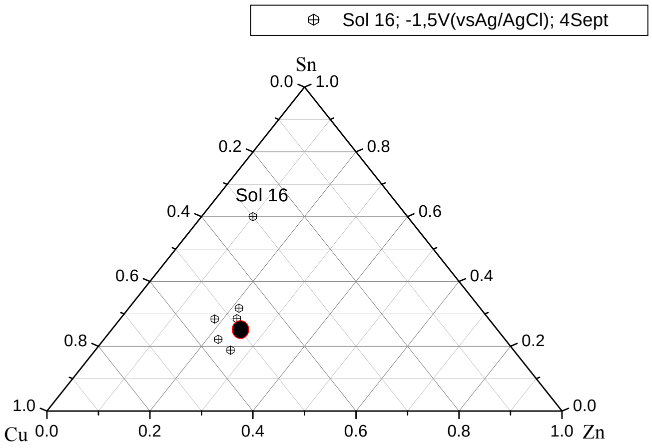

Fig. 2. Electrolyte composition with appropriate ions (Cu2+, Zn2+,Sn2+) ratio – Sol 16 and alloy thin film Cu-Zn-Sn compositions, deposited at –1500 mV

Unfortunately, the electrolyte suffers of lack of stability due to oxidizing ability of Sn^{2+} on air oxygen or on the Counter Electrode in the cell. On other side presence of Tiosulphate or/and Selenite ions in electrolyte causes precipitations. These circumstances imposed to simplify deposition process on two independent depositions of both Brass (Cu-Zn) and Bronze (Cu-Sn) sub layers. Fig. 3 a and b represent micrograms of surface morphology and cross section of a (Cu-Sn) onto (Cu-Zn) sub layers deposited on Mo covered soda lime glass substrate. The deposit is amorphous and estimated overall thickness is near 350 nm.

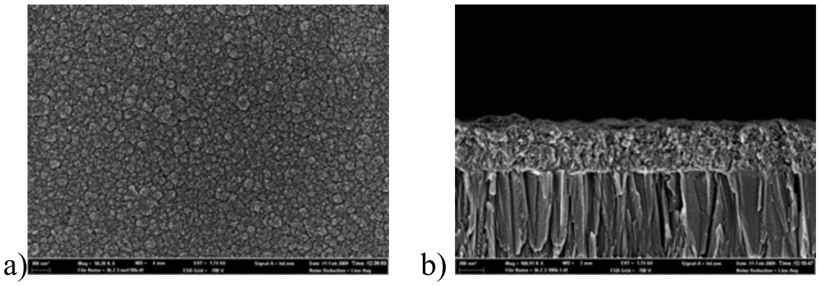

Fig. 3. Surface morphology and cross-section microgrammes of Brass (Cu-Zn) under Bronze (Cu-Sn) substrate layers, deposited on Mo covered soda lime glass electrodes.

Electrodeposition for 40 minutes of Brass layer followed by 3 minutes electrodeposition of Bronze layer ensures formation of 1.5–2 μm thick CZTSe layer after selenization.

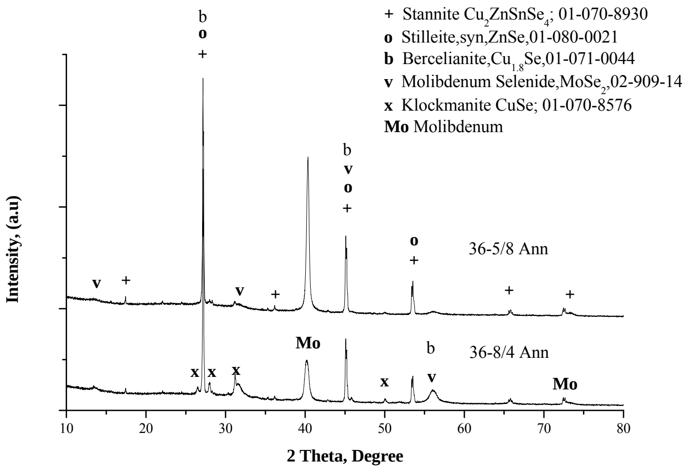

Fig. 4. X-Ray diffraction patterns of thin layers $Cu_2ZnSeSe_4$ annealed in different regimes: Sample 36-5/8 – selenization 15 minutes at 530°C and 20 minutes slow cooling down; 36-8/4 – 1 hour annealing in vacuum and1 hour selenization at 560°C

Fig. 4 presents XRD patterns of samples 36-8/4 and 36-5/8. First one had passed preliminary homogenization annealing in vacuum for 1 hour at 400°C followed by reactive isothermal anneal in Selenium vapors for 1 hour at 560°C. The second sample had been treated for short time (15 minutes) at 530^{o}C and then cooled slowly down following procedure described by Fig.1. In both cases main reflexes of CZTSe at 45.1°, 27.16° and 53.52° in scale 2Θ as well as minorities at 17.44°, 36.25°, 65.98° and 72.65° are seen. Signals are strong and sharp indicating well-crystallized Stannite – (JCDPS 01-070-8930). Well-defined reflexes from Molybdenum substrate layer at 40.18° and 73.4^{o} in 2Θ are additionally detected. The pair of reflexes at 31.66° and 56,9° together with the small peak at 11.54° are assumed to Drysdallite $MoSe_2$ (JCDPS 02-909-14) - a product of selenization of the substrate. Detailed structural analysis has revealed in both cases non-monophase thin film materials. There are minor but well distinguished reflexes at 26.58°, 28°, 31.2° and 50.02°

related obviously to CuSe (Klockmanite – 01-070-8576). It is possible that thin films consist additionally small concentrations of cubic ZnSe (Stilleite – JCDPS 01-080-0021) which pattern coincides with the Stannite at 27.16°, 45.1° and 53.52° in 2Θ scale. In addition scrupulous analysis supposes existence of another phase – $Cu_{1.8}Se$ (Bercelianite – JCDPS 01-071-0044) with possible reflexes at 27.16°, 45.1° and 56.03°.

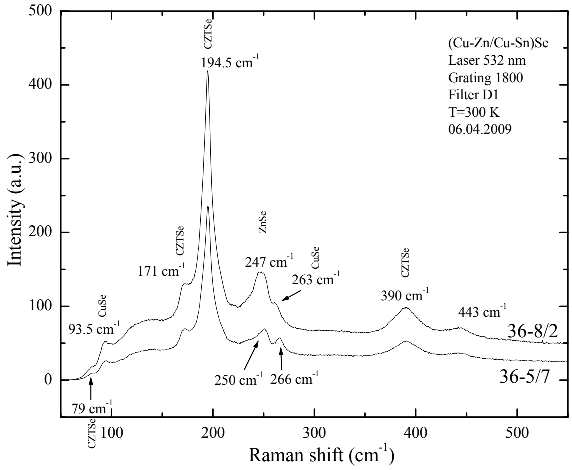

Fig. 5. Room temperature Raman spectra of Cu2ZnSnSe4 thin layers

Fig. 5 presents RT Raman spectra of samples 36-8/2 and 36-5/7 deposited and annealed on the same conditions as sample 36-5/8 from Fig.4. Patterns present defined spectra for well-formed Stannite by almost all important vibrations at 79 cm^{-1}, 173 cm^{-1}, 196 cm^{-1}, 231 cm^{-1} and 390 cm^{-1} respectively. There were two peaks that could be attributed to CuSe – at 94 cm^{-1} and near 263 cm^{-1}. Registered signal at 247 cm^{-1} may due to the presence of cubic ZnSe in films. The weak vibration at 443 cm^{-1} could be attributed to bond Si-O-Si from substrate [17].

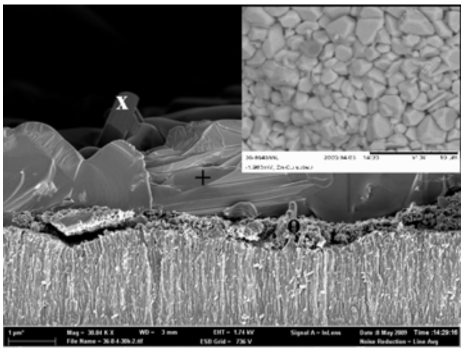

Fig. 6. SEM cross section microgram of CZTSe thin film, annealed in vacuum for 1 hour followed a selenization at 560°C for 1 hour. Insertion presents the surface morphology image of the same film

Fig. 6. presents a SEM cross section and surface morphology micrograms of sample 36-8/4 preliminary annealed in vacuum for 1 hour at 400°C and selenized at 560°C for 1 hour. As we could take insights from XRD and Raman spectra the formed thin films consist of large grains of CZTSe sized more than 1μm. More detailed observations reveal fine grains situated mainly on big grain boundaries of the bottom layer and flat hexagonal well-formed crystals

situated mainly on the surface of the layer. High definition EDX allows determining the compositional peculiarities of described objects. Big grains composition (measured at point +) indicates slightly Tin rich CZTSe (23.8 at.% Cu- 11.3 at.% Zn – 13.7 at.% Sn – 51.2 at.% Se) thin film material. Fine crystallites on the interface Mo - CZTSe pointed as **o** present composition 52.7 at.% Zn – 47.3 at.% Se that corresponds to the Stilleite phase (see Fig. 4). Flake microcrystal grains on the surface – pointed **x** were defined to correspond to the Klockmanite (Fig. 4) giving 47.5 at.% Cu – 52.5 at.% Se.

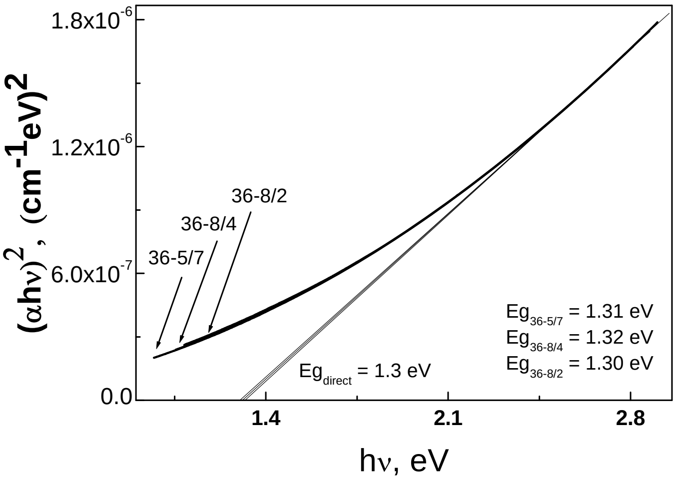

Fig. 7. Plot for determining of band gap of $Cu_2ZnSnSe_4$ films selenized at different conditions: 36-8/4 -1 hour at 400°C in vacuum +1 hour at 560°C and 36-8/2&36-5/7 for 10 minutes at 530°C. The analysis is based on the assumption that CZTSe is a direct band gap material

At Fig. 7 are presented curves of dependence of $(\alpha h\nu)^2$ on optic light energy hν for CZTSe layers deposited in similar conditions but annealed both by fast (10 minutes selenization at 530°C -36-8/2&36-5/7) or through preliminary metal alloys homogenization at 400°C for 1 hour and 1 hour selenization at 560°C – sample 36-8/4. The band gap of the CZTSe thin films was estimated to be 1.31 eV ± 0.01 eV. This value is lower than those reported earlier 1.44 eV and 1.56 eV [3, 5] but it seems to be closer to them than proposed recently for monograin materials near 1 eV [18].

Comparing the samples shift intensities on Fig. 5 it is possible to conclude that a longer annealing time acts favourably to formation of well-crystallized Stannite $Cu_2ZnSnSe_4$.

4. CONCLUSIONS

The electrochemical behavior of elements Copper, Zinc, Tin, Selenium and Sulphur were investigated in order to formulate an electrolyte composition for their co-deposition. An almost stoichiometric compound Cu_2ZnSnS_4 thin layer was deposited but electrolyte was not stable due to the oxidizing ability of Sn^{2+} ions by air Oxygen or on the counter electrode in the cell.

Electrodeposition of alloys Brass and Bronze substrate layers followed by selenization give a successful route for formation of well-crystallized Stannite thin film structures. Shorter annealing time may lead to favorable formation of Stannite thin films but the system is still multi phase. All thin layers showed similar optic properties and band gap near 1.31 eV.

5. ACKNOWLEDGEMENTS

Faculty of Chemical and Materials Technology Tallinn University of Technology

European researcher’s mobility program of Estonian national science foundation under Contract JD 98 is gratefully acknowledged.

REFERENCE

1. A Vision for Photovoltaic Technology for 2030 and Beyond, European Commission, 2004.
2. Feltrin, A. Freindlich, Material considerations for terawatt level deployment of photovoltaics, Renew. Energy 33 (2008) 180–185.
3. H.Matsushita, T.Maeda, A.Katsui and T.Takadzawa, J.Cryst.Growth 208, 416 (2000).
4. K. Ito, T. Nakazawa, Jpn. J. Appl. Phys. 27 (1988) 2094.
5. Th. M. Friedlmeier, N. Wieser, T. Walter, H. Dittrich, H.-W. Schock, Proceedings of the 14th European Conference of Photovoltaic Solar Energy Conference and Exhibition, Belford, 1997, p. 1242.
6. H. Katagiri, K. Jimbo, K. Moriya, K. Tsuchida, Proceedings of the 3rd World Conference on Photovoltaic Solar Energy Conversion, Osaka, 2003, p. 2874.
7. Ennaoui A., Lux-Steiner M., Weber A., Abou-Ras D., Kotschau I., Schock H.-W., Schur R., Holzing A., Jost S., Hock R., Voss T., Schulze J., Kirbs A., Thin Solid Films, xxx (2008) xxx-xxx.
8. Scragg J., Dale P., Peter L., Electrochemistry Communications 10 (2008) 639-642.
9. H. Kühnlein, J. Schulze, T. Voß, Metal plating composition and method for the deposition of copper–zinc–tin suitable for manufacturing thin film solar cell, Patent WO2007134843, Nov. 29, 2007.
10. R.A.Wibowo, E.S.Lee, B.Munir, K.H.Kim, Pulsed laser deposition of quaternaryCu2ZnSnSe4 thin films, Phys. Status Solidi (a)204(2007) 3373–3379.
11. R.A.Wibowo,W.S.Kim,E.S.Lee,B.Munir,K.H.Kim,Single step preparation of quaternary Cu2ZnSnSe4 thin films by RF magnetron sputtering from binary chalcogenide targets, J.Phys.Chem.Solids 68 (2007) 1908–1913.
12. O.Volobijeva, J.Raudoja, E.Mellikov, M.Grossberg, S. Bereznev, R.Traksmaa, Cu2ZnSnSe4 films by selenization of Sn-Zn-Cu sequential films, Journal of Physics and Chemistry of Solids, 2009.
13. M.Altosaar, J.Raudoja, K.Timmo, M.Danilson, M.Grossberg, J.Krustok, E. Mellikov, Cu2Zn1_x Cdx Sn(Se1_y Sy)4 solid solutions as absorber materials for solar cells, Phys. Status Solidi (a) 205 (2008) 167–170.
14. T. Todorov, K. Reuter, B. Mitzi, Adv.Mater. 2010, 22, 1–4
15. Ямпольский А.М., Ильин В.А., Краткий Справочник Гальванотехника, Ленинград “Машиностроение”, 1981.
16. Powder Diffraction File, Joint Committee on Powder Diffraction Standards, American Society for Testing and Materials, Philadelphia, Pa, 1967, PDF 40-1487.
17. Instrument Engineers' Handbook: Process measurement and analysis, Béla G. Lipták,Edition: Published by CRC Press, 2003; ISBN 0849310830, 9780849310836.
18. Grossberg M., Krustok J., Timmo K., Altosaar M., Radiative recombination in Cu2ZnSnSe4 monograins studied by photoluminescence spectroscopy, Thin Solid Films 517, 7 (2009), 2489-2492.

CYSENI 2010, May 27–28, Kaunas, Lithuania
ISSN 1822-7554, www.cyseni.com

STABLE CARBON ISOTOPE RATIO MEASUREMENTS IN AEROSOL PARTICLES, GENERATED FROM VARIOUS INTERNAL COMBUSTION ENGINES

A. Garbaras, R. Barisevičiūtė, T. Šneideris, V. Remeikis
Institute of Physics
Savanoriu av. 231, LT-02300, Lithuania
Email: Garbaras@ar.fi.lt

J. Matijošius, S. Pukalskas
Vilnius Gediminas Technical University
Faculty of Transport Engineering Department of automobile transport
J. Basanavičiaus str. 8, LT-0322, Lithuania

ABSTRACT

Aerosol particles play important role in the global climate change. The indirect effect of aerosols is their impact on the size and number of cloud droplets. A second indirect effect of aerosols on clouds, namely their effect on cloud lifetime also lead to a negative temperature forcing. Establishing aerosol particle sources is an important task. One of the methods which allows "fingerprinting" carbon origin in aerosol particles is measurement of the carbon isotope ratio. Discrimination among isotopes occurs in internal combustion engines due incomplete combustion. Fuel and combustion products (CO_2, aerosol particles) have a different isotopic signature. For determination anthropogenic carbon part in aerosol particles it is necessary to know what changes in the isotope ratio occur during combustion. In our study we used petrol, diesel and gas driven vehicles to generate aerosol particles. The aerosol particle carbon isotopic signature differs depending on the fuel used and presence of a catalytic converter in a car. We have shown that in internal combustion engines generated aerosol particles the carbon isotope ratio is overlapping with particles of natural origin and solely cannot be used for estimating carbon amount from fossil fuel combustion. Combination of stable and radioactive carbon isotope ratio measurements would be a promising tool for aerosols sources characterization.

Keywords: $\delta^{13}C$, Biofuel, Ethanol, Blend

1. INTRODUCTION

The relative contributions of different emission sources of carbonaceous aerosols to the urban atmosphere, their formation mechanisms, transformations and transport are not well understood. Stable carbon isotope composition analysis has been extensively used for establishment of the initial pollution source and permitting a semi-quantification of their respective contributions.

During real incomplete combustion, not only carbon dioxide and water steam but also carbon monoxide (CO), unburned hydrocarbons (HC), nitrogen oxide (NO_x) and particulates (PM) appear.

Highly efficient combustion can produce CO_2 that makes up over 90% of the total carbon transformation, but less efficient combustion reduces the CO_2 production to as low as 50% with the other products such as CO, methane and other volatile hydrocarbons. Incomplete combustion also produces particulate matter by condensation of volatile organic compounds onto existing aerosols as well by emission of combustible debris [1, 2].

Carbon naturally possesses two stable isotopes: ^{12}C makes up 98.89% of all carbon and ^{13}C–1.11% of all carbon. The variations of heavier isotope are of the order of 0.001÷0.05 %, so the δ notation in units of per mil (‰) is used to report changes in isotopic abundance. The partitioning of isotopes between two substances with different isotope ratios is called the isotope fractionation (noted $\Delta^{13}C = \delta^{13}C_{products} – \delta^{13}C_{reactant}$). There are two main reasons for the isotope fractionation appearance: (i) isotope exchange reactions; (ii) kinetic processes, mainly depending on differences in reaction rates of isotopic molecules.

As combustion reactions are generally not total, it can be expected that they are associated with carbon-isotope fractionation ($\Delta^{13}C$), i.e. the reaction will favor one of the stable carbon isotopes (^{13}C or ^{12}C) in the end-products.

As very little researches related with stable isotope fractionation during combustion processes has been done, the one of the aims of this work was to determine the relation between aerosol particles and used fuel.

Another aim of this work was to investigate combustion products of diesel engine using as fuel ethanol - diesel blend changing engine working parameters.

The global fuel crisis in 1970 s stimulated the development of alternative fuel sources. The ethanol-diesel blends were the subject of intense investigations in 1980s. It was shown that this blend was technically accepted for existing gasoline engines. The high ethanol production cost at that time meant that this blend could be acceptable in the fuel shortage case. In recent 10 years the dwindling fossil fuel sources force the expanding use of biofuel. Ethanol is an attractive alternative fuel because it is a renewable bio-based resource and reduction of particulate emission as having oxygen in its structure [3].

The aim of this work was to investigate the aerosol particles, generated in internal combustion engines, using stable isotope ratio mass spectrometry.

2. METHODOLOGY

For establishment of the relation between vehicle emitted aerosol particles and used fuel four cars described in Table 1 were selected.

Table 1. List of studied automobiles

Type	**Manufacture**	**Year**	**Working volume, l**	**Cleaning system**
Gasoline	Volvo	1994	2	-
Diesel	Hyunday	2000	2.5	Exhaust gas recirculation system
Gasoline	Honda Civic	2000	1.6	Three-way functional catalytic converter
Liquefied petroleum gas	Volkswagen	1993	1.8	-

For investigation of combustion products of diesel engine using as fuel ethanol -diesel blend with various engine working parameters the engine control system *КИ-5543* with 4-cylinder diesel engine was used (Fig. 1., Table 2).

As was mentioned above all carbon isotope data are reported in the delta notation ($\delta^{13}C$) relative to the Pee Dee Belemnite (PDB) standard as follows:

$$\delta^{13}C = \left(\frac{\left(\frac{^{13}C}{^{12}C} \right)_{sample}}{\left(\frac{^{13}C}{^{12}C} \right)_{s\tan dart}} - 1 \right) * 1000, ‰.$$

Analytical precision and calibration of reference gas CO_2 to PDB were estimated by repeated analysis of certified reference material BCR 657, which gave an average $\delta^{13}C$ of – 10.76‰ and SD equal to 0.08‰ (certified value – 10.76±0.04‰).

Table 2. Engine specifications (Model IZ)

Type	In-line4-cylinder
Working volume V_h, cm^3	1896
Compression ratio ε	19,5
Maximum power P_e, kW	66 (4000 min^{-1})
Maximum torque M_s, Nm	180 (2000…2500 min^{-1})
Idling torque, Nm	780…860

Aerosol particles emitted from exhaust pipes were collected on the 47 mm diameter quartz-fiber filters. The quartz-fiber filters were baked before sampling at 600 ºC for 5 hours to remove organic impurities. After sampling they were stored in a refrigerator. The filters were analyzed with the elemental analyzer (FlashEA 1112) connected to the stable isotope ratio mass spectrometer (ThermoFinnigan DeltaPlus Advantage) [4, 5].

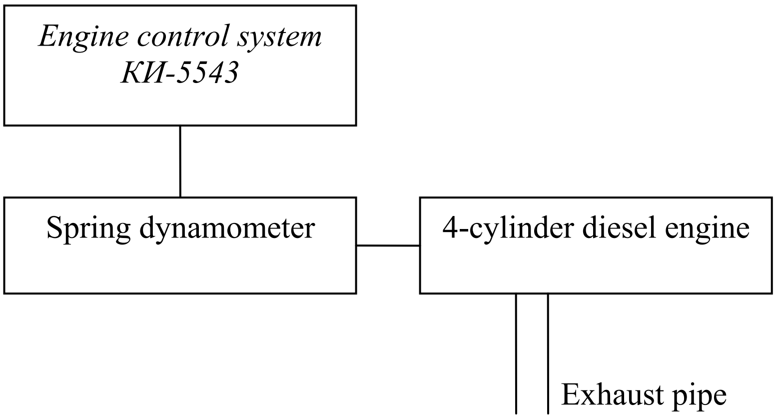

Fig. 1. Schematic diagram of experiment system

The filters were cut into 11 mm diameter pieces, placed into the tin capsule and combusted in the oxidation furnace at the 1020 ºC temperature and with the oxygen excess. Carbon of the sample oxidized into CO_2. Later this gas passed into the reduction furnace (650 ºC). The water from the sample in the He flow was removed using the magnesium perchlorate trap. Then the gas mixture was separated in the column PoraPlot Q (50º C). Separated gas passed to the mass spectrometer ionization cell through the gas distribution device ConFlow III.

3. RESULTS AND DISCUSSIONS

3.1. Carbon isotope fractionation induced by combustion processes in internal combustion engines

The measured $\delta^{13}C$ values of fuels and their combustion are presented in Table 3.

Table 3. $\delta^{13}C$ of fuel and vehicle exhaust aerosol particles.

	Gasoline without cleaning system	Diesel	Gasoline with Three-way functional catalytic converter	Liquefied petroleum gas
Fuel	-30.5 ± 0.2 ‰	-31.1 ± 0.4 ‰	-29.6 ± 0.3 ‰	
Aerosol particles	-27.8 ± 0.2 ‰	-28.2 ± 0.5 ‰	-23.6 ± 0.8 ‰	-29.3 ± 0.8 ‰

Carbon isotope discrimination ($\Delta^{13}C=\delta^{13}C_{product}-\delta^{13}C_{fuel}$) is positive in particle formation. It was determined that $\Delta^{13}C = 2.7 \pm 0.2$ ‰ for aerosol particles emitted by the gasoline automobile without a catalytic converter and $\Delta^{13}C = 2.9 \pm 0.5$ ‰ for aerosol particles emitted by the diesel automobile. These results are very similar to presented by Widory ($\Delta^{13}C = 3.3 \pm 1.1$ ‰ for aerosol particles emitted by diesel and gasoline automobiles) [2] and comparable to the results ($\Delta^{13}C \approx 2.5$ ‰ for aerosol particles emitted by diesel automobiles and $\Delta^{13}C \approx 4$ ‰ for aerosol particles emitted by Magna gasoline using automobiles) presented by López-Veneroni [6]. The biggest fractionation between fuel and the aerosol particles occurred in the engine with a catalytic converter ($\Delta^{13}C = 6 \pm 0.8$ ‰). It can be explained in the way that a catalytic converter oxidizes unburned hydrocarbons [7] to CO_2. The rest of the material with the higher oxidizing potential (and higher ^{13}C content) survive and later are present in the aerosol particles. Thus using stable isotope mass spectrometry we demonstrate that a catalytic converter play important role in the reducing of unburned hydrocarbons amount in the exhaust gas.

3.2. Effect of ethanol content in the fuel on aerosol particle formation

For investigation of combustion products of the diesel engine with different engine working parameters used blends are described in Table 4.

Table 4. Fuel blends and their $\delta^{13}C$

Fuel	**$\delta^{13}C$, ‰**
Diesel	-30.7 ± 0.1
Ethanol	-25.2 ± 0.9
90% diesel and 10% ethanol	-30.3 ± 0.5
60% diesel and 40% ethanol	-29.1 ± 0.5

Carbon isotopic values of diesel and 10% ethanol-diesel blend are similar, but isotopic values of aerosol particles, generated during combustion differ significantly when load is 49 Nm (Fig. 2). When the load is 98 Nm, the carbon isotopic values of the aerosol particles not varies despite the higher ethanol concentration in the fuel and has value about -28 ‰. The main reason for changing $\delta^{13}C$ of emitted aerosol particles is combustion efficiency. These measurements show that ethanol does not participate in the aerosol particles formation during normal load of the engine.

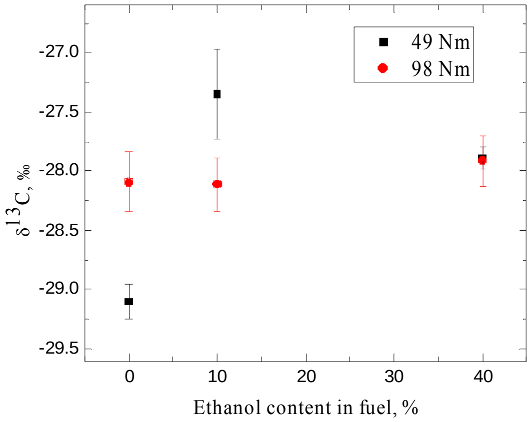

Fig. 2. Effect of ethanol content in fuel and engine load on $\delta^{13}C$ of engine emitted aerosol particles

Use of the ethanol-diesel fuel blend produces less aerosol particles comparing with pure diesel. This feature can be used when the anthropogenic particles emission must be reduced.

4. CONCLUSIONS

It has been determined that the carbon isotope discrimination is positive in particle formation. Isotope fractionation between fuel and aerosol particles differs depending on a fuel used and engine type. For gasoline engine $\Delta^{13}C = 2.7 \pm 0.2$ ‰ (without catalytic converter) and $\Delta^{13}C = 6 \pm 0.8$ ‰ (with catalytic converter). For diesel engine $\Delta^{13}C = 2.9 \pm 0.5$ ‰.

During investigation of combustion products of diesel engine at different engine's working parameters and using ethanol diesel blends it has been determined that ethanol does not participated in aerosol particle formation during normal operation conditions.

The stable isotope ratio mass spectrometry can be used as a tool for quality evaluation of combustion processes.

REFERENCES

1. HEYWOOD J. B. *Internal combustion engine fundamentals*. McGraw-Hill, 1988. 930 p. ISBN-10:007028637X.
2. WIDORY, D. Combustibles, fuels and their combustion products: a view through carbon isotopes. *CombustionTheory and Modelling*, 2006, Vol. 10, p.831–841.
3. AGARWAL, A. K. Biofuels (alcohols and biodiesel) applications as fuels for internal combustion engines. *Progress in Energy and Combustion Science*, 2007, Vol. 33, p. 233–271.
4. GARBARAS, A., ANDRIEJAUSKIENĖ, J., BARISEVIČIŪTĖ, R., and REMEIKIS, V. Tracing of atmospheric aerosol sources using stable carbon isotopes. *Lithuanian Journal of Physics*, 2008, Vol. 48, No. 3, p. 259–264.
5. GARBARAS, A., RIMŠELYTĖ, I., KVIETKUS, K., and REMEIKIS, V. $\delta^{13}C$ values in size-segregated atmospheric carbonaceous aerosols at a rural site in Lithuania. *Lithuanian Journal of Physics*, 2009, Vol. 49, No. 2, p. 229–236.
6. LOPEZ-VENERONI, D. The stable carbon isotope composition of PM2.5 and PM10 in Mexico City Metropolitan Area air. *Atmospheric Environment*, 2009, Vol. 43, p. 4491–4502.
7. NAKAGAWA, F., TSUNOGAI, U., KOMATSU, D. D., YAMADA, K., YOSHIDA, N., MORIIZUMI, J., NAGAMINE, K., IIDA, T., and IKEBE, Y. Automobile exhaust as a source of 13C- and D-enriched atmospheric methane in urban areas. *Organic Geochemistry*, 2005, Vol. 36, p. 727–738.

CHARACTERISTICS OF EROSION PLASMA COUNTER-FLOWS INTERACTION IN A CONFINED AREA

U.M. Hryshchanka, P.P. Khramtsov, O.G. Penyazkov
Heat and Mass Transfer Institute of the National Academy of Sciences of Belarus
15 P.Brouki Street, Minsk BY-220072, Republic of Belarus
Phone: +375(17)2842246
Email: furst2006@tut.by

ABSTRACT

The parameters of interaction of plasma erosion flows in a confined area are presented. The collision of plasma flows in the confined area is characterized by large energy volume density and time of existence of the cumulative zone in comparison with the collision in the unconfined area.

Keywords: erosion, plasma, accelerator, confined area, spectrum, electron temperature, electron concentration

1. INTRODUCTION

Study of physical processes of interaction of plasma erosion flows is of undoubted fundamental and practical interest to solve actual scientific and applied problems of quantum electronics, photochemistry, radiation plasma dynamics, etc.

Works [1–3] describe in detail a cumulative discharge where a plasma flow is decelerated and its kinetic energy is thermalized as a result of interaction with a similar counter-flow. The described below interaction process is based on high-current discharges of magnetoplasma compressor of erosion type in vacuum and, as a rule, in the conditions when a cumulative zone is confined in the radial direction by transparent cylindrical walls [1]. It is shown that the region of plasma flow interaction (cumulative zone) is a dense structure confined on two sides by strong shock waves, the velocity of which is by the order of magnitude less than that of incoming flows. This gives evidence both of the efficiency of dissipation processes, i.e., practically complete thermalization of kinetic energy of colliding flows, and of the plasma heating in the interaction zone.

Collision of compression plasma counter-flows gives an impetus to form rather stable quasi-steady spherical plasma structures that exist for more than 50 μs [4].

The purpose of work is research of quasi-stationary plasma formations with high energy content for practical applications in high thermal physics and diagnostic of materials under extreme conditions.

2. EXPERIMENTAL SETUP

Fig. 1 illustrates the schematic of the experimental setup for studying erosion plasma flows. An end erosion plasma accelerator is a system of two coaxial copper electrodes separated by a caprolone insulator. An outer copper electrode is shaped as a convergent nozzle having an outlet cross section 20 mm in dia. The diameter of a caprolone insert is 30 mm. The accelerator was mounted in a vacuum chamber by means of copper coaxial current supply. Visualization, photography and spectral investigation were made through special vacuum chamber optical windows.

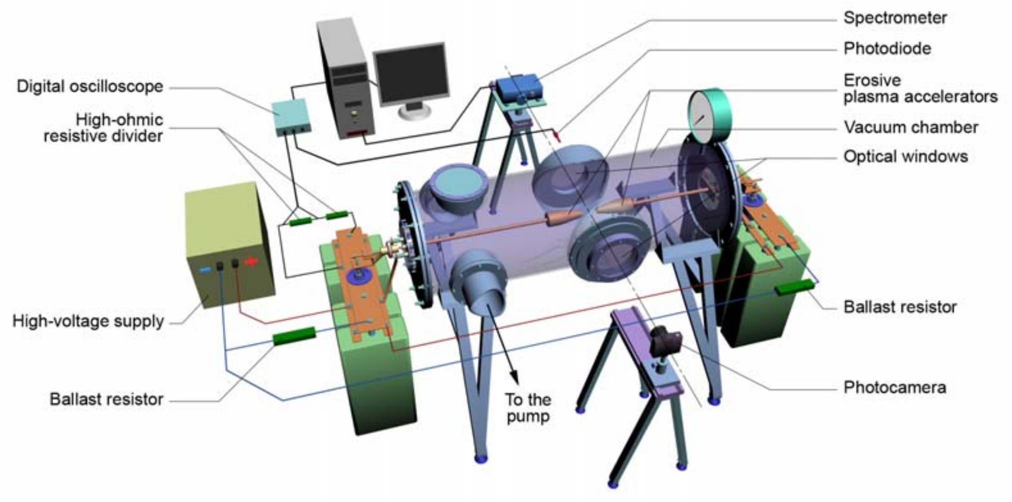

Fig. 1. Schematic of the experimental setup for studying erosion plasma flow collision

Each accelerator was put into operation by discharging a condenser battery with a total capacitance of 600 μF. Condensed batteries were charged from a high-voltage source over the range from 0 to 6 kV.

Investigations were measured at a residual air pressure in the vacuum chamber not exceeding $3 \cdot 10^{-3}$ Torr. The discharge current amplitude of the erosion accelerator was varied from 90 to 140 κA when the initial voltage of the energy accumulator was increased from 3 to 4 κV. Discharge current was measured by Rogowki's loop, and condenser battery voltage – by a high-Ohmic resistance divider.

3. INTERACTION OF EROSION PLASMA FLOWS

Fig. 2 presents the photo of simultaneous operation of the both accelerators and the time dependence of total plasma luminosity in the region of erosion plasma flow collision.

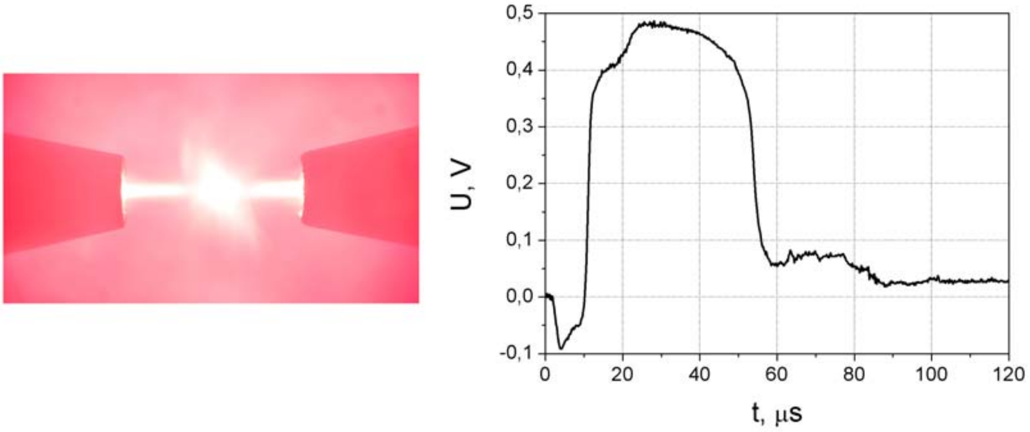

Fig. 2. Photo of simultaneous operation of accelerators and the time dependence of total luminosity of a plasma jet

Two erosion plasma counter-flows interacted in the unconfined area and also in the area confined by a quartz tube placed between the accelerators. The outer tube diameter was approximately equal to the diameter of the outlet cross section of the accelerators (20 mm). Collision dynamics is shown in Fig. 3.

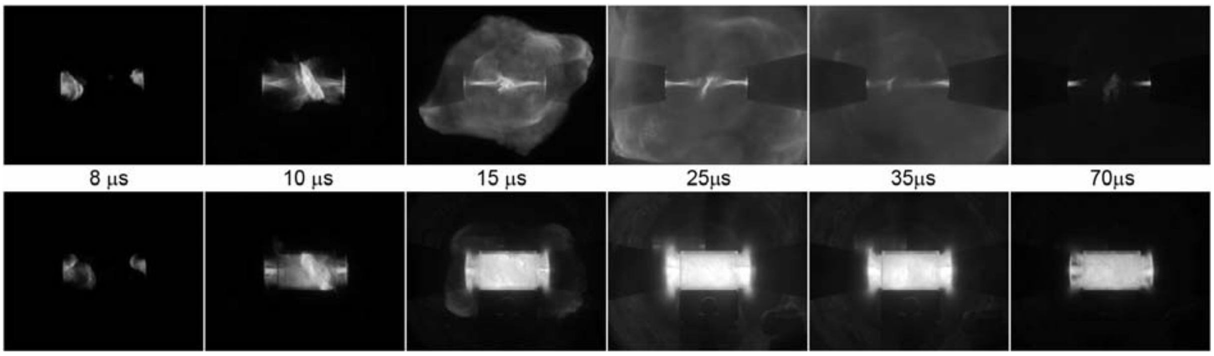

Fig. 3. Collision dynamics of erosion plasma counter-flows in the unconfined area (top) and in the area confined by a quartz tube (bottom)

Our experiments show that the collision of plasma flows in the confined area is characterized by large energy volume density and time of existence of the cumulative zone (about 120 µs) in comparison with the collision in the unconfined area.

The recorded spectral 300÷1200 nm emission regions show mainly continuum radiation, atomic hydrogen lines and the most intensive (resonance) lines of atoms of elements that are constituents of dielectric material. Caprolone (poly-ε-caproamide) served as dielectric material and its chemical formula is of the form $[-NH(CH_2)CO-]_n$. Accordingly, the erosion plasma spectra show resonance lines of hydrogen, nitrogen, oxygen and carbon (Fig. 4).

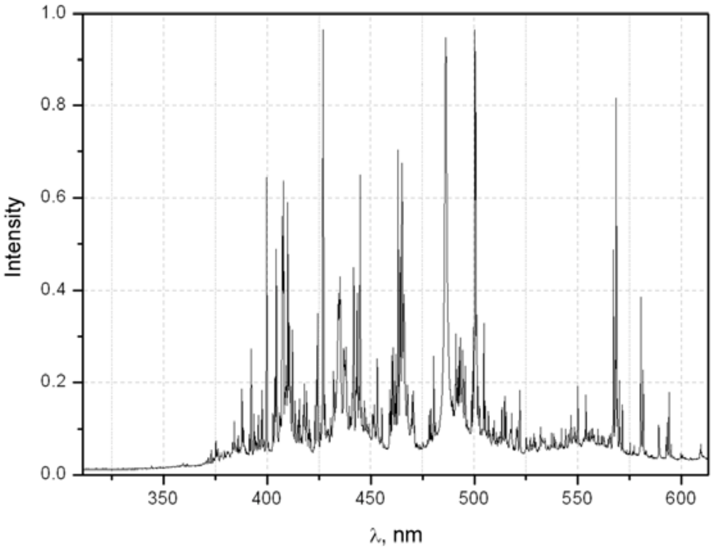

Fig. 4. Spectrum of erosion plasma emission

An electron temperature T_e in the plasma flow collision region was determined by the ratio of the intensity of the Balmer line of hydrogen H_γ in the spectral region in the vicinity of this line, assuming that local thermodynamic equilibrium exists. When the maximum value of discharge current was equal to 140 кA, the electron temperature in the plasma at a distance of 1 cm from the cathode cross section was ~ $3.8 \cdot 10^4$ K.

The electron concentration N_e was determined from Stark's broadening of the Balmer line of H_β. When the maximum discharge current was equal to 140 кA the electron concentration was $2 \cdot 10^{16}$ cm^{-3} [5].

4. CONCLUSION

Basic parameters of plasma (electron temperature and concentration) in the region of erosion flow collision are determined in experiments: plasma temperature is $3.8 \cdot 10^4$ K and plasma electron concentration is $2 \cdot 10^{16}$ cm^{-3}. The limitation on the region of plasma flow interaction allows increasing energy volume density and time of existence of a cumulative zone.

REFERENCES

1. Плазменные ускорители и ионные инжекторы. / Под ред. А. И. Морозова. М., Наука. 1984. с. 5–49.
2. Генераторы лазерного и мощного теплового излучения на основе сильноточных плазмодинамических разрядов. М., Наука. 1984. с. 50–81.
3. Протасов Ю. С., Протасов Ю. Ю. Импульсный источник коротковолнового ультрафиолетового излучения высокой плотности мощности // Приборы и техника эксперимента. 2003. № 2. с. 72–77.
4. Асташинский В.М., Ананин С.И., Аскерко В.В., Костюкевич Е.А. Исследование процессов взаимодействия двух встречно направленных компрессионных плазменных потоков // Труды VII симпозиума Беларуси и Сербии по физике и диагностике лабораторной и астрофизической плазмы (ФДП-VII’2008). Мн. 2008. с. 162–165.
5. Диагностика плазмы / Под ред. Р. Хаддлстоуна и С. Леонарда. М., Мир. 1967.

CYSENI 2010, May 27–28, Kaunas, Lithuania
ISSN 1822-7554, www.cyseni.com

ELECTRICAL CHARACTERISTICS OF DOUBLE-LAYER SUPERCAPACITORS

Ž. Kavaliauskas, L. Marcinauskas
Lithuanian Energy Institute
Breslaujos str. 3, LT-4440, Kaunas - Lithuania
Phone: +370 37 401 895
Email: zydrunas@mail.lei.lt

ABSTRACT

Supercapacitors due to their large specific capacitance, high power density, and high efficiency of charging are widely used in the electronic devices, uninterrupted power sources, hybrid car, and power distribution systems. Carbon electrodes were deposited using atmospheric pressure plasma torch in the mixture of argon and acetylene gases on stainless steel substrates. The ratio of Ar/C_2H_2 was verified in the range 15–55. The arc voltage was 36 V, arc current - 25 A, deposition time – 150 s, and the distance between plasma torch outlet and sample – 5 mm. After carbon deposition the coatings were immersed in low pressure oxygen plasma for 1 min. Surface structure and topography were characterized by scanning electron microscopy (SEM), JEOL JSM–5600. Bulk microstructure of carbon coatings were analyzed using the X-ray diffraction. The capacitance values and breakdown (stability) voltage of fabricated supercapacitors were measured. It is shown that with the increase of the ratio Ar/C_2H_2 from 15 to 55 the capacitance of supercapacitor increases from 1.6 mF up to 3.6 mF. Meanwhile, the stability voltage of supercapacitor increases from 0.40 V up to 0.50 V with the decrease of the Ar/C_2H_2 ratio from 55 to 15.

Keywords: supercapacitors, electrode, carbon

INTRODUCTION

In recent decade, a great attention is focused on the development and research of the supercapacitors. The supercacitors due to the specific properties (large capacitance, high power density, high efficiency of discharge) are widely used in the electronic devices, uninterrupted power supplies, hybrid car and power distribution systems [1–2].

Carbon materials (such as carbon black, carbon nanotubes, carbon aerogel, activate carbon) are widely use as the electrode materials of supercapacitors (SC). These materials are attractive due to high surface area, low electrical receptivity, high porosity, remarkable thermal and mechanical properties [3–4]. Plasma technologies are widely used to modify properties, such as surface composition, structure and topography of coatings [5]. It is known that a non-equilibrium nature of the processes in plasma results in a reduction of carbon density by 30–40% and formation of surfaces with an enhanced surface area. Plasma coatings, as result of the activated redistribution of atoms on the surface and in the near-surface layer, demonstrate highly developed surface topography which includes many clusters and nanoformations of complicated geometry formed under plasma interaction with growing film [6]. Recently, there is much interest in technologies of carbon materials fabricated using the atmospheric plasma torch [7]. The ability to control the material fluxes and processing conditions more precisely is a strong motivation for using plasma torch technologies to optimize the properties of supercapacitor electrodes. The quantitative assessment of the effects of plasma interaction is complicated in reactive plasma environment because of a complex mixture of atoms, molecules, activated species, ions and electrons is present in combinations of flux and energy which are currently difficult to measure and control. In this complex situation, it is possible to establish a correlation between electrical characteristics of supercapacitor and properties of electrode material which are modified changing technological parameter, as in the present work, such as gas flow ratio of Ar/C_2H_2 keeping fixed other parameters. This parameter is specific technological and is in complicated relation with the fundamental carbon growth processes.

EXPERIMENT

The atmospheric plasma torch technology was used for the fabrication of thick carbon coatings with high effective surface area on the surface of stainless steel 1X18H9T substrates. Carbon layer was deposited using the plasma torch from the mixture of argon and acetylene gases at atmospheric pressure. Argon was used as gas carrier and acetylene as precursor. The ratio of Ar/C_2H_2 was verified in the range 15–55. The arc voltage was 36 V, arc current – 25 A, deposition time – 150 s, and the distance between plasma torch outlet and sample – 0.01 m. After carbon deposition, coatings were immersed in low pressure oxygen plasma for 1 min.

The analysis of surface topography of fabricated electrodes was carried out using a scanning electronic microscope (SEM) JEOL JSM–5600. The bulk microstructure of coatings was analyzed using X-ray diffraction (XRD) in the Bragg-Brentano configuration with the 2Θ angle in the range 10–70° using CuK_α radiation in steps of 0.05°. Simple supercapacitors have been manufactured including plasma carbon electrodes. These simple devices are sandwiches of plasma carbon electrodes with an electrolyte permeating the space between and within them. Aqueous solution (dilute KOH electrolyte) was used as an electrolyte. A separator was used to keep the electrodes from contacting each other. The stainless steel was used as the current collector. The electrical characteristics (capacitance and breakdown voltage) of fabricated supercapacitors were measured using standard electrical circuit.

RESULTS AND DISCUSSIONS

The surface topography of fabricated electrodes significantly depends on the acetylene gas amount in the argon plasma (Fig. 1). It is seen that the surface structure of carbon coating deposited at $Ar/C_2H_2=15$, after the oxygen plasma treatment, includes many self-developed 10–30 μm size formations and contains many loosely adhered particles. The rough cluster formations, randomly distributed with deep holes between clusters were obtained (Fig. 1b). As the acetylene amount in the argon plasma decreases, the surface includes many 1–10 μm size formations (Fig. 1d). It may be noted that the surface roughness increases with the decrease of the Ar/C_2H_2 ratio. The increase of the surface roughness leads to the higher value of the surface area. Such phenomenon is explained considering the peculiarities of argon-acetylene plasma. The microstructure of as-deposited carbon coatings was analyzed by XRD. The XRD patterns of the etched carbon coatings showed reflections corresponding to the grapheme sheet plane at $2\theta=24.5^\circ$ (Fig. 2).

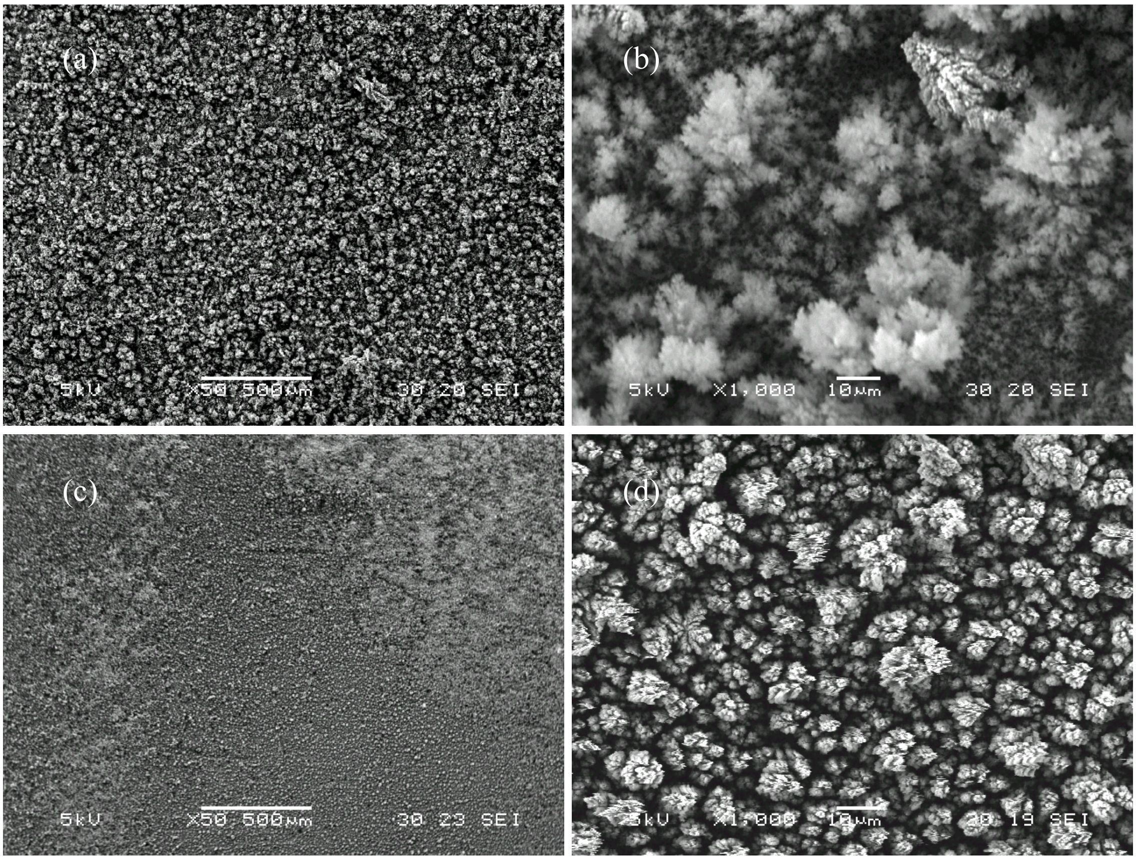

Fig. 1. SEM images of the carbon coatings after treatment in low pressure oxygen plasma: a, b – with Ar/C_2H_2=15 and c, d – with Ar/C_2H_2 =55

The large width of this peak and complete absence of other order peaks in the XRD spectra suggested a disordered amorphous structure for all considered coatings. It may be noted that as the Ar/C_2H_2 ratio decreased to 15, the graphite-like peak became narrower indicating the same ordering process in the coating.

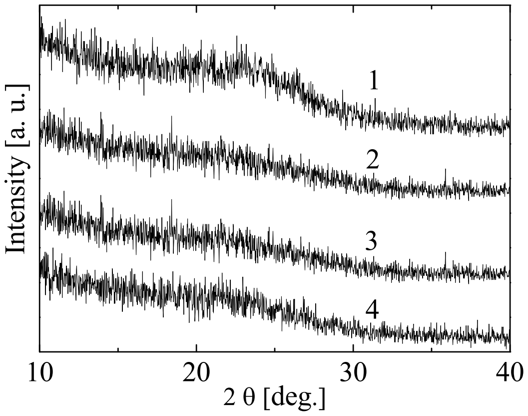

Fig. 2. X-ray diffraction patterns of as-deposited carbon coatings for different ratio of Ar/C_2H_2 values: 1 – 15, 2 – 27, 3 – 40, and 4 – 55

The dependences of the supercapacitor electrical parameters on the ratio of Ar/C_2H_2 were measured. Fig. 3 and Fig. 4 show dependences of supercapacitor capacitance and stability voltage on the ratio of Ar/C_2H_2, correspondingly. The obtained results indicated that with the increase of the ratio Ar/C_2H_2 from 15 to 55, the supercapacitor capacitance increases from 1.6 to 3.6 mF (Fig. 3). Meanwhile, the stability voltage of supercapacitors increases from 0.40 V up to 0.50 V with the decrease of the Ar/C_2H_2 ratio from 55 to 15 (Fig. 4). The volume plasma processes cannot be clearly separated from processes on the surface [1–2].

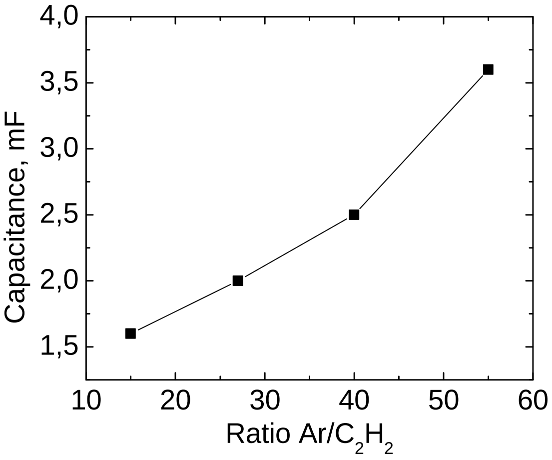

.

Fig. 3. The dependence of supercapacitor capacitance on the ratio of Ar/C_2H_2

The increase of the capacitance is related to the surface morphology of the carbon coatings. As the Ar/C_2H_2 ratio increases the surface roughness decreases. So, it should lead to lower capacitance values due to the decrease of the surface area. However, in our case the double electrical layer is formed on the top of the electrode surface [4]. Hence, the oscillation of dipoles and the Brown movement will proceed only in the upper carbon layers. Meanwhile, if the surface morphology of the electrode were very rough, the electrical layer would be formed in the internal layers of carbon electrodes. As a result of this, the Brown movement will be inhibited and the capacitance values will be lower.

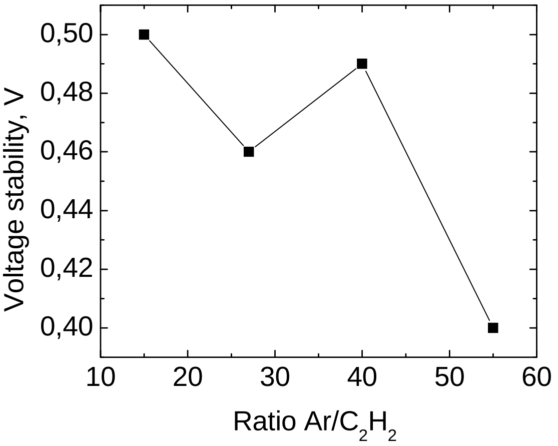

Fig. 4. The dependence of supercapacitor stability voltage on the ratio of Ar/C_2H_2

Pandolfo [3] indicated that the increasing proportion of conjugated carbon in the sp^2 state during carbonization progressively increases the conductivity of the starting material as electrons associated with π-bonds are delocalized and become available as charge carriers. As a result of this the capacitance values increase. Probably when the Ar/C_2H_2 ratio increases the carbon structure consist from the higher fraction of the sp^2 carbon sites. So, the capacitance increases due to higher conductivity of the electrode. The understanding of carbon growth using plasma torch in C_2H_2 reactive gas is not complete and interpretation of experimental results is complicated. The plasma volume reactions are necessary for the creation of species deposited. The efficiency of decomposition of the process gas depends on the ratio of Ar/C_2H_2. The variation of Ar/C_2H_2 ratio will change the plasma composition and flow density of the various hydrocarbon species.

CONCLUSIONS

1. Surface morphology analysis indicated that the surface roughness of the carbon coatings increases with the decrease of the Ar/C_2H_2 ratio.
2. The XRD diffraction measurements indicated highly disordered amorphous microstructure for all carbon coatings.
3. The increase of the Ar/C_2H_2 ratio from 15 to 55 increases capacitance value from 1.6 up to 3.6 mF.
4. The stability voltage of supercapacitors increases from 0.40 V up to 0.50 V with the decrease of the Ar/C_2H_2 ratio from 55 to 15.

REFERENCES

1. Kotz R, Carlen M. Principles and applications of electrochemical capacitors, Electrochimica Acta 45 (2000), p. 2483–2498.
2. Burke A., R&D considerations for the performance and application of electrochemical capacitors Electrochimica Acta 53 (2007), p. 1083–1091.
3. Pandolfo A, Hollenkamp A. Carbon properties and their role in supercapacitors Journal of Power Sources 157 (2006), p. 11–27.
4. Ganesh V, Pitchumani S, Lakshminarayanan V. New symmetric and asymmetric supercapacitors based on high surface area porous nickel and activated carbon Journal of Power Sources 158 (2006), p. 1523–1532.
5. Liu X, Pickup P. Ru. Oxide supercapacitors with high loadings and high power and energy densities Journal of Power Sources 176 (2008), p. 410–416.
6. Wu M, Gao J, Zhang S, Chen A. Effect of carbamate esters on neurite outgrowth in differentiating human SK-N-SH neuroblastoma cells Journal of Power Sources 159 (2006), p. 365–369.
7. Wu M, Zhang L, Wang D, Xiao C, Zhang S. Cathodic deposition and characterization of tin oxide coatings on graphite for electrochemical supercapacitors Journal of Power Sources 175 (2008), p. 669–674.

CYSENI 2010, May 27–28, Kaunas, Lithuania
ISSN 1822-7554, www.cyseni.com

NUMERICAL SIMULATION OF UPRISING GAS-SOLID PARTICLE (OIL-SHALE ASH) TURBULENT FLOW IN CFB BY DIFFERENT MATHEMATICAL MODELS

Igor Krupenski, Alexander Kartushinsky, Andres Siirde
Tallinn University of Technology
Department of Thermal Engineering
Kopli 116, 11712 Tallinn, Estonia
Phone: +372 58003989
Email: ikrupenski@gmail.com

ABSTRACT

The concentration of solid particles of the ash and inert material taken place in a combustion chamber of the circulating fluidized bed (CFB) is very high, that gives a rise to some disadvantages. At the same time, the required temperature level occurred in a combustion chamber is guaranteed by the circulation of solid particles. In this work we give an overview of numerical simulations of gas-solid particles flow, which were performed by 2-Dimenisonal Reynolds-Averaged Navier-Stokes (2D RANS) approach method and Turbulent Boundary Layer (TBL) model. The compare of the results with figures are shown in the work, which qualitatively and quantitatively describe the real-time distribution of flow parameters in real flow domain, i.e. model covers reasonable physical phenomena occured in fluidized bed conditions. The results of this work would be helpful for improving of the processes occurred in the combustion chamber of CFB.

Keywords: circulating fluidized bed, oil-shale, two-phase flow, two-fluid model

1. INTRODUCTION

Over 90% of electricity produced in Estonia is made by power plants firing local oil-shale and 25% of the boilers are of the CFB variety. Fluidized bed is the fine solid particles hovering system in gas flows, which inside motion gives it fluid properties, so arises pseudo-fluid and that is how fluidized bed is called. Solid particles layer becomes a fluidized bed layer in a gravitation field if the blown particles gas flow dynamic pressure force equilibrates the gravity force of the particles. In accordance with a widespread introduction of the CFB furnaces in power plants the concentration of the ash solid particles in the furnace gases substantially increases. The ash particles of the pulverised firing boilers can be observed in the furnace gases as an inconvenient admixture. These particles pose specific problems such as the behaviour of inorganic matter in combustion process, fouling, high temperature corrosion and wear of the steam boilers heating surfaces. In the CFB furnaces the ash solid particles are used mainly as the solid heat carrier – separated in hot cyclone and cooled in heat exchange the ash particles come back into the furnace. By the circulating ash mass the temperature level in furnace is held in the given range. While the heat capacity of ash is quite low, then the circulating ash mass must be high. The high ash concentration in furnace gases is attained a) by the high velocity of gas in the bed and that of most fuel particles carried out of bed are burned and their ash fills the whole volume of furnace and b) by the ash circulation. The CFB combustion technology enables to bind the sulphur components with the carbonate components added to the fuel or existing within the mineral part of the fuel [1].

A disadvantage of CFB is that some fuel ash particles become too fine during the circulation and therefore the size of the ash particles contained in the fuel gas exiting the hot cyclone is too small. As a result of disintegration, the mass of the fine ash particles, which are not separated from the flue gases or occurred in the connective flue ducts and in the multicyclone, increases. The high concentration of particles in the fire gases of the CFB furnace chamber contributes to the formation of the particle clusters with the solid phase concentration within 0.1–0.2 m^3/m^3. At the exit of the CFB boiler furnace the density of solid phase is within 5–20 kg/m^3 [2].

The numerical simulations are mainly performed within the Lagrangian approach by the tracking of single particles or their packages in order to capture the particle-fluid interactions. For example, the two-dimensional gas-solid particles flow taken place in the CFB riser with a total volume concentration of solids 3% has been studied in [3] by the Lagrangian approach using the particles tracking method.

In the present study the two-fluid model, i.e. the Eulerian approach, is applied for the motion of the dispersed phase. The advantage of the Eulerian method is to obtain the distributions of all flow dynamic parameters, including the particle mass concentration. This method does not depend on the number of the tracked particles which model the motion of the disperse phase, contrary to the Lagrangian approach, which convergence is determined by the number of the tracked single particles that can be up to hundreds of thousands, and it requires high computational capabilities.

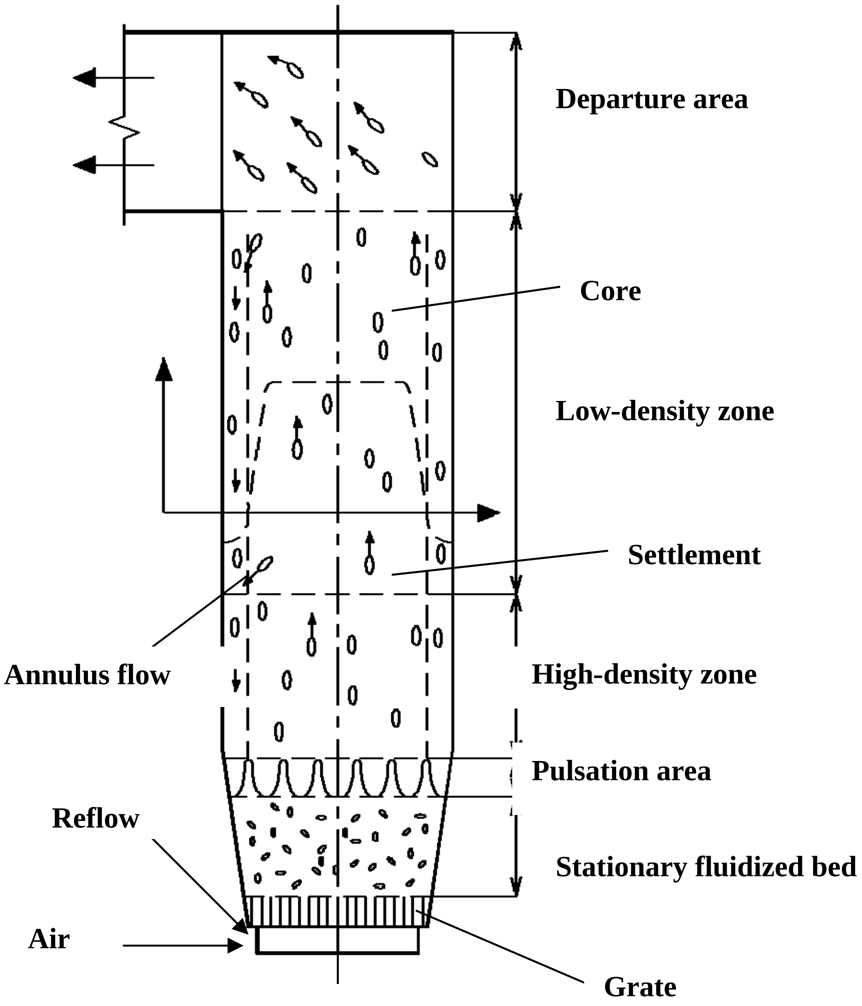

Fig. 1. Internal aerodynamics in circulating fluidized bed furnace [2]

In circulating fluidized bed furnace there is a rather complex structure of aerodynamics, which scheme is shown on Fig. 1.

The furnace internal aerodynamics is affected by the furnace dimensions and heat input (gas velocity in furnace).

Taking into account the characteristic parameters of two-phase flow, the furnace process by height (by grate surface) could be divided into four zones. The first part is situated near the grate, high-density solid-phase, which is similar to classical fluidized bed. This zone may be in turn divided into a further layer situated directly on the grate and upper layer pulsating zone. Due to high surface velocity these parts are not so clearly separable from the rest as in case of classical fluidized bed.

The first zone is followed by the high-density upper layer zone and the solid-phase low-density area in turn. The fourth one is a departure area. Furnace internal aerodynamics in the fourth zone depends on both the furnace, as well as its geometric shape and hatch dimensions, as well as speed and density of the solid-phase hatch outside the section.

Circulating fluidized bed internal furnace two-phase flow aerodynamics affects the so-called wall effect, which appears especially in case of large appliances.

Part of outgoing particles, which departure from layer and rise up are concentrated in colonies,in which solid-phase volumetric concentration is 0.1–0.2 m^3/m^3. Such colonies leave the flow, bound to the wall and under gravity fall back to the layer. Particles may also have a specific cross-flow component from the wall to the centre of the furnace, but it is not of paramount importance. Particles colonies are more likely in areas where solid phase is denser and gas surface velocity is smaller (the variation of particle concentration and velocity in furnace cross-section is shown in Fig. 1).

In the present work the gas-solid particles flow in conditions of CFB is studied, taking into account the amount of heat, which must be separated from the combustor by the sensible heat of the ash solid ash particles. This approach enables to optimize the concentrations of the ash solid particles in fire gases.

2. METHODOLOGY

In the area of multiphase flows there were developed a lot of models for particulate flows in pipes [5, 12]. “Two-fluid model” is being used in the modelling of dispersed two-phase systems, where the gas and the particles are considered as two coexisting phases that reach the entire flow domain. In the present study we perform numerical simulation using two different models: Turbulent Boundary Layer (TBL) model and 2-Dimensional Reynolds-Averaged Navier-Stokes (2D RANS) model.

2.1. Turbulent Boundary Layer (TBL)

This implies that the diffusive source terms were only retained in one direction, namely in transverse direction, and magnitude of the average transverse velocity components of the gas- and dispersed phases were much less than that of the longitudinal components of the corresponding velocities of both phases. Such approach is thoroughly valid and used in the pipe channel flows as well as in the turbulent round jets together with the flow past of the rigid shapes [6–8].

The governing TBL equations presented in the tensor form are the following (here “i” is the order number of the particles fractions, I = 1.3):

$$\frac{D\rho}{Dt} = 0 \qquad (1)$$

$$\frac{Du_j}{Dt}=\frac{\partial}{r\partial r}r(\nu_t+\nu)\frac{\partial u_j}{\partial r}-\frac{\partial p}{\rho\partial x}-\sum_{i=1,3}\alpha_i\left\{C'_{Di}\frac{(u_j-u_{sij})}{\tau_i}+C_{Mi}\left[\vec{\Omega}_i\times(\vec{v}-\vec{v}_{si})\right]_j\right\} \tag{2}$$

$$\frac{\mathrm{Dk}}{\mathrm{Dt}}=\frac{\partial}{\mathrm{r}\partial\mathrm{r}}\mathrm{r}\left(\frac{\nu_t}{\sigma_t}+\nu\right)\frac{\partial\mathrm{k}}{\partial\mathrm{r}}+\frac{\mathrm{G}}{\rho}-\frac{\varepsilon_0}{\rho}+\sum_{i=1,3}\alpha_i\left[\frac{(\mathrm{u_j}-\mathrm{u_{sij}})^2}{\tau_i}+\mathrm{k_{sci}}-\left\langle\mathrm{u'_j u'_{sij}}\right\rangle\right] \tag{3}$$

$$\frac{\mathrm{D}\rho\alpha_i}{\mathrm{Dt}}=0 \tag{4}$$

$$\frac{\mathrm{D}\alpha_i\mathrm{u_{sij}}}{\mathrm{Dt}}=\frac{\partial}{\mathrm{r}\partial\mathrm{r}}\mathrm{r}\alpha_i(\nu_s+\nu_{ci})\frac{\partial\mathrm{u_{sij}}}{\partial\mathrm{r}}-\frac{\partial\mathrm{p_{si}}}{\rho\partial\mathrm{x}}+\alpha_i\left\{\mathrm{C'_{Di}}\frac{(\mathrm{u_j}-\mathrm{u_{sij}})}{\tau_i}+\mathrm{C_{Mi}}\left[\vec{\Omega}_i\times(\vec{\mathrm{v}}-\vec{\mathrm{v}}_{si})\right]_j-\left(1-\frac{\rho}{2\rho_p}\right)\mathrm{g}\right\} \tag{5}$$

Here Eq. (1) is the continuity equation, Eq. (4) is the mass conservation equation of the polydispersed phase, Eq. (2) and (5) presented in the tensor form cover the momentum exchange for the longitudinal and radial directions for the gas and polydispersed phases, respectively. The closure of the momentum equations is performed by the transport equation of the turbulent energy (Eq. (3)) derived by [9].

2.2. 2-Dimenisonal Reynold-Averaged Navier-Stokes (2D RANS)

The general equations of this method were examined by plenty of experiments, which showed, that using this method it is possible to discover, for example, boundary conditions and it is quite easy to implement it numerically. In this work we use the RANS method with it's closure equations to find on the output needful data: axial and radial velocities, turbulent energy, mass concentration. The information on these parameters will surely be useful for particulate slow predictions.

This model is based on the complete averaged Navier-Stokes equations, without any simplifications, such as "boundary layer" simplifications. A short presentation of the governing equations for the axisymmetric pipe case is as follows:

Continuity for the gas phase:

$$\frac{\partial u}{\partial x}+\frac{\partial(rv)}{r\partial r}=0 \tag{6}$$

Linear momentum equation in the axial direction for the gaseous phase:

$$\frac{\partial}{\partial x}\left(u^2-\nu_t\frac{\partial u}{\partial x}\right)+\frac{\partial}{r\partial r}r\left(uv-\nu_t\frac{\partial u}{\partial r}\right)=-\frac{\partial p}{\rho\partial x}+\frac{\partial}{\partial x}\nu_t\frac{\partial u}{\partial x}+\frac{\partial}{r\partial r}r\nu_t\frac{\partial v}{\partial x}-\sum_{i=1,3}\alpha_i\left(\frac{u_{ri}}{\tau'_i}+C_{Mi}\Omega_i v_{ri}\right) \tag{7}$$

Linear momentum equation in the radial direction for the gaseous phase:

$$\frac{\partial}{\partial x}\left(uv-\nu_t\frac{\partial v}{\partial x}\right)+\frac{\partial}{r\partial r}r\left(v^2-\nu_t\frac{\partial v}{\partial r}\right)=-\frac{\partial p}{\rho\partial r}+\frac{\partial}{\partial x}\nu_t\frac{\partial u}{\partial r}+\frac{\partial}{r\partial r}r\nu_t\frac{\partial v}{\partial r}-\frac{2\nu_t v}{r^2}-\sum_{i=1,3}\alpha_i\left(\frac{v_{ri}}{\tau'_i}-(C_{Mi}\Omega_i+F_{si})u_{ri}\right) \tag{8}$$

Turbulence kinetic energy equation for the gaseous phase:

$$\frac{\partial}{\partial x}\left(uk-\nu_t\frac{\partial k}{\partial x}\right)+\frac{\partial}{r\partial r}\left(vk-\nu_t\frac{\partial k}{\partial r}\right)=\nu_t\left\{2\left[\left(\frac{\partial u}{\partial x}\right)^2+\left(\frac{\partial v}{\partial r}\right)^2+\left(\frac{v}{r}\right)^2\right]+\left(\frac{\partial u}{\partial r}+\frac{\partial v}{\partial x}\right)^2\right\}-\varepsilon_h+$$

$$+\sum_{i=1,3}\frac{\alpha_i}{\tau_i}\left(u_{ri}^2+v_{ri}^2+0.5(\overline{u_{si}'^2}+\overline{v_{si}'^2})_c-\frac{k}{\left(1+\frac{\tau_i}{\mathrm{T}_0}\right)}\right) \tag{9}$$

Momentum equation in the axial direction for the solids phase:

$$\frac{\partial}{\partial x}(\alpha_i u_{si}u_{si})+\frac{\partial}{r\partial r}(r\alpha_i u_{si}v_{si})=-\frac{\partial}{\partial x}\left(\alpha_i\overline{u_{si}'^2}\right)-\frac{\partial}{r\partial r}\left(r\alpha_i\overline{u_{si}'}\,\overline{v_{si}'}\right)+\alpha_i\left[\frac{u_{ri}}{\tau_i'}+C_{Mi}\Omega_i v_{ri}-g\left(1-\frac{\rho}{2\rho_\rho}\right)\right] \tag{10}$$

Momentum equation in the radial/transverse direction for the solids phases:

$$\frac{\partial}{\partial x}(\alpha_i v_{si}u_{si})+\frac{\partial}{r\partial r}\left(r\alpha_i v^2{}_{si}\right)=-\frac{\partial}{\partial x}\left(\alpha_i\overline{u_{si}'}\,\overline{v_{si}'}\right)-\frac{\partial}{r\partial r}\left(r\alpha_i\overline{v_{si}'^2}\right)+\alpha_i\left[\frac{v_{ri}}{\tau_i'}-(C_{Mi}\Omega_i+F_{si})u_{ri}\right] \tag{11}$$

Linear momentum equation in the axial direction for the solids phases:

$$\frac{\partial}{\partial x}(\alpha_i\omega_{si}u_{si})+\frac{\partial}{r\partial r}(r\alpha_i\omega_{si}v_{si})=-\frac{\partial}{\partial x}\left(\alpha_{si}\overline{u_{si}'}\,\overline{\omega_{si}'}\right)-\frac{\partial}{r\partial r}\left(r\alpha_{si}\overline{v_{si}'}\,\overline{\omega_{si}'}\right)-\alpha_i C_{\omega i}\frac{\Omega_i}{\tau_i} \tag{12}$$

3. RESULTS AND DISCUSSIONS

Both numerical simulations were performed in CFB vertical riser (the low-density zone).

3.1. TBL model

The main initial data for calculations for the TBL approach:

- flue gases temperature: 850^0C,
- flue gases velocity: 5,5 m/s,
- flue gases density: 0,27 kg/nm^3,
- ash particles density: 1300 kg/nm^3.

3.1.1. The behaviour (influence) of the solid phase concentration

Fig. 2–5 show the results of performed TBL numerical simulation. There are presented different profiles (axial and radial velocities, mass concentration, turbulent energy) for particles with different mass ratio (c1 and c10 – mass ratio of 1 kg dust/kg air and 10 kg dust/kg air, respectively), different sizes (d25 and d250 – diameters of 25 µm and 250 µm, respectively) and for the case with neglecting inter-particle collisions (mono - monofraction).

The behaviour of particles with high (10 kg dust/kg air) and low (1 kg dust/kg air) phase concentration is different, as shown in Fig. 2–5. It is known that the increase of the particle mass concentration as well as decrease of the particle size results in decrease of the velocity slip between average velocities of gas and dispersed phases [7], which is indirectly expressed via the profiles of the radial velocity component of the dispersed phase obtained at the motion of relatively small particles of 25 µm at the high flow mass ratio (bold solid line, Fig. 4) versus distribution of the same velocity at low mass ratio (solid line, Fig. 4). The effect of the mass ratio is mostly pronounced in the profile of the turbulent energy as the low level of turbulence at the high flow mass ratio (solid bold line, Fig. 3) versus the higher level of turbulence at low mass loading (solid line, Fig. 3), which is called as the turbulence modulation caused by the presence of the particles. The small changes of x-velocity and the mass concentration profiles can be seen in Fig. 2 and 5, respectively, for various flow mass ratios.

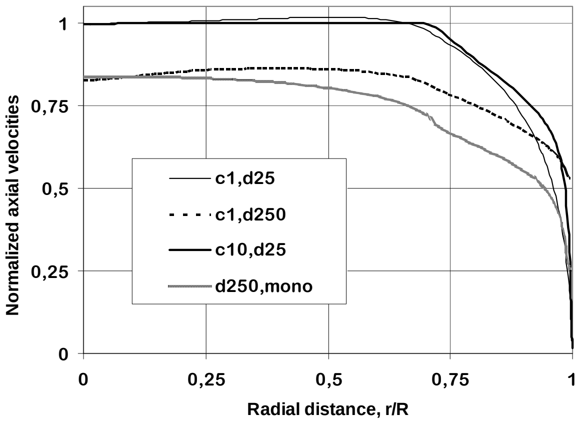

Fig. 2. x-velocity profiles of dispersed phase for different particle sizes and mass ratios

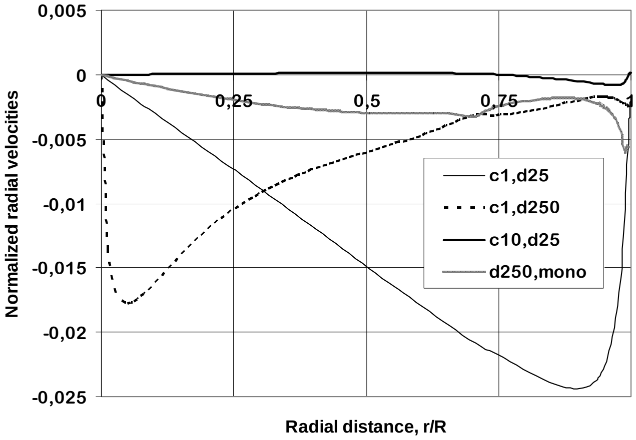

Fig. 3. Radial velocity profiles of particles for different particle sizes and mass ratios

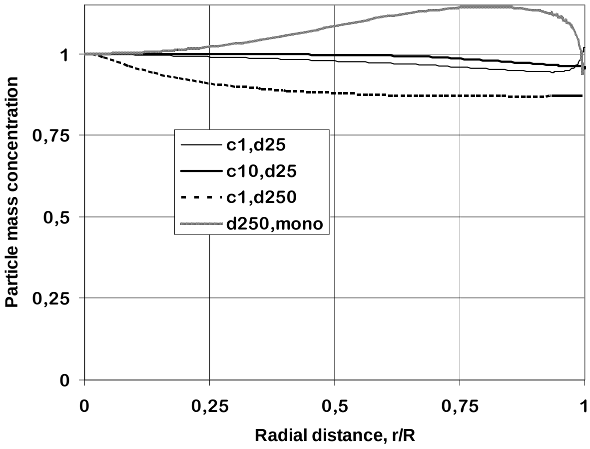

Fig. 4. Profiles of particle mass concentration for different particle sizes and mass ratio

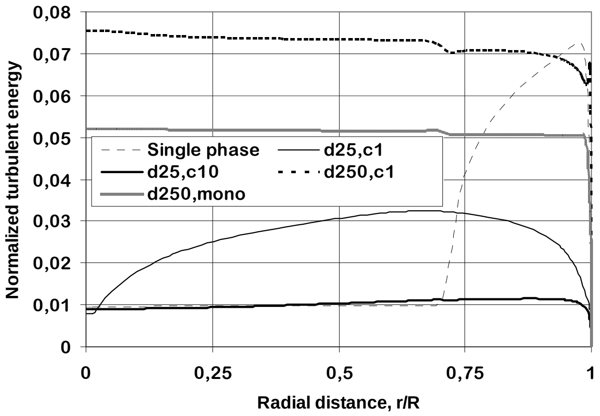

Fig. 5. Root-mean-square profiles of turbulent energy for different particle sizes and mass ratios

3.1.2. *The influence of the particle size*

This obvious effect is expressed by the distribution of the particles velocity component toward x-axis obtained at the same mass ratio of 1 kg dust/kg air for relatively small 25 μm and coarse 250 μm particles (Fig. 2), namely, the smaller particles have the higher level (solid line) that those of the larger ones (bold dotted line). With respect of the distribution of the radial velocity component, the small particles have the higher velocity in the vicinity of the wall (solid line, Fig. 4) in contrast to the velocity growth occurred close to the axis in case of a motion of the large particles (bold solid line, Fig. 4). This is due to the stronger Magnus effect of the lift force causing the lag motion of the large particles shifting them towards the axis. The manifest effect of the particle size can be seen from the distribution of the turbulent energy, namely, the larger particles generate the higher additional turbulent energy due to the vortex shedding than those of the small ones (cf. bold dotted line and solid line Fig. 3). The mass profiles of the small and coarse particles are slightly different, i.e. the concentration of the small particles has the less gradient as compared to the coarse particles (cf. bold dotted line for large and solid line for small particles, Fig. 5).

3.1.3. *The inter- particle collisions*

The effect of the inter-particle collisions is important for the particulate flows of the mass ratio larger than 1 kg dust/kg air, when $\tau_c / \tau_p < 1$, where the time of interparticle collision τ_c is less than the particle response time τ_p. We ran the calculations taking into account the inter-particle collisions described by the pseudoviscosity coefficients (Eq. (5)), using the original model of closure based on the particle collisions [10]. To show an importance of this effect one set of the calculations was performed neglecting the particles collisions (cf. bold dotted and pale lines, Fig. 2) in case of motion of the coarse 250 μm particles while comparing x-velocity profiles of the dispersed phase with mass ratio of 10 kg dust/kg air. The change of these profiles is obvious, namely, in case of no collision the x-velocity profile becomes narrower that is evidently linked with a reduction of the particles diffusion in the radial direction caused by the inter-particle collisions [10, 11]. Besides, the collision effect results in additional turbulence generation derived from the four-way coupling model of [9] (cf. bold dotted and pale lines, Fig. 3).

As a whole, the inter-particle collisions generate the high turbulence and, thus, contribute to the better particle mixing.

3.2. 2D RANS model

The main initial data for calculations for the TBL approach:

- flue gases temperature: 850^0C;
- flue gases velocity: 4 m/s;
- flue gases density: 0,329 kg/nm^3;
- ash particles density: 2000 kg/nm^3;
- ash particles concentration: 10÷20 kg/nm^3.

The results of the 2D RANS numerical simulation are shown at Fig. 6–9. There are shown different profiles (axial and radial velocities, turbulent energy) for gas flow (gas) and particles flow (solids), modelling the CFB process with different sizes of particles (0.3 mm; 1.0 mm; 1.5 mm) and different cases of inter-particle collisions (mono – neglecting the collisions and poly – taking the collisions into account).

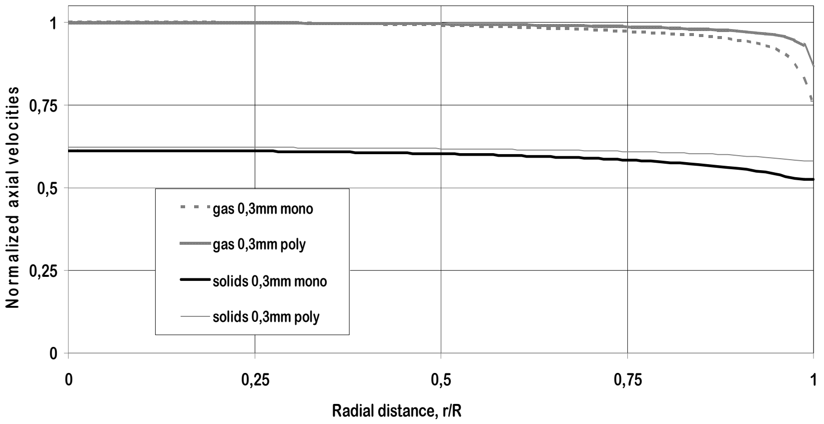

Fig. 6. Axial velocity distribution of gas- and dispersed phases for particles (0,3mm) with and without collision effect

In Fig. 6 there is axial velocity of carrier fluid (gas-phase) and dispersed phase in case of solid particles of diameter 0.3 mm, calculated for different flow conditions – with and w/o particle collisions. As one can noticed the particle collision results in alignment of velocity profiles of dispersed phase. In polydispersed case it is observed smaller velocity slip between gas-phase and average velocity of dispersed phase over three particle fractions. This is due to presence of smaller particle traction among other "mean" and large particle fractions in polydispersed phase composition which is versus the case of monofraction particle fractions composition with the same particle sizes. Eventually it produces large drag than that of polydispersed sold phase motion.

Fig. 7 shows that radial velocity of both phases which increases off axis and has highest magnitude somewhere in a middle of the flow cross-section. This indicates that radial velocity in case of two-phase flow is not negligible in comparison with axial velocity component like in single-phase turbulent pipe flow and it is formed by lift Magnus and Saffman forces along its redistribution owing to effect of particle collisions in the dispersed phase. As a result it redistributes and forms the particle mass concentration in flow cross-sections. In both cases at the motion of monodispersed and polydispersed particles (collision motion) it should take into account an important role of radial velocity of dispersed phase. The effect of particle collisions levels the radial velocity of dispersed phases.

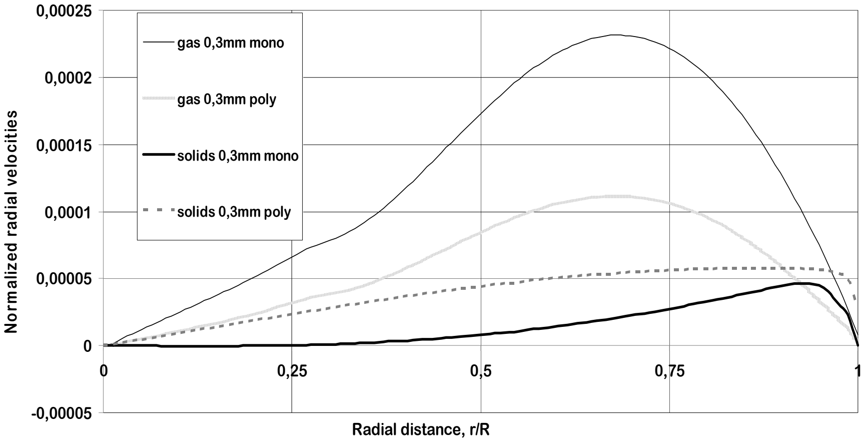

Fig. 7. Radial velocity profiles of gas- and dispersed phases for particles (0.3 mm) with and without collision effect

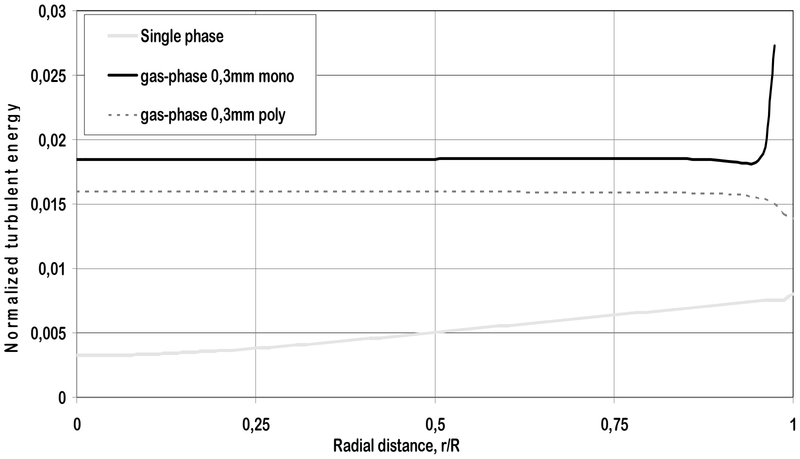

Fig. 8. Turbulent energy profiles of single and gas phases for particles (0.3 mm) with and without collision effect

The Fig. 8 shows distribution of turbulence at the motion of relatively small solid particles of 0.3 mm for two regimes – with and without particle collisions. One can indicate that the presence of particles leads to turbulence enhancement in turbulent core and in the wall vicinity in comparison with case of single-phase flow. It follows from four-way coupling model [9] by introducing square of velocity lag between gas- and dispersed phases (last term in right-hand side of Eq. (3)), which is responsible for additional turbulence generation. The physics behind this is formation of vortex shedding generated from streamlined inertia large solid particles. This process is less pronounced for polydispersed phase with lower level additional turbulence generation than for monodispersed phase because of smaller velocity slip occurred at the motion of polydispersed phase (Fig. 6).

In case of larger particles, of 1.5mm one can see jump in distributions of axial velocity (Fig. 9) The jump in distributions of radial velocity of solids and the particle mass concentration in vicinity of the wall is analyzed in [7]. It’s stemmed from finite size of such rough particles which is comparable or larger of mesh size of numerical grid. Due to comparable size of such rough particles they may occupy smaller flow domain focusing on vicinity of the wall where gas-phase may less effect of their motion and mainly they fall down along the walls. Therefore in order to keep moving such rough particles upward flow it should be some value of flow velocity holding there versus gravitation. We determined flow the region where such rough of 1.5 mm particles move upward flow.

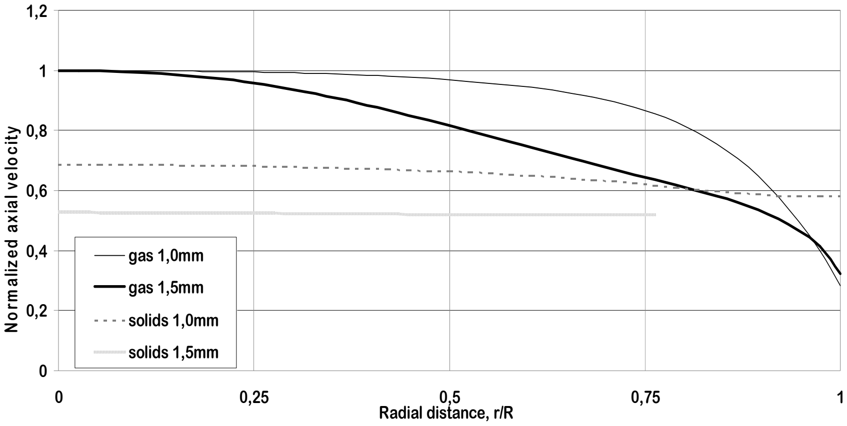

Fig. 9. Axial velocity profiles of gas- and dispersed phases for different particle sizes (1.0 and 1.5 mm)

In case of larger particles, of 1.5mm one can see jump in distributions of axial velocity (Fig. 9) The jump in distributions of radial velocity of solids and the particle mass concentration in vicinity of the wall is analyzed in [7]. It's stemmed from finite size of such rough particles which is comparable or larger of mesh size of numerical grid. Due to comparable size of such rough particles they may occupy smaller flow domain focusing on vicinity of the wall where gas-phase may less effect of their motion and mainly they fall down along the walls. Therefore in order to keep moving such rough particles upward flow it should be some value of flow velocity holding there versus gravitation. We determined flow the region where such rough of 1.5 mm particles move upward flow.

4. CONCLUSIONS

4.1. TBL model

- the inter-particle collisions generate the high turbulence and contribute to the better particle mixing and enhance the heat exchange between the ash solid particles and gases;
- the low particle mass concentration results in high velocity of both phases and high level of turbulence;
- the radial velocity of the coarse particles decreases towards the centre resulting in enhancement of turbulence;
- the modelling states that the optimal concentration can be achieved with the guaranteed inter-particle collisions, and further increasing of the mass loading would not be desirable.

4.2. 2D RANS model

The main contribution to the flow formation stemmed from the interparticle collisions and four-way coupling turbulence modulation due to presence of solids. The other forces exerted on the motion of solids are the gravitation, viscous drag and lift forces. On the basis of the performed calculations one can conclude that:

- the rough particles generate a noticeable amount of turbulent energy producing much mixing processes in the flow domain;

- the interparticle collisions along with the four-way coupling turbulence generate high level of turbulence considerably intensifying particle’s mixing process with enhance of the heat exchange between the ash solid particles and gases.

4.3. Compare of the results

Comparing the results of the both numerical simulations (TBL and 2D RANS), we can notice next remarkable facts:

- the 2D RANS approach gives more comprehensive picture of description of phenomena in CFB versus TBL (turbulent boundary layer approach) with respect distribution of average velocity components of both phases the turbulent energy and particle mass concentration. The inter-particle collision in considered RANS method results in redistribution of velocities, turbulent energy and mass concentration not only in radial direction but in streamwise direction as well. The numerical results obtained for two cases with and w/o particle collision qualitatively are close and different quantitatively underlining that in conditions of CFB operating with dense particle flow the effect of particle collision indispensably have taken into account;
- the particle mass concentration in our work is bigger, comparing coarse particles to the smaller ones. It is caused by the big turbulence diffusion in the vicinity of the wall. Also to make certain conclusions in particle mass concentration, the flow has to be fully developed, but our one is not.

The main conclusion of the performed simulations is that the main factor for improving the CFB process with ash particles as the solid phase of the flow are the inter-particle collisions. One of the possibilities for developing current work is to perform numerical simulation where the solid phase is mixture of ash and sand particles.

NOMENCLATURE

C'_D – factor of drag coefficient;
C_M – coefficient of Magnus force;
D – pipe diameter ;
F_s – Saffman force ;
g – gravitation acceleration;
k – turbulent energy;
p – pressure;
r – radial coordinate;
R – pipe radius;
t – time scale;
T_* – characteristic time of hydrodynamic process;
u – axial velocity component;
$\bar{u}$ – gas velocity over cross-section;
v – radial velocity component;
$\bar{v}$ – radial velocity over cross-section;
x – axial coordinate;
α – particle mass concentration;
σ – turbulent energy for two-phase flow;
ε – dissipation rate of turbulent energy;
Σ – summation over all particle fractions;
τ – response time;
ν – kinematic viscosity;

ω – angular velocity;
Ω – angular velocity slip between gas- and dispersed phases;

Superscripts

$'$ – fluactuation & post-collision.

Subscripts

i – i-th particle fraction of dispersed phase;
p – particle property;
si – i-th fraction of dispersed phase;
t – turbulent;
ri – slip velocity component;
h – channel width;
ω – rotation;
0 – parameters of single-phase flow & dynamic friction.

REFERENCES

1. HUSSAINOV, M., KARTUSHINSKY, A., MARTINS, A., RUDI, Ü., SHCHEGLOV, I., TISLER, S., KRUPENSKI, I., SIIRDE, A., Numerical simulation of uprising gas-solid particles flow in circulating fluidized bed. *Oil-Shale*, 2008, Vol. 2, p. 125–138.
2. OTS, Arvo. *Oil Shale Fuel Combustion*. Tallinn, 2006.
3. HELLAND, E., OCCELLI, R., TRADIST, L. Numerical study of cluster formation in a gas-particle circulating fluidized bed. *Power Technology 100*. 2000, p. 210–221.
4. KRUPENSKI, I., KARTUSHINSKY, A., SIIRDE, A., RUDI, Ü., Numerical simulation of uprising gas-solid particle flow by 2D RANS for fluidised bed conditions. *Oil-Shale*, 2010, Vol. 2
5. MICHAELIDES, E. E., A model for the flow of solid particles in gases. *Int. J. Multiphase Flow*, 1984, Vol. 10, p. 61–75.
6. HUSSAINOV, M., KARTUSHINSKY, A., MULGI, A., RUDI, Ü., TISLER, S. Experimental and Theoretical Study of the Distribution of Mass Concentration of Solid Particles in the Two-Phase Laminar Boundary Layer on a Flat Plate. *Int. J. Multiphase Flow*, 1995, Vol. 21, No. 6, p. 1141–1161.
7. HUSSAINOV, M., KARTUSHINSKY, A., MULGI, A., RUDI, Ü. Gas-solid flow with the slip velocity of particles in a horizontal channel. *J. Aerosol Science*, 1996, Vol. 27, No 1, p. 41–59.
8. FRISHMAN, F., HUSSAINOV, M., KARTUSHINSKY, A., MULGI, A. Numerical simulation of a two-phase turbulent pipe-jet flow loaded with polyfractional solid admixture. *Int. J. Multiphase Flow*, 1997, Vol. 23, No 4, p. 765–796.
9. CROWE, C. T., GILLANDT, I. Turbulence modulation of fluid-particle flows – a basic approach. *Third ICMF*, 1998, Lyon.
10. KARTUSHINSKY, A., MICHAELIDES, E. An analytical approach for the closure equations of gas-solid flows with inter-particle collisions. *Int. J. Multiphase Flow*, 2004, Vol. 30, p. 159–180.
11. KARTUSHINSKY, A., MICHAELIDES, E. E. Gas-solid particle flow in horizontal channel: decomposition of the particle-phase flow and inter-particle collision effect *Journal of Fluids Engineering, the Transaction of ASME*, 2007, Vol. 129, No 6, p. 702–712.
12. PFEFFER, R., ROSETTI, S., LICKLEIN, S. Analysis and correlation of heat transfer coefficient and heat transfer data for dilute gas–solid suspensions. *NASA Report TND-3603*, 1996.

CYSENI 2010, May 27–28, Kaunas, Lithuania
ISSN 1822-7554, www.cyseni.com

AUTO-IGNITIONS STUDIES OF METHANE – AIR MIXTURES IN RAPID COMPRESSION MACHINE

V.V. Leschevich, O.G. Penyazkov
A.V. Luikov Heat and Mass Transfer Institute
15 P. Brovka str., 2000072 Minsk, Republic of Belarus
Phone: +375 17 284 15 20
Email: V.Leschevich@dnp.itmo.by

ABSTRACT

Detailed kinetic mechanisms need to be validated with experimental results of high fidelity over a wide range of temperatures, pressures, and equivalence ratios. The aim of the study is to perform induction and reaction time measurements in high-pressure methane-air mixtures at intermediate temperatures by means of rapid compress machine (RCM) with complete current pressure and temperature control of reactive media. The auto-ignition and combustion of methane/oxygen/nitrogen/argon mixtures at the composition $\phi = 0.5–2$ and gas density of 2 kg/m^3 and 4 kg/m^3 was studied in the compressed gas temperature range from 700 to 1400 K. The ratio of total inert gases to oxidizer was similar to that of nitrogen to oxygen in air, while the N_2/Ar ratio was chosen for obtaining different temperatures of the mixture after compression for the same compression ratios. Ignition times were measured by using emission observations from side wall of combustion chamber and end wall pressure measurements. The RCM runs were performed for filling holes in experemental data for methane-air autoignition.

Keywords: rapid compression machine, auto-ignition, methane, ignition time, activation energy

1. INTRODUCTION

The availability, relative low-cost and low-emission qualities of natural gas have made it the primary fuel for many practical combustion systems and have been responsible for numerous experimental and modeling studies of methane and synthesized from methane natural gas mixtures. Experimental studies measure basic combustion characteristics such as ignition delay times, intermediate species concentrations, and laminar flame speeds. These data are used then to produce validated chemical kinetic mechanisms. The reduction of these mechanisms and further integration with Computational Fluid Dynamics (CFD) codes allows performing realistic and accurate overall simulations of real processes of practical combustion devices. These simulations are necessary for design of new more efficient and clean combustion systems and for operating behavior optimization of the existed gas turbines, internal combustion engines, boilers and etc.

Methane auto-ignition has been extensively studied for last forty years [1] because of its prominence in natural gas and because it is an important intermediate constituent in the combustion of higher-order hydrocarbons. Almost all investigations were carried out independently using specific experimental facilities which make it possible to measure ignition delay times in a narrow range of conditions. If arrange facilities in the term of test temperature the succession is the next: continuous flow devices such as flow and/or jet-stirred reactors (up to 1000 K), rapid compression machines (approximately 600–1100 K) and shock tubes (typically 1400–3000 K). The specified ranges for each facility are approximate and the auto-ignition experiments can be preformed at more higher or lower temperatures. But the data will be obtained with large uncertainties for these conditions. Measurements at high temperatures in rapid compression machines are limited by a maximum possible compression ratio (that estimates maximal temperature) and compression piston's velocity (which limits minimal ignition delay time that can be measured). The main problem is associated with a high piston's velocity because at the first the complicated systems for piston's velocity control and stopping at final position are needed and at the second because rapid piston motion can create high turbulence after compression and cause temperature inhomogeneity in test chamber. Measurements at low temperatures in rapid compression machines are difficult because heat losses to the test chamber are limited the maximal ignition time that can be measured. Usually researchers take into account heat losses when simulate experimental results in order to validate kinetic mechanism. Two methodologies are available and described in literature [2]. But it is difficult to make direct comparison of these data with measurements performed on other facilities like shock tubes. The similar problems can occur also when for example shock tubes or flow continuous devises are used for experiments at intermediate temperature region.

In the present work we developed a unique rapid compression machine in order to extend the typical for RCM range of studies and to perform auto-ignition experiments at intermediate-to-high temperatures. Special design of RCM was developed with the view of obtaining new experimental data and providing the continuous overlapping with high temperature data points previously obtained in shock tube facility [3].

2. METHANE AUTOIGNITION INVESTIGATIONS AT INTERMEDIATE TEMPERATURES

In this paper, we are concerned with methane-air mixtures as them are most extensively studied and a wide auto-ignition database is presented in literature. A summary of the ignition delay time measurements made through 1969, mostly focusing on temperatures above 1400 K and pressures near atmospheric, is provided by Spadaccini and Colket [1]. A correlation of the numerous methane ignition delay measurements reported by 13 different investigators using shock tubes and continuous flow devices was presented in their paper. But only few experimental studies were available at the intermediate temperatures ≤ 1100 K. Moreover, there was no any study for temperature range from 1000 K to 1250 K.

In recent years, the missing data for methane auto-ignition have been received. Generally these data were obtained in shock tube experiments for pressures up to 300 atm and temperatures ranging from 1000 K to 1600 K. The temperature range was extended by achieving tailored-interface conditions in the test volume. Also a few studies for temperature 950–1050 K were carried out using rapid compression machines.

Petersen et al. [4, 5] studied methane oxidation using shock tubes at equivalence ratio ranging from 0.5 to 6.0, pressures ranging from 9 atm to 480 atm and temperatures ranging from 1040 K to 2040 K for the purpose of providing validation data for chemical kinetics mechanisms. The authors found a very significant decrease in activation energy for the lower temperature region. Goy et al. [6] studied methane oxidation in shock tubes for pressures ranging from 5 atm to 20 atm and temperatures ranging from 852 K to 1428 K. Authors used specific driver and test section lengths of the shock tube setup in order to prolong a maximum observation time to approximately 6 milliseconds. They found very poor agreement between their results and predictions made by the GRI 3.0 mechanism [7], particularly at temperatures below about 1100 K. Huang et al. [8] also used a shock tube to study methane oxidation for mixtures having equivalence ratio ranging from 0.7 to 1.3, pressures 16–40 atm, and temperatures ranging from 1000 K to 1350 K. To extend an experimental time to 5 milliseconds tailored-interface conditions were achieved by adjusting the helium/air ratio of the driver gas. Petersen et al. [9] again collected methane ignition delay times for lean mixtures at pressures 0.54–25.3 atm and temperatures 1451–2001 K for the purpose of making modifications to the GRI 3.0 mechanism to reflect the data collected. Finally, de Vries and Peteresen [10] measured auto-ignition of lean methane mixtures at temperatures near 800 K and average pressures of 20 atm. The authors report that very weak ignition occurred at the low temperatures studied and suggest that further study is needed in this regime to validate the current kinetics models.

Rapid compression machines (RCM) are widely used in up-to-date auto-ignition studies as well as shock tubes. The RCM experimental time is limited only by heat losses to the cold walls. As a result, the RCM can provide a basis for combustion studies at elevated pressures and intermediate temperatures from 600 K to 1100 K. That is under conditions when the measurements are too difficult in comparison with shock tube experiments, which typically spans the high-temperature range. Since many research groups over the world used rapid compression machines for ignition delay time measurements only few studies on methane were found in literature. Moreover majority of them related to the influence of hydrogen or heavier hydrocarbons (ethane, propane, butane, and pentane) on the oxidation of methane and a little data have been reported for pure methane oxidation.

Ignition delay times in $CH_4/O_2/Ar$ mixtures using an RCM have been measured at National University of Ireland [11]. Experiments were carried out for stoichiometric methane/oxygen mixture at the postccompression pressure about 1.6 MPa and temperature ranged from 985 K to 1060 K. The obtained data were compared with predicted results by the model based on GRI and Leeds [12] mechanism. The best prediction, particular at high temperatures (> 1000 K), was observed in simulations using GRI mechanism. But at low temperatures (≤ 1000 K) the measured ignition delay times far exceed those predicted by either model.

Levinsky et al. from University of Groningen (The Netherlands) have investigated changes in the combustion behavior of methane upon hydrogen addition in rapid compression machine [13]. In the part of all experiments ignition delay times of stoichiometric methane/oxygen/argon/nitrogen mixture were measured at pressures 15–70 bar and temperatures 950–1060 K. Simulation results using various chemical mechanism and comparison with experimental data were reported. The calculations using the mechanism from Petersen et al. show excellent agreement with measurements over the range of pressures and temperatures studied.

Auto-ignition of $CH_4/C_2H_6/C_3H_8$ mixtures representative of an average natural gas composition have been recently studied in the RCM at the University of Lille [2] at pressures varied from 13 to 21 bar and temperature ranged from 850 to 925 K. But the information about pure methane auto-ignition was not reported.

A gap exists on our knowledge over the range of temperatures from 900 to 1400 K and elevated pressures, because presented intermediate temperature shock tube measurements were obtained at extreme conditions at which not well-controlled tailored-interface conditions, boundary layer effects and shocks bifurcation can effect on induction time and cause significant errors. These data should be validated by other experimental equipment. But the obtained RCM data are too spare and presented for narrow range of conditions. Moreover the experimental results obtained on various RCM facilities at the same conditions can be rather different, because induction times are effected by heat losses, temperature distribution, flow dynamics and etc. These effects can also cause discrepancies between experimental shock tube and RCM data. For propane-air mixtures at low temperatures and high pressures such discrepancies were recently reported by Petersen et al. [14]. Authors have noted that RCM ignition data have longer apparent times than the shock tube data and that some of the difference can be explained by the effects of pressure increases in the shock tube during induction period. The nature of this pre-ignition pressure increase is still not clear.

3. EXPERIMENTAL SETUP

The present RCM system consists of a driving cylinder, a compression cylinder, a pneumohydraulic system of motion control, and a driving air tank. All these parts are located along one axis. The general photo of the developed machine is shown in Fig. 1.

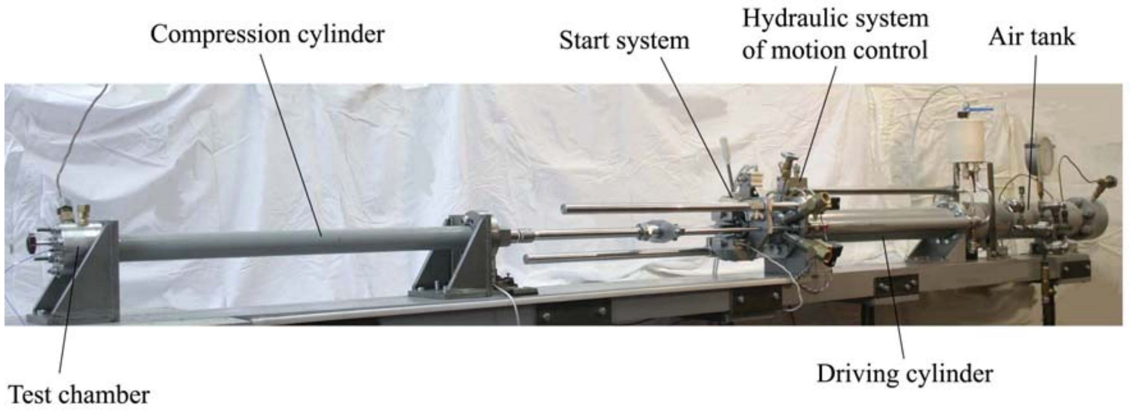

Fig. 1. General photo of the developed RCM

The key feature of an RCM is the ability to have a high compression ratio in order to produce both high pressure and high temperature at the end of compression. The driving cylinder and the compression cylinder have a bore of 100 mm and 50 mm, respectively. This allows the driving air pressure to be 4 times smaller than the final desired pressure achieved in compression cylinder. The driving piston is connected with compression piston and hydraulic dampers by rods. Initial volume variations are achieved by changing the initial position of the pistons assembly and, hence, of the piston stroke. When the test chamber height is 10 mm the compression ratio of up to 80 can be achieved.

Fig. 2 shows the general layout of the compression cylinder and measurement setup. The test chamber (4) is designed to withstand high pressures generated under compression and combustion. The end wall is equipped with a high-temperature quartz pressure sensor Kistler 6031U18 (8) with a Kistler 5015A charge amplifier (9), a gas inlet/outlet valve (6) for pumping and filling compression cilinder with a test mixture. For recording the luminescence at ignition and combustion, on cylindrical side wall of the test section was mounted quartz window (10), to the mandrel of which the biffurcated optical fiber light guide was connected. It transmitted and directed output radiation on the photomultiplier cathodes (11). Doubled narrowband interferometric filters installed in front of the photocathodes passed only emissions of OH at λ = 308.9 nm (transitions $A^2\Sigma – X^2\Pi$) and CH radicals at λ = 431.5 nm (transitions $^2\Delta – ^2\Pi$). An optical reflection probe was used for measuring a speed of the pistons assembly and the current gas volume during the compression stroke. Luminosities, pressure and piston position signals were recorded using a 4-channel Tektronix digital oscilloscope with $1.25*10^9$ samples/second.

The feature of present RCM is a two-step stopping mechanism. A main metal conical stopper (Fig. 2 (5)) was installed at the beginning of compression cylinder. This stopper ensured the coarse fixing of the moving pistons assembly at the end of compression stroke. The fine fixations of the compression piston and, correspondingly, volume of the test chamber (Fig. 2 (4)) were produced by the second cone made at the beginning of the test volume. For avoiding of the strong mechanical stresses of the test chamber and rebounds of the piston head, which are caused by collisions with a piston assembly, a doubled compression piston design with internal high-pressure gas damper was implemented (Fig. 3).

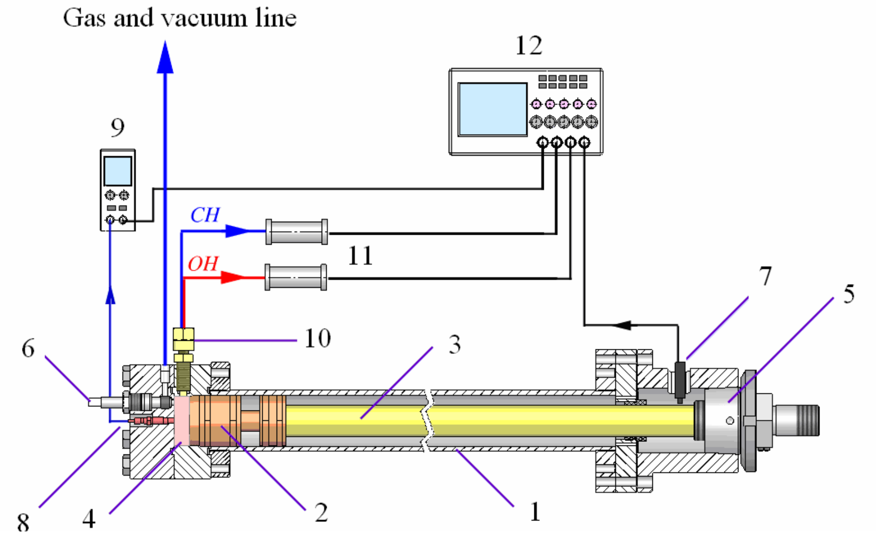

Fig. 2. The layout of the compression cylinder and measurement sytem: 1 – compression cylinder; 2 – doubled compression piston with internal high-pressure gas damper; 3 – pushing rod; 4 – test chamber; 5 – conical stopper; 6 – inlet gas and vacuum valve; 7 – optical reflection probe; 8 – high-temperature pressure sensor; 9 – charge amplifier; 10 – quartz window; 11 – photomultipliers; 12 – digital oscilloscope

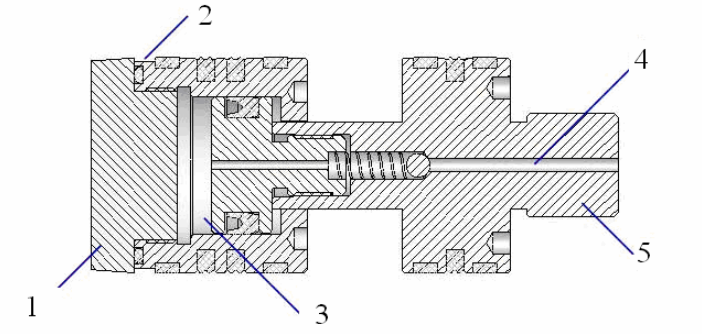

Fig. 3. Double creviced compression piston: 1 – piston head; 2 – crevice; 3 – high-pressure damping gas volume; 4 – high-pressure gas line; 5 – main pushing rod

The high-pressure gas damper inside the piston head suppressed the deformation movement of the main heavy part of the pistons assembly during the stopping of the compression piston head in the second cone.

The gas temperature was calculated using pressure measurements as in other RCM studies [2, 10, 12]. If the compression is assumed as adiabatic and isentropic the gas temperature at the end of compression, T_c, is calculated from the equation of state using initial temperature, T_0, pressure, P_0, temperature-dependent specific heat ratio for mixture, γ, and an actual pressure, P_c, measured by a pressure transducer according the following equation:

$$\int_{T_0}^{T_c} \frac{\gamma(T)}{(\gamma(T)-1)\cdot T} dT = \ln\left(\frac{P_c}{P_0}\right) \tag{1}$$

Runs were performed in stoichiometric (ϕ = 1), lean (ϕ = 0.5), and rich (ϕ = 2) methane/oxygen/nitrogen/ar mixtures (Table 1) within the range of post-shock pressures of 10–20 atm and temperatures of 700–1400 K. The ratio of total inert gases to oxidizer was similar to that of nitrogen to oxygen in air, while the N_2/Ar ratio was chosen for obtaining different post-compression gas temperatures for the same compression ratios. The N_2/Ar mixtures containing 0, 25, 50, 75 and 100% of argon were used as diluents. Commercially grade compressed methane of 99.92 % purity (additional contents: N_2-O_2 0.03%; ethane-propane 0.02% and H_2O 0.02%), nitrogen and oxygen were used for mixture preparations. All studied compositions were mixed by the method of partial pressures within the ten-liter gas vessel and kept for two days before use. Prior to the each experiment, the test volume was cleaned and evacuated to the pressure of ~ 8 Pa monitored by thermocouple vacuum gauge. An electronic pressure meter was used to control the initial pressure of the mixture with accuracy of ± 80 Pa.

Table 1. Percentege composition of the studied mixtures

ϕ	Volume percent in the total gas mixture, %		
	CH_4	O_2	Diluent (N_2/Ar)
1	9.51	19.01	71.48
0.5	4.99	19.96	75.05
2	17.36	17.36	65.28

In the present work, ignition or induction time of the mixture was defined as the time difference between pressure peak at the end of compression stroke and the onset of emission and pressure rising (5% of maximal rise) within the measuring gas volume. Fig. 4 shows typical pressure and luminosity records obtained at compression of lean (a) and reach (b) methane/oxygen/argon mixtures in developed RCM setup. To obtain a correct temperature dependence of ignition time on activation energy of the mixture and fuel/oxygen concentrations all comparative RCM experimental series were performed at constant densities (low – 2 kg/m^3 and high – 4 kg/m^3) of compressed gas mixtures. It means that fuel, oxygen, and nitrogen concentrations were kept nearly constant within a studied temperature range at the end of compression stroke.

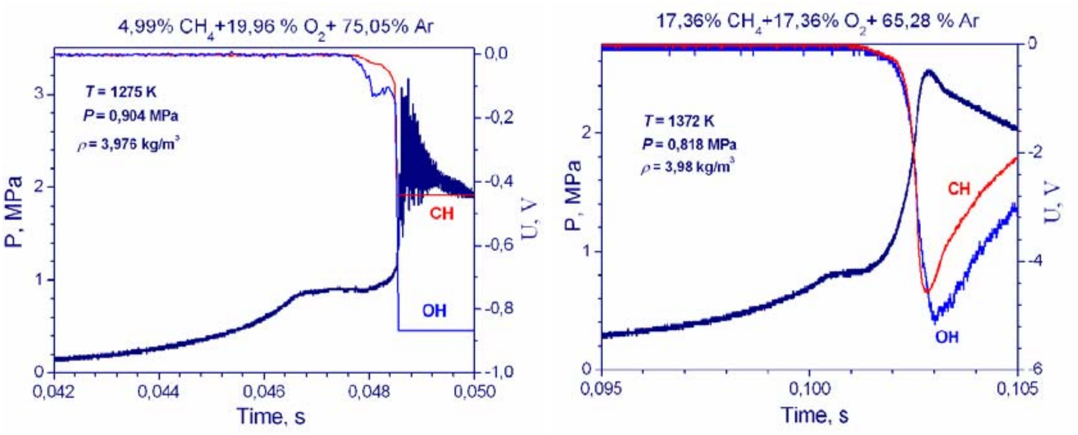

a) b)

Fig. 4. Typical pressure and luminosity records during compression and ignition of lean (a) and reach (b) methane/oxygen/argon mixtures, postcompression conditions and mixture compounds are indicated on the plot

4. RESULTS AND DISCASSION

For high – and low-density stoichiometric $CH_4/O_2/N_2$/Ar mixtures, the results of induction time measurements are plotted in Fig. 5. Experimental points correspond to ignition times measured by using emission observations from side wall of combustion chamber and the end wall pressure measurements. Global activation energy was determined using Arrhenius approximations of experimental data. It was found as 11.67 kcal/mole for low-density (2 kg/m^3) and 8.59 kcal/mole for high-density (4 kg/m^3) stoichiometric $CH_4/O_2/N_2/Ar$ mixtures.

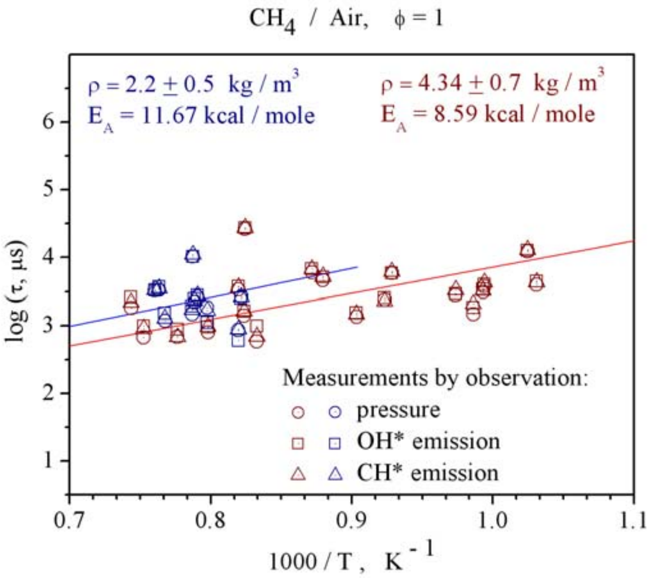

Fig. 5. Ignition delay time vs. reciprocal temperature in stoichiometric $CH_4/O_2/N_2/Ar$ mixtures: blue points correspond mixture density of 2 kg/m^3 and red points – 4 kg/m^3

At the same time, some problems are visible from experimental observations. It is a big experimental uncertainty of measured induction times for the same initial and final conditions (Fig. 6). The reason is that during the compression stroke the long pushing rod (approximately 1 m long), which is connected with the piston head, experiences the transverse vibrations affecting on the dynamic contact of the compression piston with the fixing conical part of the test chamber. Any misalignment during this contact can produce: 1) local metal-to-metal collisions ejecting small metal particles into the gas volume; 2) primary gas overcompressions in formed gas pockets within the conical clearance. These factors can produce the local hot spots, which can strongly influence on ignition timing. To reduce the role of metal particle formation we excluded duralumin containing a lot of alumina which is very high-energetic material at high temperatures, especially at micro and nanoscales. In further experimental series we have tested different non-metal materials for conical piston head. But application of plastic materials is also assotiated with some problems. Because the collision type of the plastic piston head with a fixing cone is unpredictable, the process is too stochastic. This immediately produces a big experimental scatter of the data .So, to obtain good statistics a huge amount of experiments is required.

Experimental measurements in RCM evidence, that for high- and low-density stoichiometric mixtures the ignition limits are close to the temperature of 936 K and 1190 K, respectively. At lower temperatures than those critical one’s there were not auto-ignitions of methane at RCM compression.

As for stoichiometric mixtures the global activation energies were determined for rich (Fig. 6) and lean (Fig. 7) mixtures. For rich high-density mixture, the ignition limits are close to the temperature of 1105 K. This value is much higher than corresponding one for stoichiometric mixture, i.e. 936 K. For low-density mixture the ignition limit is nearby 1347 K temperature. At lower temperatures than those critical one’s there were not auto-ignitions of rich methane/air mixtures at RCM compression. Unfortunately only two auto-ignition events were obtained. That is why the global activation energy was not careful determined for low-density conditions. For high-density mixtures rather good repeatability of measurements was observed and thus the global activation energy (21.67 kcal/mole) was determined with sufficient accuracy.

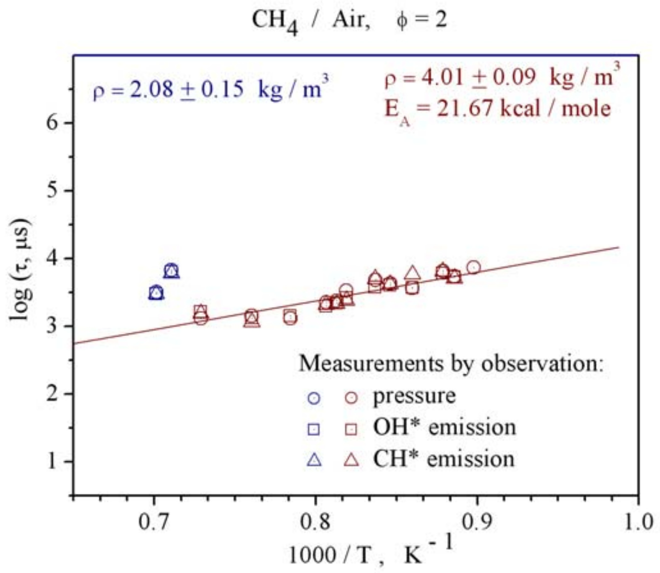

Fig. 6. Ignition delay time vs. reciprocal temperature in rich $CH_4/O_2/N_2/Ar$ mixtures: blue points correspond mixture density of 2 kg/m^3 and red points – 4 kg/m^3

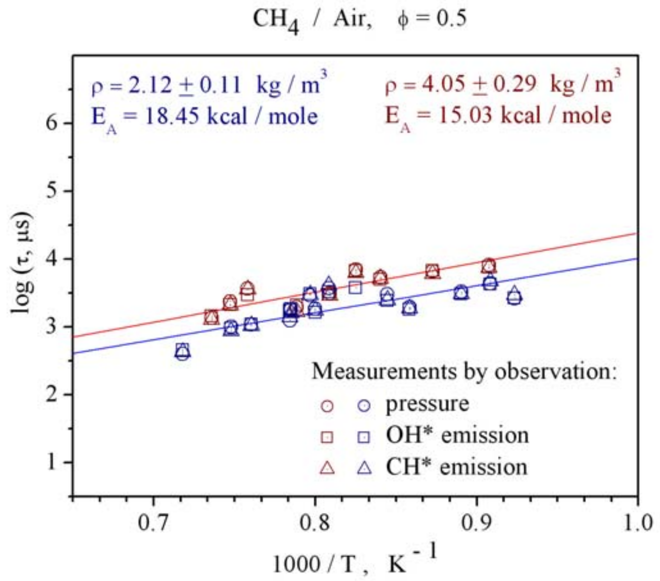

Fig. 7. Ignition delay time vs. reciprocal temperature in lean $CH_4/O_2/N_2/Ar$ mixtures : blue points correspond mixture density of 2 kg/m^3 and red points – 4 kg/m^3

For lean high-density mixture, the ignition limits are close to the temperature of 1075 K. This value is lower than corresponding one for rich mixture, i.e. 1140 K. The low-density mixture exhibits the limit at compression temperatures lower than 1020 K. A large number of repeatable measurements allowed us to determine the global activation energy for low- and high-density lean mixtures respectively 18.45 kcal/mole and 15.03 kcal/mole.

In comparison with usual auto-ignition behavior of the mixture in RCM at low temperatures for compression temperatures higher than 1200 K in lean mixture a standard knocking phenomena in the end gas were observed in experiments (Fig. 4a). Knocking produced stable self-oscillations with amplitude approximately equal to the half of the pressure rise induced by the normal combustion.

A summary of the methane auto-ignition studies founded in literature and including obtained data are presented in Fig. 8. The ignition delay times from different data sets scaled as in [1] under correlation (2) proposed by Lifshitz and co-workers [15] and improved upon by Krishnan and Ravikumar [16]. The terms $[CH_4]$ and $[O_2]$ are the molar concentrations (mol/cc) of methane and oxygen, respectively, in combustible mixture.

$$\tau = 2.21 \cdot 10^{-14} \exp(22659/T)[O_2]^{-1.05}\,[CH_4]^{0..33} \tag{2}$$

The concentrations in this equation are determined by

$$[\ ]_i = x_i\, P/RT, \tag{3}$$

where x_i is the mole fraction of fuel or oxygen, P is the pressure, T is the temperature of the mixture at the point of ignition and R is the universal gas constant.

It should be noted, that it is not correct to use plot like Fig. 8. for comparison experimental results obtained on different type facilities, because experimental conditions in test volume of each experimental setup can be different due to boundary layer effects, possible heat losses, temperature distribution, flow dynamics and etc. These effects can cause significant deviation between shock-tube measurements and RCM measurements. But nevertheless, the plot showed at Fig. 8. presents measurements performed by all researchers at wide range pressures, temperatures and equivalence ratios on one graph. From this plot it is seen that developed RCM facility can be used for investigations of auto-ignition phenomena in a wide range of temperatures. The problem of accuracy of measured ignition delay times is remain open and requires the continuous optimizing of the RCM design and used materials.

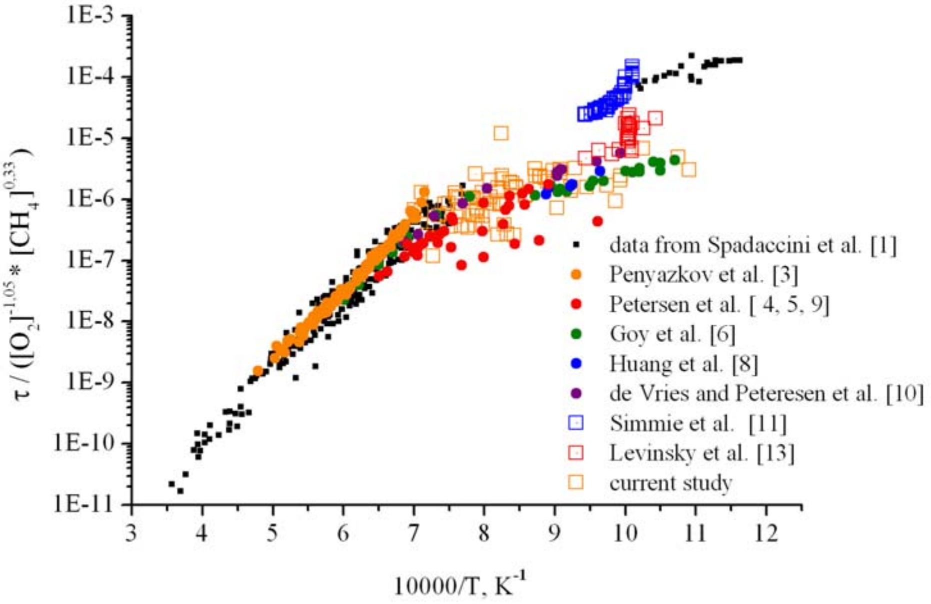

Fig. 8. Comparison of results from this study with other data in literature

CONCLUSIONS

Ignition times of $CH_4/O_2/N_2/Ar$ mixtures for pressures of 3.8–15 atm, intermediate-to-high temperatures of 900–1400 K and stoichiometries of $\phi = 0.5–2$ were measured in the developed rapid compression machine. The RCM runs were performed for filling holes in experemental data for methane-air autoignition.

Ignition times were measured by using emission observations from side wall of combustion chamber at $\lambda = 308.9$ nm (OH, transitions $A^2\Sigma – X^2\Pi$) and at $\lambda = 431.5$ nm (CH, transitions $^2\Delta – ^2\Pi$), and end wall pressure measurements. For lean high-density mixture the ignition limit in the course of RCM tests was close to the temperature of 1075 K, for stoichiometric one – 936 K, and for rich one – 1105 K.

For studied range of conditions, global activation energies of $CH_4/O_2/N_2/Ar$ mixtures were determined by linear Arrhenius approximations of experimental data. It was found as 11.67 kcal/mole for low-density (2 kg/m^3) and 8.59 kcal/mole for high-density (4 kg/m^3) stoichiometric; 21.67 kcal/mole – for high-density rich and 18.45 kcal/mole and 15.03 kcal/mole – for low- and high-density lean $CH_4/O_2/N_2/Ar$ mixtures, respectively. Sufficient accuracy was obtained for lean and rich mixtures. For stoichiometric mixtures additional experiments are needed for correction of some measurements.

For compression temperatures higher than 1200 K in lean and stoichiometric mixtures, knocking phenomena were observed in the end compressed gas. Usually, knocking produces stable self-oscillations with amplitude approximately equal to the half-height of the pressure rise induced by the normal combustion.

Comparison with other experimental data availible in litterature has showed that auto-ignition phenomena can be investigated in a wide range of conditions by means of the developed RCM facility. The problem of accuracy and repeatability of measurements is remain open and requires the continuous optimizing of the RCM design and used materials.

REFERENCES

1. SPADACCINI L.J., COLKET M.B. Ignition delay characteristics of methane fuels. Prog. Energy Combust. Sci., 1994, Vol. 20, p. 431–460.
2. HEYNE S., ROUBAUD A., RIBAUCOUR M., VANHOVE G., MINETTI R., FAVRAT D. Development of a natural gas reaction mechanism for engine simulations based on rapid compression machine experiments using a multi-objective optimization strategy. Fuel, 2008, Vol. 87, p. 3046–3054.
3. PENYAZKOV O.G., SEVROUK K.L., TANGIRALA V., JOSHI. N. Auto-ignitions of methane/air mixtures at elevated temperatures and pressures, Proceedings of 7th ISHPMIE, 2008 July 7–11, ,Vol. 1, p. 101–107.
4. PETERSEN E.L., ROHRID M., DAVIDSON D.F., HANSON R.K., BOWMAN C.T. High-pressure methane oxidation behind reflected shock waves. Twenty-Sixth Symp. (Int.) Combust./Combust. Inst., 1996, p. 799–806.
5. PETERSEN E.L., DAVIDSON D.F., HANSON R.K. Ignition delay time of ram accelerator CH_4/O_2/diluent mixtures. J. Prop. Power, 1999, Vol. 15, p. 82–91.
6. GOY C.J., MORAN A.J., THOMAS G.O. Autoignition characteristics of gaseous fuels at representative gas turbine conditions. ASME Turbo Expo 2001, New Orleans, LA, 2001, 2001-GT-0051.
7. FRENKLACH M., BOWMAN C.T., SMITH G. P., GOLDEN D. M., , MORIARTY N. W., EITENEER B., GOLDENBERG M., HANSON R., SONG S., GARDINER W. C.,

LISSANSKI V., QIN Z. GRI 3.0 mechanism, link to the internet http://www.me.berkeley.edu/gri_mech.

8. HUANG J., HILL P.G., BUSHE W.K., MUNSHI S.R. Shock-tube study of methane ignition under engine-relevant conditions: experiment and modeling. Combust. Flame, 2004, Vol. 136, p. 25–42.
9. PETERSEN E.L., HALL J.M., SMITH S.D., DEVRIES J., AMADIO A.R., CROFTON M.W. Ignition of lean methane-based fuel blends at gas turbine pressures. ASME Turbo Expo 2005, Reno, NV, 2005, GT2005-68517.
10. DEVRIES J., PETERSEN E.L. Autoignition of methane-based fuels under gas turbine conditions. Proc. Combust. Inst., 2007, Vol. 31, p. 3163–3171.
11. BRETT L., MACNAMARA J., MUSCH P., SIMMIE J. M. Simulation of methane autoignition in a rapid compression machine with creviced pistons. Combust. Flame, 2001, Vol. 124, p. 326–329.
12. Methane oxidation mechanism. Version 1.3, link to the internet http://www.chem.leeds.ac.uk/Combustion.html.
13. GERSEN S., ANIKIN N.B., MOKHOV A.V., LEVINSKY H.B. Ignition properties of methane/hydrogen mixtures in a rapid compression machine. International Journal of Hydrogen Energy, 2008, Vol. 33, 1957-1964.
14. PETERSEN E.L., LAMNAOUER M., DEVRIES J., CURRAN H., SIMMIE J., FIKRI M., SCHULZ C., BOURQUE G. Discrepancies between schock-tube and rapid compression machine ignition at low temperatures and high pressures. Proceedings of 26th International Symposium on Shock Waves, 2007, Vol. 1, p. 739–744.
15. LIFSHITZ A., SCHELLER K., BURCAT. Shock-tube investigation of ignition in methane-oxygen-argon mixtures. Combust. Flame, 1971, Vol. 16, p. 311–321.
16. KRISHMAN K.S., RAVIKUMAR R. Ignition delay of methane in reflected shock waves. Comb. Sci. Tech., 1981, Vol. 24, p. 239.

CYSENI 2010, May 27–28, Kaunas, Lithuania
ISSN 1822-7554, www.cyseni.com

INFLUENCE OF GAS FLOW RATE ON THE THERMAL CHARACTERISTICS OF PLASMA-CHEMICAL REACTOR

M. Milieška, R. Kėželis, V. Mėčius
Plasma Processing Laboratory
Lithuanian Energy Institute
Breslaujos st. 3, LT-44403, Kaunas – Lithuania
Tel.: +370 37 401 895
Email: milieska@mail.lei.lt

ABSTRACT

Novel technology for production of mineral fiber using plasma technologies is specific, so there is a lack of information in worldwide scientific literature about the influence of many operating parameters on the working conditions of plasma chemical reactor designed for melting and fibrillation of dispersed particles. Gas flow temperature has to be 500–600 K higher than melting temperature while melting ceramic materials, so the experiments for estimation of the influence of additional feeding of air and propane-butane gas to the reactor was executed. Experimental parameters of plasma torch connected to the chemical reactor were constant: plasma torch power was 65 kW, air flow rate – 11 g/s, temperature of plasma flow entering the reactor – 3400 K. The additional flow of propane-butane gas increases the temperature of plasma flow, and the increase is more significant as the amount of propane-butane is higher. The addition of air flow to the reactor decreases the temperature of plasma flow, but it is necessary for the maintenance of high (about 950 m/s) plasma flow velocity which is essential for fibrillation of the melt of dispersed particles.

Keywords: thermal plasma, plasma chemical reactor, thermal characteristics.

1. INTRODUCTION

The use of thermal plasma in industry has been expanding in recent years. The possibility of application of thermal plasma processes depends on the development of the appropriate plasma equipment, i.e. the plasma generators, furnaces and reactors [1]. In traditional applications, such as plasma cutting and welding, this technique has been ripened and developing continually [2]. Many new applied fields have been discovered. Applications in coating, material, chemical engineering and waste treatment are very active [3]. Domestic research concentrates on fine powders and chemical engineering [4]. Because of simple technical flow, control environment and low cost, it is competitive to traditional techniques [1].

One of the novel applications of thermal plasma is plasma torch connection with the chemical reactor for production of mineral fiber. As distinct from plasma spraying technique, where dispersed particles are introduced into the plasma jet, melted and propelled towards a substrate, there particles are injected into the chemical reactor, heated, melted and stretched by plasma flow and formed into fiber. The review of fiber formation mechanism can be found elsewhere [5]. The reactor is called “chemical” because many exothermic and endothermic reactions, dissociation, ionization, erosion of surfaces are taking part in plasma environment at the same time.

As this technology is not fully developed there is lack of information in worldwide scientific literature about the influence of many operating parameters to the working conditions of plasma chemical reactor designed for melting and fibrillation of dispersed materials. Main published results on electrical and thermal characteristics of plasma-chemical reactors are obtained by article authors and their colleagues [6–7]. However, influence of additional gas flows to the temperature distribution in the plasma-chemical reactor hasn't been estimated.

As it was examined [8], the best conditions for fiber production are achieved when the melt viscosity is about 5 Pa. Therefore the temperature of the gas flow leaving the reactor has to be 500–600 K higher than the raw materials like zeolite, dolomite, quartz sand and etc, to achieve suitable viscosity. The melting temperatures of mentioned materials are from 1900 K to 2800 K. So the average temperature of plasma flow must be in the range of 2400-3400 K for any particular case in any section of plasma-chemical reactor.

The purpose of this paper is to analyze the influence of additional gas flows to the thermal characteristics of particular plasma chemical reactor.

2. METHODOLOGY

The sectional direct current electric arc plasma torch used in this work consists of the button-type hot hafnium cathode, an arc ignition section, neutral rings for feeding of working gas, a neutrode and a step-formed water-cooled anode made of high purity copper. When a gas is introduced on the electrode and a dc arc is established between the electrodes, the arc is pushed through the nozzle resulting in a high temperature and velocity flame. The temperature of the electric arc is nearly 20.000 K. The button-type cathode emitter and step-formed anode lead to determining the constant location of the arc column. The arc is also stabilized by tangential air injection into the reaction chamber through a pair of injectors. The body of the torch consists of chambers for cathode and anode cooled with water [7, 9]. Precise description plasma torch and additional equipment of experimental set-up has been depicted in detail elsewhere [7].

In Plasma Processing Laboratory of Lithuanian Energy Institute such dc plasma torch (66–68 kW of power capacity) was connected to a chemical reactor which consists of four sections (Fig. 1).

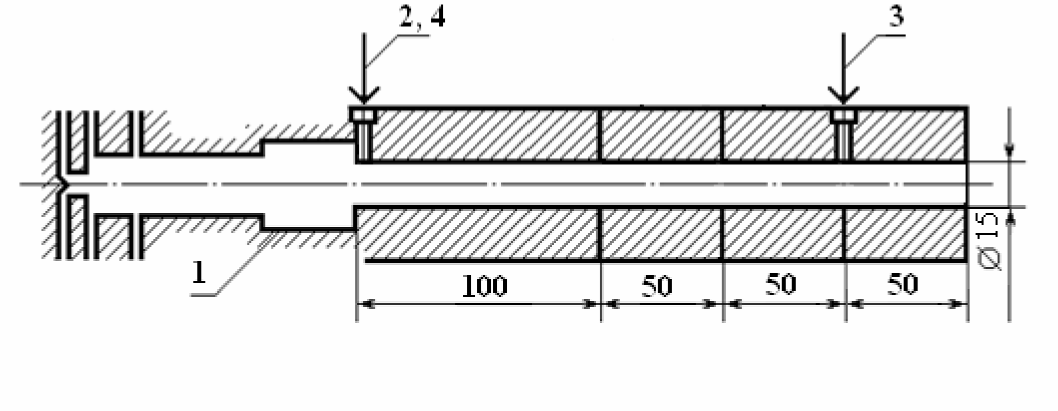

Fig. 1. Set-up of uniflow plasma chemical reactor: 1 – dc plasma torch, 2 – injection place of dispersed particles, 3 – additional feeding of air, 4 – propane-butane gas feeding. Measurements in mm

All chemical reactor sections made of stainless steel are 0.015 m of diameter and are cooled with water separately. The first section which is directly connected to the plasma torch anode is 0.01 m length. Other sections are 0.005 m length. Such design enables to change the length of the reactor, if needed. The first and the last sections have the inlets for dispersed particles and additional gases. Air for carrying of dispersed particles and propane-butane gases are introduced in the first section, and additional air flow is introduced in the fourth section.

Average plasma flow temperature in plasma torch and each section is calculated using power balance equation. Plasma torch current (I) and voltage (U), the flow rates of used gas (G_g) and water (G_w) for cooling and its temperature change (Δt_w) in each section are measured during the experiments.

General plasma torch power:

$$P = I \cdot U\ . \tag{1}$$

Power loss to the cooling water:

$$N_w = G_w \cdot \Delta t_w \cdot c_p\ . \tag{2}$$

Gas flow power:

$$N_g = P - N_w\ . \tag{3}$$

Average flow enthalpy in the section is calculated from the overall gas flow and its power:

$$H_f = \frac{N_g}{G_g} + H_0\ , \tag{4}$$

where H_0 – burning propane-butane gas enthalpy.

$$G_g = G_{pf} + G_{pc} + G_{fa}\ . \tag{5}$$

G_g – flow rate of all gases. G_{pf} – plasma forming air flow. G_{pc} – air for particle carrying. G_{fa} – air for plasma flow acceleration.

Average flow temperature in the plasma torch and each section is estimated from H_f.

3. RESULTS AND DISCUSSION

The experiments were done without any dispersed particle injection into plasma flow. The plasma torch power was constant in all our experiments and it was about 65 kW.

The experiments could be divided into four stages (each stage appends the one above) of plasma flow temperature distribution measurements in the plasma-chemical reactor:

1. Plasma flow obtained from the plasma torch;
2. Addition of air flow used for dispersed particles introduction;
3. Addition of air flow introduced in the fourth section of the chemical reactor;
4. Addition of propane-butane gases.

As it can be seen in Fig. 2, the temperature of the plasma flow without using any additional gas would be sufficient for melting of raw materials or their mixtures with low melting temperatures. The drag force between the reactor walls and plasma flow slows down the velocity of the flow, increases heat transfer from plasma flow to the reactor walls which results the flow temperature decrease. The decrease is about 400 K in the length of the reactor.

As the plasma forming air rate is bigger, the plasma temperature at the plasma torch outlet nozzle is lesser. It is because the equal thermal energy transferred from the plasma torch to the smaller air rate heats it up more than the bigger air rate.

In the different type of plasma-chemical reactor, it was found that decrease of average plasma flow temperature is about 400 K in the length, too [10].

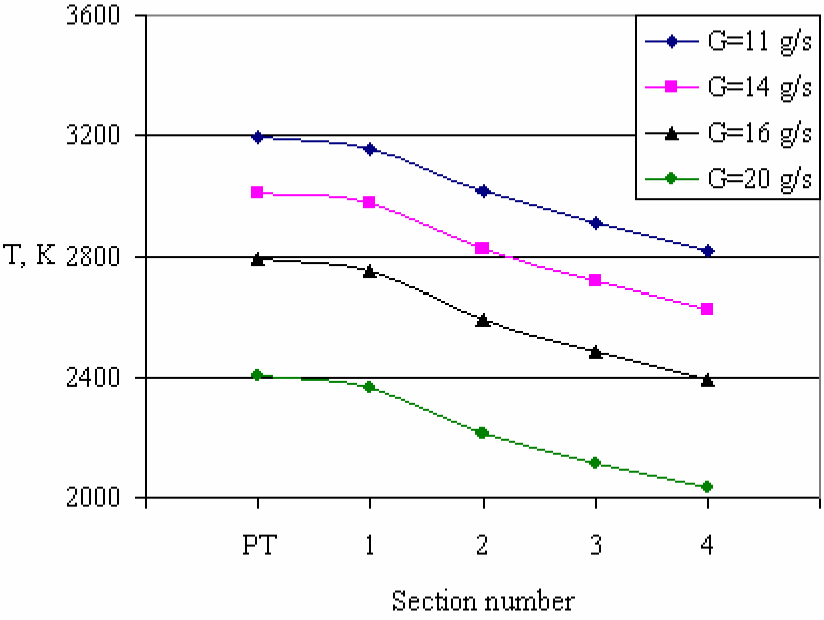

Fig. 2. The dependence of plasma flow temperature in the chemical reactor on the plasma forming air rate. PT – plasma torch

Because of the technical restrictions dispersed particles can be introduced into plasma flow with the use of gas flow only. For creation of conditions as similar as possible to the real conditions of fiber production air flow was introduced into plasma flow during further experiments. As the amount of air is bigger, the temperature drop of the plasma flow from the injection place is more significant (Fig. 3). The temperature drop occurs because of heat transfer between mixing plasma and injected room temperature air (~ 291 K).

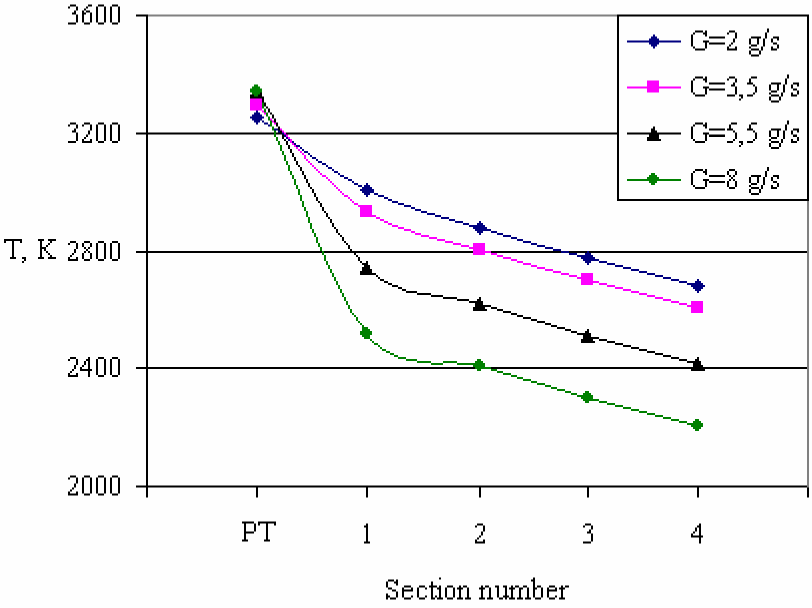

Fig. 3. The influence of dispersed particle carrying air flow on plasma flow temperature drop in the chemical reactor for 11 g/s plasma forming gas flow rate. PT – plasma torch

As we mentioned above, there is no dispersed particle injection in this experiment, only the air injection which could carry the dispersed particles in. But if the dispersed particles were injected, they would start to mix with turbulent plasma flow when they enter the chemical reactor. The smallest particles would sublimate or evaporate immediately because the flow temperature is very high. Bigger particles would stick to the reactor walls and flew out of the reactor as a melt [5]. To accelerate the plasma flow and to enhance the plasma flow kinetic energy, which drags little drops out of the melt sticked to the reactor walls, stretches them and forms a fiber, an additional air feeding is used at the end (before the fourth section) of the chemical reactor (Fig. 1). Fig. 4 shows what influence to the temperature of plasma flow has plasma flow accelerating air flow depending on its rate.

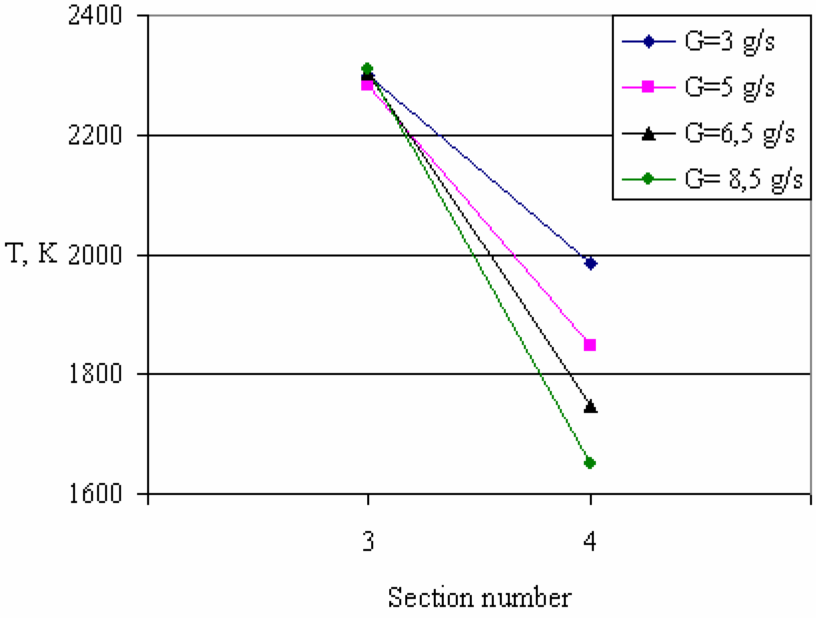

Fig. 4. The influence of accelerating air on the temperature drop in the last section of the reactor at plasma forming gas flow rate 11 g/s, particle carrying air flow rate 8 g/s

Same as the dispersed particle carrying air, the plasma flow accelerating air decreases the temperature of the plasma flow. Despite the short time of being in the reactor, the plasma flow accelerating air mixes enough with plasma flow to have a significant influence on its temperature.

The use of both (particle carrying and plasma flow accelerating) air flows is necessary. But they significantly decrease the temperature of plasma flow and the melting of dispersed materials becomes impossible. Propane-butane gases were injected into plasma flow along with the air for dispersed particle carrying to increase the temperature of plasma flow (Fig. 5). The flow rate of dispersed particle carrying air was 1 g/s and plasma flow accelerating air flow rate was 3 g/s. Propane-butane gases injected into plasma flow mixes with it, ignites and burns emitting significant energy amounts which increases the flow temperature in the reactor.

The propane-butane gas injection to the plasma flow increases the temperature in the plasma chemical reactor which becomes suitable for melting and fibrillation of dispersed materials.

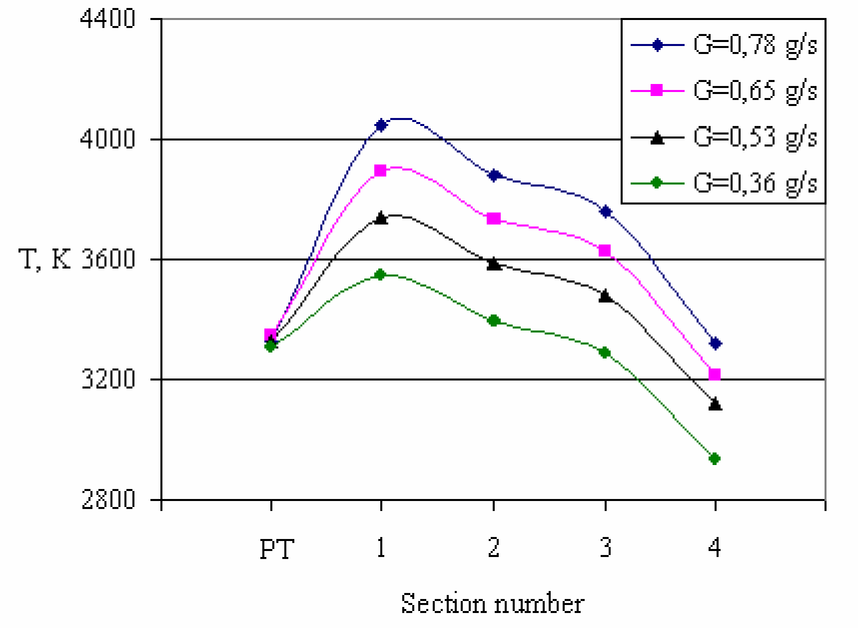

Fig. 5. The influence of propane-butane gas flow to the temperature of the plasma flow in the chemical reactor at plasma forming gas flow rate 11 g/s. PT – plasma torch.

4. CONCLUSIONS

1. The decrease of average plasma flow temperature without using any additional gases is about 400 K in the reactor length and it is caused by the drag force between the plasma flow and plasma-chemical reactor walls.
2. As the flow rate of additional air for dispersed particle carrying into plasma-chemical reactor increases from 2 g/s to 8 g/s the average plasma flow temperature decreases from 600 K to 1100 K in the length of the reactor.
3. The use of additional air flow for plasma flow acceleration from 3 g/s to 8.5 g/s decreases the average plasma flow temperature only in the last section of plasma-chemical reactor from 300 K to 600 K, as the average temperature drop in the last section without use of any additional air flow is 100 K.
4. The propane-butane gas feeding rate into the plasma-chemical reactor from 0.36 g/s to 0.78 g/s increases the average temperature of plasma flow in each section from 250 K to 850 K.

ACKNOWLEDGEMENTS

The authors acknowledge the Agency for International Science and Technology Development Programmes in Lithuania for financial support.

REFERENCES

1. RYKALIN N.N. Plasma engineering in metallurgy and inorganic materials technology. *Pure & Appi. Chem.*, 1976, Vol. 48, p. 179–194.
2. XU W.J., FANG. J.C., LU. Y.S. Study on ceramic cutting by plasma arc. *Journal of Materials Processing Technology,* 2002, Vol. 129, p. 152–156.
3. BOGAERTS, A., NEYTS E., GIJBELS R., VAN DER MULLEN J. Gas discharge plasmas and their applications. *Spectrochimica Acta Part B,* 2002, Vol. 57, p. 609–658.

4. FUKUMASA O., FUJIWARA T. Rapid synthesis of ferrite particles from powder mixtures using thermal plasma processing. *Thin solid films,* 2003, Vol. 435, p. 33–38.
5. MILIEŠKA M., KĖŽELIS R., VALINČIUS V. Realization and analysis of inorganic metal oxides plasma melting and fibrillation process. CYSENI 2009. Proceedings of annual conference of young scientists on energy issues. [CD]. Kaunas: Lithuanian Energy Institute. 2009 May 28–29.
6. VALINČIŪTĖ V., KĖŽELIS R., VALINČIUS V., VALATKEVIČIUS P., MĖČIUS V. Heat transfer in a plasma jet reactor for melting and melt fibrillation of hard ceramics. *Heat transfer research.* 2008, Vol. 39, Iss. 7, p. 609–618.
7. VALINČIUS V., KRUŠINSKAITĖ V., VALATKEVIČIUS P., VALINČIŪTĖ V., MARCINAUSKAS L. Electric and thermal characteristics of the linear, sectional dc plasma generator. *Plasma sources science and technology.* 2004, Vol. 13, p. 199–206.
8. STRAZDAS K., EIDUKEVICIUS P.. Mineral and glass fiber, Vilnius, 1985, p. 19 (in Lithuanian).
9. VENKATRAMANI, N. Industrial plasma torches and applications. *Curr. Sci.* 2002, Vol. 83, No 3, p. 254–262.
10. VALINČIUS V., KĖŽELIS R., VALATKEVIČIUS P., MILIEŠKA M. Melting and conversion into fibre dolomite and quartz sand mixtures by means of plasma spraying. *Изв. вуз. Физика.* 2007, No 9, p. 441–444.

CYSENI 2010, May 27–28, Kaunas, Lithuania
ISSN 1822-7554, www.cyseni.com

APPLICATION OF WATER VAPOR PLASMA TORCH FOR CONVERSION OF BIOMASS AND ORGANIC WASTE

A. Tamošiūnas, P. Valatkevičius
Lithuanian Energy Institute
Plasma Processing Laboratory
Breslaujos str. 3, LT-44403 Kaunas – Lithuania
Email: tamosiunas@mail.lei.lt

ABSTRACT

Conversion of biomass and organic waste into synthetic fuels using plasma technologies is investigated. Water vapor plasma torch is used to convert solid biomass to synthetic gas (CO + H_2). The potential of biomass for the generation of energy in Lithuania is reviewed. The thermal methods of conversion of solid biomass and organic waste are compared. Advantages and disadvantages is be introduced. Also, the processes proceeding in plasma reactor is overlooked. Chemical reactions how to get synthetic fuels from organic materials are supplied. Characteristics of water vapor under high temperatures, construction and features of plasmachemical reactors for the conversion of solid biomass and organic waste are analyzed.

Keywords: Plasma torch, Biomass, Synthetic fuels, Organic waste

1. INTRODUCTION

Rapid consumption of fossil fuels depends on the growth of world economy. A reserve of these fuels permanently diminishes. Supply of cheap oil stock could exhaust for the next few decades [1]. Increased demand of fossil fuels causes negative emissions of greenhouse gases. It must be stopped until humanity doesn't destroyed nature and themselves. Scientists, engineers and politicians have to take means now. There is no time to wait and do nothing.

One of the most promising stocks for the production of energy and fuels is biomass. It has been gradually and widely begun to use in nowadays for the conversion into energy, heat and the production of biofuels. Biomass is a production of the photosynthesis, where the energy is collected in leaves, branches and stems of the plants [2].

The potential of biomass and organic waste in Lithuania is very huge. One of the biggest potential is solid biomass (residues of forest logs and energetic plants), also straw, municipal waste and domestic residues and biogas and biofuels, etc.

There are created and developed a lot of methods and technologies of biomass conversion into biofuels in the world. One of the latest and less explored is plasma gasification using water vapor. So, the point of this article is to develop the water vapor plasma torch for conversion of biomass and organic waste.

2. THE PROBLEM OF BIOMASS AND ORGANIC WASTE TREATMENT, AND METHODS

2.1. The potential of biomass and organic waste for conversion into energy in Lithuania

There is accumulated a big quantity of biomass in the world and in Lithuania also. Lithuania is one of the leading countries in Europe Union according to amount of biomass per one habitant [3]. Replacement of conventional energy sources by biomass energy supports to save money and preserves energetic independency from foreign countries, also helps to deal with environmental and unemployment problems, increases security supply of energy and etc. The 3 mln. tones amount of organic waste are deposited in dumps every year. More than half is municipal waste [4]. There are some application areas of biomass and organic waste (Fig. 1) from the main biomass and organic waste resources:

- residues of forest logs and wood;
- rgricultural plants and residues (energetic plants, straw, wheat and etc.);
- residues of Food Industry (also Milk Industry and Meat Industry);
- residues of Animal Husbandry (droppings of birds, pigs and cattle);
- municipal waste.
- medical residues.

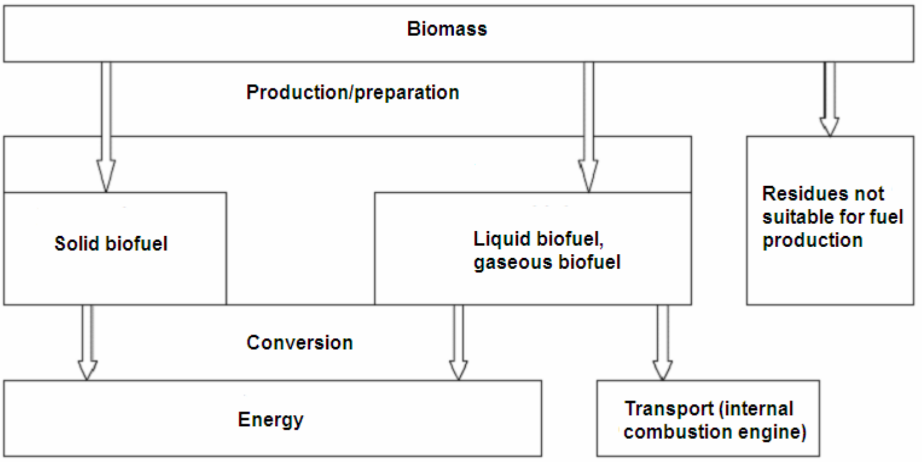

Fig. 1. The usage of biomass for energy generation [3]

Wood is one sort of biomass, which is mainly and mostly used for the production of energy. Total annual increment of wood is about 13.8 mln. m^3. Wood suitable for the production of biofuels takes 4.3 mln. m^3. This is equal to the amount of energy of 9.8 TWh per year [5]. However, the biggest amount of wood suitable for the generation of energy (residues of forest logs, constructional waste of building industry and etc.) is being transported to dumps or just left to rot in the forests. To avoid this pollution of nature, these wastes can be utilized by plasma technologies producing a synthetic gas ($CO+H_2$).

All of the mentioned sorts of biomass (solid, liquid and gaseous) appropriate for the generation of energy could be used for the production of high enthalpy synthetic gas. However, one of the most promising methods is gasification of solid biomass.

2.2. Thermal gasification of biomass and organic waste

There are developed a lot of thermal methods in the world appropriate for the conversion of solid biomass such as: pyrolysis, carbonization, thermal incineration, low temperature oxidation, catalytic oxidation, gasification and thermal plasma gasification [6–8].

Advantages of mentioned methods, except thermal plasma, are low costs, simple engineering constructions of equipments and quite easy to install. The main advantages of thermal plasma gasification is a better control of the composition of the produced gas, higher heat capacity of the gas and reduction of unwanted and even in such cases toxic contaminants like tar, CO_2 and higher hydrocarbons. Disadvantages are low effectiveness of conversion, because of low temperatures compared to thermal plasma, increasing environmental limitations on quantity of contaminants. The main disadvantage of thermal plasma gasification is relatively high cost.

Thermal plasma technology offers the possibility of decomposition of biomass by pure pyrolysis in the absence of oxygen. In this process all energy needed for gasification comes from the plasma, and the energy for decomposition by combustion is not produced. Synthetic gas obtained during gasification, could be combusted as a fuel for energy generation or used in internal combustion engines as alternative for fossil fuels. Gasification – a process that converts carbonaceous materials, such as coal, biofuel or biomass into carbon monoxide by reacting the raw material at high temperatures with a controlled amount of oxygen and/or steam. Substance during gasification is partially heated and combusted. Part of the material is turned into gases, part into tars and part into solid fraction (coke). Tars as a by-product could be used in chemical industry as a feedstock. The enthalpy of generated gas depends on sort of plasma gas and the flow rate. The production of syngas from wood using applicable current (AC) air plasma torches is discussed in [9]. The coal gasification in hydrogen, air and steam plasma was studied in [10,11] using both the direct current (DC) and AC torches.

Biomass is organic compound mostly made of carbon and hydrogen molecules, which participate in chemical reactions. Thus the equations for reactions when gasification takes place in presence of oxygen are showed below [12,13]:

$$C + O_2 \rightarrow CO_2 + 395.4\ \text{MJ/kg} \tag{1}$$

$$C + CO_2 \rightarrow 2CO - 172\ \text{MJ/kg} \tag{2}$$

$$2C + O_2 \rightarrow 2CO + 223.3\ \text{MJ/kg.} \tag{3}$$

Between carbon and water vapor two reactions proceeds. One at 500–600 ^{o}C temperature:

$$C + 2H_2O \rightarrow CO_2 + 2H_2 - 88\ \text{MJ/kg.} \tag{4}$$

And the second one, than temperature exceeds 900 ^{o}C:

$$C + H_2O \rightarrow CO + H_2 - 130\ \text{MJ/kg.} \tag{5}$$

Liquid synthetic fuels can be produced from syngas in use of special catalysts, and could be used in internal combustion engines.

2.3. Conversion of biomass and organic waste by water vapor plasma

Instead of mixture of oxygen and water, only water vapor, as a working gas, is being used in plasma gasification. It's heated up to 2000–3000 K by the electric arc of plasma torch in plasma reactor [14]. Analysis and calculations in [15] show that water vapor with organic materials forms synthetic gas ($CO + H_2$) at 1200 K temperature. In [16], syngas forms at 1100 K.

Traditional gasification process is based on chemical reactions proceeding between organic materials with limited amount of mixture of oxygen and water vapor. Plasma gasification is based on the reactions in absence of oxygen. It proceeds between biomass or organic waste with overheated water vapor only. Water vapor is a reagent and a heat carrier at once. It enhances reaction kinetics because of the high enthalpy. All energy necessary for gasification is absorbed from a plasma jet. There is no combustion in the ambience of oxygen. This allows better control the composition of synthetic gas, to gain higher enthalpy and reduce the amount of unwanted tar, carbon dioxide and hydrocarbons.

As an example, a composition of syngas after plasma gasification of crushed wood is 61.6% of hydrogen and 35.2% of carbon monoxide; enthalpy is 22.8 MJ/kg [17].

In comparison with pyrolysis after thermal plasma gasification unwanted tar is avoided, because steam of tar breaks into gas under high temperatures. So, water vapor plasma is ecologically friendly.

2.4. Characteristics of water vapor at high temperatures

As mentioned before, water vapor plasma is ecologically clean. After cooling it turns back into liquid water. That's why, this kind of plasma is very convenient to use in plasmachemical reactors for gasification of biomass and organic waste.

The mass enthalpy of water vapor is about six times higher than mass enthalpy of air at high temperatures (4000–5000 K) (Fig. 2). In comparison, distribution of oxygen and hydrogen enthalpies is showed. Decomposition of organic waste by water vapor is endothermic process. Therefore, temperature of water vapor has to be higher than temperature of chemical reactions.

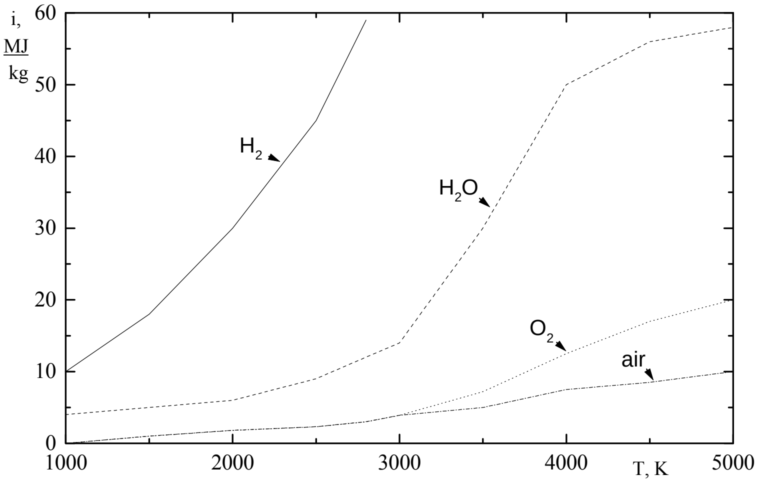

Fig. 2. The dependence of hydrogen, water vapor, oxygen and air enthalpies on the temperature at 1bar pressure [17]

To heat water vapor up to required temperature needs several times more power than the same amount of air. Water vapor begins to dissociate under 2000 K (Fig. 3). At 4000 K it is no more water vapor and flow consists only of O_2, H_2 molecules and O, H, OH atoms.

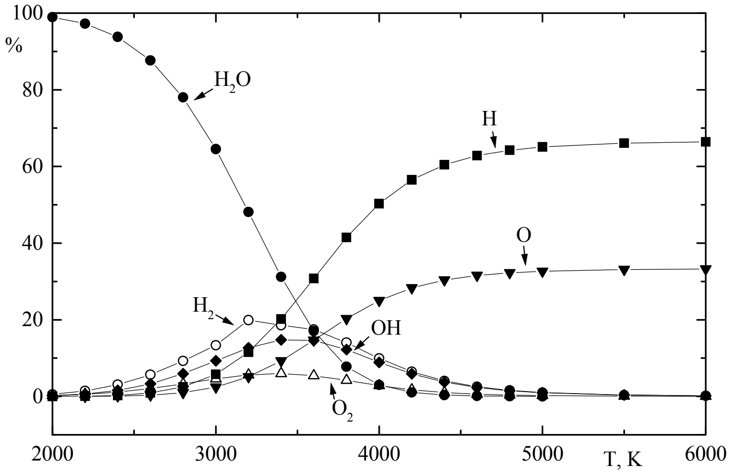

Fig. 3. The dependence of the percentage composition of water vapor on the temperature at 1bar pressure [18]

3. EXPERIMENTAL EQUIPMENT

There are two main types of plasma reactors for materials chemical processing: plasma jet reactor and electric arc reactor. In plasma jet reactor case chemical processes proceed in plasma jet, where temperatures exceed up to 2000–4000 K. The difference of electric arc reactors is that feedstock is supplied not into plasma jet, but directly into the place where electric arc forms. An electric arc discharge forms between the plasma generator (PG) and the alloy of iron, which is at the bottom of the reactor. A plasma generator – is the equipment, which allows to heat gas to very high temperatures. A temperature inside the electric arc reactor is about 1270–1370 K, and near plasma torch could exceed 2500 K [19].

An experimental linear DC water vapor plasma generator with step–formed anode has been designed and tested (Fig. 4). Electrical and thermal characteristics of PG have been measured. The DC air/water stabilized plasma torch has been employed operating at atmospheric pressure, max magnitude of current I=187 A, the voltage U=250 V, power P = 43.7 kW, air flow rate was $G_1=7\text{-}10^{-4}$ kg · s^{-1}, water vapor flow rate $G_2= (2.45\text{–}3.7)\cdot 10^{-3}$ kg · s^{-1}. The average temperature of flow at the torch outlet nozzle varied within limits of T=2600–3000 K.

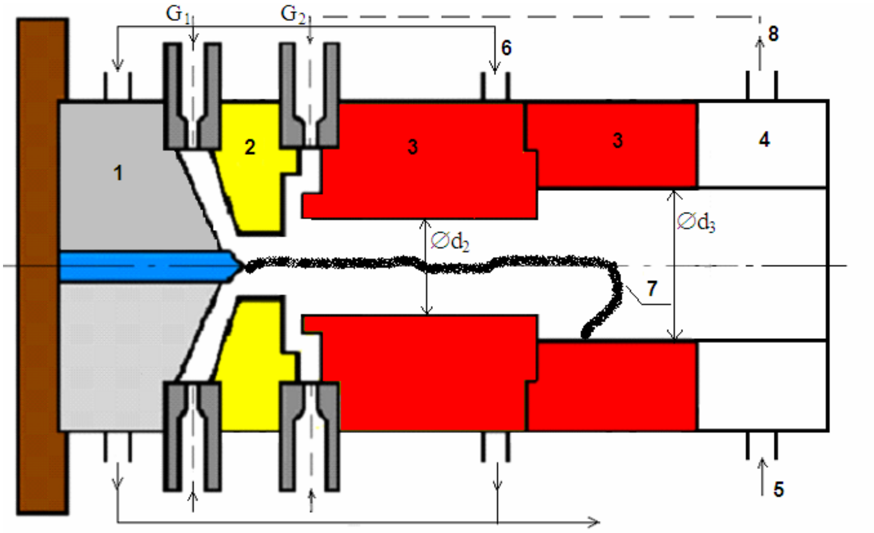

Fig. 4. A scheme of water vapor plasma generator. 1 – cathode, 2 – neutral section, 3 – stair-step anode, 4 – superheater, 5 – hole for water vapor supply, 6 – system cooling liquid, 7 – electric arc, 8 – overheated water vapor

The cathode of the plasma torch was made of copper implemented with hafnium as electron provider. The anode of the torch was made of copper also. The working gas was tangentially supplied water vapor through insulating rings contains blowholes. All parts of PG were cooled by water. Erosion of plasma generator sections takes place because of the condensation of water vapor on the walls. To avoid condensation, the temperature of electrodes walls has to be over 373 K. Before water vapor flows into PG it should be overheated up to 473–573 K temperature. For this reason a superheater is needed. The plasma generator could be a superheater itself, when saturated water vapor is supplied into the last section (4). Hot section of the PG overheats water vapor which simultaneously cools it. The overheated water vapor is tangentially supplied to the plasma generator through insulating rings. It is ionized by electric arc, i.e. dissociates into ions, atoms, neutrals and electrons.

4. RESULTS AND DISCUSSION

4.1. Thermal characteristics of water vapor plasma torch

The increased thickness of boundary layer and voltage improves the thermal efficiency of plasma generator. The increase in current strength and thermal loss into PG walls reduces the efficiency of plasma torch (Fig. 5). This is under the influence of the decline in thickness of the diameter of boundary layer. Decline in thickness of boundary layer determine the increase of diameter of the electric arc channel. Maximum plasma torch thermal efficiency than I=160 A, and water vapor flow rate $3.7 \cdot 10^{-3}$ kg · s^{-1} was 0.78.

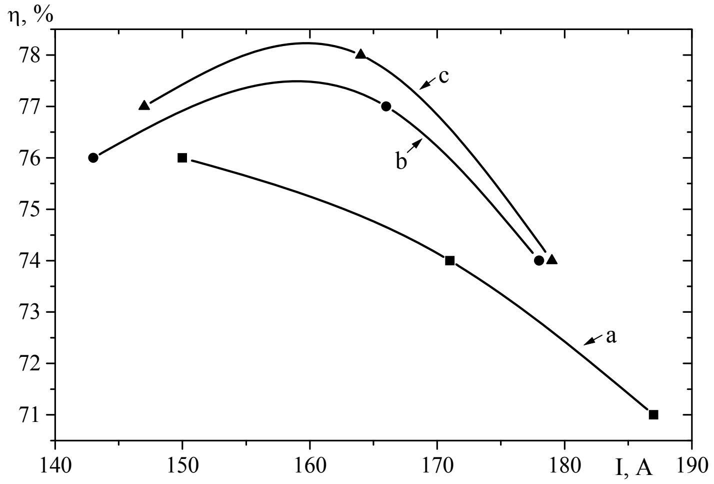

Fig. 5. The dependence of plasma torch thermal efficiency on the current strength and water vapor flow rate, 10^{-3} kg · s^{-1}: a–2.45; b–3.1; c–3.7.

The general results of plasma torch thermal efficiency (Fig. 6) were estimated using the theory of similarity and are summarized into one equation. A general estimating equation for determination of efficiency is presented below. Any magnitude of plasma torch thermal efficiency may be estimated from this equation. The results from the (Fig. 6) are taken into account designing plasma generator for decomposition of biomass and organic waste.

$$\frac{(1-\eta)}{\eta} = 1{,}65 \cdot 10^{-3} \left(\frac{I^2}{Gd_2} \right)^{0{,}26}, \tag{6}$$

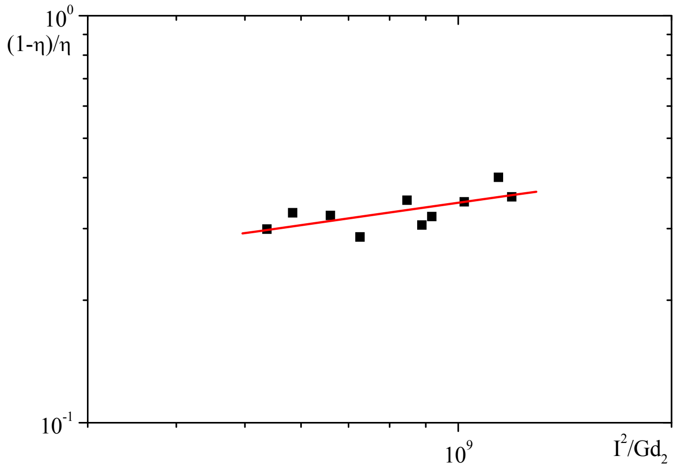

Fig. 6. A general thermal efficiency of plasma torch

4.2. Electrical characteristics of water vapor plasma torch

The voltage in an electric arc and the power of plasma torch mainly depend on the flow rate of water vapor (Fig. 8). A part of incident curve may appear as a result of the insignificant influence of the PG channel walls on an electric arc, i.e. tangentially supplied water vapor flow rate has a big influence on the thickness of the boundary layer. Thus, the diameter of an electric arc channel decreases. The part of rising curve appears than the PG channel walls influence the characteristics of electric arc, i.e. energy quantity is transferred to the channel walls. Thus, the thickness of boundary layer thins down.

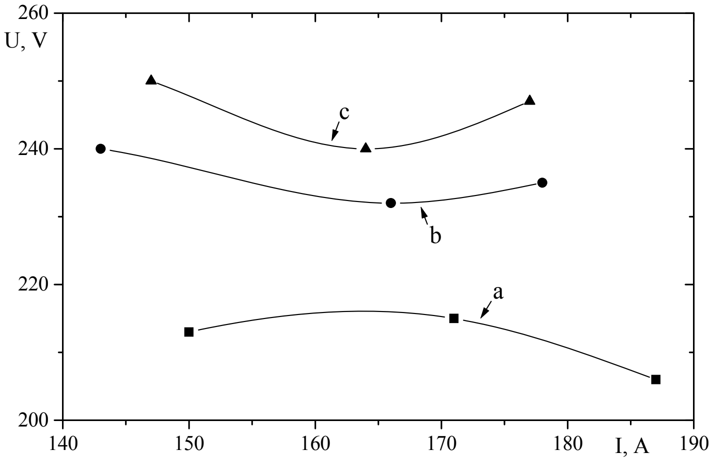

Fig. 8. Volt-ampere characteristics of water vapor plasma torch depending on water vapor flow rate, 10^{-3} kg · s^{-1}: a–2.45; b–3.1; c–3.7

A general estimating equation for determination of volt-ampere characteristics were estimated using the theory of similarity and is presented below. The general results are depicted in (Fig. 9). These results are taken into account designing plasma generator.

$$\frac{Ud_2}{I} = 182\left(\frac{I^2}{Gd}\right)^{-0,46}, \tag{7}$$

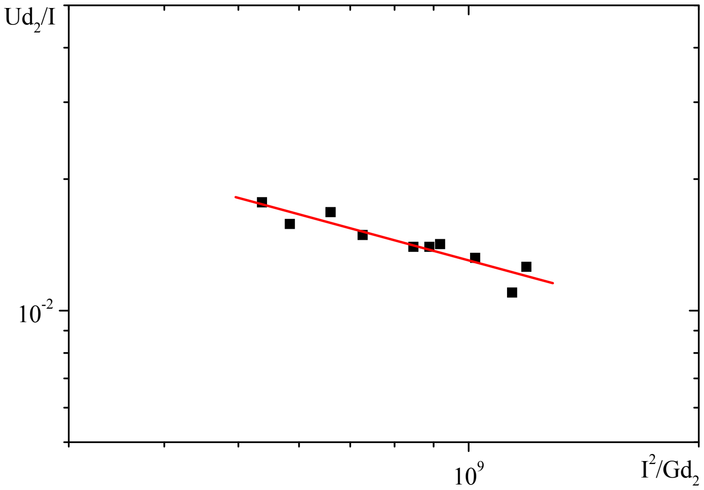

Fig. 9. A generalized volt-ampere characteristics of water vapor plasma torch

The volt-ampere characteristics of water vapor plasma torch are strongly dependent on the type of working gas and shield gas and their mass flow. It also depends on the physical characteristics of the gas, i.e. density, viscosity, conduction and etc. The knowledge of geometry of PG and its volt-ampere characteristics helps to determine the temperature and velocity of the plasma jet at the outflow nozzle. Thermal and dynamic parameters of plasma jet have the main influence on the effective thermal plasma gasification of biomass and organic waste.

5. CONCLUSIONS

An experimental linear DC water vapor plasma generator with step–formed anode has been designed and tested. The DC air/water stabilized plasma torch has been employed operating at atmospheric pressure, max magnitude of current I=187 A, voltage U=250 V, power P=43.7 kW, air flow rate was $G_1=7 \cdot 10^{-4}$ kg · s^{-1}, water vapor flow rate $G_2= (2.45–3.7)\cdot 10^{-3}$ kg · s^{-1}. The average flow temperature at the torch outlet varied within limits of T=2600–3000 K. Maximum plasma torch thermal efficiency than I=160 A, and water vapor flow rate $3.7 \cdot 10^{-3}$ kg · s^{-1} was 0.78.

The thermal and electrical characteristics of the water vapor plasma torch were carried out to ensure the stable work of the plasma generator. The results will be useful projecting new plasma equipment, designed for the decomposition of biomass and organic waste.

The water vapor plasma torch can is suitable for biomass and organic waste decomposition. More detailed examinations are required to design and test whole plasma conversion system.

REFERENCES

1. GOODSTEIN D. *Out of gas: the End of the Age of Oil*. USA: W. W. Norton & Company, 2004. 144 p. ISBN 0-393-05847-3.
2. VRUBLIAUSKAS S. Biomass for energy conversion. *Science and Life*, 2000, No 4, p. 40–42.
3. *Report of Lithuanian biomass energy association LITBIOMA*. 2010–2020 y. plan of promotion of Lithuanian renewable energy sources. Vilnius, 2008, p. 50–59.
4. http://www.lzuu.lt/nm/l-projektas/-Aplinkos_tarsa/16.htm
5. http://db1.stat.gov.lt/statbank/selectvarval/saveselections.asp?MainTable=M5020101&PLanguage=0&TableStyle=&Buttons=&PXSId=2668&IQY=&TC=&ST=ST&rvar0=&rvar1=&rvar2=&rvar3=&rvar4=&rvar5=&rvar6=&rvar7=&rvar8=&rvar9=&rvar10=&rvar11=&rvar12=&rvar13=&rvar14=
6. БЕРНАРДИНЕР М.Н., ШУРЫГИН А.Л. *Огневая переработка и обезвреживание промышленых отходов*. Москва: Химия, 1990. 304 с. ISBN 5-724-50531-2.
7. JACKMAN A. P., POWELL R. L. *Hazardous Waste Treatment Technologies*. New Jersey: Noyes publications, 1991. 276 p. ISBN 0-815-51268-6.
8. FEHLNER F.P. *Low Temperature Oxidation: The Role of Vitreous Oxides*. New York: Wiley, 1986. 257 p. ISBN 0-306-41741-3.
9. RUTBERG P.G., BRATSEV A.N., UFIMTSEV A.A. Plasmachemical technologies for processing of hydrocarbonic raw material with syngas production. *J. High Temp. Process*, 2004, Vol. 8, No 3, p. 433–446.
10. MIKHAILOV B. In: SOLONENKO O.P., ZHUKOV M.F., editors. *Plasma gasification of coal, thermal plasma and new materials technology, vol. 2*. Cambridge: Cambridge Interscience Publishers, 1995, p. 345–369.

11. ZASYPKIN I. M., NOZDRENKO G. V. *Production of acetylene and synthesis gas from coal by plasma chemical methods. In: SOLONENKO O. P., editor. Thermal plasma torches and technologies, vol. 2*. Cambridge: Cambridge Interscience Publishers, 2001. 234–243 p.
12. WEREKO-BROBBY CH. Y., HAGAN E. B. *Biomass Conversion and Technology*. Chichester: John Willey & Sons, 1996. 203 p. ISBN 0-471-96426-5.
13. BALTRUŠIS R., DEGUTIS J., DIENYS G., ir kt. *Organinė chemija, vadovėlis aukštųjų mokyklų studentams*. Vilnius: Žodynas, 1995. 379 p. ISBN 9-986-4652-9.
14. ЖУКОВ М. Ф., МИХАЙЛОВ Б. И., АНЬШАКОВ А. С. *Пароводяные плазмотроны для пиролиза и конверсии углеводородов. Плазменная газификация и пиролиз низкосортных углей*. Москва: Наука, 1987. 111–123 с.
15. VALATKEVIČIUS P. A *report of employment of plasma generators for utilization of toxic materials treatment*. Kaunas: Lithuanian Energy Institute. 1999, p. 70.
16. VAN OOST G., HRABOVSKY M., KOPECKY V., KONRAD M., HLINA M. Pyrolysis/gasification of biomass for synthetic fuel production using a hybrid gas – water stabilized plasma torch. *Vacuum*, 2009, No 83, p. 209–212.
17. JUŠKEVIČIUS R., VALATKEVIČIUS P. Thermal and plasma gasification of solid fuel. *Energetic*, 1997, No. 4, p. 24–28.
18. ВАРГАФТЫК Н. Ь. *Справочник по теплофизическим свойствам газов и жидкостей*. Москва: Наука, 1972. 625 с. ISBN 0-470-90310-4.
19. СУРИС А. Л. *Плазмохимические процессы и аппараты*. Москва: Химия, 1989. 304 с. ISBN 5-724-50584-3.

CYSENI 2010, May 27–28, Kaunas, Lithuania
ISSN 1822-7554, www.cyseni.com

IMPACT OF URBAN HEAT ISLAND ON ENERGY DEMAND AND CONSUMPTION

I.A. Balogun, A.A. Balogun, A. Oluleye,
Department of Meteorology
Federal University of Technology
PMB 704, Akure 34000 - Nigeria
Phone: +234-803-919-4212
Email: iabalogun@futa.edu.ng

ABSTRACT

It is well established that urbanisation has a significant effect on the local climate. The climate of an urban area differs from that of a nearby rural area. This paper investigates the climate modifying effect of urban heat island in Akure, a medium-sized rapid developing south western city in Nigeria which lies in the tropics. This is noted to cause significant thermal alterations which are revealed by measurement and analysis as presented in this work. The role of this urban heat island on energy demand of the city has been investigated in this study. Results showed that the elevated temperatures in the dry period, at the onset of summer monsoon in the city increase energy demand for cooling and add pressure to the electricity grid during peak periods of demand. In this period, the urban heat island (UHI) will tend to result in an increased cooling load and an increased number of human discomfort days due to longer length of hours required for cooling. But when the summer monsoon has fully developed, the UHI will tend to result in reduced cooling demand due to cooling effect of monsoon winds. This paper also investigates the roles of the developed urban heat island on the cooling degree day in the city.

Keywords: Urban heat island, cooling energy demand

1. INTRODUCTION

The modification of the natural surface, release of artificial energy and polluting materials into the atmosphere over the cities alter radiation and energy balance in urban environments. This as a result produces a peculiar local climate, termed the ‘urban climate’. The most obvious manifestation and best documented example of this inadvertent climate modification is the urban heat island (UHI) [1]. This means that warmer areas appear within settlements as compared to the surroundings. Urban areas have significant heat storage and thermal inertia from this process is believed to be instrumental in creation of the urban heat island effect [2]. The heat excess has lots of practical consequences, which may influence everyday life.

Weather has a significant impact on different sectors of the economy. One of the most sensitive is the electricity market, because power demand is linked to several weather variables, mainly to the air temperature.

It has been well documented that weather-related factors play an important role in affecting electricity consumption. For many years, utility companies and the electric power industry have been interested in the relation between energy consumption and climate, and have developed empirical weather normalization algorithms aimed at improving load forecasting subject to variations in regional climate [3]. Most of the research have been carried out by investigating the effect of increased air temperature in urban areas on energy demand of buildings [4, 5, 6].

Several researchers have published estimates of climatic influences on energy consumption. Many of the publications in this area, however, focus on energy consumption at the level of the individual residential or commercial buildings under idealized conditions. For example, [7] estimated the effects of climatic change on several prototype commercial buildings in various US cities. [8] conducted a similar climate sensitivity study using the DoE-2 building energy simulation code to simulate both residential and commercial buildings. Both authors found a significant impact of weather variations on the energy consumption of individual buildings.

There are limited studies done at regional scale level. One of such is the work of [9] that investigated the role of climate parameters in affecting the peak demand in Israel. The significance of the study was noted as it analyses peak energy consumption and was able to estimate possible implication for future generation capacity requirements and its significant national policy implications as its spatial domain was an entire country. [10] In 2001 analyzes the relationship between electricity load and daily air temperature in Spain, using a population-weighted temperature index and part of their results having isolated weather influence on electricity loads from socioeconomic factors, revealed that the sensitivity of electricity load to daily air temperature has increased along time, in a higher degree for summer than for winter. [11] In his work on Asheville, North Carolina showed that site specific energy and heating oil consumption for individual residences show a very high correlation with their National Weather Services data when transformed into heating degree days. In the United States, for example, degree day indicators are widely used in weather derivatives, energy trading, and weather risk management.

However, much of these research and related issues have been investigated in the mid-latitudes but the knowledge gap is yet to be filled in the tropics, Nigeria in particular. Few works have been done which were focused on characteristics of the heat island intensities and humidity properties [12, 13, 14, 15, 16]. This work is a pioneering research in the country trying to relate the urban heat island and its associated degree day parameters to energy demand. There are quite some limitations in directly relating energy load in terms of its distribution and consumption to the urban heat island in the country as data required for this kind of inspection are not available. Hence, is difficult to furnish us with needed information. However, we tried to assess the diurnal and seasonal magnitude of the heat island intensity and the degree day concept to establish the possible period of higher energy demands in the city.

2. DATA AND METHODS

Urban rural air temperatures were measured with portable Lascar EL-USB-2 temperature/humidity data loggers. The device has an accuracy of +/- 0.5 ^{0}C. The loggers were programmed to sample at 5 minute intervals, sheltered with radiation shields and mounted on a lamp post above head height (3 m) in the city centre classified as Built climate zone 5 (BCZ 5), and on a mast at same height in the local Airport located about 15 km east on the outskirt of the city, classified as Agricultural climate zone 3 (ACZ 3). The location of the ACZ 3 station (Observatory of the Nigerian Meteorological Agency) is nearly free from urban modifying effects and situated at a distance of about 15 km east to the city centre. Two sites considered for this work were carefully selected and appropriated based on the latest urban rural classification scheme presented by [17].

The urban heat island is the difference between the UHI = TUrban – TRural, where T is air temperature, urban represents the city centre (BCZ 5) and the rural represents the local airport (ACZ 3). Cooling degree days or heating degree days are values complied daily to assess how much energy may be needed to cool or heat buildings. In determining the cooling degree days CDD, average temperature value is calculated for a given day. If it is greater than the standard base, the standard base value is subtracted from calculated average temperature to yield the CDD. This is compiled for daily and totaled for entire month. The CDD are calculated by the following formula; CDD = Σ (ti - T) where T is the required room air temperature (25°C).

The rationale behind this technique is that whenever average temperature drops or exceeds the comfort range, some heating / cooling will be required, the requirement for heating increases with decreasing temperature and vice versa. The Cooling degree-day is a more exact measure for the comparison of the cooling energy consumption

The number of cooling days (CD) can be defined as the number of days that daily mean temperature (ti) is above or equals a critical value of 27^0C.

3. RESULTS AND DISCUSSION

3.1 Urban Heat Island

The urban heat island has been established to occur in Akure. The heat island intensity was generally noted to be weak during the day in all the season but with varying disparities in the strength of its weakness as shown in Fig. 1. The strength is observed to be seasonally dependent, but there could be likely influence of year to year variation of weather parameters noting that the data set span from 2008 to 2009 and individual year has its own peculiarity. However, it has been established and shown in this result that the urban heat island exists virtually in every time of the day. Our result also agrees with previous research works that the highest UHI intensity occurs at night between 1800 to 2200 hours. The magnitude of the heat island is also observed to be higher in the dry months (harmattan) having its peak in the month of January. Result agrees with [14] that reported urban cool island (UCI) at 1500 in October/November and higher UHI values in January/February in Akure.

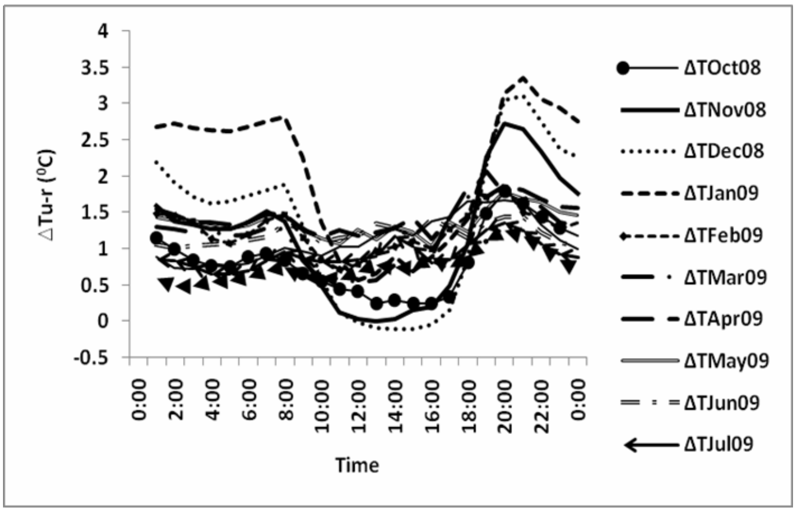

Fig. 1. Diurnal variation of mean monthly urban – rural differences of air temperature

Heat Island has increased the number of cooling days (CD) and cooling degree days (CDD), this will however increases the duration of periods that requires cooling and as a result, increase the quantity of energy demand for cooling and consumption rate in the city compared to that of the compared rural environment. For human comfort, there is a need of space cooling below a critical temperature level. The more extreme the condition, the more energy is consumed.

3.2 Cooling Days (CDs)

The comparison of the monthly means of urban and rural cooling days (CDs) show that the cooling season begins in November and lasts till June. This is observed to be predominant in both experimental sites except for the months of July and August in both sites and extending to September in the case of the rural site (airport). Monthly means of cooling days in the urban area exceed those of the rural area and the differences are between 4 and 21 days in September and January respectively as it seen in Fig. 2. Consequently, the cooling season in the rural station is more than 15 weeks shorter than experienced in the urban area (city). The month of March is noted to have the highest peak of days that requires cooling in both the urban and rural site. The least is recorded between July and September during the summer monsoon.

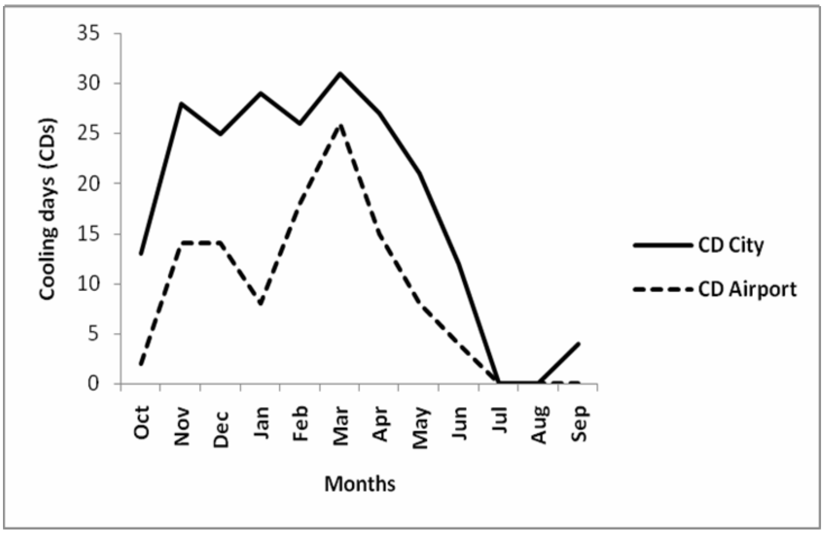

Fig. 2. Seasonal variation of the cooling days (CDs) in the two sites (urban and rural)

3.3 Cooling Degree Days (CDDs)

Fig. 3 shows the monthly mean numbers of the urban (CDDu) and rural cooling degree days (CDDr). The cooling degree day is clear measure for the comparison of the cooling energy consumption. The cooling season which has two epochs is characterized by significant cooling demand, the first which exists for a very short period in November and the other epoch which begins in February and lasts till May. These period have peculiarities as they are transitional months, November is the transitional month into harmattan period and February to April are transitional months to the period of summer monsoon The highest cooling demand is observed to peak in March at both sites. The most significant difference appears in January (about 64^0C higher in the urban than the rural site). Consequently, the effect of the city on the cooling energy demand is stronger than in other period of the cooling season. The months of July, August and September are noticed to exhibit totally different peculiarities as the three months in the both cases were absolutely typical of space heating demand rather than cooling. In this period, the summer monsoon has fully developed, resulting in reduced cooling demand due to cooling effect of monsoon winds.

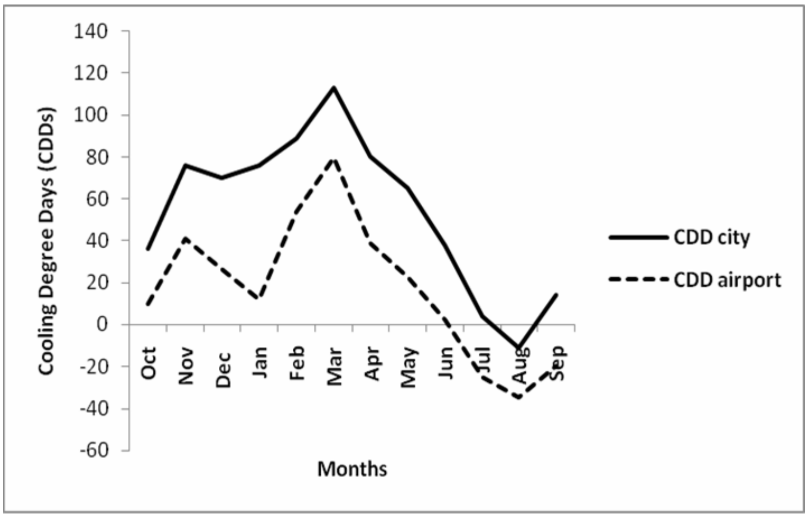

Fig. 3. Seasonal variation of the cooling degree days (CDDs) in the two sites (urban and rural)

3.4 Cooling Degree Hours (CDHrs)

Table 1. Cooling degree hours (CHr) and the time cooling demand begins at both urban (city) and the rural (airport) stations

Months	CDHr City			CDHr Airport		
	Hrs	Deg	Cooling Demand Begins at	Hrs	Deg	Cooling Demand Begins at
Oct.	11	46	9am	10	38	10am
Nov.	13	54	9am	11	55	9am
Dec.	14	64	9am	11	52	10am
Jan.	14	68	9am	10	48	10am
Feb.	15	77	-	12	59	9am
Mar.	20	87	-	13	66	9am
Apr.	15	71	9am	12	50	10am
May	14	56	8am	11	39	9am
Jun.	12	42	9am	9	27	10am
Jul.	9	22	10am	7	13	11am
Aug.	8	17	11am	6	10	12noon
Sept.	10	30	10am	7	16	11am

The cooling degree hours calculated for the period of study (October 2008 to November 2009) is presented in Table 1 shown above. A one – hour time lag in cooling demand between the urban and rural site was observed, except in February and March.. In these months, the city site exhibits comfortable range of temperature that demand for neither cooling nor heating. It is interesting to see that heating demand also exists virtually in every early hour at both sites with the exemption of February and March in the city. However, the early hours heating demand was noticed to be more intense in the rural site from October through January with the highest record in January.

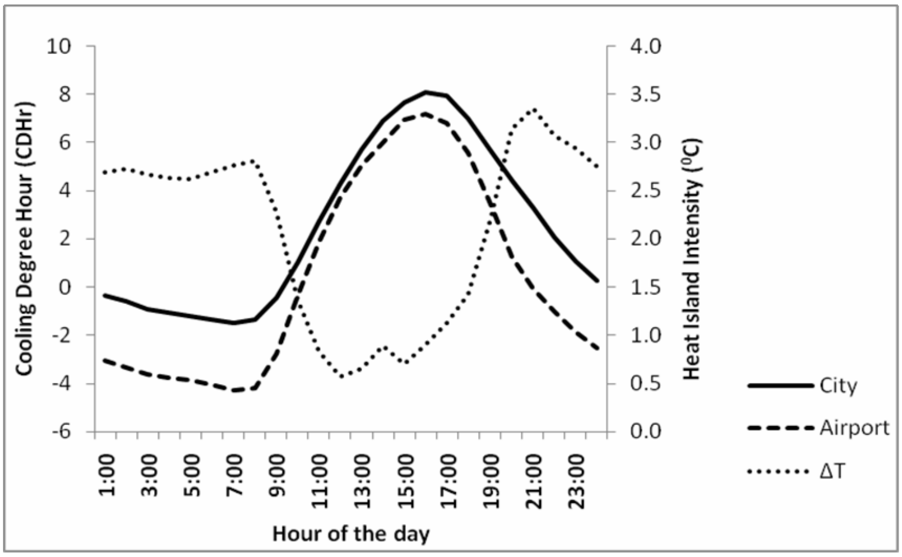

Fig. 4. Typical diurnal variation of the cooling degree hour (CDHr) and the heat island intensity (UHI)

Considering the relationship between the UHI and cooling degree hour as shown in Fig 4, on a general note, cooling demand is higher at the city than the rural site. Both the city and the rural sites cooling degree hour increases rapidly after the sunrise and gradually decreases after sunset. The degree of the demand is observed to increase diurnally relative to the air temperature pattern with its peak around 1600hrs.

The magnitude of the heat island is directly related to the degree of the hourly cooling demand. The magnitude of the urban heat island is lower during the day when there is little difference in the cooling demand between both urban and rural sites. The UHI magnitude it is noted to be higher in the early morning and late evening when the cooling demands differences are large.

4. CONCLUSION

This study examined the impact of urban heat islands (UHI) on the energy consumption and demand for space cooling and space heating comparing an urban and a rural site in Akure. Results have revealed interesting findings and supports previous research on impact of UHI on energy demand and consumption.

The UHI has been found to occur throughout the day and night except for a few hours after noon in November and December where a cool Island is observed. The heat island intensity is also noted to be generally weak during the day in all the season but with varying disparities. However, the highest UHI intensity occurs at night between 1800 to 2200 hours and the intensity is also higher in the dry than the wet seasons.

Cooling days in the urban area have been confirmed to exceed those of the rural area. The cooling degree day has also established that the effect of the city on the cooling energy demand is stronger than the rural site in every period of the cooling season.

The result also showed that the total energy consumption will increased due to the effects of UHI and that there is increase in the space-cooling but there is little existence of space heating in the city between July and August. The demand for cooling will definitely add pressure to the electricity grid during peak periods of demand. There is need to introduce mitigation measures of UHI that will not induce increase energy consumption. Part of the measures may include ensuring urban greening. This research is ongoing and part of our future researches focus on the roles of urban greening in mitigating urban heat island.

REFERENCES

1. Oke, T.R., 1987. Urban heat island. Boundary Layer climates. New York: Routledge, p. 289–292.
2. Grimmond, C.S. and T.R. Oke (1999b): Heat storage in urban areas: local-scale observations and evaluation of a simple model. *J. of appl. Meteor*., 38, p. 922–940.
3. Sailor D.J., Relating residential and commercial sector electricity loads to climate – evaluating state level sensitivities and vulnerabilities. *Energy* 26(10): 645–657.
4. Chandler, T.J., (1965): The Climate of London. Hutchinson, London. CIBSE Guide A., 2006. Environmental Design. UK, CIBSE.
5. Graves, H., Watkins, R., Westbury, P., Littlefair, P., (2001): Cooling Buildings in London – Overcoming the heat island, BR431, CRC.
6. Kolokotroni, M., Zhang, Y., Watkins, R. (2007): The London heat island and building cooling design. *Solar Energy* 81(1), 102–110.
7. Scott MJ, Wrench LE, Hadley DL. (1994): Effects of climate change on commercial building energy demand. Energy Sources; 16: 317–32.
8. Huang Y.J., Ritschard R., Bull J., Chang L. Climatic indicators for estimating residential heating and cooling loads. Lawrence Berkeley Laboratory report LBL-21101, 1986.
9. Segal M., Shafer H., Mandel M., Alpert P., Balmor V. (1992): Climatic-related evaluations of the summer peak-hours' electric load in Israel. *J Appl Meteorol*; 31: 1492–8.
10. E. Valor, V. Meneu and V. Caselles (2001): Daily Air Temperature and Electricity Load in Spain *J. App. Clim*., 40, 1413-1421.
11. Robert G., Quayle and Henry F. Diaz (1980): Heating Degree Day Applied to Residential Heating Energy Consumption. *J. Appl. Met*., 19, 241–246.
12. Adebayo YR., (1987): A note on the effect of urbanization on temperature in Ibadan. *J Climatol* 7: 185–192.
13. Adebayo, Y.R., (1991): Day-Time Effects of Urbanization on Relative Humidity and Vapour Pressure in a Tropical City. *Theor. App. Climatol*, 43: 17–30.
14. Balogun, A.A., Balogun, I.A., Adefisan, A.E., and Abatan, A.A., (2009a): Observed characteristics of the urban heat island during the harmattan and monsoon in Akure, Nigeria. *Eight Conference on the Urban Environment. AMS 89th Annual Meeting, 11–15 January, 2009, Phoenix, AZ. Paper JP4.6*, available online – http://ams.confex.com/ams/pdfpapers/152809.pdf
15. Balogun, I.A., Balogun, A.A., Adeyewa Z. D. (2009b): A note on the effect of urbanization on air temperature and humidity of Akure, Nigeria. *The seventh International Conference of Urban Climate, 29th June - 3rd July 2009, Yokohama, Japan.*
16. Balogun A. A., I. A. Balogun, A .A. Ibrahim**,** J. O. Adegoke (2009c): Resurgence of Urban Climate studies in Nigeria. *Quarterly Newsletter of IAUC*, 34: 29–34.
17. Stewart. I. (2009) Classifying urban climate field sites by "Local climate zones" The case of Nagano, Japan. *Quarterly Newsletter of IAUC*, 34: p. 8–11.

CYSENI 2010, May 27–28, Kaunas, Lithuania
ISSN 1822-7554, www.cyseni.com

PROBABILISTIC ASSESSMENT AND UNCERTAINTY ANALYSIS OF EXTREME PRECIPITATION

V. Česnulytė, R. Alzbutas
Kaunas University of Technology
Faculty of Fundamental Science
Studentų str. 50, LT 51368 Kaunas - Lithuania
Phone: +370 625 01055
Email: vaida.cesnulyte@stud.ktu.lt,

R. Alzbutas
Lithuanian Energy Institute
Laboratory of Nuclear Installation Safety
Breslaujos str. 3, LT-44403, Kaunas - Lithuania
Phone: +370 37 401 945
Email: robertas@mail.lei.lt

ABSTRACT

This paper mainly presents the probabilistic analysis of extreme precipitation. In addition, the uncertainty and sensitivity analysis is performed for probability estimate of extreme precipitation. Considering various extreme events, such as an excess rainfall, extreme wind, hail and forest fire, different classification scales are introduced. Since precipitation is one of the most frequent and dangerous nature phenomena the analysis was focused mainly on extreme precipitation and consequence of it.

The phenomena considered can do enormous damage not only to the hydro power plants, but also to others, non water related constructions as well. In order to be ready to estimate the influence of extreme precipitation on the safety of hydro power plant, the probabilistic analysis of the event occurrence has been performed: statistical data have been assembled and analyzed, probabilistic model has been built as well as modelling data uncertainty and sensitivity has been analyzed.

The probabilistic assessment is based on mathematical model, which was applied taking into account statistical data (each year extremes) from 1962 up to 2007. The historical data on extreme precipitation in Lithuanian territory were summarized according to the data of Lithuanian Hydrometeorological Service. For probability estimate of extreme precipitation occurrence the Gumbel distribution law was used. It is needed in order to evaluate the uncertainty of this estimate. Due to possible variation of probability estimate, the uncertainty and sensitivity analysis is used. They are deeply related to each other, since the aim of sensitivity analysis is to estimate the rate of change in the result of a model with respect to changes in model parameters and the task of uncertainty analysis is to estimate the distribution of considered result with respect to uncertain parameters. Such knowledge is important in order to apply the model accurately, determine parameters for which it is important to have more accurate values, and understand the behaviour of the phenomena being modelled.

The approach suggested for uncertainty and sensitivity analysis, and illustrated in this paper by an application of Software System for Uncertainty and Sensitivity Analyses, is based on well-established concepts and tools from probability calculus and statistics. This approach is also related to the so-called best estimate calculation along with the analysis of uncertainty.

Keywords: precipitation, probabilistic assessment, uncertainty analysis

1. INTRODUCTION

There is a growing public interest in the climate change and climate analysis. Detailed knowledge of natural phenomena is needed not only to extract maximum benefit from human activities but also to protect against the risk of these events. Extreme events are hazardous to the fact that they occur suddenly, unexpectedly and there is no time to prepare for them. Such events pose a significant risk to human life, health, property, agriculture and the environment and therefore may not be able to avoid them.

The main purpose of this work is to analyse the extreme events in Lithuania of which one of the most important and dangerous – extreme precipitation (rainfall). This natural element is selected because of the high occurrence frequency in Lithuania. Moreover, extreme precipitation can do enormous damage in a very short period of time.

80 percent of all naturally occurring extreme events are caused by weather events in Lithuania. Rain is the most common meteorological phenomenon that can cause extreme events (Fig. 1).

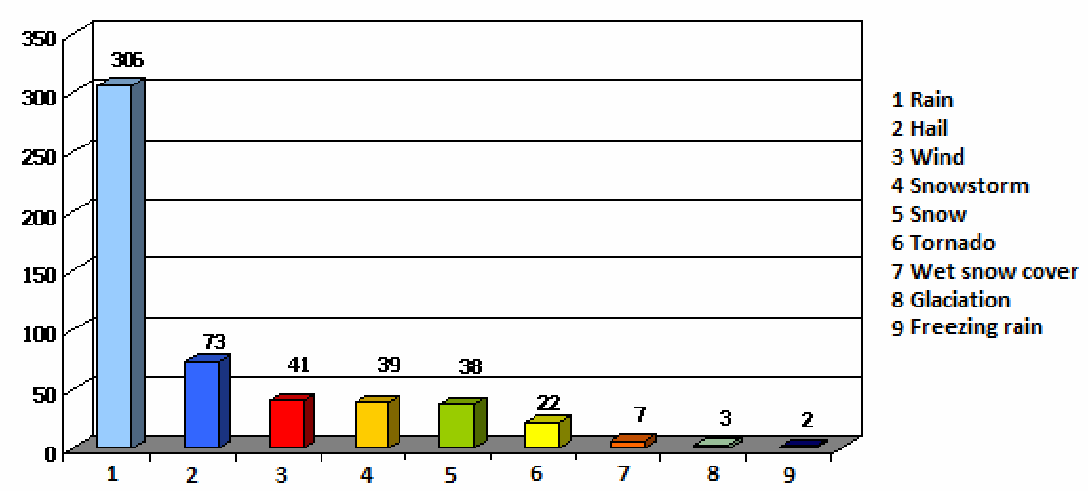

Fig. 1. Number of natural weather phenomena in Lithuania from 1961 up to 2005 [11]

In general extreme events are events that exceed the criteria set. Strong rainfall occurs when rainfalls exceeds 30 mm and if rainfalls exceeds 50 mm in shorter time period than 12 hours then it is called an elemental meteorological phenomena which can cause large-scale disasters. If rainfalls exceeds 80 mm level in less than 12 hours then phenomena is called catastrophic [12].

The probabilistic assessment is based on mathematical model which was applied taking into account statistical data (each year extremes) from 1962 up to 2007 [9, 10]. Frequency of event of Lithuanian extreme precipitation (daily, instantaneous, annual etc.) is used in the probability assessment of precipitation amount (rainfall). For probability estimate and return period of extreme precipitation occurrence the Gumbel distribution law was used.

Due to possible variation of probability estimate, the uncertainty and sensitivity analysis is used [2, 6]. They are deeply related to each other, since the aim of sensitivity analysis is to estimate the rate of change in the result of a model with respect to changes in model parameters and the task of uncertainty analysis is to estimate the distribution of considered result with respect to uncertain parameters.

2. METHODS OF PROBABILISTIC ASSESSMENT AND UNCERTAINTY ANALYSIS

2.1. Annual Rainfall Series Model

Although a high rainfall occur at varying intervals of time, it facilitates the analysis to study precipitation events within constant intervals of time, usually one year. Let the random variable X_i denote the maximum instantaneous rainfall in a year i, $i = 1, 2, ..., N$, at a gaugingstation. These X_i values are an annual maximum series. In practise, an observed sequence x_i, $I = 1, 2, ..., N$ is used to make probabilistic estimates of rainfall. Quite often the annual maxima are taken from discrete daily mean rainfalls.

In statistical rainfall studies, a particular important concept is that of the return period T. This is associated with a fixed magnitude of rainfall called the T-year rainfall and is in fact the average time interval between exceedance of that magnitude [7]. Often return periods are evaluated using applied extreme values probabilities to the given annual maxima.

The study of extreme hydrologic event involves the selection of a sequence of the largest observations from sets of data. Hence the annual maximum rainfalls have to be analysed and the probabilities of significant magnitude rainfall events have to be evaluated. Since these observations are located in the extreme tail of the probability distribution of all observations from which they are drawn, so their probability distribution is different from that of the parent (non extreme) population. In this study several types of distribution of extreme values were considered, and it appeared that in this case for extreme rainfall analysis the best fits Gumbel Extreme Value distribution [7, 8].

2.2. Extreme Value distribution

Because the Extreme Value type I distribution was extensively developed and applied to precipitation events by Gumbel [3, 4], it is often referred to as the Gumbel distribution. The Gumbel probability distribution function is

$$F(x) = e^{-e^{\left(-\frac{x-\mu}{\sigma}\right)}}, \ -\infty \le x \le \infty\text{'} \tag{1}$$

where the parameters are defined as $\sigma = \frac{\sqrt{6}s}{\pi}$ and $\pi = \bar{x} - 0.5772\sigma$.

If we substitute the value y of a reduced random value Y, where $y = (x-\mu)/\sigma$, than the basic form of the Gumbel distribution becomes:

$$F(y) = e^{-e^{-y}}, \ -\infty \le x \le \infty \tag{2}$$

Let’s define a return period. If the values Y_i are serially independent, the probability that the time interval T between exceedance of a precipitation magnitude y equals n is given by [7]:

$$P(T=n) = P(Y_1 < y) \cdot P(Y_2 < y) ... P(Y_{n-1} < y) \cdot P(Y_n > y) = \{P(Y_1 < y)\}^{n-1} P(Y_n > y) \tag{3}$$

The next assumption, that values Y_i are identically distributed and the properties of geometric distribution let determine the expected value $E(T)$, when variable n can take any value from 1 to infinity [7]:

$$E(T) = \sum_{n=1}^{\infty} nP(T=n) = \sum_{n=1}^{\infty} n\{P(Y_1 < y)\}^{n-1} P(Y_n > y) = \frac{1}{P(Y > y)}. \tag{4}$$

The return period T is commonly written instead of $E(T)$ above.

In order to estimate extreme values, which have particular return period, it is necessary to have the relationship between Gumbel variables and return period. From equation (2) and from definitions about return period above we can write:

$$1 - e^{-e^{-y}} = \frac{1}{T}. \tag{5}$$

Hence,

$$y = -\ln\{\ln(T) - \ln(T-1)\}. \tag{6}$$

From Maclaren's theorem the approximations

$$y \approx \ln\left(T - \frac{1}{2}\right) \; or \; y \approx \ln(T) \tag{7}$$

may be used in place of equation (6) for $T > 10$ years if errors (of T estimate) up to 0.5% und 2.5% respectively can be tolerated; the second approximation is sufficient for all practical purposes when $T > 25$ years.

2.3. Uncertainty and sensitivity analysis methodology

Uncertainty analysis is an attempt to quantify the degree of confidence that an analyst has in the existing data and models, based on whatever information is currently available. Estimates of risk and reliability models are becoming central to decisions about many engineering systems. However, in many important cases we do not have enough data. Rare events are a prime example. When data is scarce or physical understanding is limited, it is important to estimate the uncertainty as quantitative measure, e.g. probability. In order to estimate the uncertainty as probability there is possible to treat model parameters as random variables or as the parameters of the probability distributions of the random variables [1].

In the present research the most important and having the biggest uncertainty is real time precipitation model. This section presents uncertainty and sensitivity analysis methodology, performed for precipitation forecast model results and parameters.

Let's note that the considered model general expression [6] is

$$y = F(x_1, x_2, ..., x_N),$$

where $x_1, x_2, ..., x_N$ model parameters; N – number of model parameters; y – modelling result, $F(\cdot)$ – function relating model parameters and model result. Modelling result y is not necessary one value, in general case, also in this model y is a vector of the results.

The scheme of the link between model parameters uncertainty and modelling results uncertainty is presented in Fig. 2 [6].

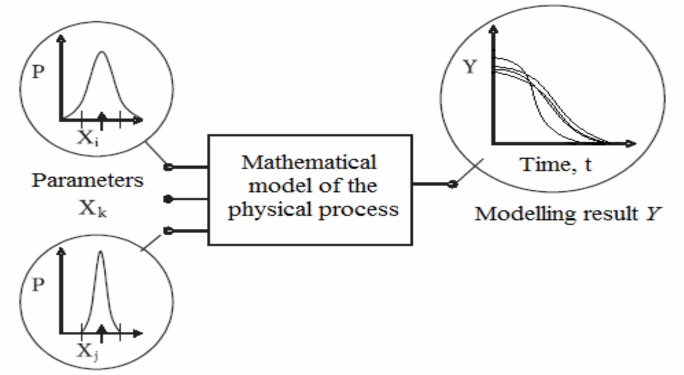

Fig. 2. Link between uncertainty of model parameters and uncertainty of modelling results

The uncertainty analysis of results was performed using the popular software SUSA [5] (Software System for Uncertainty and Sensitivity Analysis). In order use its standard procedures the following steps must be performed [13]:

1) The determination of potential uncertain model parameters, which are important for modelling results.

2) The determination of uncertainty limits for each parameter. The distribution shape, minimal and maximal parameter values are usually determined from literature, experience, engineering judgement or other reasonable sources.
3) The determination of links between uncertain parameters. It is important to note that in presence of correlated parameters, sample generation and post-processing is considerably more complicated.
4) The generation of random samples of considered parameters and simulations. The number of generated parameters values is estimated using S.S. Wilks formula. Wilks method enables to determine the minimal number *n* of model simulations that the obtained minimal and maximal values would agree with considered level and confidence interval limits. I.e. for tolerance interval (α, β) estimation, n must satisfy the following inequality [14]:

$$1-\alpha^{n}-n(1-\alpha)\alpha^{n-1}\geq\beta \qquad 8)$$

where α – limit parameter; β – confidence level.

Using this formula the two-sided tolerance interval of (95%, 95%) gives $n = 93$.

5) Evaluation of parameter uncertainties using simulation results. The uncertainty of the final result is determined by probabilistic distribution, which depends on input parameters distribution. The two-sided tolerance interval is commonly used (95%,95%), which is interpreted as follows: at least $\alpha \cdot 100\%$ of all model results will be contained within the tolerance interval with a probability of at least 0.95.

It is very efficient for large models to use the same uncertainty analysis sample to perform also sensitivity analysis. The sensitivity analysis enables to determine parameters which are the major contributors to model result uncertainty. The most commonly used sensitivity indexes are correlation coefficients, standardised regression coefficients and others.

3. PROBABILISTIC ASSESSMENT AND UNCERTAINTY ANALYSIS RESULTS

3.1. Return period of extreme precipitation

Because of the probability analysis is related to extreme precipitation the return period (see also chapter 2.2) is

$$T=\frac{1}{1-e^{-e^{-y}}}. \qquad (9)$$

Fig. 3 shows the return period of different rainfalls from 1962 up to 2007. When the rainfall peaks are around 50–60 mm the return period is no more than 10 years. When the rainfall peaks has reached and exceeded the threshold of 70 mm return period intervals becomes wider. This is because of the probability of extreme evens.

The main disadvantage of graphical analysis is that it is difficult to evaluate the return period of different extreme rainfalls *x*: 50 mm, 80 mm, 100 mm. Fig. 3 shows the return period of elemental and catastrophic extreme events of precipitation. Return period of 50 mm amount of precipitation is 1 year. This means that the performance 50 millimetres of precipitation is once in a year with probability of $9.96\cdot10^{-1}$. Return period of catastrophic extreme event is 92 years (probability $1.09\cdot10^{-2}$).

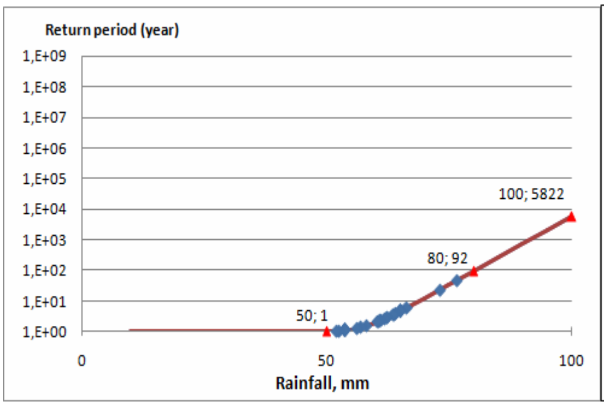

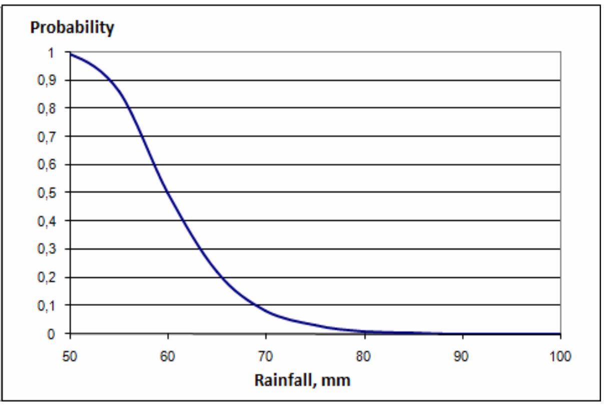

Fig. 3. Link between return period and rainfall. Fig. 4. Probability of extreme rainfall [1/year]

According to the statistics the relationship between rainfall and return period can be determined. Forecasting return period estimates they can be based on rainfall values. The extreme rainfall peaks and probability for specific return periods are evaluated using Gumbel distribution (Table 1).

Table 1. Estimated rainfalls using Gumbel didtribution for different return periods

Rainfall, mm	**50**	**80**	**100**
Probability	$9.96{\cdot}10^{-1}$	$1.09{\cdot}10^{-2}$	$2.69{\cdot}10^{-5}$
Return period, year	1	92	5 822

3.2. Probabilistic assessment and uncertainty analysis

Extreme precipitation isn’t an annual phenomenon in Lithuania, so it is necessary in this case to use at least two-year averaged values.

Since uncertainty analysis is performed in respect of mean (sample 1) and standard deviation (sample 2) estimates $\bar{X}$ and s, more comprehensive analysis is necessary of these two samples: to find distribution of samples and to evaluate main statistical characteristics, quintiles.

Table 2. Investigation of mean and standard deviation estimates distribution.

Test	**Statistics**			**p value**		
	Mean		**St.Dev**	**Mean**		**St.Dev**
Kolmogorov-Smirnov	D	0.127	0.139	Pr > D	>0.150	>0.250
Cramer-von Mises	W-Sq	0.062	0.097	Pr > W-Sq	>0.250	0.137
Anderson-Darling	A-Sq	0.470	0.649	Pr > A-Sq	0.232	0.095
Chi-Square	Chi-Sq	2.304	2.826	Pr > Chi-Sq	0.512	0.419

Table 2 shows that the annual rainfall means $\bar{X}$ are distributed by normal distribution, also gamma and lognormal distributions have similar fit. Gamma distribution has the best fit to the annual rainfall standard deviation estimate s.

The first data sample mean estimate $\bar{X} = 61.05$ standard deviation $s = 6.17$, maximum value $M = 76.62$, minimum value $m = 51.97$. The second data sample average estimate $\bar{X} = 11.45$, standard deviation $s = 9.65$, maximum value $M = 49.90$, minimum value $m = 0.49$. These data are used to sample rainfall mean and standard deviation values from normal and gamma distribution respectively.

In further analysis μ and σ values is calculated, although the probability of extreme precipitation of different rainfall x: 20, 40, 60,…, 200 mm. Because of full and particular uncertainty and sensitivity analysis 200 mm rainfall is used. Consequently, 10 groups of 100 members are obtained. It follows the probabilistic curves that were evaluated at 100 different parameters values. 100 parameters pairs were chosen so that the uncertainty of the results can be evaluated with a 0.95 confidence level.

More obvious results can be seen as maximum, minimum, average and quintiles probability curves, which are plotted separately (Fig. 5).

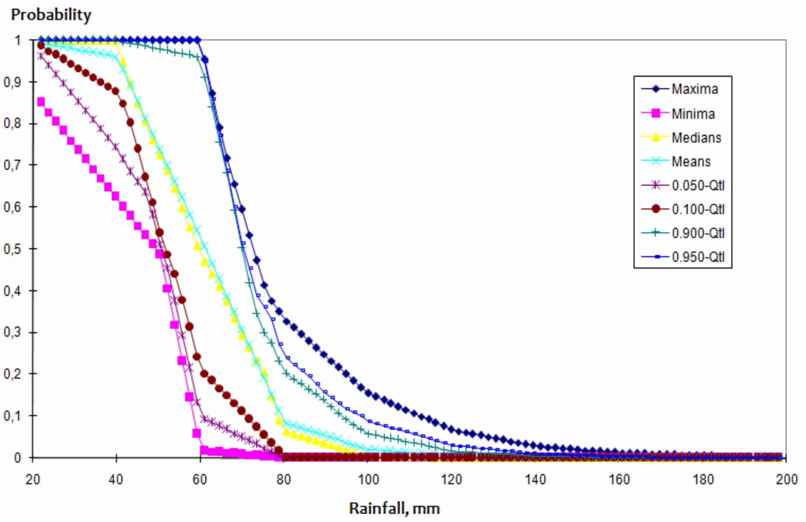

Fig. 5. Statistical characteristics of probability estimate of extreme precipitation

Sensitivity analysis may be described by regression and correlation coefficients. Fig. 6 shows the two model parameters as standardized regression coefficients change according to rainfalls x. As long as rainfall is about 40 mm, the model results are more influenced by the average, but about 80 mm in the limit situation changed and the standard deviation of standardized regression coefficient is increased, the average impact is substantially reduced and close to zero.

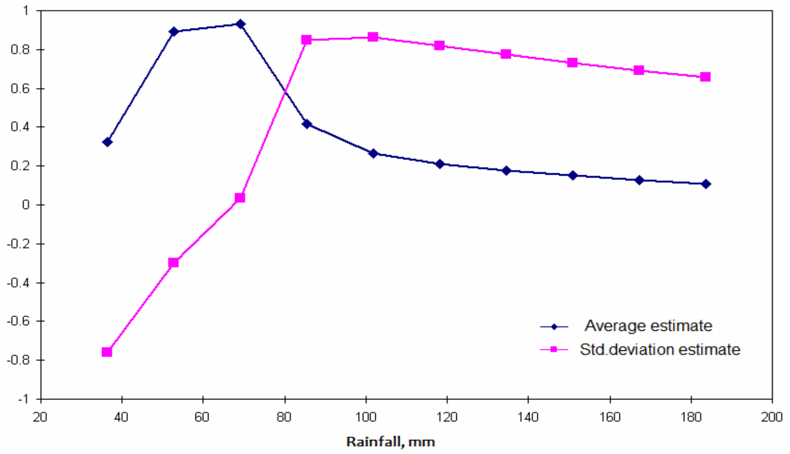

Fig. 6. Variation of standardized regression coefficient

One of the most important factors is the coefficient of determination R^2. This coefficient shows what proportion of results dispersion can be explained by linear regression.

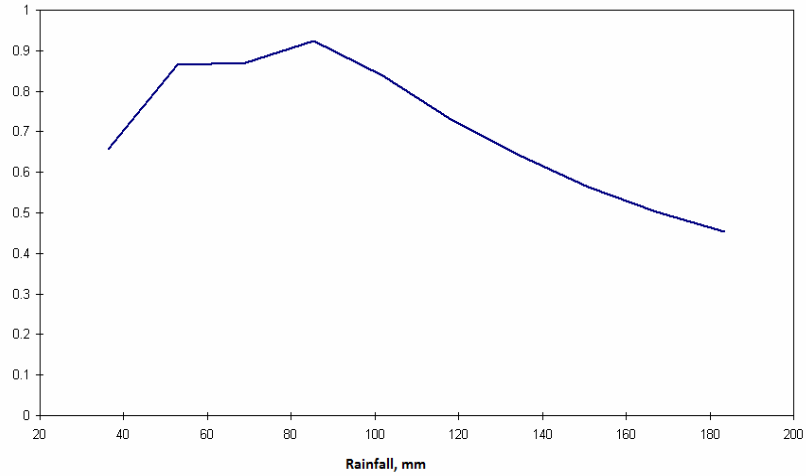

Fig. 7. Variation of coefficient of determination R^2

Fig. 7 presents the change of coefficient of determination R^2 at different rainfalls x. Regression model is able to explain over 50 percent of a probabilistic model uncertainties when rainfall x is less than 200 mm. However, when rainfall exceeds 200 mm level, uncertainty and sensitivity analysis results can be unreliable. This is because of the high dispersion of parameters and lack of information about these events.

4. CONCLUSIONS

1. The probabilistic assessment is based on mathematical model, which was applied taking into account statistical data (each year extremes) from 1962 up to 2007. According to the statistics the relationship between rainfall and return period can be determined that return period of 50 mm rainfall is 1 year and 80 mm rainfall's return period is 92 years.
2. Assess the likelihood of extreme precipitation Gumbel model was chosen which allowed to evaluate the probability of different rainfalls: 50 mm rainfall (natural phenomenon) exceedance probability is $9.96 \cdot 10^{-1}$ and 80 mm rainfall (catastrophic events) exceedance probability is $1.09 \cdot 10^{-2}$.
3. According to model uncertainty and sensitivity analysis it was found that the most sensitive parameter is mean of rainfall, when non-catastrophic rainfalls are considered, while standard deviation is the most sensitive when extreme rainfall values are considered.

REFERENCES

1. Alzbutas R. Risk minimization and reliability control of systems in nuclear power plants considering data and model uncertainty. Dissertation thesis. LEI, 2003. 144 p.
2. Alzbutas R., Augutis J., Krikštolaitis R., Ušpuras E. Uncertainty and sensitivity analysis in aircraft crash modelling, The 3-rd safety and reliability international conference KONBiN'03: conference, proceedings, Gdynia, Poland, May 27-30, 2003 / Poland, 2003. ISBN 1642-9311.
3. Alzbutas R., Kupčiūnienė K., Lysak S. Atominės elektrinės saugą veikiančių ekstremalių vėjų tikimybinis vertinimas // Energetika. ISSN 0235-7208. 2009. T.55, Nr. 1, p. 20–26. [INSPEC, IndexCopernicus].
4. Gumbel E.J. Statistics of extremes. Columbia University Press, New York, 1958.
5. Kloos M., Hofer E., SUSA Version 3.2. User‘s guide and tutorial, GRS, Garching, 1999.

6. Kopustinskas V., Alzbutas R., Augutis J. Matematinių modelių parametrų jautrumo ir rezultatų neapibrėžtumo statistiniai tyrimo metodai, Energetika, 2007. T. 53. Nr. 3, p. 10–15.
7. Kottegota N.T. Stochastic Water Resources Technology. Mac. Press LTD, Hong Kong, 1980.
8. Kotz S., Nadarajah S. Extreme value distributions. Theory and Applications, Washington 2000.
9. Lietuvos hidrometeorologijos tarnyba, Klimato žinynas. Stichiniai meteorologiniai reiškiniai 1961-1995 m., Vilnius, 2000, p. 91–134.
10. Lietuvos hidrometeorologijos tarnyba, 1996-2007 m. stichinių meteorologinių reiškinių apžvalga, Vilnius, 1997–2008.
11. Lietuvos hidrometeorologijos tarnyba. Link to the internet: <www.meteo.lt/dokumentai/naujienos/20061019/pranesimas.ppt>
12. Lietuvos Vyriausybės Nutarimas Dėl ekstremalių įvykių kriterijų patvirtinimo 2006 m. kovo 9 d. Nr. 241. Vilnius.
13. Simaitytė J. Flood discharge control based on risk assessment. Dissertation thesis. LEI, 2007.
14. Wilks S.S. Statistical prediction with special reference to the problem of tolerance limits. Annals of Mathematical Statistics, 13, 1942, p. 400–409.

CYSENI 2010, May 27–28, Kaunas, Lithuania
ISSN 1822-7554, www.cyseni.com

POLLUTION OF NITROGEN DIOXIDE IN KAUNAS IN 2008

D. Laurinavičienė, I. Januškaitienė
Vytautas Magnus University
Vileikos str. 8, 44404, Lithuania
Phone: +37037 327904
Email: dovile@gmf.vdu.lt; i.januskaitiene@gmf.vdu.lt

ABSTRACT

The aim of the present study was to assess nitrogen dioxide concentration in Kaunas city and examine its relation with meteorological conditions. We used a passive sampling method and triethanolamine as an absorbent. Sampling was carried out in 62 points of Kaunas city, 4 times per year during 2008 year period. According to measured concentration average, seasonal and annual concentration in Kaunas districts and in the whole city were calculated. The study results showed that mean NO_2 concentration in Kaunas city was 18.0 $\mu g/m^3$. The highest mean seasonal concentration was found during spring (33.1 $\mu g/m^3$) and the lowest – during summer (11.1 $\mu g/m^3$). The highest NO_2 concentration was in Centras (32.8 $\mu g/m^3$), the lowest in Panemune (9.7 $\mu g/m^3$).

Using Arc GIS software, map of nitrogen dioxide pollution dispersion in Kaunas city was plotted (according annual mean of nitrogen dioxide concentration). There were classified five areas, according to the threshold value concentration (TV = 40.0 $\mu g/m^3$).

We found a negative correlation between nitrogen dioxide concentration and precipitation ($r = -0.364$, $p = 0.006$). Correlation between nitrogen dioxide concentration wind speed ($r= -0.526$, $p= 0.474$) and temperature ($r= -0.229$, $p= 0.770$) was non significant.

Keywords: air pollution, nitrogen dioxide, seasonal variation, meteorological conditions, correlation

1. INTRODUCTION

The air quality in urban area becomes worse year by year due to the release of pollutants from industrial plants and heavy vehicle traffic and constitutes a serious hazard to human and animals' health, damages vegetation, soils, and deteriorates materials, and generally affects not only the large metropolitan areas but also the medium-sized urban areas. Therefore, it is of great importance to monitor and control such dangerous emissions [1, 2].

The primary pollutants from transportation sources are hydrocarbons (HC), nitric oxide (NO), carbon monoxide (CO), and fine particulate matter (PM2.5). Once released, NO will readily oxidize to form NO_2 and will also react with some HCs to create ground-level ozone (O_3). Typically, NO + NO_2 are collectively called oxides of nitrogen or NOx [3].

Nitrogen dioxide (NO_2), a well-known traffic-related pollutant, is currently the biggest single cause of air quality problems in urban areas [4]. However, nitrogen dioxide is far more harmful with regard to toxicity than nitrogen oxide and it is a good predictor for traffic exposure [5, 6].

Nitrogen dioxide pollution is higher along busy roads compared to background locations. Air pollution in city centers and districts near highways is related to traffic density of the highway, distance of the measuring site to the highway [7, 8, 9].

Studies show also that meteorological conditions (wind speed, temperature, relative humidity, precipitation) can influence air pollution level. High speed of wind is responsible for the effective ventilation of the air basin, under specific conditions (no thermal inversion)

[10, 11, 12]. Whereas strong temperature inversion is seen to be associated with a high concentrations of pollutants [13].

The aim of the present study was to assess nitrogen dioxide concentration in Kaunas city and examine its relation with meteorological conditions.

2. MEASUREMENTS METHODS

For determination of nitrogen dioxide concentration we used a passive sampling method and triethanolamine as an absorbent. The passive sampler has an internal diameter of 25 mm and a depth of 10 mm (Fig. 1). A disc of Whatman 1Chr filter paper impregnated with triethanolamine aqueous solution is used as the collecting element. The inside of the passive sampler is protected against wind and dust deposition by a wind screen made of a polypropylene fibre material. After sampling, the content of nitrite ions is determined spectrophotometrically following reaction with Saltzman reagent [14, 15].

Nitrogen dioxide measurements were carried out in 62 points of Kaunas city (Fig. 2) 4 times per year (in different seasons) during 2008 year period. We used mean of 1 week (7 days average) measurements of nitrogen dioxide concentration to characterize seasonal and annual mean of nitrogen dioxide in Kaunas districts and whole city.

Fig. 1. Passive sampler for determination of nitrogen dioxide concentration

Meteorological data (wind speed, temperature and precipitation) for the whole Kaunas city were obtained from air quality monitoring site [16].

Using Arc GIS software, annual map of nitrogen dioxide dispersion in Kaunas was plotted. There were classified five areas, according the threshold value (TV = 40 $\mu g/m^3$).

To assess relation with meteorological conditions, correlation coefficients between nitrogen dioxide concentration and meteorological variables were calculated.

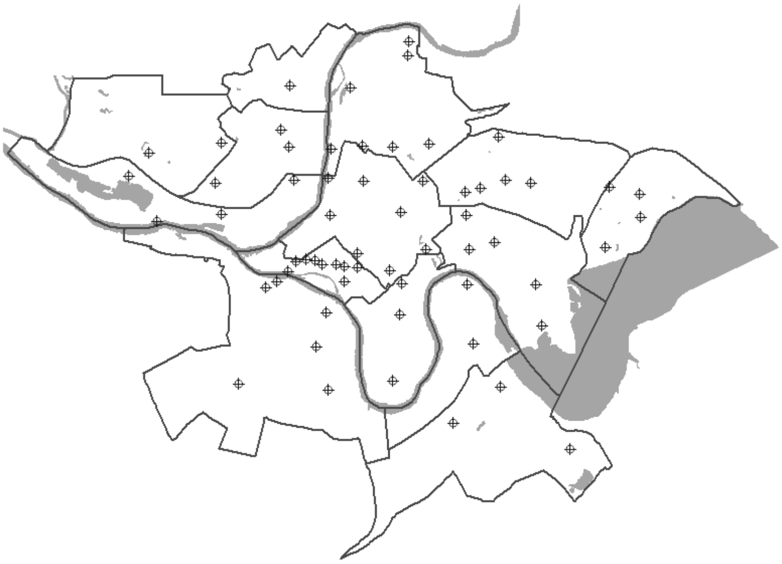

Fig. 2. Nitrogen dioxide concentration measurements points in Kaunas city

3. ESULTS AND DISCUSSION

The annual mean nitrogen dioxide concentration was 18.0 μg/m^3 for the study period. Highest seasonal nitrogen dioxide concentration was in spring 33.1 μg/m^3, lowest in summer 11.1 μg/m^3 (Fig. 3). In autumn it was 15.7 μg/m^3, in winter 11.9 μg/m^3

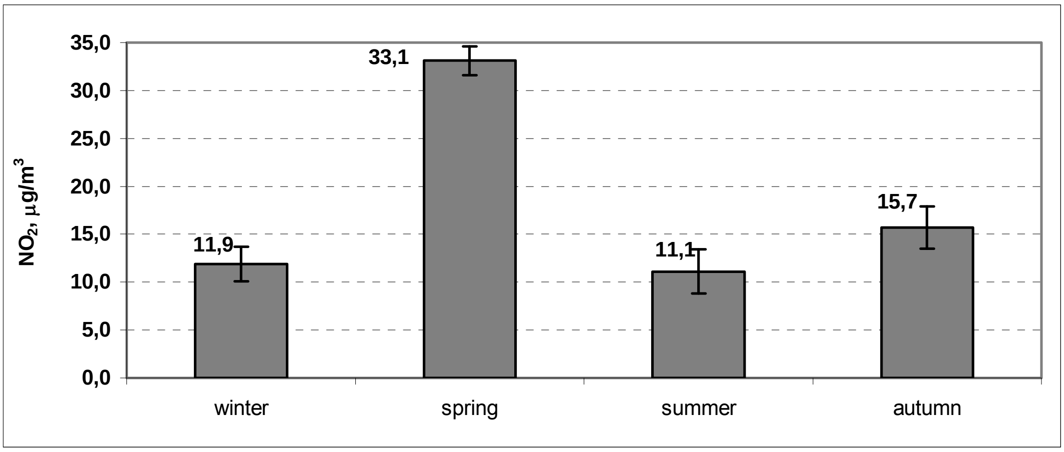

Fig. 3. Seasonal nitrogen dioxide concentration in Kaunas 2008

Fig. 4 presents variation of nitrogen dioxide concentration in districts of Kaunas city in winter season. Nitrogen dioxide concentration ranged from 19.5 μg/m^3 to 8.9 μg/m^3. Maximum concentration was in Centras district, minimum in – Panemunė. In other districts it ranged from 16.9 μg/m^3 to 9.4 μg/m^3.

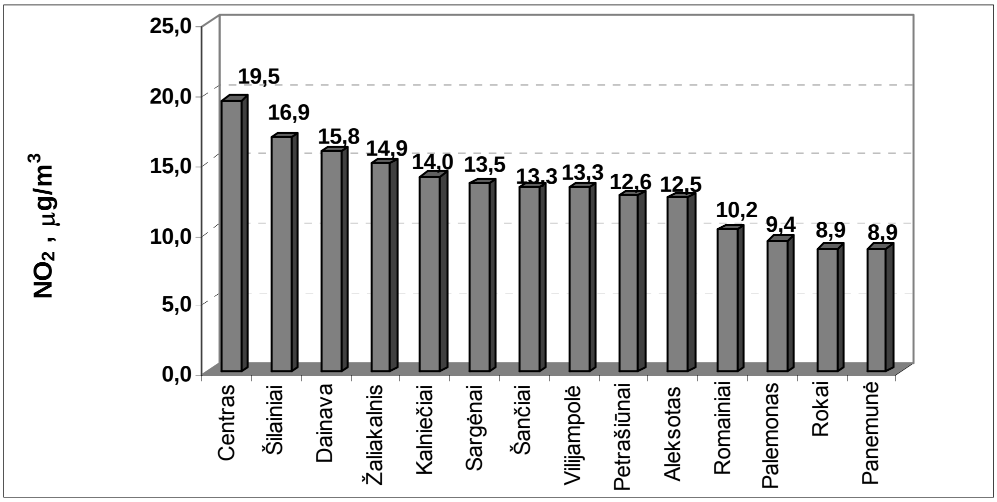

Fig. 4. Nitrogen dioxide concentration in districts of Kaunas city in winter season

Distribution of concentration of nitrogen dioxide in districts of Kaunas city in spring season presented in Fig. 5. In spring season was found highest seasonal concentration of nitrogen dioxide during year. It ranged from 69.9 µg/m^3 in Centras district to 12.3 µg/m^3 in Sargėnai district. Nitrogen dioxide concentration in Centras was on average 5 times higher than in Sargėnai district. In districts which are in central part of the city concentration of nitrogen dioxide was higher than background areas [17]. In this districts there are more busy roads and more buildings. In other districts it ranged from 33,9 µg/m^3 (Kalniečiai) to 14.7 µg/m^3 (Šančiai).

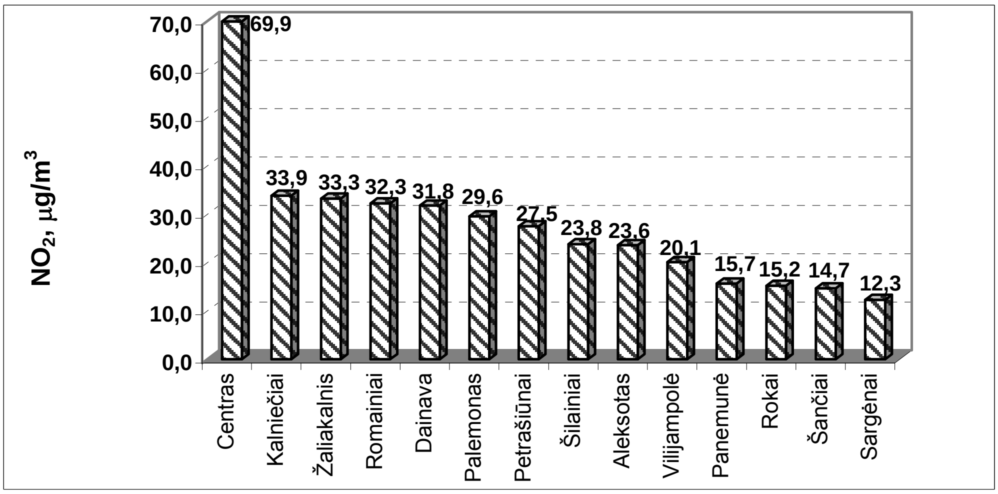

Fig. 5. Nitrogen dioxide concentration in districts of Kaunas city in spring season

Variation of nitrogen dioxide concentration (in Kaunas districts) in summer season presented in Fig. 6. Highest nitrogen dioxide concentration was found in Centras district (20.2 µg/m^3), lowest in – Panemunė (5.5 µg/m^3). In summer season it was determined lowest nitrogen dioxide concentration during study period. It might be associated with high amount of precipitation in that summer and lower traffic densities. Similar results has been presented by other authors [18].

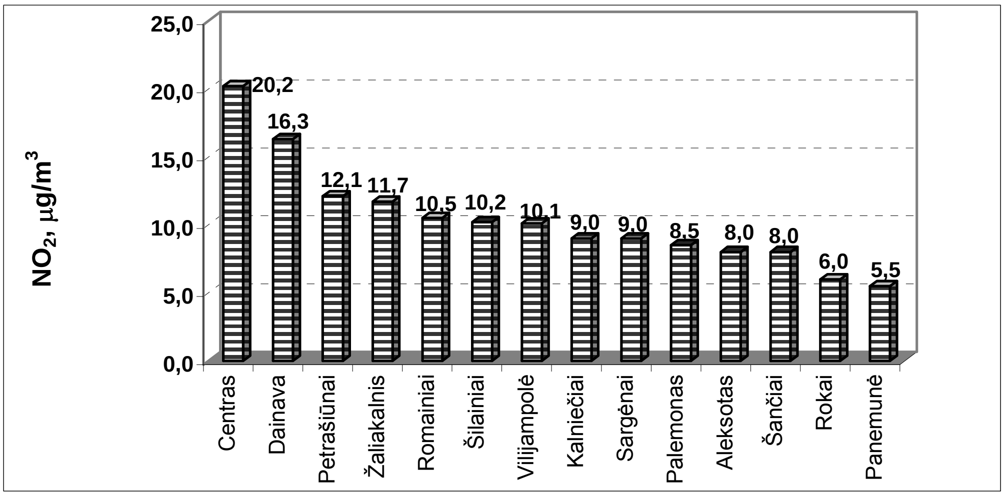

Fig. 6. Nitrogen dioxide concentration in districts of Kaunas city in summer season

In autumn season highest nitrogen dioxide was again in Centras district (21.4 µg/m^3), lowest in Panemunė district (8.9 µg/m^3, Fig. 7).

Annual mean of nitrogen dioxide concentration is presented in figure 8. From the figure we can see, that maximum annual nitrogen dioxide concentration was in Centras district (32.8 µg/m^3) and minimum in Panemunė district (9.7 µg/m^3). It is obvious that variation of nitrogen dioxide concentration is similar to that of other seasons.

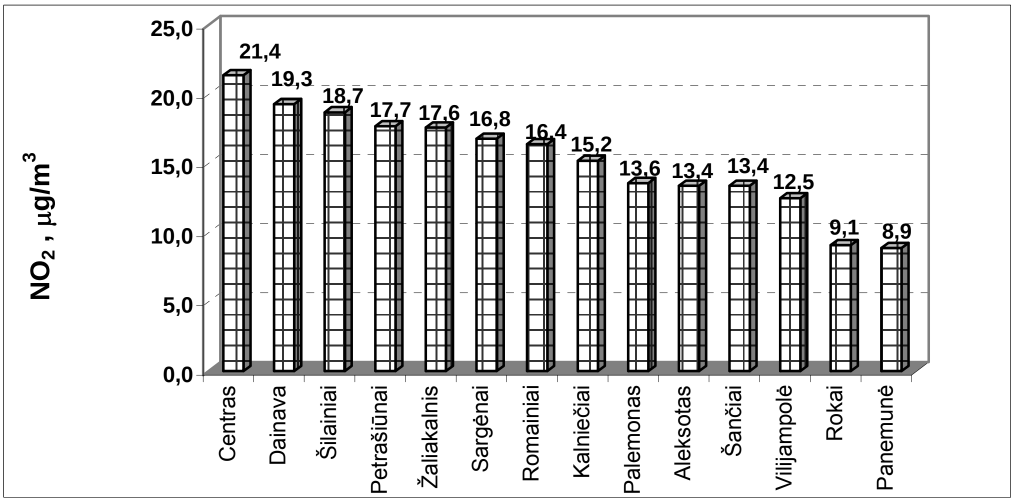

Fig. 7. Nitrogen dioxide concentration in districts of Kaunas city in autumn season

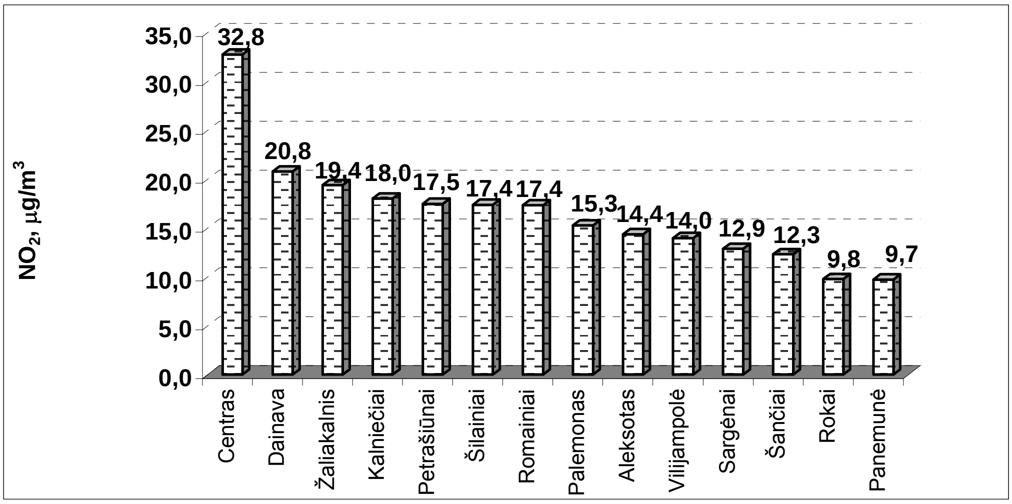

Fig. 8. Annual mean of nitrogen dioxide concentration in districts of Kaunas city

Using Arc GIS software map of nitrogen dioxide dispersion in Kaunas city was plotted (Fig. 9). There were classified five areas of nitrogen dioxide pollution.

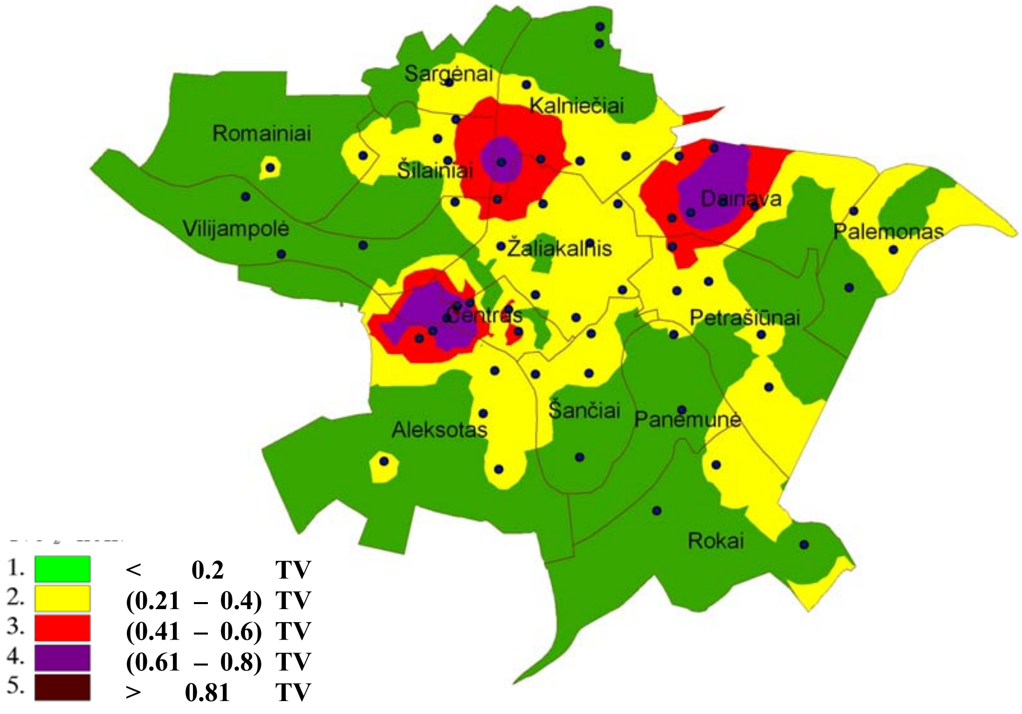

TV – treshold value (for nitrogen dioxide it is 40 µg/m^3)

Fig. 9. Dispersion of nitrogen dioxide pollution in Kaunas in 2008

Low area of nitrogen dioxide exposure have covered districts which are located in the periphery of the city (Fig. 9). The high and very high areas of nitrogen dioxide exposure have covered central or near to centre districts of Kaunas city (Centras, Aleksotas, Dainava, Kalniečiai, Šilianiai). It is caused by intensive traffic and unfavorable geographical position. Similar results were obtained from Costabile et al. [19] and Jo, Park [20]. Highest concentration of nitrogen dioxide were measured at high-traffic streets, followed by industrial and downtown locations.

To assess relation with meteorological conditions, we calculated the correlation coefficients between nitrogen dioxide concentration and wind speed, temperature and precipitation. Table 1 presented meteorological conditions during measurement period.

Table 1. Meteorological conditions during measurement period

Season	**Wind speed, ms^{-1}**	**Temperature, ^{0}C**	**Precipitation, mm**
winter	0.4	-3.6	28.5
spring	1.6	8.3	25.4
summer	0.6	18.2	44.6
autumn	0.6	10.0	52.7

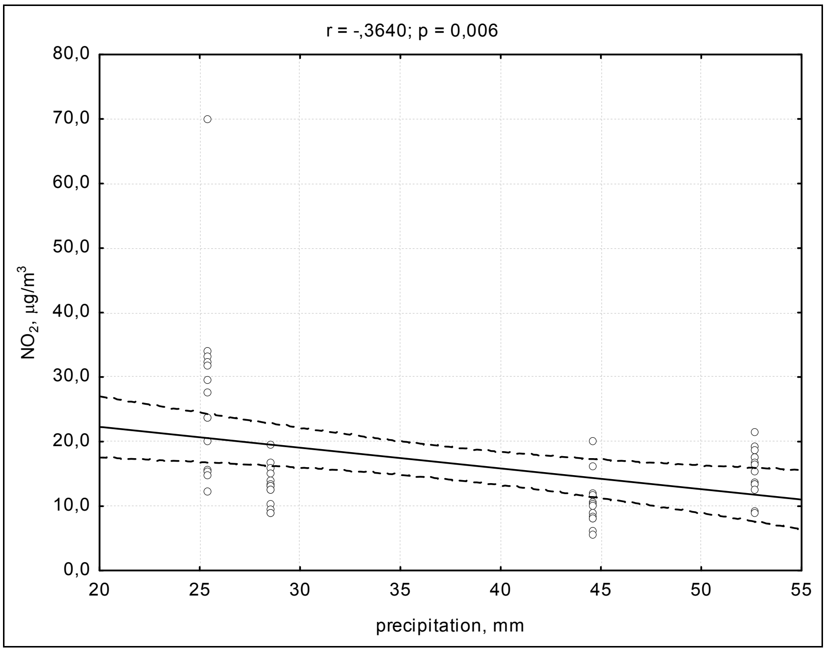

Fig. 10. Correlation between nitrogen dioxide concentration and precipitation

We found negative correlation between nitrogen dioxide concentration and precipitation (r= -0.364, p= 0.006) (Fig. 10). Negative correlation implies that lower nitrogen dioxide concentration coincide with higher precipitation. Correlation between nitrogen dioxide concentration, wind speed (r= -0.526, p= 0.474) and temperature (r= -0.229, p= 0.770) was non significant. These results revealed that low nitrogen dioxide concentration is more associated with precipitation [21].

4. CONCLUSIONS

1. Average nitrogen dioxide concentration in Kaunas city 2008, was 18.0 µg/m^3.
2. Lowest seasonal nitrogen dioxide concentration was in summer 11,1 µg/m^3, highest in spring 33,1 µg/m^3.
3. Nitrogen dioxide dispersion in Kaunas city area is uneven. Nitrogen dioxide pollution is higher along busy roads compared to the city premises. The highest annual nitrogen dioxide concentration was in Centras (32.8 µg/m^3), - the lowest in Panemunė (9.7 µg/m^3).
4. We found negative correlation between nitrogen dioxide concentration and precipitation (r = -0.364, p = 0,006).
5. Nitrogen dioxide concentration can serve as an indicator of air pollution.

ACKNOWLEDGMENTS

The authors would like to thank Audrius Dedelė who assisted in the working with Arc GIS soft.

REFERENCES

1. Al-Jeelani A. H. Air quality assessment at Al-Taneem area in the Holy Makkah City, Saudi Arabia. *Environ Monit Assess*, 2009, Vol. 156, p. 211–222.
2. Papaioannou A. B, Viras L. G., Nastos P. T., Paliatsos A. G. Temporal evolution of sulfur dioxide and nitrogen oxides in the city of Volos, Greece. *Environ Monit Assess*, 2010, Vol. 161, p. 485–494.
3. Wallace J. Kanaroglou P. Modeling NOx and NO2 emissions from mobile soures: A case study for Hamilton, Ontario, Canada. *Transportation Research*, 2008, Part D 13, p. 323–333.
4. Westmoreland E.J., Carslaw N., Carslaw D., Gillah A., Bates E. Analysis of air pollution within a street canyon using statistical and dispersion modeling techniques. *Atmospheric Environment*, 2007, Vol. 41, p. 9195–9205.
5. Soltic P., Weilenmann M. NO_2/NO emissions of gasoline passenger cars and light-duty trucks with Euro-2 emission standard. *Atmospheric Environment*, 2003, Vol. 37, p. 5207–5216.
6. Gilbert N. L., Woodhouse S., Stieb D. M., Brook J. R. Ambient nitrogen dioxide and istance from a major highway. *The Science of the Total Environment*, 2003, Vol. 312, p. 43–46.
7. Bogo H., Gomez D.R., Reich S.L., Negri R.M., San Roman E. Traffic pollution in a down-town of Buenos Aires City. *Atmospheric Environment*, 2001, Vol. 35, p. 1717–1727.
8. Beckerman B., Jerrett M., Brook J.R., Verma D.K., Arain M.A., Finkelstein M.M. Correlation of nitrogen dioxide with other traffic pollutants near a major expressway. *Atmospheric Environment*, 2008, Vol. 42, p. 275–290.
9. Carslaw D. Evidence of an increasing NO2/NOx emissions ratio from road traffic emissions. *Atmospheric Environment*, 2005, Vol. 39, p. 4793–4802.
10. Statheropoulos M., Vassiliadis N., Pappa A. Principal component and canonical correlation analysis for examining air pollution and meteorological data. *Atmospheric Environment*, 1998, Vol. 32, No.6, p. 4745–4746.
11. Plaisance H., Piechocki-Minguy A., Garcia-Fouque S., Galloo J.C. Influence of meteorological factors on the NO2 measurements by passive diffusion tube. *Atmospheric Environment*, 2004, Vol. 38, p. 573-580.
12. Hargreaves P.R., Leidi A., Grubb H.J., Howe M.T., Mugglestone M.A. Local and seasobal variations in atmospheric nitrogen dioxide levels at Rothamsted, UK, and relationscips with meteorological conditions. *Atmospheric Environment*, 2000, Vol. 34, p. 843–853.
13. Sanchez-Ccoyllo O.R., Andrade M.F. The influence of meteorological conditions on the behavior of pollutants concentrations in São Paulo, Brazil. *Environmental Pollution*, 2002, Vol. 116, p. 257–263.
14. Krochmal D, Kalina A. Measurements of nitrogen dioxide and sulphur dioxide concentrations in urban and rural areas of Poland using a passive sampling method. *Environmental Pollution*, 1997, Vol. 96, No 3, p. 401–407.

15. Grazuleviciene R., Laurinaviciene D. Ambient nitrogen dioxide dispersion in Kaunas and its relation to incidence of myocardial infarction. *Environmental research, engineering and management,* 2001, Vol. 1, No 15, p. 1–6.
16. Viešoji įstaiga „Kauno miesto aplinkos kokybės tyrimai“ http://193.219.38.28/
17. Velders G. J. M., Diederen H. S. M. A. Likelihood of meeting the EU limit values for NO2 and PM10 concentrations in the Netherlands. *Atmospheric Environment*, 2009, Vol. 43, p. 3060–3069.
18. Parra M.A., Elustando D., Bermejo R., Santamaria J.M. *The Science of the Total Environment*, 2009, Vol. 407, p. 999–1009.
19. Costabile F., Bertoni G., Desantis F., Wang F., Weimin H., Fenglei L., Allegrini I. A preliminary assessment of major air pollutants in the city of Suzhou, China. *Atmospheric Environment*, 2006, Vol. 40, p. 6380–6395.
20. Jo W-K., Park J-H. Characteristics of roadside air pollution in Korean metropolitan city (Daegu) over last 5 to 6 years: Temporal variations, standard exceedances, and dependence on meteorological conditions. *Chemosphere*, 2005, Vol. 59, p. 1557–1573.
21. Elminir H.K. Dependence of urban air pollutants on meteorology. *The Science of the Total Environment*, 2005, Vol. 350, p. 225–237.

CYSENI 2010, May 27–28, Kaunas, Lithuania
ISSN 1822-7554, www.cyseni.com

TEMPERATURE SPELLS OVER LAGOS, NIGERIA FROM 1948–2007: AN ASSESSMENT OF CLIMATE CHANGE IMPACT

A. Oluleye, I.A. Balogun
Department of Meteorology,
Federal University of Technology, PMB 704, Akure 340001, Nigeria
iabalogun@futa.edu.ng

ABSTRACT

To detect temperature spells over Lagos, this study used high quality set of National Centre for Environmental predictions – National Centre for Atmospheric Research (NCEP – NCAR) reanalysis daily temperature data spanning a period of 60 years beginning from 1948. A robust method of detection using a more stringent criterion was employed. The results revealed increasing warmer months of January – April attributable to rising annual temperature over the station. There are no warm spells observed in the months of May – August and September - December, rainy and ending of rainy seasons respectively, but there are reductions in number of cold spells days in these periods. However, frequency of normal adaptable temperatures increased within the periods. It means therefore that while the warm spells in the beginning of rainy season may cause stress, fatigue and increase attack of certain diseases such as malaria, rainy and ending of rainy seasons' warming without spells are being 'modified' to produce habitable and adaptable temperatures. We observe that with the current rate of warming these latter periods may experience warm spells in future.

Keywords: Temperature spells, harmonics, global warming

1. INTRODUCTION

The impact of global warming to aspects of human life in areas of agricultural failure, hydrology and water resources problems, possible flood as result of sea level rise, forest degradation and other has been speculated. For example, in the Sahelian region of Africa, warmer and drier conditions have led to a reduced length of growing season with detrimental effects on crops. In southern Africa, longer dry seasons and more uncertain rainfall are prompting adaptation measures [1].

Based on IPCC model predicted global temperature increase; an increase of 4.2 ^{o}C is anticipated by the year 2100. Corresponding sea level rise is 66 cm. Titus et al in OECD, (Organisation for Economic Co-operation and Development, [2]) summarises the damage as follows: "A rise in sea level would inundate wetlands and lowlands, accelerate coastal erosion, exacerbate coastal flooding, threaten coastal structures, raise water table, and increase the salinity of rivers, bays and aquifers". A one-meter rise in sea level would generally cause beaches to erode 50–100 meters from the Northeast to Maryland; 200 meters along the Carolinas; 100–1000 meters along the Florida coast and 200–400 meters along the California coast…" Lekki beech and some parts of Victoria Island in Lagos in Nigeria may not be spared. [3] notes: "in flat deltaic areas, 1 meter rise would cause shores to retreat several kilometres, displacing populations. The most vulnerable deltas include the Nile in Egypt; the Ganges in Bangladesh; the Yangtze and Hwang Ho in China; the Mekong in Vietnam; the Irrawaddy in Burma; the Indus in Pakistan; *the Niger in Nigeria*; the panama, Magdalena, Orinoco and Amazon in South America; the Mississippi in the United states; and Po in Italy". This rise in sea level is directly related to the melting of ice in the polar region as a result of increased global temperature.

One aspect that is not often mentioned is how the climate change will affect the local people life quality on daily, seasonal or annual basis. This perhaps is due partly to inadequate representation of local effects in the existing climate change forecasting models, or lack of sufficient knowledge of social aspect of climate change as related to local population. In some parts of the world, rising air temperature may lead to temperature extremes or spells (temperature spell is defined later in methodology) which could greatly impact the local population. Temperature spells may cause outbreak of some diseases leading to increased hospitalisation and increased government spending. Temperature spell may increase mosquitoes breeding and more people requiring drugs and hospitalisation due to malaria attacks as the case of highland Kakamiya, Kenya [4]. Outbreak of other diseases such as pneumonia, measles, cerebra spinal meningitis (CSM) may be triggered or exacerbated by temperature extremes.

In this study, the aim is to detect temperature spells comparatively to increasing temperature over Lagos. We also intend to assess the decadal variability of the spells. It is a well known fact that cold spell conditions (by West Africa standards) has consequent human discomfort, manifested mostly by cracked (and bloody) lips and also an itching skin due to the low temperature and the very dry air [5]. Warm spells are known to cause discomfort in terms of profuse perspiration and high demand for cooling. The cooling requires using air conditioners in homes and offices; this has great demand on electricity consumption. How these phenomena of cold and warm spells are affected in the face of increasing temperature over Lagos forms the thrust of this paper.

2. DATA AND METHODOLOGY

Mean daily temperature values over Lagos (Lat 6.5^{o}N, Lon 3.3^{o}E) were obtained from National Centre for Environmental predictions – National Centre for Atmospheric Research (NCEP – NCAR) reanalysis data [6] between 1948 and 2007. The data are from archive of improved global resolution of 2.5^o latitude by 2.5^o longitude· Temperature anomalies have been computed by subtracting from daily temperatures the value of the corresponding day in the mean annual wave, which is estimated as the sum of the first two harmonics to the series of mean daily temperatures. Such harmonics which correspond to an annual and semi annual cycle, explain about 97% of the series variance. Temperature anomaly is classified as ‘spell’ if its value is located in the third quartile of the corresponding anomaly distribution for months under consideration. The value of the third quartile (75%) is used to obtain a more robust value for extreme spell detection, since only 25% of the location’s spell exceeds that value. This criterion, according to [7] is more appropriate than sometimes using standard deviations because the third quartile indicates a probability value, which is not available from the standard deviation since the distributions are highly asymmetrical. Thus, we sub – divide the period considered into six decades starting with 1948/57 and so on for easy comparison.

3. RESULTS AND DISCUSSION

3.1 Observed temperature trend

The trend of annual temperature over Lagos is shown in Fig. 1; there have been systematic increase in temperature from the last six decades and a warming rate of about 0.03 ^{o}K per year is evident. When the warming rate is sustained for sixty years, the result is within the range of 1.5–4.5 ^{o}K globally projected increase in temperature [8]. Although this value is considerably in the lower range of the projected increase, nevertheless there is consistent increase in temperature and no sign of downward trend. The increase observed in daily temperature trend over Lagos is not unconnected with warming due to anthropogenic influences. It is important to note here that the Lagos city is the commercial hub of Nigeria characterized by increasing industrial emissions and heavy traffic volume. The release of greenhouse gases from industries and traffic has the potential to increase temperature over the city. Besides the industrial influences, there is warming on global scale which acts to reinforce the local warming.

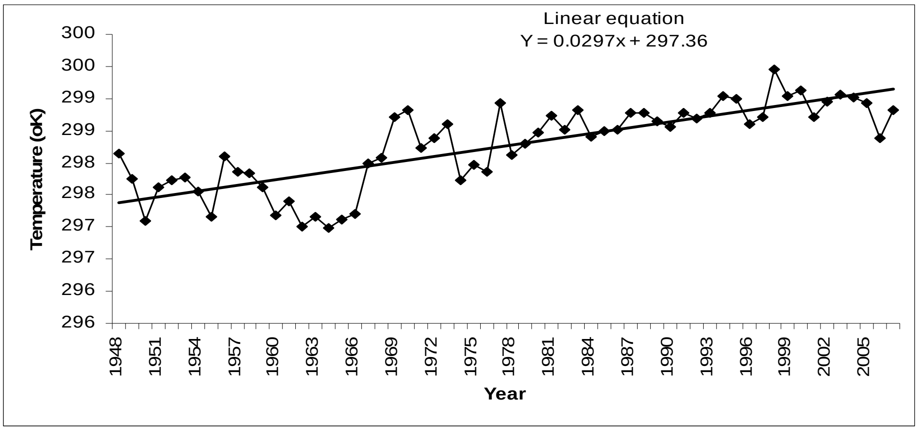

Fig. 1. Observed annual temperature trend over Lagos, Nigeria

3.2 Decadal mean temperature

Basically in Nigeria, and indeed in West Africa, two prominent seasons are known, and they are the dry season between December of previous year and March / April of following year, and wet season between April and October / November. However, the span of the seasons shrinks as we progress from the rainforest south through savannah to sahelian zones of the northern Nigeria. For the purpose of this study, a year has been demarcated into beginning of rainy season (January – April), rainy season (May – August) and ending of rainy season (September – December).

Mean decadal temperature shown in Fig. 2 reveals that temperature dropped in second decade during the beginning of rainy season but picked in the third decade. The increasing trend continued up to the sixth decade and there is yet no sign of downward trend. Meanwhile, both the rainy and ending of rainy seasons have experienced increasing mean temperature, the trends of both the rainy and ending of rainy seasons were not so severe compared to the beginning of rainy season's trend as deduced from the steeper slope of the latter's trend line. An increasing trend of about 0.5 ^{o}K per decade was detected for the months in the beginning of rainy season compared to about 0.2 ^{o}K for months in both rainy and end of rainy seasons. Comparison between the first and sixth decades only shows that there have been about 0.65%, 0.35% and 0.27% increase over the first decade in the mean decadal temperature for the beginning, rainy and end of rainy seasons respectively.

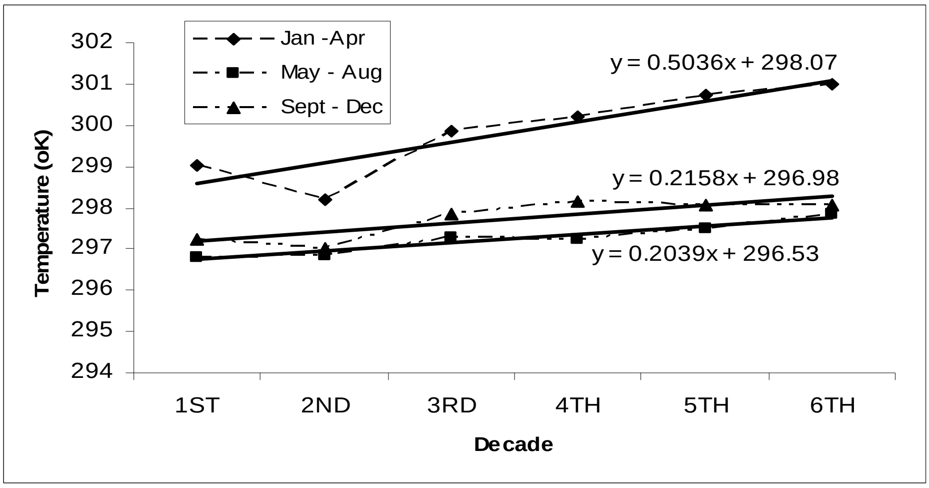

Fig. 2. Mean decadal temperature for beginning of rainy season, rainy season and ending of rainy season

3.3 DECADAL TEMPERATURE SPELL

The beginning of rainy season is characterized by moisture build up [9] when deep convective systems develop. The development of the systems signifies abundance of moisture as specific humidity anomaly becomes positive. The moisture build up is usually very deeper during the beginning of the rainy season compared to other seasons (see Fig. 3(a)–(f) in Omotosho, 2007). According to Clausius Clapeyron equation (Eq 1, which describes the relationship between temperature and saturation vapour pressure) written as:

$$e_s = e_o.\exp\left[\frac{L}{R_v}.\left(\frac{1}{T_o}-\frac{1}{T}\right)\right], \tag{1}$$

where e_o = 0.611 kPa, T_o = 273 ^{o}K are constant parameters and R_v = 461 JK^{-1} is the gas constant for water vapour [10]. We expect a corresponding increase in temperature due to moisture increase. Thus, months of the beginning of rainy season (especially March and April) are warmer than the rest of the year. Similarly, the months in rainy season are usually cold because of the cool /cold wind resulting from precipitation. And finally, months of ending of rainy season are usually cold initially due to cool / cold wind from ceasing rainy season and later due to incursion of cold harmattan wind.

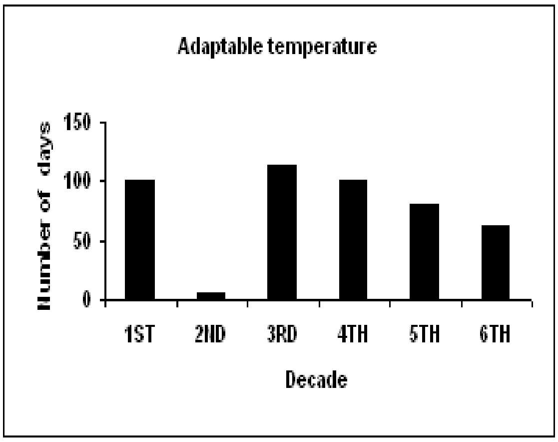

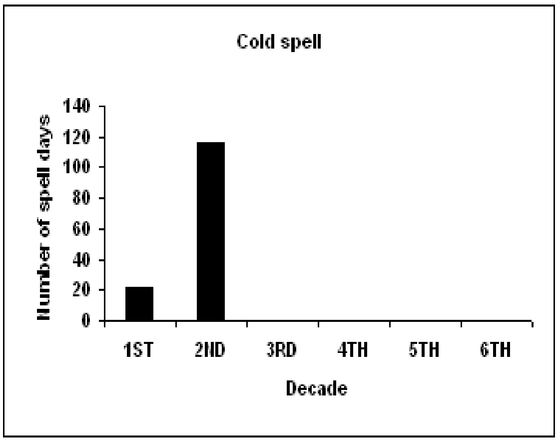

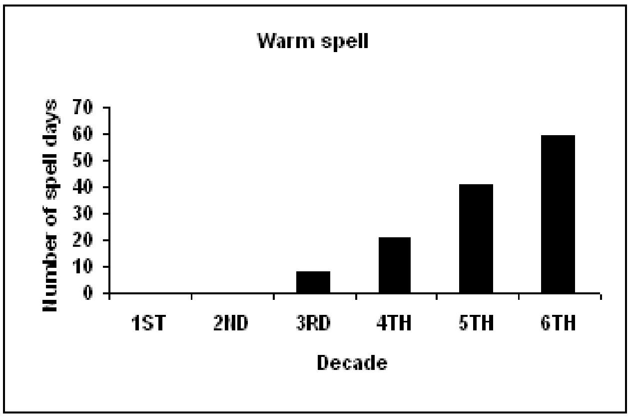

(a) January – April

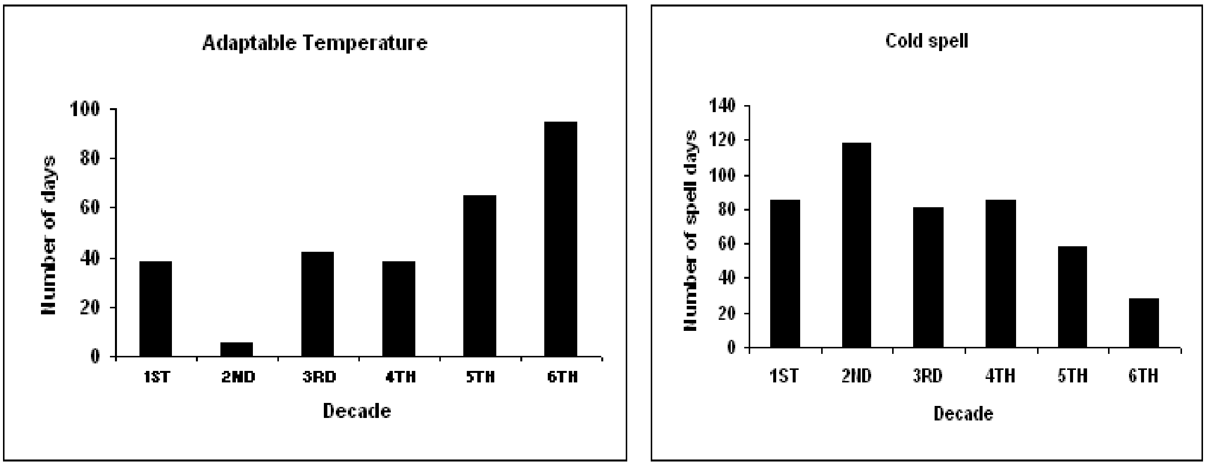

(b) May – August

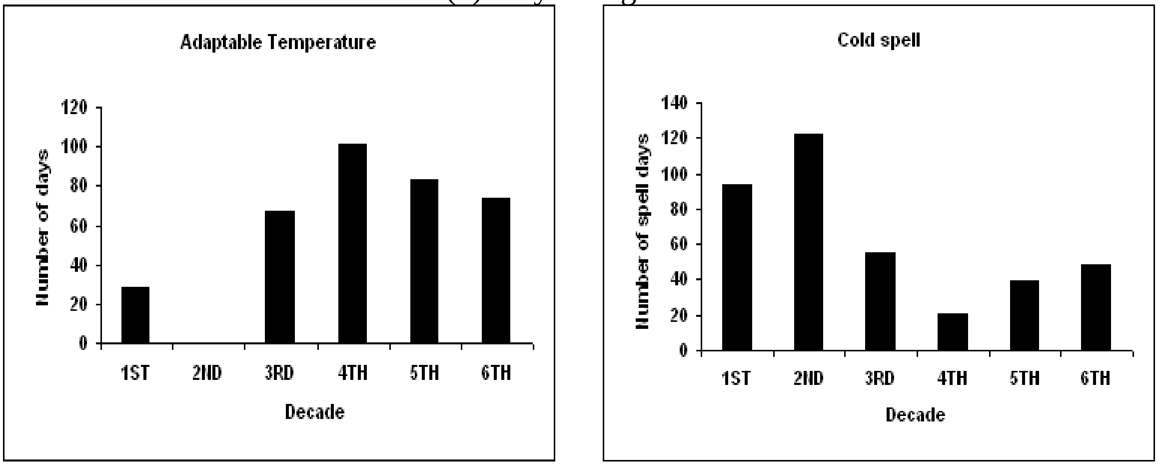

(c) September – December

Fig. 3. Decadal numbers of adaptable temperature and spells

Presented in Fig. 3(a) – (c) is number of spells days in each category of seasons. Cold spells in the months of January – April were common only in the first and second decades and disappeared completely in the rest of the decade. Second decade had the highest number of cold spell days of about 120 days thereby reducing the number of days of normal adaptable temperatures to record low.

Normal adaptable temperatures reduced considerably henceforth from third decade to sixth decade. In contrast to reducing number of days of normal adaptable temperature, warm spells increased drastically from third decade to highest value of about 60 days during the sixth decade. This is in response to increasing annual temperature over the location. Abnormally high temperatures as manifested by the increasing warm spells have tendency to exacerbate susceptibility to diseases such as malaria. Warm spells during the beginning of rainy season characterized by high humidity will increase human discomfort occurring in form of profuse perspiration, stress and fatigue. This is a commonly experienced few weeks before the proper onset of the rain. More discomfort is therefore inevitable given the current trend of increasing warm spells during these months.

May–August has high frequency of cold spells, this is expected as this corresponds to period of rainy season. However, the cold spell days have witnessed reduction attributable to rising temperature. The consequence of this is that number of days of normal adaptable temperatures has increased correspondingly. There are no warm spells detected yet during the rainy season. September – December is predominantly harmattan period when the cold often dusty winds blow from north east of the country to the station. Decreasing cold spells days is again apparent during this period in favour of increasing frequency of normal adaptable temperatures without warm spells days. Although, warm spells are visibly absent from months of rainy and ending of rainy seasons, projecting at the current rate of warming, it appears that emergence of warm spells may be unavoidable in the future.

4. CONCLUSION

Using a more robust criterion, this study has attempted to detect warm and cold temperature spells over Lagos, Nigeria between 1948 and 2007. The results have shown that rainy season (months of January – April) has witnessed increasing warm spells in the later decades. It is particular high in 1998/2007 in response to increasing temperature over the station. Analysis showed that numbers of days of adaptable temperature reduced considerable from about 100 days in the first decade (1948/57) to below 60 days in the sixth decade during the months of January to April, while number of warm spell increased correspondingly. The implication of this is that large number of people will depend on air conditional for cooling to achieve comfortability. The dependence on air conditional will increase demand for energy consumption. Within the period considered rate of increasing temperature over the station marched the projected global increase of between 1.5–4.5 ^{o}K. Observed warm temperature spells may increase or exacerbate the resurgence of certain diseases especially malaria.

ACKNOWLEDGEMENT

The author thank NCAR group for making the reanalysis data used for this study available on its website. Thanks are also due to the three anonymous reviewers. Their useful comments led to a much improved manuscript.

REFERENCES

1. IPCC, (2007): Summary for Policymakers. In: Climate Change 2007: Impacts, Adaptation and Vulnerability. Contribution of Working Group II to the Fourth Assessment Report of the Intergovernmental Panel on Climate Change, M.L. Parry, O.F. Canziani, J.P. Palutikof, P.J. van der Linden and C.E. Hanson, Eds., Cambridge University Press, Cambridge, UK, 7-22.
2. OECD, (1992): Global warming: the Benefits of Abatement. Paris: OECD bookshop.

3. IPCC, (1996): Climate Change 1995 — the Science of Climate Change. Contribution of Working Group I to the Second Assessment Report of the Intergovernmental Panel on Climate Change. J.T. Houghton, L.G. Meira Filho, B.A. Callander, N. Harris, A. Kattenberg and K. Maskell (eds). Cambridge University Press, UK. 572 p.
4. Jonathan A. Patz, Mike Hulme, Cynthia Rosenzweig, Timothy D. Mitchell, Richard A. Goldberg, Andrew K. Githeko, Subhash Lele, Anthony J. McMichael, David Le Sueur (2002): Regional warming and malaria resurgence. *Nature* 420 12.
5. Omotosho, J. Bayo (1989): Equivalent potential temperature and dust haze forecasting at Kano, Nigeria *Atmos. Res*., 23, 163-178.
6. Kalnay, E., M. Kanamitsu, R. Kistler, W. Collins, D. Deaven, L. Gandin, M. Iredell, S. Saha, G. White, J. Woollen, Y. Zhu, M. Chelliah, W. Ebisuzaki, W. Higgins, J. Janowiak, K. C. Mo, C. Ropelewski, J. Wang, A. Leetmaa, R. Reynolds, R. Jenne, and D. Joseph, (1996): The NCEP/NCAR 40-year reanalysis project. *Bull Amer Meteor Soc*, 77, 437–471.
7. Rusticucci, M.M and W.M, Vargas (2001): Interannual variability of temperature spells over Argentina. *Atmosfera*, 14, 75–86.
8. Fred B. Wood (1990): Monitoring global climate change: the case of greenhouse warming. *Bull Amer Met soc*, 71, 142–52
9. Omotosho, J.B. (2007): Pre-rainy season moisture build-up and storm precipitation delivery in the West African Sahel. *Int. J. Climatol. DOI: 10.1002/joc.1548*
10. Stull, R.B. (2000): Meteorology for scientist and engineers. Brooks/cole, USA.

CYSENI 2010, May 27–28, Kaunas, Lithuania
ISSN 1822-7554, www.cyseni.com

ANALYSIS OF WATER FLOW ENERGY OUTPUT ON RUSNĖ RIVER'S IN TWO SAME RIVER MODELS WITH DIFFERENT HYDROLOGICAL PARAMETERS VARIED TO MAXIMIZE FLOW VELOCITY

A. Pavlovas
Lithuanian University of Agriculture
Universiteto str. 10, LT-53361 – Lithuania
Phone: +370 67780497
Email: andrijanas.pavlovas@gmail.com

ABSTRACT

In paper two models of Rusnė river are analysed, where zero model based on real river parameters data gathered from archive data. Second model of river model consists of several submodels, where river flow hydrological parameters were varied. Models are prepared using water flow modelling software (MIKE 21). The main aim of study have been analysed the theoretical field how water flow velocity changed in two differents models. The results have showed that river profile correction have an influence maximizing flow velocity.

Keywords flow velocity, model

1. INTRODUCTION

River flow width (w) and river slope are the main parameters, which mainly affecting river discharge and flow velocity. River width measured as the shortest cross-sectional distance from water’s edge to water’s edge, orthogonal to the river channel. Flow widths vary constantly with discharge and, as such, differ from channel widths (i.e., bank-to-bank width). Most notably, it is one of three fundamental hydraulic variables, together with depth (d) and velocity (v), whose product determines the river discharge Q. Growing river discharge, river velocity and growing river flow kinetic energy [7]. Firstly, in recent literature is emphasized, that river flow energy in Lithuanian is costly. Flow velocity must be more 1.3 m/s, only in such situation producing electrical energy is impossible and such process profitable [9]. In Lithuania are only several rivers which have flow velocity 1.3 m/s and more. These rivers are: Nemunas, Virvytė [1]. Nemunas river is a biggest river in Lithuania. Nemunas river discharge maximized at spring period and in such period flow velocity achieving maximum value. Virvyte river‘s situation is different. Discharge and flow velocity parameters maximize at spring period. Virvytė river flow velocity is higher than on other Lithuanian rivers because river slope are different than other rivers slopes. Virvytės river‘s slope is major than other rivers slope [8]. Virvyte river flow velocity average is 1 m/s. Flow velocity is not constant parameter, it is changing during year, month, week, day. Flow velocity lenght parameter stay stable is not long. In such situation using flow energy on the rivers for electric energy produce become very problematical. Flow velocity on rivers:Nemunas, Virvytė, with velocity 1.3 m/s stay stable periods are short. To make river flow velocity more fast, we can change such hidrological river parameter as river flow width or river slope. But such practic not popular today, because flow velocity we can make faster a little, but financial sources will be high. Potentially in future river velocity less than 1.3 m/s will be enough to generate electrical energy with a potential profit and answers which hodrological parameter change to increase water flow will be topical.

2. METHODOLOGY

Selected river: Rusnė river 2 km section.

Mike 21 model parameters: water flow levels(input flow – -0,25 m, output flow – 0,23 m.), designed discharge is -228 m^3/s.

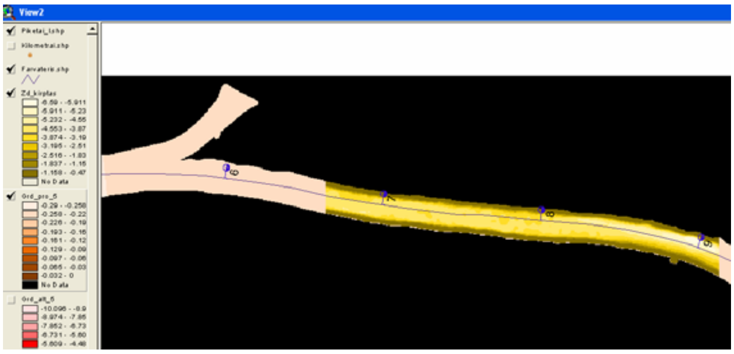

Fig. 1. Rusnė's river section bathymetry

Having bathymetry data using Mike 21 2D flow model (using Double sweep alghoritm), and model Eq. [4]:

$$\frac{\delta\zeta}{\delta t}+\frac{\delta p}{\delta x}+\frac{\delta q}{\delta y}=0$$ – flow integrity equation,

$$\frac{\delta q}{\delta t}+\frac{\delta}{\delta y}\left(\frac{q^2}{h}\right)+\frac{\delta}{\delta x}\left(\frac{pq}{h}\right)+gh\frac{\delta\zeta}{\delta y}+\frac{gp\sqrt{p^2+q^2}}{C^2\cdot h^2}-$$
$$-\frac{1}{\rho_w}\left[\frac{\delta}{\delta y}\left(h\tau_{yy}\right)+\frac{\delta}{\delta x}\left(h\tau_{xy}\right)\right]-\Omega_p-fVV_y+\frac{h}{\rho_w}\frac{\delta}{\delta y}\left(p_a\right)=0$$ – motion quantity balance equation [7]

Model discharge error limit less 5%. In model number 0 river profile not changed. In model number 1 river profile is changed (parameter - width) [2].

3. RESULTS AND DISCUSSIONS

In Fig 2. there is presented Rusnė river profile

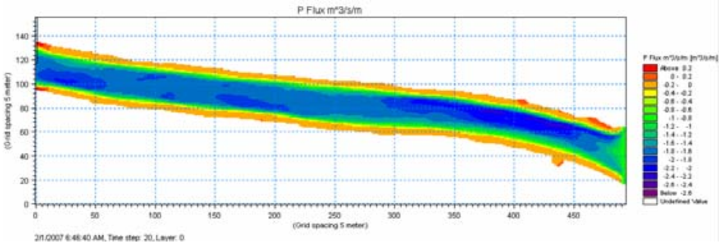

Fig. 2. Rusnė's river profile, not corrected

In Fig 3. Rusnė river profile, river width is corrected, from right and left sides of rivers banks are modified [10]. The aim of modification is to increase flow velocity in the middle of river. If equal average flow velocity in 0 model (average flow velocity= 0.35 m/s) and in 1 model(average flow velocity = 0.33 m/s) the result is that in 1 model(river profile corrected) flow velocity is less than in model 0. Such situation is paradoxical, but in detail flow velocity in model 1(river profile is corrected) increasing in the middle of flow, but near the banks after river corrected section flow velocity is decreasing [3].

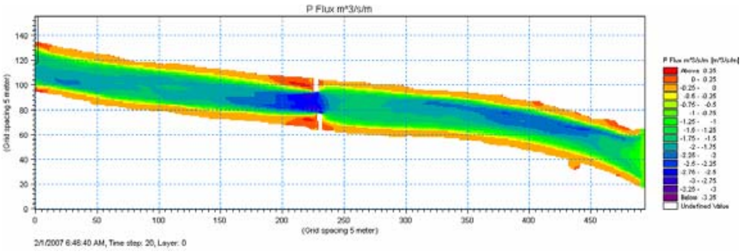

Fig. 3. Rusnė's river profile, corrected

3.1 Model 0 (model with real hydrological characteristics)

In Fig 4. Flow velocity maximized in the middle of river flow. Flow velocity are minimum near the banks.

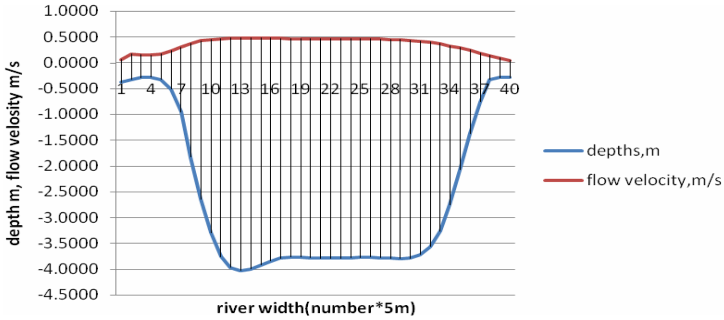

Fig. 4. Rusnė's river cross-section flow velocity across river width

Table 1. Model 0 river flow velocity

Flow velocity Model 0									
1	0.07	0.17	0.15	0.15	0.18	0.23	0.30	0.38	0.43
2	0.46	0.47	0.48	0.48	0.48	0.48	0.48	0.47	0.47
3	0.47	0.47	0.47	0.47	0.46	0.46	0.46	0.46	0.46
4	0.46	0.45	0.44	0.42	0.40	0.37	0.33	0.29	0.24
5	0.19	0.14	0.10	0.05					

3.2. Model 1 (model with changed hydrological characteristics)

In Fig 5. lFlow velocity from 0 model comparable with model 1 by river flow velocity parameter. In model 1 flow velocity after river profile corrections on the middle of river flow have been increased.

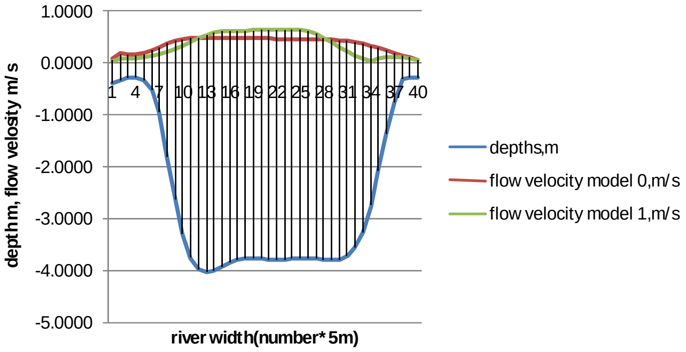

Fig. 5. Rusnė’s river cross-section flow velocity in 0 and 1 model

Table 2. Model 1 river flow velocity

	velocity		velocity		velocity		velocity
1	0.018539	11	0.390117	21	0.629043	31	0.211562
2	0.059513	12	0.462337	22	0.631009	32	0.130789
3	0.063731	13	0.529698	23	0.630816	33	0.062175
4	0.079722	14	0.582946	24	0.636575	34	0.030263
5	0.100316	15	0.611749	25	0.634361	35	0.061457
6	0.127471	16	0.620579	26	0.603602	36	0.092145
7	0.164201	17	0.622239	27	0.547622	37	0.107654
8	0.207663	18	0.622992	28	0.473446	38	0.095788
9	0.259226	19	0.624397	29	0.388292	39	0.084083
10	0.320809	20	0.626488	30	0.299036	40	0.055588

Compare model 0 and model 1 by river flow velocity fact is – river flow velocity parameter in the middle of river flow increased in the range between 17–27% (in model 1).

4. CONCLUSIONS

In model 1 river flow velocity in the middle of river increased in average about 20 %. But near the banks of river flow velocity is decreased. River profile correction was the main factor of this increasing. Rusnė river flow velocity is not enough for electric energy production today,but for future such river flow velocity increasing is a potential factor to produce electric energy and it would be possible in future.

REFERENCES

1. Gailiušis B., Jablonskis J., Kovalenkovienė M. Lietuvos upės.Hidrografija ir nuotėkis. Kaunas. Lietuvos energetikos institutas, 2001.
2. Maidment D. R. Arc Hidro:GIS for Water Resources. California:ESRI, 2002.
3. Šikšnys A. Atvirų vandens telkinių hidrodinamikos skaitmeninis modeliavimas. Mokomoji knyga, 2007, p. 47–60.
4. Littlewood I. G., Practical aspects of calibrating and selecting unit hydrograph-based models for continuous river flow simulation. Hidrological Sciences Journal, 46(5), 2001, p. 795–811.
5. Littlewood I. G., Practical continuous river flow modelling using unit hydrograph identified from commonly available hydrometeorogical data. In: G. Gergov and

I.G. Littlewood (eds), British-Bulgarian Colloboration in Hydrology. British Council, Sofia, 2000, p. 142–157.
6. Montagu R., Energy of flowing water, critical flow. 2002, Link to the internet <http://pecongress. org.pk/images/upload/books/P17-PAPER126-1.pdf>
7. Turcek P., The velocity of the river flow., Tatra Mt.Math. Publ. 39.,2008, p. 87–94. Link to the internet <http://www.sav.sk/journals/uploads/0916111609-12m-t.pdf>
8. Hagemann, S. Dumenil, L. A parameterization of the lateral water flow for the global scale, Clim. Dynam., 14, 1998, p.17–31.
9. Mosley, M. P. and McKerchar, A. I.: Streamflow, in: Handbook of Hydrology, edited by: Maidment, D. R., McGraw-Hill, New York, 1993, ch. 8.1–8.39.
10. Arnell, N. W.: A simple water balance model for the simulation of streamflow over a large geographic domain, J. Hydrol., 1999, p. 217, 314–335.

SIMULATION OF THERMODYNAMIC PROPERTIES OF LITHUANIAN MINERALS FOR CO_2 SEQUESTRATION

I. Stasiulaitiene, G. Denafas
Kaunas University of Technology
Department for Environmental Engineering
Radvilėnų pl. 19, LT-50254 Kaunas - Lithuania
Phone: 37037300182, 37061572323
Email: Inga.Stasiulaitiene@ktu.lt

R. Zevenhoven
Abo Akademi University
Biskopsgatan 8, FI-20500 Abo - Finland
Phone: 35822153223, 358503704810
Email: Ron.Zevenhoven@abo.fi

ABSTRACT

Carbon dioxide (CO_2) is the most important greenhouse gas causing global warming. Fossil fuel combustion has been the greatest contributor to increasing CO_2 concentration in the atmosphere over the past century. Carbon dioxide capture and storage (CCS; CO_2 sequestration) is considered to be one of the options for reducing CO_2 emissions caused by human activities. Mineral carbonation is a prospective technology for CO_2 storage, i.e. a process where CO_2 could be stored in the form of solid inorganic carbonates by means of chemical reactions. This process is an alternative for countries which don't have other possibilities (such as deep saline aquifers) for storing CO_2. In this study minerals abundant in Lithuanian geological layers have been evaluated for carbonation technology. Three different minerals: glauconite, opoka and serpentinites have been studied for the evaluation of their thermodynamic properties based on thermochemical calculations. The results have showed that serpentinites have potential for storing CO_2, while glauconite and opoka have limited application.

Keywords carbon dioxide, sequestration, thermodynamics, simulation

1. INTRODUCTION

Human activities are generally considered responsible for the rapidly increasing CO_2 levels in the atmosphere. Fossil fuel-based energy production is a leading contributor to the emission of CO_2. In order to reduce the amount of CO_2 emitted into the atmosphere, three main strategies are available: improvement of energy efficiency (efficient use of energy), use of renewable energy sources, and carbon sequestration (development of CO_2 capture and storage (CCS) technologies). An approach of CCS involves capturing CO_2 from energy-related and industrial sources, transporting it to a storage location and long-term storing it from the atmosphere [1]. CO_2 sequestration by mineral carbonation is one of the options for CCS.

The mineral carbonation or carbon dioxide mineralization concept was first mentioned by Seifritz in 1990s [2] and developed by Dunsmore [3]. However Lackner et al. were the first to provide details and foundation for today's research. Lackner introduced a safe and permanent method of CO_2 disposal based on the chemical fixation of CO_2 in the form of carbonate minerals. Moreover, magnesium and calcium silicate deposits are sufficiently abundant to fix the CO_2 that could be produced from the combustion of all fossil fuel sources [1, 4]. That is an option for the countries which don't have possibilities for underground geological storage. There are no suitable geological formations for storing captured CO_2 in countries, such as Finland, Sweden, Estonia, Lithuania [5–7].

Evaluation of Lithuanian minerals suitable for CO_2 mineralization provides valuable information for further research. As Lithuania has to follow the Kyoto protocol requirements under CO_2 emissions, possible storage options of CO_2 should be evaluated. Presently the CO_2 emissions do not exceed the base year (1990) limit, but the emissions are expected to grow, essentially after the closure of the Ignalina Nuclear Power Plant (the last unit was closed on the 1st of January, 2010). The aim of the paper is to describe selected Lithuanian minerals and their thermodynamic properties,i.e. glauconite, opoka and serpentinite [8].

2. LITHUANIAN MINERAL RESOURCES

The ideal source materials for carbonation are alkaline-earth species containing calcium (Ca) and magnesium (Mg) [9]. Pure oxides and hydroxides of Ca and Mg are extremely rare in nature because of their high reactivity. Ultramafic rocks containing these oxides and hydroxides in large amounts and high concentrations have been considered as primary reactants for mineral carbonation [10].

Different prospective mineral resources have been explored in Lithuania, of which eight minerals are exploited (limestone, dolomite, sand, gravel, chalky marl, peat and oil) and two of them (opoka and sapropel) exploitation was stopped in the 1980s. The current legislation allows exploiting only the mineral reserves which have been explored in detail [11].

Although such minerals as anhydrite and gypsum consist of 41.19% and 32.57% of CaO respectively, these rocks are not analysed for mineral carbonation because of complicated technology of CaO extraction and environmental consequences (emissions of SO_2) [12].

Glauconite, opoka and serpentinites rocks have been chosen for thermodynamic investigations and their suitability for a carbonation process in Lithuania. The summarized data about the reserves exploitation and hypothetically prognostic reserves of these three minerals is given in Table 1 [12]. These three Lithuanian resources have been chosen of MgO and CaO content. MgO and CaO oxide constitute 3.32 mol-% and 6.95 mol-% respectively in glauconite [13]. The content of MgO and CaO in opoka is in the range of 17.32–37.98 mol-% and 0.5–0.87 mol-% respectively [14]. In the case of serpentinite, MgO constitute 6.84 mol-% and CaO – 42.23 mol-% [15].

Table 1. Survey of Lithuanian natural resources, 2008 [12]

No.	Natural reserves	Units	Mining in 2008	Reserves explored in details	Reserves explored tentatively	Detected prognostic reserves	Hypothetically prognostic reserves
1.	Iron ore Fe>20%, Fe>45%	mln.t	-	-	219.6 142.1	71.0 9.2	441.4
2.	Glauconite sandy loam	mln.m^3	-	-	7.4	21.681	-
3.	Opoka	mln.t	-	33.7	-	-	-

The glauconite is a common mineral of the Albian and Cenomanian (Cretaceous) sands composing 15–50% of the rock volume (16). They occur at the depths of 100–200 m in the southeastern half of Lithuania. The total thickness of the Albian-Cenomanian succession is in the range of 40–75 m. The Palaeogene sediments are also enriched in glauconite. Chemical formula of glauconite in general is as following: $K_{0.73}Na_{0.04}Ca_{0.03}Fe^{3+}_{0.83}Fe^{2+}_{0.017}Al_{0.93}Mg_{0.40}Si_{3.68}O_{10}(OH)_{2.39}(H_2O)_{0.29}$ (17). The sedimentary opaline silica rocks *(opoka)* occur in the Upper Cretaceous chalky succession in west Lithuania and in the Palaeogene sediments of southern Lithuania. They occur at the depths of 10–80 m, the thickness attains a few dozens of meters (18). *Serpentinites* are distributed in the southeastern part of the Lithuania within the Varena Geological Province (18). Serpentinite bodies are well discernable on the gravity and essentially the magnetic field maps, as they associate with the magnetite (iron ore) concentrations. More than a dozen of serpentinite bodies were identified in south Lithuania.

3. METHODOLOGY

Thermodynamic behaviour of the rocks, i.e. glauconite, opoka and serpentinites, under two conditions was simulated. These conditions have been chosen aiming to research how the composition of a certain mineral changes during heating under the typical air environment and in CO_2 environment.

Thermochemical calculations are based on enthalpy H, entropy S, heat capacity C_p or Gibbs energy G values for chemical species.

Absolute values of enthalpy H of substances often cannot be measured, but enthalpy differences between two temperatures can be determined with a calorimeter. Heat capacity C_p at constant pressure (specific heat) can be calculated from this data using equation (1) [19] :

$$C_p = \left(\frac{dH}{dT}\right)_{P,n} . \tag{1}$$

Eq. (1) allows the calculation of enthalpy as following [19]:

$$H(T) = H_f(298.15) + \int_{298.15}^{T} C_p * dT + H_{tr}, \tag{2}$$

where: $H_f(298.15)$ is the enthalpy of formation at 298.15 K;

H_{tr} is the enthalpy of transformation of the substance.

Absolute entropy can be calculated from the experimental heat capacity values using Eq. (3) and numerical integration [19].

$$S = S(298.15) + \int_{298.15}^{T} \left(\frac{C_p}{T}\right) dT + \sum H_{tr} / T_{tr} \quad , \tag{3}$$

where: S(298.15) is the standard entropy of the substance which can be calculated by integrating C_p/T function from 0 to 298.15 Kelvins;

T is temperature;
H_{tr} is enthalpy of phase transformation at a temperature T_{tr}.

The absolute heat capacity of substances at constant pressure can be calculated using Eq. (1). The temperature dependence of heat capacity at elevated temperatures cannot be predicted theoretically by thermodynamics. A fully mathematical correlation is therefore adopted for fitting experimental heat capacities. The Kelley equation is used throughout the program in the following form [19]:

$$C_p = A + B * 10^{-3} * T + C * 10^{5} * T^{-2} + D * 10^{-6} * T^{2}, \tag{4}$$

where A, B, C and D are coefficients estimated from experimental data.

The mutual stability of substances (elements, compounds, ions, etc.) cannot be compared using enthalpy, entropy or heat capacity functions solely. It should be done using the Gibbs energy defined by equation (5) [19].

$$G = H - T * S \tag{5}$$

Thermodynamic analysis of Lithuanian minerals have been performed by HSC 5.11 software (8). The HSC Chemistry software enables simulation of chemical reactions and processes on the thermochemical basis as explained above. This module enables to calculate multi-component equilibrium compositions in heterogeneous systems. The program calculates the amounts of products at equilibrium in isobaric conditions. The amounts of products at equilibrium in isobaric conditions are calculated and presented graphically as functions of equilibrium composition, equilibrium amount and reaction enthalpies with respect to temperature changes. Temperature range used in the simulation was 25 °C–900 °C, with the step of 100 °C. Equilibrium calculations offer a practical way to observing the effects of process variables, such as temperature and amounts of raw materials on product composition. Thermodynamical behaviour of each rock was simulated by modeling equilibrium compositions of gas/solid mixture containing minerals comprising particular rock. Two different conditions have been chosen for modeling two-phase (gas and solid) systems. These conditions have been chosen aiming to research how the composition of a certain mineral changes during heating under the typical air environment and a mineral mutates in CO_2 environment. In the first case, heating of the minerals was simulated in the gas mixture (N_2(g), O_2(g), H_2O (g) – 78.2 mol-%, 20.2 mol-%, 1.6 mol-% respectively) under 1 bar pressure. This gas mixture corresponds to relative composition of air. In the second case, gas mixture with 90 mol-% of CO_2(g) was chosen. It was assumed that 90 mol-% of CO_2(g) takes part in the reaction, because it is unlikely that capture of CO_2 into 100 mol-% gas is technically viable. The majority of solid forms of mineral's compounds and amounts have been chosen according to their XRD analysis which has been performed in KTU at the Department of Silicate Technology. XRD data were collected with a DRON–6 X-ray diffractometer with the Bragg–Brentano geometry using Cu K_α radiation and graphite monochromator operating with the voltage of 30 kV and emission current of 20 mA. The step-scan covered the angular range 2–60^o (2θ) in steps of $2\theta = 0.02^o$. Other group of the compounds, which were unidentified from XRD analysis, has been chosen according to stoichiometrical composition of the specific rock from the database which is given by HSC software [8].

One of the main disadvantages of this method is that HSC does not take kinetic phenomena into account. It should be noted that thermodynamic analysis performed by calculating the changes in Gibbs free energy only estimates the probability to obtain certain equilibrium compositions in the systems, but gives no information about the limitations of phase contacting and mixing and kinetic parameters, in particular the time for reaching an equilibrium and the effect of activation energy.

4. RESULTS AND DISCUSSIONS

4.1. Glauconite

Equilibrium composition, amount and enthalpies of glauconite during heating (Fig. 1) and its reaction with CO_2 (Fig. 2) have been calculated using the Gibbs energy minimization method (based on Eq. 5).

Heating of glauconite in air environment. Fig. 1a shows the equilibrium compositions at various temperatures (temperature range 25 °C–900 °C) and constant pressure (1 bar) for the compounds comprising glauconite, during heating of the rock with following gaseous compounds (N_2(g), O_2(g), H_2O(g). For the first modeling case, it was assumed, as described in Chapter 3, that N_2(g) constitutes 78.2 mol-% of the whole gas mixture, O_2(g) and H_2O(g) – 20.2 mol-% and 1.6 mol-%, respectively. It was assumed that glauconite rock or its reaction products during heating process consisted of the following components: $KAl_2(AlSi_3O_{10})(OH)_2$, $KFe_3(AlSi_3O_{10})(OH)_2$, Al_2O_3, FeS_2, K_2O, $CaSO_4 \cdot 2H_2O$, SiO_2, $Al_2O_3 \cdot 2SiO_2 \cdot 2H_2O$, $CaSO_4$, CaO, MgO, $FeSO_4$, Fe_2O_3, Fe_3O_4, KOH, $K_2O \cdot Al_2O_3 \cdot 4SiO_2$, K_2SiO_3, $K_2O \cdot 4SiO_2$, $K_2O \cdot 2SiO_2$, $K_2O \cdot SiO_2$, $KAl_3Si_3O_{10}(OH)_2$, $K_3Al_3Si_3O_{10}(OH)_2$, $K_3AlSi_3O_8$, $KAlSi_3O_8$, $KAlSi_2O_6$, $KAlSiO_4$, $KAlO_2$, $Al_2O_3 \cdot 2SiO_2$. The main compounds in glauconite rock are muscovite ($KAl_2(AlSi_3O_{10})(OH)_2$) and quartz ($SiO_2$), which compose 38.96 mol-% and 31.17 mol-% of the rock, respectively. It should be noted that all amounts are assumed to be taken from XRD analysis results. Annite ($KFe_3(AlSi_3O_{10})(OH)_2$), which was used as a proxy for glauconite in the model, was assumed to comprise 6.5 mol-%. FeS_2, CaO and MgO each amounted 7.8 mol-% of the rock. The rest of the compounds, which constitue relatively small amounts in the material, were regarded as insignifficant (as 0 mol-%).

The equilibrium amount of the compounds comprising glauconite, with respect to the temperature are shown in Fig.1b. Enthalpies of the reaction mixture up to 900 °C are presented in Fig. 1c, as kJ/mol.

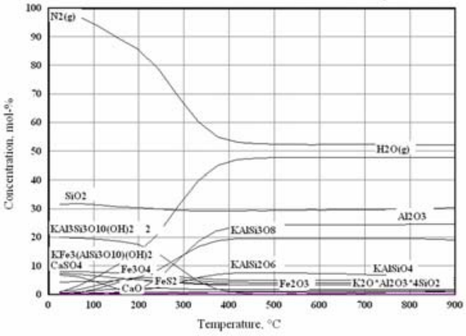

1a

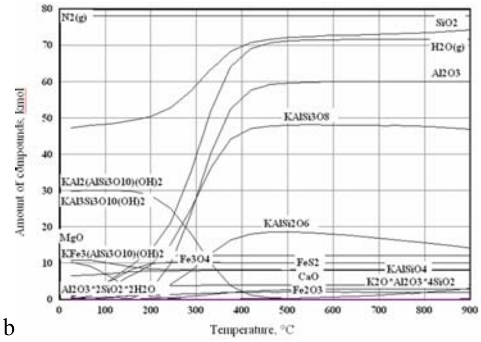

1b

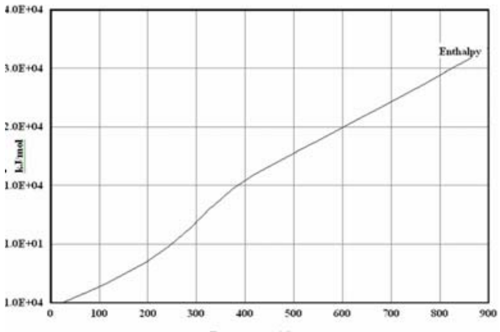

1c

Fig. 1a. Equilibrium composition of glauconite thermal dissociation products at various temperatures.
Fig. 1b. Temperature dependencies of equilibrium amounts of glauconite comprising components.
Fig. 1c. Reaction enthalpies of glauconite heating at air gas mixture.

The mathematical simulation has showed that when the rock is heated in a N_2 (g), O_2(g), H_2O(g) environment, $KAl_2(AlSi_3O_{10})(OH)_2$, $KFe_3(AlSi_3O_{10})(OH)_2$ starts to decompose at temperature higher than 200 °C. At the same time (Fig.1a), the concentrations of MgO, Fe_2O_3, Fe_3O_4 and CaO stay rather constant at the temperatures 25 °C–900 °C., while the concentration of Al_2O_3 increases with a rise of a temperature (200 °C–900 °C). The amounts of oxides (kmol) as it is presented in Fig.1b, shows that only Al_2O_3 increases drastically in 200 °C–900 °C temperatures interval. Amounts of Fe_2O_3, Fe_3O_4, MgO and CaO vary fractionally at the same temperature range.

Heating of glauconite in CO_2 environment. The second case of the modeling was simulating the behaviour of compounds composing glauconite, during heating in $CO_2(g)$ environment. Equilibrium composition, amount and enthalpies of glauconite reactions with CO_2 (g) under temperatures 25–900 °C, 1 bar pressure were simulated (Fig. 2). Fig. 2a shows the equilibrium compositions at various temperatures (temperature range 25 °C–900 °C) and constant pressure (1 bar) for the compounds comprising glauconite, during heating of the rock in $CO_2(g)$ environment. Gaseous components taking part in the reaction are $N_2(g)$, $O_2(g)$, $H_2O(g)$, $CO_2(g)$ and constitute 7.82 mol-%, 2.02 mol-%, 0.16 mol-%, 90 mol-% respectively. The forms of solid compounds and their amounts were similar to the first case, adding carbonates ($CaCO_3$, $MgCO_3$, $CaMg(CO_3)_2$, $FeCO_3$) as potentially forming materials.

The equilibrium amount of the compounds comprising glauconite with respect to the temperature are shown in Fig.2b. Enthalpies of the reaction mixture up to 900 °C are presented in Fig. 2c, as kJ/mol.

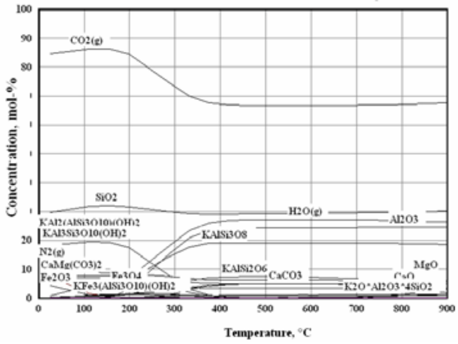

2a

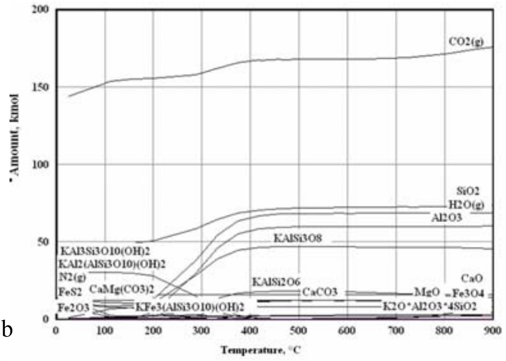

2b

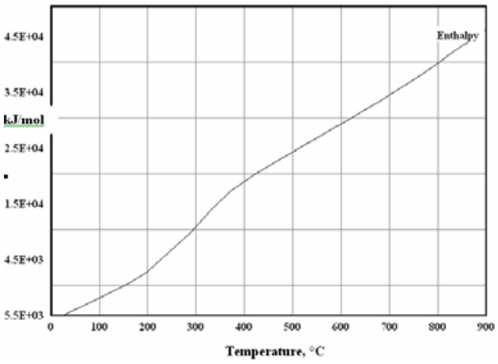

2c

Fig. 2a.Equilibrium composition of glauconite reactions depending on temperature.
Fig. 2b. Temperature dependencies of equilibrium amounts of glauconite comprising components.
Fig. 2c. Reaction enthalpies of glauconite heating at CO_2 environment.

The mathematical simulation of glauconite rock in CO_2 environment has showed that concentrations of $MgCO_3$ and $CaCO_3$ increase at temperatures around 200 °C (Fig. 2a). The biggest amounts (Fig. 2b) of $CaCO_3$ are reached at 400 °C–600 °C temperature range, while in case of $MgCO_3$, the temperature interval is 100 °C–300 °C. Carbonization of iron oxide appears to be very rapid, so that the carbonate form in glauconite rock appears immediately at low temperatures.

4.2. Opoka

Similarly to glauconite, the equilibrium composition, amount and enthalpies of opoka during heating (Fig. 3) and its reaction with CO_2 (Fig. 4) have been calculated using the Gibbs energy minimization method (based on Eq. 5). All simulations have been performed at 25 °C–900 °C temperature range and 1 bar pressure.

Heating of opoka in air environment. In the first case, heating of opoka has been simulated in $N_2(g)$, $O_2(g)$, $H_2O(g)$ atmosphere. The composition of the gases was similar to glauconite simulation. Equilibrium composition of the compounds comprising opoka is presented in graphical way in Fig. 3a, whereas equilibrium amount and reaction enthalpies of the reaction mixture up to 900 °C are shown in Fig. 3b and Fig. 3c respectively. Based on XRD analysis, it was assumed that opoka or its reaction products consisted of the following components: $KAl_2(AlSi_3O_{10})(OH)_2$, Al_2O_3, $Al_2O_3{\cdot}2SiO_2$, $3Al_2O_3{\cdot}2SiO_2$, CaO, $CaO{\cdot}Al_2O_3$, $4CaO{\cdot}Al_2O_3{\cdot}Fe_2O_3$, $CaO{\cdot}MgO{\cdot}SiO_2$, $CaO{\cdot}MgO{\cdot}2SiO_2$, $\cdot 3CaO{\cdot}SiO_2$, FeO, Fe_2O_3, $FeO{\cdot}SiO_2$, MgO, SiO_2, $CaCO_3$, of which $KAl_2(AlSi_3O_{10})(OH)_2$ constitutes 11.77 mol-%, CaO–29.41 mol-%, Fe_2O_3 – 5.88 mol-%, MgO – 5.88 mol-%, SiO_2 – 23.53 mol-%, $CaCO_3$ – 23.53 mol-%. The remaining compounds were assumed as of 0 mol-% concentration, as they comprise small amounts in opoka rock.

3a

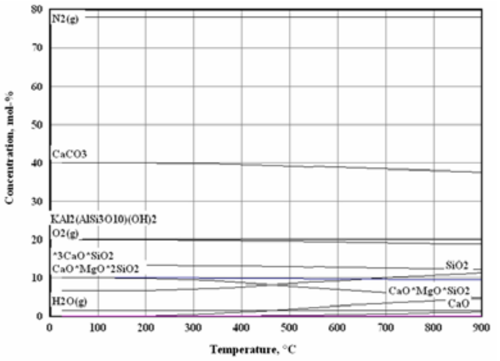

3b

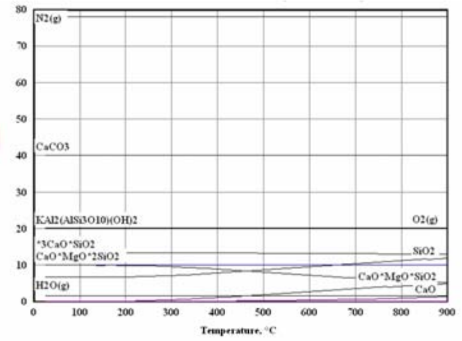

3c

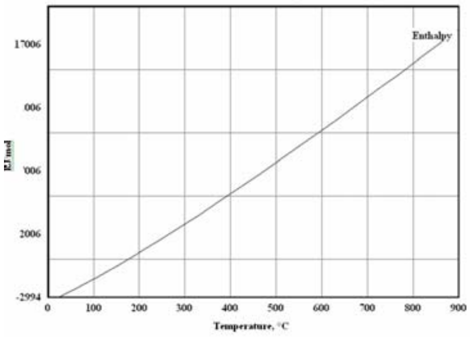

Fig. 3a. Equilibrium composition of opoka thermal dissociation products at various temperatures.
Fig. 3b. Temperature dependencies of equilibrium amounts of opoka comprising components.
Fig. 3c. Reaction enthalpies of opoka heating in the air gas mixture.

The analysis of equilibrium simulation of opoka heated at temperatures 25 °C–900 °C has showed that all the components of the rock change only slightly with a rise of temperature. Fig. 3a shows equilibrium composition of opoka; here it may be noticed that only SiO_2 concentration increases at temperatures higher than 400 °C, while concentrations of CaO and $CaO{\cdot}MgO{\cdot}SiO_2$ increase at even higher temperatures (600 °C–900 °C). Diagram of equilibrium amount (Fig. 3b) shows that components of opoka rock, i.e. $KAl_2(AlSi_3O_{10})(OH)_2$, Al_2O_3, $Al_2O_3{\cdot}2SiO_2$, $3Al_2O_3{\cdot}2SiO_2$, CaO, $CaO{\cdot}Al_2O_3$, $4CaO{\cdot}Al_2O_3{\cdot}Fe_2O_3$, $CaO{\cdot}MgO{\cdot}SiO_2$, $CaO{\cdot}MgO{\cdot}2SiO_2$, $\cdot 3CaO{\cdot}SiO_2$, FeO, Fe_2O_3, $FeO{\cdot}SiO_2$, MgO, SiO_2, $CaCO_3$, vary fractionally with a rise of temperature (temperature range 25 °C–900 °C).

Heating of opoka in CO_2 environment. In the second case, equilibrium composition (Fig. 4a), amount (Fig. 4b) and enthalpies (Fig. 4c) of opoka reactions with CO_2 (g) under temperatures 25 °C–900 °C, 1 bar pressure were performed, with the composition as described in Methods section (3 chapter). The forms of solid compounds and their amounts are the same as in the case of heating in air environment. In addition, iron and magnesium carbonates ($MgCO_3$, $CaMg(CO_3)_2$, $FeCO_3$) were included.

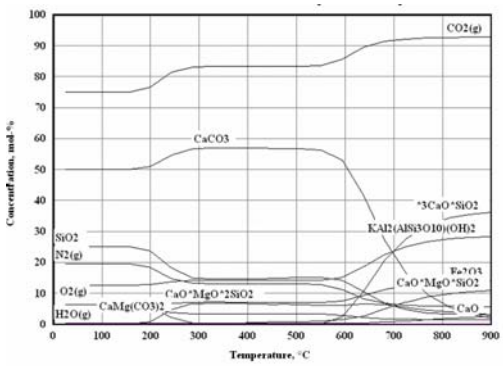

4a

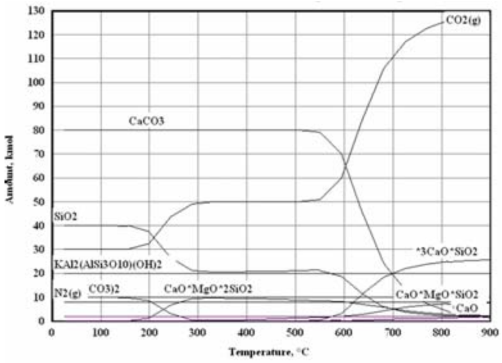

4b

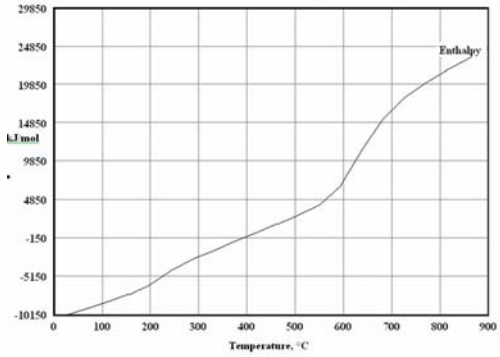

4c

Fig. 4a.Equilibrium composition of opoka reactions depending on temperature.
Fig. 4b. Temperature dependencies of equilibrium amounts of opoka comprising components.
Fig. 4c. Reaction enthalpies of opoka heating at CO_2 environment.

Mathematical simulation of opoka rock had proved that carbonates already exist in the beginning of temperature range 25 °C–900 °C. The amounts of available oxides such as MgO, Fe_2O_3, FeO and Al_2O_3 constitute relatively small amounts in opoka rock. During heating process, the formation of CaO may start as a product of the decomposition of $CaCO_3$ (also in relatively small amount) at high temperatures (600 °C–900 °C), at the same time increasing the amounts of CO_2. This process works adversely to the CO_2 storage process, thus is not feasible. Due to small amounts of available alkaline oxides, opoka's potential for dry carbonization process is rather low. On the other hand, tests of utilization of opoka in wet carbonization process should be as an option. An aqeous (wet) mineral CO_2 sequestration is a process where slurry of water mixed with pre-treated Mg- or Ca-based silicates reacts with CO_2 to produce carbonates [20].

4.3. Serpentinite

Most of the research in mineral carbonation for large scale CCS has focused on carbonation of Mg based minerals, since magnesium silicate rocks are usually richer in base ions than calcium silicate rocks [21]. The use of magnesium based silicates, $xMgO \times ySiO_2 \times zH_2O$, for carbonation is favoured also because they are worldwide available in huge amounts [22]. The storage capacity of silicate minerals has been estimated at 10.000–10.000.000 Gt of carbon, which exceeds the amount of carbon in known fossil fuel resources [23]. From the recent literature review it can be concluded that currently the most investigated mineral resources are olivine, serpentine and calcium oxide-based mineral wollastonite [24].

Heating of serpentinite in air environment. Equilibrium composition, amounts and enthalpies of serpentinite during heating under N_2(g), O_2(g), H_2O(g) environment have been calculated. The amounts of the gases were the same as for previous simulations. Fig. 5a shows the equilibrium compositions at various temperatures (temperature range 25 ^{0}C–900 ^{0}C) and constant pressure (1 bar) for serpentinite-comprising compounds. The solid components for serpentinite were assumed to be as following: $3MgO \cdot 2SiO_2 \cdot 2H_2O$, SiO_2, FeO, Fe_2O_3, MgO,

$CaSiO_3$, CaO, Al_2O_3, of which serpentine ($3MgO{\cdot}2SiO_2{\cdot}2H_2O$) constituted 61.5 mol-%, FeO - 15.4 mol-%, SiO_2, CaO, Al_2O_3 each amounted to 7.69 mol-%.

Equilibrium amount and reaction enthalpies of the reaction mixture up to 900 °C are shown in Fig. 5b, and Fig. 5c, respectively.

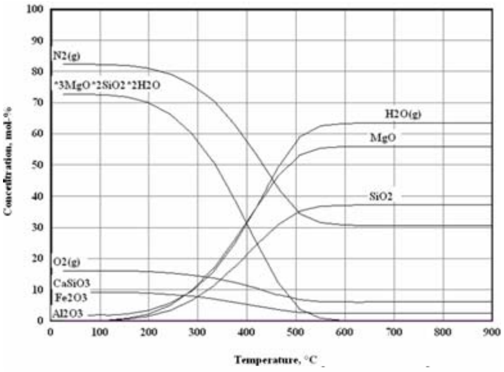

5a

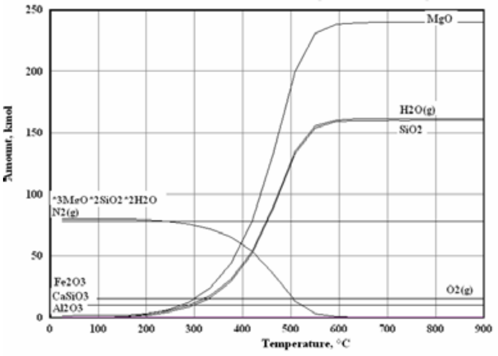

5b

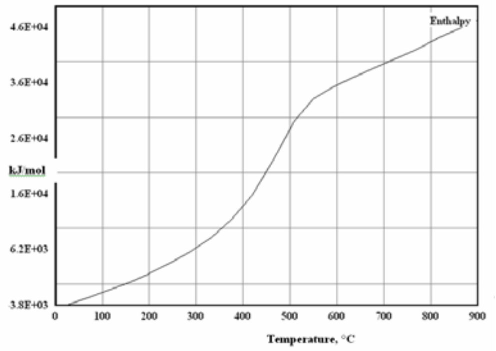

5c

Fig. 5a. Equilibrium composition of serpentinite thermal dissociation products at various temperatures.
Fig. 5b. Temperature dependencies of equilibrium amounts of serpentinite comprising components.
Fig. 5c. Reaction enthalpies of serpentinite heating at air gas mixture.

Mathematical simulation of heated serpentinite rock (Fig. 5a) has revealed that the main serpentinite component – serpentine ($3MgO{\cdot}2SiO_2{\cdot}2H_2O$) – starts decomposing at temperatures higher than 100 ^{0}C, and the concentration of MgO increases at almost the same temperature range. The amount of MgO (Fig. 5b) increases greatly from 100 °C and reaches the highest concentration at 500 °C. Fe_2O_3 concentration decreases slightly with a rise of temperature. According to results of thermodynamic simulation, heating in air environment allows producing substantial amounts of alkaline oxides (MgO, Fe_2O_3), which are suitable for subsequent sequestration of gaseous CO_2. A high content of iron in Lithuanian serpentinites may provide a unique opportunity for combined ore exploitation and CO_2 sequestration.

Heating of serpentinite in CO_2 environment. The behaviour of serpentinite-comprising compounds heated under CO_2 environment was analysed. Equilibrium composition, amount and enthalpies of serpentinite reactions with CO_2(g) under temperatures 25–900 °C, 1 bar pressure were simulated (Fig. 6), with the composition as described in Methods section. The forms of solid compounds and their amounts are similar to the case of heating in air environment, except that carbonates ($CaCO_3$, $MgCO_3$, $CaCO_3{\cdot}MgCO_3$, $CaMg(CO_3)_2$, $FeCO_3$) were included in analysis.

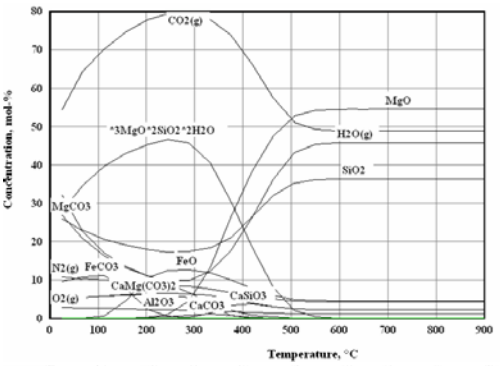

6a

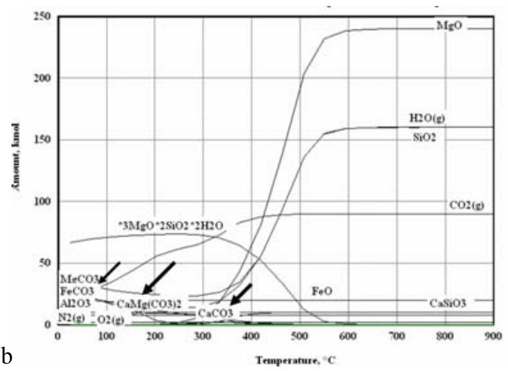

6b

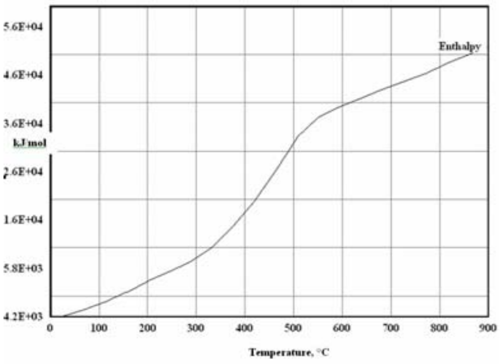

6c

Fig. 6a. Equilibrium composition of the compounds in serpentinite depending on temperature.

Fig. 6b. Temperature dependencies of equilibrium amounts of serpentinite comprising components.

Fig. 6c. Reaction enthalpies of serpentinite heating at CO_2(g) environment.

The carbonates already appear at relatively low temperatures (25 °C–200 °C), as shown in Fig. 6b, except of $CaCO_3$. which forms in 300 °C–500 °C temperature range. Thus, the results of this simulation of Lithuanian serpentinite reaction with CO_2(g) has confirmed the previous findings by Lackner (1997), that serpentines are suitable for rock carbonation [21].

4. CONCLUSIONS

A study on thermodynamical simulation of heating Lithuanian rocks, i.e. glauconite, opoka and serpentinite, in a clean air and CO_2-containing gas atmospheres has been carried out, with the aim to research the behaviour of particular rock at different temperatures. The equilibrium calculations of the rocks allowed evaluating theoretical potential of specific rocks to release alkaline oxides and bind CO_2, as well as setting the optimal conditions for experimental investigation of dry carbonation process.

Thermodynamic calculations with glauconite revealed that experimental research on dry glauconite carbonization is feasible at temperature range 200 °C–600 °C. Thus, glauconite as a raw material for dry carbonation purposes should be processed experimentally at atmospheric pressure and temperatures higher than 200 °C. The most important for carbonation purposes are Mg and Ca oxides and the carbonation of these oxides. The biggest concentrations of $MgCO_3$ were achieved at 100 °C- 300 °C, while 400 °C–600 °C was temperature range were the maximum level of $CaCO_3$ was formed. Iron is assumed to be as $FeCO_3$ in glauconite mineral.

The mathematical simulation of opoka has showed that Ca is already bound as carbonate ($CaCO_3$) in the mineral. MgO, Fe_2O_3, FeO and Al_2O_3 constitute relatively marginal amount in opoka mineral and could not be used for dry carbonation purposes. These suggests that opoka could hardly be used in dry carbonation process, although wet carbonization of opoka may be researched for its suitability for carbonation process.

In case of the thermodynamic evaluation of serpentinites, it was confirmed that the mineral is suitable for dry carbonation purposes. The temperatures between 100 °C–500 °C could be used for carbonation experiments as the highest amounts of $MgCO_3$ and $CaCO_3$ are formed.

The simulations given above were all made at atmospheric pressure. Increasing the pressure would allow for increasing the temperature to levels where the chemical reaction rates are becoming useful for technological applications while carbonates of Mg or Ca, for example, are thermodynamically stable and should not decompose.

REFERENCES

1. IPCC Special Report on Carbon Dioxide Capture and Storage; Intergovernmental Panel of Climate Change; Cambridge University Press, Cambridge, United Kingdom and New York, USA, 2005, p. 443.
2. SEIFRITZ, W. CO_2 disposal by means of silicates. *Nature*, 1990, p. 345–486.
3. DUNSMORE, H.E. A geological perspective on global warming and the possibility of carbon dioxide removal as calcium carbonate mineral. *Energy Conversion and Management*, 1992, Vol. 38, p. 259–264.
4. HOLLOWAY, S. Underground sequestration of carbon dioxide – a viable greenhouse gas mitigation option. *Energy*, 2005,Vol. 30, p. 2318–2333.
5. METZ, B.; DAVIDSON, O.; CONINCK, H.C.; LOOS, M.; MEYER, L.A. Special report on carbon dioxide capture and storage. Prepared by working group III of the intergovernemental panel on climate change. Cambridge: Cambridge University Press; 2005.
6. KOLJONEN, T., SIIKIVARTA, H., ZEVENHOVEN, R., SAVOLAINEN, I. CO_2 capture, storage and reuse potential in Finland. *Energy*, 2004, Vol. 29, p. 1521–1527.
7. SLIAUPA, S.; SATKUNAS, J.; SLIAUPIENE, R. Prospects of the CO_2 sequestration in Lithuania. *Geologija*, 2005, Vol. 51, p. 20–31.
8. HSC Chemistry for Windows, version 5.11. Outokumpu Research Oy; Pori, Finland, 2002.
9. LACKNER, K.S., WENDT, BUTT, C.H., JOYCE, D,P. SHARP, E,L.Carbon disposal in carbonate minerals. *Energy*, 1995, No. 20, p. 1153–1170.
10. GOFF, F.; LACKNER, K.S. Carbon dioxide sequestering using ultramafic rocks. *Environmental Geosciences*, 1998, Vol. 5, No 3, p. 89–101.
11. GASIUNIENE, V.E. Naudingosios iskasenos – ne vien kas auksu ziba. *Geologija-visuomenei*, 2000, Vol. 3, No 4, p. 13–19.
12. Lietuvos geologijos tarnyba. [referred on the 19th of March in 2010 y.]. Link to the internet < http://www.lgt.lt/index.php?page=68>
13. PRICKAITIENE, J. KAMINSKAS, J. GASIUNAS, K. Mineraliniu pigmentu gavimo is Lietuvos glaukonitu tyrimai. *Chemine technologija*, 1998, Vol.2, No 8, p. 41–45.
14. UAB Tavilta [referred on the 23rd of April in 2010 y]. Link to the internet <http://www.tavilta.lt/produktai_opoka>
15. STASIULAITINE, I. Denafas, G., Sliaupa, S. Lithuanian serpentines as potential carbon dioxide binders. The 32nd International Technical Conference on Coal Utilization & Fuel Systems. [CD]. Clearwater, Florida, 2007 June 10–15. ISBN 0-932066-32-1, p. 429–440.
16. SHOEGENOVA, A. FABRICIUS L.I., KORSBECH, U., RASTENIENE. V., SLIAUPA. S. Glauconitic rocks in the Baltic area: estimation of specific surface. Proceedings of the Estonian Academy of Sciences. Geology. 2003 No 52(2), p. 69–86.
17. KUUSIK, R., VIISIMAA, L. A new dual coagulant for water purification. *Water Res.* 1999. Vol. 33, No 9, p. 2075–2082.

18. SKRIDLAITE G., MOTUZA G., Precambrian domains in Lithuania: evidence of terrane tectonics. *Tectonophysics*, 2001, No 339, p. 113–133.
19. JANICKIS, J. Fizikine chemija. Vilnius: Mokslas, 1987.450 p. M 854 (08)-87.
20. HUIJGEN, W.J., COMANS, R.N.J. Carbon dioxide storage by mineral carbonation. IEA GHG report 2005/11; Energy Research Center of the Netherlands; Cheltenhem, UK.
21. LACKNER, K.S. Carbonate chemistry for sequestrating fossil carbon. *Annual review of Energy and Environment,* 2002, 27, p. 193–232.
22. ZIOCK, H. Zero emissions coal to hydrogen. [referred on the 19th of March in 2010 y]. Link to the internet <http://www.lanl.gov/energy/ziock.html> (2000)
23. LACKNER, K.S. A guide to CO_2 sequestration. *Nature*, 2003, Vol. 300, p.1677–1678.
24. SIPILA, J.; TEIR, S.; ZEVENHOVEN, R. Carbon dioxide sequestration by mineral carbonation. Literature review update 2005–2007. Report 2008 -1; Abo Akademi University, Faculty of Technology. Heat Engineering Laboratory: 2008.

THE ANALYSIS OF 40 MM DIAMETER PIPE RUPTURE IN FUSION FACILITY W7-X WITH ASTEC CODE

Tomas Kačegavičius
Lithuanian Energy Institute
Breslaujos g. 3, LT-44403 Kaunas, Lithuania
Phone: +370 37 401928
Email: tomas@mail.lei.lt

ABSTRACT

Fusion is the energy production technology, which could potentially solve problems with growing energy demand of population in the future. Wendelstein 7-X (W7-X) is an experimental stellarator facility currently being built in Greifswald, Germany. The W7-X facility shall demonstrate that in future the energy could be produced in such type of fusion reactors.

This paper presents the model of W7-X targets cooling circuits developed for ASTEC code. The analysis of loss-of-coolant accident during no-plasma operation mode “baking” (rupture of the 40 mm target cooling pipe) was performed. “Baking” is the mode of facility operation during which the vacuum vessel structures are heated to the temperature required for the plasma ignition.

The performed analysis has shown the response of W7-X “baking” and cooling circuits to the rupture of 40 mm diameter pipe. The analysis provided the amount of coolant released through the ruptured pipe into the vacuum vessel, which is needed for the assessment of the pressure build-up in the plasma vessel.

Key words: W7-X, loss-of-coolant accident, ASTEC

1. INTRODUCTION

At present there are two experimental fusion reactors under construction: International Thermonuclear Experimental Reactor ITER, which is constructed in Cadarache (France) and Wendelstein 7-X (W7-X) (in Germany). ITER will be designed to produce ~500 MW of fusion power sustained for up to 400 seconds. Wendelstein 7-X (W7-X) is a stellarator, which shall demonstrate that in the future energy could be produced in such type of fusion reactors. It is presently under construction at the Max-Planck-Institute for Plasmaphysics, Greifswald, Germany. The superconducting magnet system enables continuous operation, limited only by the plasma exhaust cooling water system whose capacity is designed for 30 minutes full power operation.

Prior to start of the operation of the facility its safety has to be demonstrated by performance of the safety analysis. The ingress of water during the W7-X no-plasma operation modes “Baking” and “Hot Liner” into the plasma vessel represents one of the most critical failure events, since primary and secondary steam production leads to a rapid increase of the inner pressure in the vessel. It should be noted that during “Baking” no plasma in the plasma vessel exists, i.e. no special models for plasma simulation are required. Such event could lead to loss of vacuum condition up to overpressure in the plasma vessel, damage of in-vessel components and diagnostics as well as bellows of the ports. Therefore increase of pressure in excess of 1.1 bar must be avoided by means of active (safety valves) and passive safety devices (burst disk, mass loaded disk).

This paper presents the analysis of loss-of-coolant accident (LOCA) in W7-X facility. This paper also includes short description of ASTEC code, which was selected for the analysis of the event, and the description of W7-X cooling system.

Since the W7-X facility is now under construction, in parallel accident analysis is carried out and the results are very important. Based on this analysis results, it may make minor design changes (change for safety systems operation algorithm, closing time of the valve and etc.).

2. W7-X TARGET COOLING SYSTEM

The plasma vessel in W7-X facility consists of the five modules having the same configuration and volume (Fig. 1). The one module is composed of two half-modules (divertors) which are divided into two sectors to allow stringing of the innermost coil during assembly. The temperature of the wall surface of the plasma vessel made of steel is 150°C. The thickness of the wall is 17 mm. According to [2,3] the plasma vessel should be modelled using a simplified geometry of the torus with a major radius of 5.5 m and a minor radius of 1 m with a free volume of 108.5 m^3. The weight of the plasma vessel is 32.6 t, the weight of the ports, which are hot too, is 62.5 t. The vessel components consist of the target plates, baffles, panels and heat shields, control coils, cryo-pumps, port protection and special port liners and the complex system of cooling water supply lines [3]. Each divertor unit is assembled from 12 separate horizontal and vertical targets (see Fig. 2). Fig. 2 shows model of one divertor target module with a total plasma facing surface of about 2 m^2. Most part of the target can withstand heat loads of up to 10 MW/m2 and the middle part of the horizontal target plate has to withstand only power loads up to 1 MW/m^2.

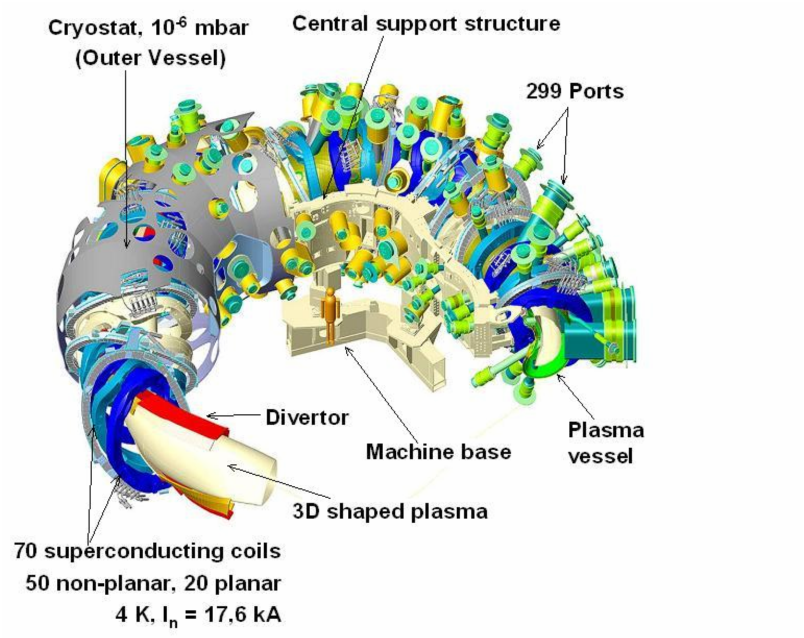

Fig. 1. Fragment of W7-X torus

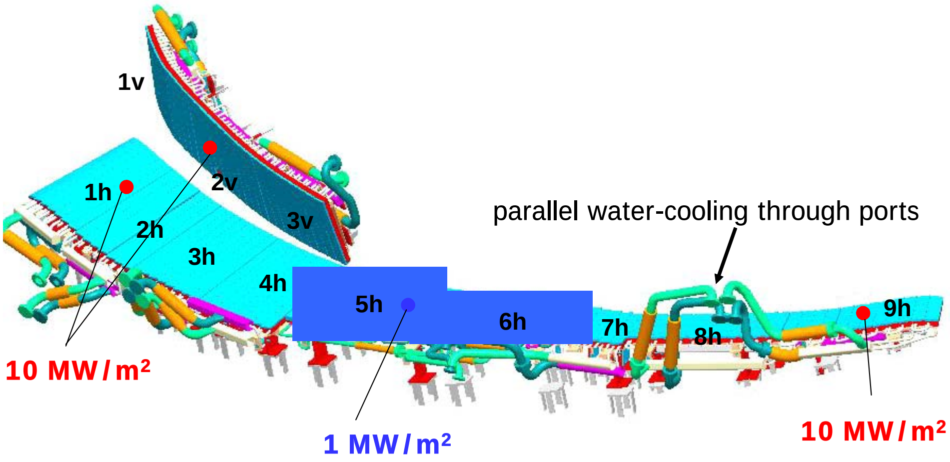

Fig. 2. W7-X divertor target module with horizontal and vertical targets

W7-X facility target cooling system consists of two circuits. One of these is called the Main Cooling Circuit (MCC) and another one the “Baking” circuit. MCC is used for cooling of targets when W7-X facility is on normal operation. Before normal operation and ignition of plasma in plasma vessel the targets and other components must be warmed up. “Baking” circuit mainly is used for this purpose. Both MCC and “Baking” circuits are connected together and supply water to the same targets. During operation of W7-X in “Baking” mode, all target inlet valves of MCC are closed, but contention with “Baking” circuit still exist by bypass. Thus, it is necessary to know all targets cooling system (Fig. 3).

The zero point for the W7-X elevation is in the centre of the torus. The highest point (pipes to the upper ports of the outer vessel) is about +3.5 m. The connections to the lower ports are at -3.5 m. The components Heater, Pump, Nitrogen Pressure Vessel are located at -8.1 m. The automatic valves at the module manifolds are at ~0 m.

The height of the pressurizer is 2850 mm (2100 mm for the cylindrical part), and the diameter is 1250 mm, leading to total volume of 2500 l. Volume ratio nitrogen/water is about 0.5. The nitrogen pressure in the pressuriser is controlled between 9-11 bar leading to 10 bar static pressure [1].

The power of the heater is 180 kW. The heater is a simple cylinder of diameter 270 mm and length 1950 mm in horizontal position. The electrical heater wires are just inside the vessel. There is no inner pipe system inside the heater.

There is only one pump for all target loops in the operation mode “Baking”. For the MCC there are other pumps available, but here for the defined analysis not of concern.

The maximum water temperature is 160 °C, the water pressure is about 1.0 MPa under the W7-X “baking” conditions. The corresponding mass flow of water in the “Baking” circuit is 177m^3/h (44.6 kg/s), the flow velocity through the cooling tubes of the target elements during “baking” operation is about 1 m/s [1].

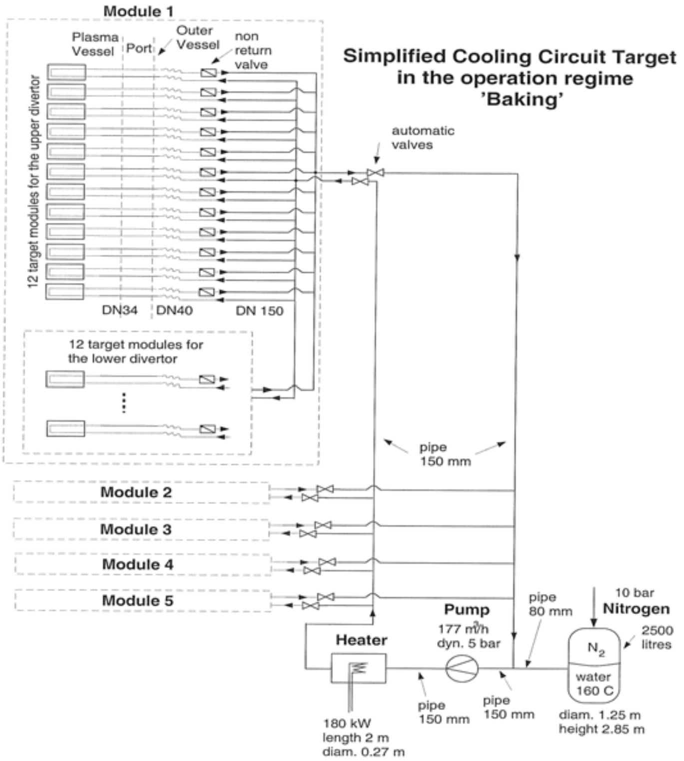

Fig. 3. Simplified scheme of Main Cooling and "Baking" circuits

This analysis assumes a rupture of the 40 mm diameter target module pipe near the flange of the outer vessel, right at the place of the inner surface of the torus, during the vessel "Baking" operation mode. It was qualified as the leading to the one of the most severe consequents [3].

3. DEVELOPMENT OF MAIN COOLING AND "BAKING" CIRCUITS MODEL USING ASTEC CODE

The analysis of LOCA in W7-X facility was performed using the integral code ASTEC. ASTEC (Accident Source Term Evaluation Code) – is an integral code for Light Water Reactors source term severe accident calculation, from the initiating event until radioactive release out of the containment [4]. Now the integral code ASTEC is used for the modelling of the ITER (International Thermonuclear Experimental Reactor). ASTEC code consists of several modules, which are developed for the analysis of separate tasks.

CESAR module simulates the whole front-end phase in the vessel (with a simplified core modelling) and in the loops, and then, after the beginning of core degradation phase, two-phase thermal-hydraulics in the loops and in the vessel upper plenum only. The models are based on a thermal-hydraulics simulator code, the physical models of which were derived from the reference French CATHARE thermal-hydraulics code [4]. Two phases are considered: water and gas (steam + 1 non-condensable gas). The system is made of 5 scalars mass and energy conservation equations associated with 5 state variables.

The reactor cooling system is discretised in volumes (one mesh), either homogeneous or with a swollen level, in axial meshed volumes and in junctions. Thermal non-equilibrium is simulated by separated mass and energy balance equations supported by interfacial mass and heat transfer models. The wall heat transfer models close the energy balance equations.

Mechanical non-equilibrium is simulated by a set of algebraic drift correlations for vertical and horizontal flow paths. The wall shear model closes the momentum balance equation. Special components could be defined to simulate pumps and ruptures of the piping.

This paper presents the analysis of W7-X target 40mm pipe rupture. The results of LOCA analysis will be further used in the plasma vessel model developed for CPA module. CPA [4] module is used for simulation of thermal-hydraulics and aerosol behaviour in containment. Lumped-parameter approach (volumes represented by nodes connected by junctions) in simple or multi-compartment containments (tunnels, pit, dome etc.) with possible leakages to the environment or to normal buildings, with more or less large openings to the environment.

The other modules DIVA, ELSA, SOPHAEROS, RUPUICUV, MEDICIS and IODE are not relevant for the selected accident scenario simulation in the fusion type facility.

For the modelling of selected accident (40 mm target pipe rupture) in “Baking” operation mode it is enough to develop detail model of “Baking” circuit. Thus, it was decided to develop detailed model of both connected circuits (Fig. 4). The measurements (pipe lengths, elevations, pump parameters, heater power and valves parameters) and configuration of pipes (it is necessary for evaluation of form loss coefficients) were taken from W7-X facility design.

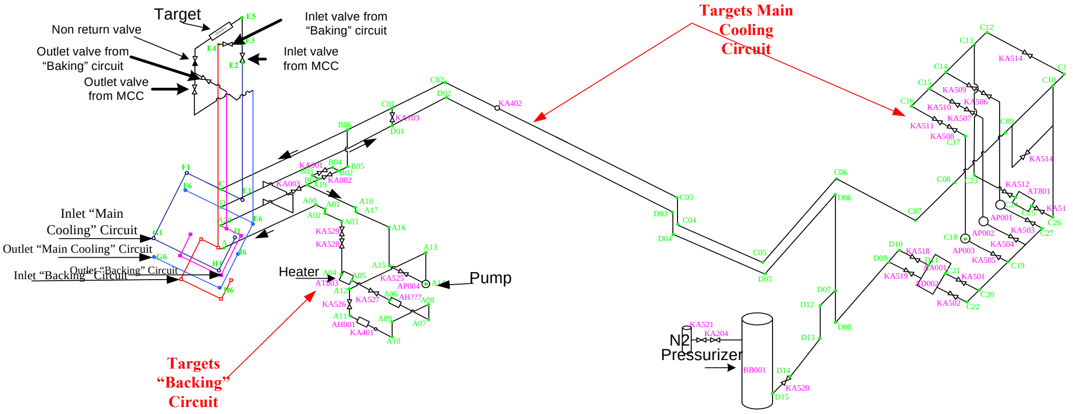

Fig. 4. Nodalisation scheme of “Baking” circuit.

The simplified scheme for modelling of targets (nodalisation scheme) was developed (see Fig. 5). As it is seen from presented scheme, four target modules are modelled as simplified one equivalent element: “F5-F5”, “G5-G5’”, “H5-H5’”, “J5-J5’”.

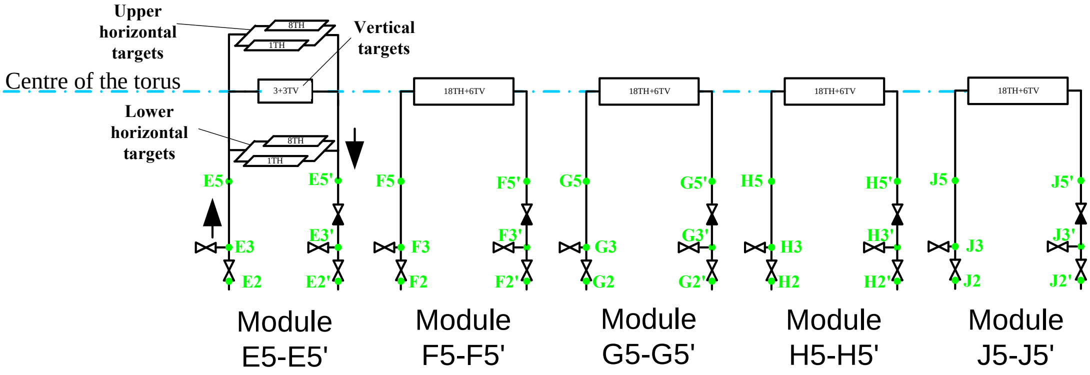

Fig. 5. Modelling of targets (nodalisation scheme)

One of target modules is modelled in more extended format: the two single targets were selected (one in upper and one in lower position). These upper and lower single elements allows to model rupture of single target feeder pipe. The Target Module "E5-E5" is modelled in more detailed manner (see **Klaida! Nerastas nuorodos šaltinis.**). The pipe elements "136", "137", "139" and "140" are used for modelling of upper and bottom horizontal Targets. Six vertical Targets are modelled by employing "138" pipe element. Element "146" is identical to "130", element "139" – to "136" and element "140" – to "137". For modelling of double ended guillotine break the ASTEC/CESAR connection module BREAK is used. Element "199" models the volume inside the plasma vessel with pressure equal 0.01 bar.

The pump in the model was described by a pressure difference as a function of the flow rate. Pump model STRU PUMP available in the ASTEC code is used. For the modelling of the pressurize a special type of node "swollen water level" was used. Volume ratio nitrogen/water is about 0.5.

The valves from MCC and "Baking" circuit on inlet and outlet were modelled using ASTEC/CESAR module STRU SYSTEMS/VALVE. The non-return valves were modelled by a difference of the proportionality coefficients used in the calculation of the local pressure loss for reverse flows.

The heater was modelled by the heat structure with defined initial temperature and the heat source of 180 kW. In this modelling the ASTEC module STRU WALL is used.

4. ANALYSIS OF 40 MM DIAMETER PIPE RUPTURE IN "BAKING" OPERATION

This section presents the calculation results of break in 40 mm feeder pipe, connecting single upper horizontal target. Double ended guillotine break of 40 mm pipe, when W7-X is operating in "Baking" mode, was modelled with the ASTEC integral code [4]. Initial conditions water temperature in the "Baking" circuit is 433.16 K (160 C) and density – 907 kg/m^3. The water flow rate through "Baking" circuit is 177 m^3/h (44.6 kg/s). Pressure in plasma vessel is equal 1000 Pa. Valves from main cooling circuit to targets are closed on inlet and on outlet. Valves from "Baking" circuit on inlet and outlet are open.

In this paper there are described the following possible scenarios of events:

1. Double ended guillotine break of DN40 pipe in the upper target.
2. Double ended guillotine break of DN40 pipe in lower target.

4.1. Double-ended guillotine break of upper target

In the model it was assumed that the break occurs in the module E5-E5' (see Fig. 5). The break occurs in DN40 mm feeder pipe, connecting single upper horizontal target (element "136" in Fig. 6). Double ended guillotine break of DN40 pipe was modelled.

Table 1 The following events were assumed to occur:

1.	T = 0.0 s	Double ended guillotine break of DN40 (inner diameter 0.0443 m) occurs.
2.	T = 1.14 s	Trip of pump on "Baking" circuit
3.	T = 1.64s	Closure of valves on Target inlets begins.
4.	T = 6.64s	Valves on Target inlets are fully closed.

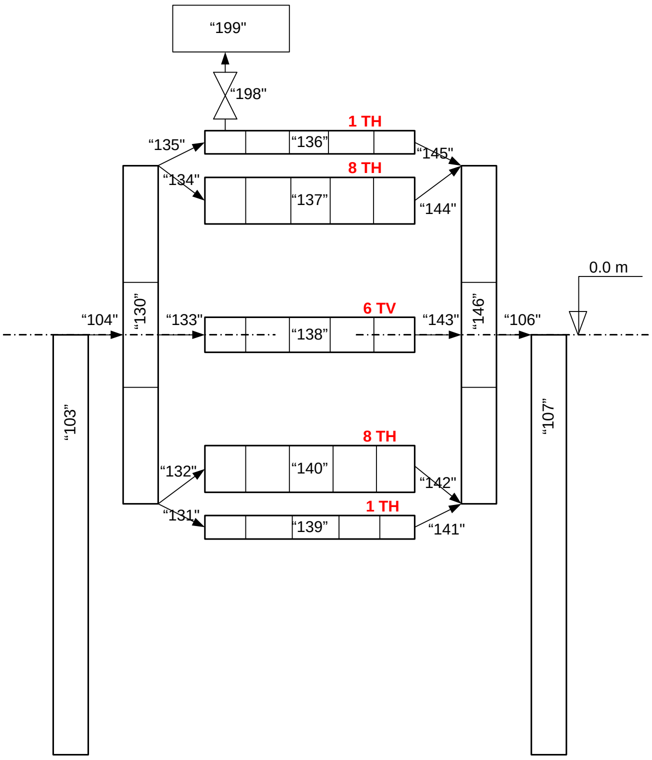

Fig. 6. Nodalisation scheme of affected module E5-E5' with failure of upper horizontal target

The discharge of coolant through the break is presented in Fig. 7. As it is presented in the figure, the water flow in the "Baking" circuit stops after the closure of automatic valves. After closure of the inlet automatic valve the discharge of the coolant through the break slightly decreases, but the water from other targets in this module is discharged till pressure in this module decreases down to the pressure in the plasma vessel. The pump trip begins about 1.14 s after the brake, thus leading to pressure decrease in the pump outlet (see Fig. 8). Since the inlet automatic valves are closed, the water is discharged only from the affected module. The pressure in other modules drops down to the approximately 0.6 MPa and remains constant, because the automatic valves have isolated them. The process of emptying of the targets in affected target module can be understood from Fig. 9. These figures show the behaviour of void fraction in the targets is presented Alfa = 0 means pure water, Alfa = 1 – pure steam. As it is shown in **Klaida! Nerastas nuorodos šaltinis.**, affected target "1TH – upper" and other targets will be empty after approximately 37 s, but small amount of water (2 kg) remains in the lower targets.

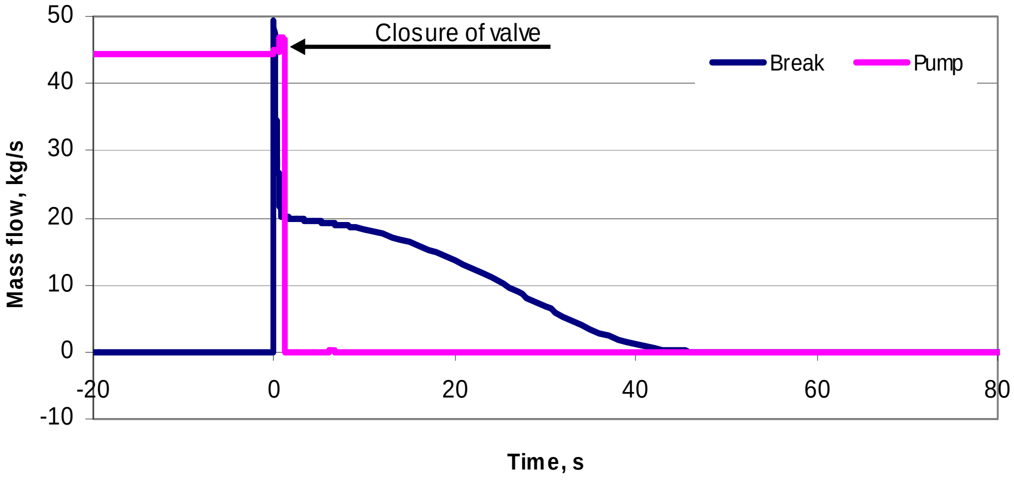

Fig. 7. Break of upper target. Water flow rate through the pump and discharge of coolant through the break

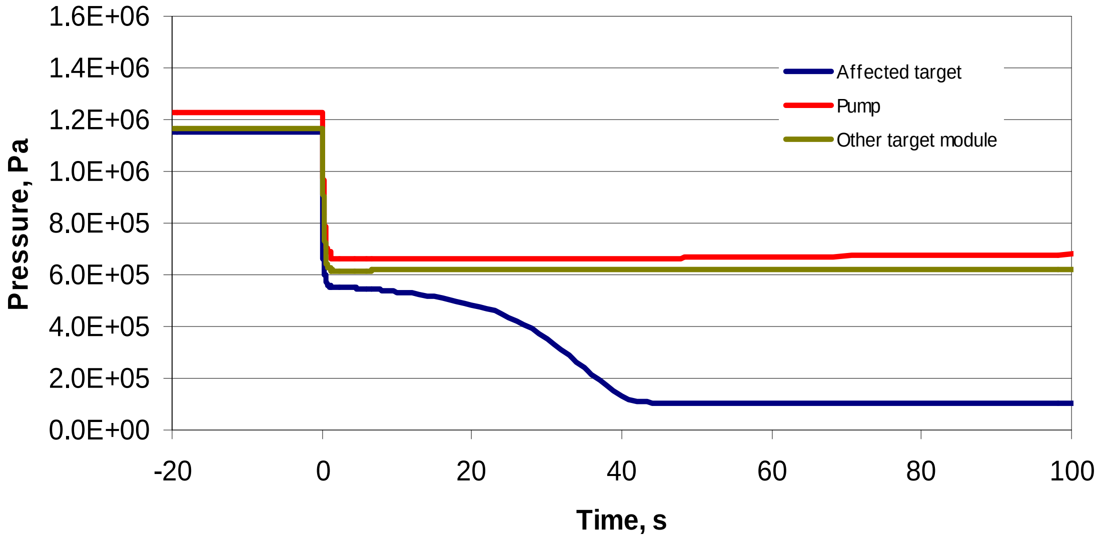

Fig. 8. Break of upper target. Pressure in “Baking” circuit

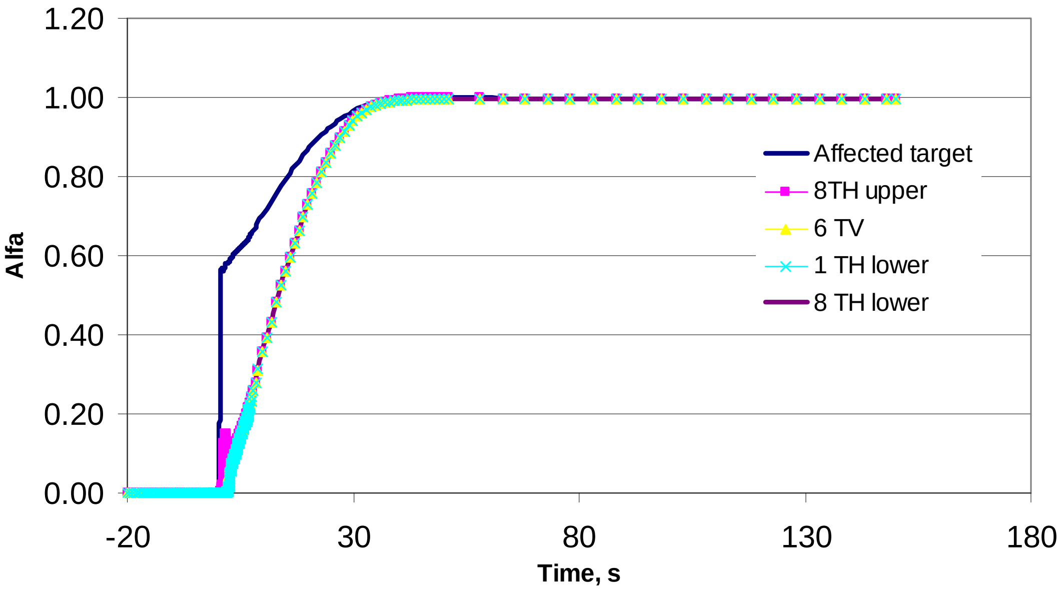

Fig. 9. Break of upper target. Void fraction in the affected target module

4.2. Analysis of double ended guillotine break of lower target

This section presents the analysis of pipe break in the lower target. In the analysis it was assumed that the break occurs in the module E5-E5’ (see Fig. 5). The break occurs in DN40 mm feeder pipe, connecting single lower horizontal target (element “139” in Fig. 10). The boundary conditions are the same as in the previous case (see section 4.1).

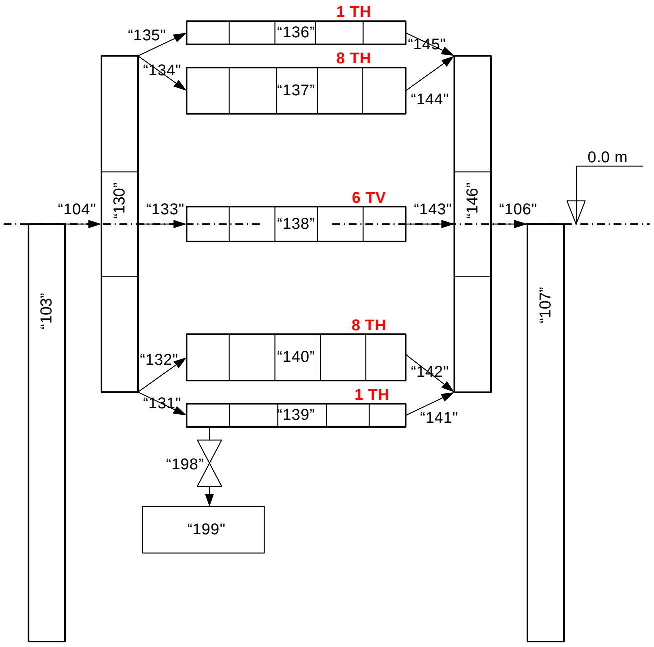

Fig. 10. Nodalization scheme of affected Module

The discharge of the coolant through the break is presented in Fig. 11. After closure of the inlet automatic valves, the discharge of coolant through the break slightly decreases, but the water from other targets in this module is discharged till pressure in the affected targets decreases down to the pressure in the plasma vessel (the same as in the previous case). Comparison of amount of water discharged through the break in both cases (break of upper and lower targets) is shown in Fig. 12. This picture shows that very small amount of water (2 kg) remains in the lower targets if the break occured in the lower target, because position of the break is lower.

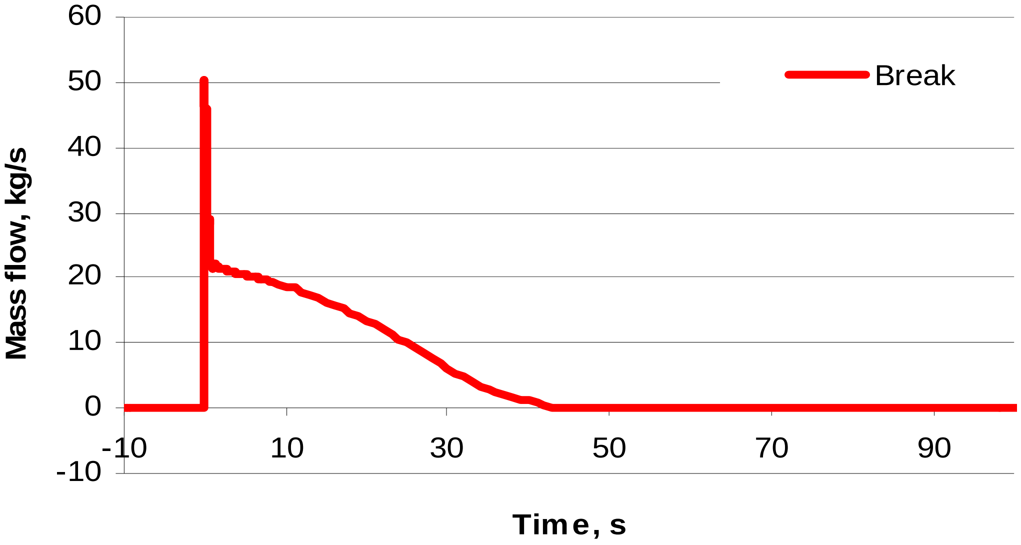

Fig. 11. Break of lower target. Water flow rate through the break

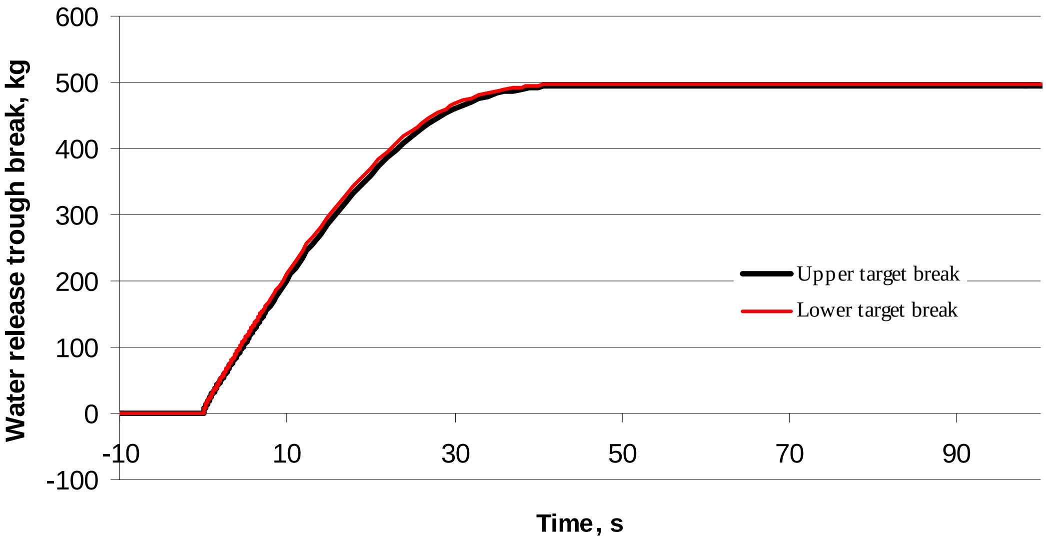

Fig. 12. Comparison of upper and lower target break scenarios. Total water release through the break

5. CONCLUSIONS

1. The models of target cooling system in W7-X facility were developed by ASTEC code. In this paper 2 scenarios of double ended guillotine break of DN40 pipe in upper and lower target inlet are presented.

2. Results of analysis showed, that the closure of automatic valves allows to decrease the amount of discharged water through the rupture, that allows to slowdown the pressure increase in plasma vessel.
3. Amount of water discharged through the break is slightly larger in case of the double ended guillotine break of the pipe in the lower target, comparing to the upper target break case.
4. Further, for the LOCA analysis the plasma vessel model, developed by employing CPA module in ASTEC code, will be used.

6. ACKNOWLEDGEMENT

Authors acknowledge the support of Agency for International Science and Technology Development Programmes in Lithuania and European Commission for preparation of this paper.

REFERENCES

1. D. Naujoks, Initial and Boundary Conditions, 1-NBF-T0008.0, Max-Plank-Institut für Plasma Physik, 2006, p. 2–4.
2. B. Streibl et al., “Manufacturing of the W7-X divertor and wall protection”, Proc. 23rd Symp. Fusion Technology, Venice, Italy (2004).
3. “Wendelstein 7-X, Overview and Status of Construction”, Hans-Stephan Bosch a and the Wendelstein 7-X Team, a Max-Planck Institut für Plasmaphysik, Branch Institute Greifswald, Euratom-IPP Association, D-17491 Greifswald, Germany, p. 1–4.
4. J.P Van Dorsselaere, B. Schings, ASTEC V1.3 rev0 Users Manuals (modules CESAR, DIVA, ELSA, SOPHAEROS and SYSINT) CD, December 2006.

ANALYSIS OF WATER HAMMER EFFECT IN W7-X FACILITY

Tadas Kaliatka
Lithuanian Energy Institute
Laboratory of Nuclear Installation Safety
Breslaujos g. 3, LT-44403 Kaunas, Lithuania
Phone: +37037401911
Email: tadas@mail.lei.lt

ABSTRACT

Fusion is the energy production technology, which could potentially solve problems with growing energy demand of population in the future. Wendelstein 7-X (W7-X) is an experimental stellarator facility currently being built in Greifswald, Germany, which shall demonstrate that in the future energy could be produced in such type of fusion reactors. Prior to start of the operation of the facility its safety has to be demonstrated by performance of the safety analyses. Rupture of the 40 mm target cooling pipe during "baking" operation was selected as the most hazardous event. This accident could lead to loss of vacuum condition up to overpressure in the plasma vessel, damage of in-vessel components. "Baking" operation mode is the regime of the facility operation during which plasma vessel structures are heated to the temperature acceptable for the plasma ignition in the vessel. One of safety systems preventing the overpressure of plasma vessel is automatic valves in target inlets. These valves must be closed during loss-of-coolant accident. Fast closure of valves means smaller amount of water discharged and the less pressure in plasma vessel. On the other hand, very fast closure of valve can lead to pressure pulse in targets cooling system - water hammer effect. The high pressure peak may lead to failure of W7-X cooling system pipelines.

This paper presents the model of W7-X target modules cooling circuits developed with RELAP5 code. The water hammer effect analyses of loss-of-coolant accident during "Baking" operation mode have been performed using developed model. The performed analysis showed, that 1s closure time of the target modules inlet automatic valve is the most predictable.

Keywords: Wendelstein 7-X, stellarator, plasma vessel, RELAP5, water hammer

1. INTRODUCTION

Fusion power is the power generated by nuclear fusion reactions as it is in the sun. In this kind of reaction, two light atomic nuclei fuse together to form a heavier nucleus and in doing so, release a large amount of energy. It has been tried for more than 60 years to recreate the basic energy process of the sun in a contained and controllable form on Earth. Results of major research attempts by numerous prominent institutions did indeed prove the possibility of nuclear fusion in controlled laboratory experiments. But experiments did not yet achieve a continuous and positive energy gain. It is therefore that were decided to build a larger scale fusion test reactors. At the present there are few experimental fusion reactors under construction: ITER, which is constructed in France, KSTAR in South Korea, Wendelstein 7-X (W7-X) in Germany and others.

In contrast to the tokamak concept (used for ITER and KSTAR), where the poloidal component of the magnetic field is generated mainly by an induced current flowing in the plasma, in stellarators, the vacuum magnetic field for plasma vessel is produced entirely by external currents allowing steady-state operation.

The stellarator W7-X is presently under construction at the Max-Planck-Institut für Plasmaphysik, Greifswald, Germany [1]. The superconducting magnet system enables continuous operation, limited by the cooling water system whose capacity to remove the plasma heat load onto the wall components is designed for 30 minutes full power operation.

Prior to the commissioning of the facility its safe operation has to be proved by dedicated safety analyses. The ingress of water during the W7-X no-plasma "baking" operation mode into the plasma vessel represents one of the critical failure events, since primary and secondary steam production leads to a rapid increase of the inner pressure in the vacuum (plasma) vessel. A rupture of the 40 mm target cooling pipe could lead to the loss of vacuum condition up to an overpressure in the plasma vessel, damage of in-vessel components and diagnostics as well as bellows of the ports [2, 3]. The amount of discharged water through the leak in the plasma vessel should be estimated in order to analyse processes, which can be harmful to the plasma vessel or other W7-X components. The amount of water discharge depends in particular on the automatic valve, which isolating the leak, operation (closure time). The fast closure of automatic valves gives smaller water discharge through the brake, but it can be a cause of water hammer effect. The water hammer effect is pressure surge wave when water in motion is forced to stop due to sudden closure of valve. In the case of sudden closure, the mass of water before the closure point is still moving forward with some velocity, building up a high pressure and shock waves. Also closure of valves means the sharp change of velocity of water flow, thus the kinetic energy of water is transformed to pressure pulse. The highest values of pressure pulsation occur in the pipelines, which are close to the automatic valve in affected target (because the highest change of water velocities is through the valve, connected to broken pipe). In our analysed case (break in target feeder pipe) the pressure pulsations occur after fast closure of automatic valves in targets inlet. Theoretically from the Joukowsky equation [4], the maximum magnitude of the water hammer is:

$$\Delta P = \rho \cdot a \cdot \Delta C, \tag{1}$$

where: ΔP is the magnitude of the pressure wave (Pa); $\Delta P = P_{max} - P_0$ (P_{max} is the maximal pressure peak; P_0 is the initial pressure in the system); ρ is the density of the fluid (kg/m^3); a is the speed of sound in the fluid (m/s), and $\Delta C = C_i - C_0$ (C_i is the initial water velocity; C_0 final water velocity) is the change in the fluid's velocity (m/s).

For the analysed case, the water density ρ is ~907 kg/m^3; the initial pressure $P_0 = 1.2$ MPa; the initial water velocity $C_{max} = 5 - 6$ m/s; the final water velocity $C_0 = 0$ m/s; $\Delta C \approx 5.5$ m/s; the speed of sound a in the water is ~1440 m/s. Thus, according Joukowsky equation, the possible maximal water hammer pressure pulse is $\Delta P \approx 7.5$ MPa.

For the above mentioned reason in this paper the water hammer effect and the influence of automatic valve closure time to water discharge in to plasma vessel were analysed.

2. W7-X TARGET MODULES COOLING SYSTEM

The plasma vessel in W7-X facility is composed of ten divertor units, which are divided in two sectors to allow threading of the innermost coils during assembly (see Fig. 1). The in-vessel components consist of the divertor units, baffles, panels and heat shields, control coils, cryo-pumps, port protection and special port liners, and the complex system of cooling water supply lines as well different diagnostics. Each divertor unit is assembled from 12 separate horizontal and vertical target modules (see Fig. 2) capable to remove maximum 10 MW/m^2 convective stationary power load [2].

The zero point for the W7-X elevation is in the centre of the torus. The highest point (pipes to the upper ports of the outer vessel) is at elevation about +3.5 m. The connections to the lower ports are at -3.5 m. Fig. 2 shows the lower divertor unit with 12 target modules and a total plasma facing surface of about 2 m^2. The high-heat-load part of the divertor unit (10 target modules) can withstand heat loads of up to 10 MW/m^2, the middle part of the horizontal target modules has to withstand only power loads up to 1 MW/m^2. These sections of the ten divertor units have a total area of about 5.6 m^2 composed of 20 target modules with a total of 240 target elements [2].

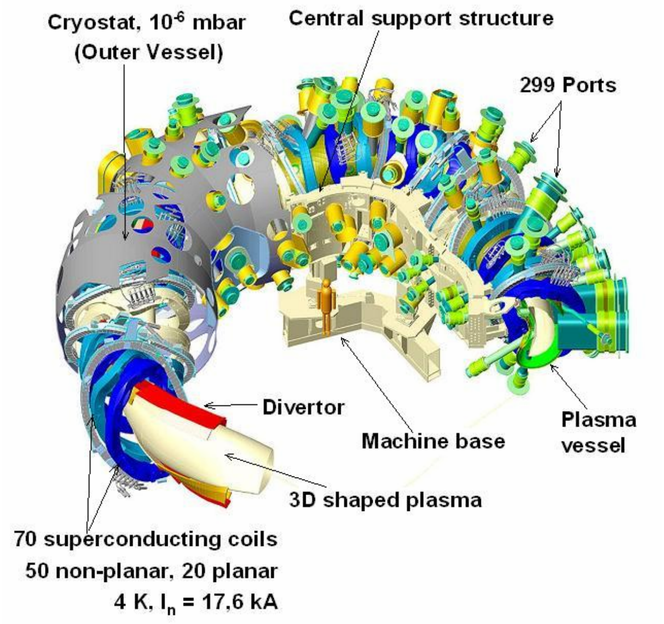

Fig. 1. Fragment of W7-X torus [1]

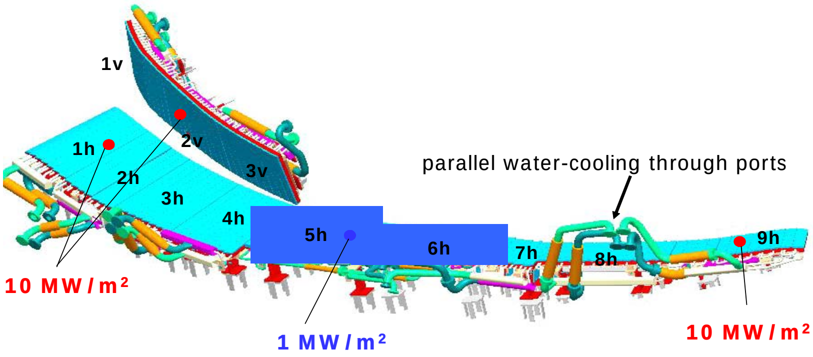

Fig. 2. W7-X divertor unit with horizontal (1h-9h) and vertical (1v-3v) target modules [6]

The W7-X facility target modules cooling system consists of two coolant circuits: The Main Cooling Circuit (MCC) and the so-called “Baking” circuit. The MCC is used for cooling of the target modules when the W7-X facility under normal operation. Before plasma operation, the target modules and other in-vessel components must be heated up in order to “clean” the surfaces by thermal desorption and the subsequent pumping out of the released volatile molecules. The “Baking” circuit is mainly used for this purpose. Both MCC and “Baking” circuits are connected together and supply water to the same target modules. During operation of W7-X in the “baking” mode, the heat, necessary for target modules heating is generated in electrical heater. There is only one pump for all target modules loops in the “baking” operation mode. For the “cooling” operation mode there are other pumps available in the MCC, but here for the defined analysis not of concern. To maintain constant pressure in “Baking” circuit, the pressurizer pressurized by nitrogen. The components heater, pump, nitrogen pressurizer are located at elevation -8.1 m. The automatic valves at the module manifolds are at elevation ~0 m. The height of the pressurizer is 2.85 m (2.10 m for the cylindrical part), the diameter is 1.25 m, with a total volume of 2.5 m^3. The volume ratio nitrogen/water is about 0.5. The nitrogen pressure in the pressurizer is controlled between 0.9 – 1.1 MPa leading to a ~1.0 MPa static pressure [1].

According the drawings presented by facility developers the amount of water in the all pipelines, connecting the target modules with the both MCC and the “Baking” circuits are 1.66 m^3. The largest amount of water is used in the MCC – 63.1 m^3, while the amount of water in “Baking” circuit is very small – 1.06 m^3. The volume of water in single torus module (two divertor units with 12 target modules each) is ~0.457 m^3, thus the total volume of water in all five tours modules is 0.457 * 5 = 2.28 m^3. The water is provided to the upper and lower target modules in each torus module through lower and upper ports. A simplified scheme of the circuits is shown in Fig. 3.

The maximum water temperature is 160 °C, the water pressure is about 1.0 MPa under the W7-X “baking” operation mode. The corresponding mass flow of water in the “Baking” circuit is 177 m^3/h (44.6 kg/s), the flow velocity through the cooling tubes of the target modules during “baking” operation mode is about 1 m/s [3].

As it was already mentioned the rupture of 40 mm diameter target module pipe near the flange of the outer vessel, close to inner surface of the tours, during “baking” operation mode was selected for the analysis. It was qualified as presumptive leading to the pressurization of the plasma vessel, which could endanger its structural integrity. It should be noted that during “baking” operation mode no plasma in the plasma vessel exists, i.e. no special models for plasma simulation are required. To stop the water discharge to the plasma vessel, the automatic valves are placed in the target modules inlets. According to the algorithm of valves control, they automatically closes when the pressure in plasma vessel exceeds 2000 Pa. Fast closure of these valves is very important, but it could induce a water hammer. Water discharge to the plasma vessel depending on closure time and the effect of water hammer are analysed in section 4.

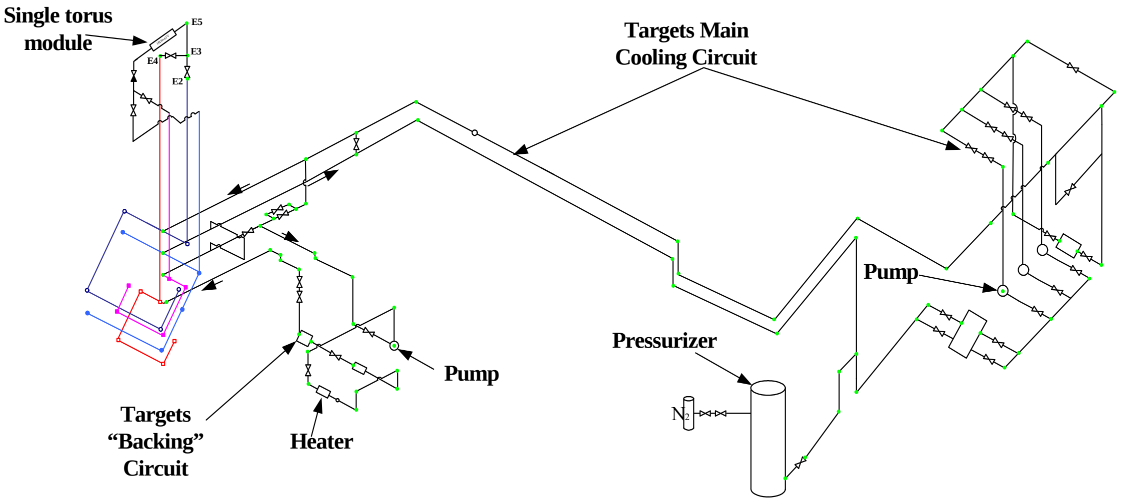

Fig. 3. Simplified scheme of Main Cooling and “Baking” circuits

3. DEVELOPMENT OF MAIN COOLING AND “BAKING” CIRCUITS MODEL

The analysis of LOCA in W7-X facility was performed using integral code RELAP5 Mod 3.3 [7]. In the Lithuanian Energy Institute, the RELAP5 code is used since 1993 for Ignalina Nuclear Power Plant licensing purposes (for the analyses of the thermo-hydraulic response of the plant to various transients). Obtained knowledge of RELAP5 application to analyse thermo-hydraulic processes was used to model the processes in targets cooling circuit of W7-X facility.

For the modeling of the selected accident (40 mm target module pipe rupture) in “baking” operation mode it is sufficient to develop a detailed model of the “Baking” circuit (see Fig. 4). However both MCC and “Baking” circuit are interconnected. Thus, it was decided to develop a detailed model of both circuits. The measurements (pipe lengths, elevations, pump parameters, heater power and valves parameters) and the configuration of pipes (necessary for evaluation of form loss coefficients) were taken from the CAD drawings provided by the W7-X design office.

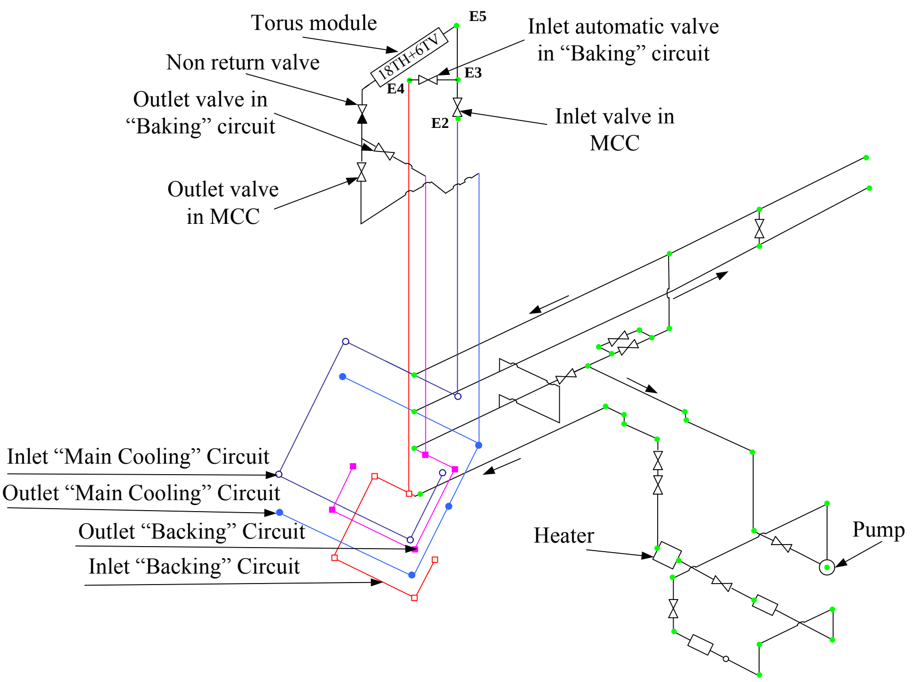

Fig. 4. Nodalization scheme of the “Baking” circuit

The W7-X cooling system supplies 5 torus modules. Each torus module is composing of 18 horizontal and 6 vertical target modules. The horizontal target modules can be grouped in 9 upper and 9 lower target modules. The simplified scheme for modeling of target modules (nodalization scheme) was developed (see Fig. 5). Four torus modules are modeled as equivalents (with the corresponding water volume and hydraulic resistance). One of torus modules is modeled in more extended format. In this torus module, the upper and lower, horizontal and vertical target modules were modeled separately. From horizontal target modules two single target modules were selected: one in upper and one in lower position (see Fig. 5). These elements of single target modules allow to model rupture of single target module. As it is seen from presented scheme, 4 torus modules are modeled as simplified one equivalent element: F5-F5’, G5-G5’, H5-H5’, J5-J5’. The main cooling circuit inlet valves are marked as E2, F2, G2, H2, I2, outlet valves - E2’, F2’, G2’, H2’, I2’; “Baking” circuit inlet automatic valves - E3, F3, G3, H3, I3, outlet valves - E3’, F3’, G3’, H3’, I3’. At “baking” operation mode the MCC inlet valves are closed and Baking” circuit inlet automatic valves – opened.

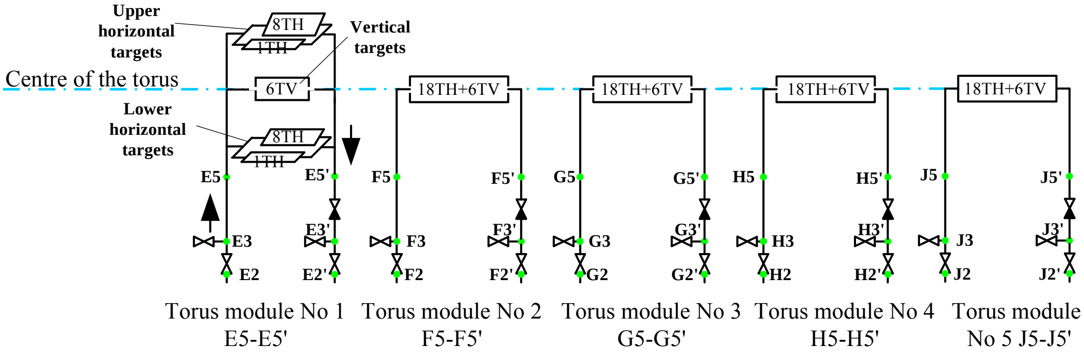

Fig. 5. Modeling of the target modules (nodalization scheme)

4. ANALYSIS OF WATER HAMMER EFFECT

This section presents the results of analysis of assumed break in 40 mm feeder pipe, connected to an upper horizontal target. In the model it was assumed, that the break occurs in the torus module E5-E5' (see Fig. 5). The nodalization scheme of the affected torus module E5-E5' is presented in Fig. 6. The pipe elements "136", "137", "139" and "140" are used for the modeling of upper and bottom horizontal targets. 6 vertical targets are modeled by the pipe element "138". Element "146" is identical to "130", element "139" – to "136" and element "140" – to "137". A simplified model of plasma vessel is element "199" (Fig. 6). The guillotine break of a pipe can be initiated by valve "198".

The initial conditions were assumed according [3, 7, 8]. The water temperature in the "Baking" circuit is 433.16 K (160 ^{o}C) and the density – 907 kg/m^3. The water flow rate through the "Baking" circuit is 177 m^3/h (44.6 kg/s). The pressure in the plasma vessel is equal to 1000 Pa (limitation of RELAP5 program code). The valves from the MCC to the targets are closed on the inlet and on the outlet. The valves from the "Baking" circuit on the inlet and the outlet are open.

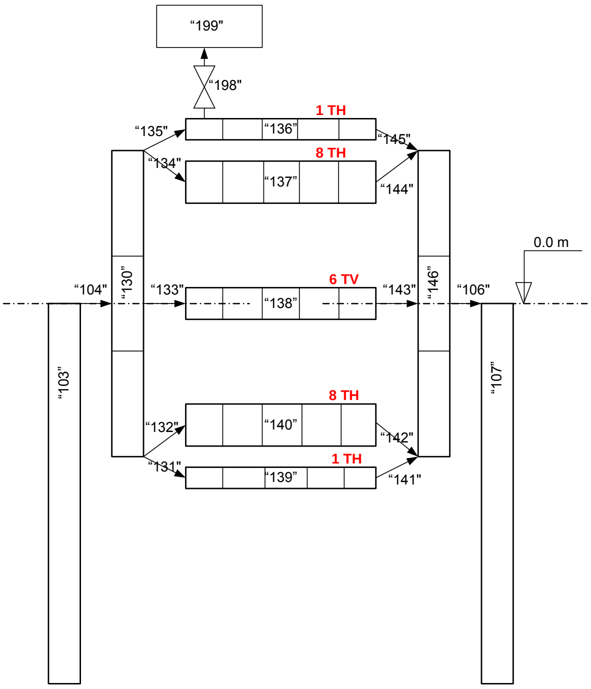

Fig. 6. Nodalization scheme of affected torus module E5-E5' with failure of upper horizontal target module

The break occurs in 40 mm feeder pipe (flow area of break is two times pipe cross-section area), connecting single upper horizontal target module (element "136" in Fig. 6). The time of break opening is 0.01 s). It was assumed, that signal for automatic valves actuation is generated when pressure in plasma vessel (element "199") reaches 2000 Pa. The preliminary calculations shows, that pressure reaches 2000 Pa in plasma vessel 0.14 s after the break initiating. It was assumed, that delay between parameter reaches the set-point and signal generation – 0.5 s, delay between signal generation and start of valve actuation – 1 s. Thus, the automatic valve in target module inlet starts to close 1.64 s after the initiation of break. The signal for automatic pump trip is the same as for valve trip (pressure in plasma vessel reaches 2000 Pa at 0.14 s). Delay between parameter reaches the set-point and pump trip – 1 s. Thus, trip of pump in "Baking" circuit occurs 1.14 s after the break. The automatic valve closure time was assumed equal to 0.5 s.

The water hammer effect depends on few parameters (valve closure time, characteristics of valves, wall roughness, flow energy loss coefficient etc.) [5]. In this paper the influences of following parameters to calculation results are investigated using RELAP5 Mod 3.3 model for water hammer event analysis:

- calculation time step;
- control volume size;
- closure time of valve.

The remaining parameters (wall roughness and flow energy loss coefficient [5]) were defined in the stage of model development. Therefore wall roughness and flow energy loss coefficient were constant during uncertainty analysis.

In the developed RELAP5 model the automatic valves were modeled using special "motor valve" model. This valve model was tested in benchmarking analysis of water hammer effects at UMSICHT facility (Fraunhofer Institute for Environmental, Safety and Energy Technology) [5].

4.1. Influence of calculation time step

Performing explicit integrated modeling of thermal hydraulic processes using system thermal hydraulic codes the calculation results can be affected by numerical errors. During calculation the close attention should be paid to selected calculation time step. As usually the smaller time step allows to decrease the numerical errors.

The acoustic wave Courant limit is the time required for a wave traveling at the sonic velocity to pass through given control volume. Since the sonic velocity can be quite high, the time step has to be reduced to a rather small number [7]. According [5] the time step, which allows receive most probable calculation results in case of water hammer simulation be calculated by formula:

$$\delta t_p = \delta x / a_w, \tag{2}$$

where: δx is the control volume length (m) and a_w – sound velocity in the fluid (m/s).

Taking in to account that the length of piping control volume size was assumed equal 1 m, and sound velocity in the fluid is ~1440 m/s, the recommended time step is 0.0007 s [5]. Feature of RELAP5 Mod 3.3 is that during the calculation the actual time step δt must be lower or equal to current courant time step ($\delta tcrnt$) $\delta t \leq \delta t_{crnt}$. Courant time step can be calculated by formula:

$$\delta t_{crnt} = \delta x / v, \tag{3}$$

where: v is velocity of flow in the control volume (m/s). The user specified maximal time step ($\delta t_{\max}$) allows to reduce the calculation time step below δt_{crnt}. Thus the actual time step of calculation $\delta t \leq \delta t_{\max}$.

For the selection of a suitable calculation time step (δt), the analysis was performed using 0.1 s, 0.01 s, 0.001 s and 0.00055 s maximal time step ($\delta t_{\max}$ referred by user).

To evaluate influence of calculation time step on results of calculation, the ratio $\delta t_{\max} / \delta t_{crnt}$ was used. In Fig. 7 there is presented first pressure pulse calculated with different calculation time steps (automatic valve closure time 0.5 s). The calculation results using 0.001 s ($\delta t_{\max} / \delta t_{crnt} = 0.2$) and 0.00055 s ($\delta t_{\max} / \delta t_{crnt} = 0.1$) time step are very similar. In this case is not necessary to use smaller time step then 0.001 s (Fig. 7). Presented analysis shoves what modeling of water hammer transients using RELAP5 the ratio $\delta t_{\max} / \delta t_{crnt}$ must be less than 0.2.

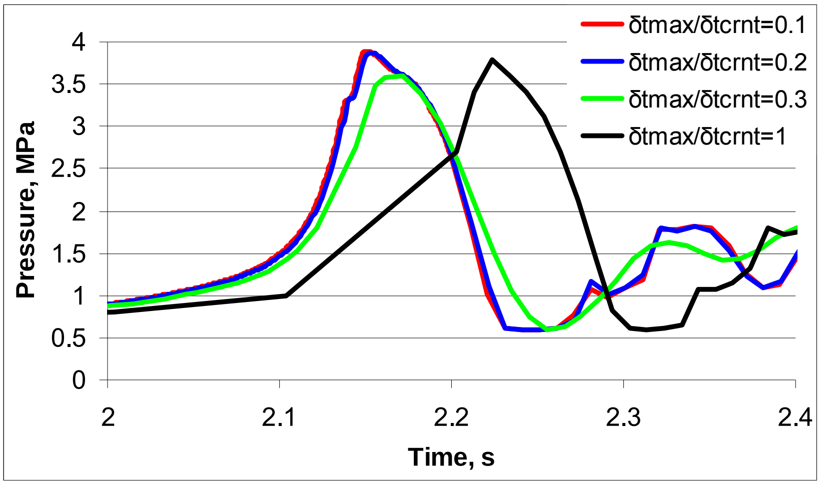

Fig. 7. Influence of calculation time step for first pressure pulse

4.2. Influence of control volume size

Employing RELAP5 code for water hammer analysis, close attention must be paid to the control volume size also. If the pressure wave is expected to have a very rapid rate of increase, then the nodalization of control volume must be implemented to give a small length dimension [9, 10]. Analysis performed to estimate the influence of control volume size in pipeline is presented in Fig. 8. As it is seen from figure the values of pressure peaks are very similar in these investigated cases. This is, because selected pipeline upstream automatic valve is short (3.445m). However, bigger difference can be found in case when pipeline was modeled as single segment. Thus, the length of one control volume should not exceed 1 m in the modeled pipelines were water hammer is expected.

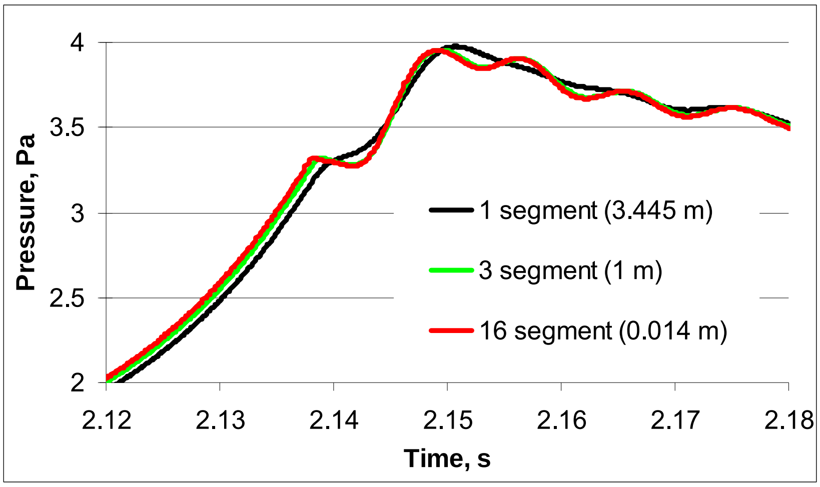

Fig. 8. RELAP5 calculation using different control volume size in pipeline

4.3. Influence of valve closure rate

After W7-X model calibration, using RELAP5 code short-term pulsation of pressure in target feeder pipe break and total coolant release through the break were calculated and it is presented in Fig. 9 and Fig. 10. In these figures are presented pressure peaks in the segment upstream the valve and total coolant release through the double ended guillotine break when automatic valve close time is 5 s, 1 s, 0.5 s and 0.05 s. The designers of W7-X facility proposed to close the automatic valves in 5 s [8]. It is obvious that fast closure of targets inlets valves will lead to high pressure pulsations. On the other hand, the fast closure of automatic valves allows to decrease the amount of discharged water through the rupture. In case if valves on targets inlets are fully closed in 0.5 s, the peak pressure in pipeline just upstream valve in failed target module reaches ~4 MPa. In Fig. 9 is shown that in the case of 0.05 s closure time of valves on targets inlets generates the higher pressure peak ~5.6 MPa. Some components of cooling system are not able to withstand this pressure peak [8]. In case of slow closure of automatic valves (closure time is 5 s), the pressure increase is insignificant. The pressure peak is just two times higher than initial in the case when closure time of automatic valves is 1 s. The total release of water through the break is very similar when closure time of automatic valves is 1 s, 0.5 s and 0.05 s (Fig. 10). Total coolant release through the break during 5 s closure time of automatic valves is much higher comparing of 1 s closure time (differences reaches ~17% in 80 s after the accident initiation). Thus, evaluating the pressure pulsations in pipelines and discharge of water through the break (Fig. 9, Fig. 10), the recommended time for automatic valves closure is 1 s, because low pressure pulsations in pipelines and discharge of coolant into plasma vessel through the break is not so high comparing to faster valves closure cases.

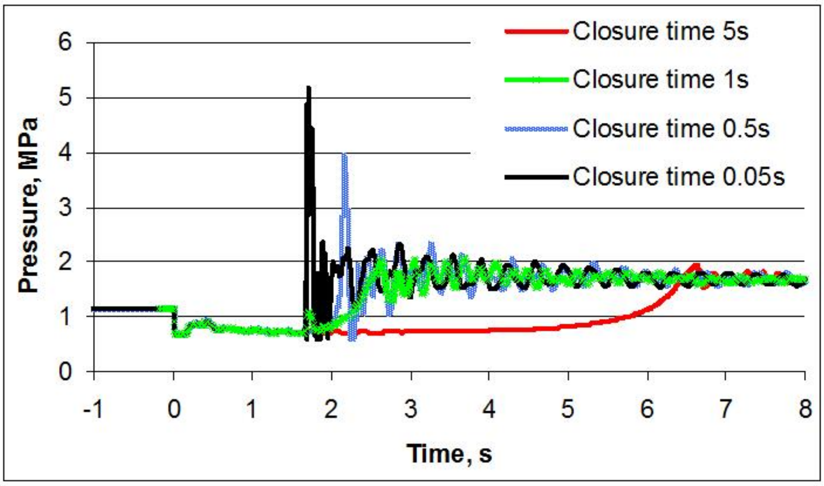

Fig. 9. Pressure peak in the segment upstream automatic valves

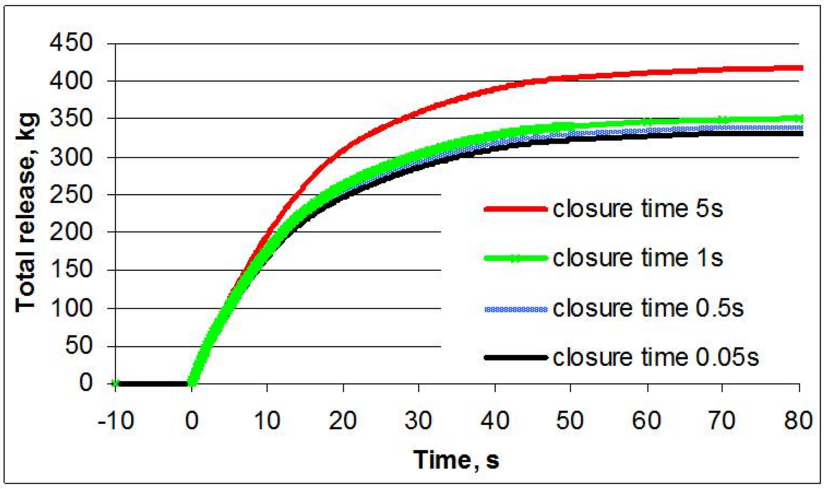

Fig. 10. Total coolant release through the break

5. CONCLUSIONS

1. The model of target modules cooling system in W7-X facility was developed for RELAP5 code. The response of W7-X “Baking” and cooling circuits and the amount of water released through the ruptured pipe into the plasma vessel in the case of double ended guillotine break of DN40 pipe in upper target module inlet is analysed.
2. Analysis shows that the fast closure of automatic valves allows to decrease the amount of discharged water through the rupture but it may lead to pressure pulsation in pipelines upstream valves, i.e. to cause water hammer.
3. The results of performed calculations of water hammer effect in “Baking” circuit showed that the ratio of recommended calculation time step to the current courant time step ($\delta t_{\max} / \delta t_{crnt}$) must be les then 0.2, and the length of one control volume should not exceed 1 m.

4. The analyses showed that the automatic valve closure time 1 s is the most acceptable: the pressure peak in pipelines reaches 2.1 MPa (only 2 times higher than initial pressure), total coolant release through the break is ~17% lower than the case of 5 s closure time of automatic valves and only 5% higher comparing to fastest (0.05s) valves closure cases.

REFERENCES

1. H.-S. Bosch, A. Dinklage, T. Klinger, R. Wolf, and the W7-X Team, Contributions to Plasma Physics (2010) DOI 10.1002/ctpp. 201010101.
2. B. Streibl et al., “Manufacturing of the W7-X divertor and wall protection”, Proc. 23rd Symp. Fusion Technology, Venice, Italy (2004).
3. L. Topilski. Consequences of the W7X in-vessel coolant pipe break at baking conditions, 1-NBF-T0015, Max-Plank-Institut für Plasma Physik.
4. Thorley, ADR, Fluid Transients in Pipelines, 2nd ed. Professional Engineering Publishing, 2004.
5. Kaliatka A., Uspuras E., Vaisnoras M. Benchmarking analysis of water hammer effects using RELAP5 code and development of RBMK-1500 reactor main circulation circuit model // Annals of Nuclear Energy. ISSN 0306-4549. 2007, Vol. 34, p. 1–12.
6. R. Stadler et al., Fusion Engineering Design 84, 305 (2009).
7. Fletcher, C.D., et. al., 1992. RELAP5/MOD3 code manual user’s guidelines. Idaho National Engineering Lab., NUREG/CR-5535.
8. Private communication with D. Naujoks, J. Boscary and L. Topilski, 2006.
9. Oran E.S., Boris J.P. Numerical Simulation of Reactive Flow. Elsevier, New York, 1987, p. 111–114.
10. Petelin S., Cebull P., Hassan Y.A., Mavko B., Ravnikar I. RELAP5 nodalization study for BETHSY experiment. In: RELAP5 International Users Seminar, RELAP5 International Users Seminar, Dallas, TX, USA, 1996.

CYSENI 2010, May 27–28, Kaunas, Lithuania
ISSN 1822-7554, www.cyseni.com

THERMAL STATE OF CONTAINERS WITH THE SPENT NUCLEAR FUEL ON A PLATFORM OF DRY STORAGE

S. V. Alyokhina
A. N. Podgorny Institute for Mechanical Engineering Problems
of the National Academy of Sciences of Ukraine
st. Dm. Pozharsky 2/10, Kharkiv, UA-61046, Ukraine
Phone: +380572942794
Email: alyokhina@ipmach.kharkov.ua

ABSTRACT

In Ukraine there is unique dry spent nuclear fuel storage on Zaporizhska nuclear power plant. For its safety the thermal processes on a platform at dry storage of ventilated containers with the spent nuclear fuel are investigated. The analysis of temperature measurements of ventilating air on exit from containers of storage is carried out. Factors which influence a thermal condition of containers are determined. Researches of thermal state of ventilated container with spent nuclear fuel were carried out by the solution of the conjugate problems of heat exchange. The free convection of ventilating air and helium into basket of storage, and radiative heat exchange in the container was considered. As a result temperature fields of solid bodies and gaseous environments, and also a vector field of speeds of ventilating air and helium are received.

Verification of calculations by taken temperatures on exits from ventilating channels of the container has been model adequacy. This model allows to estimate influence of a wind on temperature inside the container and gives recommendations on their accommodation on a platform to storage. Results of investigations can be used for construction of safety near-stations dry storages in other atomic power plants of Ukraine or at open dry storages of the spent nuclear fuel in other countries.

Keywords: spent nuclear fuel, ventilated container of storage, conjugate problems of heat exchange

1. INTRODUCTION

Interim storage of the spent nuclear fuel by dry method is supposed by “Energy strategy of Ukraine till 2030” [1]. For this purpose making the centralized storage or near-stations storage at nuclear stations is necessary. Today in Ukraine exists unique near-station dry storage of spent nuclear fuel on the Zaporizhska nuclear power plant (ZNPP).

The spent nuclear fuel of six reactors WWPR-1000 ZNPP is stored by a dry method on the open site. The storage is designed for arrangement of 380 ventilated containers. It will provide a storage of fuel for all period of operation ZNPP.

Long safe operation of this storage requires carrying out of thermal processes researches on a platform. This information is necessary for making thermal conditions of a storage which will not give to unsealing a basket with the spent nuclear fuel.

Definition of a thermal condition of containers with the spent nuclear fuel is necessary a carry by mathematical model operation [2–6]. The goal of this investigation is creation and verification of numerical definition method of a thermal condition of containers with the spent nuclear fuel on the open site of storage ZNPP.

2. PROBLEM STATEMENT

Ventilated storage container (VSC) [7], which used in dry spent nuclear fuel storage (DSNFS) at ZNPP, has prototype is VSC-24 cask of American company of Sierra Nuclear Corporation. Containers are located on the open area storage at territory ZNPP.

VSC structure is shown at Fig. 1. Twenty four spent fuel assemblies (SFA) can be placed into tight cluster storage basket (TCSB), filled with inert helium gas, which circulates in the inner space of the basket due to natural convection caused by hot assemblies and cold basket casing temperature difference. Heat transfer from assemblies to the basket casing is also made by heat radiative exchange. Storage basket is placed into a concrete casing which is the radiation protection barrier and protects the basket from mechanical damages, deposits and other effects of the environment. Heat from basket surface is removed by natural draught of ambient air through cylindrical ventilating channel which is formed by basket casing and steel shell of concrete container casing. In this case, there also is radiative heat exchange between TCSB casing and container shell.

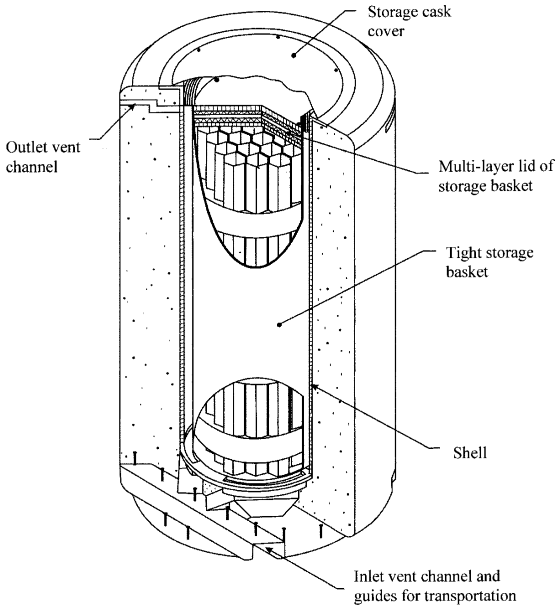

Fig. 1. Structure of ventilated container with spent nuclear fuel

The spent fuel assemblages are loaded into a basket after 5 years of storage in cooling pond. Decay heat of each is not more than 1 kW, but usually it about 0.909 kW.

For the control of thermal condition of VSC registration of temperature measurements on an exit from ventilating channels of the container is conducted. The analysis of these measurements has allowed to disclose factors which influence thermal condition of VSC [8].

In calm conditions the heating of air in each channel of the container is almost identical (Fig. 2). In calm conditions for container № 1 the maximal of ventilated air temperatures in channel 3 (numbers inside the circle, Fig. 2) and minimal – in channel 2. Such distribution of temperatures remains at different values of ambient temperature (t_a). The Fig. 2 shows that heating of ventilated air in each channel almost equally. Differences are caused by non-uniform accommodation in basket SFA with different decay heat or local wind influence.

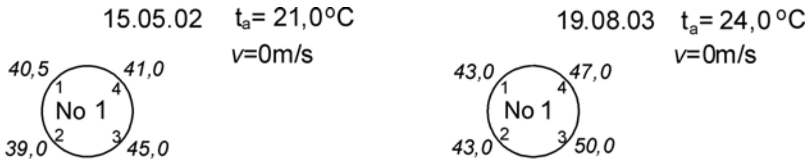

Fig. 2. Temperature measurements on exit of container ventilation channels in calm

Influence of a wind changes temperatures on an exit from ventilating channels (Fig. 3). In the channel from windward the temperature is less than in other channels. It is caused by mixture of cold atmospheric air with heated up ventilating air. The wind also causes redistribution of a cooling air stream inside VSC. Therefore detailed research of influence of a wind on the maximum temperature in the containers is necessary.

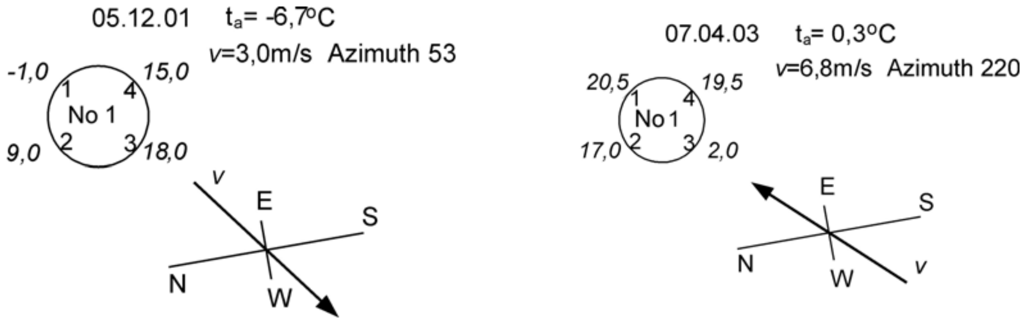

Fig. 3. Temperature measurements on exit of container ventilation channels depending on wind position

Criteria of safety establish a limit 350 °C for the spent nuclear fuel cladding temperature inside TCSB. For research of thermal processes on DSNFS it is necessary to generate mathematical model which will take into account influence of a wind on temperature of the spent nuclear fuel in the container of storage.

3. METHODOLOGY

Research of thermal processes on DSNFS was carried out by the solution of the conjugate problems of heat exchange.

The mathematical model viewed stationary process of thermal physics includes the following equations in partial derivative:

– continuity:

$$\frac{\partial}{\partial x}(\rho u)+\frac{\partial}{\partial y}(\rho v)+\frac{\partial}{\partial z}(\rho w)=0\,, \tag{1}$$

where ρ – density; u, v, w – component of velocity vector $\mathbf{v} = (u, v, w)$;

– motion of viscous fluid:

$$
\begin{gathered}
\rho u\frac{\partial u}{\partial x}+\rho v\frac{\partial u}{\partial x}+\rho w\frac{\partial u}{\partial x}=-\frac{\partial p}{\partial x}+2\frac{\partial}{\partial x}\left(\mu_{\text{eff}}\frac{\partial u}{\partial x}\right)+\\
+\frac{\partial}{\partial y}\left(\mu_{\text{eff}}\left(\frac{\partial u}{\partial y}+\frac{\partial v}{\partial x}\right)\right)+\frac{\partial}{\partial z}\left(\mu_{\text{eff}}\left(\frac{\partial w}{\partial x}+\frac{\partial u}{\partial z}\right)\right)-\frac{2}{3}\frac{\partial}{\partial x}\left(\mu_{\text{eff}}\left(\frac{\partial u}{\partial x}+\frac{\partial v}{\partial y}+\frac{\partial w}{\partial z}\right)\right),\\
\rho u\frac{\partial v}{\partial x}+\rho v\frac{\partial v}{\partial x}+\rho w\frac{\partial v}{\partial x}=-\frac{\partial p}{\partial y}+2\frac{\partial}{\partial y}\left(\mu_{\text{eff}}\frac{\partial v}{\partial y}\right)+\\
+\frac{\partial}{\partial x}\left(\mu_{\text{eff}}\left(\frac{\partial u}{\partial y}+\frac{\partial v}{\partial x}\right)\right)+\frac{\partial}{\partial z}\left(\mu_{\text{eff}}\left(\frac{\partial w}{\partial y}+\frac{\partial v}{\partial z}\right)\right)-\frac{2}{3}\frac{\partial}{\partial y}\left(\mu_{\text{eff}}\left(\frac{\partial u}{\partial x}+\frac{\partial v}{\partial y}+\frac{\partial w}{\partial z}\right)\right),\\
\rho u\frac{\partial w}{\partial x}+\rho v\frac{\partial w}{\partial x}+\rho w\frac{\partial w}{\partial x}=-\rho g-\frac{\partial p}{\partial z}+2\frac{\partial}{\partial z}\left(\mu_{\text{eff}}\frac{\partial w}{\partial z}\right)+\\
\frac{\partial}{\partial x}\left(\mu_{\text{eff}}\left(\frac{\partial w}{\partial x}+\frac{\partial u}{\partial z}\right)\right)+\frac{\partial}{\partial y}\left(\mu_{\text{eff}}\left(\frac{\partial v}{\partial z}+\frac{\partial w}{\partial y}\right)\right)-\frac{2}{3}\frac{\partial}{\partial z}\left(\mu_{\text{eff}}\left(\frac{\partial u}{\partial x}+\frac{\partial v}{\partial y}+\frac{\partial w}{\partial z}\right)\right),
\end{gathered}
\tag{2}
$$

where p – pressure; μ_{eff} – effective dynamical viscosity;

– energy:

$$
c_p\rho\left(u\frac{\partial T}{\partial x}+v\frac{\partial T}{\partial x}+w\frac{\partial T}{\partial x}\right)-\left(u\frac{\partial p}{\partial x}+v\frac{\partial p}{\partial x}+w\frac{\partial p}{\partial x}\right)=\frac{\partial}{\partial x}\left(\lambda_{\text{eff}}\frac{\partial T}{\partial x}\right)+\frac{\partial}{\partial y}\left(\lambda_{\text{eff}}\frac{\partial T}{\partial y}\right)+\frac{\partial}{\partial z}\left(\lambda_{\text{eff}}\frac{\partial T}{\partial z}\right)
\tag{3}
$$

where c_p – specific heat at constant pressure, λ_{eff} – effective heat conductivity, T – temperature;

– heat conductivity:

$$
\frac{\partial}{\partial x}\left(\lambda\frac{\partial T}{\partial x}\right)+\frac{\partial}{\partial y}\left(\lambda\frac{\partial T}{\partial y}\right)+\frac{\partial}{\partial z}\left(\lambda\frac{\partial T}{\partial z}\right)+q_V=0,
\tag{4}
$$

where λ – heat conductivity, q_V – quantity of heat.

The model has two differential equations of transport:

– for turbulent kinetic energy k:

$$
\begin{gathered}
\frac{\partial(\rho k u)}{\partial x}+\frac{\partial(\rho k u)}{\partial y}+\frac{\partial(\rho k u)}{\partial z}=\\
\frac{\partial}{\partial x}\left(\left(\mu+\frac{\mu_t}{\sigma_k}\right)\frac{\partial k}{\partial x}\right)+\frac{\partial}{\partial y}\left(\left(\mu+\frac{\mu_t}{\sigma_k}\right)\frac{\partial k}{\partial y}\right)+\frac{\partial}{\partial z}\left(\left(\mu+\frac{\mu_t}{\sigma_k}\right)\frac{\partial k}{\partial z}\right)+G_k+G_b-\rho\varepsilon,
\end{gathered}
\tag{5}
$$

where μ_t – turbulent viscosity, G_k – term featuring oscillation of turbulent kinetic energy, caused by presence of gradients of velocity, G_b – term featuring oscillation of turbulent kinetic energy, caused by action of Archimedean forces.

– for velocity of its dissipation ε:

$$
\begin{gathered}
\frac{\partial(\rho\varepsilon u)}{\partial x}+\frac{\partial(\rho\varepsilon u)}{\partial y}+\frac{\partial(\rho\varepsilon u)}{\partial z}=\\
\frac{\partial}{\partial x}\left(\left(\mu+\frac{\mu_t}{\sigma_\varepsilon}\right)\frac{\partial \varepsilon}{\partial x}\right)+\frac{\partial}{\partial y}\left(\left(\mu+\frac{\mu_t}{\sigma_\varepsilon}\right)\frac{\partial \varepsilon}{\partial y}\right)+\frac{\partial}{\partial z}\left(\left(\mu+\frac{\mu_t}{\sigma_\varepsilon}\right)\frac{\partial \varepsilon}{\partial z}\right)+C_{1\varepsilon}\frac{\varepsilon}{k}\left(G_k+C_{3\varepsilon}G_b\right)-C_{3\varepsilon}\rho\frac{\varepsilon^2}{k},
\end{gathered}
\tag{6}
$$

where $C_{1\varepsilon}$, $C_{2\varepsilon}$, $C_{3\varepsilon}$ – constant of model equal accordingly 1.44, 1.92, 0.09; $\sigma_k = 1.0$ – turbulent number of Prandtl for k; $\sigma_\varepsilon = 1.3$ – turbulent number of Prandtl for ε.

For the account of heat exchange radiation used the equation:

$$Q_{12} = \sigma_0 \varepsilon \left(T_1^4 - T_2^4\right) H_{12}, \tag{7}$$

where $\sigma_0 = 5.672 \cdot 10^{-8}$ Wt/(m^2·K^4) – Stefan-Boltzmann constant; ε – reduced of emissivity factor; T_1 – temperature of one surface (more heated) body; T_2 – temperature surfaces of the second (less heated) body; H_{12} – area of a cross surface of an irradiation which can be found from expression

$$H_{12} = \int_{F_1} dF_1 \int_{F_2} \frac{\cos\theta_1 \cos\theta_2}{\pi R_{12}^2} dF_2 ,$$

where F_1, F_2 – the areas of surfaces participating in heat exchange; θ_1 and θ_2 – corners between direct, connecting the centres of the partial surfaces dF_1, and dF_2, and the relevant normal lines to these platforms; R_{12} – and distance between these partial surfaces.

Reduced of emissivity factor may be identified as

$$\varepsilon = [1 + (1/\varepsilon_1 - 1)\varphi_{12} + (1/\varepsilon_2 - 1)\varphi_{21}]^{-1},$$

where ε_1 and ε_2 – emissivity factor of surface 1 and surface 2 accordingly; $\varphi_{12} = H_{12}/F_1$ and $\varphi_{21} = H_{12}/F_2$ – coefficients of an irradiance or the angular coefficients of radiation showing, what part of the radiation which are let out by one body, impinges on another.

This model was used for definition of a thermal condition of containers with the spent nuclear fuel on a platform of storage.

In researches it has been used two types of calculation areas:

1. The concrete container and TCSB which was considered as solid body with equivalent heat conductivity [9].
2. TCSB with detailed structure and a concrete cover with the simplified geometrical structure of channels.

4. RESULTS AND DISCUSSIONS

Using computer programs which allow to solve the equations (1)–(7) mathematical models (ANSYS Fluent, STAR-CD, PHOENICS etc.), thermal fields and fields of ventilating air velocities and helium are received.

Temperature fields of the container and air in windless day at temperature of free air 40 °C shown on Fig. 4. The form of a temperature field at others ambient temperatures same.

The free air proceeds through lower channels, passes between a basket and a concrete cover of the container, is heated up and leaves from the upper channels. Heated air rises vertically upwards above the container. Temperature of ventilating air on exit from channels about 70 °C. Heating of air does not exceed 61 °C, criteria of safety are observed. Velocity of air on exit from channels about 2 m/s.

The similar results are observed in windless conditions at other temperatures of air. In all cases heating of air makes about 20 degrees. Comparison of the measured and calculated temperatures confirm adequacy of mathematical model.

Also researches have been carried out for three directions of wind (Fig. 5).

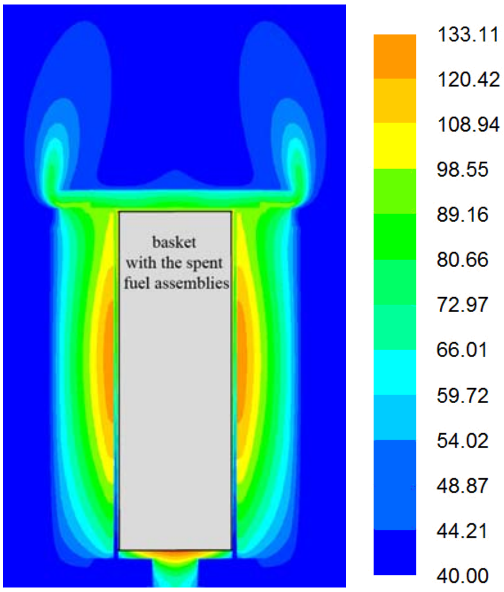

Fig. 4. Temperature fields of the container and ventilating air (°C)

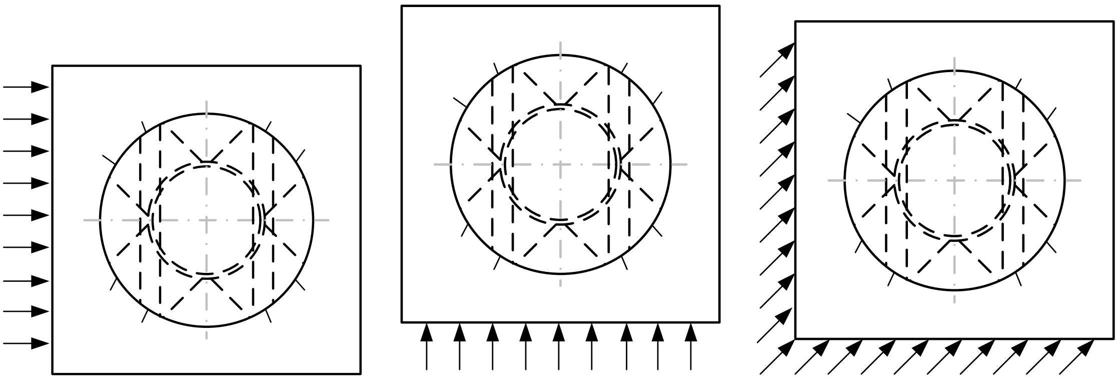

Variant A Variant B Variant C

Fig. 5. Variants of wind direction (o – outlet, i – inlet ventilation channels)

Results of calculations at various velocities of a wind are given in Table 1. Small velocities of a wind (about 1 m/s) render feeble influence on the maximum temperature in VSC in comparison with calm conditions. The maximum of temperature in VSC at 3 m/s wind velocity and this speed of wind is most dangerous at storage of spent nuclear fuel. At strong wind (10 m/s and higher) the maximum temperature in VSC decreases.

Table 1. Maximum temperature in VSC at various velocities of a wind (t_a = 24°C, decay heat of TCSB 24 kW)

Velocity of wind v, m/s	**Maximum temperature in VSC, °C**		
	Variant A	**Variant B**	**Variant C**
0	294.3		
1	302.5	297.2	301.5
3	325.6	312.7	297.7
5	305.1	318.3	288.9
10	256.8	302.9	249.1

Temperature fields of the spent fuel assemblies with identical energy-release inside the container of a storage are presented (Fig. 6).

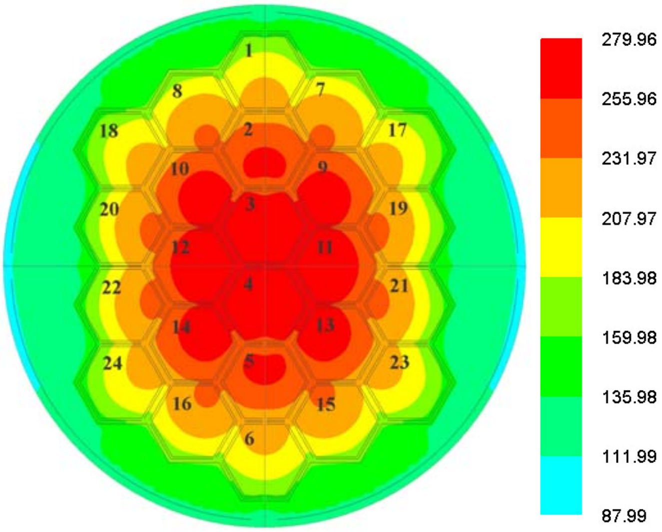

Fig. 6. Temperature fields basket with the spent fuel assemblies
(decay heat of each SFA 0.909 kW)

In TCSB small velocities of helium are observed. Maximum temperatures of SFA at the centre of a basket.

5. SUMMARY AND CONCLUSIONS

1. In this work the mathematical model for definition of thermal condition of containers with spent nuclear fuel on a platform of storage is created. At modelling the conjugate problems of heat exchange which take into account cross thermal influence of solid bodies and gases were solved.
2. Results of modelling have shown safety of operation of containers at high temperatures of a free air (40 °C), because heating of air does not exceed 61 °C.
3. Accommodation of containers on storage platform is necessary in view of an annual wind rose to lower influence of a wind on their thermal state. Results of investigations can be used for construction of wind protection system for containers.
4. Results of investigations can be used for construction of safety near-stations dry storages in other nuclear power plants of Ukraine or at open dry storages of the spent nuclear fuel in other countries.

REFERENCES

1. “Energy strategy of Ukraine till 2030” authorized by the order of Ukrainian Cabinet of Ministers No 145, 15 March 2006.
2. ALYOKHINA, S., GOLOSHCHAPOV, V., KOSTIKOV, A. Research of thermal processes taking place at dry storage of the spent nuclear fuel: actual problems and means of their solution. *Energy-saving. Energetics. Energy-audit,* 2009, No 3(61), p. 24-30 – in rus.
3. POSKAS, P., SIMONIS, V., MAKAREVICIUS, R. Thermal analysis of casks for interim storage of spent nuclear fuel. *Mechanics*, 1999, No. 2 (17), p. 47–51.

4. WALAVALKAR A. Y., SCHOWALTER D. G. 3-D CFD Simulation of a ventilated concrete cask used for spent nuclear fuel storage. WM'04 Conference, February 29–March 4, 2004, Tucson.
5. ALYOKHINA, S., GOLOSHCHAPOV, V., KOSTIKOV, A., MATSEVITY, Yu. Thermal state of ventilated concrete cask with spent nuclear fuel in the conditions of exterior airflow leaking. *Nuclear physics and atomic energy*, 2009, Vol. 10, No 2, p. 171–177 – in rus.
6. ALYOKHINA, S., GOLOSHCHAPOV, V., KOSTIKOV, A. Thermal state of ventilated containers with spent heat-generation elements of reactor WWPR-1000. *Problems of nuclear power plants' safety and of Chornobyl*, 2009, Vol. 11, p. 36–41 – in ukr.
7. BEJNER, K. Analysis of safety VSC-WWPR 1000. DYSNAI-2002. Proceedings of Symposium within XV international youth nuclear festival "DYSNAI". Visaginas, 2002, p. 22–34 – in rus.
8. ALYOKHINA, S., GOLOSHCHAPOV, V., KOSTIKOV, A., KLIMOV, S., LUCHNA, G., MOROZ, V. Analysis of storage conditions of the spent nuclear fuel on the dry storage platform. *Problems of nuclear power plants' safety and of Chornobyl*, 2010, Vol. 13, p. 76–83 – in ukr.
9. ALYOKHINA, S., VORONINA, V., GOLOSHCHAPOV, V., KOSTIKOV, A. Definition of equivalent heat conductivity of the many-placed hermetic basket of storage of the spent nuclear fuel by the decision of the inverse problem. *Nuclear and radiating safety*, 2009, Vol. 12, No 4, p. 48–51 – in rus.

CYSENI 2010, May 27–28, Kaunas, Lithuania
ISSN 1822-7554, www.cyseni.com

APPLICATION OF BAYESIAN METHODS TO ANALYZE AGE-DEPENDENT RELIABILITY OF ELECTRIC I&C COMPONENTS

T. Iešmantas, R. Alzbutas
Kaunas University of Technology
Faculty of Fundamental Sciences
Studentų str. 50, LT - 51368 Kaunas
Phone: +370 37 300300
Email: tomas.iesmantas@stud.ktu.lt, robertas.alzbutas@ktu.lt

R. Alzbutas
Lithuanian Energy Institute
Laboratory of Nuclear Installation Safety
Breslaujos str. 3, LT-44403 Kaunas
Phone: +370 37 401945
Email: robertas@mail.lei.lt

ABSTRACT

In this paper, the developed methodology of age-dependent reliability modelling and probabilistic ageing assessment is presented. Bayesian methods as having property to deal with uncertain and sparse data are used. Modelling problems, which arises in complex Bayesian models, were eliminated by usage of WinBUGS software based on Markov Chains Monte Carlo method. As a case study, the failure data of certain group of electric instrumentation and control components (I&C) were analyzed. Bayesian regression methods were applied to create model for analysis of reliability dynamics of these components. The ageing trend was modelled using several models. One model was distinguished as having property of the best flexibility and fitness to entire age-dependant failure rate curve. Effect of prior information for further failure rate forecasting was also investigated.

Keywords: ageing effect, Bayesian approach, WinBUGS, age-dependent reliability, failure rate, I&C

1. INTRODUCTION

As time passes by, the ageing phenomena is becoming more and more important in order to perform the analysis of system reliability and safety limits. However, some specific systems are not modelled adequately – reliability of passive systems (e. g. pipes or structures) or electric components were considered as having high reliability characteristics which doesn’t change over time. Economic reasons, higher safety requirements forces to evaluate ageing and its effect of systems mentioned above.

Ageing, which could be understood as a general process in which characteristics of components, systems and structures (CSS) gradually change with time or usage, eventually leads to degradation of materials subjected to service conditions and could cause a reduction in component and systems safety margins.

Ageing affects all materials to some degree and therefore may lead to degradation of safety state (i.e. integrity and functional capability) of plant components in nuclear power plants or other safety important facilities.

Most components (especially electric cables, structures or other passive systems) do not provide adequate numbers of failures to analyze statistically. Consequently, a lot of uncertainty, which is related to sparse data, is presented in the results of failure analysis. To reduce and quantify it, prior information about phenomena, historical knowledge about failures of similar components, or even subjective expert judgment can be used. However, classical frequentist[1] analysis does not have ability to integrate prior subjective information and objective data.

This imperfection of classical statistics can be overcome by Bayesian approach. In Bayesian paradigm, uncertainty is quantified in terms of a subjective probability following the axioms of probability theory.

Bayesian approach lies on Bayes theorem, which having data y in continuous way can express the posterior distribution $f(\Theta | y)$ of parameter Θ:

$$f(\Theta | y) = \frac{L(y | \Theta) f(\Theta)}{\int L(y | \Theta) f(\Theta) d\Theta}; \tag{1}$$

where $L(y | \Theta)$ is likelihood function of data y and $f(\Theta)$ is prior distribution of parameter vector Θ.

This formula expresses how prior knowledge about parameter Θ and degree of belief is updated when new data y is introduced in model.

2. AGEING MODEL CONSTRUCTION IN BAYESIAN FRAMEWORK

One of the difficulties of Bayesian inference is inability to deal with changes of age-dependant parameter as a continuous process. This problem partially can be overcome by considering ageing (or degradation) as step-wise process, which is constant in some time period and has value jump in other time period. Mathematically this can be expressed as a jump process:

$$d(t) = \sum_{i=1}^{N} 1_{\{t_i < t < t_{i+1}\}} d_i; \tag{2}$$

where $d(t)$ is any parameter under consideration and constant d_i is parameter value at each time period t_i; N – number of time intervals.

Function of parameter $d(t)$ can have any functional form. It can be linear, Weibull, or some other form. Depending on adopted form, $d(t)$ will depend on vector of parameters $\Theta = \{\theta_1, ..., \theta_n\}$:

$$d(t) = d(t, \Theta). \tag{3}$$

Parameter vector Θ estimation is one of the critical aspects in ageing analysis. When Θ is estimated, ageing impact on parameter $d(t)$ can be analyzed and other reliability characteristics can be estimated. $d(t)$ can be a degradation rate, failure rate, crack growth rate or size, etc.

One of the steps in Bayesian inference is selection of likelihood function and vector Θ prior distribution. Likelihood function should be chosen according to stochastic origin of data.

---

[1] Frequentist statistics (or frequentist inference) is the inference framework on which the well-established methodologies of statistical hypothesis testing and confidence intervals are based. Frequentist inference has been associated with the frequency interpretation of probability. In a frequentist approach to inference, unknown parameters are often, but not always, treated as having fixed but unknown values that are not capable of being treated as random variates in any sense, and hence there is no way that probabilities can be associated with them.

If it is count data or failure number data then Poisson distribution can be used, if it is failure timing data then Weibull distribution is appropriate, etc. If distribution that defines stochastic nature of observed data is $f(y)$, where $y = \{y_1, \ldots y_N\}$ is observed data, than likelihood function is:

$$L(y \mid \Theta) = \prod_{i=1}^{N} f\left(d\left(t_i;\Theta\right), y_i\right), \tag{4}$$

where $d\left(t_i;\Theta\right)$ is parameter value in *i*th time interval t_i.

Likelihood function represents all available information contained in data y sample.

Estimation of prior distribution for parameter vector Θ depends on what technique of calculations is available. WinBUGS software is capable to draw samples even from very complex distributions. Sampling difficulties can arise subject to form of prior distribution and to complexity of model.

Suppose prior distribution for $\Theta = \{\theta_1, \ldots, \theta_n\}$ is $f(\Theta)$ and prior distributions for $\theta_i, i = \overline{1,n}$ is $F(\theta_i)$. Assume that parameters in vector Θ are independent, then prior for Θ can be expressed as:

$$f(\Theta) = \prod_{i=1}^{n} F(\theta_i). \tag{5}$$

According to notations and assumptions made above, posterior distribution is proportional as follows:

$$f(\Theta \mid y) \propto \prod_{i=1}^{N} f\left(d\left(t_i;\Theta\right), y_i\right) \prod_{i=1}^{n} F(\theta_i). \tag{6}$$

Usually it is very difficult to elicit information about model parameters, and because of it, non-informative prior distributions are used in most cases. However, the use of non-informative distribution does not mean that such analysis is the same as classical frequentists analysis, because not only statistical data uncertainty is considered, as is the case in frequentists analysis, but also uncertainty of parameters. More information about informative and non-informative prior distributions and their construction can be found in [4, 6].

Calculation of various characteristics, such as mean or variance of parameters, or Bayesian credibility intervals, is straightforward and can be found in any Bayesian analysis textbook.

In Bayesian theory, predictions of future observables are based on predictive distributions:

$$f(y) = \int f(y \mid \Theta) f(\Theta) d\Theta. \tag{7}$$

By using the predictive distribution, we can quantify our knowledge about future as well as measure the probability of again observing in the future each y_i assuming that the adopted model is true. For this reason, we may use the predictive distribution not only to predict future observations but also to construct goodness-of-fit diagnostics and perform model checks for each model‘s structural assumptions [3, 4].

One numerical summary of the model diagnostic‘s for posterior distribution is the tail-area probability or as it is sometimes known, the posterior predictive p-value:

$$p = P\left(D\left(y^{rep},\theta\right) > D\left(y,\theta\right) \mid y\right) = \int\int I_{\left[D\left(y^{rep},\theta\right) > D\left(y,\theta\right)\right]} p\left(y^{rep} \mid \theta\right) p\left(\theta \mid y\right) dy^{rep} d\theta, \tag{8}$$

where $D\left(y,\theta\right)$ is discrepancy measure and can have any functional form, for example:

$$D_1\left(y;\theta\right) = \sqrt{E\left(Y - E\left(Y\right)\right)^2},\ D_2\left(y;\theta\right) = \sum \frac{\left(y_t - E\left[y_t \mid \theta\right]\right)^2}{Var\left[y_t \mid \theta\right]}. \tag{9}$$

Posterior p-value expresses the differences between statistical data and replicated data.

Bayesian approach also allows to apply “probability of model being true” concepts. Bayes factors can be used to compare different models. For this purpose, comparing probabilities of being true model Bayes factors are calculated as follows:

$$BF_{ij} = \exp\left\{-\frac{1}{2}\left(BIC_i - BIC_j\right)\right\}, \tag{10}$$

where $BIC_i = -2\ln\left(-L\left(\Theta \mid y,i\right)\right) + 2n_i \ln N$ is Bayes Information Criterion, $L\left(\Theta \mid y,i\right)$ is likelihood function, n is number of model parameters, N number of observations.

3. FAILURES OF ELECTRIC I&C COMPONENTS

3.1. Data representation

Data set represents the failure and replacement dates of electrical instrumentation and control (I&C) components. The considered data is quite similar to the real (data were encoded and places where it was collected can’t be identified) operating experience data collected in French or German nuclear power plants. In particular, it is a large sample that represents one technological group of continuously operating components. The data set contains records from type “T” reactors, which are operated by a single utility with a single management philosophy. The components are all of the same type (design, manufacturer, technology, etc.). The components operate in “A” environment having more stressful pressure and temperature. The scope of maintenance is the same for all components.

Data were collected in eleven years period, from January 1, 1990 through December 31, 2000. The components in the sample do not all have same date of being put into service, and as a consequence do not have the same ages at the beginning and end of observation. The failure counts were taken from a review of the maintenance data, so any reported date of failure is actually the date of the periodic test. A “critical” failure is one that causes the component to lose its safety function in a PSA model.

There are 20 units of type “T”, each with 20 components of type A. The data collection period is eleven years, so there would be 4400 component-year except for the fact that some of the units were commissioned after the start of the data collection.

Simple failure rate (Figure 1.) plot gives first impression about failure behaviour over time: failure rate increases in time showing equipment degradation due to ageing.

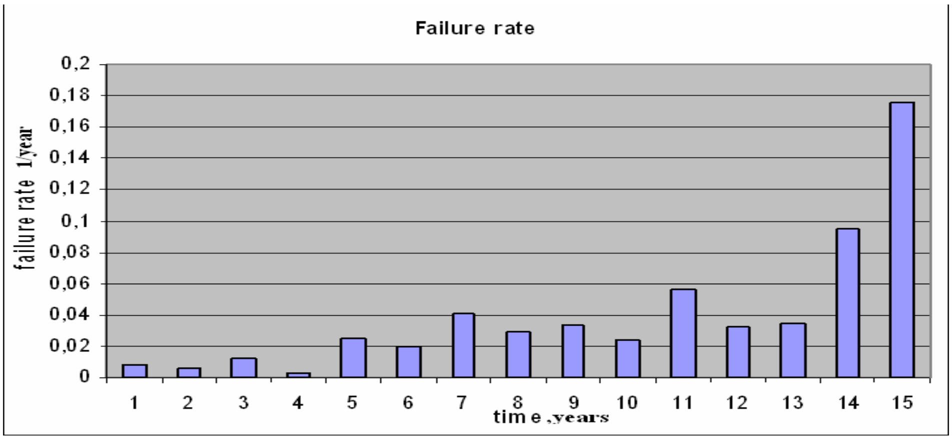

Figure 1. Failure rate[2]

In report of JRC Institute for Energy [1] full and particular frequentist analysis of data can be found. In that analysis side-by-side 90% confidence intervals are calculated and plotted, nonparametric and parametric test are performed to validate ageing in observed data.

3.2. Bayesian model application to Poisson count data

In this analysis, failure rates are considered as constant values in each year, but at every year this value jumps at the value which can be calculated from linear, Weibull or other model.

Lets consider as the model for the failure rate $\{\lambda(t); t \geq 0\}$ a jump process structure:

$$\lambda(t) = \sum_{i=1}^{N} 1_{\{t_i < t \leq t_{i+1}\}} \lambda_i \tag{11}$$

In each year period failures occurs as Poisson process (or to put in other words, likelihood of data is Poisson) but with different rate parameter $\lambda_i, i = 1, 2, ..., 15$. In every period (which is equal to one year) equipment was in operation for τ_i time (operating time). Denote number of failure that occurred in one year as N_i. According to our notations and Poisson process assumptions we can summarize:

$$P(N_i = k) = \frac{e^{-\lambda_i \tau_i} (\tau_i \lambda_i)^k}{k!} \tag{12}$$

Expression of rate parameter could be as follows ($i = 1, 2, ..., N$):

1. $\lambda_i = a$;
2. $\lambda_i = a + bi$;
3. $\lambda_i = ai^b$;
4. $\lambda_i = ae^{bi}$;

---

[2] The reason why time axis is 15 years and not 11 years is the need to equalize ages of all units, i.e. if unit was put into operatio at January 1, 1987, and we don’t know its failure history before 1990, then failures observed at January 1, 1990 will be put into third array cell where three years old failures are collected.

5. $\lambda_i = k\lambda u i^{u-1} + (1-k) b i^{b-1} \gamma e^{\gamma i^b}$ (general bathtub model);

6. $\lambda_i = \delta e^{\mu i} + \dfrac{\alpha\beta}{1+\beta i}$ (generalized Makeham model [2]).

For generality assume, that the rate parameter depends on time and on model parameter vector:

$$\lambda(t) = \lambda(t, \Theta). \tag{13}$$

Gamma distribution is assigned as prior for parameters $\theta_1, \ldots, \theta_n$. Joint distribution for vector Θ is:

$$f(\Theta) = \prod_{i=1}^{n} \frac{\beta^{\alpha} \theta_i^{\alpha-1} e^{-\beta\theta_i}}{\Gamma(\alpha)}. \tag{14}$$

Posterior parameter vector Θ is not analytically calculable, except when failure rate is constant function. In other cases, when $\lambda(t)$ has more cumbersome functional form (although it is linear function), posterior distribution can not be evaluated by using analytical methods. For this reason Markov Chain Monte Carlo estimation implemented to WinBUGS software can be used to sample from posterior distribution.

3.3. Model fitting and screening

Here we will analyze failure rate trend models described in previous chapter. Two models – Makeham and general failure rate models – were introduced additionally to the classical linear, exponential and power models. Analysis and fitting of these models is not very widely researched, which is possibly due to complexity and larger number of parameters to be estimated. However, these models are important for their ability to shape up bathtub curve, while other, simpler models like exponential, does not have such property.

Estimated posterior p-values for different failure rate models are:

Table 1. Posterior p-values for different failure rate models

	Constant	Linear	Exponential	Power	Makeham	General
p_1	0.906	0.4541	0.3696	0.3059	0.398	0.4328
p_2	0.4838	0.4899	0.4838	0.4977	0.4873	0.4886

As can be seen from posterior p-value p_2, correspondent to χ^2 discrepancy measure, carries no useful information for screening. All values are very close to 0.5 and according to p_2 all failure rate models should be considered as having good fit, however constant failure rate model is inappropriate as can be seen from Figure 2.

Bayes factors calculated for each model are presented in Table 2 (firs row represents models for which we want to calculate Bayes factors and first column represents models to which we want to compare models from first row).

Table 2 Bayes factors

	Constant	Linear	Exponential	Power	Makeham	General
Constant	1	5622262501	22799398706	1780215035	3243763284	15401878
Linear	1.77864E-10	1	4.055199967	0.31663677	0.57694981	0.002739
Exponential	4.38608E-11	0.24659696	1	0.07808167	0.14227407	0.000676
Power	5.6173E-10	3.15819291	12.80710378	1	1.8221188	0.008652
Makeham	3.08284E-10	1.73325302	7.028687581	0.54881164	1	0.004748
General	6.49271E-08	365.037468	1480.299928	115.584285	210.608298	1

Constant failure rate is not able to deal with ageing. This model replicates moderately data in the middle of the time period. This conclusion is strengthened by p-value of standard deviation discrepancy measure p_1 – it is equal to 0.906 and shows lack of fit for constant failure rate model.

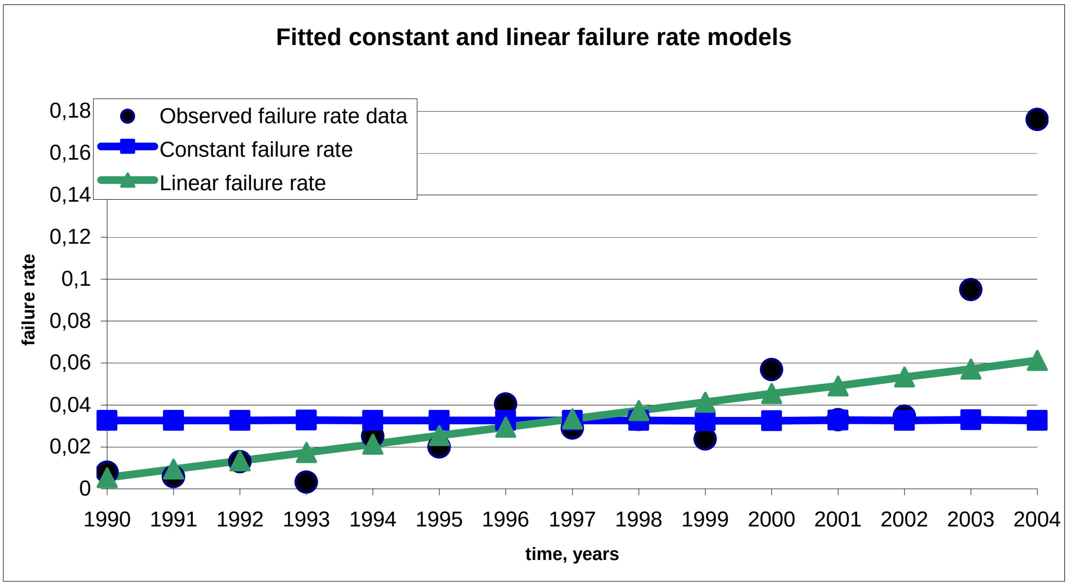

Figure 2. Application of constant and linear failure rate models

According to p-value p_1 linear, exponential, Makeham and General models fits data almost the same. However, linear failure rate model shows lack of fit for data observed in the last two years, when system degradation manifests more severely (Figure 2).

Exponential, Makeham and general failure rate models fits data almost the same (Figure 3). This conclusion is supported by p-values (Table 1). However, exponential model is the simplest failure rate model among last three models and to keep analysis more simple it could be chosen as the most reasonable.

Bayes factors, which are comparison between probabilities of different models, supports conclusions that were made above. The most unlikely model is constant (probabilities that linear, exponential, power, Makeham and general failure rate models are true are billions times greater than probability of constant failure rate model being true model). Modelling results shows that most likely among others are exponential trend model – Bayesian factors are all greater than 5 (Bayes factor of *i*th model, compared to *j*th, which is greater than 5, gives strong evidence that *i*th model is more likely than *j*th).

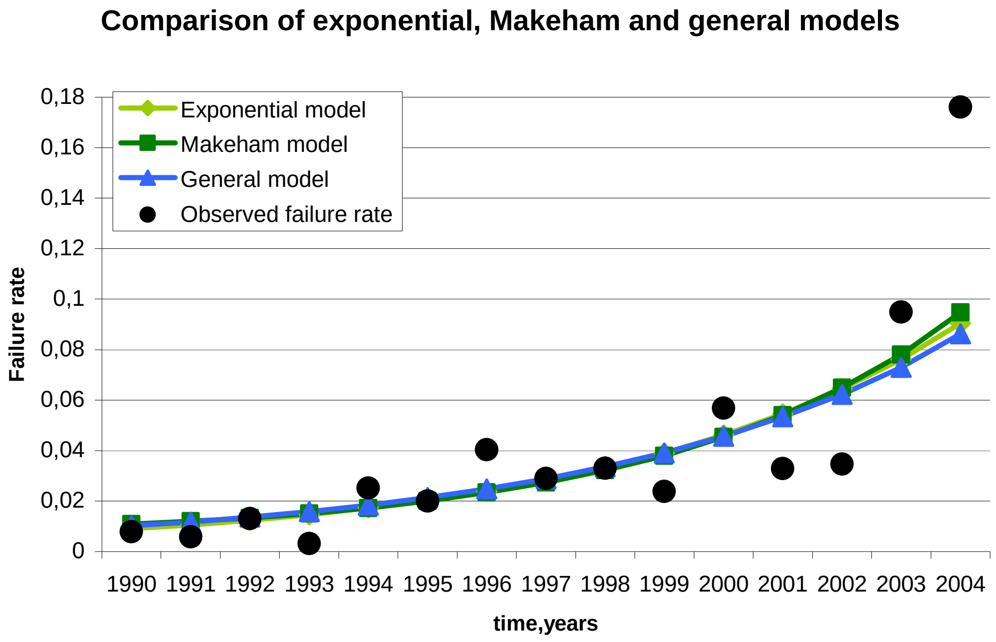

Figure 3. Exponential, Makeham and general bathtube failure rate models

According to results, obtained in this (non)linear regression analysis, exponential failure rate models receives more credits than other models. However, this does not mean, that such models as Makeham or general have to be disregarded, because they have more than good fit to the data observed in this I&C components case – it has more flexibility than exponential, which means that when burn-in failures are introduced in model, they would give more reasonable and realistic results, than exponential (or other) failure rate model.

4. BAYESIAN APPROACH APPLICATION FOR FORECASTING

Reliability forecasting is one of the most common issues of reliability analysis. It deals with prediction of the failure rate of components and future system reliability. These predictions are used to evaluate design feasibility, compare design alternatives, identify potential failure areas, trade-off system design factors, and track reliability improvement.

Dealing with uncertainty in forecast can be crucial when predicting phenomena behaviour of high risk systems, because underestimation can lead to safety limits that are not enough safe. Bayesian methods allows to quantify uncertainty in more natural way – this approach is able to account not just uncertainties in observed data, but also uncertainty that is related to unknown parameters and model screening.

Bayesian methodology can be used not just update knowledge about parameter estimates, but also to update belief about future predictions as new data becomes available.

Suppose we have data from first 9 years (until 1998) and want to forecast for next 6 years. Then, after two years of data collection, it is possible to update predictions that were made earlier. The corresponding results are presented in Figure 4.

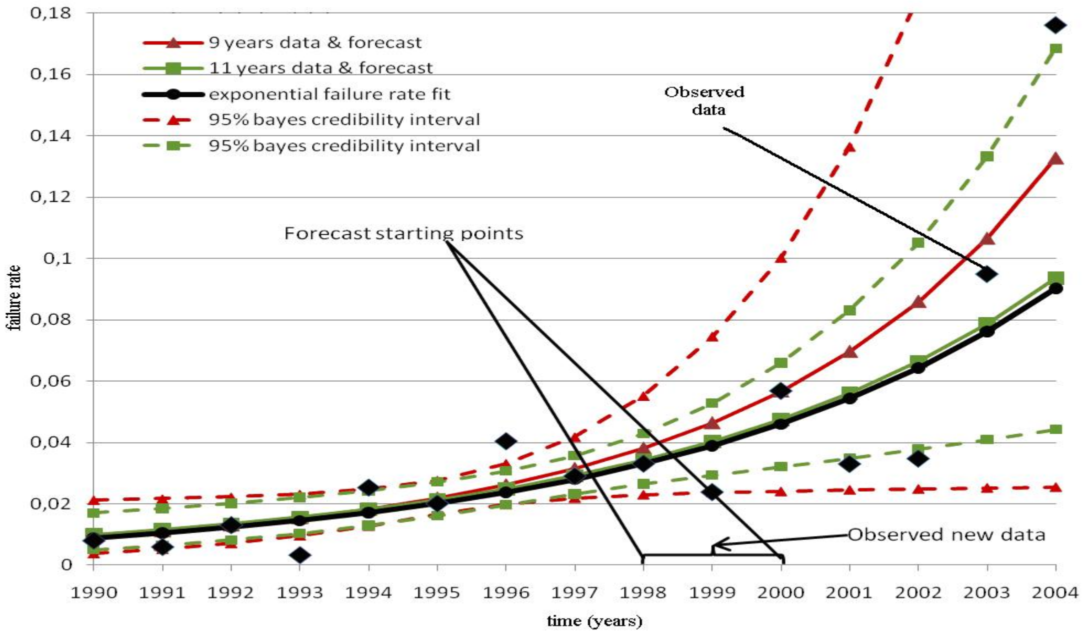

Figure 4. Dynamics of failure rate and uncertainty taking into account data updating

Exponential failure rate model was used to make predictions. Posterior distribution obtained for first 9 years was used as informative prior distribution in the next two years Bayesian analysis. Because of updating ability, Bayesian approach does not require recalculation with all data when new data is observed (eg. in 2000).

CONCLUSIONS

Developed methodology of age-dependent reliability modelling and probabilistic ageing assessment was applied to find the best fitting failure rate model. This methodology is able to deal with disperse and small data sets along with multiple parameter set. More generalized, but complex models were successfully applied together with traditional linear, exponential and other models to express the aging effect.

It was ascertained, that several goodness-of-fit approaches and measures should be used to make comprehensive and more reliable fitness analysis. Results demonstrates that chi-squared discrepancy measure, usual instrument for most researchers, may carry no important information and cannot be used for screening – calculated values were all around 0.5, which wrongly indicates good fit for all models. However, applying predictive p-values and Bayesian factors the exponential failure trend model was identified as the best-fit model for I&C components failure data.

When new methodology was applied to forecast future failure rate values – at some point it was observed that no further data collection is needed to perform satisfactory predictions. Failure rate values of fitted exponential model are almost equal to predicted values when information update was made.

REFERENCES

1. ATWOOD, C., CORNVAL, O., PATRIK, M., RADIONOV, A. Models and data used for assessing the ageing of systems, structures and components (European Network on Use of Probabilistic Safety Assessment (PSA) for Evaluation of Ageing Effects to the Safety of Energy Facilities). DG JRC Institute for Energy, 2007.
2. LAI, C. D.; XIE, M. *Stochastic Ageing and Dependence for reliability*. Springer Science 2006.
3. RAO, D. *Bayesian Thinking, Modelling and Computation.* Handbook of statistics Vol. 25, 2005.
4. NTZOUFRAS, I. *Bayesian Modelling Using WinBUGS*. Athens University of Economics and Business, Athens, Greece. 2009.
5. HAMADA, M. S.; WILSON, A. G.; C. Shane Reese, Harry F. Martz. *Bayesian Reliability*. Springer Science, New York, 2008.
6. MEEKER, W. Q.; ESCOBAR, L. A. *Statistical methods for reliability data*. United States of America, 1998.

CYSENI 2010, May 27–28, Kaunas, Lithuania
ISSN 1822-7554, www.cyseni.com

THERMO-HYDRO-MECHANICAL SIMULATION OF REFERENCE REPOSITORY FOR RBMK-1500 SPENT NUCLEAR FUEL DISPOSED IN CRYSTALLINE ROCKS

Darius Justinavičius
Nuclear Engineering Laboratory
Lithuanian Energy Institute
Breslaujos str. 3, LT-44403 Kaunas – Lithuania
Phone +370 37 401 886
E-mail: justinavicius@mail.lei.lt

ABSTRACT

The international consensus exist that spent nuclear fuel (SNF) and long–lived high level radioactive wastes are best to be disposed of in the geological repositories, using a system of engineered and natural barriers. Due to the danger of exposure arising from long-lived radionuclides to humans and the environment, SNF is not allowed to be disposed of in the near-surface repositories.

The implementation of nuclear waste repository in a deep geological formation would cause some perturbation of the geological system. The impact on the host rock is two-fold: (1) a large numbers of tunnels necessary to be constructed would lead to the appearance of excavation disturbed zones in the formations, (2) the disposed of nuclear waste would release heat for certain time period. Such a perturbation induces a number of coupled thermo–hydro–mechanical (THM) processes around the repository. Thus it is necessary to analyze their influence on the performance of the engineering barriers and the repository safety as well.

A numerical investigation of the thermo–hydro–mechanical processes occurring around a single disposal canister with RBMK-1500 SNF to be disposed of in the reference repository in the crystalline rocks has been started and the first results are presented in this paper. For the modelling the computer code COMPASS (COde for Modelling PArtly Saturated Soil) (UK) has been used.

Keywords: Thermo-hydro-mechanical behaviour, geological disposal, crystalline rocks, numerical modelling

1. INTRODUCTION

The usage of the nuclear materials in the industry and health care areas lead to appearance of the nuclear waste of different kind (activity, radionuclide inventory, etc). Some of these waste, i.e. low and intermediate level waste is being disposed of in near surface repositories [1]. The high level waste such as spent nuclear fuel, which is a minor part of all nuclear waste by volume, but contains major piece of the radioactivity, hence produce a large amount of heat. Many countries, including USA, Canada, Sweden, France, Finland, UK and Switzerland among others, have been investigating the opportunities and intent to dispose of the high level nuclear waste in the deep geological repositories [2]. Various rock types are being investigated in the different countries with geologic disposal programs (granite rocks, clay formations, rock salt, and volcanic tuff).

Recently, the demand for the performance assessment of geological nuclear waste repositories has driven the development of coupled thermo-hydro-mechanical (THM) numerical models in the fields of rock and soil mechanics [3, 4]. In this paper the thermo-hydro-mechanical (THM) behaviour around a single deposition hole has been investigated via numerical simulation using computer code COMPASS (UK), which implements a coupled THM approach to model the behaviour of saturated/unsaturated media.

2. METHODOLOGY

2.1. Theoretical formulations

One important issue is the heat release from the waste containing canisters, which gives rise to strongly coupled THM processes in clay buffers and fractured rocks surrounding disposal canisters. For example, the elevated temperature around a waste canister creates a thermal gradient with accompanying thermal stress and the deformation in the surrounding medium. The temperature gradient is also one of the main causes of groundwater movement (by diffusion) within a clay buffer. At the same time, the clay swells or shrinks as a function of its water content, causing mechanical deformation and stress changes. Due to mechanical deformation the porosity and the apertures of rock pores and fractures could be changes thus affecting the groundwater flow regime. Water flow regime depends on the material saturation, material behaviour under unsaturated conditions as well. By affecting the water pressure gradient, the heat flow is affected as well. Generally in the case of heat-generating radioactive waste, it is possible to envisage range of individual and coupled T, H and M processes that can operate. This is illustrated schematically in Fig. 1:

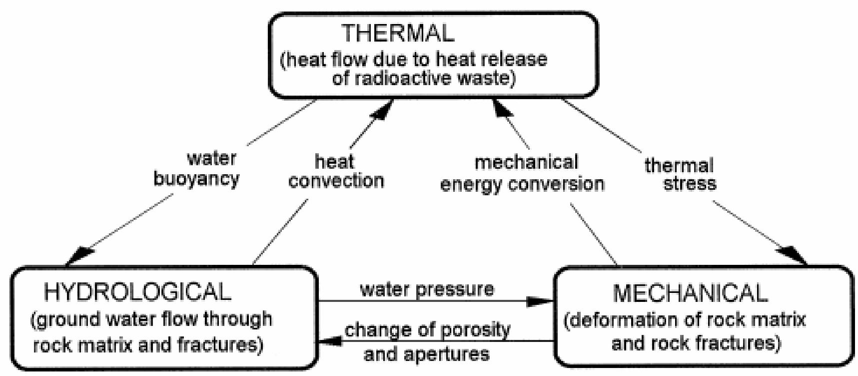

Fig. 1. Examples of thermo-hydro-mechanical (THM) couplings, from [5]

The performance of such a system can only be analyzed with a numerical model that is able to simulate the coupled and highly nonlinear behaviour of all components (canister, buffer, fractured rock, and water) and their interactions.

The materials contained within the system being analyzed (rock, buffer and backfill) are assumed to be as a three phase porous medium, consisting of solid skeleton, pore-water and pore-air. In the following formulation the flow of moisture, air and heat energy in a deformable porous medium are considered. In particular, governing differential equations are applied for moisture, dry air, heat flow and the deformation evolution. A brief summary of each governing equation will be presented below. The describing in more detail is in [6].

2.1.1. Heat transfer

Heat transfer is governed by the classical conservation of heat energy:

$$\frac{\partial \Omega_H}{\partial t} = -\nabla Q, \tag{1}$$

where Ω_H is the heat content of unsaturated soil per unit volume, includes conduction, convection and latent heat of vaporization, Q is the heat flux per unit area.

2.1.2. *Water and air transfer*

The governing equation for moisture (liquid water and water vapour) transfer in an unsaturated soil can be expressed as:

$$\frac{\partial(\rho_l \cdot n \cdot S_l)}{\partial t}+\frac{\partial[\rho_v \cdot n \cdot (S_l-1]}{\partial t}=-\rho_l \nabla \cdot v_l-\rho_l \nabla \cdot v_v-\nabla \cdot \rho_v v_a, \tag{2}$$

where v_l v_a is the velocities of pore-liquid and pore-air, based on a generalised Darcy's law, v_v is water vapour velocity is based on vapour movement due to gradients of relative humidity, n is porosity, ρ_l, ρ_v is the densities of liquid and vapour, S_l is the degree of liquid saturation.

In Eq. (2), the first two terms represent the storage of pore liquid and vapour; the third term represents the movement of liquid mass, the fourth term represents the movement of vapour mass due to a vapour pressure gradient (diffusive flow), in which the saturated vapour flow is assumed to have the same density as pore water; the fifth term represents the movement of vapour as a part of the bulk flow of air.

Air in unsaturated soils is considered to exist in two forms: dry air and dissolved air. In this approach the proportion of air contained in the pore liquid is defined using Henry's law. The governing equation for air flow:

$$\frac{\partial(S_a+H_s S_r) n \rho_{da}}{\partial t}=-\nabla \cdot[\rho_{da}(v_a+H_s v_l)], \tag{3}$$

where the dry air density ρ_{da} can be defined via Daltons law of partial pressure, H_s is Henry's volumetric coefficient of solubility and S_a is the degree of air saturation.

2.1.3. *Constitutive stress–strain relationship*

The mechanical behaviour is governed by constitutive relationship developed using an elasto-plastic relationship for a slightly swelling soil via consideration of stress equilibrium. For problems in unsaturated clays the total strain is assumed to consist of components due to stress, suction and temperature changes:

$$d\varepsilon = d\varepsilon_\sigma + d\varepsilon_S + d\varepsilon_T, \tag{4}$$

where the subscripts σ, S and T refer to net stress, suction and temperature contributions.

2.2. Modelling assumptions

2.2.1. *Repository concept*

During 2002–2005 the assessment of possibilities for disposal of spent nuclear fuel (SNF) in Lithuania was performed with the support of Swedish experts. Extended studies on selecting of suitable geological formations had led to the conclusion that crystalline rocks and argillaceous rocks are the primary candidates for disposal of SNF in Lithuania. KBS-3V concept developed by SKB (*The Swedish Nuclear Fuel and Waste Management Co.*) for disposal of the SNF in Sweden was chosen as a prototype for crystalline basement in Lithuania [7]. This concept involves SNF in a cooper canister containing a cast iron insert for strength. The canister is surrounded by a high-density expansive clay buffer and then placed into a vertical deposition hole situated in crystalline rock at approximately 400–500 m depth. The primary aim of the engineered barriers is to isolate the radioactive waste from the rock and particularly from the groundwater.

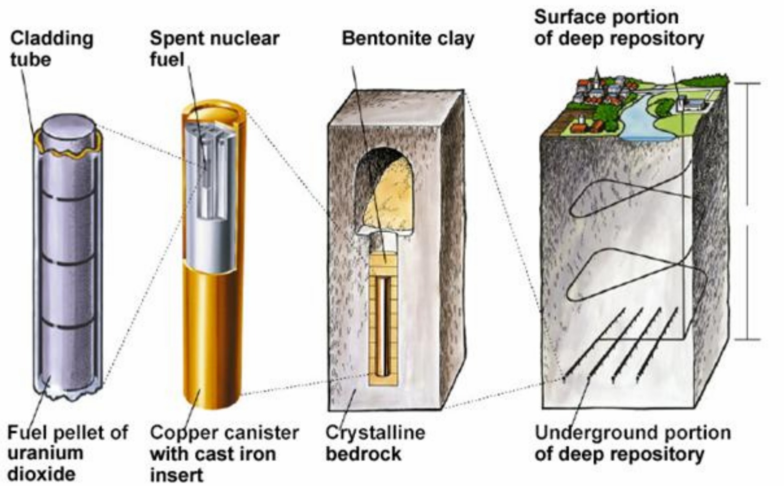

Fig. 2. Illustration of KBS-3V method for the disposal of spent nuclear fuel [8]

2.2.2. Scenario

After repository closure, the repository is sealed and thus there is no ventilation or escape of moisture. The repository cavity is then resaturated (if below the water table) and repressurized to its original hydrostatic pressure corresponding to its depth. Thermally, the temperature builds up to a certain level and then decrease. The exact temporal and spatial distribution of the heating cycle depends on the waste inventory and repository design. This is also the period when the hydraulic pressure is rebuilt in the backfilled and sealed repository opening. In general, mechanical deformation during the re-saturation and re-pressurization is an irreversible coupled THM process.

It was conservatively assumed only THM processes related to natural evolution of the repository are taking into account in this analysis. Other coupled processes have been envisaged away for the first approach. These include links involving chemical effects, seismically induced HM, glacially induced THM and erosion.

2.3. Numerical model and initial data

2.3.1. Conceptual model

A part of the emplacement tunnel and single deposition hole for the reference cooper canister with cast iron insert for RBMK-1500 spent nuclear fuel are included in model domain, which is based upon Swedish KBS-3V concept including the crystalline rocks, clayey buffer materials (bentonite and backfill) and waste canister.

The canister has a length of 4.07 m and radius of 0.525 m and is designed for 16 (32 fuel-half assemblies) fuel assemblies of RBMK-1500 spent nuclear fuel. The canister was not modelled itself, only boundary condition (time dependent heat fluxes) was used. This heat production term was applied on the bentonite next to the external surface of the canister. There is 0.35 m wide bentonite layer around the canister, 1.5 meters height above the canister and 0.5 m height of bentonite plug below the canister. The height of emplacement tunnel is 6 m, and the tunnel is backfilled with the mixture of crushed rock and 30% bentonite. The geometry of the domain is illustrated in Fig. 3:

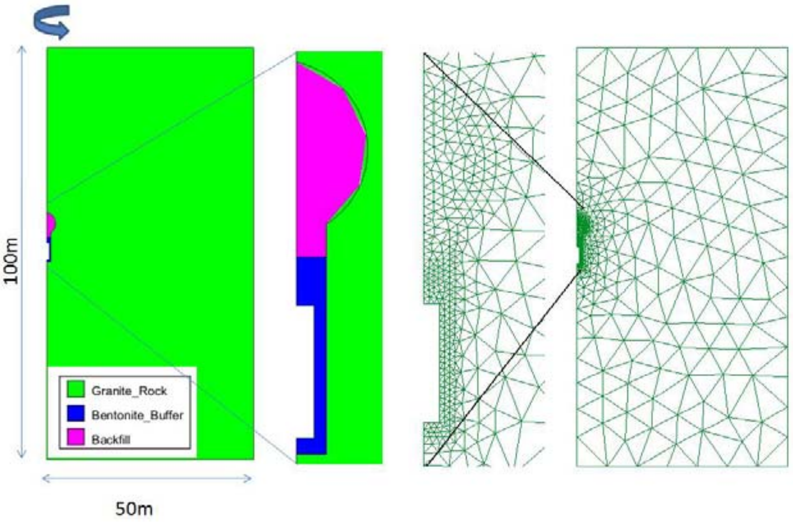

Fig. 3. Schematic view of conceptual model

A single deposition hole is virtually symmetrical therefore an axis-symmetric analysis has been undertaken to reduce computational time. The discretization of model domain shows that the mesh is more detailed in and around the repository structure due the higher parameters gradients and the finer results resolutions required.

2.3.2. *Material properties*

The model employed in this work requires a number of material parameters to define the behaviour of each individual material. Three separate materials have been considered. Each of these requires a series of material constants and constitutive relationships to describe their thermal–hydraulic–mechanical behaviour. This information has been obtained from the experimental work performed in the SKB Prototype Repository in the Äspö Hard Rock Laboratory (Sweden) [9]. Since there is a lack of geotechnical properties of geological formation in Lithuania some data were assumed to be the same as defined for Swedish site [10].

In some cases the mathematical equations have been fitted to experimental data to cast the material relationships in a form suitable for computer modelling. These equations are defined below [10]:

$$k_{unsat} = k_{sat} \cdot S_r{}^{\delta}, \tag{5}$$

$$k_{unsat} = k_{sat} \cdot \sqrt{S_r} \cdot (1 - (S_r^{1/\beta_1})^{\beta_1})^2, \tag{6}$$

$$S_r = \left[Q_{res} + \frac{Q_{sat} - Q_{res}}{\left(1 + \left(\frac{\alpha \cdot S}{\rho \cdot g}\right)^b\right)^{1-\frac{1}{b}}} \right] / n \tag{7}$$

$$S_r = \left(1 + \left(\frac{S}{P_0}\right)^{\frac{1}{1-\beta}}\right)^{-\beta}, \tag{8}$$

where k_{sat} is the saturated hydraulic conductivity, k_{unsat} is the unsaturated hydraulic conductivity, S_r is the degree of saturation, S is the suction (pore-water pressure), g is the gravitational constant, ρ is the density of liquid, n is the porosity, P_o is the air entry pressure and α, θ_{res}, θ_{sat}, β, β_1, and b are equation parameters.

A summary of the parameters is given in Table 1:

Table 1. THM material parameters used in the analysis

Parameter	**Bentonite**	**Backfill (30/70 mix)**	**Rock**
Density, ρ_s (kg/m^3)	2150	2750	2600
Initial porosity, n (-)	0.4	0.39	0.005
Initial degree of saturation, S_r (-)	0.85	0.68	1
Specific heat capacity C_{ps}(J/kg/K)	1116	850	800
Thermal conductivity (W/m/K)	0.3 – 1.35	0.3 - 2	2.8
Hydraulic conductivity	Refer to Eq. 5	Refer to Eq. 5	Refer to Eq. 6
Shear modulus, G (Pa)	$1 \cdot 10^7$	$1 \cdot 10^7$	$2.76 \cdot 10^{10}$
Poison ratio, v	0.499	0.499	0.25
Elastic stiffness (stress), κ	0.15	0.15	$1 \cdot 10^{-4}$
Elastic stiffness (suction), κ_s	0.15	0.15	$1 \cdot 10^{-4}$
Coefficient of thermal expansion, α_T (K^{-1})	$1.5 \cdot 10^{-4}$	$1.5 \cdot 10^{-4}$	0

2.3.3. Initial and boundary conditions

- For moisture (hydro-processes):

It was assumed that the rocks are fully water saturated in the beginning of simulation and the initial pore-water pressure of the rocks was assumed to be hydrostatic with the water table which is situated 350 m above the top of the domain. The buffer materials were assumed to be partly water saturated at the beginning (Table 1) and the pore-water pressure is defined from the soil-water retention curve (Eq. 7 and Eq. 8).

- For thermal processes:

The initial temperature was set 305 K in all materials according the geological data in south Lithuania. The heat flux from RBMK-1500 canister is maintained time dependent based upon the evaluation using ORIGEN-S [11] code after 50 years of interim storage of SNF.

- For mechanical processes:

For the deformation of bentonite and backfill – 200 kPa, of granite rocks – 22 MPa compressive stress in x and y directions were set. All model boundaries were restrained in x and y directions.

3. RESULTS AND DISCUSSION

The simulation work has been performed using finite element code COMPASS (Code for Modelling Partly Saturated Soil). This code is a mechanistic model where the various aspects of soil behaviour under consideration, are included in an additive manner. In this way the approach adopted describes the heat transfer, moisture migration and air transfer in the material, coupled with stress/strain behaviour. The results of fully coupled THM analyses are presented below.

3.1. Temperature evolution in the buffer and the maximum temperature

Temperature profiles obtained at various location of the buffer and the rocks are presented in Fig. 4. As it could be expected, the maximum temperature is reached at the contact with the disposal canister, after about 1.5–2 years of heating. Generally the temperature builds up to a certain level and then decrease. After about 200 years the heat power is down to a few percents of its initial value.

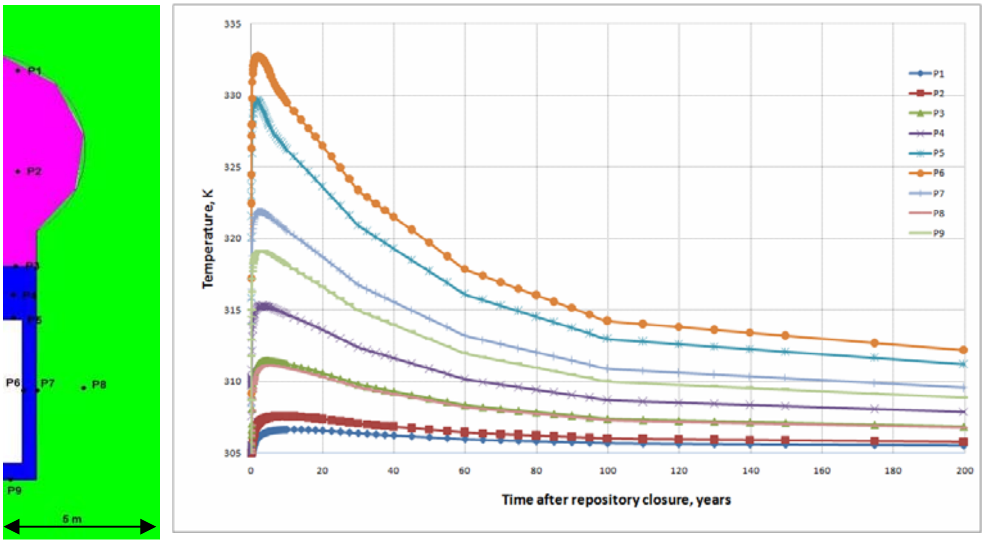

Fig. 4. Temperature profiles at selected points of interest in the buffer and rocks

The maximum temperature reached in the system is 336 K. There is a requirement that the surface temperature of the canister may not be exceeding 100˚C [12]. The results of temperature assessment around the canisters loaded with 32 RBMK-1500 SNF half-assemblies shows that a disposal canister with such a heat output would satisfy the temperature constrain.

3.2. Evolution of the buffer saturation and the time to full re-saturation

The thermal gradient induced by the waste-released heat causes a de-saturation close to the heat source and a negative fluid pressure is obtained in the near field rock, that is in the close vicinity of the buffer (the rock mass de-saturates). This effect is minor and short-term, because the incoming water from the rock will re-saturate near field rock, bentonite and backfill. A series of contour plots of liquid saturation over time are displayed in Fig. 5:

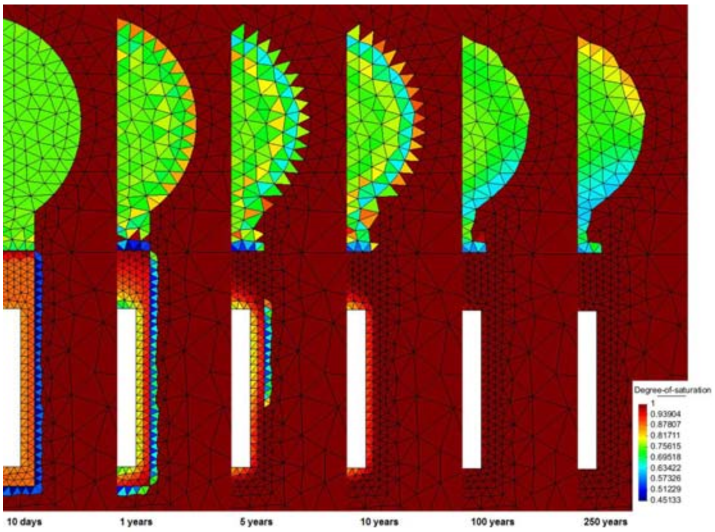

Fig. 5. Saturation contours at different time steps

The time of full re-saturation is different for bentonite, backfill and near field rocks. The faster re-saturation was in the near field rocks – after about 7 years. The bentonite buffer becomes fully water saturated after about 50 years, with exception of the area close to the canister. For the backfill material a longer time for re-saturation is required. This could be related to a different water retention and relative permeability dependence on the saturation.

3.3. Evolution of stresses induced displacements in the buffer

The results in mechanical field are closely linked to the hydraulic results, as the material used in the buffer is highly expansive. As the hydraulic results show the incoming water from the rock will increase the saturation of bentonite/backfill and cause it to swell. Also the thermal expansion may induce the stresses due to the confinement of the bentonite by the rock. The stresses noticed above will cause the deformations (vertical or horizontal displacement) of the materials. A contour plot of the displacement both in the vertical and horizontal directions is shown in Fig. 6:

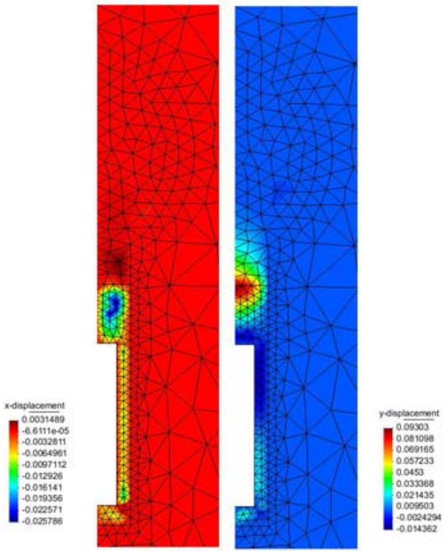

Fig. 6. Contour plots of horizontal and vertical displacements after 250 years of repository closure

As could be seen in Fig. 6 the higher radial (horizontal) displacements (about 3 cm) are seen in the bentonite at the top of deposition hole. The higher vertical displacements (about 9.3 cm) are seen in the interface between bentonite and backfill materials. There are no sensible displacements in crystalline rocks. The comparison of the mechanical displacement showed that the maximum vertical displacement scale contains values up to 3 times higher than the maximum horizontal displacement. This is related to the concept of engineering barriers around the disposal canister and mechanical properties of buffer materials.

Selected materials and its disposition allow facilitate the mechanical impact from the heat within the near field region safely.

4. CONCLUSIONS

1. A numerical model has been developed to simulate the thermo-hydro-mechanical processes occurring around a single disposal canister with RBMK-1500 SNF to be disposed of in the reference repository;
2. The results of temperature assessment around the canisters shows that the temperature builds up to a certain level and then decrease and disposal canister with such a heat output would satisfy the temperature constrain;
3. The hydraulic results show the de-saturation of materials due the thermal gradient induced by the waste released heat at early simulation stage, after that the buffer materials will re-saturated in time due the groundwater coming from the rocks. The bentonite buffer becomes fully water saturated after about 50 years with exception of the area close to the canister;
4. Incoming water increase saturation of bentonite/backfill and cause it to swell. The assessment of the mechanical displacement showed that the maximum vertical displacement scale contains values up to 3 times higher than the maximum horizontal displacement.

REFERENCES

1. ZULOAGA, P. Design and development of near surface disposal facilities for radioactive waste. IAEA Conference on Low-level Waste Disposal Safety. Tokyo, 2006.
2. IAEA. Scientific and Technical Basis for the Geological Disposal of Radioactive Wastes. Technical Report Series No. 413. Vienna: IAEA, 2003.
3. HUDSON, J.A., STEPHANSSON, O., ANDERSSON J. Guidance on numerical modelling of thermo-hydro-mechanical coupled processes for performance assessment of radioactive waste repositories. *International Journal of Rock Mechanics and Mining Sciences*, 2005, Vol. 42, p. 850–870.
4. WU, W., LI, X., CHARLIER, R., COLLIN, F. A thermo-hydro-mechanical constitutive model and its numerical modelling for unsaturated soils. Computers and Geotechnics, 2004, Vol. 31, p. 155–167.
5. HUDSON, J.A., STEPHANSSON, O., ANDERSSON, J., TSANG, C.-F., JING, L. Coupled T-H-M issues relating to radioactive waste repository design and performance. *International Journal of Rock Mechanics and Mining Sciences*, 2000, Vol. 38, p. 143–161.
6. THOMAS H.R., CLEALL P.J. Inclusion of expansive clay behaviour in coupled thermo hydraulic mechanical models. *Engineering Geology*, 1999, Vol. 54, p. 93–108.
7. POSKAS, P., BRAZAUSKAITE, A., NARKUNAS, E., SMAIZYS, A., SIRVYDAS, A. Generic repository concept for RBMK-1500 spent nuclear fuel disposal in crystalline rocks in Lithuania. ENS Conference TopSeal 2006 Transaction. [CD]. Olkiluoto, 2006 September 17–20.

8. Interim Main Report of the Safety Assessment SR-Can. SKB Technical Report TR-04-11, 2004. Swedish Nuclear Fuel and Waste Management Company (SKB), Stockholm, Sweden.
9. Äspö Hard Rock Laboratory. Annual report 2008. SKB Technical Report TR-09-10, 2009. Swedish Nuclear Fuel and Waste Management Company (SKB), Stockholm, Sweden.
10. CLEALL P.J., MELHUISH T.A., THOMAS H.R. Modelling the three-dimensional behaviour of a prototype nuclear waste repository. *Engineering Geology*, 2006, Vol. 85, p. 212–220.
11. HERMANN, O. W., WESTFALL R. M. ORIGEN-S: SCALE System Module to Calculate Fuel Depletion. Actinide Transmutation. Fission Product Build-up and Decay and Associated Radiation Source Terms. Rev.5. Oak Ridge National Laboratory. March 1997.
12. What requirements does the KBS-3 repository make on the host rock? SKB Technical report TR-00-12. 2000. 143 p.

TERMO-HIDRO-MECHANINIŲ PROCESŲ SKAITINIS VERTINIMAS MODELINIAME RBMK-1500 PANAUDOTO BRANDUOLINIO KURO KAPINYNE KRISTALINĖSE UOLIENOSE

Darius Justinavičius
Branduolinės inžinerijos laboratorija
Lietuvos energetikos institutas
Breslaujos g. 3, LT-44403 Kaunas
Telefonas 8-37 401 886
El. paštas: justinavicius@mail.lei.lt

ANOTACIJA

Šiuo metu vyrauja nuomonė, kad panaudotą branduolinį kurą (PBK) ir kitas ilgaamžes didelio aktyvumo atliekas tikslinga laidoti geologinėse formacijose naudojant inžinerinius ir natūralius barjerus. Dėl panaudotame branduoliniame kure esančių radionuklidų skleidžiamos intensyvios jonizuojančiosios spinduliuotės keliamo pavojaus žmonėms ir aplinkai šio kuro negalima laidoti paviršiniuose radioaktyviųjų atliekų kapinynuose.

Gelminių radioaktyviųjų atliekų kapinynų įrengimas geologinėse formacijose sutrikdo nusistovėjusią geologinės sistemos pusiausvyrą. Poveikis uolienoms gali būti dvejopas: 1) dėl kasamų požeminių tunelių, būtinų atliekų laidojimui, gali susiformuoti kasimo sutrikdyta zona, 2) tam tikrą laiko periodą iš palaidoto branduolinio kuro išsiskirs šiluma. Šie pokyčiai gali įtakoti giluminio kapinyno aplinkoje vykstančius ir tarpusavyje glaudžiai susijusius šiluminius, hidrogeologinius ir mechaninius (termo-hidro-mechaninius THM) procesus, todėl yra svarbu išanalizuoti ir įvertinti šių procesų įtaką inžinieriniams barjerams bei bendrai kapinyno saugai.

Pradėjus šiluminių, hidrogeologinių ir mechaninių procesų, vykstančių aplink vieną konteinerį su jame esančiu RBMK-1500 PBK modeliniame gelminiame kapinyne kristalinėse uolienose, skaitinius tyrimus, gauti pirminiai rezultatai yra pristatomi šiame straipsnyje. Procesų vertinimui buvo naudojama kompiuterinė programa COMPASS (Jungtinė Karalystė).

Raktažodžiai: šiluminiai, hidrogeologiniai, mechaniniai procesai, laidojimas, giluminis (gelminis) kapinynas, kristalinės uolienos, modeliavimas

CYSENI 2010, May 27–28, Kaunas, Lithuania
ISSN 1822-7554, www.cyseni.com

PHASOR MEASUREMENT UNIT APPLICATION IN FRAME OF INTERCONNECTION OF LARGE-SCALE POWER SYSTEMS

O. Kochukovs, A. Mutule
Institute of Physical Energetics
Aizkraukles 21, LV-1006 – Latvia
Phone: +371 67558616
Email: olegsk@edi.lv

ABSTRACT

This paper contains the analysis of existing, as well as possible future application of Phasor Measurement Units (PMU) in frame of interconnection of large-scale power systems. The work is based on the real example – interconnection between EU and Russian power systems. The paper reviews the technical specification of PMU, data concentrators and information output instruments as modern dynamic monitoring system for power grid.

The analysis have shown, that application of PMU in power system nodes gives a better opportunity to observe power system's state, to make optimal decision on planning or protection measures, to perform a forecast, to choose optimal management scheme etc.

Keyword: Power System Monitoring, Phasor Measurement Unit, Power System interconnection

1. INTRODUCTION TO COLLABORATIVE PROJECT INTELLIGENT COORDINATION OF OPERATION AND EMERGENCY CONTROL OF EU AND RUSSIAN POWER GRIDS (ICOEUR)

This chapter considers the collaborative project *Intelligent Coordination of Operation and emergency control of EU and Russian power grids (ICOEUR)* as an example of interconnection of large-scale power systems. Let us first review the largest unions of transmission system operators (TSO) in Europe.

The **UCTE** (Union for the Coordination of Transmission of Electricity) was founded in 1951 as the Union for the Coordination of Production and Transmission of Electricity consisting of interconnected companies from Switzerland, France and Germany. Over the time, most of TSOs of Continental Europe joined the association. In 1999, UCTE re-defined itself as an association of TSOs. UCTE represents 29 transmission system operators of 24 countries operating the synchronous grid of Continental Europe.

NORDEL was founded in 1963 for co-operation between the TSOs of Denmark, Finland, Iceland, Norway and Sweden for a further development of a harmonized Nordic electricity market.

The interstate integration of power grids provides multiple advantages concerning operation security as well as energy trading. As well they are concepts and objectives for the ICOEUR project [1]:

- Optimisation of the use of installed capacities
- Reliability improvements reducing the economic cost of power outages
- Improved control of system frequency to minimise major disturbances
- Sharing reserve capacities and reducing the level of reserves required
- Providing mutual support for the interconnected systems in case of emergency
- Improved energy market conditions in better integrated large scale systems

- Facilitating large scale integration of renewable energies due to higher flexibility of the interstate network operations.

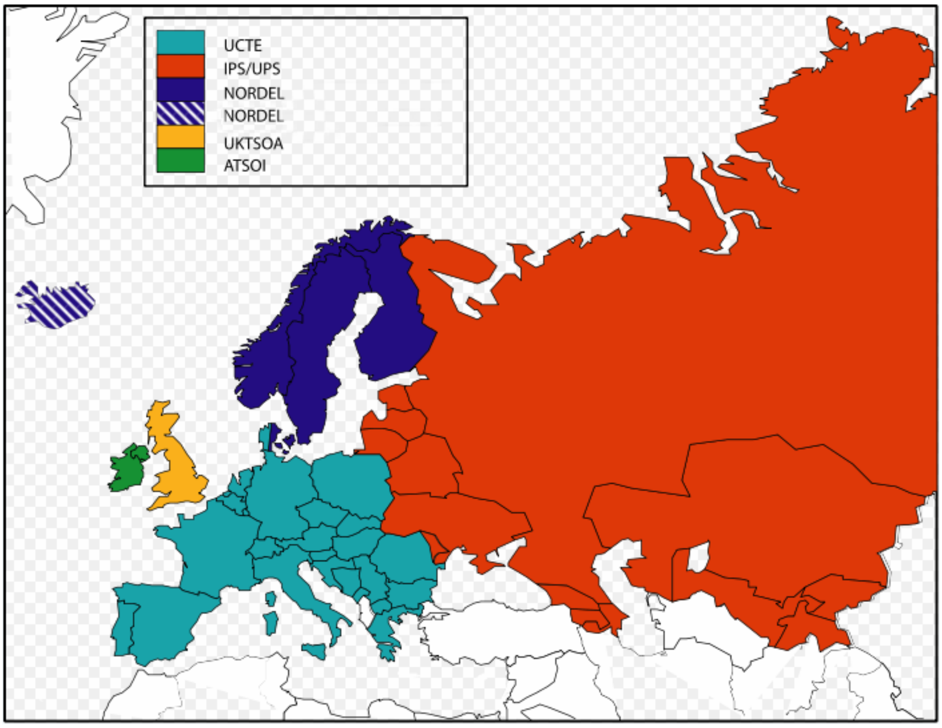

Fig. 1. The largest unions of TSOs in Europe

Due to these facts the UCTE interconnection expands continually since its establishment and the links to other interconnected systems like NORDEL grow stronger and further new links with neighbouring countries are either being constructed or planned. With large scale deployment of renewable generation, in particular large scale wind farms, interstate interconnection is of great importance to secure energy supply, optimizing the utilization of energy sources within larger areas, promote electricity trading between different regions, and meeting the requirements of economic development. Consideration is given to different scenarios of joint operation of UCTE and NORDEL with power grids on the territory of the former USSR.

These interconnections would result the largest electric synchronous interconnections worldwide, which provides a large reliable market platform to all participants.

An efficient and secure operation of the largest electrical interconnections worldwide assumes optimal choice of network interconnection and extension technologies, well defined protection functions that ensure secure operation of all partner networks in critical cases, as well as effective control and monitoring systems and strategies – it is the main issue of this paper.

2. PREPARATION FOR UCTE AND IPS/UPS SYSTEM INTERCONNECTION

During the workshops the project participants agreed to establish a common large-scale WAMS (Wide Area Measurement System) in order to investigate the technical pre-requirements and to verify the feasibility of a LS-WAMS for the interconnection of two large and extensive networks. The European and Russian power systems are governed by different rules and regulations and guidelines regarding the architecture of wide area as well as the exchange of data. In this respect the architecture of the hardware must also be examined as well as principles for data exchange [2].

A typical WAMS is shown in Fig. 2. PMUs (Phasor Measurement Units) are measuring voltage, current and frequency at substations. These measurements are sent to a PDC (Phasor Data Concentrator). A PDC correlates the data by time tag to create a wide system measurement. Then the correlated data is used for different applications.

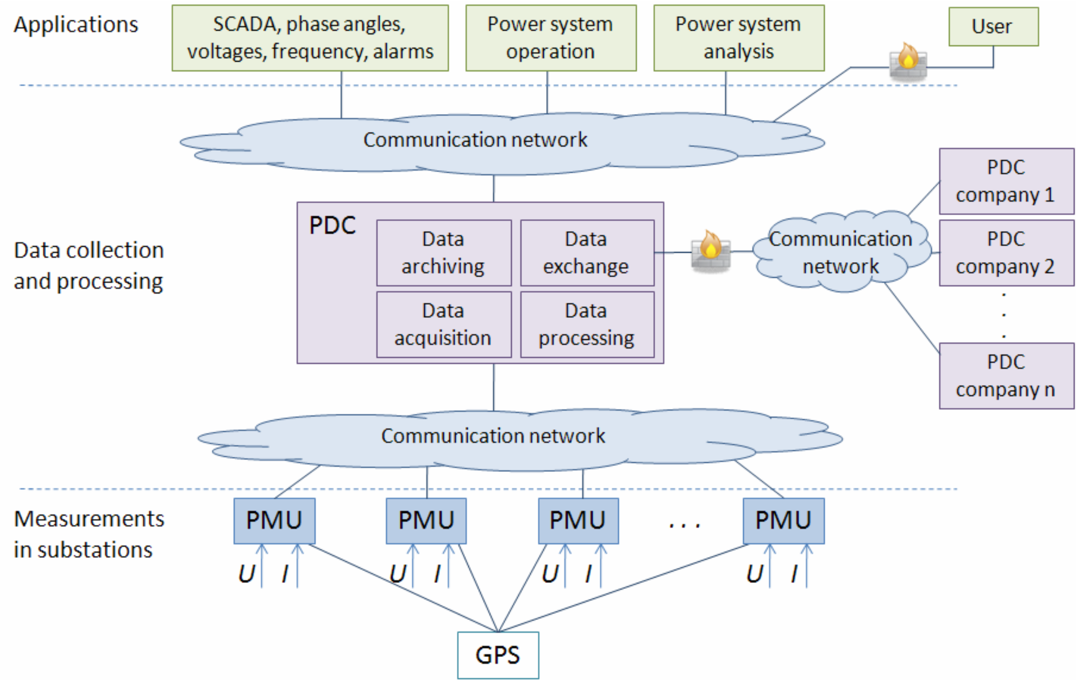

Fig. 2. Major WAMS components

Since in preparation phase for UCTE and IPS/UPS interconnection it is not possible to use the PMUs installed in transmission power systems due to some reasons, the decision inside the consortium was to build the 230 V WAMS. In this case PMUs as acquisition units are connected to an electrical socket (230 V) of the involved institution or the company. All data from PMUs are sent directly to the PDC in Ljubljana. Regardless that PMUs connection is performed on low voltage power system, frequency and inter-area voltage phase angles are quite close to the situation in high voltage power system [2].

In a first step, all available PMU will be connected to the PDC. This is done by connection of the PMU to the Internet. All PMU must have its own public IP address. The PDC is located in Ljubljana, Slovenia. The structure is shown in Fig. 2.

For measurement the PMUs are connected to an electrical socket of the involved institution or the company. All data are sent directly by the PMUs to the PDC in Ljubljana. At this stage of the project, only data on the local frequency and voltage phasors are exchanged. The frequency can always be measured at electrical sockets, and is therefore regarded as public. Aimed result of the first step is the knowledge about the hardware requirements.

In a second step, data exchange will be analyzed. The central question here is – what kind of data needs to be exchanged between the systems.

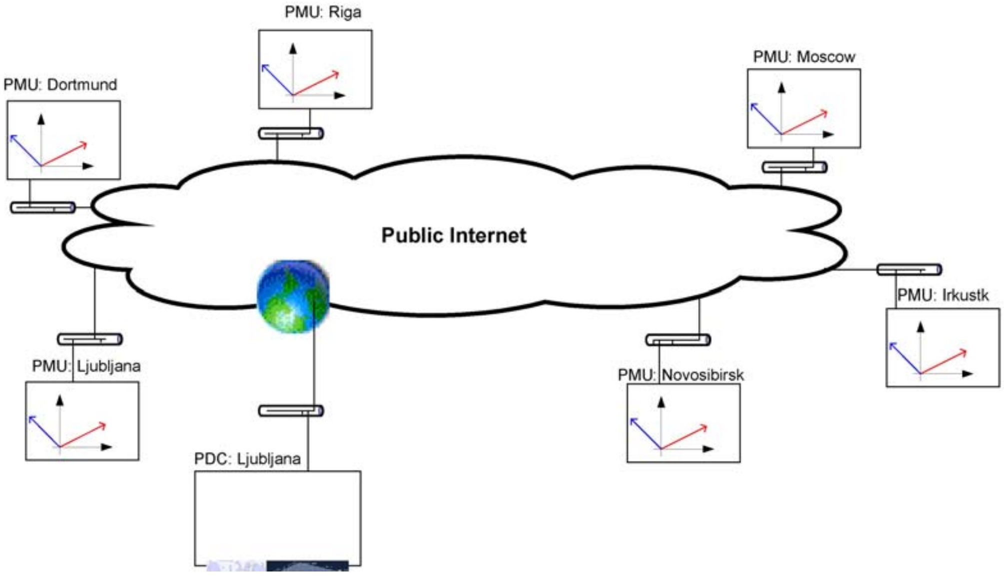

Fig. 2. First stage of large-scale WAMS

3. PMU SPECIFICATIONS

As expected outcome of the first task is to determine the requirements for the installation, set-up and operation of an LS-WAMS, in order to increase the number of the installed PMUs at different places and to examine the connection, mobile PMUs (Fig. 3) are necessary for a fast transfer to several places and for a fast installation.

The dimension and weight of a PMU are so low that such devices can be easily transported and therefore can be sent by mail. Thus PMUs can be easily distributed across a network. Similarly, the Voltage and Current Inlets can made available through laboratory plugs for a quick test setup. Then one voltage inlet can be used directly for the measurement. Devices may be adjusted according to the requirements for communication in advance. At the test site itself the device needs to be connected only to the AC socket and an Internet connection and thus can be easily taken into operation.

Fig. 3: Mobile PMU

Mobile PMU model was installed at the Laboratory of Power System Mathematical Modelling in Riga, Latvia in October of 2009.

3.1. PDC for 230V WAMS: WAProtector

WAProtector is a client-server oriented multifunctional device. WAProtector runs on the IBM server System x3650. WAProtector performs the following tasks:

- data acquisition from PMUs;
- phase angle difference monitoring;
- oscillation detection of phase angle difference;
- under/over frequency detection;
- under/over voltage detection;
- archiving of data into cycling data base. The storage is 14-day period;
- visualisation for users.

3.2. PMU Accuracy

Because PMUs are measuring instruments, the standard C37.118 contains also a definition for the accuracy of the measurements. A test signal is compared in addition to the measuring signal. The name for the divergence is Totally Vector Error (TVE). The accuracy is limited to maximum TVE of 1% besides, steady state is a precondition. However, the frequency, magnitude and phase angle can vary. Depending on how far these variations can appear and due to a TVE of less than 1%, PMUs can be divided into levels of compliance. Besides, level 1 is a proven precondition in general [2].

3.3. PMU&PDC Specification

PMUs are connected to measurement transformers in substations. The phasors are sent to a PDC. All communication links are based on Ethernet. The protocols are IP / TCP or IP / UDP, multicast, unicast or broadcast. Assuming a report frame of 100 bytes and a reporting rate of 20 ms a bandwidth of 40 kbit per second is required. That means that four percent of 1Mbit connection is occupied by a data stream of one PMU.

Let us review the main requirements for real-time data processing:

- the PDC as a client must be able to simultaneously acquire data from at least 100 PMUs with full resolution 50(60) samples per second;
- the PDC as a server must be able to simultaneously send data to at least 10 clients with full resolution of 50 (60) samples per second;
- data base have to support data storage with full resolution (50 (60) samples per second) for all data and at least for 14 days;
- events database must have the ability to archive at least 1.000.000 last events.

4. DATA VISUALISATION POSSIBILITIES

Let us review the concept of data visualization:

- multi-user graphical interface (GUI) performed as WEB SCADA system;
- data access over the Internet by the start-up from Internet browser;
- the latest version of GUI is automatically loaded on a client computer;
- GUI activates the visualisation and control according to the client rights;
- client computer requirements are: Internet browser, .NET Framework 3.0.

The visualisation system enables multi-user Web SCADA presentation of:

- real-time measurements and calculated values;
- historical database;

- events and alarms;
- event disturbance recordings;
- historical data stored on the local user computer;
- export of data into different formats (excel, etc).

The system also enables the animation of historical recorded data. In this way the event or selected time period can be reviewed and analyzed.

The user can choose between two and three-dimension time-base curves, phasor diagrams, bar charts, etc.

In the following example of visualisation we will use real data of connected PMU in four locations: 1) Dortmund (DE), 2) Ljubljana (SLO), 3) Riga (LV), 4) Helendoorn (NL). Fig. 4 presents the general review of visualization functions.

Fig. 4. Example of data visualisation

Let us now review two visualisation options in details. Fig. 5 presents windows, which shows voltage magnitude, voltage phase angle, frequency change and frequency magnitude. Here we can see historical change and current magnitudes. As we can see, at the moment Latvian PMU shows stable, comparatively high voltage magnitude about 231 V (first chart of Fig. 5, yellow curve).

Also, our historical frequency change form (last chart of Fig. 5, yellow curve) differs from the ones of Dortmund, Ljubljana and Helendoorn, as we have different frequency control systems and our power systems have not been synchronized yet.

Voltage phasors can also be observed in polar chart as shown in Fig. 6. Depends on the power system frequency voltage phasors circulate around. If the frequency is below 50 Hz then voltage phasors rotate clockwise and the opposite if the frequency is above 50 Hz. If the frequency is exactly 50 Hz phasors then voltage phasors are stable. More the frequency deviate from the 50 Hz faster is the rotation of voltage phasors.

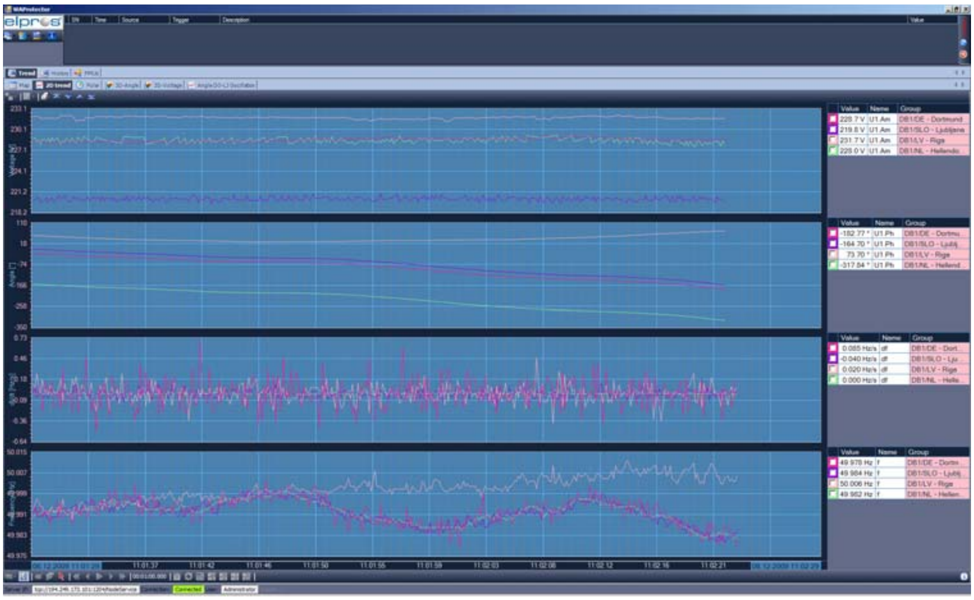

Value	Name	Group
228.7 V	U1 Am	DB1/DE - Dortmund
219.8 V	U1 Am	DB1/SLO - Ljubljana
231.7 V	U1 Am	DB1/LV - Riga
228.0 V	U1 Am	DB1/NL - Hellendo

Value	Name	Group
-182.77 °	U1 Ph	DB1/DE - Dortmu
-164.70 °	U1 Ph	DB1/SLO - Ljublj
73.70 °	U1 Ph	DB1/LV - Riga
-317.84 °	U1 Ph	DB1/NL - Hellend

Value	Name	Group
0.065 Hz/s	df	DB1/DE - Dort
-0.040 Hz/s	df	DB1/SLO - Lju
0.020 Hz/s	df	DB1/LV - Riga
0.000 Hz/s	df	DB1/NL - Helle

Value	Name	Group
49.978 Hz	f	DB1/DE - Dortm
49.984 Hz	f	DB1/SLO - Ljublj
50.006 Hz	f	DB1/LV - Riga
49.982 Hz	f	DB1/NL - Hellen

Fig. 5. One minute trend window of voltage magnitude, voltage phase angle, df/dt and frequency

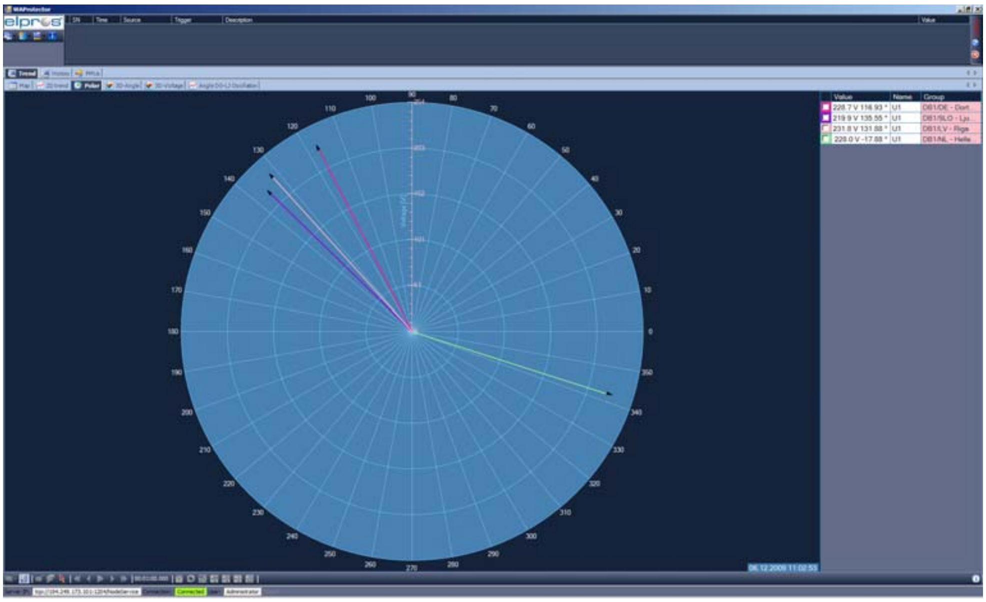

Value	Name	Group
228.7 V 116.93 °	U1	DB1/DE - Dort
219.9 V 135.55 °	U1	DB1/SLO - Lju
231.8 V 131.88 °	U1	DB1/LV - Riga
228.0 V -17.88 °	U1	DB1/NL - Helle

Fig. 6. Real-time presentation of voltage phasors

Besides, there are available such visualization options as: 3D presentation of voltage angles and voltage magnitudes, voltage phase angle difference oscillation detection, power quality monitoring (PQM), waveform data phase voltages and phase currents etc.

Let us review an example of the event detected by 230 V WAMS – outage of generation unit in Slovenia. On December 3rd the WAMS captured an event which caused the frequency drop and its damped oscillation in Slovenia region. The event also caused the change in voltage angle difference between Dortmund and Ljubljana. According to Elektro Slovenja (Slovenian TSO) Network weakly reports it was found out that the generation unit outage occurred in thermal power plant in Šoštanj. Fig. 7 shows changes in electric power system of

Slovenia at the moment of generation unit output. We can see angle difference change in the first chart and temporary frequency drop in the second chart [2].

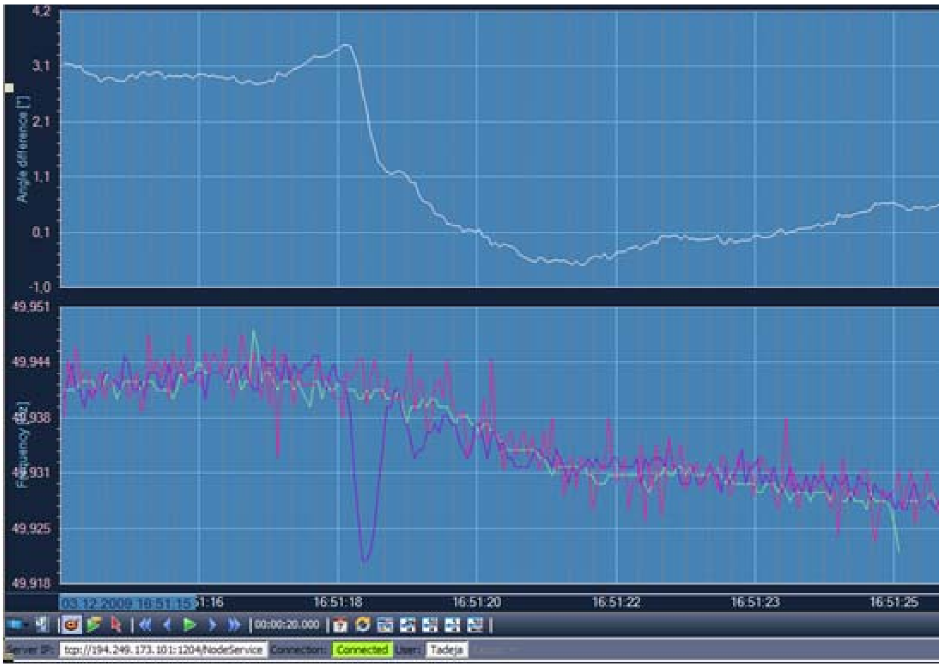

Fig. 7. Outage of generator in Thermal power plant in Slovenia:
1 chart – angle difference (^{O}), 2 chart – frequency (Hz)

5. CONCLUSIONS

Due to reviewed advantages, ICOEUR project has significant meaning in development of European, Scandinavian and Russian power systems. Definition of pre-requirements for interconnection of above mentioned systems can be done with a help of WAMS.

Building WAMS is a long and complicated process, however 230 V WAMS is easily to build and manage. In current stage of ICOEUR project it is realized by Mobile PMUs. Mobile PMU can be easily transported and installed at necessary location. Reliability of the communication over the public Internet network can vary depending on PMU location, however it is satisfying.

Even 230 V WAMS have potential to detect events, such as accidents. Based on wide area angle difference oscillation detection, WAMS can detect events occurring inside the whole power system.

REFERENCES

1. Introduction in ICOEUR project for participants.
2. ICOEUR project, report of Task 3.2.1: *Wide area power system monitoring with PMU under use of shared data concentrator.*
3. Mikhail Simonov, Riccardo Zich, Marco Mussetta (2009). *Intelligent information processing in smart grids and consumption dynamics*, p. 11–20.

CYSENI 2010, May 27–28, Kaunas, Lithuania
ISSN 1822-7554, www.cyseni.com

AEROSOL DEPOSITION IN PHEBUS CONTAINMENT DURING FPT-2 TEST

A. Kontautas, E. Urbonavičius
Lithuanian Energy Institute
Laboratory of Nuclear Installation Safety
Breslaujos g. 3, LT-44403 Lithuania
Phone: 8 37 401983
Email: aurkon@mail.lei.lt, egis@mail.lei.lt

ABSTRACT

Most of the radioactive fission products that can escape from a nuclear power plant during a severe accident will do so in the form of aerosols. One of the objectives of accident analysis is the prediction of the behaviour of these radioactive aerosols, which are small solid particles or liquid droplets suspended in a gas phase. The integral experiments performed in PHEBUS facility give possibility to simulate the release, transport and deposition processes of fission products and structural materials during accident. The performed experiments demonstrate the complex inter-linkage between different phenomena and have refined understanding of nuclear aerosols behaviour, particularly in the containment, where is possibility to measure particle sizes and compositions. The FPT2 experiment is part of the PHEBUS-FP program being conducted to investigate the key phenomena that may occur during a severe accident in Light Water Reactor. The FPT2 test is the fourth experiment of the international PHEBUS-FP program conducted by the French "Institut de Radioprotection et de Surete Nucleaire" (IRSN).

This paper presents analysis of aerosol deposition and distribution processes in PHEBUS containment using COCOSYS code. For the analysis two models of 19 and 16 nodes were developed. The calculated thermal-hydraulic parameters are in good agreement with the measured results. The correct simulation of thermal-hydraulic phenomena is a precondition for simulation of transport and deposition of the materials released from the degrading core. Analysis of aerosol deposition showed, that calculated deposition velocity is in good agreement with experimental results. Different flow paths inside the models give different deposition distribution, but in both cases deposition on the containment walls is significantly smaller than measured. Further investigation of diffusive deposition model is needed.

Keywords: COCOSYS, aerosol, severe accident, containment

1. INTRODUCTION

Generally the Nuclear Power Plants (NPP) shall be designed to be safe and operated without significant effect on individuals, society and environment. One of the most extensive international programs, which was initiated in 1988 after major accidents in Nuclear Power Plants (Chernobyl and Three Mile Island) and covers the whole spectrum of severe accidents progression, is the international program PHEBUS-FP. The PHEBUS-FP consists of five in-pile experiments being successfully performed during the period from 1993 to 2004. The main objective of the programme is to study the release, transport and retention of fission products in an in-pile facility under conditions representative of a severe accident in a Light Water Reactor (LWR) [1].

Previous analysis of thermal-hydraulic and aerosol transport results in PHEBUS FPT-1 containment started with an initial model of 11 nodes [2]. Performed thermal-hydraulic analysis showed good agreement between measured and calculated results, but aerosol deposition and deposition distribution was not sufficient. Deposition on "wet" condenser surface was too low, because of too little flows reaching condenser surface. Aerosol deposition on the external containment walls was too low as well. Consequently, the new model of 19 nodes was developed, with 8 additional nodes in the model centre. Nodes in the centre of model changed the flow paths and deposition on “wet” condenser increased and come in compliance with experiment results [3]. Later performed parametric analyses of average aerosol density and solubility parameters, showed only minor influence on aerosol deposition distribution [4]. The model of nineteen nodes was used and for parametric analyses of FPT-3 experiment. Analyses of aerodynamic mass median diameter and aerosol dynamic shape factor were investigated, but influence to deposition distribution was not in good compliance with experiment as well [5]. The reason for such deposition distribution is still not well known and additional model investigation is needed.

This paper presents the analysis of processes that occur in PHEBUS containment under FPT-2 experiment conditions. For simulation of the aerosol transport in PHEBUS containment model of 19 nodes and new model of 16 nodes for COCOSYS code was developed. The new model was developed in cooperation with scientists from company GRS mbH (Germany). The aim of cooperation with GRS is to perform an integral investigation of aerosol transport, fission products transport and iodine radiochemistry. This paper presents analysis of thermal-hydraulic parameters and aerosol deposition, i.e. the part for which Lithuanian Energy Institute is responsible in cooperation with GRS mbH. The presented results provide a basis for further investigation of iodine radiochemistry to be performed by GRS mbH.

2. DESCRIPTION OF EXPERIMENT FPT-2

2.1. Geometric conditions

The PHEBUS containment vessel is a 10 m^3 tank (see Fig. 1), made of electro-polished stainless steel (AISI 316L), in which aerosols and gases conveyed through the experimental circuit during the test are collected. Height of containment is 5 m with an inner diameter of 1.8 m. The altitude of containment vessel is shown in Fig. 1. The containment wall represents a surface of about 25 m^2. The containment has cylindrical form with rounded bottom and top. The outer vessel walls were heated to avoid steam condensation and subsequent aerosol deposition on the containment top vault and vertical walls during the test. The top vault is equipped with a group of three condensers, which are designed to control heat transfer, steam condensation and thus simulate the cold structures of a reactor building. Total surface area of condensers is 3.333 m^2. The condenser surface is divided into two parts: the cooled condensing or “wet” condenser surface (area: 0.775 m^2 per condenser) and the non-condensing or “dry” condenser surface (area: 0.336 m^2 per condenser). The lower part of each condenser is kept dry by heaters and contains equipment to collect condensate from the upper cooled part. When the collection device is full, the condensate is automatically drained into the sump. The cooled surfaces of condensers are covered with epoxy paint as a source for organic iodine formation. The sump is a lower vessel part closed by a curved bottom structure with volume of 0.1 m^3. The sump has a diameter of 0.584 m and height is 0.6 m in order to reproduce a representative atmosphere-water exchange surface. The sump was initially filled with 120 l water. The injection pipe tag to the containment of steam, hydrogen and aerosols is located -2.86 m. Pipe tag is in the centre of containment and is pointed to the condensers.

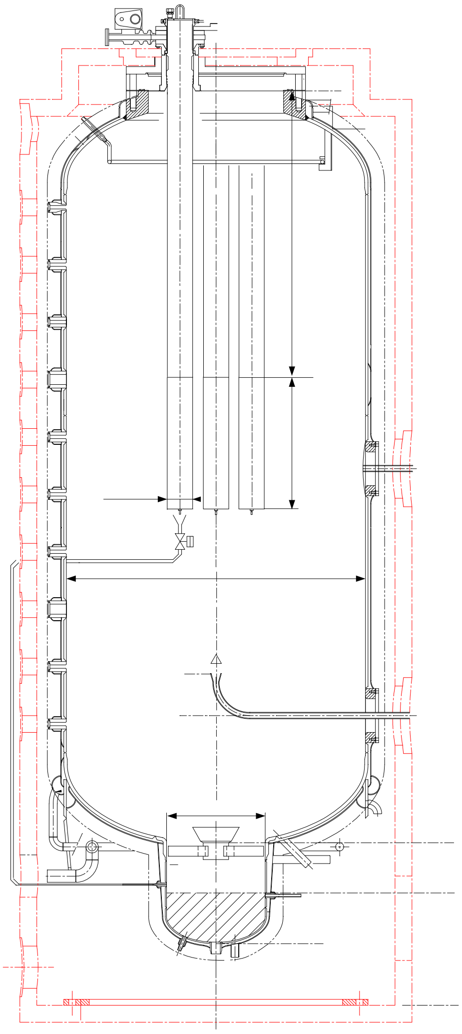

Fig. 1. Schematic view of PHEBUS containment

2.2. Initial and boundary conditions

The composition of the containment atmosphere consists of condensable gases (i. e., steam) and non-condensable gases (i.e., H_2, O_2, N_2 and He). Initially the containment atmosphere contains 397 moles of a mixture of non-condensable gases composed of 95% N_2 and 5% O_2. During the test preparation phase the nitrogen is injected into containment to avoid any explosion hazards with the possible hydrogen injection and also after depressurization to 1 bar, the desired reduced containment oxygen concentration is also 5 % O_2 in volume. Initial pressure in the containment is 1.95 bar, the average atmosphere temperature is 108 ^{o}C and average relative humidity – 51.48 %.

Measured steam and hydrogen flow rates into the containment are shown in Fig. 2. Steam injection to containment started after -3180 s. Maximum steam mass flow rate released to containment is 0.5 g/s. After 9000 s a fraction of the injected steam is converted into hydrogen as the result of oxidation process. Maximum hydrogen flow rate is ~0.05 g/s after 10000 s. After 16000 s there is another steam flow decrease, which is also related to H_2 generation. The first fuel-clad failure in the reactor was recorded at about 5630 s and around 3000 s later (8730 s) the control rod failed. As a consequence, aerosols arrived to containment after ~9000 s and finished after ~19500 s (see Fig. 3). Injected aerosol mass is 44.69 g.

Sequential samplings devoted to analysis of gases and aerosols characterisation are implemented in the containment and detailed description of sampled volumes with thermal hydraulic conditions is given in FPT-2 test Final report [1].

During the whole test period the temperature of containment walls in contact with the gas phase was 110 °C, temperature of the “wet” condensers 90 °C, temperature of the “dry” condensers 120 °C, and temperature of walls in contact with the sump 90 °C. The containment vessel boundary conditions are chosen to limit the relative humidity to from about 50 up to 70 % during the transient, in order to prevent steam condensation on the external containment. Steam condensation in the containment was controlled by the cooled condensing surfaces of the condensers [3].

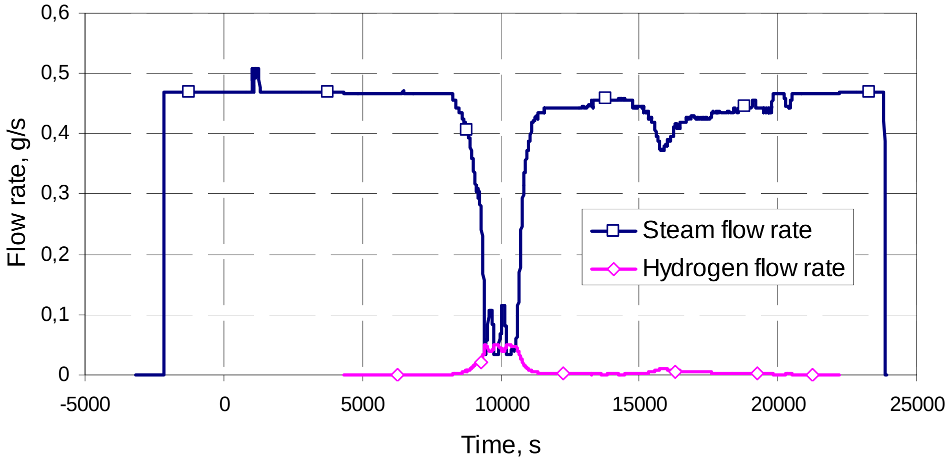

Fig. 2 Steam and hydrogen flow rates to containment during FPT-2

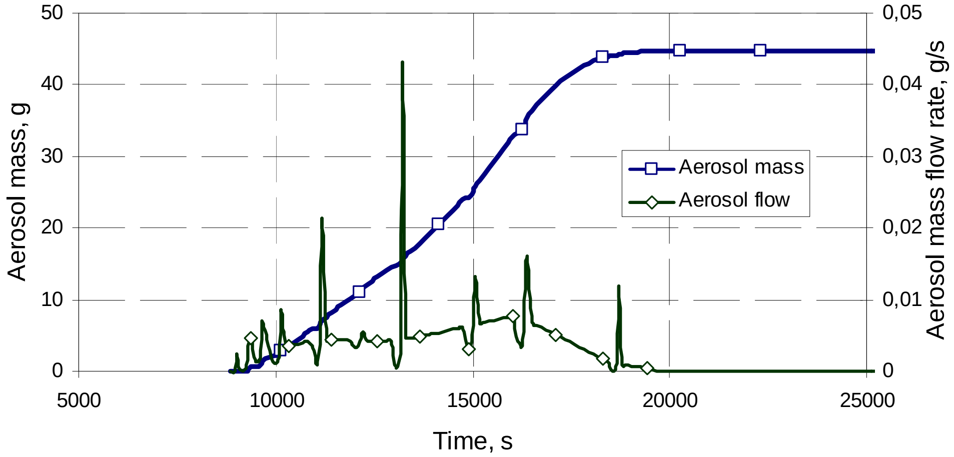

Fig. 3 Injected aerosol mass and flow rate to containment during FPT-2

3. MODELS OF PHEBUS CONTAINMENT

For simulation of the aerosol distribution and deposition in the PHEBUS containment two models for COCOSYS code were developed (see Fig. 4). The nodalization schemes of Model A and Model B are shown in Fig. 4. Model A was already used for FPT-1 and FPT-3 tests analyses [3]. New Model B of 16 nodes was developed with enlarged zones near the containment walls, only one zone for the deposition on the containment floor and one additional zone at the top. Such variations have to change gas flow paths inside the containment and get better agreement for aerosol deposition distribution with experiment results.

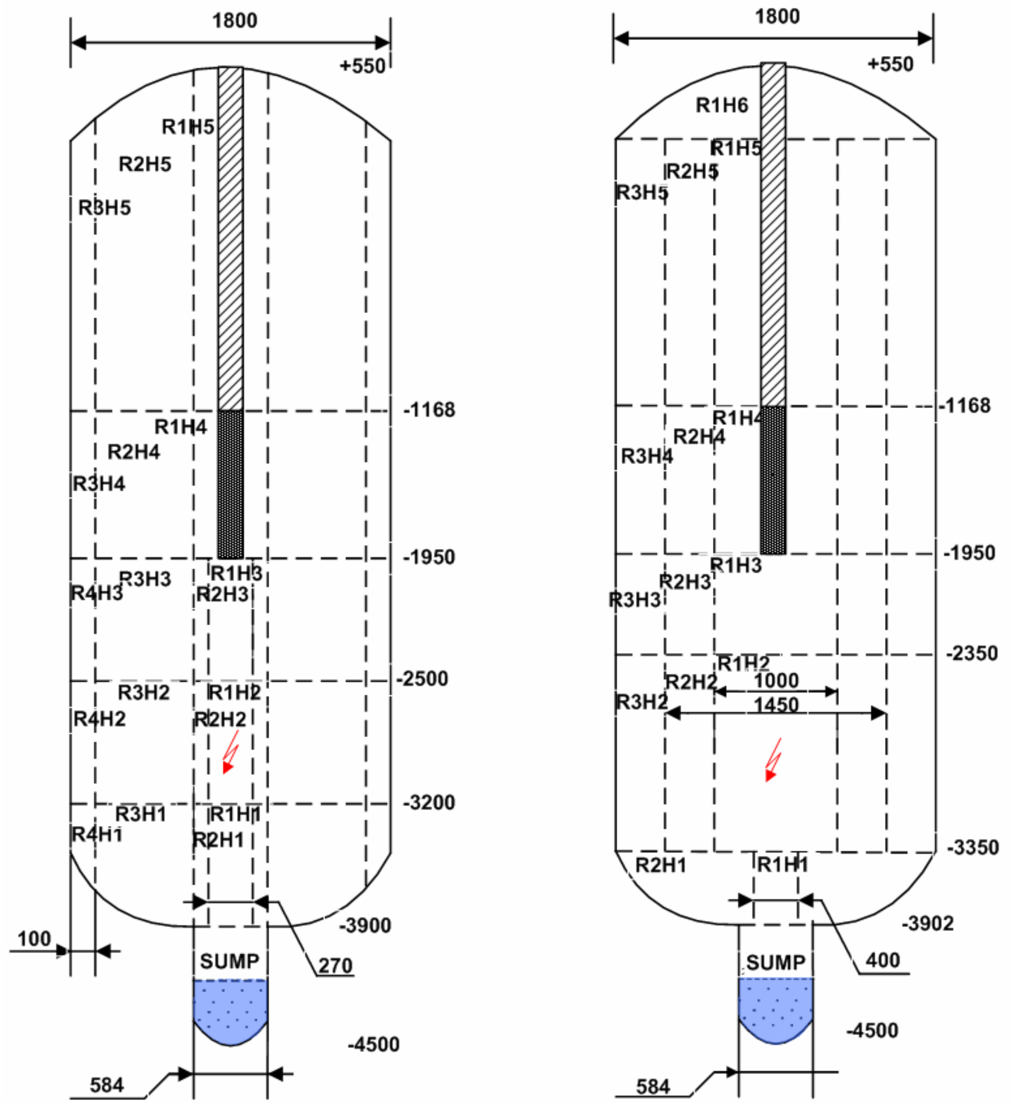

Model A Model B

Fig. 4 Nodalization schemes of PHEBUS containment

Model A radial subdivision consists of 4 rings above the sump and below condensers, and there are 3 rings at level of condensers. The diameter of one ring in radial subdivision corresponds to the diameter of the sump. The diameter of the central part of the subdivision was defined in such way that the injected plume of gases could be better defined in the model. There are defined 6 levels for vertical subdivision. Containment part between "wet" condensers bottom and sump are divided into three almost equal parts ~0.7 m height. "Wet" and "dry" condensers are in separated nodes. A more detailed description of the Model A nodalisation is presented in paper [3].

Model B radial subdivision consists of two rings in close level above the sump. There is a centre node R1H1 and node R2H1 that simulates the bottom part of the vessel. In level above -3350 mm and below 0 mm there are three almost equal area rings. The diameter of the radial subdivision was defined in such way, that the flow areas are similar. Such approach to nodalization gives similar flow velocities. A ring close to the external containment walls is enlarged to 175 mm width. At the top vault of the vessel there is one additional node. Simulation at the top vault by single node gives the well-mixed conditions at the top of facility. Similar approach is used at the bottom of facility. Above the SUMP nodes are defined in such way, that there are two junctions to the SUMP. Such approach ensures better mixing and allows avoiding dead-end node, which is not recommended in COCOSYS user's manual [7].

In both models the sump is simulated as the single node and the pipe, through which the gases and aerosols from the reactor core are injected to the containment, is located in the node R1H2.

For simulation of the gas flows between the nodes there are defined atmospheric junctions with real geometric areas. Also, there are defined junctions for simulation of the water drainage from the "wet" condenser to the sump. It is assumed that condensate is drained into the sump when is reached the thickness of 1 mm water film on the condenser.

In the developed models the initial and boundary conditions (e.g. initial pressure, temperature, humidity, etc.) are defined according to FPT-2 test specification and described in Section 2.2.

The aerosols are divided to 20 size classes assuming diameter range 10^{-8} – 10^{-4} m. The models of gravitational, diffusive and diffusiophoretic deposition mechanisms are considered in the model. It is assumed that aerosols could be washed down from the vertical walls by condensate flow and slip through the vertical junctions. Aerosol particles are spherical. The thickness of diffusive boundary layer in PHEBUS containment is assumed 10^{-4} m [6]. Considering the experiment results detected elements in PHEBUS containment can be classified into elements that are soluble (Cs,Rb and I), partly soluble (Ce, Te, Zr, Ru, Sn, In, Ag, W and U) and non-soluble (Ba, Mo, Cd, Re and Tc). The composition of elements detected in containment is given in Final test report [1]. It was supposed, that the solubility factor for soluble elements is 1.9, for partly soluble elements is 1.5 and for non-soluble elements is 1.0. Consequently, the estimated average solubility factor of generic aerosol component is 1.55, which means that aerosols are partly hygroscopic. According to PHEBUS FP programme annual progress report the average aerosol density was preliminary estimated to be ~3000 kg/m^3 [8].

4. RESULTS OF ANALYSIS

4.1. Analysis of thermal-hydraulic parameters

The correct simulation of thermal-hydraulic phenomena is a precondition for simulation of transport and deposition of the aerosols in the containment. Comparison of calculated and measured total pressure is presented in Fig. 5. At the beginning of the test transient, the steam injection of ~0.5 g/s resulted in pressure increase from initial 1.95 bar to about 2.2 bar in 20000 s. Because of steam conversion into hydrogen as the result of oxidation process after 10000 s, there is a sharp pressure decrease to 2.1 bar. After the steam injection stopped the pressure in experiment dropped to an initial value of ~1.95 bar. There is only a little difference between calculated and measured pressure during the whole test sequence. The maximal total pressure is overestimated after 45000 s, but it is less then ~0.05 bar, which is ~2% of gauge pressure.

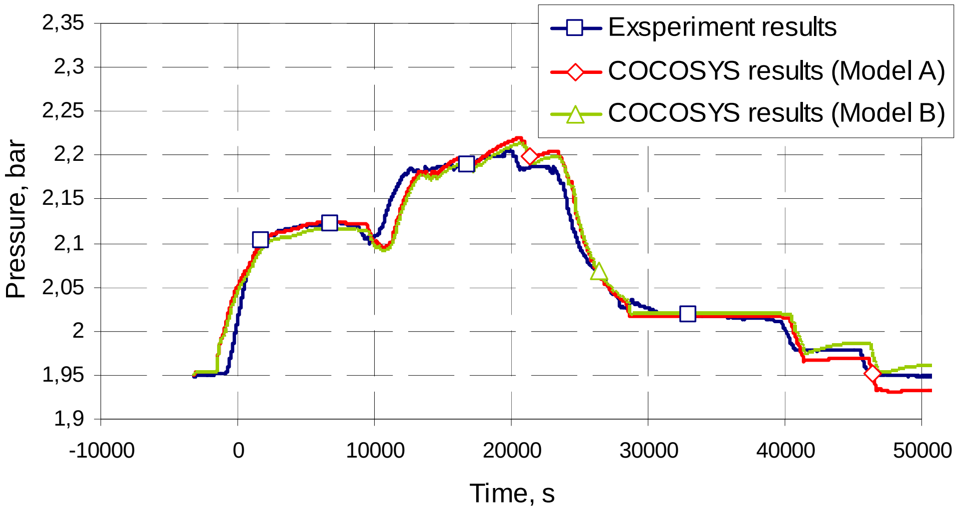

Fig. 5 Pressure in containment atmosphere

Comparison of calculated and measured gas temperature in containment is presented in Fig. 6. In general the gas temperature evolution is predicted rather well in both models and the difference between calculated and measured temperatures does not exceed 1 °C. After the containment isolation and sampling sequence the average measured and calculated gas temperature stabilised at the value close to 108.4 °C.

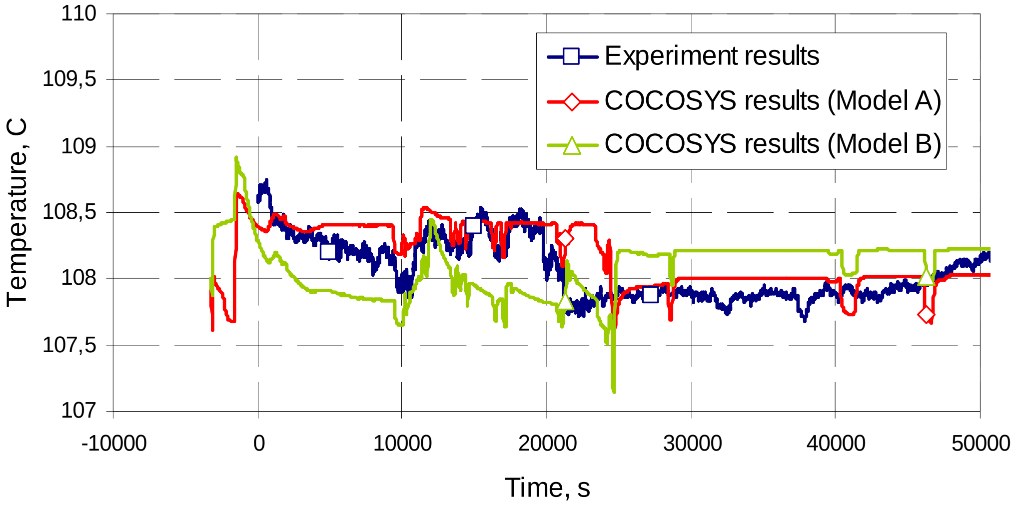

Fig. 6 Temperature in containment atmosphere

Comparison of calculated and measured condensation flow rates is presented in Fig. 7. As it was mentioned before the steam condensation in the containment, during the test, occurs only on the “wet” part of the condenser. As it could be expected from the comparison of the pressure and temperature results, the steam condensation rate is also predicted rather well. Also, there are no significant differences between the calculated values in Model A and Model B.

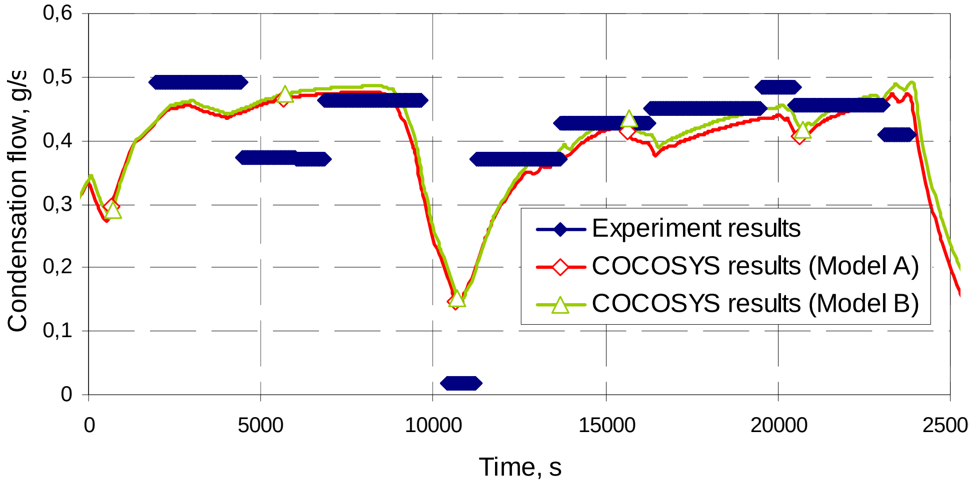

Fig. 7 Condensation flow in containment atmosphere

Taking into account the results presented in Fig. 5–Fig. 7 the thermal-hydraulic parameters in PHEBUS containment during FPT-2 in both models are predicted rather well and there are no significant differences between the measured and calculated values. Such compliance shows that the thermal-hydraulic part of containment model is developed to acceptable level and enables further analysis of aerosol transport and deposition processes, which is presented in next section.

4.2. Analysis of aerosol deposition in PHEBUS containment

Fig. 8 presents comparison between the measured and calculated aerosol mass suspended in the containment atmosphere. After ~17600 s there is observed a maximum of the suspended airborne aerosol mass in containment. In general the calculated airborne aerosol mass is overestimated during whole analysed period, but the difference is less than 2 g. The maximal measured mass is ~19 g, while calculated in Model A is ~20 g and in Model B is ~21 g. The difference between the calculated and measured mass does not change significantly, which shows that total deposition rate are rather well calculated by COCOSYS.

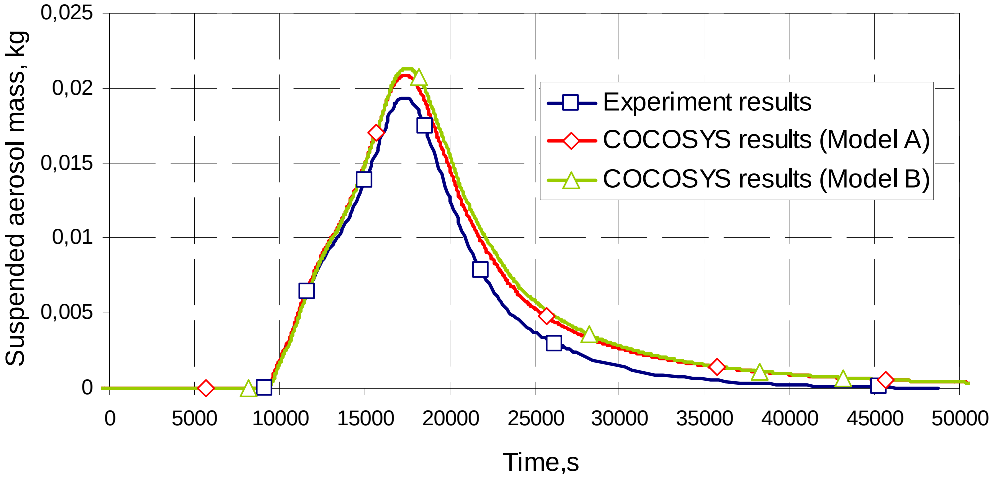

Fig. 8 Suspended aerosol mass in PHEBUS containment

Fig. 9 presents the measured and calculated results of aerosol average geometric mass median diameter (GMMD) in containment atmosphere. According to experiment results, the structure of the aerosol particle is predominantly ball shaped, with sizes typically ranging from 0.5 to 1 µm. Observations showed that these very fine particles might be agglomerated to form particles of size up to 20 µm [1]. A calculated result is ranging from 0.5 to 1 µm regarding agglomeration processes. Difference between Model A and Model B is not observable.

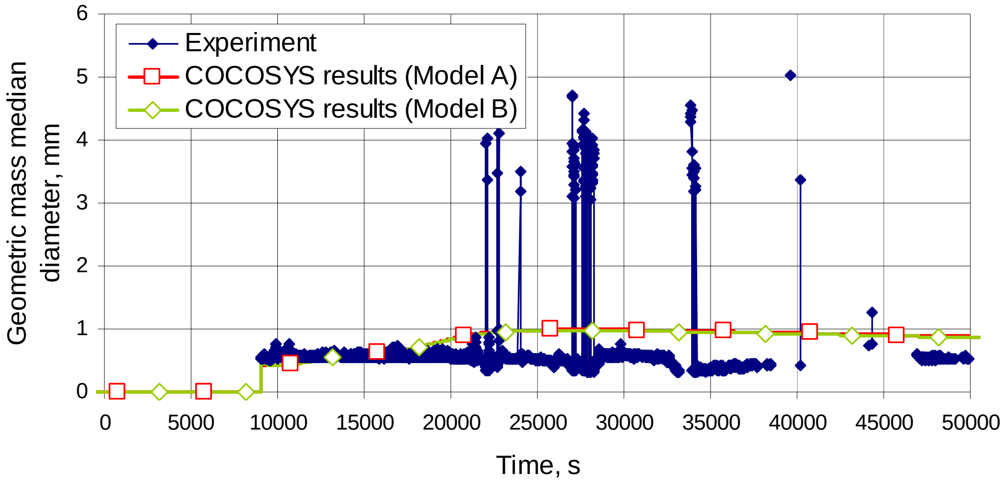

Fig. 9 Aerosol geometric mass median diameter in PHEBUS containment

Distribution of aerosol deposition on different surfaces in containment is shown in Table **1**. The largest aerosol deposition is on the containment floor around the sump, where 74% of aerosols is deposited. On the condensers and in the sump there are deposited 14% of aerosol mass, while on the vertical containment walls and removed by the sampling 12%. The results received with COCOSYS Model A shows good agreement for the particles deposition on the floor, but deposition on the containment walls and removed by the sampling is significantly lower (1% instead of measured 12%) while deposition on the condensers is overestimated. The results received with COCOSYS Model B shows a rather good agreement for aerosol deposition on condensers, while deposition on the floor is overestimated. The deposition of aerosols on the vertical containment walls is significantly underestimated again. The deposition on the vertical walls is determined by the diffusive deposition mechanism. In the paper [9] there is presented investigation of the influence of the thickness of the diffusive boundary layer on the aerosol deposition in FPT-1 test and it is shown that this parameter does not have a significant influence on the results. Therefore there should be performed further investigations on the diffusive deposition mechanism and possibly model of diffusive deposition available in COCOSYS should be updated.

Table 1. Distribution of aerosol deposition

	Floor of containment	Condenser surfaces and sump	Containment walls + samplings
Experiment	74.0%	14.0%	12.0%
Model A	74.1%	24.9%	1.0%
Model B	86.0%	13.28%	0.72%

5. CONCLUSIONS

Analysis of thermal-hydraulic parameters and aerosol deposition and distribution processes in the containment during FPT-2 test was performed using lumped parameter code COCOSYS.

The calculated thermal-hydraulic and measured results are in good agreement and enables analysis of aerosol transport and total deposition processes. The influence of nodalization on the calculated thermal-hydraulic parameters is minor.

Difference between the measured and calculated suspended aerosol mass is less than 2.5 g through all the investigated time period, thus the aerosol deposition rate is rather well calculated using both models.

Performed analyses of aerosol total deposition distribution shows that further investigation on the diffusive deposition mechanism is needed and possibly model of diffusive deposition available in COCOSYS should be updated.

REFERENCES

1. GREGOIRE, A.C., MARCH, P., PAYOT, F., RITTER, G., ZABIEGO, M., BRENAECKER, A., BIARD, B., GREGOIRE, G., SCHLUTIG, S. Final report FPT2. IRSN and Commission of the European Union Institute for Energy, 2008. 1968 psl. Batiment No 250-P 111-BP N 03.
2. KONTAUTAS, A., URBONAVIČIUS, E. Vidinių srautų modeliavimo įtaka aerozolių nusėdimo skaičiavimams PHEBUS FPT-1 eksperimente. Šilumos energetika ir technologijos 2007. konferencijos pranešimų medžiaga, Kauno technologijos universitetas, 2007 vasario 1-2. Kaunas: Technologija, 2007. ISBN 978-9955-25-338-9, p. 93–96.
3. KONTAUTAS, A., URBONAVIČIUS, E., RIMKEVIČIUS, S, Influence of the nodalisation and modelling parameters on the results calculation of aerosols deposition in PHEBUS experimental facility. Energetika, 2007, ISSN 0235-7208. T. 53, Nr. 4, p. 16–27.
4. KONTAUTAS, A., URBONAVIČIUS, E. Solubility and density parameters influence to aerosol deposition and distribution in PHEBUS FPT-1 experiment. CYSENI 2008. Proceedings of annual conference of young scientists on energy issues. [CD]. Kaunas: Lithuanian Energy Institute. 2008 May 29.
5. HERRANZ, E. L., FONTANET, J., VELA-GARCIA, M. In-Containment Thermal-hydraulic and Aerosol Behaviour during Severe Accidents: Analysis of the PHEBUS-FPT2 Experiment. Unit of Nuclear Safety Research, CIEMAT. Proceedings of ICAPP'06. Reno, NV USA, June 4–8, 2006.
6. KRESS, T.S., Proceedings of the CSNI Specialists Meeting on Nuclear Aerosols in Reactor Safety. U.S. Nuclear Regulatory Commision. Engineering technology division, NUREG/CR-1724, 601 p. 1980.
7. KLEIN-HEßLING, W., COCOSYS v1.2 Manuals GRS-P-3, in preparation Gessellshaft fur Anlagen – und Reaktorsicherheit (GRS) mbH, 2000, 469 p.
8. SIMONDI-TEISSEIRE, B., ZEYEN, R., CLEMENT, B., FABER, H., MICAELLI, J.C. PHEBUS FP programme annual progress report. PHEBUS report, September 2007 – August 2008. 35 psl. Batiment 250-BP 3.
9. KONTAUTAS, A., URBONAVIČIUS, E. Influence of diffusive layer and aerosol density on aerosol deposition in PHEBUS FPT-1 experiment. International conference Nuclear Energy for New Europe 2008, Portorož, Slovenia, September 8–11, 2008. Ljubljana: Nuclear Society of Slovenia, 2008. ISBN 978-961-6207-30-0, p. 410.1–410.8.

CYSENI 2010, May 27–28, Kaunas, Lithuania
ISSN 1822-7554, www.cyseni.com

THE BEPU CHALLENGE IN CURRENT LICENSING OF NUCLEAR REACTORS

A. Petruzzi, F.D'Auria, N. Muellner

University of Pisa, Nuclear Research Group San Piero a Grado
Via Livornese 1291, San Piero a Grado, Pisa –Italy
Phone: +39 050 2210377
Email: a.petruzzi@ing.unipi.it

ABSTRACT

Within the licensing process of the Argentinean Atucha II PHWR (Pressurized Heavy Water Reactor) the BEPU (Best Estimate Plus Uncertainty) approach has been selected for issuing of the Chapter 15 on FSAR (Final Safety Analysis Report). The key steps of the entire process are basically two: a) the selection of PIE (Postulated Initiating Events) and, b) the analysis by best estimate models supported by uncertainty evaluation. The key elements of the approach are: 1) availability of qualified computational tools including suitable uncertainty method; 2) demonstration of quality; 3) acceptability and endorsement by the licensing authority. The effort of issuing Chapter 15 is terminated at the time of issuing of the present paper and the safety margins available for the operation of the concerned NPP (Nuclear Power Plant) have been quantified

Keywords: BEPU, Licensing, FSAR, Atucha-II

1. INTRODUCTION

Among the general attributes of a methodology to perform accident analysis of a nuclear power plant for licensing purposes, the very first one should be the compliance with the established regulatory requirements.

A second attribute deals with the adequacy and the completeness of the selected spectrum of events which should consider the combined contributions of deterministic and probabilistic methods.

The third attribute is related with the availability of qualified tools and analytical procedures suitable for the analysis of accident conditions envisaged in the concerned Nuclear Power Plant. Thus, a modern and technically consistent approach has been built upon best estimate methods including an evaluation of the uncertainty in the calculated results (Best Estimate Plus Uncertainties or BEPU approach).

The complexity of a NPP and of the accident scenarios may put a challenge for a conservative analysis and may justify the choice for a BEPU approach in the licensing process. This implies two main needs: the need to adopt and to prove (to the regulatory authority) an adequate quality for the computational tools and the need for the uncertainty.

The purpose of the present paper is to outline key aspects of the BEPU process aimed at the licensing of the Atucha II Nuclear Power Plant (NPP) in Argentina. The Atucha II is a heavy-water cooled heavy-water moderated, vessel type, pressurized reactor. The moderator fluid has the same pressure as the coolant fluid, but temperature is lower. Fuel channels, which do not withstand pressure difference during nominal operation, separate the coolant from the moderator. The thermal power produced in the moderator is used to pre-heat the feed-water.

A direct link with the bases of nuclear reactor safety shall be ensured by the ‘BEPU-description document’. In the present case this is formed by the following main elements or steps:

1) Evaluation of the possibility to use a Best Estimate (BE) within the context of the current national (i.e. of the Country where the NPP is installed) Regulatory Authority (RA) requirements. A pre-application document was submitted to the national RA. This included the consideration of past interactions between the RA and the applicant as well as the analysis of the licensing practice in the Country where the NPP was designed.
2) Outline of international practices relevant for the proposed approach. The experiences acquired in the use of Best Estimate analyses for licensing purposes are reviewed: this is true for probabilistic and deterministic analyses and specifically for the determination of radiological consequences.
3) Structure of the BEPU: a) categorization of PIE, b) grouping of events, c) identification of analysis purposes, d) identification of applicable acceptance criteria, e) setting up of the ‘general scope’ Evaluation Model (EM) and of related requirements starting from the identification of scenario related phenomena, f) selection of qualified computational tools including assumed initial and boundary conditions, g) characterization of assumptions for the Design Basis Spectrum, h) performing the analyses, i) adopting a suitable uncertainty method.
4) Under the item 3g): the roadmap pursued for the analysis foresaw the use of nominal conditions for the NPP parameters and the failure of the most influential system. The implementation of such roadmap implied the execution of preparatory code run per each scenario where all NPP systems were simulated. This also required the simulation the control and the limitations systems other than the protection systems. Once the ‘nominal system performance in accident conditions (following each PIE)’ was determined, it was possible to select the worst failures and calculate a new (i.e. the ‘binding one’) accident scenario.
5) Under the general scope of item 3f): several computer codes and about two dozen nodalizations have been used, developed and, in a number of cases, interconnected among each other.
6) Qualification was necessary for the computational tools mentioned under item 5), within the framework depicted under item 3). The issue constituted by qualification of code-nodalization user was dealt with in the same context. Specific methods or procedures including acceptability thresholds have been developed and adopted.
7) Under the scope of item 3i): the uncertainty method based on the extrapolation of accuracy, developed at University of Pisa since the end of 80’s, was used to create the CIAU (Code with capability of Internal Assessment of Uncertainty) and directly used for quantifying the errors in the calculations, as needed.

The purpose of the present paper is to present an outline of the BEPU approach. At the time of preparing of the present paper a ‘rev.0’ version of the Chapter 15 of the Atucha II Final Safety Analysis Report (FSAR) has been issued. However, results are under preliminary scrutiny before being transmitted to the Regulatory Authority. Owing to this, no final results from the BE analysis of transients shall be expected in the paper.

2. ASPECTS FOR THE APPLICATION OF THE BEPU APPROACH

The BEPU approach has been adopted as the methodology for accident analyses covering the established spectrum of PIE. Procedures have been applied to derive the list of PIE and to identify applicable acceptance criteria. Finally, the application of computational tools including nodalizations required suitable boundary and initial conditions and produced results related to the Atucha II transient scenarios originated by the PIE.

The proposed BEPU approach follows current practices on deterministic accident analyses, but includes some key features to address particular needs of the application. The approach takes credit of the concept of Evaluation Models (EM), and comprising three separate possible modules depending on the application purposes:

- for the performance of safety system countermeasures (EM/CSA),
- for the evaluation of radiological consequences (EM/RCA),
- for the review of components structural design loadings (EM/CBA),

where the acronyms CSA, RCA and CBA stand for 'Core Safety Analysis, 'Radiological Consequence Analysis' and 'Component Behaviour Analysis'. It may be noted that structural resistance of Containment as well as mechanical loads on RPV (Reactor Pressure Vessel) internals are calculated in the frame of CBA.

The selection of contents for the present section has been derived based on the US NRC Regulatory Guide 1.70 [1], the US NRC Standard Review Plan [2], design industry safety documents, e.g., [3], the FSAR of recently licensed NPP and the so called (Atucha II specific) BEPU report, already endorsed by the involved Licensing Authority [4].

The evaluation of the safety of nuclear power plant Atucha II does include required analyses of the response of the plant to postulated disturbances in process variables and to postulated malfunctions or failures of equipment. For these purposes, two complementary methodologies for safety analysis are applicable. The scope of accident analyses presented in Chapter 15 of the FSAR, however, comprises only deterministic safety analyses. Probabilistic safety analyses are presented in a separate document.

The Chapter 15 sections document the results of the performed deterministic safety analysis covering a sufficiently broad spectrum of transients and accidents (i.e. PIE), aiming at demonstrating that the plant can be safely operated within the established regulatory limits related to the integrity of the components, to the preservation of the safety functions and the barriers against radioactivity releases and to the related radiological impact.

In order to confirm that the plant transient and accident analyses represent a sufficiently broad spectrum of initiating events, the transients and accidents are categorized according their expected frequency of occurrence and grouped in nine families according to the type of challenge to the fundamental safety functions. The results of these safety analyses also provide a contribution to the selection of limiting conditions for operation, limiting safety systems settings, and design specifications for components and systems to protect public health and safety of the installations.

2.1. The Basis for BEPU

A simplified flowchart of the rationale that brought to the planning and the application of the BEPU approach are given in Fig. 1 (details can be found in [4]). The steps followed by the proposed approach can also be derived from the analysis of the diagram.

In the first step, as a function of the selected scenario and of the purpose of the analysis, the complexity of the evaluation model may range from a simplified qualitative evaluation (EM/QA) to a complete combination of the three possible modules (EM/CSA + EM/RCA + EM/CBA).

In order to evaluate the plant safety performance, acceptance criteria are properly selected according to established international practice. The two main aspects which have been considered for developing the evaluation model with the ability of adequately predict plant response to postulated initiating events are intrinsic plant features and event-related phenomena characteristics.

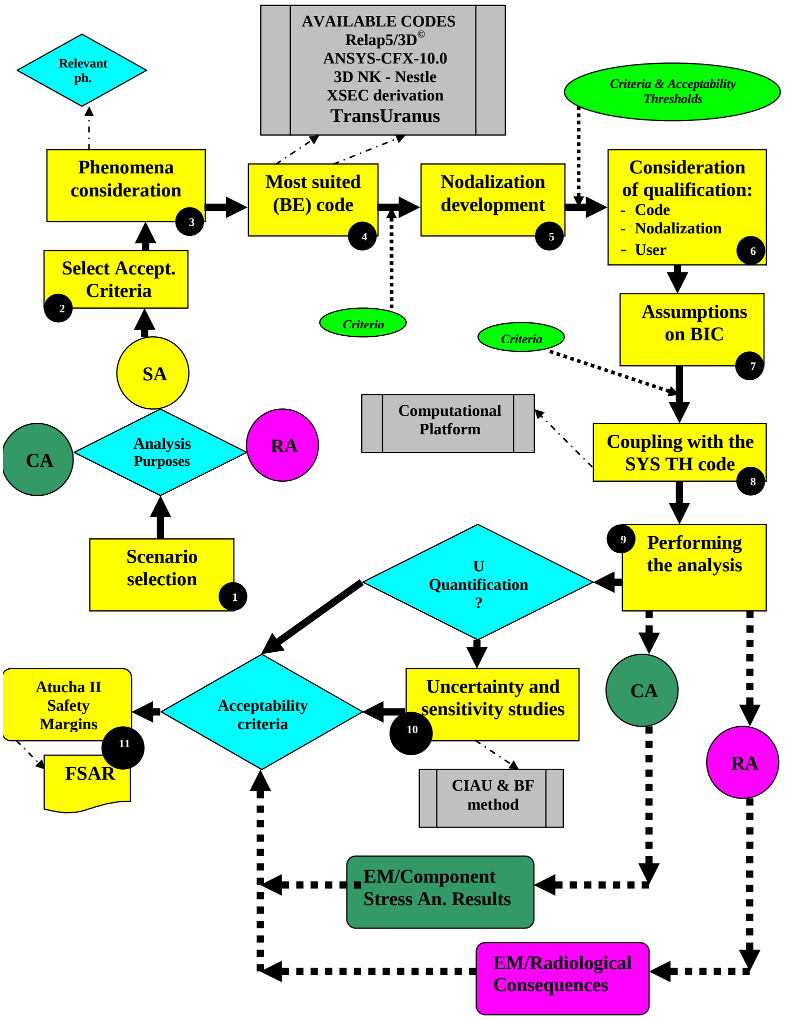

Fig. 1. The BEPU Flow-Diagram

For the two modules EM/CSA and EM/CBA, the first set of requirements for the evaluation model is imposed by the design characteristics of the nuclear power plant, its systems and components. Requirements on the capability of simulating automatic systems are of particularly importance for anticipated operational occurrences, in which control and limitation systems play a key role on the dynamic response of the plant.

It shall be noted that the concerned modelling features are consistent with the requirements that imposes the design of the limitation system according to the same standard as the reactor protection system. However, this rule does not apply to control systems. Nevertheless, the best response of the plant cannot be calculated without the detailed modelling of the control system. This has been considered in the present framework.

The second set of requirements is derived from the expected evolution of the main plant process variables and the associated physical phenomena. For the proposed approach, this is performed through the process of identifying the Phenomenological Windows (Ph.W) and the Relevant Thermal-hydraulic Aspects (RTA). The relevant timeframe for the event is divided into well defined intervals when the behaviour of relevant safety parameters is representative of the physical phenomena.

For the adequate simulation of the identified phenomena, computational tools were selected from those which have previous qualification using an appropriate experimental data base. Satisfactory qualification targets provide basis for acceptability of the postulated application.

Within the framework of the present FSAR chapter, the expression “computational tools” comprises:

- the best estimate computer codes;
- the qualified detailed nodalizations for the adopted codes including the procedures for the development and the qualification;
- the established computational methods for uncertainty quantification including the procedure for the qualification;
- the computational platforms for coupling and interfacing inputs and outputs from the concerned codes and nodalizations.

2.2. Categorization of PIE

The design philosophy of Atucha II incorporates the principle that plant states that could result in high radiation doses or radioactive releases are of very low probability of occurrence, and plant states with significant probability of occurrence have only minor or no radiological consequences.

Accordingly, for design purposes, postulated initiating events are divided into the following event categories by their anticipated probability of occurrence, consistently with Probabilistic Safety Analysis (PSA) performed for the same NPP:

Anticipated Operational Occurrences (AOO)	Probability greater than 10^{-2} / year
Design Basis Accident (DBA)	Probability less than 10^{-2} / year and greater than 10^{-5} / year
SBDBA, including ATWS and “extended spectrum” of LOCA	Probability less than 10^{-5} / year

Accident conditions which stand out of these ranges of probabilities or that are not included in the Selected Beyond Design Basis Accidents (SBDBA) category, may also involve significant core degradation. These are out of the scope of this chapter and are treated separately within the frame of PSA studies.

The third event category (SBDBA) appears to be specific of the Atucha II FSAR and addresses large break LOCA and ATWS (Anticipated Transients Without Scram). The rationale for introducing this category derives from the design characteristics of the NPP and from previously agreed licensing steps (see also [4]).

The categorization of Large Break Loss Of Coolant Accident (LBLOCA) as SBDBA is due to the exclusion of the maximum credible accident from the range of the design basis spectrum for Atucha II, and the adoption of the break size of ten percent on reactor coolant pipe (0.1 A) as the basis for fulfilling traditional regulatory requirements. So far, the double ended guillotine break is considered as a beyond design basis scenario.

Nevertheless, the demonstration of the design capability to overcome this event has still a relevant role in the safety performance evaluation. For this aim, however, currently used conservative approach for safety analysis may not be sufficient to guarantee that safety margins still exist. The use of best estimate methods is acceptable when a scenario is categorized as beyond design basis.

Regarding ATWS, similarly to some modern or evolutionary nuclear power plants, Atucha II design does present a diverse scram system (Fast Boron Injection System). In this sense, the original safety issue related to ATWS does not constitute a safety concern applicable to its design.

All selected scenarios are grouped in the nine families of events: each family covers events with similar phenomena, or events in each family are characterized by similarity of challenges in relation to the fundamental safety functions. The nine families are:

1. Increase in heat removal by the secondary system.
2. Decrease in heat removal by the secondary system.
3. Decrease in heat removal by the primary system.
4. Reactivity and power distribution anomalies.
5. Increase in reactor coolant inventory.
6. Decrease in reactor coolant inventory.
7. Radioactive release from a subsystem or component.
8. Disturbance in the refuelling system and fuel storage system.
9. Anticipated Transients Without Scram (ATWS).

An excerpt of the list including the description of 83 events is provided in Table 1 below. This also includes the type of analysis to be performed in relation to each transient. In this connection, three possible types of general evaluation purposes are foreseen for each scenario:

RCA	(Radiological Consequences Analysis) those scenarios whose radiological impacts have to be calculated.
CSA	(Core and System Analysis) those scenarios which are used for the design of safeguards or countermeasures (systems performance associated with the integrity limits for the barriers against radioactive releases).
CBA	(Component and Barrier performance Analysis) those scenarios which are used for reviewing the design of components or structures for stability or integrity (mechanical design loadings).

In relation with AOO, it has to be proved that they do not propagate into accidents. Additionally, the analysis shall demonstrate that the systems actuated by operational instrumentation and control systems and by limitation and reactor trip systems are sufficiently effective to:

- Maintain the integrity of the barriers against radioactivity release, as no fuel centerline melting, unrestricted continued operation of fuel assemblies, and ensured integrity of the reactor coolant pressure boundary (CSA related evaluation purposes).
- Maintain component loadings within the allowable limits for this category of events as it is addressed in the FSAR Chapters 4 to 6 (CBA related evaluation purposes).
- Prevent radioactive releases to the environment in excess of the allowable limits for this category of events (RCA related evaluation purposes).

For design basis accidents, even though they are not expected to occur, only limited consequences are accepted. For DBA it has to be demonstrated that the safety system countermeasures actuated by the reactor protection system are sufficiently effective to:

- Maintain adequate integrity of the barriers against radioactivity release, as limited fuel centerline melting, limited loss of integrity of fuel cladding, or integrity of the containment (CSA related evaluation purposes).
- Maintain component loadings within the allowable limits for accident conditions, and may be addressed in the FSAR Chapters 3 to 6 (CBA related evaluation purposes).
- Prevent radioactive releases to the environment in excess of the allowable limits for accident conditions (RCA related evaluation purposes).

For the SBDBA, the aim of the analyses is to demonstrate that measures for mitigation of consequences are sufficient and effective to:

- Ensure residual heat removal, maintaining sufficient integrity of the barriers against radioactivity release (CSA related evaluation purposes)
- Prevent radioactive releases to the environment in excess of the allowable limits for accident conditions (RCA related evaluation purposes).

Table 1. Excerpt from the List of PIE for Atucha II Chapter 15 of FSAR

No	**Transient**	**Section FSAR**	**Adopted Evaluation Model**	**Class of Accident**
Increase in Heat Removal by the Secondary System		**15.1**		
2	FW System Malfunctions that result in an Increase in FW Flow (Stuck Open FW Control Valve)	15.1.2	CSA	AOO
Spectrum of Steam System Piping Failures inside and outside of Containment (MSLB)		15.1.5	-	
5	Leak of MS Line inside the Containment	15.1.5.1	CSA / RCA / CBA	DBA
9	Inadvertent Closing of the Moderator Cooler Bypass CV	15.1.7	CSA	AOO
36	Uncontrolled CR Withdrawal at the particular Power Level that yields the most Severe Results	15.4.2	CSA	AOO
41	Spectrum of Rod Ejection Accidents	15.4.7	CSA	DBA
Spectrum of SGTR		15.6.3	-	
46	Single SG Tube Rupture (*“Bordihn”: SG Tube Failure*)	15.6.3.1	CSA	DBA
56	0.1A LOCA cold with Sump Swell Operation	15.6.5.1.2.4	QA	DBA
Large Break LOCA		15.6.5.1.3	-	
57	2A LOCA cold (*DEGB. Different Break Sizes and Positions are investigated*)	15.6.5.1.3.1	CSA / RCA / CBA	SBDBA
72	Leakage on the Refueling Machine and Auxiliary Equipment	15.8.2	RCA	DBA
Anticipated Transients Without Scram (ATWS)		**15.9**		
74	Mechanical Failure of the Control Rods in case of Emergency Power Mode	15.9.1	CSA	SBDBA

CV: Control Valve, CR: Control Rod, DEGB: Double End Guillotine Break, FW: Feed Water, MS: Main Steam, MSLB: Main Steam Line Break, QA: Qualitative Analysis, SG: Steam generator, SGTR: Steam Generator Tube Rupture.

In order to complete the set of targets for the analyses, event specific purposes are added, considering scenario-related safety system countermeasures or performance, as well as challenged component structural limits. To assess plant safety performance, figures of merit are derived for each purpose of the considered event.

3. ADOPTED COMPUTATIONAL TOOLS

The computational tools include a) the best estimate computer codes; b) the nodalizations including the procedures for the development and the qualification; c) the uncertainty methodology including the procedure for the qualification; d) the computational platforms for coupling and interfacing inputs and outputs from the concerned codes and nodalizations.

An idea of the interaction among the considered computational tools can be derived from Fig. 2 and Table 2, both dealing with codes, category a) above. The following to be noted:

- A chain of codes is needed for exploiting the three-dimensional neutron kinetics capability of the Nestle code.
- MCNP code has the role of providing ‘reliable-reference’ results at the steady state condition.
- Melcor is used as a back-up code to support the application of the Relap5-3D© when modeling the containment.
- The ‘ultimate’ code for calculating the Pressurized Thermal Shock (PTS) risk, deterministic analysis, is Ansys.
- Dynetz is ‘intimately’ coupled with Relap5/3D©: however, the entire control, limitation and protection systems of Atucha II are modelled and interaction with the thermal-hydraulic code is foreseen at each time step.

Table 2. List of Codes Used for BEPU Accident Analyses

No	Code Type	Code Name
1	System Thermal-Hydraulics	Relap5/3D© (TH model) including DNBR and containment
2	I&C Modelling	Dynetz
3	Computation Fluid Dynamics	CFX
4	Structural Mechanics	Ansys
5	Fuel (mechanics)	Transuranus
6	Neutron Physics (and supporting)	Nestle
7		Helios
8		MCNP
9		Scale Package: Newt-Origen (Triton), burn-up oriented
10		Scale Package: Keno, static 3D neutron physics
11		NJOY
12		Dragon
13	Radiological Consequences (and supporting)	MCNP-Origen for radioactivity source-term
14		Relap5/3D © (Radiological model)
15		Melcor-Maccs
16		Arcon96
17		Rodos

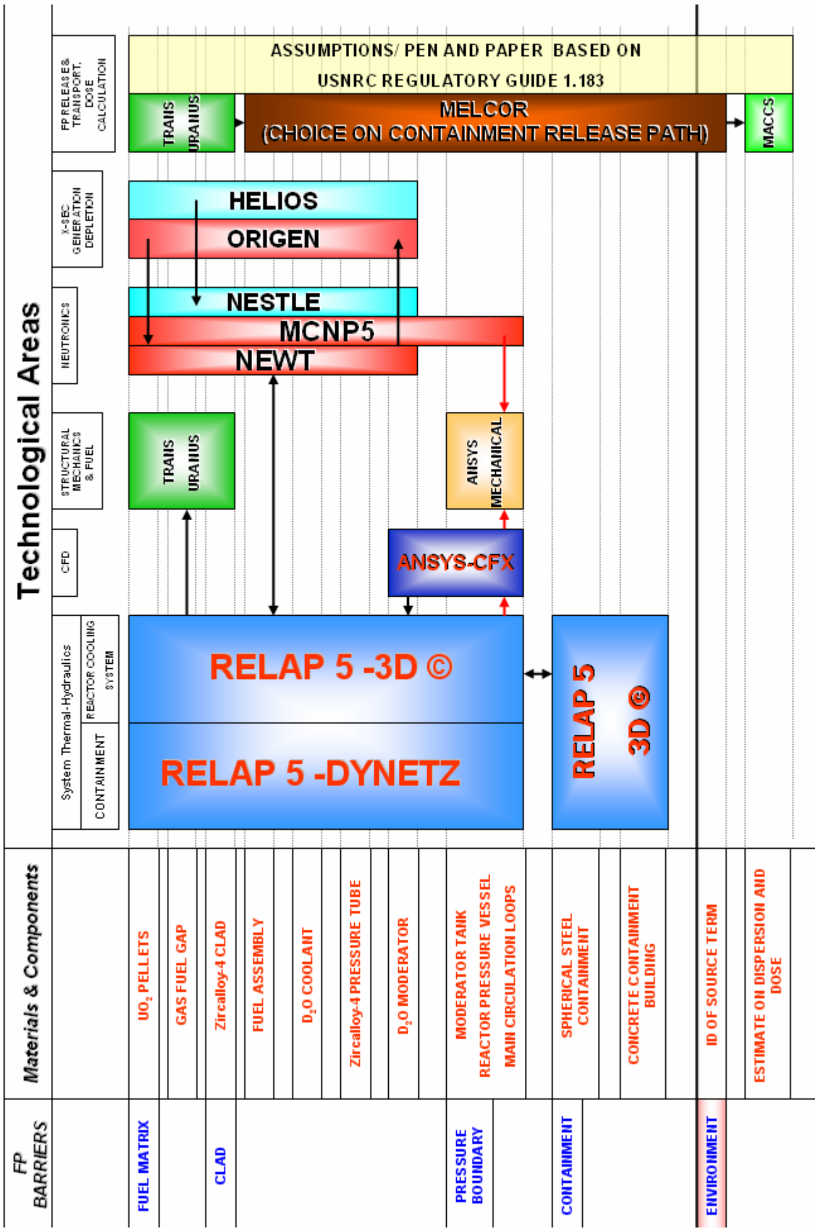

Fig. 2. The Interaction among the Computer Codes used for BEPU Accident Analyses

3.1. The Qualification

A key issue for the BEPU is represented by the qualification. This shall be demonstrated for each of the categories of computational tools discussed above. It is out of the scope of the present paper to provide details adopted to show the achievement of a suitable level of qualification. However, an idea can be derived from the section below dealing with UMAE, i.e. Uncertainty Method based upon Accuracy Extrapolation (here used to demonstrate the qualification of the thermal-hydraulic nodalizations).

3.2. The Uncertainty Method

In principle, whenever a best estimate method is applied for licensing purposes, uncertainty quantification is needed. Therefore the UMAE-CIAU procedure, or even the CIAU having UMAE as 'informatics engine', is used in the present context [4].

The UMAE [5] is the prototype method for the consideration of “the propagation of code output errors” approach for uncertainty evaluation. The method focuses not on the evaluation of individual parameter uncertainties but on the propagation of errors from a suitable database calculating the final uncertainty by extrapolating the accuracy from relevant integral experiments to full scale NPP.

Considering integral test facilities which are simulators of water cooled reactors and qualified computer codes based on advanced models, the method relies on code capability, qualified by application to facilities of increasing scale. Direct data extrapolation from small scale experiments to reactor scale is difficult due to the imperfect scaling criteria adopted in the design of each scaled down facility. The direct code application to different scaled facilities (i.e. without the availability of experimental data) and to the corresponding NPP can be biased or affected by systematic errors. So the only possible solution to ensure the best use of the code in predicting NPP behaviour is the extrapolation of accuracy (i.e. the difference between measured and calculated quantities). Experimental and calculated data in differently scaled (relevant) facilities are used to demonstrate that physical phenomena and code predictive capabilities of important phenomena do not change when increasing the dimensions of the facilities. The flow-sheet of UMAE is given in Fig. 3. The following can be added:

- The red line loop on the right of the diagram constitutes the way to qualify the code, the nodalization and the code-user in relation to the capability to model an assigned transient.
- In case the conditions (thresholds of acceptability) in the rhomboidal block ‘g’ are fulfilled, the NPP nodalization can be built-up having in mind the experience gained in setting-up Integral Test Facility (ITF) nodalizations.
- The NPP nodalization (left of the diagram) will undergo a series of qualification steps including the co-called ‘Kv-scaled’ calculation.
- Additional acceptability thresholds must be met under the block ‘k’. In case of adequate fulfilment of criteria a qualified nodalization is available for NPP analyses (so called Analytical Simulation Model – ASM).
- The FFTBM (Fast Fourier Transform Based Method) to quantify the accuracy, is used at the level of the block ‘g’ and, if requested, of the block ‘k’.
- The results of the ASM may benefit of the extrapolation of the accuracy to characterize the uncertainty.

All of the uncertainty evaluation methods, including UMAE are affected by two main limitations:

- the resources needed for their application may be very demanding, ranging to up to several man-years;
- the achieved results may be method/user dependent.

The last item should be considered together with the code-user effect, widely studied in the past, and may threaten the usefulness or the practical applicability of the results achieved by an uncertainty method. Therefore, the Internal Assessment of Uncertainty (IAU) was requested as the follow-up of an international conference jointly organized by OECD and U.S. NRC and held in Annapolis in 199. The CIAU method, [5], has been developed with the

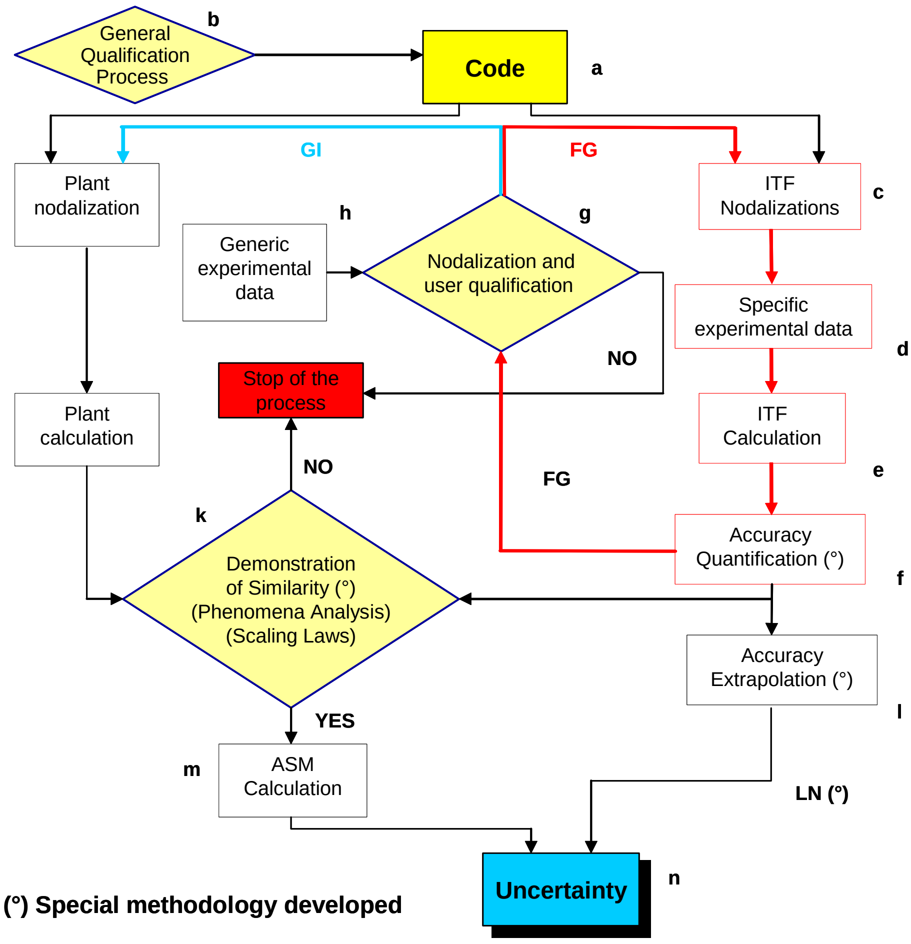

Fig. 3. The Flow-Diagram of UMAE

objective of eliminating/reducing the above limitations. The basic idea of the CIAU can be summarized in two parts, as per Fig. 4:

- Consideration of plant status: each status is characterized by the value of six relevant quantities (i.e. a hypercube) and by the value of the time since the transient start.
- Association of an ‘extrapolated error’ or uncertainty with each plant status.

Six driving quantities are used to characterize any hypercube. In the case of a PWR the six quantities are: 1) the upper plenum pressure, 2) the primary loop mass inventory, 3) the steam generator pressure, 4) the cladding surface temperature at 2/3 of core active length, 5) the core power, and 6) the steam generator down-comer collapsed liquid level.

A hypercube and a time interval characterize a unique plant status to the aim of uncertainty evaluation. All plant statuses are characterized by a matrix of hypercubes and by a vector of time intervals. Let us define Y as a generic thermal-hydraulic code output plotted versus time. Each point of the curve is affected by a quantity uncertainty (Uq) and by a time uncertainty (Ut). Owing to the uncertainty, each point may take any value within the rectangle identified by the quantity and the time uncertainty. The value of uncertainty, corresponding to each edge of the rectangle, can be defined in probabilistic terms. This satisfies the requirement of a 95% probability level, e.g. acceptable by US NRC.

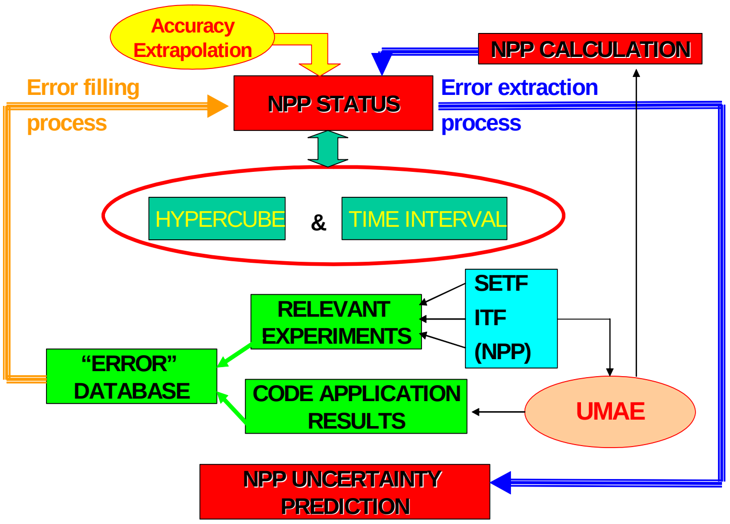

Fig. 4. Outline of the Basic Idea of the CIAU Method

4. CONCLUSIONS

An outline has been given of relevant features of the BEPU approach pursued for the Chapter 15 of the FSAR of Atucha II NPP.

The execution of the overall analysis and the evaluation of results in relation to slightly less than one-hundred PIE revealed the wide safety margins available for the concerned NPP that was designed in the 80's. Key issues for a BEPU-based Chapter 15 of any FSAR are:

a) Proper selection of PIE.
b) Simulation of I&C system response.
c) Availability of proper computational tools.
d) Qualification and quality assurance
e) Last but not least: endorsement and acceptability by the Licensing Authority.

5. ACKNOWLEDGMENTS

The work leading to the issue of BEPU Chapter 15 of Atucha II FSAR lasted more than two years and involved more than thirty scientists, including recognized international experts, working at NA-SA and at University of Pisa. The current authors coordinated the group and acknowledge the contribution of any individual.

REFERENCES

1. USNRC, *Regulatory Guide 1.70: Standard Format and Content of Safety Analysis Report for Nuclear Power Plants – LWR Edition*, NRC RG 1.70 Rev. 3, Washington, Nov. 1978.
2. USNRC, *NUREG-0800: Standard Review Plan Section 4.2: Fuel System Design, Appendix B - Interim Acceptance Criteria and Guidance for the Reactivity Initiated Accidents*, NRC NUREG 0800, Rev. 3, Washington, March 2007.
3. BORDIHN et. al., *Assessment of Radiologically Relevant Accident*, Siemens Work Report KWU NA-T/1994/053, Restricted, Erlangen, 17 Aug. 1994.
4. UNIPI-GRNSPG, *A Proposal for performing the Atucha II Accident Analyses for Licensing Purposes – The BEPU report*, Rev. 3, Pisa, 2008.
5. IAEA, Best Estimate Safety Analysis for Nuclear Power Plants: Uncertainty Evaluation, IAEA Safety Reports Series No 52, p. 1–162 Vienna (A), 2008.

CYSENI 2010, May 27–28, Kaunas, Lithuania
ISSN 1822-7554, www.cyseni.com

NUMERICAL ANALYSIS OF EXPERIMENTS PERFORMED IN THE FRAME OF INTERNATIONAL STANDARD PROBLEM NR. 49

M. Povilaitis
Lithuanian Energy Institute
Laboratory of Nuclear Installation Safety
Breslaujos str. 3, LT-44403 – Lithuania
Phone: +37037401920
Email: mantasp@mail.lei.lt

ABSTRACT

During a hypothetic severe accident involving degradation of the core of a light water reactor the hydrogen could be generated and released into the containment atmosphere posing a deflagration or even explosion hazard. In case of deflagration, the integrity of the containment would be threatened by the increase of the containment atmosphere pressure and temperature. Other risks due to turbulent flames exist, caused by high pressure pulses, shock waves and etc. For the simulation of such processes a reliable numerical codes are needed. Hydrogen combustion processes have been largely studied in case of a homogeneous hydrogen distribution in the containment atmosphere, however still lacking research on the processes in a non-uniform mixture. Moreover, in the EURSAFE program, the flame acceleration and quenching have been identified as unresolved hydrogen combustion issues especially when the concentration gradients are involved. These topics were addressed in the ongoing project ISP49 (International Standard Problem 49). The main objective of the ISP49 was the demonstration of the actual capability of hydrogen combustion models and codes. This article presents numerical analysis performed for the ISP49 using lumped parameter code ASTEC of the non-uniform hydrogen and air mixture deflagration experiments. Brief experiment description, used nodalisation schemes of the test facilities and obtained numerical results are presented.

Keywords: hydrogen deflagration, ISP49, ASTEC

1. INTRODUCTION

During a hypothetic severe accident in a light water nuclear reactor, hydrogen can be produced in case of reactor core degradation. Produced hydrogen then would be released into the reactor containment. Hydrogen accumulation in the containment atmosphere would raise a combustion hazard, because combustible mixture may ignite and cause deflagration flame propagation. Combustion process would generate loads (increase of the containment atmosphere pressure and temperature), which may threaten the integrity of the containment building and of internal structures and equipment. If flame becomes turbulent, it can cause high pressure pulses, shock waves, temperature peaks and large pressure gradients, damaging containment components, internal structures (e.g., piping) and equipment.

Flame acceleration has been largely studied for a homogeneous hydrogen distribution and only very few data are available on the behaviour of the hydrogen/air flame in a non-uniform mixture [1]. Topic of flame propagation in a presence of hydrogen concentration gradient was addressed in the International Standard Problem N°49 (ISP49). The main objective of the ISP49 is the demonstration of the actual capability of hydrogen combustion models and simulation codes [1], especially of the capability to simulate flame acceleration in the presence of hydrogen concentration gradients and steam, also flame propagation upwards in a containment-like environment.

Experiments performed in two test facilities – ENACCEF, operated by French National Centre for Scientific Research (CNRS) in the frame of collaboration with the French Institute for Radioprotection and Nuclear Safety (IRSN), France, and THAI, operated by Becker Technologies GmbH, under the sponsorship of the German Federal Ministry of Economics and Technology, Germany – were selected for the simulations (both open and blind) during the ISP49.

In this article, open simulations of experiments performed in both facilities are presented. Brief facility and experiment descriptions, used nodalisation schemes and obtained numerical results are presented.

2. EXPERIMENTS

2.1. ENACCEF facility

ENACCEF is a vertical test facility of 5 m high. It is made of stainless steel. Facility is composed of two parts (Fig. 1):

The acceleration tube, of 3.2 m length with 154 mm internal diameter. The total volume of the acceleration tube is 62.1 l. Inside the acceleration tube it is possible to insert various repeated obstacles. The acceleration tube itself is composed of five cylindrical acceleration parts and a bottom-cap (Fig. 1).

1. The dome, of 1.7 m length with 738 mm internal diameter. The total volume of the dome is 658 l.

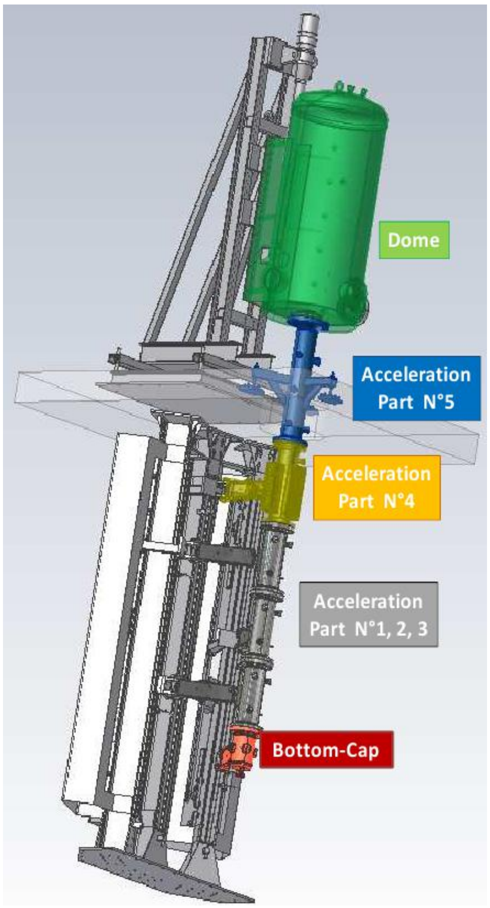

Fig. 1. Schematic view of the ENACCEF facility [1]

Five cylindrical acceleration parts (N°1–5) can be equipped with obstacles. In the simulated experiment nine annular obstacles were used (Fig. 2). Inner diameter of used obstacles was 0.093 m; distances between obstacles were 0.154 m.

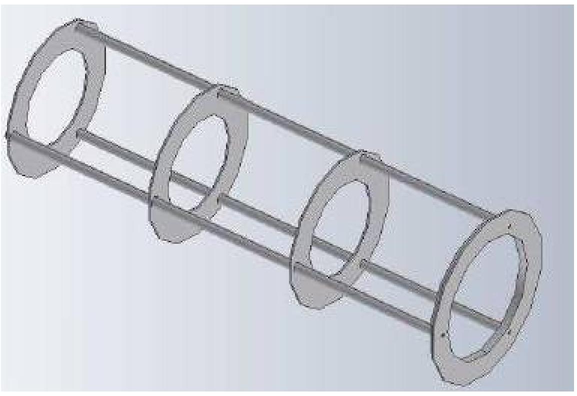

Fig. 2. Schematic view of obstacles used in the simulated experiment [1]

Experiment was performed at ambient temperature (T=23°C) and at 1 bar (normal) pressure. There was a hydrogen gradient (Fig. 3) in the dry air formed inside the facility.

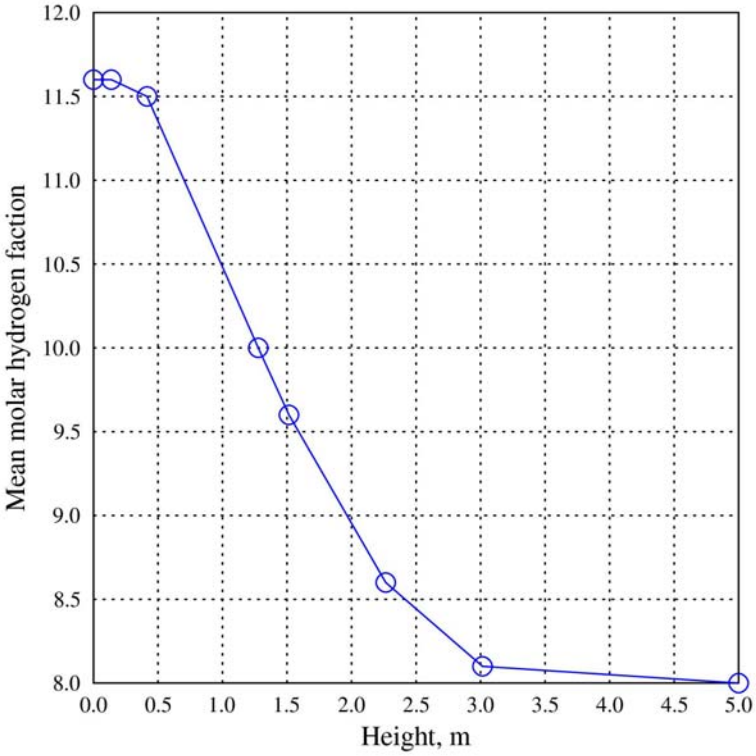

Fig. 3. Initial hydrogen gradient in the ENACCEF facility [1]

The experiment consisted of a local hydrogen ignition at the bottom of the facility (at 0.138 m height) and flame propagation upwards. It is expected that flame would accelerate when encountering obstacles and decelerate after reaching the dome.

2.2. THAI facility

Main component of the THAI facility (Fig. 4) is a cylindrical stainless steel vessel of 9.2 m height with 3.156 m internal diameter [2]. A total volume of the facility is 60 m^3. Vessel is insulated with 0.12 m width rockwool thermal insulation.

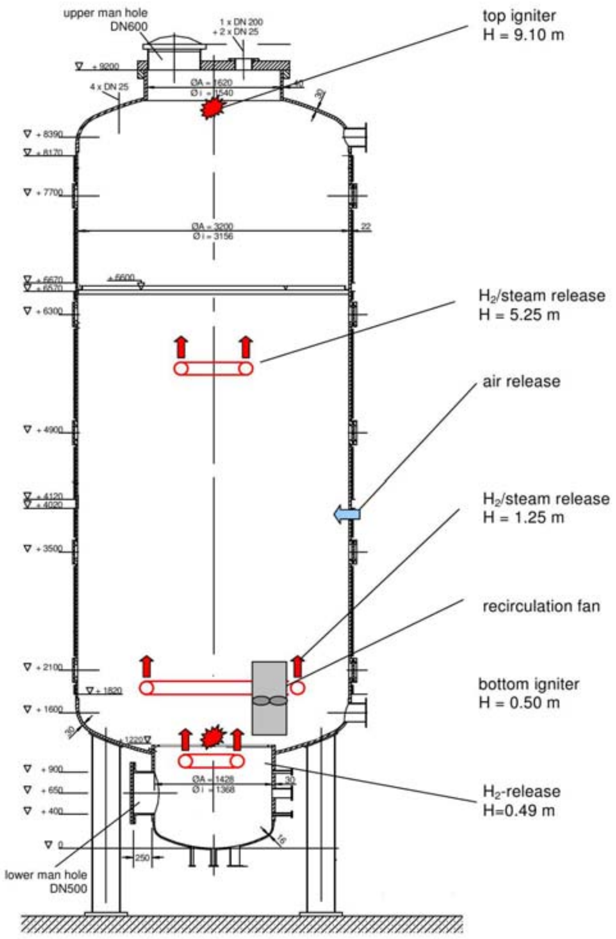

Fig. 4. THAI facility configuration used in the experiment [2]

Vessel bottom and top are formed with dished heads, both of which are penetrated in the vessel axis by cylinders with an internal diameter of 0.154 in the top and an internal diameter of 1.368 m in the bottom part.

Simulated test consisted of the combustible mixture ignition with the bottom igniter and flame propagation in upward direction. Initial conditions in the facility were homogenous – 1.485 bar pressure, 18 °C temperature and 7.98% hydrogen volume concentration. The aim of the experiment was to check the repeatability of test results. This test is suitable for simulations in the frame of ISP49, because experimental data mainly exists for horizontal flame propagation and small geometries, also current modelling of low-concentration hydrogen deflagrations is still inadequate [2].

3. SIMULATIONS

Simulations were performed using integral ASTEC (Accident Source Term Evaluation Code) V2.0 code [**Klaida! Nerastas nuorodos šaltinis.**]. The aim of the code is to simulate an entire severe accident sequence from the initiating event through to release of radioactive elements out of the containment. For the presented simulations only ASTEC thermal hydraulic module CPA was used with the additional newly-developed (testing) CPA-FRONT module for hydrogen combustion simulation. CPA uses a lumped-parameter approach, therefore simulated facilities have to be described with nodalisation schemes, in which each facility is divided into zero-dimensional zones (also called nodes or control volumes) connected by one-dimensional junctions for gas flows and flame propagation.

In the CPA-FRONT model propagation of the flame front is described by the laminar flame front velocity [4] and the turbulence velocity (flamelet model by Peters [5]). Turbulence intensity is determined by an empirical equation containing the Reynolds number.

3.1. Nodalisation schemes

3.1.1. ENACCEF facility

Nodalisation scheme of the ENACCEF facility consists of 31 layers with 41 zones. Acceleration tube is divided into 21 zones and dome into 20–10 in the middle and 10 ring shaped at side (Fig. 5). Zones in the acceleration tube and in the middle of the dome have the form of a vertical cylinder; their diameter is equal to the inner diameter of the acceleration tube. The height of the zones in the tube is 0.154 m, the same as between obstacles. The height of the zones in the dome is 0.15 m. The obstacles in the nodalisation are simulated as atmospheric junctions between zones, their areas reduced accordingly to the diameter of the obstacles. Heat losses to the environment are simulated through structures (walls of the facility), no radiation losses are simulated, since it is assumed that flame burns out quick enough for radiation losses to be negligible.

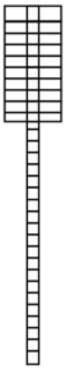

Fig. 5. ENACCEF facility nodalisation used in the simulations

3.1.2. THAI facility

THAI facility nodalisation scheme consists of 18 layers with 33 zones (Fig. 6). There are two zones in the lower sump part of the facility and one in the upper part. Main volume of the facility is divided into middle zones and ring-shaped zones at side. Outer wall are simulated as structures for heat losses into the environment.

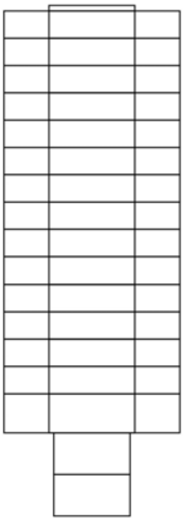

Fig. 6. THAI facility nodalisation used in the simulations

3.2. Simulation results

3.2.1. ENACCEF facility

Qualitatively the course of hydrogen deflagration was predicted in the calculations. Pressure evolution obtained from the calculations is compared with the experimental results in the Fig. 7. However, the pressure rise obtained from the calculations is too flat compared with the experiment results. Obtained value of the maximum pressure is similar to the experimental one – pressure is overestimated (conservative result) by approximately 0.023 bar. Slower pressure rise obtained from the calculations can be attributed to the slower flame propagation in the facility.

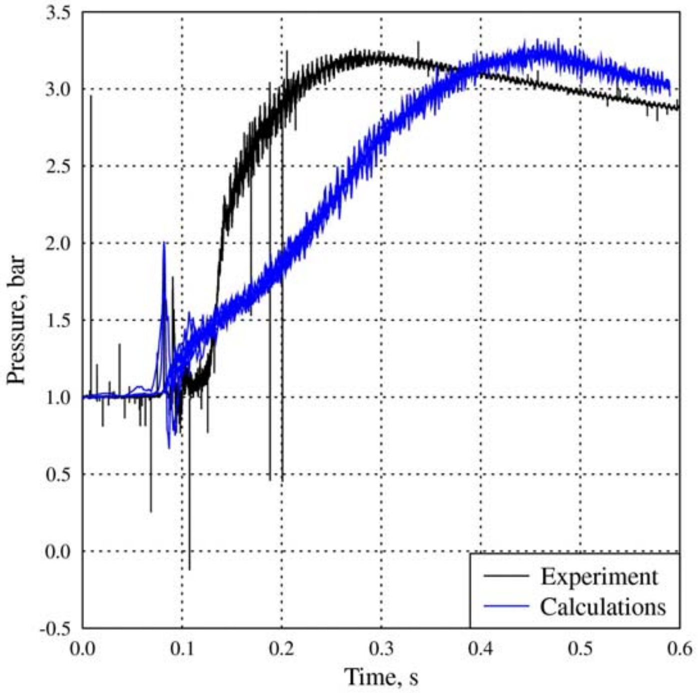

Fig. 7. Comparison of simulated and experimental pressure evolutions in the ENACCEF facility

Fig. 8 shows comparison between flame position evolution during the experiment and one obtained from the calculations. Qualitatively numerical results show the same rate of flame acceleration as in the experiment in the most part of the acceleration tube, except in its bottom part, causing a quantitative difference for the whole tube position. As it is expected, when flame comes out of acceleration tube and enters the dome, it decelerates.

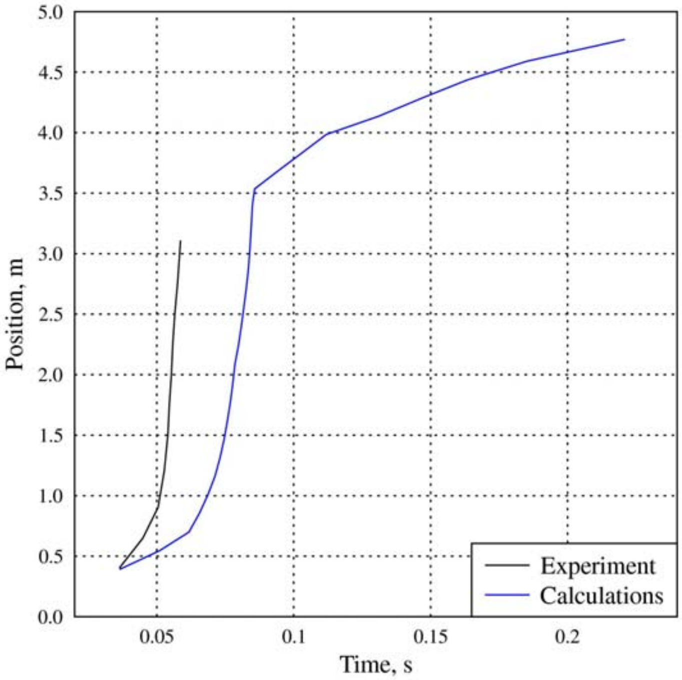

Fig. 8. Comparison of simulated and experimental flame position evolutions in the ENACCEF facility

3.2.2. *THAI facility*

Fig. 9 shows pressure evolution obtained from the calculations. Experimental results can not be presented, because by the request of experiment performers they can not be published (yet). In the THAI facility hydrogen deflagration and pressure rise are slower than in ENACCEF facility, because of different facilities geometry and initial conditions – THAI facility has bigger volume with no obstacles, and also initial concentration of hydrogen in THAI facility was lower.

Fig. 10 present flame position evolution in the THAI facility. Flame position dependency on time has nearly linear form; therefore it is possible to conclude that the speed of flame is almost constant during the propagation.

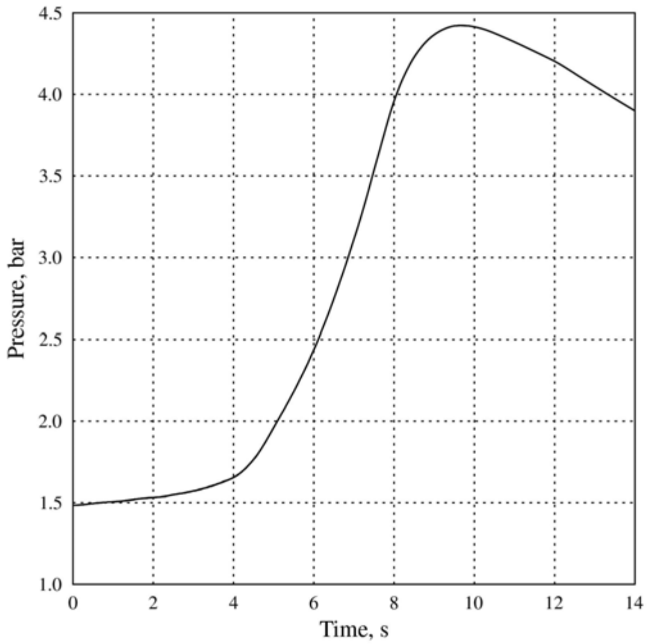

Fig. 9. Simulated pressure evolution in the THAI facility

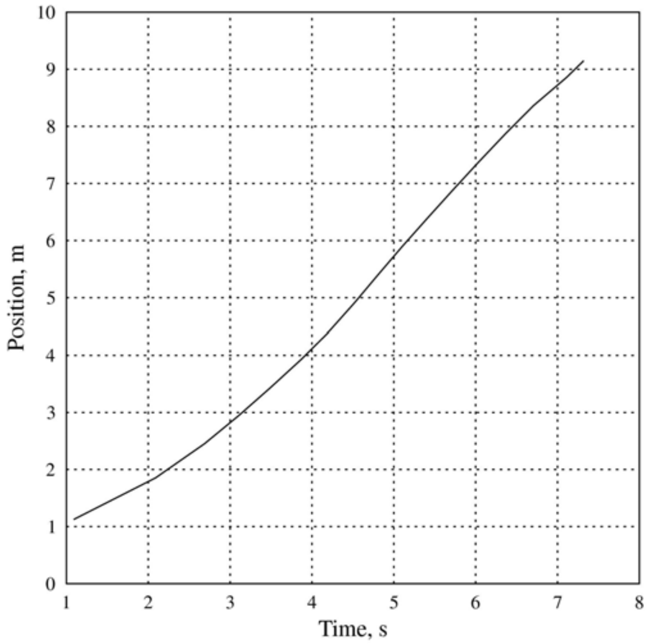

Fig. 10. Simulated flame position evolution in the THAI facility

4. CONCLUSIONS

Simulations of hydrogen deflagration tests performed in the ENACCEF and THAI facilities were performed.

1. Simulation of ENACCEF experiment qualitatively predicts the course of hydrogen deflagration.
2. Quantitative differences between the ENACCEF experiment results and simulation results arise from the too slow initial flame propagation and too slow pressure rise.
3. THAI experiment simulation results show flame propagating at constant speed.

REFERENCES

1. CHAUMEIX, N., BENTAIB A., ISP 49 Specification of ENACCEF test, Flame Propagation in a Hydrogen Gradient, Bureau de Physique des Accidents Graves Rapport DSR/SAGR N°40
2. KANZLEITER, T., LANGER G., Quick Look Report, Hydrogen Deflagration Tests HD-2R and HD-12, Becker Technologies GmbH, Eschborn, Germany, April 2008, Report No. 150 1326–HD-QLR 1
3. VAN DORSSELAERE, J.-P., SEROPIAN, C., CHATELARD, P., JACQ, F., FLEUROT, J., GIORDANO, P., REINKE, N., SCHWINGES, B., ALLELEIN, H.J., LUTHER, W., The ASTEC integral code for severe accident simulation, Nuclear Technology 165 (March (3), (2009), p. 293–307
4. LIU, D.D.S., MACFARLANE, R., Laminar burning velocities of hydrogen-air and hydrogen-air---steam flames, Combustion and Flame, Volume 49, Issues 1-3, January 1983, Pages 59–71, ISSN 0010-2180, DOI: 10.1016/0010-2180(83)90151-7.
5. N. Peters, Laminar flamelet concepts in turbulent combustion, Symposium (International) on Combustion, Volume 21, Issue 1, Twenty-First Symposium (International on Combustion), 1988, p. 1231–1250, ISSN 0082-0784, DOI: 10.1016/S0082-0784(88)80355-2.

CYSENI 2010, May 27–28, Kaunas, Lithuania
ISSN 1822-7554, www.cyseni.com

LAST MODIFICATIONS IN LWR CORES

A. Slavickas
Lithuanian Energy Institute
Laboratory of Nuclear Installation Safety
Breslaujos str. 3, LT-44403 Kaunas –Lithuania
Phone: +370 (37) 401920
Email: andriussl@mail.lei.lt

ABSTRACT

Light water reactors (LWRs) have become the preferred nuclear power generators in the World. It appears that the LWRs will dominate the nuclear power generation for the next 50 years in the 21st century. The present world of LWRs safety deals with a very small population of new reactors. New LWRs will be installed in increasing numbers but more importantly the immediate future of LWRs appears to be life extension and power up-rates of present LWRs. The most of present LWRs population are reactors which were designed and constructed 30-40 years ago. Some of these reactors has been granted life extension or have been up-rated in the power level.

The issues concerned with the thermal hydraulics and neutronics of nuclear power plants still challenge the design safety and the operation of LWRs. Nevertheless during LWRs lifetime the knowledge-base about LWR severe accidents and LWRs safety in common improved significantly. So because of the sustained development in computer technology and improved the knowledge-base about LWR safety it is possible to perform nuclear reactor design by balancing safety and economics. It influenced the applying of LWRs core modifications to improve economical characteristics of reactor cores and to fulfill more strictly safety requirements. The last modifications in LWR cores are reviewed in this paper.

Keywords: LWR cores modification, high enrichment fuel, fuel with burnable absorber, MOX fuel, hydride fuel, fuel design, core load pattern optimization.

1. INTRODUCTION

The LWRs are the preferred nuclear generators in the World because tend to be simpler and cheaper to build than other types of nuclear reactor. Many investments are being made for development of advanced technologies for LWRs too. So currently, it appears that the LWRs will dominate the nuclear power generation in the 21s century. Two types of LWRs are exploiting at this time – pressurized water reactor (PWR) and boiling water reactors (BWR). The first LWR was pressurized water reactor (PWR) installed in the first nuclear submarine (the USS Nautilus) in early 1950 s. First BWRs were developed by the General Electric with considerable private investment. The main business cycle in the development on LWRs took place in the 1970s and 1980s. Nowadays there are 359 LWRs in the operation in the world with general 328.4 GW(e) generating capacity [1].

Three Mile Island and the Chernobyl accidents changed the public opinion about nuclear energy and the look to NPPs safety. The economic, political and psychological effects were extremely large. Even today many countries have banned further construction of nuclear power plants. So the present world of LWR deals with a very small population of new reactors. The main part of nowadays LWRs reactor population is that of LWRs which were designed and constructed 30–40 years ago. Nowadays the renaissance of nuclear energy is noticeable. It is because of the knowledge-base about LWRs severe accident improved significantly since mentioned accidents. It is clear that LWRs will be the dominant source of nuclear power for the next 50 years because it appears that Generation IV NPPs application for significant nuclear generation is in distant future. The development of technologies dedicated for advanced LWRs are noticeable nowadays for this reason. These activities are covering technology improvements for current plants and development of new designs. The advanced LWRs like ABWR, AP1000, ESBWR, European Pressurized Reactor and VVER are currently offered for new NPPs.

27 new LWRs are under construction nowadays [1]. New LWRs will be installed in increasing numbers but more importantly the immediate future of LWRs appears to be life extensions and power up-rates. The life-extension trend is strongest in USA, where about half LWRs population has already been approved by the regulatory authorities for a life extension of 20 years (from 40 to 60 years life). It is expected that the remaining half will receive such approval. There are also moves underway to study the possibility of extending the life of Generation II plants from 60 to 80 years, i.e., to double the originally designed life for these plants [2].

Power up-rates have become a common practice for the power utilities owning LWRs to meet the increasing electricity demand under restrictions of constructing new nuclear power plants. Since September of 1977, more than 100 power up-rate applications have received approval of regulatory body in the United States alone [3]. Both PWRs and BWRs are being considering for power up-rates. LWRs power up-rates for PWRs are by ≤10% and for BWRs are by from 20% to 40%. The large power up-rates of the BWRs are significant because their owners have determined that the BWRs had such large safety margins incorporated in their design that even with such large increase in power levels their operation will be adequately safe.

The issues concerned with the thermal hydraulics and neutronics of nuclear power plants still challenge the design safety and the operation of LWRs. The lack of full understanding of complex mechanisms related to these issues caused the use of conservative safety limits. During LWRs lifetime the knowledge-base about LWR severe accidents and LWRs safety in common improved significantly. Thus, because of the sustained development in computer technology and improved knowledge-base about LWR safety it is possible to perform nuclear reactor design by balancing safety and economics.

LWRs core modifications are caused because safety requirements, life-extension or power up-rates issues. First modifications of LWRs were related to the upgrading of the reactor cores safety because improved the knowledge-base about LWR safety and new more strictly safety requirements appeared. The most infamous severe accidents (Three Mile Island and Chernobyl) are related with LWRs. After accidents many reactor core modifications were performed to fix defects of reactor cores designs and to fulfill more strictly safety requirements [2, 4–6]. Present world of LWR core modifications are caused because economical issues like reactors life extension and power up-rate.

The purpose of this paper is to present last LWRs core modifications like use of higher enrichment fuel, burnable absorbers, mixed oxide fuel (MOX), hydride fuel and the new design of nuclear fuel, which have significant influence on reactor economical and safety characteristics. Therefore these modifications are affecting reactor core neutronics characteristics and safety parameters. Examples of modifications affects on reactor neutronics are presented in this paper too. Some of these modifications are increasing reactor economical characteristics by keeping in the same level or increasing safety parameters. Thus, LWRs core modifications are suitable measures to increase reactor economical characteristics by balancing between reactor safety and economical characteristics.

2. HIGHER ENRICHMENT FUEL AND BURNABLE ABSORBER

Fuel management is one of the key topics in nuclear engineering. Reducing energy production cost without violating the safety requirements is very important in any means of energy production. In nuclear power generation it is possible to reduce the energy production cost by increasing the fuel burnup. Longer fuel cycles are possible with extended burnup. In order to reduce the number of spent fuel assemblies of LWRs, introduce of high burnup fuels with higher uranium enrichment occurs. In this case the fuel assemblies loaded at the beginning of a reactor cycle have some amount of excess reactivity. However, in order not to make the reactor supercritical, the amount of excess reactivity must be controlled. The enrichment of the LWRs fuel is commonly limited to 5 wt% for this reason (e.g., maximum U^{235} enrichment in LWR fuels is 4.95%) [7]. Various efforts to overcome the 5 wt% enrichment limit have been undergoing [8], but it would be require considerable cost that could offset economic benefit of high burn-up fuels.

The amount of excess reactivity must be controlled. The primary control methods are moveable control absorbers, chemical shim, soluble neutron poison in the primary coolant and burnable neutron poisons. Burnable poisons have several design advantages in comparison with other control means of reactivity excess. First of all, burnable absorbers reduce the required number of control rods. Thus, parasitical neutron loss can be reduced by this mean. Second, they do not results rapid local power density changes. Finally, their placement can be usually being coordinated with fuel assembly arrangement to avoid undesirable power peaking following burnable poison depletion. Therefore if burnable poison is chosen and in core fuel strategies managed correctly, the depletion of burnable poison compensates the reactivity loss due to fuel depletion and fission product build-up. Nuclear fuel with composite burnable absorber can be used because the purpose to control the moderator temperature coefficient too [9, 10].

The use of burnable absorbers in nuclear fuel management has acquired much importance during the last decades. Several materials for burnable absorbers and their implementation to the reactor core have been explored to achieve the desired objectives. The materials like erbia (Er_2O_3), gadolinia (Gd_2O_3), boron carbide (B_4C), zirconium diboride (ZrB_2) and so on were used for burnable poison [7, 8, 10, 11]. The use of burnable absorber in the reactor core is possible few ways too. Burnable absorber can be added in the moderator, inserted in the fuel road like integral burnable absorber (IBA) or integral with fuel (integral fuel burnable absorber – IFBA) [8, 11, 12]. The fuel can be coated in the burnable absorber material too [9].

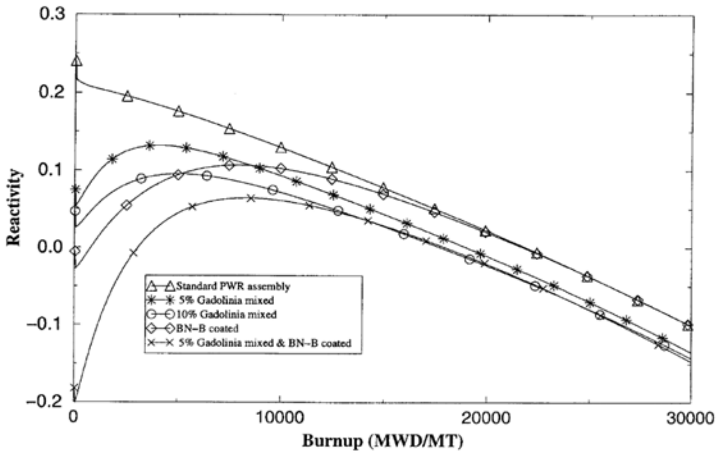

Fig. 1. Change of reactivity with burnup in a PWR assembly [9]

The variation of reactivity with burnup for different assembly configurations in a PWR and a BWR is presented in Figs. 1 and 2, respectively. Calculations were performed for both a PWR assembly with 18 x 18 square array containing 12 fuel rods bearing Gd_2O_3 and a BWR assembly with 8 x 8 array containing 4 fuel roads with Gd_2O_3. Used fuel is 3% enrichment U^{235}. It was calculated 4 different assembly configurations: fuel roads with uranium fuel contained 5% and 10% gadolinia, fuel rods with boron nitrate and boron (BN-B) coated uranium and fuel rods with urania-gadolinia fuel coated by boron nitrate and boron.

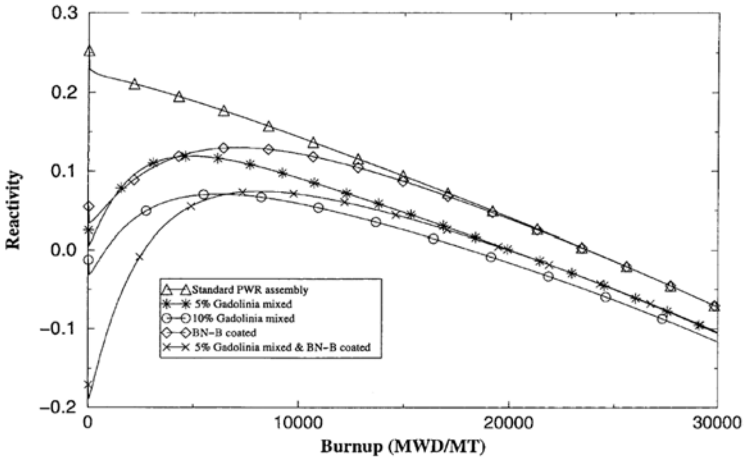

Fig. 2. Change of reactivity with burnup in a BWR assembly [9]

In order to increase the fuel cycle length, the fuel assemblies loaded at the beginning of a reactor cycle have some amount of excess reactivity. This amount of excess reactivity is needed to compensate the fuel depletion, the buildup of fission product poisons and loss of reactivity due to changes in temperature of fuel, moderator and other core constituents. The reactivity decreases due to fuel burnup, fission product buildup and temperature feedback effects. The assembly becomes subcritical beyond the burnup values of 21 000 MWD/MT PWR and 23 000 MWD/MT in BWR.

The difference between the curve of standard assemblies and any one of the curves of the assemblies with burnable absorber shows the reactivity insertion during the reactor operation due to depletion of burnable poison. It means that this amount of excess reactivity can be inserted at the beginning of the cycle, so the length of the cycle is increased. It is because the depletion of burnable absorbers that gives the variation of the curve is dictated mainly by the depletion of fuel. As the burnup increases, the reactivity decrease in the standard fuel assemblies will be compensated by the positive reactivity addition of IFBA assemblies because of the higher burnup rate of burnable absorber compared to the isotopes.

3. MIXED OXIDE FUEL (MOX)

The most widely used fuel in nuclear reactors today is low-enriched uranium dioxide (UO_2). After irradiation, UO_2 assemblies are removed from reactors core and placed in spent-fuel pools for storage. So the number of UO_2 spent-fuel assemblies and the amount of other radioactive waste increasing over time. The spent nuclear fuel has some plutonium, which is produced at some level in all reactors (i.e., both defence and commercial). Many countries (France, Great Britain, Russia, Germany, etc.) choose to separate plutonium from spent fuel and burn it again in reactors. The use of uranium-plutonium mixed oxide fuel in LWRs is a current practice nowadays. Nowadays generally 1/3 of reactor core is loaded with MOX fuel assemblies and the other 2/3 with UO_2 assemblies. It is due the meet of safety margins for partial cores of MOX fuel with the rest being pure UO_2 fuel.

Nevertheless the plutonium utilization could be more effective if the reactor core could be loaded with higher fraction or even only MOX fuel. The European Utility Requirements (EUR) document states that the next generation European Passive Plant (EPP) reactor core design shall be optimized for UO_2 fuel assemblies, with provisions made to allow for up to 50% mixed-oxide (MOX) fuel assemblies [12]. There are studies of 100% MOX fuel load in the reactor core [13, 14] too. So spent-fuel reprocessing and utilization in LWRs reactors is becoming the serious mean to decrease radioactive waste and for fuel management.

The use of MOX fuel is changing reactor core neutronics characteristics because plutonium hardens the neutron spectrum, leading to a shorter lifetime and a lower delayed neutron fraction, which could allow the reactor to go prompt critical faster. MOX has larger fission cross-section than UO_2 fuel so hot spots and power peaking concerns exist too [14]. Therefore some neutronics safety concerns existing that are related to MOX fuel use in the reactor core. First of all, control materials like control rods or soluble boron becomes less efficient [14, 15]. Second, large negative Doppler and moderate temperature coefficients occur, that is requiring additional shutdown capacity [15, 16]. Finally, the moderator void coefficient can become positive at plutonium content > ~ 10–15 wt% in heavy metal [17]. Other concerns in the use of MOX fuel include the fact that the thermal conductivity of MOX fuel is lower than that for UO2 fuel (by ~10%), leading to a higher operating temperature of the fuel [15]. This higher temperature is important in analyzing accident scenarios.

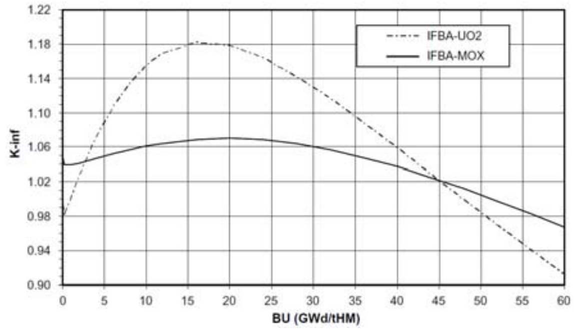

Fig. 3. K-inf vs burnup if IFBA fuel in UO_2 and MOX

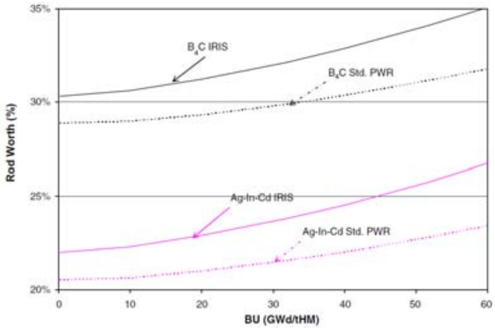

Fig. 4. Rod worth in MOX for IRIS and standard PWR fuel lattice

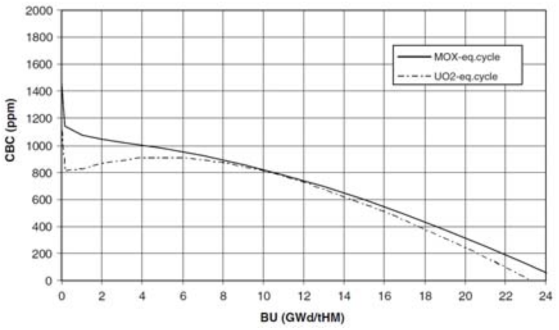

Fig. 5. Critical soluble boron concentration for the equilibrium UO_2 and MOX IRIS cores

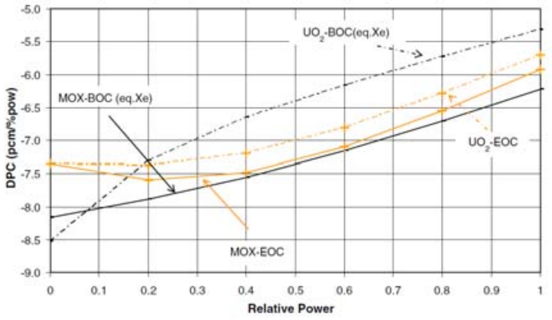

Fig. 6. Doppler power coefficient for the equilibrium UO2 and MOX IRIS cores

So sustainable use of MOX fuel can be achieved only by involvement of some design/materials changes in the reactor cores. Some neutronics characteristics comparisons in cases of full MOX and UO_2 fuel loads in IRIS core are presented in Figs. 3–6 [14]. These figures show that by enhance of moderator-to-fuel ratio and increase of the fissile content in fuel for the IRIS core with MOX fuel it is possible to met safety margins.

The smoother depletion of IFBA in the MOX fuel can be noticed in Fig. 4, which compares K-inf vs. burnup of respectively MOX and UO_2 fuel assemblies with relatively high IFBA content. It is due to the lower worth of fuel burnable absorber in the MOX fuel. MOX deplete is at lower rate than in UO_2 for this reason. Fig. 5 shows the control rod worth of a MOX fuel assembly for IRIS and standard PWR fuel lattice with either B_4C or Ag-In-CD rodlets. The MOX fuel reduces control rods worth in usually case, but control rods worth was increased due benefit of enhanced moderation in this case. So safety margin were met and the reactor power control were improved in comparison with standard PWR fuel lattice. Fig. 5 shows that critical soluble boron concentration is below 1000 pm or most of the cycle for both the UO_2 and the MOX core. This rather low level of soluble boron, especially when considering the long cycle of operation combined with the full MOX core. Besides the low soluble concentration results a lower values of reactivity coefficients, and in particular of the moderator temperature coefficient. The Doppler power coefficient, DPC, for the $_{UO2}$ and MOX cores is shown in Fig. 12. Two burnups representative of core depletion are chosen for the comparison, i.e., BOC (begin of cycle) and EOC (end of cycle) with equilibrium xenon. The DPC is negative throughout the entire power range in both core designs, again benefiting safety and reactor control.

Table 1. Operating temperatures of PWR fuel rods or oxide fuel [18].

Temperature, ^0C	$U_{0,31}ZrH_{1,6}$ (He)	$U_{0,31}ZrH_{1,6}$ (LM)	UO_2 (He)
Fuel centerline	680	555	1450
ΔT_{fuel}	170	170	665
ΔT_{gap}	125	-	125
ΔT_{clad}	46	46	46
T_{fluid}	39	39	39

4. HYDRIDE FUEL

The history of uranium-zirconium hydride as a fuel or zirconium hydride as a moderator for nuclear reactors goes nearly as far back as that oxide fuels. This fuel/moderator occupies a niche in reactor technologies with a number of proposed designs and fewer actual units. Among the former are the hydride-moderated boiling water superheat reactor investigated by the National Aeronautics Administration as early as 1960 [17].

A principal difference between oxide and hydride fuels is the high thermal conductivity of the second. This feature greatly decreases the temperature drop over the fuel during operation, thereby reducing the release of fission gases to the fraction due only to recoil. However, very unusual early swelling due to void formation around the uranium particles has been observed in hydride fuels. The avoidance of this source of swelling limits the maximum fuel temperatures to ~ 650 ^0C (the design limit recommended by the fuel developer is 750 ^0C). A liquid metal is suggested to bond the fuel-cladding gab to satisfy this temperature limitation [18]. It is due the former has a thermal conductivity ~ 100 times larger than a second. The liquid-metal bond permits operation of the fuel at current LWR linear-heat-generation rates without exceeding any design constraint.

Estimated temperatures are shown in Table 1 for three PWR fuel elements: two hydride fuels, one with helium in the fuel-cladding gap and the other with a liquid-metal bond. For comparison, the comparable temperatures in a conventional oxide-fuelled system are also given [18]. This table illustrates some of the favorable features of hydride fuel in comparison with oxide fuel. The first is much lower temperatures. This is due to the large thermal conductivity of the hydride fuel. However, the important consideration is not the temperature itself, but it is how the lower temperature affects the fuel. UO_2 fuel is hot enough for release of fission gases by diffusion then fission release in hydride fuel occurs only due to recoil mechanism. 4 times lower temperature in hydride fuel in comparison with oxide fuel means that thermal stresses in fuel pellet are low enough to avoid pellet cracking entirely.

Due to the boiling of their coolant, the cores of BWRs are undermoderated, primarily at their upper part. The oxide fuelled BWRs is also characterized as by a large degree of heterogeneity across the fuel assembly due to it compound for more than 10 different fuel rods. So moderator has large the non-uniform distribution across the assembly. This undermoderation and heterogeneity penalize the performance of BWRs in a number of ways that effect their economics and safety [19].

The use of hydride fuels instead water rods and, possibly, oxide fuels in fuel assembly regions which could benefit form additional moderation was proposed to alleviate this undermoderation in BWRs [19]. One of unique features of this newly proposed approach is that it enables to practically eliminate all the undermoderation in the BWRs without having to reduce the total length of the fuel rods in the core. The other is that it enables a more uniform distribution of the moderator across the fuel assembly. So the energy extracted per fuel assembly and the cycle length increase. So hydride fuel implementation in BWRs has both economical and safety benefits [19, 20].

5. FUEL DESIGN

While LWRs will continue to be the backbone of the global nuclear in this century, significant development effort is being applied to Generation IV reactors cooled by sodium and gas. The competition with other generating sources will motivate major efforts to reduce the cost of electricity from these reactors while maintaining or enhancing their safety. The main mean to reduce fuel cycle cost is the need to increase core power density. The development of the inverted fuel concept is aimed to increase this parameter. The term "inverted" refers to the inversion of the fuel and coolant placement from the traditional fuel pin array, e. g. fuel in cylindrical cladding rods surrounded by the continuous coolant region. The inverted fuel geometry and its variety of fuel materials are not only approach to develop advanced fuel designs. There are other promising approaches like annular fuel with both internal and external cooling, cross-shaped fuel and so on [21–23].

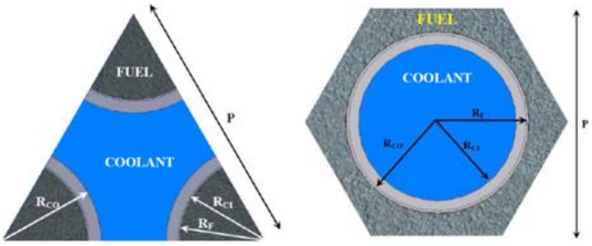

Fig. 7. Comparison of interior unit cells for the pin (left) and inverted (right) designs [21]

In the inverted fuel array, as illustrated in Fig. 7, the continuous region is the fuel, not the coolant as in the standard pin design. In both configurations the fuel region can consists of various fuel forms – a solid solution (UO2, U-Zr-hydride) or fuel dispersed in a continuous matrix materials (metals, ceramics). Inverted fuel designs offers the advantages of shorter fuel thermal path length, reduced pressure drop, elimination of fuel pin fretting and smaller coolant void fraction compared to other fuel pin geometry under comparable assembly power rating [21]. The main goal of this design is to improve the economics of PWRs by achieving higher power density than in the standard UO_2 pin assembly core.

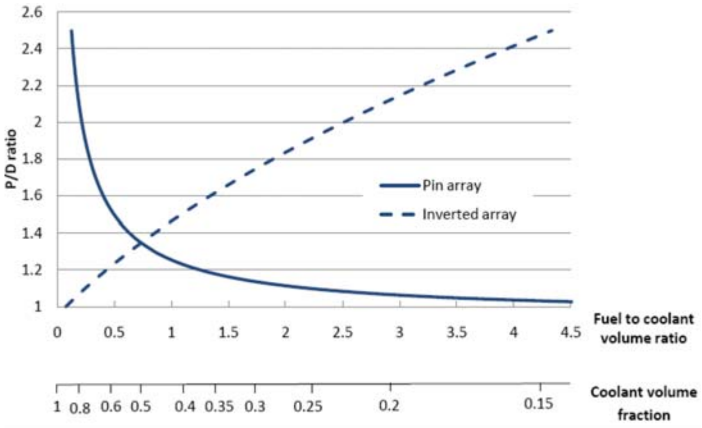

Fig. 8. Comparison of pin and inverted array geometric characteristics [21]

A central parameter in core design is the fuel-to-coolant volume ratio. Fig. 8 illustrates this parameter as a function of the pitch-to-diameter ratio, P/D. For the pin geometry the diameter is that of the fuel rod outer cladding surface while for the inverted geometry it is the coolant channel inner diameter. For LWRs an increase of coolant fraction is needed to provide the additional sufficient core cooling. But the coolant fraction increase is limited by the existence of an upper bound which arises from the need to keep the moderator temperature coefficient negative.

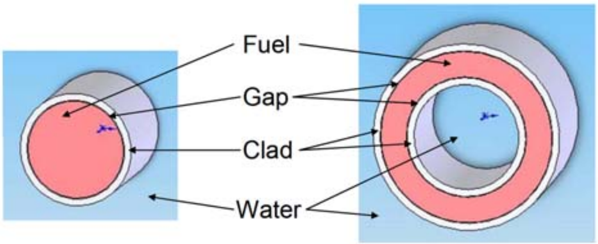

Fig. 9. Comparison of interior unit cells for the pin and for the annular designs [22]

Inverted fuel design is applied for LWRs with hydride fuel ($U-ZrH_{1.6}-ThH_2$). Some studies showed that 50% increases in a power density for UO_2 fuelled PWRs can be achieved with internally and externally cooled annular fuel while keeping the same safety margins. So new fuel design can be reasonable applied for improve of LWRs economical parameters and up-rates in power level.

6. SUMMARY

Last LWRs core modifications like uses of higher enrichment fuel, burnable absorbers, mixed oxide fuel (MOX), hydride fuel and the new design of nuclear fuel are presented in this paper. Some of these modifications are increasing reactor economical characteristics by increasing power density in fuel. Safety characteristics in the same can be kept in the same level or increased in case of application of these modifications for reactor cores. Other modifications are improving safety characteristics of reactor core, thus these modifications can be used for reactor core life extensions in case of need to fulfill more strictly safety requirements.

REFERENCES

1. *IAEA - LWR*. International Atomic Energy Agency – [referred on the 15th of March in 2010]. Link to the internet <http://www.iaea.org/NuclearPower/WCR/LWR/>
2. SEHGAL, B.R. Light Water Reactors safety: past, present and future. NURETH-13. Proceeding of the 13th International Topical Meeting on Nuclear Reactor Thermal Hydraulics. [CD]. Kanazawa City, Ishikawa Prefecture, Japan, September 27–October 2, 2009.
3. HETTIARACHCHI, S. BWR SCC mitigation experiences with hydrogen water chemistry. *The Minerals, Metals & Materials Society*, 2005, Proceedings of the 12th International Symposium on Environmental Degradation of Materials in Nuclear Power Systems – Water Reactors, Slat Lake City, UT, U.S.A., August 14–18, p. 685–699.
4. FRISCH, W., GROS, G. Improving the safety of future nuclear fission power plants. *Fusion Engineering and Design*, 56–57, 2001, p. 83–93.
5. ABU-KHADER, M. M. Recent advances in nuclear power: A review. *Progress in Nuclear Energy*, 54, 2009, p. 225–235.
6. SOROKIN, N. M., GABARAEV B.A., CHERKASHOV, Yu. M. Safe operation and life extension of RBMK-1500 plants. *Nuclear Engineering and Design*, 236, 2006, p. 1648–1656.
7. SUGIMURA, N., IMAMURA M., MORI M., YAMASAKI M. Burnup credit of erbia super-high-burnup fuel. Proceedings of the International Conference on the Physics of Reactors “Nuclear Power: A Sustainable Resource”. [CD]. Interlaken, Switzerland, September 14–19, 2008.
8. DURMAZUÇAR, H.H., ÇOLAK, U., SARIKAYA, B., GÜNDÜZ, G. Burnup characteristics and performance of boron nitride and boron coated urania and urania-gadolinia fuels. *Nuclear Engineering and Design*, 203, 2001, p. 57–64.
9. JURKEVIČIUS, A., TARASOV, A., KRIVOSHEIN, G. RBMK-1500 reactor core upgrading at Ignalina NPP. Uranium-erbium fuel and new design control rods implementation. Proceedings of the International Congress on Advanced Nuclear Power Plants ‘2003. [CD]. Córdoba, Spain, May 4–7, 2003.
10. FRANCESCHINI, F., PETROVIC, B. Fuel with advanced burnable absorbers design for the IRIS reactor core: combined erbia and IFBA. *Annals of Nuclear Energy*, 36, 2009, p. 1201–1207.
11. YILMAZ, S., IVANOV, K, LEVINE, S., MAHGEREFTEH, M. Development of enriched Gd-155 and 157 burnable poison designs for PWR core. *Annals of Nuclear Energy*, 33, 2006, p. 439–445.
12. FETTERMAN, R.J. AP1000 core design with 50% MOX loading. Proceedings of the International Conference on the Physics of Reactors “Nuclear Power: A Sustainable Resource”. [CD]. Interlaken, Switzerland, September 14–19, 2008.
13. ROUVIERE, G., BRUNA, G.B., GUILLET, J.L., PELET, J. 1300MWe PWR, A New Step in Full MOX Core Design. The Proceedings of the International Conference of Future Nuclear Systems, GLOBAL’99. JacksonHole, IL, U.S.A.
14. FRANCESCHINI, F., PETROVIC, B. Core physics analysis of 100% MOX core in IRIS. *Annals of Nuclear Energy*, 35, 2008, p. 1587–1597.
15. TREULLUE, H.R. Safety and neutronics: a comparison of MOX vs UO_2 fuel. *Progress in Nuclear Energy*, 48, 2006, p. 135–145.

16. KOO, Y., SOHN, D., VOLKOV, B. A comparative analysis of UO2 and MOX fuel behavior under reactivity initiated accident. *Annals of Nuclear Energy*, 24, 1997, p. 859–870.
17. GYLFE, J.D. Evaluation of zirconium hydride as moderator in integral boiling–water superheat reactors, NAA-SR-5943, 1960.
18. OLANDER, D., GREENSPAN, E., GARKISCH, H.D., PETROVIC, B. Uranium-zirconium hydride fuel properties. *Nuclear Engineering and Design*, 239, 2009, p. 1406–1424.
19. WANG, K., GREENSPAN, E. Performance improvement analysis of boiling water reactors by incorporation of hydride fuel. *Nuclear engineering and Design*, 231, 2004, p. 163–175.
20. GREENSPAN, E., FRATONI, M., GANDA, F., GINEX, F., OLANDER, D., TODREAS, N., DILLER, P., FERRONI, P., MALEN, J., ROMANO, A., SHUFFLER, C., TRANT, J., PETROVIC, B., GARKISCH, . Hydride fuel for LWRs – Project overview. *Nuclear Engineering and Design*, 239, 2009, p. 1374–1405.
21. TODREAS, N.E., FERRONI, P. Enhancing reactor core thermal performance through inverted fuel design. NURETH-13. Proceeding of the 13th International Topical Meeting on Nuclear Reactor Thermal Hydraulics. [CD]. Kanazawa City, Ishikawa Prefecture, Japan, September 27 – October 2, 2009.
22. ELLIS, T., HEJZLAR, P., KAZIMI, M. An advanced uranium nitride design concept of high performance annular fuel assemblies. Proceedings of the International Conference on the Physics of Reactors “Nuclear Power: A Sustainable Resource”. [CD]. Interlaken, Switzerland, September 14–19, 2008.
23. BAGLIETTO, E., NINOKATA, H. Improved turbulence modeling for performance evaluation of novel fuel designs. NURETH-13. Proceeding of the 13th International Topical Meeting on Nuclear Reactor Thermal Hydraulics. [CD]. Avignon, France, October 2–6, 2005.

CYSENI 2010, May 27–28, Kaunas, Lithuania
ISSN 1822-7554, www.cyseni.com

RADIATION DOSE MODELLING DURING DISMANTLING OF A MAINTENANCE RESERVOIR FROM RBMK-1500 REACTOR MAIN CIRCULATION CIRCUIT SYSTEM

A. Šimonis
Lithuanian Energy Institute
Nuclear Engineering Laboratory
Breslaujos str. 3, LT-44403 Kaunas – Lithuania
Phone: 370 8 37 401885
Email: audrius@mail.lei.lt

ABSTRACT

Preparation for decommissioning of the Ignalina Nuclear Power Plant involves multiple problems. One of them is personnel radiation safety during performance of dismantling works. In order to assess the optimal personnel radiation safety, modelling is performed by means of computer programs "VISIPLAN 3D ALARA Planning tool" which is developed by SCK CEN (Belgium). This program allows assessing gamma radiation exposure from various sources, shielding geometry (structure), and shielding materials. The program is used for designing of gamma radiation shielding, assessing of actual and planned accumulative effective doses to personnel when carrying out operation, maintenance, and dismantling activities.

Modelling of radiation dose during dismantling of the maintenance reservoir of RBMK-1500 reactor main circulation circuit system has been performed in this work. Also, accumulated effective doses to the operators performing dismantling works have been optimized applying (ALARA) principle,

Keywords: RBMK-1500 reactor, maintenance reservoir, dismantling, modelling of doses, optimisation

1. INTRODUCTION

The only one nuclear power plant is in Lithuania, i.e. Ignalina Nuclear Power Plant (INPP) is situated in the Northeastern part of Lithuania close to the borders with Latvia and Belarus and on the shore of Lake Druksiai. The power plant was operating two RBMK-type water cooled graphite-moderated pressure-tube reactors of a design capacity of 1500 MW(e) each. Reactors were commissioned (first grid connection) in 1983 and 1987, respectively.

In accordance with the National Energy Strategy [1] adopted by the Lithuanian Parliament, the first unit of INPP was shut down on December 31, 2004. The shutdown of the second unit was performed at the end of 2009. An immediate dismantling concept for the decommissioning of the first power unit of INPP was aproved by the Lithuanian Government‘s resolution "On State Enterprise Ignalina NPP First Unit Decommissioning Concept" [2]. After the shutdown of the first unit of INPP, the maintenance reservoir of the Main Circulation Circuit System (MCCS), located in Building V1, became redundant. It was no longer applicable for safety or operational purposes and could be progressively dismantled.

The contamination of internal surfaces of maintenance reservoir was detected, because it had been in contact with the reactor core cooling water [3].

Building V1 is the third place where dismantling is planned at Ignalina NPP. Therefore modelling information presented in this paper is quite unique and essential as it addresses future challenges.

Only one part of the Building V1 equipment has been analysed and the investigation results of the maintenance reservoir of Main Circulation Circuit System installed in Room 503 has are presented in this paper.

2. DESCRIPTION OF THE INSTALLED EQUIPMENT

A maintenance reservoir with outside diameter – 1.575 m, height – 4 m and wall thickness – 0.008 m in Room 503 has been investigated (see Fig. 1). The material of the reservoir is stainless steel; the mass of maintenance reservoir is about 3.7 tons.

Fig. 1. Photo of the maintenance reservoir in Room 503 of the Building V1

According to radiological measurements performed by INPP staff in 2007 the internal surface of maintenance reservoir was contaminated with radioactive corrosion products and deposits. Three different points on the internal reservoir's surface were chosen for the performance of contamination measurements. The internal contamination of wall was defined combining gamma spectrometry measurements from the outside of the reservoir and calculating contamination by using soft ware. Contamination at other selected points (at the top and at the bottom of reservoir) was examined by taking wipe samples and using gamma spectrometer. Maintenance reservoir‘s contamination levels that were used for modelling purposes are presented in the Table 1.

Table 1. Contamination level of internal surfaces of maintenance reservoir [3]

Nuclide	**Internal surface contamination, Bq/cm^2**		
	Top	**Wall**	**Bottom**
Co-60	16.80	192.35	972.00
Cs-137	96.00	38.01	11.10
Mn-54	0.11	9.12	95.00
Cs-134	5.21	3.04	2.12
Nb-94	0.08	1.55	6.70
Total	118.20	244.07	1086.92

Measured gamma background level was 2.0E-03 mSv/h.

The maintenance reservoir consists of a welded vertical cylinder with two circle bottoms. Metal floor for maintanance of the reservoir is located at 3 m distance from the bottom of the reservoir. So the scaffolding for a dismantling of the lower part of the reservoir below 3 m will be used.

The maintenance reservoir will be dismantled using plasma cutting equipment and lifting device. The dismantling of the maintenance reservoir will be performed downwards from the top. For beter handling the maintenance reservoir will be cut into metal pieces up to 1 m^2 (the mass of one piece will be about 50–60 kg).

3. METHODOLOGY OF MODELLING

As the maintenance reservoir is contaminated, it is necessary to register personnel doses during dismantling and apply ALARA principles for personnel collective doses.

In the first step a computer model of maintenance reservoir was prepared. Six geometery models have been prepared for each dismantling phase in total. The first model was generated for the case of dismantling of the top circle. The next four models were prepared for reservoir when a wall height was reduced to 4 m (full), 3 m, 2 m, 1.3 m. And the last model was prepared for the dismantling of the reservoir‘s bottom.

According to performed measurements the contamination of reservoir was internal. So, a radioactive source for reservoir‘s body was modeled as having cylindrical shape. Other two sources for the top and bottom of the reservoir were modeled as circles. It was assumed that all sources are homogeneous. The radionuclide content of these sources is presented in Table 1. In each model the source area was different and was dependent on the geometry of the reservoir.

It was assumed that only the maintenance reservoir is responsible for dose effects to the workers. Other possible radioactive sources present in the room were not taken into account.

Operator’s locations in each model are summarised in the Table 2.

Table 2. Operator positions in each model

No. of model	Description	Operator’s locations	
		Height	**Width**
1.	Dismantling the top of reservoir	Between 0.6 m (operator squats down) and 1.2 m (operator stands). Operator is on the top surface of reservoir.	Range of width of reservoir (3.15 m)
2.	Dismantling the wall from 4 up to 3 m height of reservoir	Between 0.6 m (operator squats down) and 1.2 m (operator stands). Operator is on the metal floor.	Range between 0.2 m and 0.6 m from reservoir wall surface
3.	Dismantling the wall from 3 up to 2 m height of reservoir	Between 0.6 m (operator squats down) and 1.2 m (operator stands). Operator is on the scaffolding at level 1.3 m.	
4.	Dismantling the wall from 1.3 up to 2 m height of reservoir		
5.	Dismantling the wall from bottom up to 1.3 m height of reservoir	Between 0.6 m (operator squats down) and 1.2 m (operator stands). Operator is on the floor.	
6.	Dismantling the bottom of reservoir	Between 0.6 m (operator squats down) and 1.2 m (operator stands). Operator is on the floor and on the reservoir botom.	Range of width of reservoir (3.15 m) and floor 0.5 m.

Based on the descriptions given in the Table 2, the grids for dose mapping were selected. In model No. 1 the grid 10x20 is selected, in models No 2–5 the grids 5x10 and in model No. 6 the grid 10x30 is selected.

The schematic views for dose mapping grids in dismantling models are presented in Fig. 2.

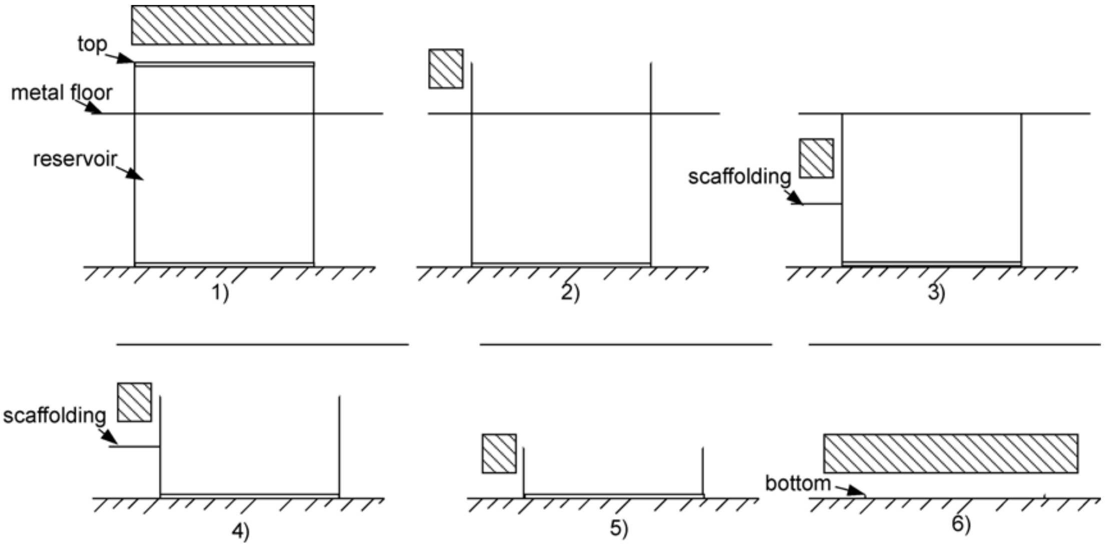

Fig. 2. The dose maps (lined areas) used for calculation in each dismantling model

3.1. The computer program

A computer program “VISIPLAN 3D ALARA Planning Tool” [4] was used for gamma dose rate modelling in this paper. This program is intended for estimation of gamma radiation dose rates in simple and complex 3D geometries. In this program the calculation of dose rate for radiation sources is based on “point kernel” method. Each small source is called a kernel and the process of integration, where the contribution to the dose of each point is added up, is called “point kernel” integration.

Before calculation with the VISIPLAN, the validation was made based on comparison of the VISIPLAN results with the results from reference calculation from ANSI/ANS 6.6.1 [5] from ESIS [6].

The photon fluence rate ϕ (cm^{-2}×s^{-1}) at a dose point near a volume source, can be determined by considering the volume source as consisting of a number of point sources. By adding the contribution of every point source to the dose at the dose point we find the photon fluence rate at the dose point from the entire source.

$$\phi = \int_V \frac{S \cdot B \cdot e^{-b}}{4 \cdot \pi \cdot \rho^2} dV \,, \qquad (1)$$

where, S is a source strength representing the number of photons emitted by the source per unit time and volume [n×s^{-1}×cm^{-3}], B - built-up factor (values tabulated according [7]), b represents the mean free paths (the attenuation effectiveness of a shield), ρ is density of material.

Based on the photon fluence rate at a point, the program can calculate the effective dose rate D, which depending on the dose conversion factors h_i. The effective dose rate D is calculated as:

$$D = \sum_i h_i \cdot \phi_i \,, \tag{2}$$

where h_i is the dose conversion coefficient [8] for photons of energy E_i, ϕ_i – the photon fluence rate of energy E_i. The dose conversion coefficient represents different exposure geometries of the person (anterior, dorsal, isotropic, rotation, lateral). The dose conversion coefficients are adapted to calculate dose rate for the standing person at the height of 1.2 m above the floor, because the most sensitive organs are located at this height.

The main input data for “VISIPLAN 3D ALARA Planning tool” are: the geometry of an analyzed system, composition and density of materials, parameters of the radiation sources and coordinates of the points where the dose rate is going to be determined.

4. RESULTS OF MODELLING

The 3D model of reservoir before dismantling is presented in Fig. 3.

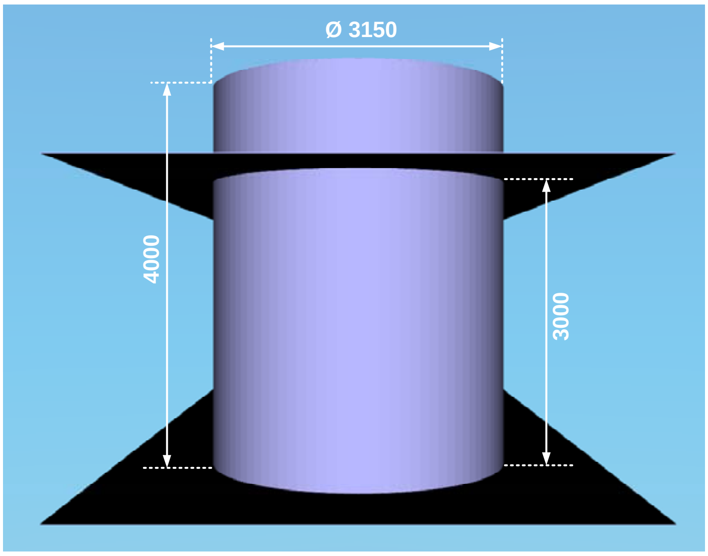

Fig. 3. 3D model of reservoir

A dose map obtained during dismantling of the reservoir‘s top (model No 1) is presented in Fig. 4, dose maps obtained dismantling the wall of reservoir (models No 2–5) are presented in Fig. 5 and dose map obtained during dismantling of the reservoir‘s bottom (model No. 6) is presented in Fig. 6.

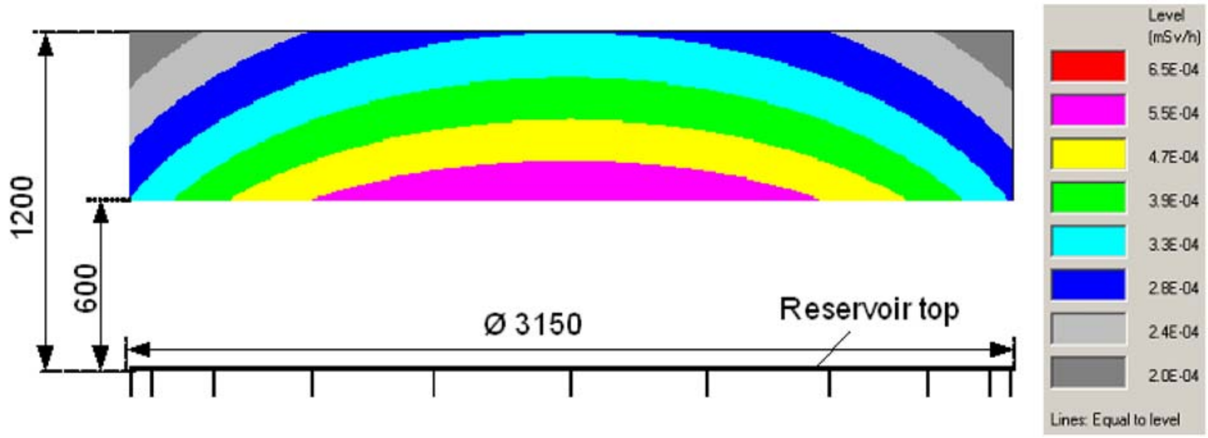

Fig. 4. The dose map obtained during dismantling of the reservoir's top (model No 1)

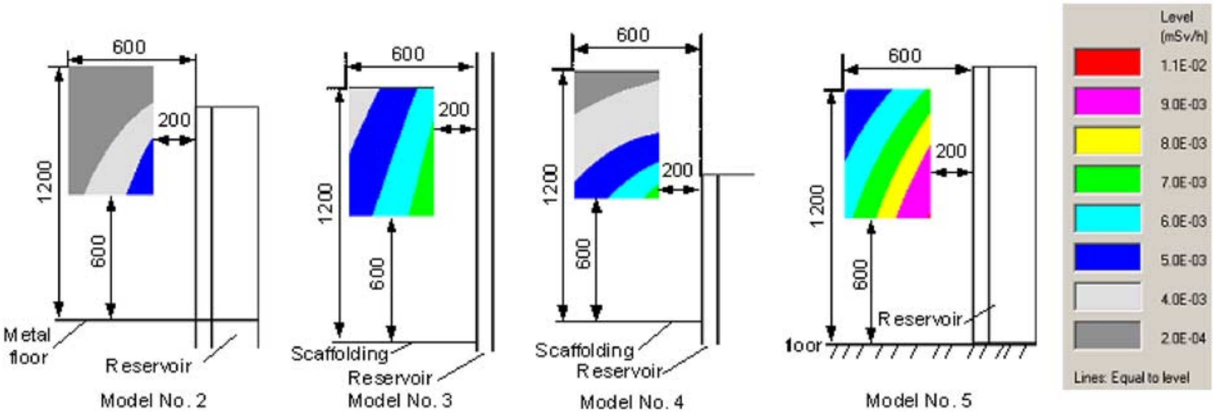

Fig. 5. The dose maps obtained during dismantling of the reservoir wall (models No 2–5)

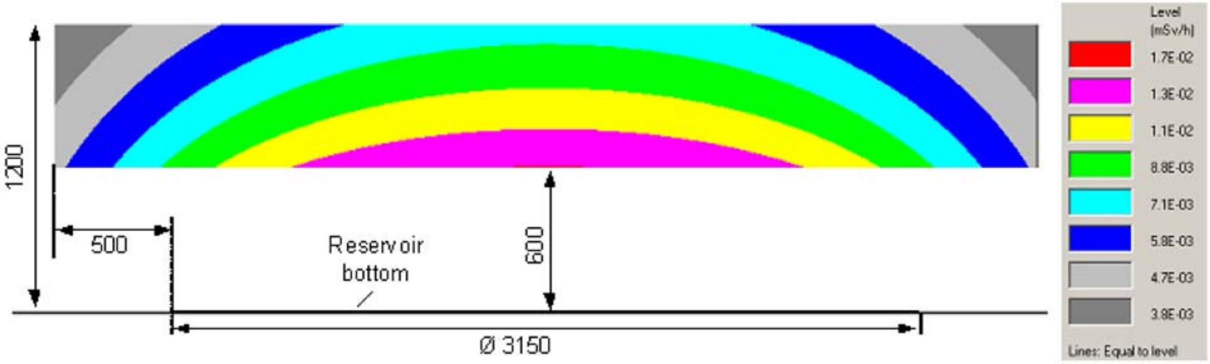

Fig. 6. The dose map obtained during dismantling of the reservoir's bottom (model No 6)

The results of dose rate calculations in each model are summarised and presented in Table 3.

Table 3. The dose rate results in models

No. of model	Dose rate, mSv/h		
	Minimum	Maximum	Average
1.	2.0E-04	6.5E-03	3.9E-04
2.	2.6E-03	5.9E-03	3.8E-03
3.	4.4E-03	7.9E-03	6.0E-03
4.	3.5E-03	7.6E-03	4.8E-03
5.	5.0E-03	1.1E-02	7.4E-03
6.	3.8E-03	1.7E-02	8.9E-03

The dose rates are in the range from 2.0E-04 mSv/h (at the top of the reservoir) to 1.7E-02 mSv/h (at the bottom of reservoir) and average dose rates are in range from 3.9E-04 mSv/h (in the model No.1) to 8.9E-03 mSv/h (in the model No.6). Calculated dose rates are higher up to 8.5 times as compared with to gamma background level in the Room (2.0E-03 mSv/h) and up to 85 times as compared to the natural background level (about 2.0E-04 mSv/h).

5. OPTIMISATION

Comparison of the dose rates evaluated using different models, has shown, that the highest dose rates are obtained during dismantling of the reservoir;s bottom (model No 6). So, it is necessary to find out how reduce the dose rate for the worker in this case. Three primary means of reducing radiation exposures exist [9]. They are:

Time. *Shortening of the time during which radioactive materials are handled.* Since the amount of exposure occurs as a function of duration of exposure, less time means less exposure. This is impossible to realize, because the dismantling time normally depends on equipment speed or rate, but not on operator.

Distance. *Increasing of the distance between operator and radioactive materials.* Dose is inversely proportional to the distance, therefore, greater distance means less dose. This is possible, if the operator works near the edge of the reservoir’s bottom, but not on the bottom (radioactive source).

Shielding. *Using of shielding wherever it is necessary to reduce exposure.* By placing an appropriate shield between the radioactive source and the worker, radiation is attenuated and exposure may be reduced to an acceptable level. It is possible to place metal slab for shielding in front of the operator.

The dose rate map for operator working on the edge of the reservoir bottom is presented in the Fig. 7a and for the operator working on the reservoir’s bottom is presented in the Fig. 7c. Results obtained using model No.6 were used for the dose optimization upon “distance” criteria.

In case of dose optimization using shielding, the additional lead slab (0.01×1000×1000 mm) placed at distance of 1 m from edge of the reservoir’s bottom was included into model No 6. The dose rate map for operator working on the edge of the reservoir’s bottom using shielding is presented in the Fig. 7b and for operator working on the reservoir’s bottom using shielding is presented in the Fig. 7d.

The results of dose rate calculations using these models are summarised in the Table 4.

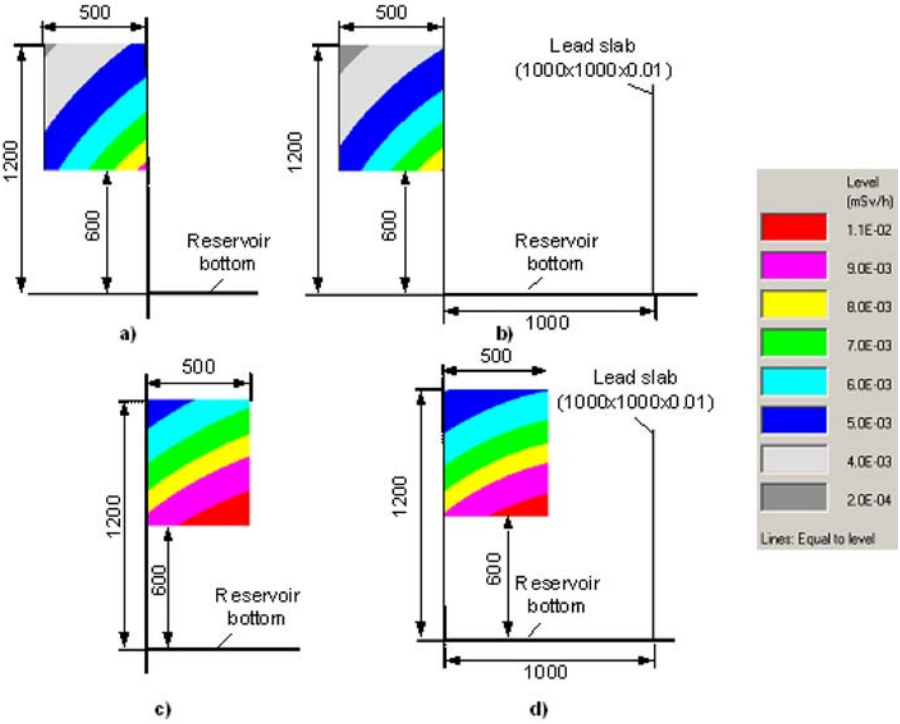

Fig. 7. The dose maps for operator: operator is on the edge of reservoir's bottom without shielding (a) and using lead slab for shielding (b); operator is on reservoir's bottom without shielding (c) and using lead slab for shielding (d)

Table 4. The dose rates in models without shielding and using lead slab for shielding

Optimization model	**Operator position**	**Shielding**	**Dose rate, mSv/h**		
			Minimum	**Maximum**	**Average**
a	Operator on the edge of reservoir bottom	No	3.8E-03	9.4E-03	5.8E-03
b		Lead slab	3.7E-03	9.1E-03	5.5E-03
c	Operator on the reservoir bottom	No	5.3E-03	1.4E-02	8.4E-03
d		Lead slab	4.9E-03	1.3E-02	7.9E-03

The lowest average dose rate was estimated for the model b (operator is on the edge of reservoir's bottom and uses a lead slab for shielding). This dose rate was decreased by 35 % as compared to the highest average dose rate value in the model c (operator is on the reservoir bottom without shielding).

When the operator stands on the edge of reservoir's bottom the benefit of using lead slab is only 5 %. So, taking into account the difficulties of handling the lead slab, the cost of it and a level of the exposure reduction, the benefit of usage the lead slab is insignificant. Comparison of doses rates during dismantling when operator stands on the edge of reservoir's bottom (model a) and on the reservoir bottom (model c), has shown that the doses rates are reduced approximately by 30 %.

After analysis of optimisation measures it is possible to conclude that working on the reservoir bottom is not the recommended position for operator. The optimum position of operator is when he stands on the edge of reservoir's bottom.

6. ACCUMULATED EFFECTIVE DOSE TO OPERATOR

After performing the modelling and optimisation of operator position during dismantling the reservoir bottom, the accumulated effective dose to operator was analysed.

It was assumed that accounting preparation works, cutting operations and removing of dismantled parts, the dismantling rate of reservoir is 15 min/m^2. The surface area of reservoir is about 55 m^2, so dismantling procedure will take about 14 working hours.

The comparison of dismantling strategies without optimisation (dose rates are presented in the Table 3) and with optimisation of dismantling the reservoir bottom (model a) is presented in Table 5.

Table 5. The comparison of individual effective doses

Dismantling	**Individual effective dose, mSv**		
	Minimum	**Maximum**	**Average**
Without optimization	4.70E-02	1.28E-01	7.40E-02
With optimization	4.70E-02	1.13E-01	6.80E-02
Benefit, %	0	12	8

The difference between calculated individual doses obtained during the dismantling of the reservoir when two strategies were applied is 1.5E-02 mSv. It is possible to reduce maximal individual dose to operator by 12 %, if the dismantling strategy with optimisation is selected.

7. CONCLUSIONS

Modeling with program “VISIPLAN 3D ALARA Planning tool” and analysis of the results according two dismantling strategies (without optimisation and with optimization) has shown, that:

1. The dose rates during dismantling of the reservoir are in the range from 2.0E-04 to 1.7E-02 mSv/h.
2. After dismantling of reservoir over 14 working hours the average individual dose to operator is 7.4E-02 mSv, when dismantling is performed without implementation of optimisation measures and 6.8E-02 mSv, when dismantling is performed implementing optimisation.
3. It is possible to reduce maximal individual dose to operator by 12%, if the dismantling strategy with optimisation is selected.

REFERENCES

1. The Republic of Lithuania Parliament Decision No. IX-1130 dated October 10, 2002, On Approval of National Energy Strategy. State news 2002 No 99-4397.
2. The Republic of Lithuania Government Resolution No. 1848 dated November 26, 2002, On State Enterprise Ignalina NPP First Unit Decommissioning Concept. State News 2002, No 114-5095.
3. Environmental Impact Assessment Report. Ignalina NPP Building V1 Equipment Decontamination and Dismantling. VT Nuclear Services Ltd, Lithuanian Energy Institute (Nuclear Engineering Laboratory), 2010.

4. F. Vermeersch. VISIPLAN 3D ALARA PLANNING TOOL. Training Guide. Exercises. Calculation Method & Validation Tests. SCK CEN, 2005, 64 p.
5. ANSI/ANS 6.6.1 “The calculation and measurement of direct and scattered radiation from LWR Nuclear Power Plants”, 1979.
6. ESIS “Specification for gamma ray shielding benchmark applicable to a nuclear radwaste facility”. Newsletter #37, European Shielding Information Service, 1981.
7. ANSI/ANS-6.4.3.-1991 „American national Standads for Gamma-Ray Attenuation Coefficients and Buildup Factors for Engineeing Materials“.
8. International Commission on Radiological Protection (ICRP 51). Data for Use in Protection Against External Radiation. A Report of a Task Group of Committee 3 of the ICRP (adopted 1987); Annals of the ICRP, Vol. 17, No 2/3, (1987).
9. Radiation Safety Manual. Michigan State University, 1996.

General sponsor:

Lithuanian
Energy
Institute

Sponsors:

AB KAUNO ENERGIJA

World Energy Council
CONSEIL MONDIAL DE L'ENERGIE
Pasaulio energetikos tarybos
Lietuvos komitetas

AB LIETUVOS ELEKTRINĖ

Lithuanian District Heating Association

KAUNAS CITY
MUNICIPALITY

CALL FOR PAPERS:

www.cyseni.com

Lithuanian Energy Institute
Young Scientists Association
Breslaujos str. 3, LT—44403 Kaunas, Lithuania
www.lei.lt, jms.lei.lt